

AD-A126 574

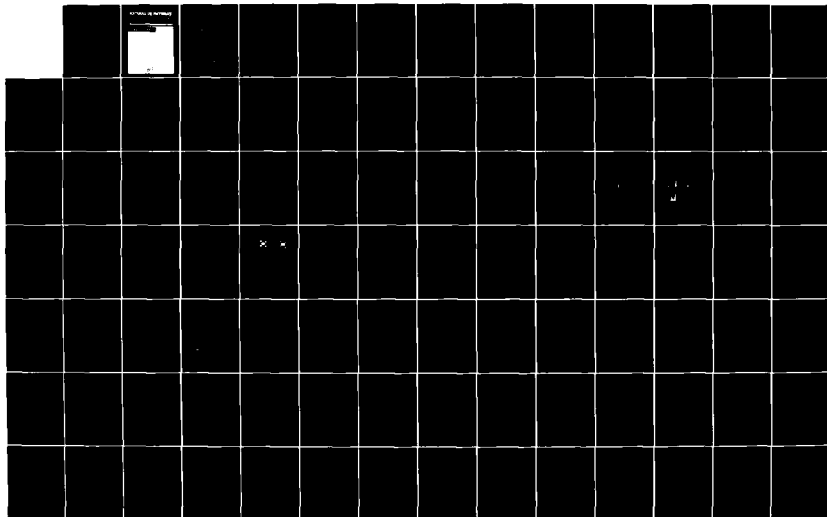
INTERNATIONAL CONFERENCE ON PHONON PHYSICS 31 AUGUST-3  
SEPTEMBER 1981 BLOOMINGTON INDIANA(U) INDIANA UNIV AT  
BLOOMINGTON W E BROW DEC 81 ARO-17340.1-PH  
MIPR-ARO-43-80

1/10

UNCLASSIFIED

F/G 20/2

NL





MICROCOPY RESOLUTION TEST CHART  
NATIONAL BUREAU OF STANDARDS-1963-A



ARO 17340.1-PH

# JOURNAL DE PHYSIQUE

Publié sous le patronage de la Société Française de Physique  
avec le concours du  
Centre National de la Recherche Scientifique

②



**Europhysics Journal**

ISSN 0449-1947  
ISBN 2-902731-33-7

COLLOQUE N° 6

Supplément au Journal de Physique, FASC. 12

C6-1981

ADA 126574

les éditions



de physique

# JOURNAL DE PHYSIQUE

Tome 42

Colloque C-6, supplément au n° 12

Décembre 1981

## International Conference on Phonon Physics

August 31 - September 3, 1981  
Bloomington, Indiana (U.S.A.)



Accession For	
NTIS GRA&I	<input checked="" type="checkbox"/>
DTIC TAB	<input type="checkbox"/>
Unannounced	<input type="checkbox"/>
Justification	
By <i>ADD</i>	
Distribution/	
Availability Codes	
Dist	Avail and/or Special
<b>A</b>	<b>21</b>

Edited by :

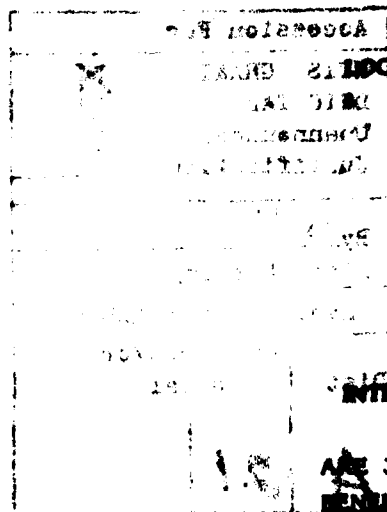
W. E. BRON

# **INTERNATIONAL ORGANIZING COMMITTEE**

BILZ H.	(W. Germany)	GRIMVALL A.	(Sweden)
BRON W.E.	(U.S.A.)	IYENGAR P.K.	(India)
BURSTEIN E.	(U.S.A.)	JOFFRIN J.	(France)
CHALLIS L.J.	(U.K.)	LEVELUT A.	(France)
CHEEKE J.D.N.	(Canada)	LIFSHITZ I.M.	(U.S.S.R.)
DEVREESE J.T.	(Belgium)	MARADUDIN A.A.	(U.S.A.)
EISENMENGER W.	(W. Germany)	MITSUISHI A.	(Japan)
ELLIOTT R.J.	(U.K.)	REBANE K.K.	(U.S.S.R.)

# **INTERNATIONAL PROGRAM ADVISORY COMMITTEE**

BENEDEK G.	(Italy)	MARIS H.J.	(U.S.A.)
CARDONA M.	(W. Germany)	NARAYANAMURTI V.	(U.S.A.)
ISHIGURO T.	(Japan)	VENKATARAMAN G.	(India)
KAPLYANSKII A.A.	(U.S.S.R.)	WIGMORE J.K.	(U.K.)
MANEVAL J.P.	(France)	YACOBY Y.	(Israel)



# **INTERNATIONAL PROGRAM COMMITTEE**

BRAY R.  
BRON W.E.  
MELTZER R.  
SENHA S.K.  
SWIHART J.C.

# **INTERIM STEERING COMMITTEE**

ALLAN J.D.	CHALLIS L.J.
BENEDEK G.	EISENMENGER W.
BILZ H.	KAPLYANSKII A.A.
BRON W.E.	MITSUISHI A.

## CONFERENCE SUMMARY

As with most fields of research, the passage of time has brought to Phonon Physics a splintering of activity into various subfields. Although any attempt to give all encompassing names to these subfields is necessarily imprecise, it is at least partially correct to characterize most of the current activity as falling into two major subfields; namely, Lattice Dynamics and Phonon Transport.

It has been the tradition over the last decade for investigators in these subfields to meet separately. And yet, as the overall field of Phonon Physics progresses, each group is becoming ever increasingly dependent on the findings of the other. It follows logically from this interdependence that the subgroups need to meet jointly from time to time for a discussion of advances and in order to provide a forum for a synthesis of results.

The 1981 International Conference on Phonon Physics was organized to fill this need. The Conference is nominally the successor of conferences on Lattice Dynamics held in Copenhagen in 1963, in Rennes in 1971 and in Paris in 1977, but it also includes the work on Phonon Transport which previously has been the subject of conferences held in Ste. Maxime in 1972, in Nottingham in 1975 and in Providence in 1979.

The call for contributions resulted in the submission of just over 350 abstracts. Papers were arranged into sessions of "long" and "short" talks and poster presentations. The selection of papers and their assignment among these sessions was accomplished through consultations with many prominent scientists in the field; particularly, with the members of the Conference's International Organizing and its Program Advisory Committees. It fell to the Local Program Committee and the Conference Chairman to assimilate and act upon this information and to arrange the various accepted contributions so as to create a coherent program.

The Conference was held in Bloomington, Indiana, U.S.A. within the facilities of Indiana University from August 31 through September 3, 1981. About 300 persons, from 30 countries (representing every continent) attended the Conference. Fifteen major topics were covered (see contents).

A number of innovations were instituted to encourage interactions among those of diverse interests. Among the more successful of these innovations were :

- i) limiting each day to four (to at most five) subjects,
- ii) to require "long" talk speakers to also present a poster during the poster session on their topic, and
- iii) to hold the poster session each day in a single room without a competing session of any kind.

Organizing a Conference of this size and diversity requires the support and efforts of a large number of persons. Of prime importance were the efforts of the Conference's Standing Committees.

During the Conference an Interim Steering Committee was formed and charged with the

mission of finding a place and date for a future meeting of similar scope.

The present Conference had an unfortunate conjunction with an economic downturn occurring throughout most of the world, which manifested itself in this regard in severely limiting the travel support available to scientists from their own countries. It became, therefore, critical to obtain some funds from sources within the U.S.A. Because of the strong demand for assistance, it turned out to be possible to give only partial support for primarily local expenses and, even then, not to all who were deserving. All the same, we are extremely grateful to those sources whose sponsorship and generous support funds made it possible for many delegates to attend the Conference. Sponsorship and support funds are gratefully acknowledged from the

International Union of Pure and Applied Physics  
American Physical Society (Sponsorship only)  
U.S. National Science Foundation  
U.S. Department of Energy  
U.S. Office of Naval Research  
U.S. Army Research Office  
Indiana University  
I.U. Department of Physics

Finally, this Conference would not have been possible without the dedicated work of its Secretariat (Vicki Woodward, Mindy Richards, Kathryn Crouch, and particularly Judy Chapple), and that of Kevin Knerr and his staff of Indiana University's Conference Bureau, as well as that of the members of the faculty and the student body who volunteered to help in the operation of the Conference itself. The support of all these persons is gratefully acknowledged.

W.E. Bron  
Professor of Physics  
Bloomington, Indiana, U.S.A.

# LIST OF PARTICIPANTS

- ALIG, R.- RCA Labs, Princeton,  
N.J. 08550 U.S.A.
- ALLDREDGE, G.P.- University of Mis-  
souri, Columbia, Physics Depart-  
ment, Columbia, MO 65211, U.S.A.
- ALMOND, D.- University of Bath,  
School of Materials Science,  
Claverton Down, Bath BA2 7AY,  
United Kingdom.
- ANASTASSAKIS, E.- National Techni-  
cal University, Physics Labora-  
tory III, Zogra fou Campus, Ath-  
ens, 624, Greece.
- ANIMALU, A.O.E.- Department of Phy-  
sics, Energy & Materials Science  
Lab., University of Nigeria,  
Nsukka, Nigeria.
- APPEL, J.C.- I. Institut f. Theore-  
tische Physik, Universitaet Ham-  
burg, Jungiusstr, 9, 2 Hamburg  
36, West Germany.
- ARNOLD, G.- University of Notre  
Dame, Dept. of Physics, Notre  
Dame, IN 46556, U.S.A.
- ARNOLD, W.- Fraunhofer-Institut for  
Non-Destructive Testing, Bldg.  
37, University, 6600 Saarbrucken,  
F.R.G.
- ASHKENAZI, J.- Dept. de la Matière  
Condensée, 32 bd. d'Yvoy, 1211  
Genève 4, Switzerland.
- AYACHE, C.- Centre d'Etudes Nuclé-  
aires de Grenoble, Service des  
Basses Températures, Laboratoire  
de Cryophysique 85 X, 38041 Gre-  
noble Cedex, France.
- BALKANSKI, M.- Université Pierre et  
Marie Curie Paris VI, Laboratoi-  
re de Physique des Solides, Tour  
13, 4 Place Jussieu, 75230 Paris  
Cedex 05, France.
- BALL, M.- University of Liverpool,  
P.O. Box 147, Liverpool L69 3BX,  
United Kingdom.
- BEHERA, S.N.- Institute of Physics,  
A/105 Saheed Nagar, Bhubaneswar,  
751007, India.
- BENEDEK, G.- Istituto di Fisica  
Dell'Università, Via Celoria, 16,  
1-20133 Milano, Italy.
- BESERMAN, R.- Technion Institute of  
Technology, Solid State Institute,  
Technion, Haifa, Israel.
- BIEM, W.- Institut für Theoretische  
Physik, Justus-Liebig-Universi-  
tät, Heinrich-Buff-Ring 16, D-  
6300 Giessen, West Germany.
- BILZ, H.- Max-Planck-Institut für  
Festkörperforschung, Heisenberg-  
strasse 1, 7000 Stuttgart 80,  
West Germany.
- BLACK, J.- Brock University, Physics  
Department, St. Catharines, On-  
tario, Canada L2S 3A1.
- BOHN, R.- The University of Toledo,  
Department of Physics & Astrono-  
my, Toledo, OH 43606, U.S.A.
- BORTOLANI, V.- Istituto di Fisica  
Università di Modena Via Campi  
213/A, 41100 Modena, Italy.
- BOSTOCK, J.- Mass. Inst. of Tech.,  
Rm. 6-204, MIT, Cambridge, Mass.  
02139, U.S.A.
- BOUILLOT, J.- Institut Laue-Lange-  
vin 156 X, 38042 Grenoble Cedex,  
France.
- BRAFMAN, O.- Technion, Physics,  
Technion, Haifa, Israel.
- BRAY, R.- Purdue University, Physics  
Department, West Lafayette, IN  
47907, U.S.A.
- BREASEALE, M.A.- Department of Phy-  
sics, The University of Tennes-  
see, Knoxville, TN 37916, U.S.A.

- BRITO-ORTA, R.- University of Connecticut, Dept. of Physics, Box 46, Storrs, CT 06268, U.S.A.
- BROKMAN, A.- M.I.T., Cambridge, MA 02139, U.S.A.
- BRON, W.E.- Indiana University, Physics Department, Bloomington, IN 47405, U.S.A.
- BROWN, R.- Division of Physics, NRC, Ottawa, Canada K1A 0R6.
- BRUNEL, L.C.- SNCI - CNRS, BP 166X, 38042 Grenoble Cedex, France.
- BUCHENAU, U.- Institut für Festkörperforschung, IFF der KFA Jülich, Postfach 1913, 517 Jülich, West Germany.
- BUEHRER, W.- Institut für Reaktortechnik ETH Zuerich, CH-5303 Wuerenlingen, Switzerland.
- BURSTEIN, E.- Physics Department, University of Pennsylvania, Philadelphia, PA 19104, U.S.A.
- BUSSMANN-HOLDER, A.- Max-Planck-Institut für Festkörperforschung, Heisenbergstrasse 1, 7000 Stuttgart 80, West Germany.
- BUTTNER, H.- Physikalisches Institut, Universität Bayreuth, Postfach 3008, D-8580 Bayreuth, West Germany.
- CAILLEAU, H.- Université de Rennes, Avenue du Général Leclerc, 35042 Rennes Cedex, France.
- CALEMCZUK, R.- Centre d'Etudes Nucléaires de Grenoble, Service des Basses Températures, Laboratoire de Cryophysique 85 X, 38041 Grenoble Cedex, France.
- CAMASSEL, J.- U.S.T.L., Lab. Electronique 2-CEES-USTL, F-34060 Montpellier Cedex, France.
- CANTINI, P.- Istituto di Scienze Fisiche dell'Università di Genova and C.N.R., Viale Benedetto XV 5, 16132, Genova, Italy.
- CARABATOS, C.- Laboratoire de Génie Physique, Université de Metz, Ile du Saulcy, 57000 Metz, France.
- CARDONA, M.- Max Planck Institut FKF, Heisenbergstr. 1, 7000 Stuttgart 80, West Germany.
- CARLONE, C.- Université de Sherbrooke, Sherbrooke, P.Q. Canada J1J 2R1
- CASELLA, R.- National Bureau of Standards, Reactor Radiation Division, Rm A-106, Bldg. 235, Washington, D.C. 20234, U.S.A.
- CERDEIRA, F.- Instituto de Física, Unicamp, 13.100 Campinas SP, Brazil.
- CHALLIS, L.- Physics Dept., Nottingham University, Nottingham NG7 2RD, England.
- CHANG, W.C.- Dept. of Physics, Purdue University, West Lafayette, IN 47906, U.S.A.
- CHASE, L.- Indiana University, Physics Department, Bloomington, IN 47405, U.S.A.
- CHEEKE, D.- Dept. of Physics, University of Sherbrooke, Sherbrooke, Québec, J1K 2R1 Canada
- CHIN, M.- Bell Laboratories, 600 Mountain Ave., Rm 1E 303, Murray Hill, NJ 07974, U.S.A.
- COLVARD, C.- University of Illinois at Urbana-Champaign, Loomis Lab of Physics, 1110 W. Green St., Urbana, IL 61801, U.S.A.
- COMPAAN, A.- Dept. of Physics, Kansas State University, Manhattan, KS 66506, U.S.A.
- COPLEY, J.R.D.- McMaster University, Department of Physics, Nuclear Res. Bldg, 1280 Main St. W. Hamilton, Ontario L8S 4K1, Canada.
- CURRAT, R.- Institut Laue-Langevin, BP 156 X, 38042 Grenoble Cedex, France.
- CZACHOR, A.- Institute of Nuclear Research, Swierk 05-400, Otwock, Poland.

- DACOROGNA, M.- Département de Physique de la Matière Condensée, 32 Bld d'Yvoy, CH-1211 Genève 4, Switzerland
- DAUDIN, B.- Centre d'Etudes Nucléaires de Grenoble, Service des Basses Températures, Laboratoire de Cryophysique 85 X, 38041 Grenoble Cedex, France.
- DEVILLE, A.- 129 Chemin Château, Gombert Val d'Azur kl, 13013 Marseille, France.
- DEVREESE, J.- University of Antwerp (UIA and RUCA), Universiteitssplein 1, B-2610 Wilrijk, Belgium.
- DE WETTE, F.- University of Texas at Austin, Dept. of Physics, Austin, TX 78712, U.S.A.
- DIERKER, S.- University of Illinois, RM. 217, Materials Research Lab., 104 S. Goodwin, Urbana, IL 61801, U.S.A.
- DIETSCH, W.- University of Illinois, Physics Dept., 1110 W. Green St., Urbana, IL 61801, U.S.A.
- DIXON, G.- Oklahoma State University, Dept. of Physics, Stillwater, OK 74078, U.S.A.
- DOLGANOV, V.- Institute of Solid State Physics, 142432 Chernogolovka Moscow distr., U.S.S.R.
- DORNER, B.- Sektion Physik, Universität München, Ludwig-Maximilians Universität, Lehrstuhl Peisl, Geschwister-Scholl-Platz 1, 8000 München 22, West Germany.
- DOUSSINEAU, P.- Université Pierre et Marie Curie, Laboratoire d'Ultrasons, Tour 13, 1er ét., 4 Place Jussieu, 75230 Paris Cedex 05, France.
- ECOLIVET, C.- Univ. de Rennes, Campus de Beaulieu, 35042 Rennes Cedex, France.
- EISENGANGER, W.- Physikalisches Institut der Universität Stuttgart, Teilinstitut 1, Pfaffenwaldring 57, Stuttgart 80, West Germany.
- ELLIOTT, R.- University of Oxford, Dept. of Theoretical Physics, 1 Keble Rd., Oxford OX1 3NP, England.
- ENGLMAN, R.- Soreq Nuclear Research Center, Yavne 70600, Israel
- EPSTEIN, J.- Research School of Chemistry, Australian National Univ., P.O. Box 4, Canberra, Act, 2600 Australia.
- ERDOS, P.- Institut de Physique Théorique, Université de Lausanne, B.S.P. Université, CH-1015 Lausanne, Switzerland.
- ERRANDONEA, G.- 196, rue de Paris, 92220 Bagneux, France.
- EVERY, A.- Witwatersrand University, Physics Dept., Johannesburg 2001, South Africa.
- FAIN, B.- Chemistry Dept., Tel-Aviv University, 69978 Ramat Aviv, Israel.
- FAY, D.- Universität Hamburg, Abteilung für Theoretische Festkörperphysik, Jungiusstrasse 11, 2000 Hamburg 26, West Germany.
- FIREY, B.M.- University of Texas at Austin, c/o Frits De Wette, Dept. of Physics, Austin, TX 78712, U.S.A.
- FONTANA, M.- Laboratoire de Génie Physique, Université de Metz, Ile du Saulcy, 57000 Metz, France.
- FONTANA, M.P.- Istituto di Fisica, Univ. of Parma, via d'Azeglio 85, Parma, Italy.
- FOSSHEIM, K.- Norwegian Inst. of Technology, Dept. of Physics, 7034-NTH, Trondheim, Norway.
- FRITSCH, G.- University of the Armed Forces-Munich, ZWE Physik, Hochschule d. Bundeswehr München, D-8014 Neubiberg, Werner Heisenberg Weg 39, West Germany.
- GALENER, F.- Xerox Palo Alto Research Centers, 3333 Coyote Hill Road, Palo Alto, CA 94304, U.S.A.



# VIII

- GERLINGER, H.- Physikalisches Institut, Universität Würzburg, Röntgenring 8, 8700 Würzburg, West Germany.
- GERVAIS, F.- CNRS Physique des Hautes Temp., 45045 Orléans Cedex, France.
- GHIJSEN, J.- Facultés Universitaires Notre Dame de la Paix, Institut de Recherche sur les Interfaces Sol., 61 rue de Bruxelles, B-5000, Namur, Belgium.
- GLEDHILL, G.- Westfield College, University of London, Kidderpore Ave., London NW3 7ST, England.
- GOMPF, F.- Kernforschungszentrum Karlsruhe, Institut für Angewandte Kernphysik, Postfach 3640, 75 Karlsruhe, West Germany.
- GOODSTEIN, D.- California Inst. of Technology, Low Temperature Physics 63-37, Pasadena, CA 91125, U.S.A.
- GOVINDARAJAN, J.- University of western Ontario, Computing Center, Natural Sciences Bldg., London, Ontario, Canada N6A 5B7.
- GRAEBNER, J.- Bell Labs, Murray Hill, NJ 07974, U.S.A.
- GREENSTEIN, M.- Univ. of Illinois, Materials Research Lab., 104 S. Goodwin, Urbana, IL 61801, U.S.A.
- GREIG, D.- University of Leeds, Dept. of Physics, Leeds LS2 9JT, England
- GRIMSDITCH, M.- Argonne National Lab., 9700 S. Cass Ave., Argonne, IL 60439, U.S.A.
- GRIMVALL, G.- Dept. of Theoretical Physics, Royal Inst. of Tech., S-100 44 Stockholm, Sweden.
- GUPTA, O.P.- J. Christian College, 145 Tularam Bagh, Allahabad, 211006, India.
- HAKE, R.- Indiana University, Physics Dept., Bloomington, IN 47405, U.S.A.
- HARDCASTLE, S.E.- University of Illinois, Dept. of Physics, 1110 W. Green St., Urbana, IL 61801, U.S.A.
- HARIDASAN, T.M.- School of Physics, Madurai Kamaraj University, Madurai, 625021, India.
- HARMON, B.- Ames Lab., Physics Dept., Iowa State University, Ames, Iowa 50011, U.S.A.
- HARRISON, J.- Queen's University, Dept. of Physics, Kingston, Ontario, Canada K7L 3N6.
- HATTORI, T.- Dept. of Applied Physics, Osaka Univ, Yamada-oda 2-1, Suita, Osaka 565, Japan.
- HAYES, W.- Clarendon Laboratory, Parks Road, Oxford, United Kingdom.
- HENKEL, J.H.- Univ. of Georgia, Dept. of Physics & Astronomy, Athens, GA 30602, U.S.A.
- HENSEL, J.- Bell Laboratories, 600 Mountain Ave., Murray Hill, NJ 07974, U.S.A.
- HERITIER, M.- Laboratoire de Physique des Solides, Bât. 510, Université Paris-Sud, 91405 Orsay, France.
- HORIE, C.- Department of Applied Physics, Tohoku University, Aramaki Aza Aoba, Sendai 980, Japan.
- HWANG, D.M.- Univ. of Illinois at Chicago Circle, Dept. of Physics, Box 4348, Chicago, IL 60680, U.S.A.
- INOUE, K.- The Physical Society of Japan, Dept. of Physics, Faculty of Sciences, Shizuoka University, 836-Ohya, Shizuoka, Japan.
- ISHIGURO, T.- Elect. Lab Umesoho 1-1-4, Sakuramura, Niharigun Ibaraki, Japan 305.
- ITOH, U.- Electrical Engineering, Osaka Univ., Suita City, Osaka 565, Japan.
- IWASA, I.- Dept. of Physics, Univ. of Tokyo, 7-3-1 Hongo, Bunkyo-ku, 113 Tokyo, Japan.

- JACKSON, H.- Univ. of Cincinnati, Dept. of Physics, Cincinnati, OH 45221, U.S.A.
- JACOBS, P.- Univ. of Western Ontario, London, Ontario, Canada N6A 5B7.
- JANG, M.S.- Inst. for Solid State Physics, Univ. of Tokyo, 7-22-1 Roppongi, Minato-ku, Tokyo, Japan.
- JANSSEN, T.- Institute for Theoretical Physics, Univ. of Nijmegen, Toernoojveld, Nijmegen, The Netherlands.
- KAJINURA, K.- Electrotechnical Lab., Sakura-Mura, Ibaraki 305, Japan.
- KAMITAKAHARA, W.A.- Iowa State Univ., Ames Lab., USDOE and Dept. of Physics, Ames, Iowa 50011, U.S.A.
- KANELLIS, G.- Univ. of Thessaloniki, First Lab of Physics, Thessaloniki, Greece.
- KAPLYANSKII, A.A.- Ioffe Physico-technical Institute, Academy of Sciences of the USSR, 190421 Leningrad, U.S.S.R.
- KENNEDY, R.J.- Physics Dept., Simon Fraser University, Burnaby, Vancouver, Canada.
- KESMODEL, L.- Indiana University, Dept. of Physics, Bloomington, IN 47405, U.S.A.
- KHODER, A.F.- Centre d'Etudes Nucléaires de Grenoble, Service des Basses Temp., Lab. de Cryophysique 85 X, 38041 Grenoble Cedex, France.
- KIM, J.J.- Korea Advanced Inst. of Science & Tech., P.O. Box 150, Chongyangni, Seoul, Korea.
- KINDER, H.- Physik Dept., Technische Universität München, James Franck Str., D-8046 Garching, West Germany.
- KING, P.J.- University of Nottingham, Dept. of Physics, University Park, Nottingham, England NG7 2RD.
- KIRCH, S.- University of Illinois, 402 Materials Research Lab, 104 S. Goodwin, Urbana, IL 61801, U.S.A.
- KLEIN, M.- Materials Research Lab, Univ. of Illinois, 104 S. Goodwin, Urbana, IL 61801, U.S.A.
- KLEMENS, P.G.- Dept. of Physics, Univ. of Conn. U-46, Storrs, CT 06268, U.S.A.
- KLITSNER, T.- Cornell Univ., LASSP Clark Hall, Ithaca, NY 14853, U.S.A.
- KNEEZEL, G.- Xerox Webster Research Center, Building 114, 800 Phillips Rd., Webster, NY 14580, U.S.A.
- KOGURE, Y.- Univ. of Illinois, Dept. of Physics, Urbana, IL 61801, U.S.A.
- KOJIMA, S.- Inst. of Applied Physics, Univ. of Tsukuba, Sakura, Ibaraki, 305 Japan.
- KRESS, W.- Max Planck Institut FKF, Heisenbergstr. 1, D-7000 Stuttgart 80, West Germany.
- KUGEL, G.- Laboratoire de Génie Physique, Ile du Saulcy, 57045 Metz, France.
- KUNC, K.- CNRS, Paris, Laboratoire de Physique des Solides, Tour 13, 4 Place Jussieu, 75230 Paris Cedex 05, France.
- KURODA, N.- Research Inst. for Iron, Steel & Other Metals, Tohoku Univ., Sendai 980, Japan.
- LAERMANS, C.- Leuven University, Dept. of Physics, Kath. Univ. of Leuven, Celestijnenlaan 200D, 3030 Leuven-Heverlee, Belgium.
- LANNIN, J.S.- Penn. State University, Dept. of Physics, 104 Davey Lab, University Park, PA 16802, U.S.A.
- LAX, M.- City College of New York & Bell Labs, 12 High St., Summit, NJ 07901, U.S.A.

X

- LEISURE, R.- Colorado State Univ., Physics Dept., Fort Collins, CO 80523, U.S.A.
- LIPSHULTZ, F.- Univ. of Connecticut, Physics Dept. U-46, Storrs, CT 06268, U.S.A.
- LOCATELLI, M.- Centre d'Etudes Nucleaires de Grenoble, Service des Basses Temp., Lab. de Cryophysique 85 X, 38041 Grenoble Cedex, France.
- LOCKWOOD, D.J.- National Research Council of Canada, Physics Division M-36, National Research Council, Ottawa, Canada K1A 0R6.
- LOONG, C.K.- Building 3025 Rm E 210, Solid State Division, Oak Ridge National Lab., Oak Ridge, TN 37830, U.S.A.
- LU, C.Y.- Institute of Electronics, National Chiao-Tung Univ., Hsin-Chu, Taiwan 300, China.
- LUDWIG, W.- Inst. Theor. Physics II, Domagstr. Corrensstr., D-4400 Münster, West Germany.
- LURIE, F.- Indiana University, Physics Dept., Bloomington, IN 47405, U.S.A.
- LUTY, T.- Technical University, Inst. of Organic & Physical Chemistry, Wyb. Wyspińskiego 27, Wrocław 50-370, Poland.
- MACDONALD, R.- National Bureau of Standards, Physics A311, Washington, D.C. 20234, U.S.A.
- MACIEL, A.- University of Oxford, Clarendon Lab., Parks Road, Oxford, OX1 3PU, England.
- MARADUDIN, A.A.- University of California, Physics Department, Irvine, CA 92717, U.S.A.
- MARTIN, D.J.- Salford University, Dept. of Physics, Salford M5 4WT, United Kingdom.
- MARTIN, R.- Univ. Pierre et Marie Curie, Dépt. des Recherches Physiques, 75230 Paris Cedex 05, France.
- MASSA, N.- Univ. of Nebraska, Dept. of Physics, Lincoln, NE 68588, U.S.A.
- MATOS GUALBERTO, G.- Instituto de Fisica, Unicamp CP 1170, 13.100 Campinas-SP, Brazil.
- MAZUR, P.- 101 N. Quincy Ave., Margate, NJ 08402, U.S.A.
- MAZZACURATI, V.- Institute of Physics, University of Rome, Piazzale Aldo Moro 2, 00185 Roma, Italy.
- MEINNEL, J.- Université de Rennes, Avenue du Général Leclerc, 35042 Rennes Cedex, France.
- MELTZER, R.- University of Georgia, Dept. of Physics & Astronomy, Athens, GA 30602, U.S.A.
- MERIAN, M.- Laboratoire d'Optique Appliquée, Ecole Polytechnique, 91120 Palaiseau, France.
- MIKOSHIBA, N.- Tohoku Univ., Research Inst. of Electrical Communication, Katahira, Sendai, Japan.
- MINNHAGEN, P.- Indiana University, Physics Dept., Bloomington, IN 47405, U.S.A.
- MITRA, S.- Univ. of Rhode Island, Dept. of Electrical Engineering, Kelley Hall, Kingston, RI 02881, U.S.A.
- MITSUISHI, A.- Dept. of Applied Physics, Osaka Univ., Yamadaoka 2-1 Suita, Osaka 565, Japan.
- MIYASATO, T.- Dept. of Physics, Univ. of Lancaster, Lancaster LA1 4YB, United Kingdom.
- MOORE, D.- University of Illinois-Chicago Circle, Gould Laboratories, 40 Gould Center, Rolling Meadows, IL 60008, U.S.A.
- MORKE, I.- ETH-Zürich, Lab. für Festkörperphysik, ETH-Honggerberg, CH-8093 Zürich, Switzerland.

- MOTIZUKI, K.- Dept. of Material Physics, Faculty of Engineering Science, Osaka Univ., Toyonaka 560, Japan.
- MULAZZI, E.- University of Milan, Istituto di Fisica, Viceloria 16, Milano, Italy.
- MÜLLER, V.- Freie Univ. Berlin Institut für Atom- u Festkörperphysik B, Königin-Luis-Strasse 28/30, D-1000 Berlin 33, West Germany.
- MURAMATSU, A.- Max Planck Institut FKF, Heisenbergstr. 1, D-7000 Stuttgart 80, West Germany.
- NAKAMURA, T.- Inst. for Solid State Physics, Univ. of Tokyo, 7-22-1 Roppongi, Minato-ku, Tokyo 106, Japan.
- NARAYANAMURTI, V.- Bell Laboratories, Rm 1 D 472, Murray Hill, NJ 07974, U.S.A.
- NATKANIEC, I.- Joint Inst. for Nuclear Research, 101000 Moscow, Head Post Office, P.O. Box 79, Dubna, U.S.S.R.
- NAVA, R.- I.V.I.C., P.O. Box 1827, Caracas, Venezuela.
- NEMANICH, R.- Xerox Palo Alto Research Center, 3333 Coyote Hill Rd., Palo Alto, CA 94304, U.S.A.
- NICKLOW, R.- Oak Ridge National Lab, Oak Ridge, TN 37830, U.S.A.
- NIELSEN, O.H.- Inst. of Physics, Univ. of Aarhus, DK-8000 Aarhus, C, Denmark.
- NORTHROP, G.- Univ. of Illinois, 1110 W. Green St., Urbana, IL 61801, U.S.A.
- NÚÑEZ-REGUEIRO, M.- Centre d'Etudes Nucléaires de Grenoble, Service des Basses Températures, Laboratoire de Cryophysique 85 X, 38041 Grenoble Cedex, France.
- OKA, Y.- Research Inst. for Scientific Meas., Tohoku Univ. 19-1 Sanjyo-machi, Sendai 980, Japan.
- OVERWEG, J.A.- Twente Univ. of Technology, P.O. Box 217, 7500 AE Enschede, The Netherlands.
- PAGE, J.- Queen's Univ., Dept. of Physics, Kingston, Ontario, Canada K7L 3N6.
- PASCUAL GAINZA, J.- Dept. Electricitat i Electronica, Facultat Ciències, Univ. Autònoma Barcelona, Bellaterra, Barcelona, Spain.
- PERRIN, B.- Département de Recherches Physiques, Université Pierre et Marie Curie, T 22, Couloir 22-23, 4e étage, 75230 Paris Cedex 05, France.
- PETITGRAND, D.- Laboratoire Léon Brillouin, CEN Saclay, 91191 Gif sur Yvette Cedex, France.
- PHILIP, J.- Univ. of Tennessee, Dept. of Physics, Knoxville, TN 37916, U.S.A.
- PICK, R.- Dept. de Recherches Physiques, Université Pierre et Marie Curie, T 22, 3e étage, 4 Place Jussieu, 75230 Paris Cedex 05, France.
- PINTSCHOVUS, L.- Kernforschungszentrum Karlsruhe, Institut für Angewandte Kernphysik, Postfach 3640, 75 Karlsruhe, West Germany.
- POIRIER, M.- Univ. of Sherbrooke, Physics Depart., Québec, J1K 2R1, Canada.
- POLIAN, A.- Laboratoire de Physique des Solides, Université P. et M. Curie, T 13 E 2, 4 Place Jussieu, 75230 Paris Cedex 05, France.
- POLLINI, I.- Univ. of Milano, c/o Istituto di Fisica-Università, Via Celoria 16, Milano, Italy.
- PRASAD, P.- State Univ. of New York at Buffalo, Dept. of Chemistry, Buffalo, NY 14214, U.S.A.
- PRIEUR, J.Y.- Laboratoire d'Ultrasons, Université P. et M. Curie, 15, Rue Campo Formio, 75013 Paris, France.

- PRITCHARD, J.- Physics Dept., Univ. of Lancaster, Lancaster LA1 4YB, United Kingdom.
- PROHOFSKY, E.- Purdue Univ., Dept. of Physics, West Lafayette, IN 47907, U.S.A.
- RAHMAN, A.- Argonne Nat. Lab., Argonne, IL 60439, U.S.A.
- RAMDANE, A.- University of Nottingham, Physics Dept., University Park, Nottingham, NG7 2RD, England.
- RAMDAS, A.- Purdue University, Dept. of Physics, West Lafayette, IN 47907, U.S.A.
- RAUH, H.- Physikalisches Institut, Universität Würzburg, Röntgenring 8, D-8700 Würzburg, West Germany.
- RAVEX, A.- CRTBT-CNRS, B.P. 166X, 38041 Grenoble Cedex, France.
- RAYNE, J.A.- Carnegie-Mellon University, Department of Physics, Pittsburgh, PA 15213, U.S.A.
- REBANE, L.A.- Institute of Physics, Estonian SSR Academy of Sciences, 142 Riia St. 202400 Tartu, Estonian SSR, U.S.S.R.
- REGIS, M.- Université de Montpellier, G.D.P.C. - U.S.T.L., 34060 Montpellier Cedex, France.
- RENK, K.- Universität Regensburg, Institut für Angewandte Physik, 84 Regensburg, West Germany.
- RESTA, R.- Institut de Physique Appliquée, Epf Lausanne, EPFL-DP, PHB Ecublens, CH 1015, Lausanne, Switzerland.
- RIVES, J.- University of Georgia, Dept. of Physics & Astronomy, Athens, GA 30602, U.S.A.
- RODRIGUEZ, S.- Purdue University, Dept. of Physics, West Lafayette, IN 47907, U.S.A.
- ROGERS, S.J.- University of Kent at Canterbury, The Physics Laboratory, Canterbury, Kent CT2 7NR, England.
- ROSENSTOCK, H.B.- Naval Research Lab (Sacks/Freeman Associates), Code 6510, Washington, D.C. 20375, U.S.A.
- ROSSINELLI, M.- Indiana University, Physics Depart., Bloomington, IN 47405, U.S.A.
- RYAN, J.F.- University of Oxford, Clarendon Laboratory, Parks Road, Oxford, England.
- SAARI, P.M.- Institute of Physics, Estonian SSR Academy of Sciences, 142 Riia St. 202400 Tartu, Estonian SSR, U.S.S.R.
- SAITO, S.H.- The Research Institute for Iron, Steel & Other Metals, Tohoku University, Sendai 980, Japan.
- SANTORO, G.- Istituto di Fisica, Università di Modena, Via Campi 213/A, 41100 Modena, Italy.
- SAPRIEL, J.- Centre National d'Etudes des Télécommunications, 196, rue de Paris, 92220 Bagneux, France.
- SASAKI, W.- Dept. of Physics, Univ. of California Irvine, Irvine, CA 92717, U.S.A.
- SASAKI, Y.- Dept. of Physics, Univ. of California Irvine, Irvine, CA 92717, U.S.A.
- SATO, M.- Brookhaven National Laboratory, Upton, New York 11973, U.S.A.
- SCHAAACK, G.- Physikalisches Institut, Universität Würzburg, Roentgenring 8, D-8700 Würzburg, West Germany.
- SCHMELTZER, D.- Max Planck Institut FKF, Heisenbergstrasse 1, D-7000 Stuttgart 1, West Germany.
- SCHNECK, J.- CNET, 196 rue de Paris, 92220 Bagneux, France.
- SCHRODER, U.- Institut für Physik I, Universität Regensburg, Universitätsstr. 31, D-8400 Regensburg, West Germany.

- SCHWARTZ, C.- Indiana University, Dept. of Physics, Bloomington, IN 47405, U.S.A.
- SHARMA, P.C.- Department of Physics, Banaras Hindu University, Varanasi 5, India.
- SHEARD, F.W.- University of Nottingham, Department of Physics, Nottingham NG7 2RD, England.
- SHEN, T.P.- Univ. of Calif. Irvine, Physics Dept., Irvine, CA 92717, U.S.A.
- SHIREN, N.- IBM T.J. Watson Research Center, P.O. Box 218, Yorktown Heights, NY 10598, U.S.A.
- SIGMUND, E.- 3. Institut für Theoretische Physik, Universität Stuttgart, Pfaffenwaldring 57, 7000 Stuttgart 80, West Germany.
- SIMMONS, R.- University of Illinois, Physics Dept., Urbana IL 61801 U.S.A.
- SIMON, C.- GPS ENS, T23 Faculté des Sciences, 2 Place Jussieu, 75005 Paris, France.
- SINHA, S.K.- Argonne National Laboratory, Solid State Science Division, Argonne, IL 60439, U.S.A.
- SINVANI, M.- California Institute of Technology, Low Temperature Physics, 63-37, Pasadena, CA 91125, U.S.A.
- SOLIN, S.- Michigan State University, Dept. of Physics, East Lansing, MI 48824, U.S.A.
- SPECTOR, H.- Department of Physics, Illinois Institute of Technology, 3301 S. Dearborn, Chicago, IL 60616, U.S.A.
- SRIVASTAVA, G.P.- New University of Ulster, Physics Department, Coleraine, Co. Londonderry, North Ireland, BT52 1SA, United Kingdom.
- STRAUCH, D.- Institut für Physik I, Universität Regensburg, Universitätsstr. 31, D-8400 Regensburg, West Germany.
- STROM, U.- Naval Research Laboratory, Code 6873, Washington, D.C. 20375, U.S.A.
- SUGAI, S.- Division of Engineering, Box D, Brown University, Providence, RI 02912, U.S.A.
- SUZUKI, K.- Max Planck Institut für Festkörperforschung, Heisenbergstrasse 1, 7000 Stuttgart 1, West Germany.
- SWIHART, J.C.- Indiana University, Physics Department, Bloomington, IN 47405, U.S.A.
- TABOREK, P.- Bell Labs, Room 1D 208, 600 Mountain Avenue, Murray Hill, NJ 07974, U.S.A.
- TATSUZAKI, I.- Research Institute of Applied Electricity, Hokkaido University, Sapporo, Kita 12-jo, Nishi, 6-chome, Hokkaido, Japan.
- THIRY, P.- Facultés Universitaires, Notre-Dame de la Paix, Laboratoire de Spectroscopie Electronique, 61, rue de Bruxelles, B-5000 Namur, Belgium.
- THORPE, M.- Physics Dept., Michigan State University, East Lansing, MI 48824, U.S.A.
- THROWE, J.- Indiana University, Physics Dept., Bloomington, IN 47405, U.S.A.
- TOLEDANO, P.- Université de Picardie, Groupe de Physique Théorique, Faculté des Sciences, 33 rue St-Leu, 80000 Amiens, France.
- TUA, P.- Indiana University, Physics Dept., Bloomington, IN 47405, U.S.A.
- TUBINO, R.- Istituto di Chimica Delle Macromolecole/CNR, Via Alfonso Corti 12, 20133 Milano, Italy.
- TUCKER, J.W.- Physics Department, Sheffield University, Sheffield S3 7RH, England.
- ULBRICH, R.G.- Institut für Physik, Postfach 500500, 46 Dortmund 50, West Germany.

XIV

- USHIODA, S.K.- University of California, Department of Physics, Irvine, CA 92717, U.S.A.
- VACHER, R.- Laboratoire de Spectrométrie Rayleigh-Brillouin, Université des Sciences et Techniques du Languedoc, Place E. Bataillon, 34060 Montpellier, France.
- VALLERA, A.M.- Faculdade de Ciencias de Lisboa, Dept. de Física, R. da Escola Politécnica, 1200 Lisboa, Portugal.
- VAN CAMP, P.- R.U.C.A., Groenenborgerlaan 171, B-2020 Antwerpen, Belgium.
- VAN DER SLUIJS, J.C.A.- Physics Department, University College North Wales, Bangor, LLSJ 2UW, United Kingdom
- VENKATARAMAN, G.- Reactor Research Centre, Kalpakkam 603 102, Tamil Nadu, India.
- VOGT, H.- Max Planck Institut für Festkörperforschung, Heisenbergstr. 1, 7000 Stuttgart 80, West Germany.
- VON GUTFELD, R.- IBM Research Center, Box 218, Yorktown Heights, New York 10598, U.S.A.
- WACHTER, P.- Laboratorium für Festkörperfysik, ETH-Z, Honggerberg, CH-8093 Zürich, Switzerland.
- WADA, N.- University of Illinois, Materials Research Lab, 104 S. Goodwin Avenue, Urbana, IL 61801, U.S.A.
- WAGH, A.- Physics Department, University of West Indies, Mona, Kingston 7 Jamaica, West Indies.
- WAGNER, M.- Institut für Theoretische Physik, Universität Stuttgart, Pfaffenwaldring 57, 7000 Stuttgart 80, West Germany.
- WALLIS, R.- Physics Department, University of California, Irvine, CA 92717, U.S.A.
- WANSER, K.- University of California, Department of Physics, Irvine, CA 92717, U.S.A.
- WASIUTYNSKI, T.- Institute of Nuclear Physics, Radzikowskiego 152, 30-074 Krakow, Poland.
- WEIMER, M.- California Institute of Technology, Low Temperature Physics 63-37, Pasadena, CA 91125, U.S.A.
- WEISS, G.- Max Planck Institut für Festkörperforschung, Heisenbergstr. 1, D-7000 Stuttgart 80, West Germany.
- WEISS, K.- Philips Research WY-3, 5600 MD Eindhoven, The Netherlands.
- WIGMORE, K.- Physics Department, University of Lancaster, Lancaster, LA1 4YB, United Kingdom.
- WOLFE, J.- University of Illinois, Dept. of Physics, Urbana, IL 61801, U.S.A.
- WOLTER, J.- Philips Research Laboratories, Eindhoven, The Netherlands.
- WORLOCK, J.- Bell Labs, Holmdell, NJ 07733, U.S.A.
- WU, A.- Dept. of Physics, Purdue University, West Lafayette, IN 47906, U.S.A.
- WU, C.C.- National Chiao Tung University, Department of Applied Mathematics, Hsinchu, Taiwan 300, Republic of China.
- WYBOURNE, M.- GEC Ltd. Hurst Research Centre, East Lane, Wembley, Middlesex, England.
- YACOBY, Y.- Hebrew University, Institute of Physics, Jerusalem, Israel 91904.
- YAGI, T.- Kyushu University, 33, Hakazaki 6-10-1, Higashiku, Fukuoka, Japan.
- YOSHIDA, Y.- Department of Material Physics, Faculty of Engineering Science, Osaka University, Toyonaka 560, Japan.
- YOSHIKAWA, S.- Faculty of Engineering, The Technological University of Nagaoka, Nagamine 1603-1, Kamitomioka, Nagaoka, Niigata, Japan 949-54.

YOUNG, E.- Perkin-Elmer Corporation, ZEYHER, R.- Max Planck Institut für  
Main Avenue, M/S 409, Norwalk, Festkörperforschung, Heisenberg-  
CT 06856, U.S.A. str. 1, D-7000 Stuttgart 80,  
West Germany.

ZARESTKY, J.- Solid State Division,  
Oak Ridge National Laboratory,  
Oak Ridge, TN 37830, U.S.A.

ZEYEN, C.M.E.- Institut Laue-Lange-  
vin, BP 156 X, F-38042 Grenoble  
Cedex, France.

ZWICK, A.- Laboratoire de Physique  
des Solides, Université Paul  
Sabatier, 118 route de Narbonne,  
31062 Toulouse Cedex, France.



## CONTENTS

### PHONONS IN MIXED VALENCE COMPOUNDS

- W. KRESS, H. BILZ, G. GÜNTHERODT and A. JAYARAMAN.- Phonons in mixed valence compounds..... C6-3
- M. CELIO, R. MONNIER and P. WACHTER.- Phonon and elastic anomalies in intermediate valent  $Tm_xSe$  and  $TmSe_{1-y}Te_y$ ..... C6-11
- I. MÖRKE and P. WACHTER.- Phonon softening in intermediate valent  $SbB_6$ ..... C6-14

### PHONONS IN AMORPHOUS AND DISORDERED SYSTEMS

- M.F. THORPE.- Phonons in amorphous materials..... C6-19
- F.L. GALEENER.- Vibrational selection rules in disordered solids : vitreous  $GeO_2$ ..... C6-24
- F. GOMPF and J.S. LANNIN.- The vibrational spectra of crystalline and amorphous phosphorous..... C6-27
- U. STROM, P.B. KLEIN, K. WEISER and S.A. WOLF.- Time-resolved phonon spectroscopy of amorphous  $As_2S_3$ ..... C6-30
- J.-Y. PRIEUR, P. DOUSSINEAU, C. FRENOIS, A. LEVELUT and R.G. LEISURE.- Low-temperature acoustical properties of Na doped  $\beta-Al_2O_3$ ..... C6-33
- A.V. BIELUSHKIN, I. NATKANIEC, V.K. DOLGANOV and E.F. SHEKA.- Vibrational density of states of amorphous and crystalline liquid crystal substances. C6-34
- W. ARNOLD, A. BILLMANN, P. DOUSSINEAU, C. FRENOIS and A. LEVELUT.- Ultrasonic absorption and dispersion in amorphous superconductors..... C6-37
- R. ZEYHER and R. DANDOLOFF.- Entropy of disordered solids at low temperatures..... C6-40
- B. JUSSEURAND, J. SAPRIEL, F. ALEXANDRE and P. DELPECH.- Raman study of the anharmonicity and disorder-induced effects in  $Ga_{1-x}Al_xAs$ ..... C6-43
- M. TEICHER, D. SCHMELTZER and R. BESERMAN.- Phonon-line-shape and disorder correlation in mixed  $GaP_{1-x}As_x$ ..... C6-46
- F. GOMPF, H.J. SCHMIDT and B. RENKER.- Inelastic neutron scattering from amorphous  $Fe_{40}Zr_{60}$  doped with different concentrations of krypton (0,1,7 at.%)..... C6-49
- G. MAISANO, P. MIGLIARDO, F. WANDERLINGH, M.P. FONTANA, M.-C. BELLISSENT-FUNEL and M. ROTH.- Local order and dynamics in liquid electrolytes : small angle neutron scattering..... C6-51
- S.T. KSHIRSAGAR and J.S. LANNIN.- Raman scattering in anneal stable amorphous silicon..... C6-54

# XVIII

P. ALIOTTA, M.P. FONTANA, G. MAISANO, P. MIGLIARDO, C. VASI and F. WANDERLINGH.- Vibrational dynamics in ionic liquids.....	C6-57
O. BETHOUX, J.C. LASJAUNIAS and A. RAVEX.- Effect of a thermal annealing on the lattice specific heat and thermal conductivity of superconducting amorphous $Zr_{.76}Ni_{.24}$ alloys.....	C6-60
E. BONJOUR, R. CALEMCZUK, R. LAGNIER and B. SALCE.- Low temperature thermal properties of cyclohexanol : a glassy crystal system.....	C6-63
T. KLITSNER, A.K. RAYCHAUDHURI and R.O. POHL.- Connection between the low temperature thermal properties of glasses and their glass transition temperature.....	C6-66
D. GREIG and N.D. HARDY.- The thermal conductivity of semicrystalline polymers at very low temperatures.....	C6-69
P. DOUSSINEAU.- Attenuation and velocity change of acoustic waves in the amorphous metal PdSiCu from 0.05 K to 90 K.....	C6-72
P.K. BANERJEE, B. BENDOW, M.G. DREXHAGE, J.T. GOLTMAN, S.S. MITRA and C.T. MOYNIHAN.- Polarized Raman scattering studies of fluorozirconate and fluorohafnate glasses.....	C6-75
A.M. DE GOËR, M. LOCATELLI and C. LAERMANS.- Thermal phonon transport study of the defects created in quartz single crystals by different irradiations ( $\gamma$ rays, electrons, neutrons).....	C6-78
V. UMADEVI, R. KESAVAMOORTHY, A.K. SOOD and G. VENKATARAMAN.- Surface polaritons in irradiated $\alpha$ -quartz.....	C6-81
D. SCHMELTZER and R. BESERMAN.- Renormalization group method for vibrational behavior in mixed crystals.....	C6-84
K. MENN and W. BIEM.- Coherent potential approximation and strongly anharmonic systems : crystals of para-hydrogen and neon resp. hydrogen atoms.....	C6-87
I.W. JOHNSTONE, G.D. JONES and D.J. LOCKWOOD.- Raman scattering from phonons in disordered $CsMg_{1-x}Co_xCl_3$ .....	C6-90
B.K. AGRAWAL.- Vibrational excitations in $\alpha$ -Si:F and $\alpha$ -Si:F:H alloys.....	C6-93
O. BRAPMAN and G. LIVESCU.- A study of polaritons and phonon peculiarities in $CuCl_{1-x}Br_x$ .....	C6-96
R. NAVA and M. RODRÍGUEZ.- Frequency dependence of acoustic saturation in smoky quartz.....	C6-99
P.G. KLEMENS.- Theory of the attenuation of elastic waves in inhomogeneous solids.....	C6-102
R. CARLES, N. SAINT-CRICQ, A. ZWICK, M.A. RENUCCI and J.B. RENUCCI.- Low frequency Raman scattering in mixed $Ga_{1-x}Al_xAs$ and $Ga_{1-x}In_xAs$ alloys.....	C6-105

## PHONON - PHONON INTERACTIONS AND NON - LINEAR LATTICE DYNAMICS

H. BÜTTNER and N. BILZ.- Some aspects of nonlinear lattice models.....	C6-111
R. BAUMGARTNER, M. ENGELHARDT and K.F. HENK.- Observation of strongly frequency dependent lifetimes of acoustic phonons in $CaF_2$ .....	C6-119

P.F. TUA and G.D. MAHAN.- Anharmonicity effects in $\text{CaF}_2$ at low temperature..	C6-122
R. VACHER and J. PELOUS.- Phonon damping in crystalline and amorphous solids at hypersonic frequencies.....	C6-125
K.H. WANSER and R.F. WALLIS.- Harmonic and anharmonic properties of silicon.	C6-128
B. PERRIN and F. MICHARD.- Phonon-phonon interactions in molecular crystals studied by ultrasonic methods.....	C6-131
M.A. BREAZEALE and J. PHILIP.- Temperature dependence of phonon-phonon interaction in silicon.....	C6-134
A.A. MARADUDIN, A.J. MARTIN, H. BILZ and R.F. WALLIS.- Non-linear dynamical excitations in solids.....	C6-137
B. BENDOW, H.G. LIPSON, R.N. BROWN, R.C. MARSHALL, D. BILLARD and S.S. MITRA.- Temperature dependence of multiphonon absorption in highly transparent cubic zirconia.....	C6-140
G. FRITSCH, W. DIETZ, R. HÄRING and E. LÜSCHER.- Anharmonic contributions to the thermal diffuse X-ray scattering intensity from single crystalline sodium.....	C6-143
J.H. HENKEL.- Lattice phonon lifetime calculations.....	C6-146
G.P. SRIVASTAVA.- Role of thermal expansion in the phonon conductivity of solids.....	C6-149
A.A. ANIKIEV, B.S. UMAROV, V.S. GORELIK and J.P. VETELINO.- Two-phonon bound states in ammonium chloride at finite temperatures.....	C6-152
T.J. SINGH and G.S. VERMA.- Four-phonon processes in solids.....	C6-155
D. SCHMELTZER and R. BESERMAN.- Anharmonic interaction in zinc selenide.....	C6-158
M. LAX, V. NARAYANAMURTI, P. HU and W. WEBER.- Lifetimes of high frequency phonons.....	C6-161

#### PHONONS IN SUPERIONIC CONDUCTORS

W. HAYES.- Phonons in superionic conductors.....	C6-167
R.J. ELLIOTT and M. DIXON.- Vibrations and diffusion of atoms in superionic crystals and melts.....	C6-175
P. BRÜESCH, T. HIMMA and W. BÜHRER.- Phonons and ionic conductivity in the two-dimensional superionic conductor $\text{AgCrS}_2$ .....	C6-178
W. SASAKI, Y. SASAKI, S. USHIODA and W. TAYLOR.- Low frequency light scattering spectra of $\text{AgI}$ .....	C6-181
D. ČIPLYS and J.Y. FRIEUR.- Ultrasonic properties of a superionic glass : $\text{B}_2\text{O}_3$ , $0.5 \text{ Li}_2\text{O}$ , $0.7 \text{ LiCl}$ .....	C6-184
D.P. ALMOND and A.R. WEST.- A new interpretation of ultrasonic attenuation in superionic conductors $\beta$ and $\beta'$ -alumina.....	C6-187
E. CAZZANELLI, A. FONTANA, G. MARIOTTO and F. ROCCA.- Vibrational dynamics of $\text{RbAg}_4\text{I}_5$ by Raman spectroscopy.....	C6-190

XX

- H. v. LÖHNEISEN, H.J. SCHINK, W. ARNOLD, H.U. BEYELER, L. PIETRONERO and S. STRÄSSLER.- Low-temperature specific heat anomaly of the one-dimensional ionic conductor hollandite..... C6-193
- V. MAZZACURATI, G. RUOCCO, G. SIGNORELLI, E. CAZZANELLI, A. FONTANA and G. MARIOTTO.- A theoretical model for the continuous order-disorder transition at 763 K in superionic  $\alpha$ -AgI..... C6-196

#### PHONON IMAGING AND PHONON FOCUSING

- W. EISENMENGER.- Phonon imaging..... C6-201
- G.A. NORTHROP, W. DIETSCH, A.D. ZDETSIS and J.P. WOLFE.- Focusing of dispersive phonons in Ge..... C6-209
- J.C. HENSEL, R.C. DYNES, F.C. UNTERWALD and A.L. SIMONS.- Singular effects in phonon focusing ; formation of phonon focusing caustics..... C6-212
- A.G. EVERY.- Phonon focusing and the shape of the ray surface in cubic crystals..... C6-215

#### PHONON TRANSPORT

- V. NARAYANAMURTI.- Transport of high energy phonons..... C6-221
- R.G. ULBRICH, V. NARAYANAMURTI and M.A. CHIN.- Ballistic transport and decay of near zone-edge non-thermal phonons in semiconductors..... C6-226
- L.J. CHALLIS, A.A. GHAZI and M.N. WYBOURNE.- Frequency crossing in bicrystals and inelastic scattering at surfaces..... C6-229
- J. MAIER and E. SIGMUND.- The influence of the dynamical Jahn-Teller effect of acceptors onto the phonon-transport mechanism in cubic semiconductors. C6-232
- A.M. DE GOËR, M. LOCATELLI and K. LASSMANN.- A study of the ground state of acceptors in silicon from thermal transport experiments..... C6-235
- M. WAGNER, W. MUTSCHELLER and H.-K. NUSSER.- Phonon and pseudo-magnon transport in cooperative Jahn-Teller systems..... C6-238
- R. ENGLMAN.- Phonon pulses from a relaxing system..... C6-241
- A. RAMDANE, B. SALCE, L.J. CHALLIS and M. LOCATELLI.- Phonon scattering by Cr ions in GaAs and the effect of uniaxial stress..... C6-244
- W. BAUERHFEIND, J. KELLER and U. SCHRÖDER.- Theory of thermal conductivity in molecular crystals. Application to alkali cyanides..... C6-247
- G.A. KNEEZEL and A.V. GRANATO.- Phonon-dislocation dipole interaction in LiF at low temperature..... C6-250
- G.P. SRIVASTAVA.- Phonon conductivity due to nondiagonal energy-flux operator C6-253
- R. BRITO-ORTA and P.G. KLEMENS.- Contribution of low-frequency longitudinal phonons to the lattice thermal conductivity of dielectric solids..... C6-256
- H. LENGFELLNER and K.P. RENK.- Detection of acoustic zone-boundary phonons by phonon difference absorption..... C6-259
- G.S. DIXON.- Two-magnon-one-phonon scattering in the lattice thermal conductivity of magnetic insulators..... C6-262

- A.M. DE GOËR, M. LOCATELLI and I.F. NICOLAU.- Low temperature thermal conductivity of  $\text{HgI}_2$  single crystals..... C6-265
- P.C. SHARMA, K.P. ROY and V. RADHAKRISHNAN.- The effect of nonmetal-metal transition due to doping on lattice thermal conductivity : application to Ge-doped InSb..... C6-268
- R.A. BROWN.- The effect of dislocations on thermal conductivity..... C6-271
- M. GREENSTEIN and J.P. WOLFE.- Modulation of ballistic phonon fluxes in Ge by a He gas film at a solid/superfluid interface..... C6-274
- B. DAUDIN, B. SALCE and S.H. SMITH.- Specific heat and thermal conductivity of  $\text{TmVO}_4$  and  $\text{DyVO}_4$  with an applied magnetic field..... C6-277

#### PHONONS IN LOW DIMENSIONAL MATTER

- S.A. SOLIN.- Phonons in graphite intercalation compounds..... C6-283
- H. ZABEL and A. MACERL.- Phonons in alkali graphite intercalation compounds. C6-289
- S.N. BEHERA.- Effect of non-magnetic impurities on the Raman scattering by superconducting gap excitation in layered compounds..... C6-292
- A. POLIAN, K. KUNC and J. ROSSAT-MIGNOD.- Inelastic neutron scattering and lattice dynamics of the layer semiconductor GaS..... C6-295
- C. HORIE, H. MIYAZAKI, S. IGARASHI and S. HATAKEYAMA.- Role of phonons in orientational intra-plane ordering in graphite intercalation compounds... C6-298
- G. BENEDEK, I. POLLINI and W. BAUHOFFER.- Two-phonon progressions associated with vibronic excitons in layered 3d-metal compounds..... C6-301
- G. FISHMAN, A. PINCZUK, J.M. WORLOCK, H.L. STÖRMER, A.C. GOSSARD and W. WIEGMANN.- Coupled electron-LO phonon excitation in a two dimensional electron system..... C6-305
- J.C. HENSEL, R.C. DYNES and D.C. TSUI.- Absorption of ballistic phonons by the 2D electron gas in a Si MOSFET..... C6-308
- W.A. KAMITAKAHARA, M. WADA and S.A. SOLIN.- Neutron spectroscopy of phonons in  $\text{RbC}_8$ ..... C6-311
- S.N. BEHERA and A. KHARE.- Dynamics and thermodynamics of a one dimensional non-linear lattice in the continuum limit..... C6-314
- S.J. ROGERS, C.J. SHAW and H.D. WIEDERICK.- Limitations on the usefulness of metallic thin film semiconductors for phonon detection..... C6-317
- S. SUGAI, T. UEDA and K. MURASE.- Raman scattering in  $\text{MoS}_2$ ,  $\text{MoSe}_2$  and  $\alpha\text{-MoTe}_2$  at high pressures..... C6-320
- C. CARLONE, N.K. HOTA, H.J. STOLZ, M. ELBERT, H. KUZMANY and R.D. HOCHHEIMER Gas phase Raman spectrum of TCNQ and pressure dependence of the modes in crystals of TCNQ..... C6-323
- S.E. HARDCASTLE and H. ZABEL.- Thermal expansion of alkali-graphite intercalation compounds..... C6-326
- A. MACERL and H. ZABEL.- Lattice dynamics of graphite intercalation compounds-modelled by the phonon dispersion of linear chains..... C6-329

N. KURODA and Y. NISHINA.- Two-exciton process resonant Raman scattering in InSe.....	C6-332
H. MIYAZAKI and C. HORIE.- Effect of electron-phonon interaction on Raman spectra of graphite intercalation compounds.....	C6-335
C. AYACHE and M. NUNEZ-REGUEIRO.- Basal thermal conductivity of $\text{TiSe}_2$ .....	C6-338
G. KANELLIS, J.F. MORHANGE and M. BALKANSKI.- Electrostatic energy and lattice vibrations in thin ionic slabs.....	C6-341
F. BATALLAN, I. ROSENMAN, C. SIMON, G. FURDIN and H.J. LAUTER.- Phonons in graphite intercalated with bromine.....	C6-344
D.M. HWANG and S.A. SOLIN.- Phonon Raman spectroscopy in graphite intercalation compounds.....	C6-347
N. WADA, M.V. KLEIN and H. ZABEL.- Raman scattering studies of folded shearing phonons in $\text{KC}_{12n}$ ( $n=2\sim6$ ).....	C6-350

#### PHONONS IN METALS

J. ASHKENAZI and M. DACOROGNA.- Phonons in metals.....	C6-355
B. DORNER, A.A. CHERNYSHOV, V.V. PUSHKAREV, A.Yu. RUMYANTSEV and R. PYNN.- Electron-phonon coupling in the nontransition metal cadmium.....	C6-365
M.V. KLEIN.- Raman scattering from anomalous phonons in transition metals and compounds.....	C6-368
C.T. YEH, W. REICHARDT, B. RENKER, N. NÜCKER and M. LOEWENHAUPT.- Lattice dynamics of $\text{YAl}_2$ and $\text{LaAl}_2$ - a further contribution to the La-Y puzzle...	C6-371
P. BERBERICH and H. KINDER.- The phonon spectrum emitted by superconducting Sn tunnel junctions.....	C6-374
G.B. ARNOLD and M. MENON.- The local phonon density of states and its influence on superconducting properties.....	C6-377
O.P. GUPTA.- Phonon dispersion and thermophysical properties of sodium.....	C6-380
A.F. KHODER, M. COUACH, M. LOCATELLI, M. ABOU-CHANTOUS and J.P. SENATEUR.- On the thermal and electrical conductivity of $\text{V}_3\text{Si}$ and $\text{V}_5\text{Si}_3$ .....	C6-383
J.R.D. COPLEY, L. BOSIO, R. CORTÈS, J. LEFEBVRE and W.D. TEUCHERT.- A neutron inelastic scattering study of phonons in metastable beta-gallium.....	C6-386
V. MÜLLER, G. SCHANZ, E.-J. UNTERHORST and D. MAURER.- Nuclear acoustic resonance investigations of the longitudinal and transverse electron-lattice interaction in transition metals and alloys.....	C6-389
R. MERLIN, S.B. DIEKKER, M.V. KLEIN, J. JØRGENSEN, S.R. RASMUSSEN, Z. FISK and G.W. WEBB.- Raman scattering in $\text{V}_3\text{Si}$ , $\text{V}_3\text{Ge}$ , $\text{Nb}_3\text{Sb}$ and $\text{Cr}_3\text{Si}$ : correlation of $E_g$ optical phonon linewidth with magnetic susceptibility.....	C6-392
U. BUCHENAU, H.R. SCHÖBER and R. WAGNER.- Coherent neutron scattering from polycrystals.....	C6-395
A.M. VALLERA.- High temperature phonons in iron.....	C6-398

- B.N. ONWUAGBA and A.O.E. ANIMALU.- Screening of the short-range potential by the local field correction in the lattice dynamics of vanadium..... C6-401
- B. STRÖBEL, K. LÄUGER, H.E. BÖMMEL and V. MÜLLER.- The ultrasound-induced electric field gradient (EFG) in metals..... C6-404

### PHONONS IN FERROELECTRICS

- A. BUSSMANN-HOLDER, G. BENEDEK, H. BILZ and B. MOKROSS.- Microscopic polarizability model of ferroelectric soft modes..... C6-409
- L.C. BRUNEL, G. LANDWEHR, A. BUSSMANN-HOLDER, H. BILZ, M. BALKANSKI, M. MASSOT and M.K. ZIOLKIEWICZ.- Influence of strong magnetic fields on ferroelectric phase transitions..... C6-412
- F. GERVAIS and J.L. SERVOIN.- Role of polar phonons in the chemical bond at structural phase transitions characterized by repetitive Fourier spectroscopy..... C6-415
- T. NAKAMURA, S. KOJIMA, M.S. JANG, M. TAKASHIGE and S. ITOH.-  $E(x) - A_1(z)$  oblique phonons in tetragonal  $\text{BaTiO}_3$ ..... C6-418
- T. NAKAMURA, M. TAKASHIGE and Y. AIKAWA.- Raman scattering from amorphous state of ferroelectric  $\text{PbTiO}_3$  and its change in the crystallization process..... C6-421
- B. SALCE, A.M. DE GOËR and L.A. BOATNER.- Study of "pure"  $\text{KTaO}_3$  and KTN single crystals by thermal conductivity measurements down to 50 mK..... C6-424
- JONG-JEAN KIM, JONG-WOOK WON and BYOUNG-KOO CHOI.- Soft-mode spectra and phase transition in KDP crystal with ADP impurities..... C6-427
- K. INOUE and N. ASAI.- Hyper-Raman scattering study of ferroelectric phase transitions in  $\text{SrTiO}_3$  and  $\text{BaTiO}_3$ ..... C6-430
- R.S. KATIYAR and J.D. FREIRE.- Dynamical study of phonons in ferroelectric lead titanate..... C6-433

### INTERACTION OF PHONONS WITH OTHER EXCITATIONS

- A.A. KAPLYANSKII, S.A. BASOON and V.L. SHEKHTMAN.- Phonons in excited ruby..... C6-439
- W. DIETSCHER, S.J. KIRCH and J.P. WOLFE.- Phonon spectroscopy of the electron-hole-liquid..... C6-447
- D.J. SON, J.E. RIVES and R.S. MELTZER.- Stimulated emission of tunable high frequency phonons in  $\text{LaF}_3:\text{Er}^{3+}$ ..... C6-450
- A. COMPAN, H.W. LO, M.C. LEE and A. AYDINLI.- Pulsed Raman measurements of inhibited electron-phonon coupling at high plasma densities in silicon... C6-453
- P.J. KING.- The effect of lattice strains on the acoustic relaxation losses in dielectric crystals due to magnetic ions..... C6-456
- Y. OKA and M. CARDONA.- Raman scattering study of correlation between phonons and electron spins in  $\text{CdS}$  and  $\text{ZnTe}$  under resonance condition..... C6-459
- A.A. KAPLYANSKII, S.A. BASOON and V.L. SHEKHTMAN.- Multiple resonant Raman spin-flip phonon scattering and  $29\text{ cm}^{-1}$  phonon transport in excited ruby in a magnetic field..... C6-462

A. DEVILLE, B. GAILLARD, C. BLANCHARD and J. LIVAGE.- Comparison of electron spin-lattice relaxation in amorphous and crystalline materials.....	C6-465
K.R. MOUNTFIELD and J.A. RAYNE.- Elastic moduli of linear antiferromagnet $\text{CeNiCl}_3$ .....	C6-468
A.S. WAGH.- A microscopic transport theory of electron-phonon systems.....	C6-471
A. BARCHIELLI and E. MULAZZI.- Homogeneous broadening of zero-phonon lines for a multilevel system in a crystal : the role of the electron-phonon interactions.....	C6-475
J.W. TUCKER.- Phonon scattering at frequencies near the exciton frequency of two-level defects.....	C6-478
CHIH-YUAN LU.- Ground-state energy of Fröhlich electron-phonon system.....	C6-481
R.C. ALIG, S. BLOOM and M. INOUE.- Optical-mode deformation potential.....	C6-484
J.M. CALLEJA, H. VOGT and M. CARDONA.- Absolute cross sections for one-phonon Raman scattering from several insulators and semiconductors.....	C6-487
D. FAY and J. APPEL.- Effect of phonons on the spin susceptibility.....	C6-490
E. MULAZZI, R. TUBINO and G. DELLEPIANE.- On the origin of the red shift of the Raman excitation profile from the absorption spectrum.....	C6-493
U. SCHRÖDER, M. WEISS, R. REIGER and J.B. PAGE.- Generalization of Fröhlich's operator for the electron-phonon coupling in polar crystals.....	C6-496
H. GERLINGER and G. SCHACK.- Magnetic field dependent reststrahlen spectra in paramagnetic $\text{CeF}_3$ .....	C6-499
P. SAARI and K. REBANE.- Phonon relaxation in crystals studied by hot luminescence.....	C6-502
L.A. REBANE and K.K. REBANE.- Phonons in resonant secondary emission of impurity molecules in crystals.....	C6-505

#### GENERAL THEORETICAL METHODS OF PHONON PHYSICS

M. PARRINELLO and A. RAHMAN.- Polymorphic transitions in alkali halides. A molecular dynamics study.....	C6-511
C. FALTER, W. LUDWIG and M. SELMKE.- Renormalized response theory with applications to phonon anomalies.....	C6-516
M.A. BALL.- The generalized pseudatom formalism in lattice dynamics.....	C6-519
E.W. YOUNG and P.B. SHAW.- A strong coupled acoustic deformation polaron in one dimension.....	C6-522
A. CZACHOR.- Gaps in phonon dispersion curves for substitutional alloys.....	C6-525
S.N. BEHERA and Sk. SAMSUR.- Hybridization of the two-phonon bound state with the local mode in imperfect crystals.....	C6-528
K. WEISS.- Attenuation of second sound in solids .....	C6-531
M. HERITIER and G. MONTANBAUX.- Interpretation of experiments in the solid-on model for rotors.....	C6-534



- E.M. ANASTASSAKIS and M. CARDONA.- Simulation of long-wavelength optical phonons by generalized internal strains..... C6-537
- B. FAIN.- Instabilities in thermal bath : phonon enhancement and saturation in a three-level system..... C6-540
- C.M.E. ZEYEN.- Improved energy resolution with neutron spin echo triple-axis spectrometers..... C6-543

#### PHONONS IN MOLECULAR AND ORGANIC SUBSTANCES

- G. VENKATARAMAN.- Phonons in molecular crystals..... C6-549
- Y. SASAKI and Y. NISHINA.- Vibrational spectra of solid and liquid sulfur... C6-557
- E.W. PROHOFKY, L.L. VAN ZANDT, M. KOHLI, K.C. LU, M.N. MEI and B. PUTMAN.- Phonons in the DNA double helix..... C6-560
- P.N. PRASAD.- Dynamics of phonon interactions in organic solids..... C6-563
- E.L. BOKHENKOV, A.I. KOLESNIKOV, T.A. KRIVENKO, E.F. SHEKA and V.A. DEMENTJEV.- Harmonic dynamics of anthracene and naphthalene crystals.... C6-566
- J.D.N. CHEEKE and G. MADORE.- Acoustoelectric interaction in p-InSb at low temperature..... C6-569
- A.K. SOOD, A.K. ARORA, S. DATTA GUPTA and G. VENKATARAMAN.- Orientational dynamics of sulphate ions in potash alum..... C6-572
- T. WASIUTYNSKI.- Self-consistent phonon calculations in solid nitrogen..... C6-575
- C. ECOLIVET.- Linear chain models and sound velocities in molecular organic crystals..... C6-578
- L.S.G. CANCELA, J.G. RAMOS and G.M. GUALBERTO.- Multiphonon process in  $\text{NiSO}_4 \cdot 6\text{H}_2\text{O}$ ..... C6-581
- S.L. CHAPLOT, A. MIERZEJEWSKI, J. LEFEBVRE, G.S. PAWLEY and T. LUTY.- Internal and external phonons in monoclinic tetracyanoethylene..... C6-584
- B. KUCHTA and T. LUTY.- Harmonic and anharmonic representation of librational motions in molecular crystals..... C6-587
- T. LUTY.- Translational - rotational coupling in s-triazine crystal..... C6-590
- N.E. MASSA.- Raman scattering spectra of  $\text{Rb}_2\text{ZnCl}_4$  under uniaxial stress.... C6-593
- F.W. SHEARD.- Spin-lattice interaction in cerium ethylsulphate..... C6-596
- T. WASIUTYNSKI, I. NATKANIEC and A.I. BELUSHKIN.- Lattice dynamics calculations for solid biphenyl in the high temperature phase..... C6-599
- B. DORNER, E.L. BOKHENKOV, E.F. SHEKA, S.L. CHAPLOT, G.S. PAWLEY, J. KALUS, U. SCHMELZER and I. NATKANIEC.- Phonon dispersion curves in the molecular crystals naphthalene and anthracene measured by inelastic neutron scattering..... C6-602
- E.L. BOKHENKOV, A.I. KOLESNIKOV, T.A. KRIVENKO, E.F. SHEKA, V.A. DEMENTJEV and I. NATKANIEC.- Neutron spectroscopy of internal phonons of naphthalene and anthracene crystals..... C6-605

- M. MERIAN and J. ETCHEPARE.- A calculation of the phonon dispersion curves in trigonal and monoclinic selenium with the help of a single vibrational potential..... C6-608
- M. BOISSIER, R. VACHER and B. PERRIN.- Ultrasonic relaxation in  $\alpha$ -sulfur.... C6-611

### PHONONS IN SEMICONDUCTORS

- R.M. MARTIN.- Recent advances in the theory of phonons in semiconductors.... C6-617
- P.E. VAN CAMP, V.E. VAN DOREN and J.T. DEVREESE.- First principles calculation of the phonon spectra of solids..... C6-625
- B.N. HARMON, W. WEBER and D.R. HAMANN.- Vibrational frequencies via frozen phonons..... C6-628
- C. COLVARD, R. MERLIN, M.V. KLEIN and A.C. GOSSARD.- Light scattering from phonons in GaAs-AlAs superlattices..... C6-631
- L. PINTSCHOVIOUS, J.A. VERGÉS and M. CARDONA.- Self-energy of phonons interacting with free carriers in silicon..... C6-634
- K.R. RAO, V.M. PADMANABHAN, P.R. VIJAYARAGHAVAN and S.L. CHAPLOT.- Neutron, X-ray and lattice dynamical studies of  $\text{Sb}_2\text{S}_3$ ..... C6-637
- K. SUZUKI, D. SCHMELTZER and A.A. MARADUDIN.- Vibrational properties of vacancies in homopolar semiconductors..... C6-640
- P.J. CARROLL and J.S. LANNIN.- Second order Raman scattering in crystalline sulphur selenium and tellurium..... C6-643
- A.Y. WU and R.J. SLADEK.- Ultrasonic phonon velocities in  $\text{Cd}_{1-x}\text{Mn}_x\text{Te}$  between 1.5 and 96 K : anomalies near the magnetic transition..... C6-646
- K. KUNC and R.M. MARTIN.- Ab initio force constants of germanium..... C6-649
- D. OLEGO, M. CARDONA and P. VOGL.- Volume and temperature dependence of the transverse charge and the ionicity of tetrahedral semiconductors..... C6-652
- CHHI-CHONG WU.- Effect of the propagation of ultrasounds on magnetoacoustic phenomena in degenerate semiconductors..... C6-655
- T. MIYASATO, M. TOKUMURA and F. AKAO.- Effect of magnetic field on ballistic heat-pulse scattering in n-type germanium..... C6-658
- R. RESTA and A. BALDERESCHI.- Local-field effects and zone-center phonons in polar and covalent cubic semiconductors..... C6-661
- M. HAMDACHE, P.J. KING, D.T. MURPHY and V.W. RAMPTON.- Phonon spectroscopy of chromium-doped gallium arsenide using superconducting tunnel junctions..... C6-664
- M.H. CHAO and R.J. SLADEK.- Ultrasonic phonons in  $\text{Hg}_{0.8}\text{Mn}_{0.2}\text{Te}$  ; dependences of elastic moduli on pressure and temperature..... C6-667
- H.N. SPECTOR and T.M. RYNEE.- Phonon assisted transitions in the free carrier absorption of semiconductors in quantizing magnetic fields..... C6-670
- O.H. NIELSEN.- Vibrations of substitutional impurities in semiconductors.... C6-673
- H.N. SPECTOR.- Parametric amplification of microwave phonons in semiconductors..... C6-676

- K. RAMACHANDRAN and T.M. HARIDASAN.- The localized modes due to phosphorous defects in cadmium telluride..... C6-679
- J. CAMASSEL, B. GIL, P. MERLE, H. MATHIEU and J. PASCUAL.- Resonant Raman scattering in  $\text{TiO}_2$ ..... C6-682
- G.A. GLEDHILL, S.S. KUDHAIL, R.C. NEWMAN, J. WOODHEAD and G.Z. ZHANG.- The low frequency absorption of gallium phosphide induced by impurities and radiation damage..... C6-685
- D. PETRITIS, C. DEVILLE CAVELLIN and G. MARTINEZ.- Resonant enhancement of the Raman linewidth of phonon modes induced by hydrostatic pressure..... C6-688

### THE ROLE OF PHONONS IN PHASE TRANSITIONS

- R. CURRAT.- The role of phonons in incommensurate phase transitions..... C6-693
- H. POULET and R.M. PICK.- Are phasons in biphenyl detectable by light scattering ?..... C6-701
- H. CAILLEAU, F. MOUSSA, C.M.E. ZEYEN and J. BOUILLOT.- Dynamics of incommensurate phases in biphenyl..... C6-704
- D. STRAUCH and U. SCHRÖDER.- On the mode softening in SnTe and PbTe..... C6-707
- G. ERRANDONEA.- Pressure dependence of the coupled optic and acoustic modes near the ferroelastic transitions of  $\text{LaP}_5\text{O}_{14}$ ..... C6-710
- R. GEICK, H. RAUH, N. LEHNER, J. BOUILLOT, W.G. STIRLING and G. HEGER.- Lattice instabilities and phase transitions in fluoride perovskites..... C6-713
- A. MACIEL and J.F. RYAN.- Lock-in type phase transition in  $\text{KFeF}_4$ ..... C6-716
- J. PASCUAL, J. CAMASSEL, P. MERLE and H. MATHIEU.- Gruneisen parameter and deformation potentials of Raman active modes in rutile structure compounds C6-719
- F. CERDEIRA, F.E.A. MELO and R.S. KATYAR.- Piezospectroscopic study of the Raman spectrum of  $\text{LiIO}_3$ ..... C6-722
- A. MACIEL and J.F. RYAN.- Observation of coupled amplitude modes in the Raman spectrum of incommensurate  $\gamma\text{-Na}_2\text{CO}_3$ ..... C6-725
- S. SUGAI, K. MURASE, S. UCHIDA and S. TANAKA.- Investigation of the charge density waves in  $2\text{H-TaSe}_2$  by one and two phonon Raman scattering..... C6-728
- T. YAGI, Y. HIDAKA and K. MIURA.- Brillouin scattering study of the incommensurate (antiferroelectric) phase transition in sodium nitrite..... C6-731
- J. SCHNECK, J.C. TOLEDANO, J. AUBREE, B. JOUKOFF and C. JOFFRIN.- Soft phonon valley near the transition to an incommensurate phase in barium sodium niobate..... C6-734
- T. JANSSEN and C. DE LANGE.- Vibration spectra of crystals in an incommensurate phase..... C6-737
- S. SUGAI, K. MURASE, S. UCHIDA and S. TANAKA.- Investigation of the charge density waves in  $1\text{T-VSe}_2$  by Raman scattering..... C6-740
- M. ZIGONE, M. VANDEVYVER and D.N. TALWAR.- Pressure dependence of impurity induced Raman scattering spectra in ZnS crystals..... C6-743

- P. TOLEDANO, G. PASCOLI and M. COIRET.- Simultaneous condensation of several modes at structural phase transitions..... C6-746
- M.D. FONTANA, G.E. KUGEL and C. CARABATOS.- Lattice dynamics of the cubic-tetragonal phase transition in  $\text{KNbO}_3$ ..... C6-749
- B. DORNER, H. BOYSEN, F. FREY and H. GRIMM.- On the Si-O-Si bond angle in  $\alpha$ - and  $\beta$ -quartz..... C6-752
- R. ENGLMAN.- Dynamics in displacive phase transitions..... C6-755
- T. SUSKI and S. KATAYAMA.- Phonon induced anomalous resistivity in structural phase transition of  $\text{PbSnTe}$ ..... C6-758
- D.J. LOCKWOOD and G.J. COOMBS.- A Raman study of the structural phase transition in disordered  $\text{KMn}_{0.85}\text{Ni}_{0.15}\text{F}_3$ ..... C6-761
- V.S. GORELIK, B.S. UMAROV and M. UMAROV.- "Non-central" peaks in light scattering spectra of lithium tantalate and quartz at phase transition... C6-764
- S. KOJIMA and T. NAKAMURA.- Raman scattering study of low frequency phonon polaritons in several crystals..... C6-767
- M. SATO, B.H. GRIER, S.M. SHAPIRO and H. MIYAJIMA.- Soft phonons and magnetic ordering in the  $\gamma$ -phase transition metal alloys  $\text{Fe}_{1-x}\text{Pd}_x$ ..... C6-770
- K. MOTIZUKI, Y. YOSHIDA and Y. TAKAOKA.- Role of phonons in structural phase transitions of transition metal dichalcogenides..... C6-773
- E. CAZZANELLI, A. FONTANA, G. MARIOTTO, F. ROCCA and M.P. FONTANA.- Observation of pretransitional effects on the shape of the  $E_2$  ( $17\text{ cm}^{-1}$ ) optical mode in  $\beta$ -AgI by Raman spectroscopy..... C6-776
- C. ECOLIVET, B. TOUDIC and M. SANQUER.- Brillouin scattering study of phase transitions in p-polyphenyls..... C6-779
- D. PETITGRAND, B. HENNION, C. ESCRIBE-FILIPPINI and S. LEGRAND.- Phonon dispersion and transverse mode softening in  $\text{RbFeCl}_3$ ..... C6-782
- D.R. MOORE, V.J. TEKIPPE, A.K. RAMDAS and J.C. TOLEDANO.- A Raman scattering study of the solid to solid phase transition in benzil..... C6-785
- N. KURODA, S. HASHIMOTO and Y. NISHINA.- Spectroscopic ionicity and lattice instability in III-VI layer compounds..... C6-788

#### PHONONS AT SURFACES AND INTERFACES

- G. BENEDEK, G. BRUSDEYLINS, R.B. DOAK and J.P. TOENNIES.- The spectroscopy of surface phonons by inelastic atom scattering..... C6-793
- P. CANTINI, G. BOATO and R. TATAREK.- Graphite surface phonons studied through He atoms resonant scattering..... C6-801
- V. BORTOLANI, F. NIZZOLI, G. SANTORO and A. MARVIN.- Theory of acoustic phonons at interfaces and Brillouin scattering..... C6-804
- D.J. MARTIN and R.P. WALKER.- How much information can low energy ion scattering give about surface phonons ?..... C6-807
- Y. ITOH, C. HAMAGUCHI and Y. INUISHI.- Resonant Brillouin scattering in opaque region of  $\text{CdS}$ ..... C6-810

- R.E. HORSTMAN and J. WOLTER.- Thermalization of high-frequency phonons in silicon single crystals..... C6-813
- N.S. SHIREN.- Surface roughness Kapitza conductance : dependence on material properties and phonon frequency..... C6-816
- T.J. SHEN, D. CASTIEL and A.A. MARADUDIN.- Effect of surface roughness on the Kapitza resistance..... C6-819
- R.J. NEMANICH and C.C. TSAI.- Phonons of the metal/amorphous silicon interface studied by interference enhanced Raman scattering..... C6-822
- P. TABOREK, M. SINVANI, M. WEIMER and D. GOODSTEIN.- Film thickness dependence of heat transmission into helium..... C6-825
- C. SCHWARTZ and W.L. SCHAICH.- Phonons at metal surfaces..... C6-828
- V. BORTOLANI, A. FRANCHINI, F. NIZZOLI and G. SANTORO.- Surface lattice dynamics of nickel..... C6-831
- A. MURAMATSU and W. HANKE.- Microscopic theory of lattice dynamics and reconstruction of semiconductor surfaces..... C6-834
- J.E. BLACK, D.A. CAMPBELL and R.F. WALLIS.- Atomic vibrations at (100) surfaces of FCC and BCC metals..... C6-837
- A. FASOLINO, G. SANTORO and E. TOSATTI.- Effective mass approximation for surface phonon states..... C6-840
- P.A. THIRY, S.MAROTTE, J.J. PIREAUX, R. CAUDANO and A. ADNOT.- Adsorbate induced vibrations measured by EELS on a CuZn  $\alpha$  75/25 (110) surface during its early stage of oxidation..... C6-843
- A. FASOLINO, G. SANTORO and E. TOSATTI.- Surface phonons and the incommensurate reconstruction of clean Mo (100)..... C6-846
- J. THROWE and W.E. BRON.- Mode conversion coefficients of acoustic waves at a crystal-vacuum interface..... C6-849
- P. TABOREK, M. SINVANI, M. WEIMER and D. GOODSTEIN.- Time constant for phonon induced desorption of helium..... C6-852
- P. TABOREK, M. SINVANI, M. WEIMER and D. GOODSTEIN.- Polarization dependence of phonon induced desorption of He atoms at low temperatures..... C6-855
- B. FRISKEN, F. GUILLON, J.P. HARRISON and J.H. PAGE.- Low frequency phonons in sintered copper..... C6-858

#### PHONON ECHOES

- K. KAJIMURA.- Phonon echoes in bulk and powdered materials..... C6-863
- F. TSURUOKA and K. KAJIMURA.- Static polarization echoes in metal powders... C6-864
- J.O. FOSSUM, H.J. AUNE, K. FOSSHEIM and R.M. HOLT.- Echo properties of BGO and CdS..... C6-867
- D.J. MEREDITH, J.A. FRITCHARD and J.K. WIGMORE.- Backward wave phonon echoes at 17 GHz in single crystals of LiTaO<sub>3</sub>, LiNbO<sub>3</sub> and Bi<sub>12</sub>SiO<sub>20</sub>..... C6-870
- S. YOSHIKAWA and T. KIMURA.- Dipolar field fluctuation effects on phonon echoes in piezoelectric powder..... C6-873

XXX

- M. POIRIER, J.D.N. CHEEKE, P. MORISSEAU and A. HIKATA.- Attenuation of a static polarization echo by  $^4\text{He}$  film..... C6-876

**PHONON IN INSULATORS**

- V.C. SAHNI.- On the possible use of optical rotation measurements for detecting weakly IR active modes..... C6-881
- G.E. KUGEL, C. CARABATOS and W. KRESS.- Lattice dynamics of cuprite ( $\text{Cu}_2\text{O}$ ).. C6-884
- A.K. RAMDAS and S. RODRIGUEZ.- Time reversal symmetry and the Raman scattering by crystals..... C6-887
- M. HERITIER.- The phonon anomaly in b.c.c.  $\text{He}^4$  : a phonon self-trapping ?... C6-890
- M. LOCATELLI, R. SUCHAIL and E. ZECCHI.- A study of the Pb precipitation in NaCl from thermal conductivity experiments..... C6-893
- I. IWASA and H. SUZUKI.- Interaction of sound with vacancies in bcc  $^3\text{He}$  crystals..... C6-896
- S. DURAISWAMY and T.M. HARIDASAN.- Mean square displacements of a substitutional defect and its nearest neighbours in KI..... C6-899
- M.L. BANSAL, S.K. DEB, A.P. ROY and V.C. SAHNI.- Anomalous temperature dependence of a LO mode in  $\text{LiKSO}_4$ ..... C6-902
- K.R. BALASUBRAMANIAN and T.M. HARIDASAN.- A green's function study of the U centre in  $\text{BaClF}$  and  $\text{SrClF}$ ..... C6-905
- N. KRISHNAMURTHY and K. KESAVASAMY.- Phonon dispersions in calcium tungstate C6-908
- M.A. BALL and W.N. LEUNG.- The dielectric function matrix and the lattice dynamics of KCl..... C6-911
- P.W.M. JACOBS, M.A.H. NERENBERG, J. GOVINDARAJAN and T.M. HARIDASAN.- Calculation of defect entropies in ionic crystals in the quasi-harmonic approximation : application to fluorites..... C6-914
- M.B. PATEL and H.D. BIST.- Librational modes of water in crystal hydrates and phase-transitions..... C6-917
- T. HATTORI, T. IMANISHI, H. KUOKAWA and A. MITSUISHI.- Brillouin scattering in silver halides..... C6-920
- R.C. CASELLA.- Detection of impurity tunneling in solids via coherent phonon coupling and direct neutron scattering..... C6-923
- AUTHOR INDEX..... C6-927

PHONONS IN MIXED VALENCE COMPOUNDS

## PHONONS IN MIXED VALENCE COMPOUNDS

W. Kress, H. Bilz, G. Güntherodt\* and A. Jayaraman\*\*

*Max-Planck-Institut für Festkörperforschung, 7000 Stuttgart, F.R.G.**\*Universität Köln, F.R.G.**\*\*Bell Laboratories, Murray Hill, NJ, U.S.A.*

**Abstract.**— Several mixed-valence NaCl-structure compounds show strong anomalies in the phonon dispersion curves. These anomalies are related to the interaction of localized f-electrons with delocalized band electrons near the Fermi surface and to the isostructural phase transitions characterized by a softening of the bulk modulus. The lattice dynamics of these compounds is reviewed and the dispersion curves are analyzed in terms of a breathing shell model including various modifications. The relation between the phonon self-energies and the electronic band structure is discussed. In addition, the polarized Raman spectra are interpreted in terms of local cluster deformabilities of breathing and quadrupolar symmetry. Similarities and differences of phonon anomalies, Raman spectra and electronic band structure in semiconducting, superconducting and mixed valence compounds are pointed out.

**I. Introduction.**— Rare earth atoms are characterized by extremely localized, partly filled 4f shells. In solids most of the rare earth ions are trivalent with the exception of Sm and Eu in the middle and Tm and Yb at the end of the series. For these ions Hund's rule couplings become important and the divalent state is favored. In Sm, Eu, Tm, and Yb as well as in Ce compounds the  $4f^n(5d6s)^m$  and the  $4f^{n-1}(5d6s)^{m+1}$  states are energetically close and may become nearly degenerate when the external parameters (pressure, temperature) are changed. The same can happen if the composition is changed (e.g. by alloying). In these cases isostructural phase transitions into a homogeneous intermediate (non integer) valence phase have been observed. Since the screening of the Coulomb attraction of the core is significantly reduced when a localized 4f electron is promoted to the delocalized (5d6s) band large changes in volume occur.

The coexistence of two neighboring, nearly degenerate configurations  $4f^n(5d6s)^m$  and  $4f^{n-1}(5d6s)^{m+1}$  at equivalent rare earth ions leads to valence fluctuations for which the charge relaxation rate may be on the same time scale as the lattice vibrations. It can, therefore, be expected that the valence fluctuations manifest themselves not only in the electronic and magnetic properties of the rare earth compounds but also in the phonon spectra. Due to strong electron-pho-



non interactions, pronounced anomalies in the phonon dispersion curves are expected for those modes which are sensitive to the isotropic deformation of the charge density of the rare earth ions.

Experimental investigations of the lattice properties have revealed a number of characteristic features: (i) A soft bulk modulus<sup>1</sup> due to  $c_{12} < 0$  and anomalous mean square sulphur displacements of  $\text{Sm}_{1-x}\text{Y}_x\text{S}$  for  $x > 0.15$ <sup>2</sup>, (ii) a softening of the zone boundary phonons in semiconducting and metallic  $\text{SmS}$ <sup>3,4</sup>, (iii) anomalies in the phonon dispersion curves of  $\text{Sm}_{0.75}\text{Y}_{0.25}\text{S}$ <sup>5,6</sup>, (iv) a softening of the bulk modulus due to  $c_{12} < 0$  and anomalies in the phonon dispersion curves of  $\text{TmSe}$ <sup>7,8</sup>, (v) strong interaction of the 4f multiplet levels with phonons in  $\text{Sm}_{1-x}\text{Y}_x\text{Se}$  and  $\text{Sm}_{1-x}\text{Y}_x\text{S}$ <sup>9</sup>, and (vi) a softening of the zone center optic modes in  $\text{CePd}_3$ <sup>10</sup>.

Several theoretical approaches have been proposed for the treatment of the electron-phonon interactions and the description of the phonon anomalies of  $\text{Sm}_{0.75}\text{Y}_{0.25}\text{S}$ <sup>11-15</sup> and  $\text{SmS}$ <sup>4,16</sup> in its semiconducting as well as in its metallic phase. Recent calculations of the variation of the charge relaxation rates of rare earth ions as a function of their valence have provided a systematic understanding of the occurrence or absence of phonon anomalies in intermediate valence compounds<sup>17</sup>.

**II. Lattice dynamics.**— The electronic densities of states<sup>18-20</sup> and the phonon dispersion curves of  $\text{EuS}$ <sup>21</sup>,  $\text{SmS}$ <sup>22,23</sup>,  $\text{Sm}_{0.75}\text{Y}_{0.25}\text{S}$ <sup>5,6</sup> and  $\text{YS}$ <sup>24</sup> are shown schematically in Fig. 1. In  $\text{SmS}$  the filled 3p bands are separated by a band gap of about 3eV from the empty 5d and 6s bands. The localized 4f states and the Fermi level lie at the bottom of the conduction band. The phonon dispersion curves of  $\text{SmS}$  look like those of a typical ionic semiconductor. A comparison between the dispersion curves of  $\text{EuS}$  and  $\text{SmS}$  reveals, however, an incipient effect of intermediate valence in  $\text{SmS}$ . Compared to  $\text{EuS}$  the LO branch of  $\text{SmS}$  is lowered and the bulk modulus is decreased. The lowering at the  $\Gamma$ -point and at the L-point is due to an increased dipolar ( $\Gamma_{15}$ ) electronic deformability of the Sm ions and a breathing ( $\Gamma_1$ )<sup>+</sup> deformability of the Sm ions respectively, which also reduces the bulk

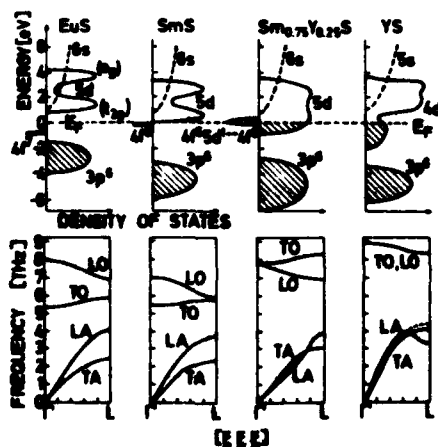


Fig. 1. Electronic densities of states and phonon dispersion curves.

modulus by about 15%. These effects are caused by the lowered 4f-5d promotion energy in SmS as compared to EuS.

When we go from SmS to YS we find a considerable change in the dispersion curves. YS is a superconductor with a partly filled 4d-5s band. The metallic screening of the conduction electrons leads to degenerate LO-TO phonons at the  $\Gamma$ -point. The degeneracy persists all along the  $\Lambda$  direction. This indicates that the long range Coulomb forces are screened out almost completely and that only nearest neighbor (nn) overlap forces are important. Therefore a neutral nn approach is a good starting point for the description of phonons in YS and in metallic intermediate valent  $\text{Sm}_{0.75}\text{Y}_{0.25}\text{S}$ .

As we have already seen in the discussion of SmS local electronic deformabilities are a very useful concept for understanding the special features<sup>25</sup> and, in particular, the anomalies in the phonon dispersion curves. Assuming radial coupling between nn in a NaCl lattice only three deformabilities are possible for each ion. Fig. 2 illustrates the different symmetry types. In an adiabatic multipole model the dynamical matrix becomes the sum of a rigid ion part and a deformability

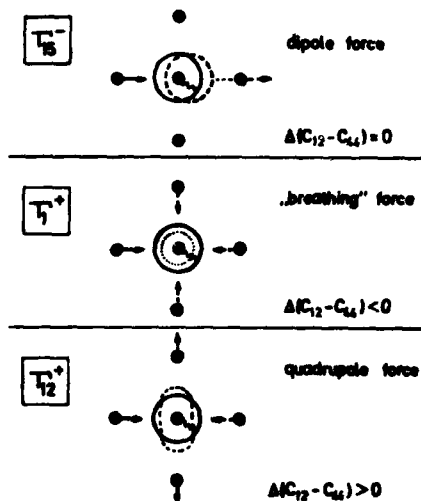


Fig. 2. Displacement-induced local deformabilities

Symm. of Deform.	Effect on	Observed in SmS	Observed in $\text{Sm}_{0.75}\text{Y}_{0.25}\text{S}$	Observed in YS	Microscopic origin
$\Gamma_1^+(\text{Sm})$	LO(L)	x	x		$4f^6 + 4f^5(5d^1)$
$\Gamma_{15}^-(\text{Sm})$	LA(CCC)	x	x		$4f^6 + 5d^1(4f^5)$
$\Gamma_{12}^+(\text{Sm})$	LO( $\Gamma$ )				
$\Gamma_{12}^+(\text{Sm})$	TO(L)				
$\Gamma_1^+(\text{S})$	LA(L)			x	$3d_{xy} + 3d_{xy}$
$\Gamma_{15}^-(\text{S})$	LO( $\Gamma$ )				
$\Gamma_{12}^+(\text{S})$	TA(L)				

Tab. 1. Local deformabilities

part which itself contains a sum over all possible symmetries. In Tab. I the effects which result in a decrease of the corresponding

phonon frequencies are summarized. We have already discussed the  $\Gamma_1^+$  and  $\Gamma_{15}^-$  deformabilities of the Sm ion in SmS. The LA(L) anomaly in YS (the dashed line in Fig. 1 indicates the normal dispersion curve) exhibits a breathing deformability of the S ion which may be caused by resonance-like valence  $d_{xy}$  conduction  $d_{xy}$  excitations near  $E_F$  since YS has not only Y  $4d_{xy}$  but also S  $3d_{xy}$  states near  $E_F$ .<sup>20</sup>

When going from YS to  $\text{Sm}_{0.75}\text{Y}_{0.25}\text{S}$ , the Fermi energy decreases

relative to the band edge and a large fraction of the  $S_{d_{xy}}$  states may become depopulated. If we look at the dispersion curves we see that the LA(L) anomaly has in fact disappeared. Instead, a new anomaly in the LA branch is found at smaller q-values where the LA-branch now lies below the TA-branch. At the same time the LO(L) frequency (which in YS was practically degenerate with the TO(L) frequency) is significantly lowered. Both effects result from a breathing deformability of the Sm ion arising from virtual Sm  $4f \rightarrow 5d$  state excitations, which are characteristic of the mixed-valent state. In addition to the splitting of the LO and TO phonons at the L-point we observe a lowering of the optic modes at  $\Gamma$ . This is consistent with a dipolar deformability at the Sm-ion caused by the hybridization of the Sm  $4f$ -levels with d-states of S, Sm and Y.

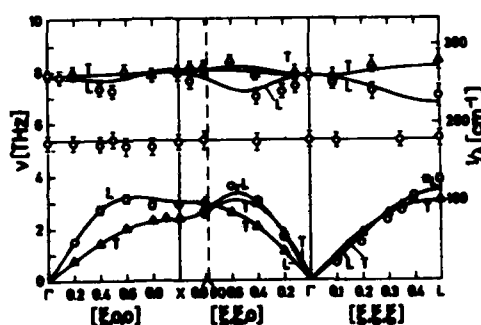


Fig. 3. Phonon dispersion curves of  $\text{Sm}_{0.75}\text{Y}_{0.25}\text{S}$ .

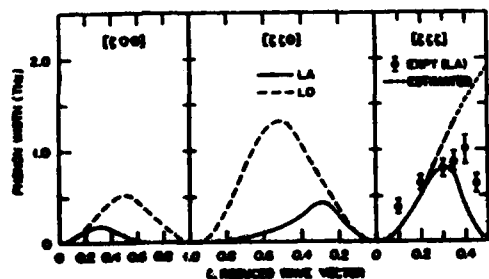


Fig. 4. Phonon width for longitudinal  
modes<sup>5,6,15</sup>

Fig. 3 shows the results of our calculations<sup>13</sup>. Only five parameters have been used: two nn overlap force constants a breathing and a dipolar S<sub>m</sub> deformability (which are assumed to be equal) and a quadrupolar S deformability which lifts the degeneracy of the TA(X) and LA(X) and may be interpreted as a remainder of the Coulomb interaction. In view of the simplicity of our model the agreement with experiment is quite satisfactory.

Recent calculations of Wakabayashi<sup>15</sup> show that the model can also account for the wave vector dependent lifetimes of the longitudinal phonons if the relaxation of the electronic system is taken into account. Fig. 4 shows that the line widths calculated<sup>15</sup> with a relaxation time of  $4 \cdot 10^{-14}$  s compare well with the experimental results<sup>5,6</sup>.

Using essentially the same model we have been able to reproduce rather well the phonon dispersion curves of TmSe measured recently<sup>26</sup>. The results are given in Fig. 5.

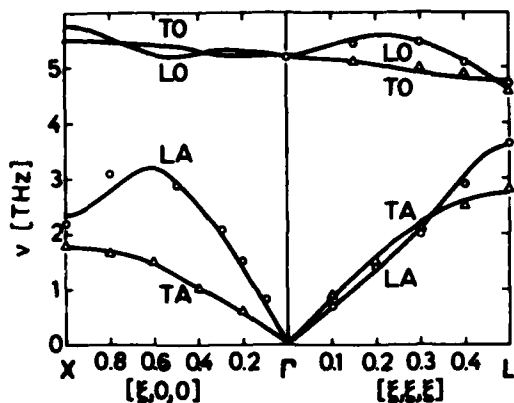


Fig. 5. Phonon dispersion curves of TmSe.

It is seen from the splitting of the LO( $\Lambda$ ) and TO( $\Lambda$ ) branches that for shorter wavelengths the Coulomb contributions play an important role and have to be included in the calculation. In addition to the parameters used for the calculation of  $\text{Sm}_{0.75}\text{Y}_{0.25}\text{S}$  we take into account screened Coulomb and weak Tm-Tm interactions.

**III. Raman Scattering.**— So far we have parametrized the electron-lattice interaction in terms of local cluster deformabilities and found that three deformabilities (breathing, quadrupolar and dipolar) were sufficient to describe the anomalous part of the phonon dispersion curves. We show now that the relevant features of the polarized Raman spectra are due to the same deformabilities which cause the strong anomalies in the phonon dispersion curves. For this purpose we expand the polarization operators  $P_{\alpha\beta}(\mathbf{r})$  into normal coordinates  $A(\mathbf{q},j)$  and impurity-induced distortions  $B(\mathbf{q},\kappa)$  at lattice site  $\kappa$ . The first-order terms read as follows

$$\sum_{\kappa} P_{\alpha\beta}(\mathbf{q},j,\kappa) B(-\mathbf{q},\kappa) A(\mathbf{q},j) = \tilde{P}_{\alpha\beta}(\mathbf{q},j) A(\mathbf{q},j)$$

This equation describes the symmetry breaking effect of the impurities with respect to the  $\mathbf{q}$  selection rule, so that  $\tilde{P}_{\alpha\beta}(\mathbf{q},j) \neq 0$  for  $\mathbf{q} = 0$ . Instead of using a many parameter fit of the expansion coefficients of  $P_{\alpha\beta}(\mathbf{q},j)$  in ordinary space we use cluster related projection operators to calculate the components of the Raman spectra which correspond to the different cluster deformabilities. The scaling factors for the partial spectra related to the cluster deformability of symmetry  $\Gamma_1$  at the central cluster ion  $\kappa$  are taken as parameters.

In Fig. 6 we compare our polarized Raman scattering data for  $\text{SmS}$ <sup>27</sup> (upper part) with the results of our calculation (lower part). The bold lines in the lower part represent the one-phonon density of states weighted by  $(n(\mathbf{q},j)+1)/\omega(\mathbf{q},j)$ . This is the simplest approach to the Raman density and gives only a very poor description of the measured

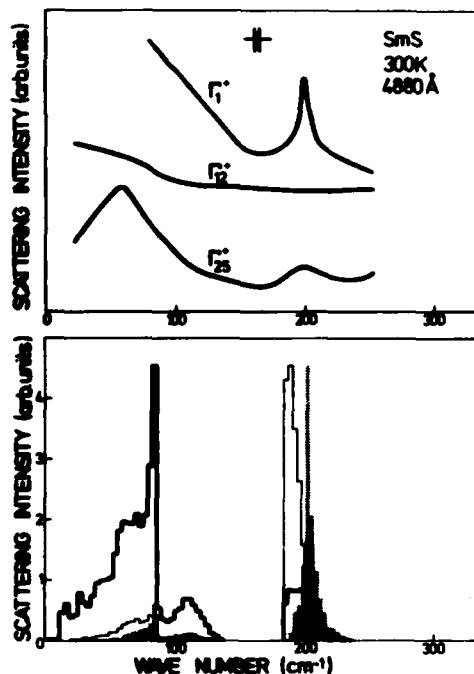


Fig. 6. Polarized Raman spectra<sup>27</sup> of SmS (upper part). Lower part; weighed one phonon density: bold line; breathing contribution: hatched area; quadrupolar contribution: thin line.

245 cm<sup>-1</sup> and the weaker one near 85 cm<sup>-1</sup>. The results of the calculation (shaded curve) show that these structures are caused by the breathing deformability of the Sm-ions.

From our lattice dynamical analysis we expect a strong  $\Gamma_1^+$  deformability of S in YS. The Raman scattering data<sup>27</sup> confirm this interpretation (Fig. 8). The intensity near 210 cm<sup>-1</sup> arises from second order acoustic phonon scattering which is not included in our calculations.

Our analysis of TiN shows that the Raman spectrum<sup>28</sup> is made out of two nearly equal contributions from the breathing and quadrupolar deformabilities at the N site which are represented in Fig. 9 by shaded spectra enclosed by full and dashed lines, respectively. This is again in agreement with the analysis of the phonon dispersion curves where the LA(L) and TA(L) anomalies indicate  $\Gamma_1^+$  and  $\Gamma_{12}^+$  deformabilities of the N ions, respectively. TiN belongs to the group of transition metal compounds for which detailed microscopic studies have been carried out<sup>30-32</sup>. TiN shows dynamical Ti(d<sub>xy</sub>)-N(2p) hybridization, which leads to periodic charge fluctuations between the open d- and p-

spectra. However, taking into account the impending valence instability of Sm by a breathing response ( $\Gamma_1^+$ ) of the charge density around the Sm ion, we obtain the shaded curve, which explains nicely the strong  $\Gamma_1^+$  Raman scattering near 200 cm<sup>-1</sup>. An effect of a quadrupolar  $\Gamma_{12}^+$  deformability of the Sm-ion has been detected neither in the Raman spectra nor in the phonon dispersion curves. The effect of such a deformability would lead to the spectrum represented by thin lines in the lower part of Fig. 6. A qualitative analysis of the  $\Gamma_{25}^+$  contribution near 60 cm<sup>-1</sup> shows that it is consistent with S-S interactions.

The most interesting spectrum is of course the mixed valent Sm<sub>0.75</sub>Y<sub>0.25</sub>S<sup>27</sup> (Fig. 7) which is clearly dominated by the prominent  $\Gamma_1^+$  scattering intensity near

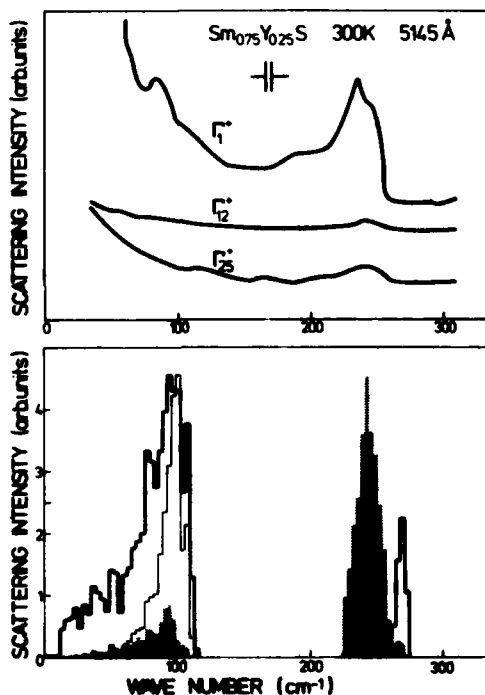


Fig. 7. Polarized Raman spectra<sup>27</sup> of  $\text{Sm}_{0.75}\text{Y}_{0.25}\text{S}$ . Notation as in Fig. 6.

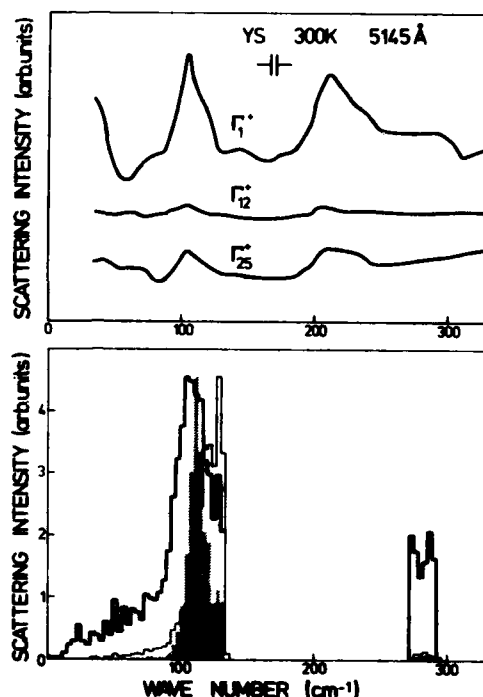


Fig. 8. Polarized Raman spectrum<sup>27</sup> of YS. Notation as in Fig. 6.

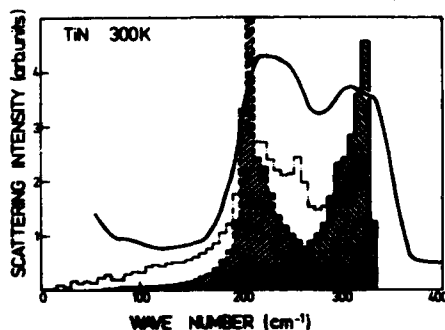


Fig. 9. Raman spectrum of  $\text{TiN}_{0.95}$ .

shells of Ti and N, respectively. The symmetry of purely radial charge deformations of the (pd $\pi$ )-overlap leads, in a first approximation, to equal strength of the breathing and the quadrupolar deformability of the N site. In YS the pd coupling is less effective and largely replaced by  $d_{xy}$ - $d_{xy}$  excitations which lead to a breathing deformation only. In  $\text{Sm}_{0.75}\text{Y}_{0.25}\text{S}$  the local symmetry of the Sm site

imposed by the Y impurities is consistent with radial  $\Gamma_1^+$  and  $\Gamma_{15}$  deformations but incompatible with the  $\Gamma_{12}^+$  quadrupolar symmetry, which has neither been observed in the Raman nor in the phonon spectra.

**IV. Summary and Conclusions.**— We have shown that the phonon dispersion curves, the phonon line width and the Raman spectra of a variety of materials ranging from semiconductors to superconducting transition metal compounds and including the mixed valent compounds can be described successfully in terms of deformabilities of breathing, dipolar and quadrupolar symmetry.

### References

1. T. Penney, R.L. Melcher, F. Holtzberg, and G. Güntherodt, AIP Conf. Proc. 29, 392 (1975)
2. P.D. Dernier, W. Weber and L.D. Longinotti, Phys. Rev. B 14, 3635, (1976)
3. G. Güntherodt, R. Keller, P. Grünberg, A. Frey, W. Kress, R. Merlin, W.B. Holzapfel, and F. Holtzberg, p. 321 in Ref. 32.
4. G. Güntherodt, R. Merlin, A. Frey, and M. Cardona, Solid State Commun. 27, 551 (1978)
5. H.A. Mook, R.M. Nicklow, T. Penney, F. Holtzberg, and W.M. Shafer, Phys. Rev. B 18, 2925 (1978)
6. H.A. Mook and R.M. Nicklow, Phys. Rev. B 20, 1656 (1979)
7. A. Treindl and P. Wachter, Solid State Commun. 32, 573 (1979)
8. H. Boppart, A. Treindl, P. Wachter and S. Roth, to be published
9. G. Güntherodt, A. Jayaraman, E. Anastassakis, E. Bucher, and H. Bach, to be published
10. B. Hillebrands, G. Güntherodt, R. Pott, A. Breitschwerdt, and W. König, to be published
11. K.H. Bennemann and M. Avignon, Solid State Commun. 31, 645 (1979)
12. N. Grewe and P. Entel, Z. Phys. 33, 331 (1979)
13. H. Bilz, G. Güntherodt, W. Kleppmann, and W. Kress, Phys. Rev. Lett. 43, 1998 (1979)
14. P. Entel, N. Grewe, M. Sietz, and K. Kowalski, Phys. Rev. Lett. 39, 2002 (1979)
15. N. Wakabayashi, Phys. Rev. B 22, 5833 (1980); see also: T. Matsura, R. Kittler, and K. Bennemann, Phys. Rev. B 21, 3467 (1980)
16. K. Baba, M. Kobayashi, H. Kaga, and J. Yokota, Solid State Commun. 35, 175 (1980)
17. E. Müller-Hartmann, Proc. Taniguchi Symp. on "Electron Correlation and Magnetism in Narrow Band Systems", to be published
18. G. Güntherodt and P. Wachter, in Proc. 12 Int. Conf. Phys. Semicond. ed. M.H. Pilkuhn (Teubner, Stuttgart, 1974) p. 899
19. B. Batlogg, E. Kaldis, A. Schlegel, and P. Wachter, Phys. Rev. B 14, 5503 (1976)
20. J.A. Appelbaum and D.R. Hamann, in Physics of Transition Metals-1977, ed. M.J. Lee, J.M. Perz and E. Fawcett, AIP Conf. Proc. 39 (1978)
21. R. Zeyher and W. Kress, Phys. Rev. B 20, 2850 (1979)
22. G. Güntherodt, R. Keller, P. Grünberg, A. Frey, W. Kress, R. Merlin, W.B. Holzapfel, and F. Holtzberg, p. 321 in Ref. 32.
23. R.J. Birgenau and S.M. Shapiro, p. 49 in Ref. 32
24. P. Roedhammer, W. Reichardt, and F. Holtzberg, Phys. Rev. Lett. 40, 465 (1978)
25. H. Bilz, in Computational Solid State Physics, ed. by F. Herman, N.W. Dalton and T.R. Koehler (Plenum, New York, 1972) p. 309
26. H.A. Mook and F. Holtzberg, in Ref. 33
27. G. Güntherodt, A. Jayaraman, W. Kress and H. Bilz, Phys. Lett. 82A, 26, (1981) and in Ref. 33
28. W. Spengler, R. Kaiser, A.N. Christensen and G. Müller-Vogt, Phys. Rev. B 17, 1055 (1978)
29. S.K. Sinha and B.N. Harmon, Phys. Rev. Lett. 35, 1515 (1975)
30. W. Hanke, J. Hafner and H. Bilz, Phys. Rev. Lett. 37, 1560 (1976)
31. C.M. Varma and W. Weber, Phys. Rev. Lett. 39, 1094 (1977)
32. Valence Instabilities and Related Narrow-Band Phenomena, ed. R.D. Parks (Plenum, New York, 1977)
33. Proc. Int. Conf. on Valence Fluct. in Solids, Santa Barbara 1981 North Holland, to be published.

# PHONON AND ELASTIC ANOMALIES IN INTERMEDIATE VALENT $\text{Tm}_x\text{Se}$ AND $\text{TmSe}_{1-y}\text{Te}_y$

M. Celio, R. Monnier and P. Wachter

Laboratorium für Festkörperphysik, ETH Zürich, 8093 Zürich, Switzerland.

**Abstract.**— In  $\text{Tm}_x\text{Se}$  and  $\text{TmSe}_{1-y}\text{Te}_y$  the degree of valence mixing can be adjusted between nearly  $3+$  for  $\text{Tm}_{0.87}\text{Se}$  and  $2.55+$  for  $\text{TmSe}_{0.7}\text{Te}_{0.3}$ . The sound velocity  $v_L$  decreases with increasing degree of valence mixing and the elastic constant  $c_{12}$  becomes negative. The first order Raman spectrum shows an additional peak at  $60\text{ cm}^{-1}$  for strong valence mixing and a softening of the LO (L) frequency. The experiments are compared with the calculation of an 8 parameter shell model resulting in projected density of phonon states.

$\text{TmSe}$  is one of the most interesting intermediate valent (IV) materials inasmuch as it is IV at ambient pressure and its degree of valence mixing can be adjusted by composition ( $\text{Tm}_x\text{Se}^{1)}$  or by alloying with other ions<sup>2)</sup>. Thus the valence as determined by the lattice constant is nearly  $3+$  for  $\text{Tm}_{0.87}\text{Se}$  and  $2.55+$  for  $\text{TmSe}_{0.7}\text{Te}_{0.3}$ <sup>3)</sup>. On these compositions we have performed Raman scattering, ultrasound velocity and elastic measurements<sup>4)</sup>. In these rocksalt type structures the Raman effect measures a defect induced weighted one phonon density of states<sup>3)</sup> which is displayed in Fig. 1a for 4 different compositions of  $\text{Tm}_x\text{Se}$ . The curve

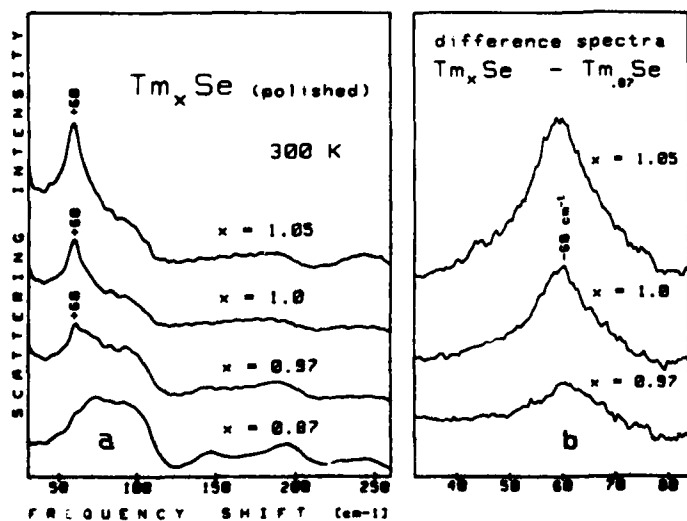


Fig. 1a: Raman spectra of trivalent  $\text{Tm}_{0.87}\text{Se}$  and intermediate valent  $\text{Tm}_x\text{Se}$ .

Fig. 1b: Contribution of the anomalous peak at  $60\text{ cm}^{-1}$  to the scattering intensity, computed by subtraction of the trivalent spectra.



for the trivalent  $x=0.87$  at the bottom of Fig.1a is identical to other trivalent selenides like GdSe or LaSe and corresponds to TA and LA phonon densities in the low energy range and TO and LO densities for the higher energy peaks<sup>5)</sup>. As one increases the degree of valence mixing,  $x \rightarrow 1.05$ , a significant peak at  $60 \text{ cm}^{-1}$  is emerging within the acoustic region which is shown in more detail in Fig.1b. Also with increasing valence mixing the high energy edge of the LO band softens and merges with the TO band. This softening of the LO band between a  $\text{Tm}_{0.87}^{3+}\text{Se}$  and a hypothetical  $\text{Tm}^{2+}\text{Se}$ , but a real  $\text{Yb}^{2+}\text{Se}$ , is shown in more detail in Fig. 2, where for comparison also the much smaller softening of the trivalent series  $\text{Tm}_{0.87}^{3+}\text{Se}$  - LaSe due to the lanthanide contraction is displayed.

The sound velocities  $v_L, v_{T1}$  and  $v_{T2}$  have also been measured and the elastic constants  $c_{11}, c_{12}$  and  $c_{44}$  have been derived<sup>4)</sup>. With increasing valence mixing  $v_L$  reduces from  $3.48 \cdot 10^5 \text{ cm/sec}$  for  $\text{Tm}_{0.37}\text{Se}$  to  $2.56 \cdot 10^5 \text{ cm/sec}$  for  $\text{Tm}_{0.99}\text{Se}$ . At the same time  $c_{12}$  becomes negative, going from  $2.1 \cdot 10^{11} \text{ erg/cm}^3$  to  $-5.7 \cdot 10^{11} \text{ erg/cm}^3$ , respectively. As a consequence the compressibility rises from  $1.46 \cdot 10^{-6} \text{ bar}^{-1}$  for  $\text{Tm}_{0.87}\text{Se}$  to  $4.61 \cdot 10^{-6} \text{ bar}^{-1}$  for  $\text{Tm}_{0.99}\text{Se}$ . These elastic anomalies persist down to 4.2 K.

A softening of LO(L)- and LA( $\Lambda$ ) phonons with increasing degree of valence mixing has been predicted already<sup>6)</sup> and is well born out by the experiment (see above). The negative  $c_{12}$  for IV TmSe has a dominant effect for  $v_L|111|$  which becomes even less than  $v_T|111|$ , forcing the LA

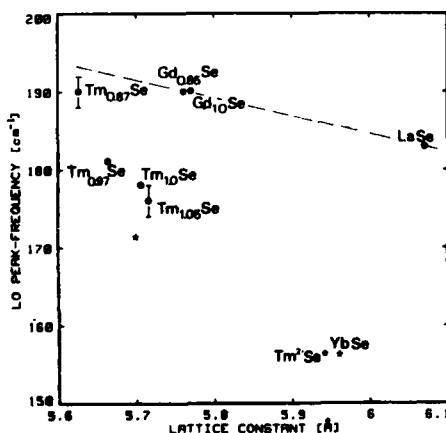


Fig.2: Peak position of the LO band of Tm Se, Gd Se and LaSe. Stars:  $\omega_{LO}(L)$  in shell model calculation.

branch below the TA branch, Since no softening of the LA(L) is expected<sup>6)</sup>, a qualitative LA $|111|$  dispersion has been constructed which indicates for the anomalous Raman peak at  $60 \text{ cm}^{-1}$  mainly a density of states effect<sup>3)</sup>. A different point of view has been taken<sup>7)</sup> by assuming that the electron-phonon matrix elements of the  $\Gamma_1^+$  breathing mode enhance the Raman intensity of those parts of the phonon dispersion curves which soften for IV.

We have calculated the phonon spectrum of IV TmSe by using an 8 para-

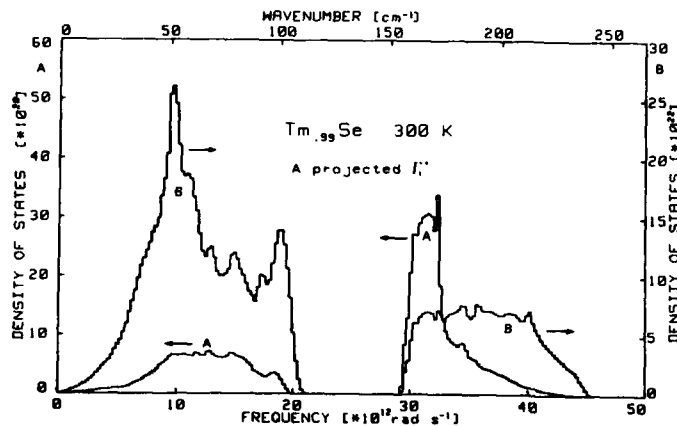


Fig. 3: Phonon density (B) and projected  $\Gamma_1^+$  density of states (A) of IV TmSe.

The parameters were adjusted using the lattice constant,  $c_{11}$ ,  $c_{12}$  and  $c_{44}$ <sup>4)</sup> and  $\omega_{TO}$  and  $\omega_{LO}$  at the  $\Gamma$  and L points<sup>8)</sup>. The continuum character of the 5d electrons is reflected in a high polarizability of the Tm ions. However, density functional results for the charge distribution around a trivalent impurity in an electron gas at the corresponding density indicate that the induced charge is too localized to effectively screen out the long range Coulomb interaction between the ions, thereby justifying the use of a shell model for the description of that system. The measured dispersion curves<sup>8)</sup> are reasonably well reproduced by our model in the  $|100|$  and  $|110|$  direction, but essential differences appear in the  $|111|$  direction, where the life time broadening of the longitudinal modes is especially large. In Fig. 3 we show the one phonon density of states (B) which should be compared with the experimental curve of Fig. 1a for Tm<sub>1.0</sub>Se. Very good agreement is obtained. In Fig. 3 (A) we also display the  $\Gamma_1^+$  projected density of states which is not very pronounced at the experimentally determined 60 cm<sup>-1</sup> peak, which thus is mainly due to a density of states effect from flat regions in the phonon dispersion along  $|100|$  and  $|110|$  near X.

meter shell model with deformable ions. The dynamical matrix  $D(\vec{q})$  is  $D(\vec{q}) = D_{RI}(\vec{q}) + D_{shell}(\vec{q}) + D_{def}(\vec{q})$  with  $D_{RI}$  the point charge rigid ion matrix,  $D_{shell}$  the matrix for a simple shell model and  $D_{def}$  accounting for the breathing ( $\Gamma_1^+$ ) of the Tm ion and a quadrupolar deformability ( $\Gamma_{25}^+$ ) of the Se

- 1) B. Batlogg, H.R.Ott, E.Kaldis, W.Thöni and P.Wachter, Phys. Rev. B 19, 247 (1979)
- 2) B. Batlogg, Phys. Rev. B 23, 650 (1981)
- 3) A. Treindl and P. Wachter, Solid State Commun. 36, 901 (1981)
- 4) H. Boppart, A. Treindl, P. Wachter and S. Roth, Solid State Commun. 35, 489 (1980)
- 5) A. Treindl and P. Wachter, Phys. Lett. 64 A, 147 (1977)
- 6) K.H. Bennemann and M. Avignon, Solid State Commun. 31, 645 (1979)
- 7) H. Bilz, G. Güntherodt, W. Kleppmann and W. Kress, Phys. Rev. Lett. 43, 1998 (1979)
- 8) H.A. Mook and F. Holtzberg, Int. Conf. Valence Fluctuations in Solids, Santa Barbara, Calif., Jan. 27-30, (1981)

PHONON SOFTENING IN INTERMEDIATE VALENT  $\text{SmB}_6$ 

I. Mörke and P. Wachter

*Laboratorium für Festkörperphysik, ETH Zürich, 8093 Zürich, Switzerland*

**Abstract.**— We have measured the Raman spectrum of a  $\text{SmB}_6$  single crystal and compared it to  $\text{LaB}_6$  and  $\text{EuB}_6$ . Beside the three high energy Raman active phonons we found additional excitations in these compounds. Most prominent is a peak at  $172 \text{ cm}^{-1}$  for  $\text{SmB}_6$ ,  $214 \text{ cm}^{-1}$  for  $\text{LaB}_6$  and  $220 \text{ cm}^{-1}$  for  $\text{EuB}_6$ . The spectra are analysed in terms of defect induced phonon scattering. The softening of the line in intermediate valent (IV)  $\text{SmB}_6$  is explained in analogy with the phonon anomalies found in other IV compounds.

$\text{SmB}_6$  is of special interest among the rare earth hexaborides because the Sm ion has a non integer valence of 2.6. To examine the influence of intermediate valence (IV) on the first order, forbidden Raman scattering, we have remeasured the spectra of a  $\text{SmB}_6$  single crystal and compared it to  $\text{LaB}_6$  and  $\text{EuB}_6$ . The hexaborides crystallize in the  $\text{CaB}_6$  structure of space group  $\text{O}_h^1$  ( $\text{Pm}\bar{3}\text{m}$ ). For this structure there are three Raman active phonon modes of  $A_{1g}$ ,  $E_g$  and  $F_{2g}$  symmetry. Beside these three modes our measurements show additional shoulders in both spectra. The most prominent structure is a peak at  $172 \text{ cm}^{-1}$  for  $\text{SmB}_6$ , and  $214 \text{ cm}^{-1}$  for  $\text{LaB}_6$  (Fig.1). The absence of magnetic ordering in  $\text{SmB}_6$  and  $\text{LaB}_6$  and of electronic excitations, in  $\text{LaB}_6$  (the ground state of  $\text{La}^{3+}$  is  $1s_0$ ) is the reason why we are going to interpret this part of the spectra in terms of phonon scattering only. The selection

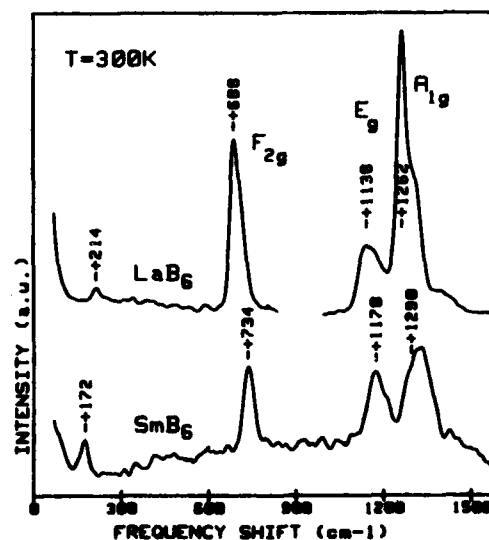


Fig.1 Room temperature Raman Spectrum of  $\text{SmB}_6$  and  $\text{LaB}_6$  single crystals.

rules for Raman scattering may be lifted by crystal defects. This effect yields a weighted phonon density of states in the spectra (1). The peak at  $172\text{ cm}^{-1}$  in IV  $\text{SmB}_6$  is of special interest because it is about  $40\text{ cm}^{-1}$  softer than the corresponding excitation in metallic  $\text{LaB}_6$ . The frequencies of the Raman active modes of the other  $\text{MB}_6$  are in semiconducting compounds always higher than in the metallic samples (2). This is confirmed on a  $\text{Eu}^{2+}\text{B}_6$  powder sample which shows a weak broad excitation at  $220\text{ cm}^{-1}$ . Furthermore a softening of the bulk modulus has been observed in  $\text{SmB}_6$ .  $B=139\text{ GPa}$ ,  $191\text{ GPa}$  and  $157\text{ GPa}$  for  $\text{SmB}_6$ ,  $\text{LaB}_6$  and  $\text{EuB}_6$ , respectively (3).

Softening of zone boundary phonons and of the bulk modulus are the striking effects caused by the electron phonon interaction in IV compounds (4). In IV compounds with NaCl structure the phonons mostly affected by the coupling to the RE ion are those where planes of anions move against planes containing only the IV ions (5). Such a vibration is expected at the X-point in the  $\text{CaB}_6$  structure. The symmetry of normal modes at this point is (we put the origin of the coordinate system in the center of the boron octahedron):

$$3A_{1g} + A_{2g} + B_{1g} + B_{2g} + 3E_g + 2A_{2u} + B_{2u} + 3E_u$$

The compatibility relations are given in Fig. 2. The two modes of  $A_{2u}$  symmetry are those where planes of B ions move in  $[100]$  direction against planes of Sm ions (Fig. 3).

Although it is not possible on the basis of the Raman scattering experiment alone to be sure that the observed low frequency line coincides with either of these  $A_{2u}$  modes, there are some important arguments which favour such an interpretation. One is by taking a suitable linear combination of both  $A_{2u}$  modes, one can deal with the movement of the center of gravity of the whole  $\text{B}_6$  octahedron. Comparing the mass of  $\text{B}_6$  with that of a single boron atom, one may expect this vibration to have a low frequency. A further argument is deduced directly from the compatibility relations (Fig.2). A mode

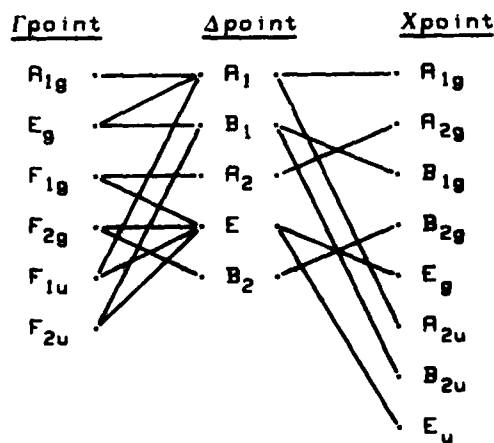


Fig. 2 Compatibility relations for different symmetry points

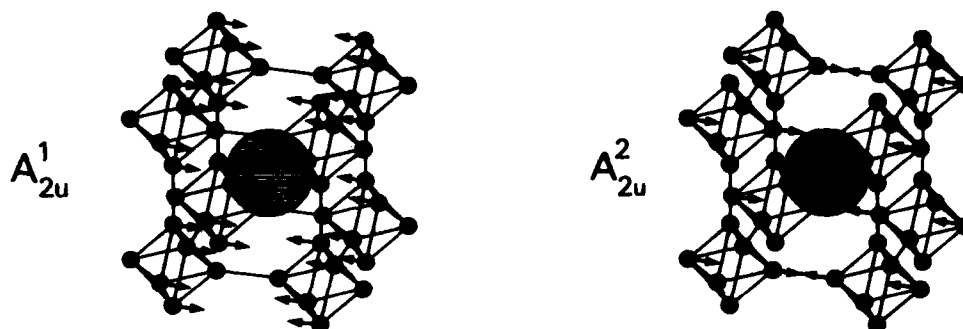


Fig.3. Normal modes of the two  $A_{2u}$  modes of  $\text{SmB}_6$  at the X-point.

of  $A_{2u}$  symmetry at the X-point may be either of  $A_{1g}$  or  $E_g$  or  $F_{1u}$  symmetry at the  $\Gamma$ -point. The  $\Gamma$ - $A_{1g}$  has the highest frequency in the hexaborides of about  $1300 \text{ cm}^{-1}$ . One would not expect this mode to be of the order of  $200 \text{ cm}^{-1}$  at the zone boundary. The same argument holds for the  $\Gamma$ - $E_g$  mode. If one looks at the  $F_{1u}$  modes, one of which is the acoustical, one finds two vibrational modes showing exactly the same atom displacements as for the two  $A_{2u}$  modes. The only difference is that at the  $\Gamma$ -point all unit cells move in phase whereas at the X-point neighboring planes of unit cells in X direction move in antiphase. The  $F_{1u}$  mode is expected to be of lower frequency than the  $A_{1g}$  mode. The softening of the low frequency line is thus tentatively explained in terms of a Raman inactive LO (X) mode which couples most strongly to the volume fluctuations.

1. A.Treindl, P.Wachter, Solid State Communications 32, 573 (1979)
2. M. Ishii, T.Tanaka, E.Bannai, S.Kawai, J.Phys. Soc.Japan 41, 1075 (1976)
3. H.E. King, Jr., S.J.La Placa, T.Penney, Z.Fisk, Int. Conf. on Val. Fluctuations in Solids St.Barbara, Jan. 1981
4. K.H. Bennemann, M.Avignon, Solid State Commun. 31, 645 (1979)
5. H.Bilz, G.Güntherodt, W.Kleppmann, W.Kress, Phys.Rev. Lett, 43, 1998 (1979)

PHONONS IN AMORPHOUS AND DISORDERED SYSTEMS

## PHONONS IN AMORPHOUS MATERIALS

M.F. Thorpe

*Physics Department, Michigan State University, East Lansing, MI 48824, U.S.A.*

**Abstract.**- A brief review is given of phonons in amorphous materials as seen in Raman scattering, infrared absorption and inelastic neutron scattering. It is shown that phonons (i.e. quantised harmonic vibrations) are well defined in network structures and a description is given of the standard theoretical technique which is to build a finite model and then use one of a number of numerical techniques to obtain the eigenvalue spectrum of the dynamical matrix. Particular emphasis is given to newer theoretical techniques that do not require the building of a model. The results are illustrated with reference to experiments in elemental semiconductors like Si and Ge and two component glasses like  $\text{SiO}_2$ ,  $\text{GeS}_2$ , etc.

1. **Introduction.**- The vibrational spectra of amorphous solids and glasses have been extensively studied particularly in the last decade. The principle experimental techniques used are inelastic neutron scattering, Raman scattering and infra-red absorption. Although there is no one theoretical approach that can explain all aspects of these vibrational spectra, the main features are now understood. However, many significant details remain to be put in place.

We will try to briefly review the most important theoretical techniques that are available to calculate the phonon spectra of glasses. The results are illustrated mainly with a. Si and a.  $\text{SiO}_2$  on which most work has been done. More exotic types of glasses have also been studied but less theoretical progress has been made on these.

2. **Model Building and Numerical Methods.**- The standard and most successful calculations of phonon spectra have involved numerical methods on particular models. It is of course essential to know the structure of a glass before proceeding to calculate the vibrational spectrum.

The earliest of these models were hand built ball and stick models of a.  $\text{SiO}_2$ <sup>(1)</sup>. These were based on the known local bonding arrangements and typically contained ~ 300 atoms in a roughly spherical cluster. Bell and Dean<sup>(1)</sup> used these models to set up a dynamical matrix using the Born model which has nearest neighbor central and non-central forces. The eigenvalue spectrum was obtained as a histogram using the negative eigenvalue theorem.

In figure 1 we show a recent comparison between theory and an inelastic neutron scattering experiment<sup>(2)</sup> for  $\text{SiO}_2$ . The experiment is done at large wave vector transfer so that essentially the density

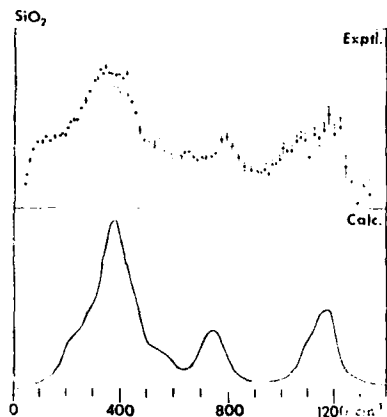


Fig. 1 : A comparison<sup>(3)</sup> between experiment and theory for inelastic neutron scattering in a.  $\text{SiO}_2$ . [Adapted from reference 3.]

of states is measured. This has the disadvantage that the multiphonon background has to be subtracted. This is indicated in the figure by the dashed line<sup>(2)</sup>. The theory is the density of states weighted by the appropriate neutron scattering lengths for Si and O. The agreement overall is impressive.

Similar calculations<sup>(3)</sup> have been performed for the Raman and I.R. spectra. Again reasonably good agreement is obtained. However, the matrix elements are difficult to put in as they are not simple as in neutron scattering. Usually some local bond polarisabilities are introduced which have the correct symmetry. This introduces a major theoretical uncertainty that is not present in inelastic neutron scattering.

Similar work has also been done on a. Si. Hand built models have been constructed by many groups. While the hand construction fixes the topology of the network, the positions of the atoms can be refined by relaxing according to a suitably chosen potential.<sup>(5)</sup> The equation of motion method has been used by Alben and collaborators to determine all quantities of interest [density of states, Raman scattering, I.R. absorption and the neutron scattering law  $S(\vec{Q}, \omega)$ ]. The method tracks the behavior of the displacements with time and then Fourier transforms. It can be used in any harmonic system that is disordered. Good overall agreement is achieved between theory and experiment using this method<sup>(4), (6)</sup>.

The negative eigenvalue theorem was used to construct histograms for the density of states<sup>(1)</sup> for  $\text{SiO}_2$  type glasses. To calculate other quantities, sample eigenvectors must be obtained. This method could also be applied to a. Si as could the equation of motion method be applied to  $\text{SiO}_2$  type glasses. It is an accident of history that this



has not happened.

It is particularly difficult to calculate the I.R. absorption in elemental glasses because there is no I.R. absorption in the corresponding crystal usually. A new mechanism must be invoked. Two have been suggested; dipole moments associated with three near neighbor atoms<sup>(4)</sup> or fluctuating dynamic charges on all the atoms.<sup>(7)</sup>

Direct diagonalisation of the dynamical matrix for a finite model is now rarely used as it is inefficient.

These numerical techniques may be regarded as providing a solution to the problem - although some effects such as those produced by the long range Coulomb forces have yet to be included. However, they do not often provide a great deal of insight and calculations must be repeated every time a change is made in the model - such as increasing the local distortions or changing the masses. For this reason, more analytic approaches are now being pursued.

3. Beyond Numerical Methods. - Some progress has been made in two directions. The phonon spectrum of a Bethe lattice<sup>8</sup> can be obtained using Born forces for a. Si. This shows many features in common with the density of states of crystalline Si although the van Hone singularities and some other features are absent. (see fig. 2)

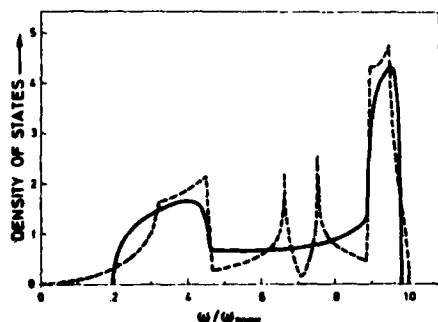


Fig. 2 : Showing the density of states for crystalline Si in the diamond structure (solid line) and the Bethe lattice (dashed line). [From reference 8.]

This or other Bethe lattices can be tied onto small pieces of network and used as a convenient boundary condition in the "Cluster - Bethe - lattice" method. This avoids the large effects that the free surfaces of small clusters can produce. A review of this method contains many of the results obtained to date<sup>(7)</sup>. Good agreement with experiment is obtained in many cases.

The other approach is to keep only the central forces and completely neglect the non-central forces. This is not an unreasonable starting point as the non-central forces are typically only ~20% of the nearest neighbor central force. Within this scheme the problem is essentially

soluble<sup>9</sup> and very simple expressions are obtained for the positions and widths of the main peaks in the density of states. These are particularly valuable when the network is modified in some simple way. For example  $O^{18}$  can be substituted for  $O^{16}$  and the Raman spectra of the two glasses compared.<sup>10</sup> It may be possible eventually to include non-central forces and Coulomb forces in this model using perturbation theory.

4. Future Prospects. Although many Raman and I.R. experiments have been performed on many glasses whose structure is known, progress has been hampered by the absence of a good knowledge of the optical matrix elements. Recent work by Martin and Galeener<sup>(11)</sup> has shown that these matrix element effects are extremely important and can produce peaks in the optical spectra where none exist in the density of states (see figure 3).

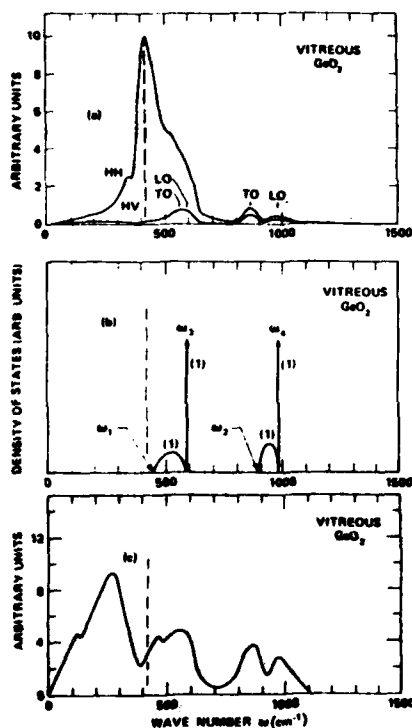


Fig. 3 : Showing the Raman scattering, density of states in the central force model, and measured weighted density of states from neutron scattering. [Reproduced from ref. 11.]

The clearest measurements to interpret theoretically are from inelastic neutron scattering. However, the measurements at large  $Q$  have problems with multiphonon scattering. It may be that measurements at smaller  $Q$  will give the most information. These can be obtained theoretically using the equation of motion technique.

I should like to thank R. J. Bell, F. L. Galeener and A. Wright for many useful discussions. Support from the O.N.R. is gratefully acknowledge.

#### References.

1. See P. Dean, Rev. Mod. Phys. 44, 127 (1972) and R. J. Bell, Reports of Prog. in Phys. 35, 1215 (1972).
2. A. J. Leadbetter and M. W. Stringfellow in "Neutron Inelastic Scattering, Proc. Grenoble Conf. 1972", p. 501, I.A.E.A. Vienna 1974.
3. R. J. Bell, A. Carnevale, C. R. Kurkjian and G. E. Peterson, J. Non Cryst. Solids 35/36, 1185 (1980).
4. R. Alben, D. Weaire, J. E. Smith and M. Brodsky, Phys. Rev. B11, 2271 (1975).
5. See for example - D. Beeman and B. L. Bobbs, Phys. Rev. B12, 1399 (1975).
6. D. Beeman and R. Alben, Ad. in Phys. 26, 339 (1977).
7. J. Joannopoulos, A. I. P. Conference Proceedings 31, 103 (1976).
8. M. F. Thorpe, Phys. Rev. B8, 5352 (1973).
9. P. N. Sen and M. F. Thorpe, Phys. Rev. B15, 4030 (1977); M. F. Thorpe and F. L. Galeener, Phys. Rev. B22, 3078 (1980).
10. F. L. Galeener and J. C. Mikkelsen, Phys. Rev. B23, 5527 (1981).
11. R. M. Martin and F. L. Galeener, Phys. Rev. B23, 3071 (1981).

VIBRATIONAL SELECTION RULES IN DISORDERED SOLIDS : VITREOUS  $\text{GeO}_2$ 

F.L. Galeener

Xerox Palo Alto Research Centers, Palo Alto, CA 94304, U.S.A.

**Abstract.** Empirical selection rules observed in the Raman and infrared spectra of vitreous germania are noted. Those for polarized Raman scattering are discussed in more detail, and are generalized to apply to glasses with different local order.

1. Observations in Vitreous  $\text{GeO}_2$ . - Fig. 1(a) shows the reduced polarized Raman spectra of vitreous (v-)  $\text{GeO}_2$ .<sup>1</sup> The dominant feature is the highly-polarized Raman line (R) at  $420 \text{ cm}^{-1}$ . Fig. 1(b) is a schematic diagram of the vibrational density of states (VDOS) for this material calculated by the method described by Galeener,<sup>2</sup> using the central forces (CF) only continuous random network (CRN) model of Sen and Thorpe.<sup>3</sup> According to this analysis,<sup>2</sup> R is to be associated with the single state  $W_1$  at the low frequency band edge in Fig. 1(b). Thus the dominant Raman line is interpreted as the result of very strong Raman scattering by a small number of select states of motion in the glass.

This inference is supported by data of Galeener, Leadbetter and Stringfellow,<sup>4</sup> reproduced in Fig. 2. Fig. 2(a) is the reduced neutron spectrum  $G(Q,W)$  obtained from inelastic neutron scattering measurements. Upon subtraction of the estimated 2-phonon contribution (dashed line), this quantity is a good experimental measure of the VDOS. (The lines at about  $125$ ,  $470$  and  $1230 \text{ cm}^{-1}$  are thought to be spurious.<sup>4</sup>) This VDOS is to be compared with the reduced polarized Raman spectra,  $I_{\text{red}}(W)$  in Fig. 2(b), and the transverse infrared response,  $W_{E_2}(W)$ , in Fig. 2(c). The vertical solid lines are drawn through peaks seen in  $I_{\text{red}}(W)$ ,  $W_{E_2}(W)$  and  $-\text{Im}(W/\epsilon)$  [the infrared energy loss spectrum, not shown<sup>7</sup>]. As predicted, R lies not at a peak in the VDOS but at the low frequency edge of the band of states centered at  $\sim 550 \text{ cm}^{-1}$ . This indicates the existence of a highly frequency-dependent matrix element, contradicting the prediction of Shuker and Gammon,<sup>5</sup> and supporting the arguments of Galeener and Sen.<sup>6</sup> It also provides additional confidence in the predictive utility of the simple CF CRN model.

Note that additional selection rule information can be found in Fig. 2. The dominant polarized Raman line R is not seen in the VDOS, nor is it seen in  $W_{E_2}$  or  $-\text{Im}(W/\epsilon)$  [indicating infrared inactivity]. The polarized Raman spectra give much of the information to be found in the neutron and ir spectra. All the peaks in the VDOS,  $W_{E_2}$  and  $-\text{Im}(W/\epsilon)$  are seen in the HV Raman spectrum alone. The HH spectrum clearly selects certain additional modes for observation, including D, a defect of uncertain origin.<sup>7</sup>

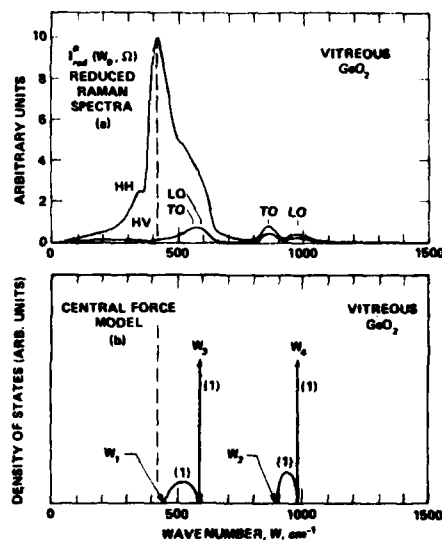


Fig. 1: The polarized Raman spectra of  $\text{v-GeO}_2$  compared with the schematic vibrational density of states computed according to Ref. 2. The dominant Raman line is associated with the SS motion in the state at  $W_1$ .

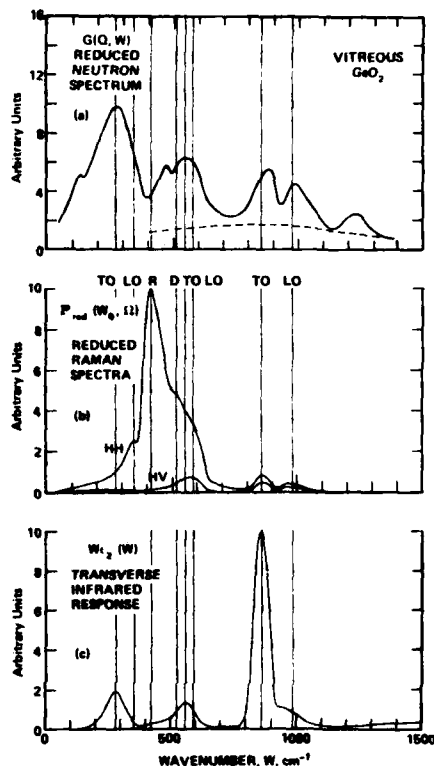


Fig. 2: Comparison of the neutron determined vibrational density of states (a) with the polarized Raman spectra (b) and the infrared dielectric constant spectra (c) of  $\text{v-GeO}_2$ .

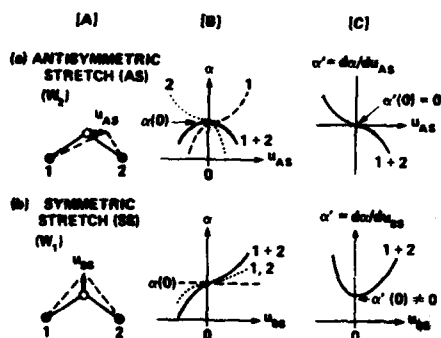


Fig. 3: Graphical construction showing that the antisymmetric stretch  $W_2$  must be Raman inactive, while the symmetric stretch  $W_1$  is expected to show Raman activity.

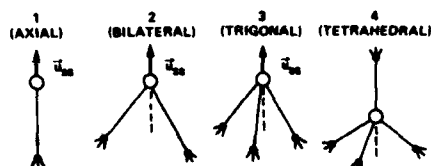


Fig. 4: Symmetric stretch (SS) motions of atoms at sites of simple symmetry in a glass. These motions are expected to give polarized Raman activity.

2. Raman Activity. - The strong Raman activity of the symmetric stretch (SS) motion at  $W_1$  is easily understood, as is the reported<sup>2</sup> inactivity of the antisymmetric stretch (AS) motion at  $W_2$  (the other low frequency band edge in the CF CRN model). The atomic motions<sup>2</sup> in  $W_2$  and  $W_1$  are shown in column A of Figs. 3(a) and (b), respectively. Following Long,<sup>8</sup> the basic rule is that Raman activity is allowed if at least one component of the derived polarizability tensor  $\alpha'(0) = (\partial\alpha/\partial u)_0$  is non-zero, where  $\alpha$  is the polarizability of the unit,  $u$  is the normal coordinate of vibration, and 0 indicates evaluation at the equilibrium position,  $u=0$ . For the normal modes at  $W_2$  and  $W_1$ , the relevant unit is the oxygen atom moving in special relation to its two *immobile* nearest neighbor Ge atoms, again as depicted in column A of Figs. 3(a) and (b), respectively. The polarizability of the unit is taken to be the sum (1 + 2) of separate contributions (1 and 2) due to the position of the oxygen atom relative to Ge atoms 1 and 2, respectively. The variation with  $u_{AS}$  (and  $u_{SS}$ ) is shown schematically in column B of Fig. 3. It is clear from Fig. 3(a) that the AS motion necessarily produces an  $\alpha$  which is even in  $u_{AS}$ . Thus, as shown in column C,  $\alpha'(0)=0$  and AS motion is Raman inactive. On the contrary, Fig. 3(b) shows that SS motion produces an  $\alpha$  which is not even in  $u_{SS}$ , so that  $\alpha'(0)\neq 0$  and Raman activity is expected. (Using a bond polarizability model, Martin and Galeener<sup>9</sup> have shown that polarized Raman activity is zero at *all* frequencies of the CF CRN model for  $AX_2$  glasses except at  $W_1$ .) The present argument supports the inference that strong polarized Raman activity arises when like bonds are stretched identically and in phase with one another.

This idea is easily generalized to include the motions of atoms which are 1-, 2-, 3- and 4-connected in the glass network, as depicted schematically in Fig. 4. The motions  $u_{SS}$  shown are the SS motions of these atoms since they result in in-phase identical stretching of the bonds. Motion at right angles to  $u_{SS}$  gives no polarized Raman scattering because  $\alpha'=0$  or, alternatively, because this motion results in out-of-phase bond stretching for which the Raman shifted radiation interferes destructively. *Thus, one should first look to SS motions like those shown in Fig. 4, in attempts to assign the origin of strong polarized Raman lines seen in disordered solids, not to wagging or rocking motions.*

3. Acknowledgments. - The author is grateful to A. J. Leadbetter and R. M. Martin for helpful discussion of portions of this work, supported by ONR Contract N0014-80-C-0713.

#### REFERENCES

1. F. L. Galeener and G. Lucovsky, *Phys. Rev. Lett.* **37**, 1474 (1976).
2. F. L. Galeener, *Phys. Rev.* **B19**, 4292 (1979).
3. P. N. Sen and M. F. Thorpe, *Phys. Rev.* **B15**, 4030 (1977).
4. F. L. Galeener, A. J. Leadbetter and M. W. Stringfellow, *in press*.
5. R. Shuker and R. W. Gammon, *Phys. Rev. Lett.* **25**, 222 (1970).
6. F. L. Galeener and P. N. Sen, *Phys. Rev.* **B17**, 1828 (1978).
7. F. L. Galeener, *J. Non-Crystall. Solids* **40**, 527 (1980).
8. D. A. Long, *Raman Spectroscopy* (McGraw-Hill, New York, 1977).
9. R. M. Martin and F. L. Galeener, *Phys. Rev.* **B23**, 3071 (1981).

## THE VIBRATIONAL SPECTRA OF CRYSTALLINE AND AMORPHOUS PHOSPHOROUS

F. Gompf and J.S. Lannin\*

Kernforschungszentrum Karlsruhe, Institut für Angewandte Kernphysik, D-7500  
Karlsruhe, Postfach 3640, F.R.G.

\*Department of Physics, The Pennsylvania State University, University Park,  
Pennsylvania PA16802, U.S.A.\*

**Abstract.** - Inelastic neutron scattering measurements are reported on polycrystalline orthorhombic black phosphorous (o-black P) and on amorphous red phosphorous (a-red P). The a-red P results indicate that the vibrational density of states is composed of three distinct spectral bands, with gaps or pseudo-gaps separating these regions. While the high frequency phonon band of o-black P occurs near to that of a-red P, considerable differences exist at lower frequencies. In particular the lowest band in a-red P is less structured and shows a strong shift towards smaller energies i.e. a pronounced softening of the lower part of the a-red spectrum is displayed. The vibrational densities of states have been employed to determine the lattice specific heats and Debye temperatures.

1. **Introduction.** - The structure of semiconducting black P is orthorhombic with lattice parameters of  $a = 4.3763 \text{ \AA}$ ,  $b = 10.478 \text{ \AA}$  and  $c = 3.3136 \text{ \AA}$  with four atoms per unit cell. Black P has a typical layer structure with a large ratio of next neighbour interlayer to intralayer distances of 1.61. This suggests a pronounced two dimensional character of this compound.

The semiconducting a-red P has only been poorly studied and its physical properties are relatively unexplored. Raman scattering and infrared absorption experiments /1/ indicate that the structure of a-red P is appreciably correlated beyond nearest neighbours rather than being build up from simple isolated structural units and it was suggested that there exists a more local layer-like atomic arrangement.

2. **Experiment.** - To help clarify some of these interesting properties of both P modifications we have performed inelastic neutron scattering experiments at TOF II, a multi detector time-of-flight spectrometer at the research reactor FR2 in Karlsruhe. The incident neutron energy was 5 meV. 60 He<sup>3</sup>-detectors covered scattering angles between 80 and 166 degrees. The experiments were carried out at room temperature.

X-ray and neutron diffraction measurements characterized a-red P to be totally amorphous and o-black P as single phase orthorhombic.

3. **Results and discussion.** - The vibrational densities of states  $F(\hbar\omega)$  for both modifications were deduced from the scattering data and partially corrected for resolution of the spectrometer. Fig. 1 shows the phonon density of states for o-black P. The very structured spectrum can be divided into two spectral bands:

- (i) A lower part with four sharp peaks at 10.5, 16.5, 25.5 and 32.5 meV which together make up about 50% of the modes in  $F(\hbar\omega)$ .
- (ii) An energetically higher lying part which has a maximum around 55 meV and is separated from the lower band by a gap at around 39 meV.

For this upper part of the spectrum the resolution of our spectrometer is rather poor so that any detailed structure cannot be registered. The broken line in Fig. 1 shows the second order Raman spectrum of o-black P from /2/ at 300K. It coincides nicely with the position of our higher optical modes and reveals a number of peaks. The difference in width, however, cannot solely be explained by difference in resolution.

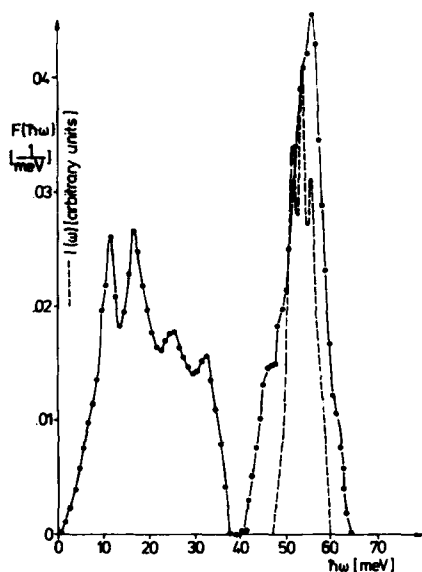


Fig. 1 : Phonon density of states of orthorhombic black phosphorous. Second order Raman spectrum - - - from /2/

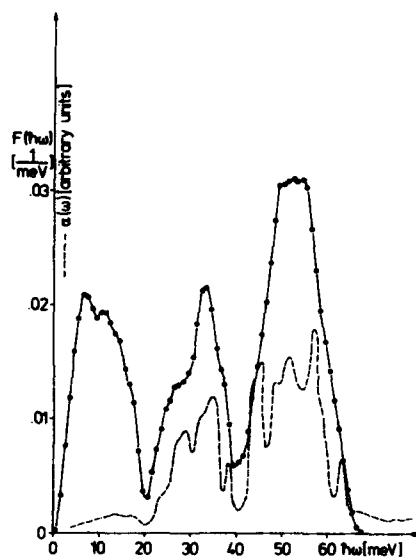


Fig. 2: Vibrational density of states of amorphous red phosphorous. Infrared absorption - - - from /1/

Fig. 2 shows the vibrational density of states of a-red P. The spectrum is composed of three distinct spectral bands with gaps or pseudogaps separating these regions:

- (i) About one quarter of the modes of  $F(\hbar\omega)$  make up the low frequency part of the spectrum. It has two peaks at 7 and 11.5 meV and shows a pronounced shift towards smaller frequencies in comparison to o-black P thus opening a gap where the crystalline phase displays a considerable overlap.
- (ii) A second quarter of modes in  $F(\hbar\omega)$  is given by the middle spectral band which has a shoulder at 26 meV and a peak at 33 meV. For them we find corresponding peaks in the o-black modification.
- (iii) The higher optical modes are separated by a gap at 40.5 meV and contribute about 50% of the modes in  $F(\hbar\omega)$ . Both gap and peak position are practically identical with the ones found in o-black P.

The broken line in Fig. 2 gives the infrared absorption,  $\alpha(\omega)$  from Ref. /2/ for a-red



P. The gap at 20 meV, the maxima in the middle part of the spectrum and the center of the high frequency band correspond well with the neutron data. Again the resolution for the higher optical modes of the neutron scattering experiments is not good enough to show details in this region while the low lying part of the spectrum cannot be detected by infrared absorption.

The comparison of  $F(\hbar\omega)$  for both modifications implies that simple phenomenological broadening of  $F(\hbar\omega)$  for the crystalline material does not yield a good representation for the noncrystalline counter part, as it occurs in group 4 semiconductors.

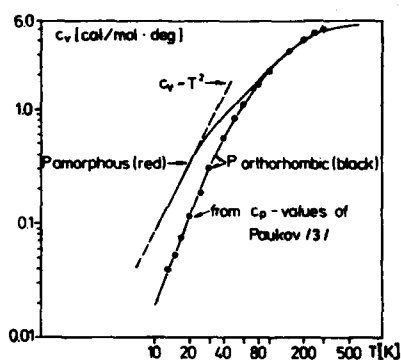


Fig. 3 : Lattice specific heats for orthorhombic black and amorphous red phosphorous

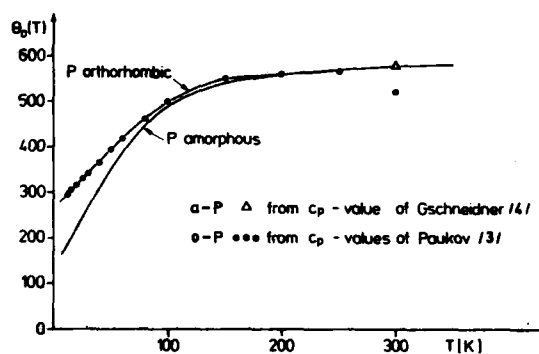


Fig. 4 : The Debye temperature  $\theta_D$  for orthorhombic black and amorphous red phosphorous

From the phonon densities of states we calculated the lattice specific heats  $C_v$  which are shown in a log  $C_v$  versus  $T$  plot in Fig. 3. The o-black P curve is in good agreement with the experimental values of Paukov /3/ after his  $C_p$  data had been transformed into  $C_v$ -data via the Nernst-Lindemann formalism. Similar to some other layer lattice structures a-red P shows a region where  $C_v \sim T^2$  holds which is consistent with the low effective dimensionality of this system as proposed by /1/.

In Fig. 4 we compare the  $\theta_D(T)$  versus  $T$  curves deduced from  $F(\hbar\omega)$  with values calculated from direct measured specific heat data. The softening of the vibrational spectrum of a-red P for small energy transfers leads to considerably smaller  $\theta_D$ -values than o-black P at low temperatures whereas both modifications are practically identical above 200K. Considering the sensitivity of this comparison the agreement with  $\theta_D$ -values determined from directly measured specific heat data for o-black P /3/ is excellent. A comparison for a-red P is only possible for 300K from a  $C_p$ -value of /4/ since to our knowledge other measurements do not exist.

- References: /1/ B.V. Shanabrook and J.S. Lannin, Proc. of the 14<sup>th</sup> Int. Conf. Phys. of Semiconductors, Edinburgh (1978)  
 /2/ J.S. Lannin and B.V. Shanabrook, Proc. of the 14<sup>th</sup> Int. Conf. Phys. of Semiconductors, Edinburgh (1978)  
 /3/ K. Paukov, Zh. Fiz. Khim 43 (1969)  
 /4/ K.A. Gschneider, Jr., Solid State Phys. 16 (1964)

TIME-RESOLVED PHONON SPECTROSCOPY OF AMORPHOUS  $\text{As}_2\text{S}_3$ 

U. Strom, P.B. Klein, K. Weiser and S.A. Wolf

Naval Research Laboratory, Washington, D.C. 20375, U.S.A.

**Abstract.**— Phonon pulses which were optically induced in thin evaporated films of amorphous  $\text{As}_2\text{S}_3$  have been studied with a superconducting NbN bolometer. The observed ballistic and diffusive heat propagation provides a measure of the phonon mean free path (m.f.p.). The results are related to the microscopic structural order of the chalcogenide glass as evidenced from previous optical and structural studies.

The present experiment examines phonons which are induced optically in thin evaporated films of the chalcogenide glass  $\text{As}_2\text{S}_3$ . The glass films are deposited on one side of a 1 mm thick sapphire disk. A NbN superconducting bolometer<sup>1</sup> (1 mm x 1 mm) deposited on the other side of the disk serves as a phonon detector. The time resolution of the experimental system was determined by measuring the ballistic phonon response induced optically in a 200 Å thick NbN metallic film. The bolometer response for an 8 nsec incident optical pulse of  $\lambda = 5796 \text{ Å}$  with total energy of  $3.5 \times 10^{-4}$  joule/pulse is shown in Fig. 1. Further details of the bolometer can be found in Ref. 1.

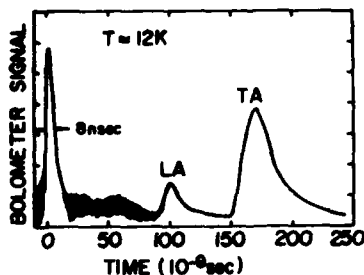


Fig. 1. Bolometer response for optically heated NbN metal film. Spike near  $t=0$  due to direct bolometer heating by partially transmitted laser pulse. Bolometer response time estimated to be less than  $10^{-10}$  sec (see Ref. 1). Delayed pulses represent ballistic TA and LA phonons propagating through 1 mm thick sapphire.

The bolometer response for a photo-excited  $\text{As}_2\text{S}_3$  film of thickness  $d \sim 1.8 \mu\text{m}$  is shown in Figs. 2 and 3. (Note: the film deposition conditions were nearly identical to those used in previous optical<sup>2</sup> and structural studies.<sup>3</sup>) For light with wavelength  $\lambda = 4882 \text{ Å}$  we find that the product of absorption coefficient  $\alpha$  and film thickness  $d$  is  $\alpha d \sim 0.7$ . This value of  $\alpha d$  typifies the glass after photodarkening,<sup>4,5</sup> i.e. the thermally reversible photo-induced band edge shift which is on the order of 0.1 eV toward the red. None of the phonon parameters discussed in this paper were affected by reversible photodarkening. As seen in Figs. 2 and 3, heat propagation in amorphous  $\text{As}_2\text{S}_3$  at  $T = 11.5 \text{ K}$  is predominantly diffusive. The ballistic components at 0.1 and 0.2  $\mu\text{sec}$  are not due to phonon propagation across the entire width of the

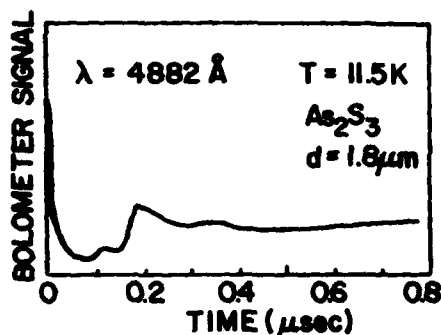


Fig. 2. Bolometer response for optically heated  $\text{As}_2\text{S}_3$  film. Ballistic pulses as in Fig. 1. Peak at  $0.35 \mu\text{sec}$  due to reflection from bolometer electrode.

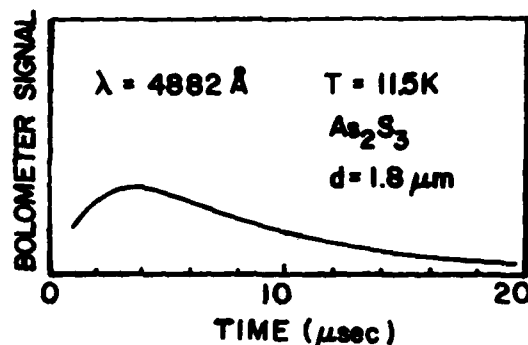


Fig. 3. Long time bolometer response due to diffusive phonon transport in  $\text{As}_2\text{S}_3$ .

film, but are due to phonon generation by the partially transmitted light in the region of the glass film closest to the sapphire substrate. The ratio of the integrated ballistic to diffusive phonon signals yields the phonon m.f.p.  $\Lambda$  in amorphous  $\text{As}_2\text{S}_3$ . The number of ballistic phonons  $I_B \sim a\lambda e^{-ad}$ , whereas the number of diffusive phonons is given by  $I_D \sim 1 - e^{-a(d-\Lambda)}$ . Since  $\Lambda \ll d$  we obtain to a very good approximation for the ratio of ballistic to diffusive phonon production  $R = I_B/I_D = a\Lambda/(e^{ad} - 1)$ . We have measured  $R$  and  $a$  for laser wavelengths  $\lambda$  from  $4771\text{\AA}$  to  $5040\text{\AA}$ . The values of  $ad$  ranged from  $ad = 1.29$  at  $\lambda = 4771\text{\AA}$  to  $ad = 0.26$  at  $\lambda = 5040\text{\AA}$ . The values of  $\Lambda$  obtained with these results were  $\Lambda = 140 \pm 30\text{\AA}$  (for  $d = 1.8 \mu\text{m}$ ). In an alternate geometry, light was incident through the semitransparent bolometer. For  $\lambda = 4000\text{\AA}$  light,  $a \sim 1.6 \times 10^5 \text{cm}^{-1}$ . From the measured value of  $R = 0.2$  we deduce  $\Lambda \approx 160\text{\AA}$ . We conclude that  $\Lambda$  is essentially independent of exciting light wavelengths between  $4000$  and  $5000\text{\AA}$ . This suggests that the thermalization time of the majority of the optically excited electron hole pairs is faster than the present  $10^{-7}$  sec time resolution.

In Fig. 4 various measurements of  $\Lambda$  for glassy  $\text{As}_2\text{S}_3$  and  $\text{SiO}_2$  are compared. The lower two curves represent  $\Lambda(T) = 3K/Cv_D$ , where the thermal conductivity  $K$ , specific heat  $C$  and Debye sound velocity  $v_D$  we obtained from low temperature thermal measurements.<sup>6,7</sup> The upper curve in Fig. 4 is the phonon m.f.p. at  $T \sim 1\text{K}$  as a function of phonon frequency  $f_D$ , measured for  $\text{SiO}_2$  by Dietsche and Kinder<sup>8</sup> using monochromatic phonon generation techniques. Temperature and frequency scales are related by  $hf_D = 3kT$ . As seen in Fig. 4,  $\Lambda$  obtained from thermal measurements is generally smaller by a factor of 3-5 than  $\Lambda$  obtained with the other two methods shown in Fig. 4. The cause for this difference cannot be addressed here. We will rather speculate on the nature of the scattering which gives rise to the  $\Lambda \sim f_D^{-2.9}$  frequency dependence observed between  $f_D = 100$  and  $300 \text{GHz}$  in  $\text{SiO}_2$ , with which our result in  $\text{As}_2\text{S}_3$  at  $11.5\text{K}$ , or at the equivalent phonon energy of  $\sim 700 \text{GHz}$ , is consistent.

The strong frequency dependent scattering above  $f_D \sim 100 \text{GHz}$  has been attributed variously to structural irregularities,<sup>9</sup> phonons,<sup>10</sup> or tunneling modes.<sup>9</sup> None of

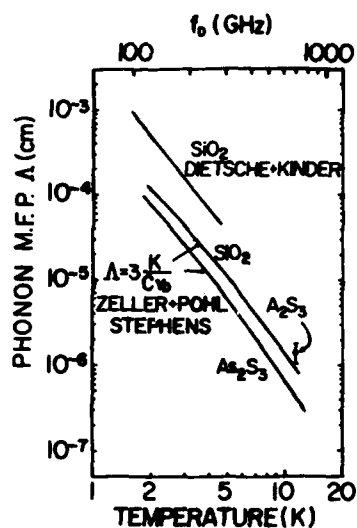


Fig. 4. Phonon mean free path in glassy  $\text{SiO}_2$ ,  $\text{As}_2\text{S}_3$  and an evaporated  $\text{As}_2\text{S}_3$  film.

these can be completely excluded. The importance of considering the local glass structure is stressed here. There exists considerable evidence for remnants of "crystal-like" or medium-range order in the glass. Specific evidence for medium-range order in  $\text{As}_2\text{S}_3$  was obtained from two-phonon vibrational<sup>10</sup> and nuclear quadrupole resonance studies.<sup>11,12</sup> Additional information comes from far infrared absorption measurements in glasses,<sup>13</sup> where correlation lengths  $\ell \sim 10\text{\AA}$  for  $\text{As}_2\text{S}_3$  and  $\sim 20\text{\AA}$  for  $\text{SiO}_2$  can be defined. Such correlation lengths represent an average spacing between static or dynamic charges in the glass and can be a direct

consequence of medium-range order. Recently Phillips<sup>14</sup> has further advanced the concept of medium-range order with specific topological proposals. Ribbon-like polymeric structures (rafts) proposed for  $\text{As}_2\text{S}_3$  do indeed exhibit a dominant width of  $\sim 10\text{\AA}$  which is comparable to  $\ell$ . Phonon scattering would deviate from Rayleigh-type scattering<sup>15</sup> ( $\sim f^{-4}$  for spheres) for phonon frequencies  $f \gtrsim v_D/2\pi\ell$ . For  $\ell = 10\text{\AA}$  and  $v_D = 1.7 \times 10^5 \text{ cm/sec}^{-1}$  this yields  $f \gtrsim 300 \text{ GHz}$ . More detailed estimates will be complicated by inelastic processes<sup>8</sup> as well as the high anisotropy of the scattering structures.

1. Weiser, K., Strom, U., Wolf, S. A. and Gubser, D. U., J. Appl. Phys. **52**, 4888 (1981).
2. Strom, U. and Martin, T. P., Solid State Commun. **29**, 527 (1979).
3. Treacy, D. J., Strom, U., Klein, P. B., Taylor, P. C. and Martin, T. P., J. Noncryst. Sol. **35+36**, 1035 (1980).
4. Keneman, S. A., Bordogna, J. and Zemel, J. N., J. Opt. Soc. Am. **68**, 32 (1978).
5. Tanaka, K., J. Noncryst. Sol. **35+36**, 1023 (1980).
6. Zeller, R. C. and Pohl, R. O., Phys. Rev. **B4**, 2029 (1971).
7. Stephens, R. B., Phys. Rev. **B 8**, 2896 (1973).
8. Dietsche, W. and Kinder, H., Phys. Rev. Lett. **43**, 1413 (1979).
9. Zaitlin, M. P. and Anderson, A. C., Phys. Rev. **B 12**, 4475 (1975).
10. Jones, D. P., Thomas, N. and Phillips, W. A., Phil. Mag. **B 38**, 271 (1978).
11. Klein, P. B., Taylor, P. C. and Treacy, D. J., Phys. Rev. **B 16**, 4511 (1977).
12. Rubinstein, M. and Taylor, P. C., Phys. Rev. **B 10**, 4258 (1974).
13. Strom, U. and Taylor, P. C., Phys. Rev. **B 16**, 5512 (1977).
14. Phillips, J. C., J. Noncryst. Sol. **43**, 37 (1981).
15. Handbook of Physics, ed. E. U. Condon and H. Odishaw, McGraw-Hill, 1958, 6-124.

LOW-TEMPERATURE ACOUSTICAL PROPERTIES OF Na DOPED  $\beta$ -Al<sub>2</sub>O<sub>3</sub>

J.-Y. Prieur, P. Doussineau, C. Frenois, A. Levelut and R.G. Leisure\*

*Laboratoire d'Ultrasons, Université Pierre et Marie Curie, Tour 13, 4 place Jussieu, 75230 Paris Cedex 05, France*

*\*Department of Physics, Colorado State University, Fort Collins, Colorado 80523, U.S.A.*

**Abstract.** - We measured the attenuation and velocity variations of ultrasonic waves, propagating parallel to the conduction plans in a Sodium doped  $\beta$  Alumina crystal. The three pure modes have been used. The results are well explained in the framework of the "two level system" (TLS) theory developed for amorphous compounds for all the temperature range studied ( $T < 70$  K). In the lowest range of temperature we observed the logarithmic variation of the velocity ( $T < 5$  K). Then for  $15 < T < 70$  K, we observed a linear variation of the velocity and a plateau for the attenuation variation, the height of which increases as the first power of the frequency. We clearly identified this plateau with the one which was theoretically predicted for the part of the sound attenuation due to the relaxation of the TLS and which is a direct proof of the distribution of the coupling constant for TLS of given energy. However we show that the relaxation of the TLS involved the direct process for  $T < 10$  K and the Raman process for  $T > 15$  K. The consideration of the Raman process and of the elastic anharmonicity let us explain the velocity variations in all the temperature range studied. [1]

[1] Amorphous-like acoustical properties of Na doped  $\beta$ -Al<sub>2</sub>O<sub>3</sub>.

P. DOUSSINEAU, C. FRENOIS, R. G. LEISURE, A. LEVELUT and J.-Y. PRIEUR  
*J. Physique* 41 (1980) 1193-1211.

## VIBRATIONAL DENSITY OF STATES OF AMORPHOUS AND CRYSTALLINE LIQUID CRYSTAL SUBSTANCES

A.V. Bielushkin, I. Natkaniec<sup>\*</sup>, V.K. Dolganov<sup>\*</sup> and E.F. Sheka<sup>\*</sup>*Joint Institute for Nuclear Research, 141980, Dubna, USSR**<sup>\*</sup>Institute of Solid State Physics, Acad. of Sciences of the USSR, 142432 Chernogolovka, USSR*

**Abstract.** - We have measured by the IOF neutron spectroscopy method the amplitude-weighted frequency distribution function of the glassy and crystalline phases of the EBBA, MBBA and PAA compounds. Evident changes in the vibrational density of states in the frequency range up to  $300\text{ cm}^{-1}$  are observed when passing from the amorphous to ordered crystalline phases. The partly deuterated  $d_6$ -PAA spectrum have shown that these vibrations are due to translational and librational motions of the whole molecule and due to low frequency oscillations of the end groups of the molecule.

Liquid crystal (LC) substances dependent on their thermal history may form different solid modifications. The PAA, MBBA and EBBA compounds are the most frequently studied LC substances and they are known to have different polymorphic crystalline phases, see ref.(1-3) and refs therein. By the fast cooling of the mesophase of these substances a glassy state (GLC) is formed. The X-ray and neutron diffraction methods as well as optical spectroscopy ones were used to investigate these GLC materials<sup>(2-6)</sup>.

It has been shown that the molecular structure and order parameter of the GLC are similar as in the nematic phase of LC. The GLC state is metastable at low temperatures and may be transformed into the ordered crystalline phases without the melting of the substance. This transformation can be stopped by the lowering of the temperature. So, any intermediate partly ordered state may be studied. Since the GLC systems exist at low temperatures, where the anharmonic effects and multiphonon scattering processes are strongly reduced, they are more suitable for dynamical studies, than LC systems. Here we present the amplitude-weighted frequency distribution function  $G_H(E)$ <sup>(7)</sup> of the GLC and crystalline states of the most popular LC substances.

The inelastic incoherent neutron scattering (IINS) spectra have been measured using the KDSOG inverted geometry time-of-flight spectrometer at the IBK pulsed reactor of the JINR Dubna<sup>(8)</sup>. The samples of EBBA, MBBA and PAA were poured in the aluminum containers of about 0.8 mm thick and with the 180 x 160 mm rectangular cross section. The GLC phases were produced by the dip in liquid nitrogen of the container placed at the bottom of the helium cryostat. The IINS spectra have been measured at 5 K at seven scattering angles from  $30^\circ$  to  $150^\circ$  every  $20^\circ$  simultaneously. Recently some of the IINS spectra from the MBBA sample were published<sup>(9)</sup>.

The measured IINS spectra have been transformed into the  $G_H(E)$  function according to the one-phonon incoherent scattering cross section formula. Such approximation is justified by the fact that IINS spectra of molecular crystals below  $300\text{ cm}^{-1}$

<sup>\*</sup>Permanent address : Institute of Nuclear Physics, 31-342 Krakow, Poland

measured at 5 K agree well with calculated ones<sup>(10,11)</sup>. The resolution function of the KDSOG spectrometer in the mentioned frequency range does not disturb significantly the  $G_H(\epsilon)$  function. The singularities of this function correspond to those of the function of phonon density of states<sup>(10-12)</sup>. So, we believe that the spectra presented here reflect the behaviour of the vibrational density of states in different phases of the LC substances.

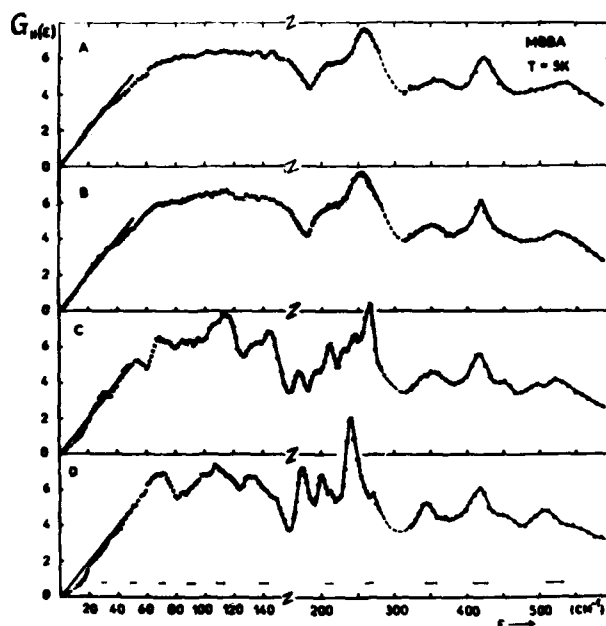


Fig.1: The hydrogen-amplitude weighted density of states  $G_H(\epsilon)$  functions obtained from the IINS spectra of different solid modifications of the MBBA (p-methoxybenzylidene p, n - butylaniline) compound.

A is the GLC sample obtained from the isotropic liquid by the fast cooling.

B is the GLC sample obtained from the nematic LC phase by the fast cooling.

C and D are the stable and metastable crystalline modifications, respectively (see refs. 1 and 3).

$\epsilon$  is the neutron energy transfer in  $\text{cm}^{-1}$ .

Horizontal bars correspond to the FWHM of the resolution function of the KDSOG spectrometer.

The  $G_H(\epsilon)$  functions of the MBBA and EBBA compounds are shown in Figs.1 and 2, respectively. One can see that the transition from the GLC structure to crystalline order does not change significantly the  $G_H(\epsilon)$  functions. Thus the large changes in vibrational spectra of the different solid modifications measured by the optical spectroscopy methods<sup>(3-6)</sup> are due to the loss of spatial coherency of vibrations and not to significant changes of the vibrational density of states.

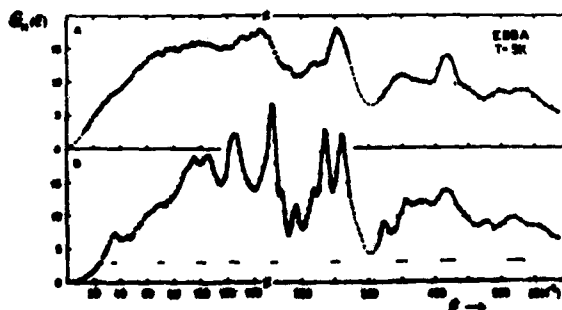


Fig.2: The  $G_H(\epsilon)$  functions of the EBBA (p-ethoxybenzylidene p,n - butylaniline) compound:

A is the GLC sample obtained from the nematic LC phase by the fast cooling.

B is the stable crystalline phase (see ref.3).

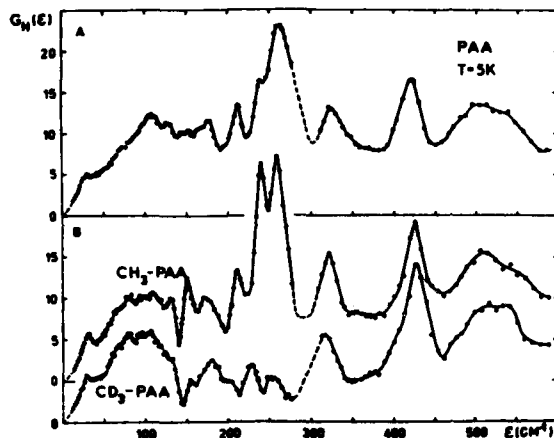


Fig. 3.: The  $G_H(E)$  functions of the PAA (p-azoxyanizole) compound:

A is the sample obtained from the nematic LC phase of the normal d-PAA ( $\text{CH}_3$ -PAA) by the fast cooling.

B is the stable crystalline sample of the d-PAA and partly deuterated d<sub>6</sub>-PAA ( $\text{CD}_3$ -PAA).

The PAA spectra will be discussed in detail in the separate publication by A.V.Bielushkin, E.L.Bokhenkov, A.I.Kolesnikov, I.Natkaniec, E.F.Sheka and S.Urban.

The essential changes of  $G_H(E)$  after the transition to the crystalline state occur in low frequency region ( $E < 300 \text{ cm}^{-1}$ ). Vibrational density of states of the GLC substances seems to be a linear function of frequency at  $E \rightarrow 0$ . In Fig.1 the slope of this function fitted to the spectrum of the sample cooled from isotropic liquid is compared with the spectra of other solid modifications. The distinct maxima in the spectra of crystalline samples at the  $E > 100 \text{ cm}^{-1}$  should correspond to the internal molecular vibrations. These low frequency bands undergo a considerable broadening when passing to the GLC state.

The comparison of the spectra of normal and partly deuterated samples of crystalline PAA (see Fig.3) show us that the lattice vibrations of this substance cut-off at about  $140 \text{ cm}^{-1}$ . The internal vibrations of this molecule in the frequency range below  $300 \text{ cm}^{-1}$  belong mainly to the oscillations of the end- $\text{CH}_3$  groups. We hope that the study of the IINS spectra of partly deuterated LC substances will help in the assignment of these oscillations and will serve to the better understanding of molecular conformations in different modifications of these substances.

#### References

1. J.A.Janik, J.M.Janik, J.Mayer, E.Sciesinska, J.Sciesinski, T.Twardowski, T.Waluga, and W.Witko, *J.de Phys.*, **36**, C1-159 (1975).
2. L.Bata, V.L.Broude, V.G.Fedotov, L.Rosta, N.Kroo, J.Szabon, K.M.Umarov and I.Visi, *Mol.Cryst.Liq.Cryst.*, **44**, 71 (1978).
3. N.Kirov, M.P.Fontana and F.Cavatora, *Mol.Cryst.Liq.Cryst.*, **54**, 207 (1979).
4. J.E.Lydon and J.O.Kessler, *J.de Phys.*, **36**, C1-153 (1975).
5. V.K.Dolganov, *Fiz.Tverd.Tela*, **21**, 2629 (1979).
6. V.K.Dolganov, N.Kroo, L.Rosta and E.F.Sheka, *Mol.Cryst.Lett.*, **64**, 115 (1981).
7. S.H.Chen and S.Yip, *Phys.Today*, Apr. 32 (1976).
8. I.M.Frank, *Sov.J.Part.Nucl.*, **2**, 805 (1973).
9. A.V.Bielushkin, V.K.Dolganov, I.Natkaniec, E.F.Sheka, *Pis'ma ZhETF*, **33**, 497 (1981).
10. I.Natkaniec, A.V.Bielushkin and T.Wasiutynski, *Phys.Stat.Sol.(b)*, **102**, 413 (1981).
11. A.V.Bielushkin, E.L.Bokhenkov, A.I.Kolesnikov, I.Natkaniec, R.Righini and E.F.Sheka, *Fiz.Tverd.Tela*, **23**, 2607 (1981).
12. J.W.White, in: "Chemical Applications of Thermal Neutron Scattering", Ed.B.T.M.Willis, Oxford University Press, 1973, p.49.



## ULTRASONIC ABSORPTION AND DISPERSION IN AMORPHOUS SUPERCONDUCTORS

W. Arnold, A. Billmann\*, P. Doussineau\*, C. Frenois\* and A. Levelut\*

*Fraunhofer-Institute, 6600 Saarbrücken, F.R.G.*

*\*Université Paris VI, Laboratoire d'Ultrasons, 75230 Paris, France*

Like disordered insulators, amorphous metals contain tunnelling centers (TLS) which dominate their low-temperature properties. This has been shown mainly by ultrasonic experiments /1/. In contrast to amorphous insulators, tunnelling centers in a-metals relax very rapidly due to their coupling to electrons /2/. It is obvious, that this coupling could be verified in amorphous superconductors.

The effect of superconductivity on the acoustic properties of a-metals has been calculated recently /3/. For instance, the absorption of ultrasound is predicted to drop rapidly for  $T < T_c$  relative to the value in the normal state. The origin of this effect is explained in the following way: the acoustic wave perturbs the population difference of the TLS and therefore gives rise to a relaxational process. In the normal state the relaxation time  $T_1$  of the TLS is extremely short because of the strong coupling between TLS and electrons. Due to the pair condensation for electrons this relaxation channel disappears in the superconducting state:  $T_1$  becomes longer and the resulting attenuation is modified greatly.

In order to verify these predictions, an experiment has been carried out on a-PdZr alloy ( $T_c = 2.62$  K), using longitudinal waves of frequencies  $\omega/2\pi = .74$  GHz and 1.3 GHz /4/. As expected, at very low temperatures ( $T = .4$  K) the relaxation attenuation becomes very small and magnetic-field dependent up to field strengths of the order of  $H_{c2}$ . Increasing the temperature, the attenuation rises rapidly and reaches the normal state value at a temperature  $T_n$  which, surprisingly, turned out to be much lower than  $T_c$  (Fig. 1). Here, we present an explanation of this unexpected behavior. We show that it is necessary to take into account not only the relaxation of the TLS by thermally excited quasi-particles still present at  $T < T_c$ , but also the relaxation of the TLS by thermal phonons. Moreover, it is necessary to involve a stronger TLS electron coupling than previously assumed. Furthermore, we corroborated these ideas by carrying out an experiment in a-CuZr with a low  $T_c$  ( $= .4$  K), such that the role of phonons becomes almost negligible.

Our explanation of the experiments in PdZr is based on the following hypotheses:

- a) When the relaxation of the TLS caused by the electrons is dominant ( $H > H_{c2}$ ), the relaxation rate becomes so strong that even at the lowest temperatures ( $.4$  K)

the condition  $\omega T_1^m \ll 1$  holds and the attenuation is then weakly temperature-dependent. This is a consequence of the distribution function of relaxation times  $P(\tau)$  inherent in the tunnelling model, and  $T_1^m$  is the fastest relaxation time of this distribution.

- b) When the relaxation of the TLS by electrons is suppressed ( $H = 0$ ,  $T < T_C$ ), the contribution of the thermal phonons to the relaxation rate becomes noticeable.

At the lowest temperatures it manifests itself by a  $T^3$ -dependence of the attenuation, indicating that as in insulators the one-phonon process dominates /5/.

- c) At  $T > 1.5$  K the relaxation rate even without any applied field is so strong that  $\omega T_1^m \ll 1$  holds and a plateau is obtained for the attenuation.

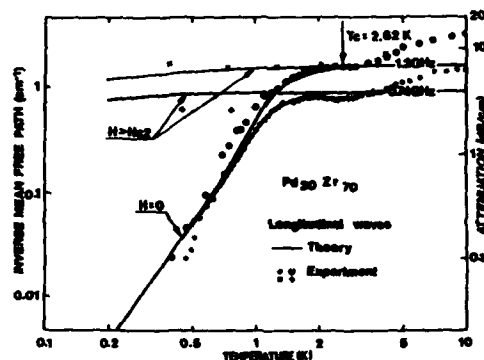


Fig. 1: Ultrasonic absorption in PdZr

We have carried out numerical calculations which can be found in detail in /6/. For the calculation of the relaxation attenuation we use the following equation /3/:

$$l^{-1} = \frac{WN\gamma^2}{\rho v^3} \int d(\beta E) \operatorname{sech}^2(\beta E) \int_{T_{\min}}^{T^m} \frac{d\tau P(\tau) \omega \tau(E, T)}{1 + \omega^2 \tau^2(E, T)} \quad (1)$$

Here  $N$  is the number of TLS per unit volume and energy,  $P$  is the density of the material,  $v$  is the sound velocity,  $\beta = (kT)^{-1}$ ,  $\gamma$  is the deformation potential between TLS and phonons,  $2E$  is the level splitting of the TLS. Similarly, the relative change of the sound velocity is given by:

$$\Delta v/v = - \frac{N\gamma^2}{2\rho v^3} \int d(\beta E) \operatorname{sech}^2(\beta E) \int_{T_{\min}}^{T^m} \frac{d\tau P(\tau)}{1 + \omega^2 \tau^2(E, T)} \quad (2)$$

In Eqs (1,2) the relaxation rate  $T_1^{-1}$  is now determined by two mechanisms:

- i) by electrons ( $<T$ ) and for  $T < T_C$  by quasi-particles (essentially  $\sim \exp(-T_C/T)$  and
- ii) by phonons ( $\sim T^3$ ) /5/. Assuming  $\gamma \approx 0.8$  eV and a rather strong coupling of  $PV_1 = 0.8$  between electron and TLS, we calculate the solid lines in Fig. 1 which agree very well with the experimental curves. Having a closer look to the behavior of the absorption in the vicinity of  $T_C$ , we can say that it is in particular the strong coupling of the TLS to electrons which dominates the relaxation mechanism at  $T_C$ , although the phonons still contribute. Because  $\omega T_1^m$  already  $\ll 1$ , the relaxation absorption exhibits a plateau, whatever the relaxation process might be /5,6/.

We have also calculated the relative variation of the velocity of sound as a function of temperature (Eq.(2)), using the parameters deduced from the fit of the attenuation

(Eq.(1)). We added the contribution due to resonant interaction of the TLS with phonons, which varies as  $C \ln (T/T_0)$ .  $T_0$  is a reference temperature. The result is that at  $T_c$  the velocity should show a change of slope in contrast to behavior of the absorption. This can easily be explained. Provided  $\omega T_1^m \ll 1$ , the inner integral in Eq. (2) results in  $\ln(\omega T_1^m(E,T))$  /6/. Therefore the relaxation rate is still explicitly present in the velocity through  $T_1^m$ , which of course contains the rapid change of  $T_1^{-1}$  caused by the electrons at  $T_c$ , and the change of slope depends on the relative weight of the phonon and electron processes. In order to verify this, we have carried out an experiment in the amorphous superconductor  $\text{Cu}_{60}\text{Zr}_{40}$  with a  $T_c = 0.4$  K (transverse waves  $\omega/2\pi = 740$  MHz). As can be seen in Fig. 2, only the familiar logarithmic contribution ( $\sim C \ln (T/T_0)$ ) due to the resonant process plays a role below 200 mK. With increasing  $T$ , however, the contribution of the relaxation process becomes noticeable. Because  $T_1$  changes rapidly with  $T$ , and also because the relaxation process decreases the sound velocity with increasing  $T$ , the total change of velocity passes through a maximum and then decreases with increasing  $T$ . For  $T > T_c$ , however,  $T_1$  only contains the weak temperature dependence due to normal electrons. Then, at temperatures for which  $\omega T_1^m \ll 1$  holds,  $\Delta v/v$  is given by  $-C/2 \ln (T/T_0)$ . Adding the contribution due to resonant interaction which is still present, this results in a positive slope of exactly one half of its magnitude at low temperatures, which we indeed observe experimentally. In summary we have shown experimentally and theoretically that tunnelling centers in an amorphous superconductor do couple to electrons as originally proposed /3/.

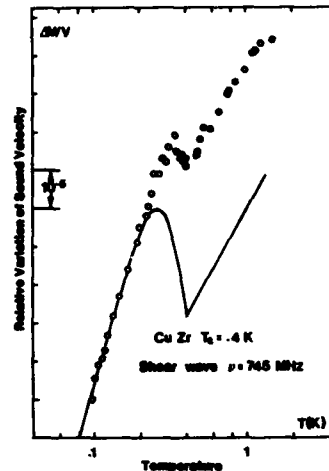


Fig. 2:  $\Delta v/v$  in CuZr,  
solid line: theory

#### References

- /1/ J.L.Black, in *Metallic Glasses*, Ed. H.J. Güntherodt (Springer, N.Y.) 1980
- /2/ B.Golding, J.E.Graebner, A.B.Kane, and J.L.Black, *Phys.Rev.Lett.* **41**, 1478 (1978)
- /3/ J.L.Black and P.Fulde, *Phys.Rev.Lett.* **43**, 453 (1979)
- /4/ G.Weiss, W.Arnold, and H.J.Güntherodt, *J.Phys.Colloq.* **41**, C8-742 (1980)
- /5/ J.Jäckle, *Z.Phys.* **257**, 212 (1972)
- /6/ W.Arnold, P.Doussineau, C.Frenois, and A.Levelut, *J.Phys.Lett.* **42**, L289 (1981)

## ENTROPY OF DISORDERED SOLIDS AT LOW TEMPERATURES

R. Zeyher and R. Dandoloff

*Max-Planck-Institut für Festkörperforschung, 7000 Stuttgart 80, F.R.G.*

**Abstract.** - It is shown that the complete set of low-lying collective excitations in a disordered solid yields in general a leading term  $\propto T^{3/2}$  in the entropy and the specific heat at low temperatures.

Omitting electronic degrees of freedom the Hamiltonian of a solid has the form

$$H = \sum_{\lambda=1}^N \frac{\vec{p}^2(\lambda)}{2 M(\lambda)} + V(\vec{u}(1), \dots, \vec{u}(N)) \quad (1)$$

The index  $\lambda$  counts the  $N$  atoms and  $M(\lambda)$  is the mass of the atom  $\lambda$ .  $\vec{u}(\lambda)$  denotes the displacement of the atom  $\lambda$  from its rest position  $\vec{x}^{(0)}(\lambda)$ ,  $\vec{p}(\lambda)$  are the corresponding momenta and  $V$  is a general potential. Eq. (1) assumes implicitly that the  $\vec{u}$ 's are finite and therefore that no mass transport is possible. As a result Eq. (1) cannot describe for instance an ionic conductor at high temperatures. At low temperatures all the atoms of a solid however can be assumed to be localized (in an "ideal" ionic conductor for instance the atoms are localized because of Anderson localization caused by unavoidable small fluctuations in the periodic potential and the large mass). The Hamiltonian (1) is therefore quite general for the discussion of low temperature properties. It includes in particular cases where no harmonic approximation exists or where the density of lattice sites and the density of particles must be considered as independent variables.

The Hamiltonian of Eq. (1) has several branches of collective, low-lying excitations caused by conservation laws and broken symmetries: a) The Fourier transform of the momentum density  $\vec{p}(\vec{k})$  is conserved in the limit  $\vec{k} \rightarrow 0$ ; b) The introduction of rest positions  $\vec{x}^{(0)}(\lambda)$  breaks the translational symmetry which is restored again by the displacement variables  $\vec{u}(\vec{k})$  in the limit  $\vec{k} \rightarrow 0$ ; c) The energy density  $e(\vec{k})$  is conserved for  $\vec{k} \rightarrow 0$ ; d) Assuming an one-component solid the total mass density  $n(\vec{k})$  is conserved for  $\vec{k} \rightarrow 0$ .

As a result of a) and b) there are three branches of propagating sound waves with linear dispersion and imaginary part  $\propto k^2$ . At low temperatures they yield a contribution  $\propto T^3$  to the entropy which is the usual Debye law. As a result of c) solids exhibit a collective diffusion mode describing the dissipation of entropy. This mode has a weight  $\propto \alpha^2(T)$ , where  $\alpha$  is the thermal expansion coefficient. If the third law of thermodynamics is valid,  $\lim_{T \rightarrow 0} \alpha = 0$  and the corresponding contribution to  $S$  is unimportant at low temperatures. Ref. 1 assumes  $\lim_{T \rightarrow 0} \alpha(T) \neq 0$ . It follows then from general thermodynamic arguments that  $S \propto T$ . However we can show that under rather general assumptions this case will not occur in real solids so we will discard it in the following. d) yields (for an one-component solid) an additional diffusion peak which describes structural rearrangements of the atoms and has been discussed in Refs. 2 and 3. Assuming that the corresponding susceptibilities and the transport coefficient is nonzero at low temperatures we calculate in the following the contribution of this diffusion mode to  $S$  at low temperatures.

The leading term in the entropy at low temperatures can be calculated from the relation  $(k_B = 1)$ :

$$S(V, T) = \int_0^\infty \frac{dx}{\pi} \frac{x e^x}{(e^x - 1)^2} \Lambda(xT, V), \quad (2)$$

$$\Lambda(\omega, V) = - \sum_{\lambda, \alpha} \left\{ \sum_{\lambda', \beta} \text{Im } G_{\alpha\beta}(\lambda, \lambda', \omega + i\eta) \text{Re}(G_{\beta\alpha}^{-1}(\lambda', \lambda, \omega + i\eta)) + \right. \\ \left. + \text{Im } \ln(-G_{\alpha\alpha}^{-1}(\lambda, \lambda, \omega + i\eta)) \right\} \quad (3)$$

$G_{\alpha\beta}(\lambda, \lambda', \omega + i\eta)$  is the retarded Green's function associated with the displacements  $u_\alpha(\lambda)$  and  $u_\beta(\lambda')$ . The inverse  $G^{-1}$  is to be taken with respect to the labels  $(\lambda\alpha, \lambda'\beta)$ ,  $\ln$  is the logarithm and  $\text{Im}$  the imaginary part. It is also understood that the spectral functions of  $G$  are to be taken in the limit  $T \rightarrow 0$  so that the  $T$ -dependence is due to the first argument of  $\Lambda$  in Eq. (2).

Eq. (2) shows that the small  $T$  behavior of  $S$  is determined by the small  $\omega$  behavior of  $\Lambda$ . Assuming that only the long-range spatial part of  $G$  is important (this assumption can be verified later) it is possible to use for  $G$  in Eq. (3) only its "hydrodynamic part". If the third law of thermodynamics holds the energy fluctuations can moreover be omitted at low temperatures. The interesting longitudinal part of  $G$  assumes then the form in  $k$ -space:

$$G(\vec{k}, z) = \frac{z + iDk^2}{z^3 - zk^2(\alpha_1 + \alpha_2) + iDk^2(z^2 - \alpha_2 k^2)} \quad (4)$$

$\alpha_1$  and  $\alpha_2$  are static susceptibilities:  $\sqrt{\alpha_2}$  and  $\sqrt{\alpha_1 + \alpha_2}$  describe the bare and the renormalized sound velocity, respectively.  $D$  is the transport coefficient associated with the extra mode.

Transforming Eq. (3) into  $k$ -space and inserting Eq. (4) the  $k$ -integration can be carried out in the complex plane. The leading contribution  $\Delta S$  to  $S$  is for  $\alpha_1 \ll \alpha_2$ :

$$\Delta S = \frac{75}{384} \zeta(5/2) V \left( \frac{\alpha_1^2}{2\pi D \alpha_2} \right)^{3/2} T^{3/2} \quad (5)$$

where  $\zeta$  is Riemann's zeta function and  $V$  is the volume of the solid. Because of  $C_V = T \delta S / \delta T$  we find that the leading term in  $C_V$  should also be  $\propto T^{3/2}$ . The next term in  $S$  is  $\propto T^3$  and contains in particular the usual Debye contribution.

Experimentally extra contributions to  $S$  of the form  $aT^\alpha$  with  $1 \lesssim \alpha \lesssim 3/2$  have been found in glasses, amorphous semiconductors and metals, polymers, superionic conductors, and ferroelectrics.<sup>5</sup> A characteristic feature of these solids is that some of the atoms can make "large" (i.e. of the order of the bond length) displacements. This also is just a condition that the above extra mode should be important<sup>2,3</sup>. Nevertheless the application of our theory to the above solids is difficult because  $\alpha_1$  and  $D$  are presently unknown and have so far also not been calculated within theoretical models.

#### References:

1. P.V. Giaquinta, N.H. March, M. Parinello, and M.P. Tosi, Phys. Rev. Letters **39**, 41 (1977)
2. P.C. Martin, O. Parodi, and P.S. Pershan, Phys. Rev. **A6**, 2401 (1972)
3. C. Cohen, P. Fleming, and J.H. Gibbs, Phys. Rev. **B13**, 866 (1976)
4. P. Fulde and H. Wagner, Phys. Rev. Lett. **27**, 1280 (1971)
5. D.A. Ackerman, D. Moy, R.C. Potter, A.C. Anderson, and W.N. Lawless, Phys. Rev. **B23**, 3886 (1981), and references therein.

# RAMAN STUDY OF THE ANHARMONICITY AND DISORDER-INDUCED EFFECTS IN $\text{Ga}_{1-x}\text{Al}_x\text{As}$

B. Jusserand, J. Sapriel, F. Alexandre and P. Delpech

Centre National d'Etudes des Télécommunications, 196 rue de Paris, 92220 Bagneux, France

**ABSTRACT.**— Raman measurements of the frequency shift and profile variations versus temperature are interpreted in terms of anharmonicity and disorder. Several disorder activated longitudinal and transverse acoustic modes have been observed and assigned. A description of their resonant behaviour is also given.

## 1. Study of the first-order Raman lines.—

The emergency of a low-energy tail in the LO-lines has been already reported in  $\text{GaAlAs}$ .<sup>1</sup> In order to analyze the origin of this asymmetry we have investigated the frequency and profile of the LO peak in  $\text{GaAs}$  and  $\text{Ga}_{0.73}\text{Al}_{0.27}\text{As}$  as a function of the temperature  $T$ .

The effective half-width  $\Gamma$  and the anharmonic shift  $\Delta$  of a Raman peak of frequency  $\omega$  are respectively given by Rel (1) and (2)

$$\Gamma = \Gamma_1 + \Gamma_3 \quad (1)$$

$$\Delta = BT + \Delta_3 + \Delta_4 \quad (2)$$

$\Gamma_3$  is due to cubic anharmonicity and  $\Gamma_1$  is a damping independent of  $T$  due to other attenuation processes. Quartic anharmonicity is neglected in (1) as it gives rise to higher order contribution to the linewidth;  $\Delta_3$  and  $\Delta_4$  are the shifts due to cubic and quartic anharmonicity respectively and  $BT$  is the contribution of the thermal expansion. The cubic process consists of the decay of the optical phonon into two acoustic phonons of frequency  $\omega/2$  and of equal and opposite wave vector. For acoustic phonons whose wave vector is far from the Brillouin zone edge, where frequency-independent density of states can be reasonably assumed, one finds <sup>2,3</sup>

$$\Gamma_3 = \Gamma_3^0 [2n(\omega/2)+1] \quad (3) \quad \Delta_3 = -\Gamma_3 A(q) \quad (4)$$

$n$  is the thermal population factor  $n(\omega) = [\exp(\hbar\omega/kT)-1]^{-1}$ ,  $q$  is the reduced wave vector of the acoustic phonons involved in the process and  $A(q) = [1/(4q^4) + 1/(3q^3) + 1/(2q^2) + 1/q + \ln(1/q-1)]/\pi$  (5)

Relations (3)-(5) are valid in the case of the LO and TO modes in  $\text{GaAs}$  and in the case of the  $\text{GaAs}$ -type modes in  $\text{Ga}_{1-x}\text{Al}_x\text{As}$  where  $q \approx 0.5$ . The constant  $B$  of equ.(2) is calculated from data of the literature relative to elastic constants, thermal expansion and Raman shifts

under hydrostatic pressure in GaAs. One finds  $B = -0.58 \times 10^{-2} \text{cm}^{-1} \text{K}^{-1}$ . Raman scattering experiments of the LO and TO modes in GaAs and of the LO GaAs-type in  $\text{Ga}_{0.73}\text{Al}_{0.27}\text{As}$  have been performed<sup>3</sup> between 20 and 450K. The peak frequency and the profile have been carefully investigated. Fitting rel (1)-(5) to our experimental results, we found  $\Delta_4$  negligible with respect to  $\Delta_3$  and obtained the values of  $\Gamma_1, \Gamma_3^0$  and  $\Omega$  ( $\Omega = \omega - \Delta$  is the frequency of the phonon in the perfectly harmonic lattice) which are reported in Table 1.

	$\Gamma_1$ $\text{cm}^{-1}$	$\Gamma_3^0$ $\text{cm}^{-1}$	$\Omega$ $\text{cm}^{-1}$
TO in GaAs	0	0.24	273
LO in GaAs	0.28	0.26	297
GaAs-type mode for $x = 0.27$	1.11	0.28	287

Table 1- Parameters determined by fitting our experimental results to relations (1)-(5); the anharmonic contribution to the residual low temperature damping is expressed by  $\Gamma_3^0$ .

One can see that  $\Gamma_3^0$  has the same value in GaAs and GaAlAs. The anharmonicity is not affected by the disorder. The asymmetry of the LO mode in GaAlAs is not a consequence of the anharmonicity. Complementary experiments on several samples for  $x$  in the range 0-0.5 have checked that the asymmetry was temperature independent. It is interpreted as a disorder induced effect, the low-energy tail being due to contribution of LO phonons in the vicinity of  $k=0$ , whose energy is smaller. A phenomenological model of this effect is given elsewhere<sup>3</sup>.

2. Study of the disorder-activated acoustic modes. As one approaches the middle-range concentration in  $\text{Ga}_{1-x}\text{Al}_x\text{As}$ , new modes appear in the low-frequency part of the Raman spectra which are very weak and clearly resolved only under resonance conditions. Such conditions were realized in a  $\text{Ga}_{0.25}\text{Al}_{0.75}\text{As}$  sample since the extrema at  $k = 0$  of the conduction and valence band are, for this composition, separated by an amount of energy which lies in the range of the argon-ion laser emitting lines. The results are given in Fig.1 for the 4880 Å and 5145 laser lines at different temperatures. One can notice two sets of lines : one around  $200 \text{ cm}^{-1}$  which compares well to one already reported (dotted line in Fig.1) generally attributed to the disorder activated longitudinal mode (DALA) and the other, never reported before in  $\text{Ga}_{1-x}\text{Al}_x\text{As}$ , which is situated between  $70$  and  $135 \text{ cm}^{-1}$ , i.e. in the short-wavelength transverse acoustical range and which we interpret as a disorder activated transverse acoustical band (DATA). The peaks I, II, III, IV, V of Fig.1 have not a second-order Raman behaviour versus temperature and one can notice that the variation of their intensities are related to the difference between the energy of the incident pho-



ton and the value of the gap at  $k=0$ . The increase of these intensities is only a consequence of the tuning of this gap to the incident light when the temperature is made to vary. Peaks I-V are therefore first order Raman lines which reflects the density of states. A linear interpolation between the values of  $\omega_{TA(L)}$  and  $\omega_{TA(X)}$  in GaAs and AlAs gives :  $\omega_{TA(L)} = 75 \text{ cm}^{-1}$  and  $\omega_{TA(X)} = 97 \text{ cm}^{-1}$  for  $x = 0.75$ . These values are very close to the frequencies of peaks I and II, whose assignment is straightforward. Peaks IV and V situated at  $200 \text{ cm}^{-1}$  and  $210 \text{ cm}^{-1}$  can be assigned as the LA(L) and LA(X) modes. Peak IV is the same as the peak reported in Ref.4. Peak V is an additional one which undergoes a resonance clearly stronger than all others. We report in Fig.2 the intensity variations of the Raman lines at 80 K for five  $\text{Ar}^+$  laser lines. The resonance behaviour of line I,II,III and IV is quite similar to that observed for the GaAs-type and AlAs-type LO modes in the allowed configurations though line V has a "forbidden resonant behaviour". The polarized Raman study shows a  $\Gamma_1$  symmetry for the DALA structure as predicted theoretically. The DATA structure is preferentially  $\Gamma_1$  polarized although the theory predicts strong components  $\Gamma_{12}$  and  $\Gamma_{15}$ .

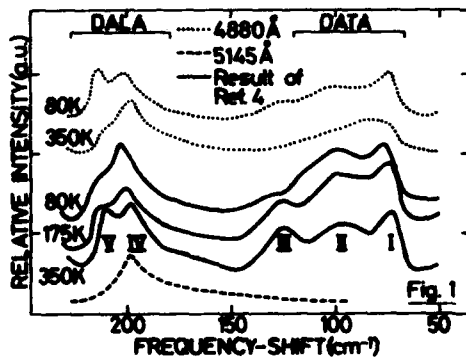


Fig.1 : Disorder-activated longitudinal-acoustic structure (DALA) and Disorder-activated transverse-acoustic structure (DATA) in  $\text{Ga}_{0.25}\text{Al}_{0.75}\text{As}$ . Peaks I, II, IV and V are assigned as TA(L), TA(X), LA(L) and LA(X) respectively.

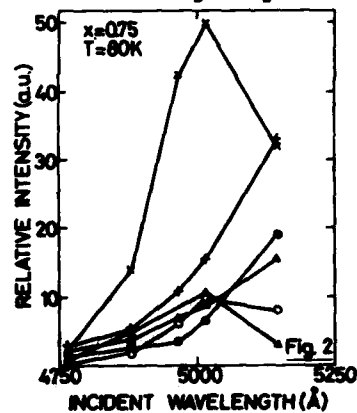


Fig.2 : Incident wavelength dependence of the intensity.  
 $\times$  AlAs-type LO (FC).  
 $+$  AlAs-type LO (AC).  
 $\circ$  GaAs-type LO (FC).  
 $\bullet$  GaAs-type LO (AC).  
 $\Delta$  Peak V ( $\times 10$ ).  
 $\triangle$  Peak I, II, IV ( $\times 10$ ) and III ( $\times 50$ ).  
 FC : Forbidden configuration.  
 AC : Allowed configuration.

- References : 1. J. Shah, A.E. Di Giovanni, T.C. Damen, and B.I. Miller, *Phys. Rev. B*, 7, 3481 (1973).  
 2. A.S. Pine and P.E. Tannenwald, *Phys. Rev. B*, 178, 1424 (1969).  
 3. B. Jusserand and J. Sapriel to be published in *Phys. Rev. B* vol.23.  
 4. R. Tsu, H. Kawamura, and L. Esaki, *Proc. of the Int. Conf. on the Physics of Semi-conductors Warsaw (1972)* p. 1135.

PHONON-LINE-SHAPE AND DISORDER CORRELATION IN MIXED  $\text{GaP}_{1-x}\text{As}_x$ 

M. Teicher, D. Schmeltzer and R. Beserman

*Solid State Institute and physics Dept., Technion, Haifa, Israel*

**Abstract.** - The disorder of  $\text{GaP}_{1-x}\text{As}_x$  is evaluated from the double phonon spectrum and compared to the amorphous material.

Combinations between zone edge Raman active phonons are used to define the disorder in a mixed crystal. These phonons have large "q" and therefore are sensitive to spatial disorder. The change in line width and shape of the double phonon spectrum of mixed  $\text{GaP}_{1-x}\text{As}_x$  is compared to the amorphous Raman width of the pure components.

$\text{GaP}_{1-x}\text{As}_x$  has a two-mode-zone center and zone-edge behaviour. The second order spectrum of  $\text{GaP}_{1-x}\text{As}_x$  is composed of combinations of zone edge phonons of GaP alone and GaAs alone. Figure 1 shows the spectra of the GaP optical double phonons as a function of As content. With increasing "x" the spectrum is shifted and broadened, we shall focus our attention on this broadening. The same results are obtained for the GaAs double phonon spectrum.

The normalized Raman spectrum  $I(\omega)$  is related to the phonon density of states  $g(\omega)$  by:

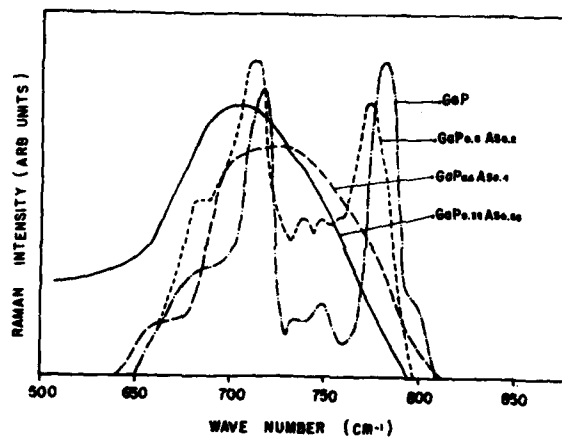
$$I(\omega) = \sum_b C_b \frac{1}{\omega} (n(\omega) + 1) g(\omega)$$

$g(\omega)$  is the double phonon Raman spectrum at half width. By fitting procedure,  $\sum_b C_b$  is taken as a phenomenological width. Figure 2 compares the double-phonon spectrum of GaP to the amorphous spectrum, the spectrum agrees well with the amorphous one.

If we make the hypothesis that the disorder which is introduced by mixing GaP with GaAs, is of the same nature than the disorder created by amorphisation, a correlation should exist between the widths of the  $\text{GaP}_{1-x}\text{As}_x$  spectrum and that of amorphous GaP.

On figure 3, we plot the GaP double phonon width as a function of As concentration this curve extrapolates to the width of the amorphous material. This result can best be understood by assuming that  $\text{GaP}(\text{GaAs})$  aggregates into microcrystallite clusters, the other component prevents the propagation of the  $\text{GaP}(\text{GaAs})$  phonon from cluster to

cluster . This results in the alternation and in the broadening of the propagating vibrational mode. When the concentration of GaP (GaAs) is small enough, the clusters are isolated one from the other, the barrier between them is too high to be overcome, this is the picture of an amorphous material.



**Fig. 1:-** GaP double-phonon Raman spectra for different As concentrations in  $\text{GaP}_{1-x}\text{As}_x$ .

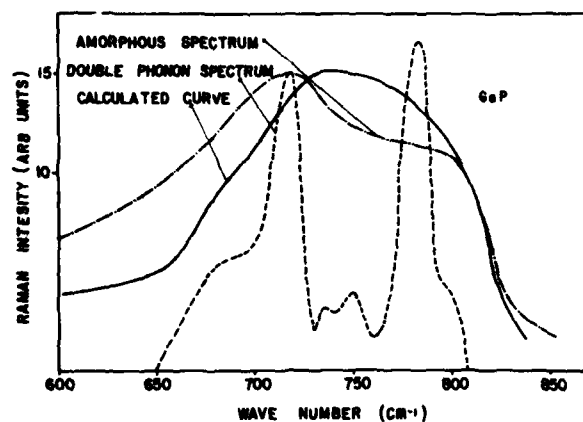


Fig. 2:- Broadened double-phonon GaP spectrum, compared to the amorphous spectrum of GaP.

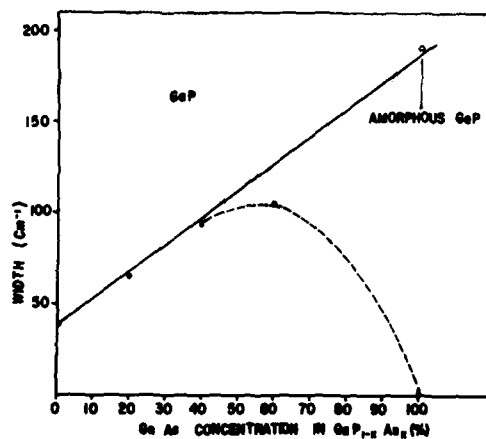


Fig. 3:- GaP double-phonon line-width, as a function of As concentration in mixed  $\text{GaP}_{1-x}\text{As}_x$ .

INELASTIC NEUTRON SCATTERING FROM AMORPHOUS Fe<sub>40</sub>Zr<sub>60</sub> DOPED WITH DIFFERENT CONCENTRATIONS OF KRYPTON (0,1,7 at.%)

F. Gompf, H.J. Schmidt and B. Renker

*Kernforschungszentrum Karlsruhe, Institut für Angewandte Kernphysik, D-7500 Karlsruhe, Postfach 3640, F.R.G.*

**Abstract.**— By means of time-of-flight neutron inelastic scattering techniques we have obtained the generalized vibrational densities of states  $G(\hbar\omega)$  of undoped polycrystalline and amorphous Fe<sub>40</sub>Zr<sub>60</sub> and of amorphous samples doped with 1 and 7 at.% Kr. The amorphous compound displays a triangular shaped  $G(\hbar\omega)$  which is very different from the strongly structured crystalline modification. Concerning the amorphous alloys, the energetic range of the additional Kr modes indicates that the Kr atoms are embedded in their host matrix as single atoms or perhaps small clusters and not as bubbles as was found in metals.

**1. Experiment.**— We have produced amorphous Fe<sub>40</sub>Zr<sub>60</sub> undoped and doped with 1 and 7 at.% Kr using a triode sputtering system as described in /1/. The structure of our samples was checked by neutron diffraction. No Debye-Scherrer-lines were observed showing the amorphous state of the materials. By means of inelastic neutron scattering techniques from powder samples we determined the generalized vibrational densities of states  $G(\hbar\omega)$ . The experiments were carried out at the FR2 research reactor in Karlsruhe using the multidetector time-of-flight spectrometer TOF II. The incident neutron energy was 5 meV, the 60 He<sup>3</sup>-counters covered scattering angles between 80 and 166 degrees.

To crystallize the alloy we heated an amorphous sample up to about 700°C in UHV. Neutron diffraction revealed that the material had completely crystallized. The largest amount had transformed to FeZr<sub>2</sub> a tetragonal CuAl<sub>2</sub> (C16)-type structure /2/ but also minor parts of other phases were present.

**2. Results and discussion.**— In Fig. 1 we show the time-of-flight distribution (background subtracted) of three amorphous Fe<sub>40</sub>Zr<sub>60</sub> alloys containing 0-1 and 7 at.% krypton. Towards smaller energy transfers we register a strong enhancement of intensity with rising Kr concentration. In fact even the sample doped with 1 at.% Kr already shows a well defined increase. From these scattering data the generalized vibrational densities of states were deduced. They are shown in Fig. 2 together with  $G(\hbar\omega)$  after crystallization of the undoped alloy. Amorphous undoped Fe<sub>40</sub>Zr<sub>60</sub> has a triangular frequency distribution which peaks around 20 meV and extends to 40 meV. Astonishing is the fact that there is no Debye like behaviour in  $G(\hbar\omega)$  down to our experimental limit of 1 meV. This shape of  $G(\hbar\omega)$  is very different from the phonon density of states curve of the crystalline modification where a pronounced decrease

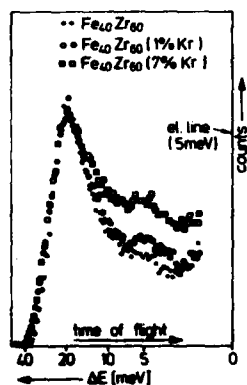


Fig. 1: Time-of-flight spectra of amorphous  $\text{Fe}_{40}\text{Zr}_{60}$  with different Kr concentrations

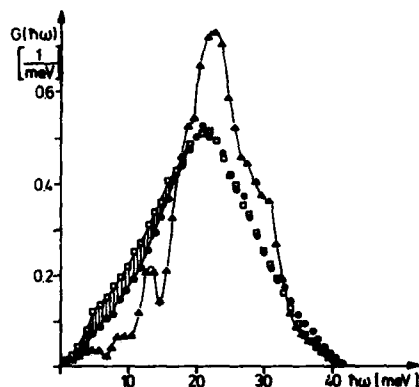


Fig. 2: Comparison of the vibrational densities of states of crystalline  $\text{Fe}_{40}\text{Zr}_{60}$  A-A with that of the amorphous alloy:  $\circ-\circ$  undoped,  $\square-\square$  doped with 7 at.% Kr

of intensity is registered below 17 meV with a dip at 6.5 meV and a rather sharp peak at 13 meV. The maximum of  $G(h\nu)$  is shifted to higher energies and now centers around 23 meV while the cut-off frequency remains the same i.e. 40 meV.

Amorphous  $\text{Fe}_{40}\text{Zr}_{60}$  with 7 at.% Kr exhibits additional intensities from 1 meV up to 20 meV with a maximum of 10 meV. From scattering power considerations these modes have been attributed to the Kr atoms i.e. one expects an intensity gain of approximately 5% for the doped sample which is nicely confirmed. For solid Kr the frequency spectrum ends at 6 meV [3] whereas we obtained a much harder Kr spectrum which is shown in Fig. 3. From this we conclude that the force constants between Kr and the

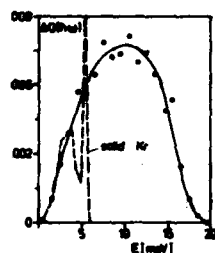


Fig. 3: The Kr vibrations in amorphous  $\text{Fe}_{40}\text{Zr}_{60}$

transition metal atoms must be about 10 times larger than the forces in solid Kr. If Kr was enclosed in its host matrix in the form of bubbles it would be in its liquid state due to its critical temperature. As the dynamical forces then were of the Van de Waals type they would be even weaker than for the solid state. From this we conclude that the Kr-atoms are embedded as single atoms or at most as very small clusters in the amorphous host matrix.

- References.** - /1/ H.-J. Schmidt, E. Henrich, T. Fritsch, F. Gompf, B. Renker, E. Mohs, Proc. of the Int. Conf. on Liquid and Amorphous Metals, Grenoble 1980  
 /2/ J. Vincze, F. van der Woude and M.G. Scott, Solid State Commun. **37**, 567 (1981)  
 /3/ J. Skalyo, Y. Erdoh, and G. Shirane, Phys. Rev. **B9**, 1957 (1974)

## LOCAL ORDER AND DYNAMICS IN LIQUID ELECTROLYTES : SMALL ANGLE NEUTRON SCATTERING

G. Maisano, P. Migliardo, F. Wanderlingh, M.P. Fontana\*, M-C. Bellissent-Funel\*\* and M. Roth\*\*\*

*Istituto di Fisica and G.N.S.M., Messina, Italy*

*\*Istituto di Fisica and G.N.S.M., Parma, Italy*

*\*\*Labo. "L. Brillouin" Orme des Merisiers, Gif-sur-Yvette, France*

*\*\*\*I.L.L., 38000 Grenoble, France*

The existence of dynamically correlated regions of intermediate range of ordering was verified for  $\text{ZnCl}_2$  solutions in  $\text{D}_2\text{O}$  by means of small angle neutron scattering. The data also show the presence of two characteristic lengths in the solutions for solute concentration below about 3 Molar. At higher concentration, the secondary "bump" due to the interference of these two distances disappears, indicating perhaps a percolation threshold. Such result is confirmed by the detection of a characteristic length in the small angle spectra of pure  $\text{D}_2\text{O}$ .

Aqueous solutions of strong II-I electrolytes have been investigated for some time because of the unusual and strong structure making effects they show (1). At sufficiently high concentrations, the local structure in the liquid is imposed by the solute and turns out to be very similar to the corresponding crystalline structure (EXAFS measurements). Raman and inelastic neutron scattering spectroscopy (see also papers B1-6 and D1-4 at this conference) show the existence of solute-connected collective vibrational excitations which indicate that the range of ordering may extend well beyond the mean interionic separation. These effects may be particularly evident in  $\text{ZnCl}_2$  solutions, and the contrast between ordered regions and the remaining fluid sufficiently high to make the intermediate range dynamical correlations detectable by small angle neutron scattering.

For monodisperse, spherical, non interacting "regions" the Guinier approximation to the structure factor yields:

$$S_{\text{Coh}}(Q) \Big|_{Q \rightarrow 0} \sim \exp \left( - \frac{R_G^2 Q^2}{3} \right) \quad (1)$$

i.e. for  $Q \rightarrow 0$ , the scattered intensity should rise exponentially. Independently of the details of the Guinier approximation, such a rise will be indicative, in a homogeneous system, of density or concentration fluctuations spatial correlations, with characteristic range  $R_G$ .

Although we performed measurements on  $\text{ZnCl}_2$ ,  $\text{CuBr}_2$ ,  $\text{NiCl}_2$  solutions, here we shall discuss mainly the data we obtained for  $\text{ZnCl}_2$  in  $\text{D}_2\text{O}$  and pure  $\text{D}_2\text{O}$ .

## Experimental

We have used the D17 and D11 small angle cold neutrons spectrometers at I.L.L. Grenoble. The working wavelength was  $10 \text{ \AA}$  and the  $Q$  ranges spanned were  $0.019 < Q < 0.25 \text{ \AA}^{-1}$  (with D17) and  $0.002 < Q < 0.25 \text{ \AA}^{-1}$  (with D11). Solutions here held in a  $2 \times 2 \times 0.1 \text{ cm}$  fused quartz cell at room temperature, and were prepared by standard methods. The data were corrected for empty cell, detector efficiency, sample absorption.

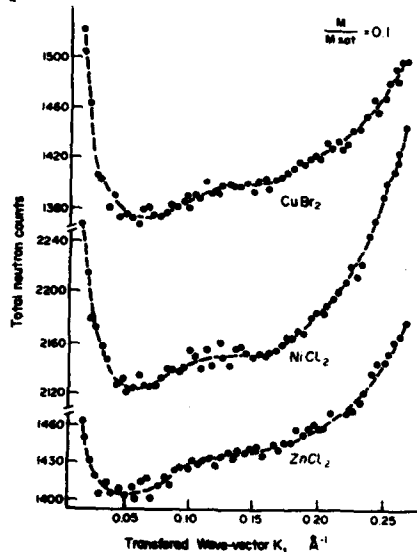


Fig.1 - Small angle data in  $\text{CuBr}_2$ ,  $\text{NiCl}_2$ ,  $\text{ZnCl}_2$  solutions in  $\text{D}_2\text{O}$ . The molar concentration is 0.1 of the saturation value.

In fig. 1 we show the  $S_{\text{coh}}(Q)$  behavior at intermediate values of the "small angle" region (data obtained with D17), for  $\text{ZnCl}_2$ ,  $\text{NiCl}_2$ ,  $\text{CuBr}_2$  solutions at 0.1 of the saturation concentration. Note the rise for  $Q \rightarrow 0$  and the bump at ca.  $Q = 0.1 \text{ \AA}^{-1}$ . The rise for larger  $Q$ 's is due to the tail of the metal-metal correlation peak and the stronger but more distant water peak in the structure factor. The study of  $S_{\text{coh}}(Q)$  vs concentration shows that the bump disappears for concentration higher than about 3 Molar for  $\text{ZnCl}_2$  in  $\text{D}_2\text{O}$  (Fig. 2).

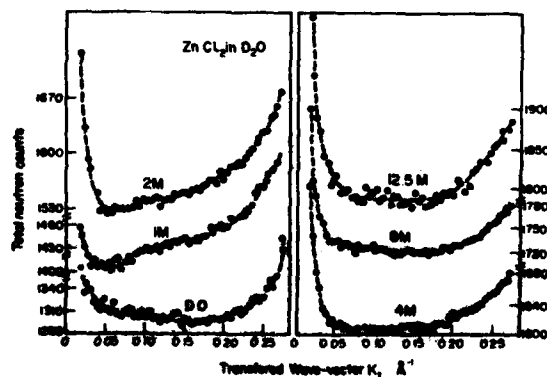


Fig.2 - Small angle scattering data for  $\text{ZnCl}_2$  solutions at various concentrations. The case of pure  $\text{D}_2\text{O}$  is also shown.



These results indicate that:

- In the solutions there are dynamically correlated regions with fairly well defined range  $d_0$ .
- The secondary maximum suggests that such regions are themselves spatially correlated with a characteristic distance  $d$ .
- Using a dumbbell model (Guinier) to perform a preliminary analysis of the spacial correlations yielding the observed  $S_{\text{Coh}}(Q)$  shape, we obtain  $d_0/d \sim 0.7$  with  $d \approx 50 \text{ \AA}$  for  $c \approx 1\text{M}$ .
- The regions loose their identity and merge into an "infinite cluster" at  $c \sim 3\text{M}$ . This effect may indicate the existence of a percolation limit in this system.

The small angle spectra obtained for  $\text{D}_2\text{O}$  confirm the validity of the application of percolation theory concepts to these systems. Since the data shown in Fig. 1 for  $\text{D}_2\text{O}$  were not sufficiently accurate, we repeated the measurements using the high resolution D11 spectrometer. Actually the measurements were repeated for the solutions also, and the data are still a under analysis and will be reported elsewhere. The data for  $\text{D}_2\text{O}$  show a clear rise of  $S_{\text{Coh}}(Q)$  all the way to  $0.01 \text{ \AA}^{-1}$ .

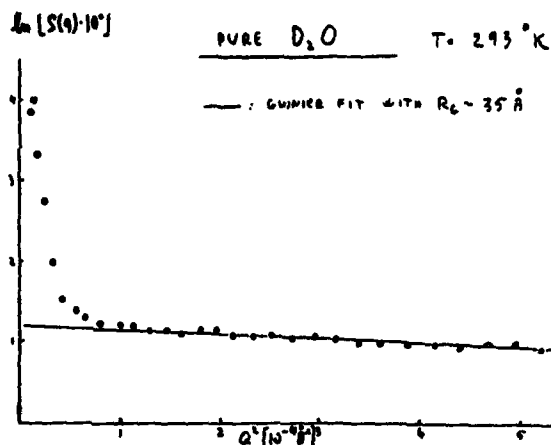


Fig.3 -

Very small angle scattering  
for pure  $\text{D}_2\text{O}$  (Guinier plot).

In Fig. 3 we show a Guinier plot of the data. From the slope of the straight line fit of  $S_{\text{Coh}}(Q)$  for  $Q \gg 0.01 \text{ \AA}^{-1}$  we obtain

$$R_G \approx 35 \text{ \AA} \quad (2)$$

This result confirms and extends to low  $Q$ 's the results obtained by Bosio et al. (2) by means of Small Angle X-Ray Scattering (their lower  $Q$  limit was  $\sim 0.015 \text{ \AA}^{-1}$ ), which they interpreted in terms of the recently proposed site percolation model for water (3), in which tetrahonded sites tend to clusterize (forming low density patches).

The sharp rise in  $S_{\text{Coh}}(Q)$  at the smallest  $Q$ 's (which would yield an apparent coherence length of about  $600 \text{ \AA}$ ) is not understood at present: it may be due to interfacial effects between water and the cell walls.

#### References

- 1) Most relevant references can be found in M.P.Fontana, G.Maisano, P.Migliardo and F.Wanderlingh, J.Chem.Phys. 69, 676 (1978).
- 2) L.Bosio, J.Teixeira, H.E.Stanley, Phys.Rev.Lett. 46, 597 (1981).
- 3) H.E.Stanley, J.Teixeira, J.Chem.Phys. 73, 3404 (1980).

## RAMAN SCATTERING IN ANNEAL STABLE AMORPHOUS SILICON

S.T. Kshirsagar\* and J.S. Lannin<sup>†</sup>*Department of Physics, Pennsylvania State University, University Park,  
Pennsylvania 16802, U.S.A.*

**Abstract.**— First order Raman scattering measurements are reported on anneal stable amorphous Si prepared by chemical vapor deposition. The results indicate substantial modifications of the Raman spectra relative to a-Si prepared by other methods. The results indicate improved short range order in CVD a-Si resulting from a narrowing of the bond angle distribution. Similarities to a-Si<sub>1-x</sub>H<sub>x</sub> spectra suggest improved short order in the hydrogen alloys.

1. **Introduction.**— Lattice dynamical calculations of amorphous semiconductors as well as metals have emphasized the important role of short range order on the phonon density of states and its relation to crystalline solids.<sup>1</sup> A number of models for amorphous (a-) Si and Ge have been developed in the past with the goal of obtaining the radial distribution function as well as properties, such as the phonon density of states. The implicit assumption in these studies is that one correct model is appropriate for elucidating most of the physical properties of these systems and that 'extrinsic' effects, such as void, defects and impurities are responsible for the diversity of electrical and optical data.<sup>2</sup> Detailed radial distribution function (rdf) studies<sup>3</sup> in a-Ge, in fact, indicated that rather small changes in short range order arise with deposition conditions. In addition, Raman scattering studies reported in a-Ge and a-Si prepared under a variety of conditions have suggested that the vibrational and Raman spectra are relatively insensitive to small changes in local order.<sup>4</sup> Recent interest in a-Si<sub>1-x</sub>H<sub>x</sub> alloys has raised the question of whether H modifies local order in these systems both in terms of saturating dangling bond defects, as well as modifying the network structure. In this study we report on Raman scattering measurements performed on the anneal stable states of a-Si and a-Ge. As the anneal stable state is believed to correspond to that of lowest free energy prior to crystallization, it is of particular interest for models which consider energy relaxation in their construction as well as for lattice dynamical studies. The present results emphasize, in contrast to earlier studies, that considerable 'intrinsic' variations in the vibrational density of states and Raman spectra occur and that these are a consequence of small changes in short range order. The results further suggest that the presence of H in certain a-Si alloys results

\* Supported in part by NSF Grant DMR 7908390 and by SERI Contract XS-8-9010-5.

† Present address: National Chemical Laboratory, Poona, 411008, India

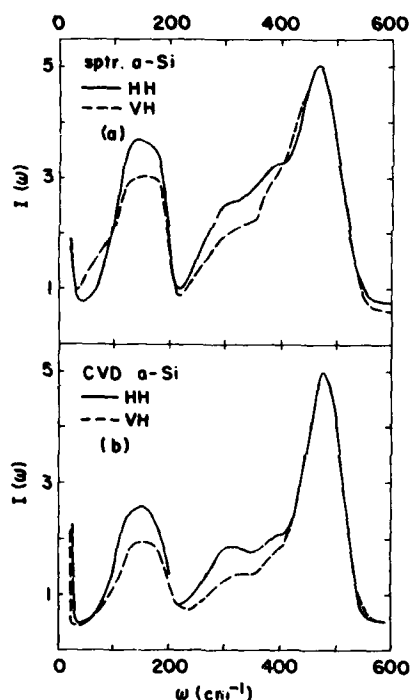


Fig. 1 : Comparison of the Raman spectra of rf sputtered a-Si ( $T \approx 120^\circ\text{C}$ )(a) and CVD a-Si(b). The solid curves represent HH and the dashed curves VH spectral components.

in an improved short range order.

2. Experiment.— Two forms of a-Si are reported here, one prepared by conventional planar rf sputtering at 7m Torr onto a substrate whose temperature is  $\approx 120^\circ\text{C}$ , and a second form prepared by chemical vapor deposition (CVD) onto substrates above  $520^\circ\text{C}$ . The latter samples were obtained from Prof. B. O. Seraphin and have been extensively characterized.<sup>5</sup> Their H concentration is  $\sim 0.2$ - $0.7$  at. %. Raman scattering measurements were performed on a Spex third monochromator system using 5145 Å excitation at room temperature.

3. Results and Discussion.— In Fig. 1 the Stokes spectra of CVD a-Si is compared to that of the film prepared by rf sputtering. The spectra clearly indicate that substantial variations in both the VH and HH Raman components occur in the anneal stable CVD a-Si material. This is particularly manifest by large changes in the width of the high frequency peak centered at  $\sim 475\text{ cm}^{-1}$  which corresponds to the crystalline TO peak of the density of

states.<sup>4</sup> In addition, the relative intensity of the low frequency TA-like peak is considerably reduced in the CVD a-Si film. Such large changes in the Raman spectra of a-Si contrast with earlier measurements which suggested no apparent changes in the spectra with preparation conditions.<sup>4</sup> Meek has performed theoretical calculations<sup>6</sup> of the phonon density of states of a number of models<sup>7</sup> of a-Ge that vary in short range order by their bond angle variations,  $\Delta\theta_{\text{rms}}$ , as well as topology. These calculations, which employed a modified bond charge model, indicated that  $\Delta\theta_{\text{rms}}$  and not topology (ring statistics) determined the form of the phonon density of states. While these calculations were performed for a-Ge, they are also applicable to a-Si, given similarities in short range order<sup>2</sup> and vibrational or Raman<sup>8</sup> spectra. The results of Meek imply that modifications of the high frequency widths of the TO-like Raman band are attributable to changes in  $\Delta\theta_{\text{rms}}$ . Thus the increased scattering intensity at low frequencies as well as the high frequency band width in the sputtered film indicate increasing disorder relative to the anneal stable CVD material. The increased order in the latter is

attributed to small changes in the bond angle distribution, since rdf measurements in a-Ge suggest that rather small modifications of this parameter ( $\sim 10^\circ$ ) are likely. The decrease in the low frequency scattering for the CVD a-Si may also be a consequence of changes in the Raman matrix elements, particularly for the depolarized, VH component. In the limit of tetrahedral symmetry the depolarized scattering from low frequency body bending type modes vanishes.<sup>9</sup> Similar trends to Fig. 1 are also observed in the Raman spectra of anneal stable a-Ge prepared by annealing evaporated films.<sup>10</sup> However, a more detailed analysis of the stray light background is required at low frequencies for quantitative changes to be assessed.

The Raman spectra of CVD a-Si shown in Fig. 1 are similar in form to those obtained by Tsai and Nemanich<sup>11</sup> on a glow discharge deposited a-Si<sub>0.92</sub>H<sub>0.08</sub> alloy. In particular, the trend of decreasing TO-like width and TA-like intensities is observed. This clearly suggests that the presence of H in the glow discharge deposited film improves the short range order relative to unalloyed a-Si prepared by other methods at the corresponding substrate temperature of  $\sim 230^\circ\text{C}$ . As the CVD a-Si film is prepared by high temperature SiH<sub>4</sub> decomposition it is possible that both the high temperature as well as the presence of H or SiH<sub>x</sub> intermediates also influence the short range order. Some small differences in TO-like width of  $\sim 10^\circ$  exist between the CVD a-Si and the glow discharge Raman spectra that suggest somewhat greater local order in the latter hydrogen alloy.<sup>10</sup>

We wish to gratefully acknowledge Prof. B. O. Seraphin for the CVD a-Si samples.

#### References

- 1) D. Weaire and P. C. Taylor, in Dynamical Properties of Solids, Vol. 4, ed. G. K. Horton and A. A. Maradudin (North Holland, New York, 198) p. 1.
- 2) N. F. Mott and E. A. Davis, Electronic Processes in Non-Crystalline Materials, (Oxford, London, 1979) and references therein.
- 3) W. Paul, G. A. W. Connell and R. J. Teskin, Adv. Phys. **22**, 529 (1973).
- 4) J. E. Smith, Jr., M. H. Brodsky, B. L. Crowder, M. I. Nathanan, A. Pinczuk, Phys. Rev. Lett. **26**, 642 (1971).
- 5) M. Janai, D. D. Allred, D. C. Booth and B. O. Seraphin, Solar Energy Materials, **1**, 11 (1979).
- 6) P. E. Meek, in Proc. 4th Intern. Conf. Physics of Non-Cryst. Solids, ed. G. H. Frischat (Trans. Tech. Publ., Aedermansdorf, 1977) p. 586.
- 7) D. Beeman and B. L. Roobe, Phys. Rev. **B12**, 1399 (1975).
- 8) J. S. Lannin, Proc. 5th Intern. Conf. Amorphous and Liquid Semicond., ed. J. Stuke and W. Brenig (Taylor and Francis, London, 1974) p. 1245.
- 9) D. Beeman and R. Alben, Adv. Phys. **26**, 339 (1977).
- 10) S. T. Kshirsagar and J. S. Lannin (to be published).
- 11) C. C. Tsai and R. J. Nemanich, Proc. 8th Intern. Conf. Amorphous and Liquid Semiconductors, ed. W. Paul and M. Kastner (North Holland, New York, 1980) p. 1205.

## VIBRATIONAL DYNAMICS IN IONIC LIQUIDS

F. Aliotta, M.P. Fontana\*, G. Maisano, F. Migliardo, C. Vasi and F. Wanderlingh

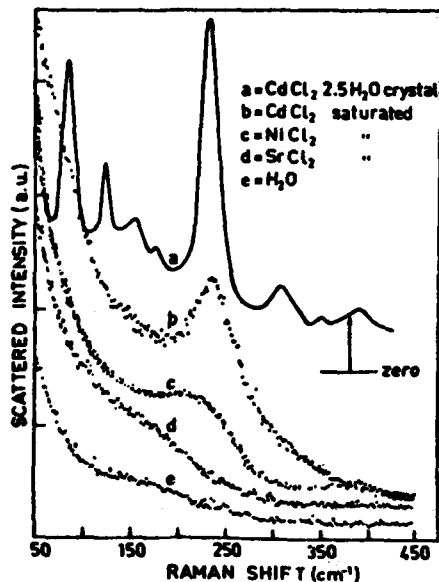
*Istituto di Fisica and G.N.S.M. del CNR, Università di Messina, Italy*

*\*Istituto di Fisica and G.N.S.M. del CNR, Università di Parma, Italy*

In recent years, the chemistry and the physics of ionic liquids as electrolytic solutions and molten salts, have been widely studied because of the structural peculiarity of these materials. In particular, as far as aqueous strong electrolytes solutions of 2-1 transition metals ( e.g.  $\text{NiCl}_2$ ,  $\text{CuCl}_2$ ,  $\text{CuBr}_2$ ,  $\text{NiBr}_2$ ,  $\text{ZnCl}_2$ ,  $\text{ZnBr}_2$ ) are concerned, thermodynamical calculations, transport and acoustic measurements, EXAFS, X-rays and neutron scattering, Raman scattering seem to indicate the possibility of a new point of view in describing the physical properties of such systems. The latter ones appear to be " structure dominated " rather than " collision dominated". The above mentioned results can be summarized in the following points: (i) At very high concentrations the solute tends to form complex ions of the  $\text{MeXn}^{2-n}$  kind. Such a process involved  $\sim 50\%$  of the cations, while the remaining ones diffuse together with their hydration shells. (ii) Ion-ion and ion-water complexes begin to interact and the structure of the hydrated crystals is locally reproduced. (iii) A concentration ( $\sim 2$  Molar) does exist at which the structure imposed by the water and the structure imposed by the solute become nearly equivalent. For this range of concentrations, many physical quantities ( shear viscosity, ultrasonic relaxational frequency, coordination numbers and so on) show an anomalous behaviour. In the present work, we discuss the dynamical properties of this system. In particular, VV and VH Raman spectra, in the range  $5 \div 500 \text{ cm}^{-1}$  and  $2800 \div 4000 \text{ cm}^{-1}$  of Stokes shift, have been taken as a function of temperature and concentration. For comparison, we have also performed measurements for  $\text{SrCl}_2$  and  $\text{SrBr}_2$  in water, for the corresponding hydrated crystals and for heavy water solutions. The results obtained ( see refs.1,2,3,4 and 5 for details) permit us to draw the following conclusions: The low frequency spectra of all solutes studied ( with the exception of  $\text{SrCl}_2$  and  $\text{SrBr}_2$ ) show a slowly varying distribution which resembles a variational density of states. This solid-like contribution becomes Raman active by breaking the momentum conservation selection rule.

Actually, the phonon density of states built up in this way becomes an effective density of states which is the convolution of the true vibrational spectrum with the mode depending matrix elements. For disordered materials, as amorphous semiconductors, glasses, superionics and associated liquids as  $\text{B}_2\text{O}_3$ ,  $\text{SbCl}_3$ ,  $\text{H}_2\text{O}$  in which the melting process gives rise to the breakdown of only a small percentage of the solid phase bonds, the vibrational modes seem to be collective in character. In our systems, in effect, at high concentrations, the structure resembles that of the corresponding crystalline state; this evidence implies the existence of interaction between the ionic complexes and the obtained density of states is a convolution of " acoustical" and " optical" modes in a coupled complex structure with

middle range order. In effect the Metal-Halogen stretching bands are evident and lie in the same frequency region of the corresponding modes of the hydrated crystals. (see fig.1).

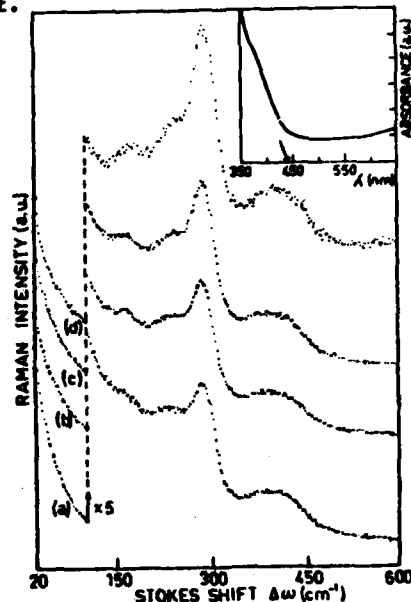


Experimental Raman spectra for the saturated solutions of (b)  $\text{CdCl}_2$ , (c)  $\text{NiCl}_2$ , (d)  $\text{SrCl}_2$  and for (e) pure water. Excitation power: 100 mW, counting time/channel 0.6 sec; scan speed  $100 \text{ cm}^{-1}/\text{sec}$ . (The top spectrum is from a single crystal of  $\text{CdCl}_2 \cdot 0.25 \text{ H}_2\text{O}$  (a)).

Fig. 1 (from ref. 1)

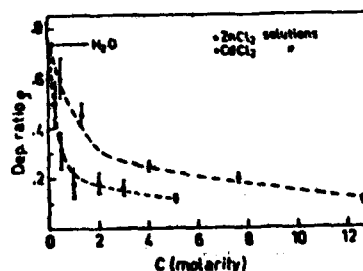
Furthermore from the behaviour of the depolarization ratio with the concentration (see fig.3), evidence has been found for a local structure transformation at  $\sim 2$  Molar, where a solute dominated structure took over the water dominated structure. Another interesting structural peculiarity appears when the anhydrous melt and glassy of the same salts are investigated.

In particular (see fig.2) with a Jet-flow technique, it has been possible to detect, by changing the  $\lambda_{\text{exc}}$ , a resonance Raman effect related to the  $A_g$  band of the complex  $\text{CuCl}_4^{2-}$ , centred at  $290 \text{ cm}^{-1}$  of Stokes shift.



Low frequency Raman spectra of  $\text{CuCl}_2$  solution for different lines: a: 5145 Å; b: 4880 Å; c: 4765 Å; d: 4579 Å. In the insert the absorption is shown.

Fig. 2 (from ref. 3)



Concentration dependence of the depolarization ratio  $\rho$  for  $\text{CuCl}_2$  and  $\text{ZnCl}_2$  solutions at 230 and  $265 \text{ cm}^{-1}$  Raman shifts, respectively.

Fig. 3 (from ref. 2)

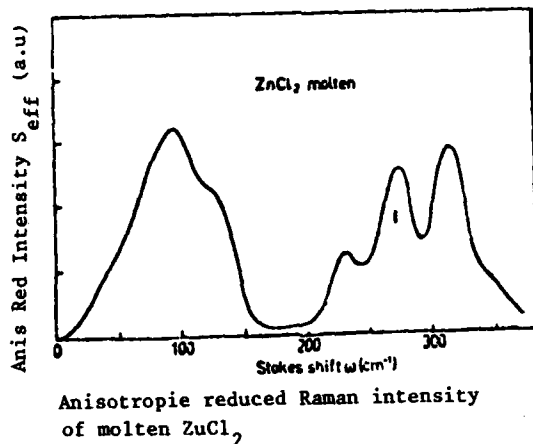


Fig. 4a (from ref. 5)

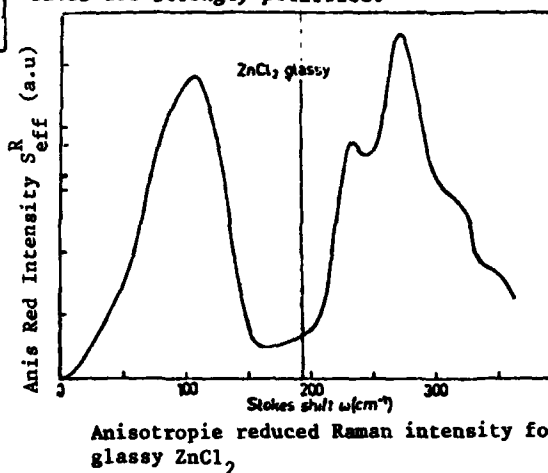
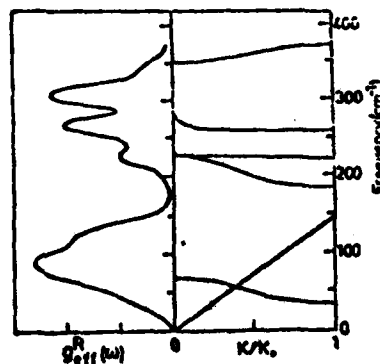


Fig. 4b (from ref. 5)

The resulting effect is a very large change of the O-H stretching region.

Representation of "average" dispersion curves (Ref. 16) on the right side and  $g_{eff}^R(\omega)$  on the left side, for molten ZnCl<sub>2</sub>.

Fig. 5 (from ref. 5)



#### References

- 1.- M.P. Fontana, G. Maisano, P. Migliardo and F. Wanderlingh, Solid State Comm. **23**, 489 (1977).
- 2.- M.P. Fontana, G. Maisano, P. Migliardo, and F. Wanderlingh, J. Chem. Phys. **69**, 676 (1978).
- 3.- F. Aliotta, M.P. Fontana, G. Maisano, P. Migliardo and F. Wanderlingh, Optica Acta, **27**, 931 (1980).
- 4.- F. Aliotta, G. Maisano, P. Migliardo and C. Vasi, Opt. Comm. **32**, 274 (1980).
- 5.- F. Aliotta, G. Maisano, P. Migliardo, C. Vasi, F. Wanderlingh, G.P. Smith and R. Triolo, J. Chem. Phys. July 15 (1981).

EFFECT OF A THERMAL ANNEALING ON THE LATTICE SPECIFIC HEAT AND THERMAL CONDUCTIVITY OF SUPERCONDUCTING AMORPHOUS  $Zr_{.76}Ni_{.24}$  ALLOYS

O. Béthoux, J.C. Lasjaunias and A. Ravex

*Centre de Recherches sur Les Très Basses Températures, C.N.R.S., B.P. 166 X, 38042 Grenoble Cedex, France*

**Abstract** - We have measured the low temperature (from 0.1 K up to 5 K) specific heat and thermal conductivity of an amorphous  $ZrNi$  superconducting alloy "as sputtered" and after annealing. We observe a variation of the Debye temperature and of the thermal conductivity related to a structural relaxation caused by the annealing.

Two amorphous  $Zr_{.76}Ni_{.24}$  alloys have been prepared by sputtering respectively at nitrogen and room temperature. They are obtained in the form of thick films (100  $\mu m$ ). The nitrogen temperature deposited sample has then been annealed under vacuum for 24 hrs at 250°C (the crystallisation temperature determined by D.T.A. was 350°C). The density measurement shows a slight increase for the annealed sample (see table) indicating a tendency to a more packed structure.

Specific Heat measurements are reported in fig.1 in a  $C/T$  versus  $T^2$  plot. From the superconducting transition temperature ( $T_c = 3.2$  K for both "as sputtered" samples and  $T_c = 3$  K for the annealed sample) to the upper limit of our measurements (about 6 K) the data are well fitted by a  $\gamma T + \beta T^3$  law. The values obtained for  $\gamma$  and  $\beta$  (see table) by this analysis are checked by comparison of the entropy in both superconducting and normal state below  $T_c$ . The presence of the  $\beta T^3$  term allows the determination of a Debye temperature  $\theta_D$  (see table) which is not possible in the case of amorphous insulators. For both "as sputtered" samples  $\beta$  values are very close. For the annealed sample the lattice contribution decreases corresponding to a variation of about 15 % of the Debye temperature. This increase of  $\theta_D$  corresponds to a hardening of the structure. Unfortunately no sound velocity measurements are available on such amorphous alloys in order to get an other determination of  $\theta_D$ . But similar conclusions have been drawn on  $PdSi$  glassy alloy (1).

Results of Thermal Conductivity measurements for both "sputtered" and annealed nitrogen deposited samples are shown in fig. 2. The superconducting transition temperatures  $T_c$  determined in the specific heat measurements are reported by arrows : they correspond very well to the change in the regime in the phonon-electron scattering due to the rapid decrease of the number of normal electrons below  $T_c$ .

Below  $T_c$ , both electron heat transport and phonon-electron scattering become rapidly negligible. Then the phonon conductivity  $K_{ph}$  is mainly limited by the interaction with the low energy excitations and the sample boundary scattering. In fact,



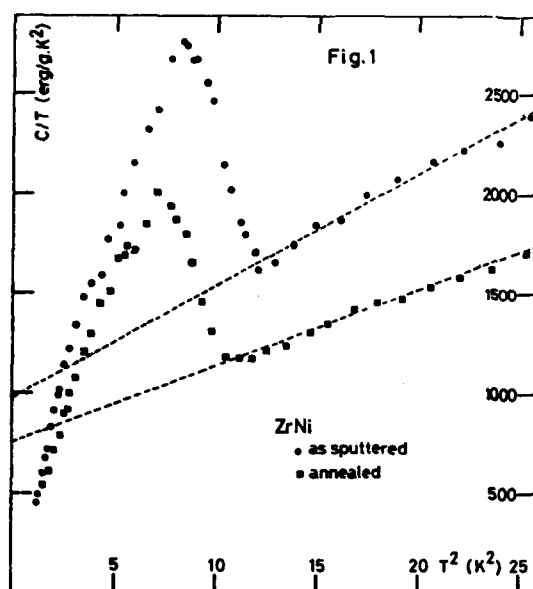
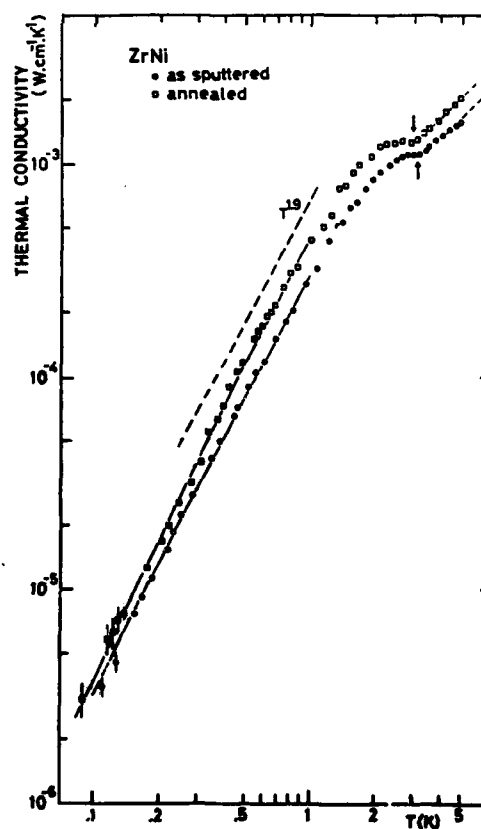


Fig. 1 : Specific heat before and after annealing.

dashed lines correspond to the  $\gamma T + \beta T^3$  laws

Fig. 2 : Thermal Conductivity before and after annealing.

The arrows indicate the superconducting transition temperatures determined by the specific heat measurements. The full lines represent the fit of the data by the phonon thermal conductivity limited by both scattering due to TLS and boundary scattering. The dashed line  $T^{1.9}$  is drawn for comparison.



above 0.3 K we observe a  $T^{1.9}$  like variation, characteristic in the amorphous materials of the resonant scattering of phonons by the two level systems (T.L.S.) : the Casimir limitation just occurs below 0.3 K. The scattering of phonons by T.L.S. is described as :

$$K_{\text{ph-TLS}} = A \frac{k_D^3}{\pi^2} T^2 \frac{v_D}{n\bar{M}^2}$$

where  $n$  is the density of states of TLS strongly coupled to the phonons and  $\bar{M}$  is an average coupling constant of TLS with phonons. Using an average Debye sound velocity  $v_D$  obtained from the  $\theta_D$  value of specific heat measurements we determine the unique adjustable parameter  $n\bar{M}^2$  (see table). To the observed increase of 50 % of thermal conductivity by annealing corresponds a significant decrease of  $n\bar{M}^2$  by a factor 1.35. This variation is well correlated to a diminution of the TLS specific heat observed in other experiments (2). Qualitatively these results are coherent and agree with a theoretical model of structural relaxation developed by Banville and Harris (3) : they assume that a TLS is a single atom moving between two or more alternate equilibrium positions within a void of the structure. This model predicts a decrease of TLS density with the disappearance of the voids during annealing.

#### References

- (1) Uichiro-Mizutani and T.B. Massalski, J. Phys. F : Metal Phys. 10 (1980), 1093-1100.
- (2) To be published in LT 16 Proceedings by the authors.
- (3) M. Banville and R. Harris, Phys. Rev. Lett. 44 (1980), 1135.

Zr <sub>0.76</sub> Ni <sub>0.24</sub>	as sputtered (both samples)	annealed
$\rho(\text{g/cm}^3)$	$6.85 \pm 0.01$	$6.95 \pm 0.01$
$\gamma(\text{mJ/mole K}^2)$	$8.15 \pm 0.2$	$6.30 \pm 0.1$
$\beta(\text{mJ/mole K}^4)$	0.465	0.315
$\theta_D(\text{K})$	161	184
$v_D(\text{cm/s})$	$1.47 \times 10^5$	$1.67 \times 10^5$
$n\bar{M}^2(\text{erg/cm}^3)$	$9.1 \times 10^7$	$6.7 \times 10^7$

Table : Experimental parameters.

## LOW TEMPERATURE THERMAL PROPERTIES OF CYCLOHEXANOL : A GLASSY CRYSTAL SYSTEM

E. Bonjour, R. Calencluk, R. Lagnier and B. Salce

*Service des Basses Températures, Laboratoire de Cryophysique, Centre d'Etudes Nucléaires de Grenoble, 85 X, 38041 Grenoble Cedex, France*

**Abstract.** - Specific heat and thermal conductivity measurements on "glassy" crystalline and crystalline cyclohexanol are reported. The glassy crystal phase shows the same anomalous behaviour found in glasses at helium temperatures.

Recently several experiments have shown that crystals containing structural disorder can at low temperatures display the same kind of anomalous behaviour found in amorphous solids. The study of this class of systems is a promising way to clear up the microscopic origin of the excitations responsible for these anomalies. Glasslike behaviour has been well established for some superionic conductors as  $\text{Li}_3\text{N}$  (1) and  $\beta$ -alumina (2), irradiated quartz (3) and others disordered crystals (4).

In this paper we present the results of specific heat  $C$  and thermal conductivity  $K$  measured between 1.5 and 20 K on a new type of disordered crystal ; namely the "glassy" crystalline phase (crystal I [5]) of cyclohexanol. We also present the results corresponding to the crystal III phase obtained by the recrystallization of the previously measured "glassy" crystalline samples.

A "glassy" crystal can be obtained by cooling through a metastability region an orientationally disordered phase such as the so-called plastic phases (6). At low temperatures the orientation disorder becomes static in the experimental time scale and on warming we observe a glass transition phenomenon.

Plastic crystalline cyclohexanol is stable between 299 K (melting point) and 265 K but it is easily supercooled and glass transition takes place around 150 K. Polymorphism of cyclohexanol has been fully described by Adachi et al [5]. Prior to the low temperature measurements we have performed a differential scanning calorimetry study on our product (Merck, Typanalyse) in order to determine the right conditions to obtain the phases investigated. Our results confirm those of Adachi. So the crystal III phase was prepared by heating the crystal I up to 240 K and then cooling to low temperatures.

The thermal conductivity  $K(T)$  was measured using standard steady state techniques from 1.5 to 20 K. The major problem arose from the low melting point (299 K) of cyclohexanol which prevented us using a classical arrangement. The most efficient way was to put the sample inside a PVC cylinder shaped cell (very thin walls) and,

to perform measurements on the sample and the cell together. Next step was to measure  $K(T)$  of the cell. Taking into account the respective cross sectional areas of the cell and the sample, it was possible to deduce the exact thermal conductivity of cyclohexanol.

The specific heat measurements were performed, between 1.5 and 20 K using an adiabatic differential method, operated at constant heating rate, as described in previous papers (6).

The specific heat results are display in Fig.1 as a  $C/T^3$  versus  $T$  plot and those of thermal conductivity  $K$  are represented in Fig.2.

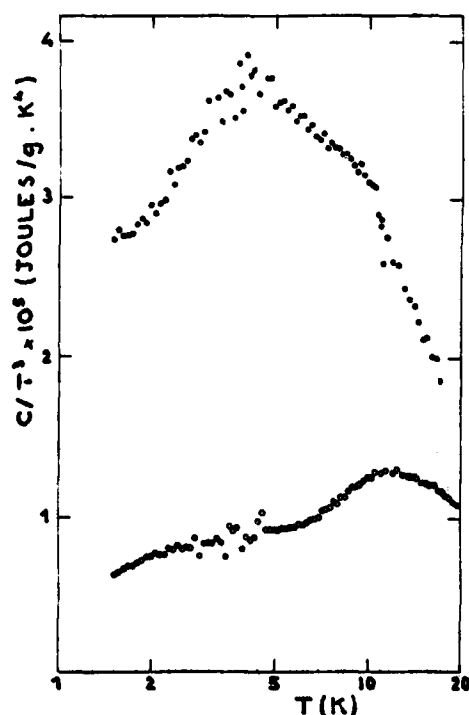


Fig.1. - Specific heat of cyclohexanol  
● "glassy" crystal I  
○ crystal III

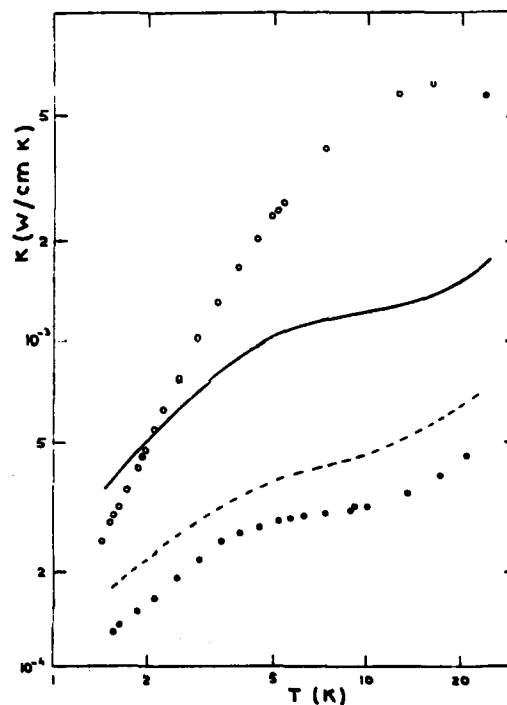


Fig.2. - Thermal conductivity of cyclohexanol  
● "glassy" crystal I  
○ crystal III  
For comparison the solid and dashed lines show the results of silica and selenium glass (literature).

In both cases the shape of the curves corresponding to the glassy crystal is identical to those found in glasses. The "plateau" of  $K$  around 5 K with a  $K$  value of the order of  $10^{-4} \text{ Wcm}^{-1} \text{K}^{-1}$  and the strong increase (faster than  $T^3$ ) of  $C$  at  $T = 3$  K, giving a peak in the  $C/T^3$  plot, are universal features of vitreous materials. In contrast the recrystallized samples behave as normal crystals. The origin of these anomalies in normal glasses is still unknown and their occurence in a glassy crystal is a useful result eliminating a certain number of possible hypothesis. As "glassy"

cyclohexanol is a good crystal, in the sense that the molecular mass centers form a periodic lattice, the existence of large scale density fluctuations (7), voids (8) or some kind of free volume (9) which are sometimes proposed should be excluded.

#### References

- (1) P.J. ANTHONY and A.C. ANDERSON, Phys. Rev. B 19 5310 (1979)
- (2) D.W. OSBORNE and H.E. FLOTOW, J. Chem. Thermodyn. 10 675 (1978)
- (3) C. LAERMANS and B. DAUDIN, in Phonon Scattering in Condensed Matter, edited by H.J. MARIS (Plenum, New York, 1980), p. 21
- (4) U.A. ACKERMAN, D. MOY, R.C. POTTER, A.C. ANDERSON and W.N. LAWLESS, Phys. Rev. B 23 3886 (1981)
- (5) K. ADACHI, M. SUGE and S. SEKY, Bull. Chem. Soc. Japan 41 1073 (1968)
- (6) R. LAGNIER, J. PIERRE and M.J. MURTIMER, Cryogenics 349 (1977)
- (7) D. WALTON Solid State Commun. 14 335 (1974)
- (8) A.S. WAGH, J. Phys. Chem. Solids 42 185 (1981)
- (9) M.H. COHEN and G.S. GREY, Phys. Rev. Lett. 45 1271 (1980)

# CONNECTION BETWEEN THE LOW TEMPERATURE THERMAL PROPERTIES OF GLASSES AND THEIR GLASS TRANSITION TEMPERATURE

T. Klitsner, A.K. Raychaudhuri\* and R.O. Pohl

*Laboratory of Atomic and Solid State Physics, Cornell University, Ithaca, NY 14853, U.S.A.*

**Abstract.** Water doping of nitrate glasses lowers their thermal conductivity. The effect, however, is smaller than expected on the basis of the increased density of states of anomalous states observed in specific heat measurements.

Addition of foreign atoms or molecules to crystalline solids changes their lattice vibrational spectrum, resulting in localized modes, resonances, and tunneling states. We are exploring whether similar effects can also be caused in amorphous solids. As host glass, we have chosen nitrate glasses of the composition 40 mole %  $\text{Ca}(\text{NO}_3)_2$  and 60 mole %  $\text{KNO}_3$ . Doping with  $\text{LiNO}_3$  and  $\text{KNO}_2$  up to their solubility limits,  $6 \times 10^{20}$  and  $4.4 \times 10^{20} \text{ cm}^{-3}$ , respectively, caused no discernible effect on the low temperature specific heat of the glass (< 2% change),<sup>1</sup> in contrast to the doping of alkali halide crystals with  $\text{Li}^+$  or  $\text{NO}_2^-$  ions, which results in low energy tunneling states in many hosts.<sup>2</sup> Doping the glass with water, however, at concentrations between 1 and  $3 \times 10^{21} \text{ cm}^{-3}$ , increased the low temperature specific heat anomaly known to be characteristic for the amorphous state.<sup>1</sup> The increase in entropy was found to scale with the water concentrations, but was approximately four orders of magnitude smaller than it would be if every water molecule would contribute one tunneling state. Thus, tunneling (or some other kind of low energy vibration) of the water also appears to be very unlikely in this case.

We did observe, however, that the specific heat anomaly of the water-doped glass scales with the reciprocal glass transition temperature  $T_G$ , i.e.,

$$a_{\text{exc}} \propto T_G^{-1}, \text{ with} \quad (1)$$

$$C_{\text{exc}} = C_v - C_{\text{Debye}} = a_{\text{exc}} T^{1.16}, \quad (2)$$

see Fig. 1. Eq. (1) suggests that the low temperature anomalous states are a measure of the disorder frozen-into the glass as it solidified, as has also been proposed independently by Cohen and Grest,<sup>3</sup> based on the free-volume theory of glasses.

In the present study, we have searched for a change in the low temperature thermal conductivity in water-doped nitrate glass. Sample preparation, determination of  $T_G$  and of the thermal conductivity have been described previously.<sup>1,2,4</sup>

\*Present address : Max-Planck-Institut für Festkörperforschung, Heisenbergstr. 1, D-7000 Stuttgart 80, F.R.G.

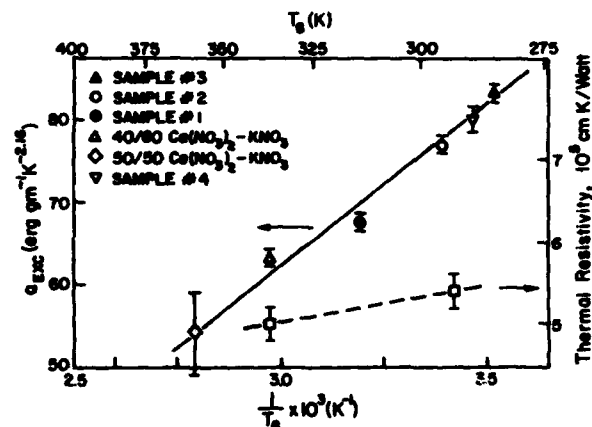


Fig. 1. The anomalous specific heat of 40/60  $\text{Ca}(\text{NO}_3)_2\text{KNO}_3$  glass increases with decreasing  $T_g$  resulting from doping with water, after Ref. 1. Water concentrations: #1, 1.1; #2, 2.4; #3, 3.8; #4, 3.3, all in  $10^{21} \text{ cm}^{-3}$ . Also shown is the thermal resistivity  $\Lambda^{-1}$  at 0.1 K, see right hand ordinate. The dashed line connecting the two data points, obviously, is only an aid for the reader. For equal changes in  $T_g$ ,  $a_{\text{exc}}$  increases approximately four times more than  $\Lambda^{-1}$ .  $T_g$  for the conductivity samples is 339 K (undoped), 292 K (doped).

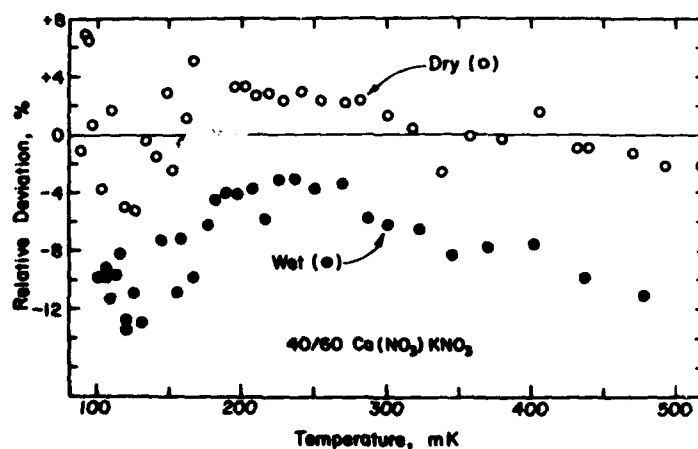


Fig. 2. Percent relative deviation, defined as  $(\Lambda_{\text{exp}} - \Lambda_{\text{fit,undoped}})/\Lambda_{\text{fit,undoped}}$  of the measured conductivity of the undoped ("dry") and the doped ("wet") samples. The best fit to the dry sample,  $\Lambda_{\text{fit,undoped}} = 1.82 \times 10^{-4} T^{1.96} \text{ (W cm}^{-1} \text{ K}^{-1})$ , with  $T$  measured in K).

The conductivity  $\Lambda$ , measured between 0.1 and 0.5 K, followed a power law for both the doped and the undoped sample. For the undoped sample,  $\Lambda = 1.82 \times 10^{-4} T^{1.96}$  (in  $W\ cm^{-1}\ K^{-1}$ ), while for the doped sample,  $\Lambda = 1.69 \times 10^{-4} T^{1.96}$ , i.e., 7% smaller. The quality of the power law fit to the conductivity of the undoped sample is shown in Fig. 2, which also shows the relative deviation of the data obtained on the doped ("wet") sample relative to the power law fit for the undoped ("dry") sample. The data for the doped sample are lower, on average, by 7% than the data for the undoped sample. Both sets of data show a peak near 0.25 K, which we believe to result from an error in calibration of our thermometer.

In Fig. 1, we have plotted the thermal resistivity  $\Lambda^{-1}$ , at 0.1 K, for the two samples. The error bars are those of the accuracy with which the sample geometry was measured ( $\pm 5\%$ ). It is seen that the increase of  $a_{exc}$ , i.e., of the density of states in the water-doped sample, is larger than the increase in thermal resistance, the latter being just barely outside the experimental error. Conceivably, the increased density of states of the scattering centers is partly offset by an increase of the speed of sound (which would increase the low temperature thermal conductivity), and/or by a decrease of the coupling constant in the doped sample. Measurements of the speed of sound in these glasses, in progress in our laboratory, will shed some light on these questions.

This research was supported in part by the National Science Foundation under Grant #DMR-78-01560 and through the Cornell Materials Science Center.

#### References

1. A. K. Raychaudhuri and R. O. Pohl, Solid State Comm. 37, 105 (1980), and submitted to Phys. Rev.
2. V. Narayanamurti and R. O. Pohl, Rev. Mod. Phys. 42, 201 (1970).
3. M. H. Cohen and G. S. Grest, Phys. Rev. Lett. 45, 1771 (1980), and Solid State Comm., in print.
4. A. K. Raychaudhuri, Ph.D. Thesis, Cornell University, August 1980, unpublished. Cornell Materials Science Center Report #4284, 1980.



AD-A126 574

INTERNATIONAL CONFERENCE ON PHONON PHYSICS 31 AUGUST-3  
SEPTEMBER 1981 BLOOMINGTON INDIANA(U) INDIANA UNIV AT  
BLOOMINGTON W E BROW DEC 81 ARD-17340.1-PH

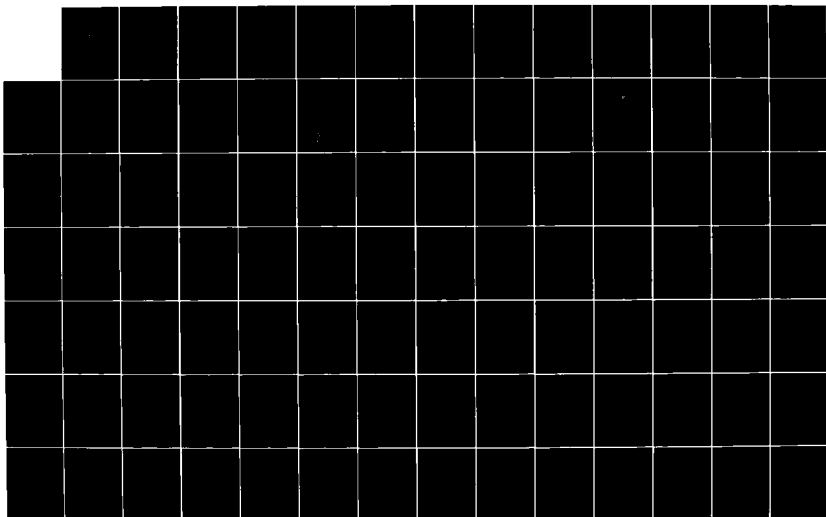
2/10

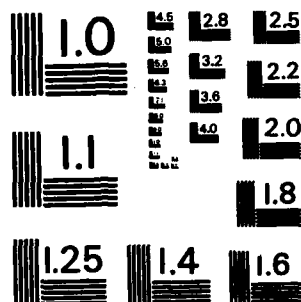
UNCLASSIFIED

MIPR-ARD-43-80

F/G 20/2

NL





MICROCOPY RESOLUTION TEST CHART  
NATIONAL BUREAU OF STANDARDS-1963-A

## THE THERMAL CONDUCTIVITY OF SEMICRYSTALLINE POLYMERS AT VERY LOW TEMPERATURES

D. Greig and N.D. Hardy

*Department of Physics, University of Leeds, Leeds LS2 9JT, England*

**Abstract.** - For polyethylene the temperature dependence of thermal conductivity decreases below a temperature  $T^*$  -- in this case 1 K -- from  $T^2$  to  $T$ . We now present experimental results on a lightly modified form of polyethylene for which  $T^*$  is raised to between 3 K and 9 K. There appears to be a correlation between  $T^*$  and the microcrystalline structure and we speculate that for semicrystalline polymers in this temperature range structure scattering is more important than 2-level tunnelling.

The general trends of the temperature dependence of the thermal conductivity,  $\kappa$ , of semicrystalline polymers have been well-established between  $\sim 2$  K and room temperature<sup>1</sup>. We have studied in detail the influence of (i) crystallinity<sup>2</sup> and (ii) crystallite orientation<sup>3</sup>, and have found that above and below  $\sim 20$  K the variations in  $\kappa$  with these two parameters are completely different. At the higher end of the range the conductivity increases both with crystallinity and with orientation. At low temperatures, on the other hand, the specimens with the greatest crystallinity have the lowest conductivity with values at  $\sim 2$  K roughly an order of magnitude lower than those found "universally" for all amorphous polymers<sup>4</sup>. These low values, furthermore, are to be more or less independent of crystallite orientation.

This rather dramatic difference in behaviour is attributed to the conditions arising at low temperatures when the phonon mean free path,  $\ell$ , becomes larger than the dimension of the structural units. As the difference in density between crystalline and amorphous regions can be as great as 20% the "structure scattering" of the composite polymer gives rise to a thermal resistance that is considerably greater than that of the amorphous material alone. For these materials this structure scattering argument seems preferable to the 2-level phonon scattering explanation that has been applied so successfully to materials that are completely amorphous<sup>5,6</sup>.

At still lower temperatures it is found that for polyethylene (PE) the variation of  $\kappa$  with  $T$  undergoes a sharp decrease in slope, changing at a temperature  $T^*$  from a dependence of about  $T^{1.8}$  to a variation that is almost linear. The anomaly, although towards the lower end of the temperatures, has been clearly established<sup>7,8,9</sup> and has been explained by the dominant phonon wavelength,  $\bar{\lambda}$ , becoming greater than the thickness of the crystallites. In the latest study it has been found to occur

at a higher value of  $T^*$  in a specimen of PE that had been extruded. It therefore appears that we can define an "ultra-low" temperature range in which the orientation properties of the crystallites are again of importance.

We are now reporting on some systematic studies of this effect by making measurements on a modified form of PE, Rigidex 40, for which the values of  $T^*$  are conveniently rather higher. Rigidex 40 is an ethylene-propylene co-polymer containing 5 methyl side groups per thousand main chain atoms.

We have obtained 2 sets of measurements both showing very marked effects. In the first (figure 1) we show the temperature variation of  $\kappa$  in the extrusion direction for a set of samples for each of which the extrusion ratio was 15 but which were extruded at 75°C, 100°C, and 110°C. Corneliusen and Peterlin<sup>10</sup> have shown that increasing the drawing temperature of PE from 40°C to 140°C results in a dramatic increase in long period,  $L$ , with values rising from about 170 Å to nearly 400 Å. Although there are no published data on extruded Rigidex 40, preliminary experiments by Hope<sup>11</sup> have shown the same trend. The most important feature of figure 1 is that the changes in  $\kappa$  appear only at very low temperatures.

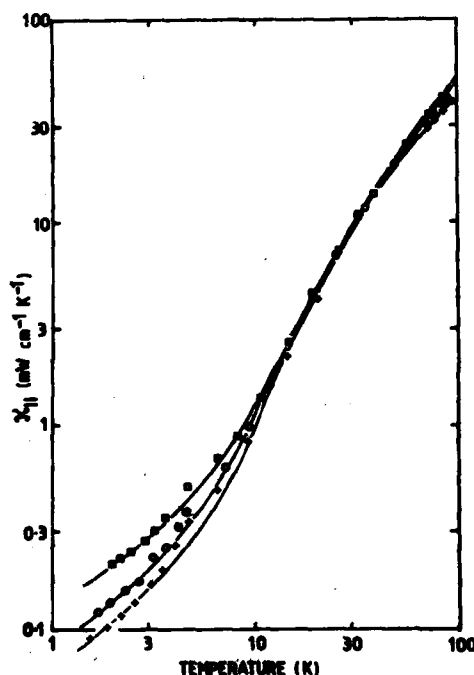


Fig. 1. Temperature variation of  $\kappa$  in the extrusion direction for samples of extrusion ratio 15 extruded at:  $\square$ , 75°C;  $\circ$ , 100°C;  $+$ , 110°C.

In figure 2 we show the temperature variation of  $\kappa$  for various values of  $\lambda$  in samples that have all been extruded at 100°C. Hope has obtained some indication of a reduction in  $L$  with increasing  $\lambda$ , but we must also consider an increase in the number of intercrystalline bridges created during the extrusion process. From figure 2 we see that the conductivity is changed both above 20 K and at "ultra-low" temperatures.

Very generally we may argue that the change in slope at  $T^*$  with falling temperature indicates a transition to a regime in which the mean free path is relatively long; that is, as the dominant phonon wavelength,  $\bar{\lambda}$ , becomes longer, phonon scattering is reduced. The results indicate that this occurs at the highest temperatures for material that has been (a) extruded at low extrusion temperatures (figure 1) and (b) extruded to the greatest possible extrusion ratio (figure 2).

This is entirely in accordance with the observation that both of these processes give rise to long periods that are relatively small, with an implication that the crystalline structure is then most broken up. This results in less scattering for 2 possible reasons. (1) When  $\bar{\lambda}$  becomes greater than the dimensions of the crystalline units some form of Rayleigh scattering takes place. When the density of scattering sites is large interference occurs between scattered wavefronts giving a relationship  $\ell \propto \nu^{-2}$ . Combined with a specific heat varying as  $T^3$  this leads to  $\kappa \propto T$  in agreement with the experimental results. (2) On a more qualitative argument orientation will tend to 'homogenize' the polymer making the amorphous material more dense and the crystalline component less so. The specimen will thus behave more like an amorphous solid with fluctuations in properties over a length  $\sim 100 \text{ \AA}$ . Morgan and Smith<sup>12</sup> have shown that this leads to a temperature variation of  $\kappa$  of exactly the form that we have found.

We should like to thank Dr P.S.Hope and Professor I.M. Ward for their interest in the work and the SERC for continued financial support.

#### References

1. See, for example, C.L. Choy, *Polymer*, **18**, 984 (1977).
2. C.L. Choy and D. Greig, *J.Phys.C*: **8**, 3121 (1975).
3. A.G. Gibson, D. Greig, M. Sahota, I.M. Ward, and C.L. Choy, *J.Polym.Sci:Polym. Letts.Edn.*, **15**, 183 (1977).
4. R.B. Stephens, *Phys.Rev.B.*, **8**, 2896 (1973).
5. P.W. Anderson, B.I. Halperin, and C.M. Varma, *Phil.Mag.*, **25**, 1 (1972).
6. W.A. Phillips, *J.Low Temp.Phys.*, **7**, 351 (1972).
7. M. Giles and C. Terry, *Phys.Rev.Letts.*, **22**, 882 (1969).
8. A. Bhattacharyya and A.C. Anderson, *J.Low Temp.Phys.*, **33**, 64 (1979).
9. D.M. Finlayson, P. Mason, J.M. Rogers, and D. Greig, *J.Phys.C*: **13**, L185 (1980).
10. A. Peterlin, *J.Polym.Sci: Part C*, **18**, 123 (1967).
11. P.S. Hope, Thesis, University of Leeds, U.K. (1978).
12. G.J. Morgan and D. Smith, *J.Phys.C*: **7**, 649 (1974).

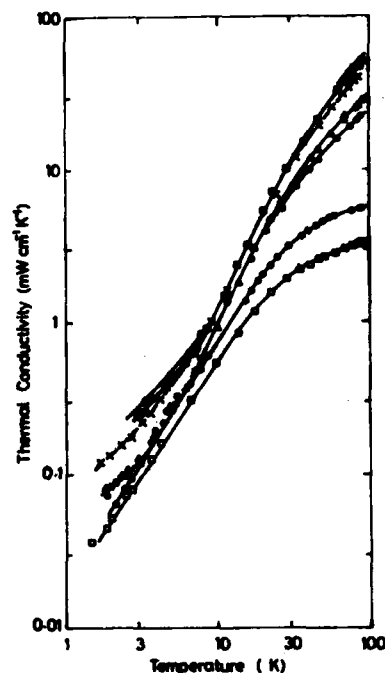


Fig.2. Temperature variation of  $\kappa$  for samples extruded at  $100^\circ\text{C}$  with extrusion ratios:  $\square$ , 10 (measured perpendicular to the extrusion direction);  $\circ$  (isotropic; 0.5;  $\Delta$ , 10;  $\times$ , 15;  $\blacksquare$ , 17; —, 20 (all measured parallel to the extrusion direction).

# ATTENUATION AND VELOCITY CHANGE OF ACOUSTIC WAVES IN THE AMORPHOUS METAL PdSiCu FROM 0.05 K TO 90 K

P. Doussineau

Laboratoire d'Ultrasons, Université Pierre et Marie Curie, Tour 13, 4 place Jussieu, 75230 Paris Cedex 05, France

**Abstract.** - Previous acoustic experiments in a-PdSiCu were extended. Attenuation and velocity change were measured at various frequencies around 500 MHz from 0.05 K to 90 K. The attenuation is interpreted as the sum of two contributions: one due to the relaxation of the TLS and the other due to an activated process. The velocity change is explained with the same two preceding contributions; however it is necessary to add not only the resonant contribution but also an electronic term varying as  $T^2$ .

1. **Experiments.** - It is now well established that two-level systems (TLS) are present in amorphous metals [1]. Among other experimental methods ultrasonic waves have proved that they are one of the best tool to study TLS in amorphous metals. I present here an extension of previous acoustic experiments in amorphous  $\text{Pd}_{0.775}\text{Si}_{0.165}\text{Cu}_{0.06}$  [2]. The attenuation and phase velocity change of transverse acoustic waves at four frequencies from 185 to 852 MHz have been measured in the temperature range 0.05 to 90 K. The results are shown in Figures 1 and 2 for the attenuation and the velocity change respectively. The main features are: - in the temperature range below 6 K the attenuation varies linearly with the temperature and with the frequency. - At higher temperatures the attenuation still increases, goes through a broad maximum near 20-25 K and then decreases slowly (Fig. 1). A similar peak has been previously reported in a  $\text{Pd}_{0.775}\text{Si}_{0.165}\text{Ag}_{0.06}$  sample for longitudinal waves [3]. - At the lowest temperatures ( $T < 2$  K) the velocity first increases roughly logarithmically when the temperature increases (Fig. 2). This behavior is now well known for amorphous metals [1]. - Then the velocity goes through a maximum and decreases on all the temperature range explored (up to 70 K). This decrease cannot be said linear if the entire temperature range (4 to 70 K) is considered, contrary to what was claimed for the same material in the range 4 to 20 K [4].

2. **Theory.** - The preceding results are explained in the framework of the TLS theory. I recall here only the results useful to what follows. Details can be found elsewhere [1,5]. The resonant interaction between TLS and ultrasonic wave leads to a velocity change given by  $\Delta v/v_0 = C \ln T/T_0$ , where  $T_0$  is an arbitrary reference temperature,  $v_0$  the sound velocity,  $C = \bar{P} \gamma^2 / \rho v_0^2$  with  $\rho$  the density,  $\gamma$  an elastic deformation potential and  $\bar{P}$  the density of states of the TLS. Besides the resonant interaction, the elastic wave undergoes a relaxational attenuation (and dispersion). In terms of the complex change of the elastic constant  $\sigma$ , it is given by

$$\frac{\Delta \sigma}{\sigma_0} = -C \int d\left(\frac{\beta E}{2}\right) \text{sech}^2\left(\frac{\beta E}{2}\right) \int_{r_m}^1 dr \frac{(1-r)^{1/2} r^{-1}}{1 + i \omega T_1}$$

where  $\beta = 1/kT$ ,  $E$  is the splitting between the two-levels,  $r = (\Delta_0/E)^2$  with  $\Delta_0$  the tunneling matrix element [5],  $\omega/2\pi$  is the frequency of the ultrasonic wave, and  $T_1$  is the longitudinal relaxation time of the TLS.  $T_1$  characterizes the return towards equilibrium of the TLS population. In a metal two channels are possible, via the thermal phonons or via the conduction electrons [1]. Consequently

$$T_1^{-1} = \left(T_1^P\right)^{-1} + \left(T_1^E\right)^{-1} \quad \text{where} \quad \left(T_1^P\right)^{-1} = r K_3 T^3 \left(\frac{\beta E}{2}\right)^3 \coth \frac{\beta E}{2}, \quad \text{with} \quad K_3 = \frac{4 k^3}{\pi \rho \hbar^4} \int \frac{\gamma_\tau^2}{v_\tau^5}$$

( $\tau = L$  or  $T$  stands for the polarization) and  $\left(T_1^E\right)^{-1} = r K_3 T \frac{\beta E}{2} \coth \frac{\beta E}{2}$ , with  $K_1 = \frac{\pi k}{2 \hbar} (\tilde{\rho} K_0)^2$ .  $\tilde{\rho}$  is the electric density of states at the Fermi level and  $K_0$  an electric deformation potential. In the general case the attenuation ( $\alpha = \frac{\omega}{v} \text{Im} \frac{\Delta c}{c_0}$ ) and the velocity change ( $\frac{\Delta v}{v} = \frac{1}{2} \text{Re} \frac{\Delta c}{c_0}$ ) are given by a numerical calculation.

Besides this first relaxational effect the acoustic attenuation in amorphous materials generally presents a broad peak attributed to some activation processes above energy barriers [6]. The corresponding change in the elastic constant is given  $\frac{\Delta c}{c_0} = -\epsilon \int_0^1 \frac{1}{1 + \tau \omega \tau(U)} n(U) dU$  where  $\epsilon$  is the relaxation strength,  $\tau(U)$  is a relaxation time given by the Arrhenius law  $\tau(U) = \tau_0 \exp \beta U$ ,  $n(U)$  characterizes the distribution of energy barriers  $U$ . Usually  $n(U)$  is taken as a constant. I found it is better to choose a gaussian distribution  $n(U) = \sqrt{\frac{2}{\pi}} \frac{1}{\sigma} \exp -\frac{U^2}{2\sigma^2}$  where  $\sigma$  has to be determined by the experiment.

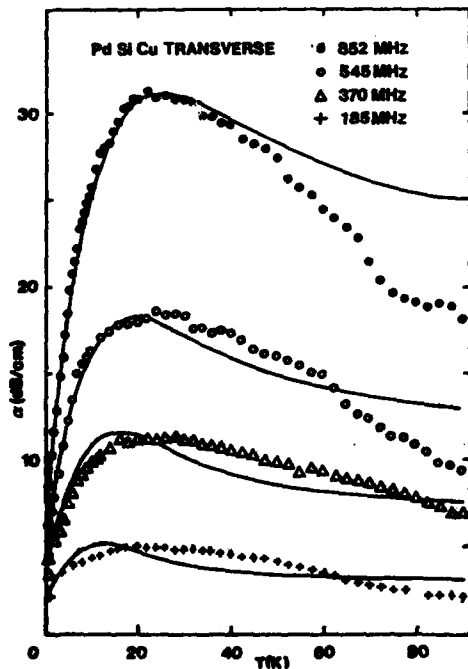


Figure 1

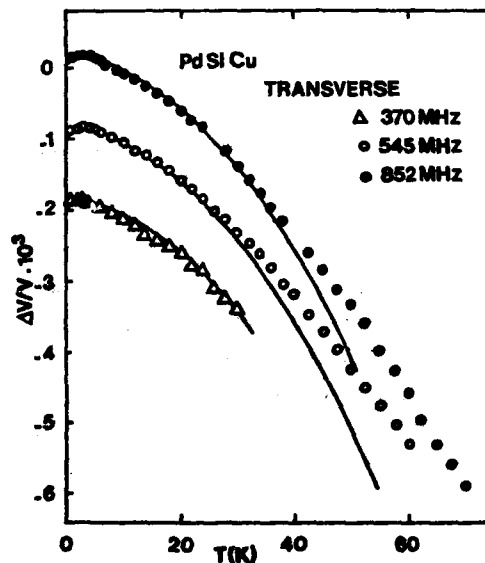


Figure 2

3. Interpretation. - The whole set of results presented in Figures 1 and 2 is described with the theory outlined above.  $C$ ,  $K_1$ ,  $K_2$ ,  $\epsilon$ ,  $\tau_0$  and  $\sigma$  are used as free parameters in the numerical computation. In fact  $C$  is given by the logarithmic increase of the velocity at the lowest temperatures, while the product  $K_1 C$  is determined from the attenuation in the same temperature range [2]. It was possible to obtain a good fit (shown by the solid lines in Fig. 1) of the attenuation results when the attenuation due to an Arrhenian process with a gaussian distribution of the energy barriers was added to the relaxational attenuation due to the TLS. The best agreement was obtained with  $C_T = 5.5 \cdot 10^{-5}$ ,  $K_1 = 1.5 \cdot 10^{10} \text{ K}^{-1} \text{ s}^{-1}$ ,  $K_2 = 2 \cdot 10^8 \text{ K}^{-3} \text{ s}^{-1}$ ,  $\epsilon = 4.4 \cdot 10^{-3}$ ,  $\sigma = 5 \cdot 10^{-15} \text{ erg}$  and  $\tau_0 = 3.5 \cdot 10^{-11} \text{ s}$ .

Then the velocity change was calculated with the same set of parameters. The logarithmic resonant contribution was also added. A good fit was obtained for temperatures up to 4 K. At higher temperatures the observed decrease of the velocity was faster than the calculated one. A good fit (shown by the solid lines in Fig. 2) up to 40 K was obtained when a decreasing term varying as  $1.6 \cdot 10^{-6} \text{ T}^2$  was added to the three preceding contributions. Such a velocity variation was expected in a metal as an electronic contribution to the elastic constant [7].

Thus a satisfactory agreement is obtained between the calculated curves and the experimental results in PdSiCu for both the attenuation and the velocity change at various frequencies in an extended temperature range. From the preceding interpretation a question arises. Have the TLS and the particles involved in the Arrhenius process a common origin? The procedure given above assumes the answer is negative because the different contributions of the attenuation (or velocity) are added. In the opposite case not the attenuation (or velocity) but the relaxation rates have to be added. Such a possibility has not yet been explored, but it will be the purpose of further research.

#### REFERENCES

- [1] BLACK, J. L., in *Metallic Glasses*, edited by H. J. Guntherodt and H. Bech (Springer Verlag, Berlin, 1980)
- [2] DOUSSINEAU, P., *J. Physique Lett.* 42 (1981) L-83, and references therein.
- [3] DUTOIT, M., *Phys. Lett.* 50 A (1974) 221.
- [4] BELLESSA, G., *Phys. Rev. Lett.* 40 (1978) 1456.
- [5] DOUSSINEAU, P., FRÉNOIS, C., LEISURE, R. G., LEVELUT, A., and PRIEUR, J. Y., *J. Physique* 40 (1980) 1193.
- [6] BELLESSA, G., *J. Physique Coll.* 40 (1980) C8-723.
- [7] ALERS, G. A., in *Physical Acoustics*, edited by W. P. Mason (Academic Press, New-York, 1966), Vol. IV-A, p. 277.



## POLARIZED RAMAN SCATTERING STUDIES OF FLUOROZIRCONATE AND FLUOROHAFNATE GLASSES

P.K. Banerjee<sup>(1)</sup>, B. Bendow<sup>(2)</sup>, M.G. Drexhage, J.T. Goltman<sup>\*(3)</sup>, S.S. Mitra <sup>\*(3)</sup>  
and C.T. Moynihan<sup>\*\* (3)</sup>

Solid State Sciences Div., Rome Air Development Center, Hanscom AFB, Massachusetts 01731, U.S.A.

<sup>\*</sup>University of Rhode Island, Kingston, Rhode Island 02881, U.S.A.

<sup>\*\*</sup>Catholic University of America, Washington, D.C. 20064, U.S.A.

**Abstract** - We report polarized Raman spectra for a set of heavy-metal multi-component fluoride glasses, containing the fluorides of hafnium, zirconium, barium, lanthanum and thorium. All the glasses have a dominant peak in their VV spectrum in the vicinity of  $580\text{ cm}^{-1}$  with a corresponding deep minimum in their depolarization spectrum. The spectra are relatively depolarized from near  $200\text{ cm}^{-1}$  to  $400\text{ cm}^{-1}$ .

1. **Introduction** - Many reports have appeared recently dealing with preparation and characterization of multicomponent heavy-metal fluoride glasses<sup>1</sup>, specifically fluorohafnates and fluorozeirconates, in which  $\text{HfF}_4$  or  $\text{ZrF}_4$  is the primary constituent, the secondary component is  $\text{BaF}_2$ , and the other components are the fluorides of rare-earths, group III elements or alkalis (either singly or in combination). One important prospective attribute of these glasses is continuous high transparency over an unusually wide range of frequencies spanning the mid-IR to the near UV. In particular, the infrared characteristics are of interest for a wide variety of applications ranging from laser windows to infrared fiber optics. Here we report selected results of polarized Raman studies aimed at obtaining information about the fundamental vibrational characteristics of this relatively new family of glasses.

2. **Experiment and Results** - The glasses utilized in the present study were synthesized at RADC and Catholic Univ. from high purity oxide or fluoride starting materials utilizing procedures described in detail elsewhere<sup>1</sup>. Samples several cm in diameter and 2-4 mm thick were prepared of compositions selected from the center of the glass formation regions. These compositions, denoted as ZBT, HBT, ZBL and HBL are indicated in Table 1.

Table 1. Fluoride Glass Compositions.

	$\text{ZrF}_4$	$\text{BaF}_2$	$\text{ThF}_4$	$\text{HfF}_4$	$\text{LaF}_3$
HBL	--	33.75	--	57.5	8.75
HBT	--	33.75	8.75	57.5	--
ZBL	57.5	33.75	--	--	8.75
ZBT	57.5	33.75	8.75	--	--

Polarized Raman spectra were taken in the  $90^\circ$  scattering geometry utilizing a Spex 1400 Spectrometer in conjunction with an argon-ion laser and a cooled FM130 photomultiplier; the spectral slit width was  $\sim 5\text{ cm}^{-1}$ . The polarized VV spectra

are shown in Fig. 1. A summary of the Raman data on these glasses is presented in Table II. The corresponding depolarization ratio,  $\rho$  (which is the ratio of HW to VV intensities) is shown in Fig. 2.

#### POLARIZED RAMAN SPECTRUM

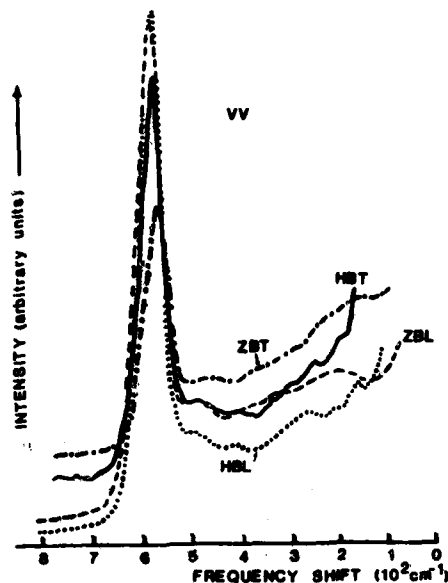


Fig. 1. Polarized VV Raman spectrum vs. frequency shift for four fluoride glasses.

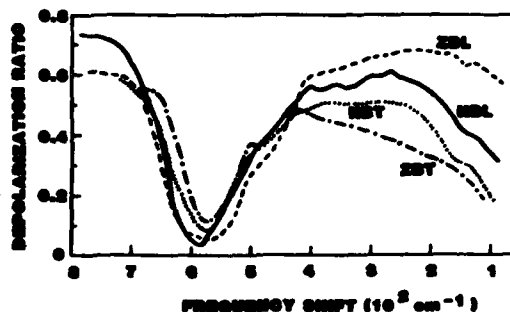


Fig. 2. Depolarization ratio vs. frequency shift for four fluoride glasses.

Table 2. Summary of Raman Data ( $\text{cm}^{-1}$ ) on Fluorozirconate and Fluorohafnate Glasses

HBT		HBL		ZBL		ZBT	
VV	HW	VV	HW	VV	HW	VV	HW
577v,p		578v,p		577v,p		578v,p	
480w		490m		480m		480m,	
400w	400m	400w	400m	390m	380m		
250m	260m	250m,sh	250m	235w,sh		230w,sh	
200w	200m	200w		200m	200m		200m,sh
160m		160m				160m	
100m		100m					

Symbols: v=very strong, p=polarized, m=medium, w=weak, sh=shoulder

3. **Discussion** - All of the VV spectra are dominated by an intense peak near  $580 \text{ cm}^{-1}$  which is associated with a corresponding deep minimum in the depolarization ratio. The position of this peak, and the major features of all of the spectra are similar for both hafnium as well as zirconium fluoride based glasses. This unexpected result may indicate a weakening of the force constants in  $\text{ZrF}_4$  as opposed to  $\text{HfF}_4$  glasses. The effect on the spectrum of changing the third component ( $\text{LaF}_3$  or  $\text{ThF}_4$ ) is relatively small, as is the case for IR reflectivity<sup>2</sup>.

The depolarization spectrum of any isotropic disordered material including glasses, liquids and gases should be characterized by  $0 < \rho < 3/4$ , which is indeed the case with the glasses studied here. The sharp pronounced minimum in  $\rho(\omega)$  near

$\sim 590 \text{ cm}^{-1}$  corresponds to the peak at  $\sim 580 \text{ cm}^{-1}$  in the VV spectrum. Based on molten salt data<sup>3</sup>, it may be identified with symmetric stretching modes of the  $\text{MF}_x^{4-x}$  coordination species (where  $x = 6$  to 8). Specifically, the latter suggests that the dominant peak be principally assigned to totally symmetric  $\text{MF}_6^{2-}$  stretching modes, in general agreement with crystalline peaks reported<sup>4</sup> in the range  $570\text{--}590 \text{ cm}^{-1}$  for both  $\text{ZrF}_6^{2-}$  and  $\text{HfF}_6^{2-}$ . The large width of this line ( $\sim 60 \text{ cm}^{-1}$ ) compared to that of crystals ( $10$  to  $20 \text{ cm}^{-1}$ ) is an expected attribute of a disordered system. The depolarization spectrum suggests that the broad Raman bands below  $400 \text{ cm}^{-1}$  are not primarily due to symmetric modes. Thus, contributions of Ba-F symmetric modes, which would be expected to occur in the general vicinity of  $250 \text{ cm}^{-1}$ , are not evident in the current spectra. The low frequency modes are more likely attributable to bending vibrations of Zr or Hf with F. It is also interesting to note the relative featurelessness of both the Raman and IR spectra of multicomponent glasses like ZBT, HBT, ZBL and HBL. This could be attributed to near coincidences of the fundamental mode frequencies of various components, and/or the one-mode behavior characteristic of certain mixed systems.

Finally, we note that IR spectra display two broad peaks in the high ( $400\text{--}600 \text{ cm}^{-1}$ ) and low ( $150\text{--}300 \text{ cm}^{-1}$ ) frequency regions. The Raman features in the vicinity of  $580$  and  $250 \text{ cm}^{-1}$  fall in-between the TO and LO modes deduced from reflectivity. This behavior is similar to that manifested in crystalline alkaline earth fluorides, where the Raman mode also falls in-between the corresponding TO and LO modes of the crystal.

- (1) IPA Appointee at RADC; permanent address: Rhode Island Junior Coll, Warwick, RI.  
 (2) Present Address: The BDM Corporation, 1801 Randolph Rd, SE, Albuquerque, NM 87106  
 (3) Research supported by Rome Air Development Center (AFSC), under Contracts No. F19628-77-C-0109 (U.R.I.) and F19628-77-C-0061 (C.U.). Present address of J. Goltman: Naval Underwater Systems Center, Newport, RI; Present address of C.T. Moynihan: Dept. of Materials Engineering, RPI, Troy, NY, 12181.

#### References

1. See, e.g. M.G. Drexhage et al, *Laser Focus* 16, 62(1980); B. Bendow and M.G. Drexhage, *Optical Engineering* (1981, in press); M.G. Drexhage et al, in "Physics of Fiber Optics", B. Bendow and S.S. Mitra, eds (Amer. Ceramic Soc., Columbus, Ohio, 1981).
2. B. Bendow et al, *Solid State Commun.* 37, 485(1981).
3. L.M. Toth et al, *J. Phys. Chem.* 77, 1384(1973).
4. See, e.g., K. Nakamoto, "IR and Raman Spectra of Inorganic Coord. Compounds" (Wiley, NY, 1978), pp 132-194.

THERMAL PHONON TRANSPORT STUDY OF THE DEFECTS CREATED IN QUARTZ SINGLE CRYSTALS BY DIFFERENT IRRADIATIONS ( $\gamma$  RAYS, ELECTRONS, NEUTRONS)

A.M. de Goër, M. Locatelli and C. Laermans\*

*Service Basses Températures, C.E.N.G., 85X, 38041 Grenoble Cedex, France**\*Lab. Vaste Stof- en Hoge Drukfysika, K.U. Leuven, Celestijnenlaan 200D, 3030 Leuven, Belgium*

**Abstract.**— Thermal conductivity measurements have been carried out between 80 mK and 30 K in quartz after  $\gamma$ , electron and neutron irradiation at different doses. All the samples were natural quartz of the same origin, in order to rule out the effects of different sample state. Electron and neutrons cause an additional phonon scattering which, below 1K, can be explained by the presence of tunneling states similar as in amorphous solids but which is very different above 1K, indicating the different origin of the glassy "plateau".  $\gamma$ -irradiation does not induce a detectable number of tunneling states.

**Introduction.**— In order to come to a better understanding of the microscopic origin of the tunneling states in amorphous solids some attention has been directed to crystalline quartz which is locally disordered by high energy neutrons and electrons, showing similar low temperature dynamical properties<sup>1-4</sup>. It is observed thereby that there are differences between the experimental results of different authors for similar experimental conditions<sup>3,5</sup> and also that some findings are attributed to impurities and inclusions<sup>4,5</sup> showing the influence of the sample state. Therefore we want to report here a set of results of thermal conductivity measurements after different kinds of irradiation, all on samples of the same origin. In addition in one of the neutron irradiated samples ultrasonic saturation experiments without<sup>1,2</sup> and in<sup>6</sup> a magnetic field have been carried out previously and the number of tunneling states and their coupling constant to phonons has been determined<sup>2</sup>.

**Experimental results.**— The thermal conductivity  $K$  measurements have been carried out between 80 mK and 30 K and the results are given in fig. 1 (a and b). Part of the data have been reported before<sup>3,6</sup>. All are natural Brazilian quartz rods of the same origin, 3mm in diameter and about 8mm in length. The value of  $K$  at the maximum, for the virgin sample, is similar to that found in earlier measurements taken into account the smaller dimensions of the present samples. Between 0.4 and 3K a  $T^3$  behavior typical for boundary scattering is found and the data agree well with the values for the boundary scattering calculated from the elastic constants (Casimir limit). This also implies that we find no evidence for the presence of inclusions as observed before in synthetic samples<sup>4</sup>. Using  $\gamma$ -irradiation, the effect of purely ionizing irradiation was measured (until now only measured above 1K). The two different doses  $5.9 \times 10^6$  and  $2.1 \times 10^8$  Roentgen give the same result, so that saturation is already achieved. The thermal conductivity is little affected above 1K and not at

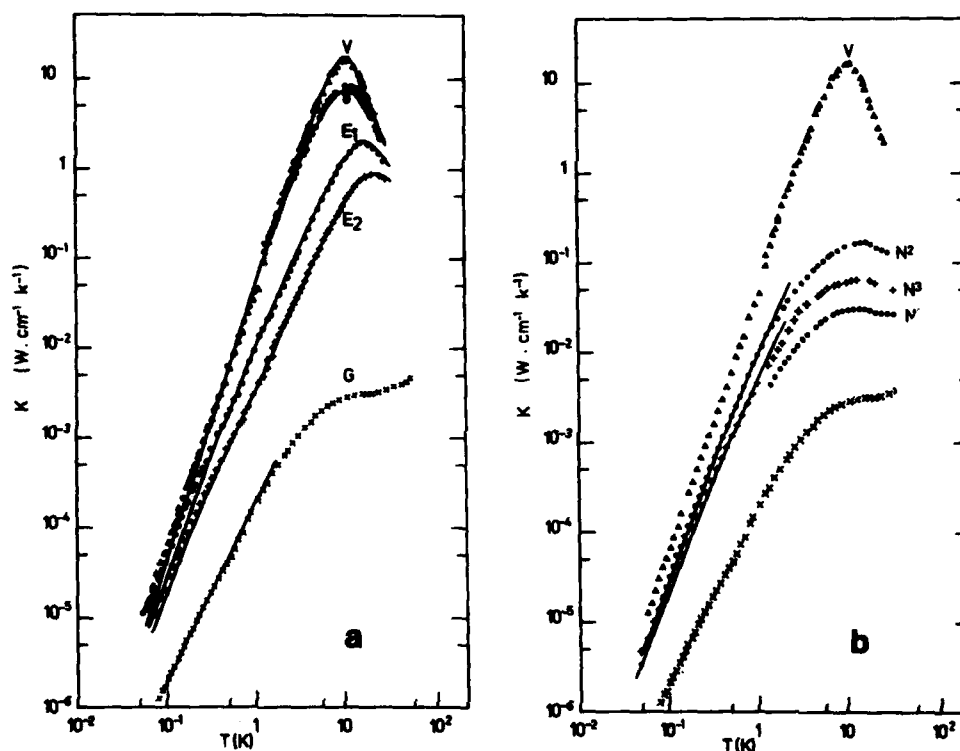


Fig. 1. Thermal conductivity as a function of temperature: V: unirradiated sample, E<sub>1</sub> and E<sub>2</sub>: electron irradiated; N<sub>1</sub>, N<sub>2</sub>, N<sub>3</sub>: neutron irradiated; G: glass sample. Irradiation dose: see table 1. Solid lines are calculated to fit the experiments.

all below 1K, were the data for the virgin sample are reproduced.

Electron and neutron irradiation induce in the whole temperature range an additional phonon scattering which increases with increasing dose, and is remarkably different above 1K but shows similarities below 1K. Above 1K, in the neutron irradiated samples, a plateau appears, similar to glasses, as already known<sup>8</sup>.

**Discussion.**— A computer fit was made using the full Debye expression for the thermal conductivity, starting from a fit for the virgin sample and introducing an additional scattering mechanism to account for the radiation damage:  $\tau^{-1} = C\omega$  and an increase of the point defect term A, the Casimir term being kept at the calculated value. The results are reported in table 1 and in fig. 1 (some only partly for clarity). More details about the fitting procedure are given in a previous paper<sup>3</sup>. At the very lowest temperatures the fit underestimates the value of the thermal conductivity as well in the virgin sample as in the irradiated samples (see also fig. 1 in the previous paper<sup>3</sup>). This effect is usually attributed to specular reflection and will not be discussed in more detail here. Apart from this small departures it was found that in the case of the electron irradiated samples the expected Rayleigh scattering, due to point defects alone, can not explain the data and that a constant

Table 1

Sample	dose <sup>+</sup> (cm <sup>-2</sup> )	A (s <sup>3</sup> )	A-A <sub>0</sub> (s <sup>3</sup> )	n <sub>0</sub> M <sup>2</sup> (erg/cm <sup>3</sup> )	$\frac{(n_0 M^2)_{\text{exp}}}{(n_0 M^2)_{\text{vitr. sil.}}}$ *
glass				$1.7 \times 10^8$	$\sim 1$
virgin		$2.7 \times 10^{-45}$	0	-	-
Y	saturation	$2.7 \times 10^{-44}$	$2.4 \times 10^{-44}$	$< 1 \times 10^4$	$< 1 \times 10^{-4}$
E <sub>1</sub>	$3 \times 10^{19}$ electr.	$1.7 \times 10^{-44}$	$1.4 \times 10^{-44}$	$2.6 \times 10^6$	0.022
E <sub>2</sub>	$1.8 \times 10^{20}$ electr.	$3.4 \times 10^{-44}$	$3.1 \times 10^{-44}$	$8.8 \times 10^6$	0.073
N <sub>2</sub>	$1 \times 10^{18}$ neutr.	-		$2.7 \times 10^6$	0.023
N <sub>3</sub>	$4 \times 10^{18}$ neutr.	-		$5.8 \times 10^6$	0.048
N <sub>1</sub>	$6 \times 10^{18}$ neutr.			$1.3 \times 10^7$ from longit. ultrasound exp <sup>2</sup>	0.065

+ electron energy 2 MeV; neutrons with energy > 0.1 MeV; neutron dose N<sub>3</sub> is preliminary

\*  $n_0 M^2 = 1.2 \times 10^8$  erg/cm<sup>3</sup> is a calculated mean value.

density of states of TLS (two level states) similar as in glasses can fit the results<sup>3</sup>. From G a value for the coupling strenght  $n_0 M^2$  of the TLS with the thermal phonons is obtained (see table 1). For the neutron irradiated samples a similar fit was carried out but only for the temperatures below 1K since the "plateau" in glasses is not yet understood. A constant density of states of TLS can, also in this case, fit the data. This is in agreement with earlier findings which show that TLS are present in neutron irradiated quartz<sup>1,2,4</sup>. For the γ-irradiated samples no evidence for the presence of TLS was found up to saturating dose which puts an upper limit to the number possibly present (see table 1).

It is surprising that in spite of the very different damaging processes, both neutron and electron irradiation induce TLS. Indeed neutrons cause displacement cascades and therefore extended damage zones, which might be amorphous, as recently observed<sup>9</sup>, while electrons are expected to cause rather simple defects.

1. C. Laermans, Phys. Rev. Lett., **42**, 250 (1979)
2. B. Golding, J. E. Graebner, W. H. Haemmerle and C. Laermans, Bull. Am. Phys. Soc. **24**, 495 (1979); B. Golding and J. E. Graebner, in "Phonon scattering in condensed matter, ed. H. J. Maris (Plenum Press, 1980) p. 11.
3. C. Laermans, A. M. de Goër and M. Locatelli, Phys. Lett. **80A**, 331, 1980.
4. J. W. Gardner and A. C. Anderson, Phys. Rev. B **23**, 474, 1981.
5. M. Hofacker and H. v. Löhneysen, to be published.
6. C. Laermans and B. Daudin in: "Phonon scattering in condensed matter", ed. H. J. Maris (Plenum Press, 1980) p. 21.
7. R. C. Zeller and R. O. Pohl, Phys. Rev. B **4**, 2029 1971.
8. R. Berman, Proc. R. Soc. London Ser. A **208**, 90 (1951).
9. D. Grasse, O. Kocar, H. Peisl, S. C. Moss and B. Golding, Phys. Rev. Lett. **46**, 261, 1981.

SURFACE POLARITONS IN IRRADIATED  $\alpha$ -QUARTZ

V. Umadevi, R. Kesavamoorthy, A.K. Sood and G. Venkataraman

Reactor Research Centre, Kalpakkam 603 102, Tamil Nadu, India

**Abstract.**— Surface polaritons (SP) in charged particle irradiated  $\alpha$ -quartz and fused quartz have been studied using the attenuated total reflection (ATR) method. It is found that on irradiation SP frequency decreases and linewidth increases. Some evidences point out that on irradiation  $\alpha$ - and fused quartz tend to become disordered in a similar way.

1. **Introduction.**— It is by now well known that at a boundary between two media with dielectric constants  $\epsilon_1 > \epsilon_2 > 0$ , surface polaritons (SP) propagate down the surface. We report below our studies on the surface polaritons in ion-bombarded  $\alpha$ -quartz and fused quartz by ATR technique in the spectral range of 1400–180  $\text{cm}^{-1}$ .

2. **Experimental.**— Irradiations were done in a Sames J-15, 150 keV neutron generator modified for charged particle work. 100 keV argon, helium and deuterium ions have been used in this study to a dose  $\leq 10^{17}$  ions/ $\text{cm}^2$ . ATR spectra of single crystals of  $\alpha$ -quartz cut with the optic axis lying in the plane of the sample were recorded in a Perkin-Elmer model 580 spectrophotometer before and after irradiation. The ATR set up used is a 25 reflections unit with a KRS-5 crystal. All the spectra reported here are recorded at a fixed angle of incidence ( $30^\circ$ ), corresponding to a fixed wave vector.

3. **Results.**— Figure 1 shows the ATR spectra of  $\alpha$ -quartz before and after charged particle irradiation. The ordinary E-type SP at 1160, 1145, 805, 690, 485 and 400  $\text{cm}^{-1}$  are seen clearly in the unirradiated spectrum. Deuterium ions seem to be more effective than argon or helium ions in causing damage. The general feature observed on irradiation is that the SP frequencies shift to lower values and that the lines are broadened. It can also be seen (figure 2) that the SP in the spectral range of 1200–1000  $\text{cm}^{-1}$  change significantly compared to the modes in the other regions.

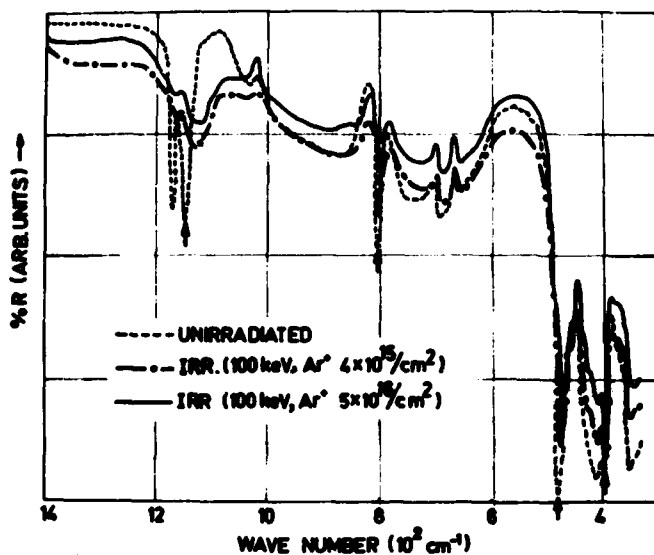


Fig. 1 : ATR spectra of unirradiated and irradiated  $\alpha$ -quartz.

Shown in figure 3 are the ATR spectra of fused quartz recorded similarly. Here also the SP frequencies decrease and linewidths increase on irradiation can be seen distinctly. The asymmetry on the higher frequency side of the SP at  $\sim 1140 \text{ cm}^{-1}$  suggests the possible presence of another mode similar to  $\alpha$ -quartz. Indications are that both  $\alpha$ -quartz and fused quartz attain a common disordered structure on irradiation. One could speculate that this is a random structure

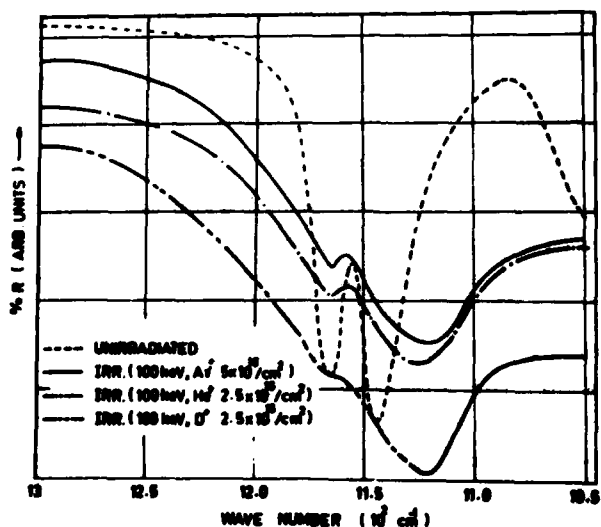


Fig. 2 : ATR spectra of unirradiated and irradiated  $\alpha$ -quartz in spectral range  $1300 - 1050 \text{ cm}^{-1}$ .



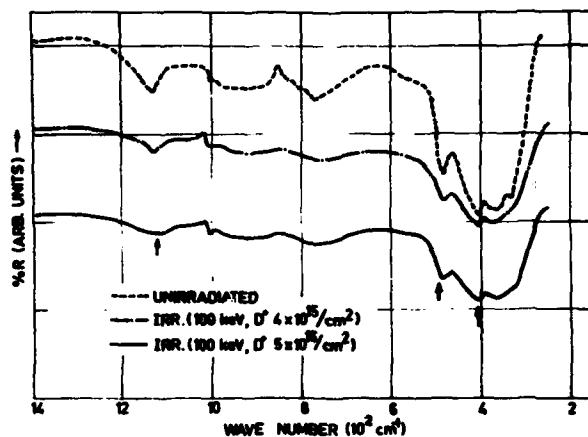


Fig. 3 : ATR spectra of unirradiated fused quartz.

with dangling bonds.

4. Discussion.— Irradiation changes the specular reflectivity spectra also<sup>1</sup>. Dielectric constant ( $\epsilon$ ) calculated from the bulk reflectivity data using Kramers-Kronig analysis does not account for the observed changes in the ATR spectra. The same conclusion was arrived at by Zhizhin et al<sup>2</sup> in nitrogen irradiated  $\alpha$ -quartz. As the projected range of the particles used for irradiation is smaller than the skin depth of infrared radiation at these frequencies, it is proposed to analyze the bulk reflectivity data itself on the basis of a two layer model. The  $\epsilon$  obtained thus should be used to generate ATR spectra calculated for a three interface case. After generating complete dispersion curve data, efforts will be made to analyze our data on these lines.

#### REFERENCES

1. Umadevi, V., Sahu, H.K., Sood, A.K. and Venkataraman, G, Proc. Nuc. Phys. and Solid State Phys. Symp. 22C, Solid State Physics, p. 755 (1979).
2. Zhizhin, G.N., Yakolev, V.A. and Shirmer, G, JETP Lett. 29, 315 (1979).

## RENORMALIZATION GROUP METHOD FOR VIBRATIONAL BEHAVIOR IN MIXED CRYSTALS

D. Schmeltzer and R. Beserman

*Solid State Institute and Physics Department, Technion - Israel Institute of Technology, Haifa, Israel*

**Abstract-** The renormalization group method has been applied to investigate vibrational properties of a diatomic mixed crystal. It has been found that there exists a fixed point which separates the one mode behavior from the two mode behavior. This transition depends on concentration, force constants and mass ratios.

It is shown that a fixed point exists which separates the extended mode behavior from a localized one which is interpreted as a transition from the one mode to two mode behavior.

We propose here a new criterion based on the renormalization group method (R.G), this gives an unstable fixed point of transition from one mode to two mode behavior.

We find a transition from one mode behavior to two mode behavior for given mass ratios and force constants (therefore the same crystal) as depending on concentration (Fig. 2). This fact is able to explain qualitatively the transition found experimentally in InSbAs. We perform the renormalization group transformation in one dimension and (with one force constant  $K_X^X$ ) for  $d=3$  we use the Migdal Kadano point moving, technique.

Our R.G. Transformation consists in comparing the eigenvalues, coupling constants and probability distribution of the initial lattice with those of a new one of spacing  $S( \gg 1)$  times larger than the original.

We consider the mixed crystal  $AB_xC_{1-x}$ .  $M_A$  is the constant mass and the random mass  $M_2(1)$  is  $M_B$  with probability  $x$  or  $M_C$  with probability  $1-x$ .

We define a disorder parameter (The root mean square deviation of the optical mode normalized by the effective coupling between the nearest cells). We study the transformation  $\lambda \rightarrow \lambda'$  for a change of the scale of the lattice constant  $a \rightarrow Sa$ .

The function  $R(\lambda)$  describes the transition from one mode to two mode behavior.

We can physically explain this claim as follows: the apparition of a localised mode is the condition for a two mode behaviour. For a localised mode, distant regions are uncoupled for our effective chain (the correlation function decreases exponentially). We calculate the coupling constant between distant cells as a coupling adjacent cells in a given state of the R.G. transformation; increasing the size of the cell during the transformation, we obtain a decrease of  $t_{\text{eff}}^{(d=3)}$  an increase of  $\lambda$  and therefore  $R(\lambda) \gg 0$ . ( $t_{\text{eff}}$  is the coupling constant between the cells).

For a one mode behavior (one type of oscillation) a long correlation exists and  $t_{\text{eff}}^{(d=3)}$  decreases slowly relatively to the decrease of the root mean square deviation of the oscillation frequencies,  $\lambda$  decreases and  $R(\lambda) < 0$ .

The fixepts  $R(\lambda)=0$  occur at  $\lambda=0$ ,  $\lambda=\infty$  (one mode, two mode) and the unstable fix point at  $\lambda=\lambda_c \neq 0$ ,  $[R(\lambda) > 0 \text{ for } \lambda > \lambda_c \text{ and } R(\lambda) < 0 \text{ for } \lambda < \lambda_c]$  which describes the point of transition from one mode to two mode behaviour.

For a given  $z, \epsilon$ , we find  $\lambda_c$  for which  $R(\lambda_c)=0$  and respectively the value of  $\tilde{f}_c$ . ( $\lambda = \lambda(z, \epsilon, \tilde{f})$ ).

We plot a graph  $\tilde{f}(\tilde{f}=\tilde{f}_c)$  for constant  $z$  and a graph of  $z, \tilde{f}(\tilde{f}=\tilde{f}_c)$  for constants  $\epsilon$ .

Fig. 1 shows our results for  $z=0.5$  which are compared to the M.R.E.I. and C.P.A. models. Fig. 2 shows the results for  $\epsilon=-1$ , which might explain the behaviour of the crystal  $\text{InSb}_{1-x}\text{As}_x$  whose  $\epsilon=-1.06$  and  $\tilde{f}=0.38$  and has been found to behave one mode for  $z=0.25$  and two mode for  $z=0.85$ .

We mention that our approximation might change the value of the unstable fixept point  $\lambda=\lambda_c$  (to smaller  $\lambda_c$ ) and as a result the function  $z = z(\tilde{f})$  (Fig. 2), appears to be shifted upwards for  $\tilde{f}$  close to 1, as approximation involves less disorder.

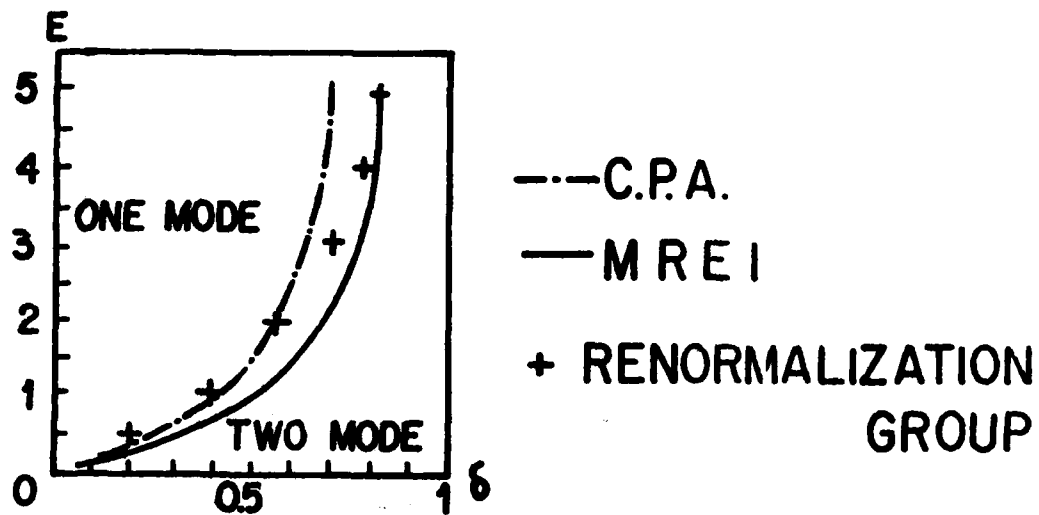


Fig. 1:- Mode behaviour  $E = E(\delta)$  for  $Z=0.5$

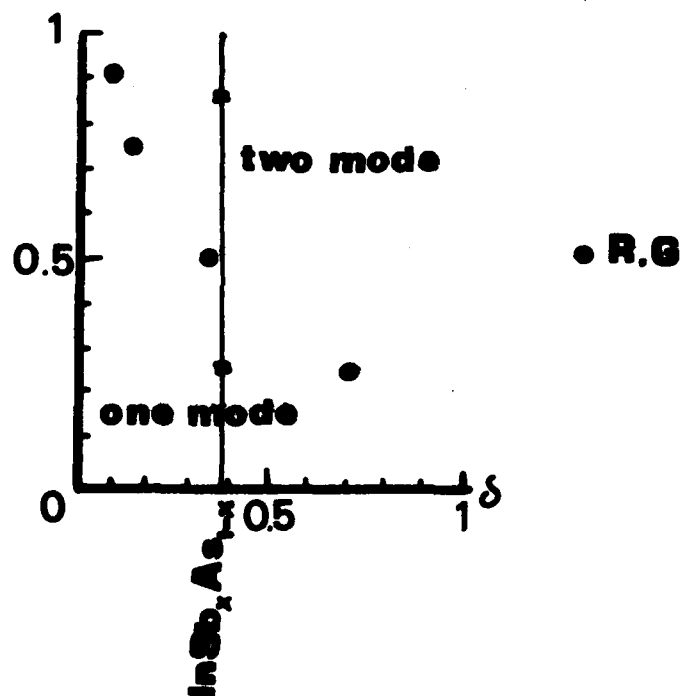


Fig. 2:- Mode behaviour for  $E = E(\delta)$  for  $c=1$

COHERENT POTENTIAL APPROXIMATION AND STRONGLY ANHARMONIC SYSTEMS :  
CRYSTALS OF PARA-HYDROGEN AND NEON RESP. HYDROGEN ATOMS

K. Menn and W. Biem

*Institute of Theoretical Physics, University of Giessen, D-6300 Giessen, F.R.G.*

**Abstract.**— For mixtures of p-hydrogen and neon in the solid state phonon calculations have been performed by combining the CPA and the self consistent phonon approximation (SCP) to include the strong anharmonicity of the system. The structure changes and the phonon spectrum have been calculated as function of the concentration. The method has also been applied to mixtures of p-H<sub>2</sub> and hydrogen atoms.

Under the solids which are known to be quantum crystals there are several systems of two or more kinds of molecules statistically mixed on the lattice positions, e.g. o-H<sub>2</sub>, p-H<sub>2</sub> mixtures, H<sub>2</sub>-D<sub>2</sub>, H<sub>2</sub>-Ne mixtures. These systems are strongly anharmonic because of changing force constants as function of the mean distance of the molecular pairs and of the large amplitudes of the zero-point motion. To calculate their phonon resp. roton spectra the theories of statistically disordered crystals which are harmonic have to be generalized to take into account strong anharmonicities.

The single site coherent potential approximation (CPA) is well known to be the best working method to calculate phonon spectra of disordered crystals abstracting from its weakness in describing pair and clustering effects. We have combined the CPA and the self-consistent phonon approximation (SCP) to get a first insight into the dynamics of anharmonic and disturbed crystals of two compounds.

One of the simplest disturbed systems seems to us to be the p-hydrogen neon system since the pair potentials are roughly equal and the mass ratio is 10 ("isotopical disorder"). The large mass ratio produces a big difference in the zero point motion. Therefore, the structure in the neighbourhood of one guest molecule in a host crystal is strongly changed and with it the force constants. We have simplified the problem to a certain extent to reduce the numerical difficulties: the structure has been face centered cubic for all concentrations though high hydrogen concentrations are stable in the hexagonal closed packed structure. We have used always the regular cubic point symmetry for every lattice site occupied by a guest molecule. We have not considered

refined quantum effects (no quantum diffusion). This may turn out to be too much simplification: There may occur deviations from statistical mixing through correlations – static or time dependent. But the problem remains complicated enough and the numerical problems grow considerably with the model of the neighbourhood of the guest molecule. We have started with a model where only the nearest neighbours could relax. This model turned out to be too rigid: the global lattice constant changed too much, the frequencies changed partly in a wrong direction. Therefore, we introduced another model with relaxations up to the fourth neighbour shell. All static and dynamic displacements were restricted not to violate the cubic symmetry.

Since hydrogen forms quantum crystals, the short range correlations have to be taken into account. We have done this with Jastrow-factors of an appropriate kind.

The whole calculation turned out to be a voluminous one to be solved self consistently with several variational parameters: the lattice constant  $a$ , the static displacements from the lattice points of molecules in four shells in the neighbourhood of a guest molecule  $\Delta R_{ij}$ , the width parameters  $\gamma_{ij}$  of the displacement-displacement correlation function, and the parameters in the Jastrowfactor. The iteration procedure turned out to be very difficult and special tricks had to be used to reach convergence. Calculations were performed mostly on the Ne-(p-H<sub>2</sub>) system, a few on p-H<sub>2</sub>-(Ne) and on p-H<sub>2</sub>-(H atoms). The table contains the static structural changes, the figures show the spectra of the crystals, some Jastrowfactors and the comparison of the mean lattice constant from which follows, that the model with relaxation of four shells is necessary to describe the local displacement field of the point defect formed by a guest molecule.

1	2	3	4					5	6	7	8
	$a(\text{\AA})$	$a(\text{\AA})$	displacement of neighbours $\Delta R(\text{\AA})$					number of iterations	short range correlations $U_2=U_0$	uncertainty of $a$ and $\Delta R$	
1) $Ne+(pH_2)_0$	0	4.4565	0.0	0.0	0.0	0.0	0.0	5	$\kappa = 0.142$	$\Delta a \pm 0.0005$	$\Delta R \pm 0.0005$
	3	4.4583	0.0542	0.0103	0.0238	0.0410	0.0410	4	0.138		
	5	4.4605	0.0558	0.0096	0.0232	0.0403	0.0403	4	0.144		
	10	4.4642	0.0555	0.0097	0.0234	0.0404	0.0404	4	0.151		
	20	4.4800	0.0537	0.0104	0.0233	0.0403	0.0403	4			
2) $Ne+(pH_2)_0$	5	4.4788	0.0191	---	---	---	---	5	$\kappa = 0.159$	$\Delta a \pm 0.0005$	$\Delta R \pm 0.0005$
	10	4.5087	0.0167	---	---	---	---	6	0.160	$\kappa = 0.04$	
	20	4.5723	0.0123	---	---	---	---	7	0.165	$\Delta a \pm 0.0005$	
	40	4.6580	0.0066	---	---	---	---	8	0.177		
3) 5) $pH_2+(Ne)_0$	0	5.2481	0.0	0.0	0.0	0.0	0.0	[21]	Horner 4)	$\Delta a \pm 0.001$	
	10	5.236	-0.078	0.036	0.003	0.001	0.001				
2) 5) $[d_2]_0+(Ne)_0$	10	5.1263	-0.0153	---	---	---	---	12	Horner 4)	$\Delta a \pm 0.0005$	
1) 5) $pH_2+(H)_0$	5	5.1927	0.0141	0.0268	0.165	0.0306	0.0306	6	without	$\Delta a \pm 0.0005$	

1) model with 4 relaxing neighbour shells  
 2) model with nearest neighbour relaxation only  
 3)  $f(r) = \exp(-r/4.1V(r))$   
 4)  $f(r) = \exp(-r/4.1V(r)) \cdot (a_0 + a_1 r + a_2 r^2)^{1/2}$   
 5) preliminary results only

6) 1) system,  
 2) concentration,  
 3) mean lattice constant as function of  $c$ ,  
 4)  $\Delta R(c)$

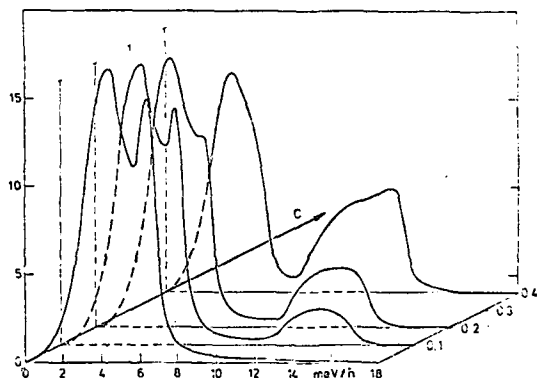


Fig. 1 : Spectrum of  
 $\text{Ne}+(\text{p-H}_2)_c$ , nearest neigh-  
 bour relaxation

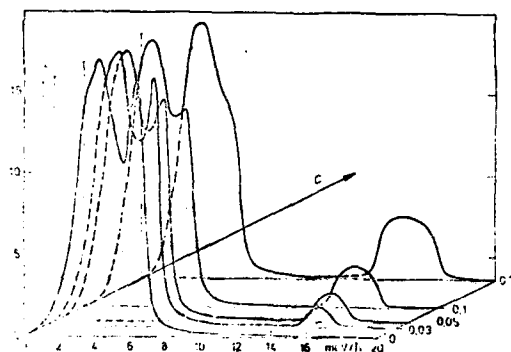


Fig. 2 : Spectrum of  
 $\text{Ne}+(\text{p-H})_c$ , four shells  
 relax

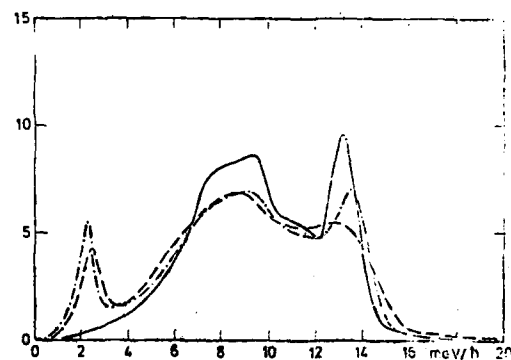


Fig. 3 :  $\text{p-H}_2+(\text{Ne})_c$ ,  
 —  $c=0$   
 - - -  $c=0,1$ , nearest neigh-  
       bour relax  
 - · -  $c=0,1$ , four shells  
       relax

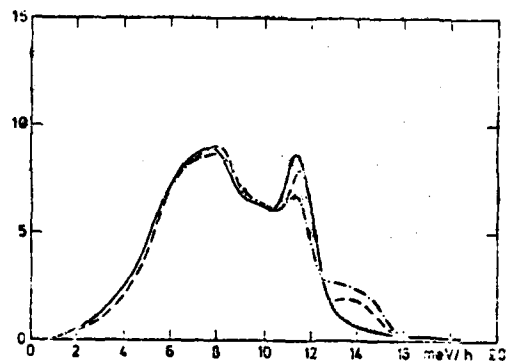


Fig. 4 :  $\text{p-H}_2+(\text{H})_c$   
 —  $c=0$   
 - - -  $c=0,05$   
 - · -  $c=0,1$

RAMAN SCATTERING FROM PHONONS IN DISORDERED  $\text{CaMg}_{1-x}\text{Co}_x\text{Cl}_3$ 

I.W. Johnstone, G.D. Jones\* and D.J. Lockwood

*Physics Division, National Research Council, Ottawa, Canada K1A 0R6**\*Physics Department, Canterbury University, Christchurch, New Zealand*

**Abstract.**— Five zone-centre phonons have been measured at low temperatures and for a range of concentrations in  $\text{CaMg}_{1-x}\text{Co}_x\text{Cl}_3$ . Three  $E_{2g}$  modes and the  $A_{1g}$  mode all exhibit the expected one-mode behaviour. A new theory is required to explain the unusual concentration dependence of the  $E_{1g}$  phonon intensity, lineshape and polarisation.

1. **Introduction.**— The lattice dynamics of  $\text{AMCl}_3$  compounds have been widely studied and many possess the  $\text{CaMgCl}_3$  structure (see figure 1) of space group  $D_{6h}^4$  with two formula units in the primitive cell. A factor group analysis predicts  $A_{1g} + E_{1g} + 3E_{2g}$  Raman active modes. The  $A_{1g}$  and  $E_{1g}$  modes comprise chlorine ion motions, perpendicular and parallel to the c (Z) axis respectively, while the  $E_{2g}$  modes involve halogen and cesium ion displacements in the hexagonal (X,Y) plane. We have studied the mixed crystal  $\text{CaMg}_{1-x}\text{Co}_x\text{Cl}_3$  to clarify assignments of phonons in  $\text{CaMgCl}_3$ ,<sup>1,2</sup> and  $\text{CaCoCl}_3$ ,<sup>1,3</sup> and thereby assist the interpretation of the highly structured magnon spectrum of  $\text{CaCoCl}_3$ .<sup>3</sup>

2. **Experiment and Results.**— Large single crystals of  $\text{CaMg}_{1-x}\text{Co}_x\text{Cl}_3$  were grown with concentrations in the ranges  $0 < x < 0.2$  and  $0.6 < x < 1$ . Raman spectra were excited with 100 mW of 476.5 nm argon laser light in the  $90^\circ$  scattering geometry  $X(\cdot\cdot)Y$ , analysed with a double monochromator ( $2 \text{ cm}^{-1}$  resolution), and recorded under computer control. Polarised Raman spectra for pure  $\text{CaMgCl}_3$  recorded at 5 K allowed unambiguous assignments of phonon lines at 55.0, 127.5, 132.0, 189.0 and  $255.0 \text{ cm}^{-1}$  to symmetry species  $E_{2g}$ ,  $E_{1g}$ ,  $E_{2g}$ ,  $E_{2g}$  and  $A_{1g}$ , respectively. The  $A_{1g}$  mode showed no anomalous (YX) intensity in contrast to that found earlier.<sup>1</sup> Figure 2 presents part of the results obtained for the mixed crystals. The scattering from  $E_{2g}$  and  $A_{1g}$  phonons follows  $D_{6h}$  selection rules for all concentrations and only the  $A_{1g}$  and  $E_{2g}$  ( $132 \text{ cm}^{-1}$ ) modes show appreciable frequency shifts with increasing x. All of these phonons exhibit one-mode behaviour as predicted by theory.<sup>4</sup>



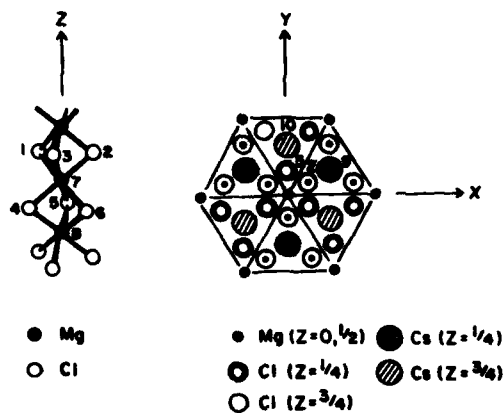


Fig. 1: Details of the  $\text{CaMgCl}_3$  crystal structure.

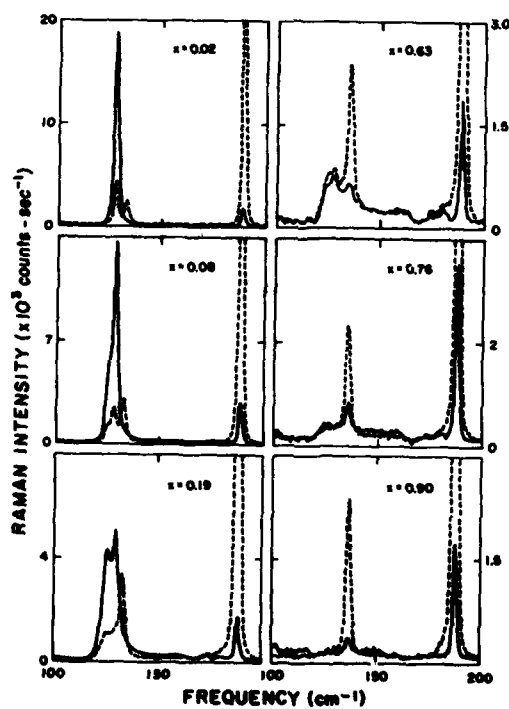


Fig. 2: Concentration dependence of the  $X(ZX)Y$  (—) and  $X(YX)Y$  (---) Raman spectra for phonons in  $\text{CaMg}_{1-x}\text{Co}_x\text{Cl}_3$  at 5 K.

Figure 2 shows the dramatic changes in band shape and intensity for the  $E_{1g}$  phonon as a function of  $x$ . The single line observed at  $127.5 \text{ cm}^{-1}$  in (ZX) polarisation for  $x = 0$  becomes a pair of lines by  $x = 0.19$ . By  $x = 0.63$  this fine structure has smeared out and the continuum of scattering to higher frequency is now more prominent and has equal intensity in (ZX) and (YX) polarisations. As  $x$  is further increased beyond  $x = 0.8$  the  $E_{1g}$  band disappears and the continuum becomes weaker, being barely visible for  $x = 0.88$ . The intensity ratio  $I_{ZX}/I_{YX}$  for the  $E_{1g}$  phonon also changes with concentration and  $I_{ZX} = I_{YX}$  for  $x > 0.63$ , contrary to  $D_{6h}$  selection rules.

3. Discussion.— The degenerate  $E_{1g}$  mode has normal mode displacements of the form<sup>4</sup>  $Z_1+Z_2-Z_4-Z_6-2Z_3+2Z_5$  and  $\sqrt{3}(Z_1-Z_2+Z_4-Z_6)$  using the atom labels of figure 1. Therefore the Raman cross-section for this mode should be relatively insensitive to substitution of the divalent metal ion, and the other Raman active modes behave sensibly in this respect. Thus although the  $E_{1g}$  mode frequency is concentration independent the lineshape, polarisation and intensity behave anomalously. Extrapolation of our data indicates a frequency of  $\sim 127 \text{ cm}^{-1}$  for the  $E_{1g}$  mode in  $\text{CeCoCl}_3$ , as opposed to an earlier assignment of  $118 \text{ cm}^{-1}$ .<sup>1,3,4</sup>

#### References

1. W. Breitling, W. Lehmann, T.P. Srinivasan and R. Weber, Solid St. Commun. 20, 525 (1976).
2. M.H. Brooker and C.-H. Huang, Mat. Res. Bull. 15, 9 (1980).
3. W. Breitling, W. Lehmann, T.P. Srinivasan, R. Weber and U. Durr, Solid St. Commun. 24, 267 (1977).
4. Further details are given in I.W. Johnstone, G.D. Jones and D.J. Lockwood, Solid St. Commun. 39, 395 (1981).

## VIBRATIONAL EXCITATIONS IN a-Si:F AND a-Si:F:H ALLOYS\*

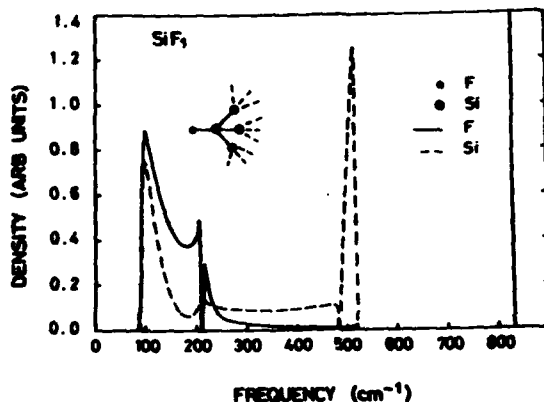
B.K. Agrawal

Department of Physics, University of Allahabad, Allahabad, India

**Abstract.**— The vibrational excitations both in the Si bulk band mode region and above it at the impurity centres in the various configurations for the a-Si:F and a-Si:F:H alloys, have been obtained by using a cluster Bethe lattice method. The predicted frequencies are in excellent agreement with the available experimental data.

We consider here only the nearest-neighbor central and non-central force constants. The force constants chosen to reproduce the experimental frequencies are shown in Table I. Figs. 1 and 2 exhibit the phonon density of states at one Si atom and at one F atom in the SiF, SiF<sub>2</sub> and SiF<sub>3</sub> configurations. All the calculated localised mode frequencies are in excellent agreement with the data of Shimada et al.<sup>1</sup>. It should be noted that a central force constant chosen for each configuration gives rise to two localised frequencies in SiF<sub>2</sub> and SiF<sub>3</sub> configurations in agreement with the measured frequencies.

We then calculated the phonon density for SiFH and SiF<sub>2</sub>H configurations (Figs. 3a and 3b) respectively. The central and angular



**Fig. 1:** Local phonon density of states for SiF configuration. The continuous and dashed curves depict the densities at F and Si atoms, respectively for  $\alpha = 4.43 \times 10^5$  dyn/cm,  $\beta = 0.34 \times 10^5$  dyn/cm where the resonance mode appears at  $224 \text{ cm}^{-1}$ . (The value of  $\beta$  is here different from that of Table I in the text). The small dashed lines at Si atoms show the connection to the Bethe lattice.

\* Work supported in parts by Science Research Council, U.K. and by University Grants Commission, New Delhi.

Table I - Assignment of the measured frequencies against the various configurations in a-Si:F and a-Si:F:H alloys.  $\alpha$  and  $\beta$  denote the central and angular force constants, respectively.

Confi- guration	Bond	Force constants ( $10^5$ dyn/cm)		Resonance and localised frequencies ( $\text{cm}^{-1}$ )	
		$\alpha$	$\beta$	Calculated	Measured
a-Si	Si-Si	1.40	0.17	510	490
SiF	Si-F	4.43	1.01	300	300 <sup>b</sup>
				830	850 <sup>a</sup> , 828 <sup>b</sup> , 830 <sup>c,d</sup>
SiF <sub>2</sub>	Si-F	5.40	1.01	300	300 <sup>b</sup>
				330	325 <sup>a</sup> (tentative)
				868	870 (827) <sup>a</sup>
				968	965, (920) <sup>a</sup> , 930 <sup>b</sup> , 950 <sup>c</sup> , 975 <sup>d</sup>
SiF <sub>3</sub>	Si-F	5.71	1.01	300	300 <sup>b</sup>
				375	380 <sup>b</sup>
				520	515 <sup>a</sup> , 510 <sup>b</sup>
				840	838 <sup>a</sup>
				1016	1015 <sup>a,d</sup> , 1010 <sup>b,c</sup>
SiFH	Si-H	2.27	0.43	529	515 <sup>a</sup> , 510 <sup>b</sup>
	Si-F	4.43	1.01	792	828 <sup>b</sup>
				877	
				902	890 <sup>b</sup> , 900 <sup>d</sup>
				2000	1985 <sup>b</sup> , 2000 <sup>d</sup>
SiF <sub>2</sub> H	Si-H	2.48	0.43	300	300 <sup>b</sup>
	Si-F	5.40	1.01	330	325 <sup>a</sup> (tentative)
				385	380 <sup>b</sup>
				529	515 <sup>a</sup> , 510 <sup>b</sup>
				820	828 <sup>b</sup>
				839	840 <sup>b</sup>
				908	890 <sup>b</sup> , 900 <sup>d</sup>
				992	975 <sup>d</sup>
				2090	2090 <sup>b</sup> , 2100 <sup>d</sup>

a : reference (1)

b : reference (2)

c : reference (3)

d : reference (4)

force constants for the Si-H bond were first fitted to reproduce the experimental frequencies in SiH, SiH<sub>2</sub> and SiH<sub>3</sub> configurations in pure hydrogenated Si material, i.e., 630 cm<sup>-1</sup> and 2000 cm<sup>-1</sup> for SiH, and 850 cm<sup>-1</sup>, 890 cm<sup>-1</sup> and 2090 cm<sup>-1</sup> for SiH<sub>2</sub>. For the SiH<sub>3</sub> configuration the calculated frequencies are 875 cm<sup>-1</sup>, 910 cm<sup>-1</sup> and 2140 cm<sup>-1</sup>. For the Si-F bonds, the values of the force constants were chosen similar to the pure-fluorinated Si materials. A perusal of Table I reveals that almost all the predicted frequencies have been seen in the infrared data.

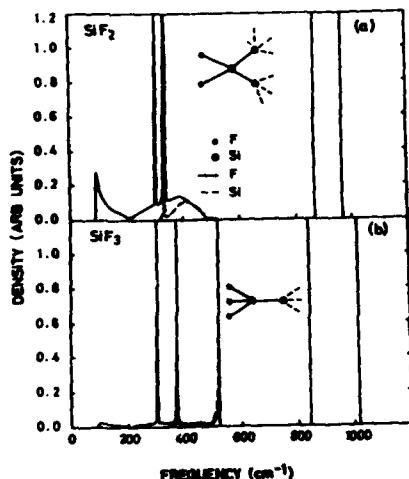


Fig. 2 : Same for Fig. 1 except that for (a) SiF<sub>2</sub> and (b) SiF<sub>3</sub> configurations.

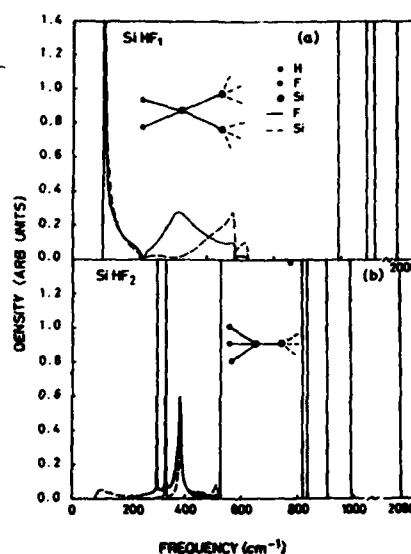


Fig. 3 : Same for Fig. 1 except that for (a) SiFH and (b) SiF<sub>2</sub>H configurations. The density at H atom appears mainly above the band mode region.

#### References

1. T. Shimada, Y. Katayama and S. Horigome, Jap. J. Appl. Phys. **19** L265 (1980).
2. L. Ley, H.R. Shanks, C.J. Pang, K.J. Grunts and M. Cardona, Phys. Rev. **B22**, 6140 (1980).
3. H. Matsumura, Y. Nakagome and S. Furukawa, Appl. Phys. Lett. **36**, 439 (1980).
4. M. Konagai and K. Takahashi, Appl. Phys. Lett. **36**, 599 (1980).

A STUDY OF POLARITONS AND PHONON PECULIARITIES IN  $\text{CuCl}_{1-x}\text{Br}_x$ \*

O. Brafman and G. Livescu

*Department of Physics and Solid State Institute, Technion-Israel Institute of Technology, Haifa 32 000, Israel*

**Abstract.**— The optic phonon anomalies found in  $\text{CuCl}_{1-x}\text{Br}_x$  by means of Raman scattering and polariton measurement are presented. These irregularities are explained in terms of a model which accounts for the phonon and other anomalies in pure Cu-halides.

The optic phonon modes in  $\text{CuCl}_{1-x}\text{Br}_x$  show an irregular behavior even at low temperatures. This is true with respect to concentration dependent phonon frequencies, their Raman intensities and especially their oscillator strengths. The oscillator strengths were deduced from fitting the calculated polariton dispersion to that measured by means of Raman forward scattering. Figure 1 shows the frequencies of the three oscillators so obtained. The notation (1) and (2) relates to the main oscillators, while d stands for disorder induced lines<sup>(1)</sup>. In fig. 2 the three oscillator strengths are presented as function of the anion concentration. The oscillator strength in a crystal is proportional to the number of oscillators participating in a given mode. Therefore both oscillator strengths in a two mode solid solution decrease gradually with mixing. This is obviously not the case in  $\text{CuCl}_{1-x}\text{Br}_x$  as shown in fig. 2 and it can not have a simple and straight forward explanation. On the other hand this behavior of  $\text{CuCl}_{1-x}\text{Br}_x$  optic phonons is not totally surprising. Even at low temperatures where CuBr phonons are well behaved, the phonon spectrum of CuCl shows numerous anomalies and those were widely discussed earlier<sup>(2)</sup>. The main feature is the appearance of two polar modes instead of a single expected one mode. The two polar modes, labeled  $\beta$  and  $\gamma$ , exhibit the same symmetry but differ considerably in linewidth and in the effect of temperature on the lines regarding intensity, frequency and width.

We shall interpret the present results with the help of a model which successfully explains the anomalies in pure CuCl<sup>(2)</sup>. It is assumed that  $\text{Cu}^+$  may occupy off center sites in CuCl giving rise to the  $\beta$  mode while those in ideal sites participate in the  $\gamma$  mode. Microscopically  $\text{CuCl}_{1-x}\text{Br}_x$  can be described<sup>(3)</sup> as being composed of five types of tetrahedra with n chlorine ions and 4-n bromine ions,  $0 < n < 4$ , with x dependent probability. The main assumption in the present work is that  $\text{Cu}^+$  may occupy off center positions, only in tetrahedra built exclusively on chlorine ions ( $n=4$ ), and that it should then occur with the same probability as in pure CuCl. On the other hand in all tetrahedra with  $n \neq 4$ ,  $\text{Cu}^+$  occupy solely

\*Work supported by the Israel commission for Basic Research and by the Fund for the Promotion of Research at the Technion.

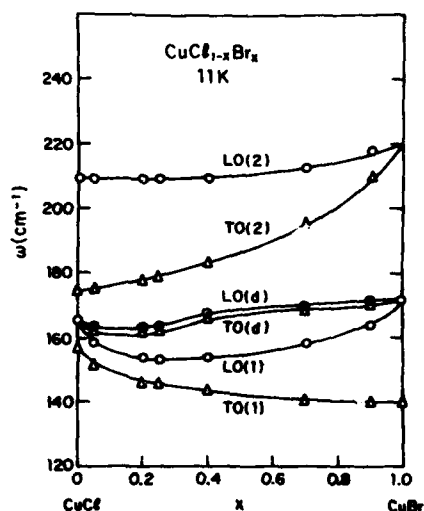


Fig. 1: The frequencies of TO(1)-LO(1), TO(d)-LO(d) and TO(2)-LO(2), at various concentrations.

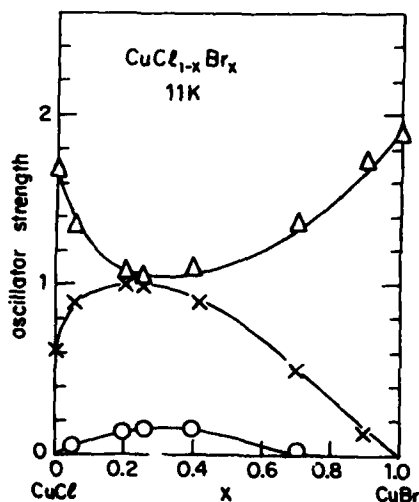


Fig. 2: The three oscillator strengths  $S_1$ ,  $S_2$  and  $S_d$  (triangles, crosses and circles respectively) for the various concentrations. The lines serve only as a guide to the eye.

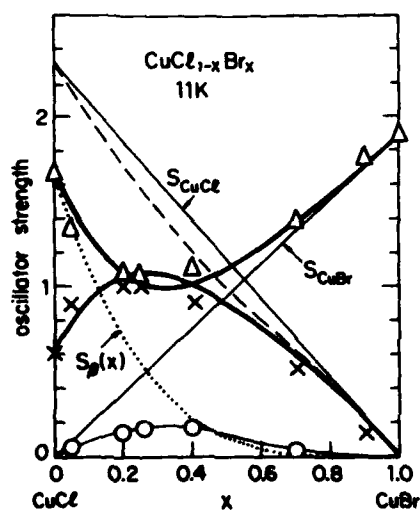


Fig. 3: A layout of the functions used for deducing the  $S_1(x)$  and  $S_2(x)$  (heavy lines).  $S_{CuCl}$ ,  $S_{CuBr}$  and  $S_p(x)$  are indicated and are explained in the text. The dashed line is  $(S_{CuCl} - S_d)$ . The triangles, crosses and circles are the  $S_1$ ,  $S_2$  and  $S_d$  values respectively deduced from polariton data and are the same as in fig. 2.

central positions. Fig. 3 presents the principal features of the calculated oscillator strengths ( $S$ ) of the various modes as function of concentration, which result in  $S_1(x)$  and  $S_2(x)$  - the main calculated oscillator strengths presented in heavy lines in the figure. The total oscillator strength of each compound is assumed to vary linearly with  $x(S_{\text{CuCl}}, S_{\text{CuBr}})$ .  $S_\beta(x) = 1.7(1-x)^4$  where  $S_\beta(0) = 1.7$  is the  $S_\beta$  of pure CuCl and  $f = (1-x)^4$  is the probability of tetrahedra with  $n=4$ . The  $\beta$  mode of CuCl and the mode of CuBr exhibit a one mode behavior thus  $S_\beta(x) + S_{\text{CuBr}}(x)$  add to  $S_1(x)$ , which is the lower frequency polar mode. The contribution of  $\beta$ -CuCl to  $S_1(x)$  decays very fast with  $x$ , corresponding to the decrease in the concentration of "all chlorine" tetrahedra in the mixed crystal.  $S_{\text{CuCl}}(x) - S_d(x) - S_\beta(x)$  yields  $S_2(x)$ . The  $S_d$  is small compared to the other two oscillators at all concentrations.  $S_d$  is the result of disorder and is affected also by the ability of  $\text{Cu}^+$  to occupy off center as well as central sites. Triangles and crosses are the experimental values of  $S_1(x)$  and  $S_2(x)$  obtained from the polariton measurements (the same as in fig. 2). Considering the fact that the only parameters we used were those employed in fitting the polariton data, the fit is self consistent and in addition it gives reasonable solutions to the problems which were presented earlier.

#### References

1. Z. Vardeny and O. Brafman, Phys. Rev. B19, 3290 (1979).
2. Z. Vardeny and O. Brafman, Phys. Rev. B19, 3276 (1979).
3. H.V. Verleur and A.S. Barker, Jr. Phys. 149, 715 (1966).



## FREQUENCY DEPENDENCE OF ACOUSTIC SATURATION IN SMOKY QUARTZ

R. Nava and M. Rodríguez

*Instituto Venezolano de Investigaciones Científicas (IVIC), Physics Center,  
P.O. Box 1827, Caracas 1010A, Venezuela*

**Abstract.**— High frequency ultrasonic measurements were performed in gamma irradiated natural quartz at 1.2 K at frequencies down to 20 MHz as a function of applied power. The two-level systems resonant attenuation shows saturation effects which decrease notably at frequencies below 200 MHz. These results are consistent with a decreasing density of states at frequencies close to  $\Delta_0$ .

A consequence of the tunneling model of TLS in amorphous and disordered solids is the existence of a gap in the density of states  $n(E)$  for energy splittings  $E = \sqrt{\Delta^2 + \Delta_0^2}$  smaller than the tunnel splitting  $\Delta_0$ . Among the observable effects of this prediction would be a departure of the low temperature specific heat from linearity in  $T$  and a rapid decrease of the resonant ultrasonic attenuation for frequencies  $\omega$  such that  $\hbar\omega < \Delta_0$  /1,2/. For TLS in crystalline matrices one expects  $\Delta_0$  to be single valued or, for small amounts of local disorder, narrowly distributed so that the change in these properties would take place in a shorter temperature (frequency) range than for glassy TLS. In this work we report the disappearance of the resonant ultrasonic attenuation of gamma irradiated Brazilian quartz for frequencies below 140 MHz in accordance with the existence of a gap in the density of states.

The intensity dependence of the resonant ultrasonic attenuation of shear waves along the AC-axis of crystals irradiated to  $1.5 \times 10^6$  Rads was measured in a non-resonant sample holder bathed by He pumped to 1.2 K. Typical acoustic intensities varied from  $20 \text{ mW/cm}^2$  to  $5 \text{ }\mu\text{W/cm}^2$ . An ultrasonic pulse length  $\tau_p$  of 1 microsecond was used throughout. The attenuation coefficient was determined from pulse-echoes separated by several hundred microseconds. The output of the video detector was averaged by means of a transient recorder coupled to a multichannel analyzer.

The experimental results show a frequency independent resonant attenuation above 200 MHz followed by a drastic reduction of  $\alpha$  for frequencies below about 170 MHz. The magnitude of the attenuation at

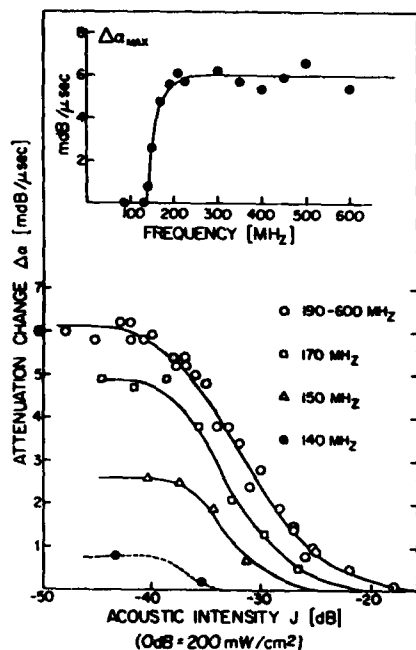


Fig. 1 : Intensity dependence of the relative resonant attenuation in smoky quartz. The inset shows the frequency dependence of the maximum attenuation change. Curves are only visual aids.

absorption ( $J < J_c$ ) takes place in a frequency range comparable to the inhomogeneous linewidth  $T_2^{-1}$ .

In the inset of Fig. 1, we have plotted the frequency dependence of the maximum resonant attenuation. The width of the transition is about 50 MHz. From this curve we estimate  $\Delta_0$  and  $T_2$  to be 130 MHz (0.5 μeV) and 3 nsecs., respectively. Taking for  $n_0$  the specific heat value ( $6 \times 10^{32} \text{ erg}^{-1} \cdot \text{cm}^{-3}$ ) we find from Eq. (1)  $\gamma_t \sim 0.14 \text{ eV}$  which is 20 times smaller than that reported for quartz glass /4/ and close to the mean value calculated from  $(\gamma\Delta_0)$  obtained by dielectric loss measurements /2/.

In summary, by studying the frequency dependence of the resonant ultrasonic attenuation due to TLS in smoky quartz we have established the existence of a gap in the density of low energy states as predicted by the tunneling model.

#### REFERENCES

- 1.- J.C. Lasjaunias, R. Maynard and M. Vondorpe, J. de Phys. **39**,

140 MHz is barely discernible above the experimental accuracy ( $5 \times 10^{-4} \text{ dB/μsec.}$ ) and undetectable below this frequency (Fig.1). We also find a frequency independent critical intensity  $J_c$  of about 35db below a reference acoustic intensity of  $200 \text{ mW/cm}^2$ .

Assuming steady state conditions at low frequencies ( $\hbar\omega \ll 2kT$ ) the attenuation coefficient of the unsaturated resonant absorption is given by:

$$\alpha = \begin{cases} \frac{\pi n(E) (\gamma_t \Delta_0)^2}{2 \hbar \rho v_t^3 kT} & \hbar\omega > \Delta_0 \\ 0 & \hbar\omega < \Delta_0 \end{cases} \quad (1)$$

For energy splittings greater than  $\Delta_0$ , a constant density of states  $n_0$  describes well these and previously reported results /3/. For energy splittings in the neighborhood of  $\Delta_0$ , assumed here to be single valued, the decrease observed in the unsaturated

C6-973 (1978).

- 2.- J. Chaussy, J. Le G. Gilchrist, J.C. Lasjaunias, M. Saint-Paul and R. Nava, J. Phys. Chem. Solids 40, 1073 (1979).
- 3.- M. Rodríguez, F. García-Golding and R. Nava, Phys. Lett. 79A, 241 (1980)
- 4.- S. Hunklinger and W. Arnold, Physical Acoustics 12. Eds. W.P. Mason and R.N. Thurston (Academic Press, New York, 1976).

## THEORY OF THE ATTENUATION OF ELASTIC WAVES IN INHOMOGENEOUS SOLIDS

P.G. Klemens

Dept. of Physics and Inst. of Materials Science, Univ. of Connecticut, Storrs,  
CT 06268, U.S.A.

**Abstract.**— Temperature variations accompanying elastic waves cause heat conduction, entropy generation and thus attenuation of the waves. In homogeneous solids the temperature variations over half a wave-length and those between different phonon groups cause comparable attenuation. In inhomogeneous solids the temperature gradients are enhanced. The resulting attenuation exceeds that due to Rayleigh scattering except at very high frequencies or at low temperatures. Small inclusions and fiber-matrix composites are discussed.

1. Introduction.— In homogeneous single crystals the attenuation of elastic waves arises from the cubic anharmonicities. Kirchhoff first proposed a heat conduction mechanism for gases,<sup>(1)</sup> which can also be applied to solids. Attenuation due to the smoothing out of temperature differences between different groups of phonons was treated by Akhieser.<sup>(2)</sup> In both cases do the elastic waves set up temperature differences, and the irreversible heat transfer generates entropy so that elastic energy is converted into heat.

There are two additional attenuation processes in inhomogeneous solids. One is Rayleigh scattering, owing to variations in the local value of the wave velocity. The other is an enhancement of the heat conduction mechanism, because temperature differences are set up between neighboring regions of different thermal expansivity, so that temperature gradients are increased. This was discussed by Zener.<sup>(3)</sup> It will be seen that the latter mechanism is more important than Rayleigh scattering except at very high frequencies or at low temperatures.

2. Homogeneous Solids.— The adiabatic temperature change due to a dilatation  $\Delta$  is given by

$$dT_S = -\gamma T \Delta \quad (1)$$

where  $\gamma$  is the Grüneisen constant. If either  $\Delta$  or  $\gamma$  varies with position,  $T$  will likewise vary and obey

$$\partial T / \partial t = D \nabla^2 T + \partial T_S / \partial t \quad (2)$$

where  $D$  is the thermal diffusivity. If  $\gamma$  is independent of position,

one can write for a wave

$$\Delta = \Delta_0 \exp i(\underline{k} \cdot \underline{r} + \omega t) \quad \text{and} \quad \partial T = T' \exp i(\underline{k} \cdot \underline{r} + \omega t) \quad (3)$$

and from (2)

$$i\omega T' = -k^2 D T' - i\omega \gamma \Delta_0 \quad (4)$$

Per unit volume, the rate of energy loss from the wave is related to the rate of entropy production by

$$-dE/dt = T dS/dt = (\kappa/T) |\text{grad } T|^2 \quad (5)$$

where  $\kappa = DC$  is the thermal conductivity, and  $C$  is the specific heat per unit volume. The energy content per unit volume of the wave is  $E = \frac{1}{2} \lambda \Delta_0^2$ , where  $\lambda$  is the bulk modulus. Thus one finds for the rate of energy loss

$$1/\tau = -E^{-1} dE/dt = \gamma^2 (T/T_0) \omega_0 \omega^2 (\omega_0^2 + \omega^2)^{-1} \quad (6)$$

where  $T_0$  is defined equal to  $\lambda/C$ , and the characteristic frequency  $\omega_0$  is defined as

$$\omega_0 = k^2 D \quad (7)$$

Now  $\omega_0$  depends on the wave frequency  $\omega$ , since  $k = \omega/v$ , where  $v$  is the wave velocity. At all but the highest frequencies  $\omega_0 \ll \omega$ , so that the Kirchhoff attenuation becomes

$$1/\tau_K = \gamma^2 (T/T_0) (D/v^2) \omega^2 \quad (8)$$

The Akhieser mechanism can also be described by (6), except that in place of  $\gamma^2$  one must now use  $\bar{\gamma}^2$ , a weighted mean square variability of  $\gamma$  for the different groups of lattice modes, while  $\omega_0$  describes the rate at which their temperature is equalized by phonon interactions. The lattice component of the thermal diffusivity is  $D_g = v^2/3\omega_0$ , if we disregard the difference between three-phonon N and U-processes. One is always in the limit  $\omega \ll \omega_0$ , so that the Akhieser attenuation becomes

$$1/\tau_A = \bar{\gamma}^2 (T/T_0) (3D_g/v^2) \omega^2 \quad (9)$$

While formally  $1/\tau_A$  exceeds  $1/\tau_K$  by a factor 3, it may well be the smaller of the two, since  $\bar{\gamma}^2$  must be less than  $\gamma^2$  and since  $D_g$  is only the lattice component, not the total  $D$ . A further reduction in  $1/\tau_A$ , perhaps by a factor 2, results from the inclusion of N-processes in the definition of  $\omega_0$ .

**3. Inhomogeneous Solids.**— Temperature gradients and entropy generation are enhanced if the thermal expansivity or  $\gamma$  depend on position. If the Fourier components of  $\gamma(\underline{r})$  have principal components of wave-number  $q$  and if the inhomogeneities are of small scale so that  $q \gg k$ ,  $\Delta$  can be treated as independent of position, so that  $q^2$  replaces  $k^2$  in (4) and (7), and (6) still holds with  $\omega_0$  redefined. However, in

place of  $\gamma^2$  one must use

$$\bar{\gamma}^2 = \sum v_i \gamma_i^2 - (\sum v_i \gamma_i)^2 \quad (10)$$

where  $v_i$  is the fractional volume of the component of Grüneisen constant  $\gamma_i$ . If the smallest diameter of the inhomogeneities is  $L$ ,  $\omega_0 = \pi^2 D/L$ , where  $D$  is the smaller of the thermal diffusivities.

4. Some Numerical Cases.— Consider small colloid inclusions such as produced by neutron irradiation in crystals, with  $L=1 \times 10^{-6}$  cm. Take  $T_0=25,000$  K,  $T=300$  K, and  $D=vL/3$ , so that  $\omega_0=3 \times 10^{11}$  sec $^{-1}$ . Now  $\gamma^2 = nV_0 \Delta\gamma^2$ , where  $\Delta\gamma$  is the difference between  $\gamma$  of the inclusion and matrix,  $n$  the inclusion density,  $V_0$  the volume of each inclusion. Let  $\Delta\gamma=1$ , then from (10) and from (6) with  $\omega \ll \omega_0$

$$1/\tau = 3 \times 10^{-14} nV_0 \omega^2 = 1.5 \times 10^{-16} \omega^2 \quad (11)$$

in inverse second units, the second value being for  $nV_0=0.005$ . This may be compared with Rayleigh scattering by these inclusions with  $\delta v/v = \frac{1}{2}$  and  $v=3 \times 10^5$  cm/sec :-

$$1/\tau_R = nV_0 (V_0/4v^3) \omega^4 = 2 \times 10^{-35} nV_0 \omega^4 \quad (12)$$

so that Rayleigh scattering is relatively weak below 6 GHz. At low temperatures attenuation by heat conduction decreases as TC.

As another example consider a composite of fibers embedded in a continuous matrix, each component occupying half the volume, with fiber diameter  $1 \times 10^{-3}$  cm and  $D=1$  cm $^2$ /sec, so that  $\omega_0=1 \times 10^7$  sec $^{-1}$ . With the same material parameters  $1/\tau=3 \times 10^{-10} \omega^2$  sec $^{-1}$  due to heat conduction, while for Rayleigh scattering  $1/\tau_R=8 \times 10^{-19} \omega^3$ . The attenuation by enhanced heat conduction is much stronger than intrinsic attenuation in either component, and exceeds Rayleigh scattering below about 10 MHz.

This work was done in collaboration with the Engineering Materials Division of the Naval Research Laboratory.

#### References

- (1) G. Kirchhoff, Poggendorff's Ann. 134, 177 (1868).
- (2) A. Akhiezer, J. Phys. (USSR) 1, 277 (1939).
- (3) C. Zener "Elasticity and Anelasticity of Metals" Univ. of Chicago Press, Chicago, 1948.

# LOW FREQUENCY RAMAN SCATTERING IN MIXED $\text{Ga}_{1-x}\text{Al}_x\text{As}$ AND $\text{Ga}_{1-x}\text{In}_x\text{As}$ ALLOYS

R. Carles, N. Saint-Cricq, A. Zwick, M.A. Renucci and J.B. Renucci

*Laboratoire de Physique des Solides, Associé au C.N.R.S., Université Paul Sabatier, 31062 Toulouse cedex, France*

**Abstract.**— We report Raman studies of disorder induced scattering in the  $\text{Ga}_{1-x}\text{Al}_x\text{As}$  and  $\text{Ga}_{1-x}\text{In}_x\text{As}$  alloys. Previous results [1] are confirmed for the  $\text{Ga}_{1-x}\text{Al}_x\text{As}$  system for a wider range of concentration. The role of the substituant is discussed through the analysis of the  $\text{Ga}_{1-x}\text{In}_x\text{As}$  system.

**Introduction.**— To extend results on a  $\text{Ga}_{0.80}\text{Al}_{0.20}\text{As}$  crystal [1] we performed experiments to a concentration of Al equals 0.50. Mass and size effects related to the nature of the substituant are analyzed on the  $\text{Ga}_{1-x}\text{In}_x\text{As}$  system.

**Results and discussion.**— All experimental details are provided in reference [1]. All the samples used in the present work were layers L.P.E. grown on a the (100) face of GaAs substrate.

Figures 1 and 2 display, respectively, the results obtained, at 300 K, for  $\text{Ga}_{1-x}\text{Al}_x\text{As}$  and  $\text{Ga}_{1-x}\text{In}_x\text{As}$ . Although the exciting laser wavelengths are different (see figure captions) resonance effects are excluded.

As in reference [1] we find that, except for the GaAs  $\text{LO}(\Gamma)$  mode, the crystal-line symmetry is also lost for the  $\text{Ga}_{1-x}\text{In}_x\text{As}$  alloys. Therefore we give only two types of spectra in figures 1 and 2. a(b) refers to crossed (parallel) polarizations of the incident and scattered lights and corresponds to the  $\Gamma_{15} (\Gamma_1 + 4 \Gamma_{12})$  Raman cross section [1].

Let us first compare for the same concentration ( $x = 0.20$ ) the spectra of the two alloys.

The main effect of the substituant appears for the long wavelength optical modes and is related to mass effects ( $m_{\text{Al}} < m_{\text{Ga}} < m_{\text{In}}$ ). Indeed a AlAs-like band stems above the frequency of the  $\text{LO}(\Gamma)$  in GaAs. This band merges into the local mode of Al in GaAs as  $x$  reaches zero. On the contrary for the  $\text{Ga}_{1-x}\text{In}_x\text{As}$  compounds a structure shows up below the  $\text{LO}(\Gamma)$  around  $235 \text{ cm}^{-1}$ . It gives for  $x = 0.09$  a shoulder (fig. 2) which materializes clearly the impurity mode of In in GaAs. As there is no gap in the phonon density of states of GaAs [2] it is an in-band mode and denoted  $\omega_b$  (In:GaAs). The symmetry of this mode is  $\Gamma_{15}$  (see fig. 2) as expected theoretically.

The structure at  $265 \text{ cm}^{-1}$  (fig. 1), which is attributed in reference [1] to GaAs

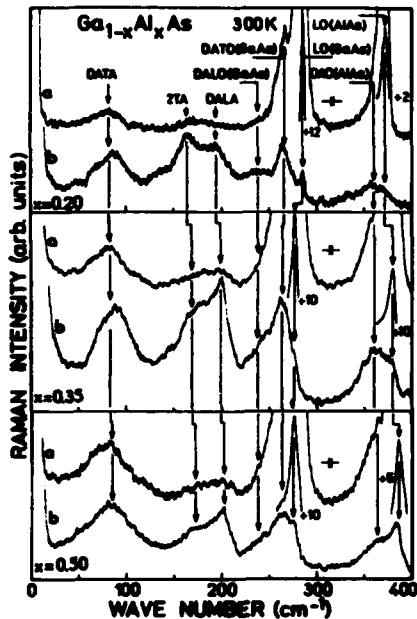


Fig. 1 - Raman spectra observed, at 300 K, for three  $\text{Ga}_{1-x}\text{Al}_x\text{As}$  samples. The exciting laser wavelengths are  $\lambda = 5308 \text{ \AA}$  for  $x = 0.20$  and  $\lambda = 5145 \text{ \AA}$  for  $x = 0.35$  and  $0.50$ .

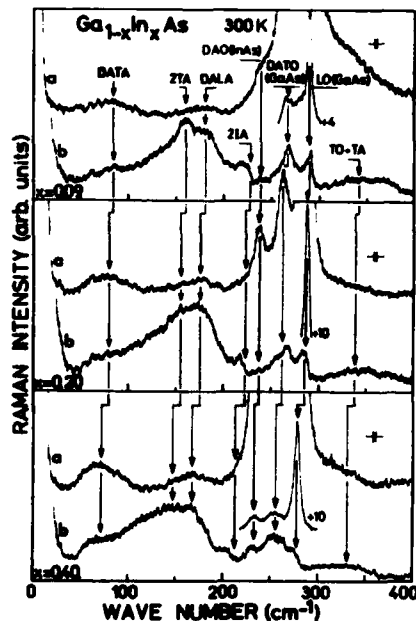


Fig. 2 - Raman spectra observed, at 300 K, for three  $\text{Ga}_{1-x}\text{In}_x\text{As}$  samples. The exciting laser wavelengths are  $\lambda = 4880 \text{ \AA}$  for  $x = 0.09$  and  $x = 0.20$ ,  $\lambda = 5308 \text{ \AA}$  for  $x = 0.40$ .

disordered activated transverse optical processes (D.A.T.O.), is also present in the  $\text{Ga}_{1-x}\text{In}_x\text{As}$  system (fig. 2) whereas the D.A.L.O. of GaAs (fig. 1) is obscured by the InAs-like band. This one is noted D.A.O. (fig. 2) as it is hard to distinguish between longitudinal and transverse processes.

In the low frequency range the D.A.T.A., 2 TA, and D.A.L.A. modes appear also in the  $\text{Ga}_{1-x}\text{In}_x\text{As}$  alloys although the structures are less resolved. Their frequencies are shifted to lower energies compared to those found in GaAs [1], due to mass effects, as expected. They increase in  $\text{Ga}_{1-x}\text{Al}_x\text{As}$  for the same reason.

The shift to lower energy of the acoustical branches in the  $\text{Ga}_{1-x}\text{In}_x\text{As}$  system allows to resolve the 2 IA band while it lies within the D.A.L.O. of GaAs for  $\text{Ga}_{1-x}\text{Al}_x\text{As}$ .

The assignment of the structures discussed above for  $x = 0.20$  are confirmed by the variations of their frequencies, widths and intensities upon concentration.

As already mentioned spectra are less structured for the  $\text{Ga}_{1-x}\text{In}_x\text{As}$  system. In the acoustical range this is related, in part, to the larger width of the 2 TA band. Due to the bigger size of In, the substitution of In to Ga introduces a distortion



of the bond length much more important than the one produced by the substitution of Al (the bond lengths in GaAs, AlAs and InAs are respectively 2.447 Å, 2.452 Å and 2.615 Å). This effect induces a larger amount of disorder in the  $\text{Ga}_{1-x}\text{In}_x\text{As}$  system and consequently should lead to wider structures.

The same reason could explain that, for each concentration, the width of the D.A.T.A. is larger by an amount of  $7\text{ cm}^{-1}$ , on the average, in the  $\text{Ga}_{1-x}\text{In}_x\text{As}$  alloys. In the same way, the width of the LO(GaAs) band increases by a factor 2.7(1.8) when the concentration of In(Al) goes from 0 to 0.5.

The intensities of the disorder induced bands reflect the degree of disorder of the alloy. As a matter of fact the relative intensities of the D.A.T.A. and the D.A.L.A. to that of the 2TA band increase (fig. 1 and 2) with  $x$  as the latter is reminiscent of the order of the perfect crystal. To evaluate more quantitatively the degree of disorder it is convenient to refer to the intensity of the D.A.T.A. which is well seen in the two alloys. Indeed the ratio  $I(\text{D.A.T.A.}) / (1-x) I[\text{LO}(\text{GaAs})]$  increases with  $x$ .

In figures 1-b one notices also that the intensities of the D.A.L.O. and the D.A.T.O. of GaAs increase in a way similar to that of the D.A.L.A. Also the D.A.O. of AlAs get stronger with  $x$ .

The "depolarization spectrum" introduced by Kobliska and Solin in the case of amorphous materials [3] can be measured in the alloys. As all the spectra have been recorded with the same instrumental transfer function, for each concentration, the depolarization ratio  $\rho$  is given by the ratio of the intensity of spectrum a over that of spectrum b. One deduces from fig. 1 and 2 that  $\rho(\text{D.A.T.A.})$ , for example, increases with  $x$  and reaches its maximum value when the disorder is the greatest for  $x=0.5$ . As displays in figures 1 and 2  $\rho$  is dispersive, indeed  $\rho(\text{D.A.L.A.}) < \rho(\text{D.A.T.A.})$ . This implies that the vibrations which correspond to the D.A.L.A. are more symmetrical than those of the D.A.T.A. in agreement with the conclusions of London [4] relative to defect activated Raman processes in zinc-blende type crystals. As a matter of fact, although longitudinal and transverse acoustical phonons at X and L become Raman active, the symmetry of the longitudinal is in part  $\Gamma_1$ -like while the one of the transverse is never  $\Gamma_1$ . One should point out that the  $\Gamma_1$  symmetry of the D.A.L.A. was well reproduced by the calculations of Talwar et al. [5].

#### References.-

- [1] N. SAINT-CRICQ, R. CARLES, J.B. RENUCCI, A. ZWICK and M.A. RENUCCI, *Solid State Commun.*, in print.
- [2] J.L.T. WAUGH and G. DOLLING, *Phys. Rev.*, **132**, 2410 (1963).
- [3] R.J. KOBLISKA and S.A. SOLIN, *Phys. Rev. B*, **8**, 736 (1973).
- [4] R. LONDON, *Proc. Phys. Soc.*, **84**, 379 (1964)
- [5] D.N. TALWAR, M. VANDEVYVER and M. ZIGONE, *Phys. Rev. B*, **23**, 1743 (1981).

PHONON - PHONON INTERACTIONS AND NON - LINEAR  
LATTICE DYNAMICS

## SOME ASPECTS OF NONLINEAR LATTICE MODELS

H. Büttner and H. Bilz\*

*Phys. Inst. Univ. Bayreuth, D-8580 Bayreuth, F.R.G.**\*Max-Planck-Inst. für Festkörperforschung, D-7000 Stuttgart 80, F.R.G.*

**Abstract.**— A theoretical study of various static and dynamic solutions in a one-dimensional lattice with anharmonic electron-ion coupling is presented. The stability of the different commensurate groundstates is investigated and both kink- and phonon-excitations are described. The coupling of nonlinear excitations to phonons is discussed in detail.

It was pointed out some time ago, that the microscopic origin of ferroelectricity in perovskites is due to the configurational instability of  $O^{2-}$  and its homologues, which leads to a strong anisotropic, anharmonic polarizability<sup>1,2</sup>. This assumption was recently tested directly by a Mössbauer study on  $LiTaO_3$ <sup>3</sup> and applied to various other materials, like  $KTa_{1-x}Nb_xO_3$ <sup>4</sup>;  $SrTiO_3$ <sup>5</sup>;  $K_2SeO_4$ <sup>6,7</sup>, and  $SnTe$ <sup>6,7</sup> in a self-consistent description of their phonon spectra. A discussion of the nonlinear excitations in a one-dimensional version of this model has been given in Ref. 8,9, and the coupling to phonons is studied in detail in Ref. 6. Extensions to two-<sup>10</sup> and three-dimensions<sup>6,11</sup> have also been successful.

In the following we shall review some results from the literature and present new investigations especially on the stability of the static nonlinear solutions and their coupling to phonon-excitations.

The essential feature of the model is a highly local electron-ion coupling. The instability of the transverse ferroelectric mode is attributed to a negative electron-shell ion-core coupling constant  $g_2$ . The paraelectric mode above the phase transition is stabilized by a fourth-order shell-core coupling  $g_4$ . For a discussion of the relation to other ferroelectric models see Ref. 8,6. In the simplest version of the model, a monatomic chain, there are additional nearest-neighbor shell-shell and core-core coupling constants  $f$  and  $f'$  (see Fig. 1).

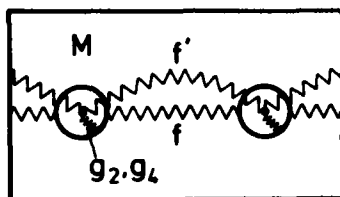


Fig 1. Part of the one-dimensional lattice model, with harmonic nearest-neighbor coupling between the electron shells  $f$  and the ions  $f'$ ; the local electron-ion coupling is described by a harmonic coupling  $g_2$  and a fourth-order term  $g_4$ .

The classical Hamilton-function of the chain is written for the displacements  $u_n$  and  $v_n$  of the ion and the electron-shell with masses  $M$  and  $m$  respectively:

$$H = \frac{m}{2} \sum_n \dot{v}_n^2 + \frac{M}{2} \sum_n \dot{u}_n^2 + \frac{g_2}{2} \sum_n (v_n - u_n)^2 + \frac{g_4}{4} \sum_n (v_n - u_n)^4 + \frac{f}{2} \sum_n (v_n - v_{n-1})^2 + \frac{f'}{2} \sum_n (u_n - u_{n-1})^2 \quad (1)$$

with the corresponding equations of motion (in the adiabatic approximation):

$$M\ddot{u}_n = g_2 w_n + g_4 w_n^3 + f' Du_n \\ 0 = -g_2 w_n - g_4 w_n^3 + f D(w_n + u_n) \quad (2)$$

where the difference displacement  $w_n = v_n - u_n$  is used and the difference operator  $Du_n = u_{n+1} - 2u_n + u_{n-1}$ .

The static periodic solutions on the lattice are the fixed points of the corresponding recurrence relations between  $w_{n+1}$  ( $u_{n+1}$ ) and  $w_n$ ,  $w_{n-1}$  ( $u_n$ ,  $u_{n-1}$ )<sup>9</sup>. Usually one has to find these points numerically, but for low-order periods the analytic results are given in Table 1. Periods of higher order are more complicated. The displacement pattern of period  $2\pi/8$  for example has two different displacements on site  $w_{8m+1} = w_{8m+3} = -w_{8m+5} = -w_{8m+7}$  and site  $w_{8m+2} = -w_{8m+6}$  related by


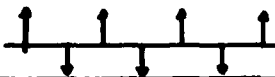
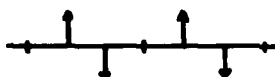


Period $2\pi/k$	Electron-Ion Displacement $w$ Displacement-Pattern	Energy
$k = 1$ (ferroelectric)	$w_0^2 = -g_2/g_4$ 	$E_1 = -g_2^2/4g_4$
$k = 2$ (antiferroelectric)	$w_0^2 = (-w_1)^2 = \frac{g_2}{g_4} \left(1 + \frac{4f_r}{g_2}\right)$ 	$E_2 = -\frac{g_2^2}{4g_4} \left(1 + \frac{4f_r}{g_2}\right)^2$
$k = 3$ (Periodon)	$w_0=0, w_1^2 = (-w_2)^2 = \frac{g_2}{g_4} \left(1 + \frac{3f_r}{g_2}\right)$ 	$E_3 = -\frac{g_2^2}{6g_4} \left(1 + \frac{3f_r}{g_2}\right)^2$
$k = 4$	$w_0=w_2=0, w_1^2 = (-w_3)^2 = \frac{g_2}{g_4} \left(1 + \frac{2f_r}{g_2}\right)$ 	$E_4 = -\frac{g_2^2}{8g_4} \left(1 + \frac{2f_r}{g_2}\right)^2$
$k = 6$	$w_0=w_3=0, w_1^2=w_2^2=(-w_4)^2=(-w_5)^2 = \frac{g_2}{g_4} \left(1 + \frac{f_r}{g_2}\right)$ 	$E_6 = -\frac{g_2^2}{6g_4} \left(1 + \frac{f_r}{g_2}\right)^2$

Table 1: Static commensurate solutions of (2) with different periods.

the equations:

$$\begin{aligned} 2w_{8m+1} &= w_{8m+2} (g_2/f_r + 2) + w_{8m+2}^3 (g_4/f_r) \\ w_{8m+2} &= w_{8m+1} (g_2/f_r + 2) + w_{8m+1}^3 (g_4/f_r) \end{aligned} \quad (3)$$

with the reduced intersite coupling  $1/f_r = 1/f + 1/f'$ .

The energy for the different commensurate states is always negative and corresponds to local minima of the Hamilton-function. For  $g_2 < 0$  and  $f, f' > 0$  the homogeneous ferroelectric state has always lowest energy. For  $g_2 < 0$  and  $f' < 0$  but  $f > 0$  there may be other states with lower energy. But this energy consideration is not sufficient to determine the stable groundstate of the chain. One has to investigate the stability of the solutions under small time-dependent perturbations and in addition to this, whether static solutions in the vicinity of the fixed points stay there under the nonlinear mapping<sup>12,13</sup> of equations (2). We rewrite these for  $w_n$  as:

$$\begin{aligned} w_{n+1} &= \left( \frac{g_2}{f_r} + 2 \right) w_n + (g_4/f_r) w_n^3 + x_n \\ x_{n+1} &= -w_n \end{aligned} \quad (4)$$

and linearize them by the ansatz:

$$w_n = w_{no} + \delta w_n \quad (5)$$

with the result

$$\begin{aligned} \delta w_{n+1} &= \left[ (g_2/f_r + 2) + (3g_4/f_r) w_{no}^2 \right] \delta w_n + \delta x_n \\ \delta x_{n+1} &= -\delta w_n \end{aligned} \quad (6)$$

For the different fixpoints we now investigate the eigenvalues of the matrix

$$M = \prod_{n=1}^k \begin{pmatrix} (g_2/f_r + 2) + (3g_4/f_r) w_{no}^2 & 1 \\ -1 & 0 \end{pmatrix} \quad (7)$$

which describes a so-called tangent space mapping<sup>13</sup>. (The method is analogous to that used by Greene<sup>12</sup> for another nonlinear mapping.)

For complex eigenvalues of  $M$  the fixpoint is elliptic stable. The stable regions are given in Table 2. Since this stability analysis is based on some (so far unproven) mathematical assumptions, we also looked for numerical stability in the vicinity of the commensurate states and found agreement with the parameters regions of Table 2.

Period $k$	Range of Parameters for Mapping Stability	Remarks
1	$0 \leq g_2/f_r \leq 2$	f or f' have to be negative
2	$-6 \leq g_2/f_r \leq -4$	
3	$-4 \leq g_2/f_r \leq -3$	
4	$g_2/f_r = -2$	method is probably too weak

**Table 2:** Range of mapping stability for low order periodic solutions.

These results mean, that in certain parameter areas only one of the fixed points is stable, although its energy may not be the absolute lowest. In the neighborhood of a stable region there may be incommensurate stable states, which can be reached by leaving the stability range of the parameters<sup>12,14</sup>.

Above these static groundstates there are linear phonon- and nonlinear static kink-like excitations. The latter ones describe, as in the usual  $\phi_4$ -theory, domain walls between the degenerate groundstates of a certain period  $k$ . As an example, we write down the equations for the kink structure in the antiferroelectric state ( $k = 2$ ), where the polarization sequence of the ions is altered from 'up, down, up ...' to 'down, up, down ...'. If we assume only small changes within the unit cell, the continuum approximation for each sublattice can be used and results in:

$$\begin{aligned}
 w_1 + aw_1' + a^2w_1'' &= \left(\frac{g_2}{2f_r} + 1\right)w_2 + \frac{g_4}{2f_r}w_2^3 \\
 w_2 + aw_2' + a^2w_2'' &= \left(\frac{g_2}{2f_r} + 1\right)w_1 + \frac{g_4}{2f_r}w_1^3
 \end{aligned}
 \tag{8}$$

where  $w_1$  and  $w_2$  describe the electron-ion displacements in the two sublattices, and  $a$  is the lattice constant of the original lattice. The boundary conditions are  $w_1 = -w_2$  for  $x \rightarrow \pm\infty$ , in contrast to the ferroelectric state. Numerical solutions show a static kink-like transitions in each sublattice. These solitary excitations will

contribute to the statistical mechanics of the antiferroelectric state. Similar solutions have been found above the periodon ( $k = 3$ ) ground-state. Details are discussed in a forthcoming paper<sup>15</sup>.

The static solutions discussed so far, can easily be extended to diatomic chains with one additional unpolarizable ion<sup>8</sup>. Furthermore there are also solutions of the same type for two<sup>10</sup> and three-dimensional<sup>6</sup> systems.

Before describing the coupling of phonons to the periodons we cite here the corresponding time dependent nonlinear solutions. They can be written as<sup>6</sup>:

$$\begin{aligned} w_n &= A(q) \sin(\omega t - nqa + \delta) \\ u_n &= B(q) \sin(\omega t - nqa + \delta) + C(q) \sin 3(\omega t - nqa + \delta) \end{aligned} \quad (9)$$

with the dispersion

$$M\omega^2 = \frac{4}{9} (f+f') \sin^2(3qa/2) \quad (10)$$

and the amplitudes

$$\begin{aligned} A^2(q) &= -\frac{4g_2}{3g_4} \left\{ 1 + \frac{4f}{g_2} \frac{M\omega^2 - 4f' \sin^2(qa/2)}{M\omega^2 - 4(f+f') \sin^2(qa/2)} \sin^2(qa/2) \right\} \\ B(q) &= -A \frac{4f \sin^2(qa/2)}{M\omega^2 - 4(f+f') \sin^2(qa/2)}, \quad C(q) = +\frac{g_4}{16f} A^3 / \sin^2(3qa/2) \end{aligned} \quad (11)$$

Note the divergent character of  $C(q)$  at  $q_c = 0; 2\pi/3$  where the frequency is zero. In order to avoid this unphysical static solutions one has to choose the phase  $\delta$  in such a way that  $\sin(3\delta) = 0$ , which results in  $C(q_c = 0; 2\pi/3) = 0$  and amplitudes given in Table 1.

The coupling of phonons to these periodons is now calculated with the ansatz:

$$w_n = w_{np} + w_{ns}, \quad u_n = u_{np} + u_{ns} \quad (12)$$



A special solution is found by rewriting the equations of motion (2) in two groups:

$$M\ddot{u}_{ns} = (f+f')\dot{u}_{ns} + f\dot{w}_{ns} \quad (13)$$

$$0 = (g_2 + 3g_4 w_{np}^2) w_{ns} + g_4 w_{ns}^3 - fD(u_{ns} + w_{ns})$$

$$M\ddot{u}_{np} = (f+f')\dot{u}_{np} + f\dot{w}_{np} \quad (14)$$

$$0 = (g_2 + 3g_4 w_{ns}^2) w_{np} + g_4 w_{np}^3 - fD(u_{np} + w_{np})$$

Our approximation is that used in the selfconsistent phonon treatment where higher powers of the phonon contribution  $w_{ns}$  are approximated by their thermal averages:

$$g_4 w_{ns}^3 \approx 3g_4 \langle w_{ns}^2 \rangle_T w_{ns} \text{ and } 3g_4 w_{ns}^2 \approx 3g_4 \langle w_{ns}^2 \rangle_T \quad (15)$$

This results in a temperature dependent coupling

$$g(T) = g_2 + 3g_4 \langle w_{ns}^2 \rangle_T \quad (16)$$

Furthermore the phonons are influenced by the periodon solution  $w_{np}$ . For low temperature we use its static value, which causes a tripling of the lattice constant:

$$g(T) + 3g_4 w_{np} \left( \frac{2\pi}{3} \right) = \begin{cases} g(T) & n = 0 \pmod{3} \\ -2g(T) - 9f_r & n = 1, 2 \end{cases}$$

For high temperature the periodons are approximated by a time average

$$g(T) + 3g_4 w_{np}^2(q) \approx g(T) + \frac{3}{2} g_4 A^2(q)$$

with  $A^2$  from (11) and  $g_2$  replaced by  $g(T)$ . This  $q$ -dependent coupling leads to a drastic change of the acoustical mode near  $q = 2\pi/3$ . An application of this method to the phonon-spectra of various materials is reported in Ref. 6. Especially the paraelectric-incommensurate and the incommensurate-commensurate phase transitions in  $K_2\text{SeO}_4$  have been successfully analysed<sup>6,7</sup>.

Furthermore it was found, that the phonon anomalies in  $\text{TaSe}_2$  and  $\text{NbSe}_3$  may be described in terms of our simple model<sup>7</sup>. This shows the interrelation of our mode-coupling treatment to the description of these metallic systems in terms of charge-density waves.

References

- 1) R. Migoni, H. Bilz and D. Bäuerle, Phys.Rev.Lett. 37, 1155 (1976)
- 2) H. Bilz, A. Bussmann, G. Benedek, H. Büttner and D. Strauch Ferroelectrics 25, 339 (1980) and to be published
- 3) M. Löhnert, G. Kaindl, G. Wortmann and D. Salomon Phys.Rev.Lett., 47, 194 (1981)
- 4) D. Rytz, U.T. Höchli and H. Bilz, Phys.Rev. B22, 359 (1980)
- 5) A. Bussmann-Holder, H. Bilz, D. Bäuerle and D. Wagner Zeitschrift Physik B41, 353 (1981)
- 6) H. Bilz, H. Büttner, A. Bussmann-Holder, W. Kress and U. Schröder, to be published
- 7) A. Bussmann-Holder, H. Bilz and H. Büttner, Proc. Ferroelectric Conf. Philadelphia, 1981
- 8) H. Büttner and H. Bilz, in Recent Developments in Condensed Matter Physics, Vol. I (ed. J. T. Devreese) p. 49, Plenum (1981)
- 9) H. Büttner in Nonlinear Phenomena at Phase Transitions and Instabilities, Nato Adv. Study Inst. Geilo 1981 (ed. T. Riste), Plenum (1981)
- 10) G. Behnke and H. Büttner, J. Phys. A14, L113 (1981) see also G. Behnke, thesis, Univ. Bayreuth, W.-Germany (1981)
- 11) U. Schröder et. al, Int. Conf. on Phonons, Bloomington 1981, Journal de Physique, to be published.
- 12) J.M. Greene, J.Math.Phys., 20, 1183 (1979)
- 13) M. Tabor, Adv. Chem. Phys. Vol. XLVI, p. 73 (1981)
- 14) P. Bak, Phys. Rev. Lett., 46, 791 (1981)
- 15) H. Büttner, to be published

OBSERVATION OF STRONGLY FREQUENCY DEPENDENT LIFETIMES OF ACOUSTIC PHONONS IN  $\text{CaF}_2$ 

R. Baumgartner, M. Engelhardt and K.F. Renk

*Institut für Angewandte Physik, Universität Regensburg, 8400 Regensburg, F.R.G.*

**Abstract.**— A strongly frequency dependent lifetime of acoustic phonons in  $\text{CaF}_2$  at low crystal temperature is observed. The phonon lifetime decreases proportionally to  $\nu^{-5}$  indicating spontaneous phonon decay. Furthermore, we report measurements of the spectral distribution of phonons generated by nonradiative transitions.

Various attempts have been made to detect spontaneous decay of high-frequency acoustic phonons without, however, conclusive results.<sup>1</sup> In this paper we report experimental evidence of spontaneous decay of acoustic phonons. Our experiment was performed on  $\text{CaF}_2$  at low crystal temperature.

The principle of our experiment is shown in Fig.1. Uniaxial stress is applied to a  $\text{CaF}_2$  crystal doped with 0.003 mole%  $\text{Eu}^{2+}$  ions. The stress leads to a splitting of the lowest excited state level of  $\text{Eu}^{2+}$  into a doublet with variable energy separation  $h\nu$  where  $h$  is Planck's constant. This system allows tunable phonon detection up to a frequency  $\nu$  of 3.2 THz.<sup>2</sup> For phonon generation the crystal is optically pumped with radiation of a nitrogen laser. The radiation is absorbed in broad bands of the  $\text{Eu}^{2+}$  ions. Nonradiative transitions lead to population of the stress split energy levels and, simultaneously, to

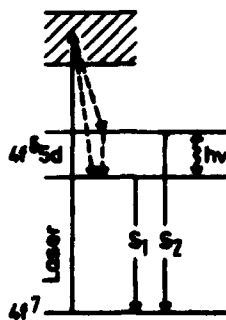


Fig.1. Principle of phonon detection.

generation of phonons with a broad frequency distribution. An additional phonon source is due to one-phonon spin-lattice relaxation in the doublet levels. Phonons are detected by the phonon induced fluorescence radiation  $S_2$  (Fig.1). Since the spin-lattice relaxation time is shorter than 1 ns the relative population of the doublet levels is in equilibrium with phonons of the frequency  $\nu$ . Therefore, we can directly measure phonon occupation numbers by observing  $S_1$  and  $S_2$  fluorescence. In addition, from the decay of

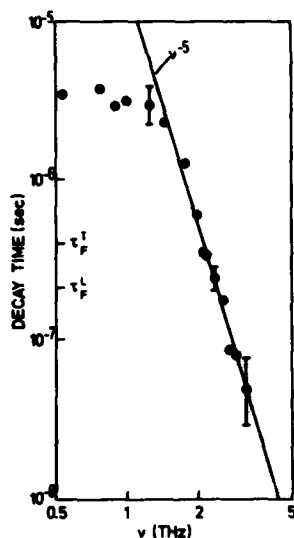


Fig.2. Phonon lifetimes in  $\text{CaF}_2$  at  $T = 2$  K.

the  $S_2$  signal phonon lifetimes are obtained.

Experimental results for phonon lifetimes are shown in Fig.2. We observe an almost frequency independent phonon decay time in the range up to 1.5 THz, but, a strong decrease as  $\nu^{-5}$  at higher frequencies. A  $\nu^{-5}$  dependence is predicted by theory for the case of phonon splitting by anharmonic three phonon processes.<sup>3</sup> We compare the lifetimes with theoretical values calculated for an isotropic dispersionless solid. Regarding that due to impurity scattering transverse and longitudinal phonons at the same frequency are in an equilibrium, and assuming that only longitudinal phonons can decay spontaneously, whereas

transverse phonons cannot decay due to energy and momentum conservation, we find that our experimental decay times in the high-frequency range are in agreement with theory.<sup>4</sup> In the low frequency range, the decay times are an order of magnitude longer than the ballistic times of flight ( $\tau_F^T$  and  $\tau_F^L$  in Fig.2) out of the optically excited volume, indicating a diffusive propagation of the phonons. The reason for a frequency independent lifetime is not known, the low frequency lifetime may be due to inelastic scattering of phonons at impurities.

In order to obtain information on the phonon spectrum, which is generated by the nonradiative transitions, we have determined phonon occupation numbers from the ratio  $S_2/S_1$  of the fluorescence intensities. In Fig.3a experimental phonon occupation numbers  $p$  are plotted for different phonon frequencies. We find that immediately after laser pulse excitation phonons with a nonthermal spectrum are contained in the crystal. In Fig.3a we have also drawn occupation numbers for a Planckian spectrum of  $T = 10$  K. This temperature is estimated using specific heat data for the case, that fast thermalization of the absorbed laser energy occurs. In the low frequency range, the observed occupation numbers are up to two orders of magnitude lower than for the 10 K spectrum, while at higher frequencies the experimental occupation numbers are larger than for the

Planckian spectrum. Our result indicates that by the nonradiative transitions mainly high-frequency phonons are created.

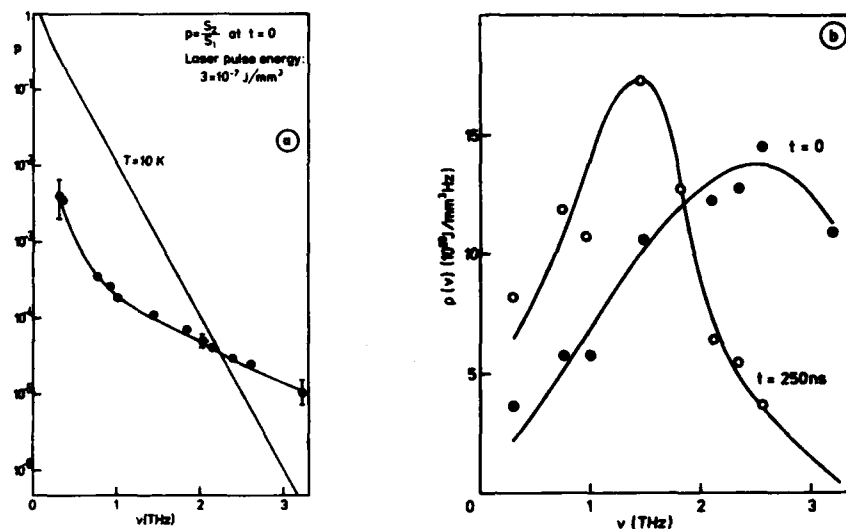


Fig.3. (a) Phonon occupation numbers  $p$  immediately after laser pulse excitation ( $t = 0$ ); (b) Phonon spectrum at different times.

From the occupation numbers the spectral energy density of the phonons is derived. In Fig.3b the spectral energy densities of the phonons for two different times  $t$  after laser pulse excitation are shown. At  $t=0$  we find a large phonon energy at high frequencies. At a later time we observe a strong decrease in the high-frequency range, while at lower frequencies the spectral phonon energy has increased. This confirms that high-frequency phonons decay spontaneously into phonons of lower frequencies.

In summary, we have studied the temporal development of a non-thermal phonon distribution in  $\text{CaF}_2$  at low crystal temperature. The results of our measurements show, that phonon decay times are strongly frequency dependent in agreement with theory.

Discussions with R. Orbach are acknowledged. The work was supported by the Deutsche Forschungsgemeinschaft.

#### References

- 1 For a survey see Bron, W.E., Phys.Rev. B **21**, 2627 (1979).
- 2 Eisfeld, W., and Renk, K.F., Appl.Phys.Lett. **34**, 481 (1979).
- 3 Slonimskii, G.L., Zh.Eksp.Teor.Fiz. **7**, 1457 (1937); Orbach, R. and Vredevoe, L.A., Physics **1**, 92 (1964); Klemens, P.G., J.Appl.Phys. **38**, 4573 (1967).
- 4 Baumgartner, R., Engelhardt, M., and Renk, K.F., to be published.

ANHARMONICITY EFFECTS IN  $\text{CaF}_2$  AT LOW TEMPERATURE

P.F. Tua and G.D. Mahan

Physics Department, Indiana University, Bloomington, IN 47405, U.S.A.

**Abstract.** - Using the framework of the rigid ion model, we have calculated the lifetime of longitudinal acoustic phonons in  $\text{CaF}_2$  at low temperature. The decay mode  $1 \rightarrow 1 + t$  is strongly anisotropic and of one order of magnitude smaller than the decay mode  $1 \rightarrow t + t$ . For each single decay mode, the long-wavelength approximation which yields the  $\nu^5$  dependence of  $1/\tau$ , is valid for  $\nu \leq 2.5$  THz. At higher frequencies, the competing decay modes show different deviances which, curiously, cancel each other so that the total life-time can be well approximated by the long-wavelength limit up to 5.5 THz. We have also calculated the temperature dependence of the second and third order elastic constants and a good agreement is found with the available experimental data.

Several new experimental techniques have been recently applied to study the lifetime of high-frequency acoustic phonons at low temperature<sup>[1]</sup>. Preliminary results<sup>[2]</sup> for longitudinal acoustic (LA) phonons in fluorites,  $\alpha$ -quartz, and ruby show a lifetime longer than the theoretical predictions of Orbach and Vredevoe<sup>[3]</sup> and Klemens<sup>[4]</sup>, which are based on an isotropic model in the long-wavelength approximation (LWLA). Bron<sup>[2]</sup> has suggested that, for  $\text{SrF}_2$ ,  $\text{CaF}_2$ , and  $\alpha$ -quartz, the discrepancy lies in the differences in the density of phonon states between the real crystal and an isotropic, dispersionless Debye solid. We believe this is

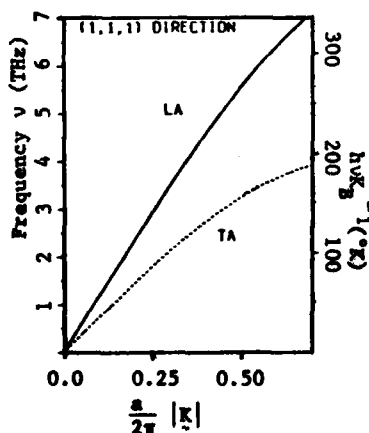


Fig. 1: Example of dispersion curves in  $\text{CaF}_2$ <sup>[8]</sup> at 295°K.

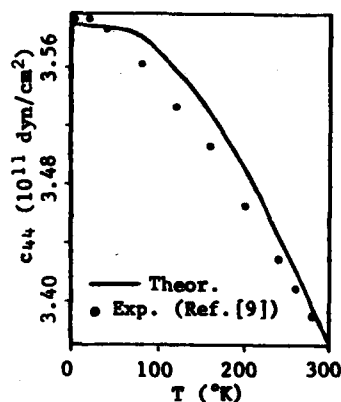


Fig. 2: Temperature-dependence of  $c_{44}$  in  $\text{CaF}_2$ .

not the case. First, the frequency  $\nu$  of the probed LA phonons lies between 1 and 3.5 THz<sup>[2]</sup> and the deviances of the dispersion relations from the LWLA are very small in that region, as shown in Fig. 1 for  $\text{CaF}_2$ . Second, the form of Orbach and Vredevoe's relation, where  $1/\tau$  is proportional to  $\nu^5$ , is independent of the anisotropy of the crystal in the LWLA, because it is a consequence of a simple scaling law<sup>[5]</sup>, the anisotropy affecting the constant of proportionality slightly.

Another possible explanation is that the three-phonon interaction matrix elements might show large deviations from the LWLA in that frequency region, even if the dispersion relations do not. In order to investigate this possibility, we have performed a numerical calculation of the LA phonon lifetime in  $\text{CaF}_2$  for frequencies between 2.5 and 5.5 THz. We have used the Landau and Rumer<sup>[6]</sup> theory for the case  $h\nu \gg k_B T$ . A simple calculation<sup>[5]</sup> shows that the umklapp processes play a minor role in the region  $\nu < 5.5$  THz, and hence they have been neglected. Strictly speaking, the calculation is at zero temperature, but the LA phonon decay is temperature-independent at sufficiently low temperature ( $< 15^\circ\text{K}$ , in our case), as shown by Orbach and Vredevoe<sup>[3]</sup>. We have used the rigid ion model where the ions have an "effective" charge and the short-range pair-potentials have the usual Born-Mayer form<sup>[7]</sup>. The parameters have been determined by fitting the neutron scattering data<sup>[8]</sup> and the temperature-dependence data of the second-order elastic constants<sup>[9]</sup>. In Fig. 2 we show the temperature-dependence of  $c_{44}$  as an example of the good agreement between theory and experimental data. We have also performed a long-wavelength expansion of the interaction matrix elements and calculated the third-order elastic constants. The values<sup>[5]</sup> are in satisfactory agreement with the available experimental data<sup>[10]</sup>, since the latter refer to the first-sound region where vertex corrections become important<sup>[11]</sup>.

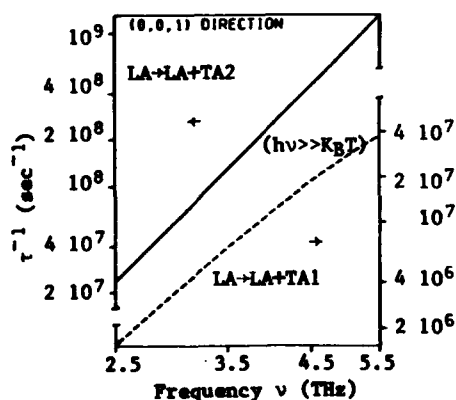


Fig. 3: Transition rate of LA phonons in  $\text{CaF}_2$  for decay  $\text{LA} \rightarrow \text{LA} + \text{TA}$ .

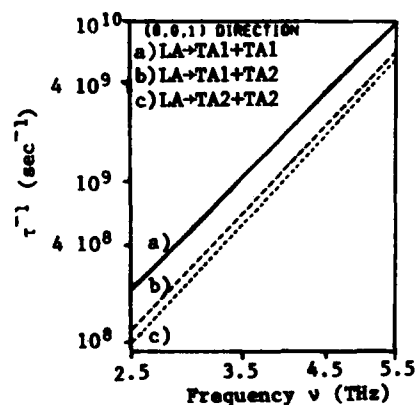


Fig. 4: Transition rate of LA phonons in  $\text{CaF}_2$  for decay  $\text{LA} \rightarrow \text{TA} + \text{TA}$ .

Table I - Lifetime ( $10^{-10}$ sec) of LA phonons with  $h\nu \gg K_B T$  in  $\text{CaF}_2$ .

$\nu$ (THz)	(0,0,1)	(0,1,1)	(1,1,1)
2.5	33.9	11.9	6.41
3.5	6.33	2.18	1.19
4.5	1.80	0.610	0.341
5.5	0.662	0.220	0.125

The calculated total LA phonon lifetimes in the three principal directions is reported in Table I. As expected, the lifetime depends upon the direction, but only within a factor of 5. The  $\nu^5$ -dependence is well satisfied. Nevertheless, as shown in Figs. 3 and 4, the single decay modes show deviations from the  $\nu^5$ -dependence but they cancel out in the total lifetime. The strong deviation of the process  $\text{LA} \rightarrow \text{LA} + \text{TA}_1$ , where  $\text{TA}_1$  is the lowest transverse acoustic branch, can be attributed only to the interaction matrix elements, because the differences between the two TA branches are minimal<sup>[8]</sup>. Besides, in the (0,0,1) direction the transition rate for  $\text{LA} \rightarrow \text{TA} + \text{TA}$  is one order of magnitude greater than that for  $\text{LA} \rightarrow \text{LA} + \text{TA}$ , to the contrary of Orbach and Vredevoe's assumption<sup>[3]</sup>. The ratio between the two decay modes becomes smaller in the other two principal directions.

In conclusion, a realistic calculation of the lifetime of LA phonons in  $\text{CaF}_2$  with  $h\nu \gg K_B T$  and 2.5 THz  $< \nu < 5.5$  THz confirms the  $\nu^5$ -dependence and suggests that a more careful interpretation of the raw experimental data is needed.

## REFERENCES:

- [1] For reviews, see W. Eisenmenger, in Physical Acoustics, edited by W.P. Mason and R. Thurston (Academic, New York, 1976), Vol. 12; W.E. Bron, Rep. Prog. Phys. 43, 303 (1980).
- [2] W.E. Bron, Phys. Rev. B 21, 2627 (1980).
- [3] R. Orbach and L.A. Vredevoe, Physics 1, 19 (1964).
- [4] P.G. Klemens, J. Appl. Phys. 38, 4573 (1967).
- [5] P.F. Tua, Ph.D. Thesis, Indiana University (unpublished).
- [6] L. Landau and G. Rumer, Phys. Zeit. Sowjetunion 11, 18 (1937).
- [7] M.P. Tosi, Solid State Physics 16, i (1964).
- [8] M.M. Elcombe and A.W. Pryor, J. Phys. C 3, 492 (1970).
- [9] D.R. Huffman and M.H. Norwood, Phys. Rev. 117, 709 (1960).
- [10] S. Alterovitz and D. Gerlich, Phys. Rev. 184, 999 (1969).
- [11] G. Nicklasson, Phys. Kondens. Mater. 14, 138 (1972).



## PHONON DAMPING IN CRYSTALLINE AND AMORPHOUS SOLIDS AT HYPERSONIC FREQUENCIES

R. Vacher and J. Pelous

*Laboratoire de Spectrométrie Rayleigh Brillouin (ERA 460), Université des Sciences et Techniques du Languedoc, Place E. Bataillon, 34060 Montpellier Cedex, France*

**Abstract.**— We present new Brillouin scattering measurements, for temperature ranging from 1 K to room temperature in a broad range of insulating solids (crystalline and amorphous solids). We analyse the temperature dependence of the attenuation of longitudinal phonons (frequency higher than 15 GHz) on the basis of the physical processes responsible for the phonon damping.

Measurements of acoustic attenuation in solids for frequencies higher than 10 GHz are scarce, because the large attenuation at these frequencies makes the ultrasonic experiments difficult, excepted at low temperatures. Brillouin scattering, which is the appropriate tool for such measurements, has been used in a broad range of insulating solids for temperatures ranging from 1 K to 300 K. We have studied ionic and molecular crystals, inorganic glasses and amorphous polymers. Our purpose is to bring out the laws for the temperature variation of the damping, to compare them with those observed at lower frequencies, and to analyse these results on the basis of the theoretical models describing the physical processes responsible for the attenuation.

(i) *Ionic crystals.* In such materials, the acoustic damping  $\alpha$  is known to originate from anharmonic phonon-phonon interaction. Sodium Chloride is used here as an example. In this crystal, previous ultrasonic measurements<sup>1</sup> have demonstrated the existence of two well-defined limiting regimes. At low temperatures (below 20 K) the condition  $\omega\tau \gg 1$  was fulfilled ( $\omega$  is the frequency of the acoustic wave and  $\tau$  the lifetime of thermal phonons). The experiment gave  $\alpha \sim T^4$  in agreement with the theory in the Landau-Rumer regime.<sup>2</sup> At higher temperatures, the Akhieser regime ( $\omega\tau \ll 1$ ) was reached: the ultrasonic attenuation  $\alpha$  was then found proportional to  $T^0$  which also agrees with theory. In contrast, Brillouin experiments around 30 GHz indicates  $\alpha \sim T^n$ , with  $n \approx 2.5$  below 60 K. At higher temperatures, the  $T^0$  law is not observed. A satisfying explanation of this surprising behaviour can be found extending the current theories of the attenuation due to phonon-phonon interactions, to the unusual temperature-frequency regime reached in our experiments.<sup>3</sup>

(ii) *Molecular crystals.* Our experiments in succinonitrile<sup>4</sup> and  $\alpha$ -sulfur<sup>5</sup> have demonstrated that a dispersion and attenuation of elastic waves can be observed by Brillouin scattering in molecular crystals. Such experiments at hypersonic frequencies show that relaxation processes with characteristic times of the order of  $10^{-11}$  s.

are present in these crystals, in addition to anharmonic phonon-phonon processes. For more details on the molecular relaxation observed in  $\alpha$ -sulfur, the reader is referred to the paper presented separately at the same Conference.<sup>6</sup>

(iii) *Inorganic glasses.* Above 1 K, two striking features are observed in most of the inorganic glasses. For temperatures around 1 K, the ultrasonic attenuation is proportional to  $T^3$  (frequencies lower than 1 GHz). In this temperature range the dominant process is the relaxational absorption via phonon-assisted tunnelling. At higher temperatures, a - more or less pronounced - absorption peak is often observed, which is assigned to thermally activated relaxation processes. Such a behaviour has been observed in glasses of very different chemical composition as, for instance, vitreous  $\text{SiO}_2$  and  $\text{LaSF}_7$ , a metallic oxide glass, for frequencies of about 100 MHz.<sup>7</sup> Our Brillouin scattering experiments in  $\text{LaSF}_7$ , plotted in Fig.1, exhibit a completely different behaviour (the frequency is about 40 GHz) :  $\alpha$  is found nearly proportional to  $T$  in the whole temperature range studied.

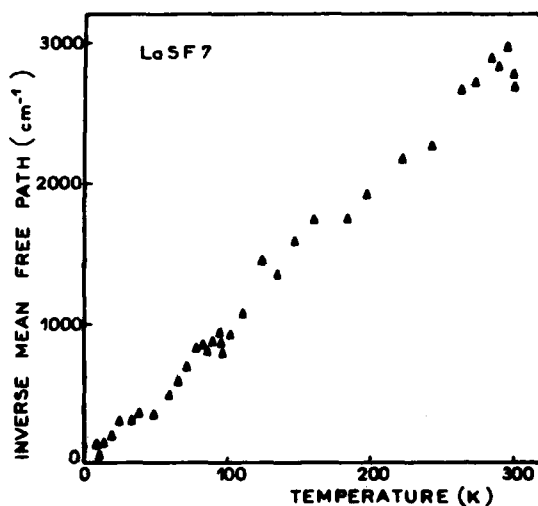


Fig. 1 - Hypersonic attenuation of longitudinal waves (42 GHz) in metallic oxide glass  $\text{LaSF}_7$ .

In vitreous  $\text{SiO}_2$ , we have already shown<sup>8</sup> that the relaxation process which accounts for all of the ultrasonic attenuation can only explain one part of the hypersonic values. Phonon-phonon interactions have been suggested to explain this excess. A similar explanation can be proposed for  $\text{LaSF}_7$  results.

(iv) *Amorphous polymers.* At ultrasonic frequencies, the peak due to thermally activated relaxations is also observed in polymers. However, at low temperatures,  $\alpha$  appears here proportional to  $\omega T$ . Our results in polystyrene (Fig.2 - the frequency is about 18 GHz) exhibit a  $T$ -dependence in a large temperature range, and agree approximately with an  $\omega T$  law where compared to the ultrasonic values below 10 K. The best candidate for explaining a  $\omega T$  law is a distribution of thermally activated relaxation processes, with a nearly constant density of activation energies.<sup>9</sup>

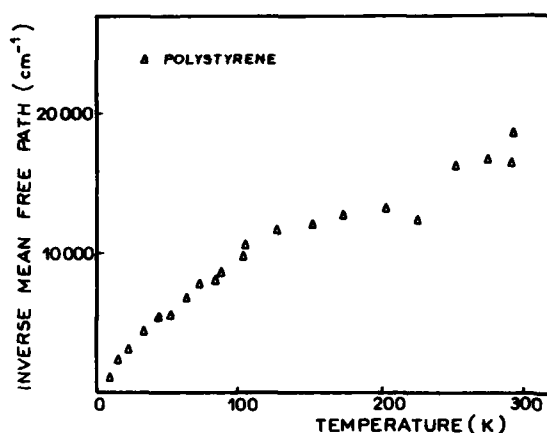


Fig. 2 - Hypersonic attenuation of longitudinal waves (18 GHz) in amorphous polystyrene.

However, as for inorganic glasses, the hypersonic results cannot be described as a whole on the basis of the ultrasonic values of the relaxation parameters.

The above results show that, for all of the insulating solids studied, the temperature dependence of acoustic damping is very different for ultrasonic and hypersonic frequencies. In amorphous materials, the thermally activated relaxations appear to be insufficient for explaining the hypersonic results above 20 K. Phonon-phonon interactions seem to contribute appreciable to the acoustic damping.

- 1 L.G. Merkulov, R.V. Kovalenok and E.V. Konovodchenko, *Sov. Phys. Solid State* **13** (1971) 968.
- 2 H.J. Maris in "Physical Acoustics" Vol. 8, W.P. Mason, Ed. (Academic, N.Y. 1974) p. 279.
- 3 J.P. Bonnet, M. Boissier, R. Vacher, (to be published).
- 4 H. Fontaine, R. Fourret, L. Boyer and R. Vacher, *J. Physique*, **33** (1972) 1115.
- 5 R. Vacher, J. Sapriel and M. Boissier, *J. Appl. Phys.* **45** (1974) 2855.
- 6 M. Boissier, R. Vacher and B. Perrin, this conference.
- 7 A. Raychaudhuri, private communication.
- 8 R. Vacher, J. Pelous, F. Plicque and A. Zarembovitch, *J. Non-Cryst. Solids*, to be published.
- 9 J.Y. Duquesne and G. Bellessa, *J. Physique (France)*, to be published.

## HARMONIC AND ANHARMONIC PROPERTIES OF SILICON

K.H. Wanser and R.F. Wallis

*Department of Physics, University of California, Irvine, California 92717, U.S.A.*

**Abstract.**— Silicon has interesting harmonic and anharmonic properties such as the low-lying transverse acoustic modes at the X and L points of the Brillouin zone, negative Gruneisen parameters, negative thermal expansion and anomalous acoustic attenuation. In an attempt to understand these properties, we have developed a lattice dynamical model for silicon employing long-range, non-local, dipole-dipole interactions. Several interesting features of this interaction are found and discussed. We present analytic expressions for the Gruneisen parameters that explain how the negative Gruneisen parameters arise. Application of this model to the calculation of the thermal expansion of silicon is made.

It is well known that comparatively long range interactions are necessary to explain the elastic constants as well as the low-lying TA[100] and [111] modes in silicon. Several models have been developed to explain this behavior. Attempts <sup>1,2</sup> to compute anharmonic properties have utilized first neighbor anharmonicity or first and second neighbor anharmonicity, one of the authors<sup>2</sup> concluding that this was sufficient to explain the mode Gruneisen parameters and thermal expansion coefficient. That this is not the case can be seen from the fact that the Gruneisen parameters for these models are in major disagreement with experiment for several modes.

The model we use employs first thru fourth neighbor central potentials, nearest neighbor angle bending and displacement induced non-local dipoles. An interesting feature of the non-local dipole interaction is that it does not affect the elastic constants or the Raman frequency. This is in contrast to the local quadrupoles used by Lax.<sup>3</sup>

A ten independent parameter preliminary fit of our model to the experimental data is shown in Fig. 1. The major feature of this dipole model is the dramatic lowering of the TA modes at the X point.

Proceeding to the anharmonic properties, we note that silicon has negative thermal expansion and thus negative Gruneisen parameters for some modes. The volume thermal expansion coefficient is given to

lowest order in the anharmonicity by

$$\alpha = \frac{1}{BV_0} \sum_{\vec{k}j} \gamma(\vec{k}j) C_E(\omega(\vec{k}j)) \quad (1)$$

Here  $B$  is the bulk modulus,  $V_0$  the volume of the bare crystal,  $\omega(\vec{k}j)$  the bare harmonic frequency,  $C_E(\omega)$  is the Einstein specific heat function and  $\gamma(\vec{k}j)$  the mode Gruneisen parameter.

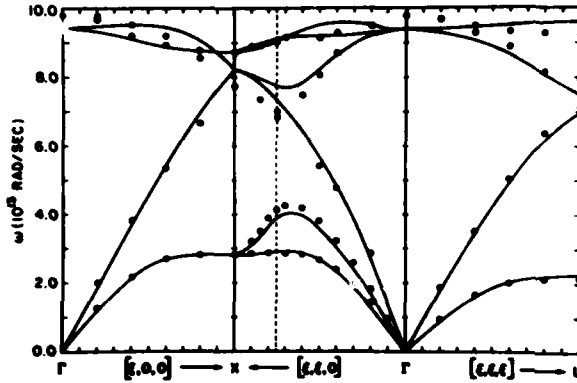


Fig. 1. Preliminary fit of dipole model to experimental data for silicon.

To illustrate the origin of the negative mode gammas, consider the analytic expressions we have found at the X point.

$$\gamma_{TAX} = \frac{-1}{3M\omega_{TAX}^2} \left[ \begin{aligned} &2\phi_1''(r_0) - \frac{2\phi_1'(r_0)}{r_0} + 2r_2\phi_2''(r_2) + 6\phi_2''(r_2) \\ &- \frac{6\phi_2'(r_2)}{r_2} + \frac{32}{11}r_3\phi_3''(r_3) + \frac{34}{11}\phi_3''(r_3) \\ &- \frac{34\phi_3'(r_3)}{11r_3} + 6\sigma^{(1)} \\ &- \frac{16\pi}{\epsilon_a^3} (16.28143)(p_1 - p_2)(p_1^{(1)} - p_2^{(1)}) \end{aligned} \right] \quad (2a)$$

$$\gamma_{TOX} = \frac{-1}{3M\omega_{TOX}^2} \left[ \begin{aligned} &\frac{4r_0\phi_1''(r_0)}{3} + \frac{2}{3}\phi_1''(r_0) - \frac{2\phi_1'(r_0)}{3r_0} + 2r_2\phi_2''(r_2) \\ &+ 6\phi_2''(r_2) - \frac{6\phi_2'(r_2)}{r_2} + \frac{12}{11}r_3\phi_3''(r_3) \\ &+ \frac{54}{11}\phi_3''(r_3) - \frac{54\phi_3'(r_3)}{11r_3} + \frac{2\sigma^{(1)}}{3} \\ &+ \frac{16\pi}{\epsilon_a^3} (10.76338)(p_1 + p_2)(p_1^{(1)} + p_2^{(1)}) \end{aligned} \right] \quad (2b)$$

In Eqs. (2)  $a$  is the conventional cube edge,  $\epsilon$  the static dielectric constant,  $p_1$  and  $p_2$  are harmonic dipole parameters,  $p_1^{(1)}$  and  $p_2^{(1)}$  are anharmonic dipole parameters,  $\sigma^{(1)}$  is an anharmonic angle-bending parameter and  $\phi_1''(r_0)$ ,  $\phi_1'(r_0)$ ,  $\phi_1'(r_0)$  are the derivatives of the

first neighbor potential function etc. The fourth neighbor interaction does not contribute at the X point. The interesting feature of Eqs. (2) is that the nearest neighbor third derivative is not present in Eq. (2a) but is in Eq. (2b). This is the explanation for why the TAX mode has a negative mode gamma and the TOX mode does not. It is due to the fact that the diamond structure has a nearest neighbor central force instability. In fact, it is just those modes that have the instability that exhibit the negative mode gamma. This point has not been recognized in the literature previously. We emphasize again that since  $\phi_1'''(r_0)$  is of opposite sign to  $\phi_1''(r_0)$ , the cancellation of  $\phi_1'''(r_0)$  in certain modes makes the mode gamma extremely likely to be negative.

A preliminary calculation of the thermal expansion is shown in Fig. 2. In this calculation the four third order potential

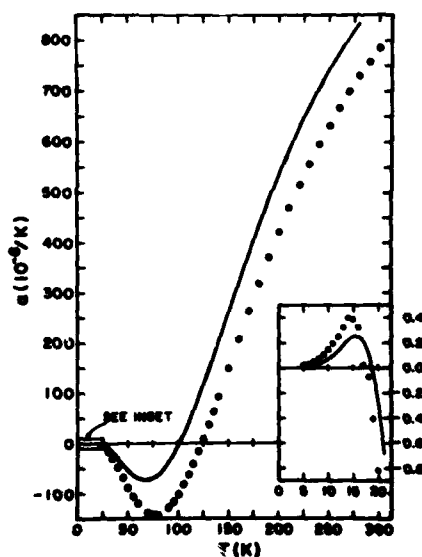


Fig. 2. Volume thermal expansion coefficient of silicon. Solid line is present calculation, circles are experimental data.

derivatives were fit to the experimental mode gammas at X, L and the elastic region. The dipole and angle-bending anharmonic parameters were fixed by theoretical considerations.<sup>4</sup>

**Acknowledgement** - Work supported in part by NASA Contract No. NSG-7472 and NSF Grant No. DMR-7809430.

#### References

1. G. Dolling and R. A. Cowley, Proc. Phys. Soc. **88**, 463 (1966).
2. H. Jex, Phys. Stat. Sol. (b) **45**, 343 (1971).
3. M. Lax, "Lattice Dynamics," Ed. by R. F. Wallis, (Pergamon, Oxford, 1965), p. 179.
4. K. E. Wanser, Ph.D. Thesis, UC Irvine, 1981 (unpublished).

## PHONON-PHONON INTERACTIONS IN MOLECULAR CRYSTALS STUDIED BY ULTRASONIC METHODS

B. Perrin and F. Michard

*Département de Recherches Physiques, Tour 22, Université P. et M. Curie,  
75230 Paris Cedex 05, France*

**Abstract.** - Internal vibrations of molecules are slightly affected by lattice effects in molecular crystals so that there are only weak interactions between internal and external phonons which give slow relaxation times in the phonon collision operator. Thus an ultrasonic relaxation may be expected in molecular crystals. In this work it is shown that this *molecular relaxation* may be taken into account in the framework of Akhiezer's theory and a relation between sound absorption and relaxation time is given. Results obtained through acousto-optic interaction on ionic-molecular crystals are also mentioned.

1. **Introduction.** - Internal vibrations of molecules are quite unaffected by lattice effects in molecular crystals so that there are only weak interactions between internal and external modes of vibrations of the molecules in these crystals. This weakness entails the existence of slow relaxation processes during the thermalization of the whole set of phonons after any perturbation of the thermal equilibrium. The times involved in these processes lying in the ultrasonic frequency range, an ultrasonic relaxation may be expected in molecular crystals. This "molecular relaxation", due to a slow transfer of energy between the internal and external degrees of freedom of molecules, has been extensively studied in molecular gases and liquids and Liebermann<sup>1</sup> was the first to suggest the extension of this phenomenon to the solid state. Since his pioneering work, some experimental studies led on organic molecular compounds have clearly shown the existence of a relaxation process which underlies a special ultrasonic behavior of molecular crystals among dielectric ones. We present in this work recent theoretical and experimental developments concerning this field.

2. **Theoretical aspect.** - The present status of the theory in this field is unsatisfying in several points. For example, Richards<sup>2</sup>' relation

given by

$$\alpha = \frac{1}{2s} \frac{C_p - C_v}{C_p} \frac{C_I}{C_v - C_I} \frac{\Omega^2 \tau}{1 + \Omega^2 \tau^2} \quad (1)$$

is used to relate the sound absorption  $\alpha$  and the relaxation time  $\tau$ ; here  $\Omega$  and  $s$  are respectively the angular frequency and the velocity of the sound beam,  $C_p$  and  $C_v$  are the specific heats at constant pressure and constant volume and  $C_I$  is the specific heat associated with the internal degrees of freedom of molecules. This expression has been derived considering specific properties of gas and liquid phases and its use in the solid state seems questionable. Moreover no mention has never been made of the fact that, although molecular crystals belong to the family of dielectric crystals, the molecular relaxation does not seem predicted by the classical theories of ultrasonic attenuation in dielectric crystals. The answer to these two points may be found by considering a solid state point of view (in contrast to Liebermann's approach). The molecular relaxation times being greater than the mean lifetime of thermal phonons, this phenomenon occurs in a hydrodynamical regime of ultrasonic propagation and may be studied with the Boltzmann equation approach. The phonon collision operator involved in this approach is usually simplified by the collision time approximation which means that all the phonons have the same status during the thermalization and which leads to the classical expression of the Akhieser loss<sup>3</sup>. This assumption obviously fails in molecular crystals for which we have to consider two phonon systems (external and internal phonons) which have only weak interactions between them. One of the author<sup>4</sup> has recently proposed a model describing the behavior of phonon-phonon interactions in molecular crystals and has shown that the ultrasonic absorption  $\alpha$  may be written  $\alpha = \alpha_A + \alpha_R$  where  $\alpha_A$  is close to the expression of the Akhieser loss and  $\alpha_R$  is a relaxation term given by

$$\alpha_R = \frac{T}{2\rho s^3} \frac{C_I}{C_v - C_I} \frac{(C_{ijkl} \beta_{kl} e_i K_j)^2}{C_v} \frac{\Omega^2 \tau}{1 + \Omega^2 \tau^2} \quad (2)$$

Here  $C_{ijkl}$  are the elastic constants,  $\beta_{kl}$  the thermal expansion tensor,  $e_i$  and  $K_j$  components of the polarization  $\vec{e}$  and normalized wave vector  $\vec{K}$  of the sound beam,  $T$  the temperature and  $\rho$  the density. For isotropic and cubic symmetries this expression may be reduced to

$$\alpha_R = \frac{1}{2s} \frac{C_p - C_v}{C_p} \frac{C_I}{C_v - C_I} \left( \frac{C_{11} + 2C_{12}}{3\rho s^2} \right) (\vec{e} \cdot \vec{K}) \frac{\Omega^2 \tau}{1 + \Omega^2 \tau^2} \quad (3)$$

which differs from Richards' expression by the existence of the



structure factor  $\left(\frac{C_{11} + 2C_{12}}{3\rho s^2}\right)$  resulting from the accounting for the properties of the solid state. Moreover for symmetries lower than cubic it is impossible to introduce in a natural way the quantity  $\left(\frac{C_p - C_v}{C_p}\right)$  in the expression of  $\alpha_R$ . Thus the Boltzmann equation approach, on the one hand, makes it possible to consider the molecular relaxation as a particular aspect of the Akhieser absorption mechanism and, on the other hand, proves that the use in the solid state of Richards' expression is indeed questionable; moreover it gives an expression of  $\alpha$  which takes into account the specific elastic properties of the solid state.

3. Experimental aspect. - Most of the ultrasonic studies on molecular compounds which have been reported up to now have been led with the classical pulse echo method. In fact, this method does not seem adapted to this problem because a careful analysis of the frequency dependence of the absorption needs to use high frequencies ( $> 100$  MHz) and moreover the attenuation is expected to be very large. On the other hand the light diffraction by elastic waves seems a suitable tool for this study whether ultrasonic waves are used (Bragg diffraction) or thermal waves (Brillouin scattering). The interest of light diffraction by elastic waves has been emphasized by an ultrasonic study<sup>5-6</sup> on the isomorphous cubic crystals  $\text{Sr}(\text{NO}_3)_2$ ,  $\text{Ba}(\text{NO}_3)_2$  and  $\text{Pb}(\text{NO}_3)_2$  (which may be termed ionic-molecular crystals) for which the ultrasonic absorption has been measured for a large range of frequency and temperature. In these compounds, a relaxation process has been identified which can be viewed as a molecular relaxation; thus this study seems to be the first experimental evidence of the molecular relaxation in ionic-molecular compounds and proves that this phenomenon is closely connected with the "molecular character" of a crystal. An other consequence of this study is that the analysis of experimental results has shown that relation (3) offers a better fit than Richards' expression for ultrasonic measurements in molecular compounds.

#### REFERENCES.

1. - L.N. Liebermann, Phys. Rev. 113, 1052 (1959)
2. - W.T. Richards, Revs. Modern Phys. 11, 36 (1939)
3. - A. Akhieser, J. Phys. (USSR) 1, 277 (1939)
4. - B. Perrin, to be published
5. - F. Michard and B. Perrin, Phonon Scattering in Condensed Matter, edited by H.J. Maris (Plenum Publishing Corporation, 1980)p. 141
6. - F. Michard, to be published

## TEMPERATURE DEPENDENCE OF PHONON-PHONON INTERACTION IN SILICON

M.A. Breazeale and J. Philip

*Department of Physics, The University of Tennessee, Knoxville, TN 37916, U.S.A.*

**Abstract.**- The generation of a second harmonic of an initially sinusoidal ultrasonic wave can be considered as collinear interaction between two identical phonons to produce the sum frequency phonon. This phenomenon has been studied in considerable detail, and the studies have led to a technique for measuring harmonic amplitudes and calculating anharmonic coupling coefficients in terms of second- and third-order elastic constants. Measurements have been made on silicon, and have resulted for the first time in a complete set of third-order elastic constants at temperatures between 3°K and 300°K. Results are presented for silicon between 3°K and 300°K and a comparison is made between TOE constants calculated by using our data in the Keating theory and TOE constants evaluated by combining our data and those of Beattie and Schirber.

**Introduction.**- Nonlinear interaction of two phonons of frequency  $\omega_1$  and  $\omega_2$  produces both sum and difference frequency phonons. This interaction can be described in terms of an interaction Hamiltonian which contains coupling parameters that can be expressed in terms of higher-order elastic constants. Specialization to collinear propagation of phonons of the same frequency leads to a sum frequency which is the second harmonic. Going to the continuum limit leads to a set of equations which contain nonlinear coefficients which can be measured at ultrasonic frequencies. We have measured the nonlinearity parameters of silicon and have interpreted our results in terms of the Keating lattice dynamical model to obtain all six third-order elastic constants as a function of temperature between 3°K and 300°K. In addition, we have combined our data with that of Beattie and Schirber to obtain the TOE constants at 300°K, 77°K, and 4°K.

**Method.**- The experimental setup and the procedure to measure the absolute amplitudes of the fundamental and generated second harmonic of an initially sinusoidal ultrasonic wave propagating through a nonlinear medium has been described in earlier publications.<sup>1,2,3</sup> In the special directions along which pure mode longitudinal wave propagation is possible, the nonlinear wave equation for a cubic crystal reduces to the form<sup>4</sup>

$$\rho_0 \frac{\partial^2 u}{\partial t^2} = K_2 \frac{\partial^2 u}{\partial x^2} + (3K_2 + K_3) \frac{\partial u}{\partial x} \cdot \frac{\partial^2 u}{\partial x^2} \quad (1)$$

where  $K_2$  and  $K_3$  are linear combinations of second- and third-order elastic constants respectively given by

$$\begin{aligned}
 K_2[100] &= C_{11} ; & K_2[110] &= \frac{1}{2} (C_{11} + C_{12} + 2C_{44}) ; \\
 K_2[111] &= \frac{1}{3} (C_{11} + 2C_{12} + 4C_{44}) , & & (2)
 \end{aligned}$$

and

$$\begin{aligned}
 K_3[100] &= C_{111} ; & K_3[110] &= \frac{1}{4} (C_{111} + 3C_{112} + 12C_{166}) ; \\
 K_3[111] &= \frac{1}{9} (C_{111} + 6C_{112} + 12C_{144} + 24C_{166} + 2C_{123} + 16C_{456}) . & & (3)
 \end{aligned}$$

Considering an initially sinusoidal disturbance at  $a=0$ , the solution to Eq. (1) is of the form

$$u = A_1 \sin(ka - \omega t) - \frac{A_1^2 k^2 a}{8} \left( \frac{3K_2 + K_3}{K_2} \right) \cos 2(ka - \omega t) + \dots \quad (4)$$

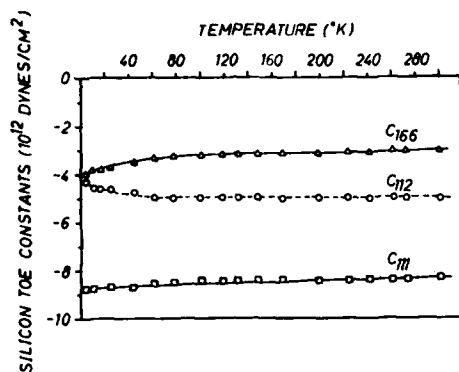
in which  $a$  is the propagation distance and  $k$  is the propagation constant. Measuring the amplitude of the fundamental wave and the amplitude of the second harmonic allows one to calculate the  $K_3$  parameters along the pure mode directions. Measurements have been made for silicon as a function of temperature between 3 and 300°K by measuring the absolute  $A_1$  and  $A_2$  values using a variable gap capacitive detector. The  $K_2$  parameters have been determined by measuring the longitudinal wave velocities along the symmetry directions.

Keating's<sup>5</sup> theory of the TOE constants of diamond-like solids is basically equivalent to the Born-Huang approach of imposing the invariance requirements on the anharmonic strain energy of the crystal. Keating has derived the expressions for the six TOE constants in terms of three anharmonic first and second neighbor force constants  $\gamma$ ,  $\delta$  and  $\epsilon$  and two harmonic force constants  $\alpha$  and  $\beta$ :

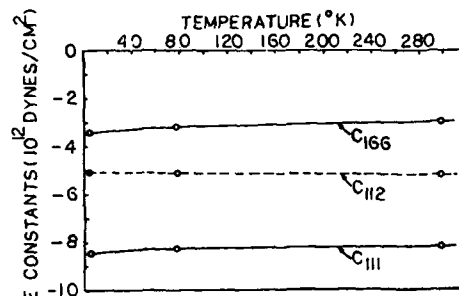
$$\left. \begin{aligned}
 C_{111} &= \gamma - \delta + 9\epsilon \\
 C_{112} &= \gamma - \delta + \epsilon \\
 C_{123} &= \gamma + 3\delta - 3\epsilon \\
 C_{144} &= \gamma(1-\epsilon)^2 + \delta(1+\epsilon)^2 + \epsilon(1+\epsilon)(3\epsilon-1) + C_{12}\epsilon^2 \\
 C_{166} &= \gamma(1-\epsilon)^2 - \delta(1+\epsilon)^2 + \epsilon(1+\epsilon)(3-\epsilon) + C_{12}\epsilon^2 \\
 C_{456} &= (1-\epsilon)^3
 \end{aligned} \right\} \quad \begin{aligned} &\text{where} \\ \epsilon &= \frac{\alpha-\beta}{\alpha+\beta} = \frac{2C_{12}}{C_{11}+C_{12}} . \end{aligned} \quad (5)$$

Combining the set of equations (3) and (5), we can write the three anharmonic force constants  $\epsilon$ ,  $\delta$  and  $\gamma$  in terms of the  $K_3$  parameters. Evaluation of  $\epsilon$ ,  $\delta$  and  $\gamma$  as a function of temperature from the temperature dependent  $K_3$  parameters leads to the determination of all the TOE constants as a function of temperature.

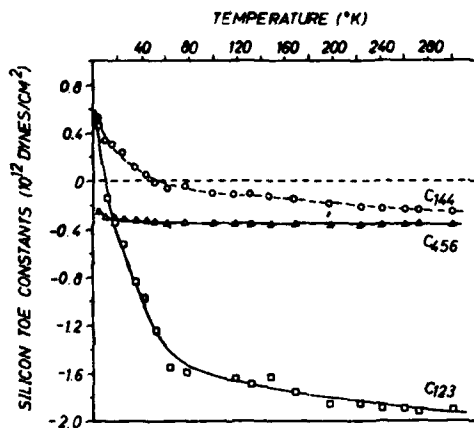
**Results and Discussion.**— The TOE constants of silicon plotted as a function of temperature are reproduced in Figs. 1(a) and 2(a). We have plotted both the calculated data points as well as the best fit curve through them to show the effect of error propagation. Beattie and Schirber<sup>6</sup> have measured the pressure derivatives of the SOE constants of silicon at 4, 77 and 300°K. Combining their results with our  $K_3$  values, we have isolated all the six TOE constants at these specific temperatures.



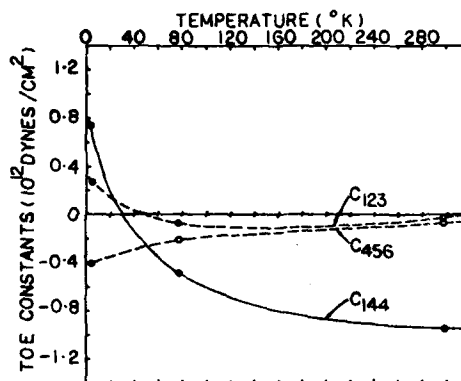
(a) Our data plus Keating theory



(b) Our data plus Beattie and Schirber data

Fig. 1. The TOE constants  $C_{111}$ ,  $C_{112}$ , and  $C_{166}$  of silicon plotted as a function of temperature.

(a) Our data plus Keating theory



(b) Our data plus Beattie and Schirber data

Fig. 2. The TOE constants  $C_{123}$ ,  $C_{144}$ , and  $C_{456}$  of silicon plotted as a function of temperature.

The calculated points and the curves joining them are given in Figs. 1(b) and 2(b). A comparison between 1(a) and 1(b) and between 2(a) and 2(b) shows the extent to which the Keating model and experimental results agree for silicon. The fact that we can measure three quantities and that the Keating model involves only three anharmonic force constants has made this approach possible. The Grüneisen parameters of silicon evaluated as a function of temperature using our TOE constant data are in better agreement with experimental curves than those reported by earlier workers who treated TOE constants as temperature independent.

**Acknowledgment.**— Research supported by the Office of Naval Research.

- References.**— 1. W. B. Gauster and M. A. Breazeale, *Phys. Rev.* **168**, 655 (1968).  
 2. J. A. Bains, Jr., and M. A. Breazeale, *Phys. Rev.* **813**, 3623 (1976).  
 3. Jacob Philip and M. A. Breazeale, *J. Appl. Phys.* **52**, 3383 (1981).  
 4. M. A. Breazeale and J. Ford, *J. Appl. Phys.* **36**, 3486 (1965).  
 5. P. M. Keating, *Phys. Rev.* **149**, 674 (1966).  
 6. A. G. Beattie and J. E. Schirber, *Phys. Rev.* **B1**, 1548 (1970).

## NON-LINEAR DYNAMICAL EXCITATIONS IN SOLIDS

A.A. Maradudin\*, A.J. Martin, H. Bilz and R.F. Wallis\*

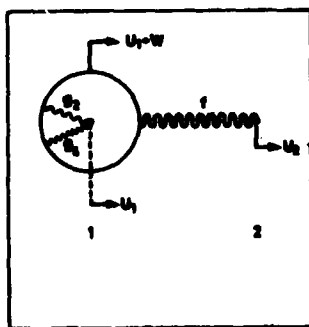
*Max-Planck-Institut für Festkörperforschung, Heisenbergstrasse 1, 7000 Stuttgart 80, F.R.G.*

**Abstract.**— Vibrational excitations can exist in non-linear systems which have no counterpart in the corresponding linear systems. In this paper we investigate such excitations in systems where the non-linearity is of an on-site character. In particular, we analyze the existence conditions for localized (and delocalized) excitations, and their interaction with external fields.

In this paper we discuss the properties of non-linear periodic lattice waves in models of perfect and imperfect crystals. Our model Hamiltonians contain a fourth-order on-site electron-ion potential<sup>†</sup> reminiscent of  $\phi^4$ -models. This approach is motivated by the success of the self-consistent phonon approximation (SPA) for the investigations of ferroelectric-type phase transitions in terms of such models (refer to Bussmann *et al.*, this Conference).

## 2. General Solution to the Dynamical Monomer Problem

The monomer (Fig. 1) consists of one anion and one cation. If the center of mass motion is factored out, the system is described by two coupled variables,



**Fig. 1** The monomer unit.  $g_4$  is the fourth order coupling constant.

which may be chosen as the displacement,  $u$ , of the cation relative to the anion core and the displacement,  $w$ , of the anion shell relative to its core. The oscillation frequency of the monomer is displayed in Fig. 2 as a function of  $w_0^2$ , where  $w_0$  is the maximum displacement from the origin. The range  $w_0^2 > w_{crit}^2$  belongs to anharmonic oscillations which traverse the origin  $w=0$  (the solution at  $w_0^2=0.4$  is the only harmonic one). The range  $w_0^2 < w_{crit}^2$

describes oscillations which are localized in one or another of two equivalent potential wells. The minimum squared displacement from the origin increases from zero to the left of  $w_{crit}^2$  until it coincides with  $w_0^2$  at  $-g_2/g_4$  (notice that the frequency does not go to zero at this point).

\*Permanent address : Department of Physics, University of California, Irvine, CA 92717, U.S.A.

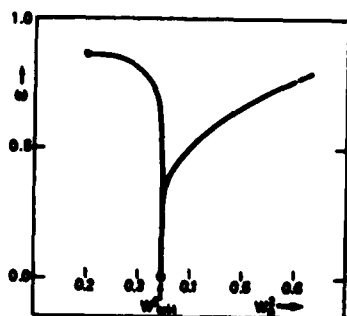


Fig. 2 Frequency vs. squared maximum amplitude.  $\beta/\alpha=0.2$ ,  $g_2/g_4 = -0.2$ ,  $\omega$  is in units of  $(2/3) \times (E/\mu)^{1/2}$ , where  $\mu$  is the reduced mass, and  $\alpha=3g_4>0$ ,  $\beta=f+g_2$ ,  $f>0$ .

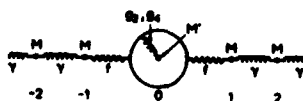


Fig. 3 A nonlinearly polarizable impurity in a monatomic linear chain.

### 3. A Nonlinearly Polarizable Impurity in a Linear Chain

We now turn to the consideration of a problem in which a nonlinearly polarizable atom is present as a substitutional impurity in a monatomic linear chain (Fig. 3). We seek a solution for the displacement field in the chain that decays exponentially with increasing distance from the impurity site, i.e. a localized mode.

We can obtain an exact solution to the equations of motion of the chain with the Ansatz

$$w_0 = A \cos \omega t \quad (3.2a)$$

$$u_0 = B^{(1)} \cos \omega t + B^{(3)} \cos 3\omega t \quad (3.2b)$$

$$u_n = (-1)^n \left[ C^{(1)} e^{-n\lambda} \cos \omega t + C^{(3)} e^{-n\mu} \cos 3\omega t \right] \quad n \geq 1, \quad (3.2c)$$

where  $w_0$  is the relative shell-core displacement of the impurity atom, and  $u_n$  is the displacement of the  $n^{\text{th}}$  core, when we assume in addition that  $u_{-n} = u_n$ . In Eq. (3.2c) the quantities  $\lambda$  and  $\mu$  are the real quantities given by  $\lambda = 2 \cosh^{-1}(\omega/\omega_L)$ ,  $\mu = 2 \cosh^{-1}(3\omega/\omega_L)$ , where  $\omega_L = (4\gamma/M)^{1/2}$  is the maximum normal mode frequency of the unperturbed chain. The frequency of the localized mode must therefore be larger than  $\omega_L$  for the solution (3.2) to exist. The equation determining  $\omega$  is

$$\frac{9M'\omega^2}{2f} \frac{9M\omega^2 - f - \gamma(1+e^{-\mu})}{9M\omega^2 - \gamma(1+e^{-\mu})} = 1. \quad (3.3)$$

With  $\omega$  determined from this equation the amplitude  $A$  is found from the relation

$$A^2 = \frac{4g_2}{3g_4} \left[ -1 + \frac{2f/g_2}{(2f/M'\omega^2) - \gamma} \right] > 0, \quad (3.4)$$

where  $X = [M\omega^2 - f - \gamma(1 + e^{-\lambda})] / [M\omega^2 - \gamma(1 + e^{-\lambda})]$ .

It should be pointed out that for  $g_2 < 0$ , Eqs. (3.3)-(3.4) have a solution even if  $M' = M$  and  $f = \gamma$  provided that  $|g_2|/\gamma > 2.8$ . In this case the localized mode has no counterpart in the harmonic approximation.

#### 4. Response to External Electric Fields

If the periodon solutions to the nonlinear equation of motion of a crystal containing atoms or ions possessing nonlinear polarizabilities are to be observed experimentally, it is likely to be through features they contribute to the functions characterizing the response of such crystals to external probes. We have therefore begun a study of the periodon-type solutions of the equations of motion of a monatomic linear crystal of this type (Fig. 4), in the presence of an external spatially and temporally varying electric field.

We consider an electric field given by  $E_n(t) = E_0 \cos(n\phi - \omega t)$ . In this case the equations of motion of the crystal have the exact solution

$$w_n(t) = A \cos(n\phi - \omega t) \quad (4.1)$$

$$u_n(t) = B_{(1)} \cos(n\phi - \omega t) + B_{(3)} \cos 3(n\phi - \omega t) \quad (4.2)$$



provided that the frequency and wave vector are related through  $\omega^2 = 4(f + f')/9M \sin^2 \frac{3}{2}\phi$ . We then have that the amplitude  $A$  is obtained in terms of the electric field amplitude  $E_0$  from the equation

Fig. 4 A monatomic nonlinear chain.

$$\frac{4f A \sin^2 \frac{1}{2}\phi}{Z E_0 - g_2 A - \frac{3}{4} g_4 A^3} = \frac{M\omega^2 - 4(f + f') \sin^2 \frac{1}{2}\phi}{M\omega^2 - 4f' \sin^2 \frac{1}{2}\phi} \quad (4.3)$$

while

$$B_{(1)} = \frac{Z E_0 - g_2 A - \frac{3}{4} g_4 A^3}{M\omega^2 - 4f' \sin^2 \frac{1}{2}\phi} \quad B_{(3)} = - \frac{g_4 A^3}{16f \sin^2 \frac{3}{2}\phi} \quad (4.4)$$

where  $Z$  is the charge on each core and  $-Z$  is the charge on each shell. Generalizations of this solution can be obtained by adding higher odd harmonics to the right hand sides of Eqs. (4.1). However, in that case a solution in finite terms, like that given by Eqs. (4.1)-(4.3), is no longer possible.

+ refer to Büttner and Bilz, (this Conference)

## TEMPERATURE DEPENDENCE OF MULTIPHONON ABSORPTION IN HIGHLY TRANSPARENT CUBIC ZIRCONIA

B. Bendow<sup>(1)</sup>, H.G. Lipson, R.N. Brown, R.C. Marshall, D. Billard\* and S.S. Mitra\*\*<sup>(2)</sup>

*Solid State Sciences Division, Rome Air Development Center, Hanscom AFB, MA 01731, U.S.A.*

*\*Centre de Recherche sur la Physique des Hautes Températures, C.N.R.S., 45045 Orléans Cedex, France*

*\*\*Dept. of Electrical Engineering, University of Rhode Island, Kingston, RI 02881, U.S.A.*

**Abstract** - We investigate multiphonon absorption in the three to five phonon regime of yttria-stabilized cubic zirconia, over an extended range of temperatures. The absorption vs. frequency curves at fixed temperature are found to display a nearly exponential decrease typical of multiphonon absorption in other ionic crystals. A theoretical model for multiphonon absorption is utilized to fit the data over the full range of frequency and temperature investigated, and good agreement is obtained between theory and experiment. A strong suppression of the temperature variation of absorption is observed at high frequency, which we attribute to the temperature dependence of the phonon spectrum itself.

1. Introduction - Cubic zirconia is an optical material of considerable interest because of its unique properties: namely, it is very hard, has a very high melting temperature, resists chemical attack and is an excellent insulator. It is readily doped with various rare-earth and transition-metal ions to provide a wide range of potential laser-host materials. The crystals utilized for this study were produced at RADC employing a relatively new process called "skull melting", in which the melt is contained within a solid "skull" of identical composition<sup>1</sup>. This procedure minimizes difficulties with reaction and contamination encountered in conventional crucible-type growth. Heating is accomplished by coupling RF energy to zirconium metal placed into the charge. Crystals are finally obtained by preferential freezing of the melt when the crucible is slowly lowered through the coil. The yttria-stabilized crystals obtained in this way possess hardness ~ 1370 Knoop, density ~ 5.9 gm/cm<sup>3</sup>, thermal conductivity ~ .018 W/cm/°C and visible refractive index ~ 2.15-2.18. The yttria concentration typically varies from around twelve to twenty-five weight percent; the sample utilized for the present study contained twenty weight percent yttria.

2. Experimental - The absorption coefficient ( $\alpha$ ) in the vicinity of the IR edge was deduced from transmission data, obtained with a Fourier spectrophotometer which was appropriately modified for both low temperature<sup>2</sup> and high temperature<sup>3</sup>

(1) Present address: The BDM Corp, 1801 Randolph Rd, S.E., Albuquerque, NM 87106.

(2) Research supported by Rome Air Dev.Center (AFSC) under contract no.F19628-77-C-0109.



measurements. Results for  $\alpha$  vs frequency at several temperatures between 80 and 1320K are displayed in Fig. 1. Note that the absorption vs. frequency curves at fixed temperature display a nearly exponential decrease typical of multiphonon absorption in other ionic crystals<sup>4</sup>. Moreover, the spectra reveal only weak

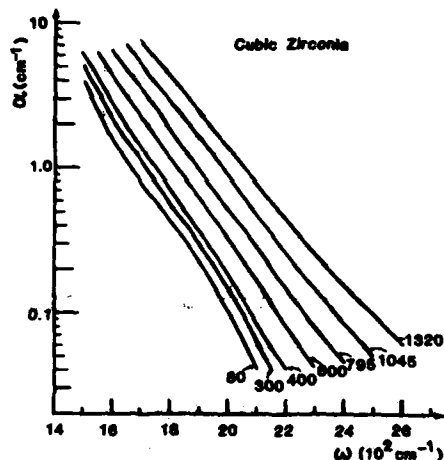


Fig. 1. IR edge absorption coefficient  $\alpha$  of cubic zirconia vs frequency  $\omega$  at several temperatures ( $^{\circ}\text{K}$ ).

structural features, which progressively disappear with increasing temperature.

3. Discussion - For ionic materials, one may model the temperature dependence of the IR edge absorption as<sup>4</sup>

$$\alpha = \alpha_0 \frac{(n(\omega_0) + 1)^{\omega/\omega_0}}{n(\omega) + 1} \exp(-A\omega/\omega_0)$$

where  $n$  is the Bose-Einstein function and  $\omega_0$  is a temperature dependent average optical phonon frequency. For the present purposes we only account for linear variations of  $\omega_0$  vs  $T$ , i.e., we take  $\omega_0 = \omega_{00}(1 - \gamma T)$ . Variation of parameters to obtain a best fit to the data over the full range of available temperatures and frequencies leads to the results indicated in Fig. 2, corresponding to the choices

$$\alpha_0 = 1.38 \times 10^5, \quad \omega_{00} = 550 \text{ cm}^{-1}, \quad A = 3.85, \quad \gamma = 2.0 \times 10^{-5}/^{\circ}\text{K}$$

The good agreement obtained between theory and experiment corroborates the interpretation of the observed spectra as multiphonon absorption. The derived average frequency  $\omega_{00} = 550 \text{ cm}^{-1}$  is consistent with fundamental IR and Raman data, and implies that the present absorption measurements span the three to five phonon regime.

A noteworthy feature of the above results is the relatively strong suppression of the  $T$ -dependence of absorption at high temperatures. This effect, which is well known from previous measurements on alkali-halides, is attributable to the strong  $T$ -dependence of the fundamental phonon spectrum itself in ionic crystals.

Further confidence in this interpretation is provided by the close proximity of the value deduced here for  $\gamma$ , to those implied by Raman scattering studies<sup>5</sup> of the  $T$ -dependence of phonons in monoclinic  $\text{ZrO}_2$ .

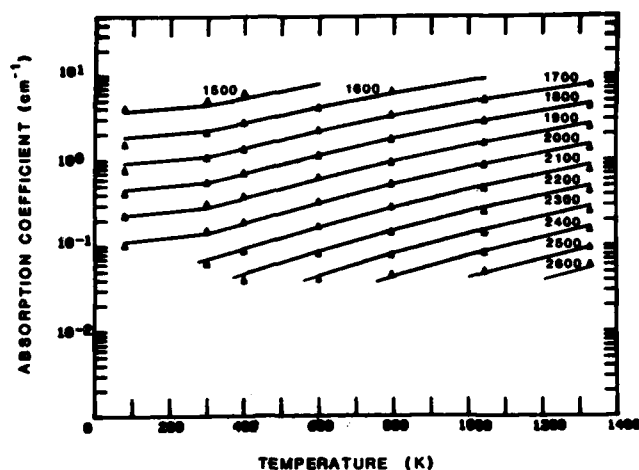


Fig. 2. Absorption coefficient vs temperature for representative frequencies (cm<sup>-1</sup>). Solid lines are theoretical calculations and triangles are experimental values.

**Acknowledgement**—The assistance of F. Gervais of CNRS with the present studies is gratefully acknowledged.

#### References

1. See, e.g., D. Michel et al, J. Cryst. Growth 43, 546 (1978).
2. B. Bendow et al, in "Basic Optical Props of Materials", NBS Spec. Pub #574 (USGPO, Wash., DC, 1980).
3. D. Billard et al, Revue de Physique Applique (1981, in press).
4. B. Bendow, Solid State Phys. 33, 249 (1978).
5. M. Ishigame and T. Sakurai, J. Amer. Cer. Soc. 60, 367 (1977).

# ANHARMONIC CONTRIBUTIONS TO THE THERMAL DIFFUSE X-RAY SCATTERING INTENSITY FROM SINGLE CRYSTALLINE SODIUM

G. Fritsch\*, W. Dietz, R. Häring and E. Lüscher

Physik-Department, Technische Universität München, D-8046 Garching, F.R.G.

\*ZWE Physik, Hochschule der Bundeswehr München, D-8014 Neubiberg, F.R.G.

**Abstract.** - We report on measurements of the thermal diffuse X-ray scattering from single crystalline Na. Data were taken with the momentum transfer being aligned along the (100), (110) and (111) directions as a function of temperature. They are discussed in terms of one, two and higher multi-phonon contributions. In addition, a part asymmetric with respect to a reciprocal lattice vector is determined and analyzed.

1. **Introduction.** - The X-ray intensity scattered diffusely from a metal single crystal is the sum of one, two and higher order phonon processes.<sup>1)</sup> At temperatures  $T > \theta_D$  interference terms caused by anharmonic interactions will also contribute.<sup>1)</sup> This picture may be complicated if deformations of the ion cores<sup>2)</sup> or elastic defect scattering<sup>3)</sup> exists. In this communication we would like to discuss our results on Na and compare them with other work in this field<sup>4-6)</sup>.

2. **Data Analysis.** - The experimental set-up used was a modified version of the one described elsewhere.<sup>6)</sup> After subtracting from the measured cross section  $(d\sigma/d\Omega)_{\text{eff}}$  the calculated one-phonon part<sup>6)</sup>, the multi-phonon contribution higher than of order two<sup>4)</sup>  $(d\sigma/d\Omega)_{\text{mp}}$  and the Compton cross section, we arrive at  $(d\sigma/d\Omega)_d$ . The latter is interpreted as a sum of the two-phonon and an asymmetric interference contribution.  $[(d\sigma/d\Omega)_{\text{mp}} = f^2 \exp(-2W) \{ \exp(2W) - 1 - 2W - 2W^2 \}]$ , where  $\exp(-2W)$  is the Debye-Waller factor<sup>4)</sup> and  $f^2$  the ionic scattering factor.]

In the main crystallographic directions the two phonon term can be written as<sup>1)</sup>:

$$(d\sigma/d\Omega)_2 = \alpha^4 \exp[-2W(\alpha)] A(\vec{q}/q) \cdot f^2(\alpha) ,$$

where  $A(\vec{q}/q)$  is symmetric with respect to the reciprocal lattice vector  $\vec{q}$ .  $\alpha = \alpha_B \pm q$ . Furthermore, we assume that only the lowest order interference term<sup>1)</sup> contributes:

$$(d\sigma/d\Omega)_{\text{anh } 1,2}^s = \alpha^3 \exp[-2W(\alpha)] \cdot B(\vec{q}/q) \cdot f^2(\alpha)$$

with  $B(\vec{q}/q)$  asymmetric with respect to  $\alpha_B$ . There is an additional symmetric term  $(d\sigma/d\Omega)_{\text{anh } 1,2}^s$  which has the same  $\alpha$ - and  $T$ -dependences<sup>1)</sup> as does  $(d\sigma/d\Omega)_2$ . Using data above and below  $\alpha_B$  the quantities  $(d\sigma/d\Omega)_2 + (d\sigma/d\Omega)_{\text{anh } 1,2}^s$  as well as  $(d\sigma/d\Omega)_{\text{anh } 1,2}^s$  may be determined. The results are given in Figs 1 and 2.

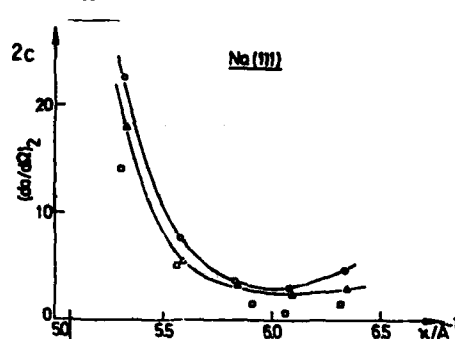
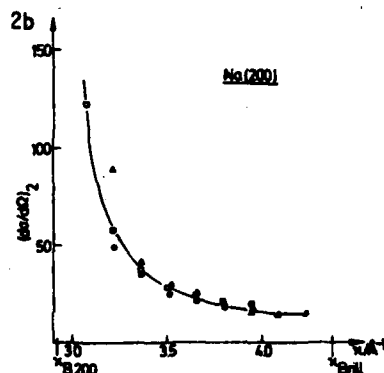
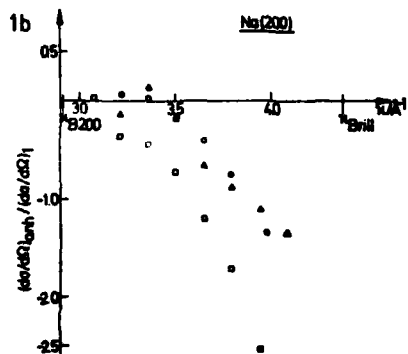
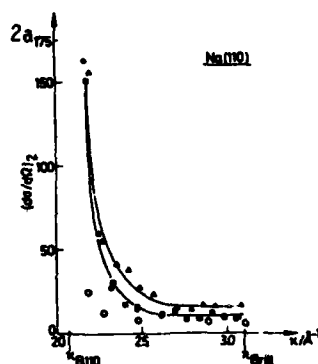
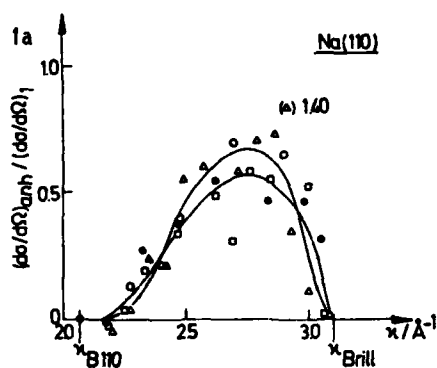


Fig.1 Results for the asymmetric anharmonic contributions  $(d\sigma/d\sigma)_{anh}^a$ .  
 a)  $\circ$ : 30°C;  $\square$ : 40°C;  $\Delta$ : 95°C and  
 $\circ$ : see ref.6 : 30°C  
 b) crystal 1:  $\square$ : 63.6°C; crystal 2:  
 $\circ$ : 52.6°C;  $\Delta$ : 69.8°C.

The lines are only guides to the eye.

Fig.2 Results for the symmetric contribution  $(d\sigma/d\sigma)_2$ .  
 a)  $\circ$ : 30°C;  $\square$ : 40°C;  $\Delta$ : 95°C and  
 $\circ$ : direct calculation 30°C  
 b) crystal 1:  $\square$ : 63.6°C; crystal 2:  
 $\circ$ : 52.6°C;  $\Delta$ : 69.8°C.  
 c)  $\Delta$ : 26.8°C;  $\circ$ : 65.0°C;  $\square$ : 94.5°C.

3. Discussion.- The asymmetric part in the (110)-direction (Fig. 1a) agrees with the one determined earlier.<sup>6)</sup> In this paper we showed that the T-dependence is the one to be expected for anharmonic interference effects between the one and two phonon process. However, the symmetric part is systematically higher than the two phonon part calculated directly (Fig. 2a). Close to the reciprocal lattice vector  $\omega_B$  the discrepancy is probably due to the approximations used in evaluating the higher order many phonon processes. In between the two  $\omega_B$  values the quantity  $(d\sigma/d\Omega)_{\text{anh}}^{S,1,2}$  might contribute.

For the (100) direction, the results for the asymmetric term (Fig. 1b) are rather puzzling, since they apparently do not show a zero at  $\omega_{\text{Brill}}$ . This fact may point towards a wrong  $\omega$ -dependence of the higher order many phonon contributions (orientational dependence). The symmetric part (Fig. 2b) is close to the (110) result, calculations of the two phonon term is in progress.

The asymmetric results (Fig. 1c) in the (111)-direction are similar to the ones in the (110)-case. However, the magnitude is much larger, increasing with temperature. The comments for the symmetric part (Fig. 2c) are the same as in the (100)-case.

In view of the temperature dependence of the asymmetric part and its  $\omega$ -dependence, we conclude that these are anharmonic contributions and deformation scattering is not present. Trinkhaus<sup>3)</sup> has shown that these defects in thermal equilibrium give a symmetric part  $\sim q^{-2}$  and an asymmetric part  $\sim q^{-1}$ . An estimation using a relative activation volume  $\Delta v/v = -0.6$  for the vacancy yields 0.16 and -0.14 respectively in the most favourable case. These values are relative to  $(d\sigma/d\Omega)_1$ .

#### Literature

- 1) H.R. Glyde, J.P. Haasen, M. Klein, Phys.Rev. B16, 3476 (1977)
- 2) W.J.L. Buyers, J.P. Pirie, T. Smith, Phys.Rev. 165, 999 (1968)
- 3) H. Trinkhaus, phys.stat.sol. b54, 209 (1972), b51, 307 (1972)
- 4) S.L. Schuster, J.W. Weymouth, Phys.Rev. B3, 4143 (1971)
- 5) H. Hervet, R. Ober, J.Phys. C 6, 3024 (1973)
- 6) W. Adlhart, H. Alt, G. Fritsch, J.Phys. F7, 2467 (1977)

## LATTICE PHONON LIFETIME CALCULATIONS

J.H. Henkel

Department of Physics and Astronomy, University of Georgia, Athens, Georgia  
30602, U.S.A.

**Abstract.**—It is shown that phonon lifetimes can be calculated using finite periodicities and discrete frequencies without going completely to the limit of infinite periodicities or quasi-continuous frequency distributions. In applying the Golden Rule equation in time-dependent perturbation theory there is a time interval over which the transition rate is very nearly independent of time and energy level differences (or periodicity). As the periodicity of the lattice increases the time interval over which the transition rate is independent of time increases and approaches infinity in the limit of infinite periodicity. Calculations are presented.

The Golden Rule of time-dependent perturbation theory relating transition rates from an initial unperturbed energy eigenstate  $E_n^{(0)}$  to one of the other energy eigenstates  $E_m^{(0)}$  induced by the perturbing Hamiltonian  $H'$  with matrix elements  $H'_{mn}$  is given by<sup>1</sup>

$$w = \frac{1}{t} \sum_m' |a_m(t)|^2 = \frac{2}{t} \sum_m' |H'_{mn}|^2 \frac{1 - \cos(\omega_{mn}t)}{\hbar^2 \omega_{mn}^2}, \quad (1)$$

where

$$\omega_{mn} = \frac{E_m^{(0)} - E_n^{(0)}}{\hbar} \quad (2)$$

and where the prime on the sum means that the term for  $m=n$  is excluded from the sum. The Golden Rule can also be written as

$$w = \frac{d}{dt} \sum_m' |a_m(t)|^2 = \frac{2}{\hbar^2} \sum_m' |H'_{mn}|^2 \frac{\sin(\omega_{mn}t)}{\omega_{mn}} \quad (3)$$

For quasi-continuous energy distributions the Golden Rule takes the form

$$w = \frac{2\pi}{\hbar} |H'_{mn}|^2 \rho(E_n^{(0)}), \quad (4)$$

where  $\rho$  is the density of states expressed as a function of  $E^{(0)}$  and where the right hand side is independent of time  $t$ .

To see how phonon lifetimes can be calculated using the Golden Rule equation without first taking the limit of quasi-continuous energy

level distributions consider the functions  $F_1(\alpha, t, L)$  and  $F_2(\alpha, t, L)$  given by

$$F_1(\alpha, t, L) = \frac{2}{L} \sum_{n=1}^L \frac{\sin \frac{2\pi}{L}(\alpha - n)t}{\frac{2\pi}{L}(\alpha - n)} \quad (5)$$

and

$$F_2(\alpha, t, L) = \frac{1}{t} \frac{2}{L} \sum_{n=1}^L \frac{1 - \cos \frac{2\pi}{L}(\alpha - n)t}{[\frac{2\pi}{L}(\alpha - n)]^2} \quad (6)$$

In the limit  $L \rightarrow \infty$  these functions are unity independent of time  $t$  provided  $0 < \alpha < L$  but not one of the integers  $1, 2, \dots, L$ . For finite  $L$  the functions are to within about 10% equal to unity independent of  $\alpha$  and  $t$  for the interval  $1 < t < L$  and for  $0 < \alpha < L$  with  $\alpha \neq 1, 2, \dots, L$ . A plot of a typical  $F_1(\alpha, t, L)$  versus  $t$  is shown in Fig. 1 while Table I lists calculated values of  $F_1(\alpha, t, 12)$ . The function  $F_1(\alpha, t, L)$  is zero

at  $t=0$ , with a slope  $\frac{dF_1(\alpha, 0, L)}{dt} = 2$ , and levels off to approximately 1 at  $t=L$ . It remains unity within small variations up to  $t=L$  independent of  $\alpha$  provided  $0 < \alpha < L$  and  $\alpha \neq 1, 2, \dots, L$ .

Two important conclusions result in examining the properties of  $F_1(\alpha, t, L)$ . One is that the value of  $F_1(\alpha, t, L)$  for  $1 < t < L$  is approximately the same as the limiting value of  $F_1(\alpha, t, \infty)$ . The other is that the convergence in  $L$  is very rapid. The main result in increasing  $L$  is the increase in time interval over which  $F_1$  is constant.

The potential energy expression of a crystal can be expanded in series form involving the atomic displacements. That part of the potential including the third degree terms in the displacements can be used as the perturbing potential utilized in the Golden Rule equation to calculate time derivatives of phonon occupation densities. When this is done the derivative takes the following form<sup>2</sup>

$$\frac{dn_\sigma}{dt} = \sum_{\sigma', \sigma''} 2 |C_{\sigma, \sigma', \sigma''}|^2 \frac{\hbar}{M \omega_\sigma \omega_{\sigma'}} \frac{\sin \Delta \omega t}{\Delta \omega} \times \quad (7)$$

$$[(n_\sigma + 1)n_{\sigma'} n_{\sigma''} - n_\sigma (n_{\sigma'} + 1)(n_{\sigma''} + 1)],$$

where

$$\Delta \omega = \omega_\sigma - \omega_{\sigma'} - \omega_{\sigma''} \quad (8)$$

This derivative can be evaluated for different times by direct summation of finite sums obtained using finite periodic boundary conditions. The above analysis of the properties of  $F_1(\alpha, t, L)$  indicates that this derivative  $\frac{dn_\sigma}{dt}$  using finite periodicity should be roughly constant over a time interval  $\epsilon < t < \frac{2\pi}{|\Delta \omega|_m}$ , where  $|\Delta \omega|_m$  is a minimum value of  $|\Delta \omega| = |\omega_\sigma - \omega_{\sigma'} - \omega_{\sigma''}|$ . The analysis also indicates that the convergence in  $L$  should be very rapid and that the constant

value obtained should be within about 10% of the value obtained in the limit of infinite periodicity.

An advantage of the use of finite periodic boundary conditions with the resulting finite sums is that the complex phase relations involving conservation of momentum and energy is automatically included in the sums.

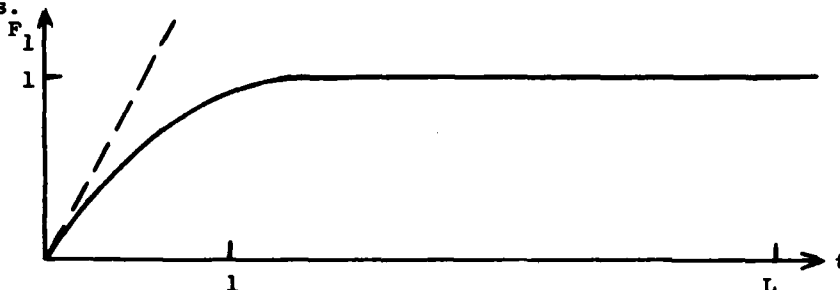


Fig. 1: Plot of typical value of  $F_1(\alpha, t, L)$  versus  $t$ . Independent of  $\alpha$  for  $0 < \alpha < L$ ,  $\alpha \neq 1, 2, \dots, L$ .

TABLE I. Calculated values of  $F_1(\alpha, t, 12)$

$t \backslash \alpha$	3.1	3.2	3.3	3.4	6.5
.4	.68	.68	.68	.69	.73
.8	.89	.90	.92	.93	1.14
1.2	.91	.92	.93	.94	1.15
1.6	1.03	1.04	1.04	1.05	.98
2.0	1.12	1.12	1.12	1.12	.90
2.4	1.08	1.08	1.07	1.07	.96
2.8	1.06	1.05	1.04	1.03	1.06
6.0	1.02	1.04	1.06	1.07	.95

#### References:

1. E. Merzbacher, Quantum Mechanics (John Wiley and Sons, Inc., New York, London, 1961), p. 470.
2. P. G. Klemens, J. Appl. Phys. 38, 4573 (1967).



## ROLE OF THERMAL EXPANSION IN THE PHONON CONDUCTIVITY OF SOLIDS

G.P. Srivastava

*Physics Department, The new University of Ulster, Coleraine, N. Ireland BT52 1SA, United Kingdom*

**Abstract.** We have studied the role of thermal expansion in the thermal conductivity of solids. By treating the Grüneisen constant as a temperature dependent semiadjustable parameter we find that the high temperature lattice thermal conductivity of Ge and Si can be explained. The fitted values of the Grüneisen constants show reasonable agreement with recent experimental and theoretical results.

The high-temperature lattice thermal conductivity of most insulators and semiconductors decreases faster than  $T^{-1}$ . Recently we<sup>1,2</sup> have concluded that consideration of three-phonon processes (both acoustic-acoustic and acoustic-optical interactions), together with mass-defect and boundary scattering, cannot explain this behaviour. Inclusion of four-phonon processes does not improve the situation<sup>3</sup>. It was suggested by Ecsedy<sup>4</sup> that thermal expansion might be helpful in this respect. In this paper we study the role of thermal expansion on the lattice thermal conductivity of Ge and Si.

The effect of thermal expansion is to make the Grüneisen constant of a material temperature dependent<sup>5,6</sup>. In our earlier work<sup>1</sup> (hereafter referred to as I) we have derived an expression for the Grüneisen constant in terms of the second- and third-order elastic constants of the material. Because of thermal expansion the elastic constants become temperature dependent. This would require calculating the Grüneisen constant at various temperatures using experimental data for elastic constants provided these were available. In view of the unavailability of elastic constants at different temperatures in our range of interest, we treat the Grüneisen constant  $\gamma$  as a temperature dependent semiadjustable parameter for the thermal conductivity calculation.

The model conductivity expression in the notation of I is

$$\kappa_m = \frac{\hbar^2 \beta^2 k_B}{3N_0 \Omega} \left[ \langle \omega^2 c^2 \tau \rangle + \frac{\langle q \omega c \tau_m \tau_N^{*-1} \rangle^2}{\langle q^2 \tau_N^{*-1} (1 - \tau_m \tau_N^{*-1}) \rangle} \right] \quad (1)$$

Here  $\beta = 1/k_B T$ ,  $\langle f \rangle = \sum_q f \bar{N}_q (\bar{N}_q + 1)$ , and  $\tau_m^{-1} = \tau_N^{*-1} + \tau_U^{-1} + \tau_R^{-1}$ ,

with  $\bar{N}_q$  as the equilibrium distribution function for phonons in mode  $q$ . Also in equation (1)  $\tau_N^*$  represents the single-mode relaxation time of a phonon in mode  $q$  due to three-phonon  $N$  processes,  $\tau_U$  is an effective relaxation time due to three phonon  $U$  processes, and  $\tau_R$  is the relaxation time due to mass defect and boundary scattering. Expressions for the relaxation times can be obtained using the first-order time dependent perturbation method. As in Refs 1 and 2 results for these are derived with the crystal Hamiltonian expressed within an isotropic continuum approximation

$$H = \sum_q \hbar c q (a_q^+ a_q + \frac{1}{2}) + \frac{1}{3} \frac{|\gamma| \hbar^2}{c \sqrt{2 \rho N_0 \Omega}} \sum_{qq'q''} \sqrt{\omega \omega' \omega''} A_q A_{q'} A_{q''} \delta_{q+q'+q'', \vec{G}} \quad (2)$$

Here  $\gamma = \gamma(T)$  is the temperature dependent anharmonic (Grüneisen) constant,  $\bar{c}$  is an average phonon speed,  $A_q = (a_{-q}^+ + a_q)$  etc. are the phonon field operators, and other symbols are the same as in I. For acoustic-optical phonon scattering we make a correction to the model presented in I: the reduction factor in the cubic anharmonic Hamiltonian is included only when dealing with interactions of the type  $ac + ac \neq op$ .

The physical parameters and boundary lengths used in our calculations are taken from I. In I a constant  $\gamma$  was adjusted to fit the low temperature lattice thermal conductivity of materials from groups IV, III-V, II-VI and I-VII. It was noticed that with a constant  $\gamma$  the isotope parameter  $A$  had to be adjusted to fit the maximum in the experimental conductivity curve. In this work we take the experimental value for  $A$  ( $2.44 \times 10^{-14}$  sec<sup>3</sup> for the Geballe and Hull's sample of Ge, and  $0.132 \times 10^{-14}$  sec<sup>3</sup> for Si) and only adjust  $\gamma(T)$  to fit the experimental conductivity curve both in low and high temperature regions. The values of  $\gamma(T)$  needed to explain the conductivity results of Si<sup>7</sup> and Ge<sup>8</sup> are listed in Table 1. It is clear that a relation  $\gamma(T) = \gamma_0 (1 + \beta T)$  with appropriate  $\gamma_0$  and  $\beta$  explains the high temperature variation of the thermal conductivity of the samples

studied here. The fitted values of  $\gamma(T)$  are in reasonable agreement with recent experimental<sup>3</sup> and theoretical<sup>6</sup> results.

In conclusion, within an isotropic continuum model for germanium and silicon we have shown that consideration of thermal expansion explains both the low and high temperature lattice thermal conductivity of these materials,

**Table 1:** Temperature dependent Grüneisen constants fitted to explain the lattice thermal conductivity of Si and Ge.

Temperature (K)	$ \gamma $ Grüneisen constant	
	Ge	Si
10	1.6	0.6
20	0.5	0.65
40	0.36	0.35
80	0.28	0.27
100	0.29	0.25
200	0.39	0.29
300	0.43	0.33
600	0.52	0.39
800	0.55	0.42
1200	-	0.45

<sup>1</sup>Srivastava, G.P., J. Phys. Chem. Solids 41, 357 (1980)

<sup>2</sup>Srivastava, G.P., Philos. Mag. 34, 795 (1976)

<sup>3</sup>Ecsedy, D.J. and Klemens, P.G., Phys. Rev. B15, 5957 (1977)

<sup>4</sup>Ecsedy, D.J., in Thermal conductivity 14 (Ed. P.G. Klemens, and T.K. Chu), Plenum Press, N.Y., 1976 p.195

<sup>5</sup>Yates, B., Thermal Expansion (Plenum Press, N.Y., 1972)

<sup>6</sup>Soma, T., J. Phys. Soc. Jpn 42, 1491 (1977)

<sup>7</sup>Holland, M.G. and Neuringer, L.J., Proc. Int. Cong. on the Phys. of Semiconductors, p.475 Exeter 1962 (The Inst. of Phys. and Phys. Soc., London 1962).

<sup>8</sup>Geballe, T.H., and Hull, G.W., Phys. Rev. 110, 773 (1958).

<sup>9</sup>Slack, G.A., and Bartram, S.P., J. Appl. Phys. 46, 89 (1975).

## TWO-PHONON BOUND STATES IN AMMONIUM CHLORIDE AT FINITE TEMPERATURES

A.A. Anikiev, B.S. Umarov, V.S. Gorelik\* and J.F. Vetelino\*\*

S. Umarov Physicotechnical institute, Dushanbe, USSR

\*P. Lebedev Physical institute, Moscow, USSR

\*\*Department of Electrical Engineering, University of Maine, Orono, Maine 04469, U.S.A.

**Abstract.**— Two-phonon density of states in  $2\psi_4$  band of ammonium chloride crystal was calculated by the method of Green's temperature functions considering anharmonic phonon-phonon interaction. Theoretically calculated temperature dependence of quasibound two-phonon state is compared to the Raman scattering experiments.

1. **Introduction.**— Along with the usual phonon shift and widening the anharmonic phonon-phonon interaction leads to the appearance of anomalous structure in crystal optical spectra. The exhibition of these peculiarities may be explained by considering the processes of resonance or bound phonon states as a particular case of their scattering on each other and decay. The detailed analysis of conditions of resonance and bound phonon states formation was carried out in work /1/ by the Green's function formalism at  $T=0$ .

Our approach is similar to the formalism used in work /1/. However, we apply the temperature Green's functions and consider the temperature effects on the optical phonon lifetime in a self-consistent manner.

2. **Results.**— The two-phonon temperature Green's function has a form /2/:

$$\hat{G}_2(x-x', \tau-\tau') = i \langle T_\tau \{ \bar{\psi}(x, \tau) \bar{\psi}(x', \tau') \bar{\psi}(x', \tau') \bar{\psi}(x, \tau) \} \rangle \quad (1)$$

Here  $\psi(x, \tau) = e^{\tau \hat{H}} \psi(x) e^{-\tau \hat{H}}$  are phonon field operators in Heisenberg's representation depending on "imaginary" time - temperature;  $\hat{H}$  is a Hamiltonian operator containing the fourth-order anharmonic term;  $T_\tau$  is a "time"-ordering operator.

In accordance with the rules of the analytical calculation of the diagrams in technique at  $T \neq 0$  we contrast one loop in Bethe-Solpeter equation with the function:  $\Pi(x-x', \tau-\tau') = i [G_2^{(0)}(x-x', \tau-\tau')]^2$ . In the momentum representation a single-phonon propagator  $G_1^{(0)}(\vec{k}, i\omega_n)$  has the following form:

$$G_1^{(0)}(\vec{k}, i\omega_n) = \frac{\omega_{\vec{k}}}{2} \left\{ [i\omega_n - \omega_{\vec{k}} + i\frac{\Gamma}{2}]^{-1} - [i\omega_n + \omega_{\vec{k}} - i\frac{\Gamma}{2}]^{-1} \right\} \quad (2)$$

where  $\omega_{\vec{k}}$  is a law of phonon dispersion, and  $\Gamma$  is a small but finite phonon width at low temperatures. The total two-phonon Green' func-

tion, obtained by summation of geometrical progression series /1/ will be written as follows:

$$G_2(\vec{k}, i\omega_n) = \Pi(\vec{k}, i\omega_n) / [1 - g_4 \Pi(\vec{k}, i\omega_n)] \quad (3)$$

where  $g_4$  is anharmonic coupling constant and

$$\Pi(\vec{k}, i\omega_n) = \frac{1}{(2\pi)^3} \int d^3\vec{k}' \sum_{\vec{k}''} G_1^{(0)}(\vec{k} - \vec{k}', i\omega_n - i\omega_{n'}) G_1^{(0)}(\vec{k}', i\omega_{n'}) \quad (4)$$

In a self-consistent treatment phonon damping  $\frac{1}{2}\Gamma$  in Eqs (2) to (4) should be replaced by  $\text{Im} \Sigma(\vec{k}, i\omega_n)$ . The self-energy  $\Sigma(\vec{k}, i\omega_n)$  was evaluated as the sum of the diagram (at low temperature approximation):

$$\Sigma = \text{---} \bigcirc \text{---} + \text{---} \bigcirc \text{---} + \text{---} \bigcirc \text{---} + \dots$$

Analytical expression for  $\Sigma(\vec{k}, i\omega_n)$  has a form:

$$\Sigma(\vec{k}, i\omega_n) = -\frac{g_4 k_B T}{(2\pi)^3} \int d^3\vec{k}' \sum_{\vec{k}''} G_1^{(0)}(\vec{k} - \vec{k}', i\omega_n) G_2(\vec{k} + \vec{k}', i\omega_n + i\omega_{n'}) \quad (5)$$

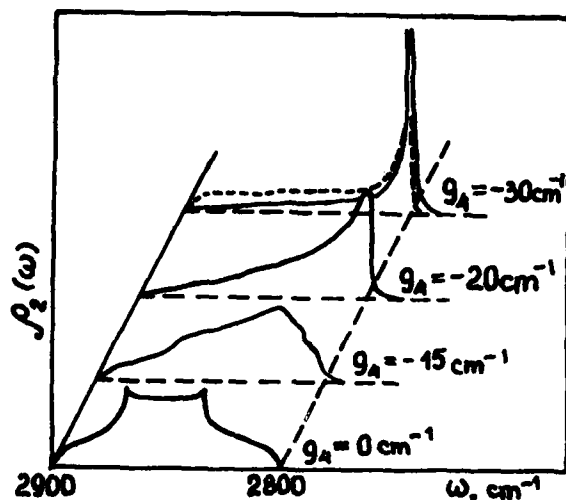
In order to evaluate the integrals in Eqs (4), (5) we consider the first term of propagator (2) and the integration interval from  $\omega_0$  to  $\omega_0 + 4\beta$  where  $\beta$  is one-phonon bandwidth. Moreover, to compare the calculated density of states to the experimental Raman scattering experiments we assumed the phonon pair momentum  $\vec{k} = 0$  and make the replacement  $\omega_{\vec{k}} \rightarrow \omega_0 = 1400 \text{ cm}^{-1}$  for  $\text{NH}_4\text{Cl}$ . The self-energy part is then rewritten in the following form:

$$\Sigma(\omega) = -\frac{2g_4}{(2\pi)^2} \int_{\omega_0}^{\omega_0 + 4\beta} d\omega' \frac{\rho_2(\omega' + \omega) \rho_2^{(0)}(\omega') [2n(\omega') + 1]}{\omega - 2(\omega_0 + 4\beta - \omega') + i\delta} \quad (6)$$

Here function  $\rho_2(\omega) = -\frac{1}{\pi} \text{Im} G_2(\omega)$  is defined by Eq. (3) at low temperature approximation and  $n(\omega)$  is Bose-factor. Function  $\Pi(\omega)$  expressed through the temperature depending phonon damping (6) is given:

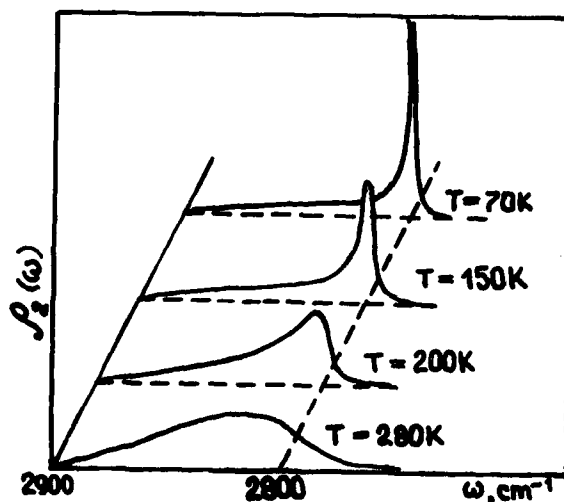
$$\Pi(\omega) = \frac{i\omega_0^2}{(2\pi)^4} \int_{\omega_0}^{\omega_0 + 4\beta} d\omega' \frac{[2n(\omega') + 1] \rho_2^{(0)}(\omega')}{\omega - 2(\omega_0 + 4\beta - \omega') - \Sigma(\omega') - \Sigma(\omega - \omega')} \quad (7)$$

The density of states of noninteracting phonons  $\rho_2^{(0)}(\omega)$  is defined in integral form obtained in work /5/ for the dispersion law  $\Omega_{\vec{k}}^2 = 4\omega_0^2 + \frac{16}{3}\beta \{ (1 - \cos k_x a) + (1 - \cos k_y a) + (1 - \cos k_z a) \}$ . We carry out the iteration procedure using Eqs (3) to (7) to calculate the temperature effect on the two-phonon band shape. First we calculate the two-phonon spectrum numerically for various values of anharmonic coupling constant at fixed temperature  $T = 70 \text{ K}$ . The results of the calculations are shown in Fig. 1. As one can see the quasibound state appears on the continuum low-frequency edge in accordance with the RS experimental data /3/. The procedure of fitting gives the constant value  $g_4 = 32 \text{ cm}^{-1}$ . As a second step, we calculated two-phonon spectrum at fixed value  $g_4 = 32 \text{ cm}^{-1}$  and various temperatures.  $\rho_2(\omega)$  spectra, plotted as the function of energy and temperature, are shown in Fig. 2. When the temperature increases, the two-phonon continuum intensity increases too, and quasibound state intensity decreases. The decay of the quasibound state occurs at  $T = 280 \text{ K}$  in a small disagreement with the experimental data /4/. It should be noted that the calcula-



**Fig.1.** Spectral function plotted as a function of frequency for different values of anharmonic coupling constant. The Raman spectrum studied in work [3] is shown by dotted line.

ted value of a coupling constant is overstated as we did not take into consideration the hybridization process between the two-phonon continuum  $2\nu_4$  and closely located one-phonon state  $\nu_1 = 3045 \text{ cm}^{-1}$ .



**Fig.2.** The two-phonon spectra  $\rho_2(\omega, T)$  as function of frequency for various temperatures. Two-phonon quasibound state is appeared at temperature  $T = 280\text{K}$ .

#### REFERENCES

1. J. Ruvalds and A. Zawadowski, Phys. Rev. B2, N4, 1172, 1970.
2. A. A. Abrikosov, L. P. Gorkov, N. E. Dzyaloshinski. Methods of field quantum theory in statistical physics. Physmatgiz, Moscow, 1962.
3. M. V. Belousov and D. E. Pogarev in "Oxidic Lattice Vibrations", "Nauka", Leningrad, 1981, p. 265.
4. G. G. Mitin, V. S. Gorelik, M. M. Sushchinski. Sol. St. Phys. (Soviet), 16, 10, 2956, 1974.
5. W. A. Bowers and H. B. Rosenstock. J. Chem. Phys., 18, 1056, 1950.

## FOUR-PHONON PROCESSES IN SOLIDS

T.J. Singh and G.S. Verma

*Physics Department, Banaras Hindu University, Varanasi, 221005, India*

**Abstract.**— The relaxation rate of four-Phonon Processes is derived using a diagrammatic field-theoretic approach. The results are in agreement with the earlier predictions of Pomeranchuk and recent perturbation results of Ecsedy and Klemens for a relatively simple model of a solid for which it is possible to obtain analytical expression.

Four-Phonon processes can arise in two ways via the perturbation terms  $\langle i | H_4 | f \rangle$  and  $\langle i | H_3 | l \rangle \langle l | H_3 | f \rangle / (E_l - E_i)$ .

$H_3$  and  $H_4$  are respectively the cubic and quartic anharmonic parts of the crystal Hamiltonian. The equivalent diagrams are shown in Fig. 1. Fig. 1(b) has a very interesting feature. It is possible to conserve energy at the interaction vertex giving rise to a resonance of the Briet-Wigner type in the Phonon-Phonon interaction. Processes depicted in Fig. 1(c) are well-behaved and hence there will be no resonance. We discuss resonance effects in a separate paper<sup>1</sup>. So for the present we concentrate on Fig. 1(a).

We start by defining a one-Phonon Green's function and calculating the phonon self energy associated with the diagrams (Fig.2.). The self-energy is found to be a complex quantity ; the real part merely serving to renormalize the phonon frequencies and the imaginary part is our relaxation rate for four-phonon processes. This rate when simplified for high temperature case, becomes

$$\Gamma(\vec{q}s, \omega) = - \frac{\pi^2 k^2 T^2}{96 N^2} \sum_{123} \Delta(-\vec{q} + \vec{q}_1 + \vec{q}_2 + \vec{q}_3) \frac{|\rho(-\vec{q}s, \vec{q}_1s_1, \vec{q}_2s_2, \vec{q}_3s_3)|^2}{\omega(\vec{q}s) (\omega_1 \omega_2 \omega_3)^2}$$

$$\times \left[ (\omega_2 + \omega_3 - \omega_1) \delta(\omega - \omega_1 + \omega_2 + \omega_3) + (\omega_1 + \omega_2 + \omega_3) \delta(\omega + \omega_1 + \omega_2 + \omega_3) \right.$$

$$+ (\omega_1 - \omega_2 - \omega_3) \delta(\omega + \omega_1 - \omega_2 - \omega_3) - (\omega_1 + \omega_2 + \omega_3) \delta(\omega - \omega_1 - \omega_2 - \omega_3)$$

$$\left. + (\omega_3 - \omega_2 - \omega_1) \delta(\omega - \omega_1 - \omega_2 + \omega_3) + (\omega_1 - \omega_2 + \omega_3) \delta(\omega + \omega_1 - \omega_2 + \omega_3) \right] +$$

$$(\omega_2 - \omega_3 - \omega_4) \delta(\omega - \omega_1 + \omega_2 - \omega_3) + (\omega_1 + \omega_2 - \omega_3) \delta(\omega + \omega_1 + \omega_2 - \omega_3) \quad (1)$$

where  $\Delta(\vec{q})$  is the lattice Kronecker delta, the summations over 123 indicate summations over all wave vectors  $q$ 's and over all polarisation branches  $S$ 's,  $K$  is the Boltzmann constant,  $N$  is the number of unit cells in the crystal and  $\varphi(q)$ 's are the atomic force constants and  $\omega_i = \omega(\vec{q}_i s_i)$  and etc.

For a f.c.c. crystal with central nearest neighbour interactions the atomic force constants  $\varphi(q)$ 's become, in the long wavelength limit

$$|\varphi(-\vec{q}s, \vec{q}_1 s_1, \vec{q}_2 s_2, \vec{q}_3 s_3)| = \frac{2\pi^4 \alpha a_0^4 A}{M^2} q_1 q_2 q_3 \dots (2)$$

where  $a_0$  is the lattice constant, and  $M$  mass of each atom,  $\alpha$  is the equilibrium force constant and the factor  $A$  contains all the

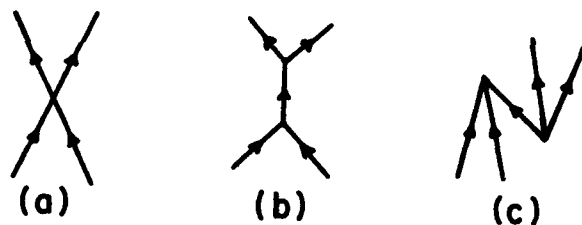


Fig.1 : Diagrammatic representations of 4-phonon processes.



Fig.2 : Diagrams contributing to the self-energy.

information regarding angular dependences of the various modes propagating through the lattice. Using (2) in (1), we get



$$\Gamma(\vec{q}s, \omega) = A' \omega^2 (\vec{q}s) T^2 \quad \dots (3)$$

$$\text{where} \quad A' = 2\pi^{16} \alpha^2 A^2 K^2 a_0^9 / 3v^9 M^4 \quad \dots (4)$$

and  $v$  is a suitably averaged phonon velocity.

Equation (3) agrees with that suggested by Pomeranchuk<sup>2</sup> and the recent perturbation result of Ecsedy and Klemens<sup>3</sup>. However, their treatment suffers from the basic assumption that all phonons except the one under consideration are in thermal equilibrium. Such an assumption is unnecessary in the present derivation which also takes care of all possible modes of combinations of phonons in a natural way. Moreover, for any model of a solid the relaxation rate of 4-phonon processes can be calculated by using eqn. (1)

Besides the real part of the self-energy function, there is another source of renormalization of phonon frequencies. Because of thermal expansion the frequencies of phonons may be changed<sup>4</sup> and such a change can be easily calculated. We find that for a purely anharmonic crystal the change is of negligible order and that so far as temperature dependence of the relaxation rate is concerned the effect of thermal expansion is negligible. Thus thermal expansion alone can not explain the  $T^2$  -dependence of the observed phonon conductivity in semiconductor, especially in Si<sup>5</sup>.

#### References.

1. T.J.Singh and G.S.Verma, Phys. Rev. B (Accepted)
2. I.Pomeranchuk, J.Phys. USSR, 4, 259(1941) ; 7, 197(1943).
3. D.J.Ecsedy and P.G.Klemens, Phys. Rev. B15, 5957(1977).
4. A.A.Maradudin and A.E.Fein, Phys. Rev. 128, 2589(1962).
5. Y.P.Joshi, M.D.Tewari and G.S.Verma, Phys. Rev. B1, 642(1970).

## ANHARMONIC INTERACTION IN ZINC SELENIDE

D. Schmeltzer and A. Beserman

*Solid State Institute and Physics Department, Technion, Israel Institute of Technology, Haifa, Israel*

**Abstract.-** Experimental evidence of anomalous temperature dependence of the double phonon Raman spectrum is brought and explained by a 4th order anharmonic coupling between two 2-phonon states.

We report experimental evidence of the fourth order anharmonic interaction in the continuum of ZnSe transverse acoustic-phonons, and its temperature dependence. The fourth order interaction produces a positive feedback which is the fourth order coupling parameter. The intensity of the response function increases with the increase of the feedback parameter.

The Raman spectrum (RS) intensity of the double-phonon band has been studied as a function of temperature. At room temperature this spectrum is mainly composed of the 2 TA peak from the X point of the Brillouin zone with some contribution from the  $\langle 110 \rangle$  direction and from subtractive phonons.

Fig. 1 shows the  $\int_1 + \int_{12}$  representation of the ZnSe R.S, Excited by the 6471 Å line, at 80K, 300K and 480K. As the temperature increases, the double phonon intensity increases with respect to the  $TO_L$  and  $LO_L$  modes. When the temperature varies from 80K to 660K, the variation of the Bose-Einstein factor ratio between  $TO_L$  and  $2 TA_X$  should be 10 while experimentally we found a factor  $\approx 100$ . The width, shape and frequency of the double phonon peak do not vary appreciatively with temperature.

These results are the same when the 6764 Å krypton laser line is used, and no anomalous behaviour is observed in the double phonon spectrum of ZnS.

These experimental facts show that at high enough temperature an instable double-phonon state exists which disappears at low temperature.

In order to analyze the behavior of the doublephonon in the acoustic range we assume a fourth order anharmonic interaction

$$H = \sum_k \hbar \omega_k \left( b_k^\dagger b_k + \frac{1}{2} \right) + \frac{g_4}{4!} \hbar \int d^3x \Phi(x)$$

The Raman Intensity is proportional to the time ordered green's function

$$I_{(\omega)}^{(2)} = - [n(\omega) + 1] 2 \hbar \frac{\omega}{2kT} \text{Im } D_2^T(q=0, \omega)$$

In the mean field approximation

$$\text{Im } D_2^T(q=0, \omega) = \frac{2 \text{Im } F(\omega)}{\left[1 - \frac{24}{2} \text{Re } F(\omega)\right]^2 + \left[\frac{24}{2} \text{Im } F(\omega)\right]^2}$$

$\text{Im } F(\omega)$  is proportional to the double phonon density of states  $\rho(\omega)$ . At high enough temperature  $1 - \frac{24}{2} \text{Re } F(\omega)$  gives the resonant condition.

For  $\frac{\hbar T}{2\omega_{ac}} \gg 1$ ,  $1 - \frac{24}{2} T I^{(2)}(\omega) = 0$  for  $T = T_0$   
 For frequencies close to  $2\omega_{ac}$ , the singularity of the density of states produces a large change in the second order Raman intensity

$$\frac{I^{(2)}(T)}{I^{(2)}(T_0)} \approx 1 - \frac{T - T_0}{T} \frac{\partial \ln \rho(\epsilon)}{\partial \ln \epsilon}, \quad \epsilon = \frac{\omega - 2\omega_{ac}}{2\omega_{ac}}$$

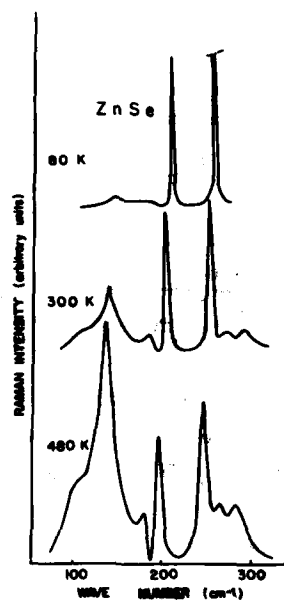
When  $T \gg T_0$  for high temperatures

$$\frac{I^{(2)}(T)}{I^{(2)}(T_0)} \propto \frac{T}{T^* - T} \quad \text{with } T^* = \frac{T_0 \sqrt{2} \epsilon}{\sqrt{2} \epsilon - \sqrt{\epsilon} T_0}$$

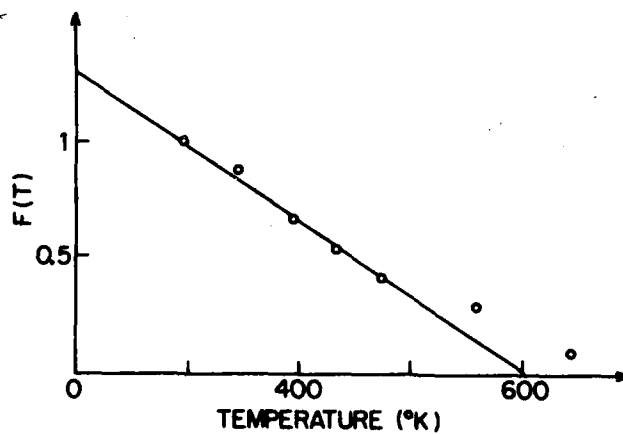
We deduce

$$F(T) = \left[ \frac{I^{(2)}(T)/T}{I^{(2)}(T_0)/T_0} \right]^{-1} \propto T^* - T$$

In fig. 2 we have plotted  $F(T)$  as a function of temperature. The graph shows that for  $T = 600$  K the linear equation given for  $F(T)$  is valid and fits our experimental results well, with  $T^* = 600$  °K.



**Fig. 1:-** ZnSe Raman Intensity at different temperatures,  $\lambda = 6471\text{\AA}$ .



**Fig. 2:-**  $F(T)$  plotted as a function of temperature this equation has been normalized to 1 for  $T=300\text{K}$ , the experimental points are indicated by circles.

## LIFETIMES OF HIGH FREQUENCY PHONONS

M. Lax\*, V. Narayanamurti, P. Hu and W. Weber\*\*

Bell Laboratories, Murray Hill, N.J. 07974, U.S.A.

**Abstract** - We discuss the inhibition of anharmonic spontaneous multiphonon decay by energy-momentum conservation and the reduction of isotope scattering by the sharing of ionic motion to permit a frequency window for long-lived transverse acoustic phonons.

**1. Introduction** - Recent high frequency phonon experiments have revealed anomalously long phonon lifetimes at low temperatures.<sup>1</sup> Indeed, for phonons generated by  $e-h$  recombination in GaAs mean free paths of a few  $\mu\text{m}$  have been observed for near zone boundary acoustic phonons.

Since elementary theories of isotope scattering and of two-phonon decay lead to scattering rates that grow as  $\omega^4$  and  $\omega^5$  respectively, the experimental results require some mechanism or mechanisms that inhibit such scattering processes at least over some frequency window near the zone boundary.

**2. Spontaneous Phonon Decay** - In an isotropic solid transverse phonons can not decay into two other phonons because of energy and momentum conservation.<sup>3</sup> Maris<sup>4</sup> recognized that the same conclusion would be likely to apply to an anisotropic crystal, but that conservation of energy and momentum would be model dependent. He demonstrated the result for a face-centered cubic crystal with central forces between nearest neighbor atoms.

Lax, Hu and Narayanamurti<sup>3</sup> proved the following theorem: A phonon can not decay by anharmonic processes of any order into a set of phonons each of whose phase velocities is higher than that of the initial phonon. This result is applicable in the presence of frequency and angular dispersion in an anisotropic crystal of arbitrary symmetry. It is applicable to  $U$  (umklapp) as well as  $N$  (normal) processes.

The above theorem does not completely preclude the possibility that a transverse acoustic phonon can decay by anharmonic processes, but as found in Maris's example, only modes with small wave-vector  $q$  can decay. The reason for this is that the phase velocity of a phonon will normally decrease with increasing  $q$  making it more difficult to find phonons of lower phase velocity to decay into.

**3. Isotope Scattering** - To explain anomalously long-lived phonons, we must also demonstrate that isotope scattering, at least over some frequency "window", is weaker than expected from the usual theoretical treatments of monatomic lattices. We have suggested<sup>5</sup> that this weakness is to be expected in multi-atomic lattices when not all of the constituents possess isotopes. If only one atom (say Ga) has isotopes, there is a reduction factor of the form  $|u_i^{Ga}(q') \cdot u_i^{Ga}(q)|^2$  where  $u_i^{Ga}(q)$  is a (normalized) amplitude for Ga in a mode of type  $i$  with propagation vector  $q$ . Here  $i$  and  $q$  refer to the initial phonon state and  $i'$  and  $q'$  refer to the final state.

For the case of GaAs, which has cubic site as well as space group symmetry, the initial and final state amplitudes can be disentangled and the decay rate  $1/\tau_i(q)$  associated with a single scattering center in a lattice of  $N$  sites is given by

$$\frac{1}{\tau_i(q)} = \frac{1}{12} \frac{\omega_i^2(q)}{N} |u_i^{Ga}(q)|^2 \frac{(\Delta M^{Ga})^2}{\langle M^{Ga} \rangle^2} W(f); \text{ where } f = \omega_i(q)/2\pi \quad (1)$$

\* M. Lax is also at Physics Dept., City College of New York, New York 10031.

\*\* W. Weber is also at Kernforschungszentrum Karlsruhe, FRG, Inst. f. Angew. Kernphys. I.

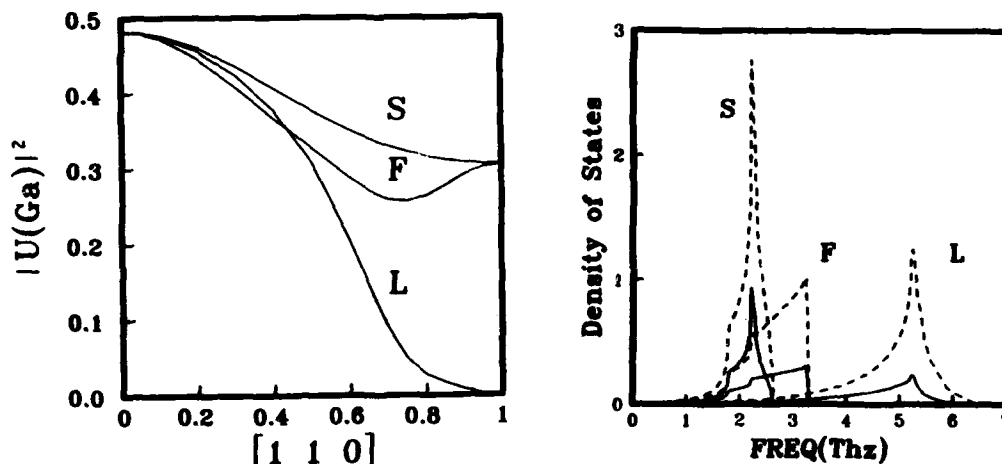


Fig. 1. (a) The Ga participation  $|u_{Ga}(q)|^2$  in the transverse acoustic mode is plotted versus  $q$  in the  $[110]$  direction. (b) Density of states  $g_i(f)$  (dashed curve) and Ga weighted density of states  $W_i(f)$  (solid curve) for the three acoustic branches is plotted against frequency  $f$  in terahertz.

Here all the initial state information is concentrated in  $\omega_i(q)$  and  $u_{Ga}(q)$  and the final state information is concentrated in the density of states weighted by the Ga motion:

$$W(f) = \sum_{i'} g_i(f) R_i(f) = \sum_{i'} W_i(f); \text{ where } g_i(f) = \langle \delta(f - f_i(q)) \rangle. \quad (2)$$

is the ordinary density of states for mode  $i'$  and

$$g_i(f) R_i(f) = \langle \delta(f - f_i(q)) |u_{Ga}(q)|^2 \rangle. \quad (3)$$

Here  $f_i(q) = \omega_i(q)/2\pi$  is the frequency in Hertz of the scattered phonon, and the amplitudes are normalized in accord with

$$|u_{Ga}(q)|^2 + |u_{As}(q)|^2 = 1. \quad (4)$$

The averages shown in Eqs. (3) and (4) are integrals over the Brillouin zone performed using the Gilat-Raubenheimer algorithm.<sup>6</sup>  $W_i(f)$  is the density of final states of type  $i'$  weighted by the Ga motion, and  $R_i(f)$  is the final state reduction factor at frequency  $f$  caused by the fact that the Ga motion contains only a portion of the kinetic energy. The factor  $|u_{Ga}(q)|^2$  is plotted versus  $q$  in the  $[110]$  direction in Fig. 1a. Plots of  $g_i(f)$  and  $W_i(f)$  for the acoustic modes are shown in Fig. 1b.

These calculations are based on a simplified extension from Ge to GaAs of Weber's adiabatic bond charge model<sup>7</sup> by adding only an ionic charge asymmetry  $\Delta$  between Ga and As.<sup>8</sup> The results for  $|u_{Ga}|^2$  are sensitive to  $\Delta$  and favor  $\Delta < 0$  for Ga.

**4. Anharmonic Two-Phonon Scattering.** - The extent to which two-phonon spontaneous decay of a phonon of wave-vector  $k$  and frequency  $\omega$  is possible is described by the two-phonon density of states

$$g_2(\omega, k) = \langle \sum_G \delta(\omega - \Omega_2(k, q)) \rangle \text{ where } \Omega_2(k, q) = \omega_i(q) + \omega_j(k - q - G), \quad (5)$$

embodies the simultaneous requirements of energy and momentum conservation with the sum over  $G$  including umklapp processes.

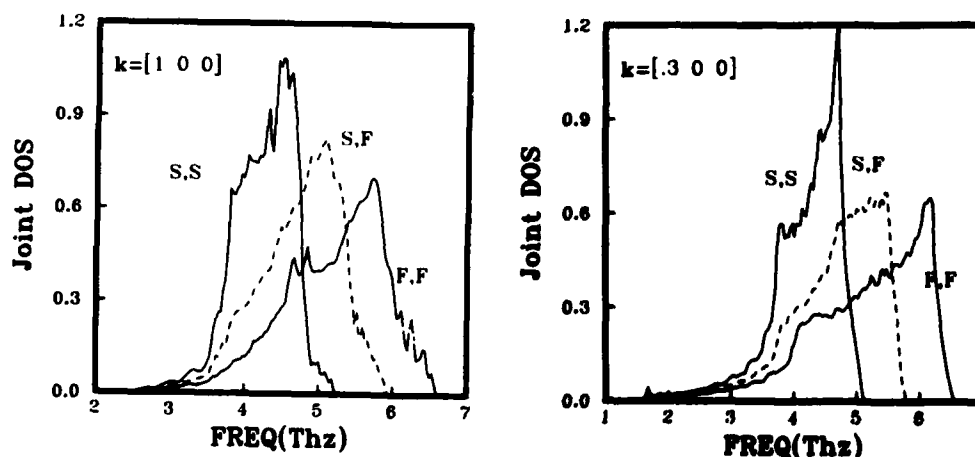


Fig. 2. The two phonon density of states for pairs of transverse acoustic (TA) phonons of the slow (S) and fast (F) variety is plotted versus frequency for (a)  $k=[1,0,0]$ , and (b)  $k=[0.3,0,0]$  phonons as slow transverse phonons.

For decay of a transverse phonon, the relevant final states are also transverse. We display  $g_{\alpha}(\omega, k)$  for  $\alpha$  and  $\alpha'$  slow (S) or fast (F) transverse (T) phonons, with  $k$  at  $[.3,0,0]$  and  $[1,0,0]=X$  (the zone boundary point) in Figs. 2a and 2b respectively. Since the two phonon density of states exists only above some minimum  $\omega_m$ , for any given  $k$ , phonons whose  $\omega(k) < \omega_m$  can not decay, such as the T phonons at X. This conclusion is undoubtedly valid in *all* directions for large enough  $k$  permitting propagation over a substantial portion of  $k$  space.

**5. Summary** - We have shown that anharmonic decay by a phonon into two (or more) phonons is rigorously prevented if the final phonons have higher phase velocities than the initial phonon, and is strongly inhibited for acoustic transverse phonons near the zone boundary. Moreover, isotope scattering in GaAs is reduced near the zone boundary by two factors involving the squared amplitude of the Ga atoms. Thus a window is available for long-lived high frequency phonons. Since these results depend on the eigenvectors they provide a more sensitive test of vibrational models than measurements of dispersion alone.

**6. Acknowledgements** - We thank M. Schlüter for his advice in the use of the Gilat-Raubenheimer code, and R. C. Fulton for programming support. Work at CCNY was supported by ARO, DOE, and PSC-CUNY.

#### References

- <sup>1</sup>For a recent review see W. Bron, *Rep. Prog. Phys.* 43, 301 (1980) and *Phys. Rev. B* 21, 2627 (1980).
- <sup>2</sup>R. G. Ulbrich, V. Narayanaswami and M. A. Chin, *Phys. Rev. Lett.* 43, 1432 (1980); P. Hu, V. Narayanaswami and M. A. Chin, *Phys. Rev. Lett.* 46, 192 (1981).
- <sup>3</sup>P. G. Klemens in *Solid State Physics* (Academic Press, New York, 1958, F. Seitz and D. Turnbull, Eds.) Vol. 7, Chap. I. R. Orbach and L. A. Vredevoes, *Physica* 1, 91 (1964).
- <sup>4</sup>H. J. Maria, *Phys. Lett.* 17, 228 (1965).
- <sup>5</sup>M. Lax, P. Hu and V. Narayanaswami, *Phys. Rev. B* 23, 3095 (1981).
- <sup>6</sup>G. Gilat and L. J. Raubenheimer, *Phys. Rev.* 144, 380 (1966).
- <sup>7</sup>W. Weber, *Phys. Rev. B* 15, 4789 (1977).
- <sup>8</sup>Code for the very elaborate model for GaAs of K. C. Rustagi and W. Weber, *Solid State Communications*, 18, 673 (1976). was not available.

PHONONS IN SUPERIONIC CONDUCTORS



## PHONONS IN SUPERIONIC CONDUCTORS

W. Hayes

*Clarendon Laboratory, University of Oxford, United Kingdom*

**Abstract** - Detailed information about the nature of disorder in superionic conductors can be obtained from the study of vibrational excitations using Raman, Brillouin and neutron scattering techniques. The present review will be concerned with the application of these techniques to materials such as AgI,  $\text{CaF}_2$  and sodium  $\beta$ -alumina, with emphasis on the latter.

1. **Introduction.** - Most ionic solids have values of the electrical conductivity  $\sigma$  immediately below the melting temperature  $T_M$  about four orders of magnitude smaller than in the melt. In LiF, for example,  $\sigma$  increases from  $10^{-10}(\Omega\text{cm})^{-1}$  at room temperature to  $10^{-3}(\Omega\text{cm})^{-1}$  just below  $T_M = 1140$  K. On melting  $\sigma$  increases discontinuously to  $10(\Omega\text{cm})^{-1}$ . However, some ionic solids have values of  $\sigma$  in the crystalline state comparable to that in molten solids and are referred to as superionics or fast-ion conductors<sup>1</sup>. This high value of  $\sigma$  is due to ionic transport and is a consequence of extensive disorder in a component sublattice of the solid. The study of ionic vibrations in disordered systems has an intrinsic interest of its own and in superionics such studies throw light on the mechanisms of conduction<sup>2,3</sup>.

The superionic materials that have been subject to the most extensive study at a fundamental level in recent years may be divided into 3 groups:

(I) Silver and copper based compounds e.g. AgI,  $\text{RbAg}_4\text{I}_5$  and CuI, in which disorder occurs in the silver and copper sublattices. Here the prototype material is AgI. At room temperature AgI has the hexagonal wurtzite structure and is referred to as  $\beta$  AgI. At  $T_C = 147^\circ\text{C}$  a first-order phase change occurs to a body-centred cubic structure, referred to as  $\alpha$  AgI. The value of  $\sigma$  just below  $T_C$  is  $\sim 3 \times 10^{-4}(\Omega\text{cm})^{-1}$ ; it increases abruptly at  $T_C$  to  $\sim 1.3(\Omega\text{cm})^{-1}$  and falls slightly from this value on melting. A variety of structural studies<sup>1</sup> indicates that in the  $\alpha$  phase the iodine ions form a fairly rigid bcc lattice and that the silver ions are randomly distributed between them in tetrahedral interstitial sites. It also appears<sup>1</sup> that the motion of  $\text{Ag}^+$  ions between nearest-neighbour tetrahedral sites is the basic step in ion conduction. Phonon studies on AgI and other materials in this group have been reviewed recently<sup>3</sup> and will not be discussed further here. However, the attempts that have been made to obtain information about the dynamics of the mobile ions using quasielastic light scattering<sup>4,5,6</sup> and quasielastic neutron scattering<sup>7</sup> should be mentioned.

(II) Materials with the fluorite structure. These will be discussed in § 2.

(iii) Materials with the  $\beta$  alumina structure. These will be discussed in § 3.

2. Crystals with the Fluorite structure. - A pronounced heat anomaly occurs in halides with the fluorite structure at a temperature  $T_C$  well below  $T_M$ ; for  $\text{CaF}_2$   $T_C = 1430$  K and  $T_M = 1633$  K. This anomaly is due to development of extensive disorder in the anion sublattice and is associated with the onset of high ionic conductivity<sup>2</sup>. A study of the effects of anharmonicity ( $T < T_C$ ) and lattice disorder ( $T > T_C$ ) on the Raman spectrum of  $\text{CaF}_2$ ,  $\text{SrF}_2$ ,  $\text{BaF}_2$ ,  $\text{SrCl}_2$  and  $\text{PbF}_2$  was made by Elliott et al<sup>8</sup>. In these materials the  $T_{2g}$  Raman-allowed phonon broadens with increasing  $T$  and the detailed shape of the Raman band below  $T_C$  can be explained quite well using third and fourth-order anharmonicity. Additional scattering develops on the low energy side of the  $T_{2g}$  phonon for  $T > T_C$  and this can be accounted for by a theory of defect-induced scattering, including effects of both anion vacancies and anion interstitials.

Effects of disorder in the superionic phase of fluorites ( $T \geq T_C$ ) on elastic constants was studied by Brillouin scattering techniques<sup>9</sup> showing a dramatic fall of  $C_{11}$  at  $T_C$ . Neither  $C_{12}$  nor  $C_{44}$  is appreciably affected by the disorder. Similar results have been obtained by neutron scattering techniques<sup>10</sup>. The different behaviour of the elastic constants may be rationalised from the fact that the contributions to  $C_{11}$  from Coulomb and short-range forces have the same sign whereas for  $C_{12}$  and  $C_{44}$  they have opposite signs. It seems that effects of defects on  $C_{12}$  and  $C_{44}$  is small because the change in Coulomb and short-range forces largely cancel each other.

It should be emphasised that the theories used to account for effects of disorder on the Raman and Brillouin spectra of fluorites<sup>8,9</sup> are not sensitive to the precise configurations of vacancies and interstitials. However, very useful information has been obtained about the structure of the superionic state of

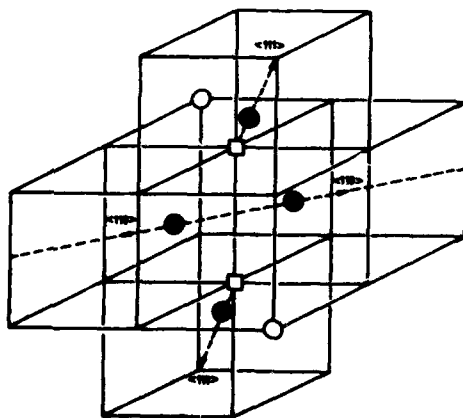


Fig 1: Model of a 2:2:2 defect in fluorite showing two anion interstitials ●, two relaxed anions ○ and two anion vacancies ○.

AD-A126 574

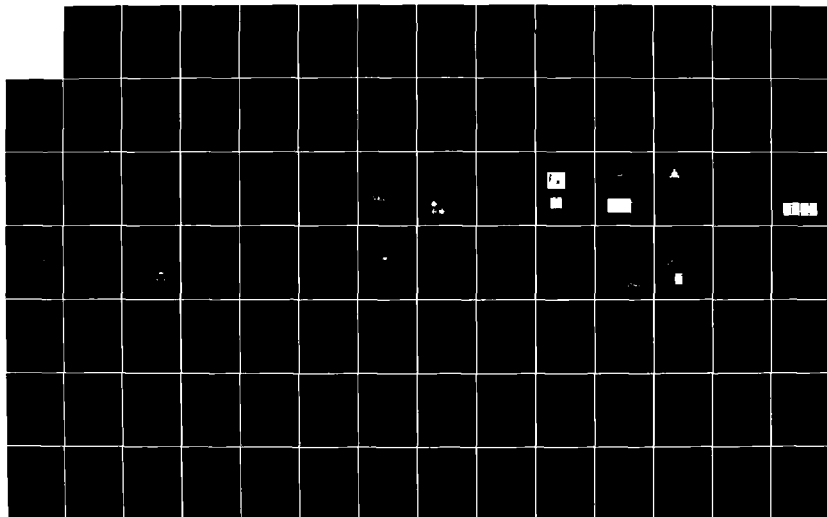
INTERNATIONAL CONFERENCE ON PHONON PHYSICS 31 AUGUST-3  
SEPTEMBER 1981 BLOOMINGTON INDIANA(U) INDIANA UNIV AT  
BLOOMINGTON W E BROW DEC 81 ARO-17340.1-PH  
MIPR-ARO-43-80

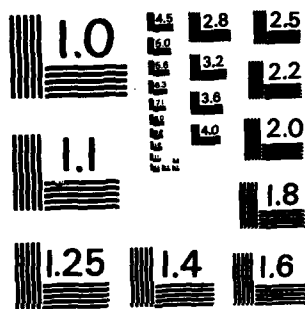
3/10

UNCLASSIFIED

F/G 20/2

NL





MICROCOPY RESOLUTION TEST CHART  
NATIONAL BUREAU OF STANDARDS-1963-A

fluorites from the  $q$ -dependence of the intensity of quasielastic neutron scattering<sup>11</sup>. These results may be explained quite well assuming the existence of a transient vacancy-interstitial complex of the so-called 2:2:2 type (Figure 1), involving two anion vacancies, two anion interstitials and two relaxed anions. The neutron linewidths suggest that these complexes survive in the superionic state for times of  $\sim 1$  ps. This type of complex is very stable and its formation contributes to the large reduction in anion Frenkel energy needed to account for the onset of cooperative disorder at  $T_c$ <sup>12</sup>.

Brillouin scattering techniques have also been used to study effects on  $T_c$  of doping with trivalent cations<sup>13</sup>. It was found, for example, that doping  $\text{CaF}_2$  with 9 mole per cent of  $\text{YF}_3$  reduces  $T_c$  from 1430 K to  $\sim 1200$  K. In the doped material 2:2:2 type complexes form, similar to that shown in Figure 1, but involving  $\text{Y}^{3+}$  in cation sites, rather than anion vacancies. Calculation showed<sup>13</sup> that such complexes act as traps for thermally generated anion interstitials, thus reducing the energy of formation of anion Frenkel pairs and also of  $T_c$ .

3. Compounds with the  $\beta$ -alumina structure. - Melt-grown crystals of sodium  $\beta$ -alumina have the formula  $(1+x)\text{Na}_2\text{O} : 11 \text{ Al}_2\text{O}_3$  where  $x \sim 0.3$  represents departure from stoichiometry. The ionic conductivity at room temperature is large ( $\sigma \sim 0.04 \text{ } (\Omega\text{cm})^{-1}$ ) due to nonstoichiometry. The crystals have a centrosymmetric structure with hexagonal symmetry. They consist of spinel-like  $(\text{Al}_{11}\text{O}_{16})$  blocks separated by mirror planes containing sodium and oxygen ions (Figure 2). The spinel blocks

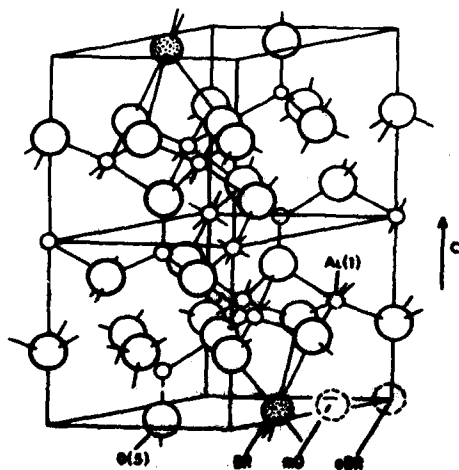


Fig. 2: Model of the  $\beta$  alumina structure.

are  $11.26 \text{ \AA}$  thick along the  $c$  axis. The oxygen ion in the mirror plane (O(5) in Figure 2) are coordinated by  $\text{Al}^{3+}$  ions in the spinel blocks, joining the blocks together. In effect, each mirror plane is a hexagonal network of O(5) ions interspersed with cation sites referred to as Beavers-Ross (BR) and anti-Beavers-Ross (aBR), which have site symmetry  $D_{3h}$ , and mid-oxygen (mo) which has site symmetry

$C_{2V}$  (Figure 2).

Neutron diffraction studies by Roth et al.<sup>14</sup> on sodium  $\beta$ -alumina at room temperature indicate that  $\sim 66\%$  of the  $Na^+$  ions are near BR sites,  $\sim 30\%$  are near mo sites and  $\sim 4\%$  are near aBR sites. These studies also led to the suggestion that charge compensation for the excess sodium in the mirror plane occurs through interstitial oxygens,  $O_i^{2-}$ , in mo sites bound by two aluminium ions (Al(1) in Figure 2) displaced from their normal positions towards the  $O_i^{2-}$ .

Studies of the Raman spectrum of sodium  $\beta$  alumina showed  $E_{2g}$  peaks at 61 and  $100\text{ cm}^{-1}$ <sup>15,16</sup>. The  $61\text{ cm}^{-1}$  peak was assigned to vibrations of  $Na^+$  ions in BR sites and the  $100\text{ cm}^{-1}$  peak to shearing of spinel blocks. The infrared absorption spectrum measured with the electric vector in the mirror plane is much more complex<sup>17</sup>. However, interpretation is assisted by measuring the absorption of material approximating to stoichiometry (Figure 3a). Here excitations are sharp (FWHM  $\sim 5\text{ cm}^{-1}$ ) compared to the widths of the overlapping bands found for the

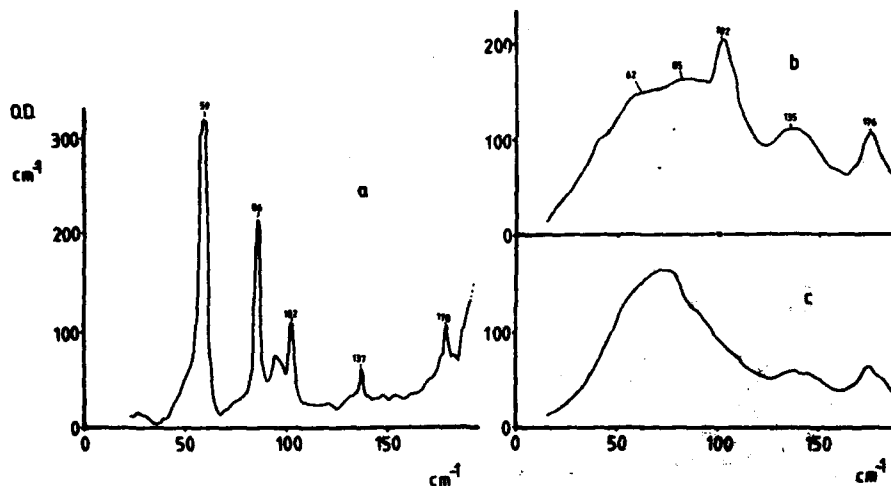


Fig. 3: Infrared absorption with  $E_{\perp c}$  of nearly stoichiometric sodium  $\beta$  alumina at 2K, (a), and of nonstoichiometric sodium  $\beta$  alumina at 2K, (b), and 300K, (c).

nonstoichiometric material (FWHM  $\sim 25\text{ cm}^{-1}$ ) (Figure 3b). Since we expect the occupation of BR sites to be predominant in the more stoichiometric material we assign the  $59\text{ cm}^{-1}$  line in Figure 3a to  $E_{1u}$  vibrations of  $Na^+$  ions near BR sites, consistent with the assignment of the Raman peak<sup>15,16</sup>. The other lines in Figure 3a are due to complexes of  $Na^+$  ions in various degrees of association with  $O_i^{2-}$ <sup>17</sup> and there is a one-to-one correspondence with the bands of Figure 3b.

Figures 3b and 3c show the change in the infrared absorption of nonstoichiometric material on going from 2 to 300 K. The intensity of the  $102\text{ cm}^{-1}$  band is very sensitive to temperature, decreasing with increasing temperature with an

activation energy of  $\sim 0.02$  eV. This may be taken to be the energy required to remove an extra  $\text{Na}^+$  ion from the vicinity of  $\text{O}_i^{2-}$ , making it available for long-range conduction. The  $85\text{ cm}^{-1}$  band decays with increasing temperature with a similar activation energy. The intensity of the  $135\text{ cm}^{-1}$  band is less temperature sensitive and the intensity of the  $176\text{ cm}^{-1}$  band shows little change between 2 and 300 K. If, in comparison with Figure 3a, we assume that the  $\text{Na}^+$  ions giving rise to the main peak in Figure 3c are near BR sites we conclude, in agreement with Roth et al.<sup>14</sup>, that 66% of the  $\text{Na}^+$  ions occupy such sites at room temperature. However, it would seem that the assignment by Roth et al.<sup>14</sup> to mo sites cannot, in our case, refer to a unique complex since at least five different centres are involved. The percentage assigned by Roth et al.<sup>14</sup> to aBR sites is too small to be readily recognisable in our studies, but it seems likely that ions in aBR sites will have a vibrational frequency comparable to that of BR sites. Our results are in general agreement with the suggestion of Wolf<sup>18</sup> that the sodium ions should be considered as two major groups, those bound with different strengths to  $\text{O}_i^{2-}$  i.e. in associated areas and those not appreciably perturbed by  $\text{O}_i^{2-}$  i.e. in unassociated areas.

We have carried out similar studies on silver<sup>19</sup> and potassium  $\beta$ -alumina<sup>20</sup> and more recently on sodium  $\beta''$  alumina and its isomorphs<sup>21</sup>. We shall give a preliminary account of our work on sodium  $\beta''$  alumina here. This material is similar in structure to sodium  $\beta$ -alumina. It has the rhombohedral space group  $D_{3d}^5$  and is composed of spinel-like blocks of aluminium oxide, but ordered in a triple stacking sequence along the c axis. These blocks are separated by conduction slabs containing sodium and oxygen ions. The ideal structure is represented by the formula unit  $\text{Na}_2\text{O} \cdot \text{MgO} \cdot 5\text{Al}_2\text{O}_3$  with  $\text{Mg}^{2+}$  ions dissolved primarily in tetrahedrally-coordinated  $\text{Al}^{3+}$  sites. Figure 4 shows a projection of the positions of  $\text{Na}^+$  ions in the conducting slab on to the plane defined by the bridging  $\text{O}^{2-}$  ions. The sites which

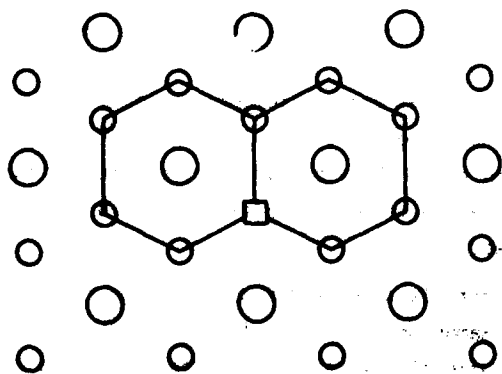


Fig. 4: Conduction slab of sodium  $\beta''$  alumina showing oxygen ions (large circles), sodium ions (small circles) and a sodium vacancy (square).

correspond to the BR and aBR positions in sodium  $\beta$  alumina (Figure 2) are in this case equivalent. It is generally assumed that the crystals are not stoichiometric, containing about 15% of  $\text{Na}^+$  vacancies, and that the high ionic conductivity ( $\sim 0.06 (\Omega \text{ cm})^{-1}$  at room temperature) is due to vacancy motion.

Figure 5a shows the Infrared absorption at 2K of a crystal of sodium  $\beta''$  alumina provided by W.L. Roth, with the electric vector of the radiation perpen-

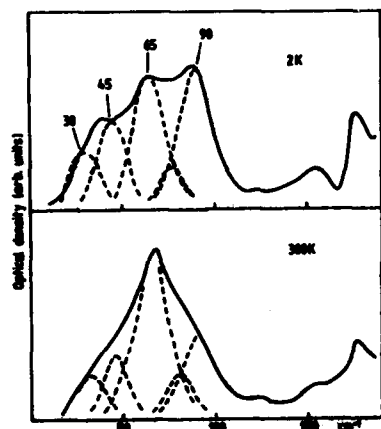


Fig. 5: Infrared absorption of sodium  $\beta''$  alumina with  $\underline{E} \perp c$ , at 2K and 300K.

dicular to the  $c$  axis. The spectrum is complex, showing some similarity to that of sodium  $\beta$  alumina (Figure 3). An approximate deconvolution of overlapping bands is shown in Figure 5. The interpretation of these bands is at present tentative awaiting the outcome of model calculations and further experiments. The bands at  $155$  and  $176 \text{ cm}^{-1}$  are probably due to  $\text{Na}^+$  ions in association with  $\text{O}_i^{2-}$ . The band at  $90 \text{ cm}^{-1}$  loses about half of its intensity on warming to room temperature (Figure 5b) and by analogy to sodium  $\beta$  alumina may be due to  $\text{Na}^+$  ions weakly bound to  $\text{O}_i^{2-}$ . The peak at  $65 \text{ cm}^{-1}$  increases in intensity on warming to room temperature and is probably due to  $\text{Na}^+$  ions on normal lattice sites without any other defects nearby. The bands at  $30$  and  $45 \text{ cm}^{-1}$  decrease on warming to room temperature and may be due to sodium-vacancy complexes. There are also indications of a weak band at  $\sim 78 \text{ cm}^{-1}$ .

The discussion given above suggests that at room temperature about 45% of the sodium ions are on lattice sites without other defects nearby and that the rest of the sodium ions form a variety of complexes. This behaviour is similar to that of sodium  $\beta$  alumina, but, again, the situation is more complex than the diffraction results for sodium  $\beta''$  alumina<sup>14</sup> suggest.

4. Conclusions. - The superionic materials already discussed divide into two categories from the point of view of Raman and infrared studies of phonons:

(1) A sublattice of the material is effectively totally disordered as in  $\alpha$  AgI or partly disordered as in fluorites. The disorder here is intrinsic and is a cooperative, thermally-induced phenomenon. The characteristic features of these materials



are a Raman spectrum corresponding to a defect-induced single-phonon density of states and a quasielastic peak associated with diffusive motion.

(11) Nonstoichiometric materials, such as sodium  $\beta$  alumina, where the disorder is present in as-grown crystals. The ions responsible for conductivity in these materials give rise to relatively sharp Raman and infrared lines, giving detailed information about environment. There is a need for quasielastic light-scattering studies of these materials.

#### References

1. Salamon, M.B., Editor, Physics of Superionic Conductors, Springer-Verlag 1979.
2. Hayes, W., Cont. Phys. 19, 469 (1978).
3. Hayes, W., Light Scattering in Solids, Vol. 11, Editors, M. Cardona and G. Guntherodt, 1982, to be published.
4. Winterling, G., Senn, W., Grimsditch, M. and Katiyar R., Lattice Dynamics (Ed. M. Balkanski) Flammarion Press, 553 (1977).
5. Field, R.A., Gallagher, D.A. and Klein, M.V., Phys. Rev. B 18, 2995 (1978).
6. Nemanich, R.J. Martin R.M. and Mikkelsen, J.C. Jr., Fast Ion Transport in Solids (Ed<sup>s</sup> P. Vashishta, J.N. Mundy and G.K. Shenoy), North Holland Pub. Co. 547 (1979).
7. Eckold, G., Funke, K., Kalus, J. and Lechner R., J. Phys. Chem. Sol. 37, 1097 (1976).
8. Elliott, R.J., Hayes W., Kleppmann W.G., Rushworth, A.J. and Ryan J.F., Proc. Roy. Soc. A360, 317 (1978).
9. Catlow, C.R.A., Comins, J.D. Germano, F.A., Harley, R.T., and Hayes, W., J. Phys. C. Sol. St. Phys. 11, 3197 (1978).
10. Dickens, M.H., Hayes, W., Hutchings, M.T. and Kleppmann, W.G., J. Phys. C. Sol. St. Phys. 12, 17 (1979).
11. Clausen, K., Hayes, W., Hutchings, M.T., Kjems, J.K., Schnabel, P., and Smith, C. Proc. Int. Conf on Superionics, Gatlinburg, 1981, to be published.
12. Catlow, C.R.A., and Hayes, W., J. Phys. C. Sol. St. Phys., 1981, to be published.
13. Catlow, C.R.A., Comins, J.D., Germano, F.A. Harley, R.T., Hayes, W. and Owen, I.B., J. Phys. C. Sol. St. Phys. 14, 329 (1981).
14. Roth, W.L., Reidinger, F. and La Placa S., Superionic Conductors (Ed<sup>s</sup> G.D. Mahan and W.L. Roth), Plenum Press 223 (1976).
15. Chase, L.L., Hao, C.H. and Mahan, G.D., Sol. St. Comm., 18, 401 (1976).
16. Hao, C.H., Chase, L.L. and Mahan, G.D., Phys. Rev. B13, 4306 (1976).
17. Hayes, W. and Holden L. J. Phys. C, Sol. St. Phys., to be published.
18. Wolf, D., J. Phys. Chem. Sol. 40, 757 (1979).

19. Hayes, W., Holden, L. and Tofield, B.C., 1981, J. Phys. C., Sol. St. Phys 14, 511.
20. Hayes W., Holden, L., and Hopper G.F., J. Phys. C. Sol. St. Phys. 13, L317 (1980).
21. Hayes, W. and Hopper, G.F., J. Phys. C., Sol. St. Phys., to be published.

## VIBRATIONS AND DIFFUSION OF ATOMS IN SUPERIONIC CRYSTALS AND MELTS

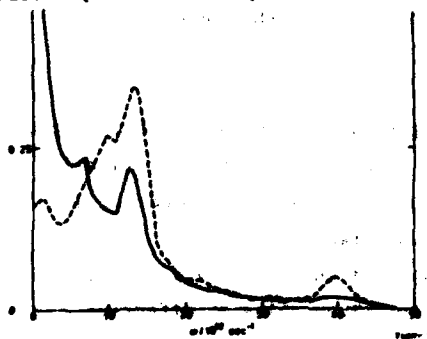
R.J. Elliott and M. Dixon

*Department of Theoretical Physics, Oxford University, Oxford, U.K.*

**Abstract.**— Recent computer simulation studies contain sufficient information about the atomic disorder and motion to allow a calculation of the dynamical response of superionic crystals and melts which may be compared with measurements of inelastic neutron scattering and Raman scattering. The high frequency part of this response is essentially that of anharmonic vibrations in a disordered lattice. The low frequency part results from correlated jump diffusion of the atoms.

1. **Introduction.** — The exact nature of the transition which occurs in superionic crystals is still imperfectly understood, in spite of the intensive study of materials like AgI and particularly the fluorites (1). In the latter the anion lattice certainly disorders to some extent (2) and these ions are able to diffuse. However it now seems unlikely that the disorder is simply due to partial occupation of the empty cube centre sites with consequential vacancies in the normal sites. Rather there appears to be a density variation along the (100) anion chains and a strongly correlated motion in these directions.

The experimental observations cannot readily be interpreted in terms of simple models of disorder. The extensive computer simulation studies of Gillan and Dixon (3) and others (4), elucidate some aspects of the problem. Most recently Gillan and Dixon (5) have studied in more detail the dynamical response in  $\text{SrCl}_2$  using a 96 ion sample and rigid ion potentials. The result for the anion structure factor (defined below) is shown in figure 1.



Partial dynamical structure factor  $S_{-}(k, \omega)$  at  $k = (2\pi/a_0)(2.5, 0, 0)$  from simulations at 938K (broken line) and  $T = 1484\text{K}$  (full line). The peaks at  $1.4$  and  $4.0 \times 10^{13} \text{ rad. s}^{-1}$  are due to longitudinal acoustic and optical phonons. The peak at  $\omega = 0$  in the full line is due to diffusive motion.

Fig. 1

Phonon structure is still visible in the high T phase although experiments by

neutron scattering (6) and Raman scattering (7) show greater broadening. This is interpreted (7) as due to anharmonicity which is effective at relatively low  $T$  and the destruction of the  $k$ -selection rule by disorder at high  $T$ .

2. Theory. - The structure factor which is related to neutron scattering is defined as

$$S_{\alpha\beta}(k, \omega) = \frac{1}{2\pi} \int dt e^{i\omega t} \langle \sum_i \sum_j \exp[ik \cdot R_i^\alpha(t) - R_j^\beta(0)] \rangle$$

where  $R_i^\alpha$  is the position of atom  $i$  of type  $\alpha$  and  $\langle \rangle$  indicates thermal average. In harmonic theory  $R(t)$  is expanded about its equilibrium position, but in the simulations the full expression is used. The motions at high  $T$  are roughly described as oscillations around some point, followed by a jump to a new position.

The Raman scattering is proportional to the correlation between the polarisabilities

$$R_{ab} = \frac{1}{2\pi} \int dt e^{i\omega t} \langle P_{ab}(t) P_{ab}(0) \rangle.$$

Here  $P$  is the polarisation due to the fields  $E_a, E_b$  of the incoming and outgoing photons.

$$P_{ab} = \sum_{ij} \alpha_{ab}^-(i) \alpha_{ab}^-(j)$$

where  $r(i)$  is the relative electron co-ordinate on atom  $i$ . There are two important contributions to  $P$ , one local when  $i=j$  involving the electronic quadrupole or the electronic orbit size, for combinations of the indices  $a, b$  appropriate to second and zero order harmonics respectively. The other arises for the induced dipoles on different atoms  $i \neq j$ , which is effectively the modulation of the van der Waals interaction (8). Extensive discussion of the latter mechanism has been given for rare gas liquids but because of the long range non-local character computer simulations are unreliable (9). We have assumed a local polarisation which depends on the relative local atomic displacements via a term like the Born-Mayer potential  $A e^{-R/\rho}$ . The two components depend on the density and quadrupole distortion of the local environment.

3. Melts. - We have estimated these effects on a computer simulation of molten NaI using a rigid ion model (10). Figure 2 shows results for the number-number and charge-charge combinations.

$$S_{nn}(S_{cc}) = S_{++} + S_{--} \pm (S_{+-} + S_{-+}).$$

The Raman scattering intensity is shown in figure 3 for the two symmetry types. Since the polarisability is due to relative atomic displacements the vibrational part is emphasised, although the 'optical phonon' peak is less pronounced than it is in  $S_{cc}$ . The narrow diffusive peak seen in  $S_{nn}$  is absent.

Computer simulations are proving extremely valuable in determining the atomic structure and atomic motion in superionics and melts. They allow an effective separation of vibrational and diffusive motions because of the jump diffusive character of these.

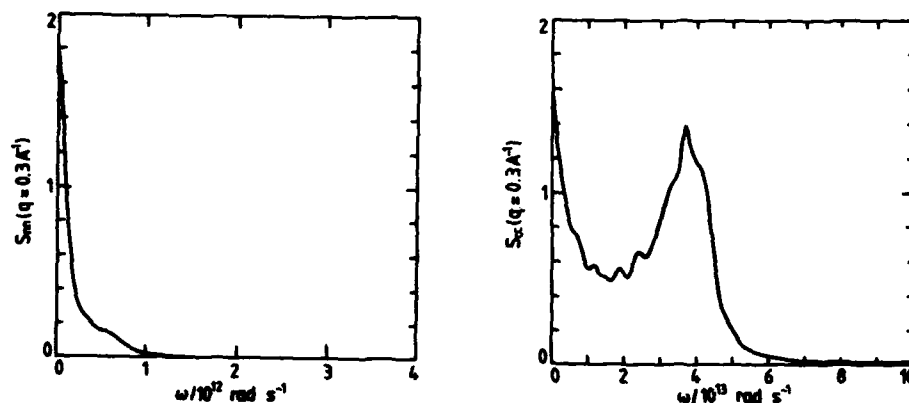


Fig.2 :  $S_{nn}(q, \omega)$  and (b)  $S_{cc}(q, \omega)$  at  $q = 0.3 \text{ \AA}^{-1}$  from a simulation of molten NaI at 1000 K.  $S_{nn}$  is largely diffusive but  $S_{cc}$  shows a peak due to optical type vibrational motion. Note the difference in frequency scale.

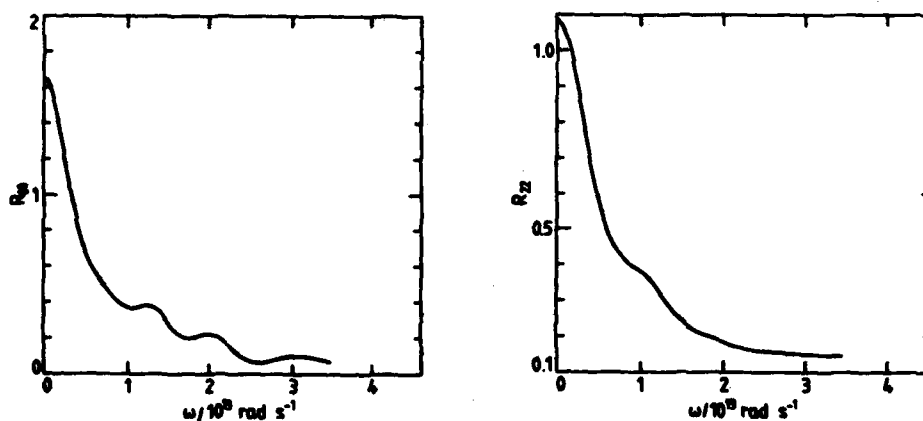


Fig.3 : Raman scattering intensities predicted from a simulation of NaI at 1000K using local polarisabilities.

#### References

- 1) W. Hayes 1978 Contemp. Phys. 19, 469.  
R. Catlow 1980 Comments on Solid State Physics 9, 157.
- 2) M.H. Dickens et al. 1978 J. Phys. C. 11, L583.
- 3) M. Dixon and M.J. Gillan 1980 J. Phys. C. 13, 1901, 1919.
- 4) G. Jacucci and A. Rahman 1978 J. Chem. Phys. 69, 4117.
- 5) M.J. Gillan and M. Dixon 1980 J. Phys. C. 13, L835.
- 6) M.H. Dickens, W. Hayes and M.T. Hutchings 1976 J. de Phys. 37, Suppl. C7-353.
- 7) R.J. Elliott et al. 1978 Proc. Roy. Soc. A360, 317.
- 8) B.J. Adler et al. 1979 J. Chem. Phys. 70, 4091.
- 9) A.J.C. Ladd et al. 1980 J. Chem. Phys. 72, 1759.  
J.H.R. Clarke and L.V. Woodcock 1981 Chem. Phys. Lett. 78, 121.
- 10) M. Dixon (to be published).

# PHONONS AND IONIC CONDUCTIVITY IN THE TWO-DIMENSIONAL SUPERIONIC CONDUCTOR $\text{AgCrS}_2$

P. Brüesch, T. Hibma and W. Bührer\*

Brown Boveri Research Center, CH-5405 Baden, Switzerland

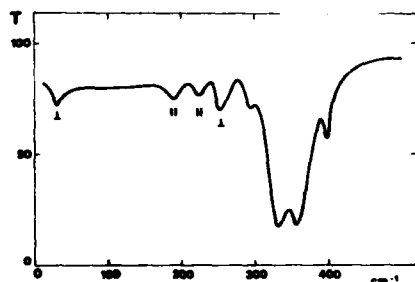
\*Institut für Reaktortechnik ETHZ, CH-5303 Würenlingen, Switzerland

**Abstract.**— Far-infrared technique, coherent and incoherent neutron scattering have been used to study the lattice dynamics of  $\text{AgCrS}_2$  at different temperatures. The low frequency TO mode shows a pronounced softening between 10 K and 700 K. The data are analyzed with a rigid-ion model and it is shown that the pattern of eigenvectors of the low energy modes ( $\nu < 45\text{cm}^{-1}$ ) give basic information for the diffusion process of the Ag ions.

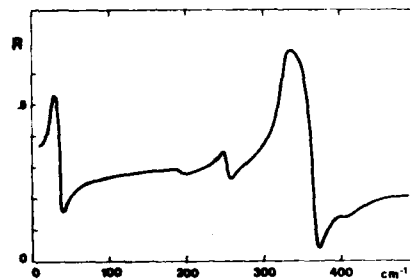
$\text{AgCrS}_2$  is a layer crystal which shows rather anisotropic behaviour in structure and macroscopic properties. At 673 K  $\text{AgCrS}_2$  exhibits a second order phase transition to a partially disordered structure where the Ag ions are distributed over a large number of available sites, resulting in a high ionic conductivity in the layers (1). Insight into the fast diffusion can be gained by investigating not only static properties such as  $\sigma(0)$  but rather the full dynamics of the crystal lattice. This paper reports results of far-infrared and neutron inelastic scattering experiments. The measurements are analysed with a rigid-ion model and the process of jump-diffusion is discussed on the basis of a reaction coordinate which is expressed in terms of the phonon structure.

$\text{AgCrS}_2$  crystallizes in a trigonal lattice (space group  $C_{3v}^5$ ) with one formula unit per primitive cell. At the zone center, the irreducible representations are  $\Gamma = 4 A_1 + 4 E$ , and both types are infrared active. Along the trigonal axis and at the point T there are again 4 one-dimensional and 4 two-dimensional representations; all other points in the Brillouin zone have lower symmetry. Single phase  $\text{AgCrS}_2$  has been prepared as described elsewhere (1). Small additions of AgCl improved the growth of single crystal platelets.

The far-infrared (FIR) measurements have been performed with a Beckmann interferometer in the polarizing mode for  $\nu < 150\text{cm}^{-1}$  and in the Michelson mode for  $150\text{cm}^{-1} < \nu < 400\text{cm}^{-1}$ . Fig. 1 shows the transmission spectrum of an  $\text{AgCrS}_2$  film on Si, and Fig. 2 displays the reflectance spectrum of a pressed pellet. The first absorption band near  $30\text{cm}^{-1}$  can be interpreted as TO mode ( $\vec{q} \parallel \vec{z}$ ,  $\vec{e}(\vec{q}) \perp \vec{z}$ ) an assignment which is based on transmission measurements of a thin single crystal.



**Fig. 1:** Far-infrared transmission of a thin film (d=4000 Å) of  $\text{AgCrS}_2$  on a silicon wafer at 295 K.



**Fig. 2:** Far-infrared reflectivity of  $\text{AgCrS}_2$  (pressed pellet) at 295 K.

A rich structure is observed between  $190 \text{ cm}^{-1}$  and  $400 \text{ cm}^{-1}$ , a tentative assignment is given on Fig. 1.

The dispersion relation of the lowest energy modes was determined by coherent inelastic neutron scattering techniques on a small but perfect single crystal. For the experiments the triple axis spectrometer at the reactor Saphir was used in its doubly focusing mode of operation (2). Results for phonons propagating along the trigonal axis ( $\Gamma - T$ ) and along ( $\Gamma - L$ ) are shown in Fig. 3. The dispersion curves show the typical behaviour of an anisotropic layer compound with its large separation in intralayer and interlayer modes.

FIR measurements as function of temperature showed a pronounced softening of the lowest TO mode, the frequency decreases from  $39 \text{ cm}^{-1}$  at 10 K to  $22 \text{ cm}^{-1}$  at the transition point, Fig. 4. This mode softening is unique in the large family of Ag based superionic conductors (3). The symmetry of the  $\text{AgCrS}_2$  lattice is low, and hence group theory gives only little information on the eigenvectors of the ions in the different modes. Therefore it is necessary to perform a model calculation, and as a starting point we used a simple rigid ion model with valence field forces for the short range term. The parameters (10 short-range stretching constants and ionic charges) were adjusted in order to reproduce the lowest frequency modes (Fig.3). A serious problem is given by the large separation between the lowest in-plane mode ( $30 \text{ cm}^{-1}$ ) and the corresponding out-of-plane mode ( $190 \text{ cm}^{-1}$ ) which could not satisfactorily be explained with our model. For a deeper understanding of this anisotropy the influence of the induced permanent dipoles on the sulphur ions must be included in the computations (4). However we obtain a good agreement for the low frequency modes and due to the large energetic separation of modes with the

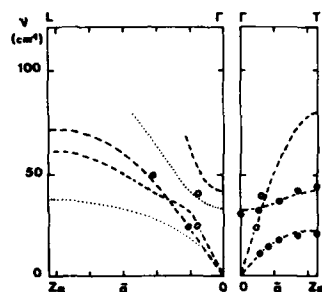


Fig. 3: Phonon dispersion curves in  $\text{AgCrS}_2$ .  $\circ$  longitudinal  $\bullet$  transverse; lines: rigid-ion model calculation.

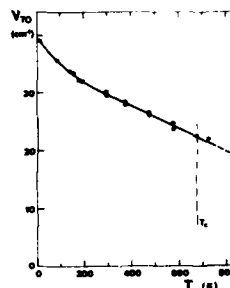


Fig. 4: Temperature dependence of the low frequency TO-mode of  $\text{AgCrS}_2$ . The peculiar behaviour below 150 K is not yet understood.

same symmetry, the eigenvectors of the lowest branches turned out to be almost model independent. We obtain the following result :  $\Gamma$  (TO) ( $30 \text{ cm}^{-1}$ ) Ag planes vibrate against the rigid S-Cr-S layer;  $\Gamma$  (TA) only Ag ions involved;  $\Gamma$  (TO) ( $45 \text{ cm}^{-1}$ ) only S-Cr-S layer in motion; L (TA) ( $45 \text{ cm}^{-1}$ ) only Ag vibrates. Atomic migration in crystals is discussed by Flynn (5). The instantaneous relative position of the migrating atom and its neighbours is of central interest in the diffusion process and is a suitable reaction coordinate which can be expressed in terms of the phonon structure (eigenvectors, density of states). Evidently low lying flat optic modes and low zone boundary acoustic branches give the main effects because they have a large density of states, strong vibrational amplitudes and are thermally easily activated; moreover in all these modes in  $\text{AgCrS}_2$  the Ag ions and the surrounding cage move not in phase. In addition the softening of the frequencies will enhance the diffusion probability (reduced barrier height). This can, in principle, give rise to a temperature dependent activation energy (1). In summary we conclude that the observed dynamical features, i.e. flat, soft, low energy modes, qualitatively explain the fast diffusion of Ag ions in  $\text{AgCrS}_2$ . For a theory of the conductivity  $\sigma(\nu, T)$  and the transition temperature  $T_c$  additional experiments at higher temperatures as well as a better lattice dynamical model are necessary.

- (1) T. Hibma, Solid State Commun. 33, 445 (1980)
- (2) W. Bührer et al., Nucl. Instr. and Meth. 179, 259 (1981)
- (3) P. Brüesch, H. Beyeler, and W. Bührer, Proc. Int. Conf. on Lattice Dynamics, Flammarion (Paris) 1978
- (4) A. Frey and R. Zeyer, Solid State Commun. 28, 435 (1978)
- (5) C.P. Flynn, Phys. Rev. 171, 682 (1968)



LOW FREQUENCY LIGHT SCATTERING SPECTRA OF AgI<sup>\*</sup>

W. Sasaki, Y. Sasaki, S. Ushioda and W. Taylor\*

University of California, Irvine, California 92717, U.S.A.

**Abstract.** The Rayleigh-Brillouin spectra of  $\alpha$ - and  $\beta$ -AgI have been measured with a Fabry-Perot interferometer in a back scattering geometry. The longitudinal acoustic phonon frequency in the  $\beta$ -phase gradually decreases with increasing temperature from 17.4 GHz at room temperature to 16 GHz just below the transition. At the transition temperature (145°C) the frequency of the LA-mode shifts suddenly to 13.5 GHz, and thereafter it remains independent of temperature. No peak corresponding to the TA phonon was observed. A broad peak was observed in the frequency region near 27 GHz where a conductivity anomaly was found by earlier infrared reflectivity measurements.

1. **Introduction.**— In the superionic phase of AgI liquid-like diffusive motions of the silver ions produce two central components in the inelastic light scattering spectra.<sup>(1)</sup> In the same low frequency region, peaks due to acoustic phonons should appear, and according to theory<sup>(2,3)</sup> they may show interference with the diffusive motions of cation ions. The purpose of the present paper is to investigate the inelastic light scattering spectra of  $\alpha$ - and  $\beta$ -AgI in the frequency range of 0.1 GHz to 300 GHz. The frequency region near 30 GHz ( $1\text{ cm}^{-1}$ ) where an anomaly in the frequency dependence of the conductivity  $\sigma(\omega)$  was observed by the far-infrared measurement<sup>(4)</sup> has been explored to find a corresponding structure in the light scattering spectrum.

2. **Experiment.**— Single crystals of  $\beta$ -AgI grown from a water solution<sup>(5)</sup> were cleaved parallel to the base plane with the c-axis of the wurtzite structure normal to the large hexagonal surface. This hexagonal plate shaped sample was mounted in an oven with one of the sides along the horizontal as indicated in the insert to Fig. 1. What we call Y-axis is normal to one of the sides of the hexagon; Z-axis is parallel to the c-axis. The oven temperature was controlled within 0.5°C. The incident light (6328 Å line of a multi-mode He-Ne laser) was directed along the c-axis and the back scattered light was analyzed by a triple-passed plane-parallel Fabry-Perot interferometer with a fineness of 30. The frequencies of the observed Brillouin spectra were calibrated by comparison with the well-known Brillouin spectra of pure fused silica.<sup>(6)</sup>

3. **Results and Discussion.**— Figure 1 shows the Brillouin spectra of  $\beta$ -AgI (125°C) with the LA phonon peak located at 16.3 GHz. In the (YY) polarization configuration a clear peak is observed, while no peak is observed in the (XY) polarization con-

\*Permanent address : Department of Physics, University of Edinburgh

<sup>\*</sup>Research supported by NSF, DMR 80-11435

figuration as shown in the figure. According to the selection rule for the wurtzite structure<sup>(7)</sup> this strong peak corresponds to the LA phonons propagating along the c-axis.

From the observed Brillouin frequency,  $\nu = 17.35$  GHz, and the refractive index, we find the sound velocity  $v_s = 2.48 \times 10^5$  cm/sec. This value is reasonable compared to the value of  $2.17 \times 10^5$  cm/sec obtained by extrapolating the neutron scattering data.<sup>(8)</sup> One of the elastic constants  $C_{33}$  was found to be  $C_{33} = 3.7 \times 10^{11}$  dyne/cm<sup>2</sup>. This value is comparable to the corresponding data for AgBr and AgCl.<sup>(9)</sup>

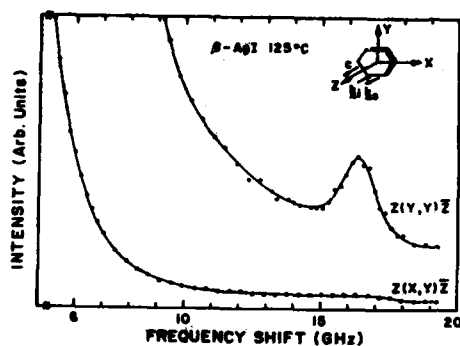


Fig. 1 : Brillouin spectra of LA phonons in  $\beta$ -AgI. The insert shows the crystal orientation.

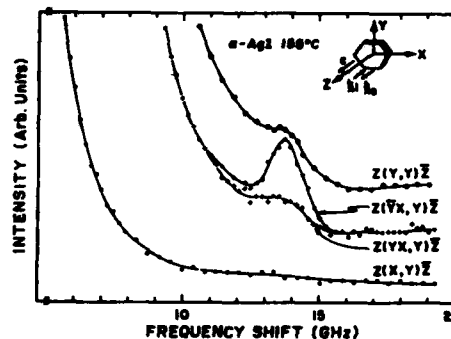


Fig. 2 : Brillouin spectra of LA phonons in  $\alpha$ -AgI. The insert shows the crystal orientation.

Figure 2 shows the Brillouin spectra of  $\alpha$ -AgI at 155°C. The frequency shift of the acoustic phonon decreases to 13.7 GHz at the transition. According to the selection rule for a bcc crystal, both the LA and the TA phonons should appear in these spectra,<sup>(7)</sup> but the TA phonon peak is not found. After the  $\beta$ -to- $\alpha$  phase transition, the c-axis of the wurtzite phase becomes the  $[110]$  axis of the cubic phase.<sup>(10)</sup> Hence, under our experimental condition (back scattering) the LA phonon propagates along the  $[110]$  direction of the cubic phase, and can scatter light for the polarization configuration (Y,Y) but not for (Y,X).<sup>(7)</sup> By rotating the polarization of the incident light, we found that the maximum intensity is obtained for the incident polarisation at  $-45^\circ$  from the vertical, i.e. (YX,Y) configuration. The intensity is significantly weaker when the incident light polarization is rotated to  $+45^\circ$ , i.e. for the (YX,Y) configuration. The reason for this polarization effect has not been

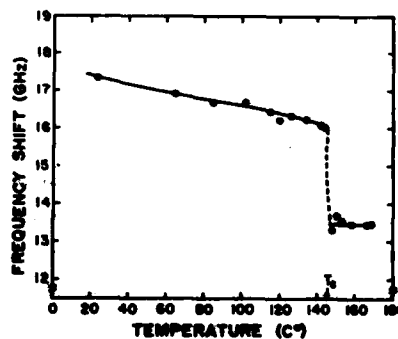


Fig. 3 : Temperature dependence of the LA phonon frequency.

determined. However, we believe that the observed effect originates from multi-domain formation at the  $\beta$ - $\alpha$  transition which is first order.

Huberman and Martin,<sup>(2)</sup> and Subbaswamy<sup>(3)</sup> have predicted the existence of interactions between the diffusing  $\text{Ag}^+$  ions and the acoustic phonons. In our experiment, no clear indication of this interaction could be found from the observed spectral shape of the LA phonon peak. The fact that the TA phonon peak could not be found in our spectra may indicate a strong interaction between the diffusive motion of  $\text{Ag}^+$  and the TA phonons resulting in heavy damping. The absence of the TA phonons is probably related to the liquid-like behavior of the  $\text{Ag}^+$  ions in the  $\alpha$ -phase.<sup>(11)</sup>

Figure 3 shows the temperature dependence of the LA phonon frequency which decreases gradually from 17.5 GHz at room temperature to 16 GHz just below the transition temperature. The frequency suddenly shifts to 13.5 GHz at the transition temperature  $T_c$  and remains constant above  $T_c$ . For our sample  $T_c$  was 145°C.

In the frequency region about 30 GHz ( $\approx 1 \text{ cm}^{-1}$ ) some structures were found in the frequency dependent conductivity  $\sigma(\omega)$  which was derived from the infrared reflectivity.<sup>(4,12)</sup> We looked for a corresponding structure in the Brillouin spectra, and found a weak and broad peak at 27 GHz. However, the nature of this peak could not be determined definitively due to its low intensity.

The diffusive central component with  $3.8 \text{ cm}^{-1}$  width<sup>(1)</sup> could not be observed in this experiment, although we looked for such a feature.

#### 4. References.

- 1) G. Winterling, W. Senn, M. Grimsditch and R. Katiyar: Proc. Intern. Conf. on Lattice Dynamics, ed. by M. Balkanski (Flammarion, Paris 1977).
- 2) B. A. Huberman, R. M. Martin: Phys. Rev. **B13**, 1498 (1977).
- 3) K. R. Subbaswamy: Solid State Comm. **19**, 1157 (1976).
- 4) P. Bruesch, L. Pietronero, H. R. Zeller: J. Phys. C: **9**, 3977, (1976).
- 5) M. E. Hills: J. Crystal Growth **7**, 257 (1970).
- 6) S. M. Shapiro, R. W. Gammon, H. Z. Cisnerios: Appl. Phys. Lett. **9**, 157 (1966).
- 7) R. Vacher, L. Boyer: Phys. Rev. **B6**, 639 (1972).
- 8) P. Bruesch, W. Buhrer, H. J. M. Smeets: Phys. Rev. **B22**, 970 (1980).
- 9) K. H. Hellwege ed: LANDOLT-BÖRNSTEIN Numerical Data and Functional Relationships in Science and Technology III/1 (Springer-Verlag 1966).
- 10) D. R. Mills, C. M. Perrott, M. H. Fletcher: J. Crystal Growth **6**, 266 (1970).
- 11) M. J. Delaney, S. Ushioda: Phys. Rev. **B16**, 1410 (1977).
- 12) H. Hayashi, M. Kobayashi, I. Yokota: Solid State Comm.: **31**, 847 (1979).

ULTRASONIC PROPERTIES OF A SUPERIONIC GLASS :  $B_2O_3$ , 0.5  $Li_2O$ , 0.7  $LiCl$ 

D. Čiplies and J.Y. Prieur\*

*Molecular Acoustics Laboratory, University of Vilnius, Knygos 4a, 232006  
Vilnius, Lithuania, U.S.S.R**\*Laboratoire d'Ultrasons, Université Pierre et Marie Curie, Tour 13, 4 place  
Jussieu, 75230 Paris Cedex 05, France*

**Abstract.** - We measured the attenuation and the phase velocity variations of longitudinal ultrasonic waves in a superionic glass of composition :  $B_2O_3$ , 0.5  $Li_2O$ , 0.7  $LiCl$ . The experimental curves show at least three different mechanisms of sound attenuation. Comparison with the result for a less conductive compound ( $B_2O_3$ , 0.5  $Li_2O$ ) is done. Two of the mechanisms are attributed to the glassy nature of the compound. One is believed to be due to the superionic properties of the material.

Among the superionic conductors there is a class of compounds which are glassy materials. These are very interesting because it is relatively easy to prepare them with a fairly large size (typically a cubic centimeter). But up to now they are not as good conductor at room temperature as the crystalline superionic. Thus there is a need for studying their properties in order to improve them.

We have measured the attenuation and the phase velocity variations of ultrasonic waves in a superionic glass with the chemical formula :  $B_2O_3$ , 0.5  $Li_2O$ , 0.7  $LiCl$ . These materials were synthesized by A. LEVASSEUR and his co-workers, from the University of Bordeaux I. Their room temperature conductivity is between  $10^{-5}$  and  $10^{-6} \Omega^{-1} \text{ cm}^{-1}$ . It is generally believed that the increase of lithium oxide will change mainly the microscopic structure of the glass when the increase of lithium chloride will increase the conductivity of the material. Thus it seemed worth to us to study a glass with the same content of lithium oxide but without lithium chloride, i.e.  $B_2O_3$ , 0.5  $Li_2O$ . In this way we expected to be able to separate the variations due to the structure of the material (glassy type variations) from those due to the superionic nature of the glass. The experimental results are displayed in Figure 1 for the attenuation and in Figure 2 for the velocity. In these figures the data for the glass with  $LiCl$  are shown with full lines when the ones for the glass without  $LiCl$  are shown with dashed lines.

At low temperatures (below 15 K) both materials have the same kind of variations. They are glassy types. The variations for the compound with  $LiCl$  have been analysed in details and the result reported elsewhere [1]. The attenuation changes as  $T^3$  up to about 1 K, then it bends around towards a plateau the height of which varies linearly with the frequency.

Between 15 K and 100 K a second mechanism of attenuation arises. It seemed clear from the results for the compound without  $LiCl$ , this mechanism is due to the relaxation of a distribution of two level systems (TLS) with a relaxation time changing with a distributed Arrhenius type law versus the temperature. Such a peak is

often found for glassy materials [2]. This behavior is less obvious for the LiCl compound. But, since an increase of the attenuation arises in the same range of temperature, we believe that the main reason for it is an Arrhenius type relaxation.

Finally, at higher temperatures ( $T > 100$  K) a new mechanism of attenuation appears in the LiCl compound. It is certainly much weaker in the other compound since we begin to see such an increase only above 250 K. This mechanism seemed to be of a new type and probably related to the lithium concentration since it exists in both materials and it is much stronger in the compound with the higher lithium concentration.

The velocity variations does not show so well defined temperature behavior. However at low temperature they are characteristic of a glassy compound. At temperatures lower than 4 K, the velocity increases as the logarithm of the temperature and is frequency independent. The slope of the curves for the LiCl doped compound is slightly lower than the ones of the other compound. These variations are known to be due to the resonant interaction between the ultrasonic waves and the TLS [1-3]. Then the curves bend around and a decrease almost linear is observed. It has been shown in Ref. [1] this variations can be explained by the relaxation interaction between the waves and the TLS. The bending appears at higher temperature and the temperature decrease is weaker in the compound without LiCl than in the other.

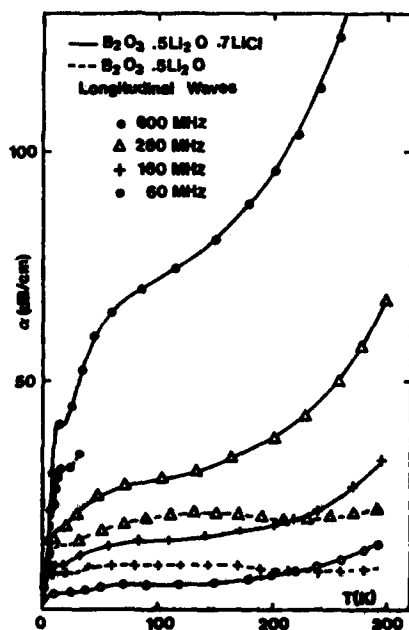


Figure 1 - Experimental variations of the attenuation of longitudinal waves in both compounds. The lines are guide for the eyes. The full lines are relative to  $B_2O_3$ , 0.5  $Li_2O$ , 0.7 LiCl and the dashed lines to  $B_2O_3$ , 0.5  $Li_2O$ .

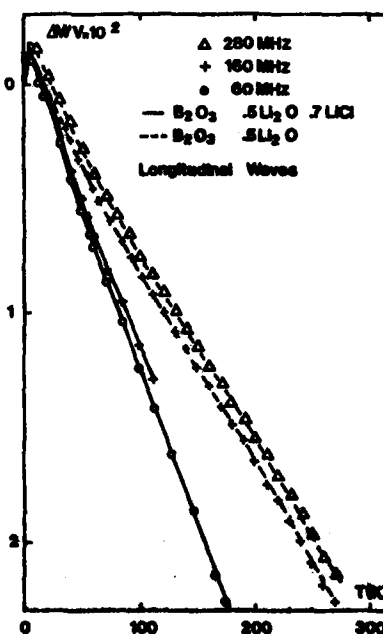


Figure 2 - Experimental velocity variations of longitudinal waves in both compounds. The lines are guide for the eyes. The full lines are relative to  $B_2O_3$ , 0.5  $Li_2O$ , 0.7 LiCl and the dashed lines to  $B_2O_3$ , 0.5  $Li_2O$ .

Around 60 K the slope of the decrease diminishes and a region with a slight dispersion starts. It is in the temperature range near the maximum of the Arrhenius peak. Then we think this change is related to the peak.

On a quantitative point of view, we must remember that the attenuation variations for any effect are at least proportional to the inverse of the third power of the sound velocity. Thus we measured the absolute sound velocity for longitudinal and transverse waves in both compounds. We found  $V_L = 6.2 \cdot 10^3$  m/sec and  $V_T = 3.75 \cdot 10^3$  m/sec in the LiCl compound, and  $V_L = 6.92 \cdot 10^3$  m/sec,  $V_T = 3.97 \cdot 10^3$  m/sec in the other. Thus the attenuation of the latter must be multiply by 1.25 before comparison with the LiCl doped compound.

If we do so, the height of the plateau is the same in both compounds. This seemed to show that the coupling constant is independent of the LiCl concentration. The slight difference in the slope of the velocity curves can be taken into account by changing the distribution of two level systems as it was done in Ref. [3].

It has been shown in [1] using the theory of Ref. [3] that the attenuation and the velocity variations in the LiCl compound can be explained quantitatively by introducing, besides the deformation potentials, two constants labeled  $K_3$  and  $K_7$ .  $K_3$  and  $K_7$  are expected to be roughly proportional respectively to  $V_T^{-5}$  and  $V_T^{-10}$ . Then with the velocity measured,  $K_3$  and  $K_7$  should be stronger by a factor of 1.3 and 1.8 in the LiCl doped compound. The accuracy is too small on the attenuation curves to see such a weak factor. But it is clear on the velocity curves that the height of the maximum is lower and the slope of the decrease, higher for the LiCl doped compound than for the other. This is exactly what is expected from the theory developed in Ref. [3].

The quantitative comparison is more difficult at higher temperature since there is no satisfying theory developed up to now to explain the Arrhenius peak. A simple way to analyse the results will be to subtract from the LiCl curve the conveniently scaled variations for the other compound. But this leads to some rather strange variations for the extra attenuation around 40 K. Then we think that the introduction of LiCl changes possibly the distribution of the barrier height. This called for a more careful analysis. Finally we note that the extra attenuation increases very roughly as the frequency.

#### REFERENCES

- [1] PRIEUR J.-Y. and ČIPLYS D., *XVth International Conference on Low Temperature Physics (LT 16)*, U.C.L.A., Los Angeles, U.S.A. (August 1981)
- [2] HUNKLINGER S. and ARNOLD W., in *Physics Acoustics*, ed. by W. P. Mason and R. N. Thurston (Academic Press, New-York, 1976), Vol. XII, p. 155.
- [3] DOUSSINEAU P., FRÉNOIS C., LEISURE R. G., LEVELUT A., and PRIEUR J.-Y., *J. Physique* 41 (1980) 1193.

# A NEW INTERPRETATION OF ULTRASONIC ATTENUATION IN SUPERIONIC CONDUCTORS $\beta$ AND $\beta''$ -ALUMINA

D.P. Almond and A.R. West\*

*School of Materials Science, University of Bath, Bath, BA2 7AY, United Kingdom*

*\*Department of Chemistry, University of Aberdeen, Aberdeen, AB9 2UE, United Kingdom*

**Abstract:** Broad asymmetrical attenuation peaks have been found in the ionic conductors  $\beta$  and  $\beta''$ -alumina which cannot be explained by Debye theory. They are interpreted as being a consequence of non-exponential decay processes and are analysed using universal dielectric response theory. Additional effects associated with water contamination of the samples are discussed.

Measurements of the ultrasonic attenuation in a single crystal sample of  $\beta$ -alumina<sup>(1)</sup> and a polycrystalline sample of predominantly  $\beta''$ -alumina<sup>(2)</sup> reveal attenuation peaks at low temperatures. The peaks are found to be thermally activated and have been associated with the hopping of  $\text{Na}^+$  ions from site to site in the ionic conductors.

Similar activation energies of 0.186 eV for  $\beta$ -alumina and 0.142 eV for  $\beta''$ -alumina were obtained from these measurements. These results were obtained using Debye theory, i.e. assuming peaks occur where the product of angular frequency  $\omega$  and relaxation time  $\tau$  equals one. The peaks were found, however, to be much broader than expected for an interaction with ions which all have the same relaxation time. In the past, broadened peaks of this type have been explained by postulating a distribution of relaxation times,  $g(\tau)$ . The attenuation  $\alpha$  was then considered to be formed from contributions corresponding to all the relaxation times in the distribution as in equation 1.

$$\alpha = \int g(\tau) \frac{\omega^2 \tau}{1 + \omega^2 \tau^2} d\tau \quad (1)$$

Examples of the attenuation peaks found in  $\beta$ -alumina and polycrystalline  $\beta''$ -alumina are shown plotted against inverse temperature in Figs. 1a and 1b. The attenuation for an appropriate single relaxation time process is shown as a dashed line in each figure. The peaks are very similar in shape and are particularly asymmetrical. Conventionally this necessitates postulating a broad highly asymmetrical distribution of relaxation times, and by implication of barrier heights, in these materials. Such a distribution seems to be physically unreasonable in crystalline solids like the  $\beta$ -aluminas. In this paper we suggest an alternative interpretation of the data based on a re-examination of the relaxation process, similar to that which has successfully explained analogous features of the electrical

response of dielectrics.

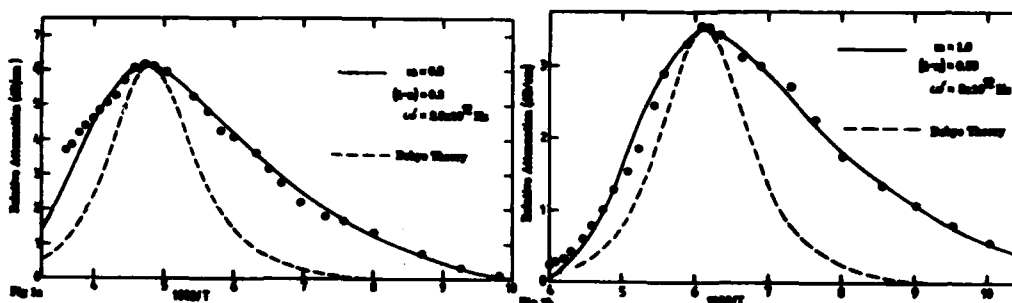


Fig.1. Attenuation of 240 MHz longitudinal waves in single crystal  $\beta$ -alumina, (Fig.1a) and 56 MHz longitudinal waves in polycrystalline  $\beta''$ -alumina (Fig.1b) versus inverse temperature. Fits of solid lines use parameters shown as explained in the text.

Jonscher<sup>(3)</sup> has shown that the dielectric loss in solids of all types cannot be explained using Debye theory and physically reasonable relaxation time distributions. He has suggested that the data indicates that the fundamental Debye theory assumption of pure exponential decay of dielectric perturbations is invalid. The "universal dielectric response"<sup>(3)</sup> of materials has been shown to be a consequence of non-exponential decay processes. In dielectric solids strong many-body interactions between electric dipoles cause non-exponential decay processes. Dielectric loss peaks are found to fit functions of the form

$$K''(\omega) \propto [(\omega/\omega_1)^{-n} + (\omega/\omega_2)^{1-n}]^{-1} \quad (2)$$

where the dielectric loss  $K''(\omega)$  is related to the thermally activated parameters  $\omega_1$  and  $\omega_2$  the relaxation time  $\tau$  has no meaning. The exponents  $n$  and  $(1-n)$  are related to the form of the decay process. In  $\beta$ -alumina and most other ionic conductors strong many-body interactions may be expected to influence the decay of perturbations in ionic concentration. The appropriate electrical response of  $\beta$ -alumina has been shown<sup>(4)</sup> to be very non Debye-like and to be fitted by a function of the form of equation 2. As both electrical and mechanical relaxation phenomena have been shown<sup>(1)</sup> to be related to  $\text{Na}^+$  ion diffusion it is suggested that equation 2 might be used in place of the usual Debye expression to account for mechanical relaxation peaks in ionic conductors. The solid lines in Figs.1a and 1b are fits of equation 3 below to the data.

$$a = 1/T [(\omega/\omega_1)^{-n} + (\omega/\omega_2)^{1-n}]^{-1} \quad (3)$$

In these  $\omega_1 = \omega_2 = a' \exp(-E_a/kT)$ , has been used with the activation energies  $E_a$  mentioned above. The other parameters used in the fits are shown in the figures. These are all similar to those employed to fit the electrical data<sup>(4)</sup> showing a detailed correspondence between electrical and mechanical relaxations in these materials. In this interpretation the highly asymmetrical loss peaks are a con-



sequence of the nonexponential decay of ionic concentrations. The value of  $(1-n)$  which controls the fit of the shallow gradient in attenuation on the low temperature sides of the peaks is similar to the value obtained in an AC conductivity study of  $\beta$ -alumina<sup>(5)</sup>. This study showed  $\beta$ -alumina to adhere to Joncher's universal law and to be very non Debye-like. Although for a non-exponential decay  $\tau$  has no meaning the parameters  $\omega_1$  and  $\omega_2$  are thermally activated and can be used<sup>(4)</sup> to obtain activation energies in the usual way.

The high temperature attenuation in  $\beta$ -alumina tends to deviate from the fitted curve. This is believed to be a residual effect of water contamination of the sample. Samples of the type studied here have been reported<sup>(6)</sup> to contain absorbed water. This appears to introduce a large additional contribution to the attenuation. The attenuation found before and after annealing<sup>(6)</sup> to remove the water is shown in Fig.2. Earlier measurements<sup>(7)</sup> were dominated by the effect of water and not the basic diffusion process. A similar phenomenon was found in the polycrystalline  $\beta''$ -alumina samples<sup>(2)</sup>.

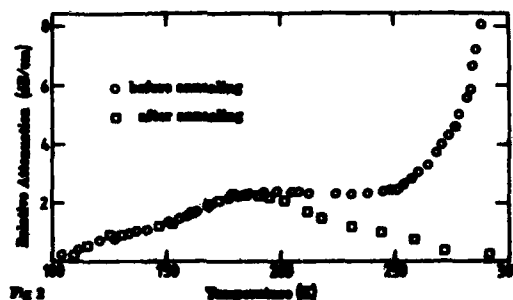


Fig.2. Attenuation of 100 MHz longitudinal waves in a single crystal sample of  $\beta$ -alumina before and after annealing to remove absorbed water.

#### References

1. D.P. Almond and A.R. West, Solid State Ionics (1981), in press.
2. D.P. Almond, H. Çallica and A.R. West, Mat. Res. Bull. 16(1981) 117.
3. A.K. Joncher, Nature, 267 (1977) 673.
4. D.P. Almond and A.R. West, Phys. Rev. Letters 47 (1981) 431.
5. R.J. Grant, I.M. Hodge, M.D. Ingram and A.R. West, Nature 266 (1977) 42.
6. T. Kameda, J.B. Bates, J.C. Wang and H. Engstrom, Mat. Res. Bull. 14 (1979) 1053.
7. D.P. Almond and A.R. West, Phys. Lett. 69A (1978) 130.

VIBRATIONAL DYNAMICS OF  $\text{RbAg}_4\text{I}_5$  BY RAMAN SPECTROSCOPY

E. Cazzanelli, A. Fontana, G. Mariotto and F. Rocca\*

*Dipartimento di Fisica, Università di Trento e Unità GNSM-CNR, Trento, Italy**\*Istituto per la Ricerca Scientifica e Tecnologica, Trento, Italy*

**Abstract.**— We have measured the temperature dependence of Raman scattering of superionic  $\text{RbAg}_4\text{I}_5$  from 20°K to melting point. We interpret our data in terms of a vibrational density of states.

The group compounds like  $\text{MAg}_4\text{I}_5$  ( $M = \text{Rb}, \text{K}, \text{NH}_4$ ) are well known for their properties of ionic conductivity at room temperature. For this reason they have been studied recently and compared with more famous compounds like  $\text{AgI}$ ,  $\text{CuI}$ , and  $\text{CuBr}$  which structure is much more simple but with the "disadvantage" to become superionic conductors at higher temperatures (1-3). The other cause of interest of  $\text{RbAg}_4\text{I}_5$  crystal is the presence of two phase transitions: the first at 120°K, the second at 208°K. After the former transition the  $\text{RbAg}_4\text{I}_5$  crystal is in superionic phase: this transition is associated to a discontinuity in ionic conductivity  $\sigma(T)$  (3). The last transition takes the crystal to an other phase (yet superionic) and it is associated with a discontinuity of  $d\sigma(T)/dT$  (4).

Both transitions are associated with a discontinuity in specific heat. The 208°K phase transition is a second order transition and it has been designated a disorder-disorder transition because neither the  $\alpha$  nor the  $\beta$ -phase can be ordered (5).

In spite of such transitions the vibrational dynamics measured by Raman spectroscopy does not change significantly in these three phases (6,7) (apart from the disappearance at 120°K of a small peak centered at  $23 \text{ cm}^{-1}$  among more of thirty peaks (7) and the appearing of a low quasi-elastic tail); while in  $\text{AgI}$  crystals we have a strong change in the shape of spectrum, with the appearing of large bands in  $\beta$ -phase and a strong quasi-elastic scattering in superionic phase (8). Finally we have no effects at 208°K transition. We have accurately measured Raman scattering in  $\text{RbAg}_4\text{I}_5$  as a function of temperature from liquid helium temperature to melting point.

Raman spectra were excited by He-Ne 6328 Å laser line with 5mW power on samples. The low power and defocalized radiation were necessary to avoid photosensitivity effects. The scattered light is dispersed by a double monochromator Jobin Yvon (2200 lines per mm); such double monochromator has a very large rejection of stray light: this rejection has allowed us to measure Raman spectra  $2 \text{ cm}^{-1}$  from laser line. Our unoriented samples were of pale yellow colour and high optical quality. They were grown from HI solution in E.T.H. in Zürich Laboratory and kindly provided us by Herbert Looser.

At liquid helium temperature the spectrum appears with a large number of peaks which are superimposed mainly in two zones centered at  $30 \text{ cm}^{-1}$  and  $100 \text{ cm}^{-1}$  respectively (Fig. 1).

The large number of peaks is not surprising because the  $\text{RbAg}_4\text{I}_5$  in its  $\alpha$ -phase has twelve molecules in unit cell (3).

The spectrum shape and the peak frequencies do not change with increasing tempe-

perature. Essentially we have a progressive broadening of peaks until the spectrum reduces to two large bands centered at the same above mentioned frequencies, showing a low unharmonicity but, too, that vibrational dynamics is not changing. Concurrently, the integrated Raman intensity between  $3 \text{ cm}^{-1}$  to  $13 \text{ cm}^{-1}$  range changes. Such intensity is reported in fig. 2, normalized by the Bose-Einstein population factor. We note that such low frequency scattering is very low and constant up to about  $80^\circ\text{K}$ , then it increases linearly until  $300\text{K}$  through the two phase transitions ( $T = 120^\circ\text{K}$ ,  $208^\circ\text{K}$ ). Above such temperature it tends to saturate. At the same time the integrated total Raman intensity has no change. In figure 3 we reports  $I_R(T)$  where

$$I_R(T) = \int_{3 \text{ cm}^{-1}}^{200 \text{ cm}^{-1}} \frac{I(\omega, T)}{n(\omega, T) + 1} d\omega$$

where  $I(\omega, T)$  is Raman intensity at  $\omega$  frequency and  $T$  temperature,  $n(\omega, T)+1$  is Bose-Einstein factor. Thus the data show that the total Raman intensity behaves as first order scattering until melting point. The different behaviour of Raman data reported by D.A. Gallagher and M. Klein near melting point, can be explained if we take in account the broadening of peaks centered at  $30 \text{ cm}^{-1}$ : there is no change in intensity but a broadening of peaks.

A possible explanation of the noted effects can be obtained if we take into account the  $\text{RbAg}_4\text{I}_5$  structure in its three phase ( $\gamma$ ,  $\beta$ ,  $\alpha$  at increasing temperature (3) and the high ionic  $\text{Ag}^+$  conductivity.

The absence of low frequency contribution to the normalized spectral density for temperatures below  $\sim 80^\circ\text{K}$  indicates that  $\text{RbAg}_4\text{I}_5$  at such temperatures is ordered, at least as far as Raman spectroscopy is concerned. Upon increasing temperatu-

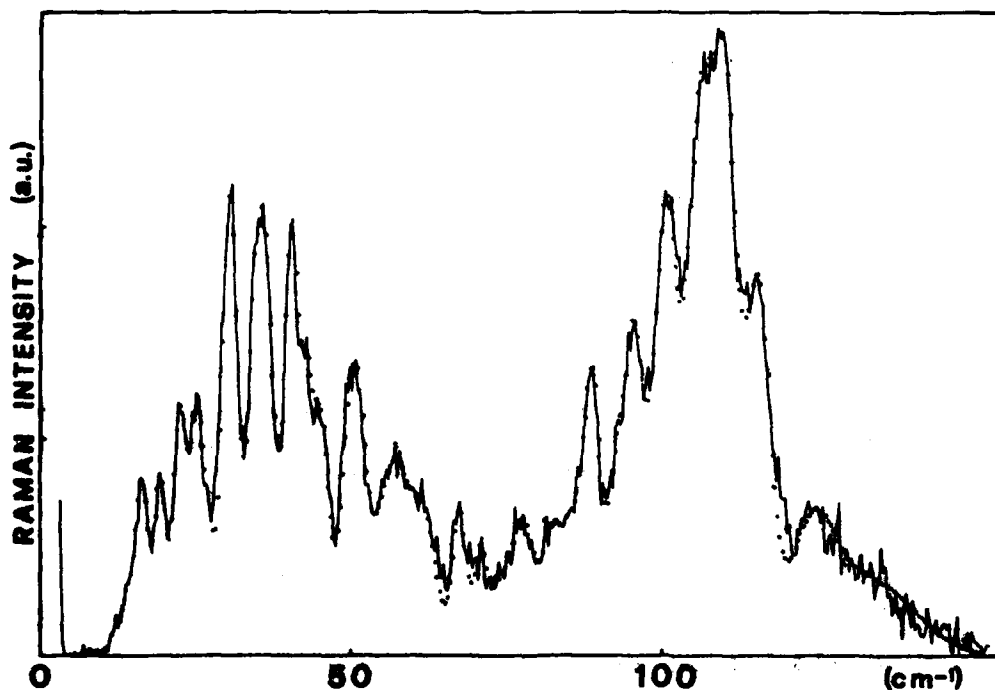


Fig. 1 :  $\text{RbAg}_4\text{I}_5$  Raman spectrum at  $22^\circ\text{K}$ . Solid line is experimental datum with  $0.5 \text{ cm}^{-1}$  resolution. The points are the fit with 30 gaussians.

re, as the remaining spectral features broaden the low frequency contribution starts to increase. This is an indication of incipient disorder in the system.

The effect of disordering will be to break wave vector conservation rule. Thus the low frequency scattering can be interpreted as a density of states contribution from the acoustic vibrational branches.

In  $\text{RbAg}_4\text{I}_5$ , such contribution is the only one that can be clearly isolated, since the remaining part of the spectrum change smoothly from the superposition of zone center normal mode peaks of the ordered system to a vibrational density of states which can hardly be distinguished from the ordered situation, given the large number of atoms in the unit cell (120) and the consequent flatness of dispersion curves. Thus the low frequency scattering intensity can be used as a probe of the progressive disordering of the  $\text{RbAg}_4\text{I}_5$  structure. Such local disordering starts in the  $\gamma$  phase and continues through the two following phase transitions. In this sense  $\text{RbAg}_4\text{I}_5$  can be considered to be always disordered, apart from the low temperature part of phase  $\gamma$  ( $T < 80^\circ\text{K}$ ), and its Raman spectrum for  $T \geq 80^\circ\text{K}$  is best described as a vibrational density of states.

The authors wish to thank prof. M.P. Fontana for valuable suggestions and discussions.

This work is partially supported by CNR contract number 80.00816.11.

- 1) W. Van Gool (editor): Fast Ion Transport in Solids, North Holland, Amsterdam, 1973
- 2) G.D. Mahan, W.L. Roth (editors): Superionic Conductors, Plenum Press, New York, 1976
- 3) S. Geller (editor): Solid Electrolytes, Springer Verlag, Berlin 1977
- 4) R. Vargas, M.B. Solomon, C.P. Flynn, Physical Rev. Lett. 37, 1550 (1976)
- 5) S. Geller, Phys. Rev. B14, 4345 (1976)
- 6) D.A. Callagher and M.V. Klein, Phys. Rev. B19, 4282 (1979)
- 7) G. Burns, F.H. Dacol, M.W. Shager, Solids St. Comm. 19, 287 (1976)
- 8) G. MacLotto, A. Fontana, E. Cassanelli and M.P. Fontana, Phys. Stat. Sol. b 101, 341 (1980)
- 9) R. Shaker and R.W. Gammon, Phys. Rev. Lett. 25, 222 (1970)

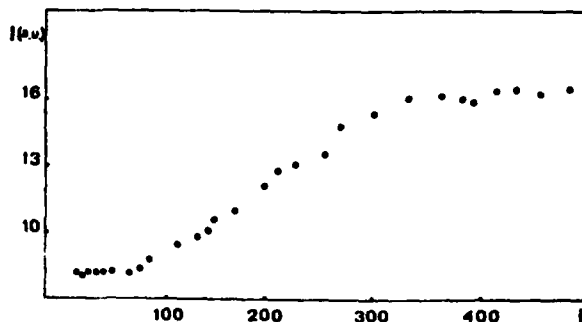


Fig. 2 : Integrated Raman scattering between  $3\text{ cm}^{-1}$  -  $13\text{ cm}^{-1}$  range as a function of temperature. The intensity is normalized by the appropriate Bose-Einstein population factor.

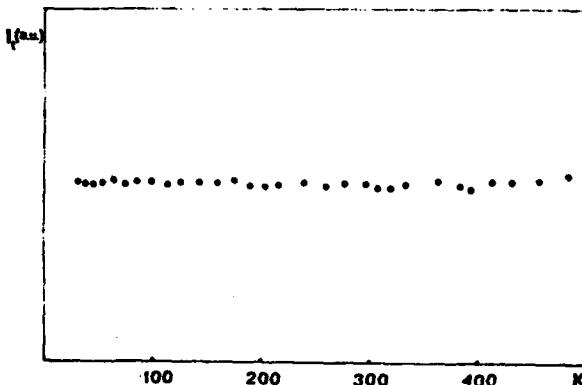


Fig. 3 : Integrated total Raman scattering as a function of temperature in the  $3\text{ cm}^{-1}$  -  $200\text{ cm}^{-1}$  range.

## LOW-TEMPERATURE SPECIFIC HEAT ANOMALY OF THE ONE-DIMENSIONAL IONIC CONDUCTOR HOLLANDITE

H.v. Löhneysen, H.J. Schink, W. Arnold<sup>\*\*</sup>, H.U. Beyeler\*, L. Pietronero\* and S. Strässler\*

2. Physikalisches Institut, RWTH Aachen, F.R.G.

\*BBC-Research Centre, Baden, Switzerland

Most amorphous materials contain localized excitations which strongly influence their low temperature properties; for example, for temperatures below a few K the specific heat varies almost linearly with temperature, and the thermal conductivity is drastically reduced compared to crystalline materials and generally exhibits a  $T^2$  dependence /1/. It is now accepted that these excitations arise from tunnelling of certain parts of the disordered network between two potential energy minima /2/. However, the question of the microscopic origin of the tunnelling systems has not been solved yet. Similar properties have been observed in superionic conductors /3/, and this seems to be particularly promising in order to elucidate the microscopic origin of these excitations because in superionic conductors the disorder can be reduced to two dimensions or even to one dimension. We have therefore carried out specific-heat measurements in the one-dimensional superionic conductor hollandite and we explain its specific heat in terms of a microscopic model.

In hollandite ( $K_{2x}Mg_xTi_{8-x}O_{16}$ ), the mobile  $K^+$  ions reside in a linear periodic potential which is substoichiometrically occupied. The channels containing the  $K^+$  ions do not communicate with neighbouring channels. By analysis of diffuse X-ray scattering a good description of the state of order has been obtained /4/. Each channel contains one site per unit cell along the c-axis and the fractional occupancy of these sites with  $K^+$  ions is equal to x. Very important is the ion-ion interaction within each channel: it removes the degeneracy of the energies of different configurations and causes the equilibrium position of the ions to shift from the local minima of the background potential. The question is: what are the configurational states in such a system and how do they contribute to the specific heat /5/? Specific-heat measurements have been carried out in two samples with  $x = 0.77$  and  $x = 0.78$  at temperatures between 70 mK and 3 K. The measurements were made in a dilution refrigerator using samples weighing about 100 mg each, and the results are plotted in Fig. 1 as a function of temperature. The specific heat first increases rapidly with temperature and then exhibits a maximum at .8 K for  $x = .78$  and at 1 K  $x = .77$ . The overall behaviour differs markedly from that found in glasses /2/ and in  $\beta$ -alumina or  $LiN_3$  /3/. Furthermore, it is very striking that a difference of only 1% in x causes the specific heat to change by a factor of four. Such a drastic effect calls for special attention.

<sup>\*\*</sup> present address: Fraunhofer-Institut, 6600 Saarbrücken, FRG

Let us start the discussion of the specific heat by defining an array of length  $n$  as a series of  $n$  consecutive wells occupied by ions which are surrounded by empty wells. For sufficiently high density of ions ( $x \geq .75$ ) we can neglect the occurrence of two or more empty wells adjacent to each other. A configuration is then specified by the set of array lengths  $[n]$ , e.g.  $[n] = 4;3;3;\dots$  indicates that we have a vacancy, then four occupied wells, a vacancy, three occupied wells etc. It has been shown that the total potential energy of a given configuration including the contribution of the ionic relaxation in each well due to the ion-ion interaction can be written in terms of a spin type Hamiltonian acting only between empty sites /4/:

$$V = \sum_{i,j} C(n^*) \sigma_i \sigma_j; \quad C(n^*) = J\alpha^{n^*} \quad (1)$$

Here  $J$  and  $\alpha$  ( $\leq 1$ ) are parameters related to the barrier height of the background potential and to the strength of the ion-ion interaction. The variable  $\sigma_j$  assumes the value 0 or 1 depending on whether the  $j$ -th site is occupied or empty, and  $n^*$  is the total number of occupied sites between the sites  $j$  and  $j'$ . The sum extends to all pairs of empty sites. With  $x=.77$  and using parameters appropriate to hollandite, a contribution to the specific heat  $T \geq 40$  K is expected due to transitions of type  $\dots;4;4;\dots \rightarrow \dots;3;5;\dots$ . The energy difference  $\Delta_1$  between these two configurations can be estimated from Eq. (1) limiting the interaction to nearest holes /4,6/:

$$\Delta_1 = C(3) + C(5) - 2C(4) = J\alpha^3(\alpha^2 - 2\alpha + 1) \quad (2)$$

However, for pairs of configurations that are degenerate with respect to the interaction between nearest holes like  $\dots;3;4;\dots \rightarrow \dots;4;3;\dots$  the interactions up to second nearest empty wells must be included. Transitions like  $\dots;4;3;4;3;\dots \rightarrow \dots;4;4;3;3;\dots$  might occur which have a characteristic gap  $\Delta_2$  /6/:

$$\Delta_2 = C(6) + C(8) - 2C(7) = \alpha^3 \Delta_1 \quad (3)$$

Because  $\alpha = .3$ ,  $\Delta_2$  is about 40 times smaller than  $\Delta_1$  and gives rise to a specific heat peak at  $T \approx 1-2$  K which agrees nicely with the experimental findings.

In order to understand the strong concentration dependence of the specific heat we need to take a closer look at the transitions that give rise to the peak. The probability of having a series of values like the starting configuration of Eq. (3) in the ground state is maximum if arrays with  $n=3$  and  $n=4$  appear with equal probabili-

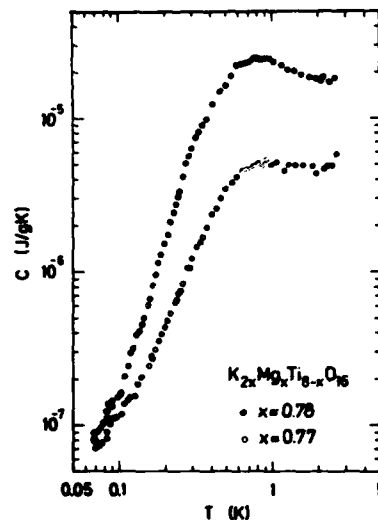


Fig.1: Specific heat of hollandite

ty. According to this argument the maximum specific heat is obtained for  $n = 3.5$  ( $x = \langle n \rangle / (\langle n \rangle + 1) = .77$ ) whilst it tends to zero for  $\langle n \rangle = 3$  ( $x = .75$ ) and  $\langle n \rangle = 4$  ( $x = .80$ ). For intermediate values of  $x$  a more detailed treatment is necessary, which, in fact, reproduces the strong variation of the specific heat by a factor of 4 /6/.

Comparing the absolute magnitude between the measured specific heat and the theoretical expected one we find that the theoretical curve is much larger. This is due to the fact that the system has been treated as an infinitely long chain, while the actual samples contain a high density of impurities so that the real system is a collection of separate segments of various lengths. The inclusion of finite chain length into theory drastically reduces the magnitude of the specific heat and we recover the experimental value if we assume the average separation between blocking ions to be about 10 lattice sites.

A further interesting question is how the transition actually occurs. In the model discussed above a configurational transition can be regarded as the hop of an ion into an empty site including the relaxation of all other ions. The tunnelling particle is therefore the jumping ion accompanied by the other relaxing ions. Taking an effective barrier of about 0.04 eV between the configurational states /4/ and taking the formula for relaxation due to tunnelling, we estimate a relaxation time  $\tau$  which is at least of the order of seconds at  $T \approx 1$  K. This value is rather uncertain owing to the unknown parameters describing the degree of overlap of the wavefunctions needed to calculate  $\tau$ . For comparison, the classical relaxation time (Arrhenius law) at this temperature would be of the order of  $10^3$  years.

In summary, we should like to point out that the low-temperature specific heat anomalies of a disordered system have been analyzed in terms of a microscopic model. Experiment and theory confirm that the disorder due to diffusing and interacting ions in an otherwise periodic potential can give rise to very low energy excitations but not to a continuous distribution of excitations. The transition between the states occurs via tunnelling.

#### References

- /1/ R.C. Zeller and R.O. Pohl; Phys. Rev. B4, 2029 (1976)
- /2/ See collected papers in Amorphous Solids, ed. W.A. Phillips, Springer, N.Y. (1981)
- /3/ P.J. Anthony and A.C. Anderson; Phys. Rev. B46, 3827 (1977)
- E. Gmelin and K. Guckelsberger; J. Phys. C, 14, L21 (1981)
- /4/ H.U. Beyeler, L. Pietronero and S. Straessler; Phys. Rev. B22, 2988 (1980)
- /5/ a more extensive report of the result presented here is given by the present authors in Phys. Rev. Lett. 46, 1213 (1981)
- /6/ L. Pietronero, W.R. Schneider and S. Straessler; to be published in Phys. Rev. B

# A THEORETICAL MODEL FOR THE CONTINUOUS ORDER-DISORDER TRANSITION AT 703 K IN SUPERIONIC $\alpha$ -AgI

V. Mazzacurati, G. Ruocco, G. Signorelli, E. Cazzanelli\*, A. Fontana\* and G. Mariotto\*

*Istituto di Fisica e Unità GNSM-CNR, Roma, Italy*

*\*Dipartimento di Fisica e Unità GNSM-CNR, Trento, Italy*

**Abstract.**— We interpret the Raman intensity behaviour and the depolarization ratio in superionic  $\alpha$ -AgI on the basis of a theoretical model.

A great deal of theoretical and experimental work has been devoted to study of solid electrolytes and especially AgI both in the superconducting "phase" ( $\alpha$ ) and in the normal one ( $\beta$ ). Recent experiments <sup>(1,2)</sup> show that the Raman spectrum of  $\alpha$ -AgI is essentially characterized by two broad bands, which are assigned to the acoustic and optical phonon density of states of the crystal respectively. The  $\text{Ag}^+$  ions (4 per unit cell) are randomly distributed and therefore their movements are essentially uncorrelated with  $\text{I}^-$  oscillations <sup>(3)</sup>. Furthermore the polarization ratio of the Raman spectrum is frequency independent and below 320°C has a value  $\rho = I_{\parallel}/I_{\perp} = 1.05$ . As a matter of fact if a liquid like distribution of  $\text{Ag}^+$  ions has to be expected, the depolarization ratio should not, in any case, exceed 0.75: only a model in which  $\text{Ag}^+$  ions are distributed randomly in a defined sublattice can in principle explain this value. An other peculiar result is that increasing the temperature both intensity and depolarization ratio decrease reaching above 430°C respectively a factor 12 less and the value of 0.68. In principle the  $\rho = 0.68$  value suggest that the disorder is increasing, while the decrease in intensity of the disorder allowed Raman spectrum can be interpreted only by supposing that the overall distribution of the  $\text{Ag}^+$  ions is more isotropic.

Following these considerations we will assume a very simple picture for our crystal (using mostly the same approximation adopted by Andreoni and Phillips in their recent paper <sup>(4)</sup>), in order to attempt an explanation of the experimental data. We suppose that the  $\text{Ag}^+$  ions can be located essentially in the d-sites obtained with the aid of a 3 interpenetrating bcc sublattices (see fig. 1). Around a given  $\text{I}^-$  we will have therefore 8  $\text{I}^-$  ions in a bcc lattice and 24 d sites that should allocate an average of 4  $\text{Ag}^+$  ions. We shall consider hereafter this 24 sites as constituting the "cage" relative to the central  $\text{I}^-$  ion. Each cage has 8 neighbouring cages, each having in common the hexagonal face evidentiated in Fig. 1.

The disorder in polarizability which gives raise to the Raman spectrum is introduced by deformation of the symmetric electronic cloud of each  $\text{I}^-$  ion by means of a randomly oriented electric field acting on this point polarizable charge due to the occupied sites of the cage. A given configuration of the  $\text{Ag}^+$  distribution in the crystal has a total energy, which is the

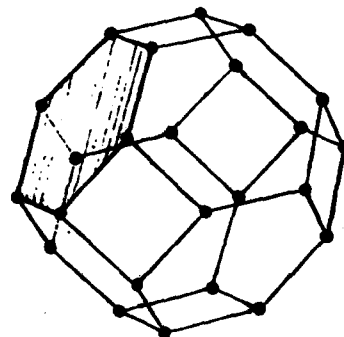


Fig. 1 : The cage with the 24 d-sites. The sketched face is that in common with the near cage.



sum of the covalent part of the bonds, the I-Ag<sup>+</sup> Coulomb attraction, and the I<sup>-</sup>-I<sup>-</sup> and Ag<sup>+</sup>-Ag<sup>+</sup> Coulomb repulsion. Supposing that both the covalent part and the screening of the electric field do not depend on the distribution considered, the only part of this energy that depends on the configuration is the Ag<sup>+</sup>-Ag<sup>+</sup> repulsion, depending on the mutual distances of the Ag<sup>+</sup> distribution. The simplest form is to assume for the induced polarizability a traceless tensor, which is diagonal in any cartesian frame having the z axis parallel to the resulting electric field ( $\vec{E}_{tot}$ ) applied in the central I<sup>-</sup> ion, the components being:  $\beta \begin{pmatrix} 1 & 0 & 0 \\ 0 & -1 & 0 \\ 0 & 0 & 2 \end{pmatrix}$  where  $\beta$  is a function of  $E_{tot}^2$  and, in a first approximation,  $\beta \propto E_{tot}^2$ . On the basis of such hypotheses, we may develop the induced polarizability in power series of atomic displacements and then obtain the Raman spectrum by Fourier transforming the correlation functions of these derivatives (5). We can write:

$$I_{ij}(\omega) \propto \int dt e^{i\omega t} \sum_{\mu, \mu'} \sum_{\alpha, \beta} \left( \frac{\partial P_{ij}^{\alpha}}{\partial x_{\mu}^{\alpha}} \frac{\partial P_{ij}^{\beta}}{\partial x_{\mu'}^{\beta}} \right) \langle \delta x_{\mu}^{\alpha} \delta x_{\mu'}^{\beta} \rangle$$

where  $\mu, \mu'$  are the I<sup>-</sup> ions, the polarizability derivatives of which have to be correlated,  $1'$  and  $1''$  are Ag<sup>+</sup> ions in two cages and  $\delta x_{\mu}^{\alpha}$  are a cartesian component of the relative displacements.  $I_{ij}$  is the 90° scattered intensity with incoming radiation polarized in the  $i$  direction and the outgoing radiation polarized in the  $j$  direction. The average  $\left( \frac{\partial P_{ij}^{\alpha}}{\partial x_{\mu}^{\alpha}} \frac{\partial P_{ij}^{\beta}}{\partial x_{\mu'}^{\beta}} \right)$  has to be taken over all possible distribution of

Ag<sup>+</sup> ion in the cages centered around  $\mu, \mu'$ . Assuming complete disorder in the orientation of the polarizability tensor, so to have only self correlation functions we have calculated the average as follows (each configuration has been chosen calculating repulsive interaction between Ag<sup>+</sup> ions). Using the stoichiometric distribution (4 Ag<sup>+</sup> in a given cage) the lowest configuration  $C_4^0$  has the Ag<sup>+</sup> located in a tetrahedral sublattice and can be realized in 6 different ways. This configuration, being symmetric, does not give any anisotropic induced polarizability, and therefore does not contribute to the disorder induced scattering. The next configuration  $C_4^1$  is clearly asymmetric and can be realized in 24 different ways. All other configurations are much more distant in the energy scale (see Table 1). For the polarizability derivatives  $\partial P_{ij}^{\alpha} / \partial x_{\mu}^{\alpha}$  it must be noticed that we will have in general 2 terms, one related to the variation of the modulus of the total electric field inducing the anisotropic polarizability and one related to the change in direction of the induced tensor. The expressions are identical to the two first terms in the polarizability modulation adopted in the paper of Alben and Burns (6). Of course both term have the effective charge again as a parameter. While for the change in direction we can presumably use the same value adopted in the repulsive energy calculation, related to the Phillips ionicity, we have to use the Szegedi charge in calculating the modulation of the electric field value. This gives in our case a fixed number to the ratio of the two coefficients limiting the choice of this polarizability expansion. By means of this number the polarization ratio calculated averaging over the 24  $C_4^1$  configuration becomes  $\rho = 0.68$ . The basic idea is to consider also cages with only three or five Ag<sup>+</sup>. Of course, if a cage has 3 Ag<sup>+</sup>, there must be elsewhere some other with 5 in order to achieve electrical neutrality. If we calculate the distribution of 3 and 5 Ag on the cage we obtain that: 1) the lowest energy configuration  $C_3^0$  and  $C_5^0$  are widely separated from the  $C_3^1$  and  $C_5^1$ , 2) the sum of the energies of isolated  $C_3^0 + C_5^0$

3		4		5	
$C_3^0$	.78	$C_4^0$	1.65	$C_5^0$	2.92
$C_3^1$	.79	$C_4^1$	1.65	$C_5^1$	2.95
$C_3^2$	.82	$C_4^2$	1.70	$C_5^2$	2.99
		$C_4^3$	1.73		

Tab. 1 : Energy in eV unit corresponding to the various configurations of N Ag<sup>+</sup> ions in the cage.

is greater than  $2 \times C_4^0$ , but not so much different. 3) the depolarization ratio is always  $\rho = 1.08$  for all the different realizations of the  $C_3^0$  and  $C_5^0$  configurations, and the same value is obtained also for the  $C_3^1$  and  $C_5^1$ . 4) Being each cage not at the stoichiometric value, if two cages with distributions  $C_3^0$  and  $C_5^0$  are close together, there is an additional attractive term which can be evaluated.

Of course the distribution of nearest neighbour cages influence one each other, so that, as an example at least two cages out of eight around a given  $C_3^0$  must be either  $C_4^0$  or  $C_5^0$ . Of course the idea of cages out of the stoichiometric population does not contradict the charge neutrality principle. Simply it states out that the correlation length of  $Ag^+$  is greater than the edge of the bcc  $I^-$  lattice.

At low temperature in the  $\alpha$ -phase we can assume "cage" structure of the crystal to be essentially that of neighbouring  $C_3$  and  $C_5$  configuration. The fraction of  $C_4^0$  and  $C_4^1$  is only a small part, and the partial correlation between  $C_3$  and  $C_5$  constitute an interconnected path, as if the system is beyond same percolation threshold. Increasing the temperature the number of  $C_4^0$  and  $C_4^1$  (in thermal equilibrium with each other) becomes more and more important and at a "critical" temperature of  $430^\circ C$  the number of  $C_4^0$  and  $C_4^1$  will be dominant, so that no interconnected paths can be found. With this picture we will have of course a decrease in the Raman intensity, connected to increasing number of  $C_4^0$  which do not contribute to the scattering process and a progressive decreases of the polarization ratio from the  $\rho_{C_3 C_5}$  value of 1.08 to the  $\rho_{C_4}$  value of 0.68. Our model has as parameter the fraction of cages  $C_4$ ,  $\eta(T)$  at every temperature. It is possible, however, to have such parameter by the Raman intensity behaviour  $I(T)$ ; in such manner the values of  $\rho(T)$  are determined without any other parameter. Fig. 2 shows  $I(T)$  and the corresponding parameter  $\eta(T)$ , while Fig. 3 shows the experimental  $\rho(T)$  and the value obtained with our model. The very good agreement gives us confidence in the validity of the proposed model and we shall try to use it to explain other experimental data, such as ionic conductivity, specific heat, etc.

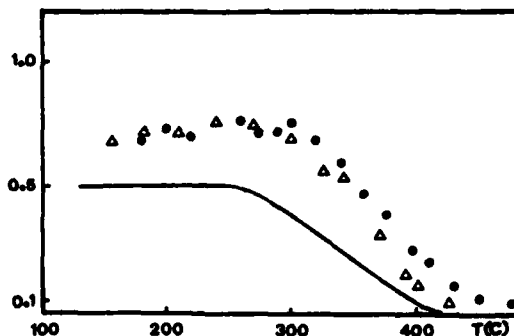


Fig. 2 : The points are the integrated Raman intensity. The solid line is the behaviour of  $\eta(T)$  by experimental data.

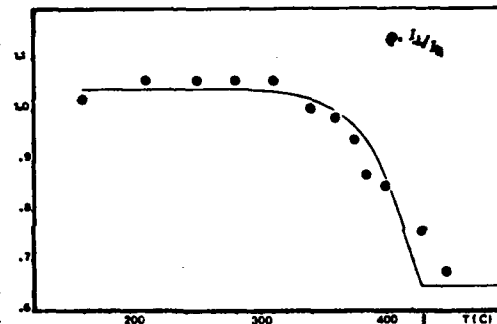


Fig. 3 : The points are the experimental data of depolarization ratio  $\rho$ . The solid line is the fit obtained by  $\eta(T)$ .

- 1) A. Fontana, G. Mariotto, M.P. Fontana, Phys. Rev. B **21**, 1102 (1980)  
G. Burns, F.H. Dacol, H.W. Shafer, Phys. Rev. B **16**, 1410 (1977)
- 2) G. Mariotto, A. Fontana, E. Cazzanelli, F. Rocca, M.P. Fontana, V. Mazzacurati, G. Signorelli, Phys. Rev. B **23**, 4782 (1981)
- 3) E. Cazzanelli, A. Fontana, G. Mariotto, F. Rocca, V. Mazzacurati, G. Ruocco, G. Signorelli, Solid State Ionics
- 4) V. Andreoni, J.C. Phillips, Phys. Rev. B **23** (1981)
- 5) To be published
- 6) P.C. Alben, G. Burns, Phys. Rev. B **16**, 3746 (1977)

**PHONON IMAGING AND PHONON FOCUSING**

## PHONON IMAGING

W. Eisenmenger

*Physikalisches Institut der Universität Stuttgart, 7000 Stuttgart 80,  
Pfaffenwaldring 57, F.R.G.*

**Abstract.**- Investigations of phonon propagation and scattering in solids use either coherent microwave phonons or incoherent phonons in the form of heat pulses<sup>1</sup> generated by current flow through thin metallic films and bolometer detection, or monochromatic incoherent phonons generated and detected with superconducting tunneling junctions<sup>2</sup>. Applying these techniques to a perfect single crystal, quantitative measurements require knowledge on phonon propagation in anisotropic media. In contrast to optic properties the acoustic propagation in anisotropic media is much more complicated by the large number of elastic constants. An additional complication arises if the dispersion of acoustic phonons is included. Whereas the propagation of coherent phonons is simply described by the anisotropic constant-energy surfaces in  $q$ -space, the propagation of incoherent phonons (generated by a point source) is determined by the distribution of group velocities. These distributions were first calculated by Taylor, Maris and Elbaum<sup>3</sup> with the result that specific propagation directions and modes show strong and sharply peaked intensity maxima. This phenomenon was called "phonon focussing". In later work also names as phonon channeling, phonon caustics etc. have been used. The pronounced sharpness of these distributions with strong intensity changes within angles of 1 degree raised strong experimental and theoretical interest for a more complete spacial description, or for imaging the phonon distributions. First, three-dimensional directivity patterns were obtained by computer analysis<sup>4</sup>. More recently, direct measurements of phonon intensity distributions<sup>5</sup> and, for instance, measurements with computer-aided spacial display<sup>6</sup> of the phonon intensity have led to impressive phonon images on crystal surfaces. Alternatively, it is also possible to obtain direct phonon images<sup>7</sup>, observing the thickness increase of a superfluid <sup>4</sup>He-film on the crystal surface by the fountain effect in regions of high phonon intensity. In this lecture the fundamentals of phonon focussing and phonon imaging techniques will be reviewed.

**1. Introduction.**- Phonon transport in solids by heat conduction is well-known as a quasi-equilibrium situation in which local thermal equilibrium is established by Normal and Umklapp processes. The heat flow vector is related to the temperature gradient by a second rank tensor equation, resulting in isotropic heat conduction for cubic crystals. At low temperatures phonon scattering by Normal and Umklapp processes becomes negligibly small, resulting in nonequilibrium phonon transport by ballistic-acoustic propagation. Stress and strain in the

acoustic waves are related by a 4th rank tensor which can be reduced to a 6 by 6 second rank tensor, resulting in 21 independent elastic coefficients for crystals of lowest symmetry. Cubic symmetry requires only three independent elastic coefficients still with a strongly anisotropic angular dependence of sound velocities for all three phonon modes. The angular dependence of sound velocity in general leads to very characteristic angular intensity variations and even singularities if phonons are excited incoherently by a point-like source. This phenomenon is called phonon focussing and is experimentally observed in all phonon propagation experiments using heater /bolometer configurations for phonon generation and detection. The same holds for phonon experiments with superconducting tunneling junctions or point-like phonon generation by optical excitation.

2. Nonequilibrium Ballistic Phonon Transport.— The first ballistic phonon pulse experiment was performed by Nethercot and von Gutfeld<sup>1</sup>. In this experiment, Fig. 1, phonons were pulse-excited at one surface of

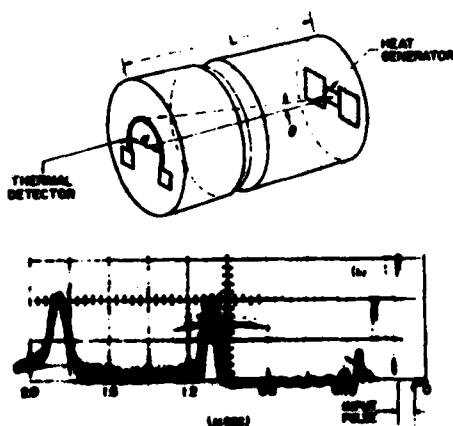


Fig. 1 Heat pulse method.

Top: c-sapphire crystal with phonon generator and detector.

Bottom: Detected phonon pulse signals at 1.2 K.

From right to left: Electric coupling signal, longitudinal phonon signal, transverse phonon signal. After R.J. von Gutfeld and A.H. Nethercot, Ref. 1

a c-cut sapphire by an evaporated metal heater and detected by a superconducting bolometer at the opposing surface. The observed signals show the expected acoustic times of flight, however, the signal amplitude ratio between transverse (degenerate) and longitudinal phonons by phonon density of states arguments should be much larger than found in the experiment. Similar unexpected results for signal amplitude ratios are observed in phonon pulse experiments with superconducting tunneling junctions<sup>2</sup>. In principle, this could be explained by mode-dependent phonon scattering or -attenuation during propagation. But changing the propagation distance should influence these ratios. This, however, was not observed; instead the signal amplitude ratios were found to be

strongly dependent on the propagation direction within the crystal. The experimental findings were properly explained as "phonon focussing"; i.e. a strong angular dependence of ballistic phonon intensities caused by crystal anisotropy; in the now classical work of Taylor, Maris and Elbaum<sup>3</sup>. Phonon focussing later has also been named phonon - channeling, - caustics, - catastrophe. Phonon focussing can be explained by the nonspherical phonon momentum surface at constant frequency,  $\omega(q) = \text{const.}$  for different phonon modes. Fig. 2 shows a section of this surface for the slow transverse, ST-mode in silicon. Since energy propagation, ac-

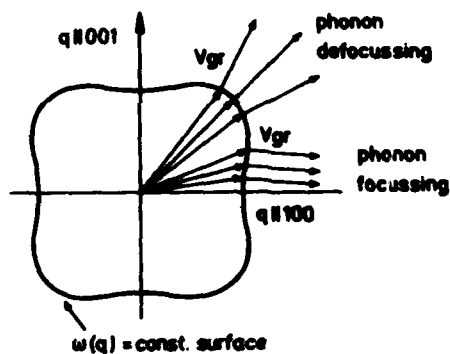


Fig. 2 Phonon focusing is shown to be caused by many q-states contributing to one group velocity from areas of the slowness surface  $\omega(q) = \text{const.}$  with small curvature. Example: 100 ST-mode-cross section for cubic crystals.

cording to the group velocity  $v_{gr} = \frac{\partial \omega}{\partial q}$  is normal to the  $\omega(q) = \text{const.}$  surface, it is evident that for regions with zero curvature (Gaussian curvature) a large number of q-states contributes to phonons with the same group velocity. Assuming equilibrium phonon occupation for all q-states, this results in high incoherent ballistic phonon intensities;

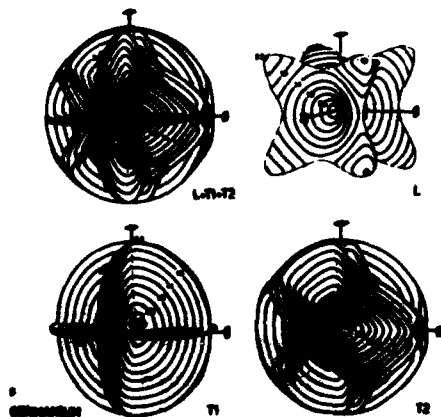


Fig. 3 Calculated phonon intensity surfaces for Ge. After F. Röscher and O. Weis, Ref. 4.

i.e. "phonon focussing" in the corresponding direction. In contrast, regions of strong curvature lead to phonon "defocussing". The  $\omega(q) = \text{const.}$  surface is called "slowness surface", since the phase velocity is small for large phonon momentum  $q$ . Based on the work of Taylor, Maris and Elbaum<sup>3</sup>, Rösch and Weis<sup>4</sup> performed computer calculations of the directivity pattern of phonon intensities caused by phonon focusing for several crystal systems. One example is shown for Ge in Fig. 3, by which the surprisingly high intensities for different modes and directions are visualized. Especially for fast transverse FT-modes and slow transverse ST-modes sharp focussing plains and also cusp structures are obtained.

3. Experiments on Directivity Patterns of Ballistic Phonon Propagation and Imaging of Phonon Intensity Distributions.— Stimulated by phonon intensity measurements in pulse experiments and the phonon wind influence on the dynamics of electron-hole droplets in semiconductors, recent experimental activity for investigating phonon focussing was forced. Indirect evidence for phonon focussing was found in phonon reflection and back-scattering experiments by Marx et al<sup>8</sup> and by Taborek and Goodstein<sup>9</sup>. First direct measurements of the angular intensity distribution of ballistic phonons propagating in Ge were performed by Hensel and Dynes<sup>5</sup>, as shown in Fig. 4. Phonons were excited by a pulse

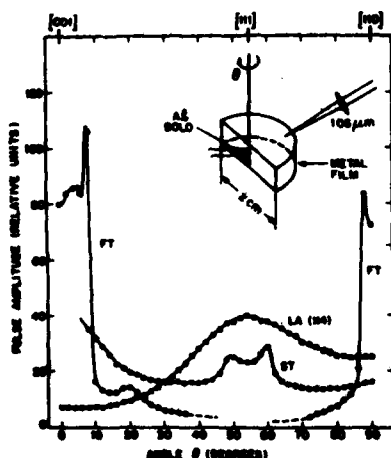


Fig. 4 Angle dependence of the phonon focusing in the (110) plane of Ge for LA, FT and ST-modes. Insert: Experimental arrangement. After. J.C. Hensel and R.C. Dynes, Ref. 5.

laser beam, moving the hot spot by crystal rotation. Different phonon modes were detected by one superconducting bolometer. The extremely high peaks for FT and ST modes, predicted by theory, could be clearly observed. The technique of moving the generator spot avoids the necessity for an array of detector bolometers.

Northrop and Wolfe<sup>6</sup> were able to "image" the angular phonon intensity

distributions in two dimensions by computer-aided visualization. Instead of crystal rotation, the movement of the laser excitation spot was achieved by x-y scanning with the help of two galvanometer mirrors. For detection, again one fixed bolometer was used. Selection of different modes is possible by delay-time-controlled signal-sampling. The very impressing phonon image, Fig. 5, obtained for Ge is equivalent to a

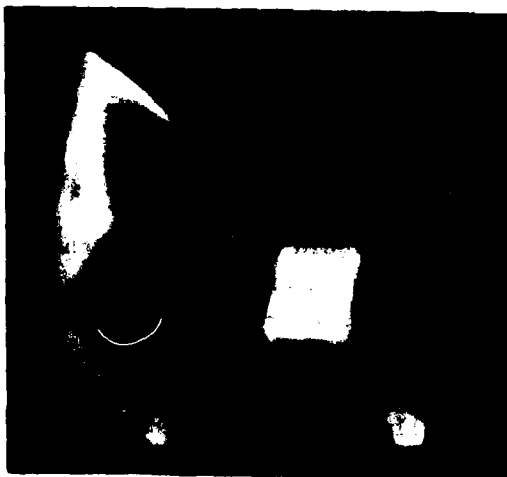


Fig. 5 Phonon focusing image for a  $1 \text{ cm}^3$  Ge crystal, obtained by computer-aided image construction, using bolometer heat pulse detection. Phonon pulse generation was performed with a pulsed laser and x-y scanning of the laser focus on the crystal surface. After G. Northrop and J. Wolfe, Ref. 6.

fixed phonon excitation point and a movable detector or an array of many detectors. This image is in full agreement with calculations<sup>3,4,5,6</sup>, see also Fig. 3. The extremely high accuracy and angular resolution of less than 1 degree is demonstrated in Fig. 6 for a larger Ge-crystal,

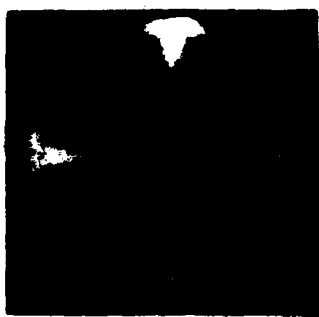


Fig. 6 High resolution ( $0.4^\circ$ ) phonon focusing image of the ST-mode near the  $[001]$  axis of Ge. Bright square width  $15^\circ$ . Computer-aided image construction. After G. Northrop and J.P. Wolfe, Ref. 6

showing the 100 phonon distribution in detail. Northrop and Wolfe<sup>6</sup> demonstrated these very complex structures again to be in agreement with theory.

A different technique<sup>7</sup> of visualizing angular phonon distributions makes use of the fountain pressure in the superfluid  $^4\text{He}$ -film covering



the crystal surface. The experimental arrangement is shown in Fig. 7,

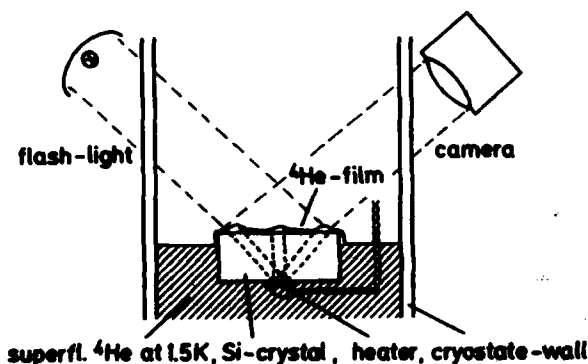


Fig. 7 Experimental arrangement for directly imaging phonon focusing by the fountain pressure in the superfluid  $^4\text{He}$ -film, covering the crystal sample. After W. Eismenger, Ref. 7.

the silicon crystal being partly immersed in liquid helium below the  $\lambda$  point. Phonons are generated by a small area heater at the crystal backside. When the heater is operated, phonons are propagating along the focusing direction and absorbed in the superfluid film covering the upper crystal surface. In these areas the temperature is raised by appr.  $10^{-4}$  K, leading to an increase of the He-film thickness by the fountain pressure. This kind of image conversion can be used to obtain directly visible phonon distribution patterns. The crystal surface is intentionally contaminated by condensed air or lampblack, increasing the optical contrast and enhancing the critical film flow velocity which sets an upper limit for film thickening by the fountain pressure, since in regions of increased film thickness evaporated helium must be replenished by superfluid film flow. The phonon distribution photographed for a 111 silicon crystal is shown in Fig. 8, revealing the threefold symmetry

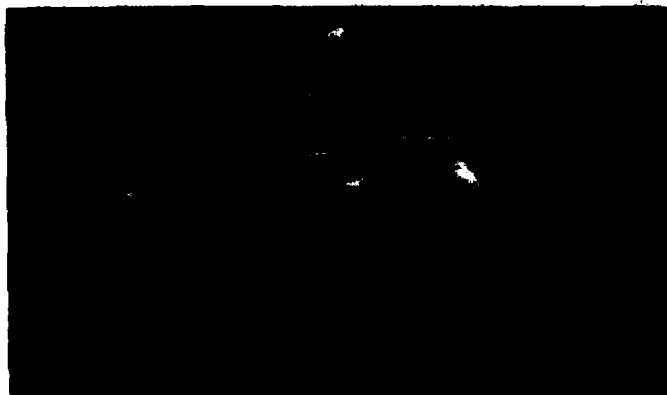


Fig. 8 Phonon focusing image at the surface of a (111)-Si-crystal. After W. Eismenger, Ref. 7.

and the phonon focusing structures expected from theory, c.f. Fig. 3. Corresponding pictures have been obtained for Ge crystals and it was also possible to photograph these distributions under vertical direction. An easy comparison with theory is possible by computer calcula-

tion of the surface phonon distribution for the crystals used by a Monte-Carlo-Method<sup>10</sup>. The corresponding result for silicon 111 is shown in Fig. 9.

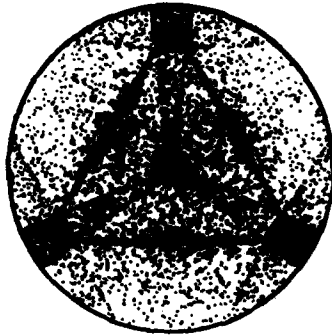


Fig. 9 Monte-Carlo simulation of the phonon focusing image in Fig. 9. After D. Marx, Ref. 10.

4. Conclusions.- Phonon imaging demonstrates the strongly anisotropic angular distributions of phonon intensities in nonequilibrium ballistic propagation, well in accord with theory and based on classical elastic theory now elaborated in detail by computer calculations. These findings are very important for absolute phonon intensity and propagation measurements which are evidently strongly influenced by phonon focusing in all crystals even in those which show little deviation from a spherical slowness surface, such as e.g. sapphire. The same applies to quantitative phonon reflection and scattering experiments and studies as to how phonon focusing images change under the influence of frequency dispersion<sup>11</sup> at high frequencies. Phonon imaging may also be applied for investigations of impurity, isotope and on general imperfection scattering, leading to smeared-out images. Therefore, phonon imaging appears as an important experimental tool in nonequilibrium ballistic phonon physics.

Acknowledgment.- I am especially indebted to G. Northrop and J. Wolfe for kindly supplying the original photography for Fig. 5. Supply of data and helpful discussions with Mrs. S. Döttinger, S. Döttinger, D. Marx, D. Schmid and Prof. O. Weis are gratefully acknowledged.

References.-

1. R.J. von Gutfeld and A.H. Nethercot Jr. Phys. Rev. Lett., 12, 641, (1964). For a review see R.J. von Gutfeld in Physical Acoustics, (W.P. Mason Ed.), Vol.5, p. 233, Academic Press New York, 1968.
2. W. Eisenmenger and A.H. Dayem, Phys. Rev. Lett. 18, 125, (1967) ; Kinder (H.) Phys. Rev. Lett. 28, 1564, (1972) for reviews see W. Eisenmenger, in Physical Acoustics (W.P. Mason and R.N. Thurston Eds.) Vol. 12, p. 79, Academic Press, New York, 1976; W.E. Bron, Rep. Prog. Phys. 43, 301, 1980;

- W. Eisenmenger, in Proceedings of NATO Advanced Study Institute on Nonequilibrium Superconductivity, Phonons and Kapitza Boundaries, (K.E. Gray Ed.), Plenum Press New York, 1981, see also V. Narayanamurti, Science, 1981.
3. B. Taylor, H.J. Maris and C. Elbaum, Phys. Rev. Lett., 23, 416, (1969) and  
B. Taylor, H.J. Maris and C. Elbaum, Phys. Rev., B3, 1462, (1971).
  4. F. Rösch and O. Weis, Z. Phys., B25, 115, (1976)
  5. J.C. Hensel and R.C. Dynes, Phys. Rev. Lett., 43, 1033, (1979), and  
J.C. Hensel and R.C. Dynes, in Proceedings of the Third International Conference on Phonon Scattering in Condensed Matter (H.J. Maris Ed.), Plenum, New York, 1980, p. 395.
  6. G.A. Northrop and J.P. Wolfe, in Proceedings of the Third International Conference on Phonon Scattering in Condensed Matter, (H.J. Maris Ed.), Plenum, New York, 1980, p. 377.  
G.A. Northrop and J.P. Wolfe, Phys. Rev. Lett., 43, 1424, (1979)  
and in Phys. Rev. B 22, (1980). See also  
J.P. Wolfe, in Physics Today, p. 44, Dec. 1980.
  7. W. Eisenmenger, in Proceedings of the Third International Conference on Phonon Scattering in Condensed Matter (H.J. Maris Ed.), Plenum, New York, 1980, p. 303.
  8. D. Marx, J. Buck, K. Lassmann and W. Eisenmenger, J. de Phys., C 6, Suppl. to No. 8 (1978) C 6 - 1015.  
D. Marx and W. Eisenmenger, Phys. Lett., 82A, (1981), 291.
  9. P. Taborek and D. Goodstein, J. Phys., C 12, 4737 (1979); Sol. St. Comm., 33, 1191 (1980) and in Proceedings of the Third International Conference on Phonon Scattering in Condensed Matter, (H.J. Maris Ed.), Penum, New York, 1980.
  10. D. Marx, Dissertation, Univ. Stuttgart, 1981, to be published.
  11. W. Dietsche, G.A. Northrop and J.P. Wolfe, 1981, to be published.

## FOCUSING OF DISPERSIVE PHONONS IN Ge

G.A. Northrop, W. Dietsche, A.D. Zdetsis and J.P. Wolfe

*Physics Department and Materials Research Laboratory, University of Illinois, Urbana, IL. 61801, U.S.A.*

**Abstract.**—Singularities in the phonon flux are observed and calculated for dispersive phonons in Ge.

The intensity of ballistic heat pulse propagation is highly anisotropic for most crystals, an effect known as phonon-focusing. Phonon focusing has been studied in many materials, both with fixed source and detector, and more recently with lasers as movable heat-pulse sources.<sup>1,2</sup> A quantitative explanation originally offered by Maris was based on calculating an enhancement factor,<sup>3</sup>  $A = |d\Omega_k/d\Omega_v|$ , the ratio of  $\vec{k}$ -space to  $\vec{v}$ -space solid angles. This factor describes how the phonon flux is increased or decreased over the isotropic case. The locus of points  $d\Omega_v = 0$  forms lines that mark directions of peak phonon flux.

These singularity lines have been observed by scanning a pulsed laser as a heat source over one surface of a crystal and recording, as a continuous function of propagation direction, the heat pulse intensity received by a fixed detector on the opposite face.<sup>2</sup> This technique, known as ballistic phonon imaging, was used to produce the picture in Fig. 1a for Ge. Here, X-Y position on the sample face corresponds to a range of propagation directions, and brightness is proportional to phonon intensity. The bright lines bounding light areas are singularity lines, in good agreement with the theoretically predicted singularity lines in Fig. 2.



**Fig.1:** Al detector (low- $v$ ) phonon image. Pb-O-Pb detector (high- $v$ ) phonon image.

In this paper we extend these experimental and theoretical results to include the effects of velocity dispersion which occur at higher phonon frequencies. To observe the effects of dispersion on the singularity directions in Ge, two modifications have been made to our phonon imaging technique:<sup>2</sup> 1) A thin sample (0.5 mm) and greater time resolution (60 ns) are used to offset the smaller mean-free-path of larger- $\vec{k}$  phonons. 2) A tunnel-junction (Pb-O-Pb) detector is used to detect phonons with  $\nu > 700$  GHz. An Al bolometer is used for detection of low- $\nu$  phonons.

Comparison of the two images for these two detectors, Fig. 1a and Fig. 1b, reveals three major differences: 1) The wedge shaped ridges (FTA mode) extending horizontally and vertically from the two diamond shapes are wider in the high frequency image than in the low frequency image. 2) The two diamond structures (STA mode) about the  $\langle 100 \rangle$  directions in the low frequency image are noticeably rounded at higher frequencies. 3) The sharp, three-fold symmetric pattern (STA mode) to the left and right of center in Fig. 1a has disappeared in Fig. 1b.

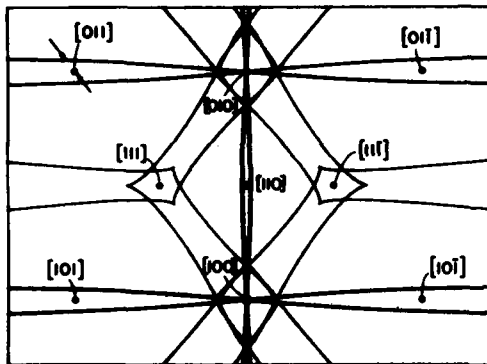


Fig.2: Zero frequency singularities.

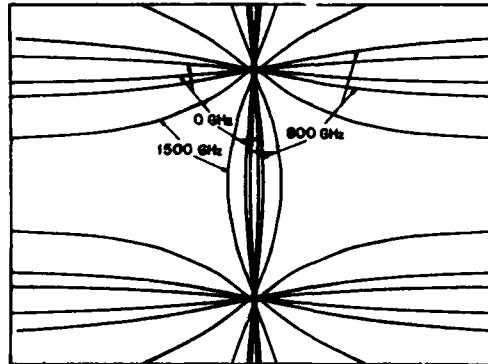


Fig.3: FTA mode frequency dependence.

In the non-dispersive phonon-focusing theory an area (solid angle) in  $\vec{k}$ -space transformed or mapped into an area (solid angle) in  $\vec{v}$ -space. This was independent on  $|\vec{k}|$ , and  $|\vec{v}|$  was fixed for each direction of  $\vec{k}$ . In the dispersive case these restrictions are removed and a more general formulation is required. Thus we define the dispersive enhancement factor  $A_3 = |d^3\vec{k}/d^3\vec{v}|$ . This is the ratio of an infinitesimal volume in  $\vec{k}$ -space to its corresponding volume in  $\vec{v}$ -space. By analogy to the non-dispersive case singularities will occur when  $d^3\vec{v} = 0$ , and, due to the increased number of dimensions, the locus of singularities will be surfaces in  $\vec{k}$ -space and  $\vec{v}$ -space. In our experiment, we study these surfaces by sectioning them at a fixed frequency.

The computation of  $A_3$  is based upon a model<sup>4</sup> of the full Brillouin-zone phonon band structure for Ge. This extended Born-Von Karman scheme parameterizes the lattice dynamics with 20 force constants representing up to fifth nearest neighbor interactions. With these constants adjusted to fit inelastic neutron spectra the model provides  $\omega(\vec{k})$  for all modes and any value of  $\vec{k}$ .

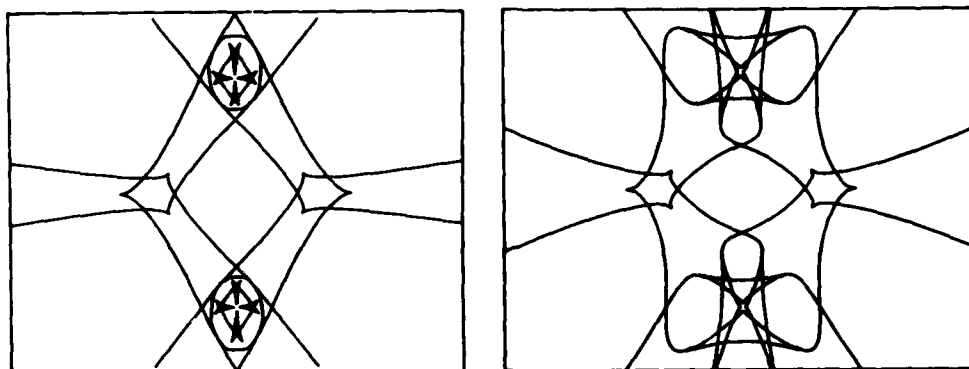


Fig. 4: STA mode at 800 GHz.

Expected STA pattern at 1500 GHz.

Since  $\vec{V}(\vec{k}) = \nabla_{\vec{k}} \omega(\vec{k})$ , and  $A_3$  is the Jacobian of this function,  $A_3$  includes second derivatives of  $\omega(\vec{k})$ , and is here determined by finite difference methods. A two dimensional root-finding routine then finds lines for which  $\omega = \text{constant}$  and  $A_3^{-1} = 0$ . These lines are projected in  $\vec{V}$ -space into the experimental geometry. These calculations have been done for both transverse modes for frequencies between 700 and 1600 GHz. The results for two frequencies are shown in Figs. 3 and 4.

The broadening of the FTA ridge singularities with increasing frequency can be seen in Fig. 3. The experimental Pb-O-Pb data agrees well with the prediction for  $\nu = 800$  GHz. The change of the STA singularity pattern is more complex, as shown in Fig. 4a. Note the rounding of the corners of the diamond structure as observed in Fig. 1b. The three-fold pattern about the  $\langle 111 \rangle$  direction in Fig. 4a has changed little, thus its absence from Fig. 1b must be due to reasons other than phonon-focusing. Fig. 4b is the  $\vec{V}$ -space (STA) pattern expected at 1500 GHz.

In summary, we have observed shifts due to dispersion in the phonon-focusing singularity patterns in Ge. These shifts agree with predictions obtained from a model of the full lattice dynamics in Ge.

This work was supported by the National Science Foundation under Grant DMR-80-20250.

#### REFERENCES

1. J. C. Hensel and E. C. Dynes, Phys. Rev. Lett. 43, 1033 (1979).
2. G. A. Northrop and J. P. Wolfe, Phys. Rev. Lett. 43, 1424 (1979); Phys. Rev. B22, 6169 (1980).
3. H. J. Maris, J. Acoust. Soc. Am. 50, 812 (1971).
4. A. D. Zdetis, Proc. Int. Conf. on Lattice Dynamics, p. 45, Paris (1978).

## SINGULAR EFFECTS IN PHONON FOCUSING ; FORMATION OF PHONON FOCUSING CAUSTICS

J.C. Hensel, R.C. Dynes, F.C. Unterwald and A.L. Simons

*Bell Laboratories, Murray Hill, New Jersey 07974, U.S.A.*

**Abstract** - We have conducted a comprehensive investigation into singular effects in phonon focusing. Measured focusing angular distributions and networks of caustics are in excellent agreement with theory.

Phonon focusing is the tendency of the flux of phonons emanating from a localized source to concentrate, owing to elastic anisotropy, along certain directions in a crystal. This phenomenon has been recognized for some time.<sup>1</sup> Only recently, however, we found<sup>2</sup> that there are certain cases where the phonon intensity becomes extremely intense, almost singular in nature. This paper gives a brief account of these investigations.

The origin of focusing can be visualized by referring to the slowness surface  $\omega(\vec{q}) = \omega[\omega(\vec{q}) \text{ and } \vec{q} \text{ being, respectively, the frequency and wavevector of the phonon}]$  shown in Fig. 1. The highly convoluted shape is responsible for a plethora of focusing structure. The directionality of the phonon flux is defined by the group velocity  $\vec{v}_g = \nabla_{\vec{q}} \omega(\vec{q})$ , a vector normal to the surface. This fact implies that focusing can be identified with a certain geometry property of the surface, namely the Gaussian curvature  $K$ , the product  $\kappa_1 \kappa_2$  of the two principal curvatures of the surface. The relationship is  $A^{-1} = q^2 K / \cos \delta$ , where  $A$  is the focusing enhancement factor and  $\delta$  is the angle between  $\vec{q}$  and  $\vec{v}_g$ .  $A$  becomes large where curvature is small. Indeed, when  $K = 0$ , as indicated in Fig. 1 by heavy solid curves called critical lines, there occur singularities in focusing.

The experiments consisted of angular scans with the geometries shown in Fig. 2. A small ballistic phonon source ( $\sim 50 \mu\text{m}$  diam. laser spot) and small detector ( $80 \times 80 \mu\text{m}^2$  bolometer) yielded an angular resolution of  $\sim 25$  minutes of arc.

An angular distribution of phonon intensity in the  $(1\bar{1}0)$  plane of Ge, obtained with the setup in Fig. 2a, is shown in Fig. 3. Its most prominent features are

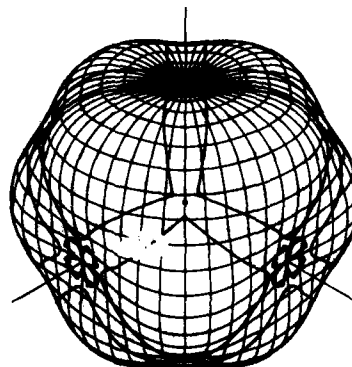


Fig. 1. T2 slowness surface.

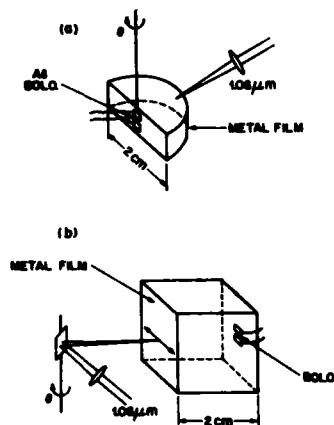


Fig. 2. Experimental geometry.

strong, sharply defined beams of focused phonons centered on the  $[100]$ ,  $[111]$ , and  $[1\bar{1}0]$  axes. This dramatic structure is typical of transverse phonons; for longitudinal phonons whose slowness surface is more nearly spherical the behavior is relatively gentle (see, e.g., Fig. 4). These beams manifest a fine structure seen as spikes, which derive from critical points (where  $K = 0$ ) on the slowness surface.

A calculation of the focusing in the  $(1\bar{1}0)$  plane of Ge is given in Fig. 4. (The units scale directly with the data in Fig. 3.) Effects of detector geometry are included in the calculation; the solid curves are for the present geometry, whereas the dotted curves represent a larger bolometer used in earlier work.<sup>2</sup> One sees excellent agreement between calculation and data.

Further insight into the nature of focusing is provided by the caustics, 2-dimensional plots of the loci of the focusing peaks. A remarkable example is the  $(100)$  pattern in Fig. 5 obtained with the scanning scheme<sup>3</sup> in Fig. 2b. One sees an intricate pattern exhibiting overall the 4-fold symmetry of the  $[100]$  axis. Both possible topological classes of phonon caustics are exemplified in Fig. 5. The

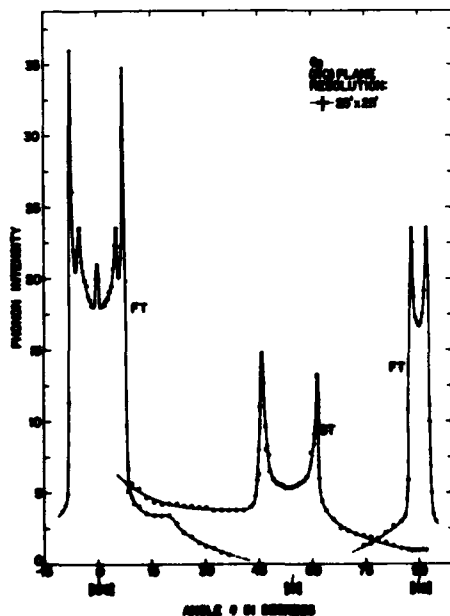


Fig. 3. Angular distributions: experimental

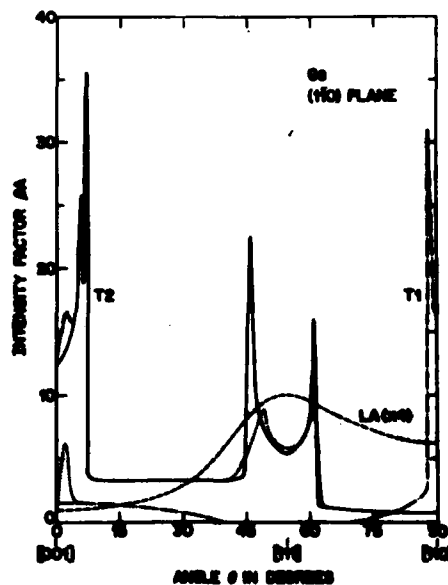


Fig. 4. Angular distributions: theory.



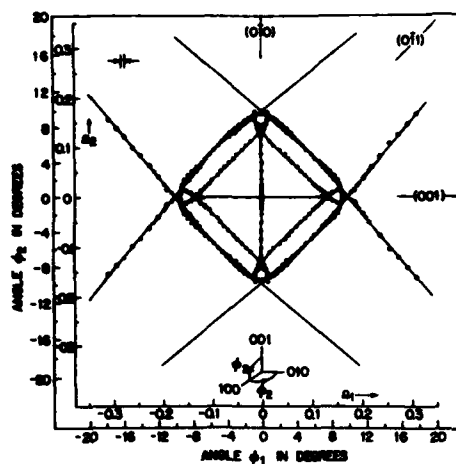


Fig. 5. (100) caustics: experimental.

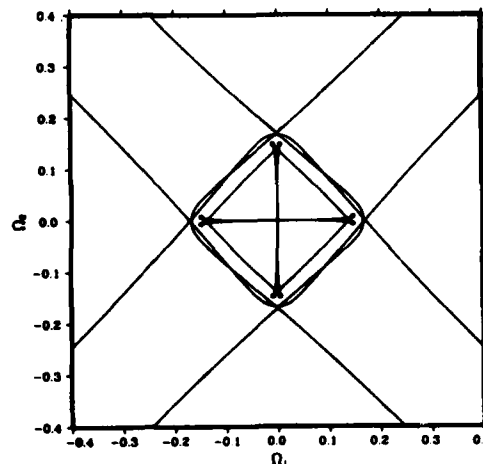


Fig. 6. (100) caustics: theory.

curves are fold caustics; but careful examination also reveals 8 cusps, 2 at each corner of the inner square.

The caustics are generated by mapping the critical lines in Fig. 1 onto the plane of observation via the vector  $\vec{v}_g$ . Results for the (100) plane are shown in Fig. 6 replicating the experimental data in Fig. 5. The cusps occur whenever the eigenvector corresponding to the nonvanishing principal curvature  $\kappa_2$  on a critical line rotates and becomes tangential to the critical line. Points satisfying this criterion are marked by small circles in Fig. 1 which map precisely onto the tips of the cusps (small circles) in Fig. 6.

To summarize, we have carried out a comprehensive study of phonon focusing which reveals sharp singularities arranged in characteristic configurations called caustics. Theory matches the data very closely with no more input than the known elastic constants.

It is a pleasure to acknowledge numerous valuable conversations with M. Lax.

#### REFERENCES

1. B. Taylor, H. J. Maris, and C. Elbaum, *Phys. Rev.* **B3**, 1462 (1971).
2. J. C. Hensel and R. C. Dynes in *Physics of Semiconductors 1978* (Institute of Physics, Bristol, 1979), p. 371 and *Phys. Rev. Lett.* **43**, 1033 (1979).
3. Photographic methods for recording caustics are described by W. Eisenmenger in *Phonon Scattering in Condensed Matter*, H. J. Maris, ed. (Plenum, New York, 1979), p. 303 and J. P. Wolfe, *et al.*, *ibid*, p. 377.

## PHONON FOCUSING AND THE SHAPE OF THE RAY SURFACE IN CUBIC CRYSTALS

A.G. Every

*Department of Physics, University of the Witwatersrand, Johannesburg, South Africa*Abstract.

A systematic study has been carried out on the dependence of the phonon ray surface of cubic crystals on elastic constants. The correspondence between folds in this surface and the presence of caustics in the flux of phonons emanating from a localised heat source is explored. The line, cusp, butterfly and hyperbolic umbilic elementary catastrophes as well as some remarkable types of structural instability are shown to occur in these caustics. A method is demonstrated for portraying the ray surface which provides an immediate indication of the number of separate components a ballistic heat pulse will split up into on propagating in various directions, and what the relative intensities and the spacings of these components will be.

1. Introduction.— In the long wavelength limit continuum elasticity theory can be used for calculating acoustic phonon phase and group velocities /1,2/. The information thus gained is conveniently displayed in the form of velocity ( $v$ ), slowness ( $S$ ) and ray ( $V$ ) surfaces /3/. The ray surface is of central importance in phonon imaging /4-6/, in that it maps out the profile of a ballistic heat pulse one unit of time after it has emanated from a point source at the origin. This surface is commonly studied in conjunction with  $S$ . The two are polar reciprocals of each other and the ray vector for a phonon is normal to  $S$ . Moreover, phonon flux is inversely proportioned to the curvature of  $S$  / 7 /. Contours of zero Gaussian curvature (parabolic lines) in  $S$  give rise to folds in  $V$  and divergent phonon flux. At conical points the curvature of  $S$  is infinite. Such points map onto circles in  $V$  at which the two transverse sheets join up smoothly and the phonon intensity is zero. The folds in  $V$  form complex patterns which are a function of the crystalline anisotropy.

2. Cubic crystals.— The folding pattern here is determined by the elastic constant ratios  $a = C_{11}/C_{44}$  and  $b = C_{12}/C_{44}$ . For stability a crystal has to lie in the wedge shaped area between the lines  $a = -2b$  and  $a = b$  in the  $(a,b)$  plane. This area may be subdivided into a limited number of regions in each of which  $V$  possesses certain distinct topological features. For instance, between the lines  $b = 1$  and  $6(a-b+1)^2(b+1)-3(a-b-2)^2(b+1)-(a-b+1)(a-b-2)(8a+13b+5) = 0$ , the folding pattern shown in fig. 1b holds for the slow transverse ( $T_1$ ) sheet of  $V$ . Fig. 1a shows the location of parabolic lines on  $S$  that map onto these folds. These lines separate regions of  $S$  which are convex (both principal curvature positive), saddle shaped (one curvature negative) and concave (both curvatures negative).

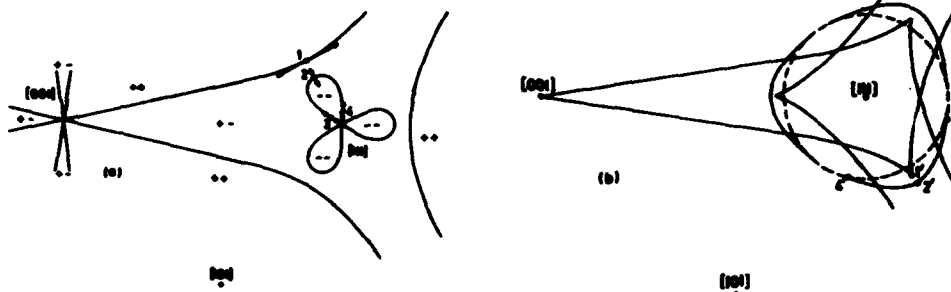


Fig. 1: Correspondence between (a) parabolic lines in  $S$  and (b) folds in  $V$  for slow transverse ( $T_1$ ) phonons. The diagrams are limited to the vicinity of the irreducible sector of the unit sphere lying within the  $[001]$ ,  $[101]$  and  $[111]$  directions.

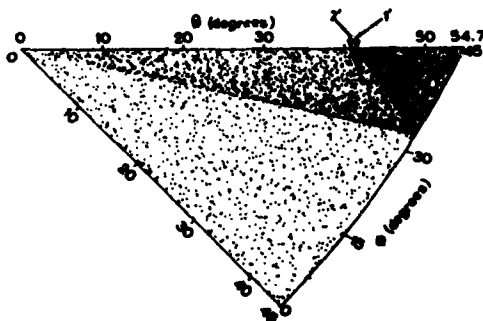


Fig. 2: Phonon enhancement map for  $T_1$  phonons in  $\text{CsCl}$ . The points represent group velocity directions for a uniform distribution of wave normals on average  $0.5^\circ$  apart.

It is noteworthy that the parabolic lines which meet at the conical point are responsible for part of a fold edge which weaves back and forth between the  $T_1$  and fast transverse  $T_2$  sheets of  $V$ , meeting the conical circle tangentially where it makes the crossing. The integrated intensity across the caustic diminishes as the caustic approaches the conical circle, as can be seen in fig. 2.

The symbol  $\uparrow$  is used to indicate the direction of the vanishing principal curvature. Where this is parallel to the parabolic line a cusp appears in the folding line of  $V$  /8/, except at conical points where the aforementioned effect takes place. For certain values of the elastic constants 8 fold lines in the  $T_1$  sheet of  $V$  converge to a point in the  $\langle 100 \rangle$  directions. This represents a structurally unstable situation which results from the degeneracy of the  $T_1$  and  $T_2$  modes in these directions. On varying the elastic constants some of the higher elementary catastrophes are exhibited. A configuration of 3 cusps which coalesce into a single one in conformity with the butterfly catastrophe can be observed in the cube planes near the  $\langle 100 \rangle$  directions. The cusp then makes contact with a neighbouring fold line to give rise to the hyperbolic umbilic catastrophe.

Fig. 3 shows the pattern of fold lines in  $V$  that obtains for the  $T_1$  sheet when the anisotropy lies between the two lines  $a^2 + (a-1)(b+1) - 2(b+1)^2 - 1 = 0$ , and  $(a-1)(a+b) + (a-2)(b+1)^2 = 0$ .

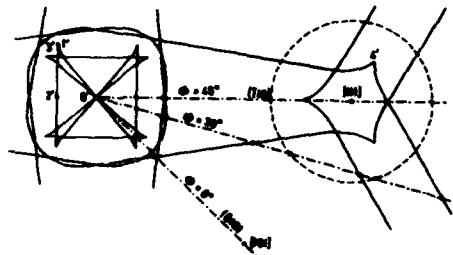


Fig. 3: A folding pattern for the  $T_1$  sheet of V.

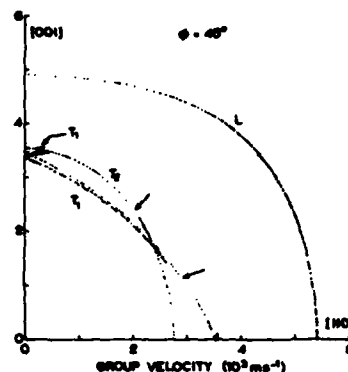


Fig. 4: A polar section of the full ray surface of Ge for  $\phi = 45^\circ$ . The mode points denote ray vectors which lie within  $0.5^\circ$  of this plane.

Fig. 4 shows a  $\phi = 45^\circ$  polar section of the full ray surface of Ge, a crystal which satisfies the above criterion. Sectioned fold edges appear as cusps in this diagram, and arrows indicate the position of the conical circle. Diagrams of this type, by the location and density of mode points, give an immediate indication of how a ballistic heat pulse can be expected to split up into components for propagation in various directions.

#### References

- /1/ Fedorov, F.I., Theory of Elastic Waves in Crystals (Plenum, New York, 1968).
- /2/ Every, A.G., Phys. Rev. B22 (1980) 1746.
- /3/ Musgrave, M.J.P., Crystal Acoustics (Holden-Day, San Francisco, 1970).
- /4/ Rösch, F. and Weis, O., Z. Phys. B25 (1976) 101; 25 (1976) 115.
- /5/ Northrop, G.A. and Wolfe, J.P., Phys. Rev. B22 (1980) 6196.
- /6/ Eisenmenger, W., in Phonon Scattering in Condensed Matter, edited by H.J. Maris (Plenum, New York, 1980) pp. 303-308.
- /7/ Lax, M. and Narayanasurti, V., Phys. Rev. B22 (1980) 4876.
- /8/ Berry, M.V., Adv. Phys. 25 (1976) 1.

PHONON TRANSPORT

## TRANSPORT OF HIGH ENERGY PHONONS

V. Narayanamurti

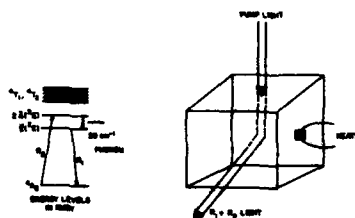
*Bell Laboratories, Murray Hill, New Jersey 07974, U.S.A.*

**Abstract.**— A brief review of high frequency phonon transport experiments in dielectric solids is presented. A major emphasis of this paper is on recent time of flight experiments on the generation and propagation of near zone-edge transverse acoustic phonon pulses in III-V semiconductors such as GaAs. The theoretical status of lifetimes of high frequency phonons is also discussed.

**Introduction.**— In recent years several experimental methods have been applied to study the transport of phonons in the thermal frequency range. Among methods which have been used include: broad band heat pulse<sup>1</sup> methods, quasimonochromatic phonon generation and detection using superconducting tunnel junctions<sup>2</sup>; far infra red laser excitation of piezoelectric materials<sup>3</sup>; resonant detection using electronic energy states of defects<sup>4</sup> in crystals which can in some cases be tuned by magnetic field<sup>5</sup> or uniaxial stress<sup>6</sup>; and phonon generation during hot carrier relaxation and recombination in semiconductors<sup>7</sup>.

The heat pulse and tunnel junction methods and results obtained from them have been extensively reviewed in the past<sup>1,2</sup>. In this paper we will concentrate mainly on energy transport by very high frequency phonons (near or above 1 THz) as studied by optical techniques using electronic states ( $\text{Al}_2\text{O}_3$ : Cr or  $\text{SrF}_2$ :  $\text{Eu}^{2+}$ ) as probes or phonon generation during carrier relaxation in semiconductors.

**Phonon Spectroscopy In Ruby.**— Extensive work<sup>8,4</sup> has been done on phonon transport using monochromatic detection of  $29\text{ cm}^{-1}$  ( $0.87\text{ THz}$ ) phonons in ruby. The frequency of  $0.87\text{ THz}$  corresponds to the  $\bar{E} + 2\bar{A}$  splitting of the  $\text{Cr}^{3+}$  ion in ruby. Broad band optical pumping causes the well-known  $R_1$  and  $R_2$  fluorescence radiation to be emitted (see Figure 1). Phonons generated by external means can cause an increase in the  $2\bar{A}$  population which in turn can be monitored through the intensity of the  $R_2$  line. This technique has been extensively<sup>8</sup> used to study the spectrum of heat pulse phonons; the resonant trapping of  $29\text{ cm}^{-1}$  phonons; and the spectrum of optically excited phonons. Using resonant light pumping stimulated emission<sup>9</sup> of  $29\text{ cm}^{-1}$  phonons has also been observed.



**Fig. 1** — Energy levels of Ruby and experimental arrangement.

**Phonon Detection Using Vibronic Sidebands.**— The technique of vibronic sideband spectroscopy utilizes the modulation of the electronic states of ions in crystals by phonons. Figure 2 shows the effect on the electronic energy due to the lattice coupling as a function of the lattice coordinate,  $Q$ . Since optical transitions occur at constant  $Q$  a large Stokes shift can take place in the luminescence spectrum. Depending on the coupling strength and the temperature the emission spectrum can consist of a 'zero phonon' line plus "stokes" and "anti-stokes" sidebands. The intensity of the anti-stokes sideband can be used for phonon detection. Considerable work on phonon transport has been done along these lines using the  $\text{W}^{3+}$  center in

diamond<sup>10</sup>, the  $I_1$  line<sup>11</sup> in CdS and  $E_u^{2+}$  ions<sup>12</sup> in  $SrF_2$ .

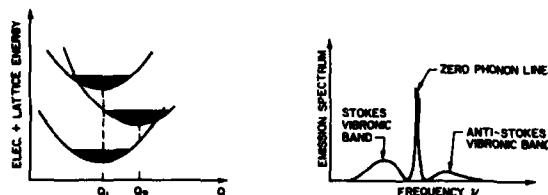


Fig. 2 - Principle of Vibronic Sideband Phonon Detection.

A survey of the results on the lifetime of high frequency phonons determined by these optical techniques has been recently given by Bron<sup>13</sup>. In almost all cases the lifetimes determined by these optical techniques are an average over all modes and direction. This is because of elastic scattering at the impurities which causes rapid mode conversion between the longitudinal (L) and transverse (T) phonons. Because of the expected long lifetime of T phonons the anharmonic decay is dominated by that of the decay rate of L phonons. The measured values are generally much longer than that calculated for an ideal dispersionless solid. We will return to this point later. We, however, will first discuss the propagation of very large wave vector T phonons in GaAs and then, turn to the theoretical situation.

**Phonon Transport in Semiconductors.**— We now discuss the role of phonons in nonradiative energy relaxation and recombination processes in semiconductors. Electrons excited high into the conduction band lose their energy to the lattice in a two step process. See Figure 3. The electrons first "cool" to the bottom of the band by emitting relaxation phonons which are primarily longitudinal optic (LO) phonons in the case of polar semiconductors such as GaAs and for excitation energies several

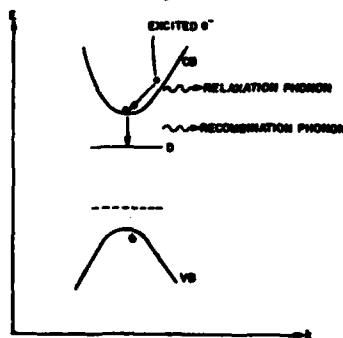


Fig. 3 - Energy Relaxation in Semiconductors.

meV above the conduction band minimum. Carriers at the bottom of the band can lose their energy through recombination processes at defect states in the semiconductor. In the case of deep defects the recombination will involve a large number of phonons in order to satisfy energy conservation. Such multiphonon capture is believed to involve mainly LO phonons and/or near zone-edge transverse phonons in certain specialized cases.

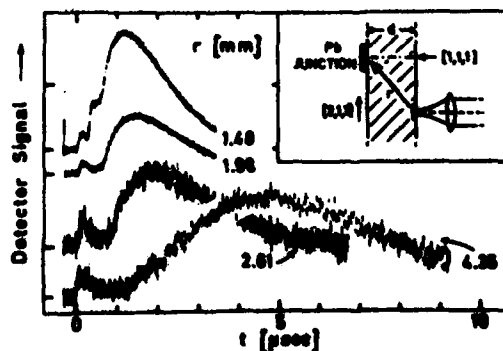


Fig. 4 - Phonon Generation in GaAs.

direct optical luminescent pickup at  $t = 0$  a single broad transverse pulse was observed. The arrival time of the leading edge, half height and peak of the pulse was shown to scale linearly with the propagation distance for distances of the order of mm. Detailed studies of the shape of the pulse showed that it could be described as consisting of ballistic propagation of phonons but with a considerable spread in velocity. The velocity corresponding to the peak of the pulse was for example  $\sim 0.7 \times 10^5$  cm/sec for the [111] direction of propagation. The low frequency ballistic velocity in this direction is, however,  $2.8 \times 10^5$  cm/sec.

These data can be interpreted from a knowledge of the phonon dispersion curves. For GaAs such a curve is shown in Figure 5. Optically excited e-h pairs lose a substantial portion of their energy by the emission of LO phonons. These phonons in turn quickly decay (in times of the order of  $10^{-11}$  sec) into lower lying LA and TA branches. Because the decay processes require the simultaneous conservation of energy and momentum most of the energy ends up in the lowest TA branch. These ultrashort wavelength phonons (wavelength  $\sim 10$  Angstroms) correspond to phonons

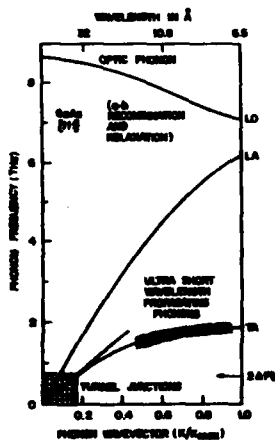


Fig. 5 - Phonon Dispersion Curves in GaAs.

well out into the Brillouin zone of the crystal and have a group velocity much less than the low frequency ultrasonic velocity. The cross-hatched area shows the regime of superconducting tunnel junction phonon spectroscopy.

These experiments show that nonradiative recombination in semiconductors occurs through large wave vector phonons, some of whom are able to propagate macroscopic distances ( $\sim$  mm) through the semiconductor. The properties of such ultrashort wavelength phonons are quite different from that of low frequency ones which correspond to continuum elasticity theory. Because of the great deal of dispersion in phonon velocity at

short wavelengths and the observed long mean free path, time resolved spectroscopy has been used to velocity select phonons<sup>14</sup> of different wavelengths. This velocity selection is achieved by scanning the photoexcited region along the direction of phonon propagation at various velocities corresponding to different dispersive points on the phonon branch. See Figure 6. This figure shows typical pulses for

three different scanning velocities. The peak of the pulse now corresponds to a well defined wavelength which can be conveniently tuned by simply altering the laser scanning speed. Such a tunable phonon source is of great potential use for physical studies of solids and for phonon optics.

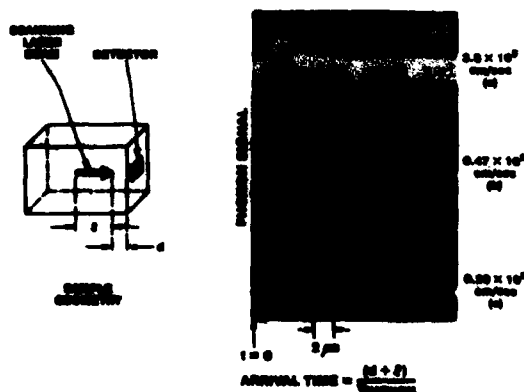


Fig. 6 - Velocity Selection of Large Wave Vector Phonons in GaAs.



**Theoretical Considerations.**- In perfect dielectric crystals the lifetime for anharmonic decay is determined by energy-momentum conservation conditions<sup>15</sup>. These considerations<sup>16</sup> show that for both normal (N) and Umklapp (U) processes the lowest transverse acoustic branch cannot spontaneously decay by anharmonic processes for any order. The phase space for decay for higher branches in crystals with anisotropy and dispersion has to be calculated from the 2-phonon density of states for the particular solid in question. Barring extreme anisotropy in most solids this phase space, for even the higher transverse branches, is expected to be small. Thus the main decay channel is expected to be the spontaneous decay of L phonons.

The momentum randomization of the transverse phonons will in ordinary crystals be affected by isotope and/or impurity scattering. Even the isotope scattering has to be calculated<sup>16, 17</sup> with care for diatomic crystals such as GaAs which have one element (As) isotopically pure. The isotope scattering is now strongly dependent on the amplitude (U) of vibration of the impure element (Ga) which in turn strongly depends on wavelength. This scattering goes as  $|U_{Ga}|^2$  times a weighted density of final states which also depends on the Ga amplitude. Numerical computations<sup>17</sup> using the real vibrational spectrum of GaAs indicate that this product can be considerably smaller than that calculated from the usual Klemen's formula valid for the monoatomic case.

The above theoretical considerations combined with the experimental results strongly suggest that in many crystals energy transport can occur via extremely short wavelength phonons whose energy relaxation time can, in favorable cases, be micro-seconds long. Thus "broad diffusive" pulses often observed in heat pulse type experiments may consist mainly of high frequency components which can play an important role in energy transport. These high frequency phonons, then, will only down convert in frequency at imperfect interfaces (surfaces) or through decay of L modes generated through impurity scattering.

**Future Directions.**- It is clear that much has been learned about the lifetimes and energy transport by high frequency phonons in several dielectric solids and semiconductors. Much, however, still needs to be done on both the experimental and theoretical sides of the problems of anharmonic decay, impurity scattering and the role of surfaces and interfaces. In situ exploration of phonon transport by generally applicable scattering techniques would be of great value. Non equilibrium phonon populations can in principle be probed by enhanced thermal diffuse scattering of X-rays. Preliminary experiments<sup>18</sup> in GaAs, reveal that optically excited phonons near the zone-boundary indeed have a long lifetime when measured by this technique and that their decay is enhanced by imperfect surfaces. This technique is capable of probing the temporal, spatial and frequency characteristics of non-equilibrium phonon populations. With the expected availability of powerful synchrotron sources this should become an extremely useful tool for phonon transport studies in solids. Tunable far IR lasers can also be valuable in probing specific decay channels for high frequency phonons. Such experiments have only recently<sup>19</sup> been attempted. Further effort also needs to be expended in proper numerical calculations of phonon decay processes (anharmonic and isotope) taking into account the real vibrational spectrum of the solid.

**Acknowledgement.**- The original parts of this work were performed in close collaboration with M. A. Chin, P. Hu, M. Lax, and R. G. Ulbrich to all of whom I owe special thanks. Helpful discussions with M. Schluter and H. L. Störmer and extensive computational aid of R. C. Fulton is also acknowledged.

#### References.-

1. R. J. von Gutfeld in "Physical Acoustics", W. P. Mason, Editor (Academic Press, 1968) Vol. V.
2. W. Eisenmenger, *ibid*, Vol. 12, 1976.
3. W. Grill and O. Weiss, *Phys. Rev. Lett.*, **35**, 588 (1975).
4. W. Bron, *Rep. Prog. Physics*, **43**, 301 (1980).
5. C. H. Anderson and E. S. Sabisky in "Physical Acoustics", Vol. 7, 1971.
6. R. C. Dynes and V. Narayanasurti, *Phys. Rev.*, **B6**, 143 (1972).
7. R. G. Ulbrich, V. Narayanasurti, and M. A. Chin, *Phys. Rev. Lett.*, **45**, 1432, (1980).

8. See e.g. K. F. Renk in Proceedings of 1979 IEEE Ultrasonic Symposium.
9. P. Hu, Phys. Rev. Lett., 44, 417 (1980).
10. M. J. Colles and J. A. Giordmaine, *ibid* 27, 670 (1971).
11. J. Shah, R. F. Leheny, and A. H. Dayem, *ibid* 33, 818 (1974).
12. W. E. Bron and W. Grill, Phys. Rev., B16, 5033, (1977).
13. W. E. Bron, Phys. Rev., B21, 2627, (1980).
14. P. Hu, V. Narayanamurti, and M. A. Chin, Phys. Rev. Lett., 46, 192 (1981).
15. R. Orbach, Phys. Rev. Lett., 16, 15 (1966).
16. M. Lax, P. Hu, and V. Narayanamurti, Phys. Rev., B23, 3095, (1981).
17. M. Lax and V. Narayanamurti, to be published.
18. D. B. McWhan, M. A. Chin, P. Hu, and V. Narayanamurti, to be published.
19. H. Lengfellner and K. F. Renk, Phys. Rev. Lett., 46, 1210, (1981).

## BALLISTIC TRANSPORT AND DECAY OF NEAR ZONE-EDGE NON-THERMAL PHONONS IN SEMICONDUCTORS

R.G. Ulbrich\*, V. Narayanamurti and M.A. Chin

*Bell Laboratories, Murray Hill, New Jersey 07974, U.S.A.*

**Abstract.**— We present results on the energy transport by near zone-edge transverse phonon pulses generated in the process of non-radiative electron-hole pair recombination at  $T=1.4$  K in GaAs and InP. Depending on orientation and distance, ballistic transport of phonons with frequencies between 1.0 and 2 THz is reported.

**Introduction.**— There has been a great deal of recent activity in high frequency phonon transport<sup>1</sup>. We recently presented a preliminary report on the propagation of non-thermal, large-wavevector acoustic phonons over macroscopic distances ( $\sim$  mm) in GaAs at low temperatures<sup>2</sup>. Here we report on the spatial, temporal and directional dependence of the phonon signals in GaAs and present also results on InP.

**Experimental.**— Bulk crystals of GaAs and InP with mechanically lapped and chemically etched surfaces were used. We studied Al bolometer and Pb junction detector signals in three geometrical configurations: a) "trans" in the plane-parallel samples with photoexcited source region and detector on opposite sides; b) "cis" with source and detector on the same crystal surface; c) "edge on" with the detector close to a sample edge and the source on the adjacent face. In the following, the necessary corrections for Lambert's Law and the cosine of the detector viewing angle have been made.

**Results.**— Figure 1 shows phonons signals  $S^* = r^2 \cdot S$ , where  $S$  is the actually measured Al bolometer signal as a function of  $t$  at different fixed distances  $r$ , for the three principal directions in a  $2.7 \times 6.5 \times 12 \text{ mm}^3$   $\langle 1,1,0 \rangle$  cut GaAs crystal with  $\langle 1,1,1 \rangle$  edge-on detector.  $S^*$  has been plotted as a function of  $t/r$  to reveal the characteristics of ballistic, dispersive transport: linear scaling of pulse shape in time and space. Close affinity is, indeed, observed in Fig. 1. The peak of the phonon distribution travels with  $0.9 \times 10^5 \text{ cm/sec}$ , and the leading and trailing halfpoints with  $\sim 2.5 \times 10^5$ , and  $\sim 0.4 \times 10^5 \text{ cm/sec}$ . respectively. The detailed shape of the velocity distributions depends on propagation direction.

The signal onset of the TA phonon signals was measured and compared to low-frequency propagation, launched in evaporated metal film stripes in situ in the same experiment. The onset edge of the "slow" signals in Fig. 1 exhibited consistently lower velocities, ranging from 88% to 93% of the low-frequency TA (resp. FTA in  $1,1,0$ ) velocities in the three directions. We therefore, conclude that all the signals we observe is due to high-frequency, i.e.  $\nu \geq 1$  THz phonons. Pb junction experiments in

\*Also at Institut für Physik, Universität Dortmund, West-Germany.

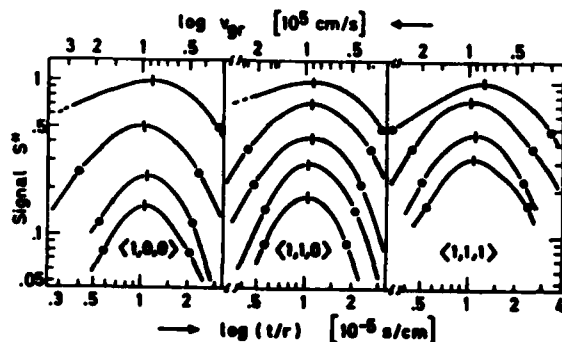


Fig. 1.- Phonon signals  $S^*(t)$  in GaAs,  $T=1.4K$ , for three directions at fixed propagation distances  $r=0.44, 0.88, 1.76, 2.6$  and  $5.2\mu m$  (from top to bottom). Pulse peak, leading and trailing edge halfpoints are indicated ( $1, 0, \cdot$ ).

the same configuration confirmed this result. To obtain frequency distributions we converted the measured velocities according to the known dispersion curves along the principal directions<sup>3</sup>. One example is shown in Fig. 2a the evolution of the frequency distribution with increasing propagation distance along  $\langle 1,0,0 \rangle$ .

The variation of  $S^*$  with increasing distance  $r$  is expected to be proportional to  $1/r \exp(-\alpha r)$ , where  $\alpha$  is a phenomenological averaged damping constant. Due to the pulse shape variations evident in Fig. 1 - a narrowing of velocity spread among the halfpoints by almost a factor of 2 is observed in all three directions in the distance range discussed here - this proportionality is modified. Evaluating the total integrated pulse signal we found  $\alpha_{\langle 111 \rangle} \approx 3\text{cm}^{-1}$ ,  $\alpha \approx 10\text{cm}^{-1}$  in the other directions. From the narrowing we conclude that both the high frequency and the low frequency parts of the initial frequency distribution are affected by attenuation. The minimum of damping occurs at frequencies of 2.05 THz in  $\langle 1,0,0 \rangle$ ,  $\langle 1,1,0 \rangle$  and 1.55 THz in the  $\langle 1,1,1 \rangle$  direction. This is an indication of anisotropic phonon propagation in the dispersive region. However, the polychromatic excitation of TA phonons (via the  $LO \rightarrow LA \rightarrow TA$  relaxation cascade) and the relatively large detector viewing angle tends to smooth out large variations in the directionality in the intensity of the phonon signals, which one would expect for monochromatic high-frequency phonon propagation (in analogy to the focussing effect in non-dispersive transport at low frequencies).

In Figure 2(b) we show some results for InP on the spatial dependence of the phonon signals for three different elapsed times. This plot shows that the phonon energy density has a peak which moves with increasing time away from  $r=0$  in a quasi ballistic fashion. This is clearly different from diffusive transport, where the excitation region would always have the maximum energy density after pulsed excitation. These data indicate that the momentum and energy relaxation time for phonons in the 1.5 THz region is microseconds long in InP.

In both materials boundary scattering of these THz phonons turned out to be completely diffuse and caused efficient down conversion into low  $\vec{q}$  phonons.

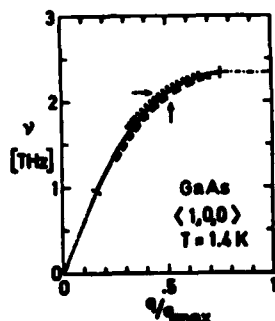


Fig. 2(a).- Phonon distributions on the lowest  $\langle 1,0,0 \rangle$  TA branch in GaAs after the pulse has propagated over a distance of  $r=0.44$  mm (—),  $0.88$  mm (---) and  $1.76$  mm (....). The arrows indicate the peak; upper and lower ends of the lines mark the halfpoints.

Pulse sharpening, presumably because of down conversion, was also observed for high excitation levels ( $\geq 10^{-6} \text{ J/mm}^2$ ).

In summary, we have observed the propagation of near zone-edge TA phonons after non-radiative e-h pair recombination in bulk GaAs and InP. Such propagation appears to be a general feature for zinc-blende semiconductors with high chemical, physical and surface perfection.

#### References.-

- 1) For a review see W. Bron, Rep. Prog. Phys. **43**, 301 (1980).
- 2) R. G. Ulbrich, V. Narayanasurti and M. A. Chin, Phys. Rev. Lett. **43**, 1432 (1980).
- 3) J. J. Waugh and G. J. Dolling Phys. Rev. **132**, 2410 (1963).

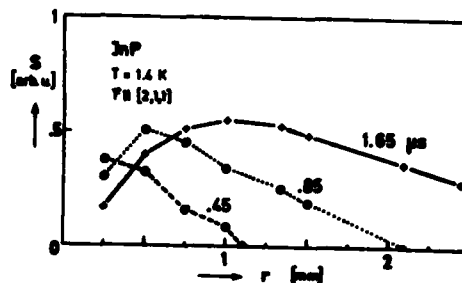


Fig. 2(b).- Phonon signals  $S^*$  as a function of distance for three different elapsed times  $t$ , after pulsed excitation at  $r=0$ ,  $t=0$  in InP.

## FREQUENCY CROSSING IN BICRYSTALS AND INELASTIC SCATTERING AT SURFACES

L.J. Challis, A.A. Ghazi and M.N. Wybourne\*

*Department of Physics, University of Nottingham, Nottingham NG7 2RD, U.K.*

**Abstract:** It has been demonstrated experimentally and theoretically that frequency crossing signals in thermal conduction can be produced between different resonant scattering centres on either side of an interface. The measurements were carried out on an  $\text{Al}_2\text{O}_3$  bicrystal doped with  $\text{Fe}^{2+}$  in one half and  $\text{V}^{3+}$  in the other. The signals are observed to decay with distance from the interface and this is interpreted as the result of inelastic scattering at the crystal surface.

When a heat current passes along a solid rod containing resonant scattering centres holes are burned in its spectrum at the resonant frequencies. If there are two scattering processes,  $\nu_A$  and  $\nu_B$ , the total phonon scattering and so thermal resistance is less when the frequencies cross (coincide) than when they are uncrossed since the area of the combined hole burned in the spectrum is less than that of the two separate holes. If the scattering centres are magnetic ions their frequencies can be tuned with a magnetic field, the fields corresponding to crossing points, which are identified by sharp minima in the temperature gradient, can provide spectroscopic information of high resolution /1/.

In the present work we have investigated experimentally and theoretically whether the technique can be used when the two types of centre are in different parts of a crystal. To simplify the theoretical analysis we have neglected inelastic phonon scattering. We consider heat conduction along a composite rod or bicrystal doped differently in its two halves A and B so that resonant scattering occurs at  $\nu_A$  in one half and  $\nu_B$  in the other. Now if the scattering is purely elastic the heat current within the channel provided by a narrow band of frequencies remains constant throughout the rod and its magnitude, for a fixed temperature difference between the ends of the rod, depends on the sum of the thermal resistances of the two halves. Therefore rather little heat will flow in the channel which contains  $\nu_A$ . The effect of adding a second scattering process  $\nu_B$  to this channel ( $\nu_B = \nu_A$ ) will reduce the heat flow along it but if it is already small it will make little difference to the total heat flow from all the channels. However if  $\nu_B$  is tuned away from  $\nu_A$  a second channel will become effectively blocked and the total heat flow will fall. So we expect the thermal resistance of the composite rod to pass through a

\*Present Address : The General Electric Co Ltd, Hirst Research Centre, Wembley, Middx, U.K.

minimum at  $\nu_A = \nu_B$ . Detailed analysis /2/ indicates that at the crossing the fractional change in the temperature differences along A is

$$\frac{\delta T_A}{\Delta T_A} = \frac{15}{2\sqrt{2}\pi^3} \left( \frac{x_0 f(x_0)}{\nu_0} \right) \left[ \Delta_A - \frac{\Delta_A^2}{(\Delta_A^2 + \Delta_B^2)^{3/2}} \right] \quad (1)$$

with a similar expression for  $\delta T_B$ .  $f(x) = x^4 e^x / (e^x - 1)^2$ ,  $x = h\nu/kT$  and  $\nu_0$  is the crossing frequency. The analysis assumes Lorentzian line shapes with scattering rates  $\tau_1^{-1}/\tau_0^{-1} = \Delta_1^2 / [(\nu - \nu_1)^2 + \Gamma_1^2]$  where  $\tau_0^{-1}$  is the background scattering rate, which will be mostly boundary scattering. It also supposes  $\Delta_1 \gg \Gamma_1$  which is believed to be the case in our experiments. Expression (1) shows that the signal size is different in the two halves of the crystal and that the bigger signal occurs in the half containing the weaker scattering process. Of particular note however is that the analysis suggests that it is possible, at least in the absence of inelastic scattering, to observe frequency crossing signals in a composite system.

To test this we have used an a-axis bicrystal of  $Al_2O_3$ , 4mm in diameter and 40 mm long made by Hrand Djevahirdjian SA. One half (V) is doped with vanadium and believed to contain  $\sim 70$ ppm of  $V^{3+}$  and 0.3ppm of  $Fe^{2+}$ . The other half (Fe) is doped with iron and believed to contain  $\sim 2$ ppm of  $Fe^{2+}$  and  $< 1$ ppm of  $V^{3+}$ . A heat current is passed along the rod and the temperature gradients measured near to the interface using a pair of thermometers as shown in fig 1. For the arrangement shown heat could be injected at  $H_{Fe}$  or  $H_V$ . Several  $V^{3+}/Fe^{2+}$  frequency crossings were examined and we report here the data for two crossings C and D involving a  $\Delta M = 1$  transition of the  $V^{3+}$  ground state at a frequency  $\nu_V = 249 - 278$  GHz. Crossing C occurs when  $\nu_V$  crosses a  $\Delta M = 1$  transition of  $Fe^{2+}$  at  $113 \pm 48$  GHz in a field of  $\sim 1.85$ T. Crossing D occurs when  $\nu_V$  crosses the  $Fe^{2+}$   $\Delta M = 2$  transition at 988 GHz in a field of  $\sim 2.05$ T. The two crossing

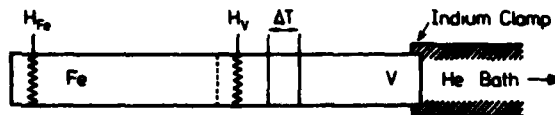


Fig 1: The experimental arrangement.

frequencies are 199 and 194 GHz respectively and the signals for the two heaters are shown in fig 2. No heat current passes through the Fe-doped end for injection at  $H_V$  and the signal is due to  $\nu_V$  crossing the hole burned by the traces of  $Fe^{2+}$  present in the V-doped end. The important feature is that when the heat is switched to  $H_{Fe}$ , the signals increase by factors of 2.7(C) and 2.1 (D) showing that the  $Fe^{2+}$  hole is now much larger. So the hole burned by  $Fe^{2+}$  ions is carried over into the  $V^{3+}$  end. A similar result is found if the sample is reversed and the temperature gradient is measured on the  $Fe^{2+}$  end. We conclude that a resonant frequency in one part of a crystal can be measured by tuning that of

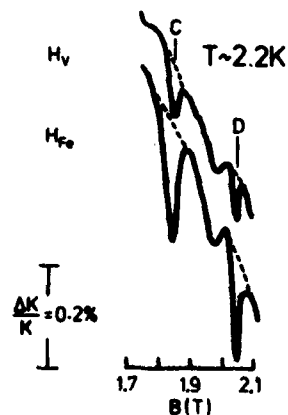


Fig 2: The frequency crossing signals.

another ion in a different part of the crystal. Using signals derived from the heat current passing between the two parts we can determine when the two frequencies are equal. This could have wider application if the second part of the crystal could be stuck or grown onto the first.

This effect can only occur if the holes burned in one part of the crystal have not decayed by the time they reach the detection region. Decay will occur as a result of inelastic scattering which will redistribute the heat current spectrum towards that corresponding to the local scattering processes. Information on this decay was obtained by measuring the size of the signals further from the interface. It was found that at  $\sim 12\text{mm}$  from the interface the holes had decayed almost completely since the signal sizes were the same whichever heater was used. From these data we deduce that at 2K and 200GHz the mean free path for inelastic scattering  $\lambda_I \approx 4\text{mm}$ . No difference was observed at 1.5K.

This value seems much too short to be due to bulk three-phonon processes. There is no direct information on these but estimates obtained by extrapolating thermal conductivity data /3/ would give values at these temperatures and frequencies of  $\sim 10^6\text{mm}$ . We prefer to believe therefore that  $\lambda_I$  is due to inelastic scattering at the surfaces and since  $\lambda_I \sim \text{diameter}$ , this suggests that the probability that a phonon striking the surface is scattered inelastically  $\sim 1$ . This is higher than that found from the decay of '2Δ' phonons /4/ and more work is needed to establish whether this is due to the nature of the surfaces - the present surfaces are fine ground to  $\sim 20\mu$  and not carefully cleaned - or for example to the fact that because of the higher resolution we are more sensitive to quasielastic scattering.

The work was supported by the Science Research Council. We are also very grateful to Mr J R MacDermott of Refractory Metals and Castings Ltd, Professor A Revcolevachi of the University of Orsay, and our colleagues Mr M Carter, Mr W Roys and Dr F W Sheard for help at various stages.

#### References

- /1/ Berman R, Brock J C F and Huntley D J, Phys Lett 3, 310, 1963; Wybourne M N, Challis L J and Ghazi A A, J Phys C 13, 6495, 1980.
- /2/ Challis L J, Ghazi A A and Wybourne M N, J Phys C, to be published.
- /3/ de Goeer A M, J Physique 30, 389, 1969.
- /4/ Trumpp H J and Eisenmenger W, Z Physik 28, 159, 1977; Bohm K, Diplomarbeit, Stuttgart University, 1975, unpublished.



# THE INFLUENCE OF THE DYNAMICAL JAHN-TELLER EFFECT OF ACCEPTORS ONTO THE PHONON-TRANSPORT MECHANISM IN CUBIC SEMICONDUCTORS

J. Maier and E. Sigmund

*Institut für Theoretische Physik, Universität Stuttgart, 7000 Stuttgart, F.R.G.*

**Abstract.**— Phonon scattering experiments of various types in cubic semiconductors doped with deep effective mass acceptors indicate an extra resonance scattering at some meV. We show, using Green's function and transformation techniques that these resonances are due to a dynamic Jahn-Teller effect of the  $\Gamma_8$ -acceptor ground state. Their influence onto the thermal conductivity is calculated in terms of a specific single mode relaxation time.

1. Introduction.— A series of phonon experiments<sup>1,2,3</sup> and optical experiments<sup>4</sup> indicate a resonance energy in the meV-range for the deeper acceptors GaAs(Mn), GaP(Zn), Si(In) and Si(B). These energies are much larger than the splitting due to random internal fields, which may be of the order of 10 to 100  $\mu$ eV in these crystals. In the following we show that these additional resonances are due to the dynamical Jahn-Teller effect and we discuss their influence onto the phonon transport mechanism.

2. The Phonon-Transport Mechanism.— The theoretical analysis of our calculation is based on the Boltzmann equation<sup>5</sup> of the phonon distribution function  $N_{\lambda q}(r, t)$ :

$$\frac{\partial}{\partial t} \delta N_{\lambda q} + v_{\lambda q} (\nabla \cdot \delta N_{\lambda q}) = \left( \frac{\partial N_{\lambda q}}{\partial t} \right)_s + \left( \frac{\partial N_{\lambda q}}{\partial t} \right)_c$$

where  $N_{\lambda q}(r, t) = N_{\lambda q}^0 + \delta N_{\lambda q}$  and  $N_{\lambda q}^0 = [\exp(\hbar \omega_{\lambda q}/kT) - 1]^{-1}$ ,  $v_{\lambda q}$  is the group velocity of the phonon and defined by  $v_{\lambda q} = \nabla_q \omega_{\lambda q}$ . The first term represents the local time-derivation, the second one arises from the drift motion of the phonons in a gradient field and the third term is the source term and describes the rate of phonon production and annihilation by the heater and detector. The fourth term is called the collision or scattering term and it reflects the physics of all phonon interaction processes arising in the studied sample. The treatment of this scattering term is the root problem in solving the Boltzmann equation. It describes the change of the phonon distribution function due to the different scattering processes. In relaxation time approximation this term is given by

$$\left(\frac{\partial N_{\lambda q}}{\partial t}\right)_c = -\frac{\delta N_{\lambda q}}{\tau_{\lambda q}}$$

$\tau_{\lambda q}$  is the single-mode relaxation time. If all relaxation rates are known the thermal conductivity can be calculated.

3. The Acceptor Ground State in Cubic Semiconductors.- The ground state of acceptors in cubic semiconductors is fourfold degenerate ( $\Gamma_8$ ) and the interaction with the lattice vibrations leads to the possibility of a Jahn-Teller effect, which may cause a dynamical splitting of the electronic levels.

The acceptor-hole-lattice interaction Hamiltonian can be written as<sup>6</sup>

$$H_I = \sum_{\lambda q} \{ D^E (\rho_1 r_1^{\lambda q} + \rho_2 r_2^{\lambda q}) + D^T \rho_3 (\sigma_1 \delta_1^{\lambda q} + \sigma_2 \delta_2^{\lambda q} + \sigma_3 \delta_3^{\lambda q}) \}$$

where  $\rho_i$  and  $\sigma_j$  are Dirac's 4x4 matrices. The coupling functions  $r_i^{\lambda q}$  and  $\delta_j^{\lambda q}$  are given by

$$r_1^{\lambda q} = \left( \frac{\hbar \omega_{\lambda q}}{2Mc_\lambda^2} \right)^{1/2} f(q) \frac{1}{3} [2\hat{q}_z e_{\lambda z} - \hat{q}_x e_{\lambda x} - \hat{q}_y e_{\lambda y}] \text{ etc.}$$

$b_{\lambda q}$  and  $b_{\lambda q}^+$  are the annihilation and creation operators for the phonon  $\lambda q$ .  $\hat{q}$  is the unit vector along  $\vec{q}$ ,  $\vec{e}_\lambda$  is the polarization vector and  $M$  the mass of the crystal.  $D^E (= D_{yy}^E)$  and  $D^T (= D_{yy}^T)$  are the deformation potential constants for a  $[1,0,0]$  and  $[1,1,1]$  strain respectively.  $f(q)$  is the cut-off function reflecting the extended nature of the defect state.

4. The Single-Mode Relaxation Time.- The scattering rate or the inverse life time of a single phonon can be related to the imaginary part of the T-matrix:

$$\tau_{\lambda q}^{-1} = -\omega_{\lambda q}^{-1} \text{Im } T(\omega_{\lambda q})_{\lambda q, \lambda q}$$

The T-matrix itself is defined by the phonon Green's functions ( $G = G_0 - G_0 T G_0$ ) of the unperturbed ( $G_0$ ) and perturbed ( $G$ ) crystal. For the calculations we used an isotropic model for the crystal, we expanded the Green's function hierarchy up to the fourth order and we calculated the thermal expectation values by use of an exponential transformation. As a final result the mean scattering rate can be written in the Lorentzian-like form<sup>6</sup>

$$\langle \tau^{-1} \rangle(\omega) = \frac{P(\omega)}{(\omega - \Delta(\omega))^2 + \Gamma(\omega)^2}$$

$P$ ,  $\Delta$  and  $\Gamma$  are rather lengthy expressions, therefore we have omitted them. In Fig. 1 the Jahn-Teller induced relaxation rate is drawn.

5. The Thermal Conductivity.— Taking into account the boundary (B) and isotopic (I) scattering as well as the phonon scattering by the acceptor states (JT) and the Umklapp processes (U) the thermal conductivity  $K(T)$  can be calculated<sup>7</sup>. In Fig. 2. the thermal conductivity of the system Si(In) for different In-concentrations is drawn. Its behaviour is in good agreement with the experimental results.

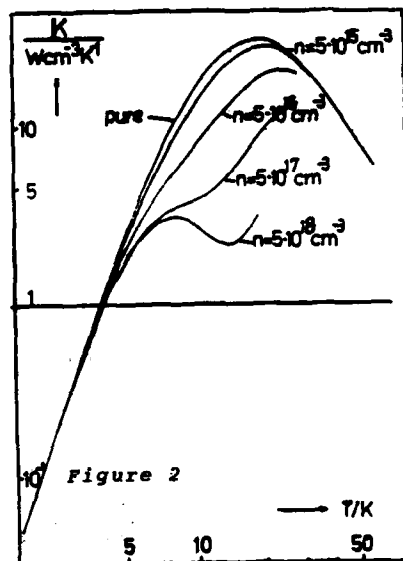
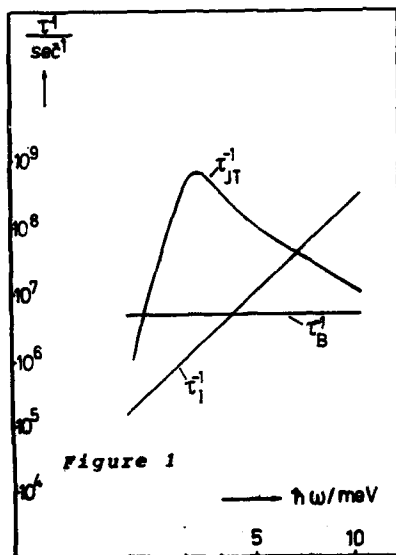


Fig.1: Relaxation rate of longitudinal phonons by the scattering by the Jahn-Teller state ( $1/\tau_{JT}$ ), by the isotopic scattering ( $1/\tau_I$ ), and by the boundary scattering ( $1/\tau_B$ ) in In-doped Si (In-concentration  $n=1 \cdot 10^6 \text{ cm}^{-3}$ ) as a function of the energy  $\hbar\omega$ . The calculated resonance energy is 3.8 meV.

Fig.2: Calculated thermal conductivity  $K$  in Si(In) as a function of temperature for different In-concentrations  $n$ .

#### References:

- (1) de Combarieu, A., Lassmann, K., Phonon Scattering in Solids, p. 340, Plenum Press (1976)
- (2) Lassmann, K., Schad, Hp., Solid State Commun. **18**, 449 (1976)
- (3) Schenk, H., Forkel, W., Eisenmenger, W., Frühjahrstagung DPG, Freudenstadt 1978
- (4) Sauer, R., Schmid, W., Weber, I., Solid State Commun. **27**, 705 (1978)
- (5) Klemens, P.G., Sol. State Phys. **7** (1958)
- (6) Sigmund, E., Lassmann, K., Phonon Scattering in Condensed Matter, p. 417, Plenum Press (1979)
- (7) Callaway, J., Phys. Rev. **113**, 1046 (1959)

# A STUDY OF THE GROUND STATE OF ACCEPTORS IN SILICON FROM THERMAL TRANSPORT EXPERIMENTS

A.M. De Goër, M. Locatelli and K. Lassmann\*

*Service des Basses Températures, Laboratoire de Cryophysique, Centre d'Etudes Nucléaires de Grenoble, 85 X, 38041 Grenoble Cedex, France*

\* *Physikalisches Institut, University of Stuttgart, 7000 Stuttgart 80, F.R.G.*

**ABSTRACT** - Thermal conductivity measurements of silicon crystals doped with B or In have shown the presence of several phonon scattering processes. The resonant effect observed below 1 K is ascribed to the existence of a distribution of splittings  $N(\delta)$  of the  $I_g$  ground state of the acceptor, which could be related to the presence of oxygen and carbon impurities. In two cases, the maximum of  $N(\delta)$  occurs for  $\delta_{\max}$  near 6 GHz, in agreement with previous ultrasonic studies ( $\delta_{\max} > 4$  GHz).

**Samples and Experiments** - The thermal conductivity of four Si single crystals doped with B or In has been measured from 50 mK to 200 K. Three crystals have been studied by ultrasonic absorption in Stuttgart and some of these results have been already published [1]. The characteristics of the samples are given in table 1.

TABLE 1

Sample	S 80 g	S 87 d	S 52	S 33 *
Dimensions (mm × mm × mm)	2.6 × 3.0 × 35	3.0 × 3.0 × 34	2.3 × 3.0 × 14	0.85 × 3.03 × 11
Acceptor	B	B	In	In
$\rho$ ( $\Omega$ cm)	10.8	2.5	0.1	2
$N_A$ ( $\text{cm}^{-3}$ )	$1.2 \cdot 10^{15}$	$5.4 \cdot 10^{15}$	$5 \cdot 10^{17}$	$5 \cdot 10^{15}$
$n_0$ ( $\text{cm}^{-3}$ )	$5.7 \cdot 10^{17}$	$\leq 2 \cdot 10^{15}$	$8 \cdot 10^{17}$	$7 \cdot 10^{17}$
$n_c$ ( $\text{cm}^{-3}$ )	$4.1 \cdot 10^{16}$	$\leq 5 \cdot 10^{15}$	?	?
Growth method	Cz	Fl. zone	Cz	-
$\delta_{\max}$ (GHz) (from ultrasonics)	$\geq 4$	1.3	$> 4$	-

\* This sample has been measured previously above 1.2 K [2]

**Results and qualitative discussion** - The experimental results are displayed in fig.1 in a log-log plot and show that three temperature ranges can be considered.

(i)  $T < 2$  K Resonant phonon scattering is present in the three samples measured in this temperature range. We ascribe this scattering to a direct process between the two energy levels arising from the  $I_g$  acceptor ground state, the splitting being variable from site to site due to random strains and electric fields. The distri-

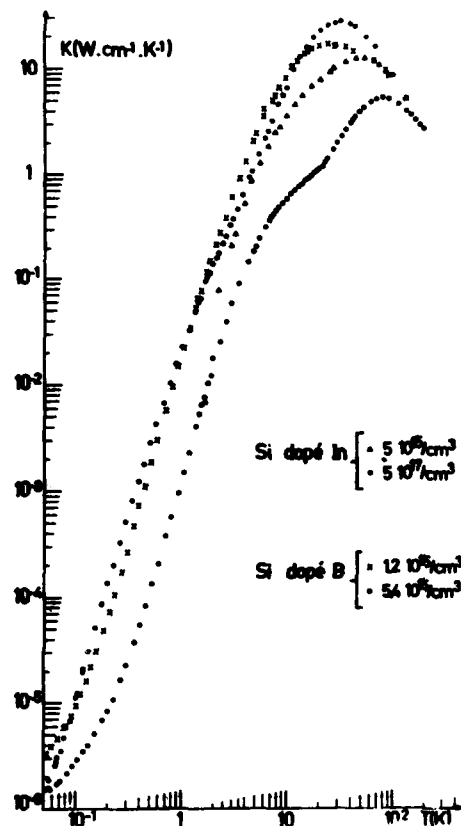


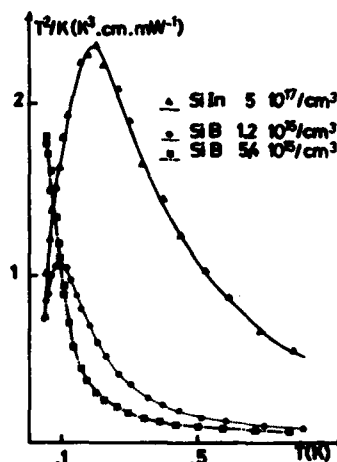
Figure 1.

butions  $N(\delta)$  have been studied at frequencies less than 4 GHz by ultrasonic attenuation and related to the presence of carbon or oxygen impurities in the crystals [1]. The phonon relaxation rate due to this process is given approximatively by :

$$\tau^{-1}(\omega) = \pi \bar{D}^2 \omega N(\delta=\omega) / \hbar \rho v^2 \quad (1)$$

where  $\bar{D}$  is a mean value of the coupling constant, and the qualitative shape of  $N(\delta)$  is given by the function  $T^2/K$  [3]. In fig. 2,  $T^2/K$  is plotted as a function of  $T$  for the three samples studied. A maximum is observed near 0.19 K in the case of Si : In ( $5.10^{17}/\text{cm}^3$ ) and 0.09 K in the case of Si : B ( $1.2.10^{15}/\text{cm}^3$ ), which would correspond very crudely to frequencies  $\delta_{\text{max}}$  of 15 and 7 GHz respectively. In the case of Si : B ( $5.10^{15}/\text{cm}^3$ ) the maximum is not reached at the lowest temperatures, so that  $\delta_{\text{max}}$  must be less than 4 GHz. These results are in very good qualitative agreement with those obtained by ultrasonic measurements and given in table 1.

(ii)  $2 < T < 30$  K A very clear dip appears near 20 K in the case of the In-doped samples, which has been already observed and attributed to an excited Jahn-Teller level of the acceptor near  $40 \text{ cm}^{-1}$  [2]. A small effect could be present near 3 K in the more highly doped Si : B sample so that the ratio of the transition energies for

Figure 2. Solid lines are not calculated

the two systems would be about 5, a value noticeably larger than previously supposed [4].

(iii)  $T > 30$  K The dip near 40 K present in the lightly doped Si : B crystal and not in the highly doped one is attributed to the presence of isolated oxygen interstitials ; the two crystals contain different amount of oxygen (see table 1) and in fact, the two curves cross near 20 K. This resonant scattering observed near 40 K is also probably present in the In-doped samples and could be related to a transition near  $80 \text{ cm}^{-1}$ , in reasonable agreement with the energy level scheme of oxygen deduced from FIR absorption measurements [5].

Quantitative analysis - A preliminary analysis of the results in the temperature range  $T < 1$  K for the two samples containing oxygen and carbon has been carried out within the Debye approximation. Only boundary scattering ( $\tau_b^{-1} = \text{constant}$ ) and scattering by the acceptors as described by equation (1) have been considered. We have used an expression of  $N(\delta)$  which gives a satisfactory description of the distribution obtained by a Monte-Carlo calculation for point defects such as carbon [1]. The general features of the experimental  $T^2/K$  curves (fig.2) can be described by such an analysis and, with the parameters given in table 2, the position and intensity of the maximum are well reproduced, but not the detailed shape of the curves. The values of  $\delta_{\text{max}}$  obtained from these fits are similar in the two crystals, in contrast with the crude estimations from the position of the pics given above.

TABLE 2

Sample	$\delta_{\text{max}}$ (GHz)	$N_A \bar{D}^2 (\text{erg}^2 \text{ cm}^{-3})$	$N_A (\text{cm}^{-3})$	$\bar{D}$ (eV)
Si : B (S 80 g)	$6.2 \pm 0.4$	$6.5 \cdot 10^{-9}$	$1.2 \cdot 10^{15}$	1.5
Si : In (S 52)	$5.6 \pm 0.4$	$5.1 \cdot 10^{-7}$	$5 \cdot 10^{17}$	0.63

This analysis also gives values of  $N_A \bar{D}^2$  and, supposing that all the acceptors contribute to the scattering, we obtain the values of  $\bar{D}$  given in table 2, which are not unreasonable. Full details will be published elsewhere.

#### References

- [1] LASSMANN K. and ZEILE H. in "Phonon Scattering in Condensed Matter" edited by MARIS H.J., Plenum Press (1980), 369.
- [2] DE COMBARRIEU A. and LASSMANN K. in "Phonon Scattering in Solids" edited by CHALLIS L.J. et al., Plenum Press (1976), 340.
- [3] CHALLIS L.J., DE GDER A.M. and HASELER S.C., Phys. Rev. Letter **39** (1977) 558.
- [4] SIGMUND E. and LASSMANN K. in "Phonon Scattering in Condensed Matter" edited by MARIS H.J., Plenum Press (1980) 417.
- [5] HAYES W. and BOSCHWORTH D.R., Phys. Rev. Letters **23** (1969), 851.

## PHONON AND PSEUDO-MAGNON TRANSPORT IN COOPERATIVE JAHN-TELLER SYSTEMS

M. Wagner, W. Mutscheller and H.-K. Nusser

*Institut für Theoretische Physik, Universität Stuttgart, 7000 Stuttgart 80, F.R.G.*

**Abstract.** - Stimulated by measurements of Daudin and Salce it is shown that in E-b<sub>1</sub>, b<sub>2</sub> systems like TmVO<sub>4</sub> one-phonon scattering is of minor importance for phonon transport. Strong effects onto the heat conductivity arise from the new transport path of the pseudo-magnon system and from the 2 phonon-1 magnon relaxation path. Explicite expressions are given.

1. **Introduction.** - This work has been stimulated by measurements of Daudin and Salce [1] on the heat conductivity of rare earth vanadates and arsenates, which are cooperative Jahn-Teller Systems of the E-b<sub>1</sub>, b<sub>2</sub> type. We specifically refer to TmVO<sub>4</sub>. These authors tentatively ascribed the resonance behaviour below T<sub>c</sub> to a 1 phonon-1 magnon scattering mechanism. But the data could not be reproduced in this way.

2. **Physical Conception.** - In our approach we suggest that, at least in E-b<sub>1</sub>, b<sub>2</sub> systems like TmVO<sub>4</sub>, where the E-b<sub>2</sub> coupling is much weaker than the E-b<sub>1</sub> coupling, one-phonon resonances do not play any appreciable role in the energy transport. Rather, the linear electron-lattice coupling is mainly used up to define new equilibrium positions of the lattice ("J.T. distortion"), thereby on the one hand establishing cooperativity in the pseudo-magnon system, and on the other hand producing a 2-phonon-magnon scattering mechanism. Thus, there is no one-phonon scattering mechanism which would have an effect onto energy transport. Therefore it is necessary that the definition of the spatial energy density, which is necessary for doing transport theory, does not contain contributions which are linear in the lattice displacements, since these would yield artifact contributions to the heat conductivity. To avoid such artifact contributions, we perform a unitary transformation of the original Hamiltonian H<sup>0</sup> [2], which removes the linear electron-phonon interaction terms [3]. The new and physically effective Hamiltonian then reads

$$(1) \quad H = U^{-1} H^0 U = H_{ph} - \sum_{\vec{m}, \vec{\delta}} \left[ \Lambda_{\vec{0}}^{\vec{z}} \sigma_{\vec{m}}^{\vec{z}} \sigma_{\vec{m}+\vec{\delta}}^{\vec{z}} + \Lambda_{\vec{0}}^{\vec{x}} \sigma_{\vec{m}}^{\vec{x}} \sigma_{\vec{m}+\vec{\delta}}^{\vec{x}} \right] + H'$$

$$(2) \quad H' = \sum_{\vec{q}\vec{q}'} [U_{\vec{q}\vec{q}'}^{12} \sigma_{\vec{q}+\vec{q}'}^{\pm} b_{\vec{q}}^{\pm} b_{\vec{q}'}^{\pm} + \text{h.c.}]$$

$$+ \sum_{\vec{q}\vec{q}'} \{ \sigma_{\vec{q}-\vec{q}'}^{\pm} [V_{\vec{q}\vec{q}'}^{12} b_{\vec{q}}^{\pm} b_{\vec{q}'}^{\pm} + V_{\vec{q}\vec{q}'}^{21} b_{\vec{q}}^{\pm} b_{\vec{q}'}^{\pm}] + \text{h.c.} \}$$

+ energy non-conserving terms

where  $\sigma_{\vec{q}}^{\pm}$  are the pseudo-spin operators [2] which describe the electronic 2-level systems at sites  $\vec{m}$ , and where the quantities  $\Lambda$ ,  $U$  and  $V$  are triple products of the original coupling constants and the inverse of the dynamical lattice matrix  $D$ ; their detailed expressions are lengthy and will be given elsewhere.

3. Heat Conductivity. - Under suitable provisions the heat conductivity expression may be written as a superposition of the different transport paths  $j$ ,  $j=1,2,s$ , each of which is characterized by an excitation energy  $\omega_{\vec{q}j}^{\pm}$ , a group velocity  $\vec{v}_{\vec{q}j}^{\pm}$  and a relaxation time  $\tau_{\vec{q}j}^{\pm}$ . We have employed a Zwanzig-Mori formalism [4] for the correlation functions leading to expressions for  $\tau_{\vec{q}j}^{\pm 1}$ . The details are given elsewhere.

The pseudo-spin part of expr. (1) constitutes a highly anisotropic Heisenberg Hamiltonian, which by means of its dispersion property opens up a new transport path. The most simplified expression for the pseudo-spin conductivity reads

$$(3) \quad \kappa_s = \kappa_s^{(0)} \beta^2 \sigma(T) \left( \frac{1}{2} - \sigma \right) \left( \frac{1}{2} + \sigma \right), \quad \beta = \frac{1}{k_B T}$$

where  $\sigma$  is the order parameter, which satisfies the well-known mean-field equation, and where  $\kappa_s^{(0)}$  may be taken as a constant. The temperature behaviour of  $\kappa_s$  is illustrated in fig. (1). On the other hand, the residual electron-phonon coupling term  $H'$  (vid. (2)) opens a new relaxation channel by means of scattering which involves two phonons and one pseudo-magnon. This leads to a resonance expression of the form

$$(4) \quad \tau(\omega)^{-1} = \Gamma(\omega) \frac{1}{\omega \sqrt{(\omega - \Omega)^2 + \epsilon^2}} \frac{e^{-\beta\omega} (e^{\beta\omega} - 1)}{(e^{\beta\Omega} + e^{-\beta\Omega}) (e^{\beta\sqrt{(\omega - \Omega)^2 + \epsilon^2}} - 1)}$$

where  $\Omega$  is the pseudo-magnon frequency and  $\Gamma(\omega)$  is slightly  $\omega$ -dependent, but is taken as a constant. Then  $\tau(\omega)$  has resonance character below  $T_c$  and a monotonic behaviour above  $T_c$ . The deviation of the phonon heat conductivity from the Casimir behaviour (i.e. boundary scattering only) is drawn in fig. 1.



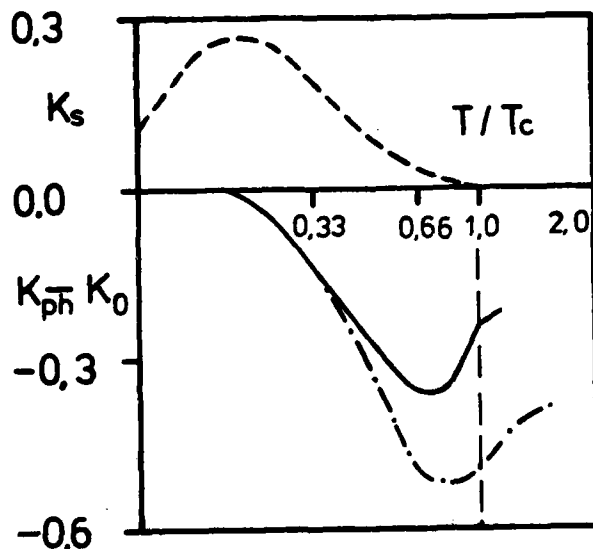


Fig. 1: Heat conductivity in Cooperative J.T. Systems. --- additional conductivity due to the pseudo-spin system. — deviation of phonon conductivity from boundary scattering behaviour in the mean field case  $\propto (1-T/T_c)^{1/2}$ . -.-.- same as before, but  $\propto (1+(T/T_c)^4)^{-1}$ .

The qualitative picture seems promising. An attempt, to achieve a quantitative fit of the measurements [1] by a suitable choice of  $\kappa_s^{(0)}$  and  $\Gamma$  will be made in the near future.

#### References:

- [1] B. Daudin a. B. Salce, accepted for publication in J. Phys. C: Sol. St. Phys. (Sept. 1981)
- [2] G.A. Gehring a. K.A. Gehring, Rep. Progr. Phys. 38, 1, (1975)
- [3] M. Wagner, Sol. State Com. 17, 527 (1975)
- [4] B.J. Berne a. G.D. Harp in: Advances in Chemical Physics, Vol. XVII, eds. I. Prigogine a. S.A. Rice, N.Y. 1970, p.63 ff.

## PHONON PULSES FROM A RELAXING SYSTEM

R. Englman

*Israel Atomic Energy Commission, Soreq Nuclear Research Center, Yavne, Israel*

**Abstract.**— The spread of polychromatic phonon pulses, following optical absorption by a defect, is calculated up to  $\sim 10^2$  lattice-spacings far. Phonon dispersion attenuates the pulse. The angular variation of the pulse peak position reflects the spectral anisotropy.

1. **Introduction.**— Recent detection of monochromatic phonon pulses explored ballistic propagation and angular dependences in the phonon spectrum.<sup>(1,2)</sup> Phonon pulses arising from a relaxing excited impurity have been described theoretically.<sup>(3)</sup> These span a broad frequency range, are easy to generate and may with some sophistication be detected (a) macroscopically, namely at a distance several times the illuminated region, or (b) microscopically, by coherent measurement of signals produced by secondary absorbers near the impurity.

2. **Results.**— As noted previously,<sup>(3)</sup> the pulse-shape depends on the frequency spectrum  $\omega(\underline{k}, j)$  as function of the wave vector  $\underline{k}$  and branch index  $j$ . In Fig. 1 the pulse, which is initially localized near the impurity, maintains its shape and height for a Debye spectrum,  $\omega \propto k$ , as far as 30 lattice spacings ( $a$ ) away but distorts and attenuates strongly by dispersion  $\omega \propto \sin ka/2$ .

The distance ( $\underline{r}$ ) and time ( $t$ ) dependence of the pulse is

$$q(\underline{r}, t) \propto \sum_{\underline{k}, j} q_0(\omega, \underline{k}, j) \exp[i\omega(\underline{k}, j)t - \underline{k} \cdot \underline{r}] \quad (1)$$

The amplitude  $q_0$  of the initial excitation is expected to follow asymptotically for small  $k$  the relationship  $q_0 \propto k^{-2}$  (or  $k^{-1}$  in 2D)<sup>(4)</sup>. The polarization vector included in  $q_0$  has a complicated behaviour especially for degenerate modes.<sup>(5)</sup> We assume an isotropic form.

Then the angular variation of the pulse intensity arises from the anisotropy of  $\omega(\underline{k})$ . Assuming a cubic form like

$$\omega^2 \propto k_x^4 + k_y^4 + k_z^4 \quad (\text{or } \propto k_x^4 + k_y^4 \text{ in 2D})$$

the outward (radial) pulse-height  $r_q(\phi, t)$  was computed as function of the azimuthal angle  $\phi$  in the (001)-plane (or of the polar angle in a cylindrical 2D-geometry).

The location of the main maximum in  $r_q(\phi, t)$  at each instant  $t$  can be derived by assuming that the main contribution to the sum in (1) comes from points in the Brillouin-zone where the group velocity satisfies

$$v_g = \frac{\partial \omega}{\partial \underline{k}} = \frac{\underline{r}}{t}$$

The maximum occurs for values of  $\underline{r}, t$  where the phase in (1)

$$\omega(\underline{k}, t) - \underline{k} \cdot \underline{r} = 2\pi \times \text{integer}$$

It can then be shown that the maximum amplitude is at points  $r_M(\phi, t)$  where

$$\frac{r_M(\phi, t)}{r_M(0, t)} = (\cos^{4/3} \phi + \sin^{4/3} \phi)^{-7/8} \quad (2)$$

The rhs of (2) is shown in Fig. 2. The values of  $r_M(\phi, t)$  obtained from computation of (1) at a time  $t = av_s^{-1}$  ( $v_s$  = velocity of sound) resemble the functional form of (2) in both 2D and 3D. [Note however from the figure that only a little later the computed maxima are distorted with respect to the simple prediction (2)].

3. Conclusion. - It follows that with suitable experimental means of detection spontaneous phonon pulses from excited, relaxing impurities can yield useful though limited information about lattice phonons and the impurity-lattice interaction.

#### 4. References

- (1) G.A. Northrop and J.P. Wolfe, Phys. Rev. B 22, 6196 (1981)
- (2) P. Hu, V. Narayanasurti and M.A. Chin, Phys. Rev. Letters 46, 192 (1980)
- (3) R. Englman, Chem. Phys. 58, 227 (1981)
- (4) R.I. Elliott and J.B. Parkinson, Proc. Phys. Soc. Lond. 92, 1024 (1967)
- (5) B. Halperin and R. Englman, J. Phys. C 8, 3975 (1975).

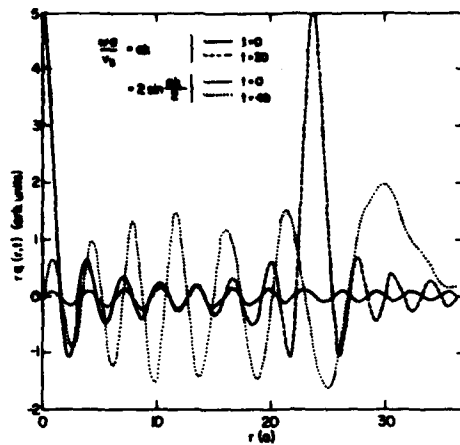


Fig. 1.-  $r_q$  vs  $r$   
Radial, weighted phonon amplitudes as function of distance in units of lattice spacing for isotropic spectra at different times. Initially the pulse is localized at the centre, later it propagates sharply outwards for a non-dispersive spectrum ( $\omega = k$ ) but gets attenuated and distorted for a dispersive spectrum. Time is in units of  $ax(\text{velocity of sound})^{-1}$ .

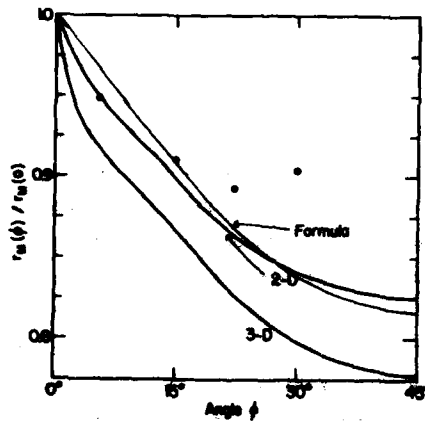


Fig. 2.- Anisotropy effect  
The position  $r_m$  of the main maximum as function of the angle of orientation  $\phi$  (in a [001]-plane) as obtained heuristically [eq.(2)], by computation in 3D and 2D at a time =  $5av_s^{-1}$ . The dots show computed results in 2D at a time =  $7av_s^{-1}$ .

## PHONON SCATTERING BY Cr IONS IN GaAs AND THE EFFECT OF UNIAXIAL STRESS

A. Ramdane, B. Salce\*, L.J. Challis and M. Locatelli\*

*Department of Physics, Nottingham University, Nottingham NG7 2RD, U.K.**\*Service B T, CENG, 85X, 38041 Grenoble Cedex, France*

**Abstract:** Thermal conductivity measurements in the range 50mK to 100K on n, p and SI samples of Cr doped GaAs show that  $\text{Cr}^{2+}$  only scatters phonons at 25 GHz while  $\text{Cr}^{3+}$  has several resonant frequencies in the range 20 to 700GHz. Measurements under uniaxial stress indicate very anisotropic behaviour qualitatively consistent with a Jahn-Teller model for  $\text{Cr}^{3+}$ .

Substitutional Cr appears to exist in GaAs in the three ionic states  $\text{Cr}^{2+}$ ,  $\text{Cr}^{3+}$  and  $\text{Cr}^{4+}$ .  $\text{Cr}^{4+}$  has an orbital singlet ( $^3A_2$ ) ground state and cannot scatter phonons strongly (neither could  $\text{Cr}^{1+}$  if it existed) but this is not necessarily the case for  $\text{Cr}^{2+}$  and  $\text{Cr}^{3+}$ . We have investigated the phonon scattering by making thermal conductivity measurements down to 50mK and under uniaxial stress. The zero stress work is an extension of earlier work /1/ and a full report on the 14 samples investigated will appear elsewhere /2/.

The thermal conductivity  $K$  correlates with the electrical characteristics and values for n, p and semi-insulating (SI) specimens are shown in fig 1. The data are plotted as thermal resistivity ( $W = 1/K$ ) divided by the resistivity characteristic of undoped GaAs to emphasise the scattering and the upper scale shows the frequency of the dominant phonons in the heat current ( $h\nu \sim 4kT$ ) attributable to Cr. The weakly p-type (GA781) and SI sample GA735(e) are not dissimilar in behaviour above 100mK and the smaller though still very substantial scattering in TI4 is consistent with the fact that the Cr concentration is about 20 times smaller than in the other 2 samples. There is also evidence of resonant scattering at 25GHz in SI GaAs which is absent in the p-type material but appears to be the only resonant scattering in n-type material containing a roughly similar amount of Cr. Since the Cr in n-type material should be very largely in the  $\text{Cr}^{2+}$  state we conclude that this ion is responsible for the low frequency scattering. So  $\text{Cr}^{2+}$  can only scatter phonons significantly at 25GHz. The absence of this scattering in weakly p-type material ( $\text{Cr}^{3+}$  and  $\text{Cr}^{4+}$ ) and its presence in SI material ( $\text{Cr}^{2+}$  and  $\text{Cr}^{3+}$ ) is consistent with the probable valence states given. The scattering above 100mK in p-type and SI material seems attributable to  $\text{Cr}^{3+}$  and from the positions of the maxima in  $W/W_0$  we deduce that the scattering is resonant at 21, 80, 150, 400 and 880GHz suggesting a fairly complex level scheme. The values at 150 and 400 GHz are broadly consistent with values obtained by tunnel junction spectroscopy /3/.

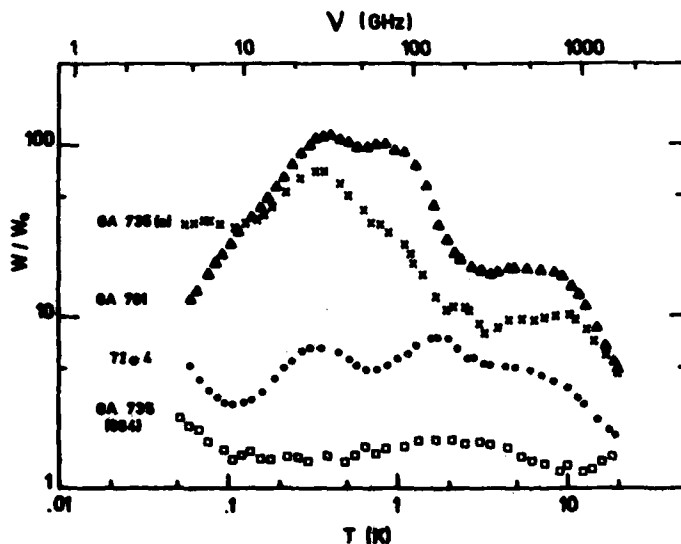


Fig 1: Reduced resistivity  $W/W_0$  of GaAs:Cr.

Both  $\text{Cr}^{2+}$  and  $\text{Cr}^{3+}$  are believed to undergo Jahn-Teller effects. In the static limit the  $^5T_2$  states of the  $T_d$  crystal field of  $\text{Cr}^{2+}$  are split by tetragonal Jahn-Teller distortions to leave a ground state orbital singlet  $^5B_2$  for each of the three wells which is then split by second order spin-orbit interaction. This can account for the EPR data /4/ but not for the phonon scattering observed here which is forbidden in this limit /2,5/. Tunnelling between the wells mixes their states and phonon scattering is now allowed between levels separated by  $3\delta_1$  where  $\delta_1$  is the tunnelling frequency /5/. The levels should be very sensitive to applied or random strain which produces relative shifts in the energies of the wells. However the phonon scattering cuts off once these shifts exceed the tunnelling splitting so no scattering can occur much above  $3\delta_1$ . From the data in fig 1 we can conclude therefore that  $\delta_1 \gtrsim 2\text{GHz}$  and so the Ham reduction factor  $\gamma \gtrsim 0.001$ . The picture is much less clear for  $\text{Cr}^{3+}$ . The  $T_d$  ground state is  $^4T_1$  and EPR data suggest that the Jahn-Teller distortion results in 6 orthorhombically placed wells /6/. The size of the reduction factors and so the relative sizes of the first and second order spin-orbit splittings are not known and the description is complicated by the possible close proximity to  $^4T_1$  of states from excited configurations /7/.

To investigate the system further, measurements have been made of the dependence of the thermal conductivity on uniaxial stress in the temperature range 2-15K. No significant effect was found in n-type material and this seems consistent with the description for  $\text{Cr}^{2+}$  given above. Stress should increase the transition frequencies to values comparable with those of the dominant phonons in the heat current so that a decrease in thermal conductivity might occur. The fact that it does not is consistent with the cut-off in scattering cross-section at these high frequencies. Data for SI (TI4) and p-type (GA781) samples are shown in fig 2 for compressive stresses along  $\langle 001 \rangle$  and  $\langle 110 \rangle$  directions. The behaviour of the two samples is very similar for  $\langle 001 \rangle$  stresses again suggesting that the scattering ion is the same. In TI4 the saturation value at high stresses is very similar to that of undoped GaAs suggesting

that the Cr scattering has been completely quenched. The anisotropy reflected by the comparatively modest changes produced by  $\langle 110 \rangle$  stress is very striking and suggests that  $\langle 110 \rangle$  stress leaves a ground state within which phonon scattering can still occur. This seems qualitatively consistent with the stress splitting for  $\text{Cr}^{3+}$  near the static Jahn-Teller limit given in ref /6/. Compressive  $\langle 001 \rangle$  stress leaves 2 orthogonal levels lowest so that phonon scattering should vanish at high stress. Compressive  $\langle 110 \rangle$  stress leaves 4 levels lowest. Tunnelling can occur between pairs so phonon scattering remains even at high stress. Further measurements and analysis are in progress to test this description.

We are very grateful for samples from M J Cardwell, P R Jay and D J Stirland and the Plessey Co and from T Ishiguro and H Tokumoto and to many of our colleagues particularly A S Abhvan, S P Austen, C A Bates, L Eaves, A M de Goër, J R Fletcher, P J King, L W Parker and D J Pooler for very helpful discussions. The work was supported by the Science Research Council and the Ministère des Affaires Etrangères and one of

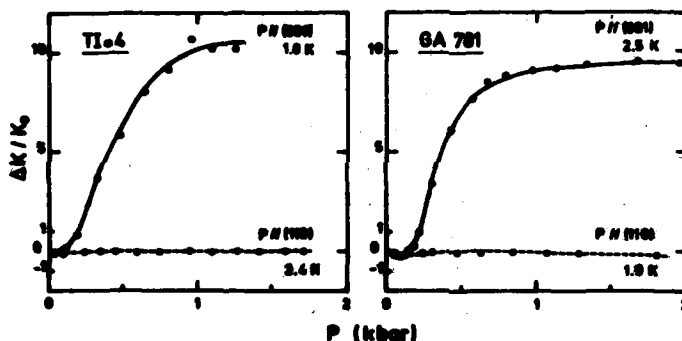


Fig 2: Effect of uniaxial stress on the thermal conductivity.

us (AR) is very grateful to the Algerian Ministry of Higher Education and Scientific Research for a maintenance grant.

#### References

- /1/ Challis L J and Randane A, 1980, Proc Int Conf on Phonon Scattering in Condensed Matter, ed H Maris (New York : Plenum) pp 121-4. Bury P, Challis L J, King P J, Monk D J, Randane A, Rampton V W and Wiscombe P C, 1980, Proc Int Conf on Semi-Insulating III-V Compounds (Nottingham), ed G J Rees (Orpington : Shiva Press).
- /2/ Challis L J, Locatelli M, Randane A and Salce B, submitted for publication.
- /3/ Hamdeche M, King P J, Murphy D T and Rampton V W, to be published.
- /4/ Krebs J J and Stauss G H, Phys Rev B **16**, 971, 1977.
- /5/ Abhvan A S, Austen S P, Bates C A, Parker L W and Pooler D J, submitted for publication.
- /6/ Stauss G H and Krebs J J, Phys Rev B **22**, 2050, 1980.
- /7/ Hammett L A and Dinnock J G, Phys Rev B **20**, 1527, 1979.

THEORY OF THERMAL CONDUCTIVITY IN MOLECULAR CRYSTALS. APPLICATION TO  
ALCALI CYANIDES

W. Bauernfeind, J. Keller and U. Schröder

*Institut für Theoretische Physik, Universität Regensburg, D-8400 Regensburg,  
F.R.G.*

**Abstract.**— We investigate the influence of coupling between translational and rotational motion on the thermal conductivity of molecular crystals and present results for KCN.

In this paper we report on calculations of the thermal conductivity of KCN, the prototype of a molecular crystal with rotational motion of molecular groups. We will show that the interaction between translational and rotational motion is a very effective relaxation mechanism for the heat current and may reduce the thermal conductivity to values as found in amorphous materials.

In our calculations we use a model proposed by Michel<sup>1</sup> for the interaction between translational and rotational motion. At  $T = 168$  K KCN undergoes a phase transition to an orthorhombic phase where the CN molecules are ordered preferentially in the  $[110]$  direction<sup>2</sup>. In our calculation we restrict ourselves to the high temperature phase where the crystal is cubic, and we treat the CN molecules as free rotators.

The thermal conductivity  $\lambda$  defined by  $J = -\lambda \nabla T$  can be calculated from the following correlating function (Kubo formula)

$$\lambda = \lim_{t \rightarrow 0} \frac{1}{V \cdot T} \int_0^\infty dt e^{-\epsilon t} \int_0^B dk \langle j_\alpha(0) j_\alpha(t + i\epsilon) \rangle \quad (1)$$

Here  $j_\alpha = j_\alpha(q=0)$  is the heat current operator.

The relaxation function (1) is most conveniently evaluated by using a Mori-Zwanzig projection technique<sup>3</sup>.

The result is

$$\lambda = \frac{1}{TV} \frac{(\langle j_\alpha | j_\alpha \rangle)^2}{N} \quad (2)$$

where the static current susceptibility is defined by

$$\langle j_\alpha | j_\alpha \rangle = \int_0^B \langle j_\alpha(0) j_\alpha(t + i\epsilon) \rangle dk \quad (3)$$



and the memory function  $M$  is given approximately by the relaxation function of the time derivative of the heat current  $A_Y = [H, j_Y]$

$$M \approx \lim_{\varepsilon \rightarrow 0} \int_0^{\infty} dt e^{-\varepsilon t} \int_0^{\beta} d\kappa \langle A_Y^{\dagger}(0) A_Y(t+i\kappa) \rangle \quad (4)$$

For the molecular crystal KCN we use the following model Hamiltonian<sup>1</sup>

$$H = \sum_{l\kappa\alpha} \frac{p_{\alpha}^2(l)}{2m_{\kappa}} + \frac{1}{2} \sum_{l\kappa\alpha} \sum_{l'\kappa'\beta} \Phi_{\alpha\beta}(l, l', \kappa, \kappa') u_{\alpha}(l, \kappa) u_{\beta}(l', \kappa') + \\ + \sum_l \frac{L^2(l)}{2I} + V^R + \sum_{\eta=1}^5 \sum_{l\kappa\alpha} Y_2^{\eta}(l, \kappa) v_{\eta\alpha} u_{\alpha}(l, \kappa) \quad (5)$$

Here the last term is the interaction between the translations  $u(l, \kappa)$  of  $K$  and the orientations  $Y_2^{\eta}(l, \kappa)$  of neighbouring CN molecules described by spherical harmonics.

From a suitable definition of the energy density  $h(\vec{r})$  and its continuity equation the following expression for the heat current is obtained

$$\vec{j} = \sum_{l\kappa\alpha} \sum_{l'\kappa'\beta} \frac{1}{2m_{\kappa}} p_{\alpha}(l, \kappa) \Phi_{\alpha\beta}(l, l', \kappa, \kappa') u_{\beta}(l', \kappa') [\vec{x}_0(l, \kappa) - \vec{x}_0(l', \kappa')] \quad (6)$$

Here we have written down only the current carried by phonons which is expected to give the largest contribution to the thermal conductivity. For the calculation of the memory function  $M$  we also need the time derivative of  $\vec{j}$ :  $A_Y = [H, j_Y]$ . It is of the form  $A \sim Y \cdot u$ . For the evaluation of the correlation function in (4) we use a mode coupling procedure by writing

$$\langle Y(t)u(t)Y(0)u(0) \rangle \approx \langle Y(t)Y(0) \rangle \langle u(t)u(0) \rangle \quad (7)$$

For a first estimate of  $\lambda$  the phonon propagator  $\langle u(t)u(0) \rangle$  and the static current susceptibility  $\langle j|j \rangle$  are evaluated in a Debye model, and for  $\langle Y(t)Y(0) \rangle$  the correlation function of a free rotator is used.

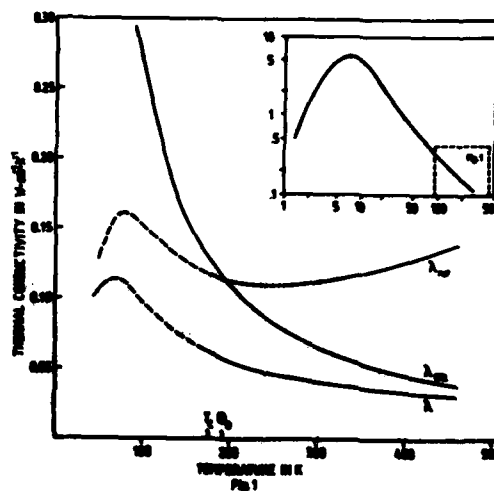
The resulting thermal conductivity  $\lambda_{\text{rot}}$  is shown in Fig. 1. Its temperature dependence is determined by the Debye temperature ( $\theta_D = 192$  K) and the typical excitation energy of a rotation  $E_{\text{rot}} = (k_B T \cdot \pi^2 / 2I)^{1/2} = 32(T/\theta_D)^{1/2}$  K where  $I$  is the moment of inertia of KCN. The magnitude of  $\lambda$  is determined by the coupling constants  $v$  between rotational and translational motion. They can be expressed by two constants  $C, B$  (see Eq. 2 of Ref. 4) which have been determined by a fit to the elastic constants:  $C = 1630$  K/Å,  $B = 860$  K/Å.

**Fig. 1:** Temperature dependence of the thermal conductivity in the cubic phase of KCN.

$\lambda_{\text{rot}}$ : thermal conductivity resulting from coupling between translational and rotational motion,

$\lambda_{\text{KCl}}$ : experimental result for KCl (also shown in the insert for a larger temperature range),

$\lambda$ : predicted thermal conductivity for KCN.



For a realistical calculation of the thermal conductivity we also have to consider anharmonic interactions in the translational motion (Umklapp processes). In order to get an estimate of this effect we compare  $\lambda_{\text{rot}}$  with the experimental result  $\lambda_{\text{KCl}}$  for pure KCl<sup>5</sup>. The total thermal conductivity  $\lambda$  shown in Fig. 1 is then obtained by

$$\lambda^{-1} = \lambda_{\text{rot}}^{-1} + \lambda_{\text{KCl}}^{-1}$$

Our result shows that in a medium temperature range  $T \approx \theta$ , the relaxation of the heat current is dominated by the interaction of phonons with rotations, whereas at high temperatures anharmonic Umklapp processes are most important. Our result has to be considered as an upper bound to the thermal conductivity of KCN above the phase transition temperature  $T_c$ .

#### References

- 1 K.H. Michel and J. Naudts, J.Chem.Phys. **67**, 547 (1977).
- 2 J.M. Rowe, J.J. Rush, and E. Prince, J.Chem.Phys. **66**, 5147 (1977).
- 3 D. Forster, Hydrodynamic fluctuations, broken symmetry, and correlation functions, Benjamin, Reading (1975).
- 4 D. Strauch, U. Schröder, and W. Barmann, Solid State Commun. **30**, 559 (1979).
- 5 E.D. Davlatkova and I.A. Smirnov, Sov. Physics Solid State **4**, 1836 (1963); **4**, 1445 (1963).

## PHONON-DISLOCATION DIPOLE INTERACTION IN LiF AT LOW TEMPERATURE

G.A. Kneezel and A.V. Granato\*

Xerox Webster Research Center, Webster, New York, U.S.A.

\*University of Illinois, Urbana, Illinois, U.S.A.

**Abstract.**--We compare the effects of isolated dislocations and a somewhat larger density of edge dislocation dipoles on thermal conductivity, specific heat, and ultrasonic velocity and attenuation in alkali halides such as LiF. The motivation for this study is to check the implications of earlier work where it was demonstrated that the effect of deformation on thermal conductivity in LiF could not be accounted for by dynamic scattering by a dislocation density equal to the etch pit density, but could be fit assuming scattering was due to the "optical" mode of vibration of a much larger density of dislocation dipoles.

By irradiating previously deformed LiF [110] rods and remeasuring the thermal conductivity, Anderson and co-workers<sup>1-2</sup> have demonstrated that the scattering of phonons by dislocations is predominantly dynamic--at least below 2 K. Although their results were qualitatively inconsistent with static strain field scattering they were also not quantitatively fit by previous calculations of dynamic scattering effects. We undertook a calculation<sup>3-4</sup> based on the vibrating dislocation string model<sup>5</sup> and taking into account several details which others have neglected--including phonon focusing, resonance angle effects, and the resolved shear stress factor for each incident phonon--and confirmed that dynamic phonon scattering by isolated dislocations of a density  $\Lambda$  equal to the etch pit density could not account for observed<sup>2</sup> effects.

It became clear that the defect responsible for scattering was a dislocation-like defect having a higher resonant frequency (with a broader distribution of resonant frequencies) and present in larger numbers. These conditions are met by the dislocation dipole, which is a pair of dislocations of opposite signs on glide planes a distance  $d$  apart. Dislocation dipoles are predominantly of edge character, as screw dislocations of opposite sign cross glide and annihilate. Because the members of the dipole attract each other there is a restoring force  $Dy$  when the dislocations move in opposite directions (the optical mode of vibration) so that the equation of motion is

$$A \frac{d^2 y}{dt^2} + B \frac{dy}{dt} + C \frac{d^2 y}{dx^2} + Dy = b \cos(kx - \omega t). \quad (1)$$

The optical resonant frequency of the  $m$ th normal mode is

$$\omega_{op}(m) = (\omega_{ac}^2(m) + D/A)^{1/2} = [(m^2 \pi^2 C/L^2 A) + (Gb^2/2\pi A(1-\nu)d^2)]^{1/2} \quad (2)$$

where  $\omega_{ac}$  is the acoustical mode resonant frequency,  $A$  is the effective mass,  $B$  is the damping constant,  $C$  is the line tension,  $\sigma$  is the resolved shear stress,  $L$  is the length between pinning points,  $b$  is the burgers vector, and  $\nu$  is Poisson's ratio. Thus the optical mode frequency is higher than the acoustical mode frequency, especially for narrow dipoles. Long wavelength ( $\lambda \gg d$ ) stress waves excite only the optical mode of vibrations because the dislocations have opposite signs.

Dislocation dipoles are believed to greatly outnumber isolated dislocations in deformed crystals. A reasonable ratio appears to be 10-100, distributed primarily at dipole widths of  $3b$  to  $300b$ <sup>6</sup> with most having widths less than a few hundred Angstroms so that they are not easily detected by electron microscopy or etch pitting techniques. A distribution of this type (for dipole

width  $nb$ ) is the exponential distribution  $\Lambda(n) = \Lambda_0 \exp(-(n-3)/N_0)$  for  $n \geq 3$ . The observed thermal conductivity effects<sup>2</sup> were fit by assuming  $N_0 = 60$  and a Koehler distribution<sup>5</sup> of lengths with average loop length equal to the ultrasonically determined value<sup>7</sup> of  $2 \times 10^{-5}$  cm. If all dipoles are on the (110) planes perpendicular to the rod axis it is found<sup>4</sup> that  $7.5 \times 10^8 \text{ cm}^{-2}$  dislocations paired into dipoles are required in order to fit the observed effects.<sup>2</sup> However if some fraction of the dipoles are on the other {110} planes which scatter the predominant heat carrying phonons along [110] LiF rods more effectively, then less dipoles are required. Because of the type of deformation used<sup>2</sup> most dislocations and dipoles are expected to be on (110) so that the number of dipoles required to fit the thermal conductivity data is 10-30 times the observed etch pit density.

Vibrating dislocations and dipoles are expected to contribute to the specific heat of a deformed crystal. The contribution by isolated dislocations (and also by the acoustical mode of dipoles which obeys the same equation of motion) at temperatures above  $T_0 = \hbar \omega_1 / k_B$  is<sup>8</sup>

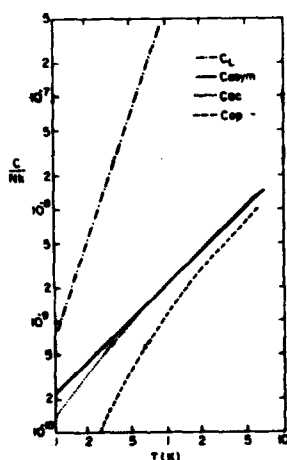
$$C_{ac} = \pi^2 p \Lambda a^2 N k_B T / 3Z\theta \quad (3)$$

where  $\omega_1$  is the lowest normal mode frequency,  $a$  is the lattice vector,  $Z$  is the number of atoms per unit cell,  $\theta$  is the Debye temperature (723 K in LiF) and  $p$  is the average sound velocity divided by  $d\omega/dk$  for the dislocation modes. At lower temperature the contribution falls off exponentially. For a delta function dislocation length distribution  $L = 2 \times 10^{-5}$  cm in LiF,  $T_0 \sim .5$  K and

$$C_{ac} \sim 2.0 \times 10^{-15} \Delta N k_B T / \theta. \quad (4)$$

This same asymptote is approached at higher temperatures by the dipole optical mode contribution  $C_{op}$ . This can be seen from equation (2) in that for the higher order modes ( $m \gg 1$ )  $\omega_{op} \sim \omega_{ac}$ . For a delta function distribution  $L = 2 \times 10^{-5}$  cm and  $d = 60b$ ,  $T_0 \sim 1.5$  K.

The background to which  $C_{op}$  and  $C_{ac}$  must be compared is the lattice specific heat at low temperature  $C_L = 234 N k_B (T/\theta)^3$ . Because of their linear temperature dependence the vibrating dislocation dipoles make their largest relative contribution at low  $T$ . At 1 K the asymptotic dipole contributions are less than 1% of the total specific heat for  $\Lambda = 7.5 \times 10^8 \text{ cm}^{-2}$ . At lower temperatures the linear asymptotic expression is no longer valid and a numerical calculation of the dipole contributions to the specific heat was performed with two objectives: 1) observe the form of the curves below the asymptote, and 2) determine the effect of assuming exponential distributions of dipole lengths and widths as in the thermal conductivity calculations.<sup>4</sup>



For a delta function distribution of lengths and widths it was found that the asymptote (4) was approached to within about 10% by  $C_{ac}$  and  $C_{op}$  around .5 K and 1.5 K as expected. The results of the calculations incorporating the exponential distributions of lengths and widths are shown in figure 1 assuming  $\Lambda = 7.5 \times 10^8 \text{ cm}^{-2}$ . Relative to the delta function case, it is found that  $C_{ac}$  is increased at all temperatures while  $C_{op}$  is increased below  $\sim .3$  K and decreased above  $\sim .3$  K. In the approximately linear regime above 1 K,  $C_{ac} + C_{op} \sim (1.5 + 1.0) \times 10^{-6} N k_B T / \theta$ . At 1 K the dipole contribution for that defect density is  $\sim .5\%$  of the lattice contribution and at higher temperature the relative contribution is proportional to  $1/T^2$ . This is consistent with recent experimental work<sup>9</sup> in which no change was observed (to within the 1% experimental accuracy) in the specific heat of a sample deformed in compression by 4.5%.

Comparison of the predicted effects of dipoles and isolated dislocations can also be made for ultrasonic velocity and attenuation. In particular the relative velocity change  $\Delta v/v$  is proportional to  $1/\omega_1^2$  and the logarithmic decrement  $\Delta$  is proportional to  $\omega^2/\omega_1^4$  for  $\omega \ll \omega_1$ . For dipoles only the optical mode of vibration is expected to be excited by the long wavelength stress waves. Numerical calculations were made to compare the effects of a Koehler distribution of screw dislocations ( $L = 2 \times 10^{-5}$  cm) and of the edge dipole distribution used in fitting thermal conductivity measurements ( $L = 2 \times 10^{-5}$ ,  $N_0 = 60$ ). Normalized to the same defect densities it was found that the screw dislocation contribution was 10 times greater for  $\Delta v/v$  and 100 times greater for  $\Delta$  than the edge dipole contributions. If the dipole density is an order of magnitude greater, dipole effects should certainly be observable--although not dominant. Irradiation pinning experiments should especially be able to discriminate between dislocation and dipole contributions because  $\omega_1$  of the dislocations is proportional to  $1/L$  while that of the dipole is given in equation (2). The length varies during irradiation according to the relation<sup>10</sup>

$$L = L_0 / (1 + \beta t). \quad (5)$$

Thus the time dependence of the velocity and attenuation changes during irradiation pinning should be less rapid if dipole effects are important. For an LIF sample deformed in [001] compression and measured by 10 MHz longitudinal waves at 4.2 K the irradiation pinning results<sup>7</sup> suggest that there are not an order of magnitude more edge dipoles than screw dislocations. However for this sample the deformation was much less so that the dislocation density was about  $1 \times 10^{-6}$  cm<sup>-2</sup>, and it is likely that the dipole density and width distribution is somewhat different for small deformation.

In conclusion we have considered the implications of assuming a large density of edge dipoles (previously deduced from thermal conductivity measurements) on the specific heat and ultrasonic velocity and attenuation in LIF. We have found the specific heat is relatively insensitive to dislocations and dipoles in the expected densities. We also found that irradiation pinning ultrasonic measurements should show the optical mode effects of edge dipoles if they are in fact present in numbers an order of magnitude greater than isolated dislocations. Such measurements should be carried out on specimens deformed by a few percent. If possible it would be useful to measure the thermal conductivity effects on the same sample. In this case, kilohertz ultrasonic measurements would be more applicable to the typically rod-shaped thermal conductivity samples.

#### References

1. A.C. Anderson and M.E. Melnowski, *Phys. Rev. B* **5**, 3199 (1972).
2. E.P. Roth and A.C. Anderson, *Phys. Rev. B* **20**, 766 (1979).
3. G.A. Kneszel and A.V. Granato, *Acta/Scripta Met Int. Conf. on Dislocation Modelling of Physical Systems*, 1980.
4. G.A. Kneszel and A.V. Granato, *The Effect of Independent and Coupled Vibrations on Low Temperature Thermal Conductivity in Alkali Halides*, to be published.
5. (a) A. Granato and K. Lücke, *J. Appl. Phys.* **27**, 583 (1956).  
(b) A. Granato and K. Lücke, *J. Appl. Phys.* **27**, 789 (1956).
6. W.G. Johnston and J.J. Gilman, *J. Appl. Phys.* **30**, 129 (1959).
7. G. Wirs, Ph.D. thesis (University of Illinois, 1972) (unpublished).
8. A.V. Granato, *Phys. Rev.* **111**, 740 (1958).
9. E.J. Cotts and A.C. Anderson, *The Low Temperature Specific Heat of Deformed Lithium Fluoride Crystals*, to be published.
10. R.M. Stern and A.V. Granato, *Acta. Met.* **10**, 358 (1962).

## PHONON CONDUCTIVITY DUE TO NONDIAGONAL ENERGY-FLUX OPERATOR

G.P. Srivastava

*Physics Department, The New University of Ulster, Coleraine, N. Ireland BT52 1SA, U.K.*

**Abstract.** Using the Zwanzig-Mori projection operator method we present calculations of renormalised phonons and their contribution to the thermal conductivity of Ge from the nondiagonal part of the heat-flux operator given by Hardy.

Recently we<sup>1</sup> have used the Zwanzig-Mori projection operator method to obtain expressions for the lattice thermal conductivity of an anharmonic crystal from the diagonal and nondiagonal parts of the heat-flux operator given by Hardy<sup>2</sup>. In the van Hove limit the diagonal contribution is the well known single-mode relaxation time result<sup>3</sup>, in which only the true phonon frequency appears. But the nondiagonal contribution includes renormalised phonons, with shifted frequencies. Here we present results of our calculations of renormalised phonons and their contribution to the thermal conductivity of Ge from the nondiagonal part of the heat-flux operator.

In the notation of Ref. 1 the expressions for the diagonal and nondiagonal contributions to the lattice thermal conductivity are as follows

$$\kappa_d = \frac{\hbar^2 \beta^2 k_B}{3N_0 \Omega} \sum_i \omega_i^2 c_i^2 \bar{N}_i (\bar{N}_i + 1) \tau_i \quad (1)$$

$$\begin{aligned} \kappa_{nd} = & \frac{\hbar^2 \beta^2 k_B}{3N_0 \Omega} \sum_{ij} \omega_i \omega_j c_{ij}^2 \left[ \frac{\bar{N}_j (\bar{N}_j + 1)}{\tau_{ij}^{-2} + (\omega_{j-i} + \Delta_{ij})^2} \right. \\ & \left. + \frac{\bar{N}_i \bar{N}_j + (\bar{N}_i + 1)(\bar{N}_j + 1)}{\tau_{ij}^{-2} + (\omega_{i+j} + \Delta_{ij})^2} \right] \tau_{ij}^{-1} \quad (2) \end{aligned}$$

Here  $i \equiv (\vec{q}, s)$ ,  $j \equiv (\vec{q}', s')$ ,  $\omega_{i \pm j} = \omega_i \pm \omega_j$ ,  $\Delta_{ij} \equiv \text{Im}(\delta_i) - \text{Im}(\delta_j) = \Delta_i - \Delta_j$

$$\tau_{ij}^{-1} \equiv \text{Re}(\delta_i) + \text{Re}(\delta_j) = \frac{1}{2}(\tau_i^{-1} + \tau_j^{-1}),$$

and  $\vec{c}_{ij} \equiv \vec{c}_{qss}$ , is a generalised group velocity.  $\Delta_i$  and  $\tau_i^{-1}$  are the frequency shift and the inverse relaxation time of a phonon in mode  $i$  and are, respectively, calculated from the imaginary and real parts of  $\delta_i$  where

$$\delta_i = \frac{-1}{\hbar^2} \int_0^\infty dt \langle [\Gamma_i(t), \Gamma_i] \rangle_0 e^{i\omega t}, \quad (3)$$

with  $\Gamma_i$  as a measure of cubic anharmonicity:  $H = H_{\text{harm}} + \sum_i \Gamma_i A_i$ . As in our previous paper in these proceedings we express  $\Gamma_i$  in terms of the Grüneisen constant of the material

$$\Gamma_i \equiv \Gamma_q = \frac{|\gamma| \hbar^{\frac{1}{2}}}{3! \sqrt{2\rho N_0 \Omega}} \sum_{q'q''} \sqrt{\omega \omega' \omega''} A_q A_{q'} \delta_{\vec{q}+\vec{q}'+\vec{q}'', \vec{G}} \quad (4)$$

$\vec{q} \equiv (\vec{q}, s)$ . With this then

$$\langle [\Gamma_q(t), \Gamma_q] \rangle_0 = \sum_{q'q''} |\Phi_{qq'q''}|^2 \langle [A_q(t), A_q A_{q'}] \rangle_0, \quad (5)$$

where

$$|\Phi_{qq'q''}|^2 = \frac{\hbar^3 \gamma^2}{2\rho c^2 N_0 \Omega} \omega \omega' \omega'' \delta_{\vec{q}+\vec{q}'+\vec{q}'', \vec{G}} \quad (6)$$

With equations (4-6) and a little bit of algebra, we can express  $\delta_i$  for three phonon processes as

$$\delta_q = \frac{-1}{\hbar^2} \sum_{q'q''} |\Phi_{qq'q''}|^2 \int_0^\infty dt \{ (N' - N'') e^{i(\omega + \omega' - \omega'')t} + \frac{1}{2} (1 + N' + N'') e^{i(\omega - \omega' - \omega'')t} \} \quad (7)$$

From this  $\Delta_q$  and  $\tau_q^{-1}$  can be evaluated using the relation

$$\int_0^\infty dt e^{i(\omega \pm \omega' - \omega'')t} = \pi \delta(\omega \pm \omega' - \omega'') - i P \left( \frac{1}{\omega \pm \omega' - \omega''} \right), \quad (8)$$

where  $P$  denotes the principal part. It is interesting to note that  $\tau_q^{-1}$  calculated in this way is the same as the result obtained using the first order perturbation method<sup>3,4</sup>.

In Fig. 1 we have plotted  $\Delta_q$  and  $\tau_q^{-1}$  for the longitudinal mode at 300 K. Although  $\tau_q^{-1}$  is an increasing function of frequency,  $\Delta_q$  shows a pronounced structure at  $\omega \sim 25 \times 10^{12} \text{ s}^{-1}$ . We find that in general  $\Delta_q > \tau_q^{-1}$  and  $(\omega_q + \Delta_q) \gg \tau_q^{-1}$ , implying that a pseudoharmonic model<sup>5</sup> is a good description for phonons in Ge. Furthermore, our calculations show that  $\kappa_{nd}$  is negligibly small in comparison to  $\kappa_d$  in the temperature range 10-900 K. A similar conclusion was reached by Hardy<sup>2</sup>, and Semwal and Sharma<sup>6</sup> using qualitative arguments.

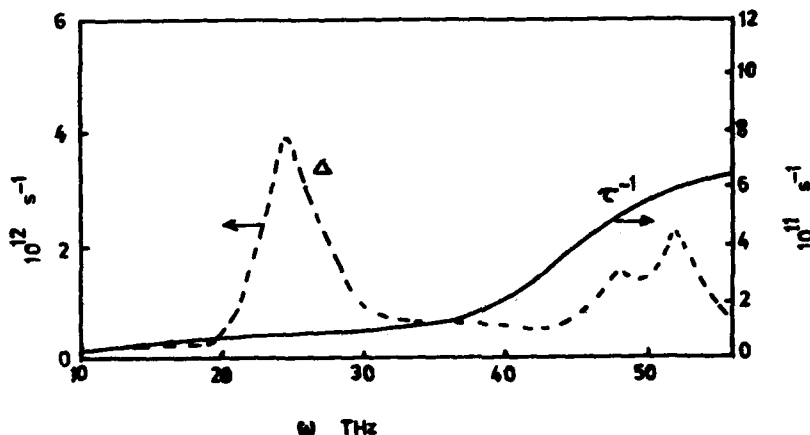


Fig. 1: The inverse relaxation time ( $\tau^{-1}$ ) and frequency shift ( $\Delta$ ) for the longitudinal acoustic phonon mode in Ge at 300 K as a function of frequency ( $\omega$ ).

#### References

- <sup>1</sup>Srivastava, G.P. and Prasad, M., Phys. Rev. B23, 4723 (1981).
- <sup>2</sup>Hardy, R., Phys. Rev. 132, 168 (1963).
- <sup>3</sup>Srivastava, G.P. Philos. Mag. 34, 795 (1976).
- <sup>4</sup>Srivastava, G.P. J. Phys. Chem. Solids, 41, 357 (1980).
- <sup>5</sup>Reissland, J.A. The Physics of Phonons (Wiley, New York, 1973).
- <sup>6</sup>Semwal, B.S. and Sharma, P.K., Phys. Rev. B5, 3909 (1972).



# CONTRIBUTION OF LOW-FREQUENCY LONGITUDINAL PHONONS TO THE LATTICE THERMAL CONDUCTIVITY OF DIELECTRIC SOLIDS

R. Brito-Orta and P.G. Klemens

*Dept. of Physics and Inst. of Material Science, Univ. of Connecticut, Storrs, CT 06268, U.S.A.*

**Abstract.**— Contributions of low-frequency longitudinal phonons to the lattice thermal conductivity are estimated using the Pomeranchuk mean free path and a cut-off given by the Akhieser theory. The temperature dependences are compared with data for rubidium halides, germanium and silicon.

1. Introduction.— Restrictions of frequency and wave-vector conservation in three-phonon anharmonic processes forbid low-frequency longitudinal phonons to interact directly with thermal phonons. This lengthens their mean free path and causes them to make a large contribution to the lattice thermal conductivity.<sup>1</sup> However, at very low frequencies, i.e. at  $\omega < \omega_c = 1/\tau_{th}$ , where  $\tau_{th}$  is the relaxation time of thermal phonons, the conservation conditions are relaxed, and longitudinal and transverse phonons have essentially the same mean free path.<sup>2</sup> The excess contribution of longitudinal phonons increases the temperature dependence of the lattice thermal conductivity.

The present treatment is confined to temperatures above the Debye temperature.

2. Phonon Mean Free Path.— For frequencies above  $\omega_c$  longitudinal phonons are scattered in a two-step process. First they participate in a three-phonon normal process with transverse phonons of about their own frequency. The transverse phonons then interact with phonons of thermal frequency. The mean free path of a longitudinal phonon of frequency  $\omega$  and velocity  $v_I$ , as limited by the first process, is estimated<sup>1,3</sup> as

$$l_I = (1/10 \pi^2 \gamma^2) (T_0/T) (\omega_D/\omega)^2 v_I \omega_D / \omega^2 \quad (1)$$

where  $\gamma$  is the Grüneisen constant,  $\omega_D$  the Debye frequency and  $T_0 = Mv^2/k$ , where  $M$  is the average atomic mass and  $k$  the Boltzmann constant. The mean free path of a transverse phonon of frequency  $\omega$  and velocity  $v_{II}$ , as limited by the second process, is<sup>4</sup>

$$l_{II} = (B/2\gamma^2) (T_0/T) v_{II} \omega_D / \omega^2 \quad (2)$$

where  $B$  is a coefficient of order unity which depends on the structure of the crystal and on the form of the dispersion curves. It will be treated as an empirical parameter. Thus, the total mean free path of the longitudinal phonons is  $\ell_I = \ell_1 + \ell_{II}$ . That of the transverse phonons is simply  $\ell_{II}$ .

Below  $\omega_c$  the picture of interactions between individual phonons is no longer valid. A phonon of very low frequency interacts with all other phonons, as in the Akhieser theory of the deformed gas of thermal phonons, and the mean free paths of longitudinal and transverse phonons are of comparable magnitude, independent of temperature and approximately given by<sup>2,3</sup>

$$\ell_A = 10 v \omega_D / \omega^2 \quad (3)$$

where  $v$  is an average velocity.

3. The Thermal Conductivity.— Given the previous considerations, and using a Debye model for the spectral specific heat  $C(\omega)$ , with  $v_I = v_{II} = v$  for simplicity, the kinetic theory expression for the lattice thermal conductivity may be written as

$$\lambda = \frac{1}{3} \int_0^{\omega_c} C(\omega) v \ell_A d\omega + \frac{1}{3} \int_{\omega_c}^{\omega_D} C(\omega) v \ell_{II} d\omega + \frac{1}{3} \int_{\omega_c}^{\omega_D} C_I(\omega) v \ell_1 d\omega \quad (4)$$

where  $C_I(\omega) = C(\omega)/3$ . Taking  $\omega_c = v/\ell_{II}(\omega_D) = (1/2B\gamma^2)(T/T_0)\omega_D$  and substituting the expressions for  $\ell_A$ ,  $\ell_I$  and  $\ell_{II}$  into Eq. (4) we find

$$\lambda = \lambda_0 + (1/30\pi^2\gamma^2)(T_0/T)\lambda_0 + \epsilon \quad (5)$$

where

$$\lambda_0 = (3B/2\gamma^2)(kv^2/a^3\omega_D)(T_0/T) \quad (6)$$

is, except for the constant  $B$ , the thermal conductivity derived by Leibfried and Schlömann,<sup>4</sup> and  $a^3$  is the volume per atom.

The second term in Eq. (5) gives the additional contribution of the longitudinal phonons due to  $\ell_1$ . The last term  $\epsilon$ , roughly proportional to  $T$ , is usually small but may be appreciable at very high temperatures for solids of appropriately high melting point. It is a result of  $\ell_A$  being the mean free path of all phonons of frequency below  $\omega_c$ .

4. Comparison with Experiments.— The deviation of  $\lambda$  from the  $1/T$  behavior at high temperatures is in part due to thermal expansion. The remaining part has often been ascribed to four-phonon processes. However, four-phonon processes are too weak, and we attribute the remaining deviation to the second term in Eq. (5). Using that equa-

tion, with  $\lambda_0$  corrected for thermal expansion, we have calculated the thermal conductivities of RbBr, RbI, and RbCl, and we have compared them to recent measurements;<sup>5</sup> those of Ge and Si were similarly compared.<sup>6</sup> Selected ratios with respect to a reference temperature are shown in the table below. The theory seems to give agreement with observed temperature variations except for Ge (and for Si at temperatures higher than 1100 K.). However, no correction has been attempted for a possible electronic component.

One of us (R.B.O) is on leave of absence from the Universidad Autonoma de Puebla, Mexico, and acknowledges support by CONACYT (Mexico).

	RbBr		RbI		RbCl		Ge		Si	
$T_R(K)$	360		360		360		600		600	
$T(K)$	280	160	280	160	280	160	800	1100	800	1100
Exp.	1.47	3.09	1.38	2.86	1.43	3.00	0.72	0.63	0.67	0.44
Calc.	1.40	2.98	1.39	2.91	1.39	2.95	0.68	0.46	0.67	0.43

Table 1: Experimental and calculated values of  $\lambda(T)/\lambda(T_R)$ .

#### References.

- <sup>1</sup> I. Pomeranchuk, J. Phys. (USSR) 4, 259 (1941).
- <sup>2</sup> A. Akhieser, J. Phys. (USSR) 1, 277 (1939).
- <sup>3</sup> P.G. Klemens, in Physical Acoustics, Ed. W.P. Mason, vol. 3B, Academic Press, New York (1965), pp 201-234.
- <sup>4</sup> G. Leibfried and E. Schlömann, Nachr. Akad. Wiss. Göttingen, 2a(4), 71 (1954).
- <sup>5</sup> J.P. Moore, R.K. Williams, and R.S. Graves, Phys. Rev. B 11, 3107 (1975).
- <sup>6</sup> C.J. Glassbrenner and G.A. Slack, Phys. Rev. 134, A1058 (1964).

## DETECTION OF ACOUSTIC ZONE-BOUNDARY PHONONS BY PHONON DIFFERENCE ABSORPTION

H. Lengfellner and K.F. Renk

*Institut für Angewandte Physik, Universität Regensburg, 8400 Regensburg, F.R.G.*

**Abstract.**— A new method for detection of zone-boundary phonons is reported. Phonons are detected by phonon difference absorption of far-infrared laser radiation. We present experimental results obtained for TlCl and TlBr crystals. Phonons are generated by nonradiative transitions in optically excited crystals. Our experiments indicate long-lived zone-boundary phonons at low crystal temperature and a strong decrease of the phonon lifetime with increasing temperature.

1. **Experiment.**— Phonon difference absorption is used to detect zone-boundary phonons in TlCl and TlBr crystals. The principle of this new

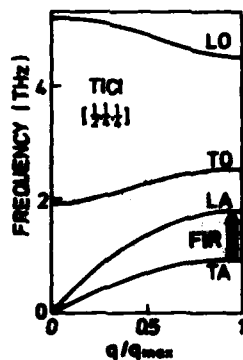


Fig.1. Principle of phonon detection.

method of detection of high-frequency phonons has recently been published<sup>1</sup> and is characterized in Fig.1. The population of transverse acoustic phonon states is determined by far-infrared phonon difference absorption. In a phonon difference process a transverse acoustic phonon (TA in Fig.1) is annihilated and a longitudinal acoustic phonon (LA) is generated. The two phonons have the same wave vector. The absorption coefficient is proportional to the difference of the occupation numbers of TA and LA phonon states.

Phonons are generated by radiationless processes induced by optical excitation of the crystal. The radiationless processes lead to generation of high-frequency phonons which decay rapidly in TA phonons of the lower phonon branches. The optical absorption is due to impurity states of unknown origin. For the optical excitation second harmonic radiation of a Nd:YAG laser is used.

The phonons are detected by time-resolved far-infrared laser spectroscopy. The radiation of a HCN laser with emission at a frequency of 0.89 THz is transmitted through the optically excited

crystal volume (typically 2 mm diameter and 4 mm thickness). The transmitted laser radiation is detected with a fast InSb detector (time resolution 0.7  $\mu$ s). The phonon induced change of sample transmission leads to a time dependent detector signal which is analyzed by a transient recorder and averaged with a computer.

The far-infrared laser radiation is absorbed mainly by phonons at the zone-boundary as has been shown by far-infrared absorption experiments at different crystal temperatures.<sup>2</sup> The TA phonons involved in the absorption process have frequencies near 1 THz.<sup>2</sup>

2. Results.— We find that the optical phonon generation leads to a reduction of sample transmission. Experimental signal curves obtained for different crystal temperatures are shown in Fig.2. At low crystal temperature ( $T \leq 5$  K) we find after the optical excitation a signal that decreases with a nonexponential slope. An analysis of the decay curve at longer times (not shown in Fig.2) indicates that a nonthermal phonon population is maintained for about 100  $\mu$ s. After this time thermal equilibrium in the optically excited crystal volume is established. The decay curve (lower curve in Fig.2) can be described

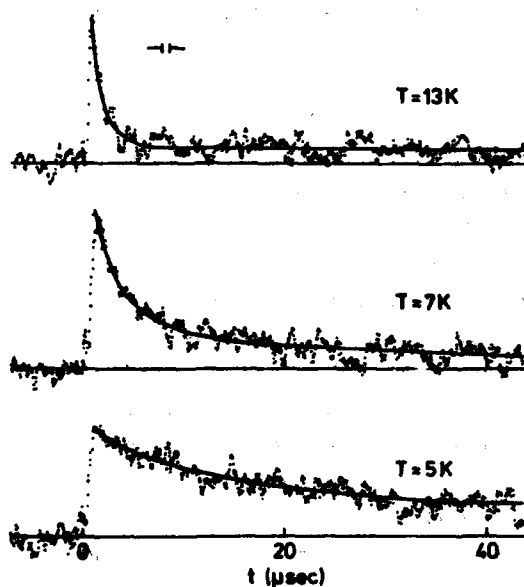


Fig.2. Far-infrared absorption at 0.89 THz after optical excitation of a TlCl crystal.

by two exponential curves, where the fast decay has a time constant of about 5  $\mu$ s. At higher temperatures the decay time of the fast decay decreases with increasing temperature, at 13 K (upper curve in Fig.2) the fast decay occurs within 1.5  $\mu$ s. After the fast decay, the signal curves reach an almost constant slope. Our results indicate that at higher temperatures thermal equilibrium is established very

fast and that heat diffusion out of the excited volume occurs very slowly. We think that the fast signals are due to long-lived TA phonons. Our results indicate that the TA phonons have a lifetime of a few microseconds at low temperature and that the lifetime decreases strongly with increasing temperature.

The temperature dependence of the phonon lifetime is shown in Fig.3 for TlCl and TlBr crystals. We find that the lifetime for TlBr has a stronger decrease than the lifetime for TlCl.

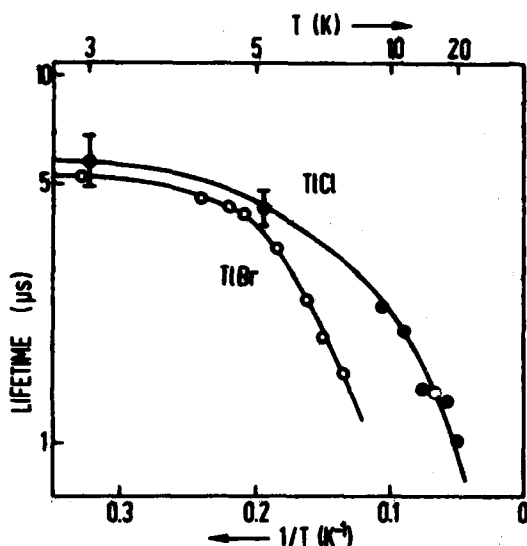


Fig.3. Lifetimes of zone-boundary phonons in TlCl and TlBr.

3. Discussion.— According to nonlinear elasticity theory for isotropic dispersionless solids<sup>3,4,5</sup> high-frequency LA phonons have short lifetimes at low crystal temperature due to anharmonic spontaneous decay, while TA phonons are not allowed to decay spontaneously. At higher temperatures TA phonons can decay by the interaction with thermal phonons.<sup>4</sup> Our results can qualitatively be explained by the nonlinear elasticity theory. We attribute the lifetime at low temperature to mode conversion of the TA phonons into LA phonons caused by impurity scattering. At higher temperatures we obtain an additional decay mechanism caused by the interaction with thermal phonons. Our results are in qualitative agreement with predictions of theory.<sup>4</sup>

- 1 Lengfellner, H. and Renk, K.F., Phys.Rev.Lett. **46**, 1212 (1981).
- 2 Lengfellner, H., Rindt, R., and Renk, K.F., Z.Phys.B **39**, 11 (1980).
- 3 Slonimskii, G.L., Zh.Eksp.Teor.Fiz. **7**, 1457 (1937).
- 4 Orbach, R. and Vredevoe, L.A., Physics **1**, 92 (1964).
- 5 Klemens, P.G., J.Appl.Phys. **38**, 4573 (1967).

## TWO-MAGNON-ONE-PHONON SCATTERING IN THE LATTICE THERMAL CONDUCTIVITY OF MAGNETIC INSULATORS

G.S. Dixon

*Oklahoma State University, Stillwater, OK 78078, U.S.A.*

**Abstract.**— A simple, but general model of magnon-phonon scattering as an extension of linear spin-wave theory is presented. Both resonant one-magnon-one-phonon and two-magnon-one-phonon scattering processes are considered. The former are included in the thermal conductivity by diagonalizing the magnon-phonon Hamiltonian to obtain coupled magneto elastic modes. The two-magnon-one-phonon processes are treated in the relaxation time approximation. This model has been used to analyze the experimental dependence of the thermal conductivity on temperature and magnetic field for several antiferromagnetic and ferromagnetic insulators. For the materials studied to date the two-magnon-one-phonon processes are found to dominate over the resonant process. This can be attributed to the greater width of the band of phonon frequencies affect by the two-magnon-one-phonon processes. In applying the model to experiment some care in the transformation of the spin-Hamiltonian of this transformation may contain important contributions to the magnetic field dependence.

The thermal conductivity of magnetic insulators is strongly influenced by magnon-phonon interactions (MPI) which arise from the sensitivity of the exchange, crystal fields, and dipole interactions among the magnetic ions to their relative displacement. To second order in the spin deviations the magnetic Hamiltonian has the general form<sup>1</sup>

$$\mathcal{H} = \sum_{\lambda} \sum_{i(m)} V_{i(m)}^{\lambda} S_{i(m)}^{\lambda} + \sum_{i(m)} \mathcal{H}'_{i(m)} + \sum_{\lambda, \nu} \sum_{i(m)j(n)} S_{i(m)}^{\lambda} U_{i(m)j(n)}^{\lambda \nu} S_{j(n)}^{\nu}$$

where  $i(m)$  refers to the  $i$ th site on the  $m$ th sublattice and  $\lambda, \nu$  stand for  $+$ ,  $-$  and  $z$ .  $\mathcal{H}'_{i(m)}$  contains the terms quadratic in the spin deviation operators on the same lattice site. When truncated to second order in the spin deviations, this forms the starting point for conventional linear spin-wave theory. Inclusion of the position-dependence of the terms in  $\mathcal{H}$  also gives the magnon-phonon interactions (MPI) up to two-magnon terms.

A general procedure for such a treatment of MPI has recently been developed. Briefly, one proceeds as follows: (1) Expand  $\mathcal{H}$  as a series in the lattice displacements. (2) Apply the Holstein-Primakoff transformations<sup>2</sup> that diagonalize  $\mathcal{H}$  with all ions at their equilibrium sites. (3) Obtain the two-magnon-one-phonon (2M1P) relaxation times from conventional perturbation theory. (4) Diagonalize the Hamiltonian for magnons and phonons, including one-magnon-one-phonon (1M1P) terms to obtain magnetoelastic coupled modes.<sup>3</sup> Details of this procedure have been given elsewhere.<sup>4,5</sup>

There are compelling reasons for using this or some similar method to obtain the MPI amplitudes and relaxation times in the analysis of experimental data. Most important is the strong dependence of the matrix elements of the Holstein-Primakoff transformation on magnetic field whenever the applied field is not parallel to the sublattice magnetization. This can provide the dominant field-dependence of the MPI. Secondly, such a procedure reveals the connections among the various MPI scattering amplitudes. This makes it possible to identify cancellations in the MPI in high-symmetry situations, and to minimize the number of potential disposable parameters when a modulation of a small subset of the contributions to  $\kappa$ , e.g. isotropic exchange, can be expected to dominate the MPI.

A comparison of the thermal conductivity as a function of field perpendicular to the easy axis to the results of this model is presented for  $\text{MnCl}_2 \cdot 4\text{H}_2\text{O}$  in Fig. 1 and  $\text{CoCl}_2 \cdot 6\text{H}_2\text{O}$  in Fig. 2. Results for fields parallel to the easy axis for a ferromagnet<sup>5</sup> and an antiferromagnet<sup>4</sup> have been presented previously. In each of these cases the 2MIP processes are found to be much more important than the 1MIP processes due to the greater band-width of the phonons that they affect.

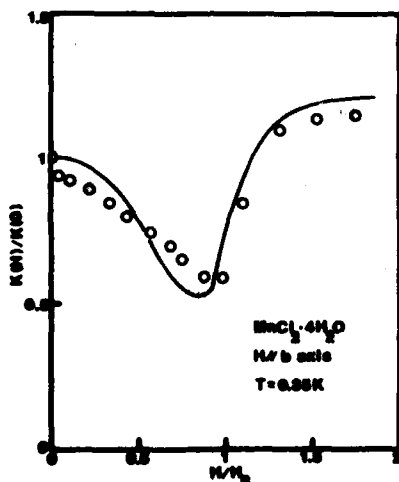


Fig. 1 : Magnetic-field dependence of the thermal conductivity of  $\text{MnCl}_2 \cdot 4\text{H}_2\text{O}$  with the field and heat flow perpendicular to the easy axis. The curve is the result of 2MIP scattering arising from exchange modulation. The phonons are strongly coupled to the lowest energy magnon branch, which is depressed by the field.



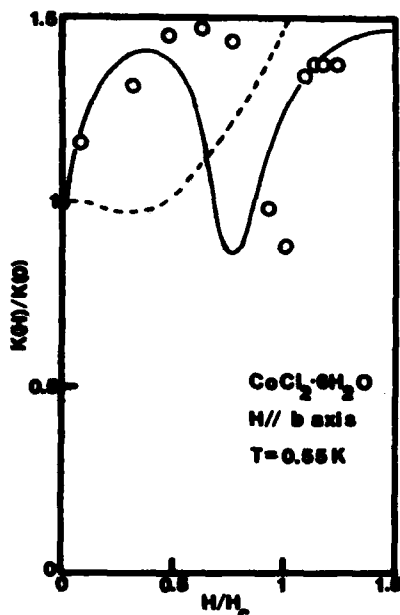


Fig. 2 : Magnetic-field dependence of the thermal conductivity of  $\text{CoCl}_2 \cdot 6\text{H}_2\text{O}$  (Ref. 6) with the field and heat flow perpendicular to the easy axis. The dashed curve is the result of 1MIP processes reported in Ref. 6. The full curve is obtained with 2MIP scattering from modulation of single-ion anisotropy. At low fields this couples the phonon to one magnon on each branch, their total energy being raised by the field. At higher fields the strongest coupling is to a pair of magnons on the lower branch.

1. L.R. Walker in *Magnetism*, Eds. G.T. Rado and H. Suhl (New York; Academic Press, 1963) Vol. I, pp. 299-381.
2. T. Holstein and H. Primakoff, *Phys. Rev.* **58**, 1098 (1940).
3. M.A. Savchenko, *Fiz. Tverd. Tela* **6**, 864 (1964).
4. G.S. Dixon, *Phys. Rev.* **B21**, 2851 (1980) and -, V. Benedict and J.E. Rives, *ibid.* **21**, 2865 (1980).
5. G.S. Dixon, *J. Phys. C: Solid State Phys.* **14**, 2147 (1981).
6. J.E. Rives and S.N. Bhatia, *AIP Conf. Proc.* **24**, 174 (1975) and private communication.

LOW TEMPERATURE THERMAL CONDUCTIVITY OF  $\text{HgI}_2$  SINGLE CRYSTALS

A.M. De Goër, M. Locatelli and I.F. Nicolau\*

*Service des Basses Températures, Laboratoire de Cryophysique, Centre d'Etudes Nucléaires de Grenoble, 85 X, 38041 Grenoble Cedex, France**\*Laboratoire d'Electronique et de Technologie de l'Informatique, Laboratoire de Cristallogénèse et Recherche sur Les Matériaux, Centre d'Etudes Nucléaires de Grenoble, 85 X, 38041 Grenoble Cedex, France*

**Abstract** - The thermal conductivity of  $\alpha\text{-HgI}_2$  single crystals has been measured from 50 mK to 200 K, and the results discussed qualitatively and quantitatively. It is concluded that phonons are scattered mainly by clusters of interstitial defects due to the lack of stoichiometry of the crystals.

**Experimental** - Several crystals have been studied, which were grown either from solution (LETI crystals) [1] or from the vapor phase (EGG-crystals) [2]. The samples are parallelepipeds of typical cross-section 3 mm  $\times$  3 mm, generally cut along a-axis except one which is parallel to c-axis. The deviation from stoichiometry of the LETI-crystals has been already studied [3].

**Results and qualitative discussion** - The results of the thermal conductivity measurements from 50 mK to 200 K are shown in fig.1. The main features of these results are : (i) the anisotropy of the thermal conductivity  $K$  in the whole temperature range (ii) the sample dependence of  $K$  below 10 K, (iii) the departure of the expected  $T^3$  variation down to the lowest temperatures, which is illustrated in the  $K/T^3$  plots (insert of fig.1). The calculated values of  $K/T^3$  in the boundary scattering limit are about  $1 \text{ W cm}^{-1} \text{ K}^{-1}$  and are not reached even in the case of the crystal LETI 14, indicating that phonons are scattered by structural defects. The shape of the  $K/T^3$  curves suggest the possibility of a resonant scattering at very low temperatures ( $T < 5 \cdot 10^{-2} \text{ K}$ ), giving some evidence of the presence of large clusters of defects, with typical dimensions equal or larger than  $0.3 \mu\text{m}$  [4].

**Quantitative analysis** - The thermal conductivity has been calculated within the simple isotropic Debye model [5] :

$$K = \frac{k}{2\pi^2 v} \left( \frac{kT}{\hbar} \right)^3 \int_0^{\theta/T} \frac{x^4 e^x / (e^x - 1)^2}{\tau^{-1}(x, T)} dx$$

with a total phonon relaxation rate :

$$\tau^{-1} = \tau_B^{-1} + A\omega^4 + \tau_{p-p}^{-1} \quad (1)$$

In a first step, the classical contributions from boundary scattering ( $\tau_B^{-1}$ ) and isotope scattering ( $A_0 \omega^4$ ) have been calculated, and the phonon-phonon interaction term adjusted to describe the results in the intrinsic temperature range  $T > 15 \text{ K}$  ( $\tau_{p-p}^{-1} = B_U \omega^2 T \exp(-\theta/\alpha T)$ , with different values of  $B_U$  and  $\alpha$  for samples // a-axis and // c-axis). The theoretical curve such calculated for the sample LETI 14 suppo-

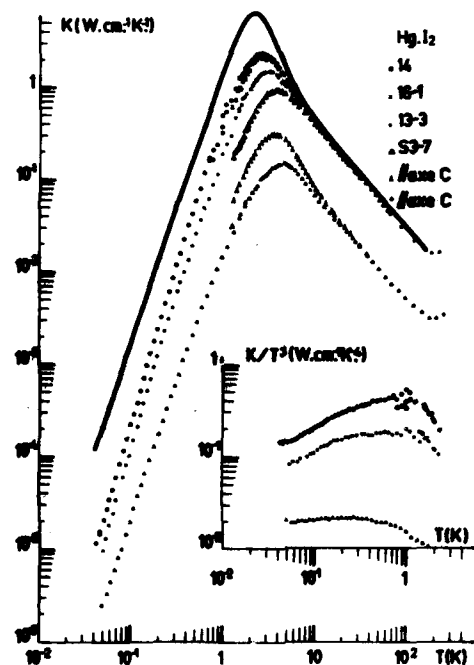


Figure 1.

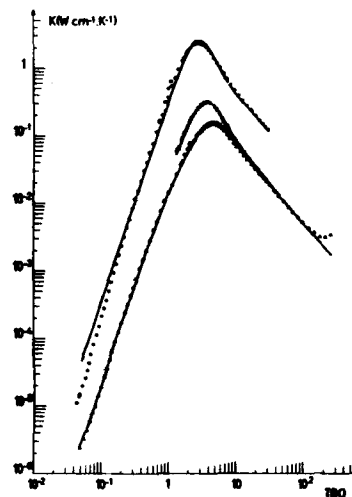


Figure 2 - Experimental points :  
o, LETI 14 ;  $\lambda$ , LETI-16 (a) ;  
A, LETI-16 (b). Solid lines  
are calculated.

sed to be perfect is shown in fig.1. The experimental results of all samples // a-axis have been fitted by adjusting the frequency independent term  $\tau_B^{-1}$  and the point defect coefficient A. Therefore phonon scattering by structural defects is described by the parameters  $\tau_C^{-1} = (\tau_B^{-1})_{\text{exp.}} - (\tau_B^{-1})_{\text{calc.}}$  and  $A - A_0$ . In the case of heat flow // c-axis, it was not possible to achieve a fit in this simple way and it was necessary to add a term  $G\omega^2$  in the total relaxation rate (1) ; this term describes phonon scattering by plane defects [6]. The parameters used are given in table 1 and examples of fits are illustrated in fig. 2.

TABLE 1

Sample	$\tau_C^{-1}$ (s <sup>-1</sup> )	$A - A_0$ (s <sup>3</sup> )	$N_C$ (cm <sup>-3</sup> )	G (s)	Orientation
LETI 14	$7.8 \cdot 10^5$	$6.10 \cdot 10^{-44}$	$9.2 \cdot 10^9$	0	// a
LETI 13	$1.6 \cdot 10^6$	$1.9 \cdot 10^{-43}$	$1.9 \cdot 10^{10}$	0	// a
EGG-S3-7	$4.6 \cdot 10^6$	$2.6 \cdot 10^{-43}$	$5.4 \cdot 10^{10}$	0	// a
LETI 16 (a)	$9.7 \cdot 10^6$	$4.3 \cdot 10^{-43}$	$1.1 \cdot 10^{11}$	$5.8 \cdot 10^{-18}$	// c
LETI 16 (b)	$1.5 \cdot 10^7$	$9.10 \cdot 10^{-44}$	$1.7 \cdot 10^{11}$	$2.3 \cdot 10^{-17}$	// c

In the limit  $\lambda \ll d$ , phonon scattering by large clusters is described by a frequency independent relaxation time :

$$\tau_c^{-1} = N_c v \pi d^2/4 \quad (2)$$

where  $N_c$  is the number of clusters /cm<sup>3</sup> [4]. The values of  $\tau_c^{-1}$  are larger for samples // c-axis than for those // a-axis by a factor 2 to 10 (cf. table 1) so that the clusters look somewhat anisotropic. If the dimension along c-axis is  $> 0.3 \mu\text{m}$  as estimated above, the dimension perpendicular to c-axis would be  $1 \mu\text{m}$  or larger, and the corresponding cluster density  $N_c \approx 1.1 \cdot 10^{10}/\text{cm}^3$  (from equ.(2)).

On the other hand, the increase of the point defect scattering  $A-A_0$ , which is relatively small, could be due to (i) chemical impurities, (ii) interstitials due to the lack of stoichiometry [3], (iii) very small precipitates, in the limit  $\lambda \gg d$ . The contribution (i) of the known chemical impurities including carbon has been calculated from mass defect alone, and found to give the correct order of magnitude of  $A-A_0$ , so that the two other scattering processes cannot be operative. In fact, the contribution (ii) leads to values of  $A-A_0$  about 30 times larger than the observed ones so that the interstitials (Hg or  $I_2$ ) cannot be isolated even in the best crystals. We suggest that the large defects discussed above are clusters of such interstitials. From the study of the stoichiometry of the crystals [3], the number of  $I_2$  interstitials in LETI 13 has been estimated to be  $\approx 2.5 \cdot 10^{19}/\text{cm}^3$ , and this number could correspond to the total cluster volume of  $\approx 3 \cdot 10^{-3}$  (calculated from  $N_c \approx 1.1 \cdot 10^{10}/\text{cm}^3$ ) if there are two interstitials per unit cell. Therefore the overall description seems to be consistent. This work will be published with full details elsewhere [7].

#### References

- [1] NICOLAU I.F. and JOLY J.P., J. Cryst. Growth **48** (1980) 61.
- [2] SCHIEBER M., SCHNEPP W.F. and VAN DEN BERG L., J. Cryst. Growth **33** (1976) 125.
- [3] NICOLAU I.F. and ROLLAND G., to be published in Mat. Res. Bull.
- [4] ABOU-GHANTOUS M., GUCKELBERGER K. and LOCATELLI M., J.P.C.S. **41** (1980) 473.
- [5] BERMAN R., in "Thermal Conduction in Solids", edited by BLEANEY B. et al. Clarendon Press (1976).
- [6] KLEMENS P.G. in "Sol. State Physics" **7** edited by SEITZ F. and TURNBULL D., Acad. Press : New-York, (1958) 1.
- [7] DE GOER A.M., LOCATELLI M. and NICOLAU I.F., to be published in J.P.C.S.

AD-A126 574

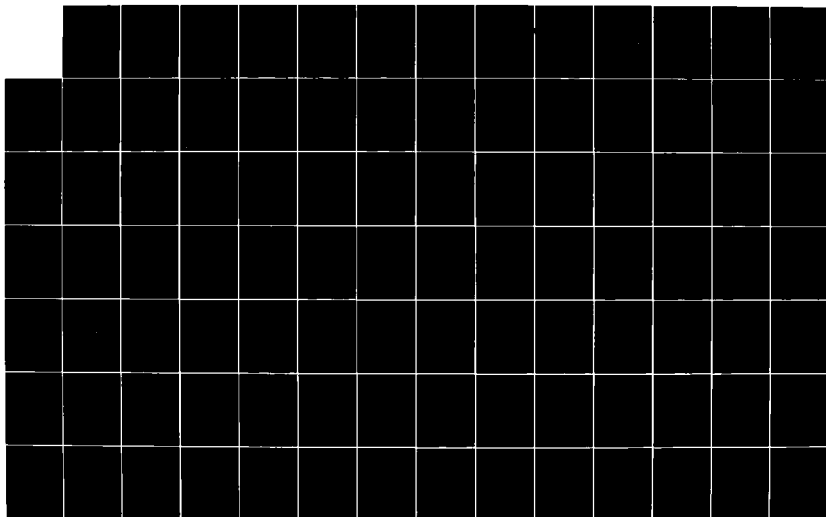
INTERNATIONAL CONFERENCE ON PHONON PHYSICS 31 AUGUST-3  
SEPTEMBER 1981 BLOOMINGTON INDIANA(U) INDIANA UNIV AT  
BLOOMINGTON W E BROW DEC 81 ARO-17340.1-PH

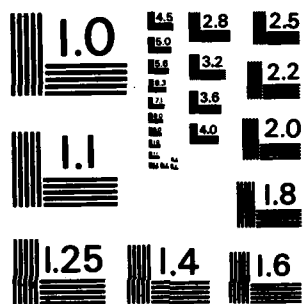
4/10

(UNCLASSIFIED) MIPR ARO-43-80

F/G 20/2

NL





MICROCOPY RESOLUTION TEST CHART  
NATIONAL BUREAU OF STANDARDS-1963-A

THE EFFECT OF NONMETAL-METAL TRANSITION DUE TO DOPING ON LATTICE  
THERMAL CONDUCTIVITY : APPLICATION TO Ge-DOPED InSb

P.C. Sharma, K.P. Roy and V. Radhakrishnan

Physics Department, Banaras Hindu University, Varanasi-221005, India

**Abstract.-** In this work we explain the phonon thermal conductivity results of Ge-doped InSb from 2 to 50 K for impurity concentrations  $7.2 \times 10^{17}$  and  $5.0 \times 10^{17} \text{ cm}^{-3}$ . Since these lie in the intermediate concentration region of the metal-nonmetal transition the theory of scattering of phonon by holes in the mixed state, i.e. both in the localised non-metallic and in the metallic state is used. The hole concentrations in the non-metallic and metallic regions are calculated for each sample by using Mikoshiba's inhomogeneity model, the theory of both bound hole-phonon and free hole phonon scattering are applied to explain the results. The value of density-of-states effective mass are kept constant ( $=0.23$ ) with the variation in temperature. The value of the dilatation and shear deformation potential constants obtained from our calculations are in good agreement with previously determined values. The effect of impurity scattering due to doped impurities alongwith isotope scattering is also taken into account.

It is reported that in the intermediate concentration range, the mixed hole-phonon scattering must be included to explain the temperature dependence of thermal conductivity of Ge-doped InSb.

**Introduction.** - The phonon thermal conductivity of p-InSb doped with Ge, has been studied experimentally [1,2] for acceptor hole concentrations from  $2.7 \times 10^{14}$  to  $6 \times 10^{18} \text{ cm}^{-3}$ . In the low concentration region well below the critical concentration for nonmetal-metal transition ( $N_0$ ) the holes are bound to the impurity atoms and in the high impurity concentration region, they are free in valence band. In the intermediate doping concentration near  $N_0$ , the holes exist in a mixed state. Using Mikoshiba's "inhomogeneity model", the acceptor hole concentration in both non-metallic and metallic region can be calculated. In the present work we have chosen two samples of p-InSb with  $N=7.2 \times 10^{17}$  and  $5 \times 10^{17} \text{ cm}^{-3}$ . Using Mott's expression the critical concentration for metal-nonmetal transition ( $N_0$ ) can be given as  $N_0 = (.25/a^*)^3$  where  $a^*$  is the effective Bohr radius of the

impurity and the concentration at which Fermi level merges with valence band is  $N_{vb} = \frac{1}{4\pi}(a^*)^{-3}$ . Using  $a^* = 38 \text{ \AA}$ , the values  $N_c$  and  $N_{vb}$  are calculated to be  $2.84 \times 10^{17}$  and  $1.46 \times 10^{18} \text{ cm}^{-3}$  for p-InSb. Using Mikoshiba's inhomogeneity model the hole concentrations in nonmetallic and metallic regions can be calculated as  $N_n = N \exp(-\frac{4}{3}\pi N r_c^3)$  and  $N_m = (N - N_n)$  where  $r_c = (144/\pi^2)^{1/3} a^*$ . For the sample of p-InSb with  $N = 7.2 \times 10^{17} \text{ cm}^{-3}$  the values of  $N_n = 0.64 \times 10^{17}$  and  $N_m = 6.55 \times 10^{17} \text{ cm}^{-3}$  and for the sample with  $N = 5 \times 10^{17} \text{ cm}^{-3}$ ,  $N_n = 0.936 \times 10^{17}$  and  $N_m = 4.06 \times 10^{17} \text{ cm}^{-3}$ . Using the relaxation rate of bound hole-phonon scattering, for the holes in nonmetallic region and the relaxation rate for free hole phonon scattering for the holes in metallic region, the phonon conductivity values of these two samples in the intermediate doping concentration are explained well between 2 and 50 K.

**Theory.-** The relaxation rate for the bound hole-phonon scattering is given as

$$(\tau_{sp}^{-1})_{\text{bound}} = \frac{N_n \omega^2 (2/3 D_{u1}^a)^4 f^4(q)}{40 \pi \rho^2 \hbar^2 v^7} \frac{20D^4 + 120D^2 + 60}{3}$$

where  $f(q) = (1 + 1/4 a^{*2} q^2)^{-2}$  and  $D = D_{u1}^a / D_{u2}^a$ .

$D_{u1}^a$  and  $D_{u2}^a$  are the shear deformation potentials for the strains along [001] and [111] directions,  $q$  is the phonon wave vector,  $v$  is the average phonon velocity and  $\rho$  is the density of the crystal.

The acceptor holes in the metallic region can be considered to be free in the valence band and the relaxation rate for the scattering of phonons by free holes for  $q \leq 2k_F$  is given as

$$(\tau_{sp}^{-1})_{q \leq 2k_F} = \frac{\pi^2 C^2 k_B T \eta_{1t}^2}{2\pi \hbar^4 \rho v} \ln \frac{1 + \exp(\eta^* - N/T - PTx^2 + x/2)}{1 + \exp(\eta^* - N/T - PTx^2 - x/2)}$$

where  $N = \pi^2 v^2 / 2k_B$ ;  $P = k_B / 8\pi^2 v^2$  and  $\eta^* = \frac{\pi^2 \hbar^2 (3N_m / \pi)^{2/3}}{2\pi^2 k_B T}$

$\pi^2$  is the density of -states effective mass and  $C$  is the dilatation deformation potential. For phonon wave vector  $q > 2k_F$ , the relaxation rate for the scattering of phonons by free holes is given as

$$(\tau_{sp}^{-1})_{q > 2k_F} = \frac{185 \pi^2 C^2 N_m \eta_{1t}^2}{\hbar^3 q^5 a^3 \rho}$$

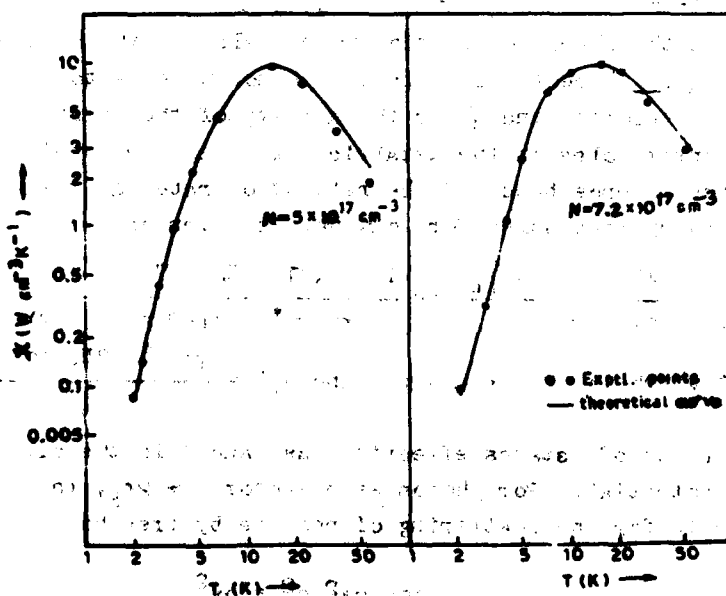
The phonon thermal conductivity can be calculated using these expressions by the method described elsewhere [5].



**Results and Discussion.**— By considering the realistic hole-phonon scattering relaxation rates for the doped samples of p-InSb in the intermediate concentration region, the phonon conductivity values are explained satisfactorily between 2 and 50 K as shown in the figure. The theoretical analysis of hole phonon scattering establishes the existence of holes in a mixed state i.e. both in bound and free impurity states in the region of present interest. The values of shear deformation potentials determined by our theoretical analysis are  $D_{II}^a = 2.8$  eV and  $D_{II}^b = 4.2$  eV; which are in agreement with experimental values. The dilatation deformation potential constants are 1.4 eV and 1.3 eV, for the two samples with  $N = 7.2 \times 10^{17}$  and  $5 \times 10^{17} \text{ cm}^{-3}$ . The scattering due to doped impurities is also considered in addition to isotope scattering in the calculation for point defect scattering parameter. The values of the parameters are given in the Table.

**Table.**— Parameters used in the calculation

$$\begin{aligned} a^* &= 38 \text{ \AA}, \quad m^*/m = 0.23, \quad v = 2.3 \times 10^5 \text{ cm s}^{-1} \\ \tau_B^{-1} &= 1.6 \times 10^6 \text{ s}^{-1}, \quad \rho = 5.76 \text{ gm cm}^{-3} \\ A &= 4.36 \times 10^{-44} \text{ s}^3, \quad B = 8.7 \times 10^{-23} \text{ s K}^{-3} \end{aligned}$$



**Figure.**— Thermal conductivity of p-InSb samples as a function of Temperature.

**References**

1. V.V.Kosarev et al. *Physica Stat. Solid (B)* **44**, 525 (1971).
2. S.S.Skalyt, P.V.Tamarin and V.S.Ivleva *Phys.Lett.* **32A**, 29 (1970).
3. V.Radhakrishnan & P.C.Sharma *Phys.Rev.* **B23**, 3004 (1981).

## THE EFFECT OF DISLOCATIONS ON THERMAL CONDUCTIVITY

R.A. Brown

School of Mathematics and Physics, Macquarie University, North Ryde, N.S.W.  
2113, Australia

**Abstract:** Phonon scattering by the strain fields of deformed crystals is formulated in terms of the third order elastic constants. The thermal resistivity due to dislocations is calculated. Theory and experiment are in accord for Cu, Al, Ge and Si but not for LiF.

1. **Aims:** To formulate the problem of phonon scattering by the static strain fields of crystal defects in terms of the third order elastic (TOE) constants, and to calculate the thermal resistivity due to dislocations.

2. **Formulation:** A classical formulation of the equations of motion of a statically deformed continuum was presented by Kogure and Hiki/1/. The system may be quantized to yield the hamiltonian

$$H = \sum_{\kappa} \hbar \omega_{\kappa} (b_{\kappa}^{\dagger} b_{\kappa} + \frac{1}{2}) + \frac{1}{V} \sum_{\kappa} (\hbar \omega_{\kappa} b_{\kappa} b_{\kappa'}^{\dagger} + \hbar \omega_{\kappa'} b_{\kappa'}^{\dagger} b_{\kappa})$$

where  $V$  is the volume of the deformed body and  $\kappa \equiv (j, k) = (\text{polarization, wavevector})$ . The operators  $b_{\kappa}$  satisfy the usual commutation rules and

$$\hbar \omega_{\kappa} = (\hbar \omega_0/4) \tilde{n}_{11} e_{\alpha}(\kappa) e_{\alpha}(\kappa') + (k_{\beta} k'_{\beta} / \rho_0 \omega_0^2) e_{\alpha}(\kappa) e_{\alpha}(\kappa') \tilde{H}_{\alpha\beta\gamma\delta} + C_{\alpha\beta\gamma\delta\epsilon\eta} \tilde{n}_{\epsilon\eta} \quad (1)$$

where repeated suffices are summed. The  $e_{\alpha}(\kappa)$  are polarization vectors and  $\rho_0$  is the density of the undeformed crystal. The  $\tilde{n}(\mathbf{k}-\mathbf{k}')$  and  $\tilde{H}(\mathbf{k}-\mathbf{k}')$  are Fourier transforms of the static strains  $n_{ij}(\mathbf{x})$  and of  $H_{ijkl} = -C_{ijkl} n_{pp} + C_{ijkp} n_{lp} + C_{ijpl} n_{kp} + C_{ipkl} n_{jp} + C_{pjkl} n_{ip}$ , respectively. the  $C$ 's are the usual elastic moduli/2/. Due to cancellation of cross-terms when (1) is squared we have, to a good approximation,

$$|\hbar \omega_{\kappa}|^2 = (\hbar^2/16 \rho_0^2 \omega_0^2) k_{\beta}^2 k'_{\beta} e_{\alpha}^2(\kappa) e_{\alpha}^2(\kappa') \left[ \tilde{H}_{\alpha\beta\gamma\delta} + C_{\alpha\beta\gamma\delta\epsilon\eta} \tilde{n}_{\epsilon\eta} \right]^2 + \rho_0^2 \omega_0^4 |\tilde{n}_{11}|^2 e_{\alpha}^2(\kappa) e_{\alpha}^2(\kappa') \quad (2)$$

The last term is negligibly small in practice and will be dropped. If we follow Klemens/3/ and set  $|\tilde{n}_{\alpha}(\mathbf{k})| = 1/\sqrt{3} = k_{\alpha}/k$  eqn. (2) becomes

$$|\hbar \omega_{\kappa}|^2 = (\hbar^2 k^2 / 12 \rho_0^2 \omega_0^2) P, \text{ where, for a cubic crystal}$$

$$P = A(|\tilde{n}_{11}|^2 + |\tilde{n}_{22}|^2 + |\tilde{n}_{33}|^2) + B(|\tilde{n}_{12}|^2 + |\tilde{n}_{23}|^2 + |\tilde{n}_{31}|^2)$$

$$+ C(\tilde{n}_{11} \tilde{n}_{22}^* + \tilde{n}_{22} \tilde{n}_{33}^* + \tilde{n}_{33} \tilde{n}_{11}^* + \text{complex conjugate}) \quad (3)$$

$$\begin{aligned}
A &= (C_{11} + 3C_{11})^2 + 4(C_{112} + C_{12})^2 + 2(C_{123} - C_{12})^2 + 2(C_{112} - C_{11})^2 \\
&\quad + 8(C_{166} + C_{44})^2 + 4(C_{144} - C_{44})^2 \\
B &= 8(2C_{166} + C_{11} + 2C_{44})^2 + 16(C_{144} + C_{12})^2 + 32(C_{654} + C_{44})^2 \\
C &= (C_{111} + 3C_{11})(C_{112} - C_{11}) + 4(C_{112} + C_{12})^2 + 2(C_{123} - C_{12})(C_{112} + C_{12}) \\
&\quad + 8(C_{166} + C_{44})^2 + 4(C_{166} + C_{44})(C_{144} - C_{44})
\end{aligned}$$

The C's are the elastic constants in Voigt notation.

3. Dislocation Thermal Resistivity: In cases where the frequencies  $\omega_j = v_j k$  are not degenerate and the dislocations not all parallel it is necessary to use the variational formula/4/

$$W_{dis} = (V/2k_B T^2) \sum_{\kappa\kappa'} (\phi_{\kappa} - \phi_{\kappa'})^2 P_{\kappa\kappa'} / \left| \sum_{\kappa\kappa'} v_{\kappa} \phi_{\kappa} dn_o/dT \right|^2, \quad (4)$$

$$P_{\kappa\kappa'} = \sum_d (8\pi/h^2 v^2) \left| h_{\kappa\kappa'}^d \right|^2 n_o (1 + n_o) \delta(\omega_{\kappa} - \omega_{\kappa'}), \quad (5)$$

where  $k_B$  is Boltzmann's constant. The sum in (5) is over all dislocations in the crystal, which are assumed straight but of random orientation and arbitrary character. When the resistivity tensor is isotropic, we expect the standard trial function  $\phi_{\kappa} = k \cdot VT$  to furnish a good approximation, particularly since it removes the singularity from the forward scattering amplitude for each dislocation. It yields in (4)

$$W_{dis} < \frac{v^2 h^2 b^2}{72 p_o^2 k_B^2 T^2} \frac{I_5}{I_4^2} \frac{S_4 S_5}{S_3^2} \frac{L_e f_e + L_s f_s}{v}; \quad S_n = \sum_{j=1}^3 v_j^{-n} \quad (6)$$

where  $L_e, L_s$  are the total lengths of edge and screw dislocation, respectively,  $f_s = B/4, f_e = (1-v)^{-2} [A(v^2 - v + 3/8) + B/16 + 2C(v^2 - v/2 + 1/16)]$

in a crystal of (average) Poisson's ratio  $v$ , and

$$I_n = \int_0^{\infty} x^n e^x (e^x - 1)^{-2} dx = 26.0, 124 \text{ for } n = 4, 5 \text{ respectively.}$$

We have followed previous authors/3,5,6/ in averaging (3) over directions in the plane normal to each dislocation. The corresponding relaxation rate for a density  $N$  (length/volume) of randomly oriented dislocations is  $\tau_j^{-1} = \Gamma_j N$  where  $\Gamma_j = b^2 S_4 (f_s + 2f_e) / 1296 p_o^2 \equiv \Gamma$ , independent of  $j$  (7)

For random characters we take  $L_s = 2L/3 = 2L_e$  in (6) for a total length  $L$  of dislocation line. The elastic constants of /7-10/ were adopted. The sums  $S_n$  were evaluated for the [100], [110] and [111] directions and the arithmetic mean was taken. The results are shown in the table. To check the reliability of the trial function we repeated the calculation for the case of parallel dislocations and degenerate polarization branches, a case which leads to a tractable Boltzmann

equation. The results suggest that the upper bound (6) overestimates the true resistivity by a factor 4/3 when either dislocation scattering or electron-phonon scattering dominate, and is exact if boundary scattering dominates. On the other hand the proportion of edge dislocations in deformed crystals is normally much greater than 2/3 of the total so this overestimation will be largely compensated.

Crystal	$\mu \equiv (L/V)(T^2 \rho_{dis})^{-1}$ ( $10^7 \text{ Wcm}^{-3}\text{K}^{-3}$ )		$r(10^{-16} \text{ cm}^2)$	
	Eqn. (6)	Experiment*	Eqn. (7)	Klemens/3/
Cu	2.1	$2.5 \pm 0.3$	77	0.61
Al	3.8	4.0	39	1.9
Si	8.9	$8 \pm 2$	11	0.24
Ge	10.6	8.4	15	0.26
LiF	6.2	$0.14 - 1.2$	14	0.59

\* We have doubled etch-pit counts to get length per unit volume.

A detailed discussion of the data will be given elsewhere.

4. **Conclusion:** The theory is in agreement with data for Cu, Al, Si and Ge. For LiF the theory underestimates the resistivity by a factor of 5 (data of /11/) or 40 (data of /12/; a similar discrepancy appears for other alkali halides /13/).

#### References:

- /1/ Y. Kogure and Y. Niki, J. Phys. Soc. Japan **36**, 1597 (1974); **38**, 471 (1975).
- /2/ K. Brugger, Phys. Rev. **133**, A1611 (1964).
- /3/ P.G. Klemens, Proc. Phys. Soc. (Lond.) **A68**, 1113 (1955).
- /4/ J.M. Ziman, Electrons and Phonons (Clarendon Press, Oxford, 1960).
- /5/ P. Carruthers, Rev. Mod. Phys. **33**, 92 (1961).
- /6/ K. Ohnishi, J. Phys. Soc. Japan **24**, 437 (1968).
- /7/ K. Salama and G.A. Alers, Phys. Rev. **161**, 673 (1967).
- /8/ H.J. McSkimin and P. Andreatch, J. Appl. Phys. **35**, 3312 (1964).
- /9/ V.K. Garg et al., Phys. Stat. Sol. (b) **80**, 63 (1977).
- /10/ J.F. Thomas, Phys. Rev. **175**, 955 (1968).
- /11/ T. Suzuki and H. Suzuki, J. Phys. Soc. Japan **32**, 104 (1972).
- /12/ R.L. Sproull et al., J. Appl. Phys. **30**, 394 (1959).
- /13/ A. Taylor et al., J. Appl. Phys. **36**, 2270 (1965).

## MODULATION OF BALLISTIC PHONON FLUXES IN Ge BY A He GAS FILM AT A SOLID/SUPERFLUID INTERFACE

M. Greenstein and J.P. Wolfe

*Department of Physics and Materials Research Laboratory, University of Illinois at Urbana-Champaign, Urbana, IL 61801, U.S.A.*

**Abstract.**—A He gas bubble may be formed at the surface of a sample which is immersed in a superfluid He cooling bath and subject to intense optical excitation. We have discovered that this bubble oscillates at 1-10 KHz, under steady state optical excitation, and this leads to a modulation of the ballistic phonon flux intensity into the sample.

Focused laser excitation is commonly used to generate free carriers and phonons in crystals at low temperatures. For samples immersed in superfluid He and under high optical excitation density ( $\lesssim 100 \text{ W/cm}^2$ ), a small He gas film or bubble may be formed at the excitation point. The existence of He gas films created by ohmic heating has been previously noted [1]. This paper deals with how the photo-produced gas bubble modifies the ballistic phonon flux into the sample. We have observed similar bubbles on Ge, Si, Al, Au, but here we concentrate on pure crystalline Ge. We have used time resolved light scattering, phonon flux detection, and infrared luminescence imaging to study this He gas bubble, its modulation of the ballistic phonon flux and the effect of the bubble on the transport of electron-hole droplets in Ge.

The most intriguing aspect of the bubble is its tendency to oscillate in size under steady state excitation conditions. The dynamic properties of the bubble may be exposed with a simple time resolved light scattering technique. An  $\text{Ar}^+$  laser ( $5145\text{\AA}$ ) is used to create the bubble, while the light from a low power He Ne probe laser ( $6328\text{\AA}$ ) is scattered off of the bubble. The scattered light is detected with a fast photodiode. The oscillation of the bubble is shown in Fig. 1 as a function of incident  $\text{Ar}^+$  laser power for focused ( $100\text{\mu m}$ ) excitation at  $T = 1.74 \text{ K}$ . Here, the  $\text{Ar}^+$  laser is chopped at 1 KHz to synchronize the bubble oscillations for display and to show the relative magnitude of the oscillatory effect on the scattered light signal. In fact, such oscillations are also observed for steady state  $\text{Ar}^+$  excitation.

The maximum bubble diameter may be measured by scanning the He Ne probe laser. The relationship between oscillation frequency and bubble diameter was obtained as a function of  $\text{Ar}^+$  excitation power, as shown in Fig. 2. The bubble frequency depends on diameter as  $\nu \sim D^{-3/4}$ ; therefore larger bubbles oscillate more slowly.

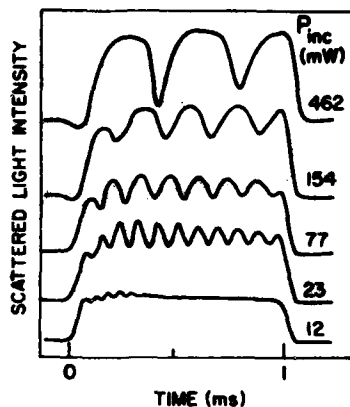


Fig. 1 : Power dependence of the bubble oscillation frequency at  $T = 1.74$  K.

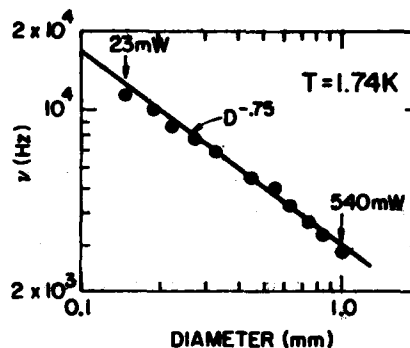


Fig. 2 : Oscillation frequency as a function of bubble diameter.

What is the cause of this oscillation? The dependence of  $\nu$  on  $D$  argues against simple capillary modes for which  $\nu \sim D^{-3/2}$ . To resolve this issue we have devised a stroboscopic imaging technique (to be reported elsewhere) that reveals a gradual growth and sudden collapse of the bubble diameter as a function of time. We therefore conclude that the oscillations arise from a mechanical instability of the bubble in the superfluid bath.

Optical excitation of Ge at low temperatures produces a ballistic phonon flux which can be detected with a superconducting bolometer. To measure the effect of the bubble on this flux, two coincident laser beams are used: A cw  $\text{Ar}^+$  laser creates the bubble, and a Q-switched YAG: Nd laser provides a reference (57W, 250 ns) heat pulse for comparison of intensity. The detected phonon signal from this experiment is shown in Fig. 3. The inset shows the heat pulse that sets the intensity scale. The phonon flux intensity modulations caused by the bubble are observed in the tail of the heat pulse. These modulations are about 1% of the heat pulse intensity.

Optical excitation of Ge at liquid He temperatures also produces a cloud of electron-hole droplets. The size and shape of the droplet cloud in Ge are determined by a "phonon wind" produced indirectly by optical excitation [2].

A modulation of the electron-hole droplet cloud size by the bubble is observed in a spatial profile of the cloud. The cloud profile is recorded by passing a focused infrared image of the recombination luminescence ( $\lambda = 1.75\mu\text{m}$ ) across the spectrometer slit. By defocusing the laser, the excitation density can be reduced below the  $100\text{W}/\text{cm}^2$  optical power density threshold for the bubble. A hysteresis is observed in the power density required for the bubble to come on and to go off.

This hysteresis effect is used to isolate the effect of the bubble on the cloud size for a given optical power. Figure 4a shows for reference a cloud profile for focused ( $100\mu\text{m}$ ) excitation. The remaining traces are for a

500 $\mu$ m excitation spot diameter. Trace b) is obtained in the hysteresis region with the bubble on. Trace c) is then obtained after momentarily blocking the laser to remove the bubble. The cloud penetrates 1.4 times as far into the sample with the bubble present. The spatially integrated total luminescence remains unchanged, indicating that this is truly a spatial redistribution. We conclude that the bubble reduces the phonon transmission into the bath, increasing the flux reflected back into the sample and thus increasing the total phonon flux.

In Fig. 4, traces a), b), c) were recorded slowly with a 0.15s time constant, so no oscillatory phenomena was observed. In Fig. 4d) we see that the cloud shape does actually oscillate in time, synchronous with the bubble. Here the cloud profile is digitized in one quick sweep with a 100 $\mu$ s time constant. This is a novel demonstration of the fundamental role that ballistic phonons play in the spatial distribution of electron-hole droplets.

This work was supported by the National Science Foundation under Grant DMR-80-24000.

#### REFERENCES

1. W. Kappus and O. Weis, J. Appl. Phys. **44**, 1947 (1972).
2. M. Greenstein and J. P. Wolfe, Phys. Rev. Lett. **41**, 715 (1978).

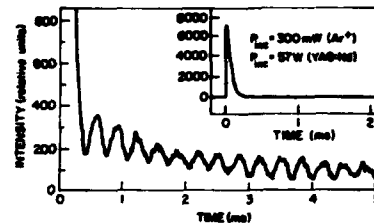


Fig. 3 : Phonon flux modulation by the bubble.

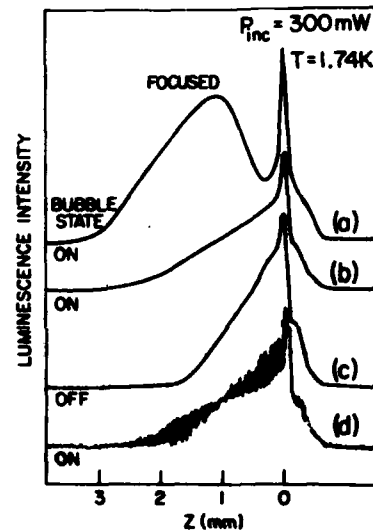


Fig. 4 : Modulation of the droplet cloud shape by the bubble.

SPECIFIC HEAT AND THERMAL CONDUCTIVITY OF  $\text{TmVO}_4$  AND  $\text{DyVO}_4$  WITH AN APPLIED MAGNETIC FIELD

B. Daudin, B. Salce and S.H. Smith\*

*Service des Basses Températures, Laboratoire de Cryophysique, Centre d'Etudes Nucléaires de Grenoble, 85 X, 38041 Grenoble Cedex, France**\*Clarendon Laboratory, Oxford University, U.K.*

**Abstract** - Specific heat and thermal conductivity measurements of  $\text{TmVO}_4$  and  $\text{DyVO}_4$  with applied magnetic field are reported. Experimental results for  $\text{TmVO}_4$  are well described by a molecular field theory whereas such a calculation fails to interpret the  $\text{DyVO}_4$  results as short range order interactions are not taken into account.

1. **Introduction.** -  $\text{TmVO}_4$  and  $\text{DyVO}_4$  belong to the  $\text{RXO}_4$  family ( $R$  = rare earth and  $X$  = V, As or P) whose most members undergo a cooperative Jahn-Teller transition at low temperature. A lot of experimental and theoretical work has been done on these compounds (1) but heat transport mechanisms are not well known. We have previously reported low temperature thermal conductivity measurements of  $\text{TmVO}_4$ ,  $\text{TmAsO}_4$ ,  $\text{DyVO}_4$  and  $\text{TbVO}_4$  samples. In addition,  $\text{TmVO}_4$  and  $\text{TmAsO}_4$  were measured with applied magnetic field and strong effects were observed in both cases (2,3). These measurements were extended to  $\text{DyVO}_4$  and specific heat of  $\text{TmVO}_4$  and  $\text{DyVO}_4$  with applied magnetic field was conjunctly measured in order to check the validity of the theoretical expression we used to calculate the thermal conductivity.

2. **Experimental results.** - The  $\text{DyVO}_4$  sample was needle shaped with a square section of approximately  $1 \times 1 \text{ mm}^2$  and a length of 6 mm. All samples are naturally oriented along the c-axis. The thermal conductivity was measured with the magnetic field,  $H$ , parallel or perpendicular to the c-axis and the results are shown in Fig.1. The main feature is a decrease of  $K(T)$  when  $H$  is parallel to the c-axis whereas a strong  $K(T)$  increase is observed when  $H$  is perpendicular to the c-axis and parallel to the a-axis of the sample.

The specific heat results for  $\text{TmVO}_4$  and  $\text{DyVO}_4$  are shown in Fig.2 and 3. The  $\text{TmVO}_4$  sample was measured with  $H$  parallel to the c-axis.  $\text{DyVO}_4$  was measured with  $H$  parallel to the a-axis. The measure was made difficult by the size of the samples whose weight was 340 mg and 193 mg respectively for  $\text{TmVO}_4$  and  $\text{DyVO}_4$ , despite the fact that a dynamical adiabatic differential technique\* was used.

\* R.LAGNIER, J.PIERRE and M.J.MORTIMER, *Cryogenics* **17**, 349 (1977).



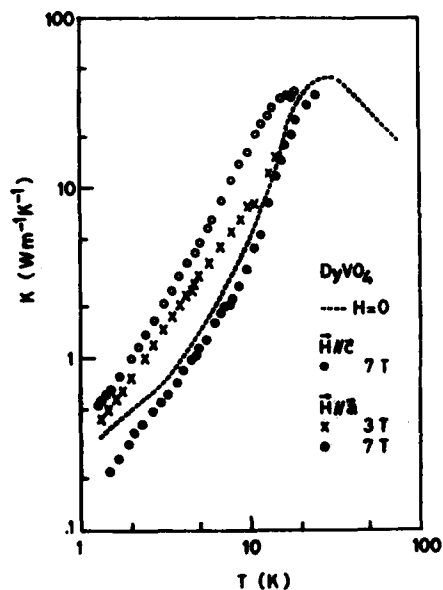


Figure 1

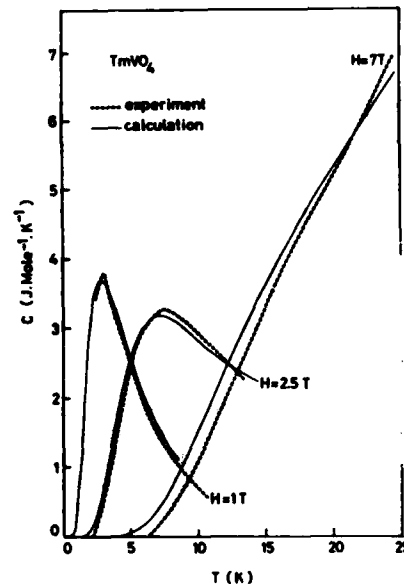


Figure 2

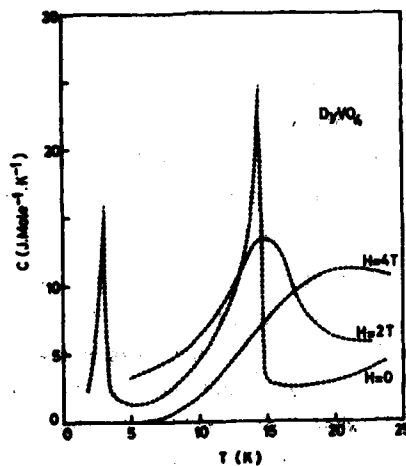


Figure 3

3. Discussion. - The specific heat of  $\text{TmVO}_4$  was previously measured in zero magnetic field (4) and was correctly described in the frame of a molecular field theory. If the two lowest energy levels of the  $\text{Tm}^{3+}$  ion are considered as an isolated doublet (the first excited is a singlet at  $54 \text{ cm}^{-1}$  (5)) the energy splitting  $2W$  in applied magnetic field is given by :  $W/kT_c = \tanh(W/kT)$  if  $\frac{1}{2}g_c \beta H < W$  and  $W = \frac{1}{2}g_c \beta H$  otherwise with  $T_c = 2.15 \text{ K}$ ,  $g_c = 10$  and  $\beta = \text{Bohr magneton}$ .

The specific heat was calculated as  $C = C_S + C_D$ , where  $C_S$  is the contribution of the Schottky anomaly due to the three lowest levels (the singlet is then assumed to be field independent and have no interaction with the ground state doublet).  $C_D$  is the lattice contribution calculated in the Debye model and was adjusted to  $C_D = 1.5 \text{ K } 10^{-4} T^3 \text{ J/K mole}$ .

The results of the adjustment are shown in Fig.2. To obtain a satisfactory agreement it was necessary to assume that the crystal was containing 13 percent of impurities, which is coherent with the presence of large flux inclusions.

The two main conclusions are as follows : a) the molecular field theory accounts well for the observed specific heat.

b) we observe no enhancement of specific heat at the maximum of the Schottky anomaly as would be expected from the presence of the coupled mode (6,7).

So far as  $\text{DyVO}_4$  is concerned, the results are more complicated. A calculation of the specific heat based on a molecular field treatment failed to explain the experiments since short range order interactions which are important in  $\text{DyVO}_4$  are not taken into account by this approach (8). On the other hand, calculations based on "compressible" Ising model fit correctly linear birefringence experiments (9) and it would be interesting to interpret our specific heat measurements within the frame of this model. Such calculations are now in progress.

As a general conclusion, it appears that the specific heat of  $\text{TmVO}_4$  is well described taking into account a Schottky anomaly associated with the thermal populations of the energy levels. Such a description is presumably correct for  $\text{DyVO}_4$  provided we are able to calculate the energy levels of the system. That means that the huge enhancement of thermal conductivity with applied magnetic field observed in both cases is not related to anomalous specific heat behaviour but is probably due to a drastic modification of phonon scattering.

#### References

- (1) G.A. GEHRING and K.A. GEHRING, Rep. Prog. Phys. 38, 1, (1975)
- (2) B.DAUDIN, A.M. DE GOER and S.H. SMITH in Phonon Scattering in Condensed Matter, H.J. MARIS ed., Plenum Publishing Corp., (1980)
- (3) B. DAUDIN and B. SALCE, accepted for publication in J. Phys. C : Sol. St. Phys.
- (4) A.H. COOKE, S.J. SWITENBY and M.R. WELLS, Sol. St. Comm. 10, 265, (1972)
- (5) K.D. KNOLL, Phys. St. sol. (b) 45, 553, (1971)
- (6) V.F. SEARS, Proc. Phys. Soc. 84, 951, (1964)
- (7) J.W. TUCKER, Proc. Phys. Soc. 85, 559, (1965)
- (8) G.A. GEHRING, A.P. MALOZEMOFF, W. STAUE and R.N. TYTE J. Phys. Chem. Solids 33, 1495, (1972)
- (9) G.A. GEHRING, R.T. HARLEY and R.M. MAC FARLANE J. Phys. C : Solid St. Phys. 13, 3161, (1981)

**PHONONS IN LOW DIMENSIONAL MATTER**

## PHONONS IN GRAPHITE INTERCALATION COMPOUNDS

S.A. Solin

*Department of Physics, Michigan State University, East Lansing, Michigan 48824, U.S.A.*

**Abstract.** - Vibrational excitations in pristine graphite and in graphite intercalation compounds are discussed. Modes associated with carbon atom intralayer motions and with the internal excitations of guest molecular species are emphasized.

1. **Introduction.** - The study of phonons in graphite intercalation compounds (GIC's) is by now a relatively mature subject.<sup>1,2,3</sup> The road towards this maturity is characterized by recent spurts in the growth of our knowledge of GIC's in general and of phonons in GIC's in particular. Not surprisingly, our understanding of phonons in-GIC's is intimately coupled to an understanding of phonons in pristine graphite itself.<sup>4,5</sup>

During the past several years research efforts on vibrations in GIC's have focused on five sub-areas: phonons in pristine graphite,<sup>5</sup> phonons associated with the intralayer motions of carbon atoms in GIC's,<sup>1-3</sup> internal molecular modes of guest species in GIC's,<sup>6,7</sup> interlayer c-axis modes involving both guest and host layers,<sup>8,9</sup> and intercalate intralayer modes.<sup>10</sup> In this brief manuscript, I would like to address the first three of the above mentioned areas. Thus, this paper constitutes an introductory setting for the latter two topics which are under active investigation and are considered in other papers in this proceedings. Space limitations also preclude the presentation of introductory material on GIC's, staging, sample preparation techniques, etc. Readers unfamiliar with those topics are referred to recent review articles.<sup>11,12</sup>

2. **Pristine Graphite.** - Hexagonal graphite crystallizes in the  $D_{6h}^{14}$  space group with four atoms in the primitive cell.<sup>13</sup> The zone center optic modes can be group theoretically decomposed into the following irreducible representation<sup>14</sup>

$$\Gamma_{\text{opt}} = 2 E_{2g} + E_{1u} + A_{2u} + 2 A_{2g}$$

of which the  $E_{2g}$  modes and the  $E_{1u}$  and  $A_{2u}$  modes are respectively Raman and infrared active in first order. All of the optically active modes have now been observed experimentally.<sup>5,1</sup> They are shown in Figs. 1 and 2 which also show the eigenvectors

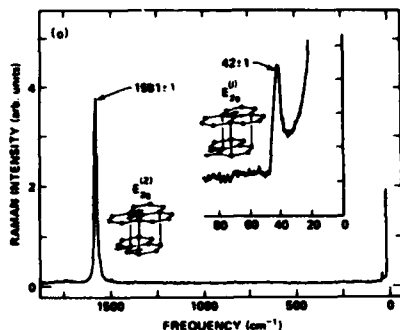


Fig. 1: The Raman spectra obtained from a cleaved surface of graphite and the atomic displacements of the Raman active  $E_{2g}$  modes.

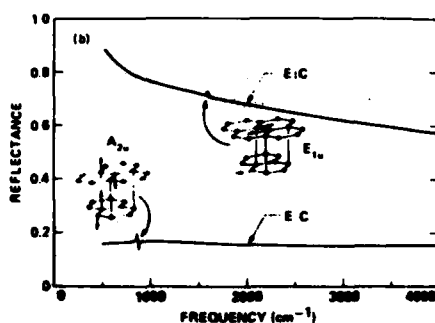


Fig. 2: The  $E_{\perp}C$  and  $E_{\parallel}C$  reflectance of graphite and the atomic displacements of the IR active modes. The  $E_{\parallel}C$  spectrum has been normalized for surface damage.

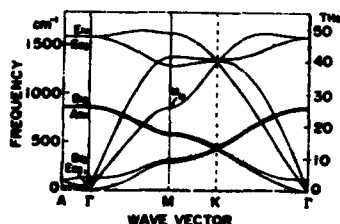


Fig. 3: Phonon dispersion curves for graphite in the [001], [100] and [110] direction. From ref. 16.

associated with each mode.

Of particular importance is the  $A_{2u}$  mode at  $848\text{ cm}^{-1}$ . Prior to its observation, the available Raman, IR and neutron scattering data (the latter of which were limited to  $< 500\text{ cm}^{-1}$ ) had been used to test several models for the phonon dispersion curves of graphite.<sup>15</sup> Although each of the available theoretical models "fit" the available data, their calculated values for the  $A_{2u}$  frequency ranged from  $800\text{ cm}^{-1}$  to  $1400\text{ cm}^{-1}$ . Armed with the crucial  $A_{2u}$  frequency, Morie and coworkers<sup>16</sup> constructed an axially asymmetric Born-von Karman model which provides phonon dispersion curves that are in excellent agreement with all the available experimental data. The results of their calculations are shown in Fig. 3. Note, in particular, that the maximum phonon energy is not at the  $\Gamma$  point, but occurs along the line between  $\Gamma$  and M.

This feature is consistent with, indeed required by, the second order Raman spectrum of pristine graphite.<sup>17</sup>

In more recent calculations<sup>18</sup> G. Dresselhaus and coworkers using a similar model to that of Horie and coworkers have improved the fit of the lower most branches to the neutron data of Nicklow et. al.<sup>4</sup> Thus, it is reasonable to assert now that the phonon dispersion curves of pristine graphite are well understood and can be accurately calculated.

3. Intralayer Modes in GIC's. - The initial approach to intralayer carbon modes in GIC's was the nearest layer model.<sup>19</sup> In this model it was noted that in an  $n^{\text{th}}$  stage GIC  $n \geq 3$ , the  $E_{2g}$   $1580 \text{ cm}^{-1}$  intralayer mode would develop a satellite caused by the small perturbation of the bounding intercalate layers. Thus for  $n \geq 3$  the Raman spectra of GIC's will contain a pair of lines at  $\approx 1580 \text{ cm}^{-1}$ . One of these is associated with interior carbon layers which have a nearest layer environment identical to that in pristine graphite. One is associated with bounding carbon layers perturbed by the intercalated layer. In stages 1 and 2 GIC's there exists only one type of nearest layer environment and thus only a single line should be observed in the  $1580 \text{ cm}^{-1}$  region. The above statements are verified by the Raman spectra of potassium graphite GIC's<sup>20</sup> which are shown in Fig. 4. These spectra are characteristic of the stage dependence of the Raman spectra of all GIC's studied to date.<sup>1</sup> Moreover, the stage dependence of the relative intensities of the members of the  $1580 \text{ cm}^{-1}$  doublet can be quantitatively accounted for by the nearest layer model.<sup>1</sup>

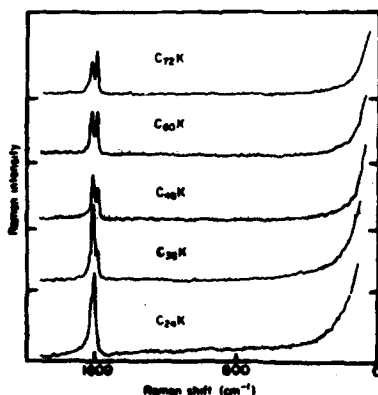


Fig. 4: Raman spectra of stage  $n$ ,  $n \geq 2$  K-GIC's with compositions  $C_{12n}K$ .

Stage 1 alkali GIC's exhibit a Raman spectrum which is characteristically different from those of Fig. 4, but which provide an elegant verification of the calculated dispersion curves of Fig. 3.<sup>1</sup> Note from the Raman spectrum of stage 1  $RbC_8$  and  $CsC_8$ <sup>21</sup> shown in Fig. 5 the polarized members of a triplet of modes in the  $580 \text{ cm}^{-1}$  region.<sup>20</sup> This triplet is quantitatively accounted for by the dispersion curves of Fig. 2 and is associated with M point out of plane motions of the carbon atoms.<sup>1</sup> These M point modes which are first order Raman inactive in pristine

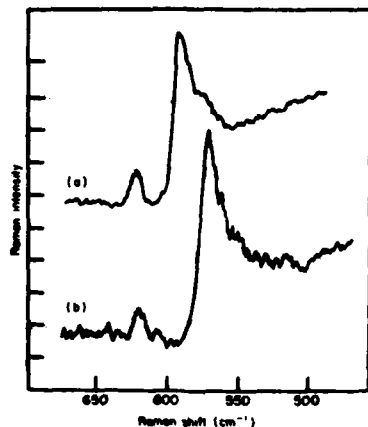


Fig. 5: Polarized Raman spectra of the triplet region for the stage 1 (a) Cs; and (b) Rb GIC's with the incident polarization perpendicular and the scattered polarization parallel to the scattering plane. Polarized modes ( $A_g$  or  $A_1$ ) are forbidden in this configuration.

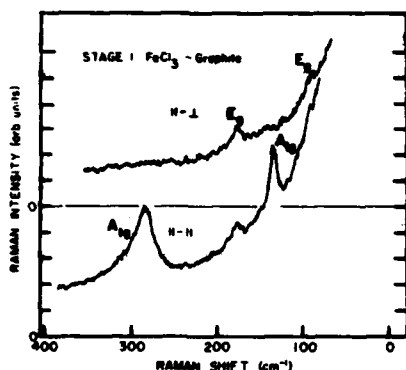


Fig. 6: Polarized Raman spectra of the intercalant intralayer modes of stage 1  $\text{FeCl}_3$ -graphite.

graphite are activated by both disorder induced scattering<sup>22</sup> and Brillouin zone folding effects<sup>3</sup> in the 3-D relatively ordered structures of stage 1  $\text{RbC}_8$  and  $\text{CaC}_8$ .<sup>23</sup> The stage 1 alkali GIC's also exhibit a broad Fano resonance at  $\approx 1500 \text{ cm}^{-1}$  (not shown) which arises from electron-phonon coupling between Raman active phonons in the  $800\text{--}1600 \text{ cm}^{-1}$  range and what appears to be an electronic continuum background.<sup>24</sup>

**4. Internal Molecular Modes.** - To date there is very little data on internal molecular modes of guest species in GIC's. This lack of data is not for want of serious efforts to observe such modes since several groups have made serious attempts in this regard.

The first observation of molecular modes in a GIC was that of  $\text{Br}_2$  molecular modes in bromine graphite.<sup>6</sup> However, the Raman spectrum of that material exhibits the multiple intense overtone peaks which are characteristic of strong resonance Raman scattering. The classic example of this phenomena is given in the Raman resonance spectrum of  $\text{CdS}$ .<sup>25</sup> To my knowledge the only other system in which internal modes of the guest species have been observed from a GIC is  $\text{FeCl}_3$  graphite.<sup>7</sup> The low frequency polarized Raman spectra of stage 1  $\text{FeCl}_3$  graphite is shown in Fig. 6.

The modes observed in that figure can be accounted for group theoretically and correspond to modes of the  $\text{FeCl}_3$  sandwich layers from which pure  $\text{FeCl}_3$  is constructed.

There is evidence that the Raman spectrum of  $\text{FeCl}_3$  graphite was also obtained under resonance enhanced conditions.<sup>26</sup> Thus it appears that resonance enhancement is required in order to observe molecular modes in the Raman spectra of GIC's. A lack of such enhancement would account for the failure to observe molecular modes in GIC's prepared with  $\text{HNO}_3$ , metal-ammonia solutions,  $\text{AsF}_5$ ,  $\text{SbCl}_5$  and other intercalants.

5. Concluding Remarks. - This paper briefly touches upon some developments in our understanding of vibrational excitations in GIC's. For GIC's the molecular modes and carbon atom intralayer modes can only be conveniently probed using optical techniques, e.g. Raman scattering and IR spectroscopy. During the past year new and exciting neutron scattering results on interlayer guest-host modes in GIC's<sup>9</sup> and on intralayer intercalate modes in monionic guest species<sup>10</sup> have been reported. In addition the former have also been observed in the Raman spectra of several stages of alkali GIC's.<sup>8</sup> These new neutron and Raman results are the subjects of other papers in this conference.<sup>8,10</sup>

6. Acknowledgements. - I gratefully acknowledge important contributions from my collaborators N. Caswell, G. Lucovsky, R.J. Nemanich and G.M. Papatheodorou.

This work was supported by the NSF under grant number DMR 80-10486.

#### References

1. Solin, S.A., *Physica* **99B**, (1980) 443.
2. Dresselhaus, M.S., and Dresselhaus, G., to be published.
3. Dresselhaus, M.S., Dresselhaus, G., Ecklund, P.C., and Chung, D.D.L., *Mat. Sci. and Eng.* **31** (1977) 141.
4. Nicklow, R., Wakabayashi, N., and Smith, H.G., *Phys. Rev.* **B5**, (1971) 4951.
5. Nemanich, R.J., Lucovsky, G., and Solin, S.A., in *Proceedings of the International Conference on Lattice Dynamics*, Balkanski, M., ed. (Flammarion, Paris, 1978), p. 619. Also, Nemanich, R.J., Lucovsky, G., and Solin, S.A., *Solid State Commun.* **23** (1977) 117.
6. Song, J.J., Chung, D.D.L., Ecklund, P.C., and Dresselhaus, M.S., *Solid State Commun.* **20** (1976) 1111.
7. Caswell, N., and Solin, S.A., *Solid State Commun.* **27** (1978) 961.
8. Wada, N., Klein, M.V., and Zabel, H., this conference and to be published.
9. Magerl, A., and Zabel, H., *Phys. Rev. Lett.* **46** (1981) 44.
10. Kamitakahara, W.A., Wada, N., and Solin, S.A., this conference and to be published.
11. Solin, S.A., *Advances in Chemical Physics*, in press.
12. Dresselhaus, M.S., and Dresselhaus, G., *Advances in Physics* **30** (1981) 139.



13. Wyckoff, R.W.G., Crystal Structures, Vol. 1 (Oxford Univ. Press, London, 1962), p. 26.
14. Mani, K., and Ramani, R., Phys. Stat. Sol. B61 (1974) 659.
15. See references 1, 8 and 9 and references therein.
16. Maeda, M., Kuramoto, Y., and Horie, C., Proc. of the Phys. Soc. of Japan, 47 (1979) 337.
17. Nemanich, R.J., and Solin, S.A., Phys. Rev. B20 (1979) 392.
18. Lueng, S.Y., Dresselhaus, G., and Dresselhaus, M.S., to be published.
19. Nemanich, R.J., Solin, S.A., and Guerard, D., Phys. Rev. B16 (1977) 2965.
20. Solin, S.A., and Caswell, N., J. Raman Spectroscopy 10 (1981) 129.
21. Solin, S.A., Mat. Sci. and Eng. 31 (1977) 153.
22. Caswell, N., and Solin, S.A., Phys. Rev. B20 (1979) 2551.
23. See references 11 and 12 and references therein.
24. Miyazaki, H., Hatano, T., Kasunoki, G., Watanabe, T., and Horie, C., Physica 105B (1981) 381.
25. Leite, R.C.C., and Porto, S.P.S., Phys. Rev. Lett. 17 (1966) 10.
26. Papatheodorou, G.N., and Solin, S.A., unpublished.

## PHONONS IN ALKALI GRAPHITE INTERCALATION COMPOUNDS

H. Zabel and A. Magerl \*

*Loomis Laboratory of Physics and Materials Research Laboratory, University of Illinois at Urbana-Champaign, Urbana, IL. 61801, U.S.A.**\*Institut Laue-Langevin, 156X, F-38042 Grenoble-Cedex, France*

**Abstract.** - The [001]L phonon branches of alkali-graphite intercalation compounds  $C_xM$  ( $x=8,24,36$ ;  $M=K,Rb,Cs$ ) have been measured by means of inelastic neutron scattering experiments. In all cases the phonon branches show zone folding effects, due to the enlarged unit cell as compared to pristine graphite, along with opening of frequency gaps at the center and boundary of the Brillouin zone. All measured [001]L phonon dispersions are describable by one-dimensional shell models with different masses and force constants to account for the graphite and alkali area-mass densities along the c-axis and their interplanar interactions.

1. **Introduction.** - Within the past year, the interest in the study of low frequency modes in graphite intercalation compounds has increased considerably,<sup>1,2/</sup> after the high frequency modes have been investigated extensively by Raman spectroscopy and infrared reflectance.<sup>3/</sup> In particular, the low lying modes with phonon propagation in the hexagonal c-direction ([001]L and [001]T) are important for the determination of the graphite-intercalant interplanar interaction. Knowledge of the coupling force constants may contribute to the solution of such important questions as the origin of long-range stacking order of graphite and intercalated planes and of intercalant in-plane order-disorder phase transitions. In addition, those modes allow to study some fundamental aspects of lattice dynamics: since the interplanar distances of the atoms are not changed for [001] modes, they may be considered as the movement of a one-dimensional (1-D) array of rigid layers. The properties of this linear chain of graphite and intercalant planes can artificially be changed, by changing the stage  $n$  of the compound ( $n$  designates the number of graphite planes between two intercalated planes), and/or the intercalant chosen, and effects like zone folding and opening of frequency gaps at the center and the boundary of the Brillouin zone can be studied in a systematic manner.

In the following the experimental results obtained for [001]L modes in alkali-graphite intercalation compounds (AGIC's) will be presented and lattice dynamical models will be discussed. A more detailed discussion is given in a separate contribution to this volume.<sup>4/</sup> The [001]T modes, which are less accessible to inelastic neutron scattering, have been studied by Raman spectroscopy.<sup>5/</sup>

2. **Experimental.** - The samples were intercalated with alkali atoms in a two-stage furnace in the usual manner,<sup>6/</sup> and homogeneity of each compound was determined by

x-ray and neutron elastic (00 $\ell$ ) scans. Relevant parameters of the samples before after intercalation will be published elsewhere.<sup>7/</sup> Constant Q scans were performed, using triple-axis spectrometers at the National Bureau of Standards research reactor, Washington, D.C.

3. **Results.** - The [001]L phonon energies obtained at C<sub>8</sub>K, C<sub>24</sub>K, C<sub>36</sub>K, C<sub>24</sub>Rb, C<sub>8</sub>Cs and C<sub>24</sub>Cs are plotted in Fig. 1. For the sake of completeness the corresponding modes of C<sub>8</sub>Rb have also been included.<sup>8/</sup> The phonon wavevectors are given in units of the intensity period C, neglecting any stacking sequence of the graphite and/or alkali planes. Each stage n compound contains n+1 planes per unit cell. Accordingly, there are n+1 phonon branches, which could all be determined: in each case one

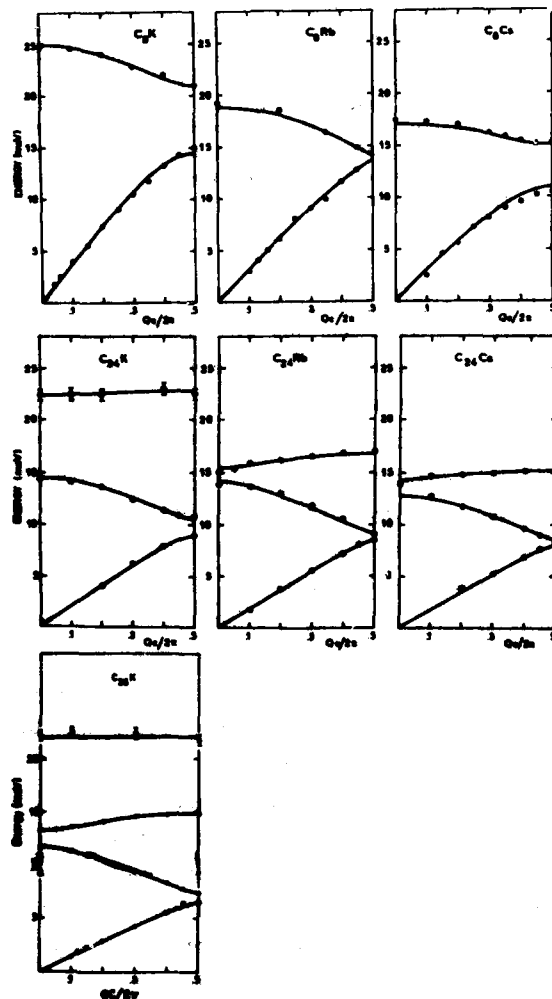


Fig. 1: Measured phonon energies for [001]L modes in alkali-graphite intercalation compounds. The phonon energies of C<sub>8</sub>Rb have been taken from Ref. 8. Full lines are best fits with 1-D ion-shell models.

acoustical branch and  $n$  optical branches. Mode splittings could be clearly resolved in most cases, with the exception of  $C_{24}Cs$ , where the carbon and cesium layers have almost identical in-plane area-mass densities. Low temperature experiments down to 80 K have been performed at  $C_{36}K$ . The results do not indicate any change of the phonon energies across the phase transition at around 130 K.<sup>9/</sup>

4. Discussion. - The data have been analyzed by several 1-D lattice dynamical models. In opposition to pure graphite,<sup>10,11/</sup> Born-von Kármán type models cannot describe the observed [001]L modes of AGIC's. Here a simple 1-D shell model

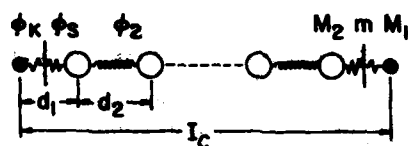


Fig. 2: Schematic representation of the 1-D ion-shell model for stage  $n$  compound  $d_1$  and  $d_2$  are the distances between alkali and graphite planes,  $I_C$  is the repeat distance of the compound in the  $c$ -direction.  $M_1$  and  $M_2$  are the alkali and graphite area-mass densities, resp. and  $m$  is the electron mass density, which is extrapolated to zero.  $\phi_K$  is the core-shell,  $\phi_S$  the shell-graphite, and  $\phi_2$  the interior graphite-graphite force constant.

yields the best result. In this model a charged layer has been introduced between alkali and adjacent graphite planes to account for the inhomogeneous charge distribution along the  $c$ -axis (Fig. 2). Best fits of the shell model to the measured phonon energies yield values for  $\phi_K$ , which are roughly an order of magnitude larger than the force constants  $\phi_S$  and  $\phi_2$ , while  $\phi_S$  is always larger than  $\phi_2$  by about 10-20%, and  $\phi_2$  is almost identical to the interplanar coupling constant of pristine graphite.

The authors acknowledge valuable discussions with J. J. Rush and J. M. Rowe. This work was supported in part by the U.S. Department of Energy under Contract DE-AC02-76ER01190, the Research Corporation and the University of Illinois Research Board.

#### References:

1. A. Magerl and H. Zabel, Phys. Rev. Lett. **46**, 444 (1981).
2. J. D. Axe, C. F. Majkrzak, L. Passell, S. K. Satija, G. Dresselhaus, and H. Masutake, to be published in Proceedings of the 15th Biennial Conference on Carbon, (1981).
3. See for a review: M. S. Dresselhaus and G. Dresselhaus, Adv. in Phys., **30**, 199, (1981).
4. A. Magerl and H. Zabel, this volume.
5. H. Wada, M. V. Klein, and H. Zabel, this volume.
6. D. E. Nixon and C. E. Parry, J. Phys. D1, 791 (1968).
7. H. Zabel and A. Magerl, to be published.
8. W. D. Ellenson, E. Semmingsen, D. Guerdard, D. G. Onn, and J. E. Fischer, Mater. Sci. Eng. **31**, 137 (1977).
9. Y. H. Jan, H. Mori, and S. C. Mann, to be published.
10. G. Dolling and B. N. Brockhouse, Phys. Rev. **120**, 1120 (1962).
11. R. Wicklow, H. Mahabadi, and H. G. Smith, Phys. Rev. **85**, 4951 (1972).

EFFECT OF NON-MAGNETIC IMPURITIES ON THE RAMAN SCATTERING BY  
SUPERCONDUCTING GAP EXCITATIONS IN LAYERED COMPOUNDS

S.N. Behera

*Institute of Physics, Bhubaneswar-751007, India*

**Abstract.**— The effect of small concentrations of substitutional non-magnetic impurities, on the observability of superconducting gap excitations, is considered. It is shown that the presence of heavy mass impurities tends to increase the strength of the Raman peak due to the gap excitations, while lowering its frequency. On the otherhand the local mode due to light mass impurities splits into two because of its coupling to the gap excitations.

1. **Introduction.**— Recently for the first time superconducting gap excitations have been observed in the layered compound  $2H-NbSe_2$  through phonon Raman scattering<sup>1</sup>. At room temperature  $2H-NbSe_2$  has two Raman lines at  $234\text{ cm}^{-1}$  and  $248\text{ cm}^{-1}$ . Below  $33^\circ\text{K}$  the system undergoes a charge density wave (CDW) transition which induces additional Raman peaks around  $40\text{ cm}^{-1}$ . On further cooling it becomes superconducting (SC) at  $7.2^\circ\text{K}$ , resulting in the appearance of still more Raman peaks at approximately  $16\text{ cm}^{-1}$ , which is close to twice the superconducting energy gap<sup>2</sup> ( $2\Delta \approx 17.2\text{ cm}^{-1}$ ). Crucial to this observation is the availability<sup>3</sup> of the CDW phonon close in energy to  $2\Delta$ . Balseiro and Falicov<sup>4</sup> (BF) interpreted this observation as a phonon self-energy effect arising because of the coupling between the CDW phonon and the SC electrons. It is well known that non-magnetic impurities, while not affecting the superconducting properties can inhibit the formation of CDW. Besides, these can give rise to impurity (local, gap and resonant) modes. It is conjectured that a suitable heavy mass impurity can produce a low lying impurity mode which in turn can couple to the SC gap excitations even in the absence of the CDW mode. On the other hand, a light mass impurity will produce a high frequency local mode which will tend to reduce the strength of CDW peak, and consequently that of the Raman line associated with the SC coupled mode. In order to test this conjecture we generalize the BF calculation to incorporate the effect of non-magnetic impurities.

2. **Theory.**— The system is described by the model Hamiltonian

$$H = H_{BF} + H_I \quad (1)$$

where  $H_{BF}$  is the Balseiro-Falicov Hamiltonian and the contribution due to non-magnetic substitutional isotopic impurities is given by

$$H_I = \lambda \sum_{i=1}^N \sum_{q,q'} U^{(i)}(q,q') (b_q + b_q^+) (b_{q'} + b_{q'}^+) \quad (2)$$

$$\text{with } \lambda = (M_I - M)/M_I \quad (3)$$

$$\text{and } U^{(i)}(q,q') = (4N)^{-1} \sqrt{\omega_q \omega_{q'}} e^{i(q+q') \cdot R_i} \quad (4)$$

$M_I$  and  $M$  being the masses of the impurity and host atoms respectively. The impurity concentration ( $c$ ) is assumed to be small. The phonon self-energy for this system turns out to be

$$\Sigma_q(\omega) = \Sigma_q^{BF}(\omega) - c\lambda D^{-1}(\omega) [\omega_q^2 + 2\omega^2(\omega^2 - \omega_q^2)^{-1} \Sigma_q^{BF}(\omega) - \lambda \omega^4 D^{-1}(\omega) \chi(\omega)] \quad (5)$$

where

$$D(\omega) = 1 + \lambda N^{-1} \sum_{q_1} \omega_{q_1}^2 (\omega^2 - \omega_{q_1}^2)^{-1} \quad (6)$$

$$\chi(\omega) = N^{-1} \sum_{q_1} (\omega^2 - \omega_{q_1}^2)^{-2} \Sigma_{q_1}^{BF}(\omega) \quad (7)$$

and  $\Sigma_q^{BF}(\omega)$  is the phonon self energy in the absence of the impurities. Since, we are interested in Raman scattering, eqn.(5) is evaluated in the limit  $q = 0$ , with the Einstein model for the host phonon, assuming that in eqn.(7)  $\Sigma_{q_1}^{BF}(\omega)$  is independent of  $q_1$ . Thus, the excitation spectrum is given by the solutions of the equation

$$(\omega^2 - 1) [1 + cF(\lambda, x)] + [1 - 2c x^2 F(\lambda, x) + c x^4 F^2(\lambda, x)] \Sigma_0^{BF}(y) = 0 \quad (8)$$

$$\text{where } F(\lambda, x) = \lambda / (x^2 - 1 + \lambda) \quad (9)$$

$$\Sigma_0^{BF}(y) = 4s y^{-1} (1 - y^2)^{-1/2} \tan^{-1} [y (1 - y^2)^{-1/2}], \text{ for } y < 1 \quad (10)$$

$$\text{with } s = \langle g^2 \rho(\epsilon) \rangle / \omega_0, \quad x = \omega / \omega_0 \quad \text{and } y = x (\omega_0 / 2\Delta) \quad (11)$$

$\omega_0$  being the frequency of the host phonon,  $\Delta$  is the superconducting energy gap,  $g$  is the electron-phonon coupling constant in the SC state and  $\rho(\epsilon)$  is the electron density of states at the Fermi surface. In this calculation the effect of the impurities on the CDW state has been ignored.

**3. Results and Discussions.**— First of all, we shall assume that  $\omega_0$  is the CDW phonon and the impurity mode arises from  $\omega_0$ . However, instead of appearing at the usual frequency of  $\omega_0(1-\lambda)^{1/2}$ , the

impurity mode splits into two, because of its coupling to the SC gap excitations, as is obvious from eqn.(8). A heavy mass impurity giving rise to a mode below  $2\Delta$ , increases the strength of the gap excitation mode and pushes it towards zero frequency, which is equivalent to increasing the coupling strength  $s$ . On the other hand a light mass impurity giving rise to a local mode decreases the strength and increases the frequency of the  $2\Delta$  excitation. Features similar to this prediction had been observed in  $2H-NbSe_2$  samples containing impurities<sup>3</sup>.

In the absence of the CDW phonon,  $\omega_0$  will be the Raman active mode in the normal state which being of high frequency  $\omega_0 \gg 2\Delta$  decreases the coupling strength considerably, resulting in the impossibility of observing the SC gap excitation. However, if the mode due to a heavy impurity falls near where the CDW mode existed then because of its coupling to the gap excitations, it is possible to observe the same under special conditions.

It is worth mentioning that substitution of heavy mass impurities in place of Nb in  $2H-NbSe_2$  may not be feasible experimentally. However, even a light mass impurity atom can produce low frequency modes provided its substitution causes nearest neighbour force constant softening. Similarly it is also possible that an impurity phonon can couple rather strongly to the SC electrons giving rise to the its bound state with SC gap excitations. These features are being investigated currently<sup>5</sup>.

**Acknowledgement.**— I would like to thank Mr.G.C.Mohanty, who is intimately associated with this work, for his help in the preparation of the manuscript. We are grateful to Prof.M.V.Klein and L.M.Palicov for sending us preprints and unpublished calculations of their work.

**References.**—

1. Sooryakumar, R. and Klein, M.V., Phys. Rev. Lett. 45, 660 (1980).
2. Clayman, B.P. and Frindt, R.F. Solid State Commun. 9, 1881 (1971).
3. Sooryakumar, R. Klein, M.V. and Frindt, R.F. preprint (1981).
4. Balseiro, C.A. and Palicov, L.M. Phys. Rev. Lett. 45, 662 (1980).
5. Behera, S.N. and Mohanty, G.C. (1981) unpublished calculations.

# INELASTIC NEUTRON SCATTERING AND LATTICE DYNAMICS OF THE LAYER SEMICONDUCTOR GaS

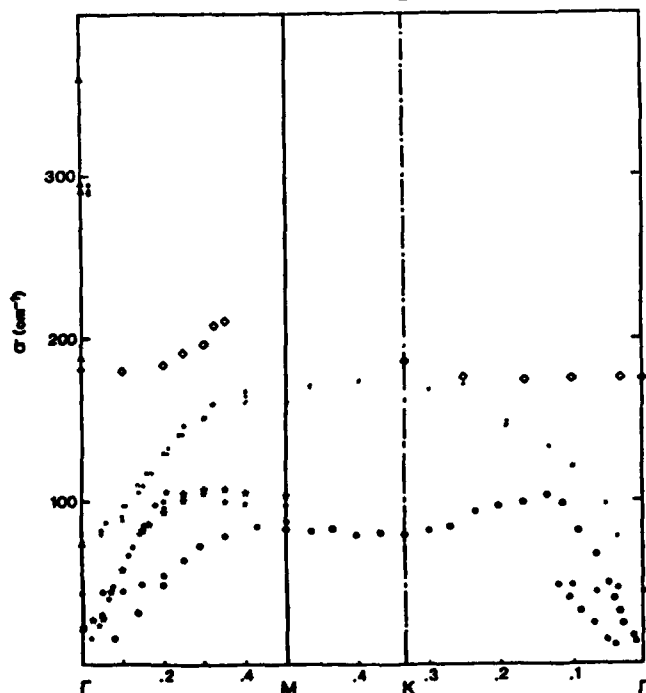
A. Polian, K. Kunc and J. Rossat-Mignod\*

*Laboratoire de Physique des Solides (Associé au C.N.R.S.), Université P. & M. Curie, 4, place Jussieu, F-75230 Paris Cedex 05, France*

*\*DRF/DN, Centre d'Etudes Nucléaires, 85 X, F 38041 Grenoble Cedex, France*

**Abstract.**— Measurements of the phonon dispersion curves of GaS in the  $\Gamma \rightarrow M$  and  $\Gamma \rightarrow K \rightarrow M$  directions by inelastic neutron scattering have been performed. They show a non dispersive behaviour of the LA phonons in both directions. A Rigid Ion Model (RIM) with anisotropic effective charges and Axially Symetric Forces (ASF) is constructed from these data and discussed.

1. **Experiment.**— Inelastic neutron scattering experiments were performed on the layer crystal GaS on the IN3 and IN8 spectrometers at the ILL and DN1 at the C.E.N.G. Two experimental configurations were used allowing to obtain the phonon dispersion in the  $\Gamma \rightarrow M$  and in the  $\Gamma \rightarrow K \rightarrow M$  directions respectively. The experimental results shown in figure 1 match the earlier measurements<sup>(1,2)</sup> and confirm the fact that, in the  $\Gamma \rightarrow M$  direction, the LA mode is non-dispersive from  $\vec{k} \cdot \vec{v}(0.25, 0, 0)$  to the zone boundary. Similar features are found in the  $\Gamma \rightarrow K$  direction and there is no dispersion between M and K. The  $B_2$  TA mode shows a similar behaviour.



**Fig. 1 :** Experimental dispersion curves in the layer plane. Each symbol corresponds to a phonon with a different symmetry. The phonons vibrating parallel to the y-axis are not shown here.



The layered nature of the crystal is reflected in the quadratic dispersion at small wave vector of the out-of-the-layer-plane TA mode  $\nu = \alpha\zeta + \beta\zeta^2$  : with frequency in Hz and reduced wave vector  $\zeta = |\vec{k}|/|\vec{k}_M|$ ,  $k_M = 4\pi/a\sqrt{3}$ , our measurements yielded  $\alpha = 5 \times 10^{-12} \text{ s}^{-1}$  and  $\beta = 10.5 \times 10^{-12} \text{ s}^{-1}$ . As  $\beta/\alpha$  is zero in usual three-dimensionnal crystals, and 10 in graphite, the present value of  $\beta/\alpha = 2$  indicates the degree of bidimensionnality.

2. Lattice Dynamics.— We used a Rigid Ion Model (RIM) associated with Axially Symetric Forces (ASF). The RIM is applied with an anisotropic effective charge tensor :

$$Z^* = \begin{pmatrix} Z_1 & 0 & 0 \\ 0 & Z_1 & 0 \\ 0 & 0 & Z_2 \end{pmatrix}$$

in order to reproduce the anisotropy of the LO - TO splits at the zone center.

The set of 5 central forces ( 10 parameters  $A_i$ ,  $B_i$ ;  $i = 1,5$ ) represents : interaction n° 1 : Ga - Ga first neighbours; n° 2 : Ga - S first neighbours; n° 3 : S - S interlayer; n° 4 : Ga - Ga second neighbours (intralayer,intercell); n° 5 : Ga - S second neighbours.

3. Discussion.— The ASF parameters  $A_3$  and  $B_3$  are calculated from the rigid layer modes  $E_{2g}$  ( $23 \text{ cm}^{-1}$ ) and  $B_{2g}$  ( $43 \text{ cm}^{-1}$ ), the other ones are obtained by least square fit to neutron data. The effective charges are obtained from LO - TO splits of the  $E_{1u}$  modes ( $Z_1 = 0.9 |e|$ ) and  $A_{2u}$  modes ( $Z_2 = 0.44 |e|$ ).

The dispersion curves calculated in the  $\Gamma \rightarrow M$  direction are compared in figure 2. In spite of its simplicity, the model accounts well for all the zone center modes and provides elastic constants in good agreement with values obtained by Brillouin scattering<sup>(3)</sup>. On the contrary, the non-dispersive behaviour of the LA phonons in the  $\Gamma \rightarrow M$  direction could not be reproduced. While a flat region in the

dispersion of TA modes was already observed in other materials like Si or Ge, a similar behaviour for the LA does not appear in other semiconducting materials.

A tentative explanation of this dispersion could be a coupling between the  $A_1$  (LA)

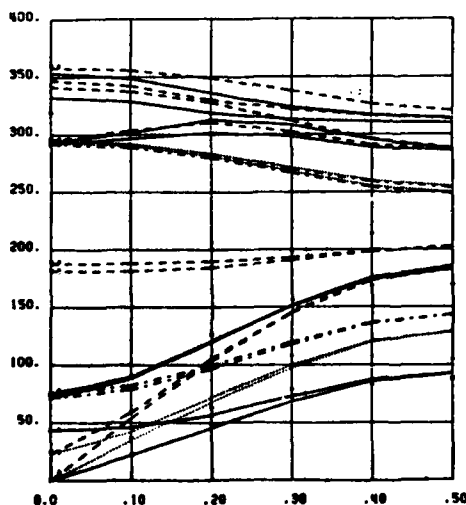


Fig. 2 : Theoretical dispersion curves in the  $\Gamma \rightarrow M$  direction.  
— :  $B_1$  modes; ... :  $B_2$  modes  
--- :  $A_1$  modes; -.- :  $A_2$  modes.

mode and the  $B_1$  ( $E_{1g}$  in  $\Gamma$ ) mode.

Owing to the use of anisotropic effective charge, the present model is able to describe the angular dispersion of the zone center polar phonons. Due to the high symmetry of GaS, the only experimental data available are those parallel and perpendicular to the c-axis so that the prediction cannot be checked. We preferred thus to show in figure 3 the dispersion predicted by the same model rather for  $\gamma$ -GaSe ( $Z_1 = 0.84 |e|$ ;  $Z_2 = 0.39 |e|$ ) a closely related structure in which, however the different stacking and consequently lowered symmetry made possible to obtain more complete data<sup>(4,5)</sup>.

Large polarisability of bonds in GaS, which is suggested by the space distribution of electronic charges<sup>(6)</sup> and shown by the high intensity of the Raman allowed lines raises some doubts about the adequacy of RIM for the description of the lattice dynamics of GaS. It is very likely that any of the standard dipole models (shell, d.d.m. etc.) would be

more satisfactory. It is questionable, however, whether the introduction of polarizable ions *alone*, would be sufficient to explain the non-dispersive behaviour of the  $A_1$  (LA) and  $B_2$  (TA) branches : looking for a description accounting explicitly for the large bond-charges showing up between the Ga atoms would probably be more appropriate.

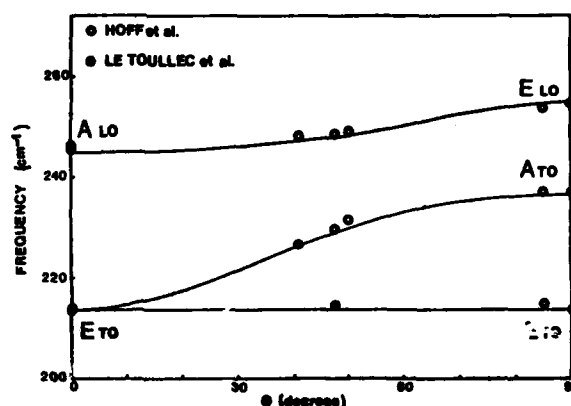


Fig. 3 : Angular dispersion of the polar modes of GaSe.

#### References

- (1) B.M. POWELL, S. JANDL, J.L. BREBNER and F. LEVY : J. Phys. C **10**, 3039 (1977)
- (2) A. POLIAN, K. KUNC, R. LETOULLEC and B. DORNER : Proc 14th I.C.P.S. Edinburgh 1978. Inst. Phys. Conf. Ser **43**, 907 (1979)
- (3) A. POLIAN, J.M. BESSON, M. GRIMSDITCH and H. VOGT : to be published, Phys. Rev. B
- (4) R.M. HOFF, J.C. IRWIN and R.M.A. LIETH : Can. J. Phys. **53**, 1606 (1974)
- (5) R. LETOULLEC, N. PICCIOLI, M. MEJATTY and M. BALKANSKI : Nuovo Cimento **38B**, 159 (1977)
- (6) A. KUHN, A. BOURDON, J. RIGOUT and A. RIMSKY : submitted to Phys. Rev.

## ROLE OF PHONONS IN ORIENTATIONAL INTRA-PLANE ORDERING IN GRAPHITE INTERCALATION COMPOUNDS

C. Horie, H. Miyazaki, S. Igarashi and S. Hatakeyama

*Department of Applied Physics, Tohoku University, Sendai, Japan*

**Abstract.-** Theoretical study of orientational intra-plane ordering in the second stage graphite intercalation compounds is presented with particular emphasis on the role of phonons. It is shown that the rotation angle of intercalant layers relative to the graphite layers is predominantly determined by intra-plane transverse modes and also depends on the ratio of lattice constants of both intercalant and graphite layers.

1. Introduction. X-ray diffraction studies of  $C_{24}Cs$  prepared from single crystal graphite demonstrate that a triangular arrangement of Cs atoms in the real space is non-registered with graphite layers in macroscopic domains, generating a hexagonal sextet of diffraction spots rotated by  $\pm 14^\circ$  about the c-axis with respect to the  $\langle 100 \rangle$  graphite direction at temperatures  $50K < T < 165K$  [1]. Similar orientational intra-plane ordering has also been studied on  $C_{24}Rb$  [2,3,4] and other compounds. In the present paper, a microscopic theory of the orientational intra-plane ordering in the second stage compounds is developed with particular emphasis on the role of phonons. The theoretical procedure follows the one developed by Novaco [5] for mono-layer films adsorbed on solid surfaces, but is extended so as to be applicable to our system consisting of intercalant layers sandwiched between a pair of graphite layers. It is shown that characteristic phonon dispersions modulated by a coupling between intercalant atoms and carbon atoms in the adjacent layers play a crucial role in determining the rotation angle in the orientational ordering.

2. Model. We assume that intra-plane structure of an intercalant layer is a triangular lattice with a lattice constant  $d_I$  and is non-registered and incommensurate with the adjacent hexagonal graphite layers with a lattice constant  $d_G$ . Then, the atomic displacements from the virtual lattice sites are modulated each other by means of the interatomic potential between intercalant and carbon atoms. This modulation yields displacements of atoms to new stable positions of intercalant and/or carbon atoms, giving rise to a rotation of the

reciprocal lattice of intercalants relative to that of carbon lattice. The free energy, then, turns out to be given by  $E_{ph} + E_{MDW}$ , where  $E_{ph}$  denotes the renormalized phonon energy and  $E_{MDW}$  corresponds to the energy gain due to the static displacement of atoms and is called the mass density wave (MDW) energy hereafter. Within the self-consistent harmonic phonon approximation,  $E_{MDW}$  is given in a form

$$E_{MDW} = - \sum_{\vec{q}, j} \frac{|g_j(\vec{q})|^2}{E_j(\vec{q})}, \quad (1)$$

where  $E_j(\vec{q})$  are phonon frequencies of  $j$ -th modes, and  $g_j(\vec{q})$  involves factors  $(\vec{G}, \vec{e}_j(\vec{q}))$ ,  $(\vec{\tau}, \vec{e}_j(\vec{q}))$  and the Kronecker's delta  $\delta_{\vec{G}+\vec{q}, \vec{\tau}}$  which select the relevant phonons to stabilize the mass density wave.  $\vec{G}$  and  $\vec{\tau}$  are the reciprocal lattice vectors of graphite and intercalant layers, respectively, and  $\vec{e}_j(\vec{q})$  is the polarization vector of  $(j, \vec{q})$  phonon. The  $g_j(\vec{q})$  depends also on the Debye-Waller factor, and the Fourier transform of the interaction potential between intercalant and carbon atoms, which consists of the Born-Mayer type repulsive part and the screened Coulomb interaction.

3. Results and Conclusions.— Figure 1 shows the renormalized phonon dispersion curves for modes with polarization parallel to the basal plane in  $C_{24}Cs$ . Other modes polarized parallel to the  $c$ -axis are omitted because they have no effect on the orientational rotation under consideration. Frequencies at the  $\Gamma$  point are determined on a simplified one-dimensional model, in which atomic arrangements and masses are taken to meet with layer stacking  $A \alpha AA \alpha AA \dots$  and with the in-plane stoichiometry of  $C_{12}M$ . Use is also made of the neutron data of  $C_8Cs$  and  $C_{36}K$  in order to estimate the effective force constants. Details of the derivation of the phonon dispersion curves and  $E_{MDW}$  will be published elsewhere.

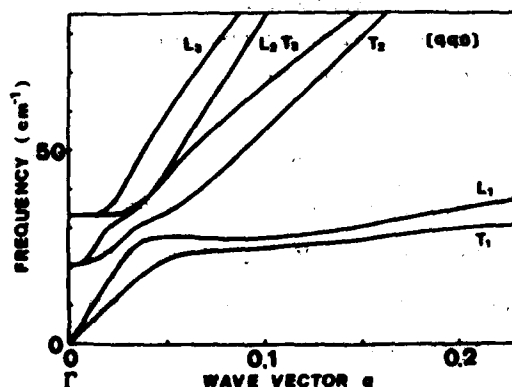


Fig. 1: Phonon dispersion curves for  $C_{24}Cs$ .  $L_1$ ,  $L_2$  and  $L_3$  represent longitudinal modes.  $T_1$ ,  $T_2$  and  $T_3$  represent transverse modes polarized parallel to the basal plane.

The  $E_{MDW}$  for  $C_{24}Cs$  is calculated by using phonon dispersion curves shown in Fig. 1, and is plotted against the rotation angle  $\theta$  between  $\hat{r}_{100}$  and  $\hat{G}_{100}$  in Fig. 2. We have taken  $d_I = 6.02\text{\AA}$  and  $d_G = 2.47\text{\AA}$  ( $z = d_I/d_G = 2.44$ ) which correspond to the layer stoichiometry  $C_{12}Cs$ .

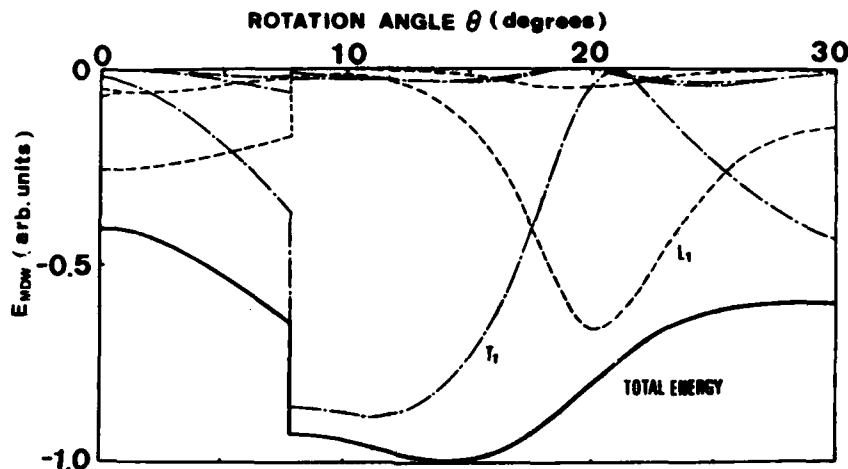


Fig. 2 : The  $\theta$ -dependence of MDW energy for  $C_{24}Cs$  calculated by using the dispersion curves given in Fig. 1. Solid curves represents the total MDW energy. The dash-dotted and dashed curves indicate contributions to EMDW from T and L modes, respectively.

The minimum of  $E_{MDW}$  is found at about  $14^\circ$  in good agreement with experiment. It seems interesting to observe from Fig. 2 that the lowest longitudinal mode always plays a role to stabilize energy at  $\theta = 19.1^\circ$ , but the lowest transverse mode is more effective in stabilizing MDW at angles below  $19.1^\circ$ . The similar feature is also seen in the case of  $C_{24}Rb$ . In this case, however, the  $E_{MDW}$  shows a flat minimum over a certain range of  $\theta$  around  $12^\circ$  for  $z = 2.45$ . It is concluded from our results that the rotation angle in the orientational ordering is determined not only by the value of  $z$ , but also by the detailed phonon dispersion curves characteristic to the compounds.

#### References

- [1] Clarke R. and Caswell N., Solin S.A. and Horn P.W., Phys. Rev. Letters **45** (1979) 2018; Physica **99B** (1980) 457.
- [2] Suematsu H., Suzuki M., Ikeda H., and Endoh Y., Synthetic Metals **2** (1980) 133.
- [3] Kambe W., Dresselhaus G. and Dresselhaus M.S., Phys. Rev. **B21** (1980) 3491.
- [4] Yamada Y., Naiki I., Watanabe T., Kiuchi T., and Suematsu H., Physica **105B** (1981) 277.
- [5] Novaco A.D., Phys. Rev. **B19** (1979) 6493.

## TWO-PHONON PROGRESSIONS ASSOCIATED WITH VIBRONIC EXCITONS IN LAYERED 3d-METAL COMPOUNDS

G. Benedek, I. Pollini and W. Bauhofer\*

Istituto di Fisica dell'Università, GNISM, Milano, Italy

\*Max-Planck Institut für Festkörperforschung, Stuttgart 80, F.R.G.

**Abstract.** - We have observed two-phonon structures in some intraconfigurational crystal field transitions of V-, Mn- and Ni-halides. We also report for the first time the crystal field spectrum of  $\text{CrBr}_2(3d^4)$ , where, despite its unfilled  $e_g$  semishell, exciton-phonon (ep) interaction vanishes to first order yielding a two-phonon sequence in  ${}^3A_1(G) + {}^3A_2(F)$  band.

Electron-phonon interaction in layered transition-metal halides yields a complex vibronic structure in crystal field spectra /1/. The quasi-molecular nature of these crystals, due to their low dimensional structure and reduced ionicity, results in a flat dispersion of both d-d excitons and optical phonons (vibronic excitons with small excitation transfer) /2/. This allows for the experimental observation of sharp phonon progressions in the absorption spectra of  $d^n + d^n$  parity forbidden transitions. From these structures we can learn much on the dynamics of the excited states. For *intraconfigurational* transitions in *half-filled shells* ( $d^3(t_{2g}^3)$ ,  $d^5(t_{2g}^3 e_g^2)$ ,  $d^8(e_g^2)$ ) the orbital ep coupling vanishes to first order /3/: thus a second-order progression is expected to be the basic vibronic structure, provided that also the *spin-dependent* ep interaction (via the phonon modulation of spin-orbit (SO) coupling) is zero. Such a selection rule is fulfilled by the transitions listed in TABLE, where 2nd-order phonon progressions are possible.

Electronic configuration	Electronic Transitions	
	predicted	observed
$d^3(t_{2g}^3)$	${}^4A_2(F) + {}^2E(G)$	${}^2E(G)$ in $\text{VCl}_2$ , $\text{VBr}_2$
$d^5(t_{2g}^3, e_g^2)$	${}^6A_1(S) + {}^4E(G) + {}^4A_1(G), {}^4E(D)$	${}^4E(G)$ in $\text{MnX}_2$ , ${}^4E(D)$ in $\text{MnCl}_2$
$d^8(e_g^2)$	${}^3A_2(F) + {}^1E(D), {}^1A_1(G)$	${}^1E(D), {}^1A_1(G)$ in $\text{NiCl}_2$ , $\text{NiBr}_2$
$d^4(t_{2g}^3, e_g)$	${}^5E(D) + {}^3E(H), {}^3A_1(G),$ ${}^3A_2(F), {}^3E(D)$	${}^3A_2(F) + {}^3A_1(G)$ in $\text{CrBr}_2$

We have included also the special case of  $d^4(t_{2g}^3 e_g)$  in  $\text{CrBr}_2$  (space group  $C_{2h}^3 / 4/$ ),

where despite its unfilled  $e_g$  semishell a vanishing  $ep$  interaction for some transitions between monoclinally split levels is found. Previously /5/ we reported a strong evidence of pure two-phonon progressions in  $\text{NiCl}_2$  and  $\text{NiBr}_2$   ${}^3A_2(F) \rightarrow {}^1E(D)$  transition. This is a rather rare case, since configurational mixing can switch on a weak 1st order  $ep$  coupling and mask two-phonon contribution. Nevertheless the theoretical prediction of a 2nd order structure often provides a key of interpretation of other complicated phonon structures we observed in other 3d-metal compounds.

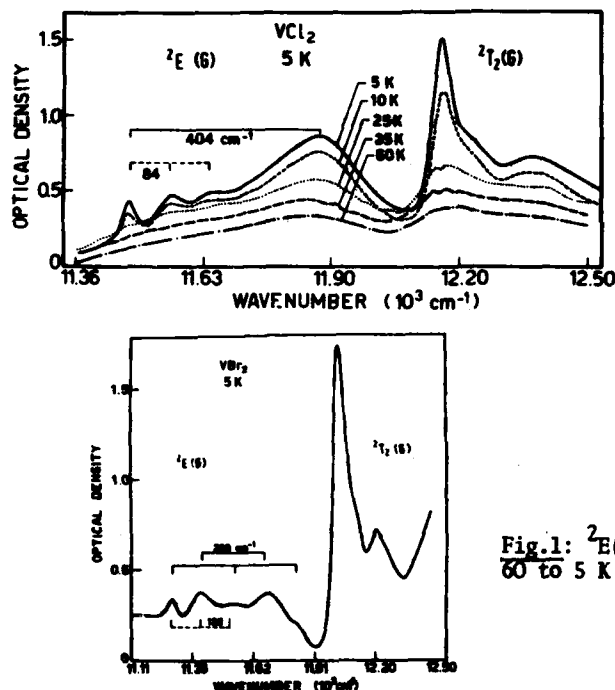


Fig.1:  ${}^2E(G)$  and  ${}^2T_2(G)$  bands in  $\text{VCl}_2$  from 60 to 5 K and in  $\text{VBr}_2$  at 5 K.

Fig.1 shows the  ${}^2E(G)$  and  ${}^2T_2(G)$  absorption bands of  $\text{VCl}_2$  and  $\text{VBr}_2$ , well separated by a deep minimum. The SO coupling accounts for the splitting observed in  ${}^2T_2(G)$ , but neither SO nor trigonal field perturbations can lift the degeneracy of  ${}^2E(G)$ . While the small splitting of  $84 \text{ cm}^{-1}$  ( $\text{VCl}_2$ ) and  $122 \text{ cm}^{-1}$  ( $\text{VBr}_2$ ) could well be due to optical magnons (quickly washed out by increasing temperature), the broad sidebands observed above the  ${}^2E(G)$  peaks cannot have but a phonon origin. The spacing of  $404 \text{ cm}^{-1}$  and  $260 \text{ cm}^{-1}$  corresponds quite well to twice the respective Raman  $E_g$  frequencies at 5 K /6/. The  ${}^6A_1(S) \rightarrow {}^4E(G) + {}^4A_1(G)$  transitions in  $\text{MnCl}_2$ ,  $\text{MnBr}_2$  /1/ and  $\text{MnI}_2$ , show a puzzling phonon structure, together with the notable common feature that the spacings between the first two sharp peaks are nearly twice the Raman  $E_g$  frequencies: they have been already discussed in /1/.

In  $\text{NiCl}_2$  and  $\text{NiBr}_2$ , besides the sharp two-phonon structure occurring in  ${}^1E(D)$ /5/, we found a pure  $E_g$  progression also in the  ${}^1A_1(G)$  bands (Fig.2). Unlike  $\text{NiBr}_2$  where the  ${}^1A_1(G)$  band occurs below  ${}^1T_2(D)$ , in  $\text{NiCl}_2$  the  ${}^1A_1(G)$  band is just atop  ${}^1T_1(D)$  and  ${}^3T_1(P)$  bands. In this case its assignment is possible thanks to the dis-

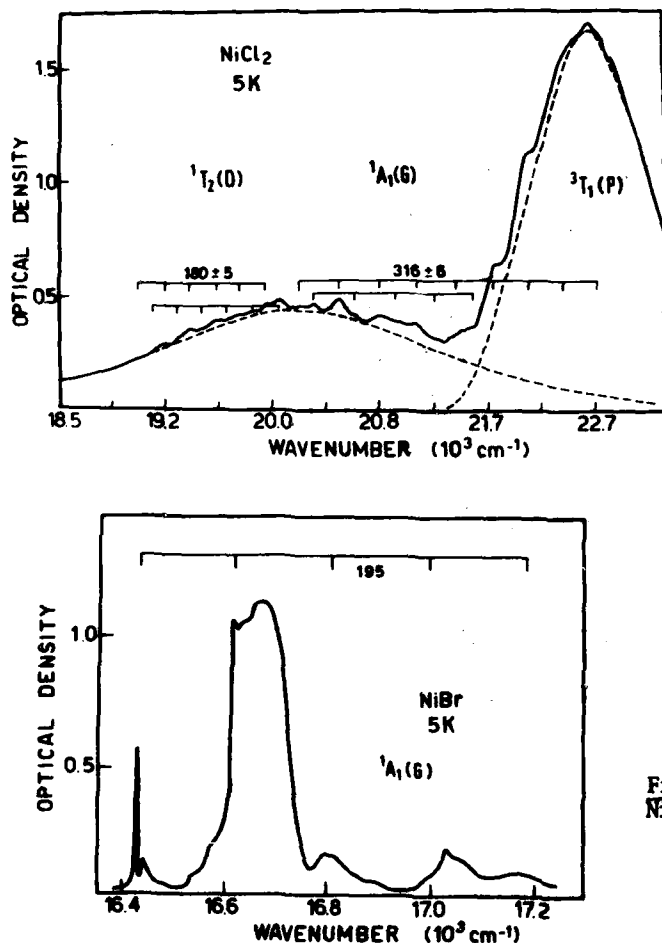


Fig.2: The  $^1\text{A}_1(\text{G})$  band in  $\text{NiCl}_2$  and  $\text{NiBr}_2$  at 5 K.

play of the two-phonon progression (spacing  $316 \pm 6 \text{ cm}^{-1}$ ): no such a structure could be brought by  $^1\text{T}_2(\text{D})$  or  $^3\text{T}_1(\text{P})$  transitions.

While in  $d^3$ ,  $d^5$  and  $d^8$  configurations a vanishing first order ep coupling descends from group theory for the listed transitions, in  $d^4$  this occurs accidentally. For this reason we have grown  $\text{CrBr}_2$  crystals by the flow system method and recorded its crystal field spectrum (Fig.3). Fitting observed transitions to octahedral crystal field diagram including spin-orbit coupling [7] gives  $Dq \approx 1200 \text{ cm}^{-1}$ . Only one vibronic structure was found in the whole spectrum. This is associated with the nearly degenerate transitions  $^3\text{A}_2(\text{F}) \rightarrow ^3\text{A}_1(\text{G})$  and has a spacing of  $306 \text{ cm}^{-1}$ . This frequency scales quite well with twice the Raman  $\text{A}_{1g}$  frequency of  $\text{VBr}_2$  ( $316 \text{ cm}^{-1}$ ) and  $\text{MnBr}_2$  ( $302 \text{ cm}^{-1}$ ) and therefore corresponds to a second-order vibronic structure.



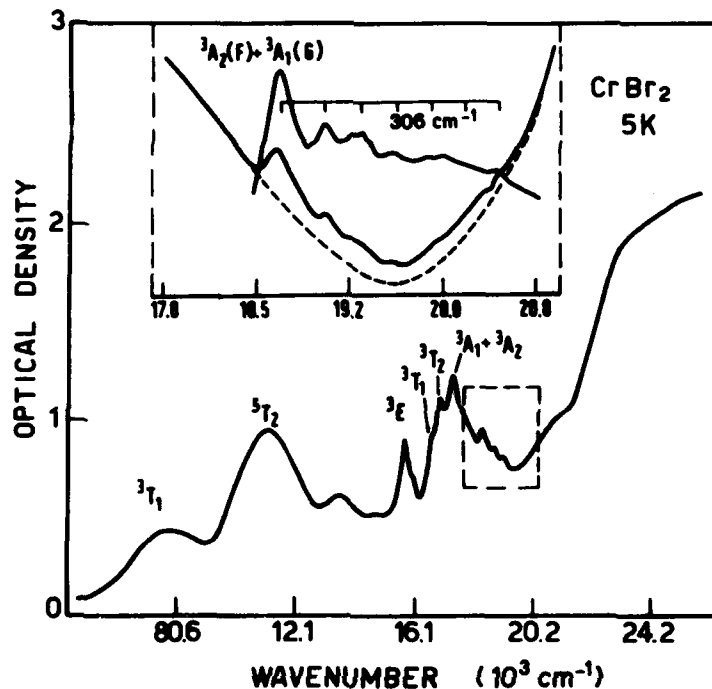


Fig.3: The crystal field spectrum of a  $\text{CrBr}_2$  crystal at 5 K. In the insert a two-phonon progression in the  ${}^3\text{A}_1(\text{G}) + {}^3\text{A}_2(\text{F})$  electronic band is shown.

#### References

- /1/ Pollini I., Spinolo G. and Benedek G., Phys. Rev. **B22**, (1980) 6369 and references quoted therein.
- /2/ Sumi H., J. Phys. Soc. Japan **36** (1974) 770; **38** (1975) 825.
- /3/ Sugano S., Tanabe Y. and Kamimura H., Multiplets of Transition Metal Ions in Crystals pag. 153, Academic Press, New York, 1970.
- /4/ Tracey J.W., Gregory N.W. and Lindgafelter E.C., Acta Cryst. **15** (1962) 672
- /5/ Benedek G., Pollini I., Piseri L. and Tubino R., Phys. Rev. **B20**, 4303 (1979).
- /6/ Bauhofer W., Güntherodt G., Anastassakis E., Frey A. and Benedek G., Phys. Rev. **B 22** (1980) 5873.
- /7/ König E. and Kremer S., J. Phys. Chem. **78**, 56 (1974).

## COUPLED ELECTRON-LO PHONON EXCITATION IN A TWO DIMENSIONAL ELECTRON SYSTEM

G. Fishman<sup>1</sup>, A. Pinczuk, J.M. Worlock, H.L. Störmer<sup>\*</sup>, A.C. Gossard<sup>\*</sup> and W. Wiegmann<sup>\*</sup>

Bell Laboratories, Holmdel, New Jersey 07733, U.S.A.

<sup>\*</sup>Bell Laboratories, Murray Hill, New Jersey 07974, U.S.A.

**Abstract** We discuss the coupling between collective intersubband excitations and LO phonons in doped GaAs - (AlGa)As multiple-quantum-well heterostructures. The analysis is applied to the interpretation of inelastic light scattering spectra and yields the Coulomb matrix elements for the intersubband transitions.

There is a sustained interest in physical systems of reduced dimensionality. Considerable effort is being devoted to two dimensional (2D) electron gases in semiconductors, where the electrons are confined in narrow ( $\sim 100\text{\AA}$ ) space charge regions at surfaces and interfaces. In polar semiconductors, the collective excitations of the confined electrons couple strongly to longitudinal optic (LO) lattice vibrations<sup>1</sup>.

The multilayer 2D electron gases in modulation-doped<sup>2</sup> GaAs - (AlGa)As multiple-quantum-well (MQW) heterostructures are an extremely interesting system, where electron-LO phonon interactions have been studied by resonant inelastic light scattering<sup>3,4</sup>. We consider here, very briefly, the coupled modes system of collective intersubband excitations, associated with transitions of confined electrons between 2D subband states, and LO phonons in the MQW heterostructures.

Electron-LO phonon coupling occurs in these systems because the polar lattice screens the depolarization electric fields, described by effective plasma frequencies<sup>5,6</sup>, of the collective intersubband excitations. In the case of isolated quantum-wells, the coupled modes are described by<sup>7</sup>

$$\det \left| \delta_{i+j, k+l} - \frac{1}{\epsilon_L(\omega)} \frac{E_P^2(i+j, k+l)}{E^2 - E_{kl}^2} \right| = 0, \quad (1)$$

which is a slight generalization of the collective mode equation derived by Dahl and Sham<sup>8</sup>. In Equation (1)  $E_{kl}$  is the energy of the vertical transition between subbands  $k$  and  $l$ .  $\delta_{i+j,k+l} = 1$  when the transitions  $i \rightarrow j$  and  $k \rightarrow l$  are identical ( $i-k, j=l$ ) and zero otherwise.  $E_p(i+j, k+l)$  is the set of effective plasma energies that describe the depolarization field effects, including coupling among the different intersubband excitations of one quantum-well.  $E_p^2(i+j, k+l)$  can be written as<sup>3,4,7,8</sup>

$$E_p^2(i+j, k+l) \sim [n_s(k) - n_s(l)] L(i+j, k+l), \quad (2)$$

where  $L(i+j, k+l)$  is the Coulomb matrix element for the transitions and  $n_s(k)$  is the charge density in level  $k$ .  $\epsilon_L(E)$  is a phonon longitudinal dielectric function of the layer, that accounts for the screening of the depolarization electric field by the lattice.

In the isolated quantum-well approximation, which is valid in the case of wide ( $\sim 50\text{\AA}$  or larger) (AlGa)As barriers, the Coulomb matrix element is given by<sup>7,8</sup>

$$L(i+j, k+l) = \int_{-\infty}^{\infty} dz \int_{-\infty}^z dz' \xi_i(z') \xi_j^*(z') \int_{-\infty}^z dz'' \xi_k(z'') \xi_l^*(z''), \quad (3)$$

where the  $\xi(z)$  are the eigenfunctions of the states of a single quantum-well. The mirror symmetry of the quantum-wells reduces the non-zero elements of  $L(i+j, k+l)$  to those in which the transitions  $i \rightarrow j$  and  $k \rightarrow l$  have the same parity. This implies that there is no coupling among intersubband excitations of opposite parity.

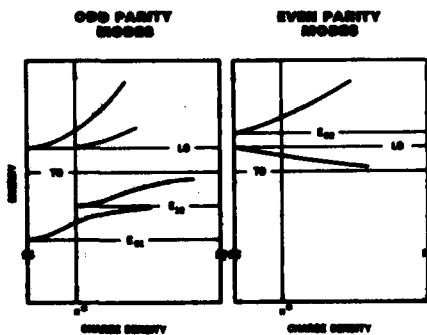


Fig. 1

Figure 1 shows schematically the energies of coupled modes as a function of areal charge density in the case in which there are three possible intersubband transitions, associated with three subbands in each quantum-well.  $n^*$  is the charge density at which the first excited subband begins to populate with electrons. For  $n < n^*$  there are only two possible transitions;  $E_{01}$  of odd parity and  $E_{01}$  of even parity. For  $n > n^*$  we

have in addition the  $E_{12}$  odd parity transition. In obtaining the curves of Figure 1 we have represented  $\epsilon_L(E)$  with the lattice dielectric function of bulk GaAs.

This approach has been applied towards the interpretation of light scattering spectra of single particle (spin-flip) and collective intersubband excitations in modulation-doped GaAs - (AlGa)As MQW heterostructures<sup>3,4,8,9</sup>. The procedure has led to a determination of Coulomb matrix elements for the intersubband transitions, that are the only adjustable parameters in the coupled modes equations (1) and (2). Coulomb matrix elements have been calculated using finite quantum-well envelope functions that include the effects of band-bending within the GaAs layers<sup>10</sup>. The results of this calculation, which has no adjustable parameters, is in excellent agreement with the Coulomb matrix elements determined from experiment.

#### References

- <sup>1</sup> On leave of absence from Groupe de Physique des Solides de l'E.N.S., Université Paris VII, 2, Place Jussieu, 75221 Paris Cedex 05, FRANCE.
1. E. Burstein, A. Pinczuk, and D. L. Mills, *Surface Sci.* **98**, 451 (1980).
2. H. L. Störmer, *J. Phys. Soc. Japan*, **49** (Suppl. A.), 1013 (1980).  
R. Dingle, H. L. Störmer, A. C. Gossard, and W. Wiegmann, *Appl. Phys. Lett.* **33**, 665 (1978).
3. A. Pinczuk, J. M. Worlock, H. L. Störmer, R. Dingle, W. Wiegmann, and A. C. Gossard, *Solid State Commun.* **36**, 43 (1980).
4. A. Pinczuk, J. M. Worlock, H. L. Störmer, R. Dingle, W. Wiegmann, and A. C. Gossard, *J. Phys. Soc. Japan* **49** (Suppl. A), 1925 (1980).
5. W. P. Chen, J. J. Chen, and E. Burstein, *Surface Sci.* **58**, 263 (1976).
6. S. J. Allen, Jr., D. C. Tsui, and B. Vinter, *Solid State Commun.* **20**, 425 (1976).
7. A. Pinczuk and J. M. Worlock, to be published in *Surface Sci.* 1981.
8. D. Dahl and L. J. Sham, *Phys. Rev.* **B16**, 651 (1977).
9. A. Pinczuk, J. M. Worlock, H. L. Störmer, A. C. Gossard, W. Wiegmann, *Bull. Am. Phys. Soc.* **26**, 422 (1981).
10. G. Fishman, to be published.

## ABSORPTION OF BALLISTIC PHONONS BY THE 2D ELECTRON GAS IN A Si MOSFET

J.C. Hensel, R.C. Dynes and D.C. Tsui

Bell Laboratories, Murray Hill, New Jersey 07974, U.S.A.

**Abstract.**— Measurements of the absorption of ballistic phonons by the two-dimensional electron gas (2DEG) in the inversion layer of a Si MOSFET are presented and compared with theory.

This paper reports measurements of the absorption of ballistic phonons by the 2DEG in the inversion layer of a (100) Si MOSFET at 2K. The rationale is to determine directly the electron-acoustic phonon interaction in 2D vis-a-vis the 3D case considered in our earlier work.<sup>1</sup>

The experimental geometry is pictured in Fig. 1. The sample consists of a Si prism upon whose (001) base is fabricated a large ( $2.5 \times 2.5 \text{ mm}^2$ ) MOSFET device (8000Å thick SiO<sub>2</sub>). A [111] beam of ballistic phonons generated from a pulsed laser heater positioned on one inclined face reflects from the interface above the gate and is detected by an Al bolometer on the opposite inclined face. A 5 Hz square wave voltage, 0 to  $V_{\text{MOD}}$ , is applied to the gate and the resulting modulation  $\Delta I$  in phonon intensity  $I$  due to absorption is detected.

Profiles of  $\Delta I/I$  for LA phonons shown in Fig. 2 were recorded as  $V_{\text{MOD}}$  was varied incrementally from 0 to  $\sim 80$  volts with excitation power density  $P/A$  a parameter. This monitors absorption as a function of  $2k_F$  in accordance with the relationship  $2k_F = 2\sqrt{\pi n} = \sqrt{V_{\text{MOD}}}$  ( $k_F$  = Fermi wavevector and  $n$  = electron areal density). The heater temperature  $T_h$  was estimated from  $P/A$  by use of the black-body formula  $P/A = \sigma T_h^4$  ( $\sigma$  is a Stephan-Boltzmann constant).

According to theory, the mechanism for absorption of a phonon with wavevector  $\vec{q}$  by a degenerate electron gas is the scattering of an electron across the Fermi surface. (See inset in Fig. 3). Such a scattering process in 2D is characterized by a transition probability shown in Fig. 3 which is peaked sharply in the vicinity of  $q \sim 2k_F$ , to an even greater degree than in 3D where it is linear in  $q$  up to  $\sim 2k_F$ . Thus, the selective absorption near  $2k_F$  acts as a "slit" in energy which

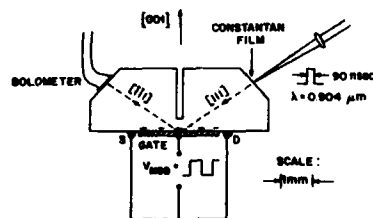


Fig. 1. Sample geometry.

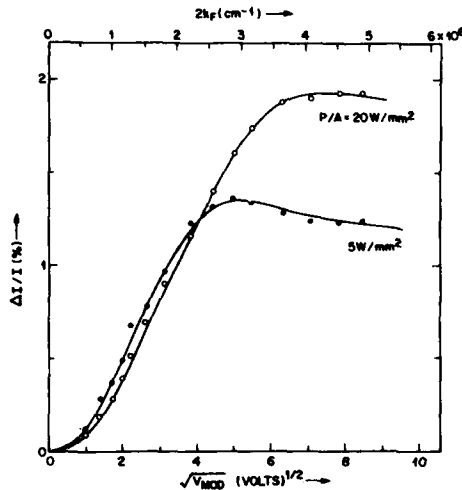


Fig. 2. Experimental absorption profiles for LA phonons:  
(o)  $T_h = 12.4\text{K}$ ; ( $\bullet$ )  $T_h = 8.77\text{K}$ .

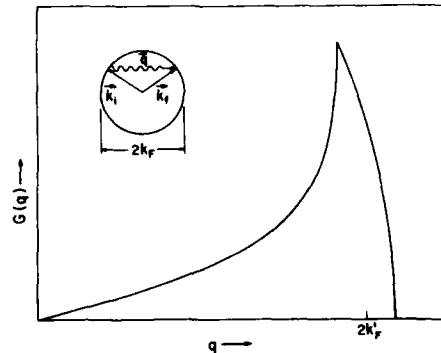


Fig. 3. Sketch of the absorption function  $G(q)$ .

can be scanned by control of  $V_{MOD}$ . Theoretical profiles representing the convolution of the sharp absorption function with a Planckian phonon distribution (including effects of isotope and umklapp scattering) are shown in Fig. 4. (The calculation assumes the electron-phonon interaction to be the same as in the bulk crystal).

Comparison of the experimental profiles with theory demonstrates generally good agreement as regard to their overall shape. The profiles are observed to have a quasi-Planckian shape and to exhibit a Wien displacement with  $T_h$ . It should be noted that the profiles trace out the phonon distribution in detail, suggesting potential application in phonon spectroscopy. We should mention that without the inclusion of isotope scattering in the calculations the peak positions would have been substantially overestimated, e.g. at  $2k_F \sim 7 \times 10^6 \text{ cm}^{-1}$  for  $T_h = 12.4\text{K}$ . (Moreover, if the acoustic mismatch model had been used to estimate  $T_h$ , the resulting  $T_h$  would have been a factor of  $\sim 2$  higher precluding any possible agreement).

Although the overall match of theory and data is definitely encouraging, there is one glaring discrepancy; and that is the absolute magnitude of the absorption is a factor  $> 10$  larger than calculated. If the structure of the theory is sound, as the close correspondence of most spectroscopic features would attest to, then the source of the discrepancy would be in the strength of the electron-phonon interaction. Two possibilities are: (1) many-body effects (not too promising inasmuch as renormalized deformation potentials are typically reduced) and (2) effects related to the interface. We have evidence that the observed phonons

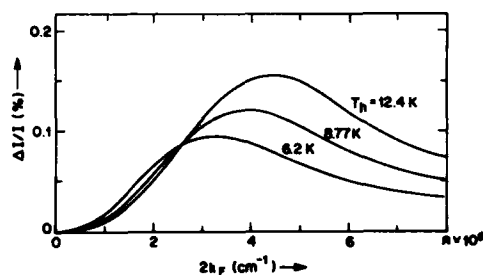


Fig. 4. Calculated absorption profiles for LA phonons.

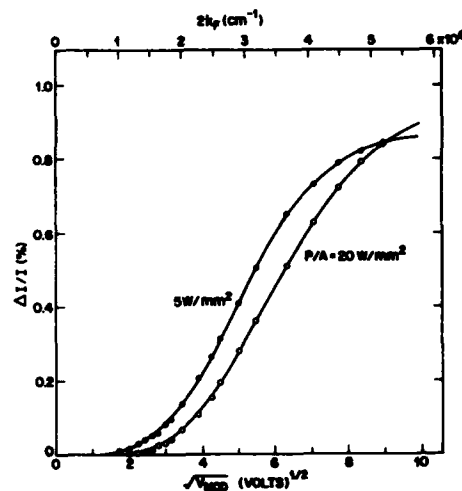


Fig. 5. Experimental absorption profiles for TA phonons:  
(o)  $T_h = 12.4\text{K}$ ; ( $\bullet$ )  $T_h = 8.77\text{K}$ .

reflect primarily from the Si-SiO<sub>2</sub> interface and hence may be significantly perturbed in the region ( $\sim$  a few phonon wavelengths thick) where the interaction occurs. One should note in this regard that there is a partial cancellation of terms comprising the effective deformation potential for LA absorption which might be rather sensitive to details of this sort.

Data for TA phonons shown in Fig. 5 are similar except that the TA profiles are shifted to substantially higher  $q$ -values by virtue of their smaller velocity. Although still sketchy, the data suggest that the magnitude of the peak absorption is nearly a factor of 2 less than LA. Theory, on the other hand, predicts a ratio  $TA/LA \sim 1.8$  dependent essentially only on the effective deformation potentials, which brings their characterization into question.

In conclusion, data are emerging from ballistic phonon experiments which demonstrate substantial phonon absorption in a ZDEC. Although the spectroscopic features are in reasonable agreement with theory, the absolute magnitude of the observed absorption of LA phonons is more than one order of magnitude greater than theoretical estimates for reasons that are still obscure.

We thank T. M. Rice and M. Lax for a number of informative discussions and G. Kaminsky for sample preparation. We are especially indebted to F. C. Unterwald for his vital role in the execution of the experiments.

#### REFERENCES

1. See, e.g., J. C. Hensel and R. C. Dynes, Phys. Rev. Letters **39**, 969 (1977).

NEUTRON SPECTROSCOPY OF PHONONS IN  $\text{RbC}_8$ W.A. Kamitakahara, N. Wada<sup>\*\*</sup> and S.A. Solin<sup>\*\*</sup>*Ames Laboratory-USDOE and Department of Physics, Iowa State University, Ames, Iowa 50011, U.S.A.**\*James Franck Institute, University of Chicago, Chicago, Illinois 60637, U.S.A.**\*\*Department of Physics, Michigan State University, East Lansing, Michigan 48824, U.S.A.*

**Abstract.**— Neutron scattering methods have been used to investigate the lattice dynamics of stage-one Rb graphite. Intercalate (Rb) modes with polarizations and wave vectors parallel to the basal plane have been observed for the first time. The experimentally-derived partial phonon density of states for intercalate modes is compared with model calculations. Phonon dispersion curves have been measured for longitudinal c-axis modes and for some transverse modes propagating in the basal plane.

1. **Experiment.**— A large ( $6 \text{ cm}^3$ ) sample was prepared by the usual two-bulb method<sup>1</sup> from Union Carbide ZYH pyrolytic graphite. The crystallites in such a sample are aligned with a common c-axis but are randomly oriented in the ab plane. A triple-axis spectrometer at the Oak Ridge Research Reactor was used to carry out the neutron scattering measurements.

2. **Intercalate Modes.**— By these we mean phonons for which the motions involved are almost completely those of the intercalate (Rb) atoms, with wave vectors and displacements parallel to the basal plane. By averaging spectra for a number of wave vector transfers  $Q$  in the basal plane, we have been able to obtain a partial phonon density of states for the intercalate modes, as shown in Fig. 1. In the low-energy region shown, for such scans with  $\vec{Q}$  parallel to the basal plane, the graphite host responds only very weakly because of the very strong forces opposing intralayer in-plane displacements of C atoms. The general room background and inelastic scattering from the graphite planes (determined by a scan on pure pyrolytic graphite) gave a smooth, gently sloping contribution to the observed spectra which was subtracted off in order to obtain the intercalate mode spectrum. The latter was then converted to a phonon density of states by dividing by well-known factors in the one-phonon neutron cross section.

The data shown in Fig. 1 were compared with several model calculations. In no case were we able to obtain good agreement with models considering only

<sup>1</sup>Present address : Materials Research Laboratory, University of Illinois, Urbana, Illinois 61801, U.S.A.



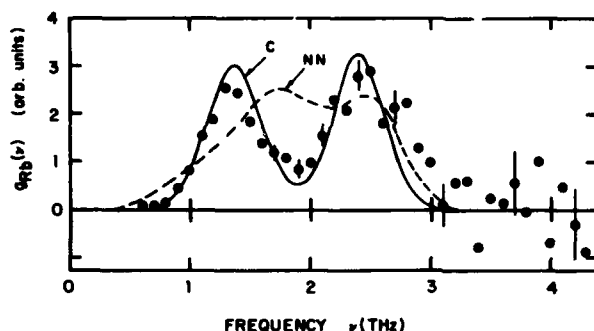


Fig. 1 : Points are the experimentally-derived partial phonon density of states for intercalate modes. Calculation NN results from a two-dimensional (2D) nearest-neighbor force model, while C represents a 3D unscreened Coulomb force model.

short-range (i.e., nearest-neighbor) forces between Rb atoms. On the other hand, it was found that a model in which the Rb-Rb forces were simply the unscreened Coulomb interactions between  $+1$  ions gave a good description of the intercalate mode phonon density of states (see curve C in Fig. 1). This model has only one adjustable parameter, representing the short-range C-Rb forces, which creates a low-frequency cutoff to the spectrum, and shifts all modes to somewhat higher frequencies. The overall shape of the spectrum and the general magnitude of the frequencies arise from the crystal structure and the Coulomb interaction, for which we need to introduce no additional parameters. The good agreement with experiment shows that conduction electron screening of the Rb motions, although it must be present, has a much less important effect on the intercalate phonon spectrum in  $\text{RbC}_8$  than on the lattice dynamics of pure Rb metal.<sup>2,3</sup> The unusual order-disorder phase transformations which occur<sup>4,5</sup> in  $\text{RbC}_8$  and similar<sup>5</sup> compounds must closely involve the intercalate-intercalate and intercalate-graphite interactions about which we have obtained detailed information through our experiment and its analysis.

**3. Phonon Dispersion Curves.**— In addition to our observations of intercalate modes, we have also made measurements on phonon dispersion in  $\text{RbC}_8$ . The longitudinal interlayer frequencies for modes propagating along the c-axis are in generally good agreement with the previous measurements of Ellenson et al.<sup>4</sup> Dispersion curves for transverse modes with polarization perpendicular to the basal plane, but with wave vector in the basal plane, were also measured, and are shown in the right hand side of Fig. 2. Because our sample is c-oriented and not a single crystal, these dispersion relations are averages over all directions in the basal plane. However, as in pure graphite,<sup>6</sup>  $\omega(\vec{q})$  is bound to be rather isotropic for  $\vec{q}$  in the basal plane. The lowest of these transverse branches lies substantially lower than in pure graphite,<sup>6</sup> despite the fact that the strong intralayer C-C forces which largely determine these modes in pure graphite are unlikely to be much different in  $\text{RbC}_8$ . Qualitatively, this points to a disproportionate participation of Rb motions (i.e., large Rb phonon

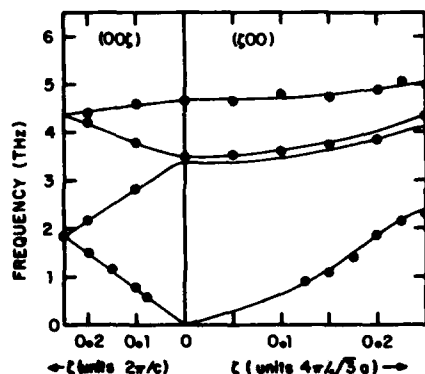


Fig. 2 : Phonon dispersion curves for  $\text{RbC}_8$ .

eigenvectors) for these modes in the intercalation compound. Recently proposed lattice dynamical models<sup>7,8</sup> should be useful in analysing our results.

The Ames Laboratory is operated for the U.S. Department of Energy by Iowa State University under contract no. W-7405-Eng-82. This research was supported by the Office of Basic Energy Sciences, WPAS-KC-02-02-01. SAS was supported by the U.S. Army Research Office under grant no. DAAG-29-80-K-0003.

#### 4. References.-

1. A. Hérol, Bull. Soc. Chim. Fr. 187, 999 (1955).
2. J. R. D. Copley and B. N. Brockhouse, Can. J. Phys. 51, 657 (1973).
3. D. L. Price, K. S. Singwi, and M. P. Tosi, Phys. Rev. B 2, 2983 (1970).
4. W. D. Ellenson, D. Semmingsen, D. Guérard, D. G. Onn, and J. E. Fischer, Mat. Sci. and Eng. 31, 137 (1977).
5. R. Clarke, N. Caswell, and S. A. Solin, Phys. Rev. Lett. 42, 61 (1979); R. Clarke, N. Caswell, S. A. Solin, and P. M. Horn, *ibid.* 43, 2018 (1979); H. Zabel, S. C. Moss, N. Caswell, and S. A. Solin, *ibid.* 43, 2022 (1979).
6. R. M. Nicklow, M. Wakabayashi, and H. G. Smith, Phys. Rev. B 5, 4951 (1972).
7. C. Horie, M. Maeda, and Y. Kuramoto, Physica 99B, 430 (1980).
8. S. Y. Leung, G. Dresselhaus, and M. S. Dresselhaus, Solid State Commun. 38, 175 (1981).

## DYNAMICS AND THERMODYNAMICS OF A ONE DIMENSIONAL NON-LINEAR LATTICE IN THE CONTINUUM LIMIT

S.N. Behera and A. Khare\*

*Institute of Physics, Bhubaneswar-751007, India**\*Department of Physics, Manchester University, Manchester, U.K.*

**Abstract.**— The dynamics of a non-linear one dimensional lattice, with the on-site potential  $V(\Phi) = (\xi^2/8) \cosh 4\Phi - \xi \cosh 2\Phi - (\xi^2/8)$  is considered in the continuum limit. Exact classical kink solutions are obtained, for  $\xi < 2$ , in which case the potential has the double well form. The free energy of the system is calculated using the ground state eigen value of the Schrodinger like equation for this potential.

1. **Introduction.**— In recent years exact classical solutions of one dimensional non-linear equations have found applications in various branches of condensed matter physics<sup>1</sup>. The non-linear problems which are of particular interest to lattice dynamics are the Toda lattice<sup>2</sup> and the lattices having on-site potentials with more than one degenerate minima, such as the  $\Phi^4$  and  $\Phi^6$  field theories<sup>3,4</sup>, the latter cases being the continuum representations of the corresponding lattice problems. In all these cases there exist exact large amplitude classical solutions called 'Solitons' (kinks) besides the well known small amplitude harmonic vibrations (phonons). It has been shown by Krumhansl and Schrieffer<sup>3</sup> for the case of the  $\Phi^4$  field theory that at low temperatures both the phonons as well as the kinks are well defined excitations of the system and hence contribute to the free energy. They further identified a part of the exact (calculated within the WKB approximation) free energy with that of an ideal gas of the kinks. Since then this identification has undergone much refinement and rigour<sup>5</sup>. In the  $\Phi^4$  field theory the on-site potential being of a double well nature serves as a model for second order phase transitions. In an earlier publication we<sup>4</sup> considered the  $\Phi^6$ -field theory (where the on-site potential has three minima) as a model for the first order phase transition. In contrast to the  $\Phi^4$ -theory, this has the advantage that the free energy of the system can be calculated exactly. However, we failed to identify this exact result with that of the ideal kink-gas phenomenology.

In the present paper we report the dynamics of yet another one-

dimensional linear lattice, which can serve as a model for second order phase transition and for which it is possible to calculate the exact free energy.

2. Dynamics of the Model. - In this model the on-site potential is of the form

$$V(\phi) = (\xi^2/8) \cosh 4\phi - \xi \cosh 2\phi - (\xi^2/8) \quad (1)$$

It can be easily checked that  $V(\phi)$  has minima at

$$\phi = 0 \quad \text{for } \xi > 2 \quad (2a)$$

$$\text{and} \quad \cosh 2\phi = 2/\xi \quad \text{for } \xi < 2 \quad (2b)$$

For the latter condition there are two degenerate minima. The values of the potential at the minima are

$$V_{\min}(\phi=0) = -\xi \quad (3a)$$

and

$$V_{\min}(\cosh 2\phi = 2/\xi) = -(1 + \xi^2/4) \quad (3b)$$

In the continuum limit the equation of motion of the corresponding classical field theory is given by

$$\frac{d^2\phi}{ds^2} - \frac{1}{2} \xi^2 \sinh 4\phi + 2\xi \sinh 2\phi = 0 \quad (4)$$

where

$$s = (x - vt)/[m(c_0^2 - v^2)]^{1/2} \quad (5)$$

$v$  and  $c_0$  being the velocity and the maximum sound velocity. It can be easily checked that eqn.(4) has exact solutions,

$$\phi(s) = \mp \tanh^{-1} \left[ (1 - \xi/2)(1 - \xi^2/4)^{-1/2} \tanh \sqrt{2}(1 - \xi^2/4)^{1/2} s \right] \quad (6)$$

In the limit of  $s \rightarrow \pm \infty$ , eqn.(6) gives

$$\tanh \phi(\pm \infty) = \mp [(2 - \xi)/(2 + \xi)]^{1/2} \quad (7)$$

which are the values of  $\phi$  corresponding to the degenerate minima. Hence, the solutions given by eqn.(6) are the kink solutions having energy

$$E_K = m_K c_0^2 \quad (8)$$

where

$$m_K = (4m/ac_0) \left[ \frac{1}{2} (1 - \xi^2/4)^{1/2} - \cosh^{-1}(2/\xi) \right] / (1 - v^2/c_0^2)^{1/2} \quad (9)$$

Besides the large amplitude kink solutions given by eqn.(6) there will also exist small amplitude harmonic solutions (phonons) around the potential minima.

3. Statistical Mechanics of the Model. - The free energy of the system can be calculated<sup>3,4</sup> from a knowledge of the ground state of the Schrodinger like equation

$$\left[ -\frac{1}{2m^*} \frac{d^2}{d\phi^2} + V(\phi) \right] \Psi_n(\phi) = E_n \Psi_n(\phi) \quad (10)$$

where the temperature dependent effective mass is given by

$$m^* = m \beta^2 c_0^2 / a^2, \quad (\beta^{-1} = k_B T) \quad (11)$$

For the potential given by eqn.(1), equation(10) can be factorized as

$$\left[ -\frac{d}{d\phi} + (\xi/2) \sinh 2\phi \right] \left[ \frac{d}{d\phi} + (\xi/2) \sinh 2\phi \right] \Psi(\phi) = 0 \quad (12)$$

to yield the exact ground state<sup>6</sup> eigen value

$$E_0 = 0 \quad (13)$$

and the eigen function

$$\Psi_0(\phi) = \exp \left[ -(\xi/4) \cosh 2\phi \right] \quad (14)$$

Hence the free energy per unit length of the system becomes

$$F/L = E_0/a - (2a\beta)^{-1} \ln(2\pi m/\beta) - (2\beta)^{-1} \ln(2\pi a^2/\beta m c_0^2) \quad (15)$$

where

$$E_0 \equiv E_0 - V_{\min} = \begin{cases} \xi & \text{for } \xi > 2 \\ (1 + \xi^2/4) & \text{for } \xi < 2 \end{cases} \quad (16)$$

Thus the free energy can be evaluated exactly. However as in the case of the  $\phi^6$ -problem, for this potential also it is not possible to identify the exact free energy with a phonon part and that of an ideal kink gas.

#### References.-

1. Bishop, A.R. and Schneider, T., Eds. "Solitons in Condensed-Matter Physics" Springer-Verlag (Berlin 1978).
2. Toda, M. Prog. Theoret. Phys. Suppl. 45, 174 (1970).
3. Krumhansl, J.A. and Schrieffer, J.R. Phys. Rev. B 11, 3535 (1975).
4. Behera, S.N. and Khara, A. Pramana 15, 245 (1980).
5. Curie, J.P. et.al. Phys. Rev. B 22, 477 (1980).
6. Razavy, M. Am. J. Phys. 48, 285 (1980).

## LIMITATIONS ON THE USEFULNESS OF METALLIC THIN FILM SEMICONDUCTORS FOR PHONON DETECTION

S.J. Rogers, C.J. Shaw and H.D. Wiederick\*

*Physics Laboratory, University of Kent at Canterbury, Canterbury, Kent, England*\* *R.M.C., Kingston, Canada*

**Abstract.**— Ultra-thin metallic films behave essentially as semiconductors. We have explored the use of Ni-Cr devices in this regime for phonon pulse detection. The evaporated films, which were typically  $\sim 20 \text{ \AA}$  thick, were deposited between layers of  $\text{SiO}_x$  on a sapphire substrate. Suitable films had room temperature resistances per square in the range  $10 - 13 \text{ K}\Omega$  and these values increased to  $10^5 - 10^6 \Omega$  at  $1^\circ \text{K}$ . By using very short ( $25 \mu$ ) conduction paths in parallel, device resistances were reduced to  $\sim 100 \Omega$  at  $1^\circ \text{K}$ . We have tested devices down to  $0.1^\circ \text{K}$  and two serious problems limit their usefulness: the low temperature resistances are quite non-ohmic for small currents; the thermal time constants are surprisingly long.

Metallic films a few atomic dimensions in thickness behave essentially as semiconductors<sup>(1)</sup>; their equivalent specific resistivity is high and the resistance variation with temperature,  $T$ , can be approximately represented by  $R = R_0 \exp(T_0/T)$ , where  $T_0$  is some characteristic temperature. The conduction mechanism is predominantly tunnelling between the island structures which are characteristic of such films. The aperiodic potential of these structures serves to localize the electrons, and this leads to infinite resistivity at  $0^\circ \text{K}$ <sup>(2)</sup>. Systems showing such localization effects have been of considerable recent interest. The thin film resistivity is in general not much affected by magnetic fields, and this suggests that it might serve to detect phonon pulses in experiments requiring such fields. Almost any non-superconducting metal could be used for a bolometer, but, following Griffin and Mochel<sup>(3)</sup> we have concentrated our work on 80/20 Ni-Cr alloy films which can be successfully deposited at room temperature.

The films studied, which were typically  $\sim 20 \text{ \AA}$  in average thickness, were deposited by evaporation (at a rate  $\sim 4 \text{ \AA/sec}$ ) between layers of  $\text{SiO}_x$  on a sapphire substrate, through which phonon pulses could be transmitted. The  $\text{SiO}_x$  layers were deposited at rates in the range  $20 - 100 \text{ \AA/sec}$  by the evaporation of SiO under a pressure  $< 10^{-5}$  torr. The first oxide layer on the substrate ( $\sim 1000 \text{ \AA}$ ) provided a chemically inert well characterised surface for the Ni-Cr, and the second protective oxide layer ( $\sim 3000 \text{ \AA}$ ) was deposited on top of the Ni-Cr film without breaking the vacuum. The variation with temperature of the resistance of the Ni-Cr films depends critically upon their thickness, and semiconductor behaviour is observed over a thickness range of only a few  $\text{\AA}$ <sup>(4)</sup>. The room temperature resistivity of our films provided a sensitive guide to their low temperature properties; films with

resistivities in the range 10 - 13 K $\Omega$  per square were most suitable for use as bolometers at 1 $^{\circ}$ K.

The resistance values for suitable films changed little in cooling to 77 $^{\circ}$ K, though in some cases there was an initial decrease of up to 10%, but the resistances typically increased to  $10^5$  -  $10^6$   $\Omega$  per square at 1 $^{\circ}$ K. Such values are inconveniently large if the bolometer circuit is to have an electrical time constant short compared with the time scale of typical phonon pulses, and in practical devices an interdigital comb geometry was adopted in which conduction was across Ni-Cr strips  $\sim 25$   $\mu$

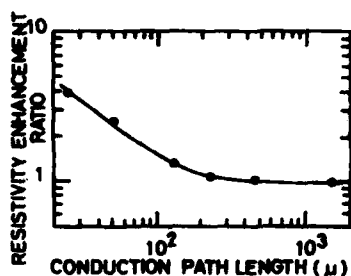


Fig. 1 Effect of film geometry on resistivity

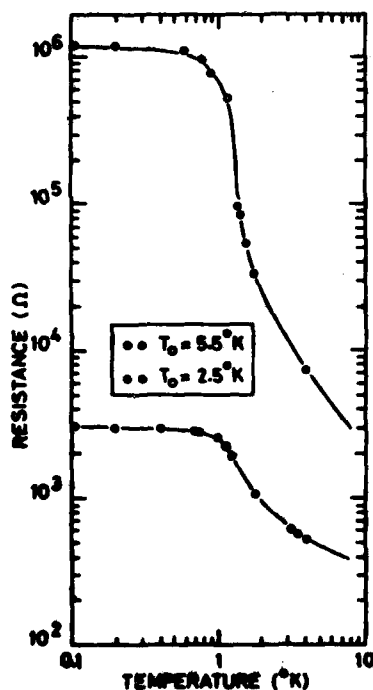


Fig. 2 Resistance of two devices (conduction path = 29  $\mu$ )

wide. The device resistance values were  $10^2$  -  $10^3$  times less than for a square film. Somewhat surprisingly, the change in geometry markedly affected the resistance characteristics of the films. In narrow geometries the equivalent specific resistivity per square was increased as compared with that for a square monitor film. Fig. 1 shows this effect for a series of simultaneously deposited films of differing conduction path length; the enhancement factor here is the ratio of the measured resistance to that calculated from geometry and the resistance of a square film. Reducing the conduction path length also changed the film thickness needed for the desired resistance variation at 1 $^{\circ}$ K; it was therefore necessary to use thinner films for the interdigital devices.

Fig. 2 shows the resistance variation in the temperature range 0.1 - 10 $^{\circ}$ K for two such devices in which the conduction path length was 29  $\mu$ . The difference in the two characteristics is a measure of the difficulty experienced in making devices to a given specification. In each case, above 1 $^{\circ}$ K the resistance variation is essentially exponential, but there is an unexpected plateau at lower temperatures. Although the measured resistances in this plateau region varied little with power dissipation, which was  $\sim 10^{-11}$  W for these measurements, it is possible that the apparent almost constant resistance arises because of non-ohmic effects. We note, however, that in this temperature range the resistance of some thin films has been observed to show a logarithmic temperature and power dependence<sup>(5)</sup>. The resistivity plateau severely limits the devices' useful

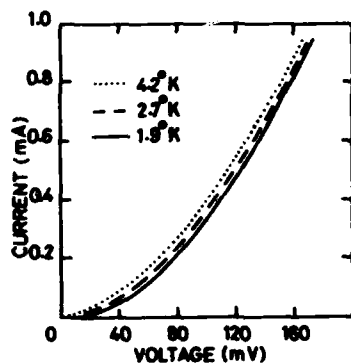


Fig. 3 I-V characteristics for an interdigital device

temperature range for phonon detection. Even at higher temperatures it is difficult to make practical use of the potential sensitivity because the film resistances are highly non-ohmic for quite small power inputs. For phonon pulse detection, the device must be fed with a biasing current, but typically a current of only 50  $\mu$ A markedly reduced the sensitivity. This will be seen in Fig. 3 which shows the I-V characteristics of an interdigital device at three temperatures; the differential resistance varies little with temperature except for small biasing currents.

In developing these devices it was thought that non-ohmic effects would arise when the voltage between metallic islands was  $\sim kT_0/e$ , and that with  $T_0$  values of a few degrees, if the film granularity was of the same scale as the film thickness (20 - 40  $\text{\AA}$ ), it would be possible to use biasing voltages  $\sim 100$  mV. This accords with the observations of Griffin and Mochel that some of their thermometers were essentially ohmic up to power levels  $\sim 10^{-4}$  W. The allowable dissipation levels for the bias power in our devices were  $10^4$  times lower than this.

The usefulness of these devices is further limited by their surprisingly long thermal time constants ( $\sim 20$   $\mu$ s). The thermal origin of these time constants was confirmed in an experiment with a superconducting Al bolometer in series with a Ni-Cr device on the same sapphire substrate. The superconducting film responded rapidly ( $< 0.1$   $\mu$ s) to the phonon flux and gave an undifferentiated signal, but the Ni-Cr film gave an integrated signal, of the opposite polarity, from which the original phonon pulse profile could be obtained by electrical differentiation.

Although their sensitivity is poor, we have made some use of the Ni-Cr devices in experiments on superconducting Al single crystals. It is not clear that they offer any real advantage over carbon films which also function as integrating devices and are similarly insensitive to magnetic fields.

#### References

- (1) Neugebauer, C.A. and Webb, M.B., J. Appl. Phys. 33, 74 (1962)
- (2) Adkins, C.J., Phil. Mag. 36, 1285 (1977)
- (3) Griffin, E.E. and Mochel, J.M., Rev. Sci. Instrum. 45, 1265 (1974)
- (4) Dynes, R.C., Garno, J.P. and Rowell, J.M., Phys. Rev. Lett. 40, 479 (1978)
- (5) Dolan, G.J. and Osheroff, D.D., Phys. Rev. Lett. 43, 721 (1979).



RAMAN SCATTERING IN  $\text{MoS}_2$ ,  $\text{MoSe}_2$  AND  $\alpha\text{-MoTe}_2$  AT HIGH PRESSURES

S. Sugai\*, T. Ueda and K. Murase

*Department of Physics, Osaka University, Toyonaka, 560 Japan.*

**Abstract.** - Lattice vibrations under hydrostatic high pressure, up to 180 kbar, were investigated in the layered materials,  $2\text{H-MoS}_2$ ,  $2\text{H-MoSe}_2$  and  $\alpha 2\text{H-MoTe}_2$ , by Raman scattering. Including the rigid layer mode, one  $A_{1g}$  and two  $E_{2g}^-$  modes were observed in each material. The energy of the rigid layer mode rapidly increased with pressure, but the increase became slow above 50 kbar. The pressure dependences of the interlayer shear force constant and intralayer shear force constant were obtained using a linear chain model.

The Group VI transition metal, molybdenum dichalcogenide  $\text{MoX}_2$  has the typical  $2\text{H}$ -type layer structure. The  $2\text{H-MoX}_2$  contains two layers in a unit cell, and therefore the rigid layer mode is observable by optical spectroscopy, and the weak van der Waals interlayer binding force can be investigated. Applying hydrostatic pressure, the interlayer distance rapidly decreases and interlayer binding force increases.

The crystal structure of  $2\text{H-MoS}_2$ ,  $2\text{H-MoSe}_2$  and  $\alpha 2\text{H-MoTe}_2$  is the hexagonal  $D_{6h}^4$ . The long wavelength optical phonons are  $A_{1g} + A_{2u} + B_{1u} + 2B_{2g} + E_{1g} + E_{1u} + 2E_{2g} + E_{2u}$ . The  $A_{1g}$ ,  $E_{1g}$  and  $E_{2g}^-$  modes are Raman active. One  $B_{2g}$  and one  $E_{2g}^-$  mode ( $E_{2g}^2$ ) are the rigid layer modes. The lattice vibration has been measured by Raman scattering,<sup>1,2)</sup> infrared spectroscopy<sup>1-4)</sup> and neutron scattering<sup>5)</sup> at atmospheric pressure. The  $A_{1g}$  and  $E_{2g}^1$  - modes in  $2\text{H-MoS}_2$  have been measured under high pressure.<sup>6)</sup>

The hydrostatic high pressure was generated by a diamond anvil cell. The pressure was measured by a wavelength shift of a ruby  $R_1$  fluorescence line ( $dP/d\lambda = 2.74 \text{ kbar} / \text{\AA}$ ). The Raman scattering experiment was executed in a back scattering configuration using a  $5145 \text{ \AA}$  argon ion laser average power 100 mW, and a double holographic grating monochromator, Spex 1400. The  $A_{1g}$  and  $E_{2g}^-$  - modes are observable in this configuration.

Figures 1(a) - (c) show the observed pressure dependence of the phonon energies. The energies of rigid layer modes increase rapidly with pressure, but the increase decreases above 50 kbar. The energies at atmospheric pressure are in good agreement with Wieting, et al's data,<sup>1,2)</sup> and the pressure coefficient of the  $A_{1g}$  and  $E_{2g}^1$  - modes near atmospheric pressure is in good agreement with Bagnall, et

\*Present address: Div. Engineering, Brown University, Providence, RI 02912

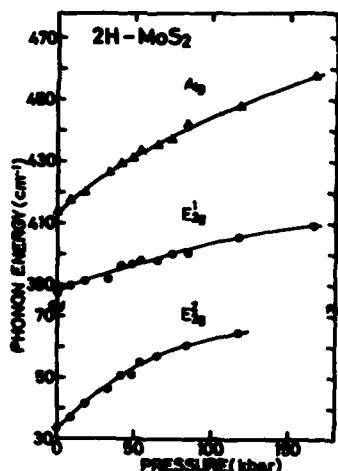


Fig. 1(a)

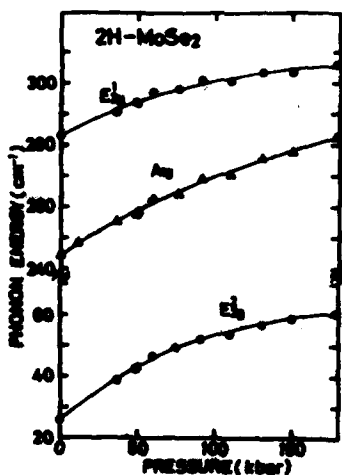


Fig. 1(b)

al's data.<sup>6)</sup> These results are summarized in Table I.

Many models have been proposed to calculate the phonon energy. In this paper, the simple linear chain model proposed by Wieting<sup>7)</sup> was adopted. The shear and compressive force constants between the chalcogen planes of the neighboring layers are expressed by  $C_b^S$  and  $C_b^C$ , respectively. The shear and compressive force constants between the molybdenum and chalcogen planes in a layer are expressed by  $C_w^S$  and  $C_w^C$ , respectively. The energy of the  $A_{1g}$  and  $E_{2g}^-$  modes are

$$\omega^2(A_{1g}) = (C_w^C + 2C_b^C)/M_x,$$

$$\omega^2(E_{2g}^1) \approx C_w^S (1 + 2C_b^S M^2 / C_w^S M_x^2) / M,$$

$$\omega^2(E_{2g}^2) \approx 4C_b^S / (M_m + 2M_x),$$

where  $M_m$  and  $M_x$  are the atomic masses of molybdenum and chalcogen, and  $M = M_m M_x / (M_m + 2M_x)$ . The shear force constant  $C_b^S$  rapidly increases with pressure as shown in Fig. 2. The ratio of the interlayer shear force constant  $C_b^S$  and the intralayer shear force constant  $C_w^S$  rapidly increases with pressure, but the value is only 8%, even at 150 kbar. Evidence of a phase transition was not observed in the pressure range of this experiment.

The authors are grateful to S. Uchida and S. Tanaka for supplying  $\text{MoS}_2$  and  $\text{MoSe}_2$  crystals.

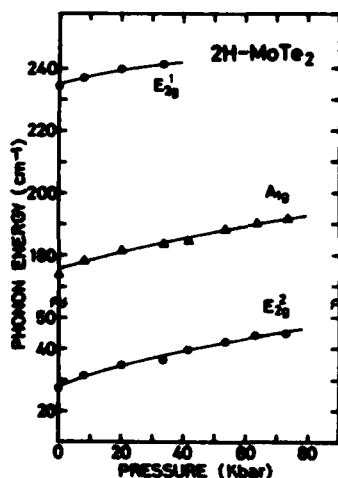


Fig. 1(c)

Fig. 1 : Pressure dependence of the phonon energies in 2H-MoS<sub>2</sub> (a), in 2H-MoSe<sub>2</sub> (b), and α2H-MoTe<sub>2</sub> (c).

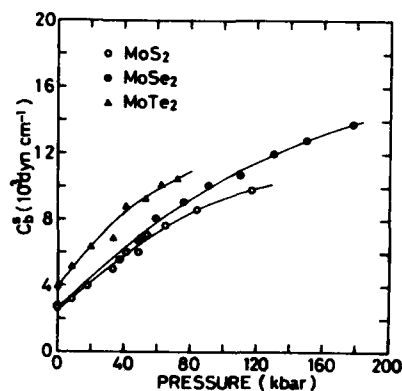


Fig. 2 : Pressure dependence of the interlayer force constant.

	$A_{1g}$ $\omega \quad \frac{\partial \omega}{\partial P} \quad \gamma$ $cm^{-1} \quad cm^{-1} \quad kbar^{-1}$			$E_{2g}^1$ $\omega \quad \frac{\partial \omega}{\partial P} \quad \gamma$			$E_{2g}^2$ $\omega \quad \frac{\partial \omega}{\partial P} \quad \gamma$		
MoS <sub>2</sub>	413.5	0.40	0.42	387	0.19	0.21	33.5	0.45	5.8
MoSe <sub>2</sub>	244	0.31		283	0.23		26	0.36	
αMoTe <sub>2</sub>	174	0.26		234	0.26		27.5	0.37	

	$C_b^s$ dyne $cm^{-1}$	$\frac{\partial C_b^s}{\partial P}$ dyne $cm^{-1} \quad kbar^{-1}$	$C_w^s$	$\frac{\partial C_w^s}{\partial P}$	$\frac{C_b}{C_w}$	$\frac{\partial (C_b/C_w)}{\partial P}$
MoS <sub>2</sub>	$2.7 \times 10^3$	70	$1.5 \times 10^5$	110	$1.6 \times 10^{-2}$	$4 \times 10^{-4}$
MoSe <sub>2</sub>	2.6	80	1.4	210	1.8	5
αMoTe <sub>2</sub>	3.9	110	1.1	230	3.5	9

Table 1 : The phonon energies, the force constants and their pressure derivatives.

#### References

- 1) T. J. Wieting and J. L. Verble, Phys. Rev. B3 (1971) 4286.
- 2) T. J. Wieting, A. Grisel and F. Levy, Physica 99B (1980) 337.
- 3) G. Lucovsky, R. M. White, J. A. Benda and J. F. Revelli, Phys. Rev. B7 (1973) 3859.
- 4) S. Uchida and S. Tanaka, J. Phys. Soc. Japan, 45 (1978) 153.
- 5) N. Wakabayashi, H. G. Smith and R. M. Nicklow, Phys. Rev. B12 (1975) 659.
- 6) A. G. Bagnall, W. Y. Liang, E. A. Marseglia and B. Welber, Physica 99B (1980) 343.
- 7) T. J. Wieting, Solid State Comm. 12 (1973) 931.

# GAS PHASE RAMAN SPECTRUM OF TCNQ AND PRESSURE DEPENDENCE OF THE MODES IN CRYSTALS OF TCNQ<sup>0</sup>

C. Carlone, N.K. Hota\*, H.J. Stolz\*\*, M. Elbert\*\*\*, H. Kuzmany\*\*\* and H.D. Hochheimer\*\*

*Département de Physique, Université de Sherbrooke, Sherbrooke, Québec, Canada, J1K 2R1.*

*\*Département de chimie, Collège militaire royal, St-Jean, Québec, Canada.*

*\*\*Max-Planck-Institut für Festkörperforschung, 7000 Stuttgart 80, F.R.G.*

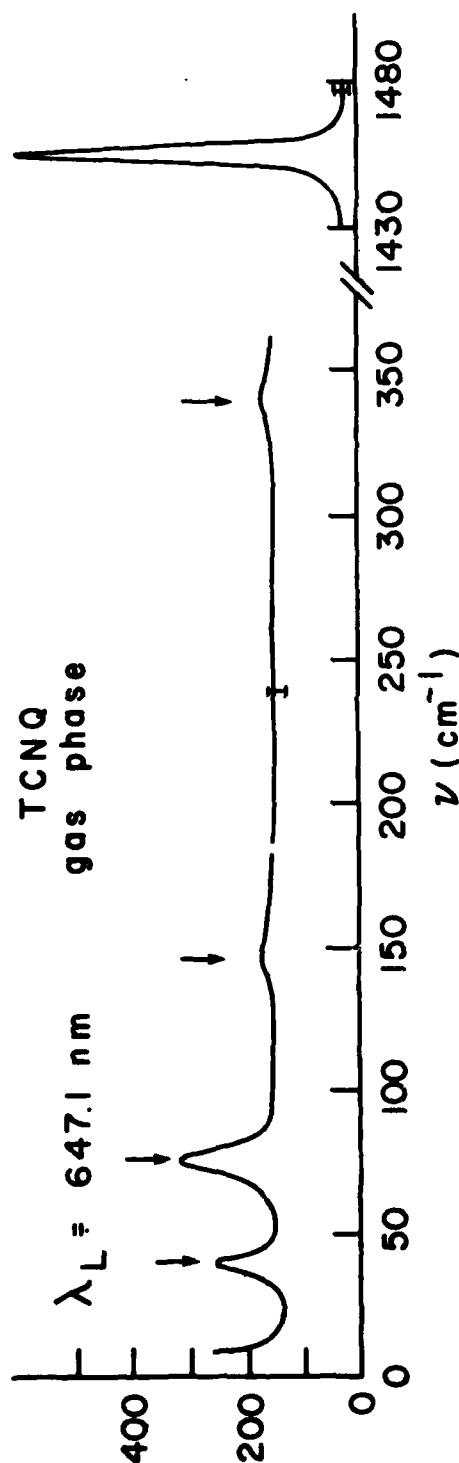
*\*\*\*Ludwig Boltzmann Institut für Festkörperforschung, and Institut für Festkörperfysik der Universität Wien, Wien, Austria.*

**Abstract.** - The Raman spectrum of gaseous TCNQ was obtained. Vibrations were detected at 40, 76, 145, 340, 1225, 1454, 1606 and 2230 ( $\pm 2$ )  $\text{cm}^{-1}$ . The pressure dependence of the Raman modes in crystals of TCNQ, TTF, K(TCNQ),  $\text{Cs}_2(\text{TCNQ})_3$ , perylene-TCNQ and phenazine-TCNQ, were obtained in a diamond cell in the pressure range 0 to 70 Kbar. The mode Grüneisen parameter were found to span several orders of magnitude. It is concluded that all of the observed low frequency modes in this class of compounds are mixed modes of internal and external characters.

The unusual physical properties of complexes involving the molecules tetrathiafulvalene (TTF) and Tetracyanoquinodimethane (TCNQ) have stimulated within the last decade considerable activity in the field of organic materials research. It has been customary to describe the lattice dynamics of these compounds in terms of internal modes and external modes, with the gap between the two regimes lying between 200 and 300  $\text{cm}^{-1}$ . We have studied the pressure dependence of the phonons in crystals of TCNQ<sup>0</sup>, TTF<sup>0</sup>, K(TCNQ),  $\text{Cs}_2(\text{TCNQ})_3$ , perylene-TCNQ and phenazine-TCNQ in order to learn about their bond anharmonicities. The pressure data was ambiguous with respect to the division of the modes and we found it necessary to perform gas phase spectra. We found by heating purified TCNQ powder in a quartz cell, gas phase vibrations at 40, 76, 145, 340, 1225, 1454, 1606 and 2230  $\text{cm}^{-1}$  (see Fig. 1). The low frequency modes indicate that the gap between internal and external modes lies below 40  $\text{cm}^{-1}$ .

The pressure dependence of the crystal phonons for TCNQ<sup>0</sup> are given in Table 1. The quantity  $\frac{1}{\nu} \frac{d\nu}{dp}$  is proportional to the mode Grüneisen parameter  $\gamma$ ; the  $\gamma$  vs frequency dependence for TCNQ<sup>0</sup> is shown in Fig. 2. The other compounds studied revealed similar plots, i.e.  $\gamma$  spans over two orders of magnitude and it decreases monotonically as a function of the frequency. Further, details are available (1).

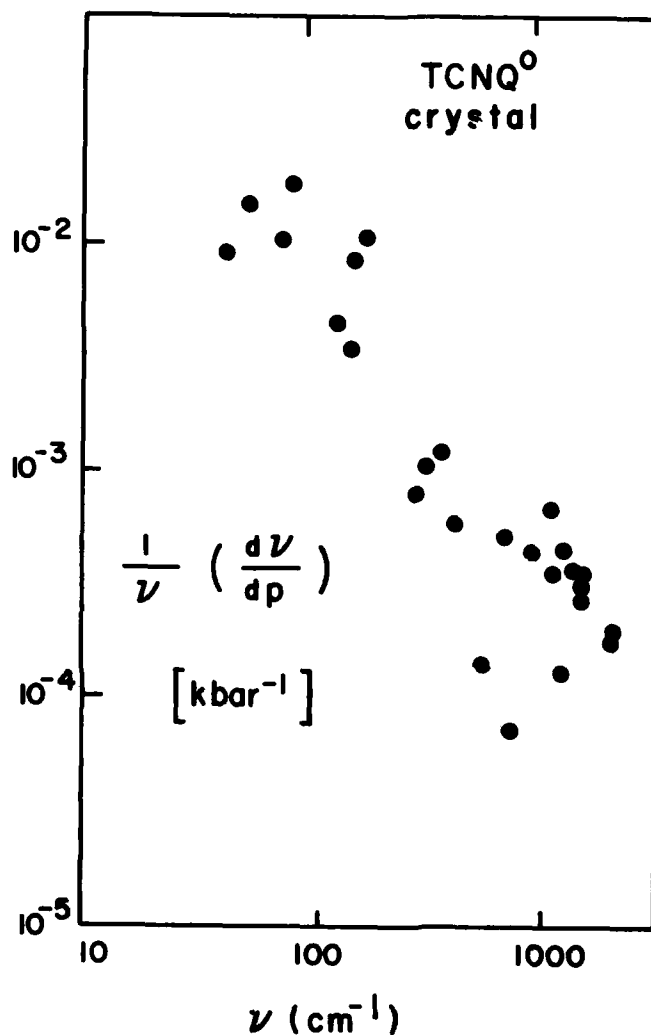
**Summary.** - From the gas phase Raman spectrum of TCNQ<sup>0</sup> and from the mode Grüneisen parameter distribution, no simple picture of mode separation between external and internal ones in TCNQ<sup>0</sup> can be derived. Stated otherwise, there is no clearcut distinction between strong intramolecular and weak intermolecular forces, but rather a continuous variation of bond strength over several orders of magnitude.



$\nu(\text{cm}^{-1})$		$\frac{d\nu}{dp}$
gas	crystal	( $\text{cm}^{-1}/\text{kbar}$ )
40	45	0.42
76	67	1.00
	85	0.83
	106	1.97
145	144	0.64
	154	0.56
	163	1.39
	180	1.78
340	300	0.25
	330	0.34
	368	0.45
	427	0.25
	590	0.08
	712	0.36
	751	0.06
	950	0.39
	1189	0.78
1225	1206	0.42
	1317	0.58
	1334	0.17
	1445	0.53
1454	1456	0.50
	1597	0.48
1606	1602	0.45
	2228	0.42
2230	2232	0.39

**Table 1.** : Gas phase vibration and crystal phonons in  $\text{TCNQ}^0$ . The pressure dependence of the phonons is given. The quantity  $\frac{1}{\nu} \frac{d\nu}{dp}$  is proportional to the mode Grüneisen parameter, and it is plotted as a function of frequency in Fig. 2.

**FIG. 1** : Raman intensity of  $\text{TCNQ}$ - gas phase.



**Fig. 2 :** Pressure dependence of the phonons in  $\text{TCNQ}^0$ . The quantity  $\gamma = \frac{1}{\nu} \frac{d\nu}{dp}$  is proportional to the mode Grüneisen parameter. For crystals having one type of bond, such as the III-V tetrahedrally bonded semiconductors,  $\gamma$  is essentially constant. For crystals having two types of bonds, such as molecular crystals and layer structures,  $\gamma$  assumes two values, one corresponding to low frequency modes and the other to the high frequency modes. For the compounds studied here,  $\text{TTF}^0$ ,  $\text{TCNQ}^0$ ,  $\text{K}(\text{TCNQ})$ ,  $\text{Cs}_2(\text{TCNQ})_3$ , perylene-TCNQ and phenazine-TCNQ,  $\gamma$  is a monotonically decreasing function of the frequency, covering several orders of magnitude.

**References. -**

1. C. Carlone, N.K. Hota, H.J. Stolz, M. Elbert, H. Kuzmany and H.D. Hochheimer. J. Chem. Phys. to appear Oct. 1981.

## THERMAL EXPANSION OF ALKALI-GRAPHITE INTERCALATION COMPOUNDS

S.E. Hardcastle and H. Zabel

*Loomis Laboratory of Physics and Materials Research Laboratory, University of Illinois at Urbana-Champaign, Urbana, ILL. 61801, U.S.A.*

**Abstract.**—The c-axis thermal expansion of several alkali-graphite intercalation compounds has been measured by means of x-ray scattering between 15 and 300 K. The thermal expansion depends strongly on the stage of the compound and is largest for C<sub>g</sub>M (M=K,Rb,Cs) compounds. The data have been analyzed in terms of an one-dimensional quasi-harmonic approximation, which yields Grüneisen parameters two or three times as large as for pristine graphite.

1. **Introduction.** — There is an intrinsic interest in the study of the thermal expansion (TE) of graphite and graphite intercalation compounds, because of their high anisotropy and unusually large anharmonic properties. The c-axis TE of pristine graphite is large ( $2.8 \times 10^{-5}/\text{K}$ ) and positive, while the a-axis TE is very small and slightly negative at room temperature.<sup>1</sup> The vibrational and thermal properties of graphite can artificially be changed by inserting monatomic layers of alkali atoms between the Van der Waals gap of graphite planes.<sup>2</sup> In these alkali-graphite intercalation compounds (AGIC's) the graphite and alkali planes form a regular stack along the hexagonal c-axis. In the following we report on a systematic study of the c-axis TE of AGIC's in dependence of the stage *n* of the compound (*n* designates the number of graphite planes between two intercalated planes) and the alkali atoms chosen by means of x-ray Bragg-scattering.

2. **Experimental.** — Highly oriented pyrolytic graphite (HOPG) was intercalated with alkali atoms by the two bulb method in the usual manner.<sup>3</sup> The homogeneity and stage of the compound was determined by (00 $\ell$ ) scans. The TE was measured between 15 and 300 K during heating and cooling cycles with MoK $\alpha$  radiation. A more detailed description of the experimental set up will be given elsewhere.

3. **Results.** — In Fig. 1a the c-axis TE of stage 1 K, Rb, and Cs GIC's is compared with pristine graphite, and in Fig. 1b the comparison is made with stage 2 K and Rb compounds. In Fig. 1c the c-axis TE's of stages 1 through 3 of K GIC's are plotted. In each case the data are normalized to the lattice constant  $c_0$ , taken at the lowest measured temperature. In all cases the TE shows a characteristic zero slope at low temperatures, due to the thermal occupation number. Stage 1 compounds exhibit the largest TE, while the TE's of higher stage compounds approach the value of pristine graphite. This behavior is not unexpected, since the frequency spectrum of the higher stage compounds is dominated by the vibration of the

interior graphite planes.

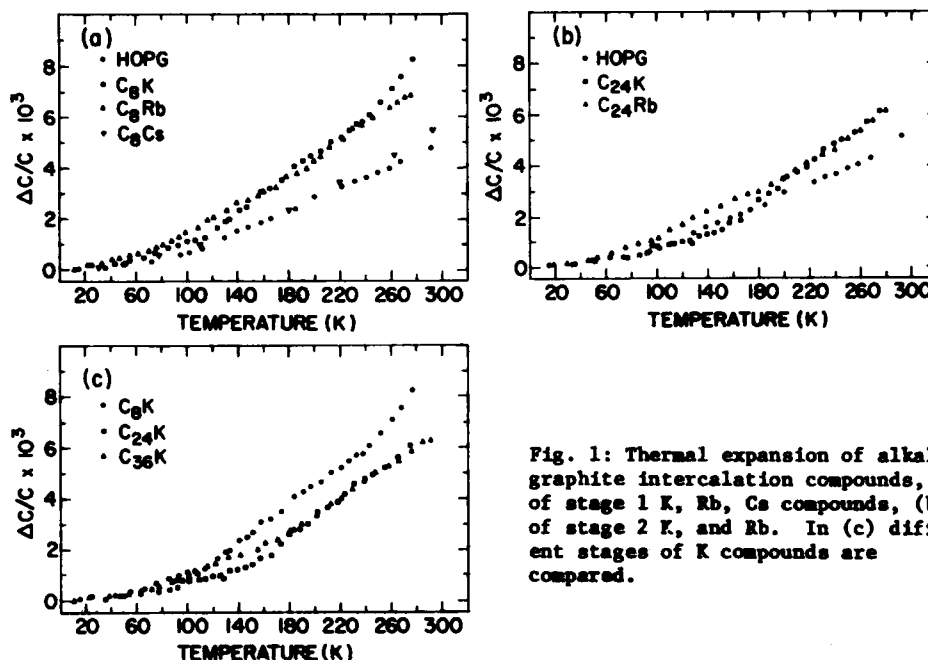


Fig. 1: Thermal expansion of alkali-graphite intercalation compounds, (a) of stage 1 K, Rb, Cs compounds, (b) of stage 2 K, and Rb. In (c) different stages of K compounds are compared.

4. Discussion. - The c-axis thermal expansion is linked to the thermal vibration of atoms with polarization in the c-direction. These are mainly the low frequency [001]L modes. The higher modes are separated from the lower by a large frequency gap and can therefore be neglected.<sup>4</sup> It has been shown recently that the [001]L modes are strongly influenced by intercalation.<sup>5</sup> The interplanar coupling constants are changed, and frequency gaps occur at the center and boundary of the Brillouin zones, creating new maxima in the density of states. There are in principal two possible reasons for an increased TE of AGIC's as compared to pristine graphite: either the phonon density of states increased and/or the anharmonicity of the vibrational potential is enhanced. To elucidate these possibilities, the TE's have been analyzed in terms of a 1-D quasi-harmonic approximation,<sup>6</sup> in which the relative change of the c-axis is given by:

$$\frac{\Delta C}{C_0} = \frac{\gamma_c}{C_{33}} V_c E_{\text{therm}} \gamma_c = - \frac{\partial \ln \omega}{\partial \ln (\Delta C/C_0)}$$

and the thermal energy is:

$$E_{\text{therm}} = \frac{C_0}{2\pi} \int \frac{d\hbar}{d\omega} \ln \coth \left( \frac{\hbar\omega}{2k_B T} \right) d\omega.$$

Here  $\gamma_c$  is the mode Grüneisen parameter, the elastic constants  $C_{33}$  for each compound have been taken from Ref. 5,  $V_c$  is the volume of a unit cell,  $\omega$  is the lattice vibrational frequency, and  $k_B$  is the Boltzmann constant. The thermal energy has been determined by numerical integration over the measured [001]L phonon dispersions.



In Fig. 2 the TE is plotted against the thermal energy for the compound  $C_8K$ . From

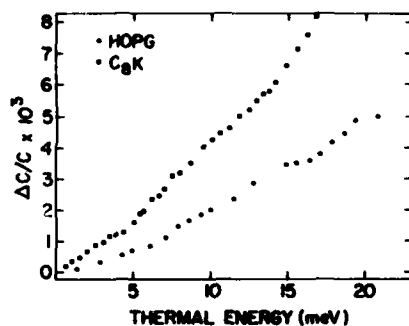


Fig. 2: c-axis thermal expansion of stage 1 K and HOPG against thermal energy, gained from [001] L phonon dispersions.

Table 1		
Compound	Temperature range (K)	$\gamma_c$
HOPG	15 - 105	.31
	120 - 300	.49
$C_8K$	15 - 105	.71
	125 - 220	1.12
	240 - 300	1.75
$C_{24}K$	15 - 150	.32
	160 - 300	.86
$C_{36}K$	15 - 70	.31
	90 - 170	.48
	190 - 300	.71

the slope, the Grüneisen parameter has been derived. In Table 1 parameters gained in this way for K compounds are listed and compared with HOPG. The Grüneisen parameter of pristine graphite is in good agreement with published data.<sup>7</sup> The anharmonicity of the lattice vibrations in c-direction seems severely influenced by the intercalation process: stage 1 compounds show a considerably higher  $\gamma_c$  at low temperatures, which even increases at higher temperatures. Also, stage 2 and 3 compounds exhibit increased Grüneisen parameters. Therefore, we believe that the dominant effect for the large TE of AGIC's is an increased anharmonicity of the lattice vibrations, rather than the higher density of states in the frequency region considered here.

We acknowledge valuable discussion with A. Magerl, R. Nicklow and R. Fiedler, donation of HOPG from A. W. Moore, and funding from U. S. DOE DE-AC02-76ER01198, Research Corporation and the University of Illinois Research Board.

#### References:

1. Thermalphysical Properties of Matter TPRC Data Series, Thermal Expansion Non-metallic solids, 13, 80 (1977).
2. For a recent review see: M. S. Dresselhaus and G. Dresselhaus, Adv. Phys. 30, 139 (1981).
3. A. Hérol, Bull. Soc. Chim. Fr. 187, 999 (1955).
4. R. Nicklow, N. Wakabayashi, and H. G. Smith, Phys. Rev. B 5, 4951 (1972).
5. H. Zabel and A. Magerl, contribution to this volume and to be published.
6. G. Leibfried and W. Ludwig, Solid State Physics 12, 275 (1961).
7. A. C. Bailey and B. Yates, J. Appl. Phys. 41, 5088 (1970).

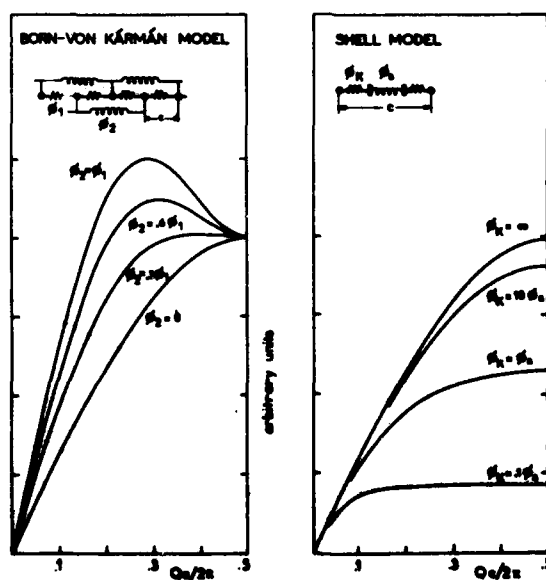
## LATTICE DYNAMICS OF GRAPHITE INTERCALATION COMPOUNDS - MODELLED BY THE PHONON DISPERSION OF LINEAR CHAINS

A. Magerl and H. Zabel\*

*Institut Laue-Langevin, 156X, 38042 Grenoble Cedex, France.**\*Loomis Laboratory of Physics and Materials Research Laboratory, University of Illinois at Urbana-Champaign, Urbana, IL 61801, U.S.A.*

**Abstract.**—The characteristic features of the phonon dispersion of a monatomic linear chain in a Born - von Kármán and a shell model formalism are outlined. Comparing model calculations with measurements of the [001]L phonon dispersion of intercalated graphite, we find that a shell model has to be used for an appropriate description.

The displacement pattern of [001]L phonon modes in graphite and graphite intercalates is determined by interplanar forces only. Because these modes show a one-dimensional character, a linear chain with two different masses representing intercalated and graphite layers provides an appropriate model. The effective repeat distance for a stage  $n$  compound extends over  $n$  graphite and 1 intercalated layer. Correspondingly, the [001] dispersion consists of 1 acoustical and  $n$  optical branches.



**Fig.1:** Comparison of the phonon dispersion of a monatomic chain calculated by a Born - von Kármán model and by a shell model.

Complete [001]L phonon dispersions are now available for stage 1 and 2 K, Rb and Cs and for stage 3 K compounds.<sup>1</sup> In a recent publication the three lower branches of  $C_{36}K$  could be well described by a Born - von Kármán model (BvK), with only nearest neighbor interactions.<sup>2</sup> However, this model fails, when including the third optical branch (compare Fig. 2a).

To improve the fit, we have extended the BvK model to include longer ranged interactions: i.) an interaction between two alkali layers, ii.) an interaction between the bonding graphite planes on both sides of an alkali layer, iii.) an interaction between an alkali layer and the second nearest neighbor graphite planes. However, with the exception of stage 1 Rb, the measurements could not be described reasonably well by any one of these four BvK models.

Shell models (SM), which treat an interaction between two mass points via an electronic shell with mass zero (adiabatic approximation), reveal a distinctively different behavior.<sup>3</sup> The phonon dispersion of a monatomic chain, calculated by

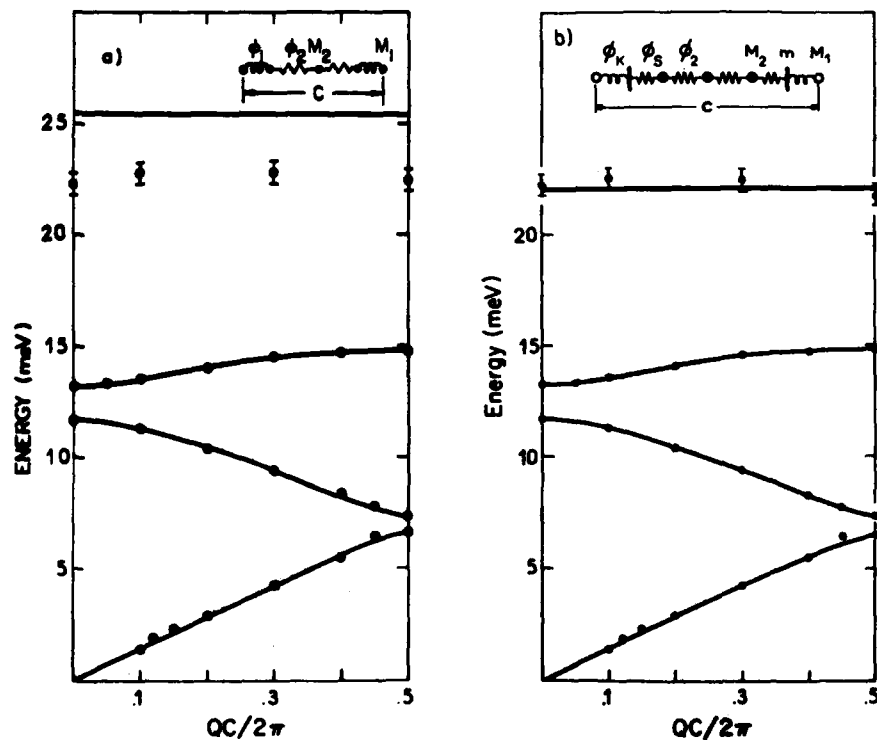


Fig.2: [001]L phonon dispersion of stage 3  $C_{36}K$ . The solid lines represent fits by (a) a Born - von Kármán model and (b) by a shell model. Fit parameters are indicated in the insertion.

a two-parameter BvK model and a two-parameter SM are compared in Fig. 1. Decreasing the second neighbor force constant  $\phi_2$  to zero for the BvK model or increasing the core shell interaction  $\phi_K$  to infinity for the SM only leaves one force constant for both models. The phonon dispersions are then identical, revealing sinusoidal functions for  $w(q)$ . Increasing  $\phi_2$  in the BvK model influences the dispersion over a large regime of the Brillouin zone (BZ). Particularly, the initial slope of the dispersion is changed, whereas the value at the edge of the BZ remains constant. However, a finite value of  $\phi_K$  in the SM mainly reduces the phonon modes at the edge of the BZ, while leaving the initial slope unchanged.

As an example, in Fig. 2 a fit of the [001]L dispersion with the BvK model and SM for stage 3  $C_{36}K$  is shown. The SM provides also a very good description for stage 1 and 2 compounds which is presented in ref. 4. We therefore believe that the interaction of alkali and graphite planes via an "electronic layer" is an essential feature of the [001]L phonon dispersion of alkali intercalates.

One of us (H.Z.) acknowledges support by the U. S. Department of Energy under Contract DE-AC02-76ER01198.

#### References

1. A. Magerl and H. Zabel, in Proceedings of the "International Conference on Physics of Intercalation Compounds," July 1981, Trieste, Italy.
2. A. Magerl and H. Zabel, Phys. Rev. Lett. 46, 444 (1981).
3. B. G. Dick Jr. and A. W. Overhauser, Phys. Rev. 112, 90 (1958).
4. H. Zabel and A. Magerl, see contribution to this volume.

## TWO-EXCITON PROCESS RESONANT RAMAN SCATTERING IN InSe

N. Kuroda and Y. Nishina

*The Research Institute for Iron, Steel and Other Metals, Tohoku University, Sendai 980, Japan.*

**Abstract.** - Resonant Raman spectra of nonpolar optical phonons in the layer compound InSe have been measured in the A-exciton region at 1.8 K and 77 K. Out-of-plane phonons exhibit their resonance dispersions typical of the one-exciton process. The in-plane phonon exhibits a dispersion which can be explained exclusively in terms of the two-exciton process where the A- and the C-exciton serve simultaneously as the resonance intermediate states. The results show that the out-of-plane phonons induce only intraband electronic scatterings, whereas in-plane ones do interband scatterings alone.

1. **Experiment.** - Measurement has been performed in the back scattering geometry by means of a conventional photon counting method. Eight oscillation lines of an Ar-ion laser are used as the light source. The laser beam is incident normal to the cleaved surface of a 3R( $\gamma$ )-InSe crystal which is immersed in liquid helium at 1.8 K or in liquid nitrogen at 77 K.

2. **Results.** - There are four nonpolar optical phonons in 3R( $\gamma$ )-InSe,  $\Gamma_1^2$ ,  $\Gamma_1^3$ ,  $\Gamma_3^2$  and  $\Gamma_3^3$  being all active for Raman scattering<sup>1)</sup> and observed at 118, 234, 43 and 182  $\text{cm}^{-1}$  at 1.8 K, respectively. Figure 1 shows resonance dispersions of cross sections of these phonons at 1.8 K. Experimental data at 77 K are also plotted in the same figure, where they are shifted by 13 meV towards higher photon energies on account of the thermal shift of the energy gap. This procedure is justified by the fact that the damping constant of the A-exciton increases only by 30 % with increase in temperature from 1.8 K to 77 K. Two out-of-plane phonons,  $\Gamma_1^2$  and  $\Gamma_1^3$ , are strongly enhanced by the resonance of excitation or scattered photons with the 1s state of the A-exciton lying at 2.547 eV. On the other hand, the in-plane phonon,  $\Gamma_3^3$ , exhibits its resonance enhancement by an order of magnitude weaker than the two  $\Gamma_1$  phonons.

3. **Discussion.** - A group theoretical analysis shows that any  $\Gamma_1$  mode is allowed for intraband scatterings within  $Z_{5,6}(A)$ ,  $Z_4(B)$  or  $Z_4(C)$  valence bands and for the interband scattering between  $Z_4(B)$  and  $Z_4(C)$

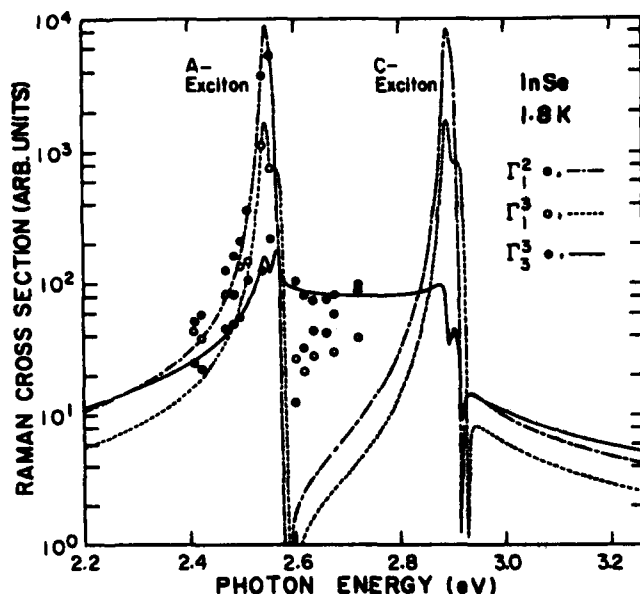


Fig. 1: Experimental and theoretical resonance dispersions of nonpolar optical phonons in layered 3R( $\gamma$ )-InSe at 1.8 K.

bands; any  $\Gamma_3$  mode can participate in any interband scattering and in intraband scatterings within  $Z_4(B)$  and  $Z_4(C)$  bands. In the quasicubic model concerning these Se p-like valence bands, no probability is found for the interband scattering by a  $\Gamma_1$  phonon nor for the intraband scattering by a  $\Gamma_3$  phonon. Hence any  $\Gamma_1$  phonon can participate only in the intraband scattering, whereas any  $\Gamma_3$  phonon can participate only in the interband scattering. This selection rule is in a remarkable contrast to the case of zincblende structure crystals in which A and B valence bands are degenerate, thereby the TO phonon participates in both intraband and interband scatterings.<sup>2)</sup> The  $Z_4(B)$  valence band in InSe is raised in energy as high as 1.209 eV above the  $Z_{5,6}(A)$  valence band by a strong uniaxial crystalline field.<sup>3)</sup> Thus the presence of the B-exciton can be neglected as far as the resonance effect in the A-exciton region is concerned. The C-exciton is separated by 0.344 eV from the A-exciton by the spin-orbit interaction of Se  $p_{x,y}$  orbitals. The following arguments show that the C-exciton as well as the A-exciton plays an essential role as the resonance intermediate state to give rise to the scattering by the  $\Gamma_3^3$  phonon.

The time dependent third order perturbation theory for the resonant Raman tensor involving exciton effect has been developed in the last several years.<sup>1,4,5)</sup> In the case where isotropic Wannier excitons with a finite damping serve as the resonance intermediate states, the Raman tensor is given by

$$\begin{aligned}
 R(\hbar\omega) = & A \sum_{\alpha, \beta} a_0^{-3} P_{\alpha} D_{\alpha\beta} P_{\beta} \left[ \sum_{n=1}^{\infty} n^{-3} (\hbar\omega + i\eta + R^* n^{-2} - E_{\alpha})^{-1} (\hbar\omega' + i\eta + R^* n^{-2} - E_{\beta})^{-1} \right. \\
 & + \frac{1}{2(E_{\beta} - E_{\alpha} + \hbar\omega_0) R^*} \left\{ \ln \left| \frac{\hbar\omega' + i\eta - E_{\beta}}{\hbar\omega + i\eta - E_{\alpha}} \right| + i \arctan \left( \frac{\hbar\omega - E_{\alpha}}{\eta} \right) - i \arctan \left( \frac{\hbar\omega' - E_{\beta}}{\eta} \right) \right. \\
 & \left. \left. + \pi i \coth \pi \left( \frac{R^*}{\hbar\omega + i\eta - E_{\alpha}} \right)^{1/2} - \pi i \coth \pi \left( \frac{R^*}{\hbar\omega' + i\eta - E_{\beta}} \right)^{1/2} \right\} \right], \quad (1)
 \end{aligned}$$

where  $\hbar\omega$  and  $\hbar\omega'$  are photon energies of incident and scattered lights, respectively,  $\hbar\omega_0$  the energy of the phonon involved in the scattering,  $R^*$  the effective Rydberg of an exciton,  $a_0$  the Bohr radius,  $\eta$  the damping constant,  $E_{\alpha(\beta)}$  the energy gap between the  $\alpha(\beta)$  valence band and the conduction band,  $P_{\alpha(\beta)}$  the optical matrix element and  $D_{\alpha\beta}$  the deformation potential. The summation over  $\alpha = \beta$  terms of eq.(1) gives the Raman tensor of the one-exciton process, and the summation over  $\alpha \neq \beta$  terms gives that of the two-exciton process. Raman cross sections,  $|R(\hbar\omega)|^2$  for the three phonons have been calculated from eq.(1) with  $R^* = 15$  meV,  $\eta = 7.6$  meV,  $E_A = 2.562$  eV and  $E_C = 2.906$  eV<sup>3)</sup> assuming  $D_{AA}(\Gamma_1^2) = D_{CC}(\Gamma_1^2)$ ,  $D_{AA}(\Gamma_1^3) = D_{CC}(\Gamma_1^3)$  and  $D_{AC}(\Gamma_3^3) = D_{CA}(\Gamma_3^3)$ . The best fit to experimental points are obtained with the ratios of  $D_{AA}(\Gamma_1^2) : D_{AA}(\Gamma_1^3) : D_{AC}(\Gamma_3^3) = 1 : 0.9 : 1.5$  as shown in figure 1. Theoretical curves for two  $\Gamma_1$  phonons calculated in terms of the one-exciton process explain the strong resonance enhancement observed. They, however, appreciably deviate from experimental values as the photon energy varies away from resonance, suggesting the presence of a background which is somewhat dependent on photon energy. The theoretical curve for the  $\Gamma_3^3$  phonon, on the other hand, is calculated in terms of the two-exciton process involving the A- and C-exciton states in accord with the selection rule mentioned above. The curve shows that the resonance enhancement is comparatively small but the cross section should be kept rather high and nearly constant for photon energies between the two exciton states. This particular feature is excellently reproduced by the experimental cross section in the whole photon energy region examined in the present work.

### References

- 1) N. Kuroda and Y. Nishina, Solid State Commun. 28, 439 (1978).
- 2) R. Trommer and M. Cardona, Phys. Rev. B 17, 1855 (1978).
- 3) N. Kuroda, I. Mumakata and Y. Nishina, Solid State Commun. 33, 687 (1980).
- 4) R. Zeyher, C.S. Ting and J.L. Birman, Phys. Rev. B 10, 1725 (1974).
- 5) F. Bechstedt, R. Enderlein, A. Kolpakov and K. Peuker, Phys. Stat. Sol. (b) 73, 141 (1976).

## EFFECT OF ELECTRON-PHONON INTERACTION ON RAMAN SPECTRA OF GRAPHITE INTERCALATION COMPOUNDS

H. Miyazaki and C. Horie

*Department of Applied Physics, Tohoku University, Sendai, Japan.*

**Abstract.**—Theoretical study is presented of effects of electron-phonon interactions on Raman spectra of acceptor graphite intercalation compounds of stages 3 and 4. It is discussed that the spectral shape of the doublet peaks observed at around  $1600\text{ cm}^{-1}$  is practically Lorentzian contrary to the case of stage 1 compounds intercalated with alkali metals. It is also shown that the coupling of Raman-active phonons with electrons localized mostly on carbon layers adjacent to intercalants yields the doublet separation of about  $10\text{ cm}^{-1}$ .

1. Introduction.— Even though there are a large amount of experimental studies of the lattice dynamics of graphite intercalation compounds (GIC), only few theoretical studies have been carried out for phonon properties mainly because of complexity of the system. In the previous paper [1], we have shown that the dynamical coupling between electron and Raman-active phonon plays an essential role in determining the anomalous line shape of Raman spectra near  $1500\text{ cm}^{-1}$  of the first stage GIC intercalated with alkali metals. The same idea is extended to higher stage GIC, in which the electronic structure is different from the first stage GIC. Our main emphasis is to show that the dynamical effect of the electron-phonon coupling still plays an important role in determining the doublet structure of Raman spectra observed near  $1600\text{ cm}^{-1}$  of GIC's with stage  $n \geq 3$ . In the present paper, we focus our attention to the case of acceptor compounds of stages 3 and 4 because of simplicity of calculations. Our results show that about one half of the magnitude of the doublet separation in the Raman spectra observed is attributed to the difference in electron-phonon couplings; one with electrons localized on carbon layers adjacent to intercalants and the other with electrons distributed on interior carbon layers. It is argued that the spectral line shape is practically Lorentzian contrary to the case of the first stage GIC intercalated with alkali metals.

2. Model.— It has been established that the lower frequency component



of the doublet of Raman spectra for acceptor GIC's is attributed to  $E_{2g_2}^o$  modes of interior graphite layers, whereas the upper component is associated with  $\hat{E}_{2g_2}$  modes of bounding graphite layers adjacent to intercalants [2]. Our main interest is to study how electron-phonon coupling contributes to the large up-shift of the  $\hat{E}_{2g_2}$  mode relative to the  $E_{2g_2}^o$  mode, which is observed to be about  $20 \text{ cm}^{-1}$  for all acceptor GIC's studied. For this purpose we start with an electronic band structure of stages 3 and 4 acceptor GIC's calculated by Blinowski and Rigaux [3]. In their model, the electronic charge distribution on carbon layers adjacent to an intercalant layer and the corresponding band structure are calculated self-consistently for a given charge transfer  $f$ , which is defined by a fraction of charge transfer per one intercalant. The band structure determined, then, is adopted to calculate self-energies of electrons by taking into account the interaction with both longitudinal and transverse acoustic phonons, because these phonons have a comparable magnitude of coupling with electrons [4]. The Raman-active phonon self-energies due to the coupling with the renormalized electrons are, then, calculated by solving the Dyson equation self-consistently. In accordance with the model described above, the phonon associated with the bounding  $\hat{E}_{2g_2}$  mode interacts primarily with electrons mostly localized on the carbon layer adjacent to intercalant layer, whereas the phonon associated with interior  $E_{2g_2}^o$  mode interacts primarily with electrons residing on interior carbon layers. Since the charge distribution along the  $c$ -axis is found to be strongly localized on the carbon layers adjacent to an intercalant layer, the renormalized phonon frequency determined is found to be different for  $\hat{E}_{2g_2}$  and  $E_{2g_2}^o$  modes, respectively. The phonon frequency difference  $\Delta\Omega$  is listed in Table I for several values of charge transfer  $f$ . The coupling constant of electron with Raman-active phonons was taken to be  $0.1 \text{ eV}$  [1]. Since the renormalized phonon frequencies fall in or are close to electronic excitation energies, the most important contribution to the Raman scattering cross-section is given by  $\sigma_1^{(c)}$  (see eq. (7) in [1]), which might give rise to a Fano-type resonance when the Fano parameter  $Q$  is close to  $\pm 1$ . In fact, the  $\sigma_1^{(c)}$  is written as

$$\sigma_1^{(c)} = C \sum_{j=B,I} \frac{n_j}{\Gamma_j} \frac{\Omega_0}{\Omega_j} \left\{ \frac{(\epsilon_j + Q_j)^2}{\epsilon_j^2 + 1} - 1 \right\}.$$

where  $n_j$  indicates a number of bounding or interior layers,  $\Omega_0$  is the  $E_{2g_2}$  mode frequency,  $\epsilon_j = (\Delta\omega - \Omega_j)/\Gamma_j$ , and the sum is taken over bounding and interior modes. Contributions other than  $\sigma_1^{(c)}$  are found to yield a broad and almost flat background. In Table I are listed

the Fano parameter  $Q$  and the  $\Gamma$  for each mode. The value of  $\Gamma$  is determined by the imaginary part of the phonon self-energy and gives a measure of the Raman line width.

**Table I :** Frequency shift  $\Delta\Omega = \Omega_B - \Omega_I$  and line shape parameter,  $Q$  and  $\Gamma$ , as a function of charge transfer  $f$ . Suffices B and I indicate bounding and interior modes, respectively.

	$f$	$\Delta\Omega(\text{cm}^{-1})$	$\Gamma_B(\text{cm}^{-1})$	$\Gamma_I(\text{cm}^{-1})$	$Q_B$	$Q_I$
$C_{36}^X$	0.35	8.71	1.42	0.37	6.90	-3.44
	0.4	10.08	1.55	0.43	7.51	-3.45
	0.45	11.42	1.66	0.49	4.99	-3.82
	0.5	12.75	1.73	0.55	4.01	-4.61
$C_{48}^X$	0.35	8.40	4.41	0.53	-4.76	-11.48
	0.4	9.68	4.87	0.49	-5.68	-10.13
	0.45	10.95	5.21	0.44	-6.09	-9.88
	0.5	12.27	5.49	0.38	-8.89	-13.89

**3. Conclusion.-** The present calculation of Raman spectra has been carried out at zero temperature. It has been found that the Fano parameters calculated are far from unity and the line shape of both  $\hat{E}_{2g_2}$  and  $E_{2g_2}^0$  peaks are practically Lorentzian. We can also conclude that the dynamical effect of electron-phonon coupling yields the doublet separation of about one half of the magnitude observed in Raman spectra of stages 3 and 4 acceptor GIC's. The remaining shift between  $\hat{E}_{2g_2}$  and  $E_{2g_2}^0$  can be attributed to the difference in ion-ion interactions [5]. It is also noticed that a slight increase of  $\Delta\Omega$  with increasing  $f$  is due to the increase in the localized charge distribution on the bounding layers adjacent to the intercalant layer. It is clear then that the doublet separation would be strongly linked with the value of charge transfer, though the value of  $f$  is not definitely known at present for all acceptor GIC's of stages 3 and 4 studied.

#### References.

- [1] Miyazaki H., Hatano T., Kusunoki G., Watanabe T., and Horie C., *Physica* 105B (1981) 381.
- [2] Underhill C., Leung S.Y., Dresselhaus G., and Dresselhaus M.S., *Solid State Commun.* 29 (1979) 769.
- [3] Blinowski J. and Rigaux C., *J. Physique* 41 (1980) 667.
- [4] Pietronero L. and Strässler S., *Proc. 15th Int. Conf. Physics of Semiconductors, Kyoto* (1980) 895.
- [5] Dresselhaus M.S. and Dresselhaus G., *Adv. Phys.* 30 (1981) 139.

BASAL THERMAL CONDUCTIVITY OF  $\text{TiSe}_2$ 

C. Ayache and M. Nuñez-Regueiro

*Service des Basses Températures - Laboratoire de Cryophysique, Centre d'Etudes Nucléaires de Grenoble, 85 X - 38041 Grenoble Cedex, France.*

**Abstract** - We present the first results on the thermal conductivity of  $\text{TiSe}_2$ . For this semimetal the heat transport is found to occur only through phonons within the investigated temperature range (1.65 - 150 K). At lower temperatures, possible origins for the nearly  $T^2$  observed law are analyzed. The other features of  $K(T)$  are also examined.

**1 - Introduction** - The semimetal  $\text{TiSe}_2$  undergoes below 200 K a phase transition essentially characterized by a superlattice formation with the doubling of the unit cell. Several mechanisms have been proposed for this transition [1-4] but no one has yet been definitely proved. As phonons are thought to play a role whose importance depends on the mechanism, they deserve special attention.

Using neutron inelastic diffraction, the phonon dispersion curves have been measured both at room [5] and low temperatures [6]. They were seen to be of a 2-dimensional nature and also to exhibit an anomalous behaviour for a transverse mode at the L-point [6-7]. Also a central peak was shown to exist [6-8]. Specific heat measurements gave only a small evidence of the transition at 200 K [9]. Zone center optical phonons were also extensively investigated. However the thermal conductivity has not been so far examined mainly due to the smallness and brittleness of the samples. Thus we have used a method specially developed for measuring such samples from helium up to room temperatures [10].

**2 - Experimental results** - Several samples were measured. These are platelets of about 50  $\mu\text{m}$  thick and  $0.2 \times 0.5$  cm for basal dimensions. They are monocrystals but certainly contain a large number of stacking faults. Their electrical resistivity at room temperature is typically  $1.1 \times 10^{-3} \Omega \text{ cm}$  and the characteristic resistivity ratios are respectively  $\rho(165 \text{ K}) / \rho(300 \text{ K}) \sim 2.5$  and  $\rho(300 \text{ K}) / \rho(4.2 \text{ K}) \sim 4$ .

On the figure is shown a logarithmic diagram of the basal thermal conductivity data obtained in the range 1.65 - 150 K. Absolute values are not defined better than 30-40 % because of a bad geometrical definition especially for the thermocouple contacts. Relative precision, however, is within a few percent.

From the lowest temperature up to about 25 K,  $K$  increases with  $T$ , following at first an approximately  $T^2$  law. The  $K/T^2$  diagram (see figure insert) shows that above 5 K a rapid deviation from this temperature dependence occurs. The maximum value at about 25 K is  $0.3 \text{ W cm}^{-1} \text{ K}^{-1}$ , much lower than the maximum values for any other semimetal of the Group V [11]. Above 30 K and up to 100-110 K a  $T^{-0.6}$  law is observed.

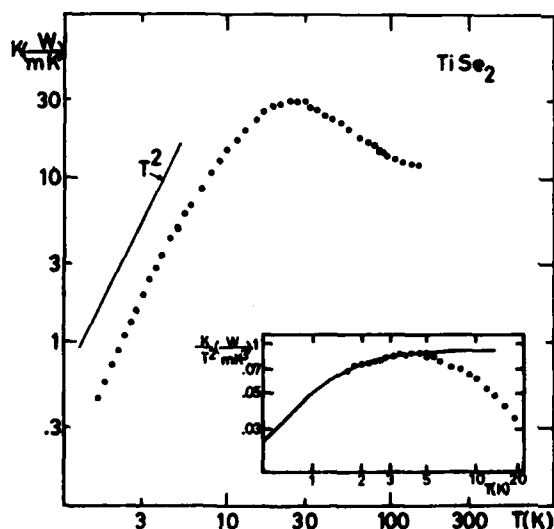


Figure - Basal thermal conductivity of  $\text{TiSe}_2$ .  $K/T^2$  below 20 K is inserted : experimental points are fitted by the theoretical curve below 5 K.

At higher temperature  $K(T)$  departs from this behaviour and appears to increase with temperature. Thermal radiation however can have some effect even with the method currently used and need more detailed examination which will be published later.

3 - Discussion - From the electrical resistivity data and the Wiedemann-Franz law it is evident that throughout the studied temperature range, heat transport is essentially due to the lattice contribution. At lower temperatures this is consistent with the absence of any  $T$ -law behaviour. A  $T^2$ -instead of a  $T^3$ -law for the lattice conductivity is not unusual in a metal or a semi-metal [11-12]. Such a behaviour is generally ascribed either to (intravalley) electron-phonon interaction or to scattering by static dislocations [12]. These explanations seem not to hold in the present case : the former because no correlative  $T^5$  behaviour is observed for the ideal electrical resistivity whereas the latter involves too large a number of dislocations ( $\approx 4 \cdot 10^{11} \text{ cm}^{-2}$ ) for layer structures, however, one also has to take into account the anisotropy of the phonon branches. Such an approach was carried out for graphite by Dreyfus and Maynard (DM) [13]. In their extension of Casimir's theory, also considering the anisotropy of crystal dimensions, they showed the basal thermal conductivity to mainly result from the so-called "in plane" modes which have their polarization parallel to the basal plane. A continuous passage from  $T^3$  to  $T^2$  is predicted which is controlled by only one parameter connected with the value of the  $C_{44}$  elastic constant. Then the phonon mean free path can be determined and is expected to be consistent with the smaller basal dimension. Qualitatively and to some extent quantitatively, analysis shows many similar features in the structural properties of graphite and  $\text{TiSe}_2$ . We thus have fitted our results to DM theory adjusting  $C_{44}$  and the phonon

basal mean free path. Results are shown in the figure insert and are seen to reproduce qualitatively the trend below 5 K. However the  $C_{44}$  value obtained ( $0.1 \cdot 10^{10}$  dynes  $\text{cm}^{-2}$ ) is much lower than the measured one from ref. [5] ( $14.3 \cdot 10^{10}$  dynes  $\text{cm}^{-2}$ ). On the other hand, if the latter value is used the  $T^2$  regime would be expected at higher temperatures (20-30 K) and in fact would hardly be visible. Also the mean free path obtained (1.6  $\mu\text{m}$ ) is much smaller than expected. These discrepancies could be explained by moving dislocations able to decrease the phonon velocity [14]. The velocity for the transverse ultrasonic wave propagating along the c-axis should be especially reduced. We have verified this prediction and measured about 350 m/s to be compared with 140 m/s deduced from our fitted  $C_{44}$ . However such a treatment is not consistent because the correlative change in the phonon mean free path must be taken into account, and so DM theory has to be extended.

The range 5-25 K seems difficult to explain in an usual way but it could perhaps be connected with observed anomalies in other transport properties. Above 25 K, the behaviour of  $K(T)$  does not present the usual features of umklapp processes resistance [12]. On the other hand, if one considers the absorption of phonons in inter-pocket transitions to be an important mechanism one can predict from the dominant phonon scheme [12] an effective temperature range starting about 30-40 K up to 100-130 K; this grossly corresponds to the extent of the  $T^{-0.6}$  law. Two other arguments also favour such an assumption: firstly, the low value of the Fermi energy in this semi-metal makes transitions possible over the whole volume of the pockets and, secondly, the thermal conductivity is mainly by transverse in-plane phonons which are seen to be most strongly affected by the transition [6]. However more data and development of calculation are needed in the range 100-300 K in order to make this point clearer.

#### References

- [1] DI SALVO F.J., MONCTON D.E. and WASZCAK J.V., Phys. Rev. **B14** 4321 (1976).
- [2] WILSON J.A. and MAHAJAN S., Comm. on Phys. **2** 23 (1977).
- [3] WHITE R.M. and LUCOVSKY G., Nuovo Cimento **38B** 280 (1977).
- [4] HUGHES H.P., J. Phys. **C10** L319 (1977).
- [5] STIRLING W.G., DORNER B., CHEEKE J.D.N. and REVELLI J., Sol. St. Comm. **18** 931 (1976).
- [6] WAKABAYASHI N., SMITH H.G., WOO K.C. and BROWN F.C., Sol. St. Comm. **28** 923 (1978).
- [7] TAKAOKA Y. and MOTIZUKI K., J. Phys. Soc. Japan **49** 1838 (1980).
- [8] MONCTON D.E., DI SALVO F.J. and AXE J.D., in Lattice Dynamics (Balkanski M. ed.) Paris Sept. 1977.
- [9] CRAVEN R.A., DI SALVO F.J. and HSU F.S.L., Sol. St. Comm. **25** 39 (1978).
- [10] LOCATELLI M. and NUNEZ-REGUEIRO M., J. Phys. **D14** 763 (1981).
- [11] ISSI J.P., Aust. J. Phys. **32** 585 (1979).
- [12] BERNAN R., Thermal Conduction in Solids, Clarendon Press, Oxford (1976).
- [13] DREYFUS B. and MAYNARD R., J. de Phys. **28** 955 (1967).
- [14] NINOMIYA T., J. Phys. Soc. Japan, **25** 830 (1968).

## ELECTROSTATIC ENERGY AND LATTICE VIBRATIONS IN THIN IONIC SLABS

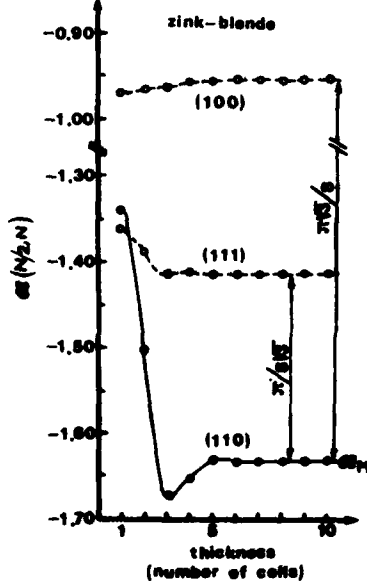
G. Kanellis\*, J.F. Morhange and M. Balkanski

*Laboratoire de Physique des Solides de l'Université Pierre et Marie Curie, associé au CNRS, 4 Place Jussieu, 75230 Paris Cedex 05, France.*

**Abstract.**— We have calculated the Electrostatic energy per cell for thin ionic slabs of any structure and any orientation, as a function of the position of the cell and the thickness of the slab. It is shown that a macroscopic depolarizing field is created inside the slabs of certain orientations. The Coulomb interaction between plane lattices is also calculated for the general case and the results are applied to GaAs.

1. The Electrostatic energy.— Considering a slab parallel to the  $(hkl)$  plane of the crystal, one can choose such a unit cell that the primitive translation vectors  $\bar{a}_1$  and  $\bar{a}_2$  lie on the plane  $(hkl)$  and  $\bar{a}_3$  out of it. The expression for the electrostatic energy per cell of the cell  $l=(l_1, l_2, l_3)$ , analogous to the Madelung constant is

$$a(l, N) = \frac{1}{2} \sum_{\kappa} \sum_{l'_3=1}^N \sum_{l'_1, l'_2, \kappa'} \frac{r_o \xi_{\kappa} \xi_{\kappa'}}{|\bar{x}(l'_1 \kappa') - \bar{x}(l \kappa)|} \quad (1)$$



where  $r_o$  is the nearest neighbor distance,  $\kappa$  and  $\kappa'$  run over all atoms in the above defined unit cell,  $l_1, l_2$  run from  $-\infty$  to  $+\infty$ ,  $\xi_{\kappa}$  is the charge fraction attributed to ion  $\kappa$  and  $N$  measures the thickness of the slab in unitcells.

By setting for each position vector

$$|\bar{x}|^2 = |\bar{x}_{||}|^2 + |\bar{x}_{\perp}|^2 \quad (2)$$

where  $||$  and  $\perp$  designate the parallel and perpendicular to the slab components of the vectors respectively, and using a variant of Ewald's method we evaluate the two-dimensional infinite sum in relation (1). For  $l=(00l_3)$  we obtain,

Fig. 1. Electrostatic energy per cell for central cells in a slab as a function of its thickness.

\*Perm. adress: First Laboratory of Physics, University of Thessaloniki - Greece.

$$\begin{aligned}
a(l_3, N) = & \frac{r_0}{2S_a} \sum_{\kappa} \sum_{l'_3 \kappa' \neq l_3 \kappa}^N \sum_{\bar{\tau} \neq 0} \frac{\xi_{\kappa} \xi_{\kappa'}}{|\bar{\tau}|} \exp\{-2\pi|\bar{\tau}||\bar{x}(l_3 \kappa; l_3 \kappa') - 2\pi i \bar{\tau} \cdot \bar{x}(l_3 \kappa; l'_3 \kappa')\} + \\
& + \frac{r_0 R}{2} \sum_{\kappa} \sum_{\kappa'} \xi_{\kappa} \xi_{\kappa'} \sum_{\substack{\bar{g} \neq 0 \\ \text{for } \kappa = \kappa'}} H(R|\bar{g} + \bar{x}(\kappa \kappa')|) - \left( \frac{r_0 R}{\sqrt{\pi}} + \frac{r_0 \sqrt{\pi}}{RS_a} \right) \sum_{\kappa} \xi_{\kappa}^2 + \\
& + \frac{r_0 \pi}{2RS_a} \sum_{\kappa \kappa'} \xi_{\kappa} \xi_{\kappa'} \sum_{\tau \neq 0} H(\pi|\bar{\tau}|/R) \exp\{-2\pi i \bar{\tau} \cdot \bar{x}(\kappa \kappa')\} - \frac{\pi r_0}{S_a} \sum_{\kappa \kappa'} \xi_{\kappa} \xi_{\kappa'} |\bar{x}(\kappa \kappa')|, \quad (3)
\end{aligned}$$

where  $\kappa''$  runs over all atoms in the unit cell lying on the same plane  $(hkl)$ ,  $\bar{g}$  and  $\bar{\tau}$  are vectors of the two-dimensional direct and reciprocal lattices respectively,  $S_a$  is the area of the two-dimensional unit cell and

$$H(x) = \frac{2}{\sqrt{\pi}} \frac{1}{x} \int_x^{\infty} \exp(-t^2) dt. \quad (4)$$

It is expected that for very thick slabs ( $N \rightarrow \infty$ ) expression (3) gives the Madelung constant of the structure. This is the case indeed only if the plane  $(hkl)$  is neutral. If not, the limit of  $a(l_3, N)$  for  $N \rightarrow \infty$  is different by the amount

$$\Delta a(\infty) = -\frac{2\pi r_0}{v_a} (\bar{P}_c \cdot \bar{v}_0)^2 \quad (5)$$

where  $\bar{P}_c$  is the dipole moment of a unit cell,  $v_a$  its volume and  $\bar{v}_0$  is the unit vector perpendicular to the plane  $(hkl)$ .  $\Delta a(\infty)$  expresses the energy of a unit cell in the macroscopic depolarizing field created by the charged planes of the slab. In fig. 1 we give some results for slabs of different orientations in the zinc-blende structure.

**II. The Coulomb Interaction.**— The field at a lattice site  $\bar{x}(l\kappa)$  due to all dipoles  $\bar{P}(l'\kappa')$  at lattice sites  $\bar{x}(l'\kappa')$  is given by,

$$E_a(l\kappa) = \sum_{l'_3 \kappa' \beta} P_{\beta}(l'_3 \kappa') \frac{\partial^2}{\partial x_a(l\kappa) \partial x_{\beta}(l'\kappa')} \sum_{l'_1 l'_2} \frac{\exp\{2\pi i \bar{q} \cdot \bar{x}(l\kappa) - 2\pi i \bar{q} \cdot \bar{x}(l'\kappa')\}}{|\bar{x}(l\kappa) - \bar{x}(l'\kappa')|}, \quad (6)$$

where  $\bar{q}$  is the wave vector.

Evaluating the above double summation by the same method mentioned above we obtain:

$$E_a(l\kappa) = \sum_{\beta} \left\{ \sum_{l'_3 \kappa' \neq l_3 \kappa} P_{\beta}(l'_3 \kappa') Q_{a\beta}(l_3 \kappa; l'_3 \kappa') \bar{q} + \sum_{\kappa''} P_{\beta}(l_3 \kappa') Q_{a\beta}(l_3 \kappa; l_3 \kappa') \bar{q} \right\} \exp\{2\pi i \bar{q} \cdot \bar{x}(l_3 \kappa)\} \quad (7)$$

where

$$Q_{\alpha\beta}(l_3\kappa''; l_3'\kappa')|\bar{q}) = \frac{4\pi^2}{S_a} \sum_{\bar{\tau}} \left\{ -\frac{(\tau_a + q_a)(\tau_\beta + q_\beta)}{|\bar{\tau} + \bar{q}|} + |\bar{\tau} + \bar{q}| \cos\alpha \cos\beta + \right. \\ \left. + i h \{ (\tau_a + q_a) \cos\beta + (\tau_\beta + q_\beta) \cos\alpha \} \exp\{-2\pi|\bar{\tau} + \bar{q}||\bar{x}(l_3\kappa; l_3'\kappa') - 2\pi i \bar{\tau} \cdot \bar{x}(l_3\kappa; l_3'\kappa')\} \right\}, \quad (8a)$$

$$Q_{\alpha\beta}(l_3\kappa; l_3'\kappa')|\bar{q}) = R^3 \sum_{\bar{g}} H_{\alpha\beta}(R|\bar{g} + \bar{x}(\kappa\kappa')|) \exp\{2\pi i \bar{q} \cdot \bar{x}(l_3\kappa)\} - \\ - \frac{4\pi^3}{RS_a} \sum_{\bar{\tau}} (\tau_a + q_a)(\tau_\beta + q_\beta) H(\pi|\bar{\tau} + \bar{q}|/R) \exp\{2\pi i \bar{\tau} \cdot \bar{x}(\kappa\kappa')\} \quad (8b)$$

$\cos\alpha$  been the direction cosines of  $\bar{v}_0$ .

As it can be seen, all terms in the above expressions are regular functions of  $\bar{q}$  for  $\bar{q} \rightarrow 0$ . Hence there is no macroscopic field lying on the plane of the slab.

By differentiating the total electrostatic energy of the slab in a field equal in magnitude and opposite in direction to the depolarizing field, the macroscopic field due to vibrations of the plane lattices along  $\bar{v}_0$  is obtained. For a slab parallel to the plane (111) of the zinc-blende structure it is,

$$E_a^{mac}(l\kappa) = \frac{4\pi}{S_a L} \cos\alpha \sum_{l_3\kappa'} \bar{P}(l_3\kappa') \cdot \bar{v}_0 \left\{ 1 - \frac{Nd}{L} (\delta l_3 N \delta \kappa_R + \delta l_3 1 \delta \kappa_1 + \delta l_3' N \delta \kappa_2 + \right. \\ \left. + \delta l_3' 1 \delta \kappa_1) + \frac{N^2 d^2}{L^2} (\delta l_3 1 \delta \kappa_1 + \delta l_3' N \delta \kappa_2) (\delta l_3' 1 \delta \kappa_1 + \delta l_3' N \delta \kappa_2) \right\}, \quad (9)$$

where  $L$  is the thickness of the slab and  $d$  the shortest distance between two successive planes.

Expression (9) gives the well known macroscopic field for infinite thickness, while for thinner slabs implies interaction between each surface plane and the rest of the slab.

We applied the above results on GaAs slabs parallel to (111) planes. The normal modes obtained belong to  $\Lambda$  branches of the infinite crystal, while the surface modes have frequencies between the  $\omega_{LO}$  and  $\omega_{LA}$  of the  $L$  point on the Brillouin zone boundary.



## PHONONS IN GRAPHITE INTERCALATED WITH BROMINE

F. Batallan, I. Rosenman, C. Simon, G. Furdin\* and H.J. Lauter\*\*

*Groupe de Physique des Solides de l'Ecole Normale Supérieure, Université Paris 7, Tour 23 - 2 Place Jussieu, 75251 Paris Cedex 05, France.*

*\*Université de Nancy I, Nancy, France.*

*\*\*Institut Laue-Langevin, Grenoble, France.*

**Abstract.** - We have investigated the phonon spectrum in stage 2 graphite intercalate with bromine by using inelastic neutron scattering. We have observed longitudinal and transverse phonons along the c direction as well as in the layer plane. Results are presented for energies up to 15 THz at 300 K. A linear chain model explains most of our results.

**1. Introduction.** - Graphite forms intercalation compounds with a large variety of atoms or molecules. Among them the acceptor compounds made by intercalating halogens or acid molecules present the most interesting properties : a metallic type of conductivity with a very large anisotropy, so that they can be considered as 2-D metals. Their electronic structure and properties are now well known<sup>(1)</sup>. But very few results on their lattice dynamics have yet been published<sup>(2)</sup> and even these concern mostly Raman active modes. A few neutron studies in donor compounds are available<sup>(3-5)</sup>. We present here the first almost complete investigation of the phonon spectrum in a graphite acceptor intercalation compound (GAC) : the stage 2 compound with bromine.

**2. Sample and experiment.** - The sample ( $0.8 \times 1.5 \times 3 \text{ cm}^3$ ) was made by direct intercalation of bromine in highly oriented pyrolytic graphite (HOPG). It should be mentioned here that it is very difficult to prepare large and homogeneous samples by intercalation. The composition as checked by elastic neutron scattering showed the presence of a non negligible amount of stage 3. However a careful analysis of the inelastic results had allowed us to separate the phonons belonging to stages 2 and 3. The experiments were made on D18 spectrometer at the high flux reactor of the Institute Laue-Langevin in Grenoble, France. We have used energies up to 15 THz and momentum resolution of  $0.01 \text{ \AA}^{-1}$ . We have made experiments at 300 K and 10 K. As our sample is obtained from HOPG, it can be considered as a 2-D powder. In the reciprocal space we have the Bragg reflexions (0,0,1) corresponding to the identity period  $I_c$  and the circles (h,k) in the basal plane of graphite or bromine. We present here only results on stage 2 obtained at 300 K.

**3. Results and Interpretation.** - We have observed phonons in four different configurations corresponding to : [001]L, [001]T, [010]L and [010]T. As the sample is a powder in the basal plane only the phonons in the configuration [001]L are

unambiguously defined. All our results in the four configurations for energies less than 15 THz are reported in Fig. 1.

We have not performed a complete calculation of the force constant model. However by using only some simple assumptions, we were able to interpret most of our experimental results. We have based our approach on the calculations for pristine graphite<sup>(6,7)</sup> which introduce force constant parameters in the Born-von Karman models. We now consider our experimental results of the phonons for each configuration :

a) - [001]L - We assume that the three experimental branches correspond to rigid modes, we then calculate the phonon branches given by a linear harmonic chain model with interactions limited to the nearest neighbors. We have used two force constants and two masses which represent an average per carbon atom, as has been previously used<sup>(5)</sup>. We find a very good agreement with the experimental results (see Fig. 2) for the following values,  $m_C = 12.01$  a.m.u.,  $m_{Br} = 11.42$  a.u.m.,  $\phi_{C-C}^x = 2849$  dyn/cm and  $\phi_{C-Br}^x = 1280$  dyn/cm. The ratio  $m_{Br}/m_C$  corresponds to the formula  $C_{14}Br$ , which results from an elastic scan studies we have made.

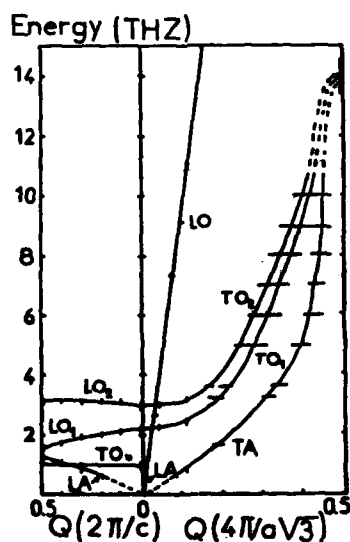


Fig. 1 : Phonons in second stage bromine intercalation compound of graphite. The vertical bars correspond to constant Q scans and the horizontal constant E scans.

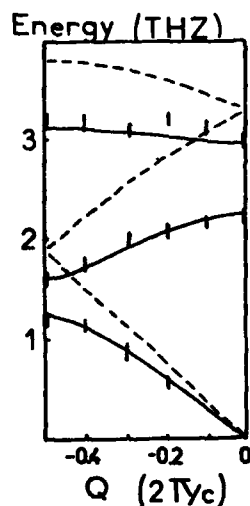


Fig. 2 : Phonons in the [001]L. The vertical bars are the experimental values. The continuous lines are the results of the computation with  $\phi_{C-Br}^x/\phi_{C-C}^x = 0.45$  and  $m_{Br}/m_C = 0.95$ . The dashed lines are the results of the calculation for pure HOPG.

b) [001]TO - Although for this branch resonances are very difficult to observe, we get an almost flat phonon branch at 1 THz. The flatness means the absence of propagation along [001] direction for the transverse optical phonons. This feature can be related to the absence of transverse coupling :  $\phi_{\text{CB}}^t = 0$ . This is confirmed by the value 1 THz which is exactly  $\sqrt{2}$  less than the value at  $\Gamma$  point in HOPG<sup>(6)</sup>. This shows also that  $\phi_{\text{CC}}^t$  in this GAC is the same as in HOPG.

c) [010]L - In the range of energy that we have investigated, the branch is linear, and gives a sound velocity of the same value as that in HOPG<sup>(6)</sup>. This means that we can take for the radial constant between carbon atoms in the graphite layer the same values as in pristine HOPG<sup>(6,7)</sup>.

d) [010]T - We have observed three branches : two TO and one TA. At the  $\Gamma$  point, these are connected to the [001]L branches. As the energy raises, the three branches merge together and give at the zone boundary the same value of HOPG. Due to the multiplicity of the interactions involved in these branches we need a more complex model in order to interpret the results.

#### References

1. C. Simon, F. Batallan, I. Rosenman and H. Fuzellier, Phys. Rev. B23, 2836 (1981)
2. S.A. Solin, Physica 99B, 443 (1980) and this conference.
3. W.D. Ellenson, D. Semmingsen, D. Guerard, D.G. Onn and J.E. Fischer, Mat. Sci. and Eng. 31, 137 (1977)
4. J. Rossat-Mignod, D. Fruchart, M.J. Moran, J.W. Milliken and J.E. Fischer, Synthetic Metals 2, 143 (1980)
5. A. Magerl and H. Zabel, Phys. Rev. Lett. 46, 444 (1981)
6. R. Nicklow, N. Wakabayashi and H.G. Smith, Phys. Rev. B5, 4951 (1972)
7. M. Maeda, Y. Kuramoto and C. Horie, J. Phys. Soc. Japan 47, 337 (1979)

## PHONON RAMAN SPECTROSCOPY IN GRAPHITE INTERCALATION COMPOUNDS

D.M. Hwang and S.A. Solin\*

*Department of Physics, University of Illinois at Chicago Circle, Chicago, Illinois 60680, U.S.A.**\*Department of Physics, Michigan State University, East Lansing, Michigan 48824, U.S.A.*

**Abstract.** - The atoms or molecules intercalated in a graphite intercalation compound are correlated spatially among themselves, resulting in a static structure factor with sharp peaks. Graphite phonons with momenta corresponding to these structure factor peaks have a higher probability of being scattered into the Brillouin zone center and becoming Raman active. With this momentum selection scheme, we can interpret the observed Raman features of graphite intercalation compounds with various in-plane structures.

1. **Introduction.** - Graphite intercalation compounds (GIC's) exhibit various ordered and disordered in-plane structures of the intercalation species. It is interesting to examine how the phonon modes of the host graphite crystal are perturbed by the intercalation structures. Stage 1 donor-type GIC's have the simplest 3-dimensional ordered structures among all intercalation compounds. Nevertheless, the interpretation of their unusual Raman features has been a vexing problem for several years.<sup>1,2</sup>

The Raman spectra for various stage 1 donor GIC's are summarized in Fig. 1. A strong frequency dependent continuum is observed in the spectra for  $\text{EuC}_6$  and  $\text{MC}_8$  ( $M = \text{K, Rb and Cs}$ ). It couples with the graphite  $E_{2g}^{(2)}$  mode, resulting in a broad Fano peak at  $1500 \pm 10 \text{ cm}^{-1}$ . For  $\text{MC}_8$ , a doublet or triplet Raman feature is also observed around  $580 \text{ cm}^{-1}$ .  $\text{LiC}_6$  only exhibits a relatively sharp peak at  $1594 \pm 5 \text{ cm}^{-1}$ . Note that at room temperature,  $\text{MC}_8$  has a  $(2 \times 2)R0^\circ$  superlattice in-plane structure, while that for  $\text{EuC}_6$  and  $\text{LiC}_6$  is  $(\sqrt{3} \times \sqrt{3})R30^\circ$ .

On the basis of phonon band structure calculations for  $\text{KC}_8$  and  $\text{RbC}_8$ ,<sup>4</sup> it is possible to associate the  $500 \text{ cm}^{-1}$  feature with the graphite  $M$  point phonons, which are rendered first-order Raman active by zone folding of the  $(2 \times 2)$  superlattice.<sup>1</sup> However, the zone folding approach can not account for the continuous background observed. Also, it has been found<sup>5</sup> that the Raman spectrum for  $\text{CsC}_8$  in its high temperature disordered phase is hardly distinguishable from that in the room temperature ordered phase. Thus, it is suggested<sup>5</sup> that both the  $580 \text{ cm}^{-1}$  feature and the continuous background are disorder-

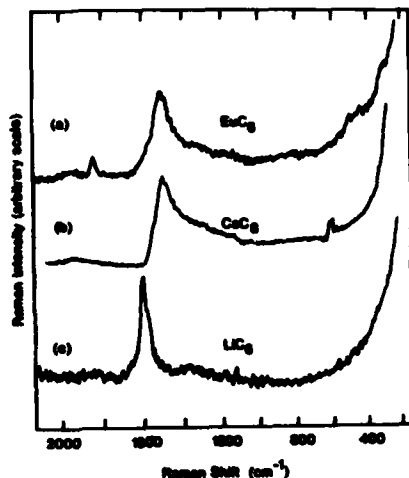


Fig. 1 : Raman spectra for (a)  $\text{EuC}_6$ , (b)  $\text{CsC}_8$  and (c)  $\text{LiC}_6$ , recorded at room temperature (from Ref. 3). The  $1840 \text{ cm}^{-1}$  peak of  $\text{EuC}_6$  is found to be sample dependent and is attributed to  $\text{EuC}_2$ , an impurity on the surface. The spectra for  $\text{KC}_8$  and  $\text{RbC}_8$  are similar to that for  $\text{CsC}_8$ .

induced scattering.

Here we present a model incorporating the static structure factor for phonon scattering and the momentum selection rules for the Raman process, and show that both the disorder-induced scattering and the zone folding effect are extreme cases of a same basic phenomenon.

2. Theory.— Due to the weak interlayer interaction, the phonon dispersion curves of graphite intralayer modes are essentially preserved in GIC's. However, the graphite phonons can be elastically scattered by the intercalation layers and exchange momentum  $\mathbf{k}$  with the intercalation lattice with relative probability  $S(\mathbf{k})$ . Here  $S(\mathbf{k})$  is the static structure factor for elastic scattering and should have the same general form for X-ray, electron, neutron, and phonon scattering.

For GIC's with perfect commensurate ordered structures,  $S(\mathbf{k})$  contains only sharp superlattice Bragg peaks. The above momentum selection scheme is identical to the zone folding mechanism. On the other hand, if the intercalation species were completely spatially uncorrelated, they would contribute a flat background to  $S(\mathbf{k})$ . The resulting disorder-induced scattering would reflect the phonon density of states of the whole Brillouin zone.

In real GIC's, the intercalation species are strongly spatially correlated. They result in a structure factor with essentially discrete peaks. Non-zone-center phonons with momenta corresponding to the peaks of  $S(\mathbf{k})$  will have a higher probability of being scattered into the zone center and becoming Raman active.

Consider  $\text{CsC}_8$  as an example. Fig. 2 shows the structure factor in its ordered and disordered phases. The structure factor for the disordered phases exhibits a strong peak at  $q = 1.50$  and  $1.43 \text{ \AA}^{-1}$  for the

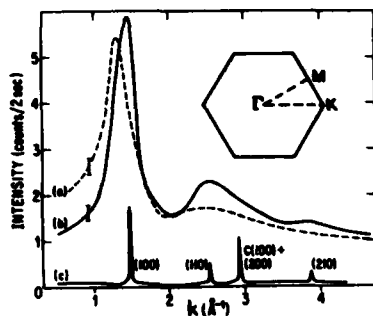


Fig. 2 : The static structure factor determined by X-ray scattering for (a) the excess sample  $\text{CsC}_8$  at 700 K, (b) the non-excess sample  $\text{Cs}_{0.8}\text{C}_8$  at 700 K and (c)  $\text{CsC}_8$  at 300 K (from Ref. 6). The momentum of the (100) peak in (c) corresponds to the  $\Gamma\text{M}$  distance in the graphite 2-dimensional Brillouin zone shown as the insert.

excess and the non-excess samples, respectively, which correspond to 90% and 100% of the  $\Gamma\text{M}$  distance in the Brillouin zone of graphite. The FWHM of these peaks are 20% of  $\Gamma\text{M}$ . Since the phonon bands near the M points are flat,<sup>4</sup> only a small shift in the Raman frequency is expected when the Cs layer undergoes the order-disorder phase transition.

Using this structure factor momentum selection scheme, we can also explain why the  $580\text{ cm}^{-1}$  peak of the density of states of the graphite phonons does not show up in the Raman spectra for other disordered GIC's, as well as why the strong Fano peak only exists in the spectra for  $\text{NC}_8$  and  $\text{EuC}_6$ . Details will be given elsewhere.<sup>7,8</sup>

**3. Conclusion.**— GIC's are a unique system of materials with a high density of "impurities" which are spatially correlated among themselves, but only weakly perturb the phonon bands of the host crystal. A momentum selection scheme based on the static structure factor must be employed to describe the disorder-induced Raman scattering.

This research is supported by the Research Board of the University of Illinois at Chicago Circle, the Atlantic Richfield Foundation Grant of Research Corporation 9422, and the NSF Grant DMR80-10486.

#### References :

1. M. S. Dresselhaus, G. Dresselhaus, P. G. Eklund and D. D. L. Chung, *Mater. Sci. Eng.* **31**, 141 (1977); M. S. Dresselhaus and G. Dresselhaus, to be published.
2. S. A. Solin, *Physica* **99B**, 443 (1980).
3. D. M. Hwang and D. Guerard, *Solid State Comm.*, to be published.
4. C. Horie, M. Maeda and Y. Kuramoto, *Physica* **99B**, 430 (1980).
5. N. Caswell and S. A. Solin, *Phys. Rev.* **B20**, 2551 (1979).
6. R. Clarke, N. Caswell and S. A. Solin, *Phys. Rev. Lett.* **42**, 61 (1979).
7. D. M. Hwang, S. A. Solin and D. Guerard, *Springer Series in Solid State Sciences*, to be published.
8. D. M. Hwang, to be published.

RAMAN SCATTERING STUDIES OF FOLDED SHEARING PHONONS IN  $KC_{12n}$  ( $n=2\sim 6$ )N. Wada\*, M.V. Klein<sup>(\*\*)</sup> and H. Zabel<sup>+</sup>

*Coordinated Science Laboratory\*, Department of Physics<sup>+</sup> and Materials Research Laboratory, University of Illinois at Urbana-Champaign, Urbana, Illinois 61801, U.S.A.*

**Abstract.**— Raman measurements were performed on  $KC_{12n}$  ( $n=2\sim 6$ ) in the very low frequency region ( $10\sim 50\text{ cm}^{-1}$ ) at room temperature. We assign the observed Raman peaks to the folded  $k_{\parallel 0}$  phonons from the c-axis transverse acoustic branch of pristine graphite. A simple linear chain model was used to deduce the shearing force constants between the layers.

1. **Introduction.**— The dynamics of inter- and intra-layer interactions in graphite intercalation compounds (GIC's) have recently attracted much research interest, especially because of its important role in understanding the various dimensionality-related structural phase transitions and the staging mechanism (a stage -n compound consists of a periodic layer sequence of an intercalant layer and n graphite layers). Frequently, the concept of Brillouin zone-folding generated by the new periodicity upon intercalation has been employed to interpret the lattice dynamics of GIC's. Neutron inelastic measurements [1,2] revealed the zone folding effects on the c-axis longitudinal acoustic phonon branches in alkali GIC's (AGIC's). Raman measurements [3,4] on stage-1 AGIC's showed some disputable evidence for the in-plane zone-folding.

In this paper we present Raman results on  $KC_{12n}$  ( $n=2\sim 6$ ) which demonstrate the zone-folding effects on the [001] TA branch. The interlayer shearing interaction will be discussed. More detailed discussion is given elsewhere [5].

2. **Experimental.**— Samples were prepared by the vapor transport method [6] from highly oriented pyrolytic graphite (HOPG). The HOPG samples were cleaved by Scotch tape, providing an atomically smooth surface before intercalation. Each sample was characterized by [001] x-ray reflection measurements before taking the Raman spectra.

Raman spectra were taken in the pseudo-Brewster angle configuration at room temperature with a 1 meter focal length home-made double-grating monochromator equipped with concave holographic gratings, using a 5145 Å  $Ar^{+}$  laser beam focused into a line image 50  $\mu$  wide by 1 mm long. The power was limited to 300 mW to avoid local deterioration of the sample.

3. **Results and Discussion.**— Figure 1 shows Raman spectra of  $KC_{12n}$  ( $n=2\sim 6$ ) taken in the cross-polarized configuration at room temperature. No apparent polarization dependence of the Raman peaks was detected in these experiments. If Fig. 1, we

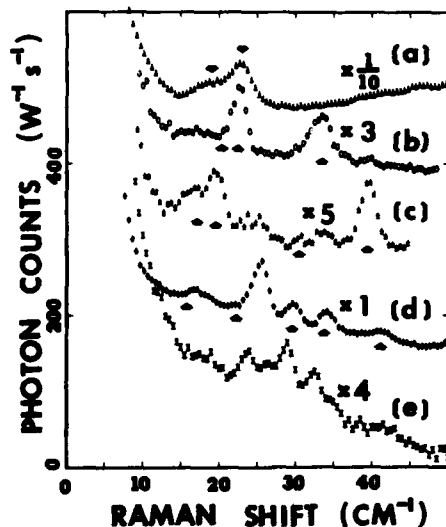


Fig. 1 : Raman spectra of  $KC_{12n}$  ( $n=2-6$ ) taken in the depolarized configuration at room temperature. The spectra (a) ~ (e) were taken from stage 2~6 samples, respectively. The background levels are not absolute. The signal-to-background ratios were about 1/2 in (a), 1/4 in (b), 1/6 in (c) and 1/10 in the other spectra. The arrows indicate the calculated values of the phonon frequencies (see text).

positively identify two peaks at 19 and 23  $cm^{-1}$  in stage 2, two peaks at 23 and 34  $cm^{-1}$  in stage 3, three peaks at 16, 19, and 39  $cm^{-1}$  in stage 4, five peaks at 17, 26, 30, 34, and 41  $cm^{-1}$  in stage 5, and three peaks at 24, 29, and 33  $cm^{-1}$  in stage 6. These observed peaks are attributed to the folded [00 $\bar{z}$ ] TA phonons because of their extremely low excitation energies and their stage dependence. Note that a stage- $n$  compound presumably possesses  $n$  zone-center shearing optical modes since a unit cell contains  $(n+1)$  layers. With use of a nearest-neighbor linear chain model, the shearing force constants (SFC's) were deduced, as is shown in Table 1. Here,

Table 1 : The shearing force constants in  $KC_{12n}$  ( $n=2-5$ ).

	$\phi_1/\phi_G$	$\phi_2/\phi_G$	$\phi_3/\phi_G$
Stage 2	0.10	0.58	
Stage 3	0.18	0.84	
Stage 4	0.14	1.03	1.13
Stage 5	0.22	1.07	1.13

$\phi_1$ ,  $\phi_2$ ,  $\phi_3$ , and  $\phi_G$  stand for potassium(K)-bounding carbon(BC), BC-interior carbon(IC), IC-IC, and pristine graphite C-C force constants, respectively. The calculated phonon frequencies using these SFC's are indicated with arrows in Fig. 1. We did not attempt to extract the SFC's of stage 6, because of the poor quality of the

spectrum. Though these SFC's should not be taken too seriously because of the missing peaks and our simple model, the following trends can be deduced from the table. First, the K-C shearing interaction in these compounds is much weaker than that of C-C in pristine graphite, and relatively stage independent. This is not surprising since the K layers are disordered at room temperature, and have a layer stoichiometry of  $KC_{12}$  [7]. Second, the SFC's of IC-IC layers is close to that of pristine graphite. This is consistent with the accepted picture [8] that the IC-IC interactions in GIC's should be similar to that in graphite. Third, the SFC of



BC-BC layers is surprisingly small in stage 2 (one might expect stronger interaction because of the excess electrons donated by K atoms), and the SFC of BC-IC layers approaches that of C-C layers in pristine graphite with increasing stage. This observation of the anomalous weak interlayer interaction is difficult to understand. Note that x-ray measurements of the compressibility at high pressure also showed an extremely soft interlayer interaction in  $KC_{24}$  [9]. Possible explanations are (1) the electrons in the  $\pi$  orbits mainly form anti-bonding orbitals along the c-axis, (2) because  $\pi$  orbits are more electron-filled in GIC's, and thus the Pauli exclusion principle repulsive force becomes stronger, or (3) because of the Coulombic interaction, the majority of  $\pi$  electrons are localized on the  $K^+$  ion side, leaving the  $\pi$  orbits on the other side relatively empty [10]. This leads to a weak BC-C interlayer interaction. Finally, we mention that stiffening of the BC-IC interlayer interaction with increasing stage suggests an extended charge delocalization in higher stage compounds.

We thank W. A. Kamitakahara, D. M. Hwang and P. C. Eklund for valuable discussions. We also thank N. Caswell for useful information about preparing high stage samples, and A. W. Moore for providing the HOPG used in these experiments. This work was supported in part by NSF 80-20550, DOE DE-AC02-76ER01198 and ONR N00014-79-C-0424.

#### References

1. W. D. Ellenson, D. Semmingsen, D. Gruérard, D. G. Onn, J. E. Fischer, *Mater. Sci. Eng.* **31**, 137 (1977).
2. A. Magerl, H. Zabel, *Phys. Rev. Lett.* **46**, 444 (1981).
3. M. S. Dresselhaus, G. Dresselhaus in *Intercalated Layered Materials*, edited by F. A. Lévy (Reidel, Dordrecht, 1979) p. 423.
4. S. A. Solin, *Physica* **99B**, 443 (1980).
5. N. Wada, M. V. Klein, H. Zabel, to be published in Proceedings of the International Conference on "Physics of Intercalation Compounds," Trieste, Italy, 1981.
6. H. Hérold, *Bull. Soc. Chim. Fr.* **187**, 999 (1955).
7. D. E. Nixon, G. S. Parry, *Brit. J. Appl. Phys. Ser. 2*, **1**, 291 (1968).
8. S. A. Safran, D. R. Hamann, *Phys. Rev. B* **23**, 565 (1981).
9. N. Wada, R. Clarke, S. A. Solin, *Solid State Commun.* **35**, 675 (1980).
10. H. Kamimura, to be published in Proceedings of the International Conference on "Physics of Intercalation Compounds," Trieste, Italy, 1981.

**PHONONS IN METALS**

## PHONONS IN METALS

J. Ashkenazi\* and M. Dacorogna

*Département de Physique de la Matière Condensée, Université de Genève, 24 Quai Ernest-Ansermet, 1211 Genève 4, Switzerland.*

**Abstract.**- By using stationarity properties within the finite temperature density functional approach, it is shown that the calculation of phonons and electron-phonon coupling processes can be based on the coupling between renormalized "bare" phonons and the HKS one-electron system, under the condition that the potential remains "frozen". This explains the success of calculations of phonon anomalies and electron-phonon coupling parameters in transition metals which were based on rigidly moving potentials. The approach is rigorously applied using the LMTO-ASA band method. It is found successful in ab initio calculations of shear moduli in transition metals, and promising for complete phonon and electron-phonon coupling calculations.

**1. Introduction.**- The success of first principles microscopic calculations of phonon spectra in metals, was limited in the past to free-electron like cases. Following the pseudopotential technique, one can start there from the jellium model assuming that the pseudopotential is weak, and expanding the energy change in powers of it. The obtained expression is separated into electronic and ionic parts /1/, and has been extensively applied for simple metals /2-4/.

This type of calculations does not succeed in transition metals and their compounds and alloys, which exhibit interesting properties (not found in general in simple metals) such as anomalies correlated with instabilities and high superconducting transition temperatures. In the last few years there have been many attempts to develop the microscopic theory of phonon-spectra and electron-phonon coupling in these metals /5-14/. However, to our knowledge, there has yet been no completely first-principles (parameterless) calculation of phonon spectra in transition metals, for general  $q$  points. In addition, recent

\* Present address: Physics Department, Technion, Haifa, Israel

explanations of phonon anomalies looked contradictory: some were based on one-electron theory, and other one many-body screening effects.

In this work we develop further the ideas initiated in ref. 14 showing that many-body effects (including non-local exchange-correlation) could be represented, under certain conditions, as one-electron effects. So the problem of screening could be avoided, simplifying first principles calculations of phonon spectra and electron-phonon coupling in transition metals for general  $q$  points.

2. Stationarity Properties.— Let us generalize to finite temperatures the ideas of ref. 14, using Mermin's generalization /15/ to the HKS approach /16-17/. One introduces a free energy functional  $F\{v, n\}$  of the variables:  $v(\underline{r})$  the external potential to the electrons system, and  $n(\underline{r})$  — a "permissible" electronic density. We consider an external potential which has a smooth dependence on a parameter  $\beta$ :  $v(\beta, \underline{r})$ , and denote by  $n(\beta, \underline{r})$  the corresponding thermally averaged density. The free energy  $F(\beta)$ , corresponding to this potential, is equal to  $F\{v(\beta), n(\beta)\}$ . In addition, this functional satisfies a minimum property under density variations, which introduces the stationarity property /14/ :

$$F(\beta_0) = F\{v(\beta_0), n(\beta)\} + 0(\beta - \beta_0)^2 \quad (1)$$

In order to calculate  $F$ , one introduces /17/ an effective system of non-interacting electrons (the "one-electron system") with the same thermally averaged density  $n(\underline{r})$ . In this system one uses the one-electron Hamiltonian  $H_n = \hbar^2 \nabla^2 / 2m + v_n(\underline{r})$ , where the effective one-electron potential  $v_n$  is given by /17/:

$$v_n(\underline{r}) = v(\underline{r}) + v_c(\underline{r}) + v_{xc}(\underline{r}) \quad (2)$$

$v_c(\underline{r})$  is the Coulomb potential due to the electrons, and  $v_{xc}(\underline{r})$  is the so called "exchange-correlation" potential.  $H_n$  satisfies the secular equation:  $H_n |b\underline{k}\rangle = E_b(\underline{k}) |b\underline{k}\rangle$ , yielding a spectrum of eigen-values and eigen-states, obtained by a band calculation. The one-electron free energy  $F_n$  can be expressed as a functional of  $v_n$ , and is given by:

$$F_n(v_n) = nE_F + T \int_{b\underline{k}} \log [1 - f(E_b(\underline{k}))] \quad (3)$$

where  $n$  is the number of electrons,  $E_F$  is the Fermi level,  $T$  is temperature, and  $f(E)$  is the Fermi function.

Let us consider a one-electron potential which has a smooth dependence on a parameter  $\alpha$ :  $v_n(\alpha, \underline{r})$  and denote by  $n(\alpha, \underline{r})$  the thermally averaged density related to it through:

$$n(\underline{r}) = \int_{b\mathbf{k}} f(E_b(\mathbf{k})) |\phi_b(\mathbf{k}, \underline{r})|^2 \quad (4)$$

where  $\phi_b(\mathbf{k}, \underline{r})$  is the wave-function corresponding to  $|b\mathbf{k}\rangle$ . The free energy functional of the real electrons system is given by /17/:

$$F\{v, n\} = G_n\{n\} + U_C\{v, n\} + F_{xc}\{n\} \quad (5)$$

where  $U_C$  is the total Coulomb energy of the electron-nuclei system,  $F_{xc}$  is the so called "exchange-correlation" free energy, and  $G_n$  is given by:

$$G_n\{n(\alpha)\} = F_n\{v_n(\alpha)\} - \int v_n(\alpha, \underline{r}) n(\alpha, \underline{r}) d^3r \quad (6)$$

On the basis of the same arguments that led to Eq. (1), and the properties of a Legendre transformation /14/ we get the following stationarity property (with respect to variations in  $v_n$ ):

$$G_n\{n(\alpha)\} = F_n\{v_n(\alpha_0)\} - \int v_n(\alpha_0, \underline{r}) n(\alpha, \underline{r}) d^3r + O(\alpha - \alpha_0)^2 \quad (7)$$

By combining Eqs. (1), (5), (7), and denoting:

$$v(\underline{r}) = v(\beta_0, \underline{r}), \quad v_n(\underline{r}) = v_n(\alpha_0, \underline{r}), \quad \tilde{n}(\underline{r}) = n(\alpha_1, \underline{r}) = n(\beta_1, \underline{r}) \quad (8a-c)$$

we get that the free energy can be expressed as:

$$F = F(\beta_0) = F_n\{v_n\} - \int v_n(\underline{r}) \tilde{n}(\underline{r}) d^3r + U_C\{v, \tilde{n}\} + F_{xc}\{\tilde{n}\} + O(\alpha_1 - \alpha_0)^2 + O(\beta_1 - \beta_0)^2 \quad (8d)$$

This expression allows us to calculate  $F$  on the basis of approximate  $\tilde{n}$  and  $v_n$ , which could be specially chosen to simplify the calculation. Let us consider for simplicity monoatomic crystals with closely packed structures. They are composed of Wigner-Seitz (WS) cells of volume  $\Omega$  and "radius"  $s = (3\Omega/4\pi)^{1/3}$ .

3. Application to Free Energy Differences.— Simple applications of Eqs. (8), for free energy differences between two crystals with the same volume, are achieved /14/ by using the "frozen potential" and the "frozen density" conditions. Namely  $v_n(\underline{r})$  and  $\tilde{n}(\underline{r})$  are taken in (8b,c) the same for both crystals in the inner parts of the WS cells, and at least on the average close to their boundaries. Considering for example the influence of an additional external potential  $V(\underline{r})$  (which changes  $v(\underline{r})$  in (8a) to  $v(\underline{r}) + V(\underline{r})$ ). It turns out, by using these conditions in (8d), that the free energy change is given to the first order in  $V$  by:

$$\delta_V F = \delta_V U_C(v, \tilde{n}) = \int V(\underline{r}) \tilde{n}(\underline{r}) d^3r \quad (9)$$

This expression can be applied for the effect of electric fields on the electrons. Its importance is that exchange-correlation effects do not appear explicitly. By introducing spin and current, one can apply a similar expression also to magnetic fields.

Another application is for the free energy change  $\delta_T F$  with temperature, assuming that the volume change is negligible, which is valid at low temperatures (the thermal expansion coefficient is connected with anharmonicity, and vanishes  $T = 0K$ ). In this case  $v(\underline{r})$  remains fixed, and for  $v_n(\underline{r})$  and  $\tilde{n}(\underline{r})$  we use the above conditions. By (8d) we get to the first order in  $\delta T$ :

$$\delta_T F = \delta_T F_n \{v_n\} + \delta_T F_{xc} \{\tilde{n}\} \quad (10)$$

$\delta_T F_n \{v_n\}$  is a one-electron term, while  $\delta_T F_{xc} \{\tilde{n}\}$  is due to thermally activated low lying collective excitations (their calculations are under the frozen potential and density conditions respectively).

Another application /14/ is for the free energy change  $\delta_V F$  under a volume conserving lattice strain (characterized by a strain parameter  $\gamma$ ). Such a strain could be a "frozen in" phonon. Let us use in this

case also the condition that  $n(\underline{r})$  is a muffin-tin (MT) density. Namely it is spherically symmetric around the WS cell centres, and flat "enough" on their boundaries. By  $n(\alpha, r)$  we denote the spherically averaged density  $n(\alpha, \underline{r})$  around the WS cell centre, and introduce the quantity  $Z(\alpha) = \Omega n(\alpha, s)$ . The band-structure value is denoted by  $Z_0 = Z(\alpha_0)$ . The corresponding density  $n(\alpha_0, r)$  has the first r-derivative  $n^{(1)}(\alpha_0, s)$  close to zero by symmetry. In order to satisfy the MT density condition, we require that also the second r-derivative  $n^{(2)}(s)$  will be zero, and denote the corresponding  $Z(\alpha)$  value by  $Z_{\text{eff}}$ . The result of the three conditions (frozen potential and density, MT density) on (8d) is /14/:

$$\delta_\gamma F = \delta_\gamma F_n \{v_n\} + Z_{\text{eff}}^2 \delta_\gamma U_M \quad (11)$$

where  $U_M$  represents the Madelung energy of unit charge point ions in a uniform neutralizing background.  $\delta_\gamma F_{xc}$  has vanished here, including the leading non-local terms, which can be expressed through an expansion in density gradients /16/ at the WS cells boundaries, and fall by the flatness of the MT density there. In the case that  $\gamma$  represents a symmetry removing strain (such as a frozen-in phonon) it can be shown /14/ that for a suitably chosen  $Z_{\text{eff}}$ , the error in Eq. (11) is reduced to order  $\gamma^3$ , and thus it (11) is valid within the harmonic approximation. This value of  $Z_{\text{eff}}$  is given by /14/:

$$Z_{\text{eff}}^2 = Z_0^2 - \alpha_0 \, dZ(\alpha_0)^2/d\alpha \quad (12)$$

where the parameter  $\alpha$  has been chosen as :  $\alpha = n^{(2)}(\alpha, s)$ , and it represents the density deviation from the flatness condition. The accuracy of Eq. (11) (to order  $\gamma^2$ ) is then linked with the validity of a linear approximation for non-flatness energy effects (such as non-local exchange-correlation). The density  $\alpha$ -derivative in Eq. (12) is obtained by perturbation expansion of the wave-functions. As was shown in ref. 14, this restricts the permissible variations, obtaining a sharply determined value of  $Z_{\text{eff}}$  for simple and transition metals.

In table I we represent the values of  $Z_0$  and  $Z_{\text{eff}}$  calculated (at  $T=0$ ) for the bcc and fcc metals of the 4th-6th rows, on the basis of self-consistent LMTO-ASA band calculations /18/ (neglecting core density contributions). We also show in the table the relative change

Table I: The calculated values of  $\bar{\epsilon}_0, \bar{\epsilon}_{\text{eff}}$  and the relative difference between them in percents.

											Element
											$\bar{\epsilon}_0$
											$\bar{\epsilon}_{\text{eff}}$
											$\frac{\bar{\epsilon}_{\text{eff}} - \bar{\epsilon}_0}{\bar{\epsilon}_0}$
K	Ca	Sc	Ti	V	Cr	Mn	Fe	Co	Ni	Cu	
1.126	2.16			3.28	3.36		3.13		2.84	2.59	
1.106	2.08			3.34	3.72		4.5		4.8	4.2	
-1.81	-3.78			1.88	11.6		448		698	628	
Nb	Sr	Y	Zr	Mo	Ru	Tc	Rh	Pd	Ag		
1.123	2.18			3.92	4.25		3.76	3.19	2.77		
1.111	2.13			3.95	4.54		5.7	5.8	4.6		
-1.18	-2.38			0.88	6.88		528	828	668		
Ce	Ba	La	Hf	Ta	W	Re	Os	Ir	Pt	Au	
1.123	2.17			4.3880	4.78			4.52	4.03	3.43	
1.101	1.99			4.3884	5.00			6.4	6.6	5.8	
-2.08	-8.38			0.018	4.68			428	648	698	

Table II: The calculated tetragonal shear moduli of fcc transition metals

$C'_{\text{calc}} = C'_D + C'_H$  at  $T = 0\text{K}$  in comparison with experiment ( $C'_{\text{exp}}$ )

Units	Cu	Rh	Pd	Ag	Ir	Pt	Au
Ryd/atm							
$C'_D$	-0.251 ± 0.01	+0.622 ± 0.01	-0.382 ± 0.01	-0.202 ± 0.01	+0.121 ± 0.01	-0.512 ± 0.01	-0.502 ± 0.01
$C'_H$	+0.382 ± 0.01	+0.682 ± 0.01	+0.682 ± 0.01	+0.412 ± 0.01	+0.852 ± 0.01	+0.882 ± 0.01	+0.852 ± 0.01
$C'_{\text{calc}}$	+0.141 ± 0.01	+0.704 ± 0.01	+0.304 ± 0.01	+0.212 ± 0.01	+0.972 ± 0.01	+0.372 ± 0.01	+0.152 ± 0.01
$10^{10} \text{ N/m}^2$							
$C'_{\text{calc}}$	2.6 ± 1.0	11.0 ± 2.0	4.4 ± 1.0	2.7 ± 1.1	14.7 ± 2.1	5.3 ± 2.0	1.9 ± 1.0
$C'_{\text{exp}}$	2.56	11.5	2.9	1.71	17.2	5.22	1.8



between  $Z_0$  and  $Z_{\text{eff}}$ . This change represents energy effects which are included in (14) indirectly, through the variation procedure, concerning among other, non-local exchange-correlation effects. In the free electron limit,  $Z_{\text{eff}}$  coincides with  $Z_0$ , and Eq. (11) with similar expressions applied using the pseudopotential technique /1,2/. From table I it turns out that, within the transition metal series, the fifth column is the closest to free-electrons concerning  $Z_{\text{eff}} - Z_0$ , while the tenth column is the farthest.

Eq. (11) was applied /14/ to calculate the tetragonal shear moduli  $C' = \frac{1}{2}(C_{11}-C_{12})$  of the non-magnetic fcc transition metals (using the LMTO-ASA band method) and the results are represented in table II.  $C'_{\text{calc}}$  is given as a sum of two terms:  $C'_b$  and  $C'_M$ , related to  $\delta_Y F_n$  and  $\delta_Y U_M$  respectively. Each of these terms has an error bar estimated from the accuracy of the calculation /14/, and the results agree with the experimental ones  $C'_{\text{exp}}$  within the error bars. For Rhodium the theoretical result preceded the experimental one /19/. For these metals the difference between  $Z_0$  and  $Z_{\text{eff}}$  is large (see Table I), and the transformation (12) is essential.

4. Electron-Phonon Hamiltonian.— The shear results correspond to low- $q$  limit phonons /8/. For finite  $q$  the strain parameter  $\gamma$  is represented by periodic displacement vectors  $\Omega_\alpha(q)$ . Let us introduce the quantities:

$$D_{\alpha'\alpha}^{(0)}(q) = Z_{\text{eff}}^2 \partial^2 U_M / \partial \Omega_{\alpha'}(q) * \partial \Omega_\alpha(q) |_{q=0} \quad (13a)$$

$$g_{b'b\alpha}^{(1)}(\underline{k}, q) = \partial \langle b' \underline{k} + q | H_n | b \underline{k} \rangle / \partial \Omega_\alpha(q) |_{q=0} \quad (13b)$$

$$g_{ba'\alpha}^{(2)}(\underline{k}, q) = \partial^2 \langle b \underline{k} | H_n | b \underline{k} \rangle / \partial \Omega_{\alpha'}(q) * \partial \Omega_\alpha(q) |_{q=0} \quad (13c)$$

where the derivatives of  $H_n$  are determined by the frozen potential condition. There are two approaches concerning the derivatives of  $|b \underline{k}\rangle / 20/$ : the Bloch approach, under which these derivatives vanish; and the Fröhlich approach under which  $|b \underline{k}\rangle$  form a complete set of "displaced" states, and the matrix elements of  $H_n$  are derivated directly.

At low temperatures one can take (by Eqs. (8) and (12)) temperature independent  $v_n$  and  $Z_{\text{eff}}$ , so that the quantities in Eqs. (13) do not depend on  $T$ . Let  $a_b(\underline{k})^\dagger$  be the creation operator of the state  $|b \underline{k}\rangle$ , and  $P_\alpha(q) = i\hbar \partial / \partial \Omega_\alpha(q)$ . The HKS one-electron Hamiltonian  $H_n$  can be generalized and expressed as:

$$\begin{aligned}
H_n = & \sum_{\underline{b}\underline{k}} E_{\underline{b}}(\underline{k}) a_{\underline{b}}(\underline{k})^\dagger a_{\underline{b}}(\underline{k}) + \frac{1}{2} \sum_{\alpha \underline{q}} [P_{\alpha}(\underline{q})^* \frac{p_{\alpha}(\underline{q})}{M} + \sum_{\alpha'} D_{\alpha\alpha'}^{(0)}(\underline{q}) \Omega_{\alpha'}(\underline{q})^* \Omega_{\alpha}(\underline{q})] \\
& + \sum_{\alpha \underline{b}\underline{k}\underline{q}} [\sum_{\underline{b}'} g_{\underline{b}'\underline{b}\alpha}^{(1)}(\underline{k}, \underline{q}) \Omega_{\alpha}(\underline{q}) a_{\underline{b}'}(\underline{k} + \underline{q})^\dagger a_{\underline{b}}(\underline{k}) + \frac{1}{2} \sum_{\alpha'} g_{\underline{b}\alpha'\alpha}^{(2)}(\underline{k}, \underline{q}) \\
& \times \Omega_{\alpha'}(\underline{q})^* \Omega_{\alpha}(\underline{q}) a_{\underline{b}}(\underline{k})^\dagger a_{\underline{b}}(\underline{k})] \\
& + \sum_{\underline{b}\underline{b}'\underline{k}} \langle \underline{b}'\underline{k} | V | \underline{b}\underline{k} \rangle a_{\underline{b}'}(\underline{k})^\dagger a_{\underline{b}}(\underline{k})
\end{aligned} \tag{14}$$

From a perturbation expansion of Eq. (11) it turns out that this Hamiltonian determines the phonon frequencies at low temperatures, and therefore also their line-widths. In addition, it turns out by Eqs. (4), (9), (10) and (11), that this Hamiltonian can be also used to describe low temperature physical processes where the (real) electrons are influenced by external fields (characterized by  $V$ ) and electron-phonon coupling (neglecting the temperature dependent contribution of other collective excitations such as spin and charge fluctuations).

So we could base the electron-phonon problem, within the harmonic approximation, on the coupling (through  $g^{(1)}$  and  $g^{(2)}$ ) between the  $D^{(0)}$  bare phonons, and the HKS one-electron system. The many-body effects are included indirectly through: (i) the renormalization of  $Z_{\text{eff}}$  which represents, among other things, non-local exchange-correlation effects; (ii) the use of the frozen potential condition under which potential and screening corrections are mutually cancelled.

**5. Discussion.**— Electron-phonon coupling calculations in transition metals are currently done using /11/ the "rigid muffin-tin approximation" (RMTA), or the "modified tight-binding approximation" (MTBA). The frozen potential condition is approximately used in both methods. So their success, within a one-electron theory, is understood on the basis of the above discussion. The RMTA has succeeded /11/ in calculations of electric resistivity, phonon line-widths, tunneling spectral functions, and the mass-enhancement parameter  $\lambda$  in transition metals; the small deviations (~10-20%) of the calculated  $\lambda$  from the values obtained by different experiments /11/ could be explained as due to spin-fluctuations /21/. The RMTA however failed /11/ in the low- $q$  limit and for the anisotropy of  $\lambda$  in Nb /22/ which has large low- $q$  contributions /11/. This is due to the fact that in the low- $q$  limit,

one calculates ratios between infinitesimal numbers, which are sensitive to inaccuracies introduced by the perturbative "shifting" of the wave-functions within the Bloch approach (used in the RMTA). This problem does not exist within the Fröhlich approach where the shifting of the wave-functions is treated rigorously, and indeed calculations using it in the MTBA, succeeded where the RMTA failed. Such calculations in Nb were successful for the anisotropy in  $\lambda$  /22,7,9/, and for shear anomalies (low- $q$  limit) in Zr-Nb-Mo alloys. Such calculations were successful in explaining  $\lambda$  values /9/ and phonon anomalies /10/ in transition metals and their compounds. The same anomalies could be also explained as a screening effect /5,6/, and this strengthens our argumentation that such effects are included in the Hamiltonian (14).

The MTBA has its limitations being based on fitting. By approaching the problem with the LMTO-ASA band method, one can rigorously interpret the frozen-potential condition. The advantages of the MTBA are restored. Furthermore, the algorithms to calculate  $Z_{\text{eff}}$  (see table I)  $D^{(0)}$ ,  $g^{(1)}$  and  $g^{(2)}$  can be naturally built within the framework of the method /23/. So complete phonon calculations for general  $q$ -values, and also rigorous calculations of electron-phonon coupling processes have become handy.

**ACKNOWLEDGEMENT.**— The authors acknowledge stimulating discussions with Professor Martin Peter, and his encouragement and suggestions.

#### REFERENCES

- /1/ W.A. Harrison, "Pseudopotentials in the Theory of Metals", Benjamin Inc. New York (1966)
- /2/ V. Heine and D. Weaire, Solid State Physics 24, 363 (1970)
- /3/ E.G. Brovman and Y.M. Kagan, in "Dynamical Properties of Solids", ed. by G.K. Horton and A.A. Maradudin, North Holland, Amsterdam (1974) vol. 1, p. 191
- /4/ S.K. Joshi and A.K. Rajagopal, Solid State Physics 22, 259 (1968)
- /5/ S.K. Sinha and B.N. Harmon, in "Superconductivity in d- and f-Band Metals" edited by D.H. Douglass, Plenum Press, New-York, (1976) p. 269; S.K. Sinha, in "Dynamical Properties of Solids" vol. 3 ed. by G.K. Horton and A.A. Maradudin North-Holland, Amsterdam (1980) p. 1
- /6/ W. Hanke, J. Hafner and H. Bilz, Phys. Rev. Lett. 37, 1560 (1976)
- /7/ M. Peter, J. Ashkenazi and M. Dacorogna, Helv. Phys. Acta 50, 267 (1977); J. Ashkenazi, M. Dacorogna and P.B. Allen, Solid State Commun. 36, 1051 (1980)
- /8/ J. Ashkenazi, M. Dacorogna, M. Peter, Y. Talmor, E. Walker and

- S. Steinemann, Phys. Rev. B18, 4120 (1978); P. Bujard, R. Sanjines, E. Walker, J. Ashkenazi and M. Peter, J. Phys. F 11, 775 (1981)
- /9/ C.M. Varma, E.I. Blount, P.Vashishta and W. Weber, Phys. Rev. B19 6130 (1979); A.L. Simons, C.M. Varma and W. Weber, Phys. Rev. B23 2431 (1981)
- /10/ C.M. Varma and W. Weber, Phys. Rev. B19, 6142 (1979); W. Weber in "Physics of Transition Metals 1980", edited by P. Rhodes (Inst. Phys. Conf. Ser. No 55) p. 495
- /11/ W.H. Butler, in "Physics of Transition Metals 1980" edited by P. Rhodes (Inst. Phys. Conf. Ser. No 55) p. 505, and references therein.
- /12/ S.J. Gale and D.G. Pettifor, Solid State Commun. 24, 175 (1977)
- /13/ B.N. Harmon and K.M. Ho, in "Superconductivity in d- and f-Band Metals", ed. by H. Suhl and M.B. Maple, Academic Press, London (1980) p. 173
- /14/ J. Ashkenazi, M. Dacorogna and M. Peter, in "Recent Developments in Condensed Matter Physics" ed. by J.T. Devreese et al. (Plenum Pub. Corp. New-York, 1981) vol. 2, p. 15; in "Physics of Transition Metals 1980" edited by P. Rhodes (Inst. Phys. Conf. Ser. No 55) p. 31; Phys. Rev. B, to be published.
- /15/ N.D. Mermin, Phys. Rev. 137, A 1441 (1965)
- /16/ P. Hohenberg and W. Kohn, Phys. Rev. 136, B 864 (1964)
- /17/ W. Kohn and L.J. Sham, Phys. Rev. 140, A 1133 (1965)
- /18/ D. Glötzl and O.K. Andersen, Adv. Phys., to be published
- /19/ E. Walker, J. Ashkenazi and M. Dacorogna, Phys. Rev. B24 (1981) in press
- /20/ J. Ashkenazi, M. Dacorogna and M. Peter, Solid State Commun. 29, 181 (1979)
- /21/ H. Rietschel and H. Winter, Phys. Rev. Lett. 43, 1256 (1979)
- /22/ G.W. Crabtree, D.H. Dye, D.P. Karim, D.D. Koelling and J.B. Ketterson, Phys. Rev. Lett. 42, 390 (1979)
- /23/ O.K. Andersen, Phys. Rev. B12, 3060 (1975); and private communication.

## ELECTRON-PHONON COUPLING IN THE NONTRANSITION METAL CADMIUM

B. Dorner, A.A. Chernyshov\*, V.V. Pushkarev\*, A.Yu. Rumyantsev\* and R. Pynn

ILL Grenoble, France

\*Kurchatov Inst., Moscow, U.S.S.R.

**Abstract.** - By inelastic neutron scattering we observed several anomalies in the group velocities of the phonon dispersion curves. They could all be allocated on the Fermi surface. Strengths and shape of the anomalies differ considerably from theoretical predictions.

After measuring the phonon dispersion curves of Cd at 80 K by inelastic neutron scattering /1/ we concentrated on the Kohn anomalies /2/ in the dispersion curves. Several anomalies (AN's) like Fig. 1 were detected and allocated on the Fermi surface. From calculations in perturbation theory, including second-order terms in the Heine Abarenkov /3/ model potential, it was expected that the group velocity at an AN should exhibit a single maximum or a single minimum depending on whether the phonon dispersion is followed from inside the Fermi surface towards outside or vice versa /4/. In Fig. 1 anomaly No. 4 should be a maximum and No. 5, practically coinciding, a minimum. The calculation shows as a resultant of both effects a maximum, while the

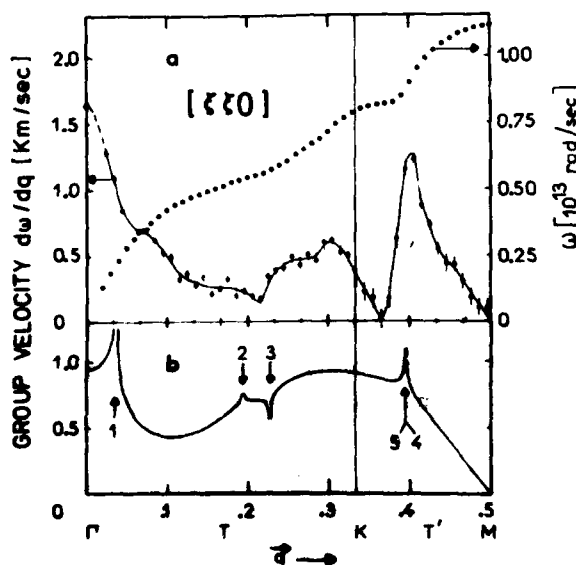


Fig. 1: a) ... Transverse phonon dispersion curve. ooo measured phonon group velocity. b) Predicted group velocity with numbered anomalies /4/.

experimental observation reveals a strong maximum at the predicted position and a strong unexpected minimum for smaller  $q$ -values.

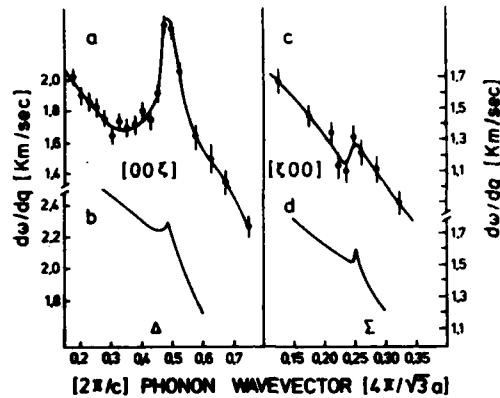


Fig. 2: Measured (open dots) and calculated (b,d) phonon group velocity.

Fig. 2 shows calculated and measured AN's /5/ for two longitudinal dispersion curves in  $|00\xi|$  and  $|\xi 00|$  directions involving the reciprocal lattice vectors  $\vec{\tau} = (002)$  and  $\vec{\tau} = (100)$ , respectively. Both calculated AN's and the experimental one in  $|\xi 00|$  directions are comparable in strength, but the observed one in  $|00\xi|$  direction is much stronger. Both AN's are related to electron transitions between spherical parts of the Fermi surface, therefore the band structure should be similar. But the strong anisotropy of the Cd structure ( $c/a = 1.886$  instead of 1.633 for ideal h.c.p.) produces probably an anisotropy in the electron phonon interaction and in the electron susceptibility via an anisotropy in the conduction electron wave function and in the electron ion potential.

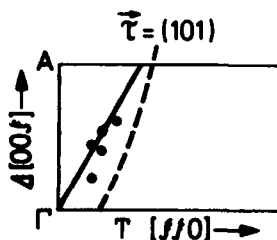


Fig. 3: Plane in reciprocal space perpendicular to  $|100|$

We investigated the AN's out of symmetry directions as well /5/ and could separate some which coincide for symmetry directions. Particular attention was paid to electron transitions between flat parts (surface of the second Brillouin zone) of the Fermi surface with  $\vec{\tau} = (101)$ . On the flat parts an energy gap must exist. The solid line in Fig. 3, going through the centre of the Brillouin zone, gives the trace for eventual AN's of this kind, while along the dashed line AN's

AD-A128 574

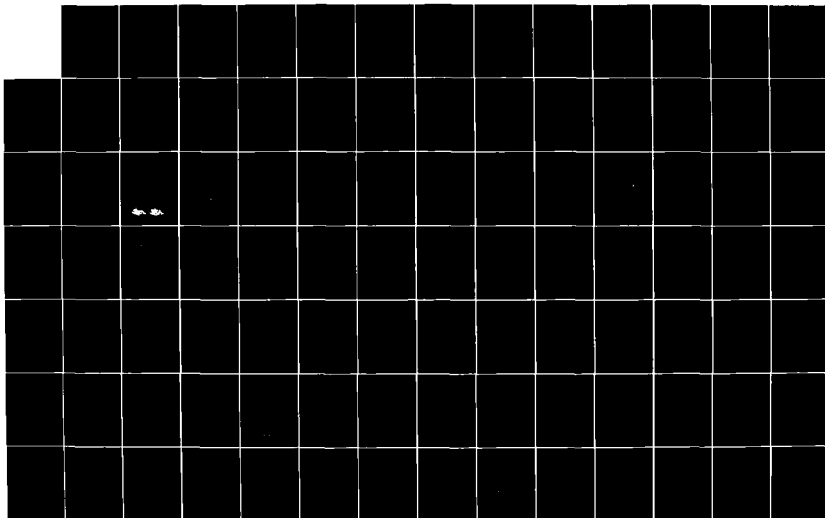
INTERNATIONAL CONFERENCE ON PHONON PHYSICS 31 AUGUST-3  
SEPTEMBER 1981 BLOOMINGTON INDIANA(U) INDIANA UNIV AT  
BLOOMINGTON W E 800M DEC 81 ARO-17340.1-PM  
MIPR ARO-43-80

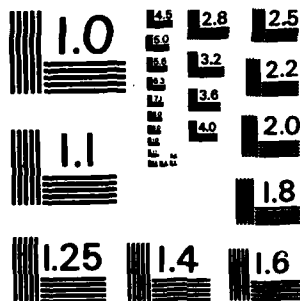
510

UNCLASSIFIED

F/G 20/2

NL





MICROCOPY RESOLUTION TEST CHART  
NATIONAL BUREAU OF STANDARDS-1963-A



would occur in the case of a spherical Fermi surface. The points in Fig. 3 indicate observed AN's. For the symmetry direction T, where the AN coincides with  $q = 0$ , we found a strong variation of the phonon group velocity for small  $q$ .

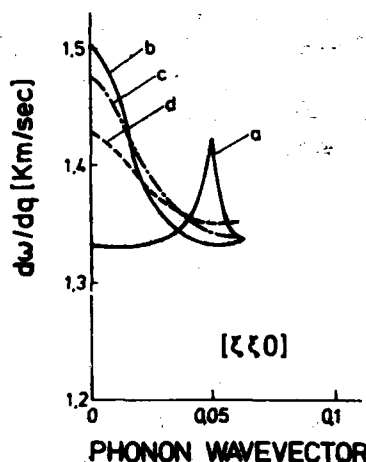


Fig. 4: Anomalous behavior of the phonon group velocity in T direction for small  $q$ 's. a) Kohn anomaly in case of a spherical Fermi surface. b-d) Case of a flat Fermi surface  $\tau = (101)$ .  
b:  $\epsilon = 0.01$ ; c:  $\epsilon = 0.02$ ; d:  $\epsilon = 0.03$ .

A calculation /5/ shows that some kind of AN appears even for flat parts of the Fermi surface, if the gap is sufficiently small. Yet, it is not a Kohn AN, as the slope of the electron susceptibility at  $2 k_F$  ( $2k_F$  being the distance between opposite parts of the Fermi surface) is finite and not infinite. The calculated effect on the group velocity for small  $q$ 's in T-direction is presented in Fig. 4. Case b resembles the observed behavior. The gap which is  $2 V_T$  was characterized by the parameter  $\epsilon = V_T/2E^0(\pi/2)$  where  $V_T$  is the value of the model potential at the point (101) and  $E^0(\pi/2)$  is the energy of an unperturbed state at the zone boundary.

- /1/ B. Dornier, A.A. Chernyshov, V.V. Pushkarev, A.Yu. Romyantsev and R. Pynn; J. Phys. F, 11, 365 (1981)
- /2/ W. Kohn; Phys. Rev. Lett. 2, 393 (1959)
- /3/ I.V. Abarenkov and V. Heine; Phil. Mag. 12, 529 (1965)
- /4/ A.A. Chernyshov, V.V. Pushkarev, A.Yu. Romyantsev, B. Dornier and R. Pynn; J. Phys. F 9, 1983 (1979)
- /5/ A.A. Chernyshov, V.V. Pushkarev, A.Yu. Romyantsev, B. Dornier and R. Pynn; J. Phys. F to be published

BAMAR - BARTLETT

D 100 800 900

ALL INFORMATION CONTAINED HEREIN IS UNCLASSIFIED  
DATE 09-01-00 BY 0056

## RAMAN SCATTERING FROM ANOMALOUS PHONONS IN TRANSITION METALS AND COMPOUNDS

M. V. Klein

*Department of Physics and Materials Research Laboratory, University of Illinois at Urbana-Champaign, Urbana, Illinois 61801, U.S.A.*

**Abstract.**—Phonon anomalies in transition-metal compounds often produce enhanced two-phonon Raman spectra. Examples are given and a theoretical explanation sketched. The anomalous  $E_g$  phonon and electronic Raman scattering in  $V_3Si$  are also discussed.

Phonon anomalies in transition-metal compounds occur when scattering of d-electrons near the Fermi surface renormalizes the phonon frequencies by giving them a self-energy  $\pi(q, \omega \sim 0)$  that is large and negative.<sup>1</sup> This alters the frequency by an amount  $\%[-\pi(q, 0)]$ . The same d-electron-phonon interactions are responsible for strong two-phonon overtone Raman scattering. There is a microscopic connection between the anomalies and the Raman cross-section.<sup>2</sup> Apart from the usual Bose factor, the latter is approximately<sup>2,3</sup>

$$\sigma(\omega) = P \int \delta(\omega/2 - \omega_q) [\pi(q, 0)]^2 \quad (1)$$

where  $P$  contains a polarizability-like factor. If  $\pi(q, 0)$  were unity the sum over  $q$  would give simply  $F(\omega/2)$ , where  $F(\omega)$  is the phonon density of states. A variable  $\pi(q, 0)$  gives selective Raman enhancement for those phonons that are anomalous.

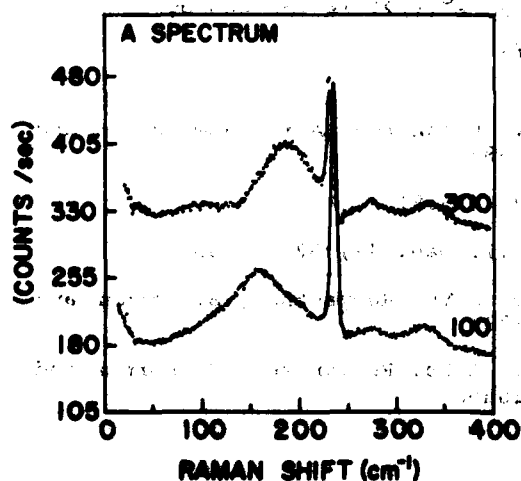


Fig. 1: The A-symmetry Raman spectrum of  $2H-NbSe_2$  at 300 and 100 K. (Ref. 4)

A clean example of this effect is found in the normal phase of the layered transition metal dichalcogenides before they undergo a charge-density-wave (CDW) type of phase transition.<sup>2</sup> For example, in  $2H-NbSe_2$  the LA phonon near  $q = (2/3)\Gamma M$  softens and eventually condenses. Its overtone gives the strongest Raman feature in the room-temperature spectrum,<sup>4</sup> as shown in Fig. 1, namely the broad peak at  $180 \text{ cm}^{-1}$ , which softens to  $160 \text{ cm}^{-1}$  at 100 K. This spectrum is clearly not the full  $F(\omega/2)$  but shows the soft LA region only.

Another example is found in the group Vb transition metal carbides, which have the rock-salt structure. The samples always occur with at least a few percent carbon vacancies, which induce a one-phonon Raman spectrum that is quite close to  $F(\omega)$ . This can be seen for acoustic modes in  $\text{TaC}_{0.99}$  in Fig. 2 in the curves labelled "1ph". The curves labelled "2ph" are two-LA-phonon spectra plotted as a function of  $\omega/2$ . These strong two-phonon peaks are not due to the vacancies, but are intrinsic and show enhancements relative to  $F(\omega)$  in the mid-frequency region, where the well-known phonon anomalies lie.<sup>5</sup>

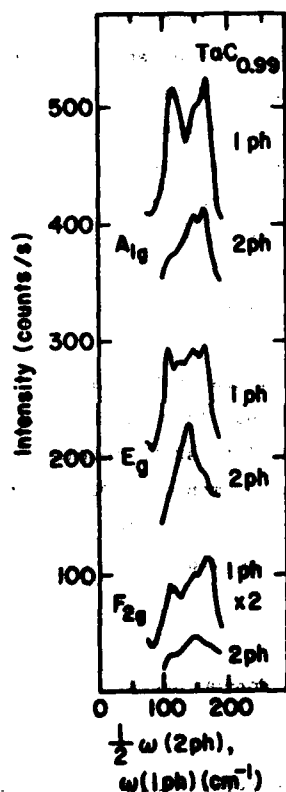


Fig. 2 Raman scattering from acoustic phonons in  $\text{TaC}_{0.99}$ . (Ref. 5) For each symmetry one and two phonon spectra are compared, the latter as a function of  $\omega/2$ .

An anomalous one-phonon Raman peak is shown in Fig. 3 for  $\text{V}_3\text{Si}$ .<sup>6</sup> This  $E_g(\Gamma_{12})$  mode "dimerizes" (100) chains of V-atoms. The frequency is lower than expected, and the mode softens and broadens upon cooling. The pronounced asymmetry suggests a Breit-Wigner-Pano type of anti-resonance. The solid lines in Fig. 3 represent a Lorentzian multiplied by an antiresonance factor superimposed on a linear background. Such an expression results when there is first-order Raman coupling both to the phonon and to a continuum, believed to be electronic, having a spectrum proportional to  $\omega$ , together with bilinear continuum-phonon coupling.<sup>6</sup>

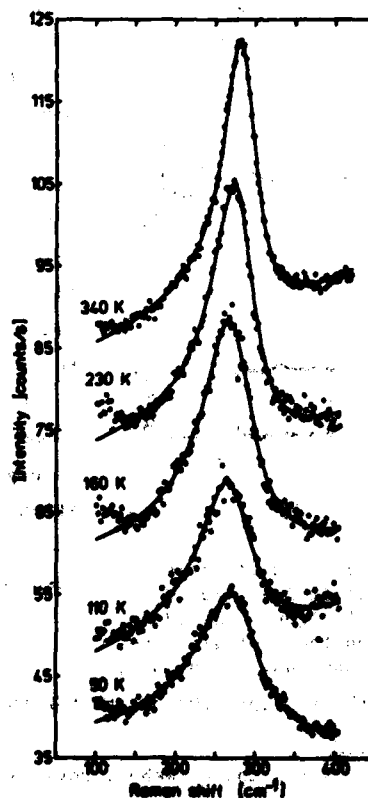


Fig. 3: The  $E_g$  Raman spectrum of  $\text{V}_3\text{Si}$  at five temperatures. (Ref. 6) Lines represent fits to a Lorentzian with anti-resonance.

A unified microscopic theory of all these effects has been presented<sup>3,7</sup>, starting with Kawabata's Greens function formalism for Raman scattering.<sup>8</sup> One must calculate essentially the imaginary part of an irreducible four-vertex function. Examples are shown in Fig. 4. The incident photon enters at vertices 1 and 4 and leaves at 2 and 3.

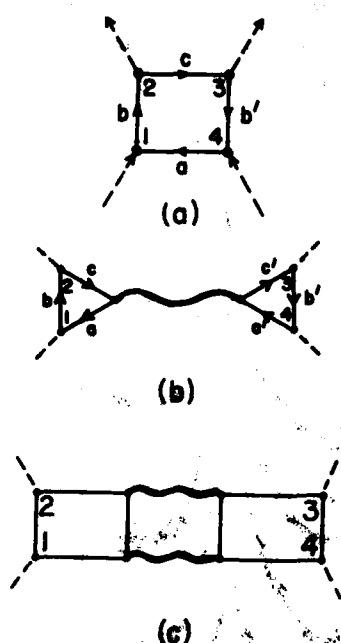


Fig. 4: Feynman diagrams for Raman scattering. Solid lines, electrons; dashed lines, photons; wiggly lines dressed phonons. (Refs. 3,7,8)

This work was supported by the NSF through the MRL grant DMR-80-20250.

#### References

1. C. M. Varma and W. Weber, Phys. Rev. B19, 6142 (1979).
2. P. F. Maldague and J. C. Tsang, in Proc. Int. Conf. Lattice Dynamics, ed. by H. Balkanski (Plenum Press, Paris, 1978).
3. M. V. Klein, Phys. Rev. B, to be published.
4. R. Sooryakumar, M. V. Klein and R. F. Frindt, Phys. Rev. B23, 3222 (1981).
5. H. Wipf, M. V. Klein and W. S. Williams, unpublished.
6. H. Wipf, et al., Phys. Rev. Lett. 41, 1752 (1978).
7. M. V. Klein, in Light Scattering in Solids, ed. by M. Cardona and G. Güntherodt, to be published by Springer-Verlag.
8. A. Kawabata, J. Phys. Soc. Japan 30, 68 (1971).
9. I. P. Ipatova and A. V. Subashiev, Sov. Phys. Solid State 18, 1251 (1976).
10. R. Merlin, et al., paper, this Conference.

LATTICE DYNAMICS OF  $YAl_2$  AND  $LaAl_2$  - A FURTHER CONTRIBUTION TO THE La-Y PUZZLE

C.T. Yeh\*, W. Reichardt, B. Renker, N. Nücker and M. Loewenhaupt\*\*

*Kernforschungszentrum Karlsruhe, Institut für Angewandte Kernphysik I, D-7500 Karlsruhe, Postfach 3640, F.R.G.**\*\*Institut für Festkörperforschung, Kernforschungsanlage Jülich, D-5170 Jülich, F.R.G.*

**Abstract.** - By means of inelastic-neutron scattering we have measured the phonon dispersion curves in the main symmetry directions of the cubic Laves phases  $YAl_2$  and  $LaAl_2$ . The phonon frequencies in  $LaAl_2$  are considerably softer than those of  $YAl_2$ , which cannot be explained solely by the different atomic masses of La and Y. The experimental dispersion curves are well described by axially symmetric Born v. Kármán models taking into account interactions up to the fifth nearest neighbors. From this analysis we find that the nearest neighbor Al-Al and TM-TM longitudinal force-constants of  $YAl_2$  are about twice those of  $LaAl_2$ , whereas the TM-Al interactions are nearly equal.

$YAl_2$  and  $LaAl_2$  belong to the group of cubic Laves-phases of type  $AB_2$ . In this structure the A-atoms form a diamond lattice. The remaining tetrahedral sites are occupied by regular tetrahedra of the B-atoms. The Bravais lattice is FCC, the primitive cell contains 6 atoms. Today more than 150 representatives of this structure are known, about 35 of which are superconducting. The motivations for our studies of  $YAl_2$  and  $LaAl_2$  are twofold: On one hand we want to have a better understanding of the lattice dynamics of such a common structure; on the other hand it is of interest that  $LaAl_2$  has a superconducting transition temperature of 3.2K whereas  $YAl_2$  is nonsuperconducting at least down to 0.34K<sup>1</sup>. Recently relations between superconducting and lattice dynamical properties have been studied for two other pairs of compounds:  $YB_6$  ( $T_c = 7.1K$ )- $LaB_6$  ( $T_c = .45K$ )<sup>2</sup> and  $YS$  ( $T_c = 2.8K$ )- $LaS$  ( $T_c = .84K$ )<sup>3,4</sup>. Note that in those cases the Y compounds have the higher  $T_c$  values. For  $YB_6$  the high  $T_c$  is correlated with a

	$M_{\text{Me}}$	$\theta_D$	$\left(\frac{M_{\text{MeAl}_2}}{M_{\text{YAl}_2}}\right)^{\frac{1}{3}} \cdot \theta_D$
$YAl_2$	88.91	484 <sup>a</sup> , 473 <sup>b</sup>	484, 473
$LaAl_2$	138.91	374 <sup>a</sup> , 352 <sup>b</sup>	435, 409
$PrAl_2$	157.25	399 <sup>a</sup>	485
$NdAl_2$	174.97	384 <sup>a</sup>	486

Table 1: Debye temperature of various  $MeAl_2$  compounds

<sup>a</sup> elastic constants <sup>b</sup> specific heat<sup>5</sup>

strong reduction of the translational phonon frequencies compared with  $LaB_6$ , whereas for  $YS$  and  $LaS$  almost identical dynamical forces have been found.

Calorimetric measurements<sup>5</sup> and investigations of the elastic constants<sup>6</sup> have shown, that the Debye temperature of  $LaAl_2$  behaves anomalously compared to other related nonsuperconducting compounds (see Table 1). After correcting the experimental  $\theta_D$ -values for their dependence on the molecular masses almost identical values are obtained for  $YAl_2$ ,

\*Present address : Institute of Atomic Energy, Academia Sinica, Peking, China

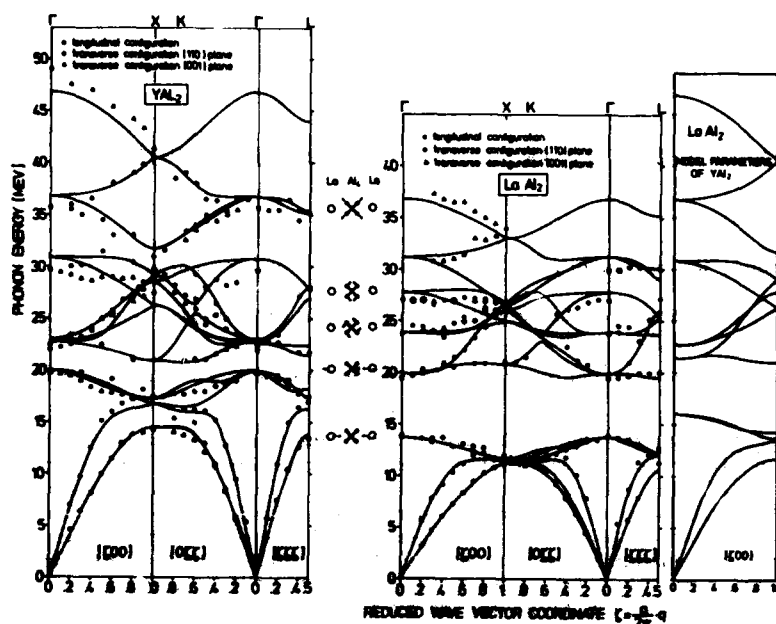


Fig. 1 Phonon dispersion curves of  $YAl_2$  and  $LaAl_2$  at 296K. Full curves were calculated with 10 parameter BvK models. For some  $\Gamma$  point frequencies the corresponding vibrational modes are indicated. The curves to the right were calculated with the parameters of  $YAl_2$  using the atomic mass of La.

$GdAl_2$  and  $LuAl_2$  whereas the values for  $LaAl_2$  are considerably lower.

We performed measurements of both the phonon densities of states and the phonon dispersion curves of  $YAl_2$  and  $LaAl_2$  at the Karlsruhe research reactor FR2 by means of inelastic neutron scattering. Fig. 1 shows the dispersion curves of  $YAl_2$  and  $LaAl_2$  at 296K in the three main symmetry directions. The full curves were calculated with a 10 parameter axially symmetric Born v. Kármán model fitted to the experimental data. The dashed lines indicate the slopes of the acoustic branches at the  $\Gamma$  point as calculated from the elastic constants<sup>6</sup>. The dispersion curves for the [100] direction on the right side of Fig. 1 have been calculated with the model parameters of  $YAl_2$  but using the atomic mass of La. By comparing this set of dispersion curves with the corresponding experimental data of  $LaAl_2$ , "trivial" effects caused by the different atomic masses of Y and La are eliminated. Besides the torsional mode at 24 meV all branches of  $LaAl_2$  are considerably lower.

Quantitative information about the interactions can be obtained from the parameters of the Born v. Kármán models which are listed in Table 2. The three longitudinal force-constants of the nearest neighbor interactions of Al-Al, Al-Me, Me-Me (Me=Y, La), respectively are dominant. They largely determine the positions of the various phonon branches. For  $YAl_2$  the force-constants for the Al-Al and Y-Y interactions are about twice as large as the corresponding values of  $LaAl_2$ . In contrast the Al-Me force-constants are about equal for the two compounds. The Table gives also the inverse third moment of the phonon densities of states calculated from the models.

INTER-ACTION	$r/a_0$		LaAl <sub>2</sub>	YAl <sub>2</sub>
Al-Al	.3536	F	15221	25117
		G	990	119
Me-Al	.4146	F	10869	11289
		G	-389	267
Me-Me	.4330	F	10230	22666
		G	2149	1131
Al-Al	.6124	F	1932	1360
		G	-65	126
Me-Al	.6494	F	3358	3374
		G	279	422
$\theta_{-3}$ (300K) model			372	493
$\theta_{-3}$ (300K) el. const.			369	475
$\theta_{-3}$ (0) spec. heat			352	473

Table 2: Force-constants [in dyn/cm] of axially symmetric Born v. Kármán models for LaAl<sub>2</sub> and YAl<sub>2</sub>.

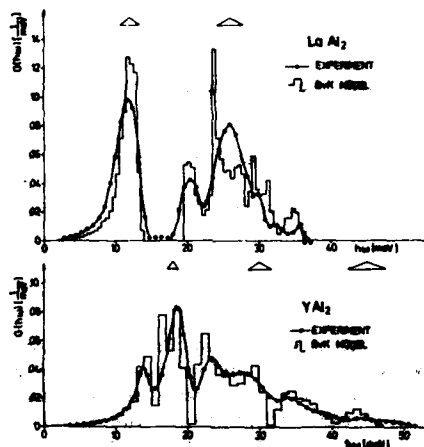


Fig. 2 Generalized phonon density of states determined from neutron scattering experiments and from models fitted to the experimental dispersion curves.

They agree well with those values obtained from the elastic constants. The comparison with the Debye temperatures from calorimetric measurements seems to indicate that the phonon densities of states do not change much between 0K and 300K. However, discrepancies exist between the calculated and experimental specific heats in the temperature range between 5 and 20K which might be explained by a phonon softening outside the elastic region at low temperatures. In Fig. 2 we compare the generalized phonon densities of states calculated from our models with those determined from scattering law measurements using powder samples. From recent bandstructure calculations of Hasegawa and Yamase<sup>7</sup> we must conclude that the anomalously soft phonon spectrum of LaAl<sub>2</sub> is not caused by the influence of f-electrons. The f-bands of LaAl<sub>2</sub> lie about 3 eV above the Fermi energy  $E_F$  and the f-components in the electron states near  $E_F$  are less than 10%. Below  $E_F$ , the bandstructures of LaAl<sub>2</sub> and YAl<sub>2</sub> are very similar, only close to  $E_F$  there are some differences which according to these authors are caused by a stronger p-d hybridization in the case of LaAl<sub>2</sub>. Whether these differences account for the occurrence of superconductivity and explain the rather soft phonon spectrum of LaAl<sub>2</sub> cannot be answered at present.

<sup>1</sup> B.W. Roberts, J. Phys. Chem. Ref. Data, Vol 5, No 3 (1976)

<sup>2</sup> G. Shell, N. Winter, R. Rietchel and P. Gompf, to be published.

<sup>3</sup> P. Reichardt, W. Reichardt and P. Holtzberg, Phys. Rev. Lett. **40**, 465 (1978)

<sup>4</sup> W. Reichardt, P. Reichardt and P. Holtzberg, KFK Report 267a, p. 1 (1978)

<sup>5</sup> R.F. Swenson and R.N. Goshwami, J. Phys. Chem. Solids **33**, 461 (1972)

<sup>6</sup> R.J. Smith and J.F. Smith, J. Appl. Phys. **45**, 4681 (1974)

<sup>7</sup> A. Hasegawa and A. Yamase, J. Phys. F **10**, 847 (1980) and J. Phys. F **10**, 2207 (1980)

## THE PHONON SPECTRUM EMITTED BY SUPERCONDUCTING Sn TUNNEL JUNCTIONS

P. Berberich and H. Kinder

*Physik-Department, Technische Universität München, D-8046 Garching, F.R.G.*

**Abstract.** - The phonon spectra emitted by superconducting tunnel junctions were directly analyzed with high resolution using tunable acceptor states of B in Si as a spectrometer. A consistent and detailed experimental picture of the different parts of the spectra under various injection conditions was obtained for the first time.

Tunnel injection of electrons into superconductors leads to energetic quasiparticles which relax by phonon emission. This is not only a subject of the growing field of "nonequilibrium superconductivity"/1/ but particularly also the basis for phonon spectroscopy/2/. There was a lot of indirect evidence for various parts of the emitted phonon spectrum/3/4/, and there were two attempts of direct spectral analysis/5/6/. But the information obtained to date was only qualitative.

In this paper we present the first quantitative measurements of the phonon spectra of superconducting junctions, revealing the shape of the recombination peak, the contribution of direct recombination, the "bremsstrahlung" or "relaxation" phonons and their reabsorption at  $\hbar\omega > 2\Delta$ , and a "background" which was not yet directly observed.

For the spectral analysis, we used the technique of "burning a hole" by resonance scattering into the spectrum of the emitted phonons on their way to the detector/7/5/. Stress tuned boron acceptors in silicon were used as resonant scatterers for the first time. These have several advantages over previous systems, e.g. Ge:Sb /5/: (i) Silicon as the host material is known to be "transparent" for ballistic phonons up to very high frequencies; (ii) the acceptor state has no "chemical shift", forming a true 2-level-system that splits strictly proportional to the applied uniaxial stress; (iii) we observe simple first order scattering which allows a quantitative interpretation of the results; (iv) the frequency resolution was improved by a factor of 10.

A Si crystal/8/ of dimensions  $2.5 \times 4 \times 15 \text{ mm}^3$ , containing  $5 \times 10^{13} \text{ cm}^{-3}$  B was used as the spectrometer. A Sn-oxide-Sn generator junction was evaporated on one  $4 \times 15$  side, an Al-oxide-Al detector junction on the opposite side. The phonon path was in  $[1\bar{1}0]$  direction. Uniaxial stress was applied perpendicularly, in  $[111]$  direction, and was monitored by a Kistler cell/9/. The apparatus for pressure generation was described by Bridges and Zoller/10/. The sample was immersed in liquid helium at 1.0 K.

In all experiments shown here we studied the "differential spectrum" of the Sn-junction which was generated in the usual way/2/ by small pulses superimposed to the dc bias voltage. The spectrum was kept constant while the resonance frequency of the acceptors was swept by stress. Only the fast transverse phonon pulse was detected because of phonon focusing. In Fig. 1, the height of this pulse is shown as a function of stress at various bias voltages as indicated. Generally, the signal is constant at low pressures, and then dips down because the phonons of the corresponding frequencies are being scattered away from their path into the detector. Eventually the signal recovers when the splitting becomes larger than any phonon frequency.

Interestingly, the signal has exactly the same height at large splitting and at zero splitting (see dashed lines) in all our experiments. At zero splitting, hence,



there is also no scattering. This is in marked contrast to donors/5/. We conclude that higher order processes are insignificant here/11/, so that the scattering can be simply described by first order resonant scattering according to the golden rule/12/:

$$I^{-1}(E, \sigma) = N \frac{\pi}{\hbar \rho v^3} M^2 E g(E - D\sigma) \quad (1)$$

for  $kT \ll E$ , where  $l$  is the phonon mean free path,  $N$  the acceptor concentration,  $E$  the phonon energy,  $\rho$  the density,  $v$  the sound velocity,  $M^2$  the coupling constant, and  $g(E - D\sigma)$  the normalized line shape function whose center frequency is given by stress  $\sigma$  times deformation potential  $D$ . For  $l$  greater than the crystal length, the signal change is proportional to  $n(E)l^{-1}(E - D\sigma)$  where  $n(E)$  is the emitted phonon power spectrum, provided the detector signal is proportional to the incident power/9/. Therefore, the deviation of the signal from 100% is essentially a direct measure of the spectrum, weighed by the factor  $E$  from (1).

Trace (a) shows the differential emission spectrum of a Sn junction ( $1\text{mm} \times 1\text{mm} \times 4\mu\text{m}$ ;  $R_{\infty} = 20\text{m}\Omega$ ) biased at the gap voltage 1.19 mV. There is a pronounced peak in the spectrum corresponding to  $2\Delta$ -phonons/3/. This peak is not symmetric but has a tail to higher frequencies. The tail can be fitted by the "extended  $T^*$  model" of Chang, Lai and Scalapino/13/ by using  $T^* = 1.1\text{ K}$  (dashed curve) while the bath was at  $T_A = 1.0\text{ K}$ . The rounding of the peak at the low frequency side is merely due to the spectrometer resolution. There is also a broad background of phonons with lower frequencies which will be discussed below.

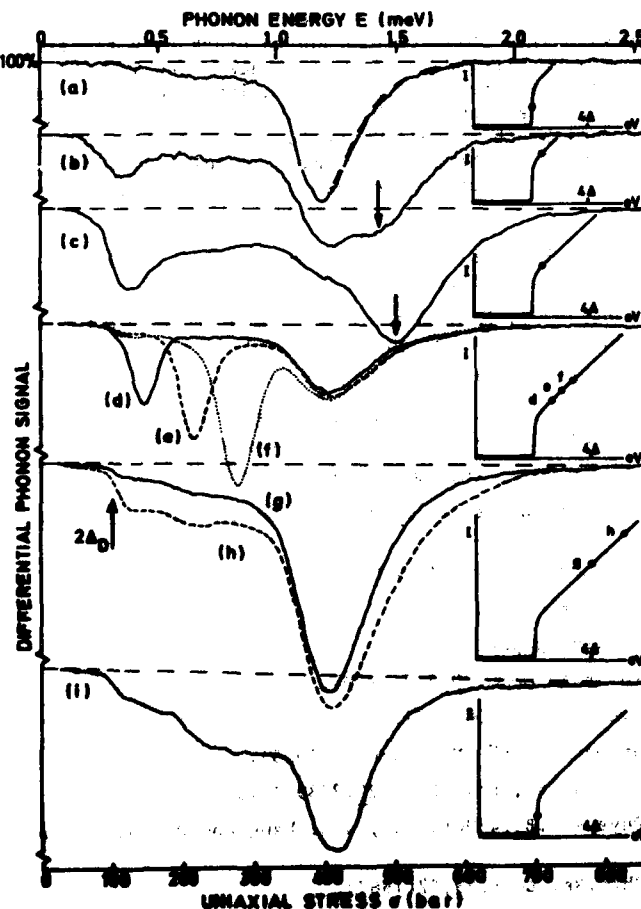


Fig. 1:

Negative replicas of phonon spectra emitted from Sn-junctions under indicated injection conditions. For details, see text.

In trace (b), the bias was increased to 1.4 mV. The differential spectrum now clearly reveals an additional peak (arrow) corresponding to  $\hbar\omega = eV$ . These phonons arise from direct recombination of the injected quasiparticles at  $E = eV - \Delta$  with thermal ones ( $E = \Delta$ )/14/. The peak is even predominant in trace (c) which was obtained from a similar junction with a lower resistance  $R_0 = 3.6 \text{ m}\Omega$ . The increased injection leads in this case to an increased steady state number of quasiparticles, making the recombination more probable/15/ than the down scattering to the gap edge ("relaxation"). The background of low frequency phonons is enhanced in traces (b) and (c) and therefore reflects very clearly the cutoff of the detector sensitivity below the gap  $2\Delta_D$ .

The traces (d), (e), and (f) were obtained from the first junction ( $R_0 = 20 \text{ m}\Omega$ ) at 1.6 mV, 1.8 mV, and 2 mV, respectively. The recombination phonon peak is obviously shifted back to  $2\Delta$ . This shows that the relaxation of quasiparticles at higher energies is faster than the direct recombination. Only  $T^* = 1.5 \text{ K}$  is now somewhat increased. As the result of the fast relaxation, the "bremsstrahlung" peaks/2/ at  $eV - 2\Delta$  have appeared. Their apparently increasing strength is due to the spectrometer weight factor  $E$  in (1). The width of the peaks is mainly determined by the spectrometer width which is increasing with stress due to stress inhomogeneity/9/. From the position of the bremsstrahlung peaks we get an accurate calibration of the stress scale which is indicated on top of Fig.1. Traces (g) and (h) were taken at 2.4 mV and 2.9 mV. Clearly the bremsstrahlung peak is now adding to the  $2\Delta$ -peak, revealing the reabsorption of the bremsstrahlung phonons at  $\hbar\omega > 2\Delta$ . However,  $T^*$  has increased to 1.6 K and 1.7 K, respectively.

Whenever there are quasiparticles in states well above the gap, the background of low frequency phonons is markedly enhanced. This can be seen from traces (b), (c) and particularly (h) in comparison with (g). This corresponds to black body radiation of these "hot" quasiparticles/13/. However, there is also some background in trace (a) where the quasiparticles are "cold". By changing the evaporation conditions (less clean/9/) we were able to enhance this background of the "cold" junction appreciably, as shown in trace (i) for a junction with otherwise similar specifications as that of trace (a). This background may be related to the loss mechanism postulated by Trumpp and Eisenmenger/16/ from a discrepancy of the calculated and observed  $2\Delta$ -phonon yield

#### REFERENCES

- /1/ Nonequilibrium Superconductivity, Phonons, and Kapitza Boundaries, ed. by K.E.Gray, NATO Adv.Study Inst.Ser.B., (Plenum Press 1981), Vol.65.
- /2/ H.Kinder, Phys.Rev.Lett.28,1564(1972); H.Kinder in: Low Temperature Physics, LT14, ed. by M.Krusius and M.Vuorio (North Holland 1975), Vol.V, p.287.
- /3/ W.Eisenmenger and A.H.Dayem, Phys.Rev.Lett.18,125(1967).
- /4/ W.Eisenmenger in: Physical Acoustics, ed. by W.P.Mason and R.N.Thurston (Acad. Press 1976), Vol.XII, p.79; M.Welte and W.Eisenmenger, Z.Phys.B41,301(1981).
- /5/ R.C.Dynes, V.Narayanamurti, and M.Chin, Phys.Rev.Lett.26,181(1971).
- /6/ W.Dietsche in: Phonon Scattering in Condensed Matter, ed. by H.J.Maris (Plenum Press 1980), p.309.
- /7/ J.P.Morton and H.M.Rosenberg, Phys.Rev.Lett.8,200(1966).
- /8/ Wacker Chemitronics, Burghausen, W.-Germany.
- /9/ Details are given in a forthcoming paper.
- /10/ F.Bridges and W.Zoller, Solid State Comm.30,717(1979).
- /11/ K.Suzuki and N.Mikoshiba, Phys.Rev.B3,2550(1971).
- /12/ See, e.g. L.I.Schiff "Quantum Mechanics" (McGraw-Hill 1955).
- /13/ J.J.Chang, W.Y.Lai, and D.J.Scalapino, Phys.Rev.B20,2739(1979).
- /14/ A.H.Dayem and J.J.Wiegand, Phys.Rev.B5,4390(1972); J.J.Chang and D.J.Scalapino, J.Low Temp.Phys.31,1(1978).
- /15/ A.Rothwarf and B.N.Taylor, Phys.Rev.Lett.19,27(1967).
- /16/ H.J.Trumpp and W.Eisenmenger, Z.Phys.B28,159(1977).

## THE LOCAL PHONON DENSITY OF STATES AND ITS INFLUENCE ON SUPERCONDUCTING PROPERTIES

G.B. Arnold and M. Menon

Univ. of Notre-Dame, Dept. of Physics, Notre-Dame, IN 46556, U.S.A.

**Abstract.** We have calculated the local phonon density of states and local electron-phonon coupling parameters for a thin metal film backed by a semi-infinite metal substrate, using the Montroll-Potts model. We find that only a small enhancement of the local electron-phonon coupling in the film can be produced by the coupling of the film lattice to the substrate. Consequently, the local density of states in the thin film is like that of the isolated film, except for some smearing of sharp structure, and a general downward shift in frequency of the gross features.

In this paper, we will consider the effect of a semi-infinite film (S) on the local phonon density of states in a thin (2l layers) film (T), and determine whether S can thereby influence the electron-phonon interaction (EPI) in T. Only the case for which S and T are good metals will be considered.

The electron-phonon coupling strength is measured by the McMillan parameter<sup>1</sup>

$$\lambda = 2 \int_0^\infty \alpha^2(u) F(u) / u \quad (1)$$

where  $\alpha^2(u)$  is a convolution of the electron band density of states and the square of EPI matrix elements, and  $F(u)$  is the phonon density of states. One can similarly define a local strength parameter for the  $n^{\text{th}}$  layer of a metal film

$$\lambda_n = 2 \int_0^\infty du \alpha^2(u, n) F(u, n) / u \quad (2)$$

In this paper we shall focus on the local phonon density of states for the  $n^{\text{th}}$  layer of metal film T,  $F_T(u, n)$ . In order to determine the effect of changes in  $F_T(u, n)$  on the local EPI coupling, we shall approximate  $\alpha^2(u, n)$  by a frequency independent parameter  $\alpha_n^2$ .

Because of the locality of the screened EPI and Coulomb interaction, one can also define a local pair potential in the thin film as the ratio  $\Delta_T(u, n) = \bar{\Delta}_T(u, n) / Z_T(u, n)$  where  $\bar{\Delta}_T(u, n)$  is the pairing self energy and  $Z_T(u, n)$  is the renormalization function in T, each depending on the local  $\alpha_n^2 F_T(u, n)$ .<sup>2</sup>

For simplicity, we have adopted the Montroll-Potts model<sup>3</sup> for the phonons. We have further assumed that both S and T lattices are simple cubic with equal lattice constants, and that the lattices are aligned, with interface perpendicular to the

[100] direction. The method of Maradudin and Wallis,<sup>4</sup> as applied by Dobryznski and Mills<sup>7</sup> then allows the exact phonon Green's function in T to be calculated. The effective spring constant of the interface plane is K, and the spring constants for S and T are  $K_S$  and  $K_T$ . We define an effective coupling parameter  $\gamma = K^2/(K_S K_T)$ . The ratio of the maximum phonon frequency in T to that in S is denoted by R.

The results for the transmission coefficient,  $|t|^2$ , for phonons normally incident from T is shown in figure (1). One can show analytically that  $|t|^2$  is a maximum for any  $\omega$  when  $\gamma=1$ . Phonons of all frequencies in T can be transmitted to S only if the maximum phonon frequency in T is less than that in S, i.e.,  $R < 1$ .

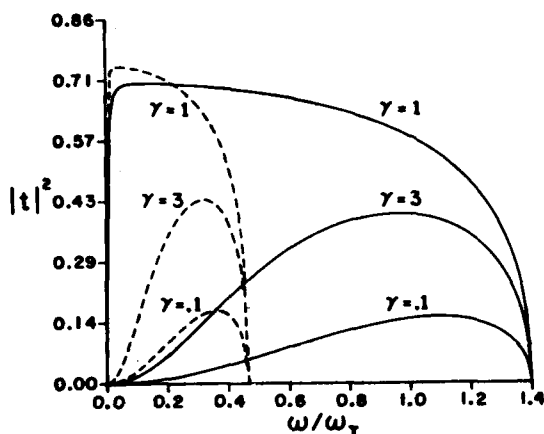


Fig. 1. Transmission coefficient  $|t|^2$  vs. frequency for an interface between two materials with various values of coupling,  $\gamma$ . The dashed curves are for  $R=3$ , the solid curves are for  $R=.30$ . The frequency  $\omega_T = (2K_T/M_T)^{1/2}$ ,  $M_T$  being the atom mass for T.

In figure (2) we compare the total density of states in bulk T material to that in an isolated ( $\gamma=0$ ) T metal film. In general,  $\omega_T F_T(\omega)$  is shifted down in frequency for the bulk ( $\gamma=1$ ,  $R=1$ ) case, but, even so,  $\omega_T(\lambda/2a^2) = .640$  for the isolated film, .643 for the bulk metal, a negligible difference.

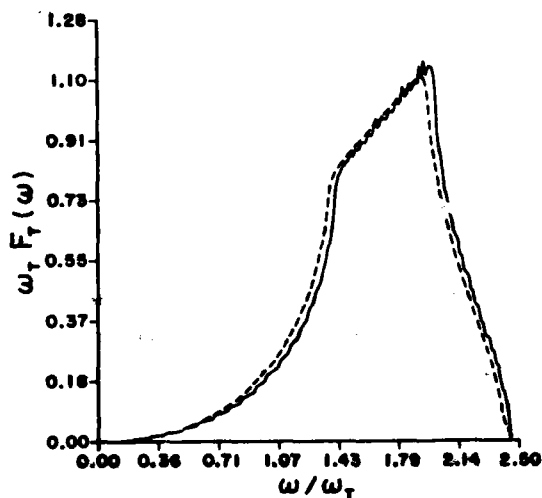


Fig. 2. Total density of states for bulk T material (dashed line) compared with same for 21 layer film of T material (solid line).

In figure (3) we compare the local density of states in T for the case of weak transmission ( $\gamma=.1$ ,  $R=3$ ) to that for optimal transmission ( $\gamma=1$ ,  $R=.3$ ). The ST

interface lies between the layers  $m=-1$  and  $m=0$ .

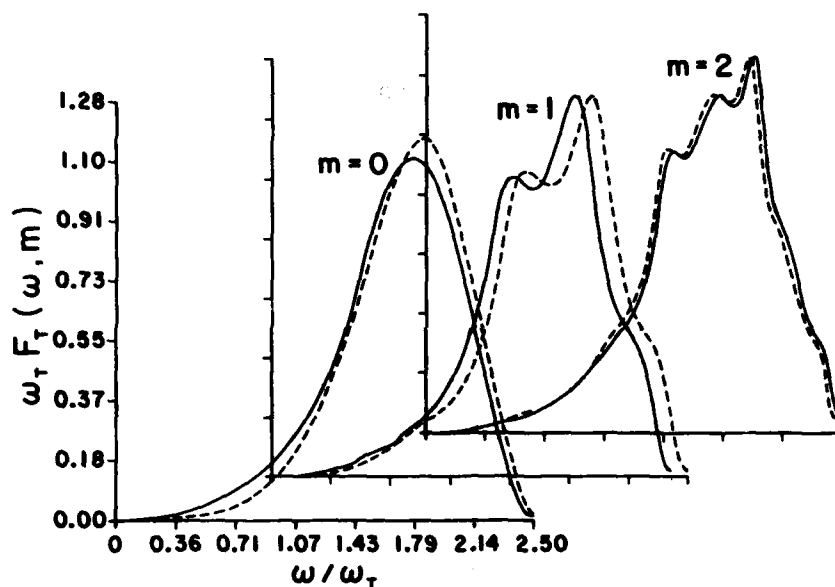


Fig. 3. Local density of states for  $R=3$  (solid lines) compared to same for  $R=3$  (dashed lines).

For optimal coupling of S and T we find local EPI parameters  $\Lambda_m = \lambda_m / (2a_m^2) = .649$  ( $m=0$ ),  $.644$  ( $m=1$ ),  $.644$  ( $m=2$ ). For weak ST coupling  $\Lambda_m = .623$  ( $m=0$ ),  $.639$  ( $m=1$ ),  $.642$  ( $m=2$ ). The difference is greatest at the ST interface, rapidly diminishing as one moves away into T.

These results show that the local pair potential in T will have energy dependence which is quite different from the bulk T dependence, but very much like that predicted for the isolated T metal film except for downward shifts in frequency and some smearing of peaks. In addition, the local energy gap value (determined by  $\lambda_m$  and  $\mu_m^*$ ) will differ negligibly from its value for the isolated film. Thus, even under optimal conditions, the coupling between the T lattice and the S lattices provides little enhancement of local superconducting properties in a T metal film of this thickness (21 layers). We have also verified this conclusion for a T metal film consisting of only four atomic layers, where we have found that  $\Lambda_m = .648$  ( $m=0$ ),  $.643$  ( $m=1$ ),  $.639$  ( $m=2$ ),  $.622$  ( $m=3$ ).

This work was supported by NEF grant DMR80-19739.

#### References

1. V.L. McMillan, Phys. Rev. **167**, 331 (1968).
2. Gerald B. Arnold, Phys. Rev. **B22**, 1171 (1981).
3. R.W. Montzall, R.B. Fette, Phys. Rev. **102**, 72 (1956).
4. A.A. Maradudin, R.F. Wallis, Phys. Rev. **148**, 945 (1966).
5. Leonard Dobrzynski, D.L. Mills, J. Phys. Chem. Solids. **30**, 1043 (1969).

## PHONON DISPERSION AND THERMOPHYSICAL PROPERTIES OF SODIUM

O.P. Gupta

Physics Department, J. Christian College, Allahabad, India.

**Abstract.**— An equilibrium condition, which preserves the crystal stability, is derived. This condition in conjunction with recent dynamical model is employed to study the phonon dispersion and thermophysical properties of Na. The theoretical results are in good agreement with the experimental values.

1. **Introduction.**— Sodium is believed to represent in many respects the prototype of a free electron metal. The experimental results on elastic constants [1,2] and their pressure derivatives [1,3-5], specific heat [6-10], Debye-Waller (DW) factor [11], and thermal expansion [1,4,12-14] can be used to test the reasonableness of the interpretation in terms of the free electron model of Na. In the present paper, we report the phonon dispersion, and temperature dependence of Debye temperature  $\Theta$ , DW factor, and Grüneisen parameter  $\gamma$  of Na on the basis of recent dynamical model [15] in conjunction with an equilibrium condition. The condition, which preserves the crystal stability, is derived by considering Fermi, exchange, and correlation energy of conduction electrons.

2. **Model.**— For equilibrium, the first derivative of the potential energy  $E$  ( $= E^i + E^e$ ) of the crystal must vanish, i.e.,

$$(dE^i/d\Omega)_a - P^e = 0, \text{ where } -P^e = dE^e/d\Omega, \quad (1)$$

where  $\Omega$  is crystal volume,  $P^e$  the electron pressure,  $E^i$  the potential energy due to ion-ion interaction, and  $E^e$  the electron energy. The Fermi, exchange, and correlation [16] parts of  $E^e$  can be written as :

$$E^e = [2.21 z^{2/3} (r_0/a_0)^{-2} - 0.916 z^{1/3} (r_0/a_0)^{-1} + 0.622 \ln(r_0/a_0 z^{1/3}) - 0.096] \quad (2)$$

The equilibrium condition Eqn.(1) with the aid of Eqn.(2) takes the form:

$$A_1 + A_2 = \frac{27.2 a}{\pi r_0} \left[ -\frac{4.41 z^{2/3}}{(r_0/a_0)^2} + \frac{0.916 z^{1/3}}{(r_0/a_0)} + 0.622 z^{-1/3} \right] \quad (3)$$

where  $a_0$  is the Bohr radius,  $z$  the chemical valence,  $r_0$  the inter electron spacing, and  $A_j$  ( $j = 1, 2$ ) are tangential pair potential force constants. Solution of Eqns. (12-15) [15], (3) determine the unknown force

constants in terms of elastic constants  $C_{ij}$  and one ZB frequency.

3. Numerical Computation.— Experimental values of  $C_{ij}$  and other parameters at 90 K used in calculations are:  $C_{11} = 0.808$ ,  $C_{12} = 0.664$ ,  $C_{44} = 0.586$  (all in units of  $10^{11} \text{ dyn cm}^{-2}$  [1],  $a = 4.24 \text{ \AA}$ , density =  $1.0014 \text{ gm cm}^{-3}$ ,  $\nu_T(100) = 3.58 \text{ THz}$  [17], and  $(m^*/m) = 1.0$  [18]. The calculated values of the force constants are:  $A_1 = 2.792$ ,  $B_1 = -1.923$ ,  $A_2 = 0.021$ ,  $B_2 = -5.301$ , and  $ake = 11.588$  (all in units of  $10^3 \text{ dyn cm}^{-1}$ ). The phonon dispersion, lattice specific heat, and DW factor are calculated as usual [15]. To calculate  $\gamma$ , we follow our paper [19]. In the present scheme the four parameters ( $A_1$ ,  $A_2$ ,  $B_1$ ,  $B_2$ ) are reduced to three ( $A_1$ ,  $B_1$ ,  $B_2$ ) by taking a suitable ratio of  $A_1/A_2$  which gives a better fit of phonon dispersion. In the present calculations, we use  $dC_{ij}/dT$  values borrowed from recent papers [1, 3-5], and temperature dependent values of  $C_{ij}$  [2] and lattice parameter [20].

4. Results and Discussion.— We display our theoretical results for phonon dispersion along with the experimental values [17] in Fig. 1. The agreement between theory and experiment is very good. Lattice specific

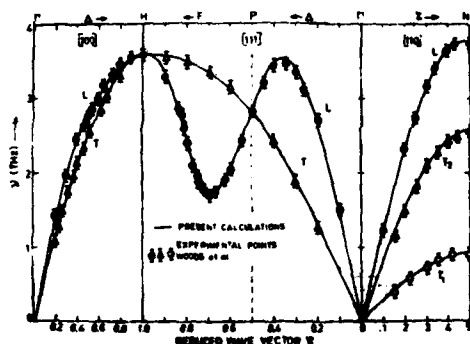


Fig. 1: Phonon dispersion curves of Na along the symmetry directions.

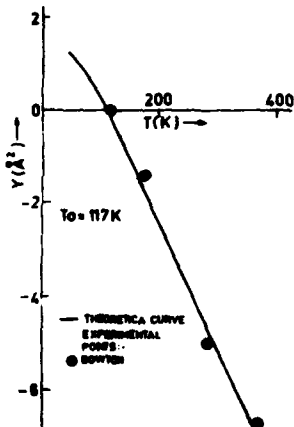


Fig. 3: DW factor of Na as a function of temperature.

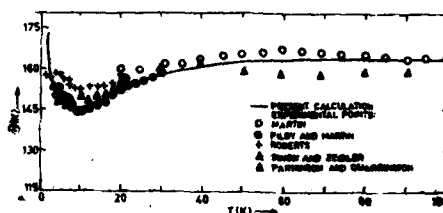


Fig. 2: Debye temperature of Na as a function of temperature.

heat extracted from experiments [6-10] and our theoretical results are converted in  $\Theta_D$ . These are plotted in Fig. 2. The theory

exhibits good agreement with the experiments down to 10 K. The various measurements are not very concordant with one another. Crystallographic transformation [21, 22] from bcc to hcp lattice phase around 35 K causes uncertainty in the experimental measurements and affects our comparison. In Fig. 3, the calculated DW factors along with the experimental points of Dawton [1] are shown. The agreement between theory and experiment is good. Fig. 4 exhibits the calculated values of  $\gamma$  along with the

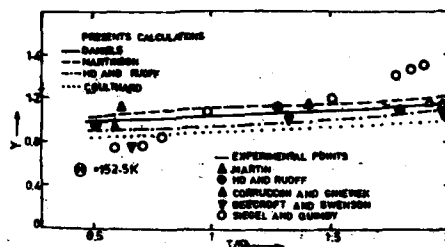


Fig.4: Grüneisen parameter of Na as a function of temperature.

values derived from the experimental measurements of thermal expansion [1,4,12-14] and specific heat [a] data. It is shown from the Fig. 4 that the general shape of the theoretical and experimental  $\gamma$ - $T$  curves is similar in spite of the fact that the measured values are not very concordant with one another. It is disconcerting to find that how

much the theoretical results deviate from the experimental points due to large scatter in experimental values. Our results corroborate the Barron's [23] prediction that  $\gamma$  remains constant to a few percent down to about  $\Theta/3$ .

The present study demonstrates that the simple model provides a good overall understanding of phonon dispersion and thermophysical properties of Na.

#### References

- [1] Daniels, W.B., Phys. Rev. **119** (1960) 1246; Quimby, S.L. and Siegel, S., Phys. Rev. **54** (1938) 293, 76.
- [2] Diederich, M. and Trivisonno, J., J. Phys. Chem. Solids **27** (1966) 637.
- [3] Martinson, R.H., Phys. Rev. **178** (1969) 902.
- [4] Ho, P.S. and Ruoff, A.L., J. Phys. Chem. Solids **29** (1968) 2101.
- [5] Coulthard, M.A., J. Phys. **C3** (1970) 820.
- [6] Roberts, L.M., Proc. Phys. Soc. **B70** (1957) 744.
- [7] Filby, J.D. and Martin, D.L., Proc. R. Soc. **A276** (1963) 187.
- [8] Martin, D.L., Proc. R. Soc. **A254** (1960) 433.
- [9] Simon, F. and Zeidler, W., Phys. Chem. **123** (1926) 383.
- [10] Perkinson, D.H. and Quarrington, J.E., Proc. Phys. Soc. **A68** (1955) 762.
- [11] Dawton, R.H.V.M., Proc. Phys. Soc. **49** (1937) 294.
- [12] Beecroft, R.I. and Swenson, C.A., J. Phys. Chem. Solids **18** (1961) 329.
- [13] Martin, D.L., Phys. Rev. **139** (1965) A150.
- [14] Corruccini, R.J. and Gniewek, J.J., Thermal Expansion of Technical Solids at low Temperatures, NBS. Washington (1961).
- [15] Gupta, O.P. and Hemkar, M.P., Il Nuovo Cimento **45B** (1978) 255.
- [16] Gellman, M. and Brueckner, K.A., Phys. Rev. **106** (1957) 364.
- [17] Woods, A.D.B., Brockhouse, B.N., March, R.H., Stewart, A.T. and Bowers, R., Phys. Rev. **128** (1962) 1112.
- [18] Weaire, D., Proc. Phys. Soc. **92** (1967) 956.
- [19] Kharoo, H.L., Gupta, O.P. and Hemkar, M.P., J. Phys. Chem. Solids **39** (1978) 45.
- [20] Pearson, W.B., A Handbook of Lattice Spacings and Structure of Metals and Alloys (Pergamon; NY, 1958).
- [21] Barret, C.S., Acta Cryst. **9** (1956) 671.
- [22] Stern, E.A., Phys. Rev. **121** (1961) 397.
- [23] Barron, T.H.K., Phil. Mag. **46** (1955) 720; Ann. Phys. (U.S.A.) **1** (1957) 77.



ON THE THERMAL AND ELECTRICAL CONDUCTIVITY OF  $V_3Si$  AND  $V_5Si_3$ 

A.F. Khoder, M. Couach, M. Locatelli, M. Abou-Ghantous\* and J.P. Senateur \*\*

*Service des Basses Températures, Laboratoire de Cryophysique, Centre d'Etudes Nucléaires de Grenoble, 85 X-38041 Grenoble Cedex, France.**\*Faculté des Sciences, Université Libanaise, Al-Hadet, Liban**\*\*ER 165, ENSIEG, BP 46, 38042 St Martin d'Hères, France.*

**Abstract.** - Thermal conductivity and electrical resistivity measurements have been performed on  $V_3Si$  and  $V_5Si_3$  single crystals. Thermal conductivity anomalies are observed on both compounds and seem likely to be related to the resistivity "saturation" behaviour exhibited by these two compounds.

**Introduction.** - It is known that the electrical resistivity of a "d" band compound (transition elements and their alloys) deviates from linearity at high temperature exhibiting a negative curvature.

Several interpretations as anharmonicity, Fermi Smearing, T dependent band structure, phonon ineffectiveness etc. (1) were proposed to explain such a behaviour.

In this paper we report and discuss results of the electrical and the thermal conductivity measurements performed on two extremely different compounds belonging to the Vanadium-Silicon system :  $V_3Si$ , an A15 compound with a high superconductivity temperature ( $T_c = 17$  K) and  $V_5Si_3$  which is normal down to 0.2 K.

Finally a correlation between these two transport properties is outlined for these compounds.

**Experimental results.** - Figure 1 shows the resistivity of  $V_3Si$  and  $V_5Si_3$  as a function of temperature, both of these curves displaying the classical saturation phenomenon. The temperatures where a change of curvature can be observed, are respectively 82 K for  $V_3Si$  and 130 K for  $V_5Si_3$ .

Recently it has been shown that the thermal conductivity of  $V_3Si$  (2) is mainly due to the electrons (Fig.2) whereas that of  $V_5Si_3$  is partly due to the phonons. In this later case this dependence appears clearly by plotting  $K \cdot \rho / T$  as a function of T (Fig.3) and shows that the contribution of the phonons which reaches a maximum at 20 K, is important around this temperature. In fact it appears difficult in the case of  $V_5Si_3$  to separate quantitatively the two contributions of electrons and phonons and one has to consider qualitative arguments in this particular case. The thermal conductivity goes through a minimum for  $V_3Si$  (Fig.2) like for  $V_5Si_3$  (Fig.4). In the case of  $V_3Si$  the temperature of this minimum  $T_m$  is the same as the temperature of the inflexion point in the  $\rho(T)$  curve. For  $V_5Si_3$ , the conductivity due to phonons decreases at high temperature because of the occurrence of anharmonic and umklapp process and then the increase of  $K(T)$  after  $T_m$  is essentially due to the electrons. More

precisely for this compound the temperature  $T_m$  of the minimum of  $K(T)$  (150 K) differs slightly from the temperature of the inflexion point on the resistivity curve (130 K). This would be a consequence of the important contribution of the phonons in the thermal conductivity for the temperature range investigated.

**Discussion.** - The semi classical treatment of Wilson (3) involves a minimum to occur in the thermal conductivity but it is likely that such a treatment is not realistic for complex compounds as  $V_3Si$  and  $V_5Si_3$ . Furthermore the behaviour of the resistivity cannot be explained satisfactorily in the framework of a semi classical theory of transport phenomena. The empirical relation of Wiesmann et al (4)

$\frac{1}{\rho} = \frac{1}{\rho_{ideal}} + \frac{1}{\rho_{max}}$  (parallel resistor) takes into account the occurrence of the saturation phenomena where  $\frac{1}{\rho_{max}}$  appears as an excess of electrical conductivity arising at high temperature. Similarly the increase of the thermal conductivity after the minimum can be understood as an excess of thermal conductivity.

Correlating the simultaneous increase of both conductivities, we suggest that such a behaviour could be explained by a growing "collectivization" of "d" electrons (5) as the temperature increases beyond  $T_m$ . This phenomenon could be interpreted as a continuous delocalization of the "d" electrons in the conduction band leading to an increase of the number of carriers contributing to the observed excess of both conductivities. For the compound  $V_3Si$ , experimental evidence of charge transfer and its redistribution with temperature has been obtained (6). Such a general process can take into account the existence of an inflexion point in the resistivity curve of transition metals and their alloys ( $Al_{1-x}Nb_x$ ,  $V$ ,  $La$ ,  $Zr_2Rh$ ,  $V_5Si_3$ , etc...) and the above correlation appears to have a general validity extending to other systems than those presently studied (7).

Moreover in the low temperature range,  $V_3Si$  and  $V_5Si_3$  exhibit a quite different behaviour : - the resistivity of  $V_3Si$  behaves as  $\rho = a + bT^n$  with  $n = 2$  contrarily to that of  $V_5Si_3$   $\rho = c + dT^m$  with  $4 < m < 5$

- in the case of  $V_3Si$  the electrons are responsible of the thermal conductivity (2) whereas for  $V_5Si_3$  an important part of this property is due to the phonon. These differences emphasize the importance of a particular electron phonon interaction related to the occurrence of superconductivity in  $V_3Si$ .

**Conclusion.** - It has been shown that at high temperature a correlation arises between the thermal and the electrical conductivity for the two compounds  $V_3Si$  and  $V_5Si_3$ . It seems likely that such a correlation could be extended to other alloys based on transition elements. These studies are in progress and more details will be published elsewhere.

**Acknowledgments :** We wish to thank Dr B.SALCE for additional information on the thermal conductivity results, P. MONNIER, Mrs COURRIOUX and J.A. FAVRE for their experimental assistance.

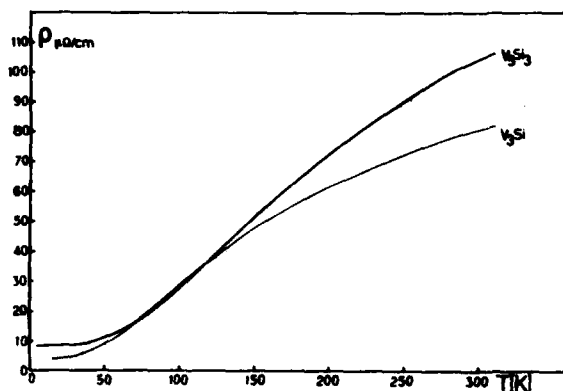


Fig. 1 - The resistivity of the  $V_3Si$  ( $MS_1b_2$ ,  $[110]$ ,  $RRR = 20.4$ ) and  $V_5Si_3$  (151A,  $RRR = 11.6$ ) single crystals.

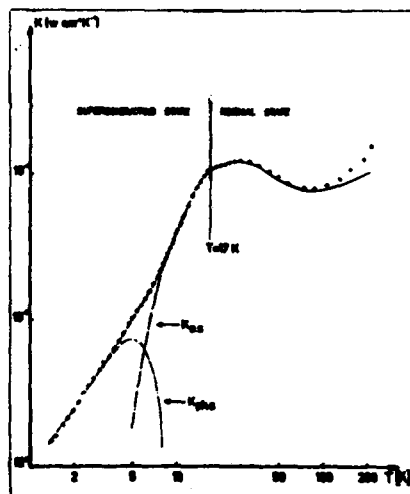


Fig. 2 - The thermal conductivity of the  $V_3Si$  sample ( $MS_1b_2$ ) with the phonon ( $K_{phs}$ ) and the electron  $K_{es}$  contributions.

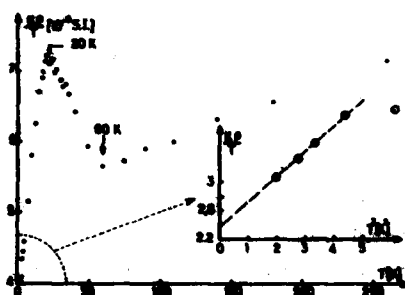


Fig. 3 - The parameter  $K_0$  for the sample  $V_5Si_3$  (151A) showing the extrapolation at  $T=0K$  which gives the Lorentz number (insert).

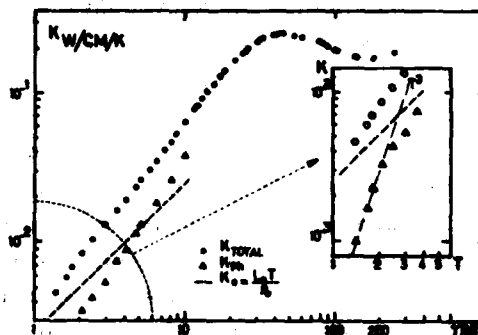


Fig. 4 - The thermal conductivity of the  $V_5Si_3$  sample with the electron contribution calculated from WFL  $K_e = L_0 T / \rho_0$ . The phonon contribution obeys the  $T$  Law below 2 K (insert).

+ WFL = Wiedemann-Franz Law

#### References

- (1) P.B. ALLEN, Superconductivity in d- and f- Band Metals P.291, ed. by H. SUHL and M.B. MAPLE, Academic Press 1980.
- (2) A.F. KHODER, M. COUACH, M. LOCATELLI, M. ABOU GHANTOUS, J.P. SENATEUR Solid State Com. 38, 1297, 1981.
- (3) A.H. WILSON, The Theory of Metals, 2d Ed. Cambridge 286 (1965).
- (4) H. WIESMANN, M. GURVITCH, H. LUTZ, A. GHOSH, B. SCHWARZ, M. STRONGIN, P.B. ALLEN J.W. HALLBY Phys. Rev. Lett. 38, 14, 782, 1977.
- (5) E.V. KUENIN and I.S. SANDALOU, Sov. Phys. JETP, vol. 41, P. 691, 1976.
- (6) J.L. STAMBERMANN Solid State Com. 26, 461, 1978.
- (7) A.F. KHODER, International Conference on electron transport in metals, Carleton Un. OTTAWA, August 1981.

# A NEUTRON INELASTIC SCATTERING STUDY OF PHONONS IN METASTABLE BETA-GALLIUM

J.R.D. Copley<sup>\*,†</sup>, L. Bosio<sup>\*\*</sup>, R. Cortès<sup>\*\*</sup>, J. Lefebvre<sup>\*</sup> and W.D. Teuchert<sup>\*x,††</sup>

<sup>\*</sup>Institut Laue-Langevin, 156X Centre de Tri, 38042 Grenoble Cedex, France

<sup>\*\*</sup>Groupe de Recherche no. 4 du C.N.R.S., Physique des Liquides et Electrochimie, associé à l'Université Paris VI, 4 Place Jussieu, 75230 Paris Cedex 05, France.

<sup>x</sup>Fachbereich Physik E21 der Technischen Universität München, 8046 Garching, F.R.G.

**Abstract.**— The phonon dispersion curves of C-centred monoclinic beta-gallium at the melting temperature have been measured along five symmetry directions. The behaviour of the lower longitudinally polarised branch in the  $E_x$  ( $S_x$ ) direction suggests a desire to double the size of the unit cell. Initial model fitting calculations indicate that the interactions in  $\beta$ -Ga are of reasonably long range.

**1. Experimental Measurements and Results.**— The phonon dispersion curves of the stable orthorhombic  $\alpha$  form of Ga were measured some years ago by Reichardt et al [1] and by Waerber [2]. In the present paper we discuss measurements and preliminary calculations of phonons in the metastable monoclinic  $\beta$  modification of this metal. The experimental details of this work are fully described elsewhere [3]. The main interest in  $\beta$ -Ga stems from its close structural and thermodynamic similarity to amorphous Ga and liquid Ga.

Three-axis spectrometer measurements were made using the IN2 and IN8 instruments at the ILL, Grenoble. Crystals were grown and oriented *in situ*, using a specially constructed goniometer and cryostat. Precautions were also necessary to reduce shock and vibration, in order to avoid accidental transformation to the stable  $\alpha$  phase. Measurements were made at the melting temperature, 256.8K, in the symmetry directions  $E_x$  ( $S_x$ ),  $A$ ,  $E_z$ ,  $S_z$  and  $R$ . Unusual features of the measured curves include the similar slopes of the three longitudinal acoustic branches, and the near mirror symmetry about (0.5,0,0) of the lower longitudinally polarised branch in the  $E_x$  ( $S_x$ ) direction (fig. 1). This latter feature suggests a desire to double the size of the unit cell by suppression of the C-centred lattice points.

**2. Calculations.**— The primitive unit cell contains 2 atoms. Its symmetry implies the following relationships between elements of the dynamical matrix  $D$ :  $D_{\alpha\beta}(q_{11}) = D_{\beta\alpha}(q_{22})$ , and  $D_{\alpha\beta}(q_{12}) = D_{\beta\alpha}(q_{21})$ . The submatrices  $D(q_k)$  are symmetric and therefore real, in the absence of many-body forces.

In order to simplify the model fitting calculations we treated

**Present address:** †Department of Physics, Mc Master University, Hamilton, Ontario, Canada, L8S 4K1

††Carl Weiss, Postfach 1369/1380, D-7082 Oberkochen, F.R.G.

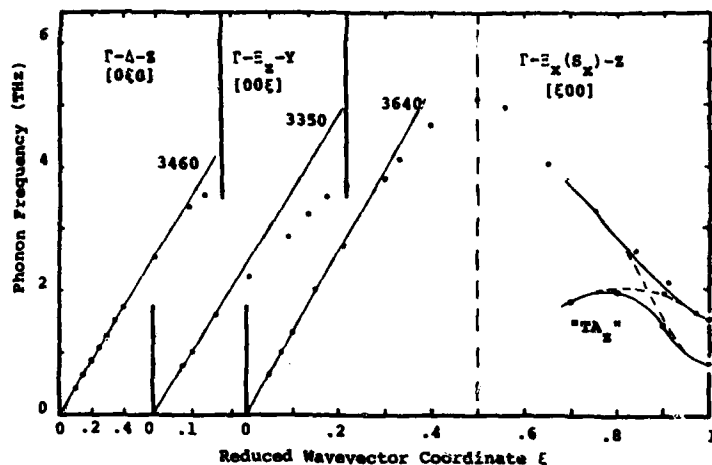


Fig. 1: The three longitudinal branches, with initial slopes in  $\text{ms}^{-1}$ . The likely behaviour of the low frequency  $[\xi 0 0]$  branches for  $\xi \geq 0.7$ , were they to belong to different irreducible representations, is suggested by the broken lines.

the unit cell as orthorhombic: this is a reasonable approach since  $\beta$  is actually  $92^\circ$ , and no new degeneracies are introduced by making it  $90^\circ$ . On the other hand, the number of irreducible representations for a given  $q$  is in general increased. Within this approximation,  $\beta$ -Ga has the same structure as  $\alpha$ -U [4], and the submatrices  $D(qkk)$  are diagonal (in the absence of many-body forces) for the symmetry directions studied.

Initial attempts to fit the parameters of simple two-body potentials to the experimental results were not surprisingly unsuccessful. Furthermore, dispersion curves computed using real space pair potentials derived from a variety of pseudopotentials calculated for gallium [5,6,7] show little resemblance to experiment.

In the axially-symmetric force model there is a radial force constant  $\phi_r(i)$  and a tangential force constant  $\phi_t(i)$  for each shell of neighbours  $i$ . Experimental data for the five symmetry directions studied, no matter how precise or detailed they may be, are insufficiently "orthogonal" to determine all the force constants. For  $i \leq 13$ , eight of the force constants linking atoms on the same sublattice may be modified as follows:  $\phi_{r,t}(1) \rightarrow \phi_{r,t}(1) + C$ ,  $\phi_{r,t}(3) \rightarrow \phi_{r,t}(3) - C/2$ ,  $\phi_{r,t}(10) \rightarrow \phi_{r,t}(10) - C$ ,  $\phi_{r,t}(11) \rightarrow \phi_{r,t}(11) + C/2$ , and six of the force constants linking atoms on different sublattices may be modified as follows:  $\phi_{r,t}(2) \rightarrow \phi_{r,t}(2) + C'$ ,  $\phi_{r,t}(4) \rightarrow \phi_{r,t}(4) + C'$ ,  $\phi_{r,t}(7) \rightarrow \phi_{r,t}(7) - C'/2$  (where  $C$  and  $C'$  are independent and arbitrary), without in any way modifying  $D$ . It is therefore necessary to impose two arbitrary constraints, e.g.  $\phi_r(11) = 0$ ,  $\phi_r(7) = 0$ .

Axially-symmetric force constant fits were made allowing interactions out to the 13th shell of neighbours, over a range of nearly

<sup>0</sup>  
6A. With 92 independent data points the "best fit" was relatively poor, having a "goodness of fit"  $\chi^2$  of  $\sim 12$ . This is not unexpected in view of the low symmetry of the system: the 13th shell in "orthorhombic"  $\beta$ -Ga (equivalent to the 19th shell in true monoclinic  $\beta$ -Ga) is only 2.15 times more distant than the nearest neighbour shell. Also the straightness of the longitudinal acoustic  $\Delta$  and  $E_x$  branches (fig. 1) implies the existence of reasonably long range forces.

3. Discussion.— The low symmetry and long range of interaction in  $\beta$ -Ga suggest that a reciprocal space analysis of the forces could be fruitful. Alternatively a "modified shell model" analysis, along the lines of Crummett et al's [4] calculations for  $\alpha$ -U, may be worth pursuing. If at all possible we would like to find a unified description of the forces in  $\alpha$ -Ga and  $\beta$ -Ga, in order to shed further light on the nature of the interactions between atoms in the liquid and amorphous states of this unusual but elusive metal.

We are grateful to Mr. Mike Pizzuto for his invaluable help with the model calculations. This work was supported in part by the Natural Sciences and Engineering Research Council Canada.

#### References

- [1] Reichardt W., Nicklow R.M., Dolling G. and Smith H.G., Bull. Am. Phys. Soc. 14, 378 (1969).
- [2] Waerber W.B., J. Phys. C2, 903 (1969).
- [3] Bosio L., Cortès R., Copley J.R.D., Teuchert W.D. and Lefebvre J., J. Phys. F11 (1981) (in press).
- [4] Crummett W.P., Smith H.G., Nicklow R.M. and Wakabayashi N., Phys. Rev. B19, 6028 (1979).
- [5] Inglesfield J.E., J. Phys. C1, 1337 (1968).
- [6] Appappillai M. and Williams A.R., J. Phys. F3, 759 (1973).
- [7] Regnaut C., Badiali J.P. and Dupont M., J. de Physique 41, C6-603 (1980).

# NUCLEAR ACOUSTIC RESONANCE INVESTIGATIONS OF THE LONGITUDINAL AND TRANSVERSE ELECTRON-LATTICE INTERACTION IN TRANSITION METALS AND ALLOYS

V. Müller, G. Schanz, E.-J. Unterhorst and D. Maurer

*Freie Universität Berlin, Fachbereich Physik, Königin-Luise-Str. 28-30, D-1000 Berlin 33, Germany*

**Abstract.** - In metals the conduction electrons contribute significantly to the acoustic-wave-induced electric-field-gradient-tensor (DEFG) at the nuclear positions. Since nuclear electric quadrupole coupling to the DEFG is sensitive to acoustic shear modes only, nuclear acoustic resonance (NAR) is a particularly useful tool in studying the coupling of electrons to shear modes without being affected by volume dilatations. By extending previous NAR measurements in Nb, Mo and Ta to superconducting alloys  $Nb_{1-x}Mo_x$  it will be shown that the combination of NAR experiments with high-pressure Mössbauer isomer-shift measurements is of interest in a deeper understanding of the coupling of shear modes and volume dilatations to s- and d-electrons in transition metals.

In cubic metals the electric field gradient (EFG) vanishes at a nuclear site. In the presence of an acoustic wave, however, the cubic point symmetry is destroyed periodically thereby giving rise to a sound-induced dynamic electric field gradient (DEFG) tensor whose components can be measured in nuclear acoustic resonance (NAR). Besides fundamental questions concerning the complex physics behind the EFG [1], measurements of the DEFG are of particular interest in studying the long-wavelength electron-phonon interaction in transition metals since, in the response of the d-electrons to acoustic shear modes, multipole fields are set up due to d-electron charge redistribution, so that the d-electrons are expected to contribute significantly to the electronic part of the DEFG.

At a nuclear site and within the range of linear response the DEFG tensor  $\{V_{ij}\}$  is related to the acoustic strain tensor  $\{\epsilon_{ij}\}$  by  $1/2 V_{ij} = \nabla_i \nabla_j \phi = \sum_{kl} S_{ijkl} \epsilon_{kl}$  where  $\phi$  is the strain induced electrical potential and  $\{S_{ijkl}\}$  is the fourth rank "field gradient-strain tensor". Choosing a coordinate system having its axes along the principal axes of the unstrained cubic crystal, the components of the traceless defined DEFG-tensor  $\hat{V}_{ij} = \{V_{ij} - \delta_{ij} \text{Tr} V / 3\}$  can be written as

$$\hat{V}_{11} = (S_{11} - S_{12}) \hat{\epsilon}_{11} \quad , \quad \hat{V}_{ij} = S_{44} \hat{\epsilon}_{ij} \quad i \neq j \quad (1)$$

where  $S_{11}$ ,  $S_{12}$  and  $S_{44}$  are the three distinct components of the S-tensor (in Voigt notation) and  $\hat{\epsilon}_{ij} = \{\epsilon_{ij} - \delta_{ij} \text{Tr} \epsilon / 3\}$  are the components of the (in first order) volume-conserving "shear tensor". Regarding that the nuclear electric quadrupole interaction is invariant against  $\text{Tr} V$ , it follows immediately that NAR investigations of the electronic contribution to the DEFG are sensitive to the coupling of elec-

trons to shear modes only. Consequently, quadrupole NAR enables one to study the coupling of shear modes to electrons without being affected by changes in the electron charge density caused by eventual volume deformations of the lattice unit cells. Confining ourselves to transition metals and applying the usual ansatz

$$\mathcal{S} = (1 - \gamma_{\infty}) \mathcal{S}_{\text{latt}} + \mathcal{S}_{\text{ce}}, \quad (2)$$

where  $\mathcal{S}_{\text{latt}}$  is the lattice contribution,  $\gamma_{\infty}$  the Sternheimer antishielding factor and  $\mathcal{S}_{\text{ce}}$  the conduction electron contribution within an atomic sphere centered around the nucleus under consideration, it follows from Eqs. (1) and (2):

- i)  $(S_{11} - S_{12})_{\text{ce}}$  refers to the conduction electron response to linear dilatations of the lattice unit cells (i.e. angular distortions of the d-bonds)
- ii)  $(S_{44})_{\text{ce}}$  refers to the conduction electron response to angular dilatations of the cubic unit cells which predominantly are associated with radial distortions of the d-bonds.

Extending the theoretical results of Watson et al. /3/ to the DEFG in transition metals and neglecting s-d transitions, within the frame of a band-orbital model /7/, we find /4/ (also see Ref. (5))

- i)  $r_{12} = (S_{11} - S_{12})_{\text{ce}} / [(1 - \gamma_{\infty})(S_{11} - S_{12})_{\text{latt}}]$  should be negligible small.
- ii)  $r_{44} = (S_{44})_{\text{ce}} / [(1 - \gamma_{\infty})(S_{44})_{\text{latt}}] \propto -N(E_F) \sqrt{n_0}$ , where  $n_0$  is the electron-phonon coupling parameter as defined in Ref. (10).

The experimental results for Mo, Ta, Nb and  $\text{Nb}_{88}\text{Mo}_{12}$  are shown in Figs. (1a) and (1b). We note that the data of Fig. (1a) are corrected for the actual values of the electric quadrupole moments and partly differ from those reported previously /6/.

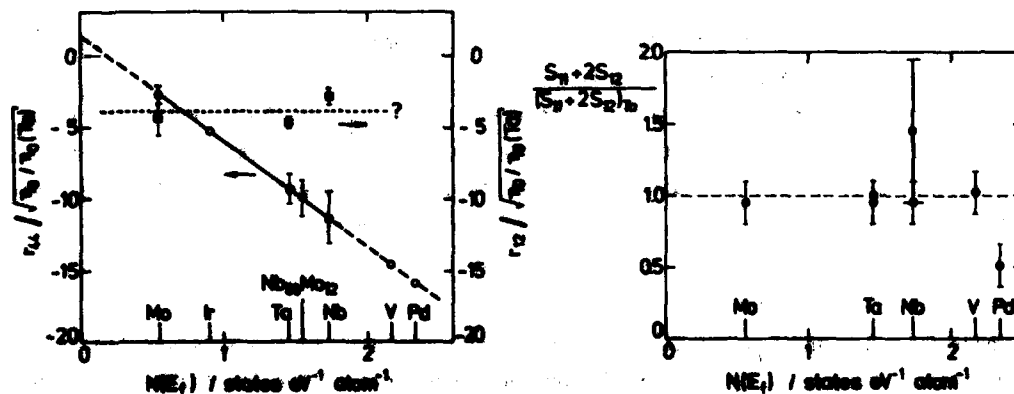


Fig. 1

a) Coupling of electrons to shear modes (o predicted data)

b) Coupling of electrons to volume dilatations



The most striking feature of these results is that within experimental error  $r_{44}$  proves to be proportional to  $N(E_F) \approx N_d(E_F)$  whereas  $r_{12}$  seems to be insensitive against  $N(E_F)$ . From Fig. (1a) we therefore may conclude that in transition metals with high densities of states (i.e.  $|r_{12}| < |r_{44}|$ ) the long-wavelength electron-phonon interaction with shear modes is dominated by "compressions" and "expansions" of d-electron bonds (transverse electron-lattice coupling). Concerning the electron coupling to the longitudinal part of shear modes (i.e. angular distortions of the d-bonds) no conclusions can be drawn yet. The coupling of electrons to volume dilata-  
tions is reflected by  $(S_{11} + 2S_{12})$  which, however, cannot be measured in NAR but may be derived /4/ from high-pressure Mössbauer isomer-shifts measurements /8/, /9/. Regarding that only s-type electrons will contribute to the Mössbauer isomer-shift, and taking into account that  $N_s(E_F)$  is nearly constant throughout the transition metal series, experimental evidence is quite in favour (see Fig. (1b)) of a relation of the form  $(S_{11} + 2S_{12}) \propto N_s(E_F)$ .

Summarizing our experimental results, we have shown that measurements of the "field gradient-strain" tensor are an important tool in studying the relative significance of s- and d-electron coupling to acoustic shear modes and volume deformations in transition metals.

#### References

- /1/ B. Strübel and V. Müller, Phys. Rev. B, in print
- /2/ E.F. Taylor, and N. Bloembergen, Phys. Rev. 113, 431 (1959)
- /3/ R.E. Watson, A.C. Gossard, and Y. Yafet, Phys. Rev. 140, A375 (1965)
- /4/ V. Müller, G. Schanz, E.J. Unterhorst, and D. Maurer, to be published
- /5/ K.H. Bennemann, Phys. Rev. Lett. 42, 676 (1979)
- /6/ E. Fischer, V. Müller, D. Ploumbidis, and G. Schanz,  
Phys. Rev. Lett. 40, 796 (1978)
- /7/ H.A. Harrison, and J.C. Phillips, Phys. Rev. Lett. 33, 410 (1974)
- /8/ G. Kaindl, D. Salomon, and G. Wortmann in "Mössbauer isomer shifts",  
North Holland Publ. Co. (1978) p. 316, and references therein
- /9/ D.L. Williamson in "Mössbauer isomer shifts", North Holland Publ. Co. (1978)  
p. 561, and references therein
- /10/ K.H. Bennemann, and J.W. Garland in "Superconductivity in d- and f-Band Metals",  
AIP Conference Proceedings 4, American Institute of Physics (1972) p. 99

# RAMAN SCATTERING IN $V_3Si$ , $V_3Ge$ , $Nb_3Sb$ , AND $Cr_3Si$ : CORRELATION OF $E_g$ OPTICAL PHONON LINEWIDTH WITH MAGNETIC SUSCEPTIBILITY

R. Merlin<sup>+</sup>, S.B. Dierker, M.V. Klein, J. Jørgensen<sup>\*</sup>, S.R. Rasmussen<sup>\*</sup>,  
Z. Fisk<sup>\*\*</sup> and G.W. Webb<sup>\*\*</sup>

*Department of Physics and Materials Research Laboratory, 104 S. Goodwin,  
University of Illinois at Urbana-Champaign, Urbana, Illinois 61801, U.S.A.*

*\*Department of Inorganic Chemistry, Aarhus University, DK-8000 Aarhus C,  
Denmark.*

*\*\*Institute for Pure and Applied Life Sciences, University of California at San  
Diego, La Jolla, California 92093, U.S.A.*

**Abstract.**— Raman scattering measurements of the  $E_g$  optical phonon in  $V_3Si$  and  $Nb_3Sn$  show it to have an anomalous width, temperature dependence, and asymmetric lineshape. We have observed a similar, although weaker, anomaly in  $V_3Ge$ . The  $E_g$  and  $T_{2g}$  phonons in  $Nb_3Sb$  and the  $T_{2g}$  phonon in  $Cr_3Si$  show no anomalous behavior and can be understood in terms of simple anharmonic interactions. In  $Cr_3Si$  the  $E_g$  phonon has an anomalous width, shape, and temperature dependence (similar to  $V_3Ge$ ) in spite of its low electronic density of states and temperature independent magnetic susceptibility. A linear correlation is shown to exist between magnetic susceptibility and  $E_g$  mode linewidth,  $\Gamma$ , in  $V_3Si$ ,  $Nb_3Sn$ , and  $V_3Ge$ . With the aid of a simple model, most of the features of the Raman data can be understood in terms of direct coupling of the  $E_g$  phonon to interband electronic transitions between the very flat bands emanating from the  $\Gamma_{12}$  level in these compounds. These results indicate that direct coupling of the  $E_g$  optical phonon to the  $\Gamma_{12}$  bands plays a major role in the splitting of the cubic  $\Gamma_{12}$  subband  $N(E)$  peak by the dimerization of the transition metal sublattice.

1. **Experiment.**— A single crystal of  $V_3Ge$  ( $T_c=6.3K$ ) was grown from buttons of stoichiometric arc-melted starting material by the Czochralski technique.<sup>1/</sup> The single crystal of  $Cr_3Si$  ( $T_c<0.015K$ ) was grown by zone refining pressed stoichiometric powder mixtures of Chromium and Silicon.<sup>2/</sup> [100] surfaces were spark cut from these samples and then mechanically polished with alumina. For the investigation on  $Nb_3Sb$ , a large single crystal was grown by closed tube vapor transport with iodine as a transporting agent. The Raman measurements were performed on a high quality, smooth, as-grown [110] face of the crystal. Laser light of 514-nm wavelength was incident at a pseudo-Brewster angle of  $70^\circ$ , collected in a direction normal to the surface, and analyzed with a home-built double monochromator employing standard photon counting electronics. Cooling was provided by either flowing cold He gas in a modified "Heli-Tran" system or a liquid He Janis cryostat. True sample temperatures were determined from Anti-Stokes/Stokes ratios of the  $E_g$  phonon.

2. **Results and Discussion.**— The  $E_g$  symmetry Raman spectra of  $V_3Ge$  taken at 340K and 50K are shown in Fig. 1. The phonon frequency hardens from 278. to 287.  $cm^{-1}$  and the linewidth increases from 37.2 to 69.6  $cm^{-1}$  (FWHM) upon cooling. The solid lines are fits to a spectral function resulting from a coupled-mode theory, wherein the asymmetric lineshape is due to a Breit-Wigner-Fano interference between the discrete phonon and an electronic continuum.<sup>3/</sup>

<sup>+</sup> Present address : Department of Physics, University of Michigan, Ann Arbor, Michigan 48109, U.S.A.

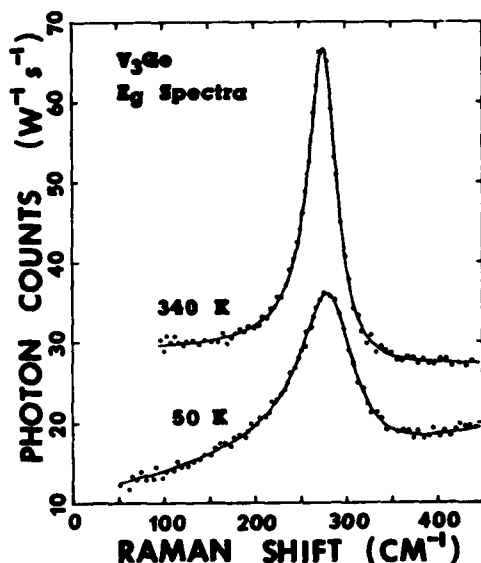


Fig. 1 : E symmetry Raman spectra in  $V_3Ge$  at 340K and 50K. The solid lines are fits to the data (see text).

are weakly damped and harden and narrow upon cooling. This is typical behavior for phonons whose self-energy is dominated by anharmonic phonon-phonon interactions. The  $E_g$  phonon in  $Cr_3Si$  is not so well understood. It appears to harden from 310. to 320.  $cm^{-1}$  and broaden from 40. to 60.  $cm^{-1}$  upon cooling from 300K to 70K. However, additional structure in the region of the phonon, possibly due to electronic Raman scattering, complicates the analysis.

The electronic nature of the  $E_g$  phonon damping in  $V_3Si$ ,  $Nb_3Sn$ , and  $V_3Ge$  is further demonstrated by plotting their magnetic susceptibility,  $\chi$ , versus their corresponding  $E_g$  mode linewidth at the same temperature, for several temperatures. This is shown in Fig. 2 for the temperature range 400K to 20K, where a strong correlation is seen to exist, with the V-based compounds following one relationship and  $Nb_3Sn$  a separate one. Such a division of V-based and Nb-based A-15 compounds into two families, with  $\eta_{Nb_3Sn} > \eta_{V_3Si}$ , where  $\eta = N(E_F) \langle I^2 \rangle$ ,  $\langle I^2 \rangle$  being the Fermi surface averaged electron-phonon matrix element squared, has already been pointed out by Klein, et. al.<sup>8/</sup> The ratio of the initial slopes of the two curves (indicated by the solid lines through the data in Fig. 2) is in good agreement with the ratio of  $\langle I^2 \rangle_{Nb_3Sn} / \langle I^2 \rangle_{V_3Si}$  as calculated by Klein, et. al.<sup>8/</sup> The temperature dependence of the magnetic susceptibility is commonly ascribed to thermal repopulation of electronic energy levels near a sharp peak in the electronic density of states. The strong correlation between the magnetic susceptibility and the  $E_g$  phonon linewidth, shown in Fig. 2, suggests that electron-phonon interactions (as opposed to anharmonic phonon-phonon interactions), subject to the same thermal repopulation effects as the magnetic susceptibility, are responsible for the temperature dependence of

We propose that the dominant damping mechanism for the  $E_g$  mode in this A-15 and in  $V_3Si$ <sup>3,4/</sup> and  $Nb_3Sn$ <sup>4/</sup> consists of inter-band processes wherein the  $E_g$  mode decays into electron-hole pairs in the  $\Gamma_{12}$  bands. These bands are within an energy comparable to the  $E_g$  phonon energy of the Fermi level throughout large regions of the Brillouin Zone.<sup>5/</sup> Due to symmetry based selection rules, the  $T_{2g}$  phonon in  $Nb_3Sn$  cannot interact with these bands and it has indeed been observed to be relatively weakly damped.<sup>4/</sup>

In  $Nb_3Sb$ <sup>6/</sup> and  $Cr_3Si$ <sup>7/</sup> the  $E_g$  phonon cannot interact with electrons in the  $\Gamma_{12}$  bands since they are  $\sim 0.35$  eV below the Fermi level and hence completely filled. Accordingly, the  $E_g$  phonon in  $Nb_3Sb$  and the  $T_{2g}$  phonons in both  $Nb_3Sb$  and  $Cr_3Si$

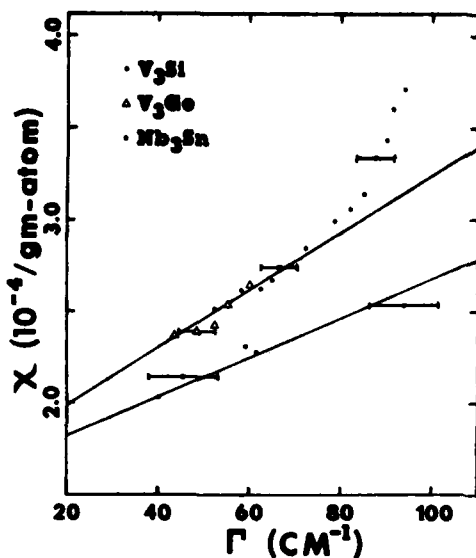


Fig. 2 : Correlation of  $\chi$  vs.  $\Gamma$  for  $V_3Si$ ,  $Nb_3Sn$ , and  $V_3Ge$ . Raman data for  $Nb_3Sn$  taken from ref. 4. data for  $V_3Si$ ,  $V_3Ge$ , and  $Nb_3Sn$  taken from refs. 9, 9', and 10, respectively.

the  $E_g$  phonon linewidth and frequency in these compounds. Indeed, a simple model of the interaction and the  $\Gamma_{12}$  bands is able to account quantitatively for the linewidth temperature dependence. Our model will be discussed more fully in a future publication. These results are in accord with the recent conclusions of Mattheiss and Weber<sup>11/</sup> that dimerization of the transition metal sublattice is the primary driving mechanism for the martensitic transition.

We thank D. A. Papaconstantopoulos for providing us with the energy band diagram for  $Cr_3Si$ . This work was supported by the National Science Foundation under the MRL Grant UMR-80-20250.

#### References

1. J. H. Wernick, G. W. Hull, T. H. Geballe, J. E. Bernardini, and E. Buehler, J. Crystal Growth **47**:73 (1979).
2. J. Jørgensen and S. E. Rasmussen, J. Crystal Growth **47**:124 (1979).
3. H. Wipf, M. V. Klein, B. S. Chandrasekhar, T. H. Geballe, and J. H. Wernick, Phys. Rev. Lett. **41**:1752 (1978).
4. S. Schickens, R. Kaiser, E. Schneider, and W. Glaser, Phys. Rev. **B22**:2386 (1980).
5. B. M. Klein, L. L. Boyer, D. A. Papaconstantopoulos, and L. F. Mattheiss, Phys. Rev. **B18**:6411 (1978).
6. B. M. Klein, D. A. Papaconstantopoulos, and L. L. Boyer in Superconductivity in d- and f-Band Metals, eds. H. Suhl and M. B. Mable (Academic Press, New York, 1980), p. 455.
7. D. A. Papaconstantopoulos, D. U. Gubser, B. M. Klein, and L. L. Boyer, Phys. Rev. **B21**:1326 (1980); and private communication from D. A. Papaconstantopoulos.
8. B. M. Klein, L. L. Boyer, and D. A. Papaconstantopoulos, Phys. Rev. Lett. **42**:530 (1979).
9. A. M. Clogston and V. Jaccarino, Phys. Rev. **121**:1357 (1961).
10. W. Rehwald, M. Rayl, R. W. Cohen, and G. D. Cody, Phys. Rev. **B6**:363 (1972).
11. L. F. Mattheiss and W. Weber, Bull. Amer. Phys. Soc. **26**:270 (1981).

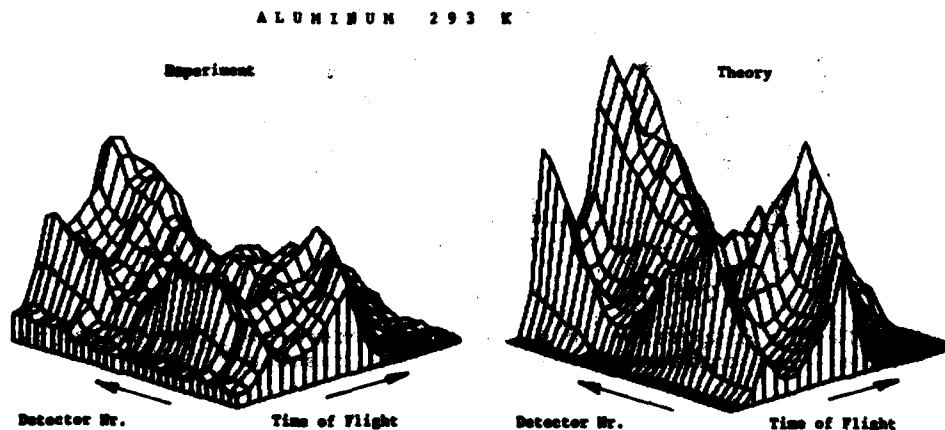
## COHERENT NEUTRON SCATTERING FROM POLYCRYSTALS

U. Buchenau, H.R. Schober and R. Wagner

*Institut für Festkörperforschung der Kernforschungsanlage Jülich, Postfach 1913, D-5170 Jülich, F.R.G.*

**Abstract.**— Phonon dispersion curves are mostly determined by coherent neutron scattering from single crystals. For a number of materials, however, large enough single crystals are not obtainable. We used the detailed structure of the coherent scattering from polycrystals to obtain as much information on the phonons as possible. Time-of-flight spectra of Al and Ca over a large area in  $Q$  and  $\omega$  have been analyzed in terms of lattice dynamical models. It turns out that, at least for these simple materials, a rough picture of the phonon dispersion may be obtained.

It is well known that phonons can be measured by coherent inelastic neutron scattering from single crystals. Much less is known about the information contained in the coherent inelastic scattering from polycrystals. Two special cases have been considered earlier: the region of high momentum transfer where the phonon spectrum may be obtained<sup>1</sup> and the regions of low energy transfer near Debye-Scherrer rings where elastic constants can be determined<sup>2</sup>. In this work we show that by measuring in an extended range of energy and momentum transfer one may even get a rough picture of the full phonon-dispersion - at least in the simple cases considered, namely polycrystalline Al and Ca at room temperature.



**Fig. 1:** Time-of-flight spectrum of polycrystalline Al at 293 K

Fig. 1 shows measured and calculated time-of-flight spectra for Al. The intensity rise at short flight times corresponds to the onset of one-phonon annihilation processes at the maximum lattice frequency of about 10 THz. The upper boundary of the time range corresponds to 3 THz. The momentum transfer increases with increasing detector number and decreases with increasing time of flight. In the region shown above it ranges from 2 to 6  $\text{\AA}^{-1}$ . The experiment was done on the time-of-flight spectrometer SV5 at the cold source of the reactor DIDO in Jülich (wavevector of incoming neutrons  $1.314 \text{ \AA}^{-1}$ , range of scattering angles 20 to 160 degrees).

The theoretical spectrum was obtained using a set of Born-v. Karman parameters from the literature<sup>3</sup>. The one-phonon scattering contributions on a fine mesh through the relevant Brillouin zones were summed up (using the symmetry as far as possible) and folded with the instrumental resolution. The result agrees reasonably well with the experiment, though there are some distinct differences. A better agreement can be achieved by fitting the Born-v. Karman parameters to the experiment. We did this assuming axially symmetric springs extending up to the sixth nearest neighbour and using the known elastic constants<sup>4</sup>. Multiphonon and multiple scattering were calculated using simple approximations. The result is summarized in Table 1. Fig. 2 shows that this fitted parameter set reproduces the experimental dispersion<sup>5</sup> along the symmetry directions astonishingly well.

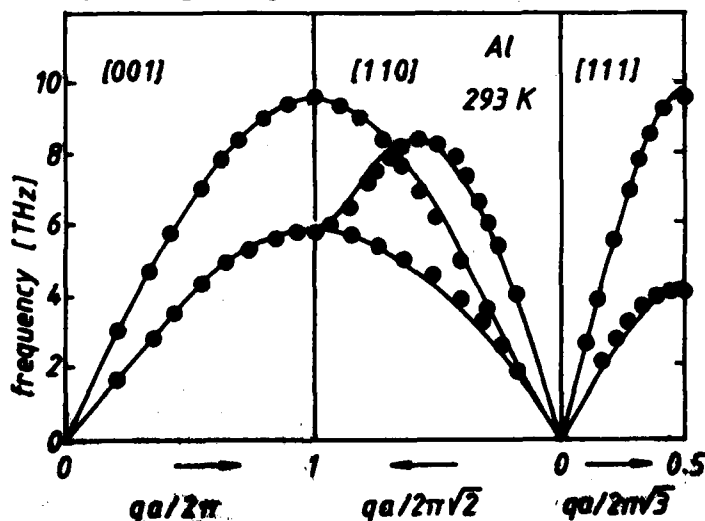


Fig. 2: Phonon dispersion in Al at 293 K determined from polycrystalline data (—) compared to single crystal results<sup>5</sup> (●).

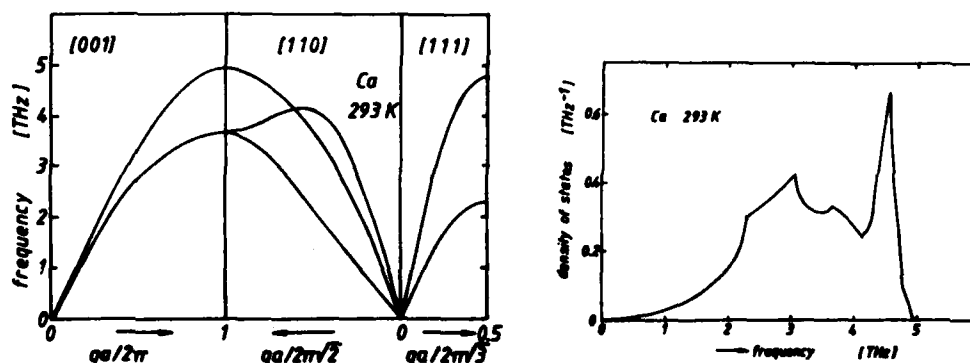


Fig. 3: Phonon dispersion and phonon spectrum in Ca at 293 K.

Table 1 and Fig. 3 show fit results for Ca at room temperature. No single crystals of this material are available because of its martensitic phase transformation at 720 K. The elastic constants determined at low energy transfer with the method<sup>2</sup>  $c_{11}=25\pm3$  GPa,  $c_{12}=15\pm1$  GPa and  $c_{44}=2\pm1$  GPa were included in the fit. The resulting bulk modulus  $B=18.3$  GPa is in reasonable agreement with the static value<sup>6</sup> of 17.2 GPa. The phonon dispersion shown in Fig. 3 corresponds rather closely to pseudopotential calculations<sup>7</sup> if these are scaled down by 16%.

Neighbour and indices	Al	Ca
1XX	10056. $\pm$ 100.	3806. $\pm$ 50.
1ZZ	-982.	-133.
1XY	11038.	3939.
2XX	1364. $\pm$ 100.	-1513
2YY	90.	227.
3XX	-629. $\pm$ 50	250. $\pm$ 20.
3YY	-19.	94.
3YZ	-203.	52.
3XZ	-407.	104.
4XX	107.	
4ZZ	-470.	
4XY	577.	
5XX	149.	
5YY	-53.	
5ZZ	-78.	
5XY	76.	
6XX	57.	
6YZ	-145.	

#### References

- 1 M.M. Bredov et al., Sov. Phys.Sol.State 9,214 (1967)
- 2 U. Buchenau, Solid State Commun. 32, 1329 (1979)
- 3 G.Gilat and R.M. Nicklow, Phys.Rev. 143, 487 (1966)
- 4 G.N.Kamm and G.A. Alera, J.Appl.Phys. 35, 327 (1964)
- 5 R. Stedman and G. Nilson, Phys.Rev. 145, 492 (1966)
- 6 C.Kittel, Intr. to Solid State Physics, 2.ed., p.99, Wiley, New York 1963
- 7 J.A. Moriarty, Phys.Rev. B6, 4445 (1972)

Table 1: Fitted Born-v.Karman parameters (dyn/cm) for Al and Ca from polycrystalline spectra at 293 K.

## HIGH TEMPERATURE PHONONS IN IRON

A.M. Vallêra

*Fac. de Ciências, Lisboa, and LNETI, Sacavem, Portugal.*

**Abstract.** - The phonon frequencies of Fe + 5 at % Si were extensively measured at room temperature, 933K, 1147K, and 1423K using neutron inelastic scattering. The most interesting features are the frequency shifts of obvious magnetic origin, with large gradients at the Curie temperature. Their interpretation in terms of magnetic contributions is discussed, and preliminary magnetic force constants are given.

We have been studying the variation with temperature of the phonon frequencies of bcc iron by neutron inelastic scattering. The data presented here refers only to Fe + 5 at % Si single crystals, although Fe samples have been also used for comparison at temperatures below the  $\alpha \rightarrow \gamma$  transition point.

Most of the data were obtained with the twin-chopper spectrometer at reactor PLUTO, Harwell. A few modes were later studied in detail with the three-axis spectrometer IN3, at the ILL, Grenoble (1). All the chopper data were obtained at four temperatures only (296K, 933K, 1147K, and 1423K) in the  $1\bar{1}0$  plane. The phonon frequencies at each temperature are well described by 5-neighbour Born-von-Karman models (2), and are consistent with the ultrasonic elastic constants (3). As an example, in Fig. 1 we show the phonon frequencies along the symmetry directions measured at 933K in Fe(Si).

In Fig. 2 we present the frequency shifts relative to room temperature. One should remark the large relative shifts occurring in low lying modes. That these

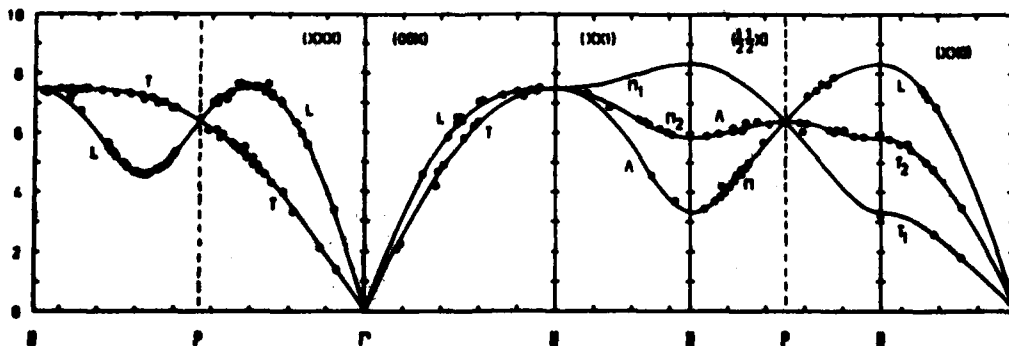


Fig. 1. Phonon frequencies of Fe(Si) at 933K : experiment (○ - chopper meas.; ● - 3-axis meas.) and fitted 5-neighbour model.



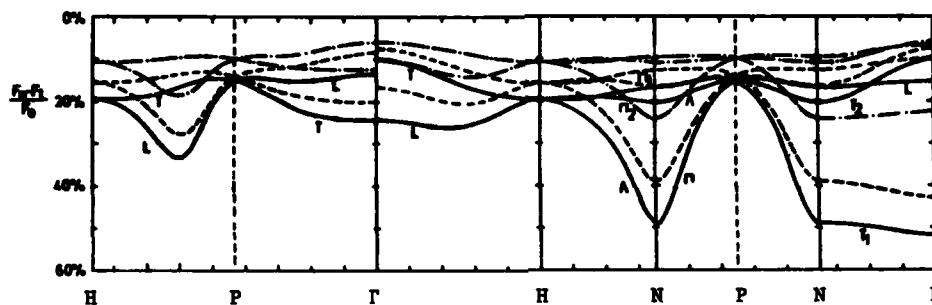
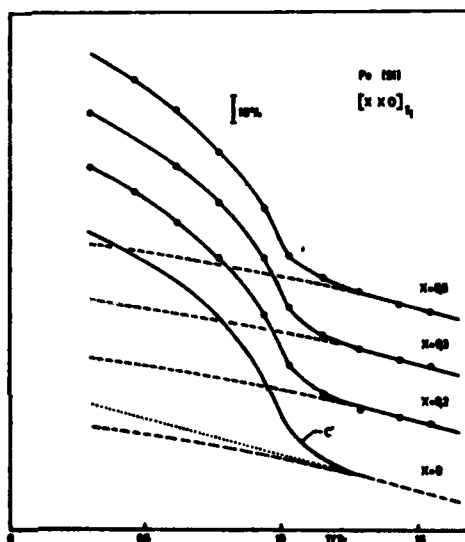


Fig. 2 Relative frequency shifts of Fe(Si) phonons.

--- 933K  
 ---- 1147K  
 ——— 1423K

$$\frac{f^2(T)}{f^2(.6T_c)}$$

Fig. 3. Variation with temperature of the frequencies of (XXO) $T_1$  modes



shifts are of magnetic origin is clearly suggested by Fig. 3. But these magnetic effects are not restricted to such modes; all of them show measurable kinks at the Curie temperature, although smaller.

Fig. 3 also suggests the possibility of separating a magnetic contribution to the phonon frequencies as the difference between the low temperature squared phonon frequency as measured and an extrapolation of the high temperature behaviour. Such contributions might be related to the space derivatives of the exchange parameters of a Heisenberg-like model, or compared with calculations within itinerant electron models of magnetism; here, however, we limit ourselves to presenting an attempt at quantifying these magnetic contributions by application a simple separation procedure to the chopper data. The fact that we only took measurements at four temperatures, and that the magnetic effect is often small, particularly in higher frequency branches, explain in part the large error bars in Fig. 4. Born-von Karman models were fitted to these points; despite the large errors, a fit could only be achieved when third neighbour magnetic force constants were introduced. The lines drawn on the figure correspond to one such 3-neighbour model, restricted to magnetic contri-

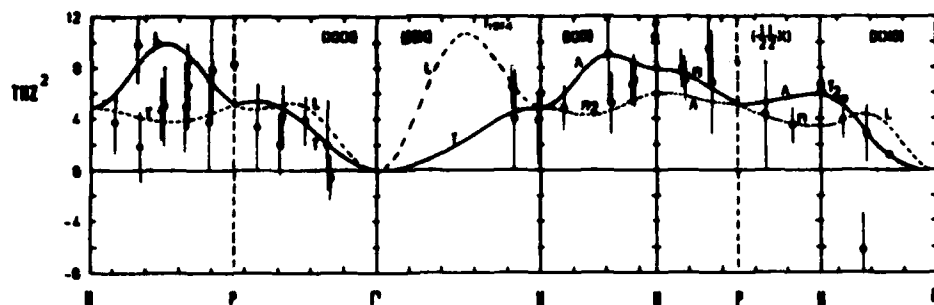


Fig. 4. The separated magnetic contribution to the phonon frequencies of Fe(Si): experiment and fitted 3-neighbour model.  $\phi$ , — higher frequency branch;  $\phi$ , — lower frequency branch. The negative point at  $3/5(1\ 1\ 0)$  was left out of the model fit. Square dots refer to 3-axis data, also not included in the fit.

butions to the shear elastic constants  $C' = 2.2$ ,  $C_{44,m} = 0.5$ , and to the bulk modulus  $B_m = 2.7$  (units of  $10^{10} \text{ Nm}^{-2}$ ), estimated from (3). The fitted force constants are given in the table below. Although a few of the important features of the experimental data have been confirmed (1) by more careful investigation of a few modes (the squares in Fig. 4), these force constants should be regarded as preliminary only, firstly because of the large errors and total absence of data in some branches, and secondly because we now feel that the value of  $B_m$  used in the fit is rather uncertain, and should be left out until low  $q$  (X00)L and (XX0)L modes are studied in detail.

Table I - Magnetic contribution to the force constants (in  $\text{Nm}^{-1}$ )

1st neighbour(111)	2d neighbour(200)	3d neighbour(220)
$\alpha_1 = 1.08$	$\alpha_1 = 3.20$	$\alpha_1 = .99$
$\beta_1 = -.98$	$\alpha_2 = -.42$	$\alpha_3 = -.96$
		$\beta_3 = 1.10$

#### References :

1. A.M. Vallêre, C.G. Windsor, being submitted to J. Phys. F.
2. A.M. Vallêre, Ph.D. thesis, Cambridge University, 1977
3. D.J. Dever, J. Appl. Phys. **43**, 3293 (1972); J.L. Routbort et al, Acta Metal. **19**, 1307(1971); L.Alberts et al, J. de Physique, Colloque C1, suppl. to n°2-3, Tome. **32**, p.415 (1971)

SCREENING OF THE SHORT-RANGE POTENTIAL BY THE LOCAL FIELD CORRECTION  
IN THE LATTICE DYNAMICS OF VANADIUM

B.N. Onwuagba and A.O.E. Animalu

*Department of Physics, University of Nigeria, Nsukka, Nigeria.*

**Abstract.**— The dielectric formulation of the local field correction to the dynamical matrix for phonon dispersion relation in d-band metals in the transition-metal model potential approximation is re-examined, with a view to explore its influence on the short-range (Born-Mayer) interatomic force contribution to the dynamical matrix. It is observed that the off-diagonal components of the inverse dielectric matrix, which determine the local field correction, make contributions that tend to cancel or "screen" the Born-Mayer contribution, just as the diagonal components of the inverse dielectric matrix tend to provide screening of the long range (Coulombic) contribution. Numerical calculation for vanadium shows that the cancellation of the Born-Mayer contribution to the dynamical matrix by the local field correction is physically significant, and leads to a better understanding of the soft modes in the phonon spectra of body-centered cubic transition metals.

1. **Introduction.** — Several years ago, Oli and Animalu<sup>1</sup> developed a theory of the local field correction to the dynamical matrix for the phonon dispersion relation in d-band metals in the transition-metal model potential approximation, with a view to elucidate the occurrence of soft modes in the body-centered cubic transition metals, vanadium and niobium. The results of this effort was subsequently reported<sup>2</sup> in the 1977 Conference on Transition Metals. The important steps in the theory may be summarised briefly, as follows. The dynamical matrix for phonon dispersion relation in a Bravais lattice is split, as in the case of simple metals, into a sum of three terms, namely the Coulombic contribution due to the long-range Coulomb interaction between the bare ions of the metal, a short-range (Born-Mayer) contribution due to the overlap of the core wavefunctions centered on neighboring ions, and the electronic contribution due to the indirect ion-ion interaction via the polarisation field of the conduction electrons. The electronic contribution involves, therefore the screening action of the gas of conduction electrons through the electron-phonon interaction matrix elements,  $g_{q,\lambda}$ , which are proportional to the screened pseudo-potential or model potential form factor,  $V(q)$ . Because of the virtual bound character of the transition-metal d-electrons, local field corrections arise in the conventional screening calculation, as the off-diagonal components of the inverse dielectric matrix. The purpose of this paper is to show that the

contribution to the dynamical matrix from the local field correction tends to cancel the Born-Mayer contribution, with the result that the effective short-range interatomic force turns out to be attractive rather than repulsive.

2. Outline of the Microscopic Theory. - The phonon frequencies in a Bravais lattice are determined by the secular equation

$$\sum_{\beta} [M\omega^2 \delta_{\alpha\beta} - D_{\alpha\beta}(q)] e_{\beta}(q) = 0 \quad (\alpha = 1, 2, 3) \quad (1)$$

where  $D_{\alpha\beta} \equiv D_{\alpha\beta}^C + D_{\alpha\beta}^R + D_{\alpha\beta}^E$  is the dynamical matrix, consisting of the three (Coulombic, Repulsive, and Electronic) contributions, as indicated. The electronic contribution, in particular, has the form:

$$D_{\alpha\beta}^E(q) = -M\omega_p^2 \sum_{g,g'} \frac{(q+g)_{\alpha}(q+g')_{\beta} G(q+g, q+g') - \sum_{g,g'} \frac{g_{\alpha}g'_{\beta}}{|g|^2} G(g, g')}{|q+g|^2} \quad (2)$$

where

$$G(q+g, q+g') = \left( \frac{4\pi z e^2}{\Omega_0 |q+g|^2} \right)^{-2} v(q+g) \chi(q+g, q+g') V_M(q+g) \times \epsilon^{-1}(q+g, q+g') V_M(q+g') \quad (3)$$

is the energy-wave-number characteristic matrix,

$$\chi(q+g, q+g') = [v(q+g)]^{-1} [\delta_{g,g'} - \epsilon(q+g, q+g')] \quad (4)$$

being the generalized susceptibility matrix,  $v(q+g)$  the Fourier transform of the electron-electron interaction,  $\omega_p = (4\pi z^2 e^2 / M\Omega_0)^{1/2}$  the ion plasma frequency,  $z$  the chemical valence and  $\Omega_0$  the atomic volume.

The expression for  $G(q+g, q+g')$  can be separated further into a diagonal part  $G_0(q+g, q+g') \delta_{g,g'}$ , which represents the screening of the Coulombic contribution, and an off-diagonal part  $G_{lc}(q+g, q+g')$  which represents the local-field correction and tends to cancel or "screen" the repulsive contribution. Explicitly,

$$G_{lc}(q+g, q+g') = \left( \frac{4\pi z e^2}{\Omega_0 |q+g|^2} \right)^{-2} \left[ \frac{v(q+g)}{[\epsilon_0(q+g)]^2} \langle k+q+g | \left( -\frac{\partial V_M}{\partial E} \right) | k+q+g' \rangle_{av} V_M^*(q+g) \right. \\ \left. \times V_M(q+g') \right] \left[ \chi_0^{-1}(q+g) - \sum_{g''} \frac{v(q+g)}{\epsilon_0(q+g'')} \langle k+q+g'' | \left( -\frac{\partial V_M}{\partial E} \right) | k+q+g'' \rangle_{av} \right]^{-1} \quad (5)$$

in which  $V_M$  is the transition-metal model potential, and  $\partial V_M / \partial E$  characterizes the depletion hole whose dependence on energy and on core electron wavefunctions is typically of the Harrison form<sup>3</sup>

$$\partial V_M / \partial E = \sum_a |a\rangle \langle a| + \sum_d |d\rangle \langle d| - \sum_d \frac{A|d\rangle \langle d| A}{(E_d - E)^2} \quad (6)$$

It is this dependence on core wavefunctions and the algebraic sign of the local field correction that make it tend to cancel the Born-Mayer term.

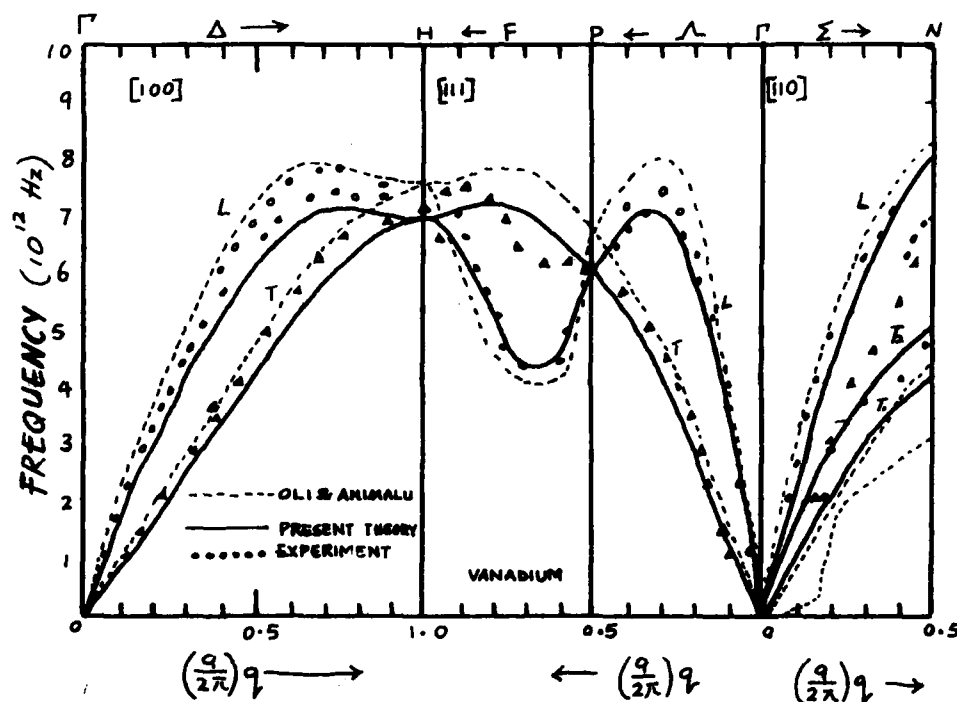


Fig. 1: Phonon spectrum of vanadium in the principal directions.

3. **Numerical Results.**— The phonon frequency reduces to the form  $\nu = (\omega_p/2\pi)(\omega_c^2 + \omega_r^2 - \omega_e^2 - \omega_{lc}^2)^{1/2}$ , in which the Coulombic contribution ( $\omega_c^2$ ) is screened by the electronic contribution given by the diagonal part of  $G(q+g, q+g')$  in the summation in Eq. (2), while the Born-Mayer contribution ( $\omega_r^2$ ) is screened by the local field correction which is well represented by  $\omega_{lc}^2 = 4.5\omega_r^2 \exp(-aq/2\pi)$ , for the longitudinal branches and by  $\omega_{lc}^2 = 0.02\omega_c^2$  for the transverse branches, the numerical factors being determined so as to fit the ab initio calculation of ref. 1 and guarantee symmetry requirements at the points P and H of the Brillouin zone, as shown in Fig. 1. We see from Fig. 1 that the overall agreement between the present theory and experiment<sup>4</sup> is quite good.

#### References.

1. Oli, B.A. and A.O.E. Animalu. Phys. Rev. B **13**, 2398 (1976)
2. Animalu, A.O.E., Transition Metals, Ed M.J.G. Lee. J.M. Parz and E. Fawcett, (1977), p. 706.
3. Harrison, W.A. Phys Rev. **181**, 1036 (1969).
4. Colella, R. and B.W. Batterman, Phys. Rev. B **1**, 3913, (1970).

## THE ULTRASOUND-INDUCED ELECTRIC FIELD GRADIENT (EFG) IN METALS

B. Ströbel, K. Läger, H.E. Bömmel and V. Müller\*

*Universität Konstanz, Fakultät für Physik, Postfach 5560, D-7750 Konstanz, F.R.G.**\*Freie Universität Berlin, Fachbereich Physik, Königin-Luise-Str. 28-30, D-1000 Berlin-33, Germany*

**Abstract.**— The method of quadrupolar nuclear acoustic resonance (NAR) allows to determine the tensor  $S$  relating the ultrasound-induced dynamic EFG (DEFG) to the ultrasonic strain. The observed temperature dependence of  $S$  in cubic Ta metal supports the "phonon-model" for the empirical  $T^{1.5}$ -law of the nuclear quadrupolar interaction in metals.

1. **Introduction.**— The study of the static EFG in non-cubic metals and around defects in metals has been of considerable interest over the past decade (for a review see Ref. 1). One of the motives for this interest is the empirical temperature dependence of the EFG as  $(1 - B \cdot T^{1.5})$  which is observed in nearly all metals. In order to explain this  $T^{1.5}$ -law, two models were propounded: a "phonon-model"<sup>2</sup> attributing the temperature dependence essentially to a Debye - Waller factor (DWF), and a "quadron-model"<sup>3</sup> based on the assumption of quadrupolar elementary interactions in non-cubic metals, in analogy to Bloch's  $T^{1.5}$ -law in ferromagnets which is explained by the excitation of magnons. A crucial test for any form of "quadron-model" would be the absence of a temperature dependence in an undisturbed cubic metal (where the static EFG vanishes, and thus no quadrupolar elementary excitations should be present).

2. **The ultrasound-induced EFG.**— Although the static EFG vanishes for cubic symmetry, one is still able to observe the DEFG accompanying an ultrasonic wave. When interacting with quadrupolar nuclei in a magnetic field, the DEFG can induce transitions between Zeeman - levels, giving rise to quadrupolar NAR<sup>4</sup>. From the intensity of the NAR signal one can determine the fourth-rank tensor  $S$  relating the DEFG  $V_{ij}$  at the site of a nucleus to the applied strain  $\epsilon_{kl}$ :

$$V_{ij} = \sum_{k,l} S_{ijkl} \epsilon_{kl}$$

The analysis of the  $S$ -tensor components allows one also to infer on the electron-phonon interaction in metals<sup>5</sup>. The present contribution is particularly concerned with the temperature dependence of  $S$  which is studied both theoretically (on the basis of the "phonon-model") and experimentally. (A detailed account can be found in Ref. 6).

3. Screened-potential approach.- In the approach of Nishiyama et al.<sup>2</sup> the EFG at a certain nucleus is given by a superposition of screened-potential contributions from all other nuclei, with the screening charges following adiabatically the thermal motions of the nuclei. For our needs we have expanded<sup>6</sup> this approach to a lattice with both thermal and ultrasonic vibrations. We obtain eventually the S-tensor components as a sum over all reciprocal lattice vector points  $\vec{G}$ :

$$S_{\alpha\beta\mu\nu}(T) = -\alpha(1-\gamma_\infty) D_{\text{eff}}(T) \sum_{\vec{G}} \{ \frac{1}{2} (G_\mu \tilde{V}_\nu + G_\nu \tilde{V}_\mu) + \delta_{\mu\nu} \} V_{\alpha\beta}^*(\vec{G})$$

where  $\alpha$  and  $(1-\gamma_\infty)$  are temperature-independent prefactors,  $D_{\text{eff}}(T)$  is an effective DWF,  $\tilde{V}$  denotes the spatial derivative in the Fourier space,  $\delta$  is the Kronecker symbol, and  $V^*(\vec{G})$  is the Fourier transform of the screened-potential EFG at the site of the reciprocal lattice vector point  $\vec{G}$ . It can be shown<sup>6</sup> that within this "phonon-model" the effective DWF (and thus the temperature dependence) for the S-tensor in a cubic metal is essentially the same as one would expect for the static EFG if the metal were non-cubic.

4. Experiment.- The temperature dependence of S has been investigated in cubic tantalum metal which due to its high nuclear quadrupole moment is especially well suited for a NAR experiment. In order to increase the experimental accuracy a novel calibration method was applied, using the magnetic-field-dependent ultrasonic attenuation known as Alpher - Rubin effect for an internal calibration standard. In Ta there are two independent linear combinations of S-tensor components. For these the following experimental results were obtained at 300 K:

$$S_{44} = \pm 6.33(29) \cdot 10^{22} \text{ V/m}^2$$

$$(S_{11}-S_{12})/2 = \mp 4.11(37) \cdot 10^{22} \text{ V/m}^2$$

(Note that with a conventional NAR experiment only the sign of the ratio of the S-tensor components is accessible.)

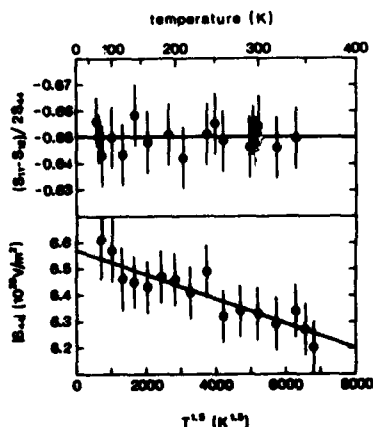


Figure: Temperature dependence of the ratio  $(S_{11}-S_{12})/2S_{44}$  (above) and of the absolute value of  $S_{44}$  (below) in tantalum, using a  $T^{1.5}$  scale. The fit for  $|S_{44}|$  corresponds to a dependence as  $|S_{44}(0)| \cdot (1-B \cdot T^{1.5})$  with  $B = +7(3) \cdot 10^{-6} \text{ K}^{-1.5}$ .

The Figure shows the measured temperature dependence of the S-tensor in Ta. The ratio of the components is found to be temperature-independent within the experimental error. In contrast to this, the S-tensor as a whole shows a decrease with temperature which can be fitted to a  $T^{1.5}$ -law, in analogy to the static EFG. From this fit the parameter B is obtained as  $+7(3) \cdot 10^{-6} \text{K}^{-1.5}$ .

5. Conclusion.— Whereas the "quadron-model" results in a zero temperature dependence for cubic metals, our observations are in complete agreement with the "phonon-model" which predicts a temperature dependence of the S-tensor as a whole. An estimation<sup>7</sup> of the parameter B from the tantalum atomic mass and Debye temperature yields  $+6 \cdot 10^{-6} \text{K}^{-1.5}$ . The observed temperature dependence in tantalum thus supports the idea that the empirical  $T^{1.5}$ -law of the nuclear quadrupolar interaction in metals can be essentially explained by the effect of lattice vibrations.

<sup>1</sup> E.N. Kaufmann and R.J. Vianden, Rev. Mod. Phys. 51, 161 (1979)

<sup>2</sup> K. Nishiyama, F. Dimmling, Th. Kornrumpf, and D. Riegel, Phys. Rev. Lett. 37, 357 (1976)

<sup>3</sup> J. Christiansen, P. Heubes, R. Keitel, W. Klinger, W. Loeffler, W. Sandner, and W. Witthuhn, Z. Physik B 24, 177 (1976)

<sup>4</sup> D.I. Bolef, in Physical Acoustics, ed. by W.P. Mason (Academic, New York, 1969), Vol. IV A, Chap. 3

<sup>5</sup> V. Müller, G. Schanz, and E.J. Unterhorst, this issue.

<sup>6</sup> B. Ströbel and V. Müller, Phys. Rev. B, in print

<sup>7</sup> P. Heubes, W. Keppner, and G. Schatz, Hyperfine Interactions 7, 93 (1979)



**PHONONS IN FERROELECTRICS**

## MICROSCOPIC POLARIZABILITY MODEL OF FERROELECTRIC SOFT MODES

A. Bussmann-Holder, G. Benedek\*, H. Bilz and B. Mokross

*Max-Planck-Institut für Festkörperforschung, 7000 Stuttgart-80, F.R.G.**\*Istituto di Fisica dell' Università and CNISM-CNR, Milano, Italy*

**Abstract.** - A simplified version of a recent microscopic model of ferroelectric soft modes<sup>1</sup> is studied. It is shown that the compensation of long-range and short-range forces<sup>2</sup> which induces the soft mode behaviour of ferroelectric systems can be expressed in terms of a simple linear chain model with a non-linear polarizability at the chalcogenide ion lattice site<sup>3</sup>. This polarizability is equivalent to an on-site electron-two-phonon coupling. The four different temperature regimes which result from the model equations are discussed. The model is applicable to completely different systems such as perovskites,  $\text{SbSI}$ <sup>4</sup>, IV-VI<sup>5</sup> semiconductors and  $\text{K}_2\text{SeO}_4$ <sup>6,7</sup>.

The dynamical properties of ferroelectric perovskites have been successfully described in terms of a strongly anisotropic non-linear polarizability of the oxygen ion<sup>1</sup>. By means of a simplified diatomic linear-chain version of this model<sup>8</sup> it was possible to describe as well the soft mode properties of other systems and to interpret the carrier<sup>9</sup> and defect<sup>10</sup> concentration dependence of the soft mode in terms of microscopic parameters. Within the model the instability of the ferroelectric soft mode is attributed to a negative electron-ion coupling constant  $g_2$  which contains strongly attractive Coulomb forces in a local approximation. Stabilization of the paraelectric modes is guaranteed by the repulsive on-site fourth-order electron-ion coupling  $g_4$  and the second nearest neighbour coupling  $f'$ .

The model has some features in common with those discussed by Pytte et al.<sup>11</sup> as it also represents a double-well problem, where the finite electron core displacement  $w$  is analogous to the static ionic displacements. The classical ground state is given by  $w_0^2 = -g_2/g_4$ .<sup>12</sup> It is however important to note that in this model the double well potential results from the non-linear interaction between electrons and ions. Similar to the double well problem a border line for displacive and order-disorder regimes may be defined which is given by  $2 \left( \frac{g_2}{2f'} \right) \left( 1 + \frac{f}{2f'} \right) < 1$ <sup>12</sup> where the second nearest neighbour repulsive Coulomb interaction  $f'$  is essential for the existence of the displacive regime.

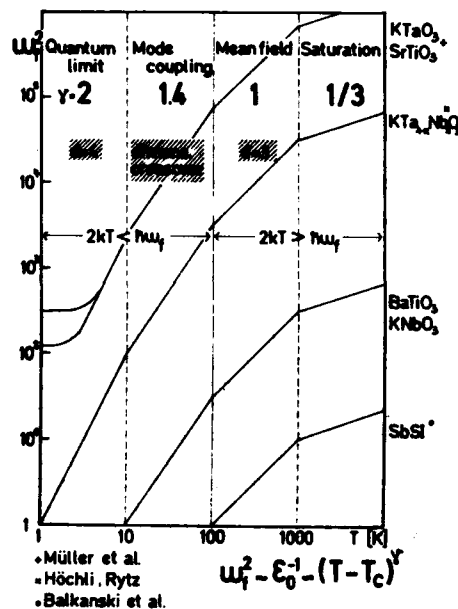


Fig. 1. Temperature regimes which result out of the model, exp.: + 14), x 15), • 4).

For finite  $T_c$  and temperature  $T > T_c$  the well-known mean-field regime occurs which governs the largest temperature region.  $\gamma=1$  has been observed for all ferroelectric systems. For  $T_c \approx 0$  and temperatures close to 0 K again strong deviations from  $\gamma=1$  are observed. In the quantum limit classical renormalization group theory predicts an unchanged exponent  $\gamma=1$ . The quantum limit leads to an apparent enhancement of dimensionality, i.e.  $d=4$ , which yields for the critical exponent:  $\gamma=2$  (refer to D. Rytz, U.T. Höchli, this Conference). The self-consistent phonon approximation (SPA) which leads to exact results in the very displacive limit predicts  $\gamma=2$ , too. The dimensionality crossover regime, appearing at low temperatures, is dominated by a "crossover" exponent,  $1.4 < \gamma < 1.6$ . All temperature regimes have been observed experimentally as indicated in Fig. 1.

An interesting extension of the model is given by the exact solutions of the non-linear equations. Besides kinks new non-linear, but periodic, solutions, "periodons"<sup>12</sup>, are found which play a major role for the description of incommensurate and lock-in transitions. The coupling between periodons and the self-consistent phonons shows completely new features in the dynamics of ferroelectric systems,

Within the model the temperature dependence of the ferroelectric soft mode is given by

$$\mu\omega_f^2 = \frac{2fg}{2f+g} \quad \begin{array}{l} \mu = \text{reduced mass} \\ f = \text{nearest neighbour core-shell coupling} \end{array}$$

where  $g(T) = g_2 + 3g_4 \langle w^2 \rangle$  and  $\langle w^2 \rangle$  is the self-consistent thermal average over the squared relative core-shell displacements at temperature  $T$ .

The different temperature regimes which result from the model are shown in Fig. 1. For high enough temperatures the soft mode saturates and the critical exponent  $\gamma$  with  $\omega_f^2 \approx (T-T_c)^\gamma$ , reaches 1/3 of its mean-field value 1. Experimentally this has been observed for SbSI,<sup>4</sup> KTaO<sub>3</sub> and SrTiO<sub>3</sub>.

(refer to H. Büttner, this Conference).

A more extended version of the SPA and the non-linear problem will be given elsewhere<sup>13,6</sup>.

#### References

1. R. Migoni, H. Bilz, D. Bäuerle, Phys. Rev. Lett. 37, 1155 (1976)
2. P.W. Anderson, Fizika dielektrikov, 1959 ed. G.J. Skanavi (Akad. Nauk SSSR, Moscow) p. 290, W. Cochran, Adv. in Physics 9, 387 (1960)
3. A. Bussmann, H. Bilz, R. Roenspiess, K. Schwarz, Ferroelectrics 25, 343 (1980)
4. M. Balkanski, M.K. Teng, M. Massot, H. Bilz, Ferroelectrics 26, 737 (1980)
5. A. Bussmann-Holder, H. Bilz, W. Kress, Proc. 15<sup>th</sup> Int. Conf. Physics of Semiconductors, Kyoto 1980, J. Phys. Soc. Japan 49, A737 (1980)
6. H. Bilz, H. Büttner, A. Bussmann-Holder, W. Kress, U. Schröder, to be published
7. A. Bussmann-Holder, H. Bilz, H. Büttner, Ferroelectrics, to be published
8. H. Bilz, A. Bussmann, G. Benedek, H. Büttner, D. Strauch, Ferroelectrics 25, 339 (1980)
9. A. Bussmann-Holder, H. Bilz, W. Kress, U. Schröder, to be published
10. A. Bussmann-Holder, H. Bilz, D. Bäuerle, D. Wagner, Z. Phys. B 41, 353 (1981)
11. E. Pytte, Phys. Rev. B 5, 3758 (1972)
12. H. Büttner, H. Bilz, in Recent Developments in Condensed Matter Physics Vol. 1 (ed. Devreese) p. 49, Plenum (1981)
13. H. Bilz, A. Bussmann-Holder, G. Benedek, H. Büttner, D. Strauch, to be published in Z. Phys.
14. K.A. Müller, H. Burkhard, Phys. Rev. B 19, 3593 (1979)
15. D. Rytz, U.T. Höchli, H. Bilz, Phys. Rev. B22, 359 (1980)

## INFLUENCE OF STRONG MAGNETIC FIELDS ON FERROELECTRIC PHASE TRANSITIONS

L.C. Brunel, G. Landwehr\*, A. Bussmann-Holder\*\*, H. Bilz\*\*, M. Balkanski\*\*\*,  
M. Massot\*\*\* and M.K. Ziolkiewicz\*\*\*

*SNCI-CNRS, 38000 Grenoble, France*

*\*Max-Planck-Institut EML, 38000 Grenoble, France*

*\*\*Max-Planck-Institut, 7000 Stuttgart, F.R.G.*

*\*\*\*Université Paris VI, Paris, France*

**Abstract.**— The ferroelectric soft mode in SbSI has been investigated by Raman scattering in strong magnetic fields up to 14 Tesla. The mode frequency shifts towards lower frequencies for a magnetic field perpendicular to the ferroelectric c-axis while the mode frequency is unaffected for a field oriented parallel to the c-axis. The effect is explained in terms of a recent theoretical model which is based on the anomalously strong electron-phonon coupling of the 3p electrons located at the sulphur ions.

1. **Introduction.**— SbSI crystals exhibit at  $\sim 290$  K a transition from a high temperature paraelectric phase to a ferroelectric phase which is triggered by the softening of a transverse optical phonon (1). Within a recent microscopic model based on the highly anisotropic non linear temperature dependent polarizability of the chalcogenide ion it was possible to calculate within the self consistent phonon approximation (SPA) the temperature dependence of the soft mode in  $\text{KTaO}_3$  crystals (2). Because of the high polarizability of the 3p orbitals of  $\text{S}^{2-}$  it seemed interesting to study the effect of a high magnetic field ( $> 10$  Tesla) on the dynamics of the soft phonon. The effect of a field should lead to a shrinkage of the 3p wave functions as it has been calculated by Larsen for  $\text{H}^-$  ions (3). The shrinkage will affect the polarizability of  $\text{S}^{2-}$  and conclusively the ferroelectric soft mode frequency.

2. **Experimental.**— The needle like samples were inside a variable temperature cryostat and surrounded by the gas at atmospheric pressure. The temperature monitored by a Pt resistance was stable to  $\pm 0.02$  degree. The 6754 Å krypton laser line was used to excite the spectra, the power was carefully kept constant (8 mW on the sample). The Raman spectra were recorded in the back scattering arrangement with the laser light incident on the 110 or  $\bar{1}\bar{1}0$  crystal faces. The spectrometer was a Jarrel-Ash double monochromator. The experiments were performed either with a split coil Bitter magnet (maximum field 13 Tesla) or with a conventional Bitter magnet (maximum field 14 Tesla).

3. **Results.**— Spectra were recorded with the magnetic field B parallel or perpendicular to the crystal c-axis. The soft mode is only Raman active in the ferroelectric phase. For each experiment the temperature of the sample  $T_s$  was kept constant below the Curie point  $T_c$  and the field turned on. For  $T_c - T_s$  less than 4 degrees the soft mode frequency shifts to lower frequencies when the magnetic field is perpendicular to the ferroelectric axis (Fig. 1). If the temperature of the sample is too low  $T_c - T_s < 5^\circ$  the field does not affect the soft phonon frequency. The soft mode frequency

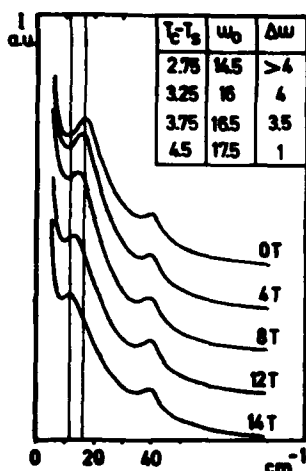


Fig. 1 : Raman spectra of SbSI,  $T_c - T_s = 3.25$  K  
(Insert : frequency of the soft mode  $\omega_0$ , shifts  $\Delta\omega$  observed at 14 Tesla for various sample temperatures.

is unaffected whatever the temperature of the sample for a magnetic field oriented parallel to the c-axis. The results are identical for experiments carried out with the laser beam incident on the  $110$  face or on the  $\bar{1}\bar{1}0$  face of the crystal.

4. Discussion. - The dynamical properties of SbSI could be well described within a simple diatomic model with quartic non linear temperature dependent polarizability at the chalcogenide ion lattice site (Fig. 2). The polarizability  $g(T)$  consists of two parts, a harmonic negative electron-ion coupling  $g_2$  which reflects strongly attractive Coulomb forces and

a non linear part  $g_4$ , which stabilizes the soft mode in the paraelectric as well as in the ferroelectric regime (4).

As has been shown for perovskites and IV-VI compounds only the harmonic part of the polarizability is affected by a charge transfer (5). For SbSI the calculations show that  $g_4$  is constant at all field strengths while  $g_2$  decreases linearly with the field (30 % for 14 Tesla). Close to  $T_c$ , within the model  $w_f^2$  is given by

$$w_f^2 \sim g_2 + 3g_4 \langle w^2 \rangle w_0^2 / 2f$$

Experimental data show that for all fields  $w_f$  as a function of  $T$  reaches the same value at  $T_c - T_B$  where  $T_B = 283$  K (Fig. 3). This behaviour can be expressed in terms of an empirical formula for both the magnetic field dependence and the temperature dependence of  $w_f^2$ ;  $w_f^2 = (T_c - T)^{1+\epsilon} \cdot \alpha_0^2 / (T_c - T_B)^\epsilon$ .

The identification of the empirical parameter with the model parameter is easily shown :

$$w_f^2(B) = \frac{w_0^2}{2f} (g_2(B) + 3g_4 \langle w^2 \rangle) = \frac{w_0^2}{2f} g(T, B)$$

$$g(T, B) = G(B) \cdot (T_c - T)^{1+\epsilon(B)}$$

$$\frac{w_0^2}{2f} G(B) = \frac{\alpha_0^2}{(T_c - T_B)^\epsilon(B)}$$

where  $\epsilon$  is linearly dependent on  $B$  as  $\epsilon = \epsilon_0 + \epsilon' \cdot B$ . The comparison of experimental data with the calculations is shown on Fig. 3.



Fig. 2 : Polarizability model.  $m_1, m_2$  ionic masses ( $S^{2-}, Sb^{3+}$ );  $f, f'$  first and second nearest neighbour coupling constants;  $g_2, g_4$  harmonic and quartic shell-shore coupling constants.

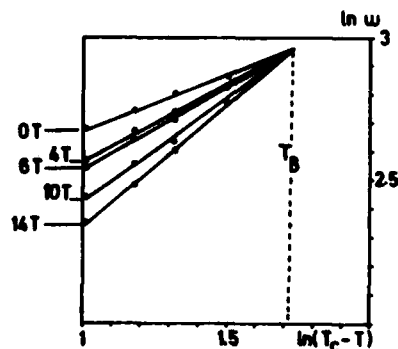


Fig. 3 : Soft mode frequency versus sample temperature for various fields (dots : experimental data - lines : calculations).

To get a more microscopic insight into the magnetic field effect we may compare our calculations with the calculations by Larsen (3) on the effect of a magnetic field on the wave functions of the  $H^-$  ion. These calculations have shown that when a magnetic field is applied the wave functions shrink and change in shape to something resembling an ellipsoid. This effect is strongly related to the magnetic field strength. As we are in the low field

limit ( $\gamma = 3 \cdot 10^{-5}$  see ref. 3) the shrinkage should be of the order of  $1 \cdot 10^{-5}\%$  at 14 Tesla, which would correspond to a directional charge transfer of  $1 \cdot 10^{-6}e^-$ ; this is too low a value to explain the shift of the soft mode we observed.

From the change of  $g_2$  with field it can be concluded that the charge transfer is of the order of  $2.5 \cdot 10^{-4}e^-$ , which corresponds to a shrinkage of  $2.5 \cdot 10^{-3}\%$  in the wave functions of  $S^{2-}$ . As has been shown for K Ta  $O_3$  (2), a charge transfer of 0.5% from the oxygen to the Ta ion leads to a shift of  $150 \text{ cm}^{-1}$  of the soft mode frequency. Taking the same value for SbSI the reorientation of charge by a 14 Tesla magnetic field would shift  $\omega_f$  by  $\sim 1 \text{ cm}^{-1}$ , which is in good agreement with experimental data. It is concluded that the strong enhancement of charge transfer, more than two orders of magnitude greater than the charge transfer calculated for  $H^-$  (2), is due to the highly anisotropic non linear polarizability of the chalcogenide ion.

#### References

1. For pertinent references see :
  - a) M. K. Teng, M. Balkanski and M. Massot, Phys. Rev. B, 5, 1031 (1972)
  - b) J.P. Pouget, S. M. Shapiro and K. Nassan, J. Phys. Chem. Solids, 40, 267 (1979)
2. A. Bussmann and H. Bilz (to be published)
3. D. M. Larsen, Phys. Rev. B, 20, 5217 (1979)
4. H. Bilz, A. Bussmann, G. Benedek, H. Büttner and D. Strauch, Ferroelectrics, 25, 339 (1980)
5. A. Bussmann-Molder, H. Bilz and W. Kress, J. Phys. Soc. Japan, 49, 737 (1980).

# ROLE OF POLAR PHONONS IN THE CHEMICAL BOUND AT STRUCTURAL PHASE TRANSITIONS CHARACTERIZED BY REPETITIVE FOURIER SPECTROSCOPY

F. Gervais and J.L. Servoin

Centre de Recherches sur la Physique des Hautes Températures, C.N.R.S., 45045 Orléans, France

**Abstract.**— The temperature dependence of dynamic effective charges carried by Ti and Nb ions which are the movable atoms involved in the ferroelectric phase transition of  $\text{BaTiO}_3$  and  $\text{KNbO}_3$ , respectively, are reported, as deduced from TO-LO splittings of polar lattice modes, including soft modes. Results below the semiconducting-metal phase transition of  $\text{NbO}_2$  are also discussed.

There is an aspect of certain structural phase transitions with displacements of atoms, but which are not properly displacive, which has been little exploited up to now. When a structural transition occurs, certain cation-anion distances are significantly changed. Such changes of bond lengths affect not only the bond strength  $k$  and, therefore, the frequency of the oscillator  $\omega_0 = (k/\mu)^{1/2}$ , but also the amount of the fractional charge which is supplied by the cation and localized on the anion. But things can be more complicated in compounds like oxides because oxygen becomes unstable, i.e. its polarisability increases rapidly with the increase of the radius of a spherical repartition of positive charges.<sup>1</sup> The knowledge of instantaneous dipole moments created by the motion of positive against negative ions, by infrared reflectivity spectroscopy, gives information not only on polar optical modes and their splitting into TO and LO components, but also on the effective charge  $Ze$ . We will use

the charge  $Ze$  introduced by Scott,<sup>2</sup> which is related to the Szigeti effective charge  $e_s$  via  $Ze = e_s (\epsilon_\infty + 2)/3 \epsilon_\infty^{1/2}$ , where  $\epsilon_\infty$  is the high frequency dielectric constant.  $Ze$  is the dynamic effective charge and incorporates the effects of polarisabilities and local fields. The dynamic effective charge has been measured in homopolar crystals such as graphite<sup>3</sup> for example, and found to be finite whereas the static charge is obviously zero.

The TO and LO frequencies as derived by Cochran,<sup>4</sup> are thus rewritten

$$\Omega_{\text{TO}}^2 = k/\mu - (Ze)^2 / 3\mu\epsilon_\infty V \quad (1)$$

$$\Omega_{\text{LO}}^2 = k/\mu + 2 (Ze)^2 / 3\mu\epsilon_\infty V \quad (2)$$

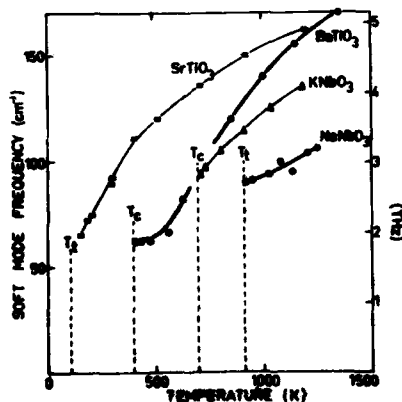


Fig. 1 : Temperature dependence of the soft mode frequency in the cubic PE phase of oxidic perovskites.



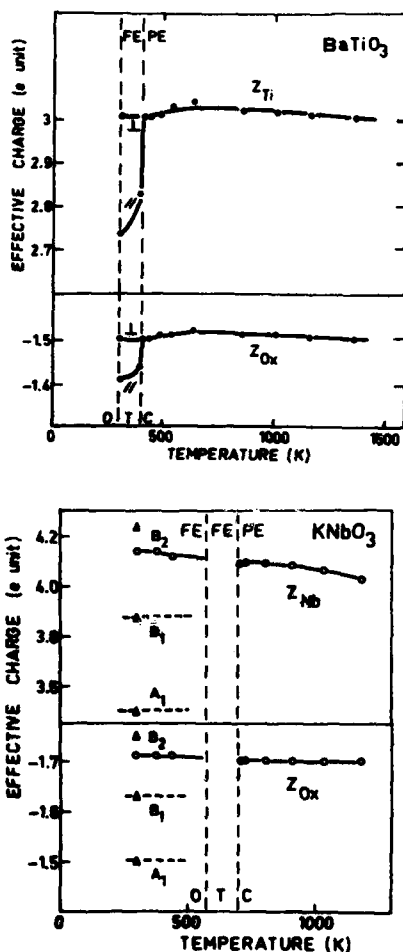


Fig. 2 : Temperature dependence of effective charges in  $\text{BaTiO}_3$  and  $\text{KNbO}_3$  with  $Z_{\text{Ba}} = 1.5$  and  $Z_{\text{K}} = 1$ .

which is most important in Eq. (4) - than in conventional spectrometers since calibrated by comparison with that of a He-Ne laser and reaches  $0.02 \text{ cm}^{-1}$ . It was found<sup>9</sup> that a crossover from a regime which has the classical displacive soft mode behavior to a regime whose features are better described in the language traditionally reserved for order-disorder systems,<sup>10</sup> occurs above the temperature of the cubic - tetragonal transition so that this is finally not the soft mode which triggers the phase transition but rather hopping motions of ions in a triple-well potential. The displacement of Ti ion with respect to the oxygen octahedron, which occurs at  $T_C$  in  $\text{BaTiO}_3$  is however visualized in Fig. 2 on inspection of the marked and sudden decrease of  $Z_{\text{Ti}}$  and  $Z_{\text{Ox}}$  which is ascribed to the shortening of the Ti - O length along the FE axis. Perpendicular to the direction of spontaneous polarization, no significant change of effective charge is observed over a wide temperature range, consis-

(2) minus (1) yields

$$\Omega_{\text{LO}}^2 - \Omega_{\text{TO}}^2 = (Ze)^2 / \mu \epsilon_v V \quad (3)$$

a relation which has been generalized by Scott<sup>2</sup> in the form

$$\sum_j (\Omega_{\text{jLO}}^2 - \Omega_{\text{jTO}}^2)_{\alpha} = (\epsilon_v V)^{-1} \sum_k (Ze)_k^2 / m_k \quad (4)$$

where  $\epsilon_v$  is the dielectric constant of vacuum and the sum on the right side is over all  $k$  ions of mass  $m_k$  in the elementary volume  $V$ .

The temperature dependence of effective charges along a polarization  $\alpha$  can thus be accurately deduced from that of TO and LO frequencies. In strongly polar crystals such as oxitic perovskites, the contribution of the heavily damped soft TO mode to Eq. (4) amounts to  $\leq 1\%$  that of the weakly damped high-frequency LO mode in the cubic phase just above the temperature of transition to the tetragonal phase. It is, therefore, reasonable to renormalize the frequencies in Eq. (4), which has been derived in the harmonic approximation, to account for anharmonic corrections. Results for the temperature dependence of the soft mode in the cubic PE phase of  $\text{SrTiO}_3$ ,  $\text{BaTiO}_3$ ,  $\text{KNbO}_3$  and  $\text{NaNbO}_3$  as obtained by the authors and coworkers,<sup>5-8</sup> are summarized in Fig. 1. Data have been deduced from i.r. reflection spectra recorded with a repetitive Fourier spectrometer and analyzed with the factorized form of the dielectric function. In such a system, the frequency accuracy is much better -

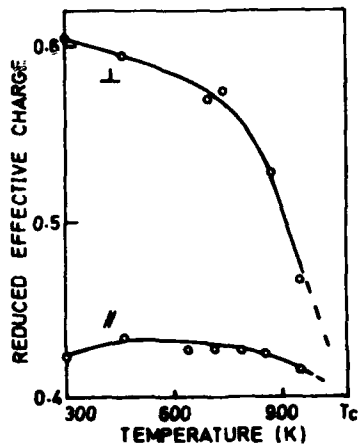


Fig. 3 : Effective charges in  $\text{NbO}_2$ , measured parallel (//) and perpendicular ( $\perp$ ) to the direction of Nb-Nb pairing.

two by two along the c axis. Such a pairing reduces the effective charge  $Z_{//}$  in this direction with respect to  $Z_{\perp}$  as shown in Fig. 3.  $Z_{//}$  would increase and tend towards  $Z_{\perp}$  at the temperature of transition to the high-temperature rutile phase which occurs at 1080 K (in agreement with the observation of isotropic charges in other rutile oxide compounds) but this increase is masked by a decrease of  $\sim 30\%$  of both charges which is understood as a consequence of the progressive delocalization of electrons consistent with a change from semiconducting to metallic character which occurs at the 1080 K transition.

#### References

1. A. Bussmann, H. Bilz, R. Roenspiess and K. Schwarz, *Ferroelectrics*, **25**, 343 (1980).
2. J.F. Scott, *Rev. Mod. Phys.*, **46**, 83 (1974).
3. R.J. Nemanich, G. Lucovsky and S.A. Solin, *Solid St. Commun.* **23**, 117 (1977).
4. W. Cochran, *Adv. Phys.*, **9**, 387 (1960); **10**, 401 (1961).
5. J.L. Servoin, Y. Laspin and F. Gervais, *Phys. Rev. B22*, 5501 (1980).
6. Y. Laspin, J.L. Servoin and F. Gervais, *J. Phys. C*, **13**, 3761 (1980).
7. A.M. Quittet, J.L. Servoin and F. Gervais, *J. de Physique*, **42**, 493 (1981).  
M.D. Fontana, G. Mètrât, J.L. Servoin and F. Gervais, *Ferroelectrics* (to be published).
8. F. Gervais, J.L. Servoin, J.F. Baumard and F. Denoyer, *Solid St. Commun.* (to be published).
9. K.A. Müller, Y. Laspin, J.L. Servoin and F. Gervais, (to be published).
10. A.D. Bruce, in "Solitons and Condensed Matter Physics", Ed. A.R. Bishop and T. Schneider, Springer Verlag (Berlin) p116 (1978).
11. Y. Laspin, J.L. Servoin, F. Gervais and A.M. Quittet, in "Symmetries and Broken Symmetries in Condensed Matter Physics", Ed. N. Boccara, Paris (1981), to be published.
12. F. Gervais, *Phys. status Sol. (b)*, **100**, 337 (1980).
13. F. Gervais, *Phys. Rev. B23*, 15 June issue (1981).

E (x) -  $A_1(z)$  OBLIQUE PHONONS IN TETRAGONAL  $BaTiO_3$ 

T. Nakamura, S. Kojima\*, M.S. Jang, M. Takashige and S. Itoh\*\*

I.S.S.P., Univ. of Tokyo, Japan

\*Inst. Appl. Phys., Univ. of Tsukuba, Japan.

\*\*Tokyo Inst. of Polytechnique, Japan.

**Abstract** - The polarized Raman scattering measurements from tetragonal  $BaTiO_3$  were made, with incident and scattered light polarized both in (x,z) scattering plane, having a crystal rotated about y-axis perpendicular to the plane. The Raman spectra were obtained at  $k_i k_s = 120^\circ$  scattering geometry. Our experimental results of angular dependence of oblique phonon frequencies were analysed by the Merten's theory.

**1. Introduction** -  $BaTiO_3$  crystals have the cubic perovskite structure with point group  $m\bar{3}m$  above  $T_C$  ( $\approx 133^\circ C$ ). It transforms successively to three ferroelectric phases: first to  $4mm$  tetragonal at  $T_C$ , then to  $mm2$  orthorhombic at  $6^\circ C$ , and finally to a  $3m$  trigonal phase at  $-90^\circ C$ . The polarization direction in the three ferroelectric phases is  $[001]$ ,  $[011]$  and  $[111]$ , respectively.

The irreducible representations are  $3T_{1u} + T_{2u} + T_{1u}$  (acoustic) in the cubic phase. In the tetragonal phase, the  $T_{1u}$  modes of cubic phase split into  $3A_1 + 3E$  modes, and the  $T_{2u}$  modes into a  $B_1$  and an  $E$  mode. The four  $E$  optic modes in the tetragonal phase have the Raman polarizability tensor,  $\alpha_{xz}$  or  $\alpha_{yz}$  for the x- or y- polarized phonon, respectively. And  $A_1$  mode has  $\alpha_{xx}$ ,  $\alpha_{yy}$  and  $\alpha_{zz}$  of the Raman polarizability tensor for the z-polarized phonon. A phonon of which wave vector is in a direction that makes an angle of  $0^\circ < \theta < 90^\circ$  to the z-axis, is an oblique phonon, where  $\theta$  is the angle between the phonon wave vector and z-axis. The polar phonons at  $\theta = 0^\circ$  are  $E(x)TO$  and  $A_1(z)LO$  phonons, and at  $\theta = 90^\circ$   $A_1(z)TO$  and  $E(x)LO$  phonons. Merten presented the general formula for the angular dependence of oblique phonon frequencies and calculated the mode frequencies of 6-oblique phonon branches using the infrared reflectivity spectra<sup>2-4)</sup> on flux grown crystals. In this work, in order to obtain Raman spectra of the oblique phonons, we made measurements on a melt grown crystal at the optical geometry with phonon wave vector in the (x,z) plane, and we discuss this experimental results on the basis of Merten's calculated results.

**2. Experiment** - A melt grown  $\text{BaTiO}_3$  single crystal was obtained from Sanders Associates. The size of sample used was about 4.5mm x 6.5mm x 5.0mm (5.0mm along the z-axis). Sample was excited 300 mW Ar-ion laser light at 5145 Å. The geometry for observing the Raman scattering peaks in the (x,z) plane was shown in Fig.1. The incident light vector  $\vec{k}_i$  and the scattered light vector  $\vec{k}_s$  were fixed. The angle between  $\vec{k}_i$  and  $\vec{k}_s$  was  $120^\circ$ . The sample was held on a goniometer which is horizontally rotatable within the accuracy of  $\pm 0.1^\circ$ . The angle  $\theta$  is varied by rotating the sample about the y-axis.

**3. Results and Discussion** - The Raman spectra of  $\vec{k}_i \vec{k}_s = 120^\circ$  scattering geometry obtained at several angle  $\theta$  are shown in Fig.2. The line shape is similar to  $A_1(z)\text{TO}$  phonon spectrum at  $\theta = 76.9^\circ$  and the peak frequencies shift to the low frequency as  $\theta$  is decreased. In order to investigate these spectra, we wrote Merten's generalized formula in to the form:

$$\tan^2 \theta = - \frac{\epsilon_3}{\epsilon_1} \frac{\prod_{i=1}^n ((\omega_{A_1}^{\text{LO}})^2 - \omega^2)}{\prod_{i=1}^m ((\omega_{E_1}^{\text{LO}})^2 - \omega^2)} \frac{\prod_{i=1}^m ((\omega_{E_1}^{\text{TO}})^2 - \omega^2)}{\prod_{i=1}^n ((\omega_{A_1}^{\text{TO}})^2 - \omega^2)} \quad (1)$$

where  $\omega_{A_1}^{\text{TO}}$  and  $\omega_{A_1}^{\text{LO}}$  are  $A_1(z)\text{TO}$  and  $A_1(z)\text{LO}$  phonon mode frequencies,  $\omega_{E_1}^{\text{TO}}$  and  $\omega_{E_1}^{\text{LO}}$  are  $E(x)\text{TO}$  and  $E(x)\text{LO}$  phonon mode frequencies, respectively.  $m$  and  $n$  denote the number of  $E(x)\text{TO}$  (or  $E(x)\text{LO}$ ) and  $A_1(z)\text{TO}$  (or  $A_1(z)\text{LO}$ ) polar modes with the phonon wave vectors in the (x,z) plane.

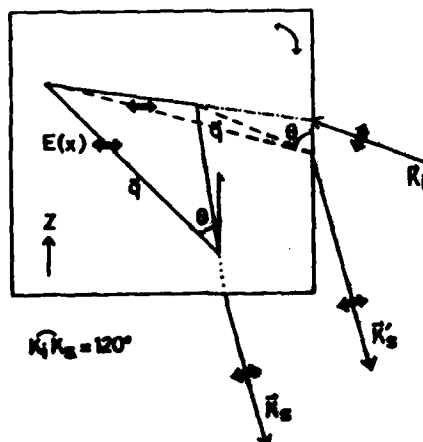


Fig.1 Scattering geometry at  $\vec{k}_i \vec{k}_s = 120^\circ$

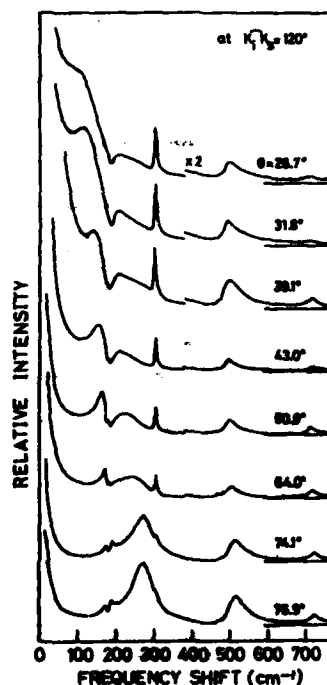


Fig.2 Angular dependence of the Raman spectra at  $\vec{k}_i \vec{k}_s = 120^\circ$

The phonon modes  $E(x)TO$  and  $A_1(z)LO$  at  $\theta = 0^\circ$  were obtained by the  $y(z,x)y+\Delta z$  and  $y(z,z)y+\Delta z$  geometry, respectively. The  $A_1(z)TO$  and  $E(x)LO$  phonon modes at  $\theta=90^\circ$  were obtained by the  $y(z,z)\bar{y}$  and  $y(x,z)y+\Delta x$  spectra, respectively. We calculated angular dependence of each oblique phonon frequency by substituting the mode frequencies into Eq.(1) using a computer. The results calculated are shown by the solid line in Fig.3. In increasing  $\theta$  from  $0^\circ$  to  $90^\circ$ , among seven branches, (1) two remain TO all the way through, TO-TO; (2) two remain LO all the way through, LO-LO; (3) Two change from TO to LO, TO-LO; and (4) one changes from LO to TO, LO-TO.

In Fig.3, the solid circles are peak frequencies of oblique phonon spectra found in Fig.2. Our experimental results of angular dependence of oblique phonon frequencies are in good agreement with Merten's calculated results except for the lowest oblique phonon branch,  $E(x)TO - A_1(z)TO$  and the phonon branch  $A_1(z)LO$  ( $191\text{ cm}^{-1}$  at  $\theta = 0^\circ$ ) -  $A_1(z)TO$  ( $280\text{ cm}^{-1}$  at  $\theta = 90^\circ$ ). The reason why these peak frequencies deviate from the solid line is attributed to the influence of the overdamped  $E(x)TO$  soft phonon which comes from the  $T_{1u}$  mode at the cubic phase

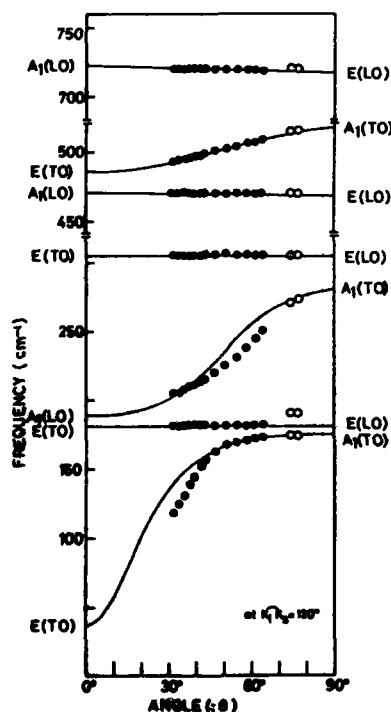


Fig.3 Solid lines are calculated oblique phonon branches and solid circles are experimental data of oblique phonon frequencies.

and that of the broad peak of  $A_1(z)TO$  at  $276\text{ cm}^{-1}$ . Since Merten's treatment does not take account of damping, our experimental plots of the frequencies of oblique phonon modes of which damping are high deviate from the solid curve. The analysis of the influence of damping is in progress.

#### References

- 1) L. Merten, Phys. Stat. Sol. **25** (1968) 125
- 2) W. G. Spitzer, Robert C. Miller, D. A. Kleinman and L. E. Howarth, Phys. Rev. **126** (1962) 1710
- 3) Joseph M. Ballantyne, Phys. Rev. **136** (1964) A429
- 4) A. S. Barker Jr., Phys. Rev. **145** (1966) 391
- 5) S. H. Wemple, M. Didomenico Jr. and I. Camlibel, J. Phys. Chem. Solids **29** (1968) 1797

# RAMAN SCATTERING FROM AMORPHOUS STATE OF FERROELECTRIC $\text{PbTiO}_3$ AND ITS CHANGE IN THE CRYSTALLIZATION PROCESS

T. Nakamura, M. Takashige and Y. Aikawa

*I.S.S.P., Univ. of Tokyo, Japan.*

**Abstract** - Amorphous state of  $\text{PbTiO}_3$  has been prepared. DTA, optical and electron-microscopic investigations has clarified the crystallization temperature and the devitrification phenomenon. In Raman spectra, low-lying response is found in the amorphous state, and the ferroelectric soft mode is found when it is crystallized.

Tsuya et al.<sup>1)</sup> first prepared amorphous flakes of ferroelectric  $\text{PbTiO}_3$  by a roller quenching method. Confirmation of their being really amorphous and neither crystallites nor ceramics, has been made by Uno using X-ray diffraction method.<sup>2)</sup>

Glass and Nassau independently prepared amorphous flakes of crystals such as  $\text{LiNbO}_3$ ,  $\text{LiTaO}_3$ , and reported unexpected high values  $10^5$  of dielectric constant in the vicinity of crystallization temperature.<sup>3)</sup> Lines published a theory, stating that the amorphous state of ferroelectrics having high symmetry structure such as perovskite may have ferroelectricity.<sup>4)</sup>

We prepared amorphous flakes of pure (99.9%)  $\text{PbTiO}_3$  by the twin roller quenching method, without adding "glass formers". Confirmation of being really in the amorphous state is made by x-ray diffractions. EXSAFS study is in progress by Terauchi et al.

Amorphous flakes obtained are about  $20 \mu$  thick, transparent, and optically isotropic, with yellowish color.

On heating the as-quenched material, DTA does not find anomaly at the ferroelectric Curie point ( $490^\circ\text{C}$ ) but does find

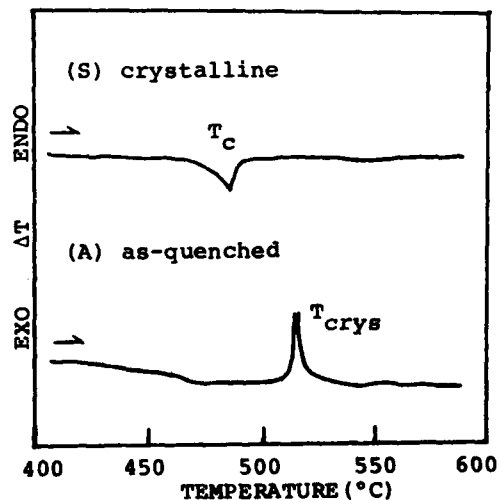


Figure 1

a sharp exothermic peak at the crystallization temperature  $T_{\text{crys}} \approx 540^\circ\text{C}$  (Fig.1).

The devitrification phenomenon is observed, when as-quenched flake is heated up to about  $950^\circ\text{C}$ .<sup>5)</sup>

The Raman scattering experiments were made on the pellets as described above.<sup>6,7)</sup>

Fig.2(A) shows Raman spectrum from as-quenched material. Soft mode does not exist, background is high, and several broad peaks exist.

Fig.2(B), (C) and (D) show effect of heat treatment on Raman spectra. After heat treatment at a temperature above  $T_{\text{crys}}$ , soft mode appears. The frequency of the damping of the soft mode is a function of annealing temperature ( $T_{\text{max}}$ ). With increasing the annealing temperature, the soft mode becomes sharp and hard, other modes than the soft mode become sharp, and the background decreases. If the annealing temperature is  $\approx T_{\text{crys}}$ , spectrum is same as that from the starting material.

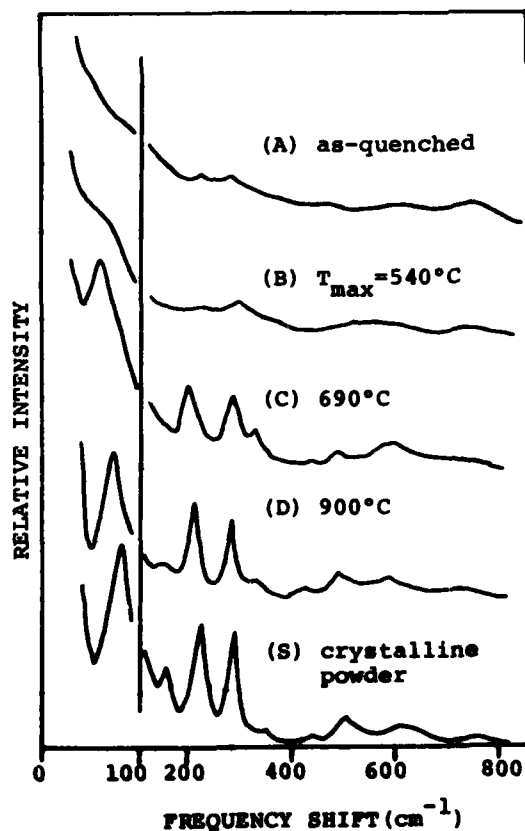


Figure 2

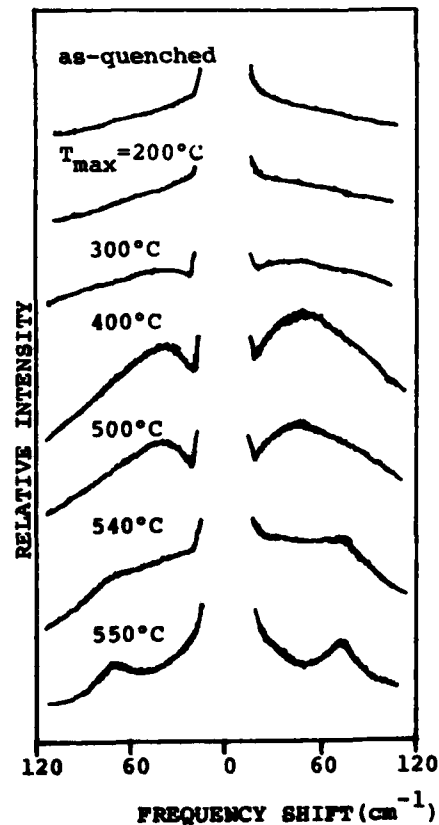


Figure 3

High resolution, low wave-number spectra (using Jobin Yvon Ramanor HG-2S) show low-lying response. Fig.3 shows the low wave-number spectra from samples which had been annealed at various temperatures. When samples had been annealed at temperatures lower than  $T_{\text{crys}}$ , broad low-lying peak was observed. This peak is definitely distinct from the ferroelectric soft mode, which is observed when a sample is annealed above  $T_{\text{crys}}$ . Theoretical investigations on this low frequency atomic vibrations in the amorphous state attract much interest.

#### References

- 1) N. Tsuya and K. I. Arai: Jpn. J. Appl. Phys. 18 461 (1979)
- 2) H. Ozawa and R. Uno : Proc. JSSF-2, Kyoto 1980, J. Phys. Soc. Jpn. 49 suppl. B 144 (1980)
- 3) A. M. Glass, M. E. Lines, K. Nassau and J. W. Shiever: Appl. Phys. Letters 31 249 (1977)
- 4) M. E. Lines: Phys. Rev. B15 388 (1977)
- 5) M. Takashige, T. Mitsui, T. Nakamura, Y. Aikawa and M. S. Jang: Jpn. J. Appl. Phys. 20 L159 (1981)
- 6) T. Nakamura and M. Takashige: Proc. JSSF-2, Kyoto 1980, J. Phys. Soc. Jpn. 49 suppl. B38 (1980)
- 7) M. Takashige, T. Nakamura, H. Ozawa, R. Uno, N. Tsuya and K. I. Arai: Jpn. J. Appl. Phys. 19 L255 (1980)



STUDY OF "PURE"  $\text{KTaO}_3$  AND KTN SINGLE CRYSTALS BY THERMAL CONDUCTIVITY MEASUREMENTS DOWN TO 50 mK

B. Salce, A.M. De Goër and L.A. Boatner\*

*Service des Basses Températures, Laboratoire de Cryophysique, Centre d'Etudes Nucléaires de Grenoble, 85 X, 38041 Grenoble Cedex, France.**\*Sol. State Division, Oak Ridge National Laboratory, Post Office Box 10, Oak Ridge, Tennessee 37830, U.S.A.*

**ABSTRACT** - We have measured the thermal conductivity of pure and doped (Nb, Na, Li, Co, Ag, etc...)  $\text{KTaO}_3$  single crystals to investigate the induced ferroelectric phase transition mechanisms. The strong phonon scattering observed in the "purest"  $\text{KTaO}_3$  is tentatively explained as well as the enhancement of this scattering by substituting Nb in the crystals. Results of preliminary numerical analysis of the curves are given.

In recent years, a substantial amount of work has been undertaken to understand the mechanisms by which a ferroelectric phase transition (FPT) can be induced by adding impurities in "incipient ferroelectrics" such as  $\text{KTaO}_3$  (1). Several authors have shown that the mixed crystals  $\text{KTa}_{1-x}\text{Nb}_x\text{O}_3$  (KTN) can undergo a FPT at a temperature  $T_c$  depending on  $x$  for  $x > x_c = 0.8$  %, but a number of questions of interest about nucleation and dynamic of FPT are not answered yet (2). Also the origin of the disorder induced Raman scattering observed in pure  $\text{KTaO}_3$  is not well understood (3).

**Experimental** - We have studied single crystals of  $\text{KTaO}_3$  (pure or doped with different ions) and KTN crystals ( $0 < x < 3$  %) by measuring the thermal conductivity  $K(T)$  in the temperature range from 50 mK to 200 K, as this property has been shown suitable to investigate samples with both isolated ions and extended defects.

All crystals were grown by a flux technique and preliminary results on  $\text{KTaO}_3$ , pure or doped with Ag or Cu, and KTN crystals, have been previously reported (3). In the present work, other crystals doped with Co, Ni, Fe, Na and Li have been measured, and the effect of heat treatments on pure  $\text{KTaO}_3$  has also been studied. The results are illustrated in figures 1 and 2 and can be summarized as follows :

- (a) The strong phonon scattering observed in "pure"  $\text{KTaO}_3$  is not significantly changed by (i) adding paramagnetic impurities such as Co, Ni, Ag or Cu at concentrations lower than .5 % (ii) annealing in air or vacuum (iii) applying a magnetic field up to 7 Teslas (fig.2 ; note the enlarged scale compared to fig.1)
  - (b) This scattering is slightly increased, together with a change of shape, by adding 1.5 % iron or 0.3 % Li ; the curves are similar to that of a semiconducting sample (fig.2).
  - (c) A strong enhancement of the scattering depending of the concentration of the dopant, and without change in shape, is observed in KTN and  $\text{K}_{1-x}\text{Na}_x\text{TaO}_3$  (fig.1)
- One crystal, namely 1 % lithium-doped  $\text{KTaO}_3$ , cannot fit in this scheme : its behaviour around 7 K is quite the same than the .3 % Li doped crystal, but below .7 K

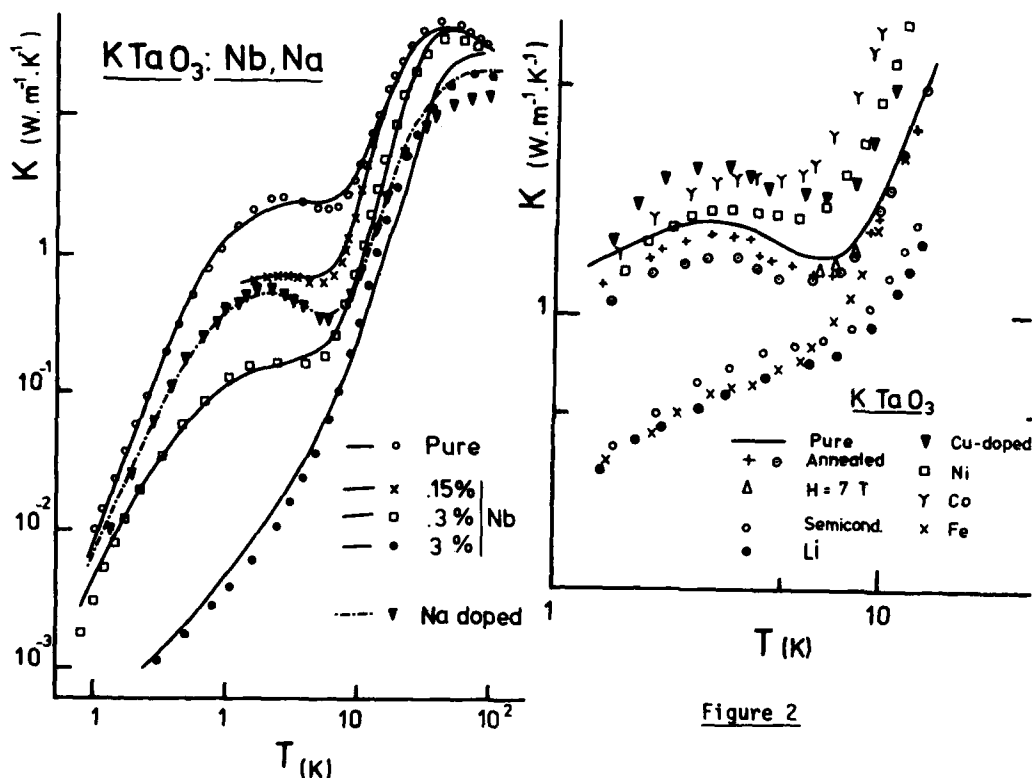


Figure 2

Figure 1

it exhibits a  $K(T) \sim T^2$  law which implies additional phonon scattering in this temperature range similar to that observed in glasses.

**Discussion** - From these results, it is clear that scattering in "pure"  $\text{KTaO}_3$  cannot be due to isolated defects such as paramagnetic impurities or oxygen vacancies or hydrogen. The other point is that Nb and Na doping lead to qualitatively comparable effects; this is not the case for Li, confirming the peculiarity of this system (especially at concentrations around 1%), which has been claimed by several authors (5)(6). Therefore we suggest that phonon scattering in "pure"  $\text{KTaO}_3$  arises from very small quantities of electric dipoles induced by residual and unavoidable Nb or Na (namely  $\sim 10$  ppm, from the more accurate available analysis). These dipoles can locally polarize the lattice over several atomic distances via long range interaction. It can be expected that these extended defects are strongly coupled with phonons. This scattering must be nearly concentration independent as long as no overlap between the perturbed regions takes place. From the less concentrated Nb-doped crystals measured (.15% and .3%) we can roughly estimate at  $\sim 1000$  ppm the mean concentration to achieve overlap so that the radius of one perturbed region would be 5-10 atomic distances. Increasing the Nb concentration results in an extension of the "ordered" part of crystal, until  $x = x_c$  where the whole sample becomes ferroelectric over this

critical concentration. Supplementary Nb do not play any role otherwise acting as ponctual defects at high temperature. Although the measurements on  $K_{1-x}Na_xTaO_3$  crystals are not so comprehensive and that the determination of reliable Na concentration is still a major problem, it can be expected that a quite similar interpretation holds for this system.

Preliminary computer calculations have been done within the Callaway model. All the Nb and Na-doped crystals can be fitted using a total relaxation time

$$\tau^{-1}(\omega, T) = v/\alpha L + A\omega^4 + \tau_R^{-1}(\omega, T) + \tau_U^{-1} + \tau_N^{-1}$$

where  $v/\alpha L$  is the boundary scattering term calculated from the size of the samples,  $A\omega^4$  the point defect scattering and  $\tau_R^{-1}$  is given by the phenomenological expression:

$$\tau_R^{-1}(\omega, T) = D(x) \cdot \omega^2 \cdot f(T) \text{ with } f(T) = \begin{cases} \exp \left[ -\alpha [(T - T_0(x))/T_0(x)]^2 \right] & \text{if } T < T_0(x) \\ \exp \left[ -\beta [T - T_0(x)] \right] & \text{if } T > T_0(x) \end{cases}$$

The parameters needed to fit the adjustments shown in figure 1 are listed in the table 1.

Table 1

	"Pure"	.15 % Nb	.3 % Nb	3 % Nb	Na
$D(x) (s^{-1})$	$3 \cdot 10^6$	$10^7$	$3 \times 10^7$	$2.5 \times 10^8$	$2 \times 10^7$
$\alpha$	2.6	2.6	2.2	1.3	3.2
$\beta$	.15	.3	.22	.18	.22
$T_0 (K)$	8	7.2	6	.35	8

It can be seen that, although  $x$  is changing by a factor 20 for the KTN samples,  $\alpha$  and  $\beta$  are nearly constant within a factor of 2. The parameter  $T_0$  decreases continuously down to  $\approx 0K$  as  $x$  increases. If we suppose that  $T_0$  defines very crudely the wavelength of the most strongly scattered phonons, this wavelength increases with  $x$  and can be related to the extension of the "ordered" part of the crystal. Also the value  $T_0 = 8 K$  for pure  $KTaO_3$  leads to a perturbed volume of about 8 unit cells, in agreement with the qualitative estimation given above.

#### References

- (1) HÜCHLI U.T., WEIBEL H.E. and BOATNER L.A., Phys. Rev.Letters, **39**, 1158 (1977).
- (2) YACOBI Y., Z.Physik B, **31**, 275 (1978).
- (3) PRATER R.L., CHASE L.L. and BOATNER L.A., Phys. Rev.B, **23**, 221 (1981).
- (4) DE GDER A.M., SALCE B. and BOATNER L.A., Proceeding of 3rd I.C. on Phonon Scattering in Condensed Matter, (Providence-US), Plenum Press N.Y., 243 (1980).
- (5) PRATER R.L., CHASE L.L. and BOATNER L.A., Phys. Rev. B, **23**, 5904 (1981).
- (6) BORSA F., HÜCHLI U.T., VAN DER KLINK J.J. and RYTZ D., Phys. Rev. Letters, **45** 1884 (1980).

## SOFT-MODE SPECTRA AND PHASE TRANSITION IN KDP CRYSTAL WITH ADP IMPURITIES

Jong-Jean Kim, Jong-Wook Won and Byoung-Koo Choi

*Physics department, Korea Advanced Institute of Science & Technology, P.O. Box 150 Chongyangni, Seoul, Korea.*

**Abstract.** - On the basis of the  $q$ -dependent coupling interactions between the proton pseudo-spin mode and the lattice phonon mode we could explain qualitatively the observation that the ferroelectric transition temperature of the KDP crystal was lowered as the ADP impurity concentration in the crystal was increased.

1. Introduction - Impurity effects on the dynamical aspects of the phase transition in KDP type crystals have been a great concern of many research workers.<sup>(1,2)</sup> The local soft-modes of the clusters around impurities are known to have a higher softening temperature  $T'_0$  well above  $T_0$  of the crystal soft-mode.<sup>(3,4)</sup>

When the impurity dependent cluster concentration or the temperature dependent cluster size increases to the extent that the nearest neighbor clusters begin to interact, the local soft-modes of the clusters will be correlated in phase to turn into the extended soft-mode of the crystal, and thereby a possible raising of the softening temperature as impurity concentration is increased.

However, we observed from the dielectric constant measurements that  $T_c$  was lowered by 2.9 K when ADP impurities were doped into KDP crystal by 0.13% (Fig. 2).

### 2. Soft-Mode Spectra vs. Phase Transition in KDP

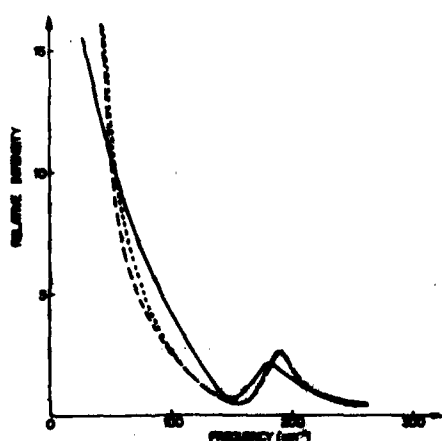


Fig. 1(a): a(ba)c Raman spectra of KDP crystal. — at 299.6 K, .... at 131.4 K and — at 124.9 K.

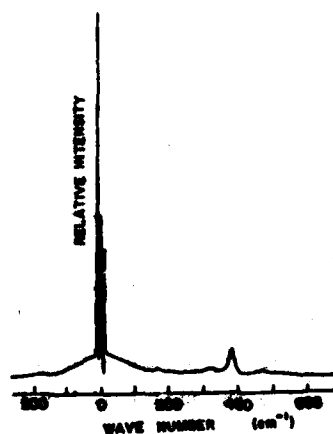


Fig. 1(b): a(ba)c low frequency Raman spectra of ADP crystal at room temperature.

The soft-mode Raman spectra of KDP and the Raman spectra of ADP obtained in the same scattering configuration are compared in Fig. 1. This wing spectrum of the soft-mode continues to remain until 90 K much below the transition temperature 122 K.<sup>(5)</sup> The phonon band at  $180 \text{ cm}^{-1}$  of  $\text{KH}_2\text{PO}_4$  does shift significantly when K or P atom is exchanged by different atoms-  $145 \text{ cm}^{-1}$  for  $\text{KH}_2\text{AsO}_4$  and  $100 \text{ cm}^{-1}$  for  $\text{C}_8\text{H}_2\text{AsO}_4$ .<sup>(6)</sup>

From Fig. 1(b) we can see that in ADP both the overdamped wing and the phonon band are extremely weak, and we see an obvious coupling between the soft-mode and a lattice phonon mode in KDP-type crystals. The uncoupled soft-mode frequency dependence on temperature obtained from the two-oscillator coupled mode analysis can be interpreted either as  $\omega_-$  of the coupled pseudo spin-phonon soft mode or as  $\Omega_T$  of the bare pseudo-spin soft-mode depending on whether we consider the  $180 \text{ cm}^{-1}$  oscillator as another simple phonon of  $B_2$  symmetry or as the  $\text{K-PO}_4$  lattice  $\omega_+$  vibration of the coupled soft-mode. We have the temperature dependence of  $\Omega_T$ ,  $\Omega_T^2 = A(T-T_0)$  different from that of  $\omega_-$ ,  $\omega_-^2 = B(T-T_0)$ . Another difficulty arises that the same observed spectra may be fitted equally well by a number of solutions<sup>(7)</sup>, and indeed we have many different results reported<sup>(8)</sup> for the temperature dependence of the KDP soft-mode,  $T_0$  from 30 K to 117.1 K. Scarparo et al.<sup>(5)</sup> recently emphasized the non-linear behaviour of the soft-mode, denouncing the fits to the  $\omega_0^2 = K(T-T_0)$  behaviour.

3. Extension of Kobayashi model - The q-dependent coupling interaction of Kobayashi<sup>(9)</sup> can be written as

$$F_q^{\text{KDP}} = \frac{1}{NM} \sum_{i,j=1}^N \vec{\epsilon}_q \cdot \vec{\nabla} v(\vec{x}_i - \vec{x}_j) e^{i\vec{q} \cdot (\vec{x}_j^0 - \vec{x}_i)} (1 - e^{-i\vec{q} \cdot \vec{a}})$$

$$= \frac{1}{NM} \sum_{i,j=1}^N \left\{ f d^3 q, \frac{1}{q^2} \vec{\nabla} e^{i\vec{q} \cdot (\vec{x}_i - \vec{x}_j)} \right\} e^{i\vec{q} \cdot (\vec{x}_j^0 - \vec{x}_i)} (1 - e^{-i\vec{q} \cdot \vec{a}}) \quad \text{for KDP crystal,}$$

where one KDP per unit cell is assumed, the Coulomb interaction energy between the i-th proton and the j-th ion,  $v(\vec{x}_i - \vec{x}_j)$ , is Fourier transformed and  $\vec{a}$ , the distance between the two minima of the double well potential, and

$$F_q^{\text{ADP}} = \frac{2}{NM} \sum_{i,j=1}^{N/2} \left\{ f d^3 q, \frac{1}{q^2} \vec{\nabla} e^{i\vec{q} \cdot (\vec{x}_i - \vec{x}_j)} \right\} \cdot e^{i\vec{q} \cdot (\vec{x}_j^0 - \vec{x}_i)} (1 - e^{-i\vec{q} \cdot \vec{A}}) (1 - e^{-i\vec{q} \cdot \vec{a}})$$

for ADP crystal, where  $\vec{A}$  is the distance between the two ADP molecules in the primitive unit cell involved in the antiferroelectric ordering. Suppose an impure KDP crystal where ADP impurities are homogeneously distributed so that an ADP molecule sees another ADP molecule at every n-th nearest neighbor site and KDP molecules in between. As in the case of antiferromagnetic impurities in a ferromagnetic crystal where the antiferro interaction persists even at large distances between impurities and a spin glass transition occurs<sup>(10)</sup>, we assume the ADP impurities persist to contribute the antiferro pseudo spin interactions. Then we have, for the ADP-doped KDP crystal where the unit cell has two ADP and  $(2n-2)$  KDP molecules,

$$F_q' = \frac{2n}{NM} \sum_{i,j=1}^{N/2n} \left\{ f d^3 q, \frac{1}{q^2} \vec{\nabla} e^{i\vec{q} \cdot (\vec{x}_i - \vec{x}_j)} \right\} e^{i\vec{q} \cdot (\vec{x}_j^0 - \vec{x}_i)} \cdot (1 + e^{-i\vec{q} \cdot \vec{A}} + e^{-i\vec{q} \cdot (2\vec{A})} + \dots$$

$$+ e^{-i\vec{q} \cdot (2n-2)\vec{A}} - e^{-i\vec{q} \cdot (2n-1)\vec{A}}) \cdot (1 - e^{-i\vec{q} \cdot \vec{a}}),$$

and we obtain

$$|F'_q|^2 \propto \frac{4n^2(1/4n^2)^2 \{6 - 4\cos(2n-1)\vec{q} \cdot \vec{A} + 2\cos 2n\vec{q} \cdot \vec{A} - 4\cos \vec{q} \cdot \vec{A}\} (1 - \cos \vec{q} \cdot \vec{A})}{(1 - \cos \vec{q} \cdot \vec{A})}$$

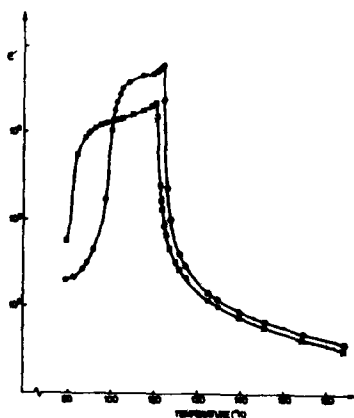


Fig. 2: Temperature dependence of dielectric constant at  $f = 1$  kHz;  $\circ$  (pure),  $\times$  (0.13% ADP)

In the limit of  $q \rightarrow 0$ , as for Raman scattering, this is reduced to give

$$\lim_{q \rightarrow 0} |F'_q|^2 \propto (n-1)^2/n^2$$

$$= 1 - 2/n + 1/n^2 \approx (1 - 2\rho^{1/3} + \rho^{2/3}),$$

where the first term 1 corresponds to  $|F_q^{\text{KDP}}|^2$  of pure KDP and  $\rho$ , the ADP impurity concentration per unit volume. Meanwhile, we have (9)

$$T_c = T_0 + nF^2/\kappa_B \Omega_0^2,$$

and substituting  $F'$  for  $F$  we obtain

$$T'_c = T_c - \alpha\rho^{1/3} + \beta\rho^{2/3}, \quad \rho \ll 1$$

Thus we can see the ferroelectric transition temperature is reduced as ADP impurity concentration  $\rho$  is increased, as depicted in Fig. 2.

#### References

1. A. D. Bruce and R. A. Cowley, *Adv. in Phys.* **29**, 219(1980).
2. V. L. Ginzburg, A. P. Levanyuk and A. A. Sobyenin, *Phys. Lett.* **C57**, 151(1980).
3. K. H. Nöck and H. Thomas, *Z. Physik* **B27**, 267(1977).
4. B. I. Halperin and C. M. Varma, *Phys. Rev.* **B14**, 4030(1976).
5. M. Scarparo, R. S. Katiyar, R. Srivastava, and S. Porto, *Phys. Stat. Sol.* (b) **90**, 543(1978).
6. R. S. Katiyar, J. F. Ryan and J. F. Scott, *Phys. Rev.* **B4**, 2635(1971).  
R. P. Lowndes, W. E. Torberg and R. C. Leung, *Phys. Rev.* **B10**, 911(1974).
7. A. S. Barker, Jr. and J. J. Hopfield, *Phys. Rev.* **135**, A1732(1964).
8. C. Y. She, T. W. Broberg, L. S. Wall, and D. F. Edwards, *Phys. Rev.* **B6**, 1847(1972) and references quoted therein.  
N. Lagakos and H. Z. Cummins, *Phys. Rev.* **B10**, 1063(1974).
9. K. K. Kobayashi, *J. Phys. Soc. Japan* **24**, 497(1968).  
R. Blinc and B. Zeks, *Adv. in Phys.* **21**, 693(1972).
10. T. Oguchi, *Theories of Random Spin Systems*, invited paper #1 - Korean Phys. Soc. spring meeting(1980). See also spin glass papers in *J. Physique* **32**, colloq. C6(1978).

HYPER-RAMAN SCATTERING STUDY OF FERROELECTRIC PHASE TRANSITIONS IN  $\text{SrTiO}_3$  AND  $\text{BaTiO}_3$ 

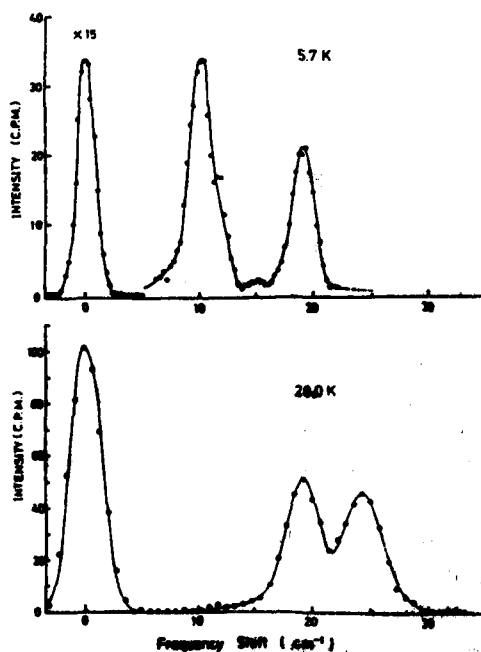
K. Inoue and N. Asai

*Department of Physics, Faculty of Science, Shizuoka University, 836 Ohya, Shizuoka 422, Japan.*

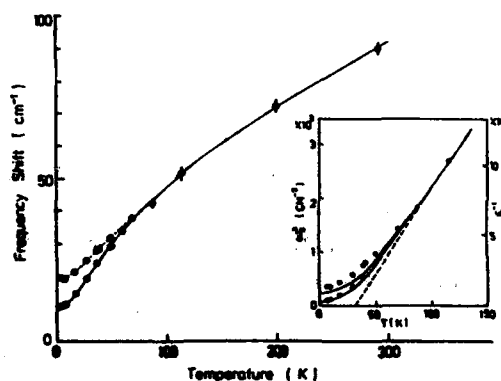
**Abstract.**— We have directly observed the "ferroelectric"  $E_u$  and  $A_{2u}$  soft modes in  $\text{SrTiO}_3$  separately in a temperature range from 50 K to 4.5 K by the hyper-Raman scattering method. Variation of the respective mode frequencies with temperature is measured and is compared to that of the dielectric constant. Further, it is found that the intensity of hyper-Rayleigh scattering light drastically increases as the temperature is lowered till 4.5 K.

As for  $\text{BaTiO}_3$ , the hyper-Raman spectra in the cubic phase have been measured with special emphasis on the spectral profile of the seemingly overdamped mode. The present result, however, seems to contradict the existence of the soft mode.

1. **Introduction.**— All phonon modes classified into  $3F_{1u} + F_{2u}$  in the cubic phase ( $O_h^1$ ) of  $\text{SrTiO}_3$  and  $\text{BaTiO}_3$  are not Raman-active but hyper-Raman-active at the Brillouin zone center. In the tetragonal phase



**Fig. 1.** Examples of Stokes hyper-Raman spectra in  $\text{SrTiO}_3$ .



**Fig. 2.** A plot of the observed mode frequency  $\omega_s$  versus temperature in  $\text{SrTiO}_3$ . The inset shows a comparison of  $\omega_s^2$  with  $\epsilon^{-1}$  (solid lines) in ref. 4.

( $D_{4h}$ ) of  $\text{SrTiO}_3$  below 105 K, the  $E_u$  and  $A_{2u}$  soft modes stemmed from the lowest  $F_{1u}$ -TO mode are still hyper-Raman-active. Consequently, the hyper-Raman scattering (abbreviated as HRS) should provide a useful tool for studying the "ferroelectric" soft mode, if any.

2. Experiment.- A standard Q-switched  $\text{Nd}^{3+}$ -YAG laser was employed at a repetition rate of 400 pps to excite the HRS at a level of peak power less than 5 kW. The sample of  $\text{SrTiO}_3$  was prepared in such a form as allowing to observe the phonons having the wavevector  $q$  parallel to one of the crystallographic axes even in the multi-domain state below 105 K. The form of the  $\text{BaTiO}_3$  sample is such that the phonons of  $q \parallel \langle 100 \rangle$  or  $\langle 110 \rangle$  can be measured in the cubic phase above 128°C. The HR spectra of both cases were measured in the right-angle geometry by using a home-made detection system with a gated photon-counter.

3. Results and Discussion.- a)  $\text{SrTiO}_3$ - Examples of the unpolarized Stokes HR spectra below 100  $\text{cm}^{-1}$  are shown in Fig. 1, where the horizontal scale is plotted as the shift relative to the harmonic frequency of the laser  $2\omega_0$ . It is found that around 50 K the soft mode starts to split into two spectral lines, the separation of which becomes larger as the temperature  $T$  is lowered. The higher- and lower frequencies can be assigned to those of the  $A_{2u}$  and  $E_u$  modes respectively, on the basis of a comparison with HR spectra<sup>2</sup> observed in the forward direction. This assignment agrees with an anticipation by pressure-induced Raman scattering<sup>3</sup>. The result on the mode frequency  $\omega_s$  versus  $T$

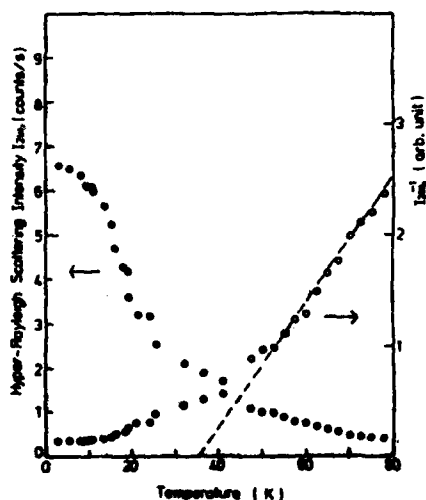


Fig. 3. A plot of the intensity of the hyper-Rayleigh scattering light,  $I_{2\omega_0}$ , versus  $T$  in  $\text{SrTiO}_3$ .

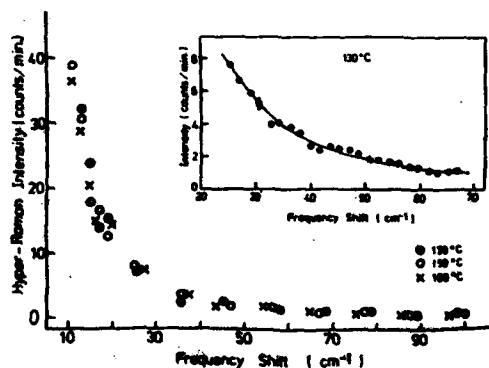


Fig. 4. Examples of hyper-Raman spectra for  $q \parallel \langle 100 \rangle$  in  $\text{BaTiO}_3$ . The inset shows that an overdamped Lorentzian shape (solid line) can be fitted to the data.



Table I Comparison of  $\omega_s$  and  $\Delta\omega$  in  $\text{SrTiO}_3$ 

mode	present work (5.7 K)		anticipation in ref. 3 (2 K)		ref. 1 (8.0 K)	
	$\omega_s$ ( $\text{cm}^{-1}$ )	$\Delta\omega$ ( $\text{cm}^{-1}$ )	$\omega_s$ ( $\text{cm}^{-1}$ )	$\Delta\omega$ ( $\text{cm}^{-1}$ )	$\omega_s$ ( $\text{cm}^{-1}$ )	$\Delta\omega$ ( $\text{cm}^{-1}$ )
$E_u$	10.3	1.3	9.1			
$A_{2u}$	19.3	0.8	19.1			< 0.5 (not split)
		15.0 (200 K)				13.8 (230 K)

Table II Mode frequency in  $\text{BaTiO}_3$  (160°C)

mode	$\omega$ ( $\text{cm}^{-1}$ )
TO-1	—
LO-1	] 185 $\text{cm}^{-1}$
TO-2	
LO-2	462
TO-3	490
LO-3	713
$F_{2u}$	312

is shown in Fig. 2. The spectral line-width  $\Delta\omega$  of both modes is found to become narrower as T is lowered. Values at 5.7 K and 200 K are shown as an example in Table I. A comparison of the result  $\omega_s$  versus T with the existing data<sup>4</sup> of the dielectric constants  $\epsilon_g$  and  $\epsilon_u$  versus T is made through the LST relation (Fig. 2). A considerable discrepancy between both curves is recognized at low temperatures. However, the present values at 5.7 K are very consistent with the deduced ones.<sup>3</sup>

Next, it is found that the relative intensity  $I_{2\omega_s}$  of the hyper-Rayleigh scattering light rapidly increases as T is lowered (Fig. 3). The inverse plot of  $I_{2\omega_s}$  vs T resembles very much that of  $\epsilon$  recently reported<sup>5</sup>, indicating another manifestation of the quantum effect.

b)  $\text{BaTiO}_3$  - Examples of the HR spectra for  $q \ll 100$  in the cubic phase are shown only in a range below  $100 \text{ cm}^{-1}$  in Fig. 4. Those are measured with all experimental conditions unchanged except the sample temperature. The phonon frequencies observed are listed in Table II. It has turned out that the spectrum does not exhibit any remarkable variation with T including the integrated intensity. Similar spectra are also observed for  $q \ll 110$  phonon. From this evidence it follows that the existence<sup>6,7</sup> of the soft optic mode related to the cubic-tetragonal phase transition might be negative in the present work. More detailed study on this problem is in progress.

The authors acknowledge the partial support by the Grant-in-Aid for Scientific Research from the Ministry of Education (Japan).

#### References

1. P. A. Fleury and J. M. Worlock, Phys. Rev. **174**, 613 (1968); Y. Yamada and G. Shirane, J. Phys. Soc. Jpn. **26**, 396 (1969).
2. K. Inoue, N. Asai and T. Sameshima, J. Phys. Soc. Jpn. **50**, 1291 (1981).
3. H. Uwe and T. Sakudo, Phys. Rev. **145**, 271 (1976).
4. T. Sakudo and H. Unoki, Phys. Rev. Lett. **26**, 851 (1971).
5. K. A. Miller and H. Burkard, Phys. Rev. **B19**, 3593 (1979).
6. A. S. Barker, Phys. Rev. **145**, 391 (1966); J. M. Ballantyne, *ibid.*, **126**, 1710 (1962).
7. J. Harada, J. D. Axe and G. Shirane, Phys. Rev. **B4**, 155 (1971).

## DYNAMICAL STUDY OF PHONONS IN FERROELECTRIC LEAD TITANATE

R.S. Katiyar and J.D. Freire

*Instituto de Física, UNICAMP, 13.100 Campinas, S.P., Brazil.*

**Abstract.**— Lattice dynamical formalism using rigid ion model with long range coulomb forces and short range axially symmetric forces has been applied to the crystal of lead titanate in tetragonal phase. All zone center phonons and a few zone boundary phonons were used in determining the force constant parameters both at room temperature and close to  $T_c$  by nonlinear least squares analysis. The results indicate that the Ti-O short range forces are at least one order of magnitude larger than the Pb-O forces. Moreover oxygens retain an effective charge of 73% of their free ion value, whereas titanium possess only 67% of their free ion charge. The eigenvector calculations of the lowest optic mode of E-symmetry correspond to the prediction by Last, whereas in  $\text{BaTiO}_3$  the computed eigenvectors confirm the description of the soft mode due to Slater. The parameters obtained, have been utilized to compute elastic and piezoelectric properties of  $\text{PbTiO}_3$ . The calculations of the zone centre phonons near  $T_c$  reveal that the small anharmonic forces could lead to the observed frequency changes.

The importance of lattice dynamics in studying the structural phase transitions in cubic perovskite structures was first realized by Cochran.<sup>1</sup> No work has, however, appeared in literature dealing with the interatomic forces in tetragonal phase and their variations with temperature. Lead titanate is one example of this class and undergoes a ferroelectric-paraelectric phase transition at 493°C, below which the crystal symmetry is tetragonal ( $C_{4v}^1$ ) with one formula unit in the unit cell. According to Shirane et al.<sup>2</sup> the unit cell structure may be described by placing Pb (K=1) at the cell corners, Ti (K=2) at  $(\frac{1}{2}, \frac{1}{2}, u)$  and oxygens (K=3,4,5) at  $(\frac{1}{2}, \frac{1}{2}, v)$ ,  $(\frac{1}{2}, 0, w)$ ,  $(0, \frac{1}{2}, w)$ ; where  $u = 0.541$ ,  $v = 0.112$  and  $w = 0.612$  with  $a_0 = 3.904$  Å and  $c_0 = 4.15$  Å. Group theoretical analysis for zone centre phonons shows that the 12 optical modes should be classified as follows:

$$3A_1(\text{Pb}, \text{Ti}, \text{O})_{x,y} + 4E(\text{Pb}, \text{Ti}, \text{O})_{x,y} + B_1(\text{O})_z$$

The subscripts x,y,z denote the displacement directions of the ions included in bracket. In the rigid ion formalism the potential energy of an ionic crystal can be written as the sum of short range repulsive and long range coulomb forces. For lead titanate considering ion pair potentials for all interactions for distances less than 3.5 Å, the short range part of potential energy may be elaborated as follows:

$$\begin{aligned} \phi_{S.R.} = & \phi_{13}(r_{13}) + \phi_{14}(r_{14}) + \phi_{14}'(r_{14}') + \phi_{23}(r_{23}) + \phi_{23}'(r_{23}') + \phi_{24}(r_{24}) + \\ & \phi_{34}(r_{34}) + \phi_{45}(r_{45}) \end{aligned} \quad (1)$$

where  $r'$  are second neighbor distances. Each short range potential is assumed to be of axially symmetric type. The potential minimum equations were worked out in the manner suggested by Katiyar.<sup>3</sup> These conditions were in turn used to compute five tangential force constant parameters, namely,  $B_{13}$ ,  $B_{14}$ ,  $B_{23}$ ,  $B_{24}$  and  $B_{25}$ . In order to reduce the number of force constant parameters further we assumed that the radial force constants may be interrelated by Born-Meyer type of potential function,<sup>4</sup> i.e.

$$A_{34} = A_{45} e^{-\alpha_{0-0}(r_{34}-r_{45})} \quad (2)$$

with similar relations for other  $A_{KK'}$ . The constant  $\alpha_{0-0}$  can be related to  $n_{0-0}$  in Pauling's potential function<sup>4</sup> as follows:

$$\alpha_{0-0} = (n_{0-0} + 1)/R_{0-0}^0 \quad (3)$$

where  $R_{0-0}^0$  corresponds to the distance between the two oxygens in contact. These transformations allowed us to reduce the number of undetermined parameters to eleven, namely,  $n_{Rb-0}$ ,  $n_{Ti-0}$ ,  $n_{0-0}$ ,  $A_{14}$ ,  $A_{23}$ ,  $A_{45}$ ,  $B_{14}$ ,  $B_{34}$ ,  $B_{45}$ ,  $Z_{Pb}$  and  $Z_0$ . The value of  $n_{0-0}$  was fixed to 7 as given by Pauling and the remaining 10 parameters were obtained by least squares fit to the zone centre phonons<sup>5</sup> and a few zone boundary phonons<sup>6</sup> using the method suggested by Katiyar and Mathai.<sup>7</sup> Reasonably good agreement between the calculated and the observed frequencies was obtained except for  $A_1(TO_3)$  phonon in which case the calculated frequency is  $578 \text{ cm}^{-1}$  whereas the observed frequency was  $646 \text{ cm}^{-1}$ . This and other small disagreements may be due to the neglect of the polarisabilities of the ions into the rigid ion model.

The values of the best fitted parameters were used to compute the axially symmetric force constant parameters and they are as follows:  $A_{13} = 19.25$ ,  $A_{14} = 38.01$ ,  $A_{15} = 6.94$ ,  $A_{23} = 192.80$ ,  $A_{24} = 48.89$ ,  $A_{25} = 122.80$ ,  $A_{34} = 4.85$ ,  $A_{45} = 6.27$ ,  $B_{13} = -2.62$ ,  $B_{14} = -7.27$ ,  $B_{15} = -2.02$ ,  $B_{23} = -25.10$ ,  $B_{24} = -0.49$ ,  $B_{25} = -14.31$ ,  $B_{34} = -1.38$  and  $B_{45} = -2.01$ ; all in the units of  $e^2/2v$ .

The parameters shown above appear to be physically acceptable. The large values of  $A_{23}$ ,  $A_{24}$  and  $A_{25}$  indicates that there are strong forces between Ti and O ions, whereas the oxygen-oxygen interactions ( $A_{34}, A_{45}$ ) are considerably weaker. The ionic charge obtained for Pb ion is  $1.695e$  and for the oxygen ion is  $-1.456e$ . These values suggest highly ionic character of the crystal.

From the eigen vector calculations the normal mode picture for the soft mode corresponding to  $E(TO_1)$  is drawn in Fig. 1. In this mode both Ti and O ions move against Pb ions along x- or y-axis. Similar movements occur in the soft mode  $A_1(TO_1)$  along z-direction. This description of the soft mode is in agreement with the proposal by Last<sup>8</sup> for  $BaTiO_3$ . We have carried out the above calculations for  $BaTiO_3$  as well and the eigen vector calculations for the lowest dipolar mode suggest that both Ba and O ions move against the Ti ions along the principal axes which is in agreement with the picture proposed by Slater<sup>9</sup> for  $BaTiO_3$ .

We have also adjusted our force constant parameters to obtain reasonably good agreement between the observed<sup>10</sup> and the calculated frequencies close to the phase

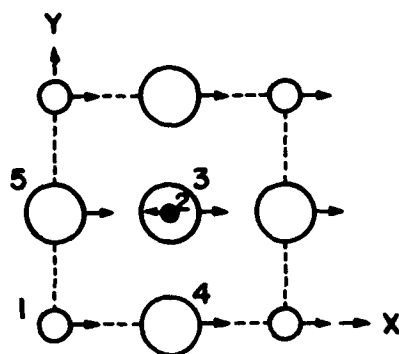


Fig. 1: Normal mode picture for  $E(TO_1)$  mode ions have been projected on the  $xy$ -plane.

transition temperature ( $\sim 493^\circ\text{C}$ ) in  $\text{PbTiO}_3$ . The lowest optic mode  $E(TO_1)$  varies from  $88\text{ cm}^{-1}$  to  $54\text{ cm}^{-1}$ , whereas the lowest  $A_1(TO_1)$  decreases to  $62\text{ cm}^{-1}$  from  $147\text{ cm}^{-1}$ . A close look at the force constant variations reveals very small changes in their values except for the parameters  $A_{24}$ ,  $A_{34}$  and  $A_{45}$ , whose values decrease by about 20-30% near  $T_c$ . Perhaps relatively small anharmonic forces could explain such changes.

The acoustic wave propagation in piezoelectric crystals has been discussed in detail by Hutson and White.<sup>11</sup> Following their approach we have computed piezoelectric and elastic coefficients for lead titanate using the force constant parameters obtained from phonon frequencies fit. The calculated values of elastic constants are as follows (in units of  $10^{11}\text{ N/M}^2$ ):  $C_{11} = 1.327$ ,  $C_{12} = 0.846$ ,  $C_{13} = 0.891$ ,  $C_{33} = 0.934$ ,  $C_{44} = 0.801$  and  $C_{66} = 0.927$ ; and those of piezoelectric coefficients are given below (in units of  $10^{-12}\text{ C/N}$ ):  $d_{15} = 45.52$ ,  $d_{31} = -15.07$ ,  $d_{33} = 51.00$ .

In above calculations we have used the values of  $\epsilon_{11}/\epsilon_0 = 125.6$  from the work of Frey and Silberman and  $\epsilon_{33}/\epsilon_0 = 30.0$  (dielectric constant along  $c$ -axis) as reported by Bhidé et al. Unfortunately no single crystal measurements exist in the literature to compare with our calculations. We have also computed these coefficients for  $\text{BaTiO}_3$  and except for  $C_{44}$  they compare well with the calculations of Devonshire.<sup>12</sup>

#### References

1. W. Cochran, *Adv. Phys.* **9**, 387 (1960); **10**, 401 (1961).
2. G. Shirane, R. Pepinsky and B.C. Fraser, *Acta Cryst.* **9**, 131 (1956).
3. R.S. Katiyar, *J. Phys.* **C3**, 1963 (1970).
4. M. Born and K. Huang, "Dynamical Theory of Crystal Lattices", Oxford Univ. Press, London, 1954.
5. R.A. Frey and E. Silberman, *Helv. Phys. Acta.* **49**, 1 (1976).
6. G. Shirane, J.D. Axe and J. Harada, *Phys. Rev.* **B2**, 155 (1970).
7. R.S. Katiyar and A.M. Mathai, *Siam J. on Scientific and Statistical Computing*, under publication.
8. J.T. Last, *Phys. Rev.* **105**, 1740 (1957).
9. J.C. Slater, *Phys. Rev.* **78**, 748 (1950).
10. G. Burns and B.A. Scott, *Phys. Rev.* **B7**, 3088 (1973).
11. A.R. Hutson and D.L. White, *J. Appl. Phys.* **33**, 40 (1962).
12. A.F. Devonshire, *Phil. Mag.* **40**, 1040 (1949).

INTERACTION OF PHONONS WITH OTHER EXCITATIONS

## PHONONS IN EXCITED RUBY

A.A. Kaplyanskii, S.A. Basoon and V.L. Shekhtman

*A.F. Yoffe Physicotechnical Institute, Academy of Sciences of the U.S.S.R., Leningrad, 194021, U.S.S.R.*

**Abstract.** - New results concerning the properties of acoustic phonons 0.87 THz in ruby are considered including (1) attenuation and anharmonic scattering of ballistic phonons and (2) kinetics of resonance phonon trapping.

Resonance interaction of the 0.87 THz ( $29 \text{ cm}^{-1}$ ) phonons with  $E-2A$  levels of  $\text{Cr}^{3+}$  ions plays an important role in many physical processes in excited ruby. Investigation of these processes provides valuable information on both the fundamental properties of the terahertz acoustic phonons proper in crystals, and phonon interaction with impurity centers. The studies have been carried out in several groups /1 - 6/. We consider below the recent results obtained in our group.

### 1. Attenuation of the $29 \text{ cm}^{-1}$ Ballistic Phonons.

Optical detection /2/ of the  $29 \text{ cm}^{-1}$ , TA and LA phonons propagating ballistically in heat pulses /3/ was used for a quantitative measurement of  $29 \text{ cm}^{-1}$  phonon attenuation in ruby with  $\text{Cr}^{3+}$  concentration  $C=0.02\%$  /7/ and  $C=0.001\%$ . Measurements were performed at  $T=1.8 \text{ K}$  for different directions h-d (heater-detector) lying in the crystal symmetry plane  $\sigma_v$  ( $\theta$  is the angle between the group velocity  $\vec{S}$  and the axis  $C_2$ ). The magnitude of mean free path  $\bar{l}$  for the LA and TA phonons depends essentially on the phonon propagation direction in the  $\sigma_v$  plane. Fig.1 shows a  $\bar{l}$  vs.  $\theta$  plot. When one goes over from  $C=0.02\%$  to  $C=0.001\%$ , the magnitude of  $\bar{l}$  for a given  $\theta$ , as a rule, increases strongly. In a 0.001% sample one observes weakly decaying LA and TA modes with  $\bar{l}$  being far in excess of sample dimensions, making only a lower estimate  $\bar{l} > 200 \text{ nm}$  possible. At the same time for some LA modes with small  $\bar{l} \sim 10 \text{ nm}$  the magnitude of  $\bar{l}$  does not change significantly with  $C$ .

The results indicate an extremely large contribution to  $\bar{l}$  from phonon scattering on the Cr ions and (or) accompanying defects. The magnitude of  $\bar{l}$  in low concentration ruby gives the lower limit for

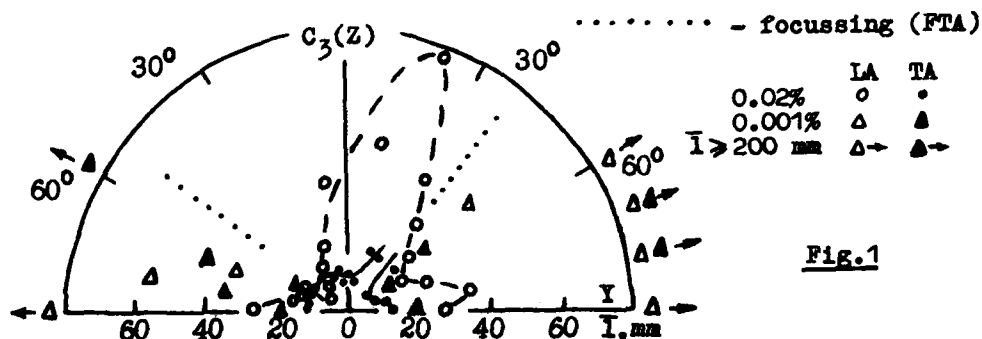


Fig. 1

$\tau_p$  decay time of LA /8/ phonons. There exist both long lived LA modes with  $\tau_p \geq 20 \mu\text{s}$  and apparently also short lived modes with  $\tau_p \sim 1 \mu\text{s}$  (for the angles  $\theta$  under which the experimentally found  $\bar{I}$  does not depend significantly on  $C$ ). The anisotropy in  $\tau_p$  is probably associated with the elastic anisotropy of the crystal and the conservation laws in the elementary events of LA phonon decay. Note that theory gives for the decay time of the  $29 \text{ cm}^{-1}$  LA phonons a value of  $\tau_p = 4.6 \mu\text{s}$  /9/ assuming the crystal to be elastically isotropic.

## 2. Decay of Mode-Averaged $29 \text{ cm}^{-1}$ Phonons.

An attempt has been made to estimate experimentally the mode-averaged phonon anharmonic lifetime by measuring the decay of the whole  $29 \text{ cm}^{-1}$  nonequilibrium phonon ensemble in the crystal immersed in superfluid helium ( $T=1.8 \text{ K}$ ). The conditions for the  $29 \text{ cm}^{-1}$  phonon escape from the bulk of the sample to its boundaries through which the phonons eventually lose energy to the helium bath were controlled. Heat pulses were injected from a heater  $h$  into cube-shaped samples with edge  $L=2+10 \text{ mm}$ . The  $29 \text{ cm}^{-1}$  nonequilibrium phonon concentration was derived from  $R_2(t)$  luminescence pulses escaping from a test volume  $\sim 0.5 \text{ mm}$ , pumped with cw laser at extremely low power. Fig. 2 shows  $R_2(t)$  pulses in a sample with  $L=10 \text{ mm}$ ,  $C=0.5\%$  measured with two detectors, one close to  $h$  and the other near the opposite face. At long times the  $R_2(t)$  pulses coincide thus indicating the  $29 \text{ cm}^{-1}$  phonons to be distributed throughout the crystal. The decay of  $R_2(t)$  at such times is exponential over  $2+3$  decades of  $R_2$  intensity. At  $L \geq 3 \text{ mm}$  the decay does not depend on the power and duration of heating, while at  $L=2 \text{ mm}$  the decay is constant only at low power inputs employed in the experiment.

Fig. 3 shows the dependence of decay time  $\tau$  on  $L$ . For the sample with  $C=0.02\%$ ,  $\tau \sim L$  (curve 1) which corresponds to the surface phonon

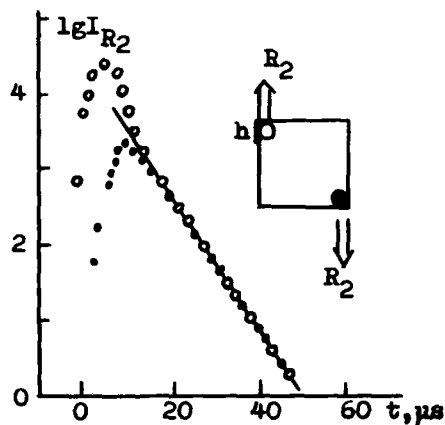


Fig. 2

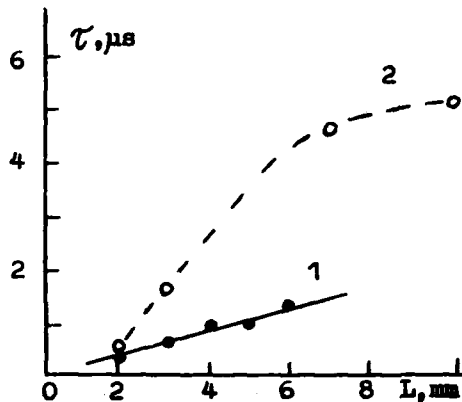


Fig. 3

decay in the ballistic regime, the decay rate being proportional to the frequency of phonon collisions with the surface, i.e.  $\tau^{-1} \sim S/L$ . In the samples with  $C=0.5\%$  the mean free path is  $\bar{l} \leq 0.4$  nm, the propagation occurring by diffusion. The phonon escape to the surface is slowed down (curve 2) and is determined by diffusion time  $\tau_d \sim L^2$ .

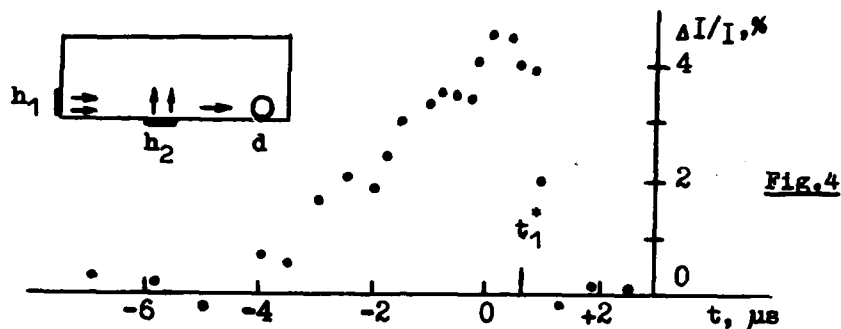
$\tau(L)$  for a sample with  $C=0.5\%$  has a trend to saturation. This might imply the existence of anharmonic decay of the  $29 \text{ cm}^{-1}$  phonons with a mode-averaged lifetime  $\tau_p \sim 10 \text{ } \mu\text{s}$ . The comparison with  $\tau_p$  for individual LA modes (Sec.1), might indicate the rather fast decay of TA phonons in ruby at 1.8 K /10/. The above interpretation of the decay time assumes that the kinetics of the  $29 \text{ cm}^{-1}$  nonequilibrium phonons at least at the final stages of their residence in a crystal is determined primarily by escape, anharmonic phonon pumping being inessential.

### 3. Anharmonic Scattering of the $29 \text{ cm}^{-1}$ Ballistic Phonons.

Phonon-phonon scattering plays an important role in physical phenomena in crystals. As for the terahertz range, we are aware of only one unsuccessful attempt /11/ to observe heat pulses interaction. We have succeeded in directly observing the merging of the  $29 \text{ cm}^{-1}$  phonons with acoustic phonons of higher frequency  $> 2 \text{ THz}$  /12/.

Heat pulses 200 ns long are injected at 50 kHz from the heater  $h_1$  into an  $\text{Al}_2\text{O}_3:0.02\% \text{ Cr}$  crystals at 1.8 K (Fig.4). The  $29 \text{ cm}^{-1}$  phonons are optically detected on the opposite side of the sample with a luminescence detector d. The line  $h_1-d$  is parallel to the direction of narrow angular focussing ( $\sim 1^\circ$ ) of FTA phonons in ruby. Therefore the FTA phonons propagating ballistically along  $h_1-d$  are focused and thus provide the major contribution to the narrow and strong  $R_2$ -luminescence pulse  $I(t)$  induced in d /13,14/. There is also heater





$h_2$  at the side face of the sample.

We have observed a decrease of the  $I(t)$  pulse amplitude in the presence of the heat pulse from  $h_2$  which directly indicates scattering of the  $29 \text{ cm}^{-1}$  FTA phonons by the phonons injected from  $h_2$ . The relative change  $\Delta I/I$  of the  $R_2$ -pulse amplitude depends on the delay  $t = t_2 - t_1$  between the current pulses through  $h_1$  and  $h_2$ . The  $\Delta I/I(t)$  dependence is shown in Fig.4 where we adopt  $t_1 = 0$  and the moment  $t_1$  of passage of the ballistic FTA phonons past  $h_2$  is specified. At delays  $t > t_1$  the effect naturally disappears. For  $t < 0$ , when the heat pulse from  $h_2$  is emitted long before the injection of  $29 \text{ cm}^{-1}$  phonons from  $h_1$ , the  $\Delta I/I$  signal decays slowly with  $|t|$ . This indicates that the effective screening phonon cloud injected from  $h_2$  decays very slowly (with  $\tilde{\tau} \sim 3 \mu s$ ).

The delayed kinetics and observed localization ( $\leq 0.3 \text{ mm}$ ) of the screening cloud near  $h_2$  demonstrate that the  $29 \text{ cm}^{-1}$  FTA phonons are scattered by high frequency phonons,  $\omega \gg 29 \text{ cm}^{-1}$ , which leave the near surface region slowly because of Rayleigh scattering /15/. This conclusion agrees with the strong frequency dependence ( $\sim \omega^4$ ) of the processes,  $TA(29) + LA(\omega) \rightarrow LA(\omega + 29)$ , and  $TA(29) + TA(\omega) \rightarrow LA(\omega + 29)$  which are apparently responsible for the observed escape of the  $29 \text{ cm}^{-1}$  FTA phonons from the ballistic mode. Knowing the FTA phonon transit time  $0.15 \mu s$  past  $h_2$  and the magnitude of their damping ( $\sim 5\%$ ), one can evaluate FTA phonon merging time as  $\tilde{\tau}_p \sim 3 \mu s$ . Hence the  $29 \text{ cm}^{-1}$  phonon anharmonic lifetime near the heat injector is determined not only by decay but also by merging which may reveal itself in experiments on  $29 \text{ cm}^{-1}$  phonon resonance trapping /16/.

#### 4. Resonance Trapping of the $29 \text{ cm}^{-1}$ Phonons.

The trapping of  $29 \text{ cm}^{-1}$  phonons in excited ruby /1,2/ is due to their multiple resonance scattering involving the  $E-2A$  levels of the  $Cr^{3+}$  metastable  $^2E$  state. The main quantitative characteristic of

trapping is the  $29 \text{ cm}^{-1}$  phonon residence time in the pumped volume which can be determined experimentally in two ways. In kinetic experiments /2,5/ one measures directly the tailing time  $\tau_1$  of the  $R_2(t)$  luminescence pulse induced by a pulsed injection of  $29 \text{ cm}^{-1}$  phonons into the volume. In stationary experiments /4/, measurement is made of the population  $\eta$  of the electronic  $2A$  level from the intensity of the R luminescence lines,  $\eta = R_2/R_1$ , under conditions of trapping. The magnitude of  $\eta$  is connected with the effective lifetime  $\tau_0 = MT$  of the  $2A$  level,  $\eta = \beta \tau_0 / \tau_R$ , where  $\beta$  is the quantum yield of  $29 \text{ cm}^{-1}$  phonon generation in an optical excitation event ( $\beta \approx 0.3$  /17/);  $\tau_R$  is the radiative time;  $T \approx 1 \text{ ns}$  /17/ the spontaneous  $2A$  level lifetime;  $M$  the number of scattering events in the time the generated phonon spends in the pumped volume. Obviously,  $\tau_1 > \tau_0$ , since  $\tau_1$ , in contrast to  $\tau_0$ , includes intervals of free phonon transit between scattering events.

In the present work, the times  $\tau_1$  and  $\tau_0$  were measured in one experiment in the same pumped volume of a ruby crystal with  $0.02\%$   $\text{Cr}^{3+}$  with a given concentration  $N^*$  of  $\text{Cr}^{3+}$  metastable ions.

(a) A pulsed copper-vapor laser ( $\lambda = 510.5 \text{ nm}$ ,  $578.2 \text{ nm}$ , repetition frequency  $f = 10 \text{ kHz}$ , energy  $2 \times 10^{-4} \text{ J}$ , pulse duration  $\Delta t = 20 \text{ ns}$ ) creates in the crystal an excited volume  $d \approx 1.5 \text{ mm}$ . Since  $f^{-1} \ll \tau_R$ , the concentration  $N^*$  is almost constant, the role of an individual Cu-laser pulse being reduced to the injection of  $29 \text{ cm}^{-1}$  nonequilibrium phonons in  $2A \rightarrow E$  transitions. The resulting pulses exhibit an exponential decay from which one could derive  $\tau_1$ . The time  $\tau_0$  was determined from the time averaged relative intensity  $\eta = R_2/R_1$ . Fig.5 shows the dependence of  $\tau_1$  and  $\tau_0$  on the average laser power  $P$ . The curves  $\tau_1(P)$  and  $\tau_0(P)$  approach one another with increasing  $P$  exhibiting a clear tendency of crossing.

(b) The crossing of  $\tau_1(P)$  and  $\tau_0(P)$  (at large  $N^*$ ) was observed in experiments with two lasers in an arrangement close to that of ref./5/. A steady-state concentration  $N^*$  was produced with cw Ar-laser ( $P = 0.1 \pm 0.8 \text{ W}$ ,  $d = 0.3 \text{ mm}$ ). A nitrogen laser beam ( $f = 100 \text{ Hz}$ ,  $\Delta t = 15 \text{ ns}$ , pulse energy  $10^{-5} \text{ J}$ ) was focussed on the same spot. The  $N_2$ -laser generates pulses of  $29 \text{ cm}^{-1}$  probe phonons which induce  $R_2(t)$  pulses. The decay of  $R_2(t)$  yields  $\tau_1$ , the time-averaged value being  $\eta = R_2/R_1 - \tau_0$ . The  $\tau_1(P)$  and  $\tau_0(P)$  curves cross at  $P \approx 0.3 \text{ W}$ ,  $\tau_0$  exceeding  $\tau_1$  at  $P \approx 0.8 \text{ W}$  by a factor of three. Note that the behavior of the  $\tau_1(P)$  and  $\tau_0(P)$  curves in experiments (a) and (b) is similar to the one observed earlier in independent pulsed /2,5,16/ and steady-state /4,16/ measurements.

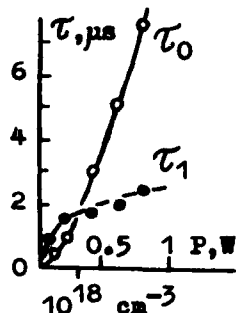
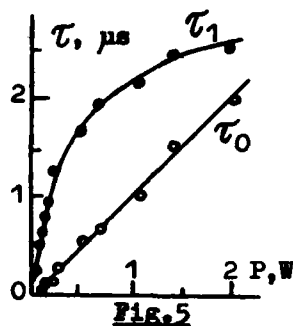


Fig. 6

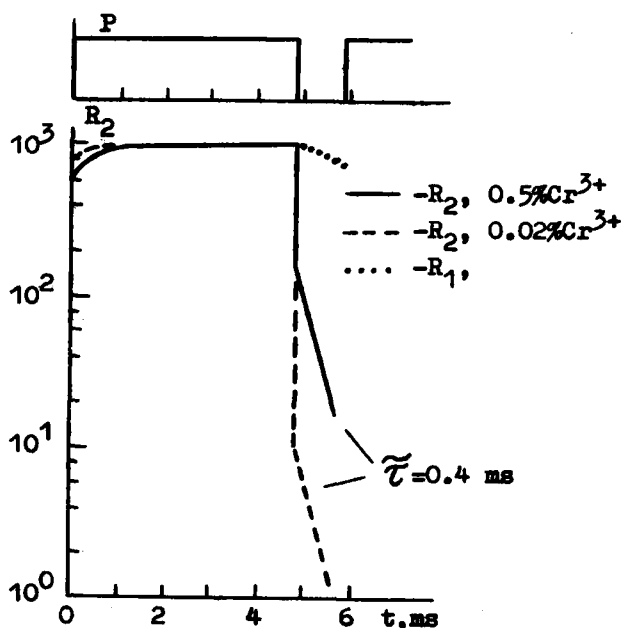


Fig. 7

Fig. 6 shows that at concentrations  $N^* < 10^{18} \text{ cm}^{-3}$ ,  $\tau_1 > \tau_0$  in full agreement with above. This interval of  $N^*$  includes: (1) a region of weak trapping where  $\tau_0 \sim TN^{*2}d^2/16, 18/$  and the phonons escape from the volume by spatial diffusion typical for the "resonance fluorescence" trapping in purely elastic phonon scattering /19,20/; and (2) a region of moderate trapping where a combined mechanism involving spatial and spectral diffusion sets in /20/, for which  $\tau_0 \sim (D_f T)^{-1/2} N^* d \sigma$  /21/, where  $D_f$  is the spectral diffusion coefficient of electronic excitations,  $\sigma \approx 10^{-13} \text{ cm}^2$  is the resonance scattering cross section ( $D_f$  does not depend on  $N^*$ ).

In the strong trapping region one observes an anomalous ratio,  $\tau_1 < \tau_0$ . The "kinetic" time  $\tau_1$  exhibits a tendency to saturation at a level of  $1.3 \mu\text{s}$ , the "steady-state" time  $\tau_0$  continuing to grow rapidly (in ref./18/ one observed  $\eta > 10^{-2}$  which corresponds to  $\tau_0 > 100 \mu\text{s}$ ). This inconsistency (pointed out earlier /22/) poses the question of which of the times,  $\tau_1$  or  $\tau_0$  is the "true" trapping time corresponding to real number of scattering events,  $M$ . Generally speaking, the large value of  $\tau_0$  may be attributed to the feeding of the  $29 \text{ cm}^{-1}$  mode by the heating accompanying optical excitation. But this suggestion would imply that up to 50% of the energy in Stokes losses ( $\sim 5000 \text{ cm}^{-1}$ ) in each optical excitation event can convert as a result of anharmonic processes into a narrow ( $\sim 0.02 \text{ cm}^{-1}$ )

$29 \text{ cm}^{-1}$  mode which is hardly conceivable. Among the facts that are at variance with this suggestion are: a strong resonance dependence of  $\eta$  on magnetic field, dependence of  $\eta$  only on the characteristics ( $N^*$ ,  $d$ ) of the pumped volume rather than on sample size. Quite to the contrary, these facts agree with the conclusion that the "true" trapping time is connected with the large  $M$  corresponding to experimental time  $\tau_0$ . The disproportion between  $\tau_1$  and  $\tau_0$  may be due to the essentially nonexponential kinetics of  $R_2(t)$  which, besides the short-lived microsecond-scale component exhibits also a long-lived tail. The existence of a tailing decay in  $R_2(t)$  in the millisecond range was mentioned in ref./22/.

Fig.7 shows the results of a special study into the nonexponential kinetics of  $R_2(t)$  luminescence excited with Ar-laser, its beam chopped mechanically for a time  $\Delta t = 1 \text{ ms}$  at a frequency of 200 Hz. Since  $\Delta t < \tau_R$ , at the times when optical excitation is interrupted  $N^*$  decreases insignificantly (by  $\sim 20\%$ ) whereas the generation of the  $2A-E$  phonons stops completely. The time profile of  $R_2(t)$  for samples with  $C=0.02\%$  and  $C=0.5\%$  shown in Fig.7 for  $P=2W$  reveals sections of rise and decay, each being characterized by a fast (microsecond-scale) kinetics in the beginning with a subsequent slow (millisecond-scale) variation. The time of the slow exponential decay does not depend markedly on  $C$ ,  $\tilde{\tau} \approx 0.4 \text{ ms}$ , its initial amplitude constituting 15% of the plateau level at  $C=0.5\%$  and  $\sim 1\%$  at  $C=0.02\%$ . The  $R_2(t)$  profile does not change over a wide range of  $N^*$  ( $P$ ) variation, the magnitude of  $\tilde{\tau}$  being practically independent of  $N^*$ . The short time of rise and decay is close in magnitude to  $\tau_1$  observed in pulsed experiments /2,5,16,22/ and exhibits a similar dependence on  $N^*$  and  $C$  (when going over from  $C=0.02\%$  to  $C=0.5\%$  it decreases for large  $N^*$  from  $3 \mu\text{s}$  to  $< 0.5 \mu\text{s}$ ).

In the interpretation of the results obtained, account should be taken of the fact that under conditions of efficient phonon trapping scattering processes of relatively low probability may come into play in the pumped volume. In particular, the scattering processes which, while not leading to an irreversible disappearance of the  $29 \text{ cm}^{-1}$  phonons, result in their being maintained for a long time in an optically inactive state, are responsible for the specific dynamics in the onset of equilibrium between the "ordinary" and "tailing"

The observed two-component decay of  $R_2(t)$  after the removal of pumping indicates the insignificant role of nonresonance feeding of the  $29 \text{ cm}^{-1}$  mode by way of optical heating (or, for instance, cooperative processes of  $E$ -excitation accumulation /23/ which have in principle millisecond-scale kinetics).

resonance phonons, which is what brings about the essentially nonexponential kinetics of  $R_2(t)$ . Among probable are the following mechanisms:

- (a) Inelastic  $29\text{ cm}^{-1}$  phonon scattering involving transfer of electronic ( $^2E$ ) excitation between the  $\text{Cr}^{3+}$  ions /22,24/ which produces, as a result of repeated scattering, spectral redistribution of the  $29\text{ cm}^{-1}$  phonons within the inhomogeneous width of the  $R_1$ -line. The delay is connected here with the mean free path of the off-resonance phonons being much larger than that at resonance (but less, at high  $N$ , than beam size  $d$ , which makes possible rescattering).
- (b) Coherent resonance transfer of electronic excitation to several ions thus creating a collective  $^2E$ -state /25/ is in principle conceivable, provided no phase relaxation of the electronic states occur. Phonon scattering accompanied by such an energy transfer in intermediate collective state could, generally speaking, exhibit a sufficiently large "electronic" tailing.

#### References

- /1/ S. Geschwind, G.E. Devlin, R.L. Cohen and R.S. Chinn : Phys. Rev. 137, A1087, 1965.
- /2/ K.F. Renk and J. Deisenhofer : Phys. Rev. Lett. 26, 764, 1971.
- /3/ A.A. Kaplyanskii, S.A. Basoon, V.A. Rachin and R.A. Titov. Pisma JETP 21, 438, 1975
- /4/ J.I. Dijkhuis, A. van der Pol and H.W. de Wijn : Phys. Rev. Lett. 37, 1554, 1976.
- /5/ R.S. Meltzer and J.E. Rives : Phys. Rev. Lett. 38, 421, 1977.
- /6/ A.P. Abramov, I.N. Abramova, I.Ya. Gerlovina and I.K. Razumova : Pisma JETP 27, 3, 1978.
- /7/ S.A. Basoon and A.A. Kaplyanskii : Fiz. Tverd. Tela 22, 3500, 1980.
- /8/ G.L. Slonimski : JETP 7, 1457, 1937.
- /9/ W.E. Bron : Phys. Rev. B21, 2627, 1980.
- /10/ D.S. Bulyanitsa : Fiz. Tverd. Tela, 1982.
- /11/ M.S. Ribbands and D.V. Osborne : J. de Phys. C4-119, 1972.
- /12/ S.A. Basoon, A.A. Kaplyanskii and S.P. Feofilov : Pisma JETP 34, No.5, 1981.
- /13/ A.V. Akimov, S.A. Basoon, A.A. Kaplyanskii, V.A. Rachin and R.A. Titov : Pisma JETP 25, 491, 1977.
- /14/ A.A. Kaplyanskii, V.A. Rachin, A.V. Akimov and S.A. Basoon : Fiz. Tverd. Tela 23, 488, 1981.
- /15/ W.E. Bron and W. Grill : Phys. Rev. B16, 5303, 5315, 1977.
- /16/ A.A. Kaplyanskii, S.A. Basoon and V.L. Shekhtman in "Light Scattering in solids". Proc. of 2nd Symposium USA-USSR, N.Y. 1979, p.95.
- /17/ J.E. Rives and R.S. Meltzer : Phys. Rev. B16, 1808, 1977.
- /18/ J.I. Dijkhuis and H.W. de Wijn : Phys. Rev. B20, 1844, 1979.
- /19/ V.A. Malyshov and V.L. Shekhtman : Fiz. Tverd. Tela 20, 2915, 1978.
- /20/ I.B. Levinson : JETP 75, 234, 1978.
- /21/ V.A. Malyshov and V.L. Shekhtman : private communication.
- /22/ R.S. Meltzer, J.E. Rives and W.C. Egbert : to be published.
- /23/ P.P. Feofilov : in "Physics of Impurity Centers in Crystals", Tallin, 1972 p.559.
- /24/ W.C. Egbert, R.S. Meltzer and J.E. Rives : in "Phonon Scattering in Condensed Matter", N.Y. 1980, p.365.
- /25/ E.M. Sedukhin and V.L. Shekhtman : Fiz. Tverd. Tela 12, 2809, 1970.

## PHONON SPECTROSCOPY OF THE ELECTRON-HOLE-LIQUID

W. Dietsche\*, S.J. Kirch and J.P. Wolfe

*Physics Department and Materials Research Laboratory, University of Illinois at Urbana-Champaign, Urbana, IL. 61801, U.S.A.*

**Abstract.**—We have observed the  $2k_F$  cut-off in the phonon absorption of electron-hole droplets in Ge and measured the deformation potential.

Photoexcited carriers in Ge at low temperatures condense into metallic droplets of electron-hole liquid (EHL).<sup>1</sup> These droplets provide a unique, tailorable system for studying the electron-phonon interaction in a Fermi liquid. The interaction of phonons with EHL was considered theoretically by Keldysh<sup>2</sup> and has been studied experimentally using heat pulses.<sup>3,4</sup> In contrast, we have employed monochromatic phonons<sup>5</sup> to examine the frequency dependence of the absorption over the range of 150 - 500 GHz. The conservation of momentum and energy in the electron-phonon scattering process implies that only phonons with wave vectors up to twice the Fermi wave vector are absorbed -- leading to a  $2k_F$  cut-off. One unique feature of the electron-hole liquid is that  $k_F$  can be changed by applying crystal stress, a feature which we have exploited.

The inset in Fig. 1 shows our experimental set-up. Two superconducting tunnel junctions, a PbBi generator (G) and an Al detector (D), were placed on opposite faces of the ultra-pure Ge crystal near one edge. A cloud of EHL droplets was created at that face using a cw Nd: YAG laser ( $\lambda = 1.06\mu\text{m}$ ). The position, size, and shape of the cloud was determined by directly imaging its recombination luminescence.<sup>6</sup>

We studied phonons propagating in the [111] direction, and found a measurable absorption only for longitudinal phonons (LA). In the [111] direction, phonon absorption is expected to be dominated by the single [111] valley, because all the other valleys (and the holes) have much smaller cut-off frequencies. Application of stress along the  $[11\bar{1}]$  direction gradually depopulates the [111] valley. This leads to a reduction of  $k_F$  along [111] and thus to a reduction in the cut-off frequency of the phonons.

Two LA phonon spectra taken at zero stress are shown in Fig. 1. The frequency is varied by sweeping the generator bias voltage, while the monochromatic signal is provided by an additional pulse modulation. Time of flight separation allowed resolution of the different modes. Two features were typical of all the data: a rise in intensity which begins at 150 GHz (F1) due to the detector threshold and a decrease which ends at 530 GHz (F2) due to isotope scattering.

\*Present address : Physik Department, TU München, F.R.G.

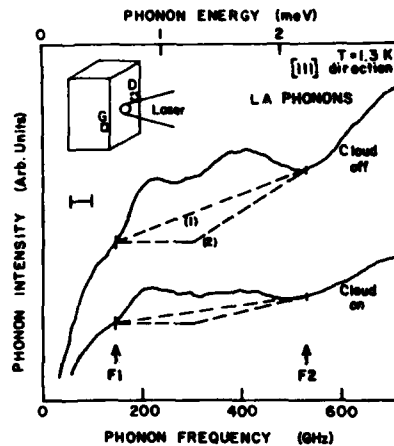


Fig. 1: Phonon signal vs. frequency, zero stress.

Between F1 and F2, the signal consists of a monochromatic part and a background. This background is a common feature in tunnel-junction spectroscopy and is attributed to  $2\Delta$ -phonons and inelastic decay products. Below F1 and above F2 only background phonons are detected. Between F1 and F2 the background will lie between the interpolations (1) and (2) as inferred from earlier spectroscopic work.<sup>5</sup> The actual cloud-on and cloud-off phonon intensities can now be compared. Assuming a phonon absorption of the form  $I = I_0 \exp(-d/l)$ , where  $d$  is the effective EHL thickness and  $l$  is the absorption length, the resulting  $d/l$  are plotted in Fig. 2a. The ends of the error bars indicate the results obtained by using the two alternative backgrounds. A similar procedure led to the plots in Fig. 2 (b) and (c) for two moderate stresses.

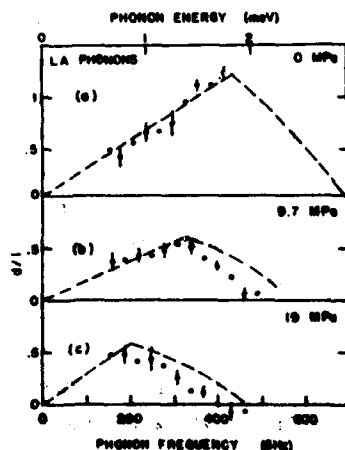


Fig. 2:  $d(\text{eff. EHL thickness})/l$  (absorption length) vs. frequency

The dashed lines in Fig. 2 are fits to deformation potential scattering theory following the procedure of Conwell.<sup>7</sup> The theoretical cut-offs are rather broad because the sound velocity is comparable to the Fermi velocity in the EHL. The frequency dependence of our data agrees remarkably well with the theory. At zero stress the experimental cut-off was obscured by the isotope scattering. At increasing stress the cut-off is observed to move through the experimental frequency range.

An effective thickness,  $d = 11 \mu\text{m}$ , was determined from an analysis of the imaging data. This value is sufficiently larger than a typical droplet radius of about  $2 \mu\text{m}$ . With this value of  $d$ , the absorption data of Fig. 2 yield the deformation potential  $\Xi^2 = (\Xi_u + \Xi_d)^2 = (15 \pm 15) \text{ eV}^2$  independent of stress. Our value of the phonon deformation potential is close to the static deformation potential,<sup>8</sup>  $49 \text{ eV}^2$  for single electrons in Ge. In contrast, a recent theoretical prediction<sup>9</sup> for the screened electrons in the EHL yielded  $149 \text{ eV}^2$ .

In summary, by using the method of phonon spectroscopy we have obtained the first experimental measurement of the phonon deformation potential of EHL in Ge and demonstrated a fundamental property of this Fermi liquid -- the  $2k_F$  cut-off.

This work was supported by NSF under the MRL Grant DMR-77-23999.

#### REFERENCES

1. T. M. Rice and J. C. Hensel, T. G. Phillips, and G. A. Thomas, *Solid State Physics* **32** (1977).
2. L. V. Keldysh, *Pis'ma Zh. Eksp. Teor. Fiz.* **23**, 100 (1976) [*JETP Lett.* **23**, 86 (1976)].
3. V. S. Bagaev, L. V. Keldysh, N. N. Sibeldin, and V. A. Tsvetkov, *Zh. Eksp. Teor. Fiz.* **70**, 702 (1976) [*Sov. Phys. JETP* **43**, 362 (1976)].
4. J. C. Hensel and R. C. Dynes, *Phys. Rev. Lett.* **39**, 969 (1977).
5. H. Kinder, *Z. Phys.* **262**, 295 (1973); H. Kinder and W. Dietsche in *Phonon Scattering in Solids* (L. T. Challis, V. W. Rampton and A. F. G. Wyatt, eds. 1976), p. 199.
6. M. Greenstein and J. P. Wolfe, *Phys. Rev. Lett.* **41**, 715 (1978).
7. E. M. Conwell, *Sol. State Phys. Suppl.* **9** (Academic, N.Y., 1967).
8. K. Murase, K. Enjouji, and E. Otsuka, *J. Phys. Soc. Jpn.* **29**, 1248 (1970).
9. R. S. Markiewicz, *Phys. Stat. Sol.* **B83**, 659 (1977).



STIMULATED EMISSION OF TUNABLE HIGH FREQUENCY PHONONS IN  $\text{LaF}_3:\text{Er}^{3+}$  \*

D.J. Sox, J.E. Rives and R.S. Meltzer

University of Georgia, Athens, GA 30602, U.S.A.

**Abstract.** We describe a case of stimulated emission of high frequency phonons ( $\sim 0.2$  THz) using optical excitation to invert the population of a pair of Kramer's states split in a magnetic field. The phonons are tunable with a magnetic field and the population inversion exists sufficiently long for phonon propagation over macroscopic sample dimensions. Analysis using rate equations suggests preferential emission along the axis of the optically excited volume.

Stimulated emission of high frequency ( $\sim 1$  THz) phonons has recently been observed in  $\text{Al}_2\text{O}_3:\text{V}^{4+}$  [1] and  $\text{Al}_2\text{O}_3:\text{Cr}^{3+}$  [2] using optical excitation techniques and superconducting bolometer detection. In these systems the spin-lattice relaxation time for the electronic levels responsible for the phonon emission is very short ( $T_1 < \text{ns}$ ). In this paper we present evidence for stimulated phonon emission in  $0.1\%$   $\text{LaF}_3:\text{Er}^{3+}$  at  $\sim 0.2$  THz which differs significantly from these earlier works in that (1)  $T_1$  for the present system is much longer ( $1\text{--}100$   $\mu\text{s}$ ) allowing propagation of the phonons over macroscopic distances during the population inversion, (2) the phonon frequency is readily tunable from  $\sim 3\text{--}20$   $\text{cm}^{-1}$  ( $0.1\text{--}0.6$  THz) with a magnetic field up to 85 kG, and (3) evidence for the stimulated emission is obtained directly by monitoring the populations of the electronic states resonant with the phonons.

The lowest  $^4\text{S}_{3/2}$  component of  $\text{Er}^{3+}$  is split in a magnetic field along the c axis as shown in Fig. 1. Level b is selectively excited with a Nd:YAG pumped tunable dye laser creating a population inversion relative to a. The system relaxes via single phonon emission at the energy difference between states b and a. The excited state populations are monitored as a function of time from optical emission C or D to the upper ground state component.

$T_1$  was first measured at several magnetic fields using small energy (50  $\mu\text{J}$ ) excitation pulses and was found to be consistent with the work of Wolfrum, Lanzinger and Renk [3]. The decay at 20.2 kG is exponential as shown by the solid curve in Fig. 2 with a decay time of

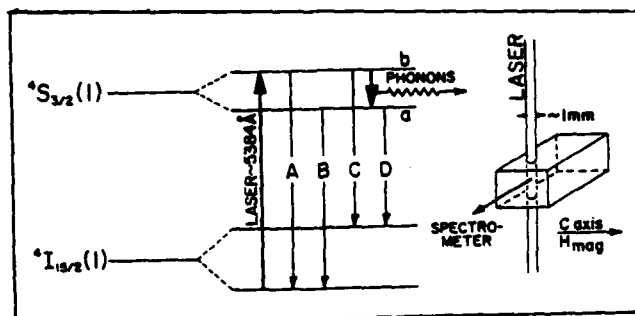


Fig. 1. Partial energy level diagram of  $\text{Er}^{3+}$  in  $\text{LaF}_3$  split in an external magnetic field. Stimulated emission of phonons occurs in the  $b \rightarrow a$  relaxation of the  $^4S_{3/2}(1)$  state after selective excitation of state b. Also shown is the experimental geometry.

46  $\mu\text{s}$ . Under conditions of much higher excitation pulse energies, non-exponential behavior was obtained as indicated by the dashed curves in Fig. 2. In these experiments the laser was focused to a  $\sim 1.5 \times 2$  mm rectangle, exciting a 5 mm length of crystal. The non-exponential decay of the upper state exhibits the following characteristics.

- (1) There is a noticeable speed-up at early times followed by (2) a slowing down of the decay at long times ( $t > T_1$ ) with both effects becoming more pronounced at higher excitation energies. (3) The cross-over between the region of enhanced and reduced decay rates always occurs between the region of enhanced and reduced decay rates always occurs near saturation and (4) there is an initial delay period ( $t \ll T_1$ ) during which the decay proceeds at a rate  $\sim T_1^{-1}$  before the enhanced decay takes over as can be seen in the insert of Fig. 2. Similar observations follow from data taken at 28.5 kG.

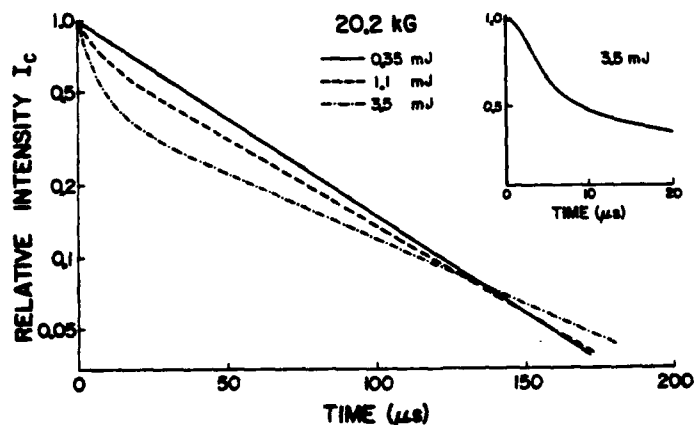


Fig. 2. Time development of the intensity of transition C as a function of excitation energy on a  $1.5 \times 2$  mm area of 0.1%  $\text{LaF}_3:\text{Er}^{3+}$ . The insert shows the 3.5 mJ data on an expanded time scale.

The time evolution of the excited state populations was analyzed with rate equations for the two excited state populations and a rate equation for the resonant phonon occupation number  $\bar{p}$ . These equations depend upon the parameters  $T_1$ , the resonant phonon lifetime  $T_{ph}$ , and  $b = N^*/\Sigma$ , the ratio of the number density of excited ions to phonon modes in the excited state resonance width. The rate equations yield an initial decay rate  $(1+\bar{p})T_1^{-1}$ . Immediately after excitation of the upper state,  $\bar{p} \approx 0$  since the sample temperature is 1.5K yielding a rate  $T_1^{-1}$ . However, when  $b \gg 1$  as in the present experiments,  $\bar{p}$  becomes  $\gg 1$  leading to a decay rate enhanced relative to  $T_1^{-1}$  where  $\bar{p}$  is strongly time dependent and its maximum value is proportional to  $T_{ph}$ . Finally, after the population inversion is lost, the decay proceeds at the reduced (bottlenecked) rate  $(T_1 + (1+b)T_{ph})^{-1}$ . The enhanced rate results from stimulated phonon emission and was termed the phonon avalanche by Brya and Wagner [4] in their work at much lower frequencies. From a quantitative analysis of the data using the rate equations we find that  $T_{ph}$  is limited predominantly by the ballistic time of flight across the excited volume. During the population inversion the fitted  $T_{ph}$  is approximately the axial propagation time whereas after saturation it is close to the radial propagation. This implies the existence of preferential stimulated emission along the axis of the excited volume. The analysis yields a resonance width of 25 MHz and an estimate of the gain for the system of up to  $10 \text{ mm}^{-1}$  for easily obtained excited ion concentrations ( $10^{17} \text{ cm}^{-3}$ ). Considering the long duration of the population inversion, during which time the phonons can propagate over macroscopic dimensions, this system offers considerable potential as a coherent phonon source of high frequency phonons.

\*Work supported by the Army Research Office, Durham.

#### REFERENCES

- [1] W. E. Bron and W. Grill, Phys. Rev. Letters, 40, 1459 (1978).
- [2] P. Hu, Phys. Rev. Letters, 44, 417 (1980).
- [3] H. Wolfrum, K. Lanzinger and K. F. Renk, Opt. Letters 5, 294, (1980).
- [4] W. J. Brya and P. E. Wagner, Phys. Rev. 157, 400 (1967).

## PULSED RAMAN MEASUREMENTS OF INHIBITED ELECTRON-PHONON COUPLING AT HIGH PLASMA DENSITIES IN SILICON

A. Compaan, H.W. Lo, M.C. Lee and A. Aydinli

*Department of Physics, Kansas State University, Manhattan, Kansas 66506, U.S.A.*

**Abstract.** - A 15 nsec duration, frequency doubled Nd:YAG laser at power densities near  $1 \text{ J/cm}^2$  has been used to create high plasma densities in silicon at room temperature. Phonon Raman scattering generated by a delayed 7 nsec dye laser probe pulse shows lattice temperatures far below the silicon melting temperature of  $1412^\circ\text{C}$ . The results suggest the presence of a dense-plasma-induced phase transition with a greatly inhibited electron-lattice coupling.

For laser energy densities of  $1 \text{ J/cm}^2$  at  $\lambda = 532 \text{ nm}$  in silicon the absorbed photon density at the surface is  $\sim 2 \times 10^{22} \text{ cm}^{-3}$ , assuming that the normal room temperature absorption coefficient is unchanged. Most absorbed photons are expected to create electron-hole pairs across the energy gap and thus photoexcited carrier densities well in excess of  $10^{21} \text{ cm}^{-3}$  may be expected for nanosecond duration laser pulses. This is a density regime far beyond that which is accessible, e.g., in the study of electron-hole droplets in silicon and is a regime where many unusual effects may be expected. The range of power densities near  $1 \text{ J/cm}^2$  is also appropriate for laser annealing of ion implanted silicon and it has been widely believed that this annealing is effected by melting of the surface layer and rapid epitaxial recrystallization. A simple calculation using the specific heat shows that the deposited energy should be sufficient to melt the silicon provided the energy is immediately thermalized to lattice system. Furthermore the occurrence of a transient reflectivity rise to a value close to that of (metallic) molten silicon circumstantially supports a melting hypothesis (see Fig. 1). However, we have performed two independent measurements which show that the normal equilibrium molten state is not produced under these circumstances. The first is a transmission measurement which shows that the extinction coefficient in the near IR is far below that of molten silicon.<sup>1</sup> The second, a measurement of optic phonon occupation factors by Raman scattering,<sup>2</sup> shows that the peak lattice temperature rise can account for only a small fraction of the deposited laser energy.

The optical transmission data were obtained using for excitation a broad band  $\text{N}_2$ -pumped dye laser focussed to  $200 \mu\text{m}$  diameter and for probes either a He-Ne laser ( $\lambda = 1152 \text{ nm}$ ) or a second pulsed dye laser focussed to  $\sim 30 \mu\text{m}$  diameter. The time-resolved transmission through a  $0.6 \mu\text{m}$  thick silicon-on-sapphire sample is shown in Fig. 1. The transmitted signal displays primarily the effects of the reflectivity change with little absorption apparent.

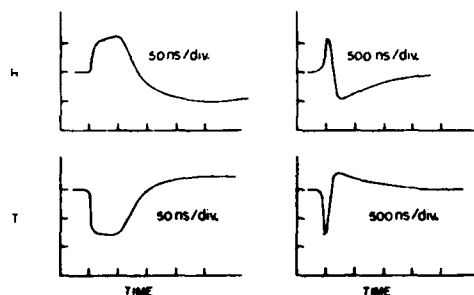


Fig. 1. Time resolved reflectivity (R) and transmission (T) of  $0.6 \mu\text{m}$  SOS for  $1152 \text{ nm}$  probe. Peak of the 8-nsec excitation pulse occurs on the first horizontal tick mark.

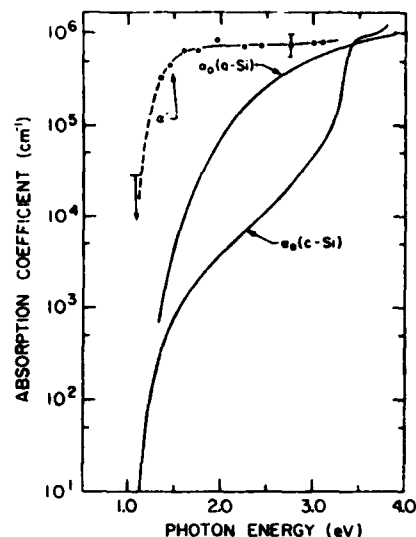


Fig. 2. Induced absorption coefficient (dots) measured 25 nsec after pulsed excitation and compared with the curves for amorphous and crystalline silicon.

The spectral dependence of the extinction coefficient was obtained with the tunable pulsed dye laser (7 nsec pulse) delayed by 25 ns (Fig. 2). The data show an abrupt increase in absorption above  $\sim 1.1 \text{ eV}$  which is directly contrary to that expected of any metallic state which should exhibit high extinction coefficients for all energies below the plasma edge. We have recently demonstrated, via a direct Kramers - Kronig analysis that the absorption shown in Fig. 1 is sufficient to explain the reflectivity rise seen in the inset.

Raman measurements of phonon occupation factors were performed using a similar excite/probe configuration. In our most recent measurements we have used a frequency doubled Nd:YAG beam ( $\lambda = 532 \text{ nm}$ ) focused to  $\sim 1 \text{ mm}$  on the sample and a  $\lambda = 405 \text{ nm}$  Raman probe pulse focussed to  $250 \mu\text{m}$  diameter with a variable electronic delay. Figure 3 shows the optic phonon temperature as a function of probe delay for an excitation energy of  $0.8 \text{ J/cm}^2$ . Note that the peak temperature observed immediately after recrystallization is completed (110 nsec) is less than  $400^\circ\text{C}$ . The cooling behavior is consistent with that expected of a thin surface layer using the known thermal diffusivity of crystalline silicon at these temperatures. However, we find no observable Raman line during the period of high reflectivity ( $\sim 10$ -80 nsec); i.e., any sharp feature between  $200 \text{ cm}^{-1}$  and  $700 \text{ cm}^{-1}$  must be less than 5% as intense as the usual Raman line at  $520 \text{ cm}^{-1}$ .

Since Raman scattering intensity in a semiconductor is directly proportional to the square of the electron-phonon coupling strength, this lack of Raman signal is consistent with a greatly reduced electron-phonon coupling. This observation

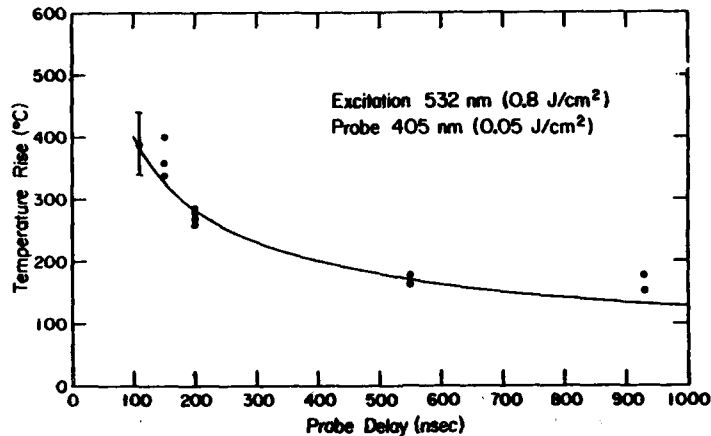


Fig. 3. Temperature rise vs. probe pulse delay.

would also explain the slow rate of energy transfer from the photoexcited carriers to the lattice. It is also possible that under intense excitation a structural phase transition occurs to a disordered, possibly fluid, state.<sup>3</sup> In this case only a very broad, density-of-states Raman spectrum would be expected which could easily be two orders of magnitude less intense than the usual sharp Raman line. However such a disordered state could not be the usual molten state of silicon since Fig. 2 shows the optical properties to be much different and Fig. 3 shows the peak lattice temperature to be far below the 1412°C melting point of silicon.

In either case we believe the low lattice temperature immediately following the high reflectivity phase gives strong evidence that the usually fast ( $\sim 10^{12}$  sec<sup>-1</sup>) electron-lattice relaxation has been inhibited. We suggest this may arise from screening effects of a dense photo-excited plasma on the deformation potential carrier-lattice coupling which prevent rapid energy transfer to the phonon system.<sup>3</sup>

The financial support of the U.S. Office of Naval Research under Contract No. N00014-80C-0419 is gratefully acknowledged.

1. M. C. Lee, H. W. Lo, A. Aydinli and A. Compaan, Appl. Phys. Lett. **38**, 499 (1981); A. Aydinli, H. W. Lo, M. C. Lee and A. Compaan, Phys. Rev. Lett. **46**, 1640 (1981).
2. H. W. Lo and A. Compaan, Phys. Rev. Lett. **44**, 1604 (1980).
3. J. A. Van Vechten and M. Wautelet, Phys. Rev. B **23**, 5543 (1981); M. Wautelet and J. A. Van Vechten, *ibid*, p. 5551.

# THE EFFECT OF LATTICE STRAINS ON THE ACOUSTIC RELAXATION LOSSES IN DIELECTRIC CRYSTALS DUE TO MAGNETIC IONS

P.J. King

*Department of Physics, University of Nottingham, University Park, Nottingham NG7 2RD, England*

**Abstract:-** Recently information on the lattice strains present at  $\text{Fe}^{2+}$  sites in  $\text{KMgF}_3$  has been obtained from electron spin resonance linewidth data. The use of this data in an empirical model previously used with success on  $\text{Fe}^{2+}:\text{MgO}$  shows that this model also gives an excellent description of the acoustic relaxation losses in  $\text{Fe}^{2+}:\text{KMgF}_3$ . In order to place this empirical model on a more sound theoretical footing a theory of relaxation losses in multi-level systems based on the rate equations for the population of each level has been studied. The empirical model results only if simplifying assumptions are made and the implications of these are described.

Acoustic relaxation losses occur when the strain of an acoustic wave modulates the energy levels of a system such as that consisting of a number of magnetic ions embedded in a dielectric lattice. The dynamic repopulation of the levels of such a system results in a loss to the acoustic wave. For a two-level system the form of the loss  $\alpha$  is:

$$\alpha = \text{constant} \cdot \frac{G^2}{v^3 kT} \cdot \frac{\omega^2 \tau}{1 + \omega^2 \tau^2}$$

where  $\omega$  is the acoustic angular frequency,  $v$  is the acoustic velocity,  $G$  is a coupling factor related to the energy level shift per unit strain and  $\tau(T)$  is the relaxation time. It may be shown that the expression for a  $n$ -level system reduces to the sum of  $n - 1$  such expressions above. Random lattice strains influence the magnitude and acoustic mode dependence of  $\alpha$  via their effect on  $G$  and on  $\tau$ , and recently a successful treatment of the effect of strains on the relaxation loss due to the Jahn-Teller ion  $\text{Ni}^{3+}$  in the  $\text{Al}_2\text{O}_3$  lattice has been given<sup>1</sup>.

It is interesting to study  $\text{Fe}^{2+}$  in cubic environments such as those provided by  $\text{MgO}$  or  $\text{KMgF}_3$  since quite different acoustic relaxation behaviour is found in the two systems<sup>2,3,4</sup>. In  $\text{MgO}$  the acoustic loss of  $T_2$  symmetry modes is much weaker than the predictions of a strain free model would suggest, while in  $\text{KMgF}_3$  it is the  $E$ -symmetry modes which are experimentally less attenuated than on such a model.

An empirical model due to King and Monk<sup>2,4</sup> treats the effect of lattice strains by considering a single two-level expression for the three-level ground state but with a coupling factor  $G^2 = (G_1 - G_2)^2 + (G_2 - G_3)^2 + (G_3 - G_1)^2$  where

$G_1, G_2, G_3$  are the shifts in the energies of the three ground state levels due to a unit acoustic strain in the presence of a much larger static lattice strain. Factors which represent reductions in the unstrained values of  $G^2$  were computed as a function of the ratio of a mean compressional to a mean shear lattice strain, using the known form of the Hamiltonian.

The anisotropy of the electron paramagnetic resonance linewidth gives a measure of this ratio<sup>5</sup> and for  $Fe^{2+}:MgO$  use of the empirical model then gives excellent predictions of the acoustic losses experimentally observed. Recently Grimshaw<sup>6</sup> has measured the anisotropy of the  $Fe^{2+}$  electron paramagnetic resonance linewidths for  $KMgF_3$ . The anisotropy is very different from that in  $MgO$ <sup>5</sup>, but again use of the empirical model gives very good estimates of the acoustic relaxation losses of the various acoustic modes.

In order to understand why this simple empirical model is so successful a treatment of the acoustic relaxation loss in a n-level system has been developed and then applied to the  $Fe^{2+}$  ion<sup>7</sup>. This treatment uses the driven rate equations for the populations of the n-levels. The energies of the n-levels are displaced by the acoustic wave, the dynamic repopulations may be calculated from the rate equations, and the overall loss derived. This involves solving the equations:

$$j\omega N_1^0 \sum_s \frac{(G'_s - G'_1)}{kT} N_s^0 = j\omega n_1 + \sum_r n_r P_{r1} - n_1 \sum_r P_{1r}$$

for the  $n_1$  and then obtaining the attenuation from the expression:

$$\alpha = \frac{2.686}{2\rho v} \cdot \sum_i \text{Im}(n_i) \cdot G'_i$$

In these equations  $N_1^0$  is the thermal equilibrium population of the 1<sup>th</sup> level,  $n_1$  is the dynamic deviation from the equilibrium which would be obtained if the levels were frozen in energy at a particular instant in time, and the  $P_{ij}$  are the probabilities of transitions between the i<sup>th</sup> and j<sup>th</sup> levels per unit time. The  $G'_i$  are linearly related to the  $G_i$  of the empirical model. This treatment gives the usual expression for a two-level system and for a three-level system yields:

$$\alpha \propto \frac{1}{(\omega^2 + \gamma_1^2)(\omega^2 + \gamma_2^2)} \left\{ \omega^2 \{ P_1(G'_2 - G'_3)^2 + P_2(G'_1 - G'_3)^2 + P_3(G'_1 - G'_2)^2 \} \right. \\ \left. + (P_1P_2 + P_2P_3 + P_3P_1) \{ P_1[(G'_1 - G'_3)^2 + (G'_1 - G'_2)^2] + P_2[(G'_2 - G'_1)^2 + (G'_2 - G'_3)^2] + P_3[(G'_3 - G'_1)^2 + (G'_3 - G'_2)^2] \} \right\}$$

where  $P_1 = P_{23} = P_{32}$  etc.  $\gamma_1$  and  $\gamma_2$  are combinations of  $P_i$ . The above expression which can be decomposed into two, two-level expressions, has to be summed over all ions. Since each ion has a different strain each has in general a different set



of  $G_1$  and  $P_1$ . If, however, we suppose that the  $P_1$  are equal then the above expression reduces to the empirical expression and the two relaxation peaks coincide.

We note that experimentally the relaxation peak is observed in MgO and  $KMgF_3$  in a region where an Orbach term involving the first group of excited states dominates the relaxation<sup>2,3,4</sup>. A single peak is observed in each case, the form of which gives a good prediction of the energy of the excited states (MgO,  $110\text{ cm}^{-1}$ ,  $KMgF_3$ ,  $96\text{ cm}^{-1}$ ). This would not occur were it described by the sum of two different two-level expressions and the single peak is consistent with the  $P_1$  being equal. Is it true then that all the  $P_1$  are equal or are there another set of simplifying circumstances? Rough calculations suggest that although the  $P_1$  will have the same temperature dependence they are not closely equal in magnitude.

We note that the rate equation method is equivalent to ignoring the off diagonal elements in a density matrix formulation such as that by Isawa et al. The use of the rate equations assumes that  $T_2$  relaxation times are much shorter than  $T_1$  relaxation times. At the temperature at which the relaxation peaks are observed this approximation may not be strictly valid. The general expressions for a three-level system involving such terms are, however, very complex and difficult to handle. It should also be noted that current Jahn-Teller theories have so far failed to predict the equal coupling of  $T_2$  and E acoustic modes to the  $Fe^{2+}$  ion.

#### Acknowledgements

I would like to thank F. Sheard & K. Lassmann for very helpful discussions and M. Grimshaw for allowing the use of his linewidth data.

#### References

1. Bankovskis, A., King, P. J. and Monk, D. J., J. Phys. C:Solid State Phys., **14**, 697, 1981.
2. King, P. J., Monk, D. J. and Oates, S. G., J. Phys. C:Solid State Phys., **11**, 1067, 1978.
3. Kim, H. and Lange, J., Phys. Rev. B, **18**, 1961, 1978.
4. King, P. J. and Monk, D. J., Acta. Phys. Slov., **30**, 11, 1980.
5. Lewis, M. F. and Stoneham, A. M., Phys. Rev., **164**, 271, 1967.
6. Grimshaw, M., Doctoral Thesis, University of Nottingham, England, 1980.
7. King, P. J. and Monk, D. J., to be published.
8. Isawa, Y., Takeuti, Y. and Mikoshiba, N., Phys. Rev. B, **15**, 4907, 1977.

## RAMAN SCATTERING STUDY OF CORRELATION BETWEEN PHONONS AND ELECTRON SPINS IN CdS AND ZnTe UNDER RESONANCE CONDITION

Y. Oka and M. Cardona\*

*Research Institute for Scientific Measurements, Tohoku University, Sanjyo-Machi, Sendai, Japan (Alexander von Humboldt Fellow)**\*Max-Planck-Institut für Festkörperforschung, Heisenbergstrasse 1, 7000 Stuttgart 80, F.R.G.*

**Abstract.** - We have observed for excitation photon energy in resonance with the lowest gap of CdS and ZnTe, intense cooperative light scattering in which incident photons are scattered by an acoustic/optical-phonon and by electron spins. From the result the interactions among the electron spins, the phonons, and the excitons are discussed.

1. **Introduction.** - Recent investigations of resonant Brillouin/Raman scattering of excitonic polaritons in semiconductors have given much information about parameters of the exciton states as well as the polariton dispersion [1]. Spin flip Raman scattering of electrons and holes arises resonantly with large scattering probability in the same region [2]. Therefore this scattering may strongly correlate with that by the phonons. In this paper, the interaction of acoustic and optical phonons with electron spins is studied by means of combined light scattering.

2. **Experiment.** - N-type CdS and p-type ZnTe containing a donor concentration of  $\sim 10^{16} \text{ cm}^{-3}$  were used. Coumarin 101 (for CdS) or coumarin 7 (for ZnTe) dye lasers pumped by an argon-ion laser were employed with a spectral width of 0.025 meV. Samples immersed in pumped liquid helium were placed in a superconducting magnet which produced magnetic fields up to 7T. The back-scattered light was analyzed with a Raman spectrometer.

3. **Results and Discussion.** - Figure 1 shows the Stokes- and anti-Stokes-shifts observed in CdS at H=7T as a function of incident photon energy,  $E_T$  being the energy of the transverse exciton. LA and TA are the dispersive Brillouin modes due to longitudinal and transverse acoustic phonons, which reflect the dispersion relation of the polariton under magnetic field [3]. The intensity of these lines decreases when the incident laser energy is lowered below 2.550 eV. The lines  $\pm A$ , however, increase in intensity in this lower energy region and resonate

at 2.5454 eV, which corresponds to the luminescence peak due to the donor-bound exciton ( $I_2$ -line). The A lines do not show any dispersion (less than 0.44 meV) in the whole energy region observed. A similar non-dispersive line of CdSe has been interpreted as TA phonon scattering via bound excitons [4].

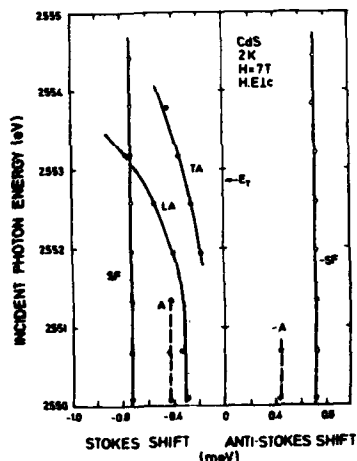


Fig. 1: Brillouin and spin-flip scattering in CdS.

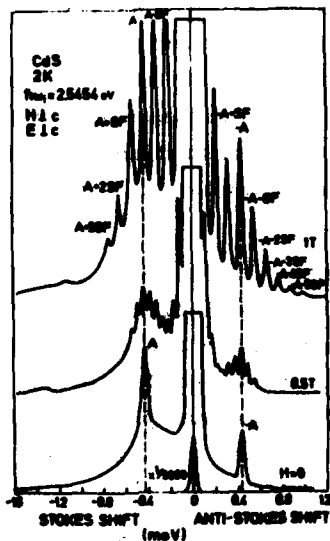


Fig. 2: Cooperative scattering spectra due to LA phonon and donor-electron spins.

As the excitation photon energy approaches 2.5454 eV (the donor-bound exciton energy) the spin-flip line increases in intensity by more than one order of magnitude, indicating that the relevant electron spins are localized in the donor states. Figure 2 shows the spectra at resonance for several values of  $H$ . In the bottom spectra at  $H=0$  the background radiation around the laser line is the  $I_2$ -luminescence while the sharp lines are the  $\pm A$  lines. At  $H=0.5T$  the spectrum changes dramatically: Multiple satellites arise around the A lines. In the top spectrum at  $H=1T$  remarkably enhanced multiplet structure can be seen with the spacing twice as large as that at  $H=0.5T$ . The  $g$ -value for these multiple lines ( $\pm A \pm SF$ ) is the same as for the  $\pm SF$  line. As  $H$  increases the SF lines become

The open circles in Fig. 1 ( $\pm SF$ ) only appear under a magnetic field; their energy shift is linearly proportional to  $H$ . The  $g$ -value calculated from the shift is 1.81 which agrees with the electron  $g$ -value in CdS [5]. Thus these lines originate from spin-flip Raman scattering by electrons. For an incident energy of 2.553 eV the Stokes shifts of the LA line and the SF line almost coincide but show no evidence of a coupling of these modes. Therefore the spin-flip process of the electron observed is not correlated with the scattering by acoustic phonons in the free exciton state. In the present sample of low impurity concentration most of the excess electrons are localized in the donor states at low temperature. Thus the dominant intermediate state for resonant scattering are different in these two scattering processes.

As the excitation photon energy approaches 2.5454 eV (the donor-bound exciton energy) the spin-flip line increases in intensity by more than one order of magnitude, indicating that the relevant electron spins are localized in the donor states. Figure 2 shows the spectra at resonance for several values of  $H$ . In the bottom spectra at  $H=0$  the background radiation around the laser line is the  $I_2$ -luminescence while the sharp lines are the  $\pm A$  lines. At  $H=0.5T$  the spectrum changes dramatically: Multiple satellites arise around the A lines. In the top spectrum at  $H=1T$  remarkably enhanced multiplet structure can be seen with the spacing twice as large as that at  $H=0.5T$ . The  $g$ -value for these multiple lines ( $\pm A \pm SF$ ) is the same as for the  $\pm SF$  line. As  $H$  increases the SF lines become

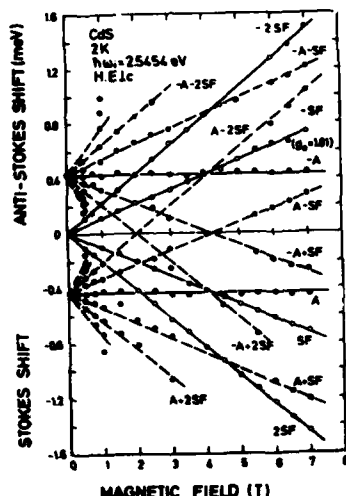


Fig. 3: Magnetic field dependence of the cooperative- and spin-flip-scatter-state relative to the impurity center [6].

Since the binding energy of the donor-bound exciton  $G_{BE}$  is 6.7 meV measured from the ground state of the free exciton,  $r_e + r_h$  is calculated as  $59 \text{ \AA}$  (hence  $q_0 = 1.7 \times 10^6 \text{ cm}^{-1}$ ) where we use the free exciton binding energy  $G_{FE}$  of 29.4 meV, the Bohr radius  $a_B$  of  $28 \text{ \AA}$  and  $G_{BE}/G_{FE} \sim (a_B/(r_e + r_h))^2$ . Thus we can conclude that the A line is caused by the LA phonon scattering via the donor-bound exciton state.

Multiple spin-flip scattering observed on donor electrons is due to exchange interaction between the donor and the donor-bound exciton [2]. As both the LA phonon and the donor electron are strongly correlated with the donor-bound exciton state, intense spin-phonon multiple scattering can take place. The appearance of the multiple spin lines as the satellites of the A line shows that donor electron spins interact considerably with the LA phonon when the magnetic field is low.

In InTe we have also observed combination scattering by an LO phonon  $\pm$  spin-flip of electrons [7].

#### References

- [1] E.S. Koteles and G. Winterling, Phys. Rev. Letters **44**, 948 (1980).
- [2] Y. Oka and M. Cardona, Phys. Rev. B **23**, 4129 (1981).
- [3] I. Broser, M. Rosenzweig, R. Broser, E. Beckman and E. Birkicht, J. Phys. Soc. Japan **49**, Supl. A 401 (1980).
- [4] C. Herman and P.Y. Yu, Solid State Commun. **28**, 313 (1978).
- [5] P.A. Fleury and J.F. Scott, Phys. Rev. B **3**, 1976 (1971).
- [6] J.J. Hopfield, Proc. Conf. on the Physics of Semiconductors, Exeter 1962, p. 75.
- [7] J.F. Scott, Phys. Rev. B **19**, 4318 (1979).

# MULTIPLE RESONANT RAMAN SPIN-FLIP PHONON SCATTERING AND $29\text{ cm}^{-1}$ PHONON TRANSPORT IN EXCITED RUBY IN A MAGNETIC FIELD

A.A. Kaplyanskii, S.A. Basoon and V.L. Shekhtman

A.F. Yoffe Physicotechnical Institute, Academy of Sciences of the U.S.S.R., Leningrad 194021, U.S.S.R.

**Abstract.**— The paper reports on the observation of an anomalous nonmonotonic dependence of trapping of the  $29\text{ cm}^{-1}$  phonons on magnetic field. The effect is due to inelastic phonon scattering processes involving the creation (absorption) of a Zeeman quantum of the  $E$ -level (resonance spin-flip phonon Raman scattering) /1/.

The trapping of  $29\text{ cm}^{-1}$  acoustic phonons in excited ruby /2,3/ is attributed to their multiple scattering by the excited  $\text{Cr}^{3+}$  ions in a resonance interaction with the  $E - 2A$  electronic states. In a magnetic field  $H$  one observes /4 - 7/ a reduction of phonon trapping. This is mainly due to a decrease of the spectral scattering cross section under the Zeeman splitting of the  $E$ ,  $2A$  levels which reduces the number  $M$  of the scattering events /4,6/.

Measurements were carried out in a field  $H \parallel C_2$  at 1.8 K on  $\text{Al}_2\text{O}_3:0.02\% \text{Cr}$  crystal, pumped with cw Ar laser (beam diameter  $L = 1.3\text{ mm}$ ). The relative intensity of the fluorescence lines  $\eta = R_2/R_1$ , which is proportional to phonon bottlenecking factor  $M$  /5,6/ has been measured.

Fig.1 shows a  $\eta(H)$  plot for different excited ion concentrations  $N^*$  determined by laser power  $W$ . At a low power, 0.05 W (curve 1), one observes a monotonic dropoff of  $\eta(H)$  /5,6/. As pump power increases (up to 0.4 and 0.8 W) the behavior of  $\eta(H)$  (curves 2 and 3) reveals a clearly pronounced anomaly, i.e. a growth of  $\eta(H)$  in the field range 0.6 to  $\sim 5\text{ kOe}$ . The relative depth of the minimum of  $\eta(H)$  at  $H=0.6\text{ kOe}$  increases with increasing  $N^*$  at  $N^* \leq 10^{17}\text{ cm}^{-3}$  (see curve 2,3). At high fields ( $H > 5\text{ kOe}$ ) one again observes a decrease of  $\eta(H)$ .

Multiple phonon scattering by the two-level system  $E$ ,  $2A$  at  $H=0$  is elastic (phonon "resonance fluorescence" trapping /8,9/). In a magnetic field, the  $E - 2A$  transition form factor becomes a quartet with resonances at the frequencies  $\Delta = \frac{\delta_1 \pm \delta_2}{2}$ , where  $\Delta = 29\text{ cm}^{-1}$ ,

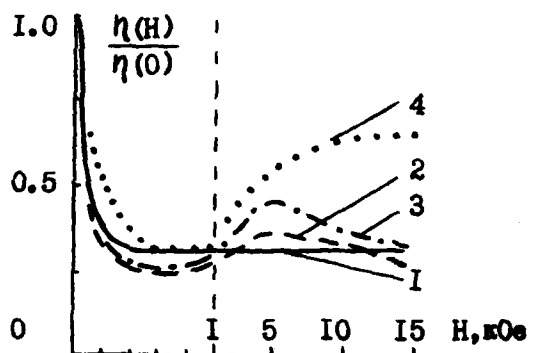


Fig. 1

$\delta_1 = g_{\bar{E}} \mu_B H$ ;  $\delta_2 = g_{2A} \mu_B H$ ;  $g_{\bar{E}} = 2.445$ ;  $g_{2A} = 1.5$  (Fig. 2). The inner components of the quartet correspond to non spin-flip transitions, the side components, to spin-flip transitions. Phonon scattering on the Zeeman four-level system includes, besides the elastic, also inelastic processes involving a change of phonon frequency  $\omega_0$  by the magnitude  $\pm \delta_1$  of the  $\bar{E}$ -level splitting /5,8/, the latter being the resonance spin-flip phonon Raman scattering (RRS). Corresponding cross section is

$$\sigma(\omega_b, \omega) = P_a [\sigma_{aa} \delta(\omega - \omega_b) + \sigma_{ab} \delta(\omega - \omega_b + \delta_1)] + P_b [\sigma_{bb} \delta(\omega - \omega_b) + \sigma_{ba} \delta(\omega - \omega_b - \delta_1)] \quad (1)$$

$$\sigma_{aa, bb}(\omega_b) = \sigma_0 \left[ \frac{\Gamma^+}{\Gamma} \frac{\Gamma^2/4}{(\omega_b - \Delta + \frac{\delta_1 - \delta_2}{2})^2 + \Gamma^2/4} + \frac{\Gamma^-}{\Gamma} \frac{\Gamma^2/4}{(\omega_b - \Delta + \frac{\delta_1 + \delta_2}{2})^2 + \Gamma^2/4} \right] \quad (1a)$$

$$\sigma_{ab, ba}(\omega_b) = \sigma_0 \frac{\Gamma^+ \Gamma^-}{\Gamma^2} \left[ \frac{\Gamma^2/4}{(\omega_b - \Delta + \frac{\delta_1 - \delta_2}{2})^2 + \Gamma^2/4} + \frac{\Gamma^2/4}{(\omega_b - \Delta + \frac{\delta_1 + \delta_2}{2})^2 + \Gamma^2/4} \right] \quad (1b)$$

Here  $\omega$  is scattered phonon frequency;  $\sigma_0$  is the cross section at line center ( $\omega_0 = \Delta$ ) at  $H=0$ ;  $P_a, P_b$  the occupancies of the  $\bar{E}$ -state sublevels  $a, b$ ;  $\Gamma^+, \Gamma^-$  probabilities of non spin-flip and spin-flip spontaneous transitions, respectively,  $\Gamma = \Gamma^+ + \Gamma^-$ .  $\sigma_{aa}$  and  $\sigma_{bb}$  ("-" and "+" in (1a)) correspond to the elastic scattering channel, and  $\sigma_{ab}, \sigma_{ba}$  ("-" and "+" in (1b)), to RRS proper. Fig. 2 shows the phonon scattering processes at frequency  $\omega_0 = \Delta + \frac{\delta_1 - \delta_2}{2}$  coinciding with one ( $a \rightarrow a'$ ) of the resonances, which corresponds to the different partial cross sections in (1).

At weak trapping the behavior of  $\eta(H)$  is determined primarily by elastic processes since the RRS cross section has a smallness

$\Gamma^-/\Gamma^+$ . Then  $\eta(H)$  decreases monotonically (curve 1 in Fig. 1) due to a decrease of spectral cross section /6,7/. At a sufficiently strong trapping, multiple RRS can yield a noticeable contribution to  $\eta$  even at  $\Gamma^-/\Gamma^+ \ll 1$ . Then in a weak field multiple change of phonon frequency by  $\pm \delta_1$  results (provided  $P_a = P_b$ ) in a spectral diffusion of phonons /5,8/ manifesting itself in a steeper dropoff of  $\eta(H)$  /7/.

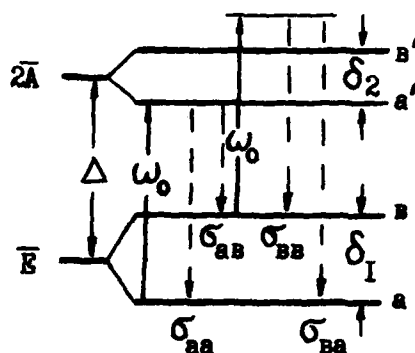


Fig. 2

An important phenomenon is the effect of multiple RRS on  $\eta$  (H) in strong fields ( $\delta_1 \gg \Gamma$ ) where the form factor undergoes splitting into four resonances. Indeed, in an inelastic scattering of a phonon of frequency  $\omega_0$  coinciding with one of the resonances (for instance, a-a' in Fig.2) phonons  $\omega_0 \pm \delta_1$ , are created. One of them ( $\omega_0 - \delta_1$ ) enters the region of another resonance (here b-a') and will again be scattered. The other phonon ( $\omega_0 + \delta_1$ ) turns out to be off the resonance quartet and can therefore leave the volume easier. Processes involving the creation of "off-resonance" phonons should apparently reduce the degree of trapping. As H increases, however, their cross section, as seen from (1b), drops to zero ( $\sigma_{ba} \sim H^{-2}$  in fields where  $\delta_1 \gg \Gamma$ ). It is this point that represents the main reason for the "anomalous" increase of  $\eta$  (H) in fields  $0.6 + 5$  kOe, since at  $\delta_1 - \delta_2 \gg \Gamma$  this inelastic process reducing the degree of trapping becomes suppressed with the growth of H.

In strong fields,  $H > 5$  kOe, only inelastic processes resulting in phonon exchange between the quartet resonances remain and  $\eta$  should become stabilized. Now the observed decrease of  $\eta$  at  $H > 5$  kOe (curves 2,3 in Fig.1) may be attributed to a different optical pumping of the a,b sublevels ( $P_a \neq P_b$ ) because of the ground state  $^4A_2$  spin memory effect /10/. At  $P_a \neq P_b$ , the pumped volume is more transparent for two of the four resonance frequencies which opens up an additional channel for phonons to escape from the volume via their transfer in inelastic scattering to weakly absorbed resonances.\*)

#### References

- /1/ S.A. Basoon, A.A. Kaplyanskii, and V.L. Sherkhtman. Fiz.Tverd.Tela 23, No 9, 1981 ; JETP in press.
- /2/ S. Geschwind, G.E. Devlin, R.L. Cohen, and R.S. Chinn. Phys. Rev. 137, A1087, 1965.
- /3/ K.F. Renk and J. Deisenhofer. Phys. Rev. Lett. 26, 764, 1971.
- /4/ A.A. Kaplyanskii, S.A. Basoon, V.A. Rachin and R.A. Titov. Pisma JTP 1, 628, 1975.
- /5/ J.I. Dijkhuis, A. van der Pol and H.W. de Wijn. Phys. Rev. Lett. 37, 1554, 1976.
- /6/ A.A. Kaplyanskii, S.A. Basoon and V.L. Shekhtman in "Light Scattering in Solids", Proc. USA-USSR Symposium, N.Y. 1979, p. 95.
- /7/ J.I. Dijkhuis and H.W. de Wijn. Phys. Rev. B20, 1844, 1979.
- /8/ I.B. Levinson. JETP 75, 234, 1978.
- /9/ V.A. Malyshev and V.L. Shekhtman. Fiz. Tverd. Tela 20, 2915, 1978.
- /10/ G.F. Imbusch and S. Geschwind. Phys. Rev. Lett. 17, 238, 1966.
- /11/ J.I. Dijkhuis, H.W. de Wijn. Phys. Rev. B20, 3615, 1979.

\*) On the other hand, multiple spin-phonon RRS produces a reverse effect on the populations  $P_a$  and  $P_b$  by equalizing them /2,11/. Under conditions of very strong trapping this equalization compensates the spin memory effect. This may account for the fact that no decrease of  $\eta$  (H) is observed at  $H > 5$  kOe under strong trapping in focused Ar-laser beam (curve 4 in Fig.1).

## COMPARISON OF ELECTRON SPIN-LATTICE RELAXATION IN AMORPHOUS AND CRYSTALLINE MATERIALS

A. Deville, B. Gaillard, C. Blanchard and J. Livage\*

*Département d'Electronique (E.R.A. 375) Université de Provence, Centre de Saint-Jérôme, Rue Henri Poincaré, 13397 Marseille Cedex 13, France.**\*Spectrochimie du Solide (L.A. 302), Université Pierre et Marie Curie, (Paris VI), 75000 Paris, France.*

**Abstract** - A quadratic law is observed for the first time in a true amorphous material with dilute electron spins. We interpret it as due to a coupling of the spins to the phonons via T.L.S. with a constant density of states up to  $2E_{\text{max}} = 56$  K.

1. Introduction. - Mechanisms and processes describing spin-lattice relaxation of electron paramagnetic centers diluted in a crystalline diamagnetic solid are well-known. The situation is somewhat different in amorphous solids, where the existence of Two-Level Systems (T.L.S.) [1] [2] strongly coupled to the phonons [3] is well established. One can then imagine that the indirect transfer of energy from the spins to the phonons via the T.L.S. will by pass the usual direct transfer from spins to phonons. This will then lead to new relaxation laws. This problem has been recently examined by S.R. Kurtz and H.J. Stapleton [4] for an amorphous-like system ( $\beta$ -Alumina doped with  $\text{Na}^+$ ... and irradiated). A similar situation has been found by J. Szeftel and H. Alloul ( $^{11}\text{B}$  in  $\text{B}_2\text{O}_3$ ...). We hereafter present results obtained for a true amorphous material and for the corresponding crystalline material.

2. Origin of the paramagnetic centers. - We studied paramagnetic defects in  $\text{V}_2\text{O}_5$ .  $\text{V}^{3+} (3d^2)$  has no permanent magnetic moment. We used non-stoichiometric oxide where paramagnetic defects were associated with oxygen vacancies. This non-stoichiometry appears because  $\text{V}_2\text{O}_5$  heated above its melting point ( $650^\circ\text{C}$ ) loses oxygen. The amorphous material was obtained by slow cooling.

In crystalline  $\text{V}_2\text{O}_5$ , we have an E.P.R. spectrum consisting of 15 lines caused by an additional electron ( $S = 1/2$ ) delocalized over two vanadium ( $I = 7/2$ ), the electron spin being coupled to both nuclear moments.

In amorphous  $\text{V}_2\text{O}_5$ , the E.P.R. spectrum consists of 8 lines; the additional electron is localized on a single vanadium ( $\text{V}^{4+} 3d^1$ ), the electron spin being coupled to the nuclear moment of the vanadium ion. Although  $\text{V}_2\text{O}_5$  is a semiconductor, in these experiments the electron may be considered bound to a given paramagnetic center (very low mobility).

3. Experimental results. - We measured  $T_1$  by the saturating pulse method. For the crystalline sample, in the temperature-range 1.4 - 50 K (fig. 1) :

$$T_1^{-1} = 12.5 T + 3.1 \cdot 10^3 / \text{Sh} \frac{15.5}{T} \quad (1) \quad (T \text{ s, K})$$



AD-A128 574

INTERNATIONAL CONFERENCE ON PHONON PHYSICS 31 AUGUST-3  
SEPTEMBER 1981 BLOOMINGTON INDIANA(U) INDIANA UNIV AT  
BLOOMINGTON W E BROW DEC 81 ARO-17340.1-PH

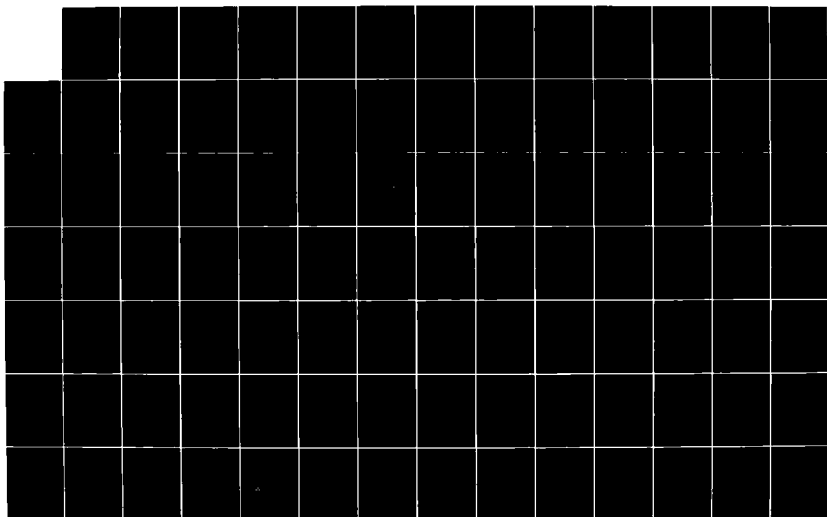
6/10

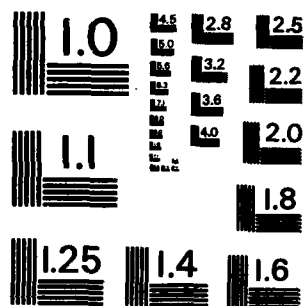
UNCLASSIFIED

MIPR-ARO-43-80

F/G 20/2

NL





MICROCOPY RESOLUTION TEST CHART  
NATIONAL BUREAU OF STANDARDS-1963-A

For  $T > 30$  K it is difficult to saturate the system because we have a broad inhomogeneous line.

For the amorphous sample (fig. 2), in the temperature-range 1.4 - 100 K :

$$T_1^{-1} = 39 T^2 \int_0^{56/T} x dx / \text{Sh}x \quad (T_1 \text{ s, Tk})$$

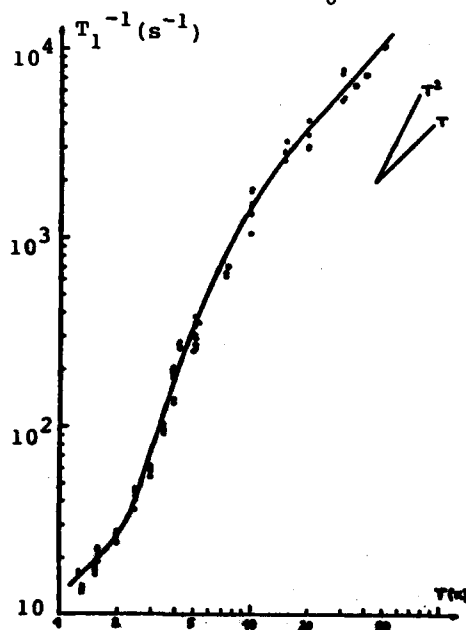


Fig. 1 : Temperature variation of the spin-lattice relaxation time of crystalline  $V_2O_5$ .  $\circ$  pulse saturation,  $\circ$  progressive saturation. The solid curve corresponds to eq. (1).

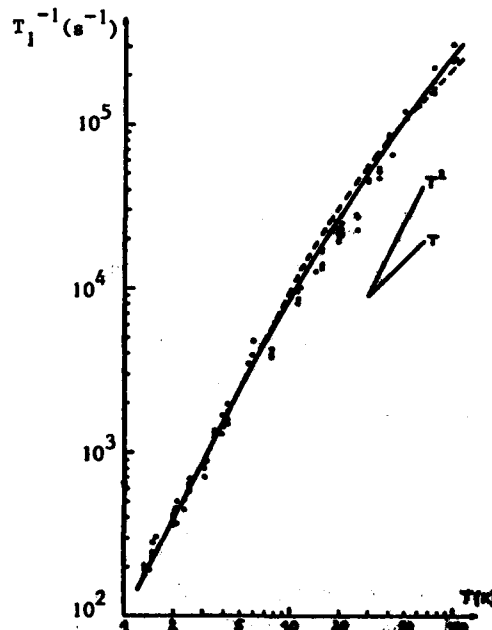


Fig. 2 : Temperature variation of the spin-lattice relaxation time of amorphous  $V_2O_5$ .  $\circ$  pulse saturation. Experimental variation corresponds to the solid curve, dashed curve corresponds to eq. (2).

4. Interpretation. - In crystalline  $V_2O_5$ , for  $T < 2$  K, we have the usual direct process. For  $T > 5$  K, the dominant process is characterized by an energy  $E_p = 16.5$  K and is also a one-phonon process since  $T_1^{-1} = T$  when  $T > 20$  K. According to Murphy model [5], the spin is coupled to the phonons via a system having two energy levels  $\phi_A, \phi_B$  separated by  $E_p$ . The efficient transitions are  $|\pm 1/2, \phi_A\rangle \leftrightarrow |\mp 1/2, \phi_B\rangle$  and use phonons with an energy  $\sim E_p$ . The origin of these two energy levels is still uncertain. An explanation is to consider that the electron is submitted to a symmetrical double well potential [6] then each vibrational state is split in two levels by tunnel effect. The energy splitting difference is much less than the vibrational energy  $\hbar\Omega$ . At low temperature we have to consider only the vibrational ground state. In amorphous  $V_2O_5$ , for  $T < 10$  K,  $T_1^{-1} = T^2$ . We rule out the possibility of a phonon-bottleneck at 10 K with our dilute system ( $10^{-3}$  centers/ $V^{5+}$ ). Near 100 K,  $T_1^{-1}$  approaches a linear dependence, which indicates a one-phonon

process. We interpret this behaviour supposing that the spins are coupled to the phonons via the T.L.S. The T.L.S.-phonon coupling is strong ; its hamiltonian, with usual notations, is [3] :

$\mathcal{H}_{T.Ph} = \frac{\epsilon}{E} \left( \frac{\Delta}{2} \right) [-\Delta_0 \sigma_X + \Delta \sigma_Z]$  where  $\sigma_X$  and  $\sigma_Z$  are Pauli matrices acting on the eigenstates of the T.L.S. The spin-T.L.S. coupling is less known ; our results suggest it is efficient in our case ; a general expression for its hamiltonian is :

$$\mathcal{H}_{T.S.} = (B_e \vec{H} \vec{\Delta} \vec{S} + \vec{I} \vec{\Delta} \vec{A} \vec{S}) \left( -\frac{\Delta_0}{E} \sigma_X + \frac{\Delta}{E} \sigma_Z \right).$$

Following S.R. Kurtz and H.J. Stapleton [4], the transition probability for a definite spin to flip through the coupling with a T.L.S. and the phonons (Debye model)

is  $\frac{\Delta^2 \Delta_0^2}{E^3 \text{Sh}(\frac{2E}{KT})}$ . Averaging over  $\Delta$  and  $\Delta_0$  with Philips distribution, one finally gets

expression (2), the cutoff value for the energy of the T.L.S. being  $2E_{\text{max}} = 56$  K. In the transition probability we have omitted an additional term leading to a  $T^4$  dependence unobserved in the present case.

The efficient process is pictured in figure 3 :

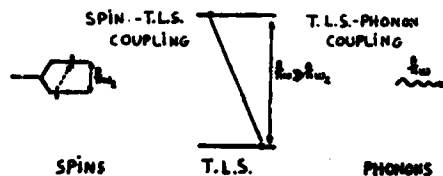


Fig. 3 : Indirect spin phonon coupling

#### References -

- [1] W.A. Philips. J. of Low-Temp. Sol., 7 (1972), 351.
- [2] P.W. Anderson, B.I. Halperin, C.M. Varma. Phil. Mag., 25 (1972), 1.
- [3] P. Doussineau, C. Frénois, R.G. Leisner, A. Levelut, J.Y. Prieur. J. Phys., 41 (1972), 1193.
- [4] S.R. Kurtz, H.J. Stapleton. Phys. Rev. B, 22 (1980), 2195.
- [5] J. Murphy. Phys. Rev., 145 (1966), 241.
- [6] R.J. Rollefson. Phys. Rev. B, 5 (1972), 3235.

ELASTIC MODULI OF LINEAR ANTIFERROMAGNET  $\text{CsNiCl}_3$ \*

K.R. Mountfield and J.A. Rayne

*Department of Physics, Carnegie-Mellon University, Pittsburgh, Pennsylvania 15213, U.S.A.*

**Abstract.** - The elastic constants of the linear chain antiferromagnet  $\text{CsNiCl}_3$  have been measured using a phase comparison method. At 295 K the measurements give  $C_{11}=3.58\pm0.07$ ,  $C_{33}=6.25\pm0.12$ ,  $C_{44}=0.60\pm0.10$ ,  $C_{66}=(C_{11}-C_{12})/2 = 1.12\pm0.02$  and  $C_{13}=1.0\pm0.2$  in units of  $10^{11}$  dyne  $\text{cm}^{-2}$ . The corresponding bulk modulus is  $2.2\pm0.4 \times 10^{11}$  dyne  $\text{cm}^{-2}$  compared to the value  $2.5 \times 10^{11}$  dyne  $\text{cm}^{-2}$  estimated from thermal expansion data.  $C_{33}$  clearly shows the effects of magnetic ordering along the chains near 30 K and of the spin rearrangement associated with three-dimensional magnetic order near 4.4 K. The former is consistent with a spin-phonon interaction involving magnetostrictive coupling through the intrachain exchange constant.

1. **Introduction.** - There is considerable interest in the properties of linear chain antiferromagnets, particularly  $\text{CsNiCl}_3$  [1]. This compound has a hexagonal  $D_{6h}^4$  structure, in which the nickel atoms form chains parallel to the c-axis. The chains are characterized by an intrachain exchange parameter  $J$  which is much larger than the interchain parameter  $J'$ , the ratio  $J/J'$  being 150. Correspondingly, short-range antiferromagnetic order develops within the chains near  $T_{\text{max}} \sim 30$  K while three dimensional ordering occurs at the much lower temperature Néel temperature  $T_N \sim 4.4$  K. A spin rearrangement, involving a ninety degree rotation of the spin component normal to the c-axis, occurs at  $T_R \sim 4.4$  K. Magnetic ordering effects have been observed in a number of properties, e.g. magnetic susceptibility [2,3], heat capacity [4,5], and thermal expansion [6].

In this paper we present the results of elastic modulus measurements on  $\text{CsNiCl}_3$  using a phase comparison method. The data at 295 K give a bulk modulus in reasonable agreement with that inferred from thermal expansion measurements. Anomalies in the temperature dependence of  $C_{33}$  are observed both in the vicinity of  $T_{\text{max}}$  and  $T_R$ . The former is consistent with a simple model for spin-phonon interaction involving magnetostrictive coupling through the exchange constant  $J(c)$ .

2. **Experiment.** - Measurements were made on single crystals of  $\text{CsNiCl}_3$  grown in sealed quartz ampoules by the Bridgmann method. Orientation of the samples was facilitated by their tendency to cleave along  $\{11\bar{2}0\}$  planes. Suitable specimens were produced by lapping the cleaved crystals to form parallel surfaces, with normals parallel, perpendicular and at  $45^\circ$  to  $[0001]$ , approximately 5mm apart.

\* Research supported by U.S. National Science Foundation under grant DMR-7923355.

Elastic modulus measurements were made at 10 MHz by a phase comparison method using X- and Y-cut co-axially plated transducers to generate longitudinal and shear waves, respectively. Room temperature data were obtained using Salol bonds, while low temperature measurements were made with Duco cement or Nonaq as bonding agents. The sample temperature was monitored by a platinum resistance thermometer down to 77 K and a calibrated germanium thermometer below 77 K. Changes in the elastic moduli in the range 4-10 K were obtained by monitoring the phase change on continuous heating with a PAR Model 162 boxcar integrator and by displaying the output against the resistance of the germanium thermometer on an X-Y recorder.

3. Results and Discussion. - Table 1 shows the results of the elastic measurements and 295 K using the X-ray density of  $\text{CsNiCl}_3$ ,  $\rho = 3.755 \text{ gm cm}^{-3}$ . There is good consistency between the redundant determinations in this table, both for the pure modes as well as the quasi-pure modes propagating off symmetry directions. From the latter we obtain the cross-coupling stiffness constant  $C_{13} = 1.0 \pm 0.2 \times 10^{11} \text{ dyne cm}^{-2}$ . The resulting value of bulk modulus at 295 K is  $B = 2.2 \pm 0.4 \times 10^{11} \text{ dyne cm}^{-2}$ , which compares well with the estimate of  $2.5 \pm 0.5 \times 10^{11} \text{ dyne cm}^{-2}$  obtained from thermal expansion data. It is of interest that the value of Debye temperature  $\theta_D$  for  $\text{CsNiCl}_3$  computed from the room temperature elastic constants is  $181 \pm 5 \text{ K}$ , which is much higher than the value  $153 \pm 5 \text{ K}$  obtained from heat capacity data [5]. The discrepancy suggests that the latter figure corresponds to a temperature range (6-15 K) in which phonon dispersion effects are still significant and that  $\theta_D$  has not reached its limited value.

Table I. - Elastic Moduli of  $\text{CsNiCl}_3$  at 295 K

Propagation Direction	Polarization Direction	Modulus	Value ( $10^{11} \text{ dyne cm}^{-2}$ )
[0001]	[0001]	$C_{33}$	$6.25 \pm 0.12$
	[1120]	$C_{44}$	$0.61 \pm 0.01$
[1210]	[1210]	$C_{11}$	$3.58 \pm 0.07$
	[0001]	$C_{44}$	$0.60 \pm 0.01$
	[0010]	$C_{66} = (C_{11} - C_{12})/2$	$1.12 \pm 0.02$
45° to [0001] in [1210]	QL	$C_{QL}^*$	$3.55 \pm 0.08$
	QT	$C_{QT}^*$	$1.45 \pm 0.02$
	[1010]	$(C_{44} + C_{66})/2$	$0.89 \pm 0.01$

\* Quasi-longitudinal and transverse modes with effective moduli  $C_{QL}, C_{QT}$  given by  $C_{QL}, C_{QT} = 1/4(C_{11} + C_{33} + 2C_{44}) \pm 1/4[(C_{11} - C_{33})^2 + 4(C_{13} + C_{44})^2]^{1/2}$ .

Figure 1 shows the temperature dependence of  $C_{33}$ , corresponding to longitudinal wave propagation along [0001]. From the dashed line, which shows the expected dependence in the absence of magnetic interactions, it can be seen that there is a pronounced anomaly near  $T_{\text{max}}$  similar to that observed in the heat capacity. This behavior is consistent with a simple hydrodynamic model for the spin-phonon interaction, involving magnetostrictive coupling between neighbouring spins though the intrachain exchange constant  $J = J(c)$ . It is readily shown that this model gives

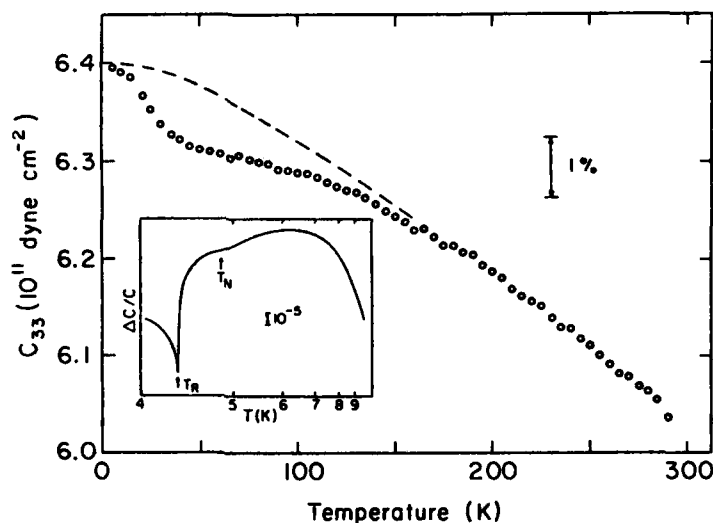


Fig. 1 : Temperature dependence of modulus  $C_{33}$ . Dashed line shows expected behavior in absence of interactions. Inset shows change in modulus below 10 K.

a velocity change

$$\frac{\Delta v}{v} = - \text{constant} \left( \frac{c}{J} \frac{dJ}{dc} \right)^2 \frac{C_M T}{Mv^2}, \quad (1)$$

where  $C_M$  is the magnetic specific heat per mole and  $M$  the corresponding molecular weight. Using the present data, the experimental values of  $C_M$  [5] and  $\gamma_{||} = -\frac{d(\ln J)}{d(\ln c)} = 21 \pm 3$  obtained from thermal expansion measurements, we find that the constant is of the order unity. It is of interest that the modulus  $C_{44}$  does not exhibit an anomalous temperature dependence. This result is easily explained on the above model, since a shear wave propagating along [0001] does not produce a modulation of the  $c$ -parameter and hence the exchange constant  $J$ .

Reference to the inset of Figure 1 shows that the modulus  $C_{33}$  exhibits a pronounced anomaly at  $T_R$  but is essentially continuous at  $T_N$ . This behavior is inconsistent with a hydrodynamic model, since  $C_M$  shows a distinct peak at both temperatures. Further experiments are being conducted to investigate the apparent anisotropy of the exchange interaction associated with the three dimensional ordering.

#### References

- /1/ See for example, deJongh Z.J. and Miedema A.R., Adv. Phys. **23** (1974) 1.
- /2/ Achiwa N., J. Phys. Soc. Japan **27** (1969) 561.
- /3/ Johnson P.B., Rayne J.A. and Friedberg S.A., J. Appl. Phys. **50** (1979) 1853.
- /4/ Adachi K. and Makata M., J. Phys. Soc. Japan **34** (1973) 269.
- /5/ Moses D., Shechter H., Ehrenfreund E. and Mahovsky J., J. Phys. C **10** (1977) 45.
- /6/ Rayne, J.A., Collins J.G. and White G.K., Solid State Comm. **33** (1980) 39.

## A MICROSCOPIC TRANSPORT THEORY OF ELECTRON-PHONON SYSTEMS

A.S. Wagh

Physics Department, University of West Indies, Mona, Kingston, Jamaica, W.I.

**Abstract** - The two-time Green functions are used to derive kinetic equations of a system of electrons and phonons interacting with Frohlich hamiltonian. A suitable connected diagram analysis is used to derive simultaneous equations similar to Kadanoff-Baym equations. The initial correlations are shown to decay in time comparable to the macroscopic time scale. The general transport equations derived in the steady state are applicable to various transport processes. It is shown that the previous assumption of considering the phonons to be in thermal equilibrium is justified only for dilute systems and phonon drag is appreciable in denser systems.

1. **Introduction.** The two-time Green functions have been extensively used by Kadanoff and Baym<sup>1</sup> to study the evolution and transport of a quantum mechanical imperfect gas. We extend this formulation to the electron phonon system. A connected diagram<sup>2</sup> analysis is used to derive the evolution equations from the theorem by Bloch and Domenicis<sup>3</sup>. We obtain four transport equations two for electrons and two for phonons, the latter describing phonon drag. Using these equations it is possible to show that the phonon drag is negligible for dilute systems such as electrons in semiconductors but can be appreciable in metals.

2. **The Evolution Equations.** The Frohlich hamiltonian for electron phonon interaction is given by

$$H = H_0 + \lambda V = \int [h_0(p) + \phi(i\frac{\partial}{\partial p}, t)] a^+(p) a(p) dp + \int \phi b^+(p) b(p) dp \\ + \lambda \int \int dp_1 dp_2 \gamma_{p_1 p_2}^{\dagger} [a^+(p_1 + p_2) a(p_1) b(p_2) + a^+(p_1) a(p_1 + p_2) b^+(p_2)] \quad (1)$$

Here  $a(p)$  and  $b(p)$  stand for annihilation operators for electrons and phonons,  $\phi$  is the external field and other symbols have their usual meaning. The partial Green functions  $g^e$  for electrons and  $n^p$  for phonons are defined by

$$g^e(1,2) = -i\text{Tr}\{p a^{\dagger}(2) a(1)\} \quad n^e(1,2) = i\text{Tr}\{p b^{\dagger}(2) b(1)\} \\ g^p(1,2) = -i\text{Tr}\{p a(1) a^{\dagger}(2)\} \quad n^p(1,2) = i\text{Tr}\{p b(1) b^{\dagger}(2)\} \quad (2)$$



where the symbols 1 and 2 stand for  $(p_1, t_1)$  and  $(p_2, t_2)$ . The evolution of  $g^Z(1,2)$  may be studied by differentiating each of these with respect to the times  $t_1$  and  $t_2$ . One obtains for example

$$\begin{aligned} i \frac{\partial g^Z(1,2)}{\partial t_1} &= -i \text{Tr} \{ \rho a^+(2) U^+(t_1) \{ a(p_1), H \} U(t_1) \} \\ &= [h_0(1) + \mu \phi(1)] g^Z(1,2) - i \text{Tr} \{ \rho \lambda / d p_3 \gamma_{p_3} [a^+(2) a(p_1 - p_3, t_1) b(p_3, t_1) \\ &\quad + a^+(2) a(p_1 + p_3, t_1) b^+(p_3, t_1)] \} \end{aligned} \quad (3)$$

This equation is not in closed form. One needs to analyze it by means of perturbation and connected diagram technique, the essential features being similar to the one obtained from Wick's theorem for an imperfect gas. Here however, we start from Bloch and Dominici's<sup>3</sup> theorem that the average  $\langle ABC... \rangle$  for operators A, B, C, etc. may be decomposed into averages of the pair-products, viz.

$$\langle ABC... \rangle = \sum_n (\pm 1)^n \langle AB \rangle \langle CD \rangle \dots \quad (4)$$

where + stands for phonons and - for electrons. The descriptions of the self-energy parts is given in the table. One obtains for  $g^Z$

$$\begin{aligned} i \frac{\partial g^Z}{\partial t_1} &= [h_0(p_1) + \mu \phi(p_1)] g^Z + \int_0^{t_2} dt_3 / d p_3 \Sigma^Z(1,3) g^Z(3,2) - t_1 \int_0^{t_2} dt_3 / d p_3 \Sigma^Z(1,3) g^Z(3,2) \\ &\quad - \int_0^{t_1} dt_3 / d p_3 \Sigma^Z(1,3) g^Z(3,2) + i \int_0^{t_1} d\beta_1 / d p_3 \Sigma^Z(1, p_3, i\beta_1) g^Z(p_3, i\beta_1, 2) \end{aligned} \quad (5)$$

where  $\Sigma^Z = \epsilon^Z + \epsilon^\pm$ . The last term in eq. (5) is due to initial correlations, which are due to our choice of initial time as  $t_1 = 0$ . In a similar manner one writes equations for  $\frac{\partial g^Z}{\partial t_2}$  and for  $n^Z$  all having same form of Kadanoff and Baym equations.

3. Decay of Initial Correlations. Though the electron-phonon interaction is a long range potential, we show here that the initial correlations die out by the time steady state is reached.

If the system is initially in thermal equilibrium, the initial Green functions for electrons obeying classical statistics are

$$g_0^<(p_1, i\beta_1, 2) = e^{-\beta_1 \epsilon(p) + i\epsilon(p) t_2 + \alpha - \beta \epsilon(p)}, g_0^>(1, p_2, i\beta_1) = e^{-\beta_1 \epsilon(p) + i\epsilon(p) t_1} \quad (6)$$

where  $p = \frac{1}{2}(p_1 - p_2)$ ,  $\epsilon$  and  $\alpha$  are particle energy and fugacity. The initial correlation term involved in eq. (5) for a linear lattice with one atom per lattice in binary collision approximation is

$$\begin{aligned} I &= \int_0^{t_1} d\beta_1 / d p_3 \Sigma^<(1, p_3, i\beta_1) g^>(-p_3, i\beta_1, 2) \\ &= \lambda^2 \int_0^{t_1} d\beta_1 / d p_3 \Sigma^<(1, p_3, i\beta_1) \gamma_{p_3} e^{-i(\beta - \beta_1) t_1} e^{i(p - p') t_1} \\ &\quad \times \exp[i\epsilon(p) t_1 + (\beta - i t_2) \epsilon(p)] \left\{ \frac{e^{-\beta \epsilon(p')}}{\epsilon \beta \epsilon(p') - 1} + \frac{e^{(\beta + \beta_1) \epsilon(p')}}{\epsilon \beta \epsilon(p') - 1} \right\} \end{aligned} \quad (7)$$

Here  $p_m$  is the maximum phonon momentum obtained at the edge of the first Brillouin zone. Assuming phonon energy to be small as compared to the electron energy and for a linear lattice

$$\xi(p) = \xi_0 \sin(p'a) = \xi_0 p'a \quad (8)$$

where  $\xi_0$  is a constant of the crystal and  $a$  is a lattice constant, we obtain

$$I = A(\beta) e^{i\xi(p)(t_1 - t_2)} \int_{\beta}^{\beta+m} P_m(p', \beta) e^{i(\frac{p'^2}{2m} + \xi_0 p'a) t_1} \left[ \frac{e^{-\frac{p p'}{m}(\beta - i t_1)} - e^{-\frac{p p'}{m}(\beta - i t_1)}}{p(\beta - i t_1)} \right] dp' \quad (9)$$

where we have used energy conservation relation  $\epsilon(p) \pm \xi(p') = \epsilon(p \pm p')$ .

$I$  decays at the most as  $\frac{1}{t_1}$  or  $\frac{1}{t_2}$ . Thus as  $t_1, t_2 \rightarrow \infty$  the whole term vanishes. Thus initial correlations are completely removed from the description of the steady state which is studied only after a long time.

4. The Steady State Transport Equations. Dropping the initial correlations and following the usual procedure<sup>1</sup>, the steady state transport equations can easily be obtained as

$$\left[ \frac{\partial}{\partial T} + \frac{p \cdot \nabla_R}{m} - \nabla \phi \cdot \frac{\partial}{\partial p} + \frac{\partial \phi}{\partial T} \cdot \frac{\partial}{\partial \omega} \right] G^{\pm} = G^{\pm} \Sigma^{\pm} - G^{\pm} \Sigma^{\pm} + \{ [G^{\pm}, \Sigma^{\pm}] - [G^{\pm}, \Sigma^{\pm}] \} \quad (10)$$

$$\text{and } \left( \frac{\partial}{\partial T} + \frac{\partial \xi(p)}{\partial p} \cdot \nabla_R \right) S^{\pm} = \epsilon^{\pm} S^{\pm} - \epsilon^{\pm} S^{\pm} + \{ \epsilon^{\pm}, S^{\pm} \} - \{ \epsilon^{\pm}, S^{\pm} \}$$

where  $G^{\pm}$  and  $S^{\pm}$  stand for electron and phonon steady state Green functions each along with the self energy parts being functions of macroscopic momentum  $p$ , particle energy  $\omega$ , position  $R$  and time  $T$ . The square brackets are generalized Poisson brackets. These equations are Markoffian and homogeneous. They can be used for the study of various transports. Here we shall use them to study the role of phonon drag in electrical conduction.

5. Phonon Drag. The equations (10) can be linearized in the electric field. To see the effect of the phonon drag, the linear parts of the Green functions  $G_L^{\pm}$  and  $S_L^{\pm}$  can be expanded for a homogeneous system as

$$G_L^{\pm}(p, \omega) = \sum_{n=0}^{\infty} \lambda^n G_{Ln}^{\pm}(p, \omega); \quad S_L^{\pm}(p, \omega) = \sum_{n=0}^{\infty} \lambda^n S_{Ln}^{\pm}(p, \omega) \quad (11)$$

Substitution of these into the linear equations and comparing the terms of the same order of  $\lambda$  yields in the lowest order

$$\begin{aligned} G_{L0}^{\pm} &= \frac{eE}{v} \cdot \frac{\partial}{\partial p} G_{eq}^{\pm}(p, \omega), \quad S_{L0}^{\pm} = 0 = G_{L1}^{\pm} = S_{L1}^{\pm}, \\ G_{L2}^{\pm} &= \frac{i\lambda^2}{v^2} \int \dots \int dp' dp'' d\omega' d\omega'' \gamma p'' \delta(p - p' - p'') \delta(\omega - \omega' - \omega'') [G_{L0}^{\pm}(p', \omega') S_{eq}^{\pm}(p'', \omega'') G_{eq}^{\pm}(p, \omega) \\ &\quad + \text{similar terms in } G_{L0}^{\pm}] + \delta(p - p' + p'') \delta(\omega - \omega' + \omega'') [G_{L0}^{\pm}(p', \omega') S_{eq}^{\pm}(p'', \omega'') G_{eq}^{\pm}(p, \omega) \\ &\quad + \text{similar terms in } G_{L0}^{\pm}] \end{aligned} \quad (12)$$

where  $v$  is the frequency of the field and  $G_{eq}^{\pm}, S_{eq}^{\pm}$  are equilibrium Green functions. It is interesting to see that  $G_{L2}^{\pm}$  has no phonon drag term. It is also a term linear in electron density. Thus in dilute systems like semiconductors, phonon drag has no contribution to the conductivity but the same cannot be said in metals.

TABLE I. Simplest self-energy diagrams and the corresponding expressions.

Symbol	Simplest Diagram	Expression in the second order
$\mathcal{E}^{<}(1,3)$		$\frac{\lambda^2}{\hbar} \{ \phi_{p_4} \{ \phi_{p_5} \gamma_{p_4}^{\frac{1}{2}} \gamma_{p_5}^{\frac{1}{2}} \mathcal{G}^{<}(p_1-p_4, t_1, p_5-p_5, t_3) \} \times n^{<}(p_4, t_1, p_5, t_3) \}$
$\mathcal{E}^{>}(1,3)$		$\frac{\lambda^2}{\hbar} \{ \phi_{p_4} \{ \phi_{p_5} \gamma_{p_4}^{\frac{1}{2}} \gamma_{p_5}^{\frac{1}{2}} \mathcal{G}^{>}(p_1-p_4, t_1, p_5-p_5, t_3) \} \times n^{>}(p_4, t_1, p_5, t_3) \}$
$\mathcal{E}^{-}(1,3)$		$\frac{\lambda^2}{\hbar} \{ \phi_{p_4} \{ \phi_{p_5} \gamma_{p_4}^{\frac{1}{2}} \gamma_{p_5}^{\frac{1}{2}} \mathcal{G}^{-}(p_1-p_4, t_1, p_5-p_5, t_3) \} \times n^{>}(p_4, t_1, p_5, t_3) \}$
$\mathcal{E}^{+}(1,3)$		$\frac{\lambda^2}{\hbar} \{ \phi_{p_4} \{ \phi_{p_5} \gamma_{p_4}^{\frac{1}{2}} \gamma_{p_5}^{\frac{1}{2}} \mathcal{G}^{+}(p_1-p_4, t_1, p_5-p_5, t_3) \} \times n^{<}(p_4, t_1, p_5, t_3) \}$
$\mathcal{E}^{\gg}(1,3)$		$\frac{\lambda^2}{\hbar} \{ \phi_{p_4} \{ \phi_{p_5} \gamma_{p_4}^{\frac{1}{2}} \gamma_{p_5}^{\frac{1}{2}} \mathcal{G}^{>}(p_1-p_4, t_1, p_5-p_5, t_3) \} \times \mathcal{G}^{<}(p_4, t_1, p_5, t_3) \}$
$\mathcal{E}^{\ll}(1,3)$		$\frac{\lambda^2}{\hbar} \{ \phi_{p_4} \{ \phi_{p_5} \gamma_{p_4}^{\frac{1}{2}} \gamma_{p_5}^{\frac{1}{2}} \mathcal{G}^{<}(p_1-p_4, t_1, p_5-p_5, t_3) \} \times \mathcal{G}^{>}(p_4, t_1, p_5, t_3) \}$

References

1. L. Kadanoff & G. Baym, The Quantum Statistical Mechanics (Benjamin, N.Y. 1962).
2. S. Fujita, Phys. Rev. A4, 1114 (1971).
3. C. Bloch & D. deDomenicis, Nucl. Phys. 7, 459 (1958).

# HOMOGENEOUS BROADENING OF ZERO-PHONON LINES FOR A MULTILEVEL SYSTEM IN A CRYSTAL : THE ROLE OF THE ELECTRON-PHONON INTERACTIONS

A. Barchielli and E. Mulazzi\*

*Istituto di Fisica dell'Università, via Celoria 16, Milano, Italy and  
Istituto Nazionale Fisica Nucleare, Sezione di Milano, Italy.*

*\*Istituto di Fisica dell'Università, via Celoria 16, Milano, Italy and  
Gruppo Nazionale Struttura Materia del CNR, Milano, Italy.*

**Abstract.-** We present the evaluation of the homogeneous broadening for a Jahn Teller centre in a crystal when interactions which cause interlevel mixing are present. Contributions coming out from one and two-phonon processes are taken into account. The special case in which the mixing is due to the presence of spin-orbit interaction is also treated.

We consider a multilevel system in interaction with the lattice phonons, e.g. an optical electron of an impurity in a crystal. This is the typical problem of discrete levels embedded in a continuum. In a first approximation, these discrete levels have an intrinsic width when the interaction with the continuum mixes them. Anyhow, the problem is not trivial if one is interested in obtaining the expressions for the widths of the zero phonon lines and the multi-phonon processes when the levels are degenerate and Jahn-Teller interactions are present. We study this problem in the framework of the open system theory, by using a method recently developed in Ref.1. As it has already been shown in Ref.2, the optical response function can be written as  $(1+M(t)) \exp Gt$ , where  $\exp Gt$  represents the "Markovian" behaviour which dominates in the long time limit, and  $M(t)$  represents the "memory" corrections to the Markovian behaviour which dominate in the short and intermediate times.  $M(t)$  is determined by the multi-phonon processes, while the real part of  $G(\text{Re}G=-\gamma/2)$  gives the width  $\gamma$ , and therefore, the homogeneous broadening of the zero-phonon line. In this short report we limit ourselves to show the expressions of such widths for a simple model: only three electronic levels are considered, the ground and two excited levels; the interaction with the lattice phonons is treated in the linear approximation. The electron-phonon interaction  $H_{ep}$  can be written as

$$H_{ep} = \sum_{r,v} \sum_{i,j=1}^2 h_{ij}(r,v) u(r,v) \quad (1)$$

where  $r$  labels the symmetry group representations according to which the various operators transform,  $v$  is the partner index; the  $u(r,v)$  are the  $(r,v)$ -symmetric displacements and the  $h_{ij}(r,v)$  are the electron-phonon interaction matrices ( $i,j=1,2$  refer to the two excited levels); for  $i=j$  they represent the interactions on the two

excited electronic levels (Jahn-Teller interactions), while for  $i \neq j$  they represent the interactions which mix the two excited levels (mixing interactions). No interaction involves the electronic ground level.

We give in the following the perturbative expressions (up to the fourth order) of  $\gamma$  for the higher excited level (level 2) by considering two different cases:

a)  $\omega_{21} < \omega_{\max}$  ; b)  $\omega_{\max} < \omega_{21} < 2\omega_{\max}$

where  $\omega_{21}$  is the frequency difference between the two excited levels and  $\omega_{\max}$  is the maximum frequency of the one-phonon spectrum.

a) In this case the electron can decay from the level 2 to the 1 through emission of one phonon. This process gives  $\gamma_D^{(1)}$ , the second order contribution to  $\gamma$ . We neglect all the fourth order terms but the one containing the Jahn-Teller interactions only ( $\gamma_{JT}$ ). This term can be comparable to  $\gamma_D^{(1)}$  if the Jahn-Teller interaction couplings  $\lambda_{JT}$  are stronger than the mixing ones  $\lambda_M$  (say  $\lambda_{JT} \approx \sqrt{\lambda_M}$ ). Under these assumptions we have

$$\gamma = \gamma_D^{(1)} + \gamma_{JT}. \quad (2)$$

$$\gamma_D^{(1)} = \frac{2\pi}{N} \sum_{r,v} \frac{1}{N} \text{Tr}(h_{21}(r,v)h_{12}(r,v))(n(\omega_{21})+1)\rho_r(\omega_{21}^2) \quad (3)$$

$$\gamma_{JT} = \frac{2\pi}{N^2} \sum_{\substack{r,v \\ r',v'}} \frac{1}{N} \text{Tr}(-[h_{21}(r,v), h_{12}(r',v')]^2).$$

$$\int_0^{\omega_{\max}} d\omega n(\omega)(n(\omega)+1) \frac{1}{\omega^2} \rho_r(\omega^2)\rho_{r'}(\omega^2) \quad (4)$$

where  $N$  is the degeneracy of the level 2,  $n(\omega)$  is the phonon population and the  $\rho_r(\omega^2)$  are the densities of one-phonon states of  $r$  symmetry.  $\gamma_D^{(1)}$  is due to the emission process of one phonon whose frequency is equal to  $\omega_{21}$ . These processes are more important as the  $\rho_r(\omega^2)$  for  $\omega=\omega_{21}$  are more intense. In Eq.(3) we have excluded the exceptional case that all  $\rho_r(\omega_{21}^2)$  vanish. The expression of  $\gamma_D^{(1)}$  is well known in the framework of open system theory.<sup>3</sup>  $\gamma_{JT}$  is determined by phonon absorption and re-emission virtual processes (note that  $\gamma_{JT}$  too is positive). It is worthwhile to note that  $\gamma_D^{(1)}$  is the only one contribution to the homogeneous broadening  $\gamma$  at  $T=0^\circ\text{K}$ .

b) In this second case the principal contribution  $\gamma_D^{(2)}$  to  $\gamma$  is due to the decay of the electron from level 2 to 1 through the emission of two phonons. Moreover, also phonon absorption and re-emission processes contribute to  $\gamma$ . Now the expression of  $\gamma$  is:

$$\gamma = \gamma_D^{(2)} + \gamma_{JT} + \gamma_M \quad (5)$$

where  $\gamma_{JT}$  is given by Eq.(4) and

$$\gamma_D^{(2)} = \frac{2\pi}{N^2} \sum_{\substack{r,v \\ r',v'}} \frac{1}{N} \text{Tr}((h_{22}(r,v)h_{21}(r',v') - h_{21}(r',v')h_{11}(r,v)) \cdot (\text{h.c.})) \quad (6)$$

$$+ \int_{-\omega_{\max}}^{+\omega_{\max}} d\omega \frac{f_r(\omega)f_{r'}(\omega_{21}-\omega)}{\omega^2}$$

$$\gamma_m = \frac{2\pi}{\hbar^2} \sum_{\Gamma, \nu} \frac{1}{N} \text{Tr}(h_{12}(\Gamma, \nu) h_{21}(\Gamma, \nu) h_{12}(\Gamma', \nu') h_{21}(\Gamma', \nu')).$$

$$\int_{-\omega_{\max}}^{\omega_{\max}} d\omega \frac{f_{\Gamma}(\omega) f_{\Gamma'}(-\omega)}{(\omega - \omega_{21})^2} \quad (7)$$

The function  $f_{\Gamma}(\omega)$  is given by

$$f_{\Gamma}(\omega) = \begin{cases} (n(\omega)+1) \rho_{\Gamma}(\omega^2), & \omega \geq 0 \\ n(-\omega) \rho_{\Gamma}(\omega^2), & \omega < 0 \end{cases} \quad (8)$$

Note that  $\gamma_D^{(2)}$  is determined by both the Jahn-Teller interactions ( $h_{ij}(\Gamma, \nu)$ ) and the mixing ones ( $h_{ij}(\Gamma, \nu)$ ,  $i \neq j$ ). In fact, the two phonon emission can be determined only through a two steps process, where the two different kinds of interactions are involved. A two phonon emission through a one step process could happen only if we had considered quadratic interactions.

At  $T=0^\circ\text{K}$  the expression of  $\gamma$  is given by

$$\gamma(T=0) = \gamma_D^{(2)} = \frac{2\pi}{\hbar^2} \sum_{\Gamma, \nu} \int_0^{\omega_{\max}} d\omega \frac{\rho_{\Gamma}(\omega^2) \rho_{\Gamma'}((\omega_{21}-\omega)^2)}{\omega^2}.$$

$$\cdot \frac{1}{N} \text{Tr}((h_{22}(\Gamma, \nu) h_{21}(\Gamma', \nu') - h_{21}(\Gamma', \nu') h_{11}(\Gamma, \nu)) \cdot (\text{h.c.})) \quad (9)$$

Note that  $\gamma_{JT}$  and  $\gamma_m$  do not contribute at  $T=0^\circ\text{K}$ , because they involve phonon absorption and re-emission processes.

The former expressions for the homogeneous broadening  $\gamma$  hold also in the case where the mixing interaction is determined only by the spin-orbit interaction. Let the Hamiltonian we consider have the expression

$$H = H_e + H_{ep} + H_{SO} + H_{ph} \quad (10)$$

$H_e$  is now the electron Hamiltonian where the spin-orbit interaction acting on the degenerate levels has been already taken into account;  $H_{SO}$  is the part of the electronic spin-orbit interaction which mixes the electron levels and  $H_{ep}$  is the e-p interaction Hamiltonian on the degenerate levels. Let us consider now the case of spin-orbit coupling comparable with the e-p one. Taking into account two excited levels as before, when  $\omega_{21} < \omega_{\max}$  (case a), the homogeneous broadening is given by Eq.(2) where  $\gamma_{JT}$  is given by Eq.(4) and  $\gamma_D^{(1)}$  by

$$\gamma_D^{(1)} = \frac{2\pi}{\hbar^2} \sum_{\Gamma, \nu} \frac{1}{N} \sum_{k_1, k_2} |\sum_{k_3} \{ \langle 2; k_1 | H_{SO} | 1; k_3 \rangle \langle 1; k_3 | h_{11}(\Gamma, \nu) | 1; k_2 \rangle$$

$$- \langle 2; k_1 | h_{22}(\Gamma, \nu) | 2; k_3 \rangle \langle 2; k_3 | H_{SO} | 1; k_2 \rangle \}|^2 \frac{n(\omega_{21})+1}{\omega_{21}^2} \rho_{\Gamma}(\omega_{21}) \quad (11)$$

The  $|1; k\rangle$  are the electronic states;  $i=1,2$  numbers the two levels and  $k$  is the degeneracy index; all the other symbols have been given before. Note that  $\gamma$  is determined by the combined action of  $H_{ep}$  which does not mix the electronic levels and  $H_{SO}$  which mixes them.

1. G.W. Ford, J.T. Lewis and J.R. McConnell, Phys. Rev. A **19**, 907 (1979).
2. A. Barchielli, E. Mulazzi and G. Parravicini, to appear in Phys. Rev. B.
3. H. Spohn, Rev. Mod. Physics **53**, 569 (1980).

## PHONON SCATTERING AT FREQUENCIES NEAR THE EXCITON FREQUENCY OF TWO-LEVEL DEFECTS

J.W. Tucker

*Physics Department, Sheffield University, Sheffield S3 7RH, England.*

**Abstract.**— In the diagrammatic temperature-dependent perturbation theory of coupled spin-phonon systems an essential quantity determining the poles of the phonon Green function is the polarisation matrix,  $M$ , of the generalised spin susceptibility. Near the spin exciton frequency the resonance contribution from the polarisation matrix to all orders is required. Hitherto only the chain-like diagrams that occur in the theory have been retained. For  $M_4$  we show that an important contribution also arises from other diagrams previously neglected, whose inclusion is essential if  $M_4$  is to remain finite in the high temperature limit.

1. **Introduction.**— In recent years there has been considerable interest in the excitation spectrum of localised defects (for example, paramagnetic ions) interacting with the phonons of the host lattice in which they are embedded. In addition to knowledge of the excitation frequencies the lifetimes of the coupled excitations are of interest because they enter into a calculation of the thermal transport properties of the system /1/ as well as contributing to the linewidth in spectroscopic measurements, for example, in phonon spectroscopy /2/ or in neutron scattering experiments /3/. One system that has been widely studied is that of paramagnetic ions having an effective spin  $\frac{1}{2}$  coupled to the phonons of the host crystal through an interaction linear in the strain. Among the theoretical approaches to the problem of determining the lifetime of the coupled mode excitations are those based on the application of diagrammatic temperature-dependent perturbation theory /2,4,5/. The work embodied in /2/ and /4/ was primarily concerned with finding the lifetime of the coupled mode spectrum in the phonon regime sufficiently removed from the spin resonance frequency for a low-order perturbation theory to be applicable. The work of Care and Tucker /5/ was an attempt to extend the theory to frequencies close to the exciton frequency of the two-level defects by incorporating higher order terms in the self energy of the phonon Green function. An expression was obtained for the lifetime of the excitations in that regime, but recent work by Memos and Loudon /6/ points out an unsatisfactory feature of the result as far as the wave-vector dependence of the relaxation rates is concerned. While the result of Memos and Loudon for the lifetime of the excitations over the whole frequency range is intuitively more attractive it has nevertheless not been deduced rigorously in a proper coupled mode theory but is rather an extrapolation of results obtained in two limiting regimes. Although an improved theory is still awaited, the work of Memos and Loudon has at least caused

us to re-examine our earlier work in an attempt to resolve some of the conflicting theoretical predictions.

2. The Polarisation Matrix.— In /5/ the poles of the phonon Green function were expressed in terms of the polarisation matrix associated with the generalised spin susceptibility. Only the zeroth and second-order contributions to the polarisation matrix  $M$  were derived completely, which is all that is needed in the low-order theory applicable to the phonon regime well away from the spin resonance frequency. In the spin exciton frequency range higher order terms in the polarisation matrix have to be included. In the work of /5/ the important contributions (referred to below as resonance terms) were isolated from the higher order terms in the polarisation matrix and a summation of these was achieved in the low temperature limit for the fully concentrated lattice. More recently, the complete expression for the fourth-order contribution to  $M$  has been reported /7/. However, when singling out the resonance-like terms in /5/ it was thought that the only diagrams that could contribute were those having a simple chain-like structure. However we now realise after a more careful examination of the complete expression for  $M_4$  that this is not the case, a point also not appreciated in /7/. In the present work we have therefore evaluated the resonance contribution to the polarisation matrix arising from the diagrams of  $M_4$  not having a chain-like character. By the resonance terms of  $M_4$  we mean those containing a denominator  $(\omega_0 - \omega)^3$ .

3. The Resonance contribution to  $M_4$ .— The resonance contributions that were missed from  $M_4^{xx}(\lambda)$  arise in fact from the terms

$$2\beta^2 \gamma^4 g(\lambda) b^{(0)} \sum_{p,q} [ F_7(p,q,-\lambda) + F_8(p,q,-\lambda) + F_9(p,q,-\lambda) + g(\lambda) \{ F_5(p,q,-\lambda) + F_6(p,q,-\lambda) \} ] \quad (1)$$

in the notation of equation (12) of /7/. On performing the analytic continuation  $i\lambda \rightarrow \omega + i\delta$  the evaluation of the wave-vector summations over  $p$  and  $q$  leads to both real and imaginary parts. The wave-vector summations are evaluated in the Debye limit and only the leading terms in an inverse expansion with respect to the Debye frequency are retained. From equation (1) we find that the real part of  $M_4^{xx}$  has a contribution

$$\frac{\gamma^4 (\pi/V)^2 b^{(0)} \operatorname{cosech}^2(\beta\omega_0/2)}{2\beta(\omega_0 - \omega)^3} - \frac{\gamma^4 (\pi/V)^2 \operatorname{cosech}(\beta\omega_0)}{2\beta(\omega_0 - \omega)^3} \quad (2)$$

arising from the non chain-like diagrams, and an imaginary part

$$K(\omega) b^{(0)} \operatorname{cosech}^2(\beta\omega_0/2) = K(\omega) \operatorname{cosech}(\beta\omega_0) \quad (3)$$



with

$$K(\omega) = (3/2)i\pi(N/V)^2 \gamma^4 (\omega/\omega_m)^3 / [\beta (\omega_0 - \omega)^3]$$

As found in /7/, the chain-like diagrams A(3), B(1), C(3) and D(2) give a resonance contribution through the terms

$$8\beta^2 \gamma^4 g(\lambda)^3 g(-\lambda) \sum_{p,q} 2\beta\omega_0 [b^{(0)} F_1(p) F_1(q) - 2b^{(1)} A_0(q, \lambda) F_1(p) + b^{(2)} A_0(p, \lambda) A_0(q, \lambda) + b^{(0)} b^{(1)} A_0(p, \lambda)^2] \quad (4)$$

of  $M^{\text{xx}}(\lambda)$ . From equation (4) the real and imaginary parts of  $M^{\text{xx}}_4$  of interest are

$$\frac{\gamma^4 (N/V)^2}{2\beta (\omega_0 - \omega)^3} [b^{(0)} \coth^2(\beta\omega_0/2) - 4b^{(1)} \coth(\beta\omega_0/2) + 4b^{(2)} + 4b^{(0)} b^{(1)}] \\ - \frac{\gamma^4 (N/V)^2}{2\beta (\omega_0 - \omega)^3} [(1/2) \tanh^3(\beta\omega_0/2) - \text{cosech}(\beta\omega_0)] \quad (5)$$

and

$$K(\omega) [-2b^{(1)} \coth(\beta\omega_0/2) + 4b^{(2)} + 5b^{(0)} b^{(1)}] \\ = K(\omega) [-\text{cosech}(\beta\omega_0) - (3/8) \tanh(\beta\omega_0/2) \text{sech}^2(\beta\omega_0/2)] \quad (6)$$

respectively. It is noticed that the contributions, equations (2) and (3) from the non chain-like diagrams exactly cancel the terms involving  $\text{cosech}(\beta\omega_0)$  in both equations (5) and (6). This has the satisfying result that the total resonance term from  $M^{\text{xx}}_4$  remains finite in the infinite temperature limit. In the dilute situation when the  $b^{(n)}$  are replaced by  $b^{(n)}_0$  the same cancellation occurs. That is, contributions from the non chain-like diagrams exactly cancel the  $\text{cosech}(\beta\omega_0)$  terms in both equations (18) and (19) of /7/.

#### References

- /1/ Elliott R.J. and Parkinson J.B., Proc. Phys. Soc., 92 (1967) 1024-39
- /2/ Tucker J.W., J. Phys. C., 5 (1972) 2064-76
- /3/ Challis L.J., Fletcher J.R., Jeffries D.J., Sheard F.W., Toombs G.A., De Goffe A.M., and Hutchings M.T., Phys. Rev., B 19 (1979) 296-9
- /4/ Toombs G.A. and Sheard F.W., J. Phys. C., 6 (1973) 1467-88
- /5/ Care C.M. and Tucker J.W., J. Phys. C., 9 (1976) 2681-93
- /6/ Memos T. and Loudon R., J. Phys. C., 13 (1980) 1657-68
- /7/ Barker G.C. and Tucker J.W., phys. stat. sol. (b), 104 (1981) 313-23

## GROUND-STATE ENERGY OF FRÖHLICH ELECTRON-PHONON SYSTEM

Chih-Yuan Lu

*Institute of Electronics, National Chiao Tung University, Hsin-Chu, Taiwan 300, Republic of China.*

**Abstract** — Recently Feynman's path-integral formalism of the Fröhlich optical polaron problem is generalized, by which it is easy and natural to get the second-order perturbation result in the weak-coupling case and the Pekar's result in the strong-coupling case, even in the crudest ground-state approximation. By using numerical method to the equations which are given by the ground-state approximation, the ground-state energy of the electron-optical phonon system can be obtained for the overall range of coupling strength. In addition, a self-consistent set of equations is derived for a central optimized potential without using the ground-state approximation. This effective local, central potential is the solution of a linear integral equation which was similar to the extensive work of optimized-potential model (OPM) in atomic physics. By using OPM formalism, no particular choice of interaction form is taken, therefore, except the approximation by Jensen's inequality, the ground-state energy of the electron-optical phonon interacting system can be obtained without any approximation.

The Hamiltonian of the idealized Fröhlich optical polaron problem is given by

$$H = \frac{\vec{p}^2}{2} + \sum_j \frac{1}{2}(p_j^2 + q_j^2) + \sum_j W_j(\vec{x}) q_j \quad (1)$$

where we use the units  $\hbar = m = \omega = 1$ .  $\vec{p}$ ,  $\vec{x}$  are the momentum and coordinate operators of electron,  $p_j$ ,  $q_j$  are those of phonons of mode  $j$ , and the interaction terms  $W_j(\vec{x}) q_j$  are  $(8/\sqrt{2} \pi \alpha / V)^{1/2} [\cos(\vec{k}_j \cdot \vec{x})/k_j + \sin(\vec{k}_j \cdot \vec{x})/k_j] q_j$ .  $\alpha$  is the dimensionless coupling strength. The generalized model comes from an intuitive belief that in some sense the reaction of the lattice system to the motion of an electron might be represented approximately by a fictitious particle coupled to the electron. We assume the variational Hamiltonian as

$$H_v = \frac{\vec{p}^2}{2} + \frac{\vec{p}^2}{2M} + v(\vec{x} - \vec{R}) \quad (2)$$

Feynman has used a specific form of interaction-harmonic interaction between the electron and the fictitious particle. We formulate the upper bound of the polaron energy for the general form of variational

potential  $v(\vec{x}-\vec{R})$ , then the result is given by<sup>[1]</sup>

$$E_0 \leq E_v = \langle u_0 | \vec{p}^2 / 2\mu | u_0 \rangle - \frac{\alpha}{\sqrt{2}\mu} \sum_{i=0}^{\infty} \iint d\vec{r} d\vec{r}' \frac{u_0^*(\vec{r}') u_0(\vec{r}) u_1^*(\vec{r}) u_1(\vec{r}')}{|\vec{r} - \vec{r}'|} \left( \frac{1 - \exp[-2C(1+\Delta\epsilon_i)^{1/2} |\vec{r}-\vec{r}'|]}{\Delta\epsilon_i + 1} \right) \quad (3)$$

$$\text{where } C = M/[2(M+1)]^{1/2} \quad (4) \quad \text{and } \Delta\epsilon_i = \epsilon_i - \epsilon_0 \quad (5)$$

$\mu$  is the reduced mass,  $\mu = M/(M+1)$ , and  $u_i(\vec{r})$  and  $\epsilon_i$  are the eigenstates and eigenvalues of the Schrödinger equation of the system

$$\left( -\frac{1}{2\mu} \nabla^2 + v(\vec{r}) \right) u_i(\vec{r}) = \epsilon_i u_i(\vec{r}) \quad (6)$$

From Eq.(3) it is obvious that if we take only the ground state term ( $i=0$  only) in the energy expression, because every term is positive in the summation and of decreasing importance by the energy difference denominator of increasing magnitude of  $i$ , then the right hand side of Eq.(3) is still an upper bound of the polaron energy. Even within this ground-state approximation, the second-order perturbation result in the weak-coupling case and Pekar's result in the strong-coupling case is obtained very naturally.<sup>[1]</sup> By using numerical direct integration or Ritz variational method the ground state energy can be obtained for the overall range of coupling strength, and the phase-transition-like behavior such as abrupt changes of slope of the ground state energy at some coupling strength  $\alpha_c$  is found<sup>[2]</sup> similar to that of Shoji and Tokuda.<sup>[3]</sup>

In order to calculate the Eq.(3) without using ground-state approximation, a self-consistent set of equations is derived for a central optimized potential, this effective local, central potential is the solution of a linear integral equation which is similar to the extensive work of optimized-potential model in atomic physics.<sup>[4][5]</sup> The  $v(\vec{r})$  above is to be varied to minimized the functional  $E_v$ , therefore a system of self-consistent equations is derived for this problem, in which  $v(\vec{r})$  is the solution of an integral equation. It can be seen that in our case the exchange terms in atomic physics will not appear. The variational problem to be solved is

$$0 = \frac{\delta E_v}{\delta v(\vec{r})} = \sum_i \int d\vec{r}' \frac{\delta E_v}{\delta u_i(\vec{r}')} \times \frac{\delta u_i(\vec{r}')}{\delta v(\vec{r})} \quad (7)$$

The variational derivatives

$$\frac{\delta E_v}{\delta u_1(\vec{r})} = \frac{\hbar^2}{2\mu} u_0(\vec{r}) \delta_{01} + w_{1,0}(\vec{r}') u_0^*(\vec{r}') + \sum_n w_{n,0}^*(\vec{r}') u_n^*(\vec{r}') \quad (8)$$

$$\text{where } w_{1,0}(\vec{r}') = -\frac{\alpha}{\sqrt{2\mu}} \int d\vec{r} \frac{u_1^*(\vec{r}) u_0(\vec{r})}{|\vec{r} - \vec{r}'|} \left( \frac{1 - \exp[-2C(1 + \Delta\epsilon_1)^{1/2} |\vec{r} - \vec{r}'|]}{\Delta\epsilon_1 + 1} \right) \quad (9)$$

$$\text{and } \frac{\delta u_1(\vec{r}')}{\delta v(\vec{r})} = -G_1(\vec{r}', \vec{r}) u_1(\vec{r}) \quad (10)$$

$$\text{where } G_1(\vec{r}', \vec{r}) = \sum_{j \neq 1} \frac{u_j^*(\vec{r}') u_j(\vec{r})}{(\epsilon_j - \epsilon_1)} \quad (11)$$

The results (8) and (10) can now be substituted into (7), and if the Eq.(6) is used, it is found that

$$\int d\vec{r}' v(\vec{r}') H(\vec{r}', \vec{r}) = Q(\vec{r}) \quad (12)$$

$$\text{where } H(\vec{r}', \vec{r}) = u_0^*(\vec{r}') G_0(\vec{r}', \vec{r}) u_0(\vec{r}), \quad (13)$$

$$Q(\vec{r}) = \sum_i \int d\vec{r}' w_{i0}^*(\vec{r}') u_0^*(\vec{r}') G_1(\vec{r}', \vec{r}) u_1(\vec{r}) + \sum_n \int d\vec{r}' w_{n0}^*(\vec{r}') u_n^*(\vec{r}') G_0(\vec{r}', \vec{r}) u_0(\vec{r}) \quad (14)$$

Therefore the variational problem has now been reduced to the problem of obtaining self-consistent solution of Eqs.(6) and (12).

In our problem there is another parameter  $\mu$  which should be determined by another variational equation. But it is suggested that we may choose some appropriate value which might come from ground state approximation or Feynman's harmonic model to the Eqs.(6) and (12), and then substitute the solutions of the self-consistent equations (6) and (12) into the  $\partial E_v / \partial \mu = 0$  to check our choice, or we may plot the  $E_v$  versus  $\mu$  to determine it.

#### References

- 1 J. M. Luttinger and Chih-Yuan Lu, Phys. Rev. **B21**, 4251(1980).
- 2 Chih-Yuan Lu and Chi-Kuang Shen, to be published.
- 3 H. Shoji and N. Tokuda, J. Phys. C: **14**, 1231(1981).
- 4 J. D. Talman and W. F. Shadwick, Phys. Rev. **A14**, 36(1976).
- 5 K. Aashamar, T. M. Luke and J. D. Talman, Phys. Rev. **A19**, 6(1979).

## OPTICAL-MODE DEFORMATION POTENTIAL

R.C. Alig, S. Bloom and M. Inoue\*

RCA Laboratories, Princeton, U.S.A.

\*RCA Laboratories, Tokyo, Japan.

**Abstract.**— From measurements in the literature of the average energies,  $\epsilon$ , required to create electron-hole pairs with ionizing radiation in several semiconductors, a value of the optical-mode deformation-potential constant,  $KD_t$ , has been obtained. A recent analysis has been extended to include scattering by the polar-mode electron-phonon interaction as well as by the optical-mode deformation potential. Expressions for these scattering rates were developed in the free-particle approximation. The only unknown in the ratio of these rates is  $KD_t$ . These values are  $KD_t = 1.8 \times 10^8 \times \sqrt{\rho \text{ eV/cm}}$ , where  $\rho$  is the semiconductor density in  $\text{gm/cm}^3$ .

When a high-energy particle enters a semiconductor, it loses energy by creating electron-hole pairs and phonons. For a particle of energy  $E_0$ , the average number  $n$  of pairs can be measured to determine the average pair-creation energy  $\epsilon = E_0/n$ . The value of  $n$  can also be calculated, as described in Ref. 1. The rate at which a particle creates optical phonons, relative to the rate at which it creates electron-hole pairs, will have a marked effect on the value for  $\epsilon$ . In Ref. 1, this relative phonon scattering rate is determined empirically from the measured and calculated values for  $\epsilon$ . In this paper the optical-phonon scattering rate due to the deformation-potential interaction is isolated from the rate due to the polar-mode electrostatic interaction, and these rates are determined empirically from the measured and calculated values for  $\epsilon$  in the elemental and binary semiconductors. In this way the value of the optical-mode deformation-potential constant,  $KD_t$ , is ascertained.

In Ref. 1 only the energy dependence of the deformation-potential electron-phonon interaction was considered. Here the explicit forms of both the deformation-potential and polar-mode electrostatic electron-phonon interactions are introduced. The scattering rates due to these interactions are<sup>2</sup>

$$r'_{DP}(E) = \frac{(KD_t)^2 n^{3/2}}{\sqrt{2} \pi \hbar^2 \rho} \left[ \frac{\sqrt{E}}{\hbar \omega_0} \right] \quad (1)$$

and

$$r'_{PE}(E) = \frac{\sqrt{E} e^2}{\sqrt{2} \pi^2} \left[ \frac{\hbar \omega_0}{\epsilon \sqrt{E}} \ln \left( \frac{4E}{\hbar \omega_0} \right) \right] \quad (2)$$

where  $E$  is the particle kinetic energy,  $\hbar\omega_0$  is the optical-mode phonon energy,  $\epsilon^*$  is the effective dielectric constant,  $\rho$  is the semiconductor density, and  $e$  and  $m$  are the free electron charge and mass.

The scattering rate for ionization, i.e., the creation of electron-hole pairs, is<sup>1</sup>

$$r(E) = |C|^2 \left[ \frac{2\pi}{105} (E - E_g)^{7/2} \right] \quad (3)$$

where  $C$  is proportional to the matrix element of the Coulomb interaction,  $E \geq E_g$ , and  $E_g$  is the semiconductor bandgap.

As in Ref. 1, the ratio of Eqs. (1) and (3) was set to a constant<sup>3</sup>,

$$A' = (KD_t / \hbar |C|)^2 m^{3/2} / \sqrt{2} \pi \rho, \quad (4)$$

times the ratio of the factors in the square brackets. In Ref. 1,  $A'$  was assumed independent of the particle energy and invariant for electrons and holes and for different materials. From measurements of  $\epsilon$  in Si, this constant was determined empirically in Ref. 1 to be  $A' = 0.33 \text{ eV}^4$ .

Here, the ratio of Eqs. (2) and (3) is set, in the same way, to another constant,

$$B' = \sqrt{m/2} (e/\hbar |C|)^2, \quad (5)$$

times the ratio of the factors in the square brackets. As with  $A'$ ,  $B'$  is assumed independent of the particle energy and invariant for electrons and holes and for different materials. From measurements of  $\epsilon$  in CdS, and using  $A'$  to account for the deformation-potential scattering,  $B'$  was determined empirically to be  $B' = 5300 \text{ eV}^3$ . The values of  $\epsilon$  calculated with  $A'$  and  $B'$  were in good accord with the measured values in 13 other semiconductors. The addition of the polar-mode electrostatic interaction had only a small effect on most of the calculated values of  $\epsilon$  given in Ref. 1.

Using  $B' = 5300 \text{ eV}^3$  in Eq. (5), the value<sup>4</sup> of  $|C|^2$  is  $1.05 \times 10^{12} \text{ eV}^{-7/2} \text{ sec}^{-1}$ . Using this value of  $|C|^2$  and  $A' = 0.33 \text{ eV}^4$  in Eq. (4) gives

$$KD_t = 1.8 \sqrt{\rho} \times 10^8 \text{ eV/cm} \quad (6)$$

where  $\rho$  is the numerical value of the semiconductor density in  $\text{gm/cm}^3$ . Since there is no ionization scattering for  $E < E_g$ , and since  $r(E)$  dominates both  $r'_{DP}(E)$  and  $r'_{PE}(E)$  for  $E \geq 5E_g$ , this value of  $KD_t$  is valid for kinetic energies between one and five bandgaps above the band minimum. Since no distinction has been made between electrons and holes, it is an average of the values for electrons and holes.

Measurements of  $KD_t$  have been reported for germanium and silicon. A large number of values have been given for Ge<sup>5</sup>, ranging from  $4$  to  $12 \times 10^8$  eV/cm. There are fewer measurements for Si because the zero-order value of  $KD_t$  for the conduction band is zero by symmetry<sup>6</sup>. The value<sup>7</sup> in first order is  $9 \times 10^8$  eV/cm.

#### References

1. R. C. Alig, S. Bloom, and C. W. Struck, Phys. Rev. **B22**, 5565 (1980).
2. E. M. Conwell, High Field Transport in Semiconductors, (Academic Press, NY, 1967).
3. The constant A of Ref. 1 is related to A' by  $A' = \hbar\omega_0 A$ .
4. Although this value of  $|C|^2$  is an order of magnitude smaller than the value found by fitting Eq. (3) to Fig. 1 of E. O. Kane, Phys. Rev. **159**, 624 (1967) for Si, differences of this size may arise when band structure is introduced.
5. A. L. Smirl, in Physics of Nonlinear Transport in Semiconductors, (edited by D. K. Ferry, J. R. Barker, and C. Jacoboni, Plenum, NY, 1980) p.367.
6. W. A. Harrison, Phys. Rev. **104**, 1281 (1956).
7. D. K. Ferry, Phys. Rev. **B14**, 1605 (1976).

## ABSOLUTE CROSS SECTIONS FOR ONE-PHONON RAMAN SCATTERING FROM SEVERAL INSULATORS AND SEMICONDUCTORS

J.M. Calleja, H. Vogt and M. Cardona

*Max-Planck-Institut für Festkörperforschung, Heisenbergstr. 1, 7000 Stuttgart 80, F.R.G.*

**Abstract.**— Using the Brillouin-Raman method we have measured the Raman scattering efficiencies for the  $\Gamma$  phonons of GaP, ZnTe, ZnSe, ZnS as well as  $\text{CaF}_2$ ,  $\text{SrF}_2$ ,  $\text{BaF}_2$ . The results for the zincblende-type materials allow us to calibrate in absolute scattering efficiency units the resonance Raman curves found in the literature. From the calibrated resonances the deformation potential  $d_0$  is deduced on the basis of a parabolic band model. For the fluorides the scattering efficiency is attributed to the edge exciton. The deformation potential of the  $\Gamma_{15}$  valence band following from this interpretation is compared with pseudopotential and LCAO calculations.

**1. Introduction.**— Raman resonances of semiconductors in the neighbourhood of interband critical points have usually been studied by measuring the Raman scattering efficiency  $S_R$  in relative, arbitrary units as function of photon energy.<sup>1</sup> A full understanding of the Raman process, however, requires the knowledge of absolute values of  $S_R$ . Such values yield information on electron-phonon coupling constants or deformation potentials.<sup>1,2</sup>

Here we investigate with the Brillouin-Raman technique the Raman scattering efficiency of four typical zincblende-type materials (GaP, ZnTe, ZnSe, ZnS) and three fluorides ( $\text{CaF}_2$ ,  $\text{SrF}_2$ ,  $\text{BaF}_2$ ). The latter have non-dispersive Raman polarizabilities and are often used as standards for Raman measurements.

**2. Experimental Method.**— We determined  $S_R$  by measuring the Raman-Brillouin scattering efficiency ratio  $S_R/S_B$  and calculating  $S_B$  from data measured independently by other experimental techniques.<sup>3</sup> Using a five-pass piezoelectrically scanned Fabry-Perot interferometer we recorded Raman and Brillouin lines under exactly identical scattering conditions.  $S_R/S_B$  was obtained from the relative intensities integrated over the full linewidth.

**3. Results.**— Raman polarizabilities  $\alpha$ , scattering efficiencies  $S_R$ , and differential cross sections  $d\sigma/d\Omega$  at 1.92 eV are listed in Table 1.  $\alpha$  is defined by :



$$\alpha = \frac{1}{N} \frac{d\chi_{12}}{du_3} \quad (1)$$

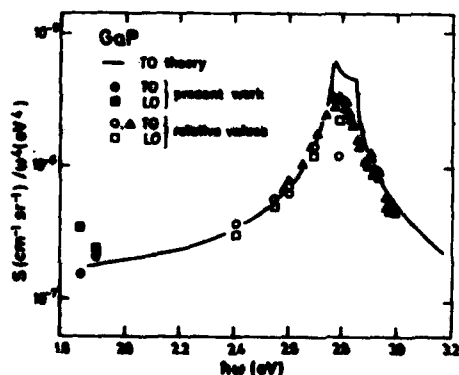
where the indices refer to the cubic axes,  $\chi$  is the dielectric susceptibility, and  $u$  the relative displacement of the two sublattices involved in the Raman vibration.

Table 1. Raman polarizabilities  $\alpha$ , scattering efficiencies  $S_R$ , and differential cross sections  $d\sigma/d\Omega$  at 1.92 eV (6471 Å).

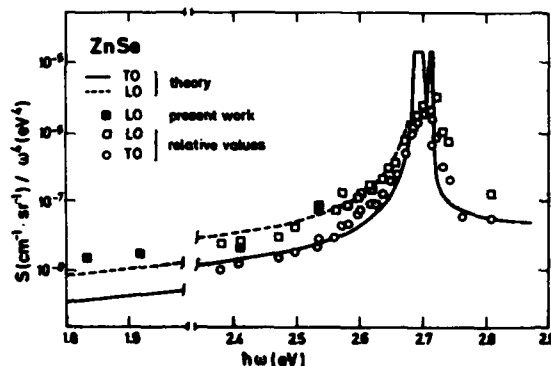
material	$ \alpha $ (Å <sup>2</sup> )	$S_R$ (10 <sup>-8</sup> sr <sup>-1</sup> cm <sup>-1</sup> )	$d\sigma/d\Omega$ (10 <sup>-30</sup> cm <sup>2</sup> sr <sup>-1</sup> per primitive cell)
GaP, LO	25	330	530
GaP, TO	23	300	490
ZnTe, LO	24	240	540
ZnSe, LO	7.0	26	47
ZnS, LO	2.5	3.8	6.0
CaF <sub>2</sub>	0.47±0.09	0.34	0.14
SrF <sub>2</sub>	0.61±0.05	0.56	0.27
BaF <sub>2</sub>	0.84±0.08	1.1	0.69

Within the indicated limits of accuracy the Raman polarizabilities of the fluorides turn out to be constant in the visible spectrum. Therefore we quote the average of the values obtained for 5 different laser lines.

The data for the zincblende-type materials were used to calibrate the resonance curves found in the literature.<sup>4,5</sup> Examples are given in Figs. 1 and 2. The solid curves in these figures are theoretical fits. The underlying formulas<sup>2</sup> mainly take into account the contribution of the direct gap  $E_0$ ,  $E_0 + \Delta_0$  to the Raman polarizability and allow to deduce values of the deformation potential  $d_0$  from the calibrated resonances. In Table 2 we compare these values with LCAO and pseudopotential calculations.



Figs. 1 and 2 : Reduced Raman efficiencies of GaP and ZnSe as function of photon energy. Empty symbols represent relative values originally measured in arbitrary units. Full symbols represent absolute values obtained in this work.



In the case of the fluorides we attribute the whole of  $\alpha$  to the strong edge exciton dominating the optical absorption spectrum. We have:<sup>6</sup>

$$\alpha = \frac{a_0^2 N_{\text{eff}} d_0}{4 E_0^3} \quad (2)$$

where  $a_0$  is the lattice constant,  $N_{\text{eff}}$  the "effective electron density", and  $E_0$  the exciton energy. Like in

the case of zincblende the deformation potential  $d_0$  is introduced as :

$$d_0 = -a_0 \frac{dE_0}{du_3} \quad (3)$$

Values of  $d_0$  following from Eq. (2), the optical absorption spectrum, and our experimental data are also listed in Table 2 and compared with the results of LCAO and pseudopotential calculations.

Table 2. Deformation potential  $d_0$  (in eV) obtained by various methods.

material	Raman	LCAO	pseudopotential
GaP	27	39.4*	26.5*;26.3*
ZnTe	37	24.4*	28*
ZnSe	12	28.1*	21.6*;27*
ZnS	4	30.4*	30.5*;25*
CaF <sub>2</sub>	49	38.8	45.1
SrF <sub>2</sub>	50	37.8	37.8
BaF <sub>2</sub>	66	34.2	30.0

\* values obtained by other authors (see Ref. 6)

1. W. Richter, Springer Tracts in Modern Physics, Vol. 78 (Springer Verlag, Heidelberg, 1976)
2. M. Cardona, Atomic Structure and Optical Properties of Solids, ed. by E. Burstein (Academic Press, New York, 1972) p. 514
3. M. Cardona, M.H. Grimsditch, and D. Olego, Light Scattering in Solids, ed. by J.L. Birman and H.Z. Cummins (Plenum Press, New York, 1979) p. 249
4. M.H. Grimsditch and A. Ramdas, Phys. Rev. B **11**, 3139 (1975)
5. B.A. Weinstein and M. Cardona, Phys. Rev. B **8**, 2795 (1973)
6. R.L. Schmidt, B.D. McCombe, and M. Cardona, Phys. Rev. B **11**, 746 (1975)
7. R.L. Schmidt and M. Cardona, Physics of Semiconductors, ed. by F.G. Fumi (Tipografia Marves, Rome, 1976) p. 239
8. J.M. Calleja, H. Vogt, and M. Cardona, to be published in Phil. Mag. (1981)

## EFFECT OF PHONONS ON THE SPIN SUSCEPTIBILITY

D. Fay and J. Appel\*

*Abteilung für Theoretische Festkörperphysik, Universität Hamburg, Hamburg, F.R.G.**\*I. Institut für Theoretische Physik, Universität Hamburg, Hamburg, F.R.G.*

**Abstract.**— That phonons do not affect the Pauli spin susceptibility seems to be a standard, well-accepted result. Since the recent suggestion by Enz and Matthias that phonons might play a decisive role in the ferromagnetism of  $\text{ZrZn}_2$ , this question has been "reopened". We review both the old and new work on this problem and try to clarify the present situation.

The suggestion by Enz and Matthias<sup>1</sup> that phonons might play an important role in the paramagnetic to ferromagnetic transition in  $\text{ZrZn}_2$  has led to renewed interest in the question of to what extent phonons affect the spin susceptibility. This is really an old question and has been (briefly) discussed in many books and articles. A good discussion was given by Herring<sup>2</sup> and a detailed model calculation was done by Quinn<sup>3</sup>. Quinn considered the change in energy  $\Delta E$  due to a spin polarization induced by an external magnetic field and wrote  $\Delta E = \Delta E_d + \Delta E_{\text{int}}$  where  $\Delta E_d$  is the "displacement" energy caused by transferring spin-down electrons from below the Fermi surface to empty spin-up states above the Fermi surface and  $\Delta E_{\text{int}}$  is the change in the interaction energy arising from phonon exchange. Here  $\Delta E_d$  is proportional to  $1/m^*$ , where  $m^*$  is the phonon-induced mass enhancement. Quinn showed that these two contributions to  $\Delta E$  cancel exactly to leading order in  $\lambda$ , i.e.,  $O(\lambda)$ , where  $\lambda = O(1)$  is the usual electron-phonon mass renormalization parameter. The correction terms were not estimated and would presumably enter first at order  $\lambda(\omega_D/E_F) \sim \lambda(m/M)^{1/2} \sim 0.01$  where  $\omega_D$  is the Debye energy and  $m$  and  $M$  are the electron and ion masses, respectively. This is in contrast to the  $O(\lambda)$  correction proposed by Enz and Matthias.

Fay and Appel<sup>4</sup> considered the diagrammatic expansion in which, using the RPA-contact interaction model for the Coulomb part  $I_c$  of the exchange interaction, the susceptibility can be written as

$$\chi(q) = \chi_{\text{phon}}(q) / (1 - I_c \chi_{\text{phon}}(q)) \quad (1)$$

where  $q \equiv (\vec{q}, q_0)$  and the first few terms in the expansion of  $\chi_{\text{phon}}$  are shown in Fig. 1.

In order to estimate the relative importance of the phonons we would now like to cast Eq. (1) into the simple RPA form  $\chi = \chi_0 / (1 - I \chi_0)$  with  $I = I_c + I_{\text{el-ph}}$  where  $\chi_0$  is the susceptibility of the non-interacting electron system. Clearly, one cannot in general define a constant effective  $I_{\text{el-ph}}$ . However, since we are

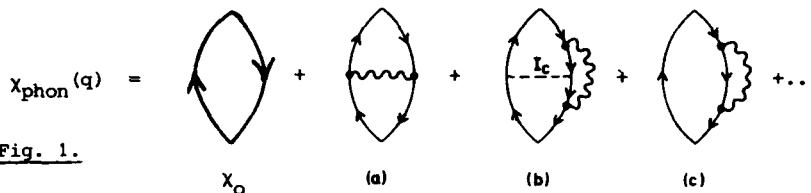


Fig. 1.

primarily interested in the effect of phonons on the ferromagnetic transition, it is sufficient to consider  $\lim(q \rightarrow 0) \lim(q_0 \rightarrow 0) \chi(q)$ . In Ref.4 it was argued that all contributions to  $\chi_{\text{phon}} - \chi_0$  are  $O(\omega_D/E_F)^2$  or higher, except diagrams (a) and (b) of Fig.1. Our procedure is to evaluate these two diagrams for  $q \rightarrow 0$  and identify  $I_{\text{el-ph}}$  by writing  $\chi_{\text{phon}} = \chi_0 + I_{\text{el-ph}} \chi_0^2$  and making use of the relation  $\chi_0(0) = N(E_F)$ . For  $\bar{I}_{\text{el-ph}} \equiv N(E_F) I_{\text{el-ph}} \ll 1$ ,  $\chi$  now has the desired RPA form. In Ref.4 we found

$$\bar{I}_{\text{el-ph}} = \epsilon(\omega_D/E_F) \lambda. \quad (2)$$

Here  $\epsilon$  is  $O(1)$  but unfortunately diagram (b) has not yet been evaluated accurately enough to determine the sign. The appearance of the small factor  $(\omega_D/E_F)$  can be considered as a manifestation of Migdal's theorem as discussed in Ref.4. Our procedure of course really only determines the effect of phonons on the static, uniform susceptibility, i.e., on the Stoner factor. Indeed, only for  $q_0 \rightarrow 0$  does it seem reasonable to neglect the retarded nature of the phonon-induced electron-electron interaction and to simulate the effect by a constant  $I_{\text{el-ph}}$ . A consistent treatment at finite  $q$  would be much more difficult and has not yet been attempted. We have also neglected spin fluctuation effects which could be important near the ferromagnetic transition. These corrections could be included in our calculation of the Stoner factor in the manner of Moriya<sup>5</sup>. At finite  $q_0$ , additional phonon-spin fluctuation interaction effects might occur.

Enz<sup>6</sup> has suggested that under certain circumstances (eg., anisotropic Fermi surface, 1-dimensional soft phonon) it may be possible to "beat" Migdal's theorem and have  $\bar{I}_{\text{el-ph}} \sim \lambda$ . It is of course true that Migdal's theorem is not a general law that applies in all situations; it is well-known, for example, that it does not hold in the limit  $|\vec{q}|/q_0 \rightarrow 0$ . In the present case however, we have been able to show rather generally, using Ward identities, that the theorem is valid for the limit  $q_0/|\vec{q}| \rightarrow 0$ ,  $|\vec{q}| \rightarrow 0$  which is appropriate here.

A good test of the importance of phonons is given by the isotope effect on the Curie temperature. Appel and Fay<sup>7</sup> found

$$\alpha = (M/T_C) (dT_C/dM) = M(d\bar{I}/dM)/2\bar{I}(\bar{I}-1) \quad (3)$$

The  $M$ -dependence of  $\bar{I}$  arises solely from the  $\omega_D$  in the small "Migdal factor" in Eq.(2).  $\bar{I}_C$  is not a function of  $M$ : The  $N(E_F)$  factor in  $\bar{I}_C$  comes from  $\chi_0$  and thus

has no phonon renormalization to order  $\lambda$  and the  $O(\omega_D/E_F)$  correction is already accounted for by  $\bar{I}_{el-ph}$ . Thus, assuming  $\lambda$  is independent of  $M$ , in the absence of the Migdal factor there is no isotope effect at all. Another formula for  $\alpha$  has been given by Enz<sup>8</sup>. Unfortunately, the experiments that could distinguish among the theoretical possibilities are quite difficult, at least in  $ZrZn_2$ .<sup>7,9</sup>

Recently Kim<sup>10</sup> has calculated  $I_{el-ph}$  by a different method and finds  $\bar{I}_{el-ph} = S(\omega_D/E_F)$  where  $S = 1/(1-\bar{I})$  is the Stoner factor and can compensate the small Migdal factor. We believe that Kim has calculated only part of  $\bar{I}_{el-ph}$  and that, in the part he has calculated, the full Stoner factor should not appear. Kim calculates  $\bar{I}_{el-ph}$  by separating the free energy into an electron part  $F_{el}$  and a phonon part  $F_{ph} = (1/2) \sum_q \hbar \omega_q$  (at  $T=0$ ). Kim's  $\bar{I}_{el-ph}$  arises from the change of the screened phonon frequency  $\omega_q$  due to a spin polarization. The separation into  $F_{el}$  and  $F_{ph}$  is however an adiabatic approximation<sup>2</sup> and does not include the non-adiabatic contributions which enter at order  $(\omega_D/E_F)$ . At this order one should also include a term  $F_{el-ph}$  which arises from the electron-phonon part of the Hamiltonian in second order perturbation theory. We doubt that the full Stoner factor occurs in the contribution Kim has calculated since the diagrams which provide the screening in  $\omega_q$  are bubble diagrams containing particle-hole pairs in a singlet spin state while the Stoner factor arises from the particle-hole triplet spin channel. We conclude that our diagrammatic approach<sup>4</sup> seems preferable in that one can identify more clearly all contributions.

#### References

- <sup>1</sup>Enz, C. P. and Matthias, B. T., *Science* **201**, 828 (1978); *Z. Phys.* **B33**, 129 (1979).
- <sup>2</sup>Herring, C., in *Magnetism*, edited by G.T. Rado and H. Suhl (Academic Press, New York, 1966), Vol. IV, Chap. XII.
- <sup>3</sup>Quinn, J. J., in *The Fermi Surface*, edited by W. A. Harrison and M. B. Webb (Wiley New York, 1960), p. 58.
- <sup>4</sup>Fay, D. and Appel, J., *Phys. Rev. B* **20**, 3705 (1979).
- <sup>5</sup>Moriya, T., *Physica (Utrecht)* **91**, 235 (1977).
- <sup>6</sup>Enz, C. P., in *Superconductivity in d- and f-band Metals*, edited by H. Suhl and M. B. Maple (Academic Press, New York, 1980) p. 181.
- <sup>7</sup>Appel, J. and Fay, D., *Phys. Rev. B* **22**, 1461 (1980).
- <sup>8</sup>Enz, C. P., *Phys. Rev. B* **22**, 1464 (1980).
- <sup>9</sup>Knapp, G. S., Corenzwit, E., and Chu, C. W., *Solid State Commun.* **8**, 639 (1970).
- <sup>10</sup>Kim, D. J., *Solid State Commun.* **34**, 963 (1980).

## ON THE ORIGIN OF THE RED SHIFT OF THE RAMAN EXCITATION PROFILE FROM THE ABSORPTION SPECTRUM

E. Molazzzi, R. Tubino\* and G. Dellepiane\*\*

*Istituto di Fisica dell'Università, via Celoria 16, Milano, Italy.**Gruppo Nazionale Struttura Materia del CNR, Milano, Italy.**\*Istituto di Chimica delle Macromolecole del CNR, via Corti, 12, Milano, Italy.**\*\*Istituto di Chimica Fisica, Dipartimento di Chimica, via Elce di Sotto, 8, Perugia, Italy.*

**Abstract.**— A red shift of the position of the Resonant Raman Scattering excitation profile with respect to the position of the maximum of the electronic absorption band has been observed in a number of compounds. The variation of the inverse vibronic lifetime  $\gamma_n$  in the excited state with the quantum number  $n$  is believed to be the most relevant contribution to the shift of the Raman excitation profile. Calculations based on this model for a molecule in a crystalline matrix are reported.

A detailed knowledge of the properties of the excited states of a molecule in a crystal can be obtained from the analysis of the electronic absorption spectrum and Raman excitation profile (REP). As a matter of fact, the electronic absorption band shape and the resonant Raman cross section are determined by the electron vibrational coupling and by the vibrational relaxation processes in the excited electronic state. While generally the REP closely mimicks the experimental absorption spectrum, in some compounds<sup>1,2,3</sup> the maximum of the REP is considerably redshifted with respect to the maximum of the absorption coefficient. This effect cannot be explained within the existing theoretical approaches which are based on linear electron vibrational interactions, harmonic potential function and a constant vibrational decay width  $\gamma$  of the vibrational states. In fact the commonly accepted approximation  $\gamma = \text{const.}$  cannot be considered any longer valid for a molecule in a solid matrix, for which the impinging laser beam creates many vibrational quanta in the excited electronic state, which rapidly decay through anharmonic interactions with the surrounding. The dependence of the vibronic lifetime on the vibrational quantum number has been quoted<sup>2,3</sup> as a possible explanation for this phenomenon. However no quantitative theoretical calculations have been reported so far. A simple theoretical model based on this hypothesis is worked out in this report and calculations for a two singlet level diatomic molecule in a crystal are presented. The model Hamiltonian for a diatomic molecule with one vibrational normal mode interacting with the lattice phonons of the host crystal is:

$$H = H_e + H_{ph} + H_{e-ph} + H_{int}, \quad H = 1 \quad (1)$$

where  $H_e = E_0 a_0^\dagger a_0 + E_1 a_1^\dagger a_1$ ;  $H_{e-ph} = V(b + b^\dagger) a_1^\dagger a_1$ ;  $H_{ph} = \omega(b + b^\dagger) \frac{1}{2}$ ;  $E_0, a_0, a_0^\dagger, a_1, a_1^\dagger$ ;  $E_1$  represent the energies and the electron operators for the ground (0) and the excited electronic state (1);  $V$  is the linear electron phonon coupling in the excited electronic state;  $b, b^\dagger$  are the vibrational operators;  $\omega$  is the frequency of the vibration-

al normal mode;  $H_{int}$  represents all the anharmonic interactions between the molecule normal mode with the phonons of the host crystal and determines the relaxation properties of the vibrational states. We assume for simplicity that  $H_{int}$  is the same in the ground and in the excited state. We note that the introduction of  $H_{int}$  influences the time evolution of the vibrational operators  $b$  and  $b^+$  both in the absorption and in the Raman scattering processes, thus introducing a variable decay width  $\gamma_n$  in both the expressions. Within the approximation we just sketched the electronic absorption coefficient can be written as

$$\alpha(\Omega) = \frac{\Omega}{N(\Omega)} I(\Omega) \quad (2)$$

where  $\Omega$  is the light beam frequency,  $N(\Omega)$  is the refractive index and  $I(\Omega)$ , the optical response function, is

$$I(\Omega) = e^{-S(T)} \sum_{n=0}^{\infty} \left(\frac{V^2}{\omega^2}\right)^n \frac{1}{n!} \left\{ \sum_{j=0}^n \binom{n}{j} (n(\omega)+1)^{n-j} (n(\omega))^j \right. \\ \left. \times \frac{\gamma_{n-j} + \gamma_j}{(\gamma_{n-j} + \gamma_j)^2 + (\Omega - \Omega_0 - n\omega + 2j\omega)^2} \right\} M_{\omega}^2 \quad (3)$$

In Eq.(3)  $S(T) = \frac{V^2}{\omega^2} (2n(\omega)+1)$  is the Huang Rhys factor,  $n(\omega)$  is the occupation number for the vibrations,  $\Omega_0$  is the zero phonon frequency, and  $\gamma_n$  is the vibrational decay width of the  $n^{\text{th}}$  vibrational state. We note that  $\gamma$  depends on  $n$  as a result of the anharmonic interactions of  $H_{int}$  in the evolution of  $b$  and  $b^+$ . In Eq.(3) we have taken into account that the  $n^{\text{th}}$  term is determined by a process in which  $(n-j)$  vibrational quanta are created in the excited state and  $j$  vibrational quanta are destroyed in the ground electronic state.

By considering the approach of the secondary emission developed in Ref.(4), the resonant Raman cross section for the  $k$ -th Stokes processes, can be written as

$$\frac{d^2\sigma}{d\omega d\Omega} \sim n(\omega)+1 \left(\frac{V^2}{\omega^2}\right)^k \frac{M_{\omega}^k}{k!} \sum_{j=0}^k (-)^j \binom{k}{j} R(\Omega - j\omega)^2 \quad (4)$$

$$R(\xi) = e^{-S(T)} \sum_{n=0}^{\infty} \left(\frac{V^2}{\omega^2}\right)^n \frac{1}{n!} \sum_{j=0}^n \binom{n}{j} (n(\omega)+1)^{n-j} (n(\omega))^j \\ \times \frac{\gamma_{n-j} + \gamma_j + i(\xi - \Omega_0 - n\omega + 2j\omega)}{(\gamma_{n-j} + \gamma_j)^2 + (\xi - \Omega_0 - n\omega + 2j\omega)^2} ; \quad (5)$$

for simplicity in Eq.(4) we have neglected the contribution to the Raman cross section coming from the terms in which  $V^2$  and the occupation number (in front to the square modulus) appear with a power higher than  $k$ .

In Fig.1 we show the results of the calculations for the absorption and the REP for the first and second order processes by considering  $\Omega_0 = 17600 \text{ cm}^{-1}$ ;  $V = 700 \text{ cm}^{-1}$ ;  $\omega = 215 \text{ cm}^{-1}$ ,  $\gamma_n (\text{cm}^{-1}) = 5 + n^2 + 0.35n^3$  at  $300^\circ\text{K}$ .

The following comments can be made: i) a significant red shift between absorption and the first and second order REP is observed ( $\sim 170 \text{ nm}$ ); ii) the intensity of the

first overtone is much lower than the fundamental one. Calculation performed using a different functional dependence of  $\gamma$  on  $n$  show that a steeper variation of  $\gamma$  with  $n$  yields lower overtone intensity, larger red shift and larger halfwidth of the absorption band. Indeed this effect has been experimentally observed in Ref.(1) where REP's and visible absorption spectra of  $I_2$  in different solutions are reported.

The model we have proposed here for the origin of the red shift of the REP should be applied to the case of  $Br_2$  in solid argon<sup>2</sup> and to the molecular center in Ref.3. Unfortunately in both cases the absorption band shape is not resolved and therefore the lack of this important experimental information does not allow us to perform exact calculations for these cases. Moreover good quality absorption spectra for both cases would make it possible to give a more precise interpretation of the dependence of  $\gamma$  on  $n$  in terms of realistic anharmonic interactions between the vibrational mode and the crystal phonons. We would like to point out that in an actual case of  $I_2$  in argon matrix, the Debye frequency of  $75\text{ cm}^{-1}$  of the host crystal implies anharmonic interaction of order higher than the third one. As a consequence of this fact a non linear dependence of  $\gamma$  on  $n$  should be expected.

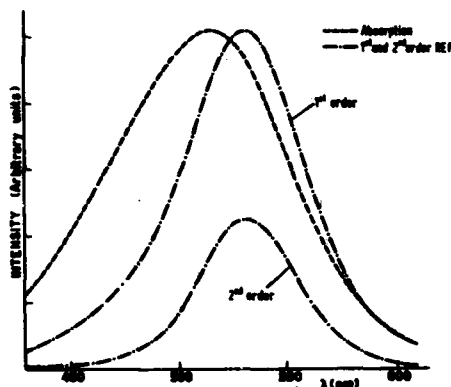


Fig.1 - Calculated absorption response function (Eq.3) and first and second order REP (Eqs.4-5), using the parameters given in the text.

#### REFERENCES

1. S. Matsuzaki and S. Nagda, Phys. Letters 28, 27 (1974);  
P.R. Fenstermacher and R.M. Callender, Optics Communications 10, 181 (1974).
2. J.M. Friedman, D.L. Rousseau and V.E. Bondybey, Phys. Rev. Letters 37, 1610 (1976).
3. T.P. Martin, Phys. Rev. B 11, 875 (1975).
4. V.V. Hizhnyakov and I. Tehver, Phys. Stat. Solidi 21, 755 (1967).



## GENERALIZATION OF FRÖHLICH'S OPERATOR FOR THE ELECTRON-PHONON COUPLING IN POLAR CRYSTALS\*

U. Schröder, M. Weiss, R. Reiger and J.B. Page\*\*

*Institut für Theoretische Physik, Universität Regensburg, D-8400 Regensburg, F.R.G.**\*\*Physics Department, Arizona State University, U.S.A.*

**Abstract.**— A formalism is developed for the coupling of excess electrons to phonons in polar crystals whose lattice dynamics are describable in terms of a shell model. Phonon dispersion and coupling to other than the usual  $\vec{q} = 0, LO$  phonons are included. Numerical results for polarons in III-V and II-VI compounds are reported.

The interaction of an electron (or hole) with phonons in a polar semiconductor is usually described by Fröhlich's Hamiltonian<sup>1</sup>. This ansatz is very fruitful for the understanding of various problems of the solid state and leads, for example, to the concept of the large polaron. As an essential assumption, the Fröhlich Hamiltonian describes the lattice vibrations by a continuum model. In this paper we develop a theory for the electron-phonon interaction with the full lattice Hamiltonian, where the phonons are treated in the harmonic approximation and are described in terms of a shell model<sup>2,3</sup>.

We start from the Hamiltonian for the electron-phonon coupling given by

$$H_{el-phon} = \sum_{l,b} \{V(\vec{r}, \vec{R}(l,b)) - V(\vec{r}, \vec{R}_0(l,b))\}, \quad (1)$$

where  $\vec{R}(l,b)$  denotes the position of the  $b$ -th ion in the  $l$ -th cell and  $\vec{R}_0(l,b)$  its equilibrium position, and  $\vec{r}$  is the position of the electron. We assume that the ions have the charge  $Z_b e$  and the electronic polarization  $\vec{P}_b[\vec{u}(l,b)]$ , which is a function of the displacements  $\vec{u}(l,b) = \vec{R}(l,b) - \vec{R}_0(l,b)$ . The potential energy is then given by

$$V(\vec{r}, \vec{R}) = - \frac{Z_b e^2}{|\vec{r} - \vec{R}|} - \frac{e(\vec{r} - \vec{R}) \cdot \vec{P}_b(\vec{u})}{|\vec{r} - \vec{R}|^3}. \quad (2)$$

In the continuum approximation  $\vec{P}_b$  can be written in terms of the macroscopic constants  $\epsilon_\infty$  and  $\epsilon_0$ . This leads to the well-known Fröhlich Hamiltonian. A fully microscopic generalization of Fröhlich's treatment is difficult, since the full dielectric tensor must be used in

order to account for local field effects. It is therefore convenient to describe the polarization field in terms of the shell model. We get

$$\vec{P}_b = Y_b e (\vec{V}(l, b) - \vec{U}(l, b)) \quad (3)$$

where  $Y_b e$  is the charge of the shell of atom  $b$  and  $\vec{V}(l, b)$  the displacement of the shell.

For small deviations from the equilibrium, we can expand the potential and use the harmonic approximation. We then write the displacements  $\vec{U}(l, b)$  in terms of normal coordinates

$$\vec{U}(l, b) = \sum_{\vec{q}, j} \sqrt{\frac{\hbar}{2N M_b \omega_j(\vec{q})}} \{ \vec{e}_c(b|\vec{q}j) e^{i\vec{q} \cdot \vec{R}_0(l, b)} a_{\vec{q}j} + \text{h.c.} \} \quad (4)$$

A similar formula holds for the shell displacements  $\vec{V}(l, b)$  with  $\vec{e}_s(b|\vec{q}j)$  replacing  $\vec{e}_c(b|\vec{q}j)$ .

After an expansion into a Fourier series and the evaluation of the sum over the lattice cells we get as a final result for the generalization of the Fröhlich operator

$$H_{\text{el-phon}} = \sum_{\vec{q}, j, \vec{G}} \{ V_{\vec{q}j\vec{G}} a_{\vec{q}j} e^{i(\vec{q}+\vec{G}) \cdot \vec{r}} + \text{h.c.} \} \quad (5)$$

with

$$V_{\vec{q}j\vec{G}} = \sum_b \frac{-4\pi e^2 i}{\Omega_0} \sqrt{\frac{\hbar}{2N M_b \omega_j(\vec{q})}} \frac{1}{|\vec{q}+\vec{G}|^2} e^{i\vec{G} \cdot \vec{R}_0(0, b)} \times \\ \times (\vec{q}+\vec{G}) \cdot \{ X_b \vec{e}_c(b|\vec{q}j) + Y_b \vec{e}_s(b|\vec{q}j) \} \quad (6)$$

Here  $\vec{G}$  is a reciprocal lattice vector,  $X_b e$  and  $Y_b e$  are the charges of the core and the shell of ion  $b$ , respectively,  $M_b$  is the mass of ion  $b$ ,  $\Omega_0$  is the volume of the unit cell, and  $N$  is the number of unit cells.

If the lattice dynamics of a crystal is known in terms of the shell model, the sums in (6) can be evaluated. Since the Hamiltonian contains the interaction with all phonons it also includes the piezoelectric coupling in crystals without inversion symmetry.

As a simple application, we investigate the case of the free polaron in semiconductors. Here the Hamiltonian is given by

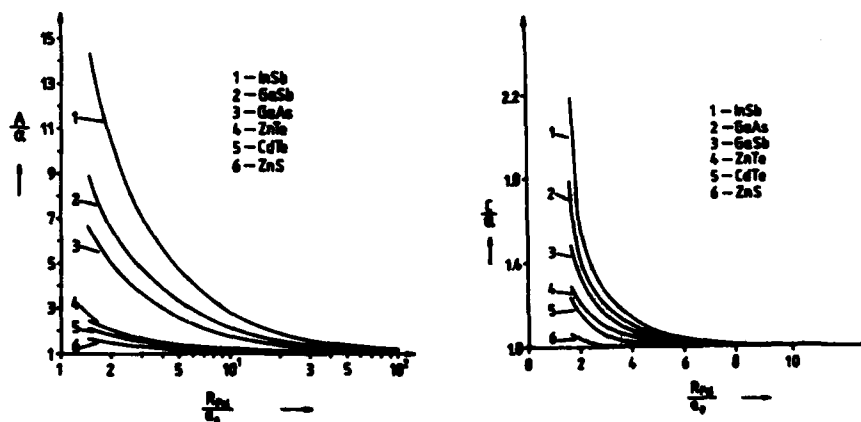
$$H = \frac{p^2}{2m^*} + \sum_{\vec{q}, j} \hbar \omega_j(\vec{q}) a_{\vec{q}j}^\dagger a_{\vec{q}j} + H_{\text{el-phon}} \quad (7)$$

In the intermediate-coupling case the method of Lee, Low and Pines<sup>4</sup> can easily be extended to this Hamiltonian. For the energy we get

the result

$$E = \frac{p^2}{2m^*(1+C/6)} - A\hbar\omega_{LO} \quad (8)$$

Numerical results for  $A$  and  $C$  are given in Figs. 1 and 2 for some III-V and II-VI compounds. The continuum approximation yields  $\alpha$  for both constants.



Figs. 1 and 2: The self-energy  $A$  and the mass correction  $C$  as a function of the polaron radius  $R_{pol}$ .  $a_0$  is the lattice constant.

Since the polaron radii for electrons and holes range from  $1.7 a_0$  (holes in ZnS) to  $16 a_0$  (electrons in InSb) the self-energy is considerably affected, but the polaron mass is only slightly different from that in the continuum approximation. A detailed analysis and an application to more polar crystals will be given in a forthcoming paper.

#### References

- 1 H. Fröhlich, H. Pelzer and S. Zienau: *Philos.Mag.* **41**, 221 (1950).
- 2 See for example M. Cochran and R.A. Cowley in *Handbuch der Physik* Vol. 25/2a, (Springer, Heidelberg 1967).
- 3 The electron-phonon interaction in a shell model was also treated by J.M. Vail, *J.Phys.* **C10**, 2399 (1977), by a different approach.
- 4 T.D. Lee, F.E. Low and D. Pines: *Phys.Rev.* **90**, 297 (1953).

\* Work supported in part by grants from the Deutsche Forschungsgemeinschaft and the National Science Foundation.

MAGNETIC FIELD DEPENDENT RESTSTRAHLEN SPECTRA IN PARAMAGNETIC  $\text{CeF}_3$ 

H. Gerlinger and G. Schaack

*Physikalisches Institut der Universität Würzburg, Roentgenring 8, 87  
Würzburg, F.R.G.*

**Abstract.** - Magnetic field dependent changes in the  $E_u$ -reststrahlen spectra of  $\text{CeF}_3$  (frequency shifts, splittings and reduction of bandwidths) have been observed at  $T = 1.6$  K,  $B = 7$  T, differing in Voigt- and Faraday-configuration.

**Introduction.** - The magnetoelastic interaction between 4f-electrons and Raman-active optical phonons in ionic Rare Earth (R. E.) compounds gives rise to a splitting of degenerate  $E_g$ -modes in an external magnetic field  $B$  parallel to the optical axis  $Z$  of an uniaxial crystal. This interaction also shifts the phonon frequencies with respect to a diamagnetic material without 4f-electrons /1, 2/. The wavenumber difference of the split phonon modes, which are complex conjugates, follows:

$\Delta\tilde{\nu} = \Delta\tilde{\nu}_s \tanh(g\mu_B H/2kT)$  (1), where  $\Delta\tilde{\nu}_s$  is the saturation splitting. This effect has been theoretically interpreted /3/, assuming a phonon-induced multipolar deformation of the R. E.-ion due to virtual transitions within the 4f-configuration. Theory also predicts/4, 5/ the splitting of degenerate infrared-active  $E_u$ -modes. Again the split  $E_u$ -modes are oppositely circularly polarized and should follow (1).

We have investigated the infrared active  $E_u$ -modes of the  $\text{CeF}_3$  in reflection at  $T = 1.6$  K in a magnetic field  $B \leq 7$  T parallel to  $Z$ . We studied two magnetic configurations: 1. Voigt-configuration (V. c.):  $K \perp Z$ ,  $B \parallel Z$ ,  $E \perp Z$ ; 2. Faraday-configuration (F. c.):  $K \parallel Z$ ,  $B \parallel Z$ ,  $E \perp Z$ . The measurements were made with a Fourier-spectrometer in the spectral range between  $60 \text{ cm}^{-1}$  and  $650 \text{ cm}^{-1}$ . The crystals were immersed in superfluid helium.

**Experimental Results.** - In Fig. 1 the reststrahlen spectra for different external magnetic fields in F. c. are shown. Fig. 2 shows the corresponding spectra in V. c.. The spectra at  $B = 0$  T are identical with each other within experimental accuracy, but differ in small but meaningful features from the reststrahlen spectra published by Lowndes et al. /6/. At  $B > 0$  effects of the magnetic field appear in both configurations surprisingly in different manner, especially near  $320 \text{ cm}^{-1}$  and near  $170 \text{ cm}^{-1}$ . In Fig. 1 the anomalous slope at the high-wavenumber edge of the reflection band near  $300 \text{ cm}^{-1}$  disappears with increasing magnetic field and gives rise to a reflection dip. The intense band at  $170 \text{ cm}^{-1}$  shows a distinct change in its form and a second maximum seems to appear at high fields. Generally the reststrahlen-bands appear more distinctly with increasing field and develop steeper slopes. This obvious reduction of the bandwidth occurs even more clearly in the V. c. (Fig. 2). In the

same spectral range as before a new band appears at  $340 \text{ cm}^{-1}$  and the splitting of the band near  $170 \text{ cm}^{-1}$  shows up more clearly. The reststrahlen spectra in both configurations differ with increasing fields beyond the experimental uncertainty (Fig. 4). This difference has according to our knowledge not been predicted theoretically up to now.

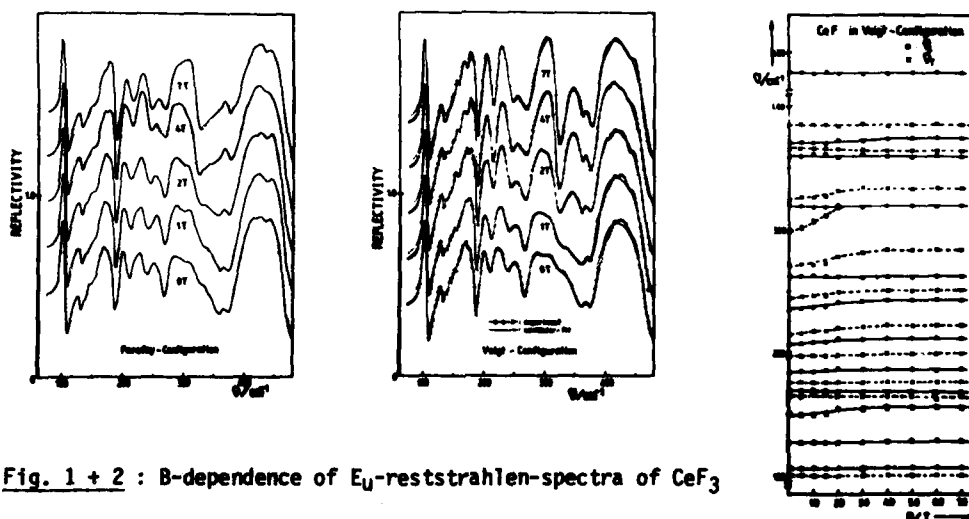


Fig. 1 + 2 : B-dependence of  $E_U$ -reststrahlen-spectra of  $\text{CeF}_3$

Fig. 3 : Wavenumber shift of transverse and longitudinal phonons,  $B \parallel Z$ , in V. c.

For the evaluation of the experimental data we have used Kramers-Kronig-analysis and, more successfully, a Lorentzian oscillator-fit. The Faraday-spectra are the superposition of two orthogonally circularly polarized spectra /5/, which can only be analyzed by an oscillator-fit. Here we present the results for the V. c.. We have calculated the reflection spectra, using the generalized Kurosawa relation as given in /7/.

$$\epsilon(\tilde{\nu}) = \epsilon(\infty) \prod_j \frac{(\tilde{\nu}_j^L)^2 - \tilde{\nu}^2 - i\gamma_j^L \tilde{\nu}}{(\tilde{\nu}_j^0)^2 - \tilde{\nu}^2 - i\gamma_j^0 \tilde{\nu}} \quad (2)$$

where  $\tilde{\nu}_j^L$  means the complex longitudinal frequency,  $\tilde{\nu}_j^0$  the transverse frequency and  $\gamma_j^L, \gamma_j^0$  the damping factors respectively.

The magnetic field dependence of  $\tilde{\nu}_j^L, \tilde{\nu}_j^0$  is shown in Fig. 3. The oscillator fit yields for the band near  $170 \text{ cm}^{-1}$  three oscillators, which are clearly separated at high fields (Fig. 2). A very unusual behaviour shows the band at  $300 \text{ cm}^{-1}$ . At low fields it was difficult to obtain a satisfying fit in this region. We had to take into account an additional oscillator which disappears at higher fields (see below). We find one case where the transverse and longitudinal frequencies of one  $E_U$ -mode ( $\approx 367 \text{ cm}^{-1}$ ) shift in opposite directions, like the two components of a split  $E_g$ -mode. In this case the oscillator strength of this mode is growing up with magnetic

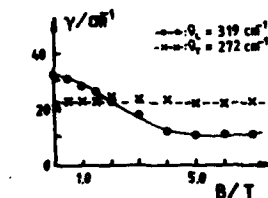
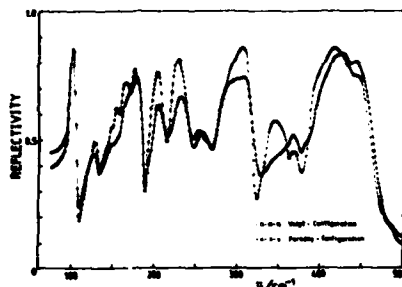


Fig. 5 :  
B-dependent  
phonon damping

Fig. 4 : Eu-reststrahlen spectra in  
V. c. and F. c., B = 7 T.

field. Frequency shifts in the order of  $7 \text{ cm}^{-1}$  to higher frequencies are observed in several cases. These shifts behave like a split  $E_g$ -phonon component according to (1) and saturate at 3 - 4 T, they are not explained by existing theory. The damping factor of the longitudinal mode at  $319 \text{ cm}^{-1}$  decreases with increasing fields from  $32 \text{ cm}^{-1}$  to  $11 \text{ cm}^{-1}$  in the same form as found in Raman-experiments /2/.

Discussion. - Magnetic field dependent frequency shifts and changes of intensity of  $E_g$ -phonons were predicted by Anastassakis et al. (e. g. /4/) using symmetry arguments alone. Our observations are in full agreement with these considerations. A splitting of a reststrahlen-band due to magnetoelastic interaction and predicted by Thalmeier and Fulde in a microscopic treatment /5/ is observed perhaps in one case ( $170 \text{ cm}^{-1}$ ).

The additional oscillator at low magnetic fields near  $300 \text{ cm}^{-1}$  is tentatively attributed to magnetic fluctuations, which are traced by the phonons. Optical phonons with a large magnetoelastic interaction seem to split already at  $B = 0 \text{ T}$  when the timescale of these fluctuations exceeds the phonon lifetime. These fluctuations are suppressed with increasing magnetic field. The differences in the spectra of the two configurations, obtained at high fields, have to be attributed to the macroscopic Coulomb-field, which couples with the phonon in V. c. but not in F. c. and has to be taken into account in addition to the magnetoelastic interaction. The joint effects of both interactions require an elliptical polarization of split phonon modes in V. c. with the appearance of a quasi-longitudinal component in the spectrum as a consequence (Fig. 2,  $340 \text{ cm}^{-1}$ ).

#### References:

- /1/ Ahrens, K. and G. Schaack: Phys. Rev. Lett. 42, 1488 (1979)
- /2/ Ahrens, K. and G. Schaack: Proc. Conf. Lattice Dynamics, ed. by M. Balkanski, Flammarion, Paris, 257 (1978)
- /3/ Thalmeier, P. and P. Fulde: Z. Physik B 26, 323 (1977)
- /4/ Anastassakis: Dynamical Properties of Solids Vol. 4, ed. by G. K. Horton and A. A. Maradudin, North Holland, Amsterdam p. 157 (1980)
- /5/ Thalmeier, P. and P. Fulde: Z. Physik B 32, 1 (1978)
- /6/ Lowndes, R. P., J. F. Parrish and C. H. Perry: Phys. Rev. 182 (3), 913 (1969)
- /7/ Lamprecht, G. and L. Merten: Phys. stat. sol. (b) 55, 33 (1973)

Acknowledgment. - The authors are indebted to W. Dürfler and K. Strössner for supplying several efficient computer programs.

## PHONON RELAXATION IN CRYSTALS STUDIED BY HOT LUMINESCENCE

P. Saari and K. Rebane

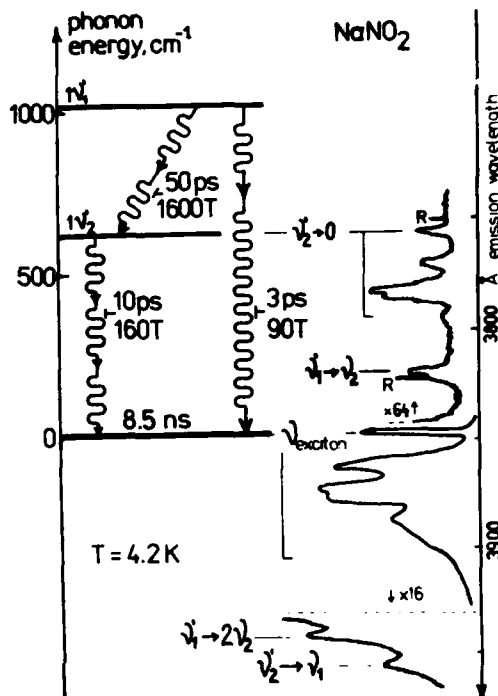
*Institute of Physics, Estonian SSR Academy of Sciences, Tartu 202400, U.S.S.R.*

**Abstract.** - We have developed a method for studying phonon interactions in picosecond timescale, which manifest themselves in optical emission spectra. In sodium nitrite transition rates between high-frequency internal and lattice phonon states have been evaluated and their correlation with the order of anharmonicity has been observed. For anthracene the kinetics of vibron relaxation up to acoustic phonons has been revealed.

1. **Introduction.** - Phonons display themselves in optical spectra of crystals through electron(exciton)-phonon interaction. For example, the luminescence pure-electronic spectral line may possess a phonon sideband which reflects the phonon density-of-states spectrum rather precisely [1]. The same interaction enables one to excite optically various phonon states through the absorption of photons whose energy exceeds that of the electronic excitation by the energy of the phonon state chosen. Although phonon states decay much faster than electronic excitations are re-emitted as luminescence there is a small part of the emission, hot luminescence (HL) [2], which occurs in the course of the phonon state transformation/decay process. As spectral bands of HL can be ascribed to phonon states involved in the process, the state lifetimes display themselves in the temporal behaviour of the HL bands or, in the case of steady-state excitation - in band intensities. Making use of these circumstances an extensive study of ultrafast phonon relaxation in luminescence centres of various impurity crystals has been carried out [3]. Here we demonstrate the possibilities of the approach on pure monocrystals possessing intramolecular phonon modes, where we study, in fact, the decay of exciton-phonon complexes created initially by light absorption.

2. **Results on sodium nitrite.** - This crystal represents an example of strong binding between intramolecular phonons and the (Frenkel) exciton: the frequencies of O-N-O stretching and bending modes,  $\nu_1 = 1330$  and  $\nu_2 = 830 \text{ cm}^{-1}$  decrease to  $\nu'_1 = 1020$  and  $\nu'_2 = 630 \text{ cm}^{-1}$ , if the exciton is created in the cell. Thus, the exciton-phonon complex (vibron) can

**Fig. 1** : On the right - emission spectrum around the pure excitonic luminescence line (+ its phonon sideband) at cw excitation by Ar<sup>+</sup> laser 3638 Å line; for HL bands initial/final phonon states are indicated; "R" labels Raman replicas (on  $\nu_1$ ,  $\nu_2$ ) of the laser line. On the left - the scheme of lowest  $\nu_1$ ,  $\nu_2$  vibron states and decay routes; transition times are given in picoseconds and periods (T) of the decaying phonon, the length of the shorter wavy line corresponds to the energy of an effective lattice phonon, the longer one - to that of  $\nu_2$ -phonon.



decay only through anharmonic coupling between internal and lattice phonons.

The obtained picture of relaxation is shown in Fig. 1 [4] (see also [5]). By virtue of the fact that the maximum energy of lattice phonons is as low as  $260 \text{ cm}^{-1}$ , the high-energy internal vibrations should decay through multiphonon processes caused by higher-order anharmonic coupling terms (or by higher-order transitions on lower terms). This is clearly expressed in the transition times which allow also some quantitative comparison of the effectiveness of couplings: the decay of a  $\nu_2$ -phonon (4-phonon process - at least 3 lattice phonons should be created) is five times faster than the conversion of a  $\nu_1$ -phonon into  $\nu_2$  and 2 lattice ones, while the direct decay of a  $\nu_1$ -phonon is surprisingly fast (due to the possibility of a 3-phonon process arising through the coupling to  $\nu_2$ -vibrations not disturbed by exciton). The latter argument is supported by the fact that in  $\text{NO}_2$ -doped alkali halides with no high-frequency vibrations in the vicinity of the excited molecule the direct decay of a  $\nu_1$ -phonon is not observed [3,4]. In general, we see that the energy gap law of multiphonon relaxation holds at a given case only after being modified by the account of the details of anharmonic coupling mechanism.

**3. Results on anthracene.** - This crystal represents an example of vanishing binding of internal phonons to the exciton but of strong interaction between excitons and photons. The first peculiarity means that here HL from excited states of internal vibrations should display the



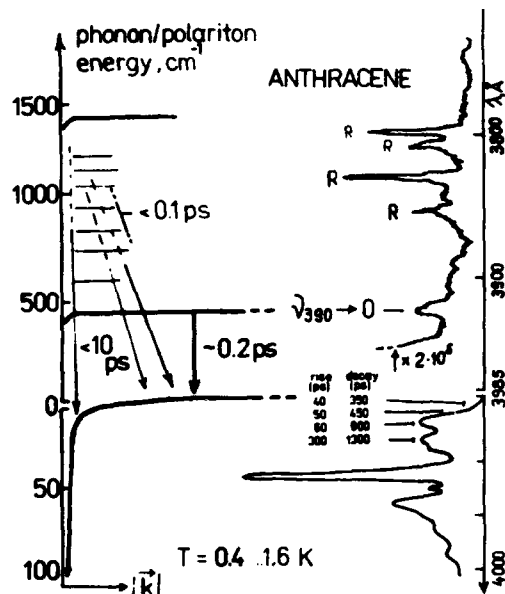


Fig. 2 : On the right - emission spectrum in the region of exciton energy at cw excitation by the 3638 Å laser line. HL band appearing through annihilation of  $A_u$   $390\text{ cm}^{-1}$  internal phonon is indicated. For the emission in "bottle-neck" region rise/decay times have been measured at picosecond pulsed excitation, reflecting polariton relaxation on acoustic phonons. On the left - dispersion curves for polaritons originating from a pure exciton and its strong interaction with 390 and  $1400\text{ cm}^{-1}$  phonons, respectively.

dissociation of vibron rather than the decay of the phonon. Indeed, emission spectra measured at various excitation conditions [6] show weak HL background under Raman lines [7] and one weak HL band. These data

give for the dissociation/decay times of higher states an estimation  $\leq 0.1\text{ ps}$  and for that of the  $390\text{ cm}^{-1}$  phonon -  $0.2\text{ ps}$  (Fig. 2). Time resolved measurements [8] led to the following conclusions: decay of high-energy states can populate within  $10\text{ ps}$  directly the states in polariton "bottle-neck", where the population distribution is formed within  $100\text{ ps}$ . From an intriguing fact that the spectrum does not change with lowering temperature to  $0.4\text{ K}$  we deduce that in this crystal phonon-stimulated processes do not take part in polariton relaxations and the relaxation mechanism could be understood if phonon-dressed polaritons are introduced [9].

1. K.K.Rebane, L.A.Rebane, J. Pure Appl. Chem. **37** (1974) 161; see also Fig. 1.
2. P.Saari, K.Rebane, Solid State Comm. **7** (1969) 887.
3. K.Rebane, P.Saari, J. Luminiscence, **16** (1978) 223.
4. J.U.Aaviksoo, A.O.Anijalg, P.M.Saari, T.A.Scovik, Sov. Phys. Sol. St. **19** (1977) 477.
5. M.Hangyo, H.Yamanaka, R.Kato, J. Phys. Soc. Japan, **50** (1981) 895.
6. J.U.Aaviksoo, P.M.Saari, T.B.Tamm, Pis'ma JETP, **29** (1979) 388.
7. On meaning of HL-to-Raman ratio see: L.A.Rebane, K.K.Rebane, in present issue and Ref. [3].
8. J.Aaviksoo, P.Saari, T.Tamm, in: Ultrafast Phenomena in Spectroscopy, Proc. Sec. Int. Symp., Reinhardtbrunn, 1980, G.D.R., p. 479.
9. J.Aaviksoo, G.Liidja, P.Saari, Phys. Stat. Sol. (b) (to be published).

# PHONONS IN RESONANT SECONDARY EMISSION OF IMPURITY MOLECULES IN CRYSTALS

L.A. Rebane and K.K. Rebane

*Institute of Physics of the Estonian SSR Academy of Sciences, Tartu, U.S.S.R.*

**Abstract.** - Resonant Raman scattering (RS), hot luminescence (HL) and ordinary luminescence (OL) were studied in the spectra of  $S_2$  and  $Se_2$  impurity molecules in KI at various frequencies of laser excitation and temperatures. Characteristic times of phase relaxation in the excited electronic state caused by phonon scattering were estimated. In contradiction with the simple version of the RSE theory no resonance in the Raman scattering cross section was observed when the excitation frequency was close or in resonance with a sharp no-phonon absorption line.

1. Model and theoretical formulas. - Theory of RSE of a rapidly relaxing center predicts three components in the spectrum  $I(\nu_1, \nu_2)$  corresponding to the three stages of the transformation of the primary photon  $\nu_1$  into the emitted secondary phonon  $\nu_2$ . A model with only one local vibration  $\Omega$  interacting with lattice phonons is considered [1,2]. The anharmonic decay  $\Gamma_m$  and the phase relaxation  $\Gamma_2$  due to phonon scattering are taken into account. Under monochromatic steady excitation in resonance with the vibronic transition  $\nu_1 = \nu_e + \Omega_m'$  ( $\nu_e$  - frequency of the electronic transition; prime refers to the excited electronic state) in the low-temperature limit

$$I(\nu_1, \nu_2) = B\kappa(\nu_1 - \nu_e) [RS(\nu_1 - \nu_2) + HL(\nu_2 - \nu_e) + OL(\nu_2 - \nu_e)]. \quad (1)$$

Here  $\kappa(\nu_1 - \nu_e)$  is the absorption spectrum of the photon  $\nu_1$ . RS is the spectrum of photons  $\nu_2$  emitted before any relaxation has taken place:

$$RS(\nu_1 - \nu_2) = \Gamma_2^{-1} \sum_{n=0}^{\infty} F_{mn}^2 \Gamma_n [(\nu_2 - \nu_1 + \Omega_n)^2 + \Gamma_n^2]^{-1}, \quad (2)$$

where  $F_{mn}^2$  is the Franck-Condon factor. HL is the emission from the states where the phase memory is lost, but the population of vibrational levels has not yet reached thermal equilibrium with the lattice:

$$HL(\nu_2 - \nu_e) = \sum_{l=1}^{m-1} \Gamma_l^{-1} \eta_{ml} \sum_{n=0}^{\infty} F_{ln}^2 (\Gamma_l + \Gamma_n) [(\nu_2 - \nu_e - \Omega_l' + \Omega_n)^2 + (\Gamma_l + \Gamma_n)^2]^{-1}; \quad (3)$$

where  $\eta_{ml}$  is the population of the vibrational level  $l$  under excitation to the level  $m$ . OL is the emission from vibrational levels in thermal equilibrium with phonons (from  $l=0$  at low temperatures):

$$OL(\nu_2 - \nu_e) = \gamma^{-1} \sum_{n=0}^{\infty} F_{on}^2 (\Gamma_n + \gamma) [(\nu_2 - \nu_e + \Omega_n)^2 + (\Gamma_n + \gamma)^2]^{-1}, \quad (4)$$

where  $\gamma^{-1}$  is the radiative lifetime. It should be pointed out that the model and formulas do not take into account the phonon sidebands and the excitation via them.

2. Results. - The impurity molecules  $S_2^-$  and  $Se_2^-$  in KI were chosen because of their single local (intramolecular) vibration of a relatively high frequency and the presence of a long series of sharp no-phonon lines in their low temperature luminescence spectra [3,4]. It enables us to construct the potential curves and to calculate the Franck-Condon factors. The RSE spectrum of  $Se_2^-$  containing all three components - RS, HL and OL, is shown in figure 1 (see also [5]). The dependence of

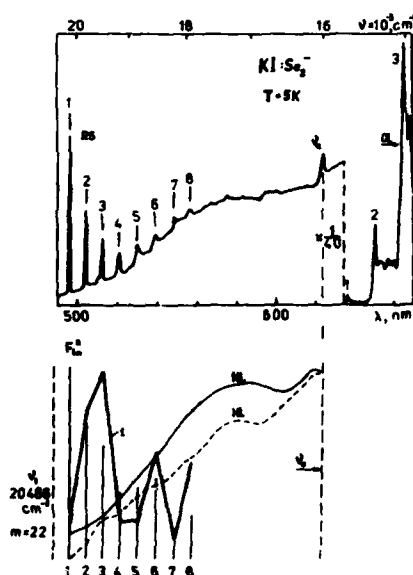


Fig. 1

the intensities of RS overtones on their order (vertical lines in the lower part of figure 1) is non-monotonic in accordance with calculated Franck-Condon factors (curve 1). The experimental HL spectrum (solid line) is in accordance with the theoretical one (dashed line) obtained from (3) as a smoothed sum of many HL transitions. From the relation of the summary intensity of RS lines to that of the OL the phase relaxation time  $\tau_2^{-1}$  was found to be  $10^5$  times shorter than the optical lifetime  $\gamma^{-1}$ . The absence of no-phonon lines in the HL spectrum of  $Se_2^-$  may be caused by relatively short lifetimes of the excited local modes: there is not enough time for thermalization of the phonon excited at the impurity. So, when the HL transition takes place, the phonons at the centre are still hot (the Debye-Waller factor is considerably smaller than for OL). For this interpretation (1) no-phonon lines are absent in the OL already at 30 K; (2) the local mode of  $Se_2^-$  can decay into only two lattice phonons.

Figure 2 shows the RSE spectrum of  $S_2^-$  in KI under excitation in resonance with the no-phonon line of  $l=4$ . On a broad background the RS lines are well displayed [6], and some of the HL no-phonon lines may be indicated. The background and its considerable increase with temperature is due to RS and HL transitions in which lattice phonons are involved. The intensity relation of  $RS_1$  (first-order) line to the HL

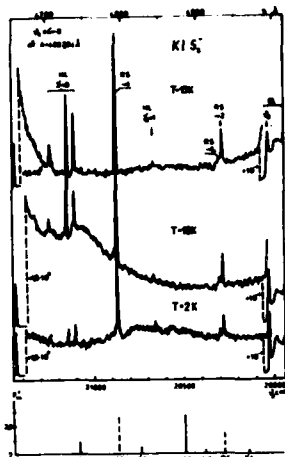


Fig. 2

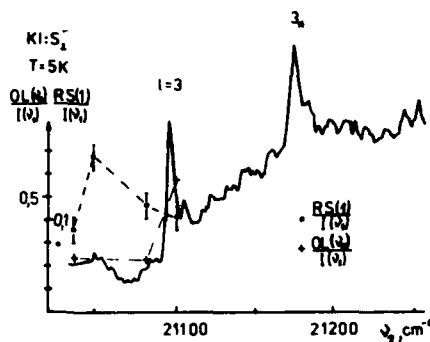


Fig. 3

(3 → 0) line is 4.2, 2.8 and 2.3 at  $T = 2, 10$  and  $15$  K, respectively. It indicates that the phase relaxation rate increases with temperature more rapidly than that of the energy relaxation.

Both RS and OL intensities should follow the absorption spectrum when the excitation frequency is varied (see formula (1)). Figure 3 shows that it is the case with the purely-electronic line of OL for excitation frequencies in the vicinity of the no-phonon line  $l = 3$  (the OL excitation spectrum is shown), but not so with the  $RS_1$  line. Definitely, there is no resonance in the RS cross section, i.e. the very simple formulas (1), (2) for RS are inadequate. A more elaborated version of the theory taking account the non-resonant levels, phonon wings and the dependence of the electronic matrix elements on vibrations is needed.

#### References

1. V.Hizhnyakov and I.Tehver, *phys. stat. sol. (b)* **82** (1977) K89.
2. K.Rebane, P.Saari, *J. Luminescence*, **16** (1978) 223.
3. C.J.Vella, J.Rolfe, *J. Chem. Phys.* **61** (1974) 41.
4. K.Rebane, L.Rebane, *J. Pure and Appl. Chem.* **37** (1974) 161.
5. L.A.Rebane, T.J.Haldre, *ZhETP Pis. Red.* **26** (1977) 674; (*JETP Lett.* **26** (1973) 515).
6. C.A.Sawicki, D.B.Fitchen, *Chem. Phys. Letters*, **40** (1976) 420.

GENERAL THEORETICAL METHODS OF PHONON PHYSICS

## POLYMORPHIC TRANSITIONS IN ALKALI HALIDES. A MOLECULAR DYNAMICS STUDY

M. Parrinello and A. Rahman\*

U. of Trieste, Trieste, Italy

\*Argonne National Laboratory, Argonne, IL 60439, U.S.A.

**Abstract.**- Using constant pressure molecular dynamics method, B1  $\rightarrow$  B2 transition in  $K^+Cl^-$  has been studied. The microscopic detail of the transition is found to be different from the one conjectured about in the literature.

1. **Introduction.**- In Born and Huang<sup>1</sup> can be found a short summary on the subject of the relative stability of the zincblend, rocksalt and cesium chloride polymorphs of alkali halides. A more detailed account was given by Tosi and Arai.<sup>2</sup> The theoretical work has only been concerned with the evaluation of the potential energy of the system using various short range interactions between the ions.

In their study Tosi and Fumi<sup>3</sup> used high pressure data in parametrizing their potential and argued that at high density the potentials needed are different from the ones relevant under more normal conditions; they also found it necessary to make the pair potentials structure dependent.

Cohen and Gordon<sup>4</sup> used the parameter free potential functions developed by Gordon and Kim<sup>5</sup>, to study the rocksalt to cesium chloride transition pressure and this study was extended by Boyer<sup>6</sup> who included the effect of harmonic vibrations in the calculation of the free energy; this however did not materially affect the conclusions based on static calculations.

In the work presented here we have used the Gordon-Kim<sup>5</sup> potentials in the parametrized form developed by Boyer.<sup>6</sup> The key element in this study is the use of new molecular dynamics methods briefly summarized in the following section. These methods make it possible for a system of classical particles to rearrange into new crystalline patterns if the ambient conditions of temperature and pressure are favorable for such rearrangement.

2. **Periodic Boundary Conditions Varying in Time.**- A system of  $N$  particles confined by periodic boundary conditions is in crystallographic language, equivalent to a Bravais lattice defined by  $\underline{a}, \underline{b}, \underline{c}$ , the unit cell having volume  $a = a.(b \cdot c)$  and containing  $N$  particles with fractional coordinates  $\underline{s}_i$ , spreading the system in the unit cell in some prescribed fashion.

Parrinello and Rahman<sup>7</sup> introduced the possibility of making the vectors  $\underline{a}, \underline{b}, \underline{c}$

dynamical variables in addition to the usual ones, namely all the  $\underline{s}_i$ . Let  $\underline{h} = (\underline{a}, \underline{b}, \underline{c})$  be the tensor formed by the vectors  $\underline{a}, \underline{b}, \underline{c}$ . Then  $\alpha = \det \underline{h}$ , the position vector is  $\underline{r} = \underline{h} \underline{s}$  and the distance square is given by  $\underline{r}^2 = \underline{s}^T \underline{h}^T \underline{h} \underline{s} = \underline{s}^T \underline{G} \underline{s}$  where  $\underline{G}$  is therefore the metric tensor; the prime denotes a transpose in the usual way.

The equations of motion generated by the Lagrangian introduced<sup>7</sup> are as follows:

$$\ddot{\underline{s}}_i = m_i^{-1} \underline{h}^{-1} \underline{f}_i - \underline{G}^{-1} \underline{\dot{G}} \underline{\dot{s}}_i, \quad i = 1, \dots, N, \quad (1)$$

$$\ddot{\underline{h}} = W^{-1} (\underline{\dot{g}} - p) \underline{g}, \quad (2)$$

where the various symbols are defined as:

$$\underline{g} = (\underline{b} \wedge \underline{c}, \underline{c} \wedge \underline{a}, \underline{a} \wedge \underline{b}) \quad (3)$$

$$\alpha \underline{g} = \sum (m_i \underline{v}_i \underline{v}_i + \underline{f}_i \underline{r}_i), \quad (\text{dyadic notation}) \quad (4)$$

$$\underline{f}_i = - \nabla V / \alpha \underline{r}_i, \quad (5)$$

$$\underline{v}_i = \underline{h} \underline{\dot{s}}_i, \quad (6)$$

$p$ , the externally applied pressure,

$V$ , the potential of particle interactions,

$W$ , has dimension of mass; it gives inertia to the temporal change of the  $h_{\lambda\mu}$ .

Results based on these equations have been published<sup>7</sup> already and a generalization from  $p$  to a general anisotropic stress tensor has also been made and the results presented elsewhere.<sup>8</sup> A discussion of the role played by  $W$  is also given there.<sup>8</sup>

Eq. (2) shows that the vectors  $\underline{a}, \underline{b}, \underline{c}$  i.e. the nine lengths  $h_{\lambda\mu}$  change in time because of the imbalance between the external pressure and the momentary, internally generated, stress from particle moments and from internal forces.

In parenthesis it is worth mentioning that the old molecular dynamics methods implicitly assumed the external stress to change with time in such a way as to balance out  $\underline{\dot{g}}$  and give  $\ddot{\underline{h}} = 0$ ; this coupled with initial condition  $\underline{\dot{h}} = 0$  automatically gave a non-varying Bravais cell  $\underline{a}, \underline{b}, \underline{c}$ .

3. Molecular Dynamics Model for Crystalline KCl.— A neutral system of 500 ions (250  $K^+$  and 250  $Cl^-$ ) was given a rocksalt structure at genesis in the following unusual manner (see section 5 below). In a rectangular parallelepiped formed by vectors  $\underline{a}, \underline{b}, \underline{c}$  of lengths  $5S, 5S, 5\sqrt{2}S$ , a body-centered tetragonal lattice with 250 sites ( $2 \times 5^3$ ) was constructed, the lattice constants being  $S, S, \sqrt{2}S$ . A displacement of  $(S/2, S/2, 0)$  produced a similar lattice of 250 sites for the other species in a rocksalt structure.

The method of molecular dynamics was used to study this system of 500 particles confined, with periodic boundary conditions, in a cell formed by vectors  $\underline{a}, \underline{b}, \underline{c}$ . The equations of motion were given in section 2. The potential function  $V$  was written as a sum of pair interactions; these were taken from Gordon-Kim<sup>5</sup> and used in

the convenient parametrized form given by Boyer.<sup>6</sup> The  $1/r$  Coulomb potential of course makes it necessary to use Ewald's summation; this has to take proper account of the ever changing vectors  $\underline{a}, \underline{b}, \underline{c}$  which define the periodically repeating cell with 500 particles. The unit of mass was taken to be the reduced mass of a K, Cl pair; in these units  $W$  was chosen to be 20. The integration was done in steps of  $0.29 \times 10^{-14} \text{ s}$ .

4. Behavior in Time of a KCl System under High Pressure.— A rocksalt KCl system of 500 ions was equilibrated at zero pressure and  $300^\circ \text{ K}$ ; the pressure was increased to 44 kb within one molecular dynamics integration step. The density and temperature are shown in Fig. 1 as functions of time after the moment of sudden pressure change.

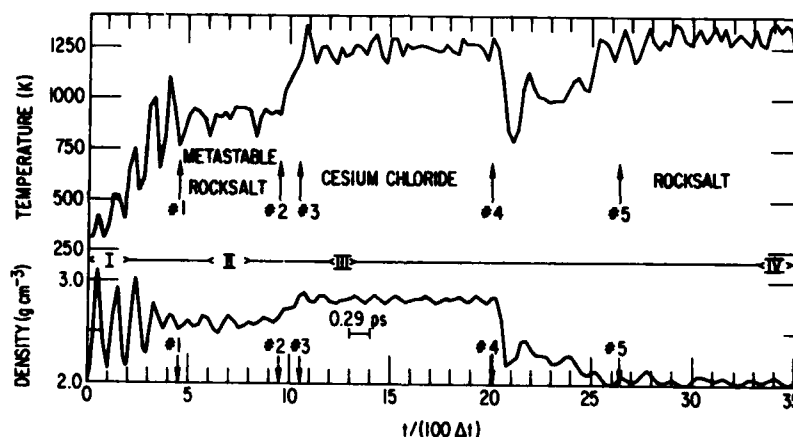


Fig. 1: Time history of a compression and decompression run. The points plotted are 25 Å apart hence the non-smooth appearance. In regions <I> to <IV> the pair correlations were monitored. These have not been shown in this paper. Significance of the numbered vertical arrows is discussed in sections 4 and 6.

We note that

- i) in about 1.3 ps the system acquires a new state at  $925^\circ \text{ K}$ ,  $2.6 \text{ g cm}^{-3}$
- ii) this turns out to be a metastable state which lasts for 1.5 ps more, the region of time between arrows marked #1 and #2 in Fig. 1.
- iii) the region between arrows #2 and #3 is clearly one of rapid changes; the density rises to  $2.85 \text{ g cm}^{-3}$  and the temperature to  $1250^\circ \text{ K}$ , within about 0.3 ps.

All the pair correlations were monitored during the regions of time indicated by bracketed Roman numerals <...> in Fig. 1.



The K-K, K-Cl, Cl-Cl pair correlations all showed that the shell distances and coordination numbers had changed from those of the rocksalt structure to those of cesium chloride: the like ions changing from an fcc to a simple cubic arrangement and the unlike ones changing from an octahedral, 6 coordination, to the cubic, 8 coordination, of unlike nearest neighbors.

5. Microscopic Detail of the Transformation.- A particle by particle analysis of the transformation just described reveals (Fig. 2) how the B1  $\rightarrow$  B2 transformation occurs.

Figure 2A shows a body-centered tetragonal lattice, lattice vectors  $\underline{a}, \underline{b}, \underline{c}$ , lengths  $a, a, \sqrt{2}a$  respectively. The atoms are indicated by  $\bullet$ . This is an fcc lattice of  $\bullet$  ions. The other species, shown as  $\circ$ , completes the rocksalt structure.

Operation #1: Uniform dilatation of amount  $\sqrt{2}$  in the direction of  $\underline{a}$  as indicated by the thick arrow in Fig. 2A. The result is shown in Fig. 2B:  $\underline{a}, \underline{b}, \underline{c}$  become  $\underline{a'}, \underline{b}, \underline{c}$ .

Operation #2: A move of alternate planes in the  $\underline{c}$  direction as indicated by the fine arrows in Fig. 2B. The result is shown in Fig. 2C; the center of the square face formed by  $\underline{a'}, \underline{c}$  is now occupied by  $\bullet$ . An atom of the same type occupies the opposite square face; it is the shadowy filled circle in Fig. 2C.

Fig. 2C shows a simple cubic lattice of like ions, the like and unlike ions together forming a cesium chloride structure.

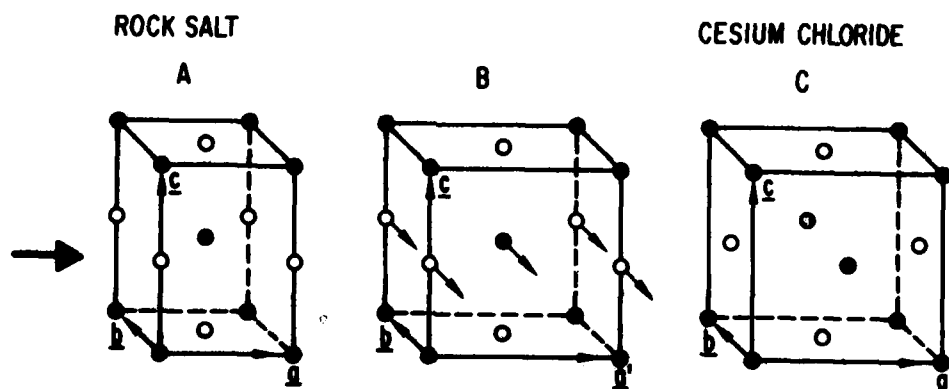


Fig. 2: Detail of rocksalt to cesium chloride found to occur in this calculation. Thick arrow in A indicates a dilatation, resulting in B. Fine arrows in B indicate displacements of particles with a common  $\underline{c}$  direction coordinate, resulting in the final structure C. A is a B1 and C a B2 structure.

In the conventional coordinate system used for B1 structures the transformation is a dilatation in the (1,1,0) direction and a transverse, (0 0 1), zone boundary phonon with polarization vector in the (-1,1,0) direction. The rock salt + cesium chloride transformation described in the previous section occurs according to the pattern just described.

The speculation in the literature<sup>9</sup> is therefore not substantiated by our calculation. It was conjectured that the change occurred by a trigonal lattice of angle 60° (sfcc) becoming a trigonal lattice of angle 90° which is a simple cubic lattice.

6. Effect of Decompression.— The region of time between arrows #3 and 4 in Fig. 1 shows the high pressure, high temperature cesium chloride structure in a state of equilibrium. At the time indicated by arrow #4 the pressure was dropped from the ambient value, 44 kb to zero in one molecular dynamics time step. Analysis of the structure between arrows #4 and 5 shows that the system was in the process of changing from a B2 to a B1 structure. Beyond arrow #5 the system is a hot, zero pressure, stable rocksalt structure.

7. Conclusion.— The above example shows that with constant pressure molecular dynamics calculations it is possible to study the kinetic detail of polymorphic transitions. In the case of KCl several other similar calculations have shown that large pressures and high temperatures are needed to trigger the transition. Thus in studying polymorphic transitions it is necessary not only to inquire into the thermodynamic transition parameters but also, using e.g. the method exemplified above, into the height of the various barriers that hinder the transition.

#### References

1. M. Born and K. Huang, "Dynamical Theory of Crystal Lattices," (Oxford, 1954).
2. M. Tosi and T. Arai, in "Advances in High Pressure Research," Vol. I, 1966. Ed. R. S. Bradley (Academic Press).
3. M. Tosi and F. Fumi, J. Phys. Chem. Solids, 23, 359 (1962).
4. A. J. Cohen and R. G. Gordon, Phys. Rev. B12, 3228 (1975).
5. R. G. Gordon and Y. S. Kim, J. Chem. Phys. 56, 3122 (1972).
6. L. L. Boyer, Phys. Rev. B23, 3673 (1981).
7. M. Parrinello and A. Rahman, Phys. Rev. Lett. 45, 1196 (1980).
8. M. Parrinello and A. Rahman, J. App. Phys. (1981) (In Press).
9. M. J. Buerger in "Phase Transformation in Solids," Eds. R. Smoluchowski, J. E. Mayer, W. A. Weyl (John Wiley, New York 1951).

## RENORMALIZED RESPONSE THEORY WITH APPLICATIONS TO PHONON ANOMALIES

C. Falter, W. Ludwig and M. Selmke

*Institut für Theoretische Physik II der Universität Muenster, Domagkstr. 75,  
D-4400 Muenster, F.R.G.*

**Abstract.**—A recently developed renormalization method for the electron response problem in effective ion-interactions is applied to phonon anomalies. A microscopic mechanism for the anomalies is proposed and its relation to the electron-phonon-coupling parameter  $\lambda$  and thus to  $T_c$  is discussed.

The renormalization method proposed in [1,2] for various applications allows for a division of the electronic density response function  $D$  into a part  $\bar{D}$ , which renormalizes the potential (and other quantities) thus leading to screened interactions and a part which acts in the renormalized system containing the relevant degrees of freedom in a special situation. This method is able to isolate certain features of the electronic structure like the Fermi surface effect in metallic compounds, the local field effect in covalent crystals or special many body effects. The characteristic items of a definite phenomenon are prepared by decomposing the polarizability function  $\pi$ , which is defined in terms of quasiparticles, into a part  $\bar{\pi}$  describing the screening (renormalization) and a complementary part  $\Delta$ , containing the relevant aspects of the response in a special case:  $\pi = \bar{\pi} + \Delta$ . (1)

This division can be shown to achieve a renormalization of  $D$ , which is related to the interactions of bare particles. With Coulomb-interaction  $v$  and dielectric function  $\epsilon$  we obtain

$$D = \bar{D} + (\bar{\epsilon}^{-1})^+ D_r \bar{\epsilon}^{-1} ; \quad \epsilon^{-1} := \epsilon_r^{-1} \cdot \bar{\epsilon}^{-1} ; \quad \bar{D} = \bar{\pi} \bar{\epsilon}^{-1} \quad (2a)$$

$$D_r = \Delta \epsilon_r^{-1} ; \quad \epsilon_r^{-1} = (1 + v \Delta)^{-1} ; \quad \bar{\epsilon} = 1 + v \bar{\pi} ; \quad v = \bar{\epsilon}^{-1} v. \quad (2b)$$

$$\text{In lowest order we can replace } D_r \rightarrow \Delta, \quad D \approx D + (\bar{\epsilon}^{-1})^+ \Delta \bar{\epsilon}^{-1}. \quad (3)$$

The effective ion-ion-interaction between two ions at  $\vec{A} + \vec{B}$  [1,2] is given by

$$\phi(\vec{A}, \vec{B}) = v^{II}(\vec{A}, \vec{B}) - v_A^I D v_B^I, \quad (4)$$

where  $v^{II}$  is the direct ion-ion-interaction and  $v_A^I$  the ion-(pseudo-)potential;  $\vec{A} = (\vec{a}, \alpha)$  contains indices for unit cell and basis, resp.. The Fourier-transformed effective interaction splits according to (4,2a) into additive parts, the anomalous one being [3] ( $Q' = \vec{q} + \vec{G}'$ ;  $Q'' = \vec{q} + \vec{G}''$  etc.)

$$\phi_{Q,Q'}^{r \alpha \beta} = -v_\alpha(Q) (\bar{\epsilon}^{-1})^+_{Q,Q''} D_r Q'' Q''' (\bar{\epsilon}^{-1})_{Q''' Q'} v_\beta(Q') \quad (5)$$

so that the renormalized part of the dynamical matrix can be written as ( $V_c$ : volume of unit cell;  $\vec{G}$ : reciprocal lattice vector)

$$\epsilon_{ij}^{r \alpha \beta}(\vec{q}) = (M_\alpha M_\beta)^{-1/2} \{ \Lambda_{ij}^{r \alpha \beta}(\vec{q}) - \delta_{\alpha\beta} \sum_{\vec{G}} \Lambda_{ij}^{r \alpha \gamma}(\vec{G}) \} \quad (6)$$

with

$$\Lambda_{ij}^{\alpha\beta}(\vec{q}) = V_z^{-1} \sum_{\vec{G}, \vec{G}'} (\vec{q} + \vec{G})_i (\vec{q} + \vec{G}')_j e^{i(\vec{G} - \vec{G}') \cdot \vec{R}} \phi_{\vec{q} + \vec{G}, \vec{q} + \vec{G}'}^{\alpha\beta} \quad (7)$$

The problem of phonon anomalies and especially the correlation of soft-phonon modes to high  $T_c$  is often dealt with but it is not solved in a unique way (see [4] for a review). In [3,5,6] a general explanation for the phonon anomalies is proposed. As a minimal assumption for the use of the renormalization method in  $\Delta$  we separate off the Fermi surface effect as the relevant part of the metallic binding component which we assume to be dominant in screening. The only characteristic property of a special material which enters the theory are the small critical wave vectors  $\vec{q}_{cr}$  (nesting vectors), which occur in Fermi surfaces with a special geometry (high density of states at the Fermi level  $\epsilon_F$ , [7]). We define  $\Delta$  (eq.(1)) to be the difference in the polarizabilities of the anomalous and the normal system (e.g. TaC and HfC), one having Fermi energy  $\epsilon_F + \delta\epsilon$ , the other one  $\epsilon_F$ :  $\Delta = \pi(\epsilon_F + \delta\epsilon) - \pi(\epsilon_F) \quad (8)$

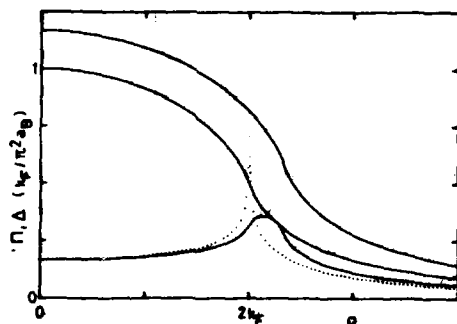
$\Delta$  contains all the effects originating from the different topologies of the Fermi surfaces in the two materials. In our model calculations [3,5,6] we use eq.(5) with a diagonal renormalization for the potentials and obtain, linear in  $\Delta$ ,

$$\phi_{\vec{q} + \vec{G}, \vec{q} + \vec{G}'}^{\alpha\beta} = -\bar{V}_\alpha(\vec{q} + \vec{G}) \Delta(\vec{q} + \vec{G}) \bar{V}_\beta(\vec{q} + \vec{G}') \delta_{\vec{G}\vec{G}'} \quad (9)$$

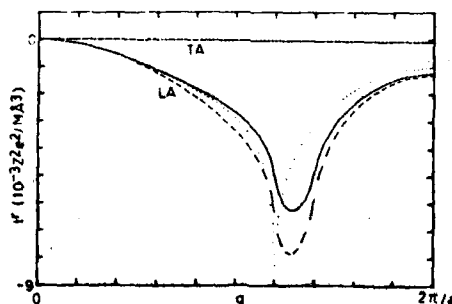
$\Delta$  can be shown to be essentially the difference of the free electron polarizabilities  $\pi_{FE}$

$$\Delta \equiv \pi_{FE}(\epsilon_F + \delta\epsilon) - \pi_{FE}(\epsilon_F) \approx \frac{\partial}{\partial \epsilon_F} (\pi_{FE}) \cdot \delta\epsilon = \frac{\delta k}{|\vec{q} + \vec{G}|} Z(\epsilon_F) \ln \left| \frac{2k_F + |\vec{q} + \vec{G}|}{2k_F - |\vec{q} + \vec{G}|} \right| \quad (10)$$

In general  $\Delta$  will have a pronounced  $\vec{q}$ -space resonance structure at the  $\vec{q}_{cr}$  (or at  $2k_F$  in the model, resp.) of the Fermi surface (Fig. 1). This resonance then occurs in the effective ion-interaction (9) and finally in the dynamical matrix (6,7). The magnitude of the anomaly effect is determined by the competition between the strength of the renormalized electron-ion-interaction and the density of states  $Z(\epsilon_F)$ , eqs. (9,10). If the resonance condition  $|\vec{q} + \vec{G}| \approx 2k_F$  is satisfied for  $\vec{G} = 0$  (i.e. small



1. Exact value for  $\Delta$  together with the corresponding free electron polarizabilities (full lines) and estimated value according to eq.(10) (dotted line).



2. Anomalous part of the dynamical matrix  $t^i$  for the (1,0,0)-direction of cubic symmetry.  $t^i$  is shown for the exact  $\Delta$  (full line), the estimated  $\Delta$  (dotted line) and with Hubbard-correction for exchange and correlation in  $\Delta$  and  $E^{-1}$  (dashed line).

critical wave vectors), we have strong potentials  $\bar{V}_\alpha[3,5,6]$  and thus an observable anomaly effect if  $Z(\epsilon_F)$  is high (Fig.2). The corresponding frequency shift is  $\Delta\omega \approx t^r/2\bar{\omega}$ ,  $\bar{\omega}$  being the frequency of the reference system. The factor  $\vec{q}_i \cdot \vec{q}_j$  in (7) tells us, that the anomaly only occurs in LA-modes. In the case of a second sublattice (NaCl-structure) there is a coupling between LA/LO- and TA/TO-modes; then the frequency-shift in (1,0,0) is approximately (linearly in  $t^r$ ) given by

$$\Delta\omega_\pm \approx (4\bar{\omega}_\pm)^{-1} \{t_{MM}^r + t_{CC}^r \pm [\gamma_1(t_{MM}^r - t_{CC}^r) + \gamma_2 t_{MC}^r]\} \quad (11)$$

where  $t^r$  denotes the anomalous components of the dynamical matrix (6), M stands for metal, C for carbon, resp. and  $\pm$  denote optical or acoustical modes, resp.. Eq.(11) shows the scaling of  $\Delta\omega_\pm$  with the inverse frequency  $\bar{\omega}_\pm$  of the reference system; this explains the suppression of the anomaly in the optical modes relatively to the acoustic ones.

We will now trace how the anomalies due to the Fermi surface effect enter the electron-phonon-coupling parameter  $\lambda$  and thus the critical temperature  $T_c$  of a superconductor. According to [4] the (isotropically) averaged expression for  $\lambda$  is

$$\lambda = \sum_\alpha Z(\epsilon_F) \frac{\langle J_\alpha^2 \rangle}{M_\alpha \langle \omega^2 \rangle} ; \quad \langle J_\alpha^2 \rangle = \langle |\vec{k}| \frac{\partial}{\partial \vec{k}} V_\alpha^{SC}(\vec{r}-\vec{k}_\alpha) |\vec{k}'\rangle |^2 \rangle_{FS} ; \quad (T_c)_{BCS} = \theta_D \exp(-1/\lambda) \quad (12)$$

The gradient of the total self-consistent crystal potential  $V_\alpha^{SC}$  (harmonic theory) in (12) can be calculated in linear response theory. Thus the same effects which produce the phonon anomalies enter  $\langle J_\alpha^2 \rangle$  quadratically via  $\Delta$ , eq.(8); the anomalous contribution is given by [3,6]

$$\epsilon^{-1} V_\alpha = \epsilon_r^{-1} (\bar{\epsilon}^{-1} V_\alpha) \approx (1-\bar{\epsilon}\Delta) \bar{V}_\alpha \quad (13)$$

This indicates clearly, that the squared matrix element  $\langle J_\alpha^2 \rangle$  in (12) is reduced in general compared to the reference system. On the other hand the high  $Z(\epsilon_F)$ -values of the special Fermi-surfaces under consideration produce an increase in  $\lambda$ . Thus the product  $Z(\epsilon_F) \cdot \langle J_\alpha^2 \rangle$  to a certain extent is limited or at least, it should vary less than either  $Z(\epsilon_F)$  or  $\langle J_\alpha^2 \rangle$ ; but  $\langle \omega^2 \rangle$  likewise involves the electron-phonon-coupling and varies similarly as  $\langle J_\alpha^2 \rangle$  (phonon-softening), so that we can expect an approximate proportionality between  $\lambda$  and  $Z(\epsilon_F)$ . These theoretical predictions are supported empirically on the basis of experimental data for the transition metals and compounds [8].

**References.** - 1.C.Falter and M.Selmke, Phys.Rev. B21, 2078(1980); 2.C.Falter, W.Ludwig and M.Selmke, Phys.Lett. 82A, 195(1981); 3.C.Falter, Habil.Schrift (to be published); 4.S.K.Sinha, P.B.Allen, Dynamical Properties of Solids 3, North Holland, Amsterdam (1980); 5.C.Falter and M.Selmke, Phys.Rev. B24 (to appear 1981); 6.C.Falter, W.Ludwig and M.Selmke, Phys.Lett. A (to be published); 7.B.M.Klein, L.L.Boyer and D.A.Papacostasopoulos, Solid State Comm. 20, 937(1976); 8. C.M.Varma and W. Weber, Phys.Rev. B19, 6142(1974).

## THE GENERALIZED PSEUDOATOM FORMALISM IN LATTICE DYNAMICS

M.A. Ball

D.A.M.T.P., University of Liverpool, Liverpool L69 3BX, U.K.

Abstract.

The change  $I$  in potential due to a phonon is expressed in terms of the susceptibility and the effective charge vector. It is analytic in metals or where  $\epsilon^{\text{eff}}$  is zero, and hence can be uniquely split into parts which rigidly follow the ions and parts which deform as the ions move. This 'generalised pseudoatom' is neutral. The dynamical matrix is expressed in terms of  $I$  both in the reciprocal lattice representation and other representations.

We show first that the charge density of a finite system is a sum of uniquely-defined pseudoatoms, each consisting of a part moving rigidly with an ion and a part which deforms [1]. Suppose the ion at  $R_j^0$  moves to  $R_j^0 + \delta R_j$ . The change in charge density to first-order is  $f_j(r) \cdot \delta R_j$ . Now  $f_j(r)$  can be written

$$f_j(r) = -\nabla \rho_j(r - R_j^0) + \nabla \times B_j(r - R_j^0) \quad (1)$$

Thus to first order in  $\delta R_j$ , the total charge density of the system is

$$n_0(r) + \sum_j [\rho_j(r - R_j) + \delta R_j \cdot \nabla \times B_j(r - R_j^0)] \quad (2)$$

Translational invariance [1] makes  $n_0(r)$  zero. The term  $\rho_j(r - R_j)$  is the part which moves rigidly with the ion and the other term is the deformation.

In crystals the ions move collectively as phonons. For (2) to be valid, the charge density must be analytic in  $q$ , the wave-vector of the phonon. Let the equilibrium position vector of the  $\kappa$  ion in the unit cell at  $\underline{l}$  be  $R^0(\underline{l}, \kappa) \equiv \underline{l} + R^0(\kappa)$ . This is displaced  $\delta R(\kappa) \exp[iq \cdot R^0(\underline{l}, \kappa)]$  by the phonon. The change in the electronic charge density is written

$$\frac{1}{\tau} \sum_{\kappa} \delta R(\kappa) \cdot f_e(q + g, \kappa) \exp[iq \cdot R^0(\underline{l}, \kappa)] \exp[i(g + g') \cdot R(\kappa)] \quad (3)$$

where  $g$  are reciprocal lattice vectors and  $\tau$  is the cell volume. The change in the total charge density is written  $f(q + g, \kappa)$ . We write the potential of the nucleus and the core electrons as  $W(r - R(\underline{l}, \kappa); \kappa)$ . Then

$$f_e(q + g, \kappa) = i \sum_{g'} q \cdot (q + g, q + g') (q + g') W(q + g', \kappa) \exp[i(g - g') \cdot R(\kappa)] \quad (4)$$

The electron-phonon operator can be expressed in terms of  $f$  and  $H$ .

$$I(q + g, \kappa) = i(q + g) W(q + g, \kappa) + v(q + g) f_e(q + g, \kappa) \quad (5)$$

where  $v$  is the Coulomb interaction. Then

$$I(q + g, \kappa) = i \sum_{g'} \epsilon^{-1}(q + g, q + g') (q + g') W(q + g', \kappa) \exp[i(g - g') \cdot R(\kappa)] \quad (6)$$

where  $\epsilon$  is the dielectric function matrix. Inverting /2/

$$(q + g)W(q + g, \kappa) = i \sum \epsilon(q + g, q + g') I(q + g', \kappa) \exp[i(g - g') \cdot R(\kappa)] \quad (7)$$

$I$  is the change in potential felt by a classical point charge.  $I'$  is the change felt by a valence electron: it includes exchange and correlation.

To investigate the analyticity of  $I$ , we write  $I(q + g, \kappa)$  in terms of the 'susceptibility'  $\chi^\Lambda$  and the effective charge vector  $\underline{z}(q, \kappa)$  /3/:

$$\chi^\Lambda = \chi + \chi \left( \frac{\Lambda}{v} - v \right) \chi^\Lambda \quad (8)$$

$$\underline{z}(q + g, \kappa) = -i((q + g)W(q + g, \kappa)/v(q + g) + \sum_{g' \neq 0} \hat{\chi}(q + g, q + g') (q + g')W(q + g', \kappa) \exp[i(g - g') \cdot R(\kappa)]) \quad (9)$$

$$\text{In insulators and metals } \lim_{q \rightarrow 0} \underline{z}(q, \kappa) = i \underline{z}^{\text{eff}}(\kappa) \cdot q \quad (10)$$

where  $\underline{z}^{\text{eff}}(\kappa)$  is the effective charge tensor. Hence

$$I(q, \kappa) = -\epsilon^{-1}(q, q) v(q) \underline{z}(q, \kappa) \quad (11)$$

and

$$I(q + g, \kappa) = -v(q + g) (\underline{z}(q + g, \kappa) + \hat{\chi}(q + g, q) \epsilon^{-1}(q, q) v(q) \underline{z}(q, \kappa)) \quad (12)$$

There can only be non-analytic behaviour in the limit  $q \rightarrow 0$ . In insulators the second term in (12) is non-analytic if  $\underline{z}^{\text{eff}}(\kappa)$  is non-zero so  $I(q + g, \kappa)$  is analytic if and only if  $\underline{z}^{\text{eff}}(\kappa)$  is zero. In a metal  $v(q) \epsilon^{-1}(q, q) \rightarrow 1/\chi^\Lambda(q, q)$ , both  $\chi^\Lambda(q, q)$  and  $\chi^\Lambda(q + g, q)$  tend to a finite limit and  $I(q + g, \kappa)$  is always analytic. Thus in metals, and in those insulators where  $\underline{z}^{\text{eff}}(\kappa)$  is zero  $I$  is analytic and so are  $I'$  and  $f$ . Each such vector field can be uniquely decomposed into vectors parallel and perpendicular to  $q + g$ , i.e.

$$f(q + g, \kappa) = i(- (q + g) \rho(q + g, \kappa) + (q + g) \times B(q + g, \kappa)) \quad (13)$$

$$I'(q + g, \kappa) = i(-q + g) u(q + g, \kappa) + (q + g) \times \omega(q + g, \kappa) \quad (14)$$

In real space, this decomposition gives (2) for  $f$  and a similar result for  $I'$ . In insulators where  $\underline{z}^{\text{eff}}(\kappa)$  is non-zero  $f$  is not analytic and the charge density cannot completely be described in terms of pseudoatoms /2/.

One advantage of the formalism is that the pseudoatom is neutral

$$\lim_{q \rightarrow 0} \rho(q, \kappa) = i \cdot q \cdot \underline{z}^{\text{eff}}(\kappa) \cdot q \epsilon^{-1}(q, q) v(q) / 4\pi e^2 = 0 \quad (15)$$

Another is that it gives the potential which an electron sees when a phonon is present. The rigid part of this potential is

$$u(q + g, \kappa) = (q + g) \cdot I'(q + g, \kappa) / |q + g|^2 \quad (16)$$

The main part of the effective interaction between the ions is /3,2/

$$V(q + g, \kappa; q + g', \kappa) = W(q + g, \kappa) \epsilon^{-1}(q + g, q + g') W(q + g', \kappa) / v(q + g) \quad (17)$$

Using (17) and the inversion procedure (7), the dynamical matrix becomes

$$\frac{(m_{\kappa} m_{\kappa'})}{\sqrt{q \cdot q'}} \sum_{g, g'} I(q + g, \kappa) \otimes I(q + g', \kappa') \epsilon^{-1}(q + g, q + g') \exp[i(q + g) \cdot R(\kappa) - i(q + g') \cdot R(\kappa')] / v(q + g) \quad (18)$$

This expression is in the reciprocal-lattice representation. It can be

generalised to other representations by considering  $\epsilon$  as a matrix and  $\underline{I}$  as a 'vector'. Then the dynamical matrix in a general representation is

$$\left(\frac{M(\underline{k})M(\underline{k}')}{\uparrow}\right)^{-\frac{1}{2}} \sum_{\mu_1, \mu_2} (\underline{I}(\underline{q}, \underline{k}))_{\mu_1} \otimes (\underline{I}^*(\underline{q}, \underline{k}')/\nu(\underline{q}))_{\mu_2} (\underline{\epsilon}^*(\underline{q}))_{\mu_1 \mu_2} \exp[i\underline{q} \cdot (\underline{R}(\underline{k}) - \underline{R}(\underline{k}'))] \quad (19)$$

This expression (19) avoids the inversion procedure needed to derive  $\chi$  from  $\chi^0$ .

Using the R.P.A. expression for  $\underline{\epsilon}$ , the dynamical matrix becomes  $\underline{C}' + \underline{D}'$  where

$$\underline{C}' = \left(\frac{M(\underline{k})M(\underline{k}')}{\uparrow}\right)^{-\frac{1}{2}} \sum_{\mu} (\underline{I}(\underline{q}, \underline{k}))_{\mu} \otimes (\underline{I}^*(\underline{q}, \underline{k}')/\nu(\underline{q}))_{\mu} + \text{exchange, etc., terms} \quad (20)$$

$$\underline{D}' = \left(\frac{M(\underline{k})M(\underline{k}')}{\uparrow}\right)^{-\frac{1}{2}} \sum_{\mu_1, \mu_2} (\underline{I}(\underline{q}, \underline{k}))_{\mu_1} \otimes (\underline{I}^*(\underline{q}, \underline{k}'))_{\mu_2} (\chi^0(\underline{q}))_{\mu_1 \mu_2} \quad (21)$$

Sinha /4/ has obtained a similar formula to this with  $\chi$  in place of  $\chi^0$ ;

however, his definition of  $\underline{I}$  is different from ours.

Equations (20) and (21) are useful when we can use the pseudoatom concept. Then we replace  $\underline{I}$  by  $\underline{I}'$  and incorporate all the exchange, etc., effects into  $\underline{C}'$ .  $\underline{I}'$  can then be written in the pseudoatom form (17), i.e.

$$(\underline{I}'(\underline{q}, \underline{k}))_{\mu} = (\nabla u(\underline{q}))_{\mu} - (\nabla \times \underline{\omega}(\underline{q}))_{\mu} \quad (22)$$

The neutrality of the pseudoatom means that the cancellation between the large Coulombic attractive and repulsive terms has already been accomplished. If there is a suitable approximation for the potential  $u$ , and  $\underline{\omega}$  can be neglected, it is practical to calculate  $\underline{I}'(\underline{q}, \underline{k})$  in certain representations, e.g. (l,m) orbitals or the tight-binding representation /4/.

When  $\underline{z}(\underline{q}, \underline{k})$  is pure imaginary in a cubic material, the only direction for  $\underline{z}(\underline{q}, \underline{k})$  is along  $\underline{q}$ , so that  $\underline{I}'(\underline{q}, \underline{k})$  has no deformation part. When there is inversion symmetry,  $\chi(\underline{q}, \underline{q} + \underline{g})$  is real, so that  $\underline{z}(\underline{q}, \underline{k})$  is pure imaginary provided  $\underline{g} \cdot \underline{R}(\underline{k})$  is an integer times  $\pi$ . This occurs in cubic crystals with one ion per unit cell or with the NaCl structure, but not with the diamond structure or the A15 structure. Thus  $\underline{I}'(\underline{q}, \underline{k})$  has no deformation in the alkali metals, nor in Nb, Mo, MoC and TaC, but may have significant deformation in Ge and Si and the A15 metals. It would be of interest to measure the change in electron-phonon coupling and in  $T_C$  in Nb, Pb and Mo caused by strains which alter the symmetry and thus allow deformation.

The second term of (12) is in the  $\underline{q}$ -direction, so that if  $\underline{q}$  is perpendicular to  $\underline{g}$  it contributes a deformation part to  $\underline{I}(\underline{q} + \underline{g}, \underline{k})$ . If  $\underline{I}(\underline{q} + \underline{g}, \underline{k})$  is calculated from a band-structure calculation, this term is neglected, but in metals it contributes to the elastic constants.

#### References

- /1/ Ball, M. A., J. Phys. C: Solid State Phys. **8** (1975) 3328.  
Pickett, W. E., J. Phys. C: Solid State Phys. **12** (1979) 1491.
- /2/ Ball, M. A. J. Phys. C: Solid State Phys. **10** (1977) 4921.
- /3/ Sham, L. J., Dynamical Properties of Solids I (1974)  
ed. by G. K. Horton and A. A. Maradudin (North-Holland, Amsterdam)
- /4/ Sinha, S. K., Dynamical Properties of Solids III (1980)  
ed. by G. K. Horton and A. A. Maradudin (North-Holland, Amsterdam)



## A STRONG COUPLED ACOUSTIC DEFORMATION POLARON IN ONE DIMENSION

E.W. Young\* and P.B. Shaw

Pennsylvania State University, U.S.A.

**Abstract.** - A study is undertaken of the system comprised of an electron interacting with acoustic phonons via the deformation potential in one dimension. A strong coupling adiabatic perturbation theory is developed in which an effective-phonon Hamiltonian is generated and determined by the solution of an iterative equation. Modified phonon modes are obtained which represent excitations of the deformed lattice. One of the modes is a translation which is interpreted as a polaron. The effective mass of the polaron is determined. The density of modified phonon modes is obtained by a Green's function method and the shift from the constant unperturbed density is computed. The energy, to the next order in inverse coupling constant beyond the strong coupling limit, involves this shift in the density of modes due to the electron-phonon interaction. Interpretation of this shift is facilitated by the introduction of a scattering phase shift. The behavior of this scattering shift clearly indicates the presence of a bound state, the polaron, and a resonance.

We develop a method for studying the coupled system of conduction electrons and acoustic phonons. The method we employ has been used previously to study the coupled system of conduction electrons and optical phonons<sup>1</sup>. We make a displaced oscillator transformation on the standard Hamiltonian and treat the displacement  $d_k$ , which is a real even c-number of  $k$ , as a variational parameter. The result, upon substituting the value obtained for  $d_k$  into the Hamiltonian, is  $H = H_0 + H_1 + H_2$ ,

$$H_0 = -\frac{1}{2} \frac{d^2}{dx^2} - \text{sech}^2 x + \frac{1}{3} \quad H_1 = \frac{1}{(2\pi\alpha\ell)^{1/2}} \sum_k |k| q_k (e^{ikx} - \rho_k)$$

$$H_2 = \frac{1}{8\pi\alpha} \sum_k (p_k p_{-k} + k^2 q_k q_{-k} - |k|). \quad (1)$$

This Hamiltonian is the basis of the strong coupling perturbation theory we present. The eigenstates of  $H_0$  are comprised of one bound state and a continuum originally analyzed by Yukon<sup>2</sup>. To carry out this perturbation theory we expand the eigenstates of  $H$  in terms of the complete set  $u(x)$  and  $u_p(x)$ ,  $|\psi(x)\rangle = u(x)|\phi\rangle + \sum_p u_p(x)|\phi_p\rangle$ , where  $|\phi\rangle$  and  $|\phi_p\rangle$  are normalizable phonon state vectors. We do not present the general method to determine these state vectors to arbitrary order in  $\alpha^{-1}$  but rather to one high power in  $\alpha^{-1}$  than the strong coupling limit<sup>3</sup>. This method generates an effective phonon Hamiltonian,  $H_{ph}$ , involving only the phonon degrees of freedom, of the form  $H_{ph} |\phi\rangle = E |\phi\rangle$ . Explicitly we calculate this phonon Hamiltonian with the result

\*Present address : Perkin-Elmer Corporation, Main Avenue, M/S 409, Norwalk, CT 06856

$$H_{ph} = -\frac{1}{6} + \frac{1}{8\pi\alpha} \sum_k \left( p_k p_{-k} + \sum_k R_{kk'} q_k q_{-k'} - |k| \right), \quad R_{kk'} = |kk'| \left( \delta_{kk'} - v_{kk'}^{opt} \right) \text{ and} \\ v_{kk'}^{opt} = \left( \frac{2\pi}{\ell} \right)^2 \sum_p \frac{kk'}{(p^2+1)^2} \operatorname{sech} \frac{\pi}{2} (p-k) \operatorname{sech} \frac{\pi}{2} (p-k'). \quad (2)$$

By writing the phonon Hamiltonian in this form, we can identify  $v_{kk'}^{opt}$  as the matrix element that appears in the optical phonon model.

The lattice we consider has a large number of sites  $N$ , therefore  $R_{kk'}$  can be thought of as an  $N \times N$  matrix with  $N$  real eigenvalues  $\Omega_n^2$  and eigenvectors  $g_{kn}$ . Introducing the Hermitean operators  $\eta_n = \sum_k g_{kn} q_k$ ,  $\xi_n = \sum_k g_{kn}^* p_k$ , we can cast  $H_{ph}$  in the diagonal form

$$H_{ph} = -\frac{1}{6} + \frac{1}{8\pi\alpha} \left[ \sum_n \left( \xi_n^2 + \Omega_n^2 \eta_n^2 \right) - \sum |k| \right]. \quad (3)$$

It can be shown that one of the eigenfrequencies vanishes and that the corresponding mode is a translation. If we further introduce phonon annihilation operators

$$A_n = (2\Omega_n)^{-1/2} (\Omega_n \eta_n + i \xi_n), \quad (n \neq 1); \quad [A_n, A_m^\dagger] = \delta_{nm}, \quad (4)$$

we can write

$$H_{ph} = -\frac{1}{6} + \frac{\Pi^2}{2m^*} + \frac{1}{4\pi\alpha} \left[ \sum_{n \neq 1} A_n^\dagger A_n \Omega_n + \frac{1}{2} \sum_n \Omega_n - \frac{1}{2} \sum_k |k| \right], \quad (5)$$

where  $\Pi$  is the generator of translations. The physical model this effective Hamiltonian describes is that of a free polaron, the acoustic deformation polaron, of mass  $m^*$  given by  $m^* = 4\pi\alpha \sum_k k^2 d_k^2 = \frac{2}{3} (4\pi\alpha)^2 m$  and free phonons with frequencies  $\Omega_n$ .

The spectrum of modes in the presence of the electron-phonon interaction is the same as the unperturbed spectrum. The quantity of interest is the shift in the density of vibrational modes  $\Delta(\omega)$  given by  $\Delta(\omega) = \sum_{n \neq 1} \delta(\omega - \Omega_n)$ ,  $\Omega_n \geq 0$ , in terms of the unknown modes of the deformed lattice. To calculate the density of modes we define a retarded Green's function  $D_{kk'}(t)$  and its Fourier transform  $G_{kk'}(\omega)$ . The density  $\Delta(\omega)$  is given by  $\Delta(\omega) = \frac{2\omega}{\pi} \sum_k \operatorname{Im} G_{kk}(\omega)$ , in terms of the non-interacting wave vectors  $k$ . We further introduce a continuum scattering amplitude  $T(k, k', \omega)$  in terms of which the shift generated by the electron-phonon interaction  $\bar{\Delta}(\omega)$  can be written

$$\bar{\Delta}(\omega) = \frac{1}{\pi} \int_{-\infty}^{\infty} dk \operatorname{Im} \left[ T(k, k; \omega) \frac{\partial}{\partial \omega} \frac{1}{k^2 - (\omega + i\eta)^2} \right]. \quad (6)$$

In the Born approximation in the continuum limit,  $T(k, k', \omega)$  is replaced  $V(k, k')$  and Eq. (6) becomes

$$\bar{\Delta}(\omega) = \bar{\Delta}_B(\omega) \equiv \frac{d}{d\omega} \frac{V(\omega, \omega)}{\omega}. \quad (7)$$

The result is plotted in Fig. 1. The shift in the density of modes in this approximation has the behavior

$$\bar{\Delta}_B(\omega) \rightarrow 0(\omega^2), \quad \omega \rightarrow 0; \quad \bar{\Delta}_B(\omega) \rightarrow 0(\omega^{-2}), \quad \omega \rightarrow \infty; \quad \int_0^\infty d\omega \bar{\Delta}_B(\omega) = 0. \quad (8)$$

As a result of the high frequency behavior of  $\bar{\Delta}_B(\omega)$ , the shift in zero point energy diverges. This divergent contribution is given by  $E_{div} = -8\pi m^2 \ln(\hbar \omega_{max}/m s^2)$  which is the result of Reference (1).

To facilitate calculation of  $\bar{\Delta}(\omega)$  without approximation we first write in matrix notation  $V = BB^T$  ( $T$  = transpose). If we define a matrix  $R(\omega)$  by the relation  $R(\omega) = B^{-1} T(\omega) (B^T)^{-1}$ , then the shift in the density of modes can be cast in the form

$\bar{\Delta}(\omega) = \frac{1}{\pi} \text{Im Tr } R^{-1}(\omega) \frac{\partial}{\partial \omega} R(\omega)$ . Further we can obtain an even simpler expression for the shift  $\bar{\Delta}(\omega) = \frac{1}{\pi} \frac{d}{d\omega} \delta(\omega)$ , where  $\delta(\omega)$  and  $R(\omega)$  are related by  $\det R(\omega) = r(\omega)e^{i\delta(\omega)}$  ( $r(\omega)$  real). Gaussian quadrature has been used to compute  $\delta(\omega)$ , which is plotted in Fig. 2. The full shift in the density of modes exhibits the behavior

$$\int_{-\infty}^{\infty} d\omega \bar{\Delta}(\omega) = [\delta(\omega) - \delta(0)]/\pi = -1 \quad (9)$$

which is analogous to Levinson's theorem in potential theory in the presence of a bound state. The absence of one vibrational mode (the translational mode) results in a depletion of modes concentrated at zero frequency, with lesser depletion at higher frequency.

The phase shift does not fall monotonically to zero as it would in the presence of a bound state alone. In fact, the shift rises abruptly at  $\omega \sim 0.5$ , reaches a maximum at  $\omega \sim 1$ , and falls monotonically to zero thereafter. This behavior suggests the presence of a resonance as well as a bound state. The enhancement occurs naturally at wavelengths comparable to the size of the polaron. These "resonating" phonons interact most strongly; hence they are lowered in frequency the most. As a result, we observe a bunching of phonon modes slightly below  $\omega = 1$ .

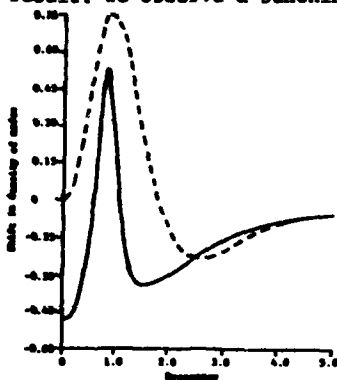


Fig. 1: The shift in density of modes versus  $\omega$ . Dashed curve is Born approx., solid without approx.

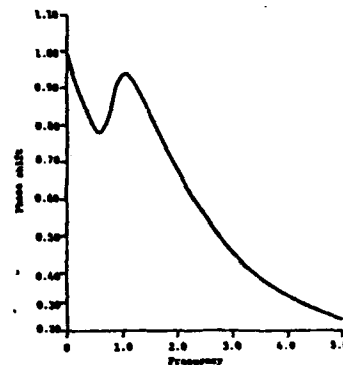


Fig. 2: The phase shift  $\delta(\omega)/\pi$  versus  $\omega$ .

Finally we calculate numerically the shift in zero point energy resulting from the shift in the phonon density of modes. Using this result, we can write the ground state energy momentum relation at low  $p$  in dimensional units in the form

$$E_G(p) = - (4\pi\alpha)^2 \frac{m^2}{6} + \frac{p^2}{2m^*} + 0.178 \, 4\pi\alpha \, m^2 - 8\alpha \, m^2 \ln \left[ \frac{\hbar \omega_{\max}}{4\pi\alpha \, m^2} \right]. \quad (10)$$

- (1) G. Whitfield and P.B. Shaw, Phys. Rev. **B14**, 3346 (1976).
- (2) S.F. Yukon, Ph.d. Thesis (Brandeis University, 1968).
- (3) P.B. Shaw and E. Young, Phys. Rev. B, to be published.
- (4) M.L. Goldberger and K.M. Watson, Collision Theory (John Wiley and Sons, Inc., New York, 1964).

## GAPS IN PHONON DISPERSION CURVES FOR SUBSTITUTIONAL ALLOYS

A. Czachor

*Institute of Nuclear Research, Swierk, Poland.*

**Abstract.** - Neutron inelastic coherent scattering (NICS) crosssection for alloy crystals often show multipeak structures and very low intensities between the peaks, the effects hardly within the reach of the CPA predictions. It is shown, on the example of the force-defect linear chain, that the average local-information transfer approximation (ALITA) [3] leads to such effects.

In order that the potential energy be invariant with respect to an uniform translation of a solid, the self-force matrix  $\tilde{\Phi}_{11}$  must be

$$\tilde{\Phi}_{11} = - \sum_{l' \neq l} \tilde{\Phi}_{ll'} \quad , \quad 1$$

where  $\tilde{\Phi}_{ll'}$  is the force matrix between lattice sites  $\tilde{l}$  and  $\tilde{l}'$ .

Let us consider a substitutional alloy with two components A, B in concentrations  $1-c$ ,  $c$ . Except in the additive limit [1],  $\tilde{\Phi}^{AB} = (\tilde{\Phi}^{AA} + \tilde{\Phi}^{BB})/2$ , it is difficult to fully incorporate the fundamental condition (1) into the CPA-type theories of disordered alloys [2]. On the other hand the ALITA [3], being rather crude in the decoupling procedure used to obtain the displacement-displacement Green's function  $G_{11'}(t-t') = \langle \langle \tilde{u}_1(t) \tilde{u}_{1'}(t') \rangle \rangle$ , accounts exactly for the translational invariance. With the locator  $\tilde{L}$

$$\tilde{L}_{ll'} = [\omega^2 M_l \tilde{I} - \tilde{\Phi}_{ll}]^{-1} \delta_{ll'} \equiv \tilde{L}_l \delta_{ll'} \quad ,$$

where  $M_l$  is a quasimass at the site  $\tilde{l}$  /in general complex/ and  $\omega$  is a frequency.

The time and space Fourier transform of the configuration average of the  $\tilde{G}$ ,  $\langle \tilde{G}_{1-1'} \rangle = N^{-1} \sum_{l'} \tilde{G}_{1+l', l'+l}$ , has here the form [3, 4]

$$\langle \tilde{G}(\tilde{q}, \omega) \rangle = [\omega^2 \tilde{M}^{\text{eff}}(\omega) - \tilde{\Phi}_q^{\text{eff}}(\omega)]^{-1} \quad ,$$

where  $\tilde{M}^{\text{eff}} = \langle \tilde{I} \rangle^{-1} \langle \tilde{L} M \rangle$ ,  $\tilde{\Phi}_q^{\text{eff}} = \sum_l e^{-i\tilde{q} \cdot \tilde{l}} \langle \tilde{I} \rangle^{-1} \langle \tilde{L} \tilde{\Phi}_l \rangle$ ,  $\langle \tilde{L} \tilde{\Phi}_l \rangle = N^{-1} \sum_{l'} \tilde{L}_{l'} \tilde{\Phi}_{l', l-1}$ ,  $\langle \tilde{L} M \rangle = N^{-1} \sum_l \tilde{L}_l M_l$ ,  $\langle \tilde{I} \rangle = N^{-1} \sum_l \tilde{I}_l$ .

The ALITA correctly predicts the dispersive local-mode branches and the in-band phonon frequency shifts for light impurities; for the heavy ones it leads to gaps in phonon spectra; usually the results appear in close analytic form. To give an example, Fig. 1 shows the mass-defect splitting in the  $[001]$  T phonon branch for  $\text{Al}_{.965}\text{Ag}_{.035}$  [4].

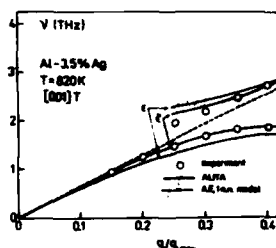


Fig. 1. Gap in the  $[001]$  T phonon branch of  $\text{Al}_{.965}\text{Ag}_{.035}$  - experimental data [7] and two ALITA fits [4]. Dashed line - dispersion in pure Al.

The experimental NICS profiles usually show two peaks, but with a structure superimposed, which may be not due to experimental scatter - see data for  $\text{Rb}_{.71}\text{K}_{.29}$  [5]; the valley between the peaks is often deep and sharp - see data for  $\text{Ni}_{.7}\text{Pt}_{.3}$  [6]. Qualitatively, such features are typical to the ALITA-plots; the CPA-approaches so far gave at most two smooth peaks with a rather shallow minimum between them [1, 2, 5].

To show it clearly, we shall examine within ALITA a simple system - the one-dimensional force-defect case; one can calculate here the Green's function (3) analytically at arbitrary concentration  $c$ . It is the two-species linear chain of identical masses and different coupling between different species (nearest neighbours only):  $\Phi_{AA} = \Phi_{BB} = 1$ ,  $\Phi_{AB} = \Phi_{BA} = 1(1-\lambda)$ ,  $M=1$ , where  $\lambda$  is the force defect. Eight 3-particle configurations pertinent to the case: AAA, AAB, ... BBB, weighted:  $(1-c)^3$ ,  $(1-c)^2c$ , ...  $c^3$ , respectively, provide 8 contributions to the averages in eqn 3. With the notation:  $r = (1-c)c$ ,  $\xi = M\omega^2/2k = \omega^2/\omega_E^2$ , the "dispersion relation"  $\langle \tilde{G} \rangle^{-1} = 0$  takes the form

$$q = 2 \arcsin X(\nu)$$

4

$$X^2(\nu) = \frac{1}{2} \frac{(\nu+1)(4-A)}{1-(\nu+1)A}, \quad A = \lambda \tau \left( \frac{1}{\nu+1} + \frac{1}{\nu+2} \right), \quad \nu = \xi - 1,$$

showing two force-defect gaps about the frequencies, at which there appear the poles of the locators, corresponding to the local configurations with one and two different neighbours. One should note, that with more distant interactions and with a higher dimensionality, a number of different local configurations and locators would be greater - there would be more gaps, and a multipeak structure in neutron scattering.

To introduce finite widths, let us put  $M \rightarrow M(1+i\alpha)$ . The NICS cross section is proportional to  $\text{Im}G$  and we have

$$-2l \text{Im} G(q, \omega) = \frac{\alpha \xi}{(\xi - B)^2 + \alpha^2 \xi^2}, \quad 5$$

with  $B = \xi \sin^2 q / X^2(\phi)$ . Fig. 2 shows this function for several wavevectors and  $\alpha = .05$ , whereas Fig. 3 shows the effect of broadening of the NICS peaks, when  $\alpha$  increases. We can see that the broadening is practically the one-side effect - in the gap regions the intensity is always extremally low.

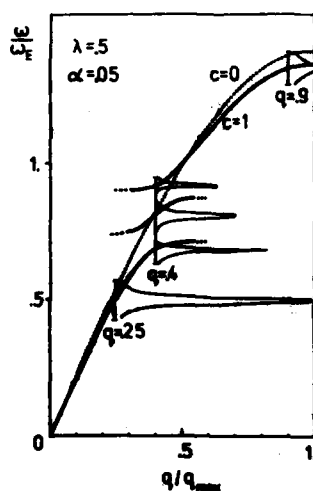


Fig. 2. Phonon dispersion in the force-defect ( $\lambda = .5$ ) linear chain at three  $q$ -values, and the NICS profiles in the ALITA quasimass scheme:  $\alpha = -\text{Im}M = .05$ .

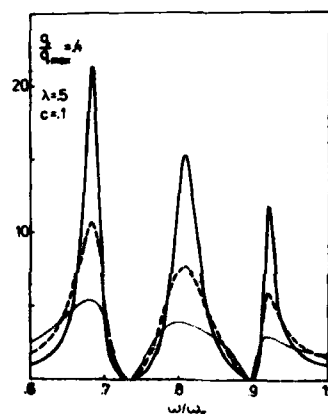


Fig. 3. Study of the peak broadening in the  $q = .4q_{\text{max}}$  NICS profile from Fig. 2, as a function of parameter  $\alpha = .1$  - heavy line, .2 - dashed, .4 - dotted.

The ALITA calculations for 3-dimensions clearly lead to similar features: multippeak NICS structures and low intensity between the peaks. Qualitative correlation of the predicted trends with the experimental findings emphasises the crucial role of the condition (1) in the theory of dynamics of disordered systems.

#### References

1. M. Mostoller and T. Kaplan, Phys. Rev. B16, 2350 (1977).
2. G. Grunevald, J. Phys. F.: Metal Phys. 6, 999 (1976).
3. A. Czacor, Report IMA No 173/II/PS/A, Warsaw, (1977).
4. A. Czacor, Phys. Rev. B21, 4458 (1980).
5. W.A. Kamitakahara and J.K.D. Copley, Phys. Rev. B18, 3772 (1978).
6. N. Kunimoto et al., Y. Tsunoda, N. Wakabayashi, R.M. Nicklow and H.G. Smith, Sol. St. Comm. 25, 921 (1978).
7. A. Zinken et al., U. Buchenau, H.J. Fenzl and H.R. Schober, Sol. St. Comm. 22, 639 (1977).

## HYBRIDIZATION OF THE TWO-PHONON BOUND STATE WITH THE LOCAL MODE IN IMPERFECT CRYSTALS

S.N. Behera and Sk. Samsur

*Institute of Physics, Bhubaneswar-751007, India.*

**Abstract.**— The possibility of the hybridization of a two-phonon bound state with an impurity local mode in an anharmonic imperfect crystal, is demonstrated. The one-phonon density of state around the local mode frequency shows the two peak structure because of this hybridization.

1. **Introduction** . - Recently it has been shown that two-phonon bound states could exist in anharmonic imperfect crystals,<sup>1</sup> which can be detected in either the second order infrared or Raman spectra. However, these can as well be seen in the first order spectrum, through their hybridization to suitable single phonons<sup>2</sup>. Evidence in support of this has been reported in the literature<sup>3</sup>. Light mass substitutional impurities, give rise to local modes of vibration with frequencies higher than the maximum allowed phonon frequency of the host lattice. Hence a two-phonon bound state caused by the anharmonic interactions (which falls slightly above twice the maximum allowed phonon frequency of the host) can hybridize with the local mode provided the latter has nearly the same frequency as the former. This condition can be achieved by suitably choosing the mass of the substitutional impurity atom. In the present paper we report the calculation of the one-phonon density of state in the presence of such hybridization.

2. **Theory** . - The anharmonic, imperfect crystal is characterized by a model Hamiltonian with cubic and quartic anharmonic terms with coupling constants  $\gamma$  and  $\delta$  respectively and the substitutional impurities which are isotopic in nature are described by the mass defect parameter  $\lambda = (M_I - M)/M_I$ .  $M_I$  and  $M$  are respectively the masses of the impurity and host atoms. Furthermore, the impurity concentration is assumed to be low. For such a system the one-phonon Green's function satisfies the equation,

$$G_{k,-k}^1(\omega) = g_k^0(\omega) + g_k^0(\omega) \chi_{k,-k}(\omega) g_k^0(\omega) \quad (1)$$

where

$$\chi_{k,-k}(\omega) = (\pi\gamma)^2 \sum_p V(k,-k,p) G_{k,k,p,-p}^2(\omega) V(-k,k,p) \quad (2)$$

$$g_k^0(\omega) = G_k^0(\omega) [1 + g_k(\lambda, \omega) G_k^0(\omega)] \quad (3)$$

$$g_k(\lambda, \omega) = -c\pi\lambda \tilde{\omega}_k [1 + \pi\lambda N^{-1} \sum_q \omega_q G_q^0(\omega)]^{-1} \quad (4)$$

and

$$G_k^0(\omega) = (\tilde{\omega}_k/\pi) [\omega^2 - \tilde{\omega}_k^2]^{-1} \quad (5)$$

is the free phonon propagator and  $V(k, -k, p)$  is the coefficient of the cubic anharmonic term. In writing eqn.(1) it is assumed that the quartic anharmonic term simply renormalizes the phonon frequencies to  $\tilde{\omega}_k$ . From eqn.(1) the phonon self energy can be written as

$$\Sigma(k, \omega) = (\omega_k/\pi) [g_k(\lambda, \omega) + \{1 + g_k(\lambda, \omega) G_k^0(\omega)\}^2 \chi_{k,-k}(\omega)] \quad (6)$$

It is clear from eqns.(1) and (5) that the phonon self energy involves besides the impurity contribution  $g_k(\lambda, \omega)$  the two-phonon propagator  $G_{k,k,p,-p}^2(\omega)$  which in turn carries the information regarding the two-phonon bound state brought about by the quartic anharmonic interaction. Because of our interest in the two-phonon bound state the later need be evaluated simply for the perfect anharmonic (quartic) crystals. This has been calculated in ref.1 (eqns.(17)-(19)) and we shall use that result.

In order to simplify the calculations we adopt the Einstein Oscillator model for the host lattice with a single optical phonon of frequency  $\omega_0$ . With this simplifying approximation the impurity local mode frequency as calculated from eqn.(3) turns out to be

$$\omega_L = \omega_0 (1 - \lambda)^{1/2} \quad (7)$$

and the two-phonon bound state frequency is given by<sup>1</sup>

$$\omega_{BS} = 2\omega_0 (1 + \eta/4)^{1/2} \quad (8)$$

where

$$\eta = \delta\omega_0/8 \quad (9)$$

the later being evaluated at zero temperature. The dimensionless quartic anharmonic coupling constant  $\delta$  being a small quantity, the bound state appears just above  $2\omega_0$ . It is obvious from eqn.(7) that for  $\lambda = -3$  i.e.  $M_1 = M/4$ , the local mode frequency becomes  $2\omega_0$ , thus giving rise to the possibility of its hybridisation with the two-phonon bound state.

Since we are interested in the one-phonon density of states



around the frequency  $\omega_L$  or  $\omega_{BS}$ , the Green's function of eqn.(1) and (6) can be approximated as

$$G_{00}^1(\omega) = (\omega^2 - \omega_L^2)(\omega^2 - \omega_{BS}^2) / 3\pi \omega_0 D(\omega) \quad (10)$$

where

$$D(\omega) = (\omega^2 - \omega_L^2)(\omega^2 - \omega_{BS}^2) + c\lambda \omega_0^2(\omega^2 - \omega_{BS}^2) - \tilde{\gamma}^2 \omega_0^2(\omega^2 - \omega_L^2) + 2c\tilde{\gamma}\lambda \times \omega_0^4 \quad (11)$$

with  $\tilde{\gamma}^2 = \gamma^2/4g$ . Equating  $D(\omega) = 0$  one obtains the two hybridized frequencies as

$$\omega_{\pm}^2 \cong \frac{1}{2} \left\{ [\omega_L^2 + \omega_{BS}^2 + (c|\lambda| + \tilde{\gamma}^2)\omega_0^2] \pm [(10\tilde{\gamma}^2 - 2\eta)c|\lambda|]^{1/2} \omega_0^2 \right\} \quad (12)$$

In calculating eqn.(12) terms of order  $\delta^2$  are neglected. Making use of the result (12) the one-phonon density of states around the frequency  $2\omega_0$  can be easily shown to be

$$\rho_1(\omega) = B_+ \delta(\omega - \omega_+) + B_- \delta(\omega - \omega_-) \quad (13)$$

where

$$B_{\pm} = \frac{[(c|\lambda| + \tilde{\gamma}^2)(10\tilde{\gamma}^2 - 2\eta)^{1/2} \pm (6\tilde{\gamma}^2 - \eta)(c|\lambda|)^{1/2}]}{12(5\tilde{\gamma}^2 - \eta)^{1/2} [8 + \eta + c|\lambda| + \tilde{\gamma}^2 \pm \{(10\tilde{\gamma}^2 - 2\eta)c|\lambda|\}^{1/2}]} \quad (14)$$

Thus we see that there will be two peaks of unequal strength. It is obvious from eqn.(12) that in the degenerate case of  $\omega_L = \omega_{BS}$  the hybridisation first shifts the frequency slightly and then the mode splits symmetrically. Such a hybridisation persists even when the two-phonon propagator is evaluated for the imperfect crystal.<sup>4</sup>

**3. Discussion.** - It has been shown that in an anharmonic crystal containing a low concentration of light mass substitutional impurities it is possible for the local mode to hybridise with the two-phonon bound state and acquire a structure. Such hybridisation can be best observed in imperfect ferroelectric crystals, because of their strong anharmonic nature, and of the availability of a soft mode whose frequency decreases with temperature above the transition temperature. Hence the two-soft mode bound state can be swept across the local mode to hybridise with it.

#### References. -

1. Behera S.M. and Samsur Sk. *Pramana* **15**, 375 (1980)
2. Ruvalds J. and Zawadowski A. *Phys. Rev. B* **2**, 1172 (1970)
3. Scott J.F. *Phys. Rev. Letters* **24**, 1107 (1970).
4. Samsur Sk. Thesis Submitted to Utkal University (1981)

## ATTENUATION OF SECOND SOUND IN SOLIDS

K. Weiss\*

*Philips Research Laboratories, 5600 MD Eindhoven, The Netherlands.*

**Abstract.** — The small-amplitude plane-wave solutions of the Boltzmann-Peierls equation for phonons in solids are classified and the propagation properties of second sound are discussed in a simple way. Specifically the transition (e.g. with rising temperature) from the case where momentum non-conserving phonon collision processes are much slower than the N-processes (second sound regime) to the case where the U-processes dominate (heat diffusion regime) is examined in detail.

**0. Introduction.** — Second sound in solids [1] is a density wave of the phonons which can be detected as a temperature wave propagating through the sample. It is not easy to create the experimental conditions [2] which allow these observations because the rate  $\tau_N^{-1}$  of phonon-phonon collisions which conserve momentum and energy must be large compared to the frequency  $\Omega$  of the wave (local thermal equilibrium) while the rate  $\tau_{\text{dis}}^{-1}$  of the collisions which do not conserve these four quantities must be low compared to  $\Omega$ . This "window condition"  $\tau_N^{-1} > \Omega > \tau_{\text{dis}}^{-1}$  puts rather severe restrictions on the experimental conditions: the sample must only contain very few impurities, dislocations, etc., it must be fairly large to avoid excessive boundary scattering, and the temperature must be low (but not too low because otherwise ballistic propagation results in a pure sample) in order to ensure that Umklapp (U) processes are much less frequent than Normal (N) processes.

The consequences of this last condition are the topic of the present paper. We will therefore assume that the U-processes are faster than all the other dissipative processes which we will ignore. Our discussion will be concerned with the transition (with rising temperature) from the regime where  $\tau_N^{-1} > \tau_U^{-1}$  (second sound) to the regime  $\tau_N^{-1} < \tau_U^{-1}$  (diffusion). It is based on the Boltzmann-Peierls equation [3] in the relaxation time approximation to which we will apply a general method [4] which allows the small-amplitude plane-wave solutions of such an equation to be classified.

**1. The Boltzmann-Peierls Equation in Relaxation Time Approximation.** — In the absence of external forces the kinetic equation for phonons with group velocity  $\mathbf{v}(\vec{p}) = \partial \epsilon / \partial \vec{p}$  ( $\epsilon$  = phonon energy) in a pure and large crystal in the relaxation time approximation is [5]

$$\left( \frac{\partial}{\partial t} + \vec{v}(\vec{p}) \cdot \vec{\nabla} \right) f(\vec{p}) = -\frac{1}{\tau_N} (f(\vec{p}) - f_{L,N}(\vec{p})) - \frac{1}{\tau_U} (f(\vec{p}) - f_{L,U}(\vec{p})). \quad (1)$$

$f_{L,N}(\vec{p})$  and  $f_{L,U}(\vec{p})$  are the local equilibrium distribution functions towards which  $f(\vec{p})$  develops as a function of time in the two limiting cases that all collisions conserve momentum and energy (N) or energy only (U). They are

\* Present address: HILTI A.G. FL-9494 Schaan, Fürstentum Liechtenstein.

$$f_{L,N}(\vec{p}) = (\exp[(\epsilon - \vec{p} \cdot \vec{u}(\vec{x},t))/k_B T_1(\vec{x},t)] - 1)^{-1} \quad (2)$$

and

$$f_{L,U}(\vec{p}) = (\exp[\epsilon/k_B T_2(\vec{x},t)] - 1)^{-1} \quad (3)$$

Here  $T_1(\vec{x},t)$  and  $T_2(\vec{x},t)$  are the local temperatures in the two cases and  $\vec{u}(\vec{x},t)$  is the local drift velocity established in the case that only N-processes are driving the system towards equilibrium. The relaxation times  $\tau_N$  and  $\tau_U$  are assumed not to depend on the phonon energy and we will restrict the discussion to phonons of one polarization. At the end we will comment on both of these assumptions.

The five unknown local parameters  $T_1$ ,  $T_2$ , and  $\vec{u}$  (the hydrodynamic variables) can be determined for a given  $f(\vec{p})$  from the five conservation laws which must be imposed on the collision terms. If we define for any function  $g(\vec{p})$  the average

$$\langle g \rangle = (2\pi\hbar)^{-3} \int d^3p g(\vec{p})$$

these conservation laws can be written as

$$\langle \frac{1}{\tau_N} (f - f_{L,N}) \epsilon \rangle = \langle \frac{1}{\tau_N} (f - f_{L,N}) \vec{p} \rangle = 0 \quad \text{and} \quad \langle \frac{1}{\tau_U} (f - f_{L,U}) \epsilon \rangle = 0 \quad (4)$$

In what follows we will be interested in small-amplitude plane-wave solutions about total equilibrium  $f_0(\vec{p})$  with (complex) frequency  $\Omega$  and real wave vector  $\vec{K}$  and we will restrict the discussion to the hydrodynamic regime, i.e.

$$|\Omega| \tau \ll 1 \text{ and } K \bar{v} \tau \ll 1 \text{ with } \tau^{-1} = \tau_N^{-1} + \tau_U^{-1} \quad (5)$$

where  $\bar{v} = \langle v f_0 \rangle / \langle f_0 \rangle$  is the mean phonon velocity.

After expanding the hydrodynamic variables about their total equilibrium values we are now ready to apply the classification scheme of Ref. 4 to discuss the physical properties of the solutions of Eq. (1) as the ratio  $\tau_N/\tau_U$  varies from values much smaller than one to very large values.

**2. Transition from second sound to the diffusive regime.**— As shown in Ref. 4 the relevant information needed to interpret the modes resulting from an analysis of the Boltzmann equation as sketched in the previous section is the number of collisional invariants, i.e. conserved quantities belonging to the fastest relaxation mechanism. If  $\tau_N^{-1} \gg \tau_U^{-1}$  this number is four and therefore the analysis in Ref. 4 implies that four of the five nontrivial solutions belonging to the five conservation laws Eqs (4) are compatible with the conditions of Eqs (5). The fifth solution belongs to a collisional mode which implies that  $T_1(\vec{x},t) = T_2(\vec{x},t)$  on a time scale  $\tau \cong \tau_N$  which is much faster than the time scale of the hydrodynamic modes. Solving the fourth order polynomial for the four solutions to second order in the small quantities of Eqs (5) yields two purely damped transverse modes and, more interestingly, the two propagating damped second sound modes [6,7]

$$\Omega = \Omega_0 \left( \pm 1 + \frac{2i}{5} \Omega_0 \tau_N + \frac{i}{2} \frac{1}{\Omega_0 \tau_U} \right) \quad (6)$$

where  $\Omega_0 = Kc\sqrt{3}$  and  $c$  is the velocity of ordinary sound. The damping is seen to consist of two contributions: the first occurs because the rate at which the N-processes establish local equilibrium is, of course, not infinite while the second one is due to the U-processes which tend to destroy the collective (oscillating) drift velocity because they do not conserve momentum. Both contributions are small compared to one and a weakly attenuated second sound wave results.

As the temperature of the sample is increased the rate of U-processes increases much faster than the rate of N-processes. Therefore as  $\tau_U$  becomes of the same order as  $\tau_N$ , the damping  $(\frac{1}{2}(\Omega_0\tau)^{-1})$  becomes comparable to the velocity (which is lower in this case) of the strongly damped wave. At still higher temperatures we have  $\tau_U^{-1} \gg \tau_N^{-1}$  and only one (i.e. the number of collisional invariants of the U-processes) of the five solutions remains compatible with the conditions (5). The other four solutions imply (on a time scale of the order of  $\tau_U \ll \Omega^{-1}$ )  $T_1(\vec{x},t) = T_2(\vec{x},t)$  as before and in addition  $\vec{u}(\vec{x},t) = 0$ , which is plausible from the physics involved. The only remaining solution describing a collective mode is

$$\Omega = i\Omega_0^2\tau_U \quad (7)$$

i.e. a purely diffusive mode in the phonon gas: heat diffusion in the crystal.

**Concluding Remarks.** — We have made two assumptions which are not in fact necessary for the argument as we have developed it: we have considered phonons of only one polarization and relaxation times which were independent of the phonon energies (and of the polarization, of course). Dropping these assumptions still allows to carry the argument through, and as far as phonons of more than one polarization are concerned earlier results (obtained by different methods) are reproduced [1,6,7].

Admitting energy dependent relaxation times introduces the interesting possibility of time-dependent local equilibrium distribution functions [4] but does not change the classification of the modes as given in this paper.

#### References

1. H. Beck, P.F. Meier, and A. Thellung, Phys. Stat. Sol. A29, 11 (1974).
2. in NaF: T.F. McNelly, S.J. Rogers, D.J. Channin, R.J. Rollefson, W.M. Gobau, G.E. Schmidt, J.A. Krumhansl, and R.O. Pohl, Phys. Rev. Lett., 24, 100 (1970); H.E. Jackson, C.T. Walker, and T.F. McNelly, Phys. Rev. Lett., 25, 26 (1970); S.J. Rogers, Phys. Rev., 3, 1440 (1971).  
in solid helium: C.C. Ackermann, B. Bertram, H.A. Fairbank, and R.A. Guyer, Phys. Rev. Lett., 16, 789 (1966); C.C. Ackermann and R.A. Guyer, Ann. Phys. (New York) 50, 128 (1968); C.C. Ackermann and W.C. Overton, Phys. Rev. Lett., 22, 764 (1969). in bismuth: V. Narayanamurti and R.C. Dynes, Phys. Rev. Lett., 28, 1461 (1972), V. Narayanamurti, R.C. Dynes, and K. Andres, Phys. Rev., B11, 2500 (1975).
3. R.E. Peierls, Quantum Theory of Solids, Oxford 1955.
4. D. Polder and K. Weiss, Phys. Rev., 17, 1478 (1978).
5. J.A. Sussmann and A. Thellung, Proc. Phys. Soc. 81, 1122 (1963).
6. R.N. Garzli, Sov. Phys. Sol. State, 7, 2838 (1966); JETP, 19, 490 (1964).
7. A. Thellung and K. Weiss, Phys. Kondens. Materie, 9, 300 (1969).

## INTERPRETATION OF EXPERIMENTS IN THE SOLIDON MODEL FOR ROTONS

M. Héritier and G. Montambaux

*Laboratoire de Physique des Solides, Université de Paris-Sud, 91405 Orsay, France.*

**Abstract** - A roton in superfluid Helium can be described as a phonon self-trapped in a region possessing the translation symmetries of the metastable solid. This picture can account for various experimental data, such as the roton wavevector in bulk Helium II and Helium films, the temperature dependence of the roton gap, the roton-roton collision time.

It has been shown recently that, under certain conditions, a longitudinal phonon in a quantum liquid can be self-trapped in a region of the liquid possessing the translation symmetries of the metastable solid (1). The first condition is a favourable balance between, on the one hand, the phonon energy lowering at a wavevector belonging to the reciprocal lattice of the solid, and, on the other hand, the phonon localization energy within the "solid-like" volume and the formation thermodynamic potential of this volume. (In principle, volume and surface terms are to be included. Another condition for the existence of a well-defined self-trapped excitation is a large enough lifetime. Helium II, which is a "nearly solid" quantum liquid (2) (first condition) and superfluid (second condition) is a good candidate. This picture, given as an example of collective excitation self-trapping, led to a new description of the roton, somewhat analogous to the Feynman's vortex ring (3), but with a large "solid-like" core in which the atoms undergo a translation motion. At present time, this model (the "solidon model") seems to give the best account for various experimental data.

A very simple variational procedure gives the roton gap by minimization of the solidon free energy with respect with the number of atoms involved in the core radius  $N$ . Three terms are to be included : the phonon localization energy  $q^2/2Nm$  (the "recoil" energy), where  $m$  is the atomic mass, and  $q$  the wavevector, the solidification free enthalpy, proportional to  $N$ , and the surface tension  $\sim N^{2/3}$ . Near enough to the solidification curve, the interface energy term predominates. A good estimate of the roton gap at low temperature can be obtained, simply from the knowledge of the solid-liquid surface tension. The corresponding values of  $N$  range from 25 to 40 depending on

the pressure.

The gap is now a thermodynamic quantity which can vary with temperature, even in the case of independent rotons. (In the Feynman model, the temperature dependence comes only from the roton-roton interactions and seems to be weaker than observed experimentally). In fact, the temperature dependence due to the variation of the solidification free enthalpy is weak. A larger effect is obtained when one takes into account the entropy flow associated with the atom dynamics. This entropy flow is necessary to preserve entropy conservation because the solid and liquid phases have different entropy, particularly at temperatures above 1 K. Because the momentum of this flow depends on temperature, so does the roton gap. Then a good agreement with the observed variation of the roton gap is obtained.

An important prediction of the model is the roton wavevector : it should correspond to the shortest reciprocal lattice wavevector of the metastable solid with the lowest free enthalpy. Both surface and volume enthalpy terms are to be included in determining this lattice. This property is an essential and simple feature of the model. In bulk Helium II, at low pressure, where the volume term predominates, the metastable solid with the lowest volume free enthalpy has a b.c.c. lattice. This is no longer true near the solidification curve at low temperatures (the lowest volume free enthalpy lattice is h.c.p.), but in these conditions the interface energy term predominates and the lowest solid-liquid surface tension is obtained for a b.c.c. lattice. Therefore, one expects a solidon core with a b.c.c. structure at any temperature and at any pressure. Indeed, the observed roton wavevector agrees well with this prediction.

Thin Helium films exhibit a roton-like excitation at a wavevector  $q \approx 2 \text{ \AA}^{-1}$  (4), much larger than expected in the Feynman model (5). In our model, two interpretations are possible. In the first, the excitation is a solidon bound state at the solid-liquid interface, due to image forces, stable because of the finite size of the solidon core. Then,  $q$  should correspond to a b.c.c. lattice distorted by the Van der Waals attraction to the substrate. In the second interpretation, the excitation is a truly two-dimensional roton. Then,  $q$  should correspond to the metastable 2 D triangular lattice. Both interpretations give about the same values for  $q$ , in agreement with experiment.

If the roton velocity field was a perfect dipolar field, the dispersion curve should be phonon-like at any wavevector. The roton mini-

mum at a wavevector  $q$  shows the existence of a finite size core, with a radius of order  $2\pi/q$ , in agreement with the previous estimate. This departure from the dipolar behaviour, noted by Castaing and Libchaber (6) in the roton-roton interaction potential, should exist also in the velocity field of a single roton. Roton-roton scattering can provide a test of the model. According to various experiments (see references in (6)), the roton-roton collision frequency can be written  $\tau_{RR}^{-1} = Bn_R$ .  $n_R$  is the thermal roton density and  $B \approx 1.7 \times 10^{-10} \text{ cm}^3/\text{s}$  (7). The contribution of the dipolar backflows to the collision frequency is small (7). Assuming a large core size, the interaction is written, in the hydrodynamic approximation as a core-core interaction. Using the Lippman-Schwinger method, the solidon core radius  $R$  is determined from  $B$ . We find  $R \approx 7.5 \text{ \AA}$  at 25 bars, i.e. about 35-40 atoms in the core. Castaing and Libchaber (6) calculation also fits the data. In fact, their theory is consistent with our model since they arrive to a roton-roton interaction non dipolar at distances shorter than  $2\pi/q$ .

These ordered "grains" may have been observed in neutron experiments (8). A new structure was observed in the structure factor below the  $\lambda$  transition, consisting of a single peak at about  $2 \text{ \AA}^{-1}$  momentum transfer. The intensity of this peak increases as approaches  $T_\lambda$  or when the pressure is increased. It is tempting to ascribe these effects by a larger number of excited rotons (with their cores modulated at  $q \sim 2 \text{ \AA}^{-1}$ ), when  $T$  increases or when the roton gap decreases with applied pressure.

- 1) M. Héritier, G. Montambaux and P. Lederer, J. Phys. (Paris), 40, L. 493 (1979).
- 2) B. Castaing and P. Nozières, J. Phys. Paris, 40, 257 (1979).
- 3) R.P. Feynman and M. Cohen, Phys. Rev. 102, 1189 (1956).
- 4) W. Thomlinson, J.A. Tarvin and L. Passell, Phys. Rev. Letters, 44, 266 (1980).
- 5) W. Götze and M. Lucke, J. of Low Temp. Phys., 25, 671 (1976).
- 6) B. Castaing and A. Libchaber, J. of Low Temp. Phys., 31, 887 (1978).
- 7) F. Toigo, Nuovo Cimento, 62B, 103 (1969).
- 8) B. Mozer and B. Le Neindre, Proceedings of the E.P.S. Conference, Haifa (1974), p. 63.

## SIMULATION OF LONG-WAVELENGTH OPTICAL PHONONS BY GENERALIZED INTERNAL STRAINS

E.M. Anastassakis<sup>+</sup> and M. Cardona\**National Technical University, Athens, Greece.**\*Max-Planck-Institute for Solid State Research Stuttgart, F.R.G.*

**Abstract.**— A generalized external force applied to a crystal can introduce new atomic position parameters known as internal strains. Each internal strain may be looked as a "frozen"  $q = 0$  optical phonon of appropriate symmetry. Explicit forms can be worked out for the internal strains produced by any type of force and crystal class. Related crystal parameters can be determined in any case with X-ray diffraction techniques.

The concept of internal strain will be generalized to include all possibilities of microscopic relative displacements of the various Bravais sublattices which are produced by any type of external force  $F$ . When  $F$  is applied to the crystal a macroscopic strain  $\eta$  may be produced. The mechanism which produces  $\eta$  depends on the nature of  $F$  [e.g. piezoelectricity (electrostriction) when  $F$  is an electric field  $E$  in first (second) order, piezomagnetism (magnetostriction) when  $F$  is a magnetic field  $H$  in first (second) order, etc]. Because of  $F$  the  $k^{\text{th}}$  atom in the  $i^{\text{th}}$  cell moves from its initial position  $r_{i,k}$  to a new one

$$r'_{i,k} \approx (1 + \eta) r_{i,k} + u_k \quad (1)$$

The first term is the macroscopic contribution to  $r'_{i,k}$  while the second term ( $u_k$ ) represents a microscopic strain due to  $F$ . It is the same for all atoms of type  $k$  in the crystal, i.e., it represents a microscopic displacement of the entire  $k^{\text{th}}$  Bravais sublattice and as such it constitutes an internal strain<sup>1</sup>. Both terms in (1) depend on the symmetry of the crystal independently of each other.

There are  $3(N-1)$  different sublattice displacements, where  $N$  the no. of atoms per unit cell.  $3(N-1)$  also gives the no. of  $q = 0$  optical phonons of the crystal. The normal coordinate  $u_j$  of the phonon  $j$  and the internal strain  $u_k$  (or  $u_{k,\lambda}$ ,  $\lambda = x, y, z$ ) are qualitatively similar in the sense that both represent sublattice displacements and transform alike under the crystal symmetry operations. When "frozen" each phonon will look exactly like one of the  $u_k$ 's. The symmetry of  $u_j$  will determine the type of  $F$  which is necessary to produce its internal strain  $u_k$ . This symmetry is described by one of the point group irreducible representations  $\Gamma(j)$ . Thus  $\Gamma(j) \in \Gamma(u_k)$ . The various  $\Gamma(j)$ 's are obtained

<sup>+</sup> Partial support by the National Research Council and by the Research Committee of the Technical University of Athens.



ned from the reduction of  $\Gamma_{\text{opt}}$ , the reducible rep of the most general displacement of the  $q = 0$  optical phonon of the crystal.

The connection between  $F$  and  $u_k$  is derived thermodynamically. Let  $f$  be the intensive parameter which corresponds to  $F$ . ( $F$  is treated as an extensive parameter<sup>2</sup>). To first order of  $u_k$  we can write

$$F = G \cdot u_k \quad \text{or} \quad f = g \cdot u_k \quad (2)$$

This results in a contribution to the internal energy of the crystal

$$\delta U(k) = F \cdot f = F \cdot g \cdot u_k = g_{\mu,\lambda} F_{\mu} u_{k,\lambda} \quad (3)$$

where  $\mu$  may be a composite index. Since  $\delta U(k)$  is a scalar, the only products  $F_{\mu} u_{k,\lambda}$  entering (3) are those which transform like scalars. This allows one to determine the type  $F$  necessary to produce a specific  $u_k$  and vice versa. The criterion is that  $\Gamma(j)$ , or  $\Gamma(u_k)$ , be included in the reduction of  $\Gamma(F)$  at least once, in general  $n_j$  times. The number  $n_j$  indicates the number of independent components of the tensor coefficient  $g$ . The form of  $g_{\mu,\lambda}$  is identical to that of known mode coefficients<sup>3</sup>. Typical examples for various forces are given next.

**1. Electric field  $E$ .** The reduction  $\Gamma(E)$  includes only IR-active phonons. Eq. (3) yields  $g_{\mu,\lambda} = (\partial^2 U^{(k)} / \partial E_{\mu} \partial u_{k,\lambda})$ , i.e.,  $g_{\mu,\lambda}$  transforms like the phonon effective charge tensor<sup>3</sup>  $e_{\mu,\lambda}^{(j)*} = (\partial^2 U(j) / \partial E_{\mu} \partial u_{j,\lambda})$ .

**2. Elastic stress or strain  $\eta$ .** The reduction  $\Gamma(\eta)$  includes only Raman-active phonons in symmetric scattering<sup>3,4</sup>. Since  $g_{\rho\sigma,\lambda} = (\partial^2 U^{(k)} / \partial \eta_{\rho\sigma} \partial u_{k,\lambda})$  it transforms like the Raman tensor  $a_{\rho\sigma,\lambda}^{(j)} = (\partial^2 U(j) / \partial \epsilon_{\rho} \partial \epsilon_{\sigma} \partial u_{j,\lambda})$ .

**3. Electric field gradient  $\nabla_{\rho} E_{\sigma} = (\partial E_{\sigma} / \partial x_{\rho})$ .** The reduction  $\Gamma(\nabla E)$  includes only Raman-active phonons in non-symmetric scattering.  $g_{\sigma\rho,\lambda}$  transforms like the non-symmetric Raman tensor<sup>3</sup>.

**4. Strain gradient  $\nabla_{\rho} \eta_{\sigma\tau}$ .** The reduction of  $\Gamma(\nabla \eta)$  is the same as that of the piezo-electric tensor.  $g_{\sigma\tau\rho,\lambda}$  transforms like the electric field-induced Raman tensor<sup>3</sup>.

**5. Hydrostatic pressure  $P$ .** The reduction  $\Gamma(P)$  coincides with  $A_1$ , the totally symmetric rep. Hence there are as many internal strains  $u_k$  produced by  $P$  as the number of phonons  $A_1$ . This also is the same as the number of atomic position parameters which cannot be uniquely determined by symmetry arguments<sup>4</sup>. The tensor  $g_{\mu,\lambda}$  becomes a scalar.

**6. Magnetic field  $H$ .**  $u_{k,\lambda}$  will transform like an axial vector.  $g_{\mu,\lambda}$  is like a second-rank polar tensor which reverses sign upon time reversal (c-type tensor<sup>5</sup>). It can only exist for the 90 magnetic crystal classes. The matrices of such tensors are given in tables 7 and 4 of Ref. 5.

As an example we consider  $\alpha$ -quartz ( $N=9$  point group  $D_3$ ). We have<sup>3</sup>

$$\begin{aligned} \Gamma_{\text{opt}} &= 4A_1 + 4A_2 + 8E & \Gamma(\nabla E) &= 2A_1 + A_2 + 3E & \Gamma(P) &= A_1 \\ \Gamma(E) &= A_2 + E & \Gamma(H) &= A_2 + E \\ \Gamma(\eta) &= 2A_1 + 2E & \Gamma(\nabla \eta) &= 2A_1 + 4A_2 + 6E \end{aligned}$$

According to these reductions there are 16 independent internal strains grouped into 3 types, 4 of type  $A_1$  (non-degenerate), 4 of type  $A_2$  (non-degenerate) and 8 of type E (doubly degenerate). Type  $A_1$  can be produced by  $\eta, \nabla E, P$  and  $\nabla \eta$  with 2,2,1,2 independent components each, for each of the corresponding tensors  $g$ . Type  $A_2$  can be produced by  $E, \nabla E$  and  $\nabla \eta$  with 1,1,4 components each for the tensors  $g$ , etc. For a magnetic crystal with  $N=9$  and magnetic structure  $D_3$ , a field  $H$  will produce 4 internal strains of type  $A_2$  and 8 of type E with only one component each for the tensor  $g$ . Once the forms of  $g$  are written, similar ones hold for  $G$  of (2) and its inverse  $\gamma$ , where  $u_k = \gamma \cdot F$ . This is because  $g, G$  and  $\gamma$  have the same symmetry<sup>4</sup>. We will consider the case of  $F = \nabla \eta$  for the  $A_2$  type of internal strains of  $\alpha$ -quartz.  $\gamma$  follows from the electric field-induced Raman tensor, according to the scheme<sup>3</sup>

$$a_{\sigma\tau\rho,\lambda}^E = (\partial^4 U^{(j)} / \partial \epsilon_\sigma \partial \epsilon_\tau \partial E_\rho \partial u_{j,\lambda}) \Rightarrow (\partial^2 U^{(k)} / \partial \nabla_\rho \eta_{\sigma\tau} \partial u_{k,\lambda}) \Rightarrow \gamma_{\sigma\tau\rho,\lambda} \quad (4)$$

The results for  $\gamma$  and  $u_k = \gamma \cdot \nabla \eta$  are

$$\gamma_{\sigma\tau\rho,z} = \begin{pmatrix} . & . & . & . & \gamma_3 & 2\gamma_2 \\ \gamma_2 & -\gamma_2 & . & \gamma_3 & . & . \\ \gamma_1 & \gamma_1 & . & . & . & \gamma_4 \end{pmatrix} \quad (5)$$

$$u_{A_2,z} = \gamma_1 \left( \frac{\partial \eta_{xx}}{\partial z} + \frac{\partial \eta_{yy}}{\partial z} \right) + \gamma_2 \left( \frac{\partial \eta_{xx}}{\partial y} + \frac{\partial \eta_{yy}}{\partial y} + 2 \frac{\partial \eta_{xy}}{\partial x} \right) + \gamma_3 \left( \frac{\partial \eta_{xz}}{\partial x} + \frac{\partial \eta_{yz}}{\partial y} \right) + \gamma_4 \left( \frac{\partial \eta_{xy}}{\partial z} \right) \quad (6)$$

There are 4 sets of values for  $\gamma_1 \dots \gamma_4$ , since we expect 4 independent internal strains of type  $A_2$  due to  $\nabla \eta$ . From (6) one can easily derive the selection rules for inducing a desired term of  $u_{A_2,z}$ .

Internal strains due to external stresses have been studied for some materials through the observation of forbidden X-ray diffractions<sup>4</sup>. In principle similar techniques can be employed to manifest internal strains due to forces other than stresses.

#### References

1. M. Born and K. Huang, Dynamical Theory of Crystal lattices, Clarendon Press Oxford 1962.
2. H.B. Callen, Thermodynamics, J. Wiley, N.Y. 1960.
3. E. Anastassakis, in Dynamical Properties of Solids, vol.4 ed. G.K. Horton and A.A. Maradudin, N. Holland 1980 and references therein.
4. E. Anastassakis and M. Cardona, phys. stat. sol. (b) **104**, 589 (1981).
5. R.R. Birss, Symmetry and Magnetism, N. Holland, N.Y. 1964.

# INSTABILITIES IN THERMAL BATH : PHONON ENHANCEMENT AND SATURATION IN A THREE-LEVEL SYSTEM

B. Fain

Chemistry Department, Tel-Aviv University, Ramat-Aviv, Tel-Aviv, 69978, Israel.

**Abstract.** - The equations, determining temporal behavior of coupled electronic and phonon subsystems in the electromagnetic field, are analyzed. The steady state solution describing saturation of the three level in such a system is achieved. It is shown that laser-like self-excitation of phonons cannot be obtained though essential phonon enhancement may be gained provided certain conditions are fulfilled. Field induced transparency is predicted between first two levels when the field saturates ground and highest levels, and the concentration of ions is high.

1. Introduction. - Usually, in various non-equilibrium processes, it is tacitly assumed that phonons play a passive role. They form a thermal bath that is assumed to be preserved all the time in its state of thermal equilibrium. But as it has been stressed in paper [1] by the author, this is not always the case. Under certain conditions or at certain stages of the non-equilibrium process, instabilities may arise in the phonon system. These instabilities correspond to stimulated emission of phonons. In the papers of Bron and Grill [2], observations have been reported of a stimulated phonon emission achieved by the inversion of a three-level electronic system of  $V^{4+}$  ions in  $Al_2O_3$ . The theoretical analysis of the three-level system influenced by the strong coherent electromagnetic field, under circumstances when phonons are not necessarily in the equilibrium, is the aim of the present paper.

2. Basic equations and steady state of the ensemble of inhomogeneously broadened three-level systems interacting with monochromatic field and phonons. - The above mentioned paper [1] of the author was devoted to the derivation of the equations describing temporal behavior of the electronic subsystems coupling with phonons. The specific example of the electronic system consisted of two-level subsystems was explored. It is easy to perform generalization to the case of many-level electronic subsystems interacting with the electromagnetic field and phonons both. The corresponding equations have the form:

$$\dot{\sigma}_{mn} + \frac{i}{\hbar} [E + V(t), \sigma]_{mn} = - \begin{cases} \sum_k (W_{mk} \sigma_{mm} - W_{km} \sigma_{kk}) ; m=n \\ \frac{1}{2} \sum_k (W_{mk} + W_{nk}) \sigma_{mn} ; m \neq n \end{cases} \quad (1)$$

$$W_{mk} = \frac{2\pi}{\hbar^2} \sum_q |A_{qmk}|^2 (n_q + 1) \delta(\omega_{mk} - \omega_q); \quad \omega_{mk} > 0 \quad (2)$$

$$W_{km} = \frac{2\pi}{\hbar^2} \sum_q |A_{qmk}|^2 n_q \delta(\omega_{mk} - \omega_q);$$

$$\dot{n}_q = \frac{2\pi}{\hbar^2} \sum_{(mk)} |A_{qmk}|^2 \{ (n_q + 1) \sigma_{mm} - n_q \sigma_{kk} \} \delta(\omega_q - \omega_{mk}) - W_q (n_q - n_q^0) \quad (3)$$

Here  $\sigma_{mn}$  - the density matrix of certain ion (defect) interacting with phonons of the solid,  $E$  - its Hamiltonian,  $V(t)$  - the energy of the interaction of this ion with the electromagnetic field;  $n_q$  - mean values of the phonon numbers with the frequency  $\omega_q$  and wave-vector  $q$ ,  $W_q$  - the relaxation rate of  $n_q$  to its equilibrium value  $n_q^0$ .  $A_{qmn}$  - matrix elements of interaction operator between electronic system and phonons. The summation in (3) over  $(mk)$  means the summation over various ions with various  $\omega_{mk}$ , i.e. the inhomogeneous broadening is assumed. The equations (1)-(3) are the system of coupled equations for  $\sigma_{mn}$  and  $n_q$  both.

We will assume that each ion has three levels  $E_n < E_k < E_m$  (or just these levels are essential for the problem). These levels are inhomogeneously distributed and grouped with certain bandwidths. We suppose that the monochromatic electromagnetic field

$$V = V^+ e^{-i\omega_0 t} + V^- e^{i\omega_0 t}, \quad \omega_0 \approx \omega_{mn}; \quad (V^+)^* = V^- \quad (4)$$

is imposed on the crystal. Then the steady state solution may be looked for in the form  $\sigma_{mn} = \bar{\sigma}_{mn} e^{-i\omega_0 t}$ ;  $\sigma_{nm} = \bar{\sigma}_{nm} e^{i\omega_0 t}$  where  $\bar{\sigma}_{mn}$ ,  $\bar{\sigma}_{nm}$  do not depend on time as well as  $\sigma_{mm}$ ,  $\sigma_{nn}$ ,  $\sigma_{kk}$  and  $n_q$ . From the equation (3) we obtain the steady state equation for  $n_q$  with the solution

$$n_q = [\bar{n}_q^0 + (\gamma_q / W_q) \sigma_{mm}] / [1 - (\gamma_q / W_q) (\sigma_{mm} - \sigma_{kk})] \quad (5)$$

Here

$$\bar{n}_q = \frac{2\pi}{\hbar^2} \sum_{(mk)} |A_{qmk}|^2 \delta(\omega_q - \omega_{mk}), \quad (6)$$

$\sigma_{mm}$ ,  $\sigma_{kk}$  are the mean values of the probabilities of the states  $m$  and  $k$  and we assume that

$$\sigma_{mm} + \sigma_{kk} + \sigma_{nn} = 1 \quad (7)$$

From equation (2), we obtain for the transition probabilities  $W_{mk}$ ,  $W_{km}$  the expressions

$$W_{km} = \Gamma_{mk} [\bar{n}_q^0 + (\gamma_q / W_q) \sigma_{mm}] / [1 - (\gamma_q / W_q) (\sigma_{mm} - \sigma_{kk})], \quad W_{mk} = W_{km} + \Gamma_{mk} \quad (8)$$

where

$$\Gamma_{mk} = \Gamma_{km} = \frac{2\pi}{\hbar^2} \sum_q |A_{qmk}|^2 \delta(\omega_{mk} - \omega_q) \quad (9)$$

It is easy to see from Eqs.(3),(6) that the threshold condition of the self-excitation of phonons has the form (see also [1])

$$(\gamma_q / W_q) (\sigma_{mm} - \sigma_{kk}) > 1 \quad (10)$$

This condition being satisfied, the steady state solution does not exist. It can be seen from Eqs.(5),(8), since the quantities  $n_q$ ,  $W_{km}$  could not be negative.

To simplify the calculations we will assume that the temperature of the crystal equals zero (or it is very low) so that  $n_q^0=0$ ;  $W_{nk}=W_{nm}=0$ . As to  $W_{mk}$  and  $W_{km}$ , we take into account their dependence on  $\sigma_{nn}$  and  $\sigma_{kk}$ . (We consider the situation when  $\sigma_{nn}-\sigma_{kk}$  can be positive and may lead to the essential enhancement of  $n_q$  and  $W_{km}$ ,  $W_{mk}$ , and at the same time  $\sigma_{kk}-\sigma_{nn}$  and  $\sigma_{nn}-\sigma_{nn}$  being negative cannot essentially influence on the quantities  $W_{nk}$ ,  $W_{kn}$ ,  $W_{nm}$ ,  $W_{mn}$ ). After transformations we obtain from (1)-(9) the following equations:

$$f^2[(1-g)(1-2g)-(1+g)d](1-gg-d)=\eta[(1-d)e+(1-gg-d)](1-gg)e \quad (11)$$

Here  $f^2=4V^2/W_{nn}^2$ ;  $g=\gamma_q/W_q$ ;  $e=r_{mk}/W_{nn}$ ;  $d=r_{mk}/W_{kn}$ ;

$$\sigma_{nn}=\eta(1-gn)/(1-gn-d); \sigma_{kk}=\sigma_{nn}-n; \sigma_{nn}=1-2\sigma_{nn}+n; n=\sigma_{nn}-\sigma_{kk}; W_{km}=r_{mk}\frac{gn}{(1-gn-d)} \quad (12)$$

The necessary condition for the inversion of the populations  $\sigma_{nn}$  and  $\sigma_{kk}$  ( $n>0$ ) is  $W_{kn}>r_{mk}$  or  $d<1$ . Solving equation (11) and finding  $\eta$  as a function of dimensionless field strength  $f$  we can find all the populations  $\sigma_{nn}$ ,  $\sigma_{kk}$  and  $\sigma_{nn}$  from (12). It can be shown that  $g$  is proportional to the concentrations of ions (defects)[1]. In the case of low concentrations ( $g=0$ ) we obtain for  $n=\sigma_{nn}-\sigma_{kk}$  and for  $\sigma_{nn}-\sigma_{nn}$  the usual expression describing the saturation in three-level system (see e.g. [3]).

3. Conclusions. - According to (3),(5),(10) the threshold field corresponding to self-excitation of phonons could exist provided  $1-gn=0$  is the solution of the equation (11). But the analysis shows that such field does not exist. The first conclusion is that in three-level system, the self-excitation of phonons cannot be achieved. When the difference of populations  $n=\sigma_{nn}-\sigma_{kk}$  begins to increase with the increasing of the field  $f$  the number of phonons (5) and  $W_{km}$ ,  $W_{mk}$  also increase. This leads to the saturation of levels  $m$  and  $k$  which in its turn prevents the fulfillment of the self-excitation condition (10).

The second conclusion is that, still, essential enhancement of the phonon numbers may be achieved for  $g>1$ :  $n_q=\frac{g}{3d} \gg 1$  (for  $g>1$ );  $n_q=\frac{g-2}{3d} \gg 1$  ( $d<g-2$ ).

The third conclusion is that at large enough concentrations (when  $g>1$ ) we should anticipate the quenching of the laser effect at the levels  $n,k$  since the difference of (inverted) populations  $n=\sigma_{nn}-\sigma_{kk}$  tends to zero when the saturation effect between levels  $m$  and  $n$  holds ( $f^2 \gg 1$ ):  $n_u=(1-d)/g-3d(1-d)/g$  ( $g>1$ ) and  $n_u=g'-d(1+g)/g(g-2)$  ( $d<g-2$ ).

And last, but not least, we predict field induced transparency in the first two levels  $n$  and  $k$  of three level system, when field saturates levels  $n$  and  $m$  and  $g>1$ . In this case  $\sigma_{nn}-\sigma_{kk}=n_u \rightarrow 0$  when  $g \rightarrow \infty$  while the absorption of the probe light signal (at the frequency  $\omega_{kn}$ ) is proportional to  $\sigma_{nn}-\sigma_{kk}$ .

#### References

1. B. Fain, Phys. Rev. (in press).
2. M.E. Bron and W. Grill, Phys. Rev. Lett. **40**, 1459(1978); W. Grill, in Phonon Scattering in Condensed Matter ed. by Humphrey J. Maris, Plenum Press, N.Y. (1980).
3. B. Fain, Y.I. Khanin, Quantum Electronics, Vol. I, Pergamon Press, Oxford (1969).

## IMPROVED ENERGY RESOLUTION WITH NEUTRON SPIN ECHO TRIPLE-AXIS SPECTROMETERS

C.M.E. Zeyen

*Institut Laue-Langevin, 156X, 38042 Grenoble Cedex, France*

**Abstract.** - A spin echo option added to a classical Triple Axis spectrometer is capable of significantly improving the Energy Resolution. The design and construction of such a machine is described. In particular it is shown that intensity problems can well be overcome by using new focussing polarizer/analyser devices. The method has proven to be very successful for high resolution quasielastic scattering. Preliminary phonon experiments with the aim of lifetime determination have been performed.

**Introduction.** - Neutron Triple-Axis Spectrometers (TAS) have been a very productive and rather unique tool for the investigation of dispersion surfaces in solids. Furthermore in certain cases the same technique has been useful to determine the energy linewidth of excitations. In general, however, the latter applications are handicapped by the limited resolution characteristics of TAS.

Their energy resolution is determined by the beam collimations and monochromatisations necessary to precisely measure the neutron energies and momenta before and after the scattering process. Hence the practical limits are conditioned by the limited flux of the available continuous neutron sources. In practice relative energy resolutions  $\frac{\Delta E}{E_0}$  of about 1 % are typical ( $E_0$  is the incident neutron energy). Thus the very best energy resolutions ( $\sim 50$   $\mu$ eV FWHM) are obtained with very low energy neutrons with the corresponding limited momentum transfer obtainable.

The neutron spin echo (NSE) technique proposed by Mezei<sup>1</sup>, if added to a Triple Axis spectrometer can be used to improve the energy resolution significantly. This is due to the fact that in NSE rather than obtaining the excitation energy as the difference between incoming and outgoing neutron energies it is measured directly. The principle of the method is analogous to the spin echo method used in NMR<sup>2</sup> with the difference that the time variable is replaced here by a spatial variable : the distance the neutrons travel through magnetic fields with their spins executing Larmor precessions. The total amount of precession angle accumulated by one neutron is proportional to the time spent in the field and the integral of the magnetic field along its trajectory. Thus the well polarized incoming neutron beam will quickly lose its polarization due to its velocity spread but the Larmor phase angle of each neutron spin taken separately will still remain a measure of its own energy.

By arranging two magnetic field areas before and after the scattering sample in such a way as to produce precession in opposite sense and properly tuning the

difference in field magnitude to the neutron energy change by the inelastic process under study one can recover the mean beam polarization at the end of the second magnetic field area. This is called obtaining the "Echo". The decay of this final NSE polarization as a function of magnetic field asymmetry around the Echo value can be shown to be related to the energy width of the excitation studied.

The resolution of such a spectrometer is improved by increasing the number of Larmor precessions through stronger magnetic fields. The limit is set by the obtainable field homogeneities. Indeed field inhomogeneities introduce parasitic Larmor precessions which may destroy the final NSE polarization.

The spectrometer. - The basis of our NSE TAS is the thermal neutron triple-axis spectrometer D10<sup>3</sup> of the I.L.L.. In its classical mode of operation the spectrometer is equipped with sets of both PG and copper vertically focussing monochromator/analysers. The useful wavelength band is inbetween 1 and 3.5 angstrom and below 1.5 Å the cut-off of the curved neutron guide is indeed very useful because  $\lambda/2$  filters are not needed. This is a particularly relevant feature where Heusler crystals are used as the second order reflexion is very strong.

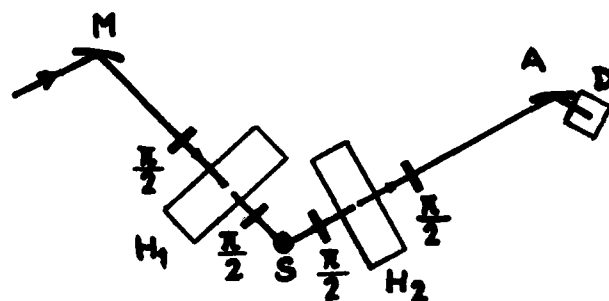


Fig. 1 : Schematic arrangement of the spin-echo TAS

M : focussing crystal monochromator/polarizer

A : focussing crystal analyser/spin analyser

D : detector

S : sample

$\pi$  : spin-turn coils (the  $\frac{\pi}{2}$  coils around the sample can be replaced by a single  $\pi$  coil)

$H_1, H_2$  : precession fields.

In order to transform the spectrometer into a polarization analysis spectrometer vertically focussing composite Heusler systems were especially developed for this purpose. These systems give a focussed beam of 30 x 30 mm cross section starting from a white beam of 120 x 30 mm. The polarization efficiency obtained is 96 %. The final polarization of the spectrometer including the flipper efficiency reaches 92 % provided the sample presents no spin incoherent scattering. In order to keep the spectrometer rather compact an Iron core precession magnet-type with the field transverse to the neutron trajectories was chosen. The magnets have a wide window frame iron core dimensioned so that the iron does not saturate anywhere at maximum field. The windings were chosen of the racetrack type because they give a maximum of homogeneity. The maximum field in the magnet gap is 1.5 k Oersted. For particular

small sample geometries extra pole pieces may be added to give a maximum field of 3 k Oersted. For NSE the relevant property of the precession magnets is the line integral of the magnetic field  $H$  along neutron path and over the distance  $l$  where the neutron spins are allowed to precess around the field direction. This integral was calculated to be about  $\int H dl \sim 5 \cdot 10^4$  Oe.cm the value depending of course on the precise integration length  $l$ . In practice and at maximum field the value of  $5.63 \cdot 10^4$  Oe.cm was found. This corresponds to 1000 Larmor precessions for 2.4 Å ( $N = 7.37 \cdot 10^{-3} \lambda \int H dl$ ). This number of precessions  $N$  has to be as homogeneous as possible for all neutrons of identical wavelength. For our magnets experiments have shown that practical beam sizes lead to a loss of NSE signal of about 30 % at maximum field mainly due to field inhomogeneities. Further experimental details can be found in <sup>4</sup>.

Performance and results. - From the point of view of polarized neutron flux the present solutions are very satisfactory. The flux loss with respect to the standard graphite crystal monochromator/analyser is of a factor 5 only.

The quantity measured in an NSE experiment is the beam average of the final NSE polarisation. As extensively discussed in <sup>1</sup> this quantity is related to the scattering function  $S(Q, \omega)$  of the sample by

$$P_{NSE} = P_0 \int S(Q, \omega) \cos \omega t d\omega$$

where  $t$  is a Fourier time variable depending on the machine constants and the incident wavelength.  $P_0$  is a normalising polarization which contains eventual changes of polarisation by the sample. This relation can be specialised to particular scattering examples. For quasi-elastic Lorentzian scattering the polarisation is just given by

$$P_{NSE} = P_0 \exp(-\Gamma t)$$

where  $\Gamma$  is the linewidth parameter of the Lorentzian.

For phonon linewidth studies the measured polarisation is given by

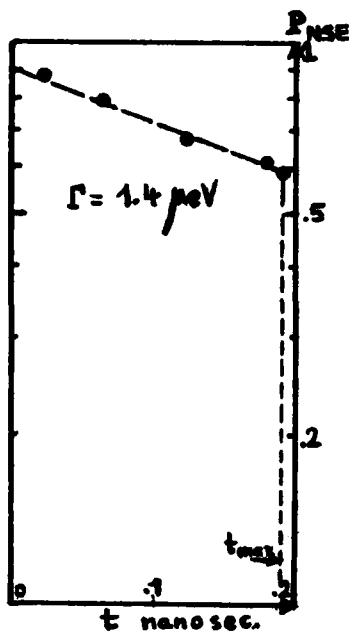
$$P_{NSE} = P_0 \cos 2\pi (N_1 - N_2)$$

where  $N_1$  and  $N_2$  stand for the mean numbers of spin precessions in the initial and final beams. The quantity  $P_0$  describes the decay of the echo signal as a function of  $N_1$  and contains both the energy width of the classical resolution function of the spectrometer as the standard deviation of the phonon lineshape.

The resolution function of an NSE spectrometer is given by the decay of the NSE polarisation with increasing precession field strength. Fig. 2 shows a typical resolution curve of D10-NSE for an incident wavelength of 2.4 Å. One sometimes defines the spectral resolution which gives rise to a 5 % change in  $P_{NSE}$  at the maximum Fourier time  $t_{max}$  obtainable. In our case this quantity amounts to 0.3 μeV. We have verified that for quasi-elastic scattering this is indeed measurable.

Concerning the measurement of phonon lifetimes only very preliminary measurements have been made. It can be stated that there is no experimental problem for non dispersive branches although the data treatment and corrections are not yet completely under control. More experimentation is needed to determine the resolution





improvements obtainable for strongly dispersive phonon branches.

Fig. 2 : Example of D10-NSE Resolution as a function of the Fourier time ( $\lambda_0 = 2.4 \text{ \AA}$ ).

#### References

1. MEZEI F., Z. Physik, 255, 146-160 (1972), a more detailed account on NSE can be found in Proceedings of Neutron Spin Echo Workshop, Grenoble 1979, Lecture Notes in Physics 128, Springer-Verlag, F. Mezei Editor.
2. HAHN, E.L. (1950) SPIN ECHOES, Phys. Rev. 80, 580.
3. I.L.L. YELLOW BOOK, Neutron Beam Facilities at the HFR, R. Maier (1980).
4. ZEYEN, C.M.E., Proceedings of the Symposium on Neutron Scattering, Argonne, August 1981, to be published by AIP.

PHONONS IN MOLECULAR AND ORGANIC SUBSTANCES

## PHONONS IN MOLECULAR CRYSTALS

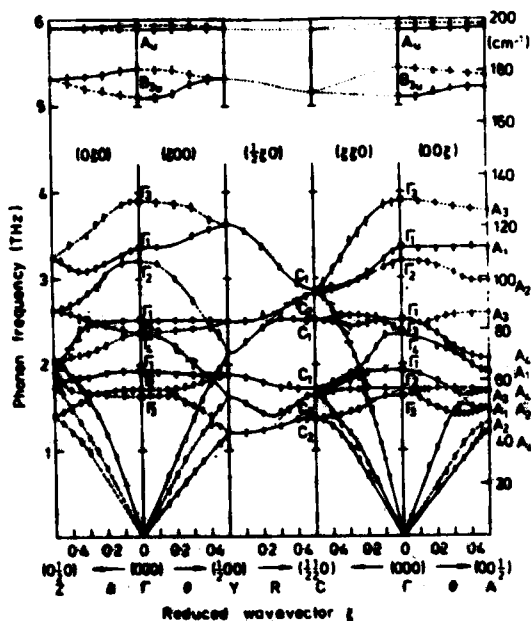
G. Venkataraman

Reactor Research Centre, Kalpakkam 603 102, Tamil Nadu, India

**Abstract.**— This paper reviews recent developments concerning phonons in molecular crystals.

1. **Introduction.**— A molecular crystal may be operationally defined as one in which there exist well-bound groups of atoms. In this paper, a broad survey is given of recent developments concerning phonons in such crystals. To start with, these developments are viewed by analogy with similar happenings earlier for 'simple' crystals. Later, features (like rotations) specific to the presence of atomic clusters, are given special attention.

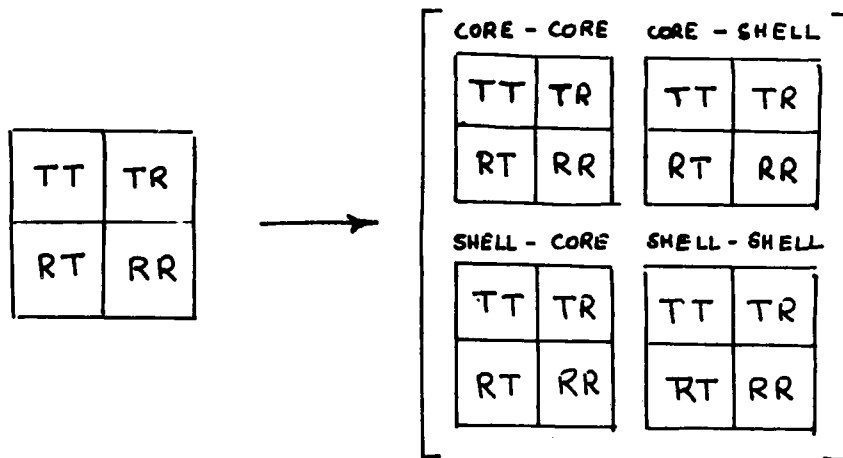
2. **Dispersion curves.**— As in the case of simple crystals, a serious study of molecular phonons commenced only when efforts were launched to make complete maps of dispersion curves. However, since the number



**Fig. 1** : Phonon dispersion curves for naphthalene (after ref.1).

of branches (even of external modes) is usually large, such experiments are time consuming and therefore confined to the large reactors. Figure 1 shows the results for naphthalene<sup>1</sup>, and probably represents the limit attainable at present. Other crystals similarly explored in detail include anthracene and TCNE. In a few cases, e.g., anthracene<sup>2</sup>, neutron scatterers have ventured to go even further and study eigenvectors. Here, for instance, it was possible to establish the extent to which the butterfly and twist internal modes (both of  $\Gamma_4$  symmetry), become mixed in the crystal.

3. Shell model.— On the theoretical side, one has witnessed the emergence of a molecular shell model<sup>3,4</sup>. As in the simple shell model of Cochran, one first visualizes the (polarizable) atoms in the molecule to be composed of cores and shells. To simplify matters, one next supposes that all the cores in a molecule are rigidly tied as also the shells. However, relative motion between the two clusters is permitted. The dynamical matrix now gets enlarged as below:



Unlike the Cochran shell model, the molecular shell model is yet to find extensive use. However, experimental results currently becoming available seem to be increasingly favouring the use of this model.

4. Ab initio calculations.— Ab initio calculations in molecular crystals in the sense of starting from ions and electrons hardly exist, in sharp contrast to, say, the metals. What is more common is to make calculations based on assumed forms for atom-atom interactions.

Initial work concentrated on non-bonded interactions. The potentials were usually assumed to be of the Buckingham - 6 exp type, the parameters often being derived from Kitaigorodsky. It is important in such calculations to ensure that the static configuration about which

the dynamics is calculated, is an equilibrium one. Chaplot *et al*<sup>5</sup> have drawn attention to the implications of this vis-a-vis the so-called self-terms in the force constants.

Naphthalene<sup>1,6</sup> has received much attention, especially in the context of comparison with experiment. It has generally emerged that while Buckingham-type potentials are by and large useful, "we are now near the stage where a more sophisticated model of the intermolecular forces is required"<sup>6</sup>. A somewhat similar programme of calculation (and limited comparison with experiment) has been implemented by Rao *et al*<sup>7</sup> for  $\alpha$ -KNO<sub>3</sub>. A notable feature of these calculations was the explicit evaluation of the various Coulombic contributions via the detailed expressions given for the molecular case earlier by Venkataraman and Sahni<sup>8</sup>.

Not infrequently, near-neighbour interactions involve hydrogen or covalent bonding, and in such cases one must obviously make modifications to the above scheme. One example of such a crystal is solid chlorine. Here, initial attempts via Buckingham-type potentials failed<sup>9</sup>. The crystal was never stable. Thereafter, Pasternak *et al*<sup>10</sup> introduced bond-charge type interactions (similar to those used earlier in diamond) to take care of covalency effects. The success of such an approach may be judged from fig.2.

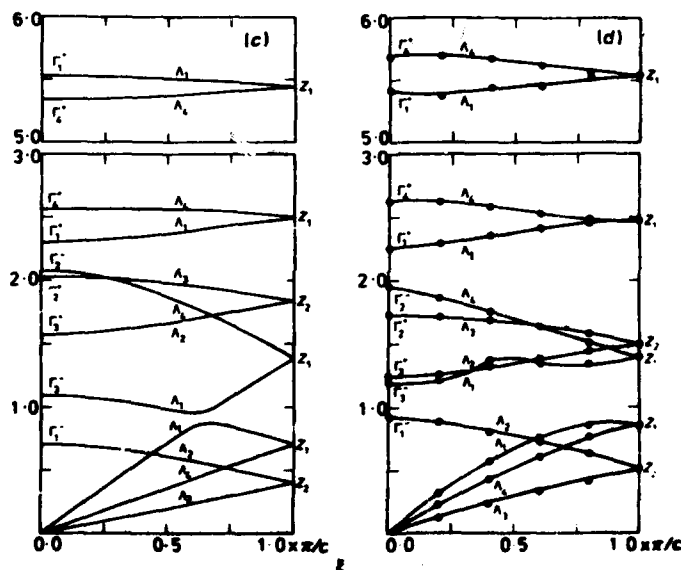


Fig. 2 : Calculated<sup>10</sup> and measured<sup>11</sup> curves for solid iodine.

5. Molecular dynamics.— Another development of significance is the study of phonons by molecular dynamics. Klein *et al* have used the technique to study solid- $N_2$ , solid  $\gamma$ - $O_2$ , DCl and  $CH_4$ . In  $\gamma$ - $O_2$ , the structure is similar to that of the famous A-15 compounds. It consists of linear chains of disordered "disk-like" molecules along 001 directions and spherically disordered "sphere-like" molecules on a bcc lattice. Broad features related to these two distinct types were detected in the simulation studies<sup>12</sup>. In  $CH_4$ , dispersion curve plots were obtained as in fig.3<sup>13</sup>. It was inferred that the potential used (deduced by Williams from crystal structure of aliphatic compounds) gave too soft a crystal. Another useful finding of this work was the general validity of the theory of neutron scattering from plastic crystals as given earlier by Dolling *et al*<sup>14</sup>.

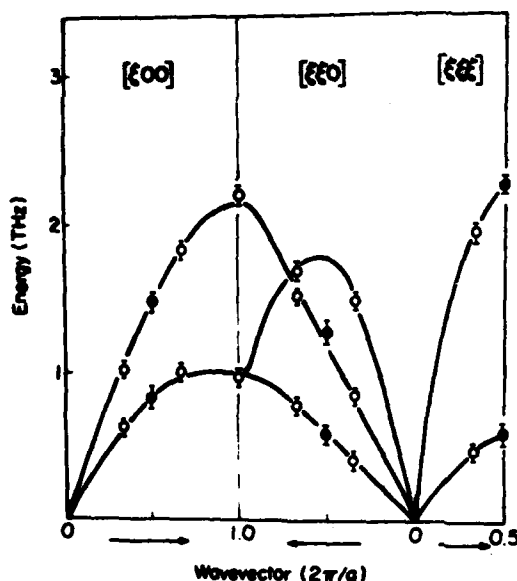


Fig. 3 : Dispersion curves for solid methane obtained by simulation (after ref. 13).

6. Rotations.— The rotational behaviour of molecules is essentially controlled by the potential they see in the field of their neighbours. Considering the single-particle behaviour first, the quantity of interest is  $V^1(\omega_i, t)$ , the net orientational potential seen by the  $i$ th molecule at time  $t$ . This potential can be expressed as the sum of a static and a fluctuating (time-dependent) part. The scenario that emerges depends very much on the relative magnitudes of the rotational constant ( $\hbar^2/2I$ ), the temperature, and the static and fluctuating components of  $V^1$ . Figure 4 illustrates the energy-level scheme for a rotor in an orientational potential. Examples of such

behaviour are now available. Particularly in  $(\text{NH}_4)_2\text{SnCl}_6$ , Prager et al<sup>15</sup> have demonstrated the presence of both librations and tunneling. Turning next to coupling between rotations, an interesting example is provided by the work of Sod et al<sup>16</sup> who have noted the possibility of coupled reorientations of two ions (between two available configurations) in a flip-flop mode.

Bates et al<sup>16</sup> have examined the role of ammonia rotations in transition metal hexammine halides  $\text{M}(\text{NH}_3)_6\text{X}_2$ . These crystals have the  $\text{CaF}_2$  structure; all show phase transitions, which, it is believed, is connected with the freezing of the protonic motions in  $\text{NH}_3$ . The

### ENERGY LEVELS OF UNIAX. ROTATOR

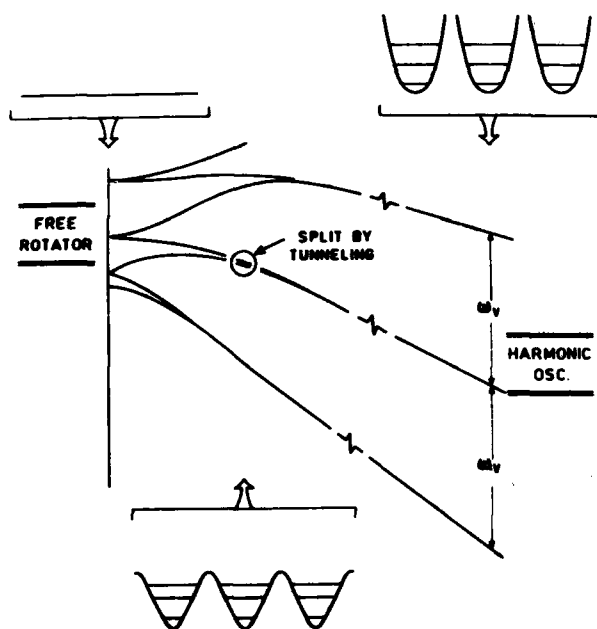


Fig. 4 : Energy levels of uniaxial rotor in a crystalline field.

calculations of Bates et al support this view, and are in general accord with Raman experiments.

In KCN, the analysis of the rotation-translation coupling has been taken to further levels of sophistication. Since relaxation effects are specifically in focus, the familiar Born-von Karman equation

$$M\omega^2(q)U(q) = D(q)U(q)$$

(1)

is inadequate. Let us first recast (1) as

$$\left(z - i\sqrt{\frac{D}{M}}\right)\Phi(z) = i\Phi(t=0) \quad (2)$$

where  $z$  is a complex frequency, and

$$\Phi(t) = \int_t^\infty dt' e^{-\epsilon t'} \langle [U^\dagger(t'), U(0)] \rangle, \quad \Phi(z) = \int_0^\infty dt e^{izt} \Phi(t). \quad (3)$$

When many dynamical variables are present and relaxation effects occur, (3) gets extended as

$$(z\mathbb{1} - \underline{\underline{\Omega}} + \underline{\underline{\Sigma}})\Phi(z) = \underline{\underline{\chi}}(0) \quad (4)$$

where  $\underline{\underline{\Sigma}}$  is the relaxation matrix and  $\underline{\underline{\chi}}(0)$  is the static susceptibility. Equation (4) is the Mori equation.

In KCN there is a phase transition at 168 K to an orthorhombic structure, with  $\text{CN}^-$  (which were initially disordered), becoming parallel to the  $b$  axis. Michele *et al*<sup>18</sup> have successfully used the above formalism both to explain the anomalous decrease of  $C_{44}$  as  $T \rightarrow T_c^+$ , and the neutron scattering results of Rowe *et al*<sup>19</sup>. In particular, they have been able to show why a central peak is absent when  $q$  is small and is present when  $q \sim 0.5 \text{ BZ}$ .

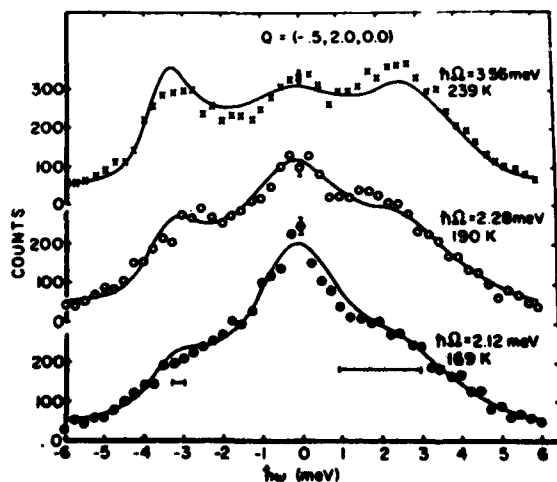


Fig. 5 : Measured and calculated phonon profiles in KCN near  $T_c$ . Note the central peak (after ref.19).

It is obvious from the above that one now knows a good deal more about rotations of molecules in crystals. In particular, one is now



able to get a detailed feel both via theory and experiments about how rotations can influence structural changes.

7. Fluctuation Spectroscopy.— Finally, a brief reference will be made to intensity-correlation spectroscopy<sup>20</sup> as a possible tool for studying slow molecular motions. The idea is as follows: Conventional spectroscopy is restricted in the study of slow relaxational processes since the latter produce negligible line broadening. Suppose now that besides the usual rapid fluctuations, there is a slow component on a very different time scale. When intensity in a spectral band is measured as usual, the experiment will average only over the fast relaxation modes. As such, repeated measurements at the same spectral setting will yield a slowly fluctuating intensity  $I(t)$ . From the correlation function  $\langle I(0)I(t) \rangle$ , the relaxation time of the slow fluctuations can be determined. Thus, one can envisage tagging a molecule by its internal vibrations, and studying the (slow) rotational dynamics by correlation spectroscopy. It is pertinent to mention that correlation spectroscopy is already popular in other fields like chemical kinetics and biophysics. Hopefully, one will hear about application to phonons in the next Conference.

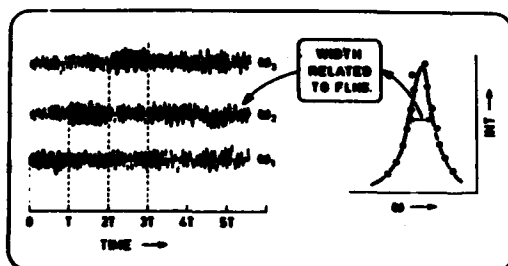
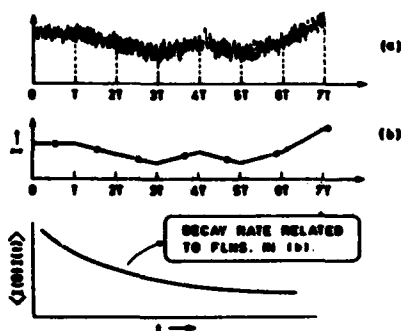


Fig. 6 : Schematic illustration of intensity fluctuation spectroscopy. The box indicates the essence of conventional spectroscopy.



7. Acknowledgements.— I would like to thank Ajay Sod and Sibba Rax for valuable assistance with the preparation of the manuscript.

REFERENCES

1. Natkaniec, I., Bokhenkov, E.L., Dorner, B., Kalus, J., Mackenzie, G.A., Pawley, G.S., Schmelzer, U and Sheka, E.F., J. Phys. C 13, 4265 (1980).
2. Chaplot, S.L., Pawley, G.S., Bokhenkov, E.L., Dorner, B., Jindal, V.K., Kalus, J., Natkaniec, I. and Sheka, E.F., (to be published).
3. Luty, T. and Pawley, G.S., Phys. Stat. Solidi B 66, 309 (1974).
4. Pawley, G.S. and Leech, J.W., J. Phys. C 10, 2527 (1977).
5. Chaplot, S.L., Sahni, V.C. and Rao, K.R., Acta Cryst. 37 (to appear (1981)).
6. Mackenzie, G.A., Pawley, G.S. and Dietrich, O.W., J. Phys. C 10, 3723 (1977).
7. Rao, K.R., Chaplot, S.L., Tyengar, P.K., Venkatesh, A.H. and Vijayaraghavan, R.R., Pramana 11, 251 (1978).
8. Venkataraman, G. and Sahni, V.C., Rev. Mod. Phys. 42, 409 (1970).
9. Leech, J.W. and Pawley, G.S., Mol. Phys. 31, 1663 (1976).
10. Pasternak, A., Anderson, A. and Leech, J.W., J. Phys. C 10, 3261 (1977).
11. Smith, H.G., Nielsen, M. and Clark, C.B., Chem. Phys. Lett. 33, 75 (1975).
12. Klein, M.L., Levesque, D. and Weis, J.J., Phys. Rev. B 21, 5785 (1980).
13. Bounds, S.G., Klein, M.L. and Patey, G.N., J. Chem. Phys. B 21, 5348 (1980).
14. Dolling, G., Powell, B.M. and Sears, V.F., Mol. Phys. 37, 1859 (1979).
15. Prager, M., Press, W., Alefeld, B. and Huller, A., J. Chem. Phys. 67, 5126 (1977).
16. Sod, A.K., Arora, A.K., Dattagupta, S and Venkataraman, G., See this Conference Proceedings.
17. Bates, A.R., Crick, I.L.A. and Davies, R.O., J. Phys. C 9, 3013 (1976).
18. Michele, K.H. and Naudts, J., J. Chem. Phys. 67, 547 (1977); 68, 216 (1978).
19. Rowe, J.M., Rush, J.J., Chesser, N.J., Michele, K.H. and Naudts, J., Phys. Rev. Lett. 40, 455 (1978).
20. Venkataraman, G., Lecture notes, Enrico Fermi School, Course LXXXII (1981) - to be published.

## VIBRATIONAL SPECTRA OF SOLID AND LIQUID SULFUR

Y. Sasaki<sup>†</sup> and Y. Nishina\**Department of Physics, University of California, Irvine, California 92717, U.S.A.**\*The Research Institute for Iron, Steel and Other Metals, Tohoku University, Sendai 980, Japan*

**Abstract.**— We have measured the Raman spectra of intermolecular vibrations of sulfur in the temperature regions of orthorhombic-monoclinic, solid-liquid, and polymerization transitions. The evolution of the Raman spectrum at the first phase transition is discussed in terms of the disorder-induced Raman scattering. The Raman spectra in liquid suggest ordering in the liquid phase. The appearance of the  $S_n$ -polymer above the polymerization temperature changes the slopes of the exponential Raman spectra in the liquid.

**1. Experiment.**— The Raman spectra were measured by conventional Raman scattering equipment with a He-Ne laser and by a system designed to obtain spatially-resolved Raman spectra with an Optical Multichannel Analyzer (OMA) and an Ar<sup>+</sup> laser (5145Å). In the latter case, a sample cell was placed in a vertical oven with the temperature gradient of about 10 deg./mm along the vertical direction. Then, the temperature dependence of the Raman spectra across the liquid-solid phase boundary was obtained from the spatially-resolved Raman spectra with the spatial resolution of 10  $\mu$ . The use of the OMA system made it possible to determine the temperature dependence of the Raman spectra very quickly with a small temperature increment of less than 0.5 K. All the data were taken with 99.999 % sulfur sealed in a glass cell in a back scattering configuration.

**2. Results.**— Figure 1 shows the depolarized Raman spectra of (a) orthorhombic ( $\alpha$ ), (b) monoclinic ( $\beta$ ), and (c) liquid ( $\ell$ ) sulfur that were measured when we increased the temperature from 290 K to above the melting point  $T_m = 391$  K. The Raman spectrum for  $\alpha$ -sulfur in Fig. 1(a) agrees well with the results of Anderson and Loh.<sup>1)</sup> The Raman bands at 83 and 153  $\text{cm}^{-1}$  have been assigned to intramolecular vibrations of the  $S_8$ -ring.<sup>1)</sup> Intermolecular vibrations are responsible for the other parts of the spectra in Fig. 1. The spectrum in Fig. 1(d) was taken at the same temperature as Fig. 1(b), but the two spectra are quite different.

<sup>†</sup> Permanent address : Tohoku University, Sendai 980, Japan

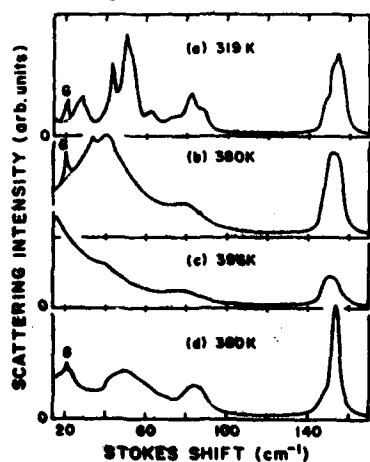


Fig. 1. Depolarized Raman spectra of sulfur. The peak, G, is the monochromator ghost.

The reason for the difference arises from the fact that the sample for Fig. 1(b) was obtained through the  $\alpha + \beta$  phase transition at about 369 K while the crystal for Fig. 1(d) was solidified from liquid. The quality of the  $\beta$ -sulfur obtained by the solidification of liquid is expected to be better.

Figure 2 shows the spatially-resolved Raman spectra across the liquid-solid phase boundary. The data were taken for five different temperature regions at 0.5 K intervals simultaneously. Figures 2(a) and 2(b) correspond to the  $\beta$ -, and 2(d) and 2(e) to the  $\delta$ -sulfur region, respectively. Since the resolution in Fig. 2 ( $\approx 7 \text{ cm}^{-1}$ ) is not as high as in Fig. 1 ( $\approx 0.75 \text{ cm}^{-1}$ ), the fine structure in Fig. 1(b) is not resolved in Fig. 2(a) or 2(b). The intermolecular Raman band appears at the same frequency ( $\approx 37 \text{ cm}^{-1}$ ) for  $\Delta T \equiv T_m - T = 11 \text{ K}$  (Fig. 1(b)),  $\Delta T = 1.0 \text{ K}$  (2(a)), and  $\Delta T = 0.5 \text{ K}$  (2(b)). The width of the band, furthermore, stays almost constant from  $\Delta T = 11 \text{ K}$  to  $\Delta T = 1.0 \text{ K}$ , and it increases slightly at  $\Delta T = 0.5 \text{ K}$ .

Figure 3 shows a logarithmic plot of the Raman spectra of the liquid. The spectral shape is approximated by

$$I \propto \exp(-\hbar\omega/\Delta) \quad (1)$$

where  $\hbar\omega$  and  $\Delta$  denote the Stokes shift and a constant, respectively. Humps at 40 and 80  $\text{cm}^{-1}$ , however, are superposed on the exponential curves in the low temperature spectra for  $T \leq 510 \text{ K}$ . The 80  $\text{cm}^{-1}$  hump is due to an intramolecular vibration. The intensity of the hump at 40  $\text{cm}^{-1}$  decreases with temperature, and the hump disappears above 440 K. Figure 4 shows the

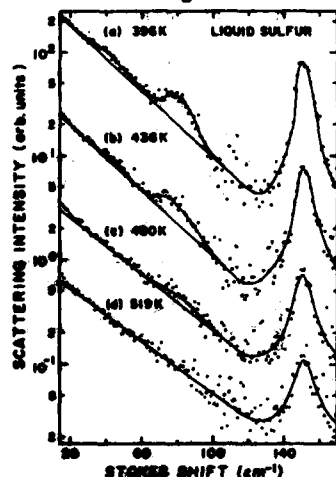


Fig. 3. Logarithmic plot of Raman spectra of  $\delta$ -sulfur. Vertical displacements of the spectra have been made for clarity.

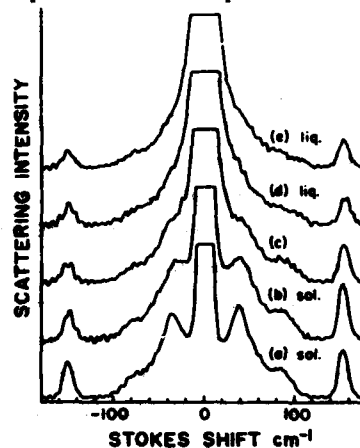


Fig. 2. Spatially-resolved Raman spectra of sulfur across the solid-liquid phase boundary.

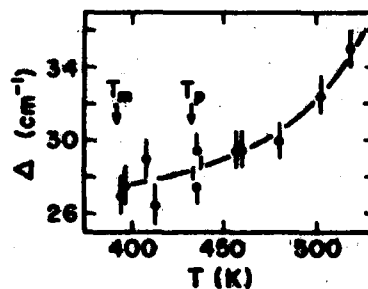


Fig. 4. Temperature dependence of  $\Delta$  in  $\delta$ -sulfur.

temperature dependence of  $\Delta$  as deduced from the slopes of the straight lines in Fig.

3. The melting point,  $T_m$ , and the polymerization temperature,  $T_p = 432$  K, are shown as a reference in Fig. 4.

3. Discussion.— Since one-third of the  $S_8$  molecules of  $\beta$ -sulfur are twofold disordered at  $T > 198$  K,<sup>2)</sup> the broad intermolecular Raman band of  $\beta$ -sulfur centered at  $37\text{ cm}^{-1}$ , similar to Fig. 1(b), was attributed to the disorder-induced one-phonon scattering due to the breakdown of the k-selection rule.<sup>3)</sup> The intermolecular Raman spectrum of the sulfur solidified from liquid (Fig. 1(d)) is similar to the spectrum of  $\alpha$ -sulfur rather than that of  $\beta$ -sulfur obtained through the  $\alpha \rightarrow \beta$  transition (Fig. 1(b)). This fact seems to suggest that the degree of disorder is lower in the  $\beta$ -sulfur obtained by the solidification than in the sulfur procured through the  $\alpha \rightarrow \beta$  transition.

The position of the hump ( $40\text{ cm}^{-1}$ ) in the Raman spectra of the liquid agrees well with the Stokes shift of the disorder-induced Raman band of the solid. The observation of this hump indicates that order in liquid sulfur exists over the range of a few molecules at  $T \leq 440$  K.

As shown in Fig. 3,  $\beta$ -sulfur shows an exponential Raman spectrum in contrast to many kinds of molecular liquids, which show non-exponential spectra approximated by  $\omega^{12/7} \times \exp(-\hbar\omega/\Delta)$ ,<sup>4)</sup> for instance. The exponential spectra have been observed in atomic liquids.<sup>4,5)</sup> According to the theory of collision-induced Raman scattering in liquids,<sup>4)</sup> the exponential spectra suggest that the molecular frame distortion does not play an important role for the collision-induced polarizability anisotropy compared with the contribution from the electronic overlap effect.

The theories available for the interpretation of high frequency Raman scattering in liquids predict that the value of  $\Delta$  in Eq. (1) is expected to vary as  $\Delta \propto \sqrt{T}$ <sup>5)</sup> or  $\sqrt{T}/[1 - (2/\pi)\arctan \sqrt{\epsilon/T}]$ ,<sup>4)</sup> where  $\epsilon$  is the energy constant for the Lennard-Jones potential. Figure 4, however, shows that  $\Delta$  varies more rapidly than  $\sqrt{T}$ , especially above  $T_p$ . Gee<sup>6)</sup> has reported that the weight fraction of  $S_8$ -ring in the liquid decreases above  $T_p$  while the fraction of  $S_n$ -polymer increases abruptly, and the fraction of polymer reaches 50 % at about 510 K. The extraordinary increase in  $\Delta$  above  $T_p$ , therefore, may be attributed to the appearance of polymeric chains.

Acknowledgements.—The authors would like to thank Prof. S. Ushioda for valuable discussions. This work was supported in part by a Grant-in-Aid for Scientific Research (1979, 1980) from the Ministry of Education in Japan and by a grant from the National Science Foundation (DMR 80-11435) in the U.S.A.

#### References

- 1) A. Anderson and Y. T. Leh, *Canad. J. Chem.*, **47**, 879 (1969).
- 2) L. M. Goldsmith and C. E. Strouse, *J. Am. Chem. Soc.*, **99**, 7580 (1977).
- 3) K. Gautier and M. Debeau, *Spectrochim. Acta* **32A**, 1007 (1976).
- 4) J. A. Bucaro and T. A. Litovitz, *J. Chem. Phys.*, **54**, 3846 (1971).
- 5) P. A. Fleury, J. M. Worlock and H. L. Carter, *Phys. Rev. Letters*, **30**, 591 (1973).
- 6) G. Gee, *Trans. Faraday Soc.*, **48**, 515 (1952).

## PHONONS IN THE DNA DOUBLE HELIX\*

E.W. Prohofsky, L.L. Van Zandt, M. Kohli, K.C. Lu, M.N. Mei and B. Putman

Dept. of Physics, Purdue University, West Lafayette, IN 47907, U.S.A.

**Abstract.**— We have calculated a model for the phonon modes of the DNA double helix. We have used these modes in a number of applications to biological problems which use lattice concepts such as soft modes, local modes and quasi-momentum.

1. **Phonons.**— The double helix is a long chain polymer made of units called base pairs. There are four possible base pair units and these units contain two hydrogen bonded bases and two backbone segments. The backbone segments are identical. DNA can be produced in which the base pairs have a repeating structure. For long polymer DNA's a screw axis operation is a symmetry operation, and the vibrational normal modes can be characterized as traveling wave phonon bands. We have used standard lattice dynamics methods to calculate these phonon bands. The polymers can carry out many biological functions and one can learn much about these mechanisms by studying the polymers.

The unit cell in the double helix is still large. We have used a common approximation which assumes that all hydrogen atoms are rigidly bound to their bonded atom. This reduced the number of degrees of freedom by about half. Even so in the simplest polymers the secular determinant is  $\sim 120 \times 120$ . More complicated homopolymers exist in which the repeating unit cell has several base pairs and the matrices here are several times  $120 \times 120$ .

2. **Force Constants.**— An initial estimate of the force constants was taken from refined values for the separate chemical entities which make up the bases, backbone, etc. The choice of constants followed the traditional valence force field choices. Calculations were made and the force field was refined by fitting to Raman and infrared data on the vibrational modes of the helix. The size of the unit cell required the development of new refinement procedures. The Raman and infrared data were limited to frequencies above  $200\text{--}300\text{ cm}^{-1}$  and only fairly strong force constants such as compression and angle bend constants could be refined with any confidence. In addition to the valence force field constants which are tied to chemical bonds and link nearby atoms, we have also studied "nonbonded" interactions. These interactions are important in determining the conformation of the helix. The acoustic velocity along the helix was determined by Brillouin scattering. This velocity was fitted for several models of the nonbonded forces. The results indicated

\*This work supported by NSF DMR 78 20602, NIH GM 24443, FDA FD 00949 and USAF S33615-78-D-0617.

that long range (electrostatic like) forces were needed to explain the observed velocity. These long range forces have also been incorporated in our calculations of the phonon bands of the double helix.

3. Soft Modes.— Conformation changes play an important role in biological processes. We have used the method of soft mode analysis to explore the onset of conformation change. The double helix undergoes a B  $\rightarrow$  A conformation change when the polar nature of its environment is reduced. We have calculated the effect of reduced polar shielding on our electrostatic nonbonded interactions and found that a soft mode develops in one DNA polymer that does undergo the conformation change. No soft mode developed in a polymer that does not undergo the transition. The soft mode displacements were a good predictor of the displacive changes in the transition.

4. Melting.— In some biological processes the base message of DNA is read. This requires a partial separation of the two strands and this is called melting of the double helix. Using our calculated eigenvalues and eigenvectors we can plot the amplitude of the stretch of the hydrogen bonds that hold the strands together as a function of temperature for several DNA polymers. We have established an empirical Lindeman's law of helix melting based on these amplitudes and comparisons of observed melting temperatures. We believe that this can be used to explore whether phonon emission by enzymes can influence localized melting without the creation and disruption of strong chemical bonds. The modes involved in stretching the H-bonds are at  $\approx 70 \text{ cm}^{-1}$  in our calculations.

5. Local Modes.— The double helix has many special sites which act as initiators and terminators of reading processes. The probability is high that these regions have unique dynamic properties which can bring about altered conformations or enhanced tendency to melt. Unique dynamic properties can on a simpler level aid in recognition by enzymes. By assuming the unique feature to be an impurity in an otherwise perfect lattice the local mode Green function method can be used to determine the local modes associated with the unique features. We have carried out a local mode analysis of the terminus of a helix by putting in the negative values for all the force constants that connect a particular two base pairs. End modes were found which were localized to the first few base pairs from the terminus. The hydrogen bond stretch modes were effected and the rms amplitude was  $\approx 2$  times that for a central base pair indicating an enhanced tendency to initiate melting from a terminus.

6. Quasi-Momentum Conservation.— In many biological processes enzymes move along the double helix. We have been interested in what can be learned about such processes by analysing the way in which real momentum and quasi-momentum are conserved. One should be able to describe the processes of propulsion in terms of processes by which enzymes emit phonons into the helix. One very interesting but far out speculation has arisen in this context. In our calculations on several DNA

polymers we find that a few bands occur which have large amplitude of H-bond stretch associated with melting. These modes have negative group velocity as well. We have proposed that the emission of wave packets in these bands by certain enzymes may be responsible for both the propulsion of the enzymes as well as aiding in maintaining and propagating a melted region of helix near the enzyme. These phonons emitted preferentially in the forward direction would both increase the H-bond stretch amplitude and cause a forward recoil in the emitting enzyme due to the negative group velocity. From the calculated band energy one can estimate the maximum momentum vs energy and very small amounts of energy can give rise to more than enough motive power. The energy needed is much less than energy known to be degraded during processes associated with enzyme motion in which high energy bonds are dissociated and lower energy chemical bonds formed.

7. Interaction with Surroundings.- The double helix is always surrounded by varying amounts of water and counterions. Removal of this water and counterions causes the helix to denature and change to a random coil conformation. We have carried out several calculations aimed at taking into account the effects of interaction with water and counterions on the vibrational modes. The first approach has been to treat the water as a continuous fluid whose response to motion is governed by the Navier-Stokes equations. The helix is treated as a continuous cylinder with vibrational properties determined by our lattice solutions. The motion of the water boundary layer is made to conform to the motion of the helix boundary and the self consistent solutions of the complex are solved for. The results indicate that the longitudinal acoustic mode for one helix in much water is critically damped below 200 GHz. Similar calculations for many stacked helices indicated reduced damping. Another approach we use is to calculate the behavior of water near a helix by using molecular dynamics methods. The water is found to order. We plan to determine the water behavior for a distorted helix which mimics the oscillatory motion of the helix. Such calculations have been done with free counterions in the system as well.

8. Microwave Absorption.- The acoustic modes of the helix span the microwave region and we have calculated the probable absorption because of the concern over genetic hazard of microwave radiation. Using our solutions for DNA in water these overdamped modes give rise to a broad absorption  $\approx 40$  times that of water per equivalent mass. Observations in good agreement have been reported. In chromosomes the DNA is wound into nucleosomes which can be resonant structures for absorption into acoustic modes. Little water is present and the damping is small. We calculate that nucleosomes could resonantly absorb at  $\approx 50$  GHz. The actual rate of absorption is still unknown as the behavior of the water in such a concentrated system is unknown.



## DYNAMICS OF PHONON INTERACTIONS IN ORGANIC SOLIDS

P.N. Prasad

Department of Chemistry, State University of New York at Buffalo, Buffalo,  
New York 14214, U.S.A.

**Abstract.** - Investigations carried out on three aspects of phonon interactions are presented in this paper. The phonon dephasing induced by anharmonic phonon-phonon scattering is investigated by temperature dependence of linewidths, lineshapes and frequencies in the Raman spectra. The dephasing of phonons in organic solids is found to be primarily caused by a  $T_1$ -relaxation involving a three-phonon inelastic scattering. Second, a similar investigation on dephasing of vibrations within the molecule suggests that for these intramolecular vibrations with frequencies greater than twice the Debye cut-off frequency, it is the fourth-order anharmonic coupling with phonons leading to an elastic scattering which provide the dominant mechanism for dephasing in organic solids. Finally, the role of phonon interactions in determining solid state reactivity is discussed and a new concept of phonon assisted reaction is introduced. A thermal intermolecular reaction is found to be assisted by a phonon mode softening. A photochemical dimerization reaction is shown to be assisted by a strong-electron phonon coupling in the excited state whereby a polaron is formed.

Phonons in organic solids are lattice vibrations derived from hindered external motions of both rotational and translational characters. Phonon interactions play an important role in determining physical and chemical properties of molecular solids.<sup>1</sup> This paper presents the results of investigations on three aspects of phonon interactions: (i) phonon relaxation and dephasing induced by anharmonic phonon-phonon scattering; (ii) phonon induced dephasing of intramolecular vibrations (relative atomic motions within the molecule); and (iii) phonon assisted solid state reactions.

The dephasing of an optical phonon can occur by two mechanisms: (a)  $T_1$ -relaxation caused by an inelastic phonon-phonon scattering which also leads to a population relaxation; (b)  $T_2$ -relaxation caused by an elastic phonon-phonon scattering which creates only a phase relaxation. The  $T_1$ -relaxation can occur by both third and fourth order anharmonic interactions, where as the leading contribution to the  $T_2$ -relaxation is derived from the fourth order anharmonicity term. We have investigated the nature of phonon dephasing by studying the temperature dependence of the phonon frequencies, lineshapes and linewidths of optical transitions in the Raman spectra in the range 2°K to room temperature. The 2°K linewidth and lineshape are assumed to represent the 0°K limit. To correct for the finite slit width, a computer convolution simulation program was developed. Such a study for the  $33\text{ cm}^{-1}$  Raman active phonon of *m*-dichlorobenzene

shows that the lineshapes are Lorentzian at all temperatures. The linewidths (corrected for slit width) are obtained as a function of temperature. A theoretical fit for these data points is provided by a model which assumes a  $T_1$ -relaxation of the optical phonon ( $33\text{ cm}^{-1}$ ) into two phonons of half the frequency. This fit of the relaxation into such a simple model appears to hold only for very low frequency optical phonons which can decay into acoustic phonons having a monotonic and smooth-density of states distribution. In the case of naphthalene optical phonons ( $\omega > 55\text{ cm}^{-1}$ ) it is found that one has to use a combination of  $T_1$ -relaxation processes to account for the observed temperature dependence of the linewidth.<sup>2</sup> In structurally disordered crystals it is found that the phonons still remain delocalized and a temperature dependence study can be used to separate the linewidth contributions due to disorder and that due to anharmonic interactions. The general conclusion of this study is that the dephasing of optical phonons in organic crystals occurs predominantly by a  $T_1$ -relaxation involving cubic anharmonic interaction terms. Also, another general observation is that the higher the phonon frequency, the faster is the relaxation time. This result can be explained by the increased number of relaxation pathways which become available at higher frequencies.

An important approximation used to describe the lattice dynamics of organic crystals is the rigid-body approximation which decouples the external lattice phonons from the intramolecular vibrations. Coupling between the intramolecular vibrations and the lattice phonons play an important role in dephasing of the intramolecular vibrations in organic solids. Again temperature dependence of the linewidth, the lineshape and the frequency of an intramolecular vibration observed in the Raman spectra is used to investigate the vibrational dephasing. It is found that for a vibration whose frequency is larger than twice the Debye cut off frequency, the dephasing is predominantly caused by an elastic scattering with phonons involving a mixed mode fourth order anharmonic interactions. This process requires population of phonons and, thus, are highly inefficient at liquid helium temperatures giving rise to sharp spectral transitions of intramolecular vibrations at the liquid helium temperature.

The third aspect of phonon interactions discussed in this paper is the concept of phonon assisted reactions introduced recently by this research group.<sup>3</sup> This concept also unifies the understanding of both physical and chemical transformations in terms of importance of phonon interactions. We show that, like phase transitions in solids, a thermal reaction can be assisted by mode softening which leads to overdamped large amplitude oscillations. Such large amplitude motions can provide pathways for the reaction to occur especially if the reaction is intermolecular in nature. The case of thermal rearrangement reaction of methyl-p-dimethylaminobenzene sulfonate which involves an intermolecular transfer of a methyl group was investigated by the Raman phonon spectra. The

AD-A128 574

INTERNATIONAL CONFERENCE ON PHONON PHYSICS 31 AUGUST-3  
SEPTEMBER 1981 BLOOMINGTON INDIANA(U) INDIANA UNIV AT  
BLOOMINGTON W E BROW DEC 81 ARO-17340.1-PH

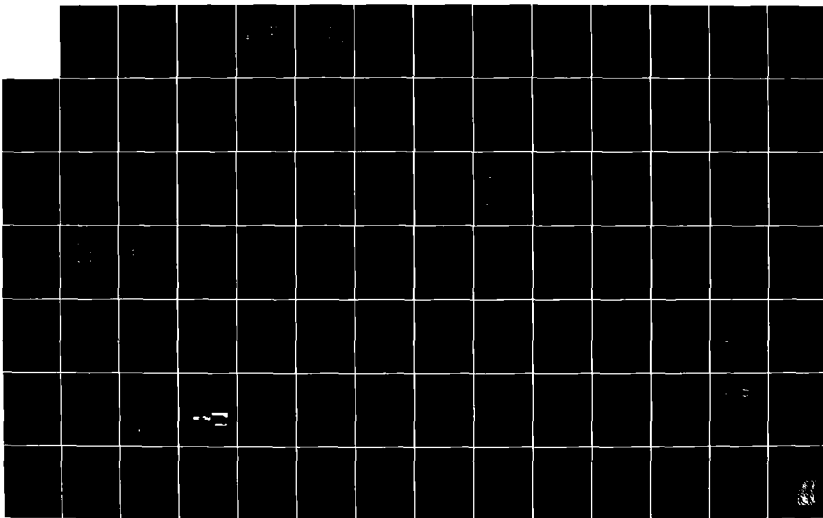
7/10

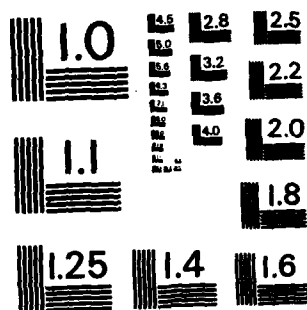
UNCLASSIFIED

MI PR ARO-43-80

F/G 20/2

NL





MICROCOPY RESOLUTION TEST CHART  
NATIONAL BUREAU OF STANDARDS-1963-A

softening of a phonon mode of frequency  $25\text{ cm}^{-1}$  was observed supporting the concept of a phonon assisted thermal reaction. Similarly, a photochemical reaction (particularly dimerization and polymerization) can be assisted by a strong electron-phonon coupling which can trap the excitation as well as provide a preformation of the product lattice configuration. The photodimerization reaction of 2,6-dimethylbenzoquinone was investigated. The 6°K electronic absorption spectra of this crystal showed most of the intensity in the phonon side band as compared to the zero-phonon line. This clearly indicated the formation of a polaron due to strong electron-phonon coupling. Thus, the reaction is assisted by the formation of a polaron.

Finally, our work shows that phonon spectroscopy can be used in a number of practical applications. The phonon spectra can readily be used to identify various polymorphs of a solid drug. It can also be used to investigate if a reaction proceeds by a homogeneous mechanism where the reactant and the product form a solid solution.

#### References

1. Prasad, P. H., Mol. Cryst. Liq. Cryst. 52, 63 (1979).
2. Bellows, J. C. and Prasad, P. N., J. Chem. Phys. 70, 1864 (1979).
3. Dwarakanath, K. and Prasad, P. N., J. Am. Chem. Soc. 102, 4254 (1980).

## HARMONIC DYNAMICS OF ANTHRACENE AND NAPHTHALENE CRYSTALS

E.L. Bokhenkov, A.I. Kolesnikov, T.A. Krivenko, E.F. Sheka and V.A. Dementjev\*

*Institute of Solid State Physics, Academy of Sciences of the U.S.S.R.,  
Chernogolovka, U.S.S.R.*

*\*Timiryazev Academy of Agriculture, Moscow, U.S.S.R.*

**Abstract.**— A method has been proposed for calculating both the dispersion and density of states of multimode phonon spectrum of molecular crystal.

The following solution of the dynamical problem of anthracene and naphthalene crystals is based on the method advanced by Taddei et al.<sup>(1)</sup> of constructing the dynamical matrix in the basis of internal and external coordinates of a free molecule.

**Phonon spectrum in  $\Gamma$ -point.**— Substitution of four equations of the 36th (anthracene) and 27th (naphthalene) orders for the secular equations of the 144th and 108th orders, correspondingly, enables exact numerical computation of the dynamical problem. The computations resulted in obtaining the values of 141 and 105 optical frequencies at  $q=0$  and revealed considerable gas-crystal shifts of the frequencies ( $\sim 20 \text{ cm}^{-1}$  and  $\sim 4 \text{ cm}^{-1}$  for out-of-plane and in-plane free molecule vibrations, respectively). The values of factor-group (Davydov) splittings were determined for all internal modes <sup>(2)</sup>.

**Dispersion and density of phonon states.**— The approach to the computation of dispersion and density of states was prompted by the mode structure of the eigenvector matrix in  $\Gamma$ -point. The mode structure was found to be nonuniform. The dominant components are grouped near the diagonal and form well-isolated groups. Hence it was possible to divide the full dynamical matrix into 7 for anthracene and 6 for naphthalene blocks that join large groups of phonons in the mode structure of which a limited basis of normal coordinates of a free molecule prevails. Thus, the replacement of the 144th-order equation for anthracene and the 108th-order one for naphthalene by the group of equations of no higher than the 24th-order permitted the dispersion and density of phonon states of these crystals to be calculated. The accuracy of this method proved to be rather high <sup>(2)</sup>.

Fig. I shows the results of calculating the phonon dispersion of anthracene crystal in five directions of Brillouin zone (BZ). Modes that are symmetric with respect to the two-fold screw axis

(  $\Gamma \rightarrow Z$  ) or to the glide plane (  $\Gamma \rightarrow B$  and  $\Gamma \rightarrow A$  ) are shown in solid lines. The dashed lines in these directions correspond to the asymmetric modes.

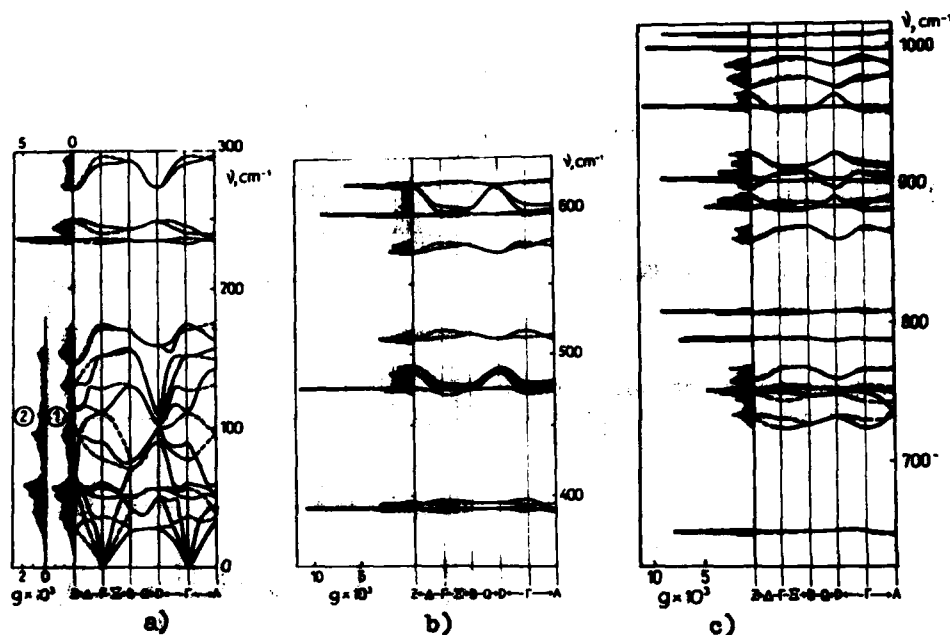
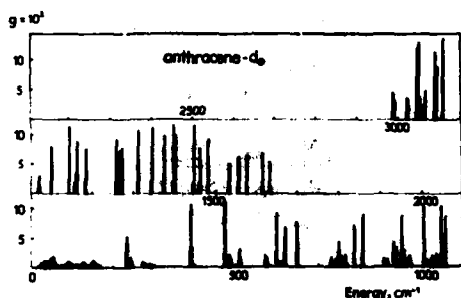


Fig.1 : Dispersion curves and density of states of anthracene crystal in the following energy regions: a) 0-300  $\text{cm}^{-1}$ ; b) 350-650  $\text{cm}^{-1}$ ; c) 650-1050  $\text{cm}^{-1}$ .

The low-frequency range (0-200  $\text{cm}^{-1}$ ) in Fig.1a embraces 16 branches with pronounced dispersion. Twelve of them are originally connected with external modes and four with two internal ones (symmetry  $B_{3u}$  and  $A_u$ ). The density of states in this range is shown by a black-shaded region (1). The density of states (2) calculated in the rigid molecule approximation is shown for a comparison. As is seen, the incorporation of internal modes reconstructs the density of states significantly. Referring to Fig.1, a great number of phonon modes have low factor-group splitting in  $\Gamma$ -point and considerable dispersion over BZ. With respect to the optical studying, such modes can be termed as the modes of "latent" dispersion. The calculated dispersion curves of anthracene crystal within the range 0-200  $\text{cm}^{-1}$  agree qualitatively well with those obtained experimentally for anthracene- $d_{10}$  at low temperature (3).

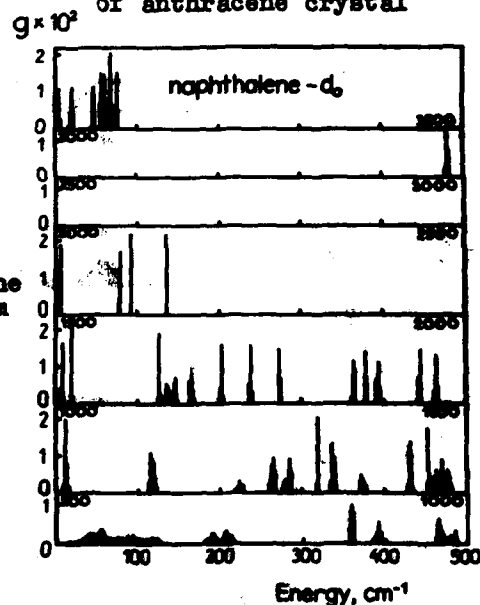
The densities of states were calculated over 1900 points in the irreducible ( $1/4$ ) part of BZ by the histogram method via 1  $\text{cm}^{-1}$  ( see Figs. 2 and 3 ). The densities weighted on the square amplitudes of the hydrogen atom displacements have been calculated as

as well. The results allowed the experimental spectra of inelastic incoherent neutron scattering of the both crystals at low temperature to be described quantitatively well within the range of both external <sup>(4)</sup> and internal <sup>(5)</sup> phonons.



**Fig. 3 :** Density of states of the 108-mode phonon spectrum of naphthalene crystal

**Fig. 2 :** Density of states of the 144-mode phonon spectrum of anthracene crystal



In conclusion the authors will express their deep gratitude to Prof. S. Califano and Dr. R. Righini for the fruitful discussions and for placing at our disposal the BENZ program.

#### References

1. G. Taddei, H. Bonadeo, M.P. Marzocchi and S. Califano, J. Chem. Phys. **72**, 966 (1973)
2. T.A. Krivenko, V.A. Dementjev, E.L. Bokhenkov, A.I. Kolesnikov and E.F. Sheka, in press
3. B. Dorner, E.L. Bokhenkov, E.F. Sheka, S.L. Chaplot, G.S. Pawley, J. Kalus, U. Schwalzer and I. Natkaniec, these Proceedings, p.
4. A.V. Belushkin, E.L. Bokhenkov, V.A. Dementjev, A.I. Kolesnikov, T.A. Krivenko, J. Maier, I. Natkaniec, V.G. Padotov and E.F. Sheka, to be published
5. E.L. Bokhenkov, A.I. Kolesnikov, T.A. Krivenko, E.F. Sheka, V.A. Dementjev and I. Natkaniec, these Proceedings, p.



## ACOUSTOELECTRIC INTERACTION IN p-InSb AT LOW TEMPERATURE

J.D.N. Cheeke and G. Madore

*Département de Physique, Université de Sherbrooke, Sherbrooke, Prov. Québec, Canada J1K 2R1*

**Abstract.** - We have measured the ultrasonic attenuation in p-InSb in the range 1 - 20 K in the 30 - 600 MHz frequency range under magnetic fields up to 7T, concurrently with magnetoresistance measurements. Both the relaxation peak observed near 10 K and the low temperature field dependence are governed by the piezoelectric interaction and both effects are in good agreement with the acoustoelectric theory of Hutson and White.

There have been many recent ultrasonic studies of resonance, relaxation and magnetic field effects associated with absorption by impurities in p type semiconductors at low temperatures (1). Our first results on p-InSb were interpreted in this way (1) (2). However more recent results to be presented here suggest that the relaxation and low temperature magnetic field effects observed in this system are in fact due to a piezoelectric interaction with free or bound carriers.

The experiments were carried out in the usual way with a Matec 6600 system and PAR two channel Boxcar integrator. LiNbO<sub>3</sub> 30 MHz transducers were grease bonded to the polished faces and a double calorimeter was used for temperature stability and control. Experiments were carried out on Ge doped InSb specimens with concentrations of  $10^{14}$ ,  $2.10^{15}$  and  $8.10^{16}$  cm<sup>-3</sup>. Only the first will be discussed here, the second showing similar results and the third, which appears to be degenerate, shows no unusual behaviour.

Typical results for the relaxation peak are shown in Figure 1. The peak height and position scale with  $\omega$ , such that  $\omega\tau \sim 1$  with  $\tau = \tau_0(H) e^{\Delta/k_B T}$ ,  $\Delta \sim 10$  meV, as described previously (2). Looking at all the pure modes, we have found such a relaxation peak only for the two piezoelectrically active modes in this system; a typical non piezoelectric mode behaviour is also shown in Figure 1. The peak position is very sensitive to applied magnetic field and can be shifted upwards by about 5K by application of 7T (2). Previous resistivity measurements (2) also showed that above about 7K the sample is in the  $c_1$  conduction regime due to free holes in the valence band. This strongly suggests the possibility of a piezoelectric interaction between the ultrasonic wave and the free holes, a situation which has been studied in the acoustoelectric effect on the basis of the theory of Hutson and White (3). In particular due to bunching of the charge carriers and their

subsequent relaxation, a relaxation peak is predicted by this theory, of the form:

$$\alpha = \left( \frac{K^2 \omega_c}{2 V_{so}} \right) \left( \frac{1}{1 + \left( \frac{\omega_c}{\omega} + \frac{\omega}{\omega_D} \right)^2} \right) \text{ where } K^2 = \text{electromechanical coupling coefficient,}$$

$V_{so}$  = sound velocity,  $\omega_c = \sigma/\epsilon =$  dielectric relaxation frequency,  $\sigma =$  d.c. electrical conductivity,  $\epsilon =$  static dielectric constant,  $\omega =$  applied angular frequency,  $\omega_D = V_{so}^2/D$ ,  $D = \mu k_B T/e$ , the Einstein relation with  $\mu =$  carrier mobility. The important term in the relaxation is that involving  $\omega_c$  and to first approximation this gives a simple relaxation  $\tau = \omega_c^{-1}$ . This corresponds roughly to what is observed although there is some trouble with the magnetic field dependence of the prefactor of  $\tau$ . Using known values of the above parameters and using a mobility determined from the 77K Hall effect measurements a numerical calculation gives good agreement between the above expression and the experimental results as regards peak attenuation and frequency, temperature and magnetic field dependence.

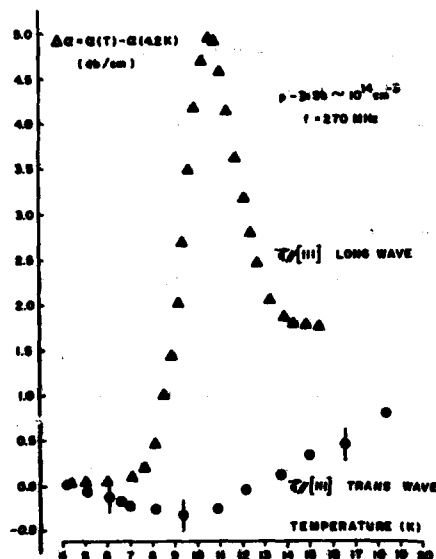


Figure 1

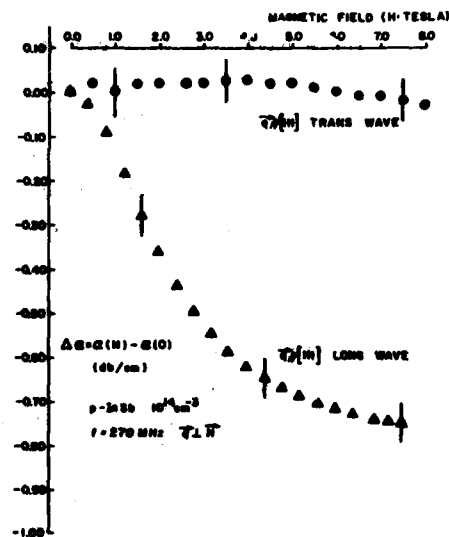


Figure 2

It is now interesting to regard the low temperature behaviour ( $T < 7K$ ) where the mobile carriers are thermally frozen out and the electrical conduction is by hopping of carriers between compensated impurity sites. In this temperature region we observe an important decrease of attenuation with applied magnetic field. As indicated for one case in Figure 2 this magnetic field effect follows the same selection rule as for the relaxation peak. We thus deduce that the interaction mechanism is again piezoelectric, although a numerical calculation clearly shows that this attenuation decrease is not the tail of the relaxation peak. In fact the

situation corresponds physically to that described by Chaikovskii and Gitis (4), who modify the Hutson and White treatment for the case of hopping conduction. For  $\omega > \omega_c$  this gives  $\alpha \sim \text{cte } \sigma$ . At present it is not easy to test this relation regarding the temperature dependence as this is quite weak and the residual attenuation is unknown. However the magnetic field variation of the attenuation is in good agreement with that estimated from the above expression although at present we only have results for the DC magnetoresistance. The crucial test will be provided by comparing the field dependence of the attenuation with the ac magnetoresistance. This study is currently being undertaken.

In summary the present results are in good agreement with the acoustoelectric theory for interaction with free and hopping charge carriers. Further experiments are in progress in an attempt to distinguish unequivocally between this model and that involving absorption by isolated impurity centres.

This work was supported by the Natural Science and Engineering Council of Canada and the Groupe de Recherches sur les semiconducteurs et diélectriques. We are grateful to A. Hikata for participation in some of the early experiments.

#### REFERENCES

- 1) K. Lassman and other papers in Phonon scattering in condensed matter (edited by H.J. Maris) Plenum Press New York (1980).
- 2) J.D.N. Cheeke, G. Madore and A. Hikata, Solid State Communications 38, 755, (1981).
- 3) A.R. Hutson and D.L. White, Jour. App. Phys. 33, 40, (1962).
- 4) I.A. Chaikovskii and M.B. Gitis, Soviet Physics Solid State 22, 1417, (1980).

## ORIENTATIONAL DYNAMICS OF SULPHATE IONS IN POTASH ALUM

A.K. Sood, A.K. Arora, S. Dattagupta and G. Venkataraman

Reactor Research Centre, Kalpakkam 603 102, Tamil Nadu, India

**Abstract.**— The  $A_g$  internal mode of sulphate ion in potash alum is studied by Raman scattering as a function of temperature. Our data suggest that over and above the thermally-activated reorientations of sulphate ion, there is an additional orientational relaxation mechanism which has its origin in cooperative interaction between sulphate ions.

1. **Introduction.**— In potash alum ( $KAl(SO_4)_2 \cdot 12H_2O$ ), the sulphate ion has two orientations<sup>1</sup> with the S-O bonds pointing towards  $Al^{3+}$  or  $K^+$  with probabilities  $p_1$  or  $p_2$  ( $p_1 > p_2$ ). This causes a splitting of the  $A_g$  internal mode of the sulphate ion into two lines<sup>2,3</sup> near  $990\text{ cm}^{-1}$ . In this paper, the area ratio i.e. the ratio of the number of sulphate ions in the two orientations is studied as a function of temperature to unravel features related to reorientations.

2. **Experimental.**— Single crystals of potash alum were cut perpendicular to the (100) axis into a parallelepiped of approximate size  $6 \times 6 \times 5\text{ (mm)}^3$ . The details of the Raman spectrometer are same as reported earlier<sup>4</sup>. The experiments were done at 24 different temperatures between 297 K and 93 K.

3. **Results.**— Figure 1 shows the area ratio. At 297 K, we obtain  $(p_1/p_2) = 2.46 \pm 0.08$ , in agreement with x-ray studies<sup>1</sup>.

In order to interpret the data, we assume first that ions make thermally activated jumps between the two orientations at rates

$$w_{12}^{ph} = \nu_0 \exp(-E'/k_B T), \quad (1)$$

$$w_{21}^{ph} = \nu'_0 \exp - [(E' - E)/k_B T], \quad (2)$$

where  $\nu_0$ ,  $\nu'_0$  are the attempt frequencies.  $E$  is the energy separation between the two orientational potential minima, and  $E'$  is the barrier height as seen from the bottom of the deeper well (see Figure

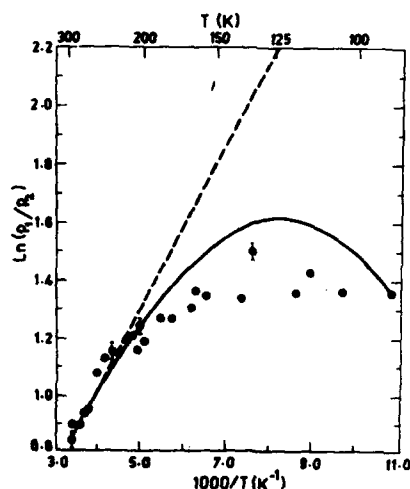


Fig. 1 : Area ratio as a function of temperature. The dots are the observed values. The dashed line corresponds to eq. (3) ( $\gamma = 0$ ) and the solid line is based on a model which includes a temperature-independent relaxation mechanism (i.e.  $\gamma \neq 0$ ).

2). From detailed balance,  $p_1 \overset{\text{ph}}{w}_{12} = p_2 \overset{\text{ph}}{w}_{21}$ , whence

$$\ln(p_1/p_2) = \text{Const.} + E/k_B T \quad (3)$$

The dashed line in figure 1 shows that (3) is obeyed for  $T > 240$  K but is inadequate at lower temperatures.

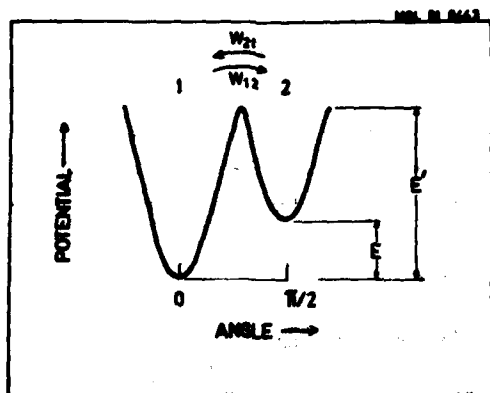


Fig. 2 : Schematic drawing of the angular dependence of the potential well in which  $(\text{SO}_4)^{2-}$  ions reside. 1 and 2 refer to the two orientations of the ion.

The Arrhenius-type approach being inadequate, we now postulate the existence of an additional temperature-independent reorientation mechanism, and write the rates as

$$w_{12} = \overset{\text{ph}}{w}_{12} + \gamma \quad \text{and} \quad w_{21} = \overset{\text{ph}}{w}_{21} + \gamma \quad (4)$$

A plausible physical origin of  $\gamma$  is discussed in Section 5.

4. Raman line shape.— For the  $A_g$  internal mode, the Raman line shape is proportional to

$$F(\omega) = \int_{-\infty}^{\infty} dt \exp(-i\omega t) \langle Q(0) Q(t) \rangle,$$

where  $Q$  denotes the vibrational coordinate. Owing to the random jumps of the two possible orientations, the vibrational frequency of the  $A_g$  mode fluctuates between  $\omega_1$  and  $\omega_2$ . For this situation, the line shapes can be calculated from<sup>5</sup>

$$F(\omega) = \text{Re} \left[ \sum_{a,b=1}^2 p_a (a | [sI - \underline{W} - i\underline{\Omega}]^{-1} | b) \right], \quad (5)$$

Where

$$s = i\omega, \quad \underline{W} = \begin{pmatrix} -W_{12} & W_{12} \\ W_{21} & -W_{21} \end{pmatrix}, \quad \text{and} \quad \underline{\Omega} = \begin{pmatrix} \omega_1 & 0 \\ 0 & \omega_2 \end{pmatrix}.$$

After including the effects of anharmonicity and instrumental resolution<sup>4</sup>, eq. (5) along with (1), (2) and (4) were used to compute the line shapes and also the area ratios. The parameters which resulted in good agreement for the line shapes are:  $\nu_0 = \nu'_0 = 3 \times 10^{11} \text{ sec}^{-1}$ ,  $E = 0.527 \text{ KCal/mole}$ ,  $E' = 1.239 \text{ KCal/mole}$  and  $\gamma = 1.65 \times 10^9 \text{ sec}^{-1}$ . The area ratio extracted by such an analysis is shown with a solid line in figure 1. Clearly it represents better the observed ratios.

5. Origin of .- We now consider the origin of  $\gamma$ . As discussed in detail elsewhere<sup>6</sup>, conceivably arises due to a flip-flop relaxation, i.e. when ion  $i$  makes the orientational jump 1-2 (say), another ion  $j$  simultaneously makes a reverse jump 2-1. Calculations<sup>6</sup> show that flip-flop mechanism does lead to a temperature-independent rate .

#### REFERENCES

1. Larson, A.C. and Cromer, D.T., *Acta Cryst.* **22**, 793 (1967).
2. Krishnan, R.S., Narayanan, P.S. and Venkatesh, G.M., Proc. Fifth Int. Conf. Raman Spec., ed. Schulz (FRG: Freiburg).
3. Eysel, H.H. and Schumacher, G., *Chem. Phys. Lett.* **47**, 168 (1977).
4. Sod, A.K., Arora, A.K., Unadevi, V. and Venkataraman, G., *Pramana* **16**, 1 (1981).
5. Anderson, P.W., *J. Phys. Soc. Japan*, **9**, 316 (1954).
6. Sod, A.K., Arora, A.K., Dattagupta, S. and Venkataraman, G., To appear in *J. Phys. C* (1981).

## SELF-CONSISTENT PHONON CALCULATIONS IN SOLID NITROGEN

T. Wasiutynski

*Institute of Nuclear Physics, Krakow, Poland*

**Abstract.** - Phonon calculation in the self-consistent harmonic approximation were performed for temperature range 0 - 40 K at zero pressure and for pressures range 0 - 10 kbar. The parameters of the intermolecular potential of the "6-exp" form were optimized.

1. **Model.** - On the basis of the earlier formulated self-consistent phonon approximation for the molecular crystals /1/ we studied solid nitrogen at different temperatures and pressures. The approximation is essentially the same as for the atomic crystals /2/ regardless the fact that we have here three extra rotational degrees of freedom for each molecule. The harmonic equation of motion is solved with the effective potential which is given by the convolution of the bare potential with gaussian distribution function. The width of the gaussian is given by the inverse of the displacement-displacement correlation function. Since the latter depends on the phonon frequencies one has to solve the equations selfconsistently.

$$\langle V(\mathbf{R} + \mathbf{u}) \rangle = \frac{1}{\Omega} \int d^3 R' V(\mathbf{R} + \mathbf{R}') \exp[-\frac{1}{2} \mathbf{R}'_{\alpha} \mathbf{R}'_{\beta} \langle u u \rangle_{\alpha\beta}^{-1}] \quad (1)$$

As the bare potential  $V(\mathbf{r})$  we use the empirical atom-atom potential of the "6-exp" form:

$$V(\mathbf{r}) = A \exp(-B\mathbf{r}) - C\mathbf{r}^{-6} \quad (2)$$

Three empirical parameters  $A$ ,  $B$  and  $C$  were optimized in order to get the proper lattice constant  $a = 5.86 \text{ \AA}$  at  $T = 15 \text{ K}$ , lattice energy  $U = 1.73 \text{ kcal/mole}$  and the best overall agreement of the phonon frequencies at  $q = 0$  in the cubic phase. The values of the parameters are listed in table 1 together with the recently published parameters from the ab-initio calculations /3/. As one can see from that table the two sets do not differ very much. The units are of kcal/mole and  $\text{\AA}$ .

Table 1

	A	B	C
present calc	128645	4.0	383
ab-initio /3/	183770	4.037	361

2. **Results.** - The comparison of the calculated and experimental /4/ phonon frequencies in  $\text{cm}^{-1}$  at  $q = 0$  for the  $\alpha\text{-N}_2$  is shown in table 2.

Table 2

Symmetry	Experiment T=15 K /4/	Present calculation	ab-initio calculation /5/
$E_g$	32.3	38.1	39.5
$T_g$	36.3	42.8	48.5
$T_g$	59.7	51.8	70.3
$A_u$	46.8	48.5	48.8
$T_u$	48.4	51.7	48.4
$E_u$	54.0	57.3	55.5
$T_u$	69.4	75.3	72.0

The temperature dependence of the lattice constant and two phonon modes: one of the translational and one of the rotational character are shown on figures 1 and 2.

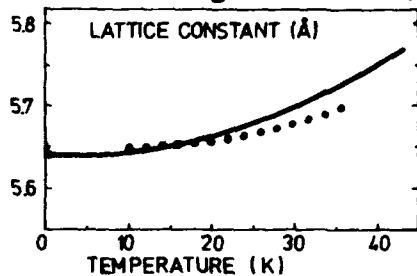


Fig. 1: Temperature dependence of the lattice constant in  $\alpha\text{-N}_2$ . Experimental points from /6/.

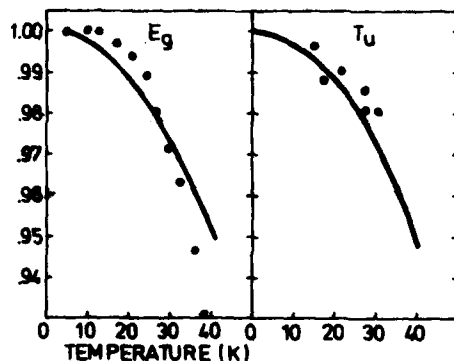


Fig. 2: Temperature dependence of the lowest  $E_g$  and  $T_u$  modes. Experimental points on  $E_g$  /7/ and on  $T_u$  from /8/.



Table 3 shows the comparison between calculated and experimental phonon frequencies in  $\text{cm}^{-1}$  at  $q = 0$  for different pressures in  $\gamma\text{-N}_2$ .

Table 3

Symmetry	p = 4 kbars		p = 5 kbars		p = 8.75 kbars	
	exper	/9/ calo	exper	/7/ calo	exper	/9/ calo
$E_g$	54.2	58.6	58.4	61.4	64.0	72
$E_{1g}$	97.2	82.3	103.6	86.3	114.4	99
$A_{2g}$	-	97.4	-	102.3	-	119
$E_u$	-	68.5	-	71.9	-	84
$E_{1u}$	-	110.9	-	116.7	-	137

3. Discussion. - The temperature dependence presented in figures 1 and 2 shows qualitatively good agreement with the experimental data. One has to notice, however, that the calculated thermal expansion is bigger than the measured one. The opposite situation takes place in the case of the temperature dependence of the rotational mode  $E_g$ . As a conclusion we can say that different anharmonic terms contribute to these two phenomena. Another point with mentioning here is that the intermolecular potential derived for the cubic phase is also valid for high pressure tetragonal phase. Usually this is the weak point because of the difficulties with precisely determining the repulsive part of the intermolecular potential.

#### References

- /1/ T. Wasiutynski, phys.stat.sol.(b)
- /2/ T.R. Keebler, Lattice dynamics of quantum crystals in the book "Dynamical properties of solid", vol.2, p.1, North Holland, 1974
- /3/ R.M. Berns, A. Van der Aveird, J.Chem.Phys. 72, 6107 (80)
- /4/ J.K. Kjems, G. Dolling, Phys.Rev. B11, 1639 (1975)
- /5/ T. Luty, A. Van der Aveird, R.M. Berns, J.Chem.Phys. 73, 5305 (1980)
- /6/ I.N. Krupskii, A.I. Prekhatilev, A.I. Erenburg, Fiz.Niskkhikh Temp. 1, 359 (1975)
- /7/ F.B. Medina, W.B. Daniels, J.Chem.Phys. 64, 150 (1976)
- /8/ R.N. St. Louis, O. Schnepp, J.Chem.Phys. 50, 5177 (1969)
- /9/ M.M. Thiery, V. Chandrasekaran, J.Chem.Phys. 67, 3659 (1977).

## LINEAR CHAIN MODELS AND SOUND VELOCITIES IN MOLECULAR ORGANIC CRYSTALS

C. Ecolivet

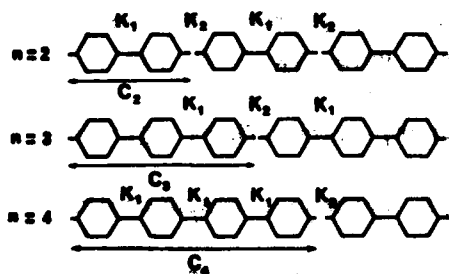
Groupe de Physique Cristalline, E.R.A. au C.N.R.S. n°070015, Université de Rennes, Campus de Beaulieu, 35042 Rennes Cedex, France

**Abstract** Longitudinal sound velocities in crystals of elongated aromatic molecules have been measured by Brillouin scattering and are found to be faithfully described by a simple linear chain model, whereas a similar behaviour is observed for compressibility and thermal expansion. A particular attention has been paid to the p-polyphenyls and polyacenes series.

**1. INTRODUCTION** Despite the width of the aromatic rings ; p-polyphenyls and polyacenes are good examples of chain-like molecules which crystallizes in parallel stacks, themselves parallel to the molecular long axis. This kind of stacking is far from being unusual in molecular and specially in flat molecules crystals which most of the time belong to the monoclinic  $P 2_1/a$  symmetry group. This is exactly what happens for naphthalene, biphenyl, dibenzyl and many others.

We will consider here a simple chain model for crystals of molecules composed of a various number of aromatic rings and look at the sound longitudinal velocities along the stacking direction, intra and intermolecular bonds will be represented by springs of force constants resp.  $K_1$  and  $K_2$ .

**2. LONGITUDINAL SOUND VELOCITIES IN p-POLYPHENYLS and POLYACENES** Let us



consider first the p-polyphenyls which are represented on Fig.1 as a function of the molecular ring number ; the  $C_n$  parameter being the length of the crystallographic period.

It can be shown very easily that the longitudinal sound velocity along the molecular long axis can be written for a molecule with  $n$  rings as :

$$v_n = \frac{C_n}{\sqrt{M_n \left( \frac{1}{K_2} + \frac{n-1}{K_1} \right)}}$$

Fig. 1 Polyphenyls chain model for longitudinal wave propagation.

Where  $M_n$  is the mass of the molecule.

The  $K_1$  value can be obtained from I.R. experiments on biphenyl which frequency mode is about  $334 \text{ cm}^{-1}$  this gives  $K_1 = 450 \text{ N/m}$ . We report in Table 2 the  $K_2$  values

obtained at 300 K and 5 K of the 3 first elements of the polyphenyls series from sound velocities obtained by Brillouin scattering <sup>(1)</sup>.

n	2	3	4
$C_n(\text{\AA})$	9.51	13.62	17.85
$N_A M_n(g)$	154	230	306
300 K {	$V_n(m/s)$	4730	5210
	$K_2(N/m)$	4.60	4.32
5 K {	$V_n(m/s)$	5440	6010
	$K_2(N/m)$	6.08	5.75

Table 1 Intermolecular force constant  $K_2$  for biphenyl p-terphenyl, p-quaterphenyl at room temperature and near liquid helium temperature.

We see on this table an excellent agreement at low temperature when vibrations are more harmonic, it is also noticeable that the effect of  $K_1$  is negligible and it should only be detectable for  $n > 10$ .

n	2	3	
$C_n(\text{\AA})$	8.66	11.16	a) TESLENKO } <sup>(2)</sup> b) AFANASSIEVA }
$N_A M_n(g)$	130	178	
$V_n(m/s)$	3540 <sup>a</sup> 3620 <sup>b</sup>	3860 <sup>c</sup>	c) HUNTINGTON <sup>(3)</sup>
$K_2(N/m)$	3.55 3.71	3.54	

Table 2 Intermolecular force constant  $K_2$  for naphtalene and anthracene at room temperature.

Table 2 give the same results taken from ultrasonic measurements previously reported in the litterature for the 2 first elements of the polyacenes at room temperature.

From these data one can clearly see that these organic crystals which look rather complicated can be surprisingly well described by simple chain models ; moreover these models also describe the effect of deuteration and the absence of sound velocity variation in directions perpendicular to the chains when  $n$  varies.

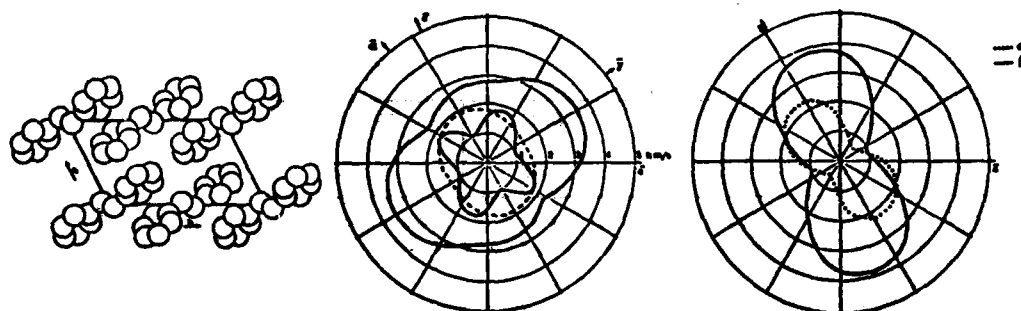
**3. COMPRESSIBILITY and THERMAL EXPANSION ANISOTROPIES** The linear compressibility  $\beta$  which can be expressed as a function of the elastic compliance moduli  $S_{ik}$  writes down for monoclinic crystals

$$\beta = A_1 n_x^2 + A_2 n_y^2 + A_3 n_z^2 + A_5 n_x n_z$$

where  $A_i = \sum_k S_{ik}$

For all the crystals studied here experimental data show the same anisotropy for compressibility and thermal expansion. A counter example found in the littera-

ture was dibenzyl and it motivates a new determination of its elastic properties, for the maximum of compressibility found along the molecular long axis looked rather unrealistic. Structure, sound velocities compressibility and thermal expansion in the  $(\vec{a}, \vec{c})$  plane can be seen on figure 2.



**Fig. 2** Structure, sound velocities, linear compressibility and thermal expansion (left to right) of dibenzyl. The dashed curve in the center diagram is related to the transverse mode polarized along  $\vec{b}$ , whereas the dotted line in the right diagram corresponds to the thermal expansion  $\alpha$  ( $.25 \cdot 10^{-3} \text{ K}^{-1}$  per division) and the other curve to the linear compressibility  $\beta_s$  ( $15 \cdot 10^{-12} \text{ m}^2 \text{ N}^{-1}$  per division)

This is a typical example of the results we can expect for such kind of crystals where the forces have a short range nature.

#### References

1. C. ECOLIVET, Thesis 1981 Rennes.
2. V.F. TESLENKO and G. AFANASSIEVA, quoted in "Molecular Crystals and Molecules" A.I. KITAIGORODSKY Acad. Press New-York, 1973.
3. H.B. BUNTINGTON, S.G. GANGOLI, J.L. MILLS, J. Chem. Phys., **50**, (1969), 3844.

MULTIPHONON PROCESS IN  $\text{NiSO}_4 \cdot 6\text{H}_2\text{O}$ 

L.S.G. Cancela\*, J.G. Ramos and G.M. Gualberto \*

*Instituto de Física Gleb Wataghin, UNICAMP, 13100 Campinas, SP., Brasil*

**Abstract.** - We have measured the Raman spectrum of  $B_2$  phonons in  $\text{NiSO}_4 \cdot 6\text{H}_2\text{O}$  as a function of temperature in the range 80K to 300K. One of these line ( $42\text{cm}^{-1}$  at  $T=300\text{K}$ ) has a temperature dependence of its intensity characteristic of difference combination of two others phonons. Another line of the same symmetry, which would be the sum combination of those two phonons, has a temperature dependence of its intensity characteristic of an one phonon line.

1. **Experiment.** - The single crystals of nickel sulfate used in these experiments were grown at a temperature of  $38^\circ\text{C}$  from a saturated solution. Using the Laue technique, we verified that the crystals grow along the  $[001]$  direction in the form of a truncated pyramid with the  $a$  and  $b$  axes parallel to the edges of the base. The  $A$  and  $B$  faces of the crystal were polished using cerium oxide and mineral oil while the  $C$  face was obtained by cleaving the sample. Since the crystal is hygroscopic, the spectra are obtained soon after the crystal is polished. The source used was the  $4880\text{\AA}$  line of an argon laser since we confirmed that the absorption of this crystal<sup>(1)</sup> is lowest around this line. The power used was limited to 50mW since, with larger powers, the crystal soon becomes opaque. The scattered light was analyzed with a double spex monochromator equipped with F.W. 130 photomultiplier. For measurements ranging from 80K to 300K the sample was mounted in a cold finger Dewar with a temperature control of  $\pm 1\text{K}$ . In this work the usual Raman notation<sup>(2)</sup>  $z(xy)x$  was used, corresponding to  $B_2$  phonons. Raman spectra using several other symmetries were presented elsewhere<sup>(3)</sup>, where the anomalous temperature behavior of the  $42\text{cm}^{-1}$  of the  $B_2$  mode was reported.

2. **Results.** - In Fig. 1 we show the Raman spectrum of  $\text{NiSO}_4 \cdot 6\text{H}_2\text{O}$  obtained using  $z(xy)x$  geometry. We note that the temperature behavior of the two ( $A$  &  $B$ ) lines of  $B_2$  symmetry are different.

\* On leave of absence from Depto. de Física, UFFa.

\* CNPq Research Fellow

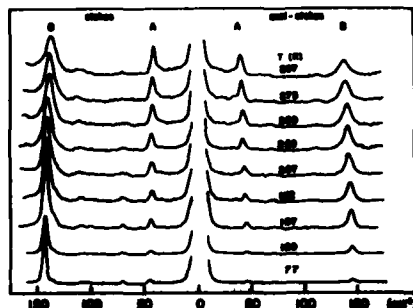


Figure 1. Temperature behavior of the lines A and B of the  $B_2$  symmetry.

In Fig. 2 we present the temperature dependence of the Stokes intensity of the low frequency  $B_2$  line. This behavior suggests the combination phonons process. In the figure we also present the plotting of expression  $(4) n(\nu_a)[n(\nu_b) + 1]$ , where  $\nu_a = 92\text{cm}^{-1}$  and  $\nu_b = 50\text{cm}^{-1}$ , which is the intensity temperature dependence of a difference combination of two phonons.

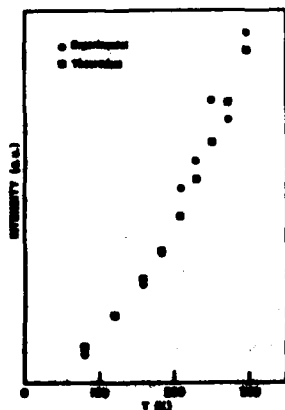


Fig. 2 Temperature dependence of the Stokes intensity of the line A compared with a difference combination process.

In the Fig. 3 we compare the temperature dependence of the two lines (A & B) of the  $B_2$  symmetry. We should note that the high frequency line has a behavior which is characteristic of one phonon processes.

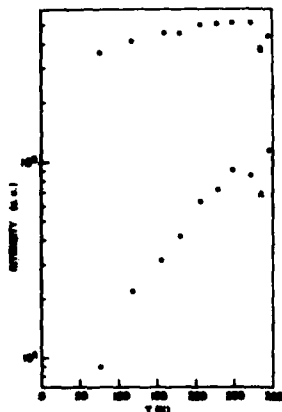


Fig. 3 Temperature dependence of the Stokes intensities of the lines A and B.

**Discussion.** - Our results (Fig. 2) show that the  $B_2$  line which appears at  $42\text{cm}^{-1}$  (A) at room temperature has a temperature dependence of its Stokes and anti-Stokes intensities characteristic of a difference combination of two phonons. The best fit of the experimental data gives  $92\text{cm}^{-1}$  and  $50\text{cm}^{-1}$  for the two phonon frequencies involved in that difference combination. This behavior is characteristic of crystals containing molecular groups, as is the one under study<sup>(4)</sup>. The sum combination of these two phonons, another  $B_2$  phonon at  $142\text{cm}^{-1}$  (B) at room temperature, is also observed; however the temperature dependence of its intensity is characteristic of an one phonon process. This could be due to accidental degeneracy of the two phonons combination with an one phonon line.

#### References.

1. S.V. Grun-Grzhimeilo, N.A. Brilliantov, R.K. Sviridova and O.N. Sukhanova, *Sov. Phys. Crystallography* 5, 2, 268 (1960).
2. T.C. Damen, S.P.S. Porto and B. Tell, *Phys. Rev.* 142, 570 (1966).
3. L.S.G. Cancela and G.M. Gualberto, *J. of Phys. Chem. Solids*, submitted.
4. S.S. Mitra in "Optical Properties of Solids" Ed. by S. Nudelman and S.S. Mitra, Plenum Press, p. 333 (1969).

## INTERNAL AND EXTERNAL PHONONS IN MONOCLINIC TETRACYANOETHYLENE

S.L. Chaplot<sup>\*\*\*</sup>, A. Mierzejewski<sup>\*\*</sup>, J. Lefebvre<sup>\*</sup>, G.S. Pawley<sup>\*</sup> and T. Luty<sup>\*\*</sup><sup>\*</sup>Department of Physics, University of Edinburgh, Scotland<sup>\*\*</sup>I-4, Technical University of Wrocław, Wrocław, Poland<sup>\*\*\*</sup>ILL, Grenoble, France<sup>\*\*\*</sup>Nuclear Physics Division, Bhabha Atomic Research Center, Bombay, India

**Abstract.**— Dispersion curves of 12 external and 10 internal phonon modes have been measured in the  $a^*$ ,  $b^*$  and  $c^*$  directions. The internal dispersion curves correspond to the 5 low-frequency vibrations of the free molecule and they exhibit a significant proportion of lattice mode character involving both translational and librational motions. Recent lattice dynamical calculations, in which several internal modes are included, have yielded neutron scattering cross-sections which have made possible to assign the observed molecular vibrations.

1. **Introduction.**— Tetracyanoethylene (TCNE), one of the most common acceptors in electron donor-acceptor (EDA) complexes, forms two crystalline phases, monoclinic ( $P2_1/n$ ) stable above 292 K and cubic ( $Im\bar{3}$ ) stable below this temperature. Warming the cubic phase causes the transition to the monoclinic structure, but this phase can be cooled down to helium temperatures without a reverse transition, enabling inelastic neutron scattering experiments to be made at the most favourable temperature. The measurements of phonon dispersion curves are complete in the low frequency range, 0-6 THz and are presented here. As the TCNE molecule has many internal vibrations at low frequencies, it is essential to include the vibrations in calculations of one-phonon neutron scattering cross-sections. Here, we report shortly a model for the same.

2. **Experimental.**— The crystal of monoclinic TCNE of about  $9 \text{ cm}^3$  was grown by the vapour deposition technique and slowly cooled to 5 K ( $\pm 0.5 \text{ K}$ ) at rate of 10 K/hour. The phonon dispersion curves have been measured at the Institute Laue-Langevin on the triple axes spectrometer IN3. Focussing monochromators of pyrolytic graphite (002) and Cu (111) were used in the low and high frequency region, along with pyrolytic graphite (002) analyser. Graphite (002) filter was used in either the incident or scattered beam as convenient. The FWHM in a vanadium scan was 0.1 THz. The crystal was



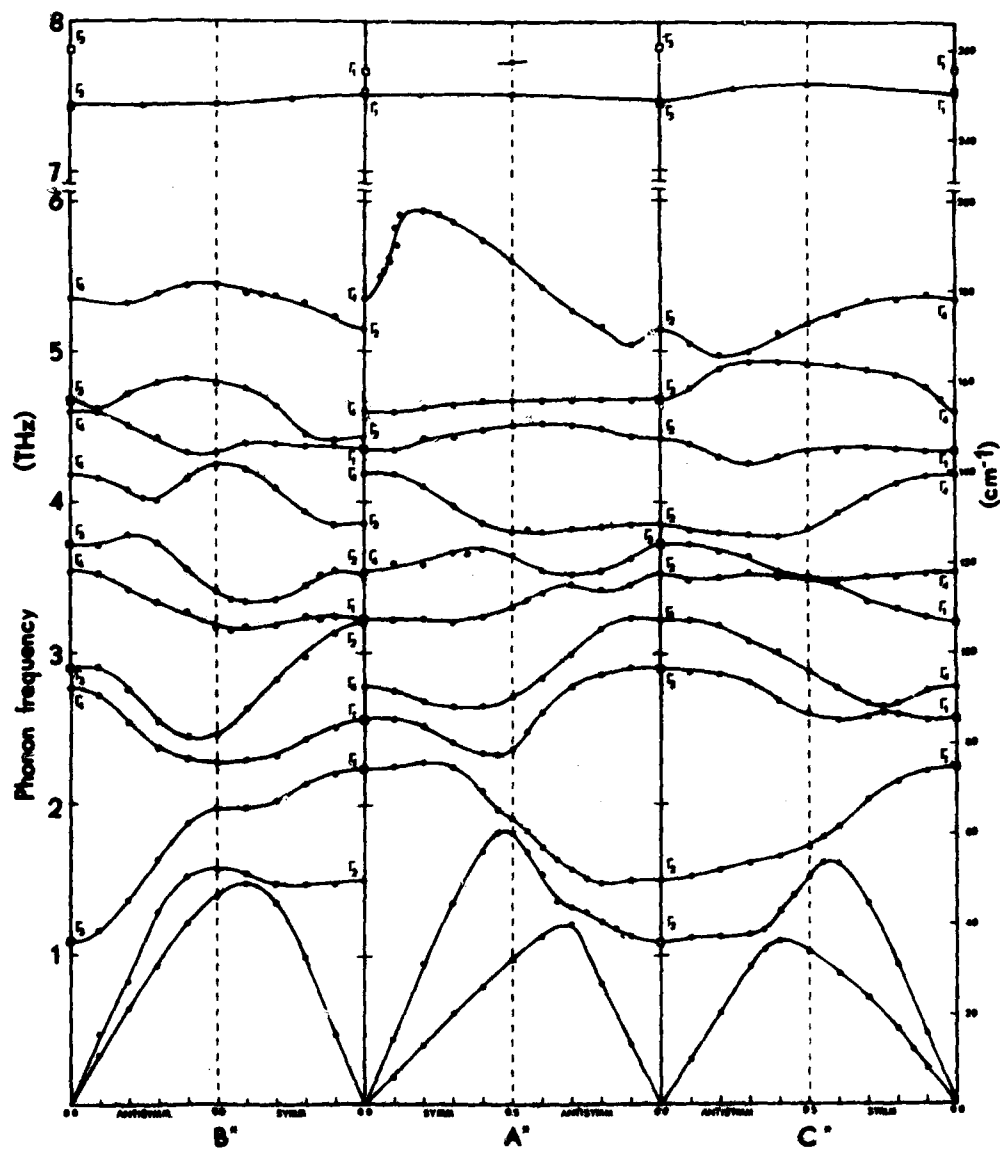


Figure 1. Experimental phonon dispersion curves in the monoclinic TCNE at 5 K. Frequencies measured by Raman spectroscopy are indicated by the square points.

oriented in  $a^*b^*$ ,  $b^*c^*$  and  $c^*a^*$  planes in different experiments. Constant Q scans were usually employed with constant E scans in a few cases.

Results of the measurements are shown on Figure 1. Most of the phonon frequencies are confirmed to within 0.05 THz. All the zone centre frequencies are well confirmed and assigned experimentally using group theoretical selection rules. The dispersion of the highest frequency branch in  $a^*$  direction needed special attention. This unusual dispersion has been confirmed in both  $a^*b^*$  and  $a^*c^*$  orientations; however, its origin has to be further investigated.

3. Theory.— The external and lowest internal phonon dispersion relations have been calculated for  $a^*$ ,  $b^*$  and  $c^*$  directions, within an extended lattice dynamical model. The secular equation,

$$\underline{D}(q) \underline{U}(q) = \omega^2(q) \underline{m} \underline{U}(q),$$

has been solved. The  $26 \times 26$  /with 7 free molecule vibrations included/ dynamical matrix has been constructed from the second derivatives of the crystal potential, assumed to be the sum of an external and an internal part. The internal potential contributes to the self force constant only and is related to the free molecule internal frequencies. The contribution to the force constants from the external potential can be easily obtained using nonbonded atomic pair potential of "6-exp" type. The mass matrix  $\underline{m}$  has elements

$$m_{\alpha\beta}(kk') = \delta_{kk'} \sum_i m(i) \{ \underline{e}_{\alpha}(ik) \cdot \underline{e}_{\beta}(ik) \},$$

where  $\underline{e}_{\alpha}(ik)$  is the atomic displacement per unit displacement of an atom  $i$  within the molecule  $k$  in the  $\alpha$ -th degree of freedom. From the calculations we note that the phonons of frequencies below 5 THz cannot be labelled as purely external or internal. The phonon eigenvectors were used to estimate the one-phonon neutron scattering cross-sections. These were largely consistent with the experiments, thus supporting assignments of the phonon eigenvectors. The agreement between the calculated and experimental phonon frequencies was usually about 10 - 20%. This leaves scope for an improvement of the assumed external potential function. We feel, however, that a molecular shell model would be necessary for a correct description of the lattice dynamics.

## HARMONIC AND ANHARMONIC REPRESENTATION OF LIBRATIONAL MOTIONS IN MOLECULAR CRYSTALS

B. Kuchta and T. Luty

*Institute of Organic and Physical Chemistry, Technical University, 50-370 Wrocław, Poland*

**Abstract.**— The orientational crystal potential, represented as a surface in  $n$ -dimensional space spanned on librational normal coordinates, has been calculated for  $\alpha$ -N<sub>2</sub>,  $\alpha$ -O<sub>2</sub> and  $\beta$ -O<sub>2</sub> crystals and compared with its harmonic representation. Significant differences in symmetries of the surfaces show that molecular librations are highly anharmonic and that any proper description of the excitations in molecular crystals has to take into account the full symmetry of an exact orientational crystal potential.

1. Introduction.— The harmonic approximation which is commonly used in the lattice dynamics calculations of molecular crystals is believed to be well satisfied for translational degrees of freedom but not for rotational ones. Results of calculations /librational phonon frequencies/ for diatomic molecular crystals, in particular for solid nitrogen [1], support the conclusion. In the present paper we shall discuss the problem of a description of librational excitations at the center of Brillouin zone in crystals, where a rotational part of the crystal potential can be separated. For the discussion we choose nitrogen and oxygen crystals for the following reasons: the ab initio intermolecular N<sub>2</sub>-N<sub>2</sub> potential is known [2], and the crystal structures of oxygen phases /one molecule in a unit cell/ simplify a representation of the rotational potential.

2. Rotational potentials.— In crystals where molecules occupy center of inversion sites, the rotational crystal potential for zero wave vector can be separated from translational part and written as an expansion with respect to a complete set of rotational coordinates. It is convenient, for our purpose, to expand the potential in terms of normal coordinates of librational excitations and to represent as a surface spanned on the coordinates. The librational normal coordinates are the eigenvectors of the harmonic dynamical matrix corresponding to the particular normal mode / A<sub>g</sub>, B<sub>g</sub> for monoclinic  $\alpha$ -O<sub>2</sub>, E<sub>g</sub> for hexagonal  $\beta$ -O<sub>2</sub> and E<sub>g</sub>, T<sub>g</sub>, T<sub>g</sub> for cubic  $\alpha$ -N<sub>2</sub>/. A qualitative difference between harmonic and anharmonic represen-

tation of the librational excitations is clearly seen from Figures 1 and 2. In the calculations of the rotational energy surfaces we have used the "6-exp" atom-atom potential, optimized to the crystal structures of solid oxygen. The striking differences in the sym-

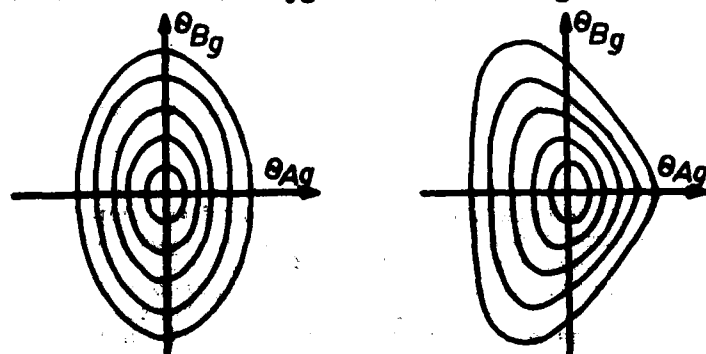


Fig. 1

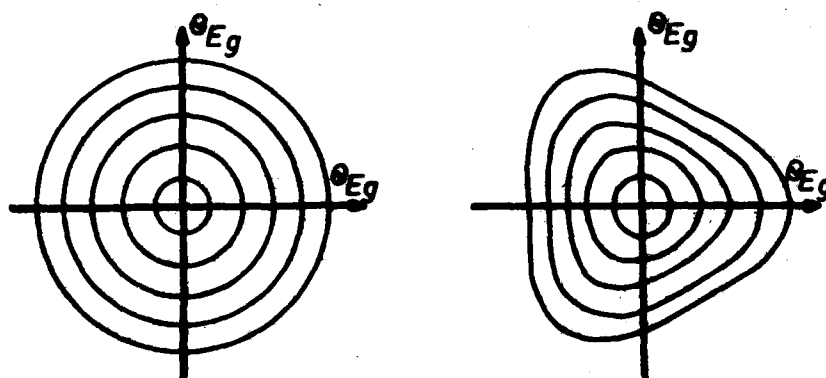


Fig. 2

Figures 1 and 2. The rotational energy surfaces for  $\alpha$ -O<sub>2</sub> /Fig. 1/ and  $\beta$ -O<sub>2</sub> /Fig. 2/ crystals in harmonic /on left/ and anharmonic /on right/ representations.

metry of the surfaces suggest that the angular motions of the molecules can be quite different in character than the librational oscillations around a fixed axis. It is also seen that any quadratic /harmonic/ or multiquadratic /quasi-harmonic/ representation of the potential increases its symmetry and cannot properly describe the librational excitations in the crystal. The important point is to take into account the odd powers in the potential expansion.

3. Librational frequencies.— An application of the perturbation theory allows one to take into account an influence of the anharmonic terms in the rotational potential on librational phonon frequencies [3]. Within the method, librations of the molecules are treated as coupled anharmonic oscillators in an exact rotational crystal potential. Figure 3 shows cross-sections of the irreducible part of the rotational energy in the cubic phase of nitrogen crystal, cor-

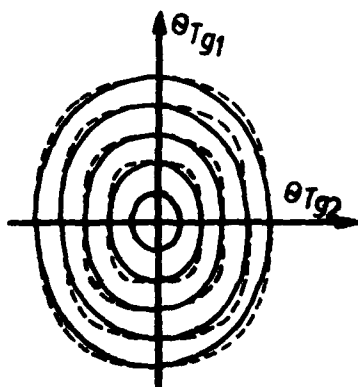


Fig. 3 /see text/

Table - Librational phonon frequencies /in  $\text{cm}^{-1}$ / at  $q = 0$  in  $\alpha\text{-N}_2$  crystal.

Mode	Harmonic [1]	SCP [1]	Anharmonic [3]	Experiment [4]
$E_g$	40.8	39.5	32.0	32.3
$T_g$	50.7	48.5	36.3	36.3
$T_g$	74.3	70.3	60.5	59.7

anharmonic representation of the librational excitations. Although the perturbation theory does reproduce the librational phonon frequencies very well, it does not give however a unique interpretation of the molecular motions. The symmetry of the real orientational potential suggests that angular molecular motions can be quite different in character than an oscillator and that any proper description of the excitations in molecular crystals has to take into account the full symmetry of the crystal potential.

#### References.

- [1] T. Luty, A. van der Avoird and R.M. Berns, J. Chem. Phys., **73**, 5305 (1980);
- [2] R.M. Berns and A. van der Avoird, J. Chem. Phys., **72**, 6107 (1980);
- [3] B. Kuchta and T. Luty, in preparation,
- [4] I.K. Kijems and G. Dolling, Phys. Rev., **B11**, 1639 (1975).

## TRANSLATIONAL - ROTATIONAL COUPLING IN s-TRIAZINE CRYSTAL

T. Luty

*Institute of Organic and Physical Chemistry, Technical University,  
50-370 Wrocław, Poland*

**Abstract.**— An anomalous dispersion of transverse acoustic phonons, related to the ferroelastic phase transition in s-triazine crystal, have been analyzed. The dispersion relation has been found from the harmonic dynamical matrix which includes translational-rotational coupling. For the nearest neighbours interactions, the relation contains two competitive terms followed from direct and indirect translational-translational coupling. When the indirect interactions are assumed to be temperature dependent, the relation reproduces the observed dispersion curves almost exactly.

1. **Introduction.**— It has long been known that in molecular crystals there should be a static coupling between rotations and translations of molecules. Recently well studied s-triazine crystal is a good example to illustrate the problem of the coupling in ordered molecular crystals. A weakly first order transition at 200 K is from a high temperature, trigonal phase  $/R\bar{3}c/$  to a low temperature, monoclinic phase  $/C2/c/$  [1]. The ferroelastic distortion of s-triazine is assisted by a pronounced softening of the transverse acoustic modes in trigonal  $\Sigma$  and  $\Lambda$  directions [2], causing an instability of the  $c_{44}$  elastic constant. The anomalous behaviour of the elastic constant has been recently interpreted [3] in terms of the mean field theory as a result of coupling between the shear strain  $e_{xz}/e_{yz}/$  and molecular rotations  $R_y/R_x/$ . The aim of the present treatment is to interpret the anomalous and extended in the Brillouin zone dispersion of the transverse acoustic modes in terms of translational-rotational coupling. As the phonons in s-triazine have been found to be well defined and underdamped down to  $T_c$ , the analysis is based on harmonic dynamical matrix.

2. **Dynamical matrix.**— The harmonic potential energy of a molecular crystal can be written in terms of dynamical matrix elements as,

$$V_h = \frac{1}{2} \sum_q \sum_{kk'} \sum_{ij} \left[ D_{ij}^{TT}(q, kk') u_i(qk) u_j^*(qk') + D_{ij}^{TR}(qkk') u_i(qk) \theta_j^*(qk') \right. \\ \left. + D_{ij}^{RT}(qkk') \theta_i(qk) u_j^*(qk') + D_{ij}^{RR}(qkk') \theta_i(qk) \theta_j^*(qk') \right] \quad (1)$$

where  $\underline{u}(\mathbf{qk})$  and  $\underline{\theta}(\mathbf{qk})$  are translational and rotational displacements of the sublattice  $k$ , respectively. The energy is decoupled into noninteracting parts, each designated by a specific direction of wave-vector  $\mathbf{q}$ . A further decoupling can be done by a group-theoretical analysis. For the high temperature, trigonal phase of s-triazine, the 12 dispersion curves in the  $\Lambda$  direction can be classified as:  $2\Lambda_1 \oplus 2\Lambda_2 \oplus 4\Lambda_3$  with  $\Lambda_3$  being double degenerate mode. As the transverse acoustic mode which shows an anomalous dispersion transforms according to  $\Lambda_3$  irreducible representation /as well as 3 optical branches/ we have to extract a part of the crystal potential energy which corresponds to this symmetry. It is easy done when a new set of coordinates /as follow from projection operators/ is introduced,

$$v_j(\mathbf{q}) = \frac{1}{2} [u_j(\mathbf{q1}) + u_j(\mathbf{q2})], \quad w_j(\mathbf{q}) = \frac{1}{2} [u_j(\mathbf{q1}) - u_j(\mathbf{q2})],$$

$$\varphi_j(\mathbf{q}) = \frac{1}{2} [\theta_j(\mathbf{q1}) + \theta_j(\mathbf{q2})], \quad \vartheta_j(\mathbf{q}) = \frac{1}{2} [\theta_j(\mathbf{q1}) - \theta_j(\mathbf{q2})],$$

for  $j = 1, 2$ . Now, the irreducible part of the crystal energy corresponding to the two-dimensional representation  $\Lambda_3$  contains two parts with identical eigenvalues and for further discussion we can use only one of them, reducing the problem to 4-dimensional one. We have,

$$\begin{aligned} v_h(\Lambda_3) = \frac{1}{2} \sum_{\mathbf{q} \in \Lambda} [ & a_+(\mathbf{q}) v_1^2(\mathbf{q}) + a_-(\mathbf{q}) w_2^2(\mathbf{q}) + 2A_-(\mathbf{q}) w_2(\mathbf{q}) \varphi_2(\mathbf{q}) + \\ & + 2A_+(\mathbf{q}) v_1(\mathbf{q}) \vartheta_1(\mathbf{q}) + 2D_+(\mathbf{q}) v_1(\mathbf{q}) \varphi_2(\mathbf{q}) + \\ & + 2D_-(\mathbf{q}) w_2(\mathbf{q}) \vartheta_1(\mathbf{q}) + \omega_+(\mathbf{q}) \varphi_2^2(\mathbf{q}) + \omega_-(\mathbf{q}) \vartheta_1^2(\mathbf{q}) + \\ & + 2\delta(\mathbf{q}) \varphi_2(\mathbf{q}) \vartheta_1(\mathbf{q}) ], \end{aligned} \quad (2)$$

with coefficients being proper combinations of dynamical matrix elements. The translational-rotational coupling is given by  $D$ 's and  $A$ 's coefficients. It has to be stressed that in the limit  $\mathbf{q} \rightarrow 0$  the above expression reduces to the harmonic part of the internal energy in the mean field theory.

To analyze dispersion of the transverse acoustic mode we have to solve an equation of motion for the coordinates and, with an assumption that internal strains given by coordinates  $w_2, \varphi_2$  and  $\vartheta_1$  respond statically to the strain given by  $v_1$  /the acoustic mode/ one gets,

$$\omega_{TA}^2(q) = \frac{1}{m} \left[ a_+(q) - D_+(q) G_{22}^{-1}(q,0) D_+^*(q) - A_+(q) G_{33}^{-1}(q,0) A_+^*(q) \right] \quad (3)$$

$G^{-1}(q,0)$  is the static phonon susceptibility corresponding to the optical phonons which are coupled /the same symmetry/ to the acoustic phonon. An exact analysis of the susceptibility shows that the element  $G_{22}^{-1}(q,0)$  follows from an effective orientational potential: a sum of rotational-rotational self term and indirect orientational potential given by translational-translational interactions,  $a_-(q)$  and translational-rotational coupling  $A_-(q)$ .

3. Results.— In general, the relation (3) is rather complicated but in the case of s-triazine crystal, where the short range interactions are dominant we can limit ourselves to the nearest neighbours and then the relation can be written in a simplified form as,

$$\omega_{TA}^2(q) = B_q \sin^2 \beta(q) - C_q \sin^2 2 \beta(q), \quad (4)$$

with the phase factor  $\beta(q)$ . The first term describes dispersion of the acoustic phonon due to the direct translational-translational coupling, while the second term, responsible for an anomalous dispersion, follows from indirect interactions due to translational-rotational coupling. When the relation is generalized by making the indirect interactions temperature dependent /as in the mean field theory, for example/ it does reproduce the observed dispersion curves [2], at different temperatures, almost exactly. As it is seen from relation (4) a stability limit is achieved for  $C_q(T_c) = \frac{1}{4} B_q$ .

#### References.

- [1] J.H. Smith and A.I.M. Rae, J. Phys., **C11**, 1761 (1978),
- [2] I.U. Heilman, W.D. Ellenson and J. Eckert, J. Phys., **C12**, 1485 (1979),
- [3] J.C. Raich and E.R. Bernstein, J. Chem. Phys., **23**, 1955 (1955) (1980).



RAMAN SCATTERING SPECTRA OF  $\text{Rb}_2\text{ZnCl}_4$  UNDER UNIAXIAL STRESS

N.E. Massa

*Behlen Laboratory of Physics, University of Nebraska, Lincoln, Nebraska  
68588, Canada*

**Abstract.** - The Raman scattering of  $\text{Rb}_2\text{ZnCl}_4$  under uniaxial stress up to 300 bars on the  $c$  and  $a$  axis (orthorhombic  $D_{2h}^{16} - P_{\text{nam}}$ ) has been measured in the incommensurate phase at room temperature and at 82 K. A downward shift in frequency has been observed in those bands related with bending and stretching modes of the  $\text{ZnCl}_4$  free molecule. Unlike  $\text{K}_2\text{SeO}_4$  in the same stress range, the study of the soft mode, assigned as amplitude by Wada et al.<sup>(1)</sup>, does not show a shift toward lower frequencies.

$\text{Rb}_2\text{ZnCl}_4$  is among the family of  $\text{ABX}_4$  compounds that are being intensively studied and have a structurally modulated incommensurate phase. It undergoes three phase transitions at  $T_I = 303$  K,  $T_{II} = 94$  K,  $T_{III} = 75$  K<sup>(2)</sup>, from the prototypic orthorhombic paraelectric ( $D_{2h}^{16} - P_{\text{nam}}$ ;  $Z = 4$ ) into the incommensurate phase at room temperature to the ferroelectric (ferrielectric?)<sup>(3)</sup> ( $C_{2v}^9 - Pna2_1$ ;  $Z = 12$ ) to a likely monoclinic phase, respectively. The axes are choiced such that in the orthorhombic phase  $b > a > c$  ( $b = \sqrt{3}c$ ,  $a$ : pseudo hexagonal axis).

Crystals were obtained from slow evaporation of an aqueous solution of  $\text{RbCl} : \text{ZnCl}_2$  in a 2:1 ratio. They resulted in oriented single crystal plates about  $2 \times 3$  cm ( $a \times c$ ) and 3 mm thick from where samples of about  $3 \times 1.2 \times 3.5$  ( $a \times b \times c$ ) mm were cut. These, after polished and under the microscope, showed good extinction and no macroscopic defects.

Measurements were made with the stress apparatus<sup>(4)</sup> inserted in a conventional dewar. Data were collected on floppy disks and plotted on a digital  $x - y$  recorder. Uniaxial stress was applied at room temperature and 82 K in steps of about 40 bars along the paraelectric  $a$  and  $c$  axis.

Lattice and bending internal modes are found in the  $0 - 160 \text{ cm}^{-1}$  spectra span and those associated with stretching are in the  $260$  to  $320 \text{ cm}^{-1}$  region. In zero stress measurements at 298 K and 82 K, the spectral features agree with those reported by Wada et al.<sup>(1)</sup> and will not be discussed here. Fig 1 (a,b) shows the room temperature results of spectra under stress for the  $a(cc) b$  and  $c(aa) b$  orientations. It can be seen that the most intense bands, associated with molecular bending, have a definitive frequency downshift that becomes more pronounced in the stretching region, shown in fig 1b. A small but reproducible increase in the splitting between the line at  $145 \text{ cm}^{-1}$  and its lower frequency shoulder at about  $124 \text{ cm}^{-1}$  seems

to occur at about 30 - 50 bars as shown in fig 2. This may be interpreted as if  $\text{Rb}_2\text{ZnCl}_4$  goes from an elastic region at lower stress to a plastic like behavior in which the downward frequency shift occurs. Much weaker lattice modes show some increase in relative intensity but no change in the apparent peak position.

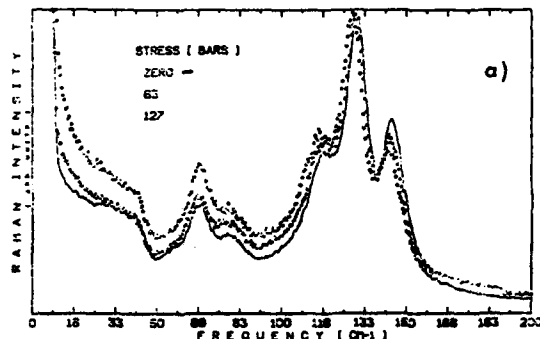
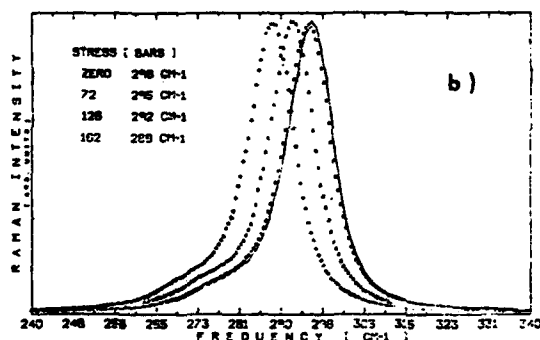


Fig 1.

(a) Effect of uniaxial stress on Ag phonons at room temperature in the a(cc)b geometry. stress along a



(b) Same but c(aa)b geometry in the stretching region. stress along c

To discuss the effect of stress on the internal modes one should first remember that, due to the chlorine natural isotopic abundance, the spectra will contain the normal modes of  $\text{ZnCl}_4^{35}$ ,  $\text{ZnCl}_3^{35}\text{Cl}^{37}$ ,  $\text{ZnCl}_2^{35}\text{Cl}_2^{37}$ ,  $\text{ZnCl}^{35}\text{Cl}_3^{37}$ ,  $\text{ZnCl}_4^{37}$ . A basic internal mode spectrum can be thought as a number of Raman components of an envelope, that is resultant from the Raman spectra of the most abundant varieties.<sup>(\*)</sup> Thus, any interaction of the  $\text{ZnCl}_4$  sublattice will be disrupted by the effect of stress on the short range interactions. An increase in uniaxial stress will tend to lower the symmetry resulting in Raman frequencies closer to those found for glassy  $\text{ZnCl}_2$ .<sup>(6)</sup>

This point is emphasized by similar band profile of the stretching region in the glass (vv) and that for the a(cc)b geometry in the crystal. Three weak features observed with crossed polarizers in the glass also appear in  $\text{Rb}_2\text{ZnCl}_4$  as

<sup>(\*)</sup> Wu and Sutherland<sup>(5)</sup> estimated the relative percent age of various isotopic compositions for  $\text{CCl}_4$  to be 31.6, 42.2, 21.2, 4.7 and 0.4 respectively.

weak overlapping bands raising the likelihood that tetrahedral  $\text{ZnCl}_4$  units form a polymer-chain-like structure in  $\text{Rb}_2\text{ZnCl}_4$ .

Further,  $\text{Rb}_2\text{ZnCl}_4$  is known to contain commensurate domains and incommensurate domain walls <sup>(7)</sup> that will justify plastic behavior and a lower yield to stress in the incommensurate phase.

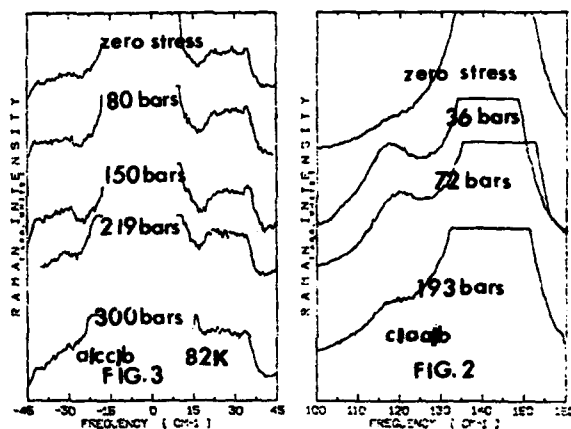
On the other hand, the Ag and B2g spectra have been studied in the ferroelectric phase at 82 K. No change in frequency has been found. Particularly, the broad features assigned as amplitudon and a temperature dependent phonon (shown in fig. 3) do not go down in frequency either as stress is applied along a or c in contrast with the  $\text{K}_2\text{SeO}_4$  amplitudon behavior <sup>(8)</sup>, at 82 K and in the same stress range. This result is consistent with the view that in  $\text{Rb}_2\text{ZnCl}_4$  long range interactions are weak and the folding of the Brillouin zone, i.e. reduction of the coherent length by the tripling of the unit cell below 94 K, is still operative at 82 K and precludes the observation of any significant stress induced change on those anharmonically coupled phonons.

Fig 2 Uniaxial stress induced changes on the shoulder of  $145\text{ cm}^{-1}$  band.

stress along c

Fig.3 Amplitudon - phonon coupled band from zero to 300 bars

stress along a



**Acknowledgments:** The author is thankful to Professor R. Kirby for fruitful discussions during the development of the present investigation and to Professor S.S. Jaswal for reading the manuscript.

- (1) M. Wada, A. Sawada, Y. Ishibashi, J. Phys. Soc. (Japan) **47**, 1185 (1979).
- (2) P. Gunter, R. Santuary, F. Rohner, H. Arend, W. Seidenbusch, Sol St. Comm. **37**, 883 (1981). Also M. Wada, A. Sawada, Y. Ishibashi, J. Phys. Soc. (Japan) **50**, 531 (1981).
- (3) S. Sawada, T. Yamaguchi, N. Shibayama, J. Phys. Soc. (Japan) **48**, 1395 (1980).
- (4) W. Nieveen, R.D. Kirby, unpublished.
- (5) C.K. Wu, B.G.G.M. Sutherland, J. Chem. Phys. **6**, 114 (1938).
- (6) F. Aliotta, G. Maisano, P. Migliardo, C. Vasi and F. Wanderlingh, G.P. Smith, R. Triolo, J. Chem. Phys. **75**, 613, (1981). Also, S. Biggin, J.E. Enderby, J. Phys. C **14**, 3129 (1981).
- (7) R. Blinc, V. Rutar, B. Topic, F. Milia, J.P. Aleksandrova, A.S. Chaves, R. Gassinelli, Phys. Rev. Lett. **46**, 1406, (1981) and references there in.
- (8) M.E. Massa, F.G. Ullman, J.R. Hardy, Proc, VIIth International Conference in Raman Spectroscopy, Ottawa, Canada, 1980.

## SPIN-LATTICE INTERACTION IN CERIUM ETHYLSULPHATE

F.W. Sheard

*Department of Physics, University of Nottingham, Nottingham NG7 2RD, England*

**Abstract:** The enhancement of the Schottky specific-heat peak of cerium ethylsulphate has been explained by Fletcher and Sheard using a model in which the  $\text{Ce}^{3+}$  ion levels are coupled to a temperature dependent lattice strain mode. This theory is used to calculate the temperature dependence of the magnetic susceptibility, which is most sensitive to the effects of the lattice mode when the magnetic field is perpendicular to the trigonal axis. The experimental results support the theory but a detailed comparison is not possible owing to absence of data in the crucial 4-13K range.

The thermodynamic behaviour of cerium ethylsulphate has been studied by Fletcher and Sheard<sup>1</sup> using a model in which the two lowest crystal-field levels of the  $\text{Ce}^{3+}$  ion are coupled to a lattice strain mode. This model has accounted for the observed enhancement of the Schottky specific-heat peak<sup>2</sup> and also for the temperature dependence of the electric susceptibility<sup>3</sup>.

A basic feature of the model is the temperature dependence of the energy separation  $E_s$  between the two lowest  $\text{Ce}^{3+}$  Kramers doublets, which form an effective spin- $\frac{1}{2}$  system. This temperature dependence arises from the coupling of the spin- $\frac{1}{2}$  system to a lattice strain. A thermodynamic analysis showed that for zero external stress the level separation and lattice strain varied smoothly between high and low temperature limits. At temperature  $T$  the separation  $E_s(T)$  is determined self-consistently by the equation

$$E_s(T)/E_{s0} = 1 + \Gamma \tanh\{E_s(T)/2kT\},$$

where  $\Gamma$  is a dimensionless spin-lattice coupling parameter and  $E_{s0}$  is the high-temperature splitting. At low temperatures the splitting is  $E_s(0) = E_{s0}(1 + \Gamma)$ .

Assuming that an external magnetic field does not affect the separation  $E_s$  but serves only to split the two Kramers doublets, the magnetic susceptibility is given by

$$\chi = \frac{N\mu^2}{4kT} \left[ (g_1^2 + g_2^2) + i(g_1^2 - g_2^2) \tanh\left\{\frac{E_s(T)}{2kT}\right\} \right],$$

where  $g_1$  and  $g_2$  are the g-factors of the lower ( $m_j = \pm 5/2$ ) and upper ( $m_j = \pm 1$ ) Kramers doublets,  $\mu$  is the Bohr magneton and  $N$  is the number of Ce ions.

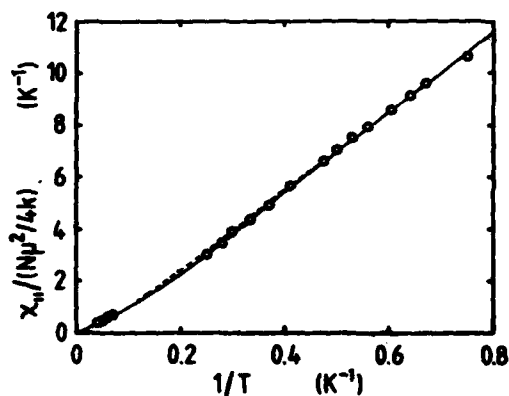


Fig 1: Temperature dependence of parallel susceptibility. See text for explanation of theoretical curves.

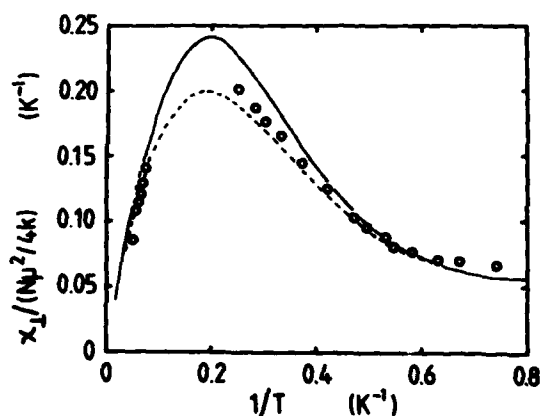


Fig 2: Temperature dependence of perpendicular susceptibility.

In both low and high temperature limits  $\chi$  varies linearly with  $1/T$ :  $\chi \propto N\mu^2 g_1^2/4kT$  ( $kT \ll E_s$ ) and  $\chi \propto N\mu^2 \frac{1}{2}(g_1^2 + g_2^2)/4kT$  ( $kT \gg E_s$ ). This behaviour is illustrated in figure 1 for the parallel susceptibility  $\chi_{||}$  (field parallel to three-fold axis). The solid curve corresponds to the Fletcher and Sheard model with the parameters used to fit the specific-heat data ( $E_s(0) = 7.1K$ ,  $\Gamma = 0.68$ ) and the  $g$ -values taken from EPR data<sup>4</sup> ( $g_1^H = 3.7$ ,  $g_2^H = 1.0$ ). The dashed curve corresponds to a constant separation  $E_s = 7.1K$ , equal to the low-temperature value of the Fletcher-Sheard model. There is a small difference between these curves in the 3-10K range but the experimental data of van den Broek and van der Marel<sup>5</sup> cannot distinguish between them.

For the perpendicular susceptibility  $\chi_{\perp}$  shown in figure 2 the temperature dependence is more dramatic since, when the field is perpendicular to the three-fold axis,  $g_1^{\perp} = 0.20$  is much less than  $g_2^{\perp} = 2.2$ <sup>4</sup>. The experimental points deviate significantly from the dashed curve (constant  $E_s$ ) in the direction of the curve for the spin-lattice coupling model but the parameters obtained from the specific-heat data do not give a good fit. Unfortunately there are no experimental data on the

4-13K range where the theoretical curves differ most markedly. A closer fit to the Fletcher-Sheard model may be obtained with a smaller value of the coupling parameter ( $\Gamma \sim 0.3$ ) but for a detailed comparison between theory and experiment a more complete set of data is desirable.

1. J R Fletcher and F W Sheard, Solid St Commun 9, 1403 (1971).
2. H Meyer and P L Smith, J Phys Chem Solids 9, 285 (1959).
3. D R Taylor, D B McColl, J P Harrison, R J Elliott and L L Goncalves, J Phys C 10 L407 (1977).
4. C B P Finn and B M Najafabadi, J Phys C 3, 330 (1970).
5. J van den Broek and L C van der Marel, Physica 29, 948 (1963).

## LATTICE DYNAMICS CALCULATIONS FOR SOLID BIPHENYL IN THE HIGH TEMPERATURE PHASE

T. Wasiutynski, I. Natkaniec and A.I. Belushkin\*

Institute of Nuclear Physics, Krakow, Poland

\*Joint Institute of Nuclear Research, Dubna, USSR

**Abstract.** The lattice dynamics model with explicitly included interphenyl modes was formulated. The intermolecular potential of the "6-exp" form with Williams parameters was used. The phase transition to the incommensurate phase was interpreted as a phonon instability for the wave vector inside the Brillouin zone  $q = (0, 0.4, 0)$ .

1. **Model.** - The potential energy of the crystal under study is expressed in the form:

$$V = \frac{1}{2} \sum_m [K_1 \psi_m^2 + K_2 \chi_m^2 + K_3 (r_m - r_0)^2 + K_4 \sin^2 \psi_m + \sum_n V_{mn}] \quad (1)$$

The first term in (1) describes in-plane deformation of the C-C bond, the second term describes out-of-plane deformation, the third term stretching, the fourth torsion. The last term describes interaction between chemically nonbonded atoms and has the well known "6-exp" form:

$$V_{mn} = \sum_{ij} [A_{ij} \exp(-B_{ij} r_{ij}) - C_{ij} r_{ij}^{-6}] \quad (2)$$

The empirical parameters A, B and C were taken from Williams /1/. The remaining parameters in (1) were adjusted in order to obtain the best agreement with the experiment. The final values in units of kcal/mole and Å are:

$$K_1 = 126 \quad K_2 = 45 \quad K_3 = 97.8 \quad K_4 = 52.5 \quad r_0 = 1.2937$$

2. **Results.** - The lattice dynamics calculations have to be performed at the minimum of the lattice energy. This is the condition for the lattice stability. As the first step the lattice energy was minimized with respect to all structural parameters. The results are presented in table 1.

Table 1

The comparison of calculated and experimental crystal structure of solid biphenyl at high temperature phase

	a	b	c	$\beta$	$\omega_1$	$\omega_2$	$\omega_3$
calculated	7.797	5.499	9.510	98.5	99.4	105.4	98.1
experimental /2/	7.82	5.53	9.44	94.6	99.2	103.7	99.0

where  $a$ ,  $b$ ,  $c$  and  $\beta$  are unit cell parameters  $\omega_1$ ,  $\omega_2$ ,  $\omega_3$  are Euler angles of the molecule. With the help of the intermolecular potential of the form (1) the phonon dispersion curves in harmonic approximation were calculated. Figure 1 presents 16 low lying phonon branches.

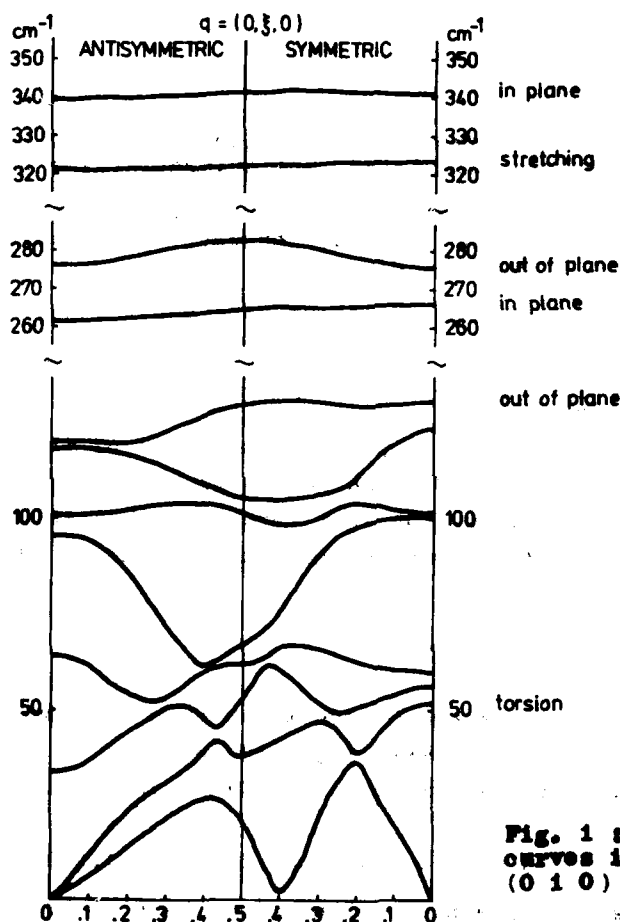


Fig. 1 : Phonon dispersion curves in biphenyl for the (0 1 0) direction.

As can be seen from the figure there is strong mixing between external modes of the biphenyl molecule and the two internal modes: out-of-plane deformation and torsion. All the modes show large dispersion. The close inspection of the eigenvectors of the lowest branch gives us information about the character of the motion. For small  $q$  values the character of the motion is translational. For larger  $q$  values the character of the curve changes to the torsional one. For the  $q = 0.4$  where there is a deep minimum in the curve it is predominantly of the torsional type. The position of the minimum is



very sensitive to the value of  $K_4$ . It is connected with the instability of the torsional mode. This fact was confirmed experimentally by coherent neutron scattering by Caillean et al. /3/. They found soft mode like behaviour of the phonon at  $\xi = 0.47$  which is in quite good agreement with the present calculations.

#### References

- /1/ D.E. Williams, J.Chem.Phys. 47, 4680 (1967)
- /2/ G.P. Charboneau, Y. Delugeard, Acta Crystallogr. B32, 1420(1976)
- /3/ H. Caillean, F. Moussa, J. Mons, Solid State Commun. 31, 521 (1979).

# PHONON DISPERSION CURVES IN THE MOLECULAR CRYSTALS NAPHTHALENE AND ANTHRACENE MEASURED BY INELASTIC NEUTRON SCATTERING

B. Dorner, E.L. Bokhenkov\*, E.F. Sheka\*, S.L. Chaplot\*\*, G.S. Pawley\*\*, J. Kalus\*\*\*, U. Schmelzer\*\*\* and I. Natkaniec\*\*\*\*

ILL Grenoble, France

\*Inst. Sol. Stat. Physics, Chernogolovka, USSR

\*\*Physics Dept. Univ. Edinburgh, U.K.

\*\*\*Physics Dept. Univ. Bayreuth, F.R.G.

\*\*\*\*Inst. Nucl. Phys. Krakow, Poland

**Abstract.** - We determined the 12 external and the 4 lowest internal dispersion branches for several symmetry directions in naphthalene at 6 K and anthracene at 12 K. The zone centre modes have been assigned unambiguously. The temperature dependence was studied for both crystals, while the pressure dependence only for naphthalene. At constant volume the frequencies of naphthalene would increase much more with temperature than those of anthracene.

By inelastic neutron scattering we determined the 16 lowest phonon dispersion branches for several symmetry directions for deuterated naphthalene at 6 K and for deuterated anthracene at 12 K. These two molecules crystallize in the same monoclinic structure  $P2_1/a$  with two molecules per unit cell. Under the assumption of rigid molecules one expects 12 external modes. This assumption is acceptably well fulfilled for naphthalene, where an energy gap of about 1 THz was observed between the external and the lowest internal modes while in the case of anthracene the four lowest internal modes are in the region of the external modes and a strong interaction is observed, see Fig. 1

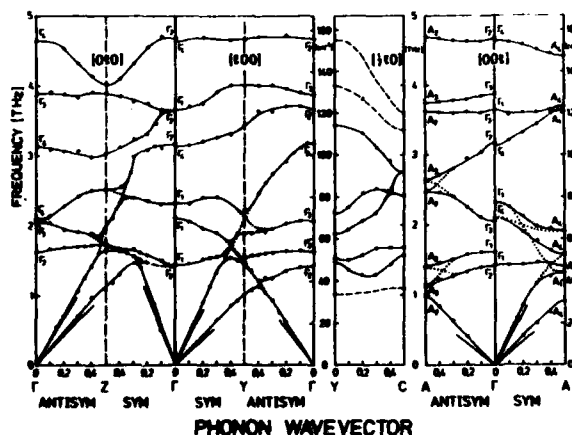


Fig. 1: The 16 lowest phonon dispersion branches in Anthracene at 12 K. The dotted lines visualize experimentally determined anticrossings and eigenvector exchanges. Sound velocities at 300 K are indicated by straight lines.

To perform the experiment it was crucial to have a lattice dynamics model calculation beforehand. The model is based on atom-atom potentials between different molecules /1,2/.

With help of the calculated eigenvectors the phonon intensities in different Brillouin zones have been predicted and nicely confirmed by the experiment (3,4) for the centres of the Brillouin zones. For finite phonon wavevectors many anticrossings of modes and eigenvector exchanges have been observed and analysed experimentally. For these two molecular crystals we obtained a complete set of experimentally determined dispersion curves. All zone centre modes have been assigned unambiguously to their group theoretical representations. The agreement between measured and calculated /5/ frequencies was qualitatively good but differed by up to 20%. The inclusion of a quadrupol moment /6/ improved the agreement very much.

In the case of anthracene we analysed the lowest internal modes further by an eigenvector determination /7/. The four lowest internal modes correspond to the  $B_{3u}$  (Butterfly) and the  $A_u$  (twist around the long axis) modes of the free molecule.

The temperature dependence at normal pressure has been investigated as well /8,9/. All phonon frequencies decrease with increasing temperature and the signals broaden such that many branches become unobservable at room temperature. We tried to include anharmonic effects by calculating the third and fourth order terms of the potential experienced by a particular mode with its proper eigenvector /10/. The amplitudes of all other modes were kept zero. The calculated anharmonic contributions had the right tendency but were much smaller than the observed ones.

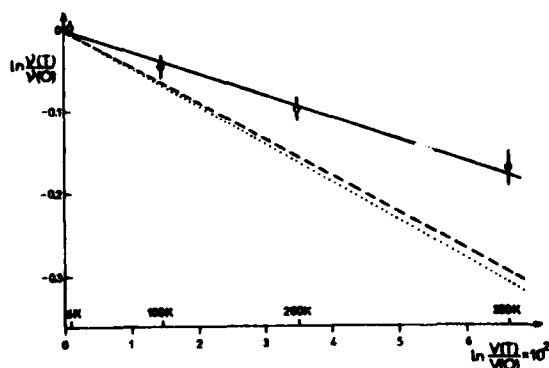


Fig. 2: Temperature dependence of librational frequency (2.52 THz at 6 K) versus temperature dependent volume. Measured (----) and calculated (.....) Grüneisen-parameters give frequency dependence at const. T.

The pressure dependence is so far studied only for naphthalene at 100 K and a hydrostatic pressure of 3 K bar /11/. We found very good agreement between measured mode-Grüneisenparameters and calculated

ones /12/. This good agreement sollicitated a calculation for negative pressure, this means for an increased volume. The decrease of the libration frequency at normal pressure with increasing temperature is plotted in Fig. 2 versus the temperature dependent volume change together with the calculated ones for the expanded volume at const. temperature. Apparently the experimental frequency decreases less than predicted from the Grüneisenparameters. Thus we conclude that in naphthalene frequencies at constant volume would increase with increasing temperature. This observation agrees with results from pressure dependent Raman scattering /13/. Encouraged by the good agreement between measured and calculated Grüneisenparameters for naphthalene we calculated them for anthracene /9/, and made a comparison like the one in Fig. 2. We found that in anthracene the frequency shift at const. volume would be smaller than in naphthalene, again in agreement with /13/. Nevertheless we plan to measure the pressure dependence in anthracene as well.

- /1/ A.I. Kitaigorodsky; J. Chim. Phys. 63, 9 (1966)
- /2/ D.E. Williams; J. Chem. Phys. 45, 3770 (1966), 47, 4680 (1967)
- /3/ I. Natkaniec, E.L. Bokhenkov, B. Dorner, J. Kalus, G.A. Mackenzie, G.S. Pawley, U. Schmelzer and E.F. Sheka; J. Phys. C. 13, 4265 (1980)
- /4/ B. Dorner, E.L. Bokhenkov, S.L. Chaplot, J. Kalus, I. Natkaniec, G.S. Pawley, N. Schmelzer and E.F. Sheka; J. Phys. C submitted
- /5/ G.S. Pawley; Phys. Stat. Sol. 20, 347 (1967)
- /6/ R. Righini, S. Califano and S.H. Walmsley; Chem. Rphys. 50, 113 (1980)
- /7/ S.L. Chaplot, G.S. Pawley, E.L. Bokhenkov, B. Dorner, V.K. Jindal, J. Kalus, I. Natkaniec and E.F. Sheka; Chem. Phys. 57, 407 (1981)
- /8/ E.F. Sheka, E.L. Bokhenkov, B. Dorner, J. Kalus, G.A. Mackenzie, I. Natkaniec, G.S. Pawley and U. Schmelzer; to be published
- /9/ V.K. Jindal, J. Kalus, E.L. Bokhenkov, S.L. Chaplot, B. Dorner, I. Natkaniec, G.S. Pawley and E.F. Sheka; J. Phys. C submitted
- /10/ J. Kalus, B. Dorner, V.K. Jindal, N. Karl, I. Natkaniec, G.S. Pawley, W. Press and E.F. Sheka; J. Phys. C submitted
- /11/ U. Schmelzer, E.L. Bokhenkov, B. Dorner, J. Kalus, G.A. Mackenzie, I. Natkaniec, G.S. Pawley and E.F. Sheka; J. Phys. C 14, 1025 (1981)
- /12/ G. S. Pawley and K. Mika; Phys. Stat. Sol. b 66, 679 (1974)
- /13/ R. Zallen and E.M. Conwell; Solid State Comm. 31, 557 (1979)

## NEUTRON SPECTROSCOPY OF INTERNAL PHONONS OF NAPHTHALENE AND ANTHRACENE CRYSTALS

E.L. Bokhenkov, A.I. Kolesnikov, T.A. Krivenko, E.F. Sheka, V.A. Dementjev\* and I. Natkaniec\*\*

*Institute of Solid State Physics, Academy of Sciences of the USSR, Chernogolovka, USSR*

\**The Timiryazev Academy of Agriculture, Moscow, USSR*

\*\**Joint Institute for Nuclear Research, Dubna, USSR*

**Abstract.**— Inelastic incoherent neutron scattering (IINS) spectra from anthracene and naphthalene crystals were measured at  $T=4.7\text{K}$  in the energy range  $200\text{--}1500\text{ cm}^{-1}$ . Experimental data are well described by the calculated spectra of one-phonon scattering.

The IINS spectra from anthracene- $\text{d}_0$  and naphthalene- $\text{d}_0$  polycrystalline specimens were obtained at  $4.7\text{K}$  using the KDSOG inverted geometry time-of-flight spectrometer at the IBR pulsed reactor of the JINR Dubna (1). The spectra measured result from a three-dimensional convolution in the form

$$N(t_0) = \Delta t_0 \iiint dE_0 dE dt F(E_0, E, t_0, t) G(E_0, E, \varphi, T)$$

where  $F$  is the apparatus function of the spectrometer and  $G$  is the cross-section of neutron scattering. A detailed description of all the quantities that appear in Eq. is given in Ref.2.

Proceeding from the solution of the harmonic dynamics of a polyatomic crystal (3) we calculated the cross-section of one-phonon IINS computing previously the weighted density of states.

In the top of Fig.1 the function  $g(\nu)$  is the density of states of the  $144\text{-mode}$  phonon spectrum of anthracene crystal; in the middle part  $G(\nu)$  depicts the weighted density integrated over all hydrogen atoms. The cross-section of one-phonon IINS is shown in the bottom of Fig.1.

Experimental spectrum of IINS from anthracene crystal is shown in Fig.2a. Fig.2b demonstrates the calculated spectrum of the one-phonon IINS in the range of the internal phonon modes which is the result of the convolution of the scattering cross-section (Fig.1, bottom) with the apparatus function of the instrument. As seen from Fig.2 this spectrum fits the experimental one rather well. It should be noted that though the energy resolution of the instrument is not high and amounts to an average of  $7\%$ , neglect of the phonon dispersion and replacement of  $G(\nu)$  by a set of  $\delta$ -function lead to a considerable deviation of the computation from the experiment.

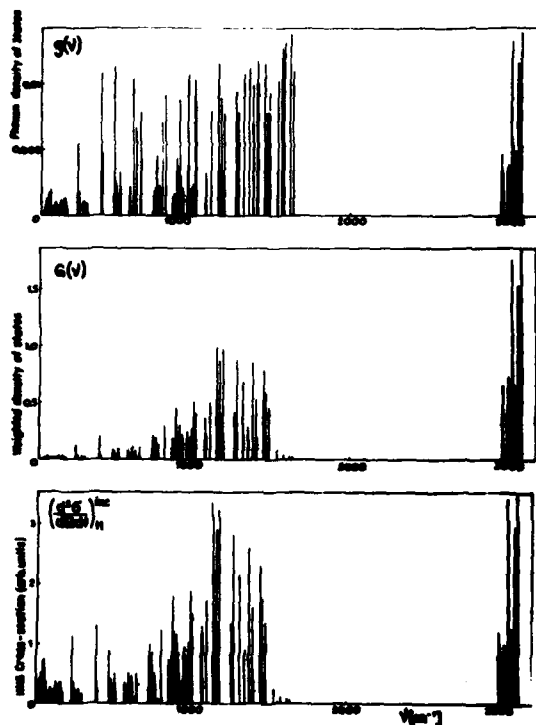
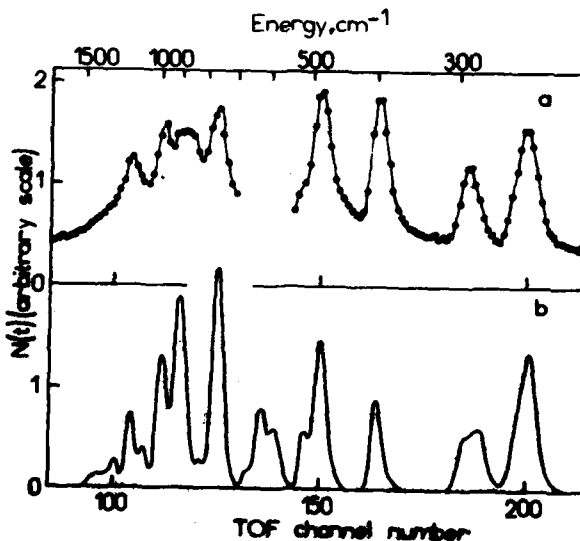


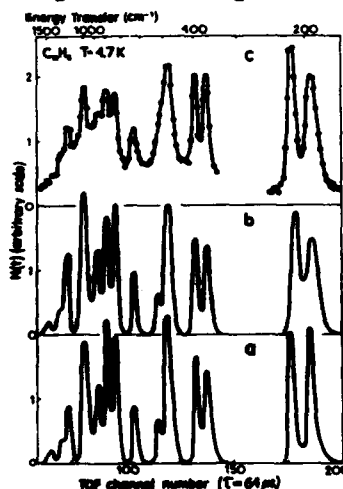
Fig.1 : Calculated  $g(v)$  (top);  $G(v)$  (midpart); one-phonon cross-section (bottom) for the 144-mode phonon spectrum of anthracene- $d_0$  crystal

Fig.2 : IINS TOP spectra from anthracene- $d_0$  crystal in the energy region 200-1500  $\text{cm}^{-1}$ ; a. Experiment,  $T=4.7\text{K}$ ; b. Calculated spectrum of one-phonon IINS



Experimental spectrum of IINS from naphthalene crystal is shown in Fig.3c. Spectrum in Fig.3b is calculated in the same way as it was made above for anthracene crystal. Spectrum in Fig.3a is calculated approximating the internal phonon density of states by a set of  $\delta$ -functions. As is seen from Fig.3 both calculated spectra describe the main features of the experimental one well, since in the energy range 300-1500  $\text{cm}^{-1}$  the phonon dispersion turned out to be compar-

able to or less than the instrument resolution. But in the range  $200\text{ cm}^{-1}$  and lower only the inclusion of phonon dispersion enables the experimental spectrum to be properly described.



**Fig.3** : IINS TOF spectra from naphthalene- $d_8$  crystal in the energy region 170-1900  $\text{cm}^{-1}$ ;  
a. Calculated one-phonon IINS spectrum in the  $\delta$ -approximation for non-interacting molecules;  
b. Calculated spectrum on the basis of solution of the dynamical problem for 108 crystal phonon modes;  
c. Experimental spectrum,  $T=4.7\text{K}$

**Fig.4** : Calculated and measured dispersion of the lowest internal modes ( $B_{2u}$ -lower,  $A_{1u}$ -upper) of naphthalene- $d_8$  crystal

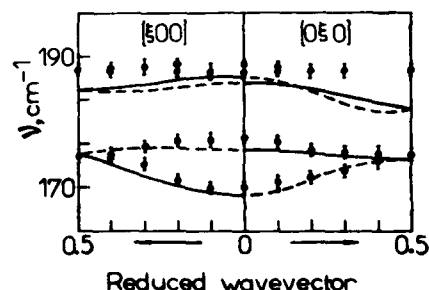


Fig.4 illustrates the comparison between the measured dispersion of the two low-frequency internal modes of naphthalene- $d_8$  crystal<sup>(4)</sup> and calculations (solid and dashed lines). The calculations performed by the method described in Ref.3 fit the experiment very well.

#### References

1. I.M.Frank, Sov.J.Part.Nucl., **2**, 805 (1973)
2. E.L.Bokhenkov, I.Natkaniec and E.F.Sheka, Sov.Phys.-JETP **43**, 536 (1976)
3. E.L.Bokhenkov, A.I.Kolesnikov, T.A.Krivenko, E.F.Sheka and V.A.Dementjev, these Proceedings, p.
4. E.L.Bokhenkov, E.F.Sheka, B.Dorner and I.Natkaniec, Solid State Commun., **23**, 39 (1977)

# A CALCULATION OF THE PHONON DISPERSION CURVES IN TRIGONAL AND MONOCLINIC SELENIUM WITH THE HELP OF A SINGLE VIBRATIONAL POTENTIAL

M. Merian and J. Etchepare

*Laboratoire d'Optique Appliquée, Ecole Polytechnique, Ecole Nationale Supérieure de Techniques Avancées, Batterie de l'Yvette, 91120 Palaiseau, France*

**Abstract.**— We present phonon dispersion curves in trigonal Selenium (chains) and zone center phonons in  $\alpha$  monoclinic Selenium (rings) calculated with the same internal force constants. Most of their differences in phonon energies can be explained by intermolecular interactions which in both case promote a tetrahedral neighbouring leaving some dangling bonds in monoclinic Se. Long range forces of the Van der Waals type were neglected in first approximation.

Helicoidal infinite chains in trigonal Se (t-Se) and eight membered rings Se<sub>8</sub> in both  $\alpha$  and  $\beta$  monoclinic Se ( $\alpha$  and  $\beta$ -Se) exhibit very close values of their first neighbours bond lengths  $r_{k,k+1}$  and bond angles  $\theta_k = (\vec{r}_{k,k-1}, \vec{r}_{k,k+1})$  and very close absolute values of their dihedral angles  $\tau_k$ . An harmonic potential  $V_{int}^{(2)}$ , which is internal to the molecular unit and written in the Wilson coordinates  $\Delta r_{k,k+1}$ ,  $\Delta \theta_k$ ,  $\Delta \tau_k$  should then contains similar force constants  $f$  :

$$V_{int}^{(2)} = \sum_k f_r (\Delta r_{k,k+1})^2 + f_\theta (\Delta \theta_k)^2 + f_\tau (\Delta \tau_k)^2 + \text{cross terms} \quad (1)$$

To describe the intermolecular binding energy, we take :

$$V_{ext} = A \sum_{kK} \left[ \exp\left(-\frac{R_{kK}}{\rho}\right) - \frac{C}{R_{kK}^6} \right] + B \sum_{kK} V(\alpha_{kK}) \quad (2)$$

A, B and C are constants. The  $R_{kK}$  are the external interatomic distances between k in one molecule and K in the others, up to  $R_{kK} = 8 \text{ \AA}$ .  $V(\alpha_{kK})$  is a four atoms term due to angles  $\alpha_{kK}$  between the  $R_{kK} < 4.366 \text{ \AA}$  (second external neighbour length in t-Se) and their equilibrium position. It will be explained elsewhere why the first terms in (2) play little role on phonons frequencies in t-Se,  $\alpha$  and  $\beta$ -Se ; it will therefore be ignored here.

The first order variations  $s_n$  of  $\alpha_{kK}$  may be expressed as linear combinations of Wilson coordinates and thus are linear combinations of first order cartesian atomic displacements  $\vec{u}_k$  :

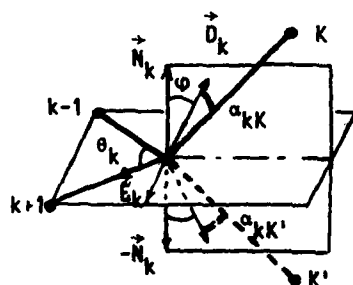
$$s_n = \Delta \alpha_{kK} = \sum_{k'} \vec{B}_{nk'} \cdot \vec{u}_{k'} \quad \text{where } k' = \begin{cases} k-1 \\ k \\ k+1 \\ K \end{cases} \quad (3)$$



Then the force acting on atom  $k$  is :

$$\vec{F}_k = - \sum_{k'K'} \frac{dV(\alpha_{k'K'})}{d\alpha_{k'K'}} \cdot \vec{B}_{nk} \quad (4)$$

We almost obtain zero forces on each atom  $k$  in  $\alpha$ -Se (and  $\beta$ -Se) by choosing  $V = (1 - \cos^2 \alpha_{kK})$  and by taking into account only those angles  $\alpha_{kK}$  which are within  $10^\circ$  from the two equilibrium directions  $\vec{D}_k$  and  $\vec{D}'_k$ . These directions are in the bisector plane of the angle  $\theta_k$ , at an angle  $\varphi$  - the same for all  $k$  - of  $12^\circ$  from the normal  $\vec{N}_k$  (or  $-\vec{N}_k$ ) to the intra molecular plane ( $k-1, k, k+1$ ) (figure 1).



$$\begin{aligned} \vec{D}_k &= \pm \cos \varphi \frac{\vec{e}_{k,k-1} \wedge \vec{e}_{k,k+1}}{\sin \theta_k} \\ &\quad - \sin \varphi \frac{\vec{e}_{k,k-1} + \vec{e}_{k,k+1}}{2 \cos \frac{\theta_k}{2}} \end{aligned} \quad (5)$$

$$\vec{E}_k = (\vec{e}_{k,k+1} - \vec{e}_{k,k-1}) / (2 \sin \frac{\theta_k}{2}) \quad (6)$$

Figure 1

The  $\vec{e}_{kk'}$  in (5) and (6) are unit vectors along the bonds. The appearance of  $\vec{E}_k$  will be explained below.

In t-Se both of these directions are occupied by a bond within  $3^\circ$  (fig. 2). In monoclinic Se at least one of them is occupied by a bond within  $10^\circ$ . This is true for each atom (fig. 3 for  $\alpha$ -Se). No in-plane equilibrium direction roughly along first internal neighbours bonds is found for  $\alpha$ -Se as opposed to the case of t-Se.

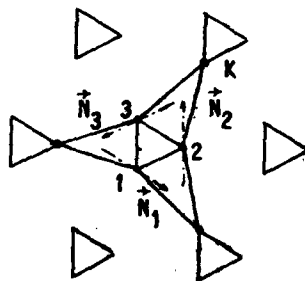


Figure 2 : projection on the  $(\vec{a}, \vec{b})$  plane (normal to the screw axis  $\vec{c}$ ) of the 3 atoms  $k = 1, 2, 3$  of one unit cell of t-Se and of their two first external neighbours roughly along  $\vec{N}_k$  and  $-\vec{N}_k$ .

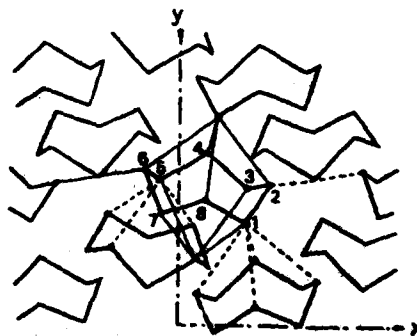


Figure 3 : projection on the  $xy$  plane of the 8 atoms  $k = 1$  to 8 of one ring of the  $\alpha$ -Se unit cell and of the external bonds  $\vec{R}_{kK}$  which are roughly along  $\vec{N}_k$  or  $-\vec{N}_k$  (full lines) or  $\vec{N}_k, -\vec{N}_k$  (dotted lines).

Using first order  $\vec{u}_k$  for  $\Delta\alpha_{kK}$  only gives those variations of  $\alpha_{kK}$  which are in the plane  $(\vec{D}_k, \vec{R}_{kK})$  or  $(\vec{D}'_k, \vec{R}_{kK})$ . For very small  $\alpha_{kK}$  the variations of the angle of  $\vec{R}_{kK}$  with the normal to these plane must also be used with about the same weight as  $\Delta\alpha_{kK}$ . We then decided to use two angular coordinates instead of the  $\Delta\alpha_{kK}$ : the Wilson out-of-plane variation  $\Delta\beta_{kK}$  of the angle  $\beta_{kK}$  between  $\vec{R}_{kK}$  and  $\vec{N}_k$  or  $-\vec{N}_k$  and the variation  $\Delta\gamma_{kK}$  of the angle between  $\vec{R}_{kK}$  and the unit vector  $\vec{E}$  or  $-\vec{E}_k$  normal to the bissector plane (fig. 1 and Eq. 6). The external vibrationnal potential then becomes:

$$V_{\text{ext}}^{(2)} = f_{\alpha} \sum_{kK}^{\alpha_{kK} < 10^\circ} [(\Delta\beta_{kK})^2 + (\Delta\gamma_{kK})^2] + f_{ra} \sum_{kK}^{\alpha_{kK} < 10^\circ} (\pm\Delta\beta_{kK} \pm \Delta\gamma_{kK}) (\Delta r_{k,k-1} + \Delta r_{k,k+1}) \quad (7)$$

The last term with the force constant  $f_{ra}$  in Eq. 7 is the best one we found to describe the quite strong dispersion of the highest frequency branche  $\Gamma$ -K in t-Se (fig. 4). The signs + or - has to be taken such that the forces push K in the bissector plane toward  $\vec{D}_k$  or  $\vec{D}'_k$  (fig. 2). The first term in Eq. 2 does not give this dispersion with the coefficients which were calculated for equilibrium in  $\alpha$ -Se and t-Se:  $\rho = .54 \text{ \AA}$  and  $C = 3.00 \text{ \AA}^6$ .

Solving the eigen values equation of the total dynamical matrix  $V_{\text{int}}^{(2)} + V_{\text{ext}}^{(2)}$ , we obtained the following results with the same force constants for t-Se and  $\alpha$ -Se:  $f_r = 1.256$  and  $f_{rr} = .047 \text{ md/\AA}$ ,  $f_\theta = .949$  and  $f_\alpha = .150 \text{ md.\AA/rd}^2$ ,  $f_{ra} = .092 \text{ md/rd}$ .

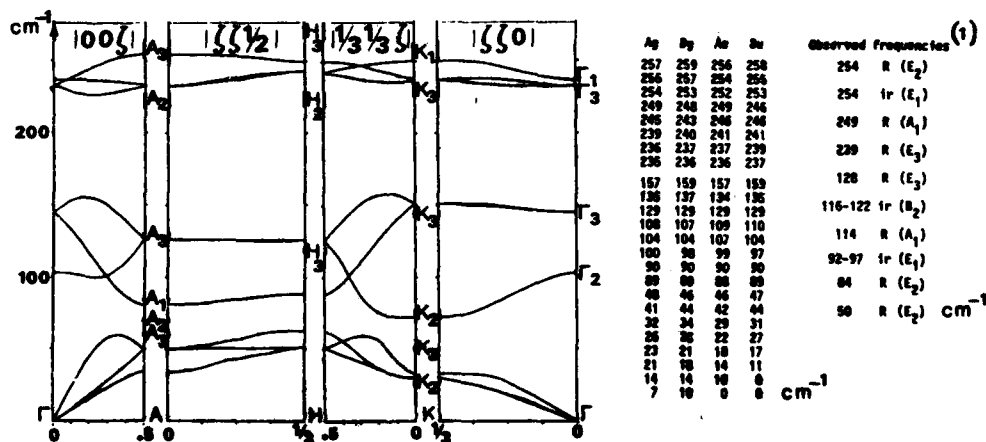


Fig. 4 : phonons in t-Se. The dashes with symmetry assignments are experimental data on the zone edges (2).

table 1 : The first four columns give the zone center frequencies of  $\alpha$ -Se in its  $C_{5h}^5$  space group.

In the fifth column of table 1 are the experimental results and assignments for isolated rings with  $D_{4d}$  symmetry.

The other force constants will be used to obtain a better fit between theoretical and experimental phonon energies for both t-Se and  $\alpha$ -Se.

#### References

1. G. LUCOVSKY et al. Solid State Com. 5, 113, 1967.
2. W.D. TRUCHERT et al. Phys. C. Solid State Phys. 8, 3725, 1975.

ULTRASONIC RELAXATION IN  $\alpha$ -SULFUR

M. Boissier, R. Vacher and B. Perrin\*

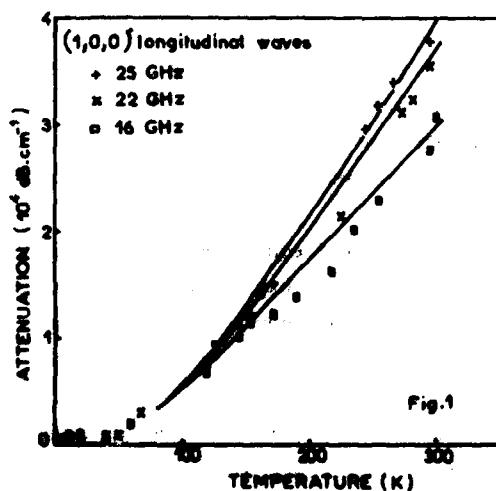
Laboratoire de Spectrométrie Rayleigh Brillouin (ERA 460), Université des Sciences et Techniques du Languedoc, Place E. Bataillon, 34060 Montpellier Cedex, France

\*Département de Recherches Physiques (LA 71), Tour 22, Université P. et M. Curie, 75230 Paris Cedex 05, France

**Abstract.**— We present new measurements of the temperature dependence of acoustic damping in  $\alpha$ -sulfur. The anomalous elastic properties observed in this crystal are described in terms of a "molecular relaxation".

Previous studies of the longitudinal acoustic wave propagation in  $\alpha$ -sulfur have revealed an unusual behaviour. The sound absorption is very high for a dielectric crystal.<sup>1</sup> Furthermore, Brillouin scattering measurements have given evidence of a large departure from the usual  $\omega^2$ -dependence of the attenuation and shown the related velocity dispersion in the frequency range 10-25 GHz.<sup>2</sup> A phenomenological description of these properties has already been given in terms of a relaxational process involving a single relaxation time.<sup>3</sup>

We want to discuss here several arguments either qualitative or quantitative allowing to interpret the relaxational process as a "molecular relaxation". We also present recent Brillouin scattering measurements of the acoustic absorption  $\alpha$  as a function of temperature. The results, shown in Fig.1, indicate a temperature dependence of  $\alpha$  very different from that observed in others dielectric crystals. This confirms that the Akhieser damping mechanism<sup>4</sup> (which, in most cases, accounts well for the acoustic damping in dielectric crystals for the frequency-temperature range



considered here) is insufficient to explain the results in  $\alpha$ -sulfur.

In molecular crystals, the internal vibrations of molecules are slightly affected by the lattice vibrations. Therefore, internal and external vibrations of molecules are weakly coupled in such crystals. If an external perturbation is applied to the crystal, this weak coupling corresponds to long relaxation times of the phonon populations during the thermalization of the phonon gas. This effect, which can give rise to an ultrasonic relaxation, will be called "molecular re-

laxation" in the following. The existence of such a phenomenon in solids has first been suggested by Liebermann.<sup>5</sup> More recently,<sup>6</sup> it has been shown that, for this relaxation mechanism, the amplitude of the relaxational term reflects the anisotropy of the solid. In contrast, the frequency dependence is not affected. Furthermore, a new expression for the relaxation amplitude has been proposed ; when the relaxation spectrum reduces to a single time, the following expression for  $\alpha$  is obtained

$$\alpha_R = \frac{1}{2s} \left( \frac{c_{ijkl} \beta_{kl} e_i k_j}{C_V} \right)^2 \frac{TC_V}{\rho s^2} \frac{C_I}{C_V - C_I} \frac{\omega^2 \tau}{1 + \omega^2 \tau^2} \quad (1)$$

where  $s$  and  $\omega$  are the velocity and frequency of the elastic wave, respectively,  $\rho$  the mass density,  $T$  the absolute temperature,  $C_V$  the specific heat at constant volume,  $C_I$  the specific heat associated with internal vibration modes,  $c_{ijkl}$  the elastic constants,  $\beta_{kl}$  the components of the thermal expansion tensor,  $e_i$  and  $k_j$  the components of the polarization and normalized wave vector of the wave, and  $\tau$  the relaxation time.

On the basis of the following arguments, we propose the "molecular relaxation" for explaining the anomalous acoustic properties of  $\alpha$ -sulfur :

(i) According to (1), the transverse waves propagating along the symmetry axes of the (orthorhombic) crystal do not give rise to "molecular relaxation", in agreement with experiment.<sup>3</sup>

(ii) As the coefficient of the relaxation in (1) varies strongly with temperature, it can be shown that this variation is compatible with the experimental results for  $\alpha$  plotted in Fig.1.

(iii) The analysis of the frequency dependence of the attenuation shows that the expression  $\alpha = (A\tau/(1+\omega^2\tau^2) + C)\omega^2$  (2) can be fitted to the experimental results. The coefficients  $A$ , related to the amplitude of the relaxation,  $C$ , describing that of the Akhieser damping and  $\tau$  are given in Table 1. In this Table,  $\tau$  appears nearly insensitive to the anisotropy, in agreement with an interpretation in terms of a "molecular relaxation".

(iv) By comparing Eqs. (1) and (2), an estimate of  $C_I$  can be deduced for each of the propagation directions studied, the other quantities appearing in (1) being known. This value has, obviously, to be the same for all directions. The results, shown in Table 2, indicate a (statistical) dispersion smaller than 4 % for  $C_I$ . Therefore, the anisotropy of the relaxation amplitude is well described by the "molecular relaxation" model.

(v) Finally,  $C_I$  was calculated directly from the frequencies of the internal modes measured in Raman scattering and infrared absorption experiments. In this calculation, we neglected the spatial dispersion of internal modes. Such an estimate gives  $0.98 \times 10^6 \text{ J.m}^{-3}.\text{K}^{-1}$ , which is close enough from the average value of  $C_I$  in Table 2 ( $0.81 \times 10^6 \text{ J.m}^{-3}.\text{K}^{-1}$ ).

In conclusion, we suggest that the relaxational behaviour of the acoustic properties of  $\alpha$ -sulfur would be the first evidence of "molecular relaxation" in an

Table 1 -

Propagation direction	(100)	(010)	(001)	(110)	(101)	(011)
$(10^{-6} \frac{\text{\AA}}{\text{m}^{-1}} \times \text{s})$	5.6	9.0	3.2	8.2	6.2	4.1
$(10^{-18} \frac{\text{C}}{\text{m}^{-1}})$	5.7	2.6	6.4	3.3	1.5	3.9
$\tau$ (ps)	10.3	10.3	10.5	10.5	10.5	10.5

inorganic molecular crystal. It seems therefore that this phenomenon is a characteristic property of what we can term, in a broad sense, the "molecular" crystals.

- <sup>1</sup> J. Sapriel, L. Rivoallan and J.L. Ribet, *J. Phys. (Paris)* **33** (1972) C6-150.
- <sup>2</sup> R. Vacher, J. Sapriel and M. Boissier, *J. Appl. Phys.* **45** (1974) 2855.
- <sup>3</sup> R. Vacher, M. Boissier and F. Michard, in "Light Scattering in Solids", (Flammarion, Paris, 1975) p. 651-5.
- <sup>4</sup> A. Akhiezer, *J. Phys. (U.S.S.R.)* **1** (1939) 277.
- <sup>5</sup> L.N. Liebermann, *Phys. Rev.* **113** (1959) 1052.
- <sup>6</sup> B. Perrin, *Phys. Rev.* (to be published).

Table 2 - Experimental estimate of  $C_I$  at 293 K from relation (1)

( $\rho = 2.07 \times 10^3 \text{ Kg.m}^{-3}$  ;  $C_V = 1.39 \times 10^6 \text{ J.m}^{-3}.\text{K}^{-1}$ ).

$\vec{k}$	1,0,0	0,1,0	0,0,1	$\frac{\sqrt{2}}{2}(1,1,0)$	$\frac{\sqrt{2}}{2}(1,0,1)$	$\frac{\sqrt{2}}{2}(0,1,1)$
$s(\text{m} \times \text{s}^{-1})$	2641	2493	2997	2484	2628	3144
$\frac{1}{C_V}(c_{ijkl}\beta_{kl}e_i k_j)$	0.909	0.983	0.871	0.943	0.879	0.919
$C_I(10^5 \text{ J.m}^{-3}.\text{K}^{-1})$	0.780	0.827	0.747	0.820	0.830	0.843

**PHONONS IN SEMICONDUCTORS**

## RECENT ADVANCES IN THE THEORY OF PHONONS IN SEMICONDUCTORS

R.M. Martin

Xerox Palo Alto Research Centers, 3333 Coyote Hill Road, Palo Alto, CA 94304,  
U.S.A.

Université P. et M. Curie, Dept. Recherches Physiques, 4 place Jussieu,  
75230 Paris, France.

**Abstract** - Calculations of structural energies of solids have recently reached a new stage, in which it has been shown to be feasible to calculate directly crystal structures of minimum energy and distortion energies that determine harmonic phonon eigenmodes and anharmonic terms. In this paper are discussed 1) calculational methods, 2) recent results, which have been shown by several groups to give accurate results for Si, Ge, GaAs and Se with no adjustable parameters, 3) the corresponding electronic charge densities, which show graphically the bonding and suggest interpretations for the origins of the atomic forces. Comparisons of direct computations of total energy differences with second-order perturbation calculations of harmonic coefficients shows the advantages and disadvantages of each method and how each can complement the other.

## I. Introduction

The structural properties of solids consist of the equilibrium structure and the dynamics of the motion of the atoms around their equilibrium positions. The subject of this conference is indicative of the division of this field of study into separate areas—both experimentally and theoretically—with the interest here focused upon dynamics. Within this division there are many subdivisions into harmonic phonons, anharmonic interactions, coupling of phonons and photons, etc. However, it has been shown recently<sup>1-8</sup> that all of these structure-related properties can be considered theoretically in a unified manner so that equilibrium positions, harmonic and anharmonic forces, effective charges, etc., can be calculated directly from the underlying Hamiltonian of the electron-ion system. The methods that have been devised are particularly well-suited for semiconductors, and complete calculations on Si,<sup>2,4</sup> Ge,<sup>3,5</sup> GaAs<sup>6,7</sup> and Se<sup>8</sup> have shown that very good agreement with experiment (and confident predictions of quantities not known experimentally) can be achieved with *ab initio* calculations having no adjustable parameters. In this paper I will attempt to present a brief review of this work, oriented to emphasize the dynamical aspects and to provide relations among many theoretical papers presented at this conference.<sup>4,5,10-13</sup>

Structural energies and forces are determined by the total energy of the system of ions and electrons. Within the adiabatic approximation, the electrons respond instantaneously on the time scale of atomic motions and the total energy can be considered a function only of the positions of the ions, which we denote schematically by  $R$ . The total energy can be written<sup>2,14,15</sup>

$$E_{\text{tot}}(R) = E_{\text{ii}}(R) + E_{\text{el}}(R), \quad (1)$$

where  $E_{\text{ii}}$  is the direct ion-ion interaction energy, and  $E_{\text{el}}$  is the total energy of the electrons moving in the potential field of the ions, including the quantum mechanical kinetic, exchange, and correlation energies. The equilibrium structure is determined by minimization of the total energy, a necessary condition for which is that the force on every atom is zero at its equilibrium position. This is the first step in any *ab initio* calculation of structural energies.

Distortion energies that determine the stability of the structure, phonon frequencies, etc., are given by  $E_{\text{tot}}(R)$  for positions  $R$  away from equilibrium. There are two primary ways to proceed at this point: 1) the "direct" method,<sup>1,2</sup> in which  $E_{\text{tot}}(R)$  is calculated directly for the distorted crystal and 2) the perturbation method,<sup>14</sup> in which the energy is expanded to second order in  $\Delta R$  to determine harmonic phonon energies. The latter approach, also termed the dielectric function formulation of lattice dynamics,<sup>14</sup> has a long history<sup>15</sup> and has been successfully applied in free-electron-like metals,<sup>15</sup> however, crystals with covalent bonding are much more difficult and explicit evaluation of these formulas has been reported in only a few instances.<sup>9-13,17,18</sup> The advantage of the perturbation method is that any harmonic phonon at any wavevector  $q$  can be treated. The disadvantage is that it requires a heavy machinery and it is limited to harmonic properties. We will first describe the "direct" method, which shows most clearly the unity of the theory of structural properties, and in the later sections we will return to other formulations.

## II. The Direct Method

The "direct" or "frozen phonon" method<sup>1,2</sup> provides a unified approach for calculation of structural energies. It discards the notion of the orders of perturbation theory and treats the distorted crystal directly as a new crystal with a new structure having symmetry lower than the undistorted crystal, whether the magnitude of the distortion is large or small. Exactly the same methods are used for undistorted and distorted crystals and the total energy is calculated directly as a function of the positions of the ion centers. In a unified manner one can find the equilibrium structure, harmonic and anharmonic energies, and properties of the electrons, such as polarizabilities and dipole moments.<sup>6,7</sup> Previously, such direct calculations have been restricted to simple high-symmetry crystal structures.<sup>19</sup> The extension to distorted structures greatly extends the usefulness of total energy calculations and it provides a very severe test for current theories of exchange and correlation energies in interacting electron systems.

The approach which has proved very successful and feasible for calculation of exchange and correlation energies is the density functional method of Hohenberg, Kohn, and Sham,<sup>20</sup> who proved that the total energy is uniquely related to the ground state charge density  $n(r)$  through a functional  $E_{\text{el}} = F[n]$ . Even though the exact form of  $F[n]$  is unknown, it is extremely useful that the theory is formulated in terms of  $n(r)$  which is itself a measurable quantity. For example, changes in charge density are directly related to the distortion energies, forces are determined rigorously by  $n(r)$  as shown by the Hellman-Feynman theorem,<sup>5,15,21</sup> and dielectric response functions can be uniquely related to functional derivatives of  $F[n]$ .<sup>2,21</sup> Explicit solutions for  $n(r)$  result from the variational requirement that  $F[n]$  is minimum for the correct  $n(r)$ . In Ref. 20 it was shown how one could define tractable self-consistent solutions to the variational



equations if the exchange-correlation part of the functional  $\epsilon_{xc}$  is assumed to be local. Within this local density functional (LDF) approximation the function  $\epsilon_{xc}(n(r))$  must be the same as for a uniform electron gas  $\epsilon_{xc}(n)$  for which various functions have been proposed and utilized: the well-known  $n^{1/3}$  form with coefficient  $\sim 0.7-0.8$ ,<sup>2,5-7</sup> the Wigner interpolation formula<sup>4</sup> and others.<sup>3,19</sup> These forms are very similar in the range of  $n$  considered here. The results given below strongly support the conclusion that the LDF approximation is very good in the semiconductor crystals and that the agreement with experiment is better than can be justified by rigorous analysis.

The most important advance in the recent work is the development of techniques to solve the self-consistent electronic equations rapidly and accurately enough to calculate the small energy differences between distorted and undistorted crystals (the non-systematic errors must be less than 0.01% on the total energy). The method to make this feasible in semiconductors is given in Ref. 2: the important simplifications are the use of pseudopotentials for the ion cores, the "special points" method<sup>22</sup> whereby the sums over the Brillouin Zone can be reduced to a few points, Lowdin perturbation theory for higher plane waves, and schemes to quickly reach convergence.<sup>23</sup> All these steps can be checked and it has been found possible to achieve essentially arbitrary accuracy in the solutions. Let us note, in particular, that the use of a pseudopotential is just a convenient procedure for eliminating the deep core electrons. It can be generated in an *ab initio* manner to reproduce very accurately the valance charge density.<sup>24</sup> The only essential approximation is the assumption that the core is rigid. Even this has been tested by Harmon, Weber, and Hamann<sup>4</sup> who have carried out all-electron calculations and have shown that the rigid ionic pseudopotential is very accurate except possibly for very large deformations where effects of non-rigidity of the core were detected.

### III. Results of Direct Calculations

The most systematic and complete investigation of the structural properties of a crystal has been carried out for Si<sup>2-4</sup> using the direct calculations of  $E_{tot}$ . The original work of Wendel and Martin<sup>2</sup> on the equilibrium and harmonic and anharmonic energies has now been extended in Refs. 3 and 4. Yin, Ihm, and Cohen<sup>3</sup> have utilized more accurate potentials and considered many crystal structures and phonons. It is remarkable that the lattice constant, bulk modulus, and phonons at  $\Gamma$ , X, and L, and Gruneisen parameters are all calculated to within a few percent of experimental values.<sup>3</sup> Harmon, Weber, and Hamann<sup>4</sup> have derived many of these quantities in all-electron calculations and have in addition calculated the internal strain parameter and the cubic anharmonicity of the TO( $\Gamma$ ) phonon. Based upon these results, it is clear that Si is one of the best understood of all crystals from a structural point of view, and that confidence can be placed in other results, e. g. anharmonicity, not known experimentally.

Aside from the interesting results for the energies, particularly to low frequency TA(X) modes and its negative Gruneisen parameter,<sup>2-4</sup> the calculations show directly the role of the electrons in determining the forces. For example, it is shown in Ref. 2 that the ion-ion forces destabilize the TA(X) and the closely-related shear  $C_{11}-C_{12}$  elastic constant. It is the covalent electron contributions that give the shear stability. Furthermore, the low TA(X) frequency results from relaxation of the bonding charge density between certain atoms as is shown in Fig.

5 of Ref. 2.. This rotational-type relaxation is very similar to the displacement of bond-charges in the adiabatic bond-charge model of Weber,<sup>25</sup> however, the upper part of figure shows that there is also charge transfer between the bond charges. This is especially important in the bond stretching modes, such as TO ( $\Gamma$ ), and is not included in the bond-charge models.<sup>25</sup> This is an example of the electronic effects that determine the atomic forces and which can be given in *ab initio* calculations. It may be possible to include such effects in future model calculations, but it is essential to have the *ab initio* calculation to determine what is the appropriate model.

In the cases of GaAs<sup>6,7</sup> and Se<sup>8</sup> new features enter the theoretical considerations. GaAs is an example of an ionic crystal in which there are long-range electrostatic forces which cannot be included in the types of calculations used for Si and Ge.<sup>1-5</sup> It is shown in Ref. 7 how long-ranged Coulomb forces can be included in finite cell calculations with a cell size which is feasible (8-12 atoms per cell<sup>6,7</sup>). The key quantity is the effective charge which may be determined by displacing planes of atoms in the crystal and calculating the dipole moment resulting from the bare ion plus the electronic contributions.<sup>6,7</sup> In Fig. 1 are given change in electronic charge density calculated as described in refs. 6 and 7 for GaAs crystals with displaced (001) planes of atoms, Ga planes in the upper part and As planes in the lower part of the figure. The ionic plus electronic charge contributions define the longitudinal effective charge<sup>7</sup> and the calculations give +0.155 for Ga, and -0.148 for As compared to the experimental value of  $\pm 0.197$ , where the sign is unknown experimentally. The close agreement for Ga and As taken from two independent calculations shows internal accuracy of the calculations. The power of the direct method illustrated by the fact that exactly the same computer programs and convergence criteria can be used for such apparently diverse problems as the effective charge<sup>7</sup> in GaAs and the electronic potential for Ge-GaAs interfaces<sup>23</sup>.

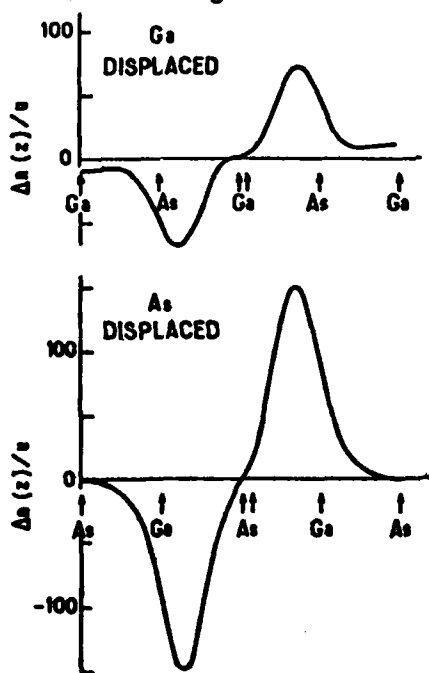


Fig. 1. The change in charge density per unit displacement of the central plane of atoms, Ga in the upper curve and As in the lower. The double arrows indicate the displacement to the right. The coordinate is in the [001] direction and the density is averaged over (001) planes. The longitudinal effective charge is the sum of the ionic part plus the moment of the electronic density shown here. Details are given in Ref. 7.

Another problem of general importance encountered in GaAs is that, at points such as X, the phonon eigenvectors are not known experimentally. Eigenvectors are just as important as eigenfrequencies for a complete description of lattice dynamics, yet they are difficult to measure and generally are unknown except when determined by symmetry. It is possible to determine eigenvectors from cross terms in the total energy and this has been done via direct calculations for GaAs at the X point,<sup>6</sup> in the first *ab initio* calculation of eigenvectors to the knowledge of the author. The results are discussed in detail in Ref. 6 where it is shown that the calculated eigenvectors provide a very stringent test for phenomenological models: of six different models, all of which fit all known frequencies extremely accurately, there is complete disagreement on the eigenvectors and only one (and perhaps a second) is even close to the present results.

The unique advantage of the direct method is the ability to calculate energies for large displacements of the ions. Let us consider one example, perhaps the most interesting of the results reported so far. In calculations described in Ref. 6, it was found that for several displacement patterns in GaAs the energy has the form  $E_{\text{tot}}(\mathbf{R}) = E_0 + A u^2 + B u^4 + C u^6$ , with  $A, C > 0$ , but  $B < 0$ . This can lead to interesting results as shown in Fig. 2 for the TA(X) mode in GaAs. The harmonic frequency of this mode decreases with pressure (decreasing lattice constant in the figure) so that a second minimum develops which eventually has lower energy than the undistorted crystal. Thus the calculations predict a first order phase transition to a lower symmetry structure at a pressure where the squared TA frequency is reduced by a factor of about 2, which may occur before the known transition to the metallic NaCl phase.

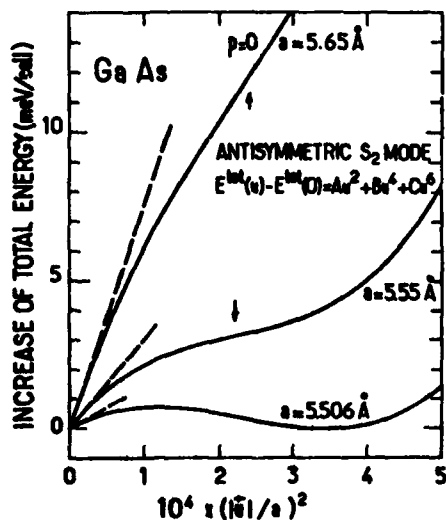


Fig. 2. Variation of the calculated total energy of a GaAs crystal with the square of the displacement which is approximately the TA(X) mode. The curves are shown at several pressures and we see the decrease of the harmonic part (dashed lines) with decreasing lattice constant  $a$ . Anharmonicity becomes relatively more important until a second minimum develops at finite displacement indicating a possible first order phase transition. From Ref. 6.

In Se<sup>8</sup> the new feature is the low symmetry of the equilibrium structure, so that determining the equilibrium lattice structure is obviously the first theoretical problem. There are three independent variables describing the structure  $a$ ,  $c/a$ , and chain radius  $r$ . The positions of the atoms for zero forces conjugate to each of these variables determines the structure and the curvature determines  $B$ ,  $C_{11}$  and the  $A(\Gamma)$  phonon frequency. Vanderbilt and Joannopoulos<sup>8</sup> have shown the calculations can be done, with reasonable agreement with experiment, and furthermore have proceeded to look for new metastable minima for large displacements corresponding to three-fold and one-fold coordination of atoms. These large changes are thought to be very important in the electronic properties of chalcogenides and their work is an extremely important step going far beyond the phonon approximation to look for new stable or metastable structures.

It is also important to mention that approximate versions of the direct method have been used to predict surface reconstructions on a variety of semiconductor surfaces<sup>26</sup>, and density functional calculations has been reported for a Si surface<sup>27</sup> and a Ge-GaAs interface.<sup>23</sup> These involve changes in bonding and are very important application of ideas similar to those in Se for prediction of entirely new situations.

Finally, at this conference is presented an entirely new use of the direct method to calculate entire dispersion curves.<sup>5,28</sup> The idea is to displace one plane of atoms represented by one atom in a large cell (8 or 12 atoms "supercells") and to use the Hellman-Feynman theorem to calculate the forces on all the planes of atoms in the vicinity of the displaced plane. It is shown in Ref. 7 that interplanar forces are always short range even in ionic crystals and, provided the cell is large enough, complete, accurate dispersion curves can be calculated. The set of harmonic forces, changes in electronic charge density, many different anharmonic terms, effective charges, etc., can be considered in a unified manner calculated simultaneously from a small number of self-consistent calculations. Results are given in Refs. 5 and 28 which show that complete dispersion curves, eigenvectors, and dielectric properties such as effective charges and dielectric constant, can all be calculated, providing a very complete description of forces in the crystal.

#### IV. Perturbation Methods

As was mentioned in the introduction, perturbation methods are very powerful for calculating linear response functions and harmonic forces. Using perturbation theory on the perfect crystal, it is much more straightforward than in the direct method to calculate dielectric functions and harmonic phonons of arbitrary points in the Brillouin Zone; thus this approach will always be preferable for some problems. A comparison of the two approaches is given in Ref. 21, where it is shown that ideas from each method can be used to aid calculations in the other method. In particular the usefulness of the density functional can be transferred to the perturbation method<sup>10,21</sup> and the perturbation theory can be used to increase the rapidity of convergence in the self-consistent cycles required in the direct calculations.<sup>23</sup>

The most complete perturbation calculations<sup>9,10,17,18</sup> have been for Si, as was the case with the direct method. The only complete dispersion curves have been published by Bertoni, et al<sup>17</sup>

and by Van Camp, Van Doren, and Devreese<sup>9</sup> with more recent results presented at this conference.<sup>10</sup> The current results do not agree with experiment as well the results of direct calculations<sup>3,4</sup> because they have not been done with accurate pseudopotentials. However, the method has the capability to give very complete information on the harmonic lattice dynamics. Let us note also the calculation by Muramatsu and Hanke<sup>12</sup> (using different methods for exchange and correlations) who apply the dielectric function method to look for phonon softening and instability to reconstruction on the Si (111) surface.

One of the powers at the perturbation method is the ability to consider long range forces and take the  $q \rightarrow 0$  limits<sup>14</sup> much more easily than in the direct method<sup>7</sup>. If the dielectric function matrix  $\epsilon$  is known, the transverse effective charge  $e_i^*$  for ion  $i$  is given by<sup>14</sup>

$$e_i^* = \lim_{q \rightarrow 0} \sum_G q \epsilon^{-1}(q, q+G) (q+G) V_i(q+G), \quad (2)$$

where  $V_i$  is the same bare ionic potential that determines the electronic states of the undistorted crystal. This has been calculated for many ionic semiconductors in papers at this conference by Resta and Baldereschi<sup>11</sup> and by Olego, Vogl, and Cardona,<sup>13</sup> who consider volume dependence of the charge. The trends among several crystals can be seen in the results of Ref. 11, however, there are inconsistencies in the use of  $V_i$  and  $\epsilon^{-1}$  that affect the values of  $e_i^*$ .

## V. Summary

In conclusion, recent calculations<sup>1-8</sup> of energies and forces using electronic Hamiltonians, have brought our understanding of structural properties to a new stage in which the equilibrium structure and lattice dynamics can be treated in a unified manner. Because of the computational simplicity of the density functional method,<sup>20</sup> the very difficult problem of electronic exchange and correlation can be handled accurately enough to calculate equilibrium lattice constants and atomic positions, harmonic and anharmonic force constants, ground state electronic properties, such as effective charges, etc. The computational technique which has made this possible is the "direct" method<sup>2</sup> and the greatest advantage of this approach is the ability to deal with many different situations—perturbative and non-perturbative—on the same basis. Extensive results on Si,<sup>2,4</sup> Ge,<sup>3,5</sup> GeAs,<sup>6,7</sup> and Se<sup>8</sup> have firmly established the power of this method. The development of perturbation methods<sup>9-14,17,18</sup> is also very useful and can potentially provide a more detailed description of the harmonic parts of the restoring forces. Together these two calculational methods hold the promise of providing very complete structural information on many systems including semiconductor crystals, surfaces, and interfaces.

This work was supported in part by Department of the Navy contract N00014-79-c-0704 issued by the Office of Naval Research. The United States Government has a royalty-free license throughout the world in all copyrightable material contained herein.

## REFERENCES

1. D. J. Chadi and R. M. Martin, *Solid State Commun.* **19**, 643 (1976).
2. H. Wendel and R. M. Martin, *Phys. Rev. B* **19**, 5251 (1979).

3. M. T. Yin and M. L. Cohen, Phys. Rev. Lett. 45, 1004 (1980); J. Ihm, M. T. Yin, and M. L. Cohen, Solid State Commun. 37, 491 (1981); M. T. Yin and M. L. Cohen, to be published.
4. B. N. Harmon, W. Weber, and D. R. Hamann, this conference and to be published.
5. K. Kunc and R. M. Martin, this conference and to be published.
6. K. Kunc and R. M. Martin, Phys. Rev. Rapid Commun., in press.
7. R. M. Martin and K. Kunc, Phys. Rev., in press.
8. D. Vanderbilt and J. D. Joannopoulos, to be published.
9. P. E. Van Camp, V. E. Van Doren, and J. T. Devreese, Phys. Rev. Lett. 42, 1224 (1979).
10. P. E. Van Camp, V. E. Van Doren, and J. T. Devreese, this conference.
11. R. Resta and A. Baldereschi, to be published and this conference.
12. A. Muramatsu and W. Hanke, to be published and this conference.
13. D. Olego, M. Cardona, and P. Vogl, this conference.
14. L. J. Sham, Phys. Rev. 188, 1431 (1969); R. M. Pick, M. H. Cohen, and R. M. Martin, Phys. Rev. B1, 910 (1970).
15. J. Ihm, A. Zunger, and M. L. Cohen, J. Phys. C12, 4409 (1979).
16. See, for example, the review by S. K. Sinha, Crit. Rev. Solid State Sci. 3, 273 (1973).
17. C. M. Bertoni, V. Bortolani, C. Calandra, and E. Tosatti, Phys. Rev. Lett. 28, 1578 (1972).
18. S. G. Louie and M. L. Cohen, Phys. Rev. B17, 3174 (1978).
19. See, for example, V. L. Moruzzi, A. R. Williams, and J. P. Janak, Phys. Rev. B15, 2854 (1977).
20. P. Hohenberg and W. Kohn, Phys. Rev. B136, 864 (1964); W. Kohn and L. J. Sham, Phys. Rev. B140, 1133 (1965); L. J. Sham and W. Kohn, Phys. Rev. B145, 561 (1966).
21. R. M. Martin and K. Kunc, Proc. of CECAM Conf. on Ab Initio Calculations of Phonon Spectra, Antwerp, 1981, to be published.
22. D. J. Chadi and M. L. Cohen, Phys. Rev. B8, 5747 (1973); H. J. Monkhorst and J. D. Pack, Phys. Rev. B13, 5188 (1975).
23. K. Kunc and R. M. Martin, Phys. Rev., to be published.
24. D. R. Hamann, M. Schluter, and C. Chiang, Phys. Rev. Lett. 43, 1494 (1979).
25. W. Weber, Phys. Rev. B15, 4789 (1977).
26. D. J. Chadi, Phys. Rev. Lett. 41, 1062 (1978).
27. J. Ihm and M. H. Cohen, Phys. Rev. B21, 1527 (1980).
28. K. Kunc and R. M. Martin, to be published.

## FIRST PRINCIPLES CALCULATION OF THE PHONON SPECTRA OF SOLIDS\*

P.E. Van Camp, V.E. Van Doren and J.T. Devreese\*\*

*University of Antwerpen, Belgium.*

**Abstract.**- In this article, a first principles microscopic calculation of Si is presented and compared with results of other methods.

In the last few years several groups have achieved first principles microscopic calculations of phonon frequencies of semiconductors. Two different approaches have been used. The first results published<sup>1</sup> were obtained by calculating the total ground state energy of the crystal as a function of the lattice parameter. In this method the unit cell of the crystal has to be adapted to satisfy the symmetry requirements imposed by the lattice displacements of a particular phonon mode. This implies that such a method is in practice restricted to phonon frequencies of high symmetry points ( $\Gamma, X, L$ ). Recently, refinements of this method have lead to calculations of the phase transformations of covalent semiconductors and of a few phonon frequencies of Si.

In the second approach, the electronic contribution to the dynamical matrix is treated by means of the dielectric screening theory which describes the linear response of the electronic system to the displacements of the ions. This formalism has been known for a long time<sup>2</sup>. The advantage of the dielectric screening method over the above mentioned total energy difference approach is that it is not restricted to high symmetry points but can be used to calculate the complete phonon dispersion curves.

In this dielectric screening method, the essential quantity is the polarizability matrix  $\tilde{\chi}$ . The present authors have calculated the Hartree expression of the dielectric matrix by expanding  $\tilde{\chi}$  in terms of moments. This procedure incorporates the effect of all conduction bands, which is impossible to achieve in a direct summation over the bands. The results for Si where the zeroth moment is evaluated explicitly and the ratio of the first to the zeroth moment is a calculated constant are given in fig. 1. Details of this calculation can be found elsewhere<sup>3</sup>. It was found that in order to obtain realistic phonon curves it is crucial to achieve consistency between the

\*Work supported in part by a CDC-grant.

\*\*Also at T.N. Eindhoven, The Netherlands.

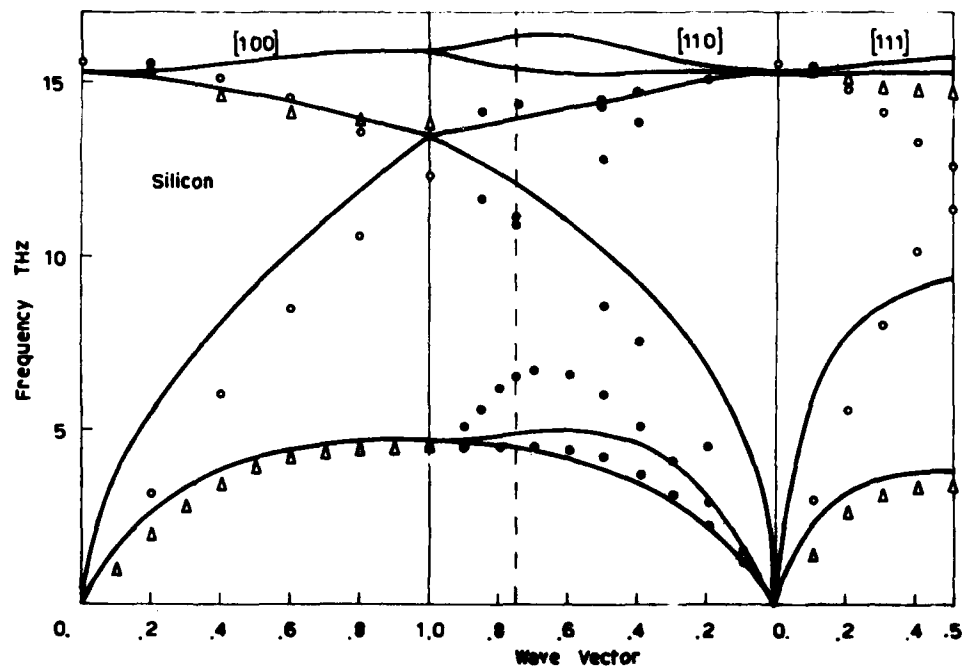


Fig. 1.

electron-ion potential and the crystal potential used to calculate the electron wave functions.

Recently, the present authors have investigated the exchange-correlation contribution to the phonon frequencies. The same exchange-correlation effects ( $p^{1/3}$  approximation) are included in both the Hamiltonian and in the dielectric matrix (see eq. (1) in ref. 4). The summations over the conduction bands have been performed explicitly. Furthermore, the lattice constant is not taken from experiment but is calculated from minimising the total energy of the crystal - as it should be done in order to have a system without stress - the following results are obtained in  $10^{12}$  Hz

a	$\Gamma$	TO(X)	LOA(X)	TA(X)
5.37	18.74	17.28	14.36	4.38

In conclusion, the dielectric screening approach shows that realistic phonon frequencies for all wavevectors are obtained from a first principles calculation.



References

- <sup>1</sup> D.J. Chadi and R.M. Martin, Sol. Stat. Comm. 19, 643 (1976).
- <sup>2</sup> See for example:  
L.J. Sham, Phys. Rev. 188, 1431 (1969).  
R.M. Pick, M.H. Cohen, R.M. Martin, Phys. Rev. B1, 910 (1970).
- <sup>3</sup> P.E. Van Camp, V.E. Van Doren, J.T. Devreese, Phys. Rev. Lett. 42, 1224 (1979).
- <sup>4</sup> P.E. Van Camp, V.E. Van Doren, J.T. Devreese, Phys. Rev. B24, 1096 (1981).

## VIBRATIONAL FREQUENCIES VIA FROZEN PHONONS \*

B.N. Harmon<sup>\*(1)</sup>, W.Weber\* and D.R. Hamann\*\*

\*Kernforschungszentrum Karlsruhe, Institut für Angewandte Kernphysik I,  
D-7500 Karlsruhe, F.R.G.

\*\*Bell Laboratories, Murray Hill, NJ 07974, U.S.A.

**Abstract.**— We have used a first principles linear combination of atomic orbitals (LCAO) method to calculate the total ground state energy for crystals of Si, Nb and Mo involving lattice distortions. From these calculations the equilibrium lattice constant, cohesive energy, and bulk modulus as well as the vibrational frequencies for selected phonons were determined.

1. **Introduction.**— Band theoretical methods are finding increased use in the study of electronic response to lattice distortion (caused by compression, stress, phonons, etc.). These techniques provide a tool for accurately calculating from first principles the frequency and charge density response for phonons at selected wavevectors. These techniques have already been applied to Si with considerable success using the pseudopotential <sup>1,2</sup> and LCAO <sup>3</sup> methods. Here we briefly present our LCAO method and our results for Si and then discuss the application of the method to metals giving preliminary results for Nb and Mo.

2. **Method.**— We have used the local density approximation for exchange and correlation<sup>4</sup> combined with a first principles tight binding method, the details of which have been described elsewhere.<sup>3,5,6</sup> The method employs an atomic basis composed of Gaussian functions which allow easy analytic evaluation of all three center integrals. The potential is expanded in a second Gaussian basis set and is general (i.e., no muffin-tin approximation is made). The calculations are iterated until the total energy is stable to seven significant digits. Absolute errors, for example those associated with the approximate treatment of exchange and correlation, are of course larger, but they are expected to cancel since we consider only energy differences.

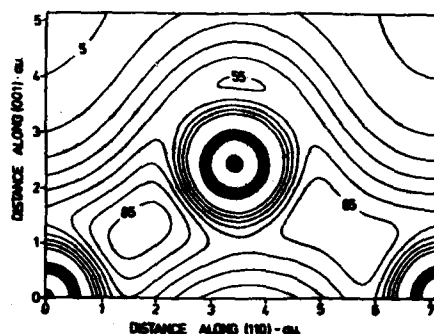
3. **Application to Si.**— Si was used as a test case to first avoid complications caused by a Fermi surface. Using the frozen core approximation the total energy was evaluated at eight values of the lattice constant and least squares fit with

<sup>5</sup>Operated for the U.S. Department of Energy by Iowa State University under contract no. W-7405-Eng-82. This work was supported by the Office of Basic Energy Sciences.

(1) Also Ames Laboratory and Department of Physics, Iowa State University, Ames, Iowa 50011, U.S.A

a fourth order polynomial. The corresponding equilibrium lattice constant, bulk modulus and cohesive energy are listed in Table 1. The total energy was also calculated as a function of displacement for lattice distortions corresponding to particular normal vibrational modes. These yield essentially classical potential wells whose curvature gives the phonon force constant or frequency. The frequencies for the transverse optic phonon at  $\Gamma$  [ $\text{TO}(\Gamma)$ ] and the transverse acoustic phonon at X [ $\text{TA}(X)$ ] are also listed in Table 1. There is good agreement with experiment, and the detailed analysis of the contributions to the total energy agree with previous studies.<sup>1,2</sup> The charge density for the  $\text{TO}(\Gamma)$  phonon is shown in Figure 1.

Fig. 1 : The charge density in the (110) plane for the lattice distortion corresponding to the  $\text{TO}(\Gamma)$  phonon with a displacement of  $-0.137\text{\AA}$  along the (111) direction. (atomic units  $\times 10^3$ ).



4. Application To Metals.— For metals small distortions of the lattice cause changes in the band occupation near the Fermi level which must be accounted for in calculating changes in total energy. Indeed such effects frequently give rise to phonon anomalies in transition metals.<sup>7</sup> One approach for metals is to simply keep increasing the number of  $\vec{k}$  points sampled until convergence is reached, however, this is costly and not necessary. Our approach has been to divide the irreducible Brillouin zone into a number of large tetrahedrons (32 for the H point phonon in Nb and Mo) and take the center of mass  $\vec{k}$  vectors as a sample grid. At each iteration a tight binding (TB) fit (see Ref. 7) is made to the eigenvalues on this grid and is used to determine an accurate Fermi energy and surface. The occupied volume as determined by the TB fit using 64 smaller tetrahedrons inside each large one is used to weight the  $\vec{k}$  points. Calculations using a mixed basis pseudopotential technique for phonons in Nb and Mo also confirm the importance of carefully weighting the  $\vec{k}$  points.<sup>8</sup>

The equilibrium lattice constant, bulk modulus and cohesive energy are listed in the table and again indicate the method is functioning well for the evaluation of bulk properties. To date we have only tested the method for the H-point phonon in Nb and Mo with the results listed in the table. This phonon in Mo is particularly anomalous as a result of a nesting feature in the Fermi surface.<sup>7</sup> The accurate modeling of changes in the Fermi surface as provided by the TB fit was required before the theoretical frequency was reduced from 9.9 THz to 5.7 THz. The frequency was determined by fitting (rms error =  $10^{-6}$  Ry/atom)

a parabola to the energy calculated for displacements of 0.064Å, 0.078Å, and 0.092Å, which are comparable to the displacement caused by the real phonon. Very small displacements led to numerical problems because of the linear interpolation used inside the small tetrahedrons, and much larger displacements caused previously unoccupied portions of bands to dip below the Fermi level, giving rise to anharmonic or non-parabolic behavior in the total energy vs displacement curve.

5. Conclusion.— Our encouraging results suggest that modern band theory techniques are capable of becoming a useful tool in studying the details of electronic response to certain high symmetry lattice distortions.

6. Acknowledgment.— One of the authors (B.N.H.) would like to thank the staff of the Institut für Angewandte Kernphysik I, Kernforschungszentrum, Karlsruhe, for their kind hospitality during his stay.

Table 1. Calculated and experimental properties

		a Lattice Constant (a. u.)	B Bulk Modulus (Mbar)	Cohesive Energy (eV/atom)	Phonon Frequency (THz)	
Si	calc.	10.40	0.89	4.92	4.9	15.0
	exp.	10.26	0.99	4.84	TA(X), 4.5	TO(Γ) 15.4.
Nb	calc.	6.32	1.62	6.63	6.6*	H point
	exp.	6.23	1.74	7.57	6.4	
Mo	calc.	5.99	2.57	6.28	5.7	H point
	exp.	5.95	2.63	6.82	5.5	

\*This is a preliminary value based on a fewer number of small tetrahedrons and both large and zero displacements so that it is less precise than the value for Mo (see text).

#### 7. References.—

1. H. Wendel and R. M. Martin Phys. Rev. **B19**, 5251 (1979).
2. M. T. Yin and M. L. Cohen Phys. Rev. Lett. **45**, 1004 (1980).
3. B. N. Harmon, W. Weber, and D. R. Hamann Phys. Rev. B (in press).
4. The approximate correlation functional was obtained from E. Wigner, Phys. Rev. **46**, 1002 (1934).
5. H. Szebe and R. H. Felton, J. Chem. Phys. **62**, 1122 (1975).
6. J. A. Appelbaum and D. R. Hamann, p. 111, *Transition Metals*, Eds. M. J. G. Lee, J. M. Perez and E. Fawcett (Inst. of Physics, Bristol, 1978), and P. J. Feibelman, J. A. Appelbaum and D. R. Hamann, Phys. Rev. **B20**, 1433 (1979).
7. C. M. Varma and W. Weber, Phys. Rev. **B19**, 6142 (1979).
8. K.-H. Ho, private communication.

## LIGHT SCATTERING FROM PHONONS IN GaAs-AlAs SUPERLATTICES

C. Colvard<sup>\*(1)</sup>, R. Merlin<sup>\*(1),(2)</sup>, M. V. Klein<sup>\*(1),(2)</sup> and A.C. Gossard<sup>\*\*</sup><sup>\*</sup>Materials Research Laboratory, University of Illinois at Urbana-Champaign, Urbana, Illinois 61801, U.S.A.<sup>\*\*</sup>Bell Laboratories, Murray Hill, New Jersey 07974, U.S.A.

**Abstract.** Raman scattering data have been taken on several GaAs-AlAs superlattices with  $d < 40$  Å. Folded LA and TA modes are both seen whose frequencies are well fit by an elastic model involving the bulk sound velocities of GaAs and AlAs. A number of peaks appear near the bulk LO and TO frequencies. Selection rules and a partial examination of resonance behavior are presented.

In a semiconductor superlattice composed of alternating layers of GaAs and AlAs one expects the increased lattice period  $d$  along the [001] growth direction to fold the Brillouin zone and produce new zone-center modes derived from bulk wavevectors  $q_z = 2\pi n/d$ , where  $n$  is an integer. Raman scattering spectra, which probe  $q \approx 0$ , clearly show the presence of these modes in the acoustic region  $< 100 \text{ cm}^{-1}$ . The optical region around the bulk LO and TO phonons, however, is more difficult to probe because the smaller dispersion of these branches causes many peaks in the spectra to overlap. In addition, light scattering from phonons with  $\vec{q} \parallel [001]$  may in some cases become allowed. We have used the resonant enhancement of the light scattering when the laser energy nears the band gap to try to separate these peaks.

The samples are single crystal superlattices  $\sim 4$  microns thick grown by molecular beam epitaxy on GaAs substrates. We have looked at three samples, designated A=(4.81, 4.03), B=(7.3, 4.4), and C=(9.4, 3.85). Here  $(\ell, m)$  means  $\ell$  monolayers of GaAs and  $m$  monolayers of AlAs per period, where one monolayer is  $\sim 2.83$  Å. Light scattering is done in backscattering geometry from the (001) surface.

Several folded acoustic modes have been seen in addition to those reported in Ref. 1. They are identified by their selection rules and their proximity to frequencies calculated by the elastic model described in that paper. The transverse modes have E symmetry and appear in both the  $(x, x)$  and  $(x, y)$  spectra. Here  $(x, y)$  denotes incident light polarized along [100], scattered along [010]. Such E modes become partially allowed when the laser is incident at the Brewster angle, giving an angle in the sample of  $\sim 15^\circ$  to the normal. We see them in sample A at 43 and  $47 \text{ cm}^{-1}$  and in sample B at 35 and  $38 \text{ cm}^{-1}$ , corresponding to the first zone-center gap  $q = 2\pi/d$ . The longitudinal modes, which should have  $A_1$  and  $B_2$  symmetry, appear only in  $(x, x)$ . The appearance of  $B_2$  in  $(x, x)$  and not in  $(x, y)$ , even apparently out of resonance, is puzzling since the Raman tensor for the  $D_{2d}$  point group implies that  $B_2$  only should be seen in  $(x, y)$ . These modes appear in sample A at 63.1 and

(1) Also at Dept. of Physics, Univ. of Illinois at Urbana-Champaign

(2) Also at Coordinated Science Laboratory, Univ. of Illinois at Urbana-Champaign

(3) Present address : Dept. of Physics, Univ. of Michigan, Ann Arbor, MI

66.9  $\text{cm}^{-1}$ , in B at 52 and 57  $\text{cm}^{-1}$ , and in C at 39 and 45  $\text{cm}^{-1}$ , corresponding to  $q=2\pi/d$ , and in sample C at 80 and 85  $\text{cm}^{-1}$  corresponding to the next higher zone-center gap  $q=4\pi/d$ . In addition, when the laser is tuned near the gap energy, the (x,x) spectrum shows peaks in sample A at 30 and 36  $\text{cm}^{-1}$  which apparently correspond to scattering from the zone edge  $q=\pi/d$  gap. Possible reasons for their appearance are i) a doubled periodicity folding this gap to the zone center, resulting for example from an odd number  $\ell+m$  of monolayers in one compositional period, or ii) momentum conservation relaxation due to the presence of disorder. A broad structure ( $\sim 30 \text{ cm}^{-1}$  wide) that may be due to higher gaps is also seen near 100  $\text{cm}^{-1}$  in both samples A and B.

An example typical of the structure in the optical region is shown in Fig.1, taken near resonance in sample B at 180 K.

Brewster angle backscattering gives  $q$  in the x-z plane inclined  $\sim 7^\circ$  to [001]. Five peaks are clearly visible, none corresponding exactly to the bulk GaAs values of 270.4  $\text{cm}^{-1}$  for TO and 293.7  $\text{cm}^{-1}$  for LO at this temperature. The peak labeled 1 is E(TO) and disappears in exact backscattering. It corresponds to the unfolded GaAs TO phonon shifted down in frequency by the superlattice. Other spectra show a clear shoulder on this peak in (x,y) around 255  $\text{cm}^{-1}$ . Peak 2 is similar to that labeled E( $\text{LO}_1$ ) in Ref.2, where it is attributed to an interface-like mode propagating parallel to the layers. Such a peak may become allowed near resonance.<sup>[4]</sup> Its frequency is rather well described by a dielectric constant model,<sup>[2]</sup> but in these

thin-layer samples it is also near predictions for the position of the first folded LO mode.<sup>[3]</sup> More samples need to be studied to see if the frequency is dependent upon total period, as for folding, or only dependent upon the ratio of layer thicknesses as our model predicts for E( $\text{LO}_1$ ). The thickness of the superlattice and sample absorption of the laser make angle-dependent studies of this mode difficult. It appears at 276, 280, and 283  $\text{cm}^{-1}$  at room temperature in samples A, B, and C respectively.

Peaks 4 and 5 were originally interpreted in sample A as the allowed and forbidden scattering from a single  $B_2(\text{LO}_1)$  unfolded mode.<sup>[2]</sup> Their splitting is now well established. At 300K peak 5 occurs at 287, 288.5, and 290.5  $\text{cm}^{-1}$  in samples A, B, and C, and peak 4 is seen at 284.3 and 287.5  $\text{cm}^{-1}$  in samples A and B, respectively. A possible explanation of peaks 2 through 5 is that they show the folding

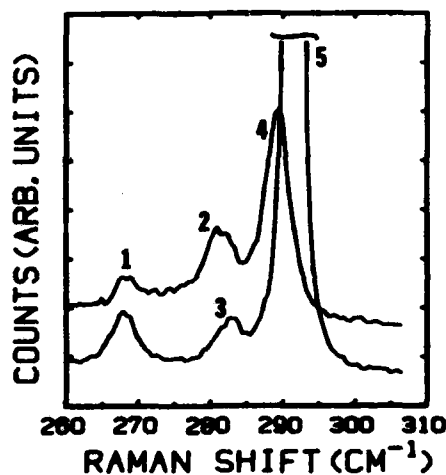


Fig. 1 : Spectrum of sample B at 180K. Upper curve (x,x), lower is (x,y). (x,x) shifted upward for clarity.

of the GaAs-like LO branch, in which case the symmetry assignments would be  $B_2$  for peaks 3 and 5 and  $A_1$  for peaks 2 and 4. However, a linear chain model for a (4,4) superlattice by Barker et. al.<sup>[3]</sup> suggests that the highest folded mode should lie closer to peak 2 in sample A, as mentioned above. If q-dependence is involved as in Fröhlich type forbidden scattering,  $B_2$  modes may appear in the (x,x) spectrum. It is not clear why no forbidden scattering is seen at resonance for peak 5 in (x,x) or why it might be shifted to the position of peak 4.

The resonance behavior of these peaks is demonstrated in Fig. 2. The spectra were taken on sample B with 1.833 eV laser light by changing the gap with temperature between 100K and 300K. The photoluminescence peak was measured by exciting well above the gap. The energy of the room temperature peak is 1.805 eV. The curve labeled A is the folded acoustic mode at  $50 \text{ cm}^{-1}$ . Both peaks 1 and 3 show little change with laser energy.

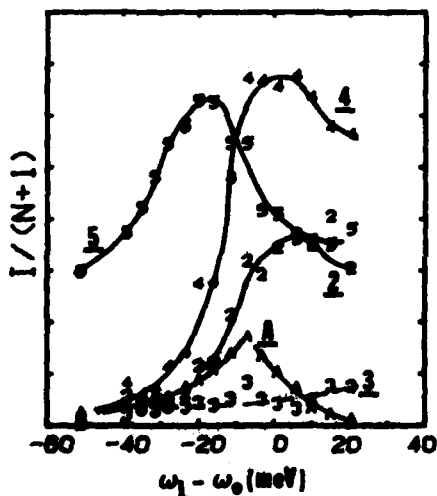


Fig. 2: Resonance behavior of peaks in Fig. 1.  $\omega_0$  is energy of the photoluminescence peak. Corrected for thermal factor but not absorption.

This work was supported in part by the Joint Services Electronics Program (U.S. Navy, U.S. Army and U.S. Air Force) under Contract No. N00014-79-C-0424, the National Science Foundation under Grant No. DMR 7902780, and profited from institutional support by the National Science Foundation for the Materials Research Laboratory under Grant No. DMR 7723999.

- [1] C. Colvard, R. Merlin, M.V. Klein, and A.C. Gossard, Phys. Rev. Lett. 45, 298 (1980).
- [2] R. Merlin, C. Colvard, M.V. Klein, H. Morkoç, A.Y. Cho, and A.C. Gossard, Appl. Phys. Lett. 36, 43 (1980).
- [3] A.S. Barker, Jr., J.L. Merz, and A.C. Gossard, Phys. Rev. B17, 3181 (1978).
- [4] S. Permogorov and A. Reznitsky, Solid State Commun. 18, 781 (1976).

## SELF-ENERGY OF PHONONS INTERACTING WITH FREE CARRIERS IN SILICON

L. Pintschovius, J.A. Vergés\* and M. Cardona\*

*Kernforschungszentrum Karlsruhe, F.R.G.**\*Max-Planck-Institut für Festkörperforschung, 7000 Stuttgart, F.R.G.*

**Abstract.** - The dispersion in the self energy of acoustic phonons produced by free electrons and holes in silicon has been measured with neutron scattering. The corresponding electron-phonon interaction mechanisms are discussed.

**Introduction.** - Doping, either n- or p-type, is known to change the frequencies of acoustic phonons in silicon<sup>1</sup>. This change is the real part of the self energy of the phonons produced by the free carriers via electron phonon interaction. Similar effects have been observed for the Raman phonons<sup>2</sup>. Recent measurements in p-type Ge have shown that those self energies can depend strongly on phonon momentum  $q$ .<sup>3</sup> Since conventional ultrasonic and light scattering techniques are not suitable for a detailed study of this  $q$ -dependence we have undertaken such study by means of inelastic neutron scattering. The acoustic branches of n- ( $n = 5 \times 10^{19} \text{ cm}^{-3}$ ) and p-type ( $p = 1.7 \times 10^{20} \text{ cm}^{-3}$ ) Si were measured with respect to intrinsic Si throughout the (100) and (111) directions of the Brillouin zone. The results yield information about hydrostatic and uniaxial deformation potentials for electrons and holes and the g-type intervalley coupling of electrons.

**Results and discussion.** - The normalized self energy ( $\Delta\omega/\omega$ ) of the TA phonons of n-Si along (111) at 300K is shown in Fig. 1. The data for  $q=0$  were obtained by ultrasonic methods and agree with those in (1). The self-energies are found to be, using second order perturbation theory:

$$\frac{\Delta\omega}{\omega} = -|\xi_2|^2 \frac{\chi_e(q)q^2}{C_{11}-C_{12}+C_{44}} \quad (1)$$

where  $\xi_2 = 8.7 \text{ eV}$  (4) is the shear deformation potential of the electron valleys,  $C_{ij}$  are the stiffness constants and  $\chi_e(q)$  the Lindhard susceptibility of a single electron valley ( $\epsilon = \epsilon_L + 24\pi\chi_e$ ) at  $T=300\text{K}$  (obtained numerically). The solid curve, calculated with Eq. (1), decays faster than the experiments with increasing  $q$ . We believe it is additionally broadened by the finite mean free path  $\ell = 62 \text{ \AA}$  ( $\Delta q = 2\pi/\ell = 0.09(2\pi/a)$ ).

The results for LA phonons along (100) in n-Si are in Fig. 2.



They show definite structure for  $q \approx 0.3(2\pi/a)$ . The solid curve in Fig. 2 was obtained with:

$$\frac{\Delta\omega}{\omega} = - \frac{q^2}{c_{11}\epsilon^2} \left\{ \left( \mathcal{E}_1 - \frac{2}{3}\mathcal{E}_2(1+24\pi\chi_{\perp}) \right)^2 \chi_{\parallel}(q) \right. \quad (3)$$

$$\left. + 2 \left( \mathcal{E}_1 + \frac{1}{3}\mathcal{E}_2(1+24\pi\chi_{\parallel}) \right)^2 \chi_{\perp}(q) \right\} + \left( \frac{\Delta\omega}{\omega} \right)_g$$

where  $(\Delta\omega/\omega)_g$  is the effect of  $g$ -coupling between (100) and  $(\bar{1}00)$  valleys, resonant for  $q \approx 0.28(2/a)$ , with coupling constant  $0.8 \text{ eV/\AA}(5)$ ,  $\chi_{\parallel}$  and  $\chi_{\perp}$  are Lindhard susceptibilities parallel and perpendicular to the valley axis, and  $\mathcal{E}_1$  is the "absolute" hydrostatic deformation potential of the electrons at  $\Delta_1$  (we take  $\mathcal{E}_1 = -7 \text{ eV}(6)$ ). The structure at  $q \approx 0.3(2\pi/a)$  is mostly produced by  $\epsilon_1$  with a small contribution of  $(\Delta\omega/\omega)_g$ . The  $\mathcal{E}_1$  effect is completely screened by the free carriers for  $q=0$  but becomes unscreened for finite  $q$  thus giving the bump observed at  $q \approx 0.3(2\pi/a)$ .

Fig. 3 discusses TA-phonons along (100) in n-Si. The effect at  $q=0$  is due to coupling of the  $\Delta_1$  with the  $\Delta_2$  states along (010) and (001) (deformation potential  $\mathcal{E}_2^*(7)$ ). The calculated curve explains the  $q=0$  effect but fails to account for the observations for  $q \neq 0$ .

Figure 4 describes TA(111) phonons in p-Si. The effect is mainly produced by heavy holes along {110} directions. The solid curve was calculated in this manner with the deformation potentials  $b=-2.2 \text{ eV}$  and  $d=-4.9 \text{ eV}(4)$ . For  $q=0$  it agrees with Ref. 8 about it falls short of the measured values for  $q \neq 0$ . The additional mean free path  $q$ -broadening  $\Delta q = 2\pi/l \approx 0.09(2\pi/a)$  suffices to explain the difference.

Figure 5 shows  $\Delta\omega/\omega$  for LA(100) phonons in p-Si. In this case the screened effect of the hydrostatic deformation potential  $a_V = \epsilon_1 - a = -8.5 \text{ eV}$  ( $a$  = hydrostatic deformation potential of indirect gap) produces the maximum at  $q \approx 0.2(2\pi/a)$ . The calculated curve describes qualitatively this observed effect.

#### References

1. R. Keyes, in Solid State Physics 20, 37, (1967)
2. M. Chandrasekhar, J.B. Renucci and M. Cardona, Phys. Rev. B 17, 1623(1978)
3. D. Olego and M. Cardona, Phys. Rev. 23, 6592(1981)
4. O. Madelung, Landoldt-Börnstein Tables, in press
5. C. Jacoboni and L. Reggiani, Adv. Phys. 28, 493 (1979)
6. D. Glötzl, O.K. Andersen, J.A. Verges and M. Cardona, to be published
7. F. Cerdeira and M. Cardona, Phys. Rev. B8, 4723 (1973)
8. C.K. Kim, M. Cardona and S. Rodriguez, Phys. Rev. 13, 5429(1976)

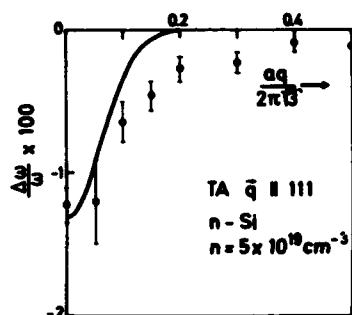


Fig. 1. - Selfenergy of TA [111] phonons in n-Si.

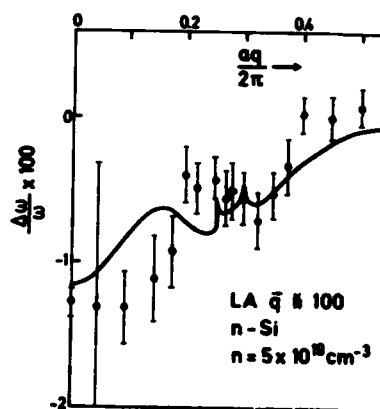


Fig. 2. - Selfenergy of LA [100] phonons in n-Si: it remains constant from  $aq/2\pi = 0.5$  to edge of BZ.

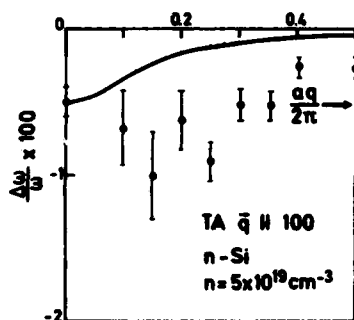


Fig. 3. - Selfenergy of TA [100] phonons in n-Si: it remains constant from  $aq/2\pi = 0.5$  to edge of BZ.

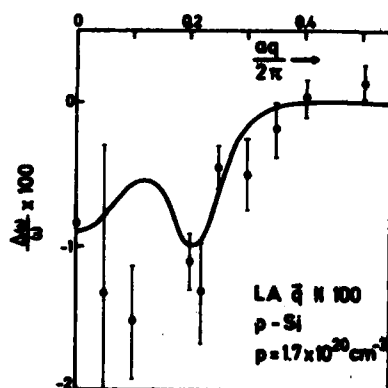


Fig. 4. - Selfenergy of TA [111] phonons in p-Si.

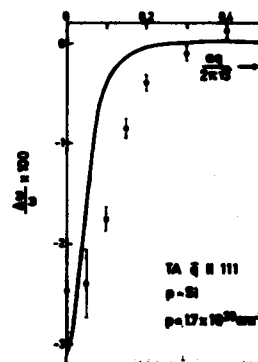


Fig. 5. - Selfenergy of LA [100] phonons in p-Si: it remains constant from  $aq/2\pi = 0.5$  to edge of BZ.

NEUTRON, X-RAY AND LATTICE DYNAMICAL STUDIES OF  $\text{Sb}_2\text{S}_3$ K.R. Rao<sup>\*\*</sup>, V.M. Padmanabhan<sup>\*\*\*</sup>, P.R. Vijayaraghavan<sup>\*\*</sup> and S.L. Chaplot<sup>\*\*</sup><sup>\*</sup> Bhabha Atomic Research Centre, Trombay, Bombay 400 085, India<sup>\*</sup> Nuclear Physics Division<sup>\*\*</sup> Neutron Physics Division

**Abstract.** - 'Elastic' neutron and x-ray diffraction patterns from crystals of  $\text{Sb}_2\text{S}_3$  (mineral stibnite) show that the crystals, while ordered along  $\langle 010 \rangle$  (the chain axis), are disordered about  $\langle 010 \rangle$ . Extensive diffuse intensity perpendicular to  $\langle 010 \rangle$  direction is observed. Inelastic scattering studies using  $1.4\text{\AA}$  neutrons did not lead to any soft TA modes with  $q$  in the  $(0k0)$  plane and polarised along  $\langle 010 \rangle$ . A few longitudinal phonons along  $\langle 010 \rangle$  are seen. Results from lattice dynamical calculations based on a rigid ion model (with covalent bonding included) are discussed in the context of these observations.

1. **Structure.** -  $\text{Sb}_2\text{S}_3$  is an interesting photo-conductive ferroelectric semiconductor which crystallises at room temperature in orthorhombic form with spacegroup  $D_{2h}^{16}$  containing four molecules per unit cell. The crystallographic structure shown in Fig.1 consists of ribbons or chains of  $(\text{Sb}_4\text{S}_6)$  in the  $b$ -direction. ( $a = 11.3107\text{\AA}$ ,  $b = 3.8363\text{\AA}$ ,  $c = 11.2285\text{\AA}$ ).

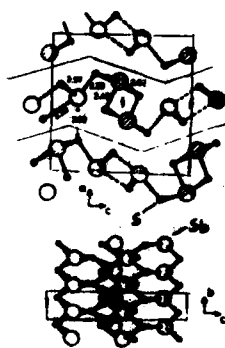


Fig.1 Crystal structure of  $\text{Sb}_2\text{S}_3$ .

2. **Experimental** - We studied a large natural crystal of mineral stibnite at room temperature (paraelectric) by neutron and x-ray scattering techniques to understand the dynamical properties of the system. Fig.2 is data from 'elastic' neutron diffraction experiments in the  $(h0l)/(0kl)$  plane (we were unable to distinguish between the  $a$  and  $c$  axes due to the extensive disorder in the plane). This figure is reminiscent of features observed in case of  $\text{CaB}_2\text{PO}_4$  by others. The diffraction pattern around  $(040)$  given in Fig.3 clearly shows that the diffraction intensity appears elongated perpendicular to the  $b$ -axis. Such intensity patterns are expected of quasi-one-dimensional lattices.

perpendicular to the  $b$ -axis. Such intensity patterns are expected of quasi-one-dimensional lattices.

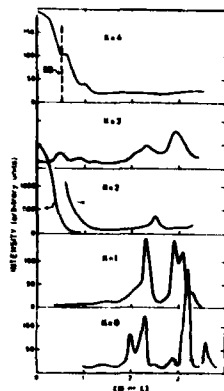


Fig.2 'Elastic' neutron diffraction patterns from  $\text{Sb}_2\text{S}_3$  in the (h0l)/(0kl) plane.

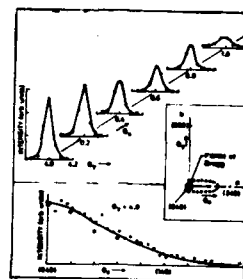


Fig.3 Details of the diffraction intensity around (040).

Fig.4 shows the rotation and Weissenberg x-ray patterns from fibres from the same specimen corroborating neutron results namely, that one observes disorder about  $\langle 010 \rangle$  axis showing extended diffuse streaks; additional diffuse lines are also observed.

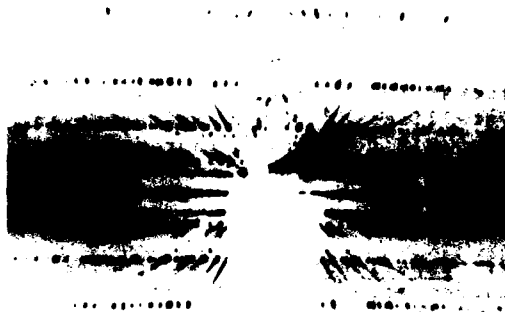


Fig.4 Rotation x-ray photograph of  $\text{Sb}_2\text{S}_3$ . Rotation about b-axis



Fig.5 Weissenberg photograph of zero layer of b-axis.

Inelastic neutron scattering experiments permitted us to measure only a longitude branch along  $\langle 010 \rangle$  direction. Experiments to look for TA modes along  $\langle 100 \rangle$  /  $\langle 001 \rangle$  direction with polarisation along  $\langle 010 \rangle$  were unsuccessful due to presence of extensive diffuse scattering and poor resolution of the experimental set-up. Fig.6 shows the neutron groups associated with the longitudinal  $\langle 010 \rangle$  modes.

**3. Lattice Dynamical Results** - We have carried out lattice dynamical calculations based on a rigid ion model with charges and radii of ions as parameters of the model. Covalent bonding between Sb-S pairs (limited to a distance of 2.6Å) are included. Results of calculations along three high symmetry directions are given in Fig.7.

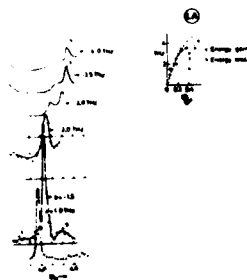


Fig.6 Longitudinal lattice modes as observed by inelastic neutron scattering experiments.

The parameters of the model were chosen so as to provide reasonable cohesive energy and lattice frequencies which cover the infrared and Raman spectral ranges. We observe that there is an extremely soft TA-TO branch in the  $\langle 100 \rangle$  direction; a similar branch may also be noted along  $\langle 001 \rangle$  direction. These branches could give rise to diffuse scattering in neutron and x-ray diffraction patterns. Since these modes are of very low frequency ( $< 0.5$  THz), it is difficult to observe these phonons because of poor resolution. The displacement of atoms at  $q = 0$  for TO mode represents out-of-phase motions of the two chains (each of  $\text{Sb}_4\text{S}_6$  configuration) in the unit cell against each other. Note this can represent interlayer modes if the crystal is thought of as layer-like system.

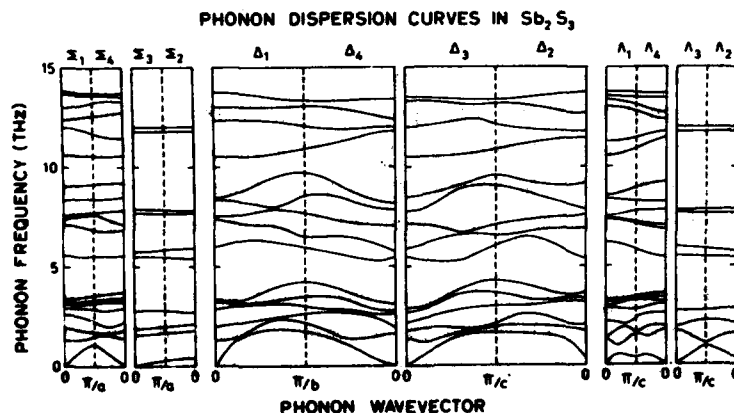


Fig. 7 Calculated phonon dispersion relation in  $\text{Sb}_2\text{S}_3$ .

Details of the experimental observations, dynamical interpretation of calculated results, comparison with data in  $\text{SbSI}$  etc. are to be published elsewhere.

## VIBRATIONAL PROPERTIES OF VACANCIES IN HOMOPOLAR SEMICONDUCTORS

K. Suzuki, D. Schmeltzer and A.A. Maradudin

*Max-Planck-Institut für Festkörperforschung, Heisenbergstrasse 1, 7000 Stuttgart 80, F.R.G.*

**Abstract.** Spectral densities of phonons in the immediate vicinity of a vacancy in Si and Ge are calculated in the continued fraction/recursion method. The results indicate that both in Si and Ge the presence of vacancy gives rise to a sharp decrease in the DOS in the optical frequency range and a rather diffuse increase in the acoustic frequency range.

1. Introduction. - At moderately high concentrations of hydrogen in amorphous Si, four hydrogen atoms tend to cluster as they saturate groups of four dangling bonds pointing towards a counterpart of the crystalline vacancy.<sup>1</sup> Infrared absorption<sup>1,2</sup> and Raman scattering<sup>3</sup> experiments on amorphous and crystalline Si or Ge with H, D, or F as impurities show that the frequency of the resonant vibration in the acoustic range depends only very slightly on impurity species. This suggests that such vibrational modes involve a large number of atoms of the host and leads one to suspect that the vacancy in whose vicinity the clustering occurs may itself give rise to resonant modes in the frequency range where they have been observed.

As a step in the direction of elucidating the nature of the resonant modes we have studied vibrational properties of crystalline Si and Ge containing an isolated vacancy. Use has been made of the real space version of the continued fraction/recursion method<sup>4</sup>, which does not require a periodic arrangement of atoms. The method has been applied successfully to several types of lattice dynamical defect problems involving a lowering of symmetry<sup>5</sup>, although not to point defects as far as we are aware.

The local density  $\rho_{\alpha\alpha}(l, l; \omega)$  of vibrational modes of polarization  $\alpha$  at site  $l$  and frequency  $\omega$  is directly related to the diagonal element of the Green's function of the dynamical matrix  $D_{\alpha\beta}(l, l')$ <sup>6</sup>. In the recursion method<sup>4</sup> the latter is expressed in a continued fraction

$$U_{\alpha\alpha}(l, l; \omega) = \frac{1}{\omega^2 - a_0 - \frac{b_0^2}{\omega^2 - a_1 - \frac{b_1^2}{\omega^2 - a_2 \dots}}} \quad (1)$$

where the coefficients  $(a_0, a_1, \dots)$  and  $(b_0, b_1, \dots)$  can be obtained as functions of  $l$  and  $\alpha$  algebraically once  $D_{\alpha\beta}(l, l')$  of the system is given.

2. Perfect Crystal. - To examine the applicability of the recursion method we first calculate the phonon spectrum of Si crystal without vacancy. On the one hand the phonon spectrum is obtained in the recursion method by considering a finite crystal containing up to 18 000 atoms, at the surface of which all bonds are terminated. The dynamical matrix is such that includes only the first and second neighbor forces.<sup>7</sup> This requires six independent force constants, of which five have been chosen to give a best least-squares fit to the experimental phonon frequencies at  $\Gamma$ , X, and L points.<sup>8</sup> The last one, the second neighbor force constant  $\delta$ , which affects none of the above phonons, has been either fixed on the basis of the valence force field model<sup>9</sup> ( $\delta = (\mu - \nu - \lambda)/2$ ) or equated to zero. The first 21 coefficients ( $a_0, \dots, a_{20}$ ) and ( $b_0, \dots, b_{20}$ ) in Eq. (1) were directly calculated and the remaining part of the continued fraction was replaced by an asymptotic form

$$T = \{ \omega^2 - a_\infty - [(\omega^2 - a_\infty)^2 - 4b_\infty^2]^{1/2} \} / (2b_\infty^2) \quad (2)$$

where  $a_\infty$  and  $b_\infty$  are chosen either from an extrapolation of the calculated coefficients or from the requirement that the obtained phonon spectrum extends from zero to the experimental highest frequency (namely that of the optical phonons at  $\Gamma$ ). The phonon LDOS  $\rho_{\alpha\alpha}(\mathbf{l}, \mathbf{l}; \omega)$  calculated from Eq. (1) is independent of  $\alpha$  and  $\mathbf{l}$  (provided  $\mathbf{l}$  is close to the center of cluster) and is represented by the upper curve in Fig. 1.

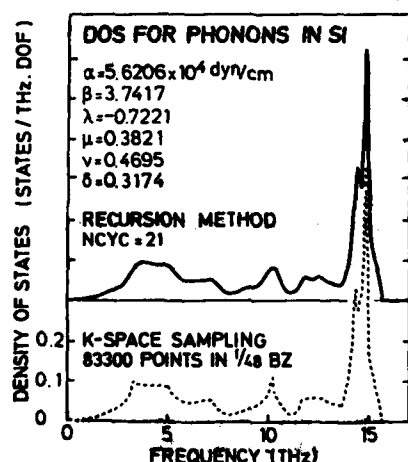


Fig. 1. Lattice vibration spectrum of Si using first and second neighbor forces in the recursion and in the k-space sampling method. The force constants are those defined by Herman.

On the other hand the phonon spectrum is calculated for an infinite lattice using the same force constants in the usual k-space sampling method. With about 80 000 sample points in 1/48 of the Brillouin zone we obtain a phonon DOS which is shown by the lower curve in Fig. 1.

With only up to second neighbor forces neither of the DOS reproduces the sharp peak in the acoustic region which would be present if the substantial flattening of acoustic phonons in the vicinity of BZ edge were properly taken into account.<sup>10</sup> Except for this, both of the curves reproduce the general features of the known phonon spectrum fairly well. The two curves are very similar, the only difference being that the recursion method generally smoothes sharply edged van Hove singularities characteristic of infinite crystals.<sup>11</sup>

3. Vacancy. - To model a vacancy in the simplest way we remove the central Si atom at  $\lambda=0$  and equate to zero all forces connected to this atom. In contrast to the preceding case, the LDOS does depend on the lattice site  $\lambda$  and we evaluate it at one of the four nearest neighbors of the vacancy. The recursion calculation proceeds in a similar way as before using the same set of force constants, except that we equate  $\delta=0$ , which is required if the translational invariance condition<sup>6</sup> is to be satisfied without introducing new force constants. No relaxation of atomic position is assumed. The spectral density for the perfect crystal ( $\delta=0$ ), that of the vacancy and their difference are shown in Fig. 2.

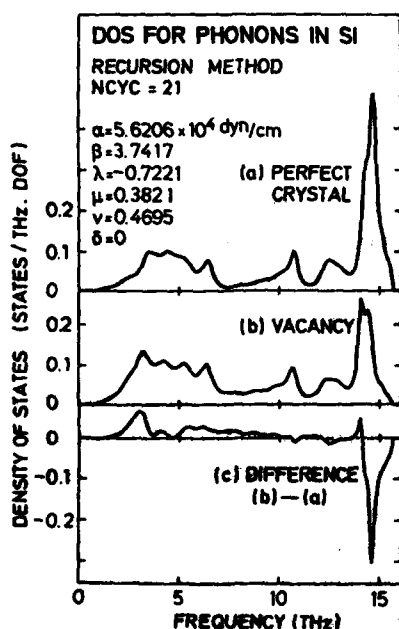


Fig. 2. Vibration spectrum of the single vacancy in Si calculated in the recursion method.

4. Discussion. - In Fig. 2 we see a diffuse increase of DOS in the lower acoustic frequency region and a decrease in the optical region. This is expected if we consider the presence of a vacancy as a partial softening of the force acting on its neighbors. The introduction of H or F, on the other hand, corresponds to a hardening (decreased ionic mass) and gives rise to a rather sharp resonant mode at the upper edge of the acoustic spectrum, as has been observed. A further discussion on the change of DOS for various point defects can be made on the basis of the function (1) for the perfect crystal. Essentially similar results are obtained for a vacancy in Ge.

5. Acknowledgement. - We are indebted to M. Cardona, H. Bilz, and W. Kress for discussions and to H.J. Stärke for advice on numerical work.

#### References

1. S.C. Shen, C.J. Fang, H. Cardona, and L. Genzel, *Phys. Rev. B* **22**, 2913 (1980).
2. H. Shanks, C.J. Fang, L. Lay, M. Cardona, F.J. Demon, and S. Kätbitzer, *Phys. Stat. Sol. (b)* **100**, 43 (1980); S.C. Shen, C.J. Fang, and M. Cardona, *Phys. Stat. Sol. (b)* **101**, 451 (1980).
3. D. Bermejo and M. Cardona, *J. Noncryst. Solids* **32**, 405 (1979).
4. R. Haydock, *Solid State Phys.* **35**, 215 (1980), M.J. Kelly, *ibid* **35**, 295 (1980).
5. M. Mostoller and U. Landman, *Phys. Rev. B* **20**, 1755 (1979), J.E. Black, B. Laks, and D.L. Mills, *Phys. Rev. B* **22**, 1818 (1980).
6. A.A. Maradudin et al., *Solid State Phys. Suppl.* **3** (2nd ed.), 1 (1971).
7. Our notation of force constants is the same as F. Herman, *J. Phys. Chem. Solids* **8**, 406 (1959).
8. H. Bilz and W. Kress, *Phonon Dispersion Relations in Insulators*, Springer, 1979.
9. K. Kunc, H. Balkanski, and M. Nussimovici, *Phys. Rev. B* **12**, 4346 (1975).
10. W. Weber, *Phys. Rev. B* **15**, 4789 (1977).
11. Similar conclusions have been obtained for a simpler case by P.E. Meek, *Phil. Mag.* **33**, 897 (1976). See also C. Herscovici and M. Fibich, *J. Phys. C* **13**, 1635 (1980) and V. Heine, *Solid State Phys.* **35**, 1 (1980).



## SECOND ORDER RAMAN SCATTERING IN CRYSTALLINE SULPHUR SELENIUM AND TELLURIUM

P.J. Carroll\* and J.S. Lannin\*

*Department of Physics, The Pennsylvania State University, University Park, Pennsylvania 16802, U.S.A.*

**Abstract.**— The second order Raman spectrum of orthorhombic(o-) S is reported and compared with the spectrum of monoclinic(m-) Se. The spectra of these ring systems exhibit very similar structure. Three regions of scattering are observed, two of which suggest a predominance of overtone scattering. The features of the other region arise from combination processes. A comparison between the high frequency bands of trigonal(t-) Te, t-Se, m-Se and o-S is also presented. Differences in these spectra are qualitatively explained in terms of the molecular unit of the crystal (ring or chain) and changes in inter-unit and intra-unit coupling.

The crystalline forms of S and monoclinic(m-) Se are composed of the same basic molecular unit, an 8-membered-puckered ring. Trigonal(t-) Se and t-Te are also composed of similar units, parallel helical chains, which are bonded together in a hexagonal lattice. Large inter-unit to intra-unit distance ratios in these solids imply that the dominant bonding is within the unit. However, interchain bonding is more significant than the van der Waals coupling exhibited between rings and is stronger in t-Te than in t-Se.

The role of this inter-unit bonding as well as the influence of the molecular unit in the group VI elements of S, Se and Te are studied here through second order Raman scattering. The second order Raman spectra of crystals provides valuable information about the one phonon density of states under the conditions of predominant overtone scattering and matrix element effects which are a smooth function of frequency. This is observed to be the case in previous studies of group IV and V elements.<sup>1</sup> A dominance of overtone scattering is also suggested in the second order Raman spectra of t-Te and t-Se which have been presented in earlier papers.<sup>2,3</sup> In these spectra the positions of most of the features are in good agreement with twice the frequency of features in the phonon density of states as obtained from theory and neutron scattering.

The second order Raman spectrum of orthorhombic(o-) S is displayed in Figure 1 with, for the purpose of comparison, the spectrum of m-Se, which has been studied in detail previously.<sup>3</sup> The spectra are scaled so that the high frequency regions are aligned. The dashed lines indicate the tails of the very intense first order peaks. The arrows in the o-S spectrum indicate twice the frequency of the  $k = 0$  modes at room temperature<sup>4</sup> and are labeled with the vibrational

\* Present address : Bell Laboratories, Murray Hill, NJ 07974

\* Supported by National Science Foundation Grant DMR 7908390

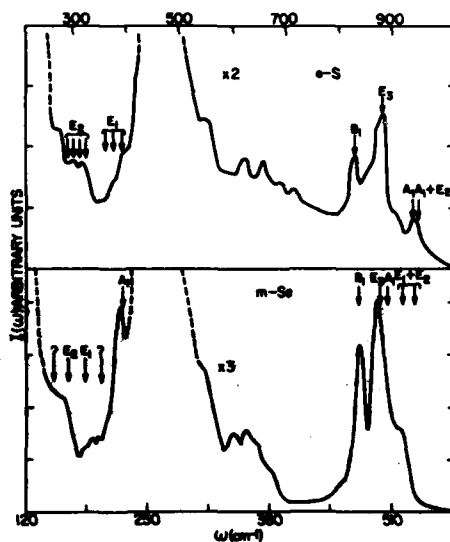


Figure 1. The second order Raman spectra of o-S and m-Se.

mode assignments of an isolated  $S_8$  molecule as calculated by Scott et al.<sup>5</sup>

Three regions of the second order scattering can be observed in Figure 1 containing similar structure in both spectra. The region which extends from  $255\text{ cm}^{-1}$  to  $420\text{ cm}^{-1}$  in the o-S spectrum contains features which are near twice the frequency of  $E_2$  and  $E_1$  first order modes. This suggests that overtone scattering occurs here from phonon branches corresponding to these lower optic modes. A second region, between  $500\text{ cm}^{-1}$  and  $760\text{ cm}^{-1}$ , exhibits features which can only be interpreted as originating from combination processes between high and low frequency optic modes. Notice that the m-Se spectrum has very similar structure here which is not as well resolved. A high frequency band consisting of second

order scattering from the higher optic modes is the third region. The main features at  $822\text{ cm}^{-1}$ ,  $876\text{ cm}^{-1}$  and  $937\text{ cm}^{-1}$  are centered very near to twice the frequency of  $k = 0$  modes suggesting that these three peaks are due to overtone scattering. This band may consequently be a good indication of the density of states for the higher optic modes. The narrowness of these peaks indicates that relatively little dispersion occurs in these phonon branches. The similarity of the high frequency bands of m-Se and o-S also suggests a revised mode assignment for the first order peaks in m-Se and is discussed elsewhere.<sup>6</sup>

A comparison of the second order Raman spectra of the high frequency bands of t-Te, t-Se, m-Se, and o-S is shown in Figure 2. A scaling factor of 1.64 is used to align the  $257\text{ cm}^{-1}$  peak of the t-Te spectrum to the  $441\text{ cm}^{-1}$  peak of the t-Se spectrum and a factor of 1.77 was used to scale the most intense peaks of o-S and m-Se. These empirical factors are greater than the square root of the mass ratios of the respective elements which indicates a trend of weaker intra-unit bonding in t-Te than in t-Se and in m-Se than in o-S. In addition, the shift to lower frequencies of the t-Se band with respect to the m-Se band is attributed to weaker bonding within a t-Se chain than within a m-Se ring. This demonstrates that intra-unit covalent bonding increases as inter-unit bonding decreases in these group VI elements.

Dultz et al.<sup>7</sup> and Meek<sup>8</sup> have suggested that a two peaked structure in the phonon density of states is characteristic of isolated chains. Figure 2 shows that

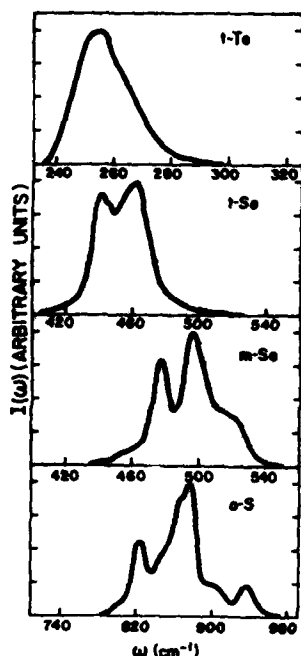


Figure 2. The high frequency second order Raman bands of t-Te, t-Se, m-Se and o-S.

this may also be true of a system of isolated rings and therefore of two-fold coordination in general. The fact that the t-Te spectrum does not have a double peaked structure demonstrates that t-Te should not be viewed as a system of isolated chains with respect to its vibrational properties, as interchain interactions are important. Although very similar, the features in the o-S spectrum are spread out more than in m-Se so that a high frequency feature that appears as a shoulder in m-Se is a peak in o-S. Additional features are also observed in the density of valence electron states of o-S compared to m-Se as obtained by x-ray photoemission spectra.<sup>9</sup> Thus both the electronic and vibrational densities of states indicate greater molecular character in o-S as is expected structurally.

In general, it is observed that significant changes occur in the phonon density of states as obtained from second order Raman scattering as a function of atomic weight in the group VI elements. These changes can be qualitatively explained in terms of the molecular unit and the relative strength of inter-unit and intra-unit forces.

- 1) J. S. Lannin and B. V. Shanabrook, in *Physics of Semiconductors*, 1978, ed. by E. L. Wilson (Inst. of Physics, Bristol and London, 1979) p. 643, and refs. therein.
- 2) P. J. Carroll and J. S. Lannin, in *Proc. 7th Int. Conf. Raman Spectroscopy*, ed by W. F. Murphy (North Holland, NY, 1980) p. 66.
- 3) P. J. Carroll and J. S. Lannin, *J. Phys. Soc. Japan*, **49**, 669 (1980) Suppl. A.
- 4) Measured from our room temperature first order Raman spectrum with some extrapolation from A. Anderson and Y. T. Lo, *Can. J. Chem.*, **47**, 879 (1969).
- 5) D. W. Scott and J. P. McCullough, *J. Mol. Spec.*, **13**, 313 (1964).
- 6) P. J. Carroll and J. S. Lannin (to be published).
- 7) W. Dultz, H. D. Hochheimer and W. Müller-Lierheim, in *Proc. 5th Int. Conf. Amorphous and Liquid Semicond.*, ed. by J. Stuke and W. Brenig (Taylor and Francis, London, 1974) p. 1281.
- 8) P. E. Mack, *Philos. Mag.*, **34**, 767 (1976).
- 9) W. R. Salaneck, C. B. Duke, A. Paton, C. Griffiths and R. C. Keeser, *Phys. Rev. B*, **15**, 1100 (1977).

ULTRASONIC PHONON VELOCITIES IN  $\text{Cd}_{1-x}\text{Mn}_x\text{Te}$  BETWEEN 1.5 AND 96 K :  
ANOMALIES NEAR THE MAGNETIC TRANSITION

A.Y. Wu and R.J. Sladek

*Department of Physics, Purdue University, West Lafayette, IN 47907, U.S.A.*

**Abstract.**— Transit times of 30 MHz ultrasonic waves have been measured from 1.5 K to 96 K for  $\text{Cd}_{1-x}\text{Mn}_x\text{Te}$  samples with  $0.05 \leq x \leq 0.65$ . Below 60 K the velocities for higher concentrations exhibit anomalous features which depend on  $x$  and are stronger for shear modes than for longitudinal modes. The shear mode anomalies are flattening of the temperature dependence for  $x = 0.20$  and  $0.35$  at low temperatures and a wide minimum centered around 22 K for samples with  $x \geq 0.55$ . The location of each minimum indicates that it is connected with a transition to the spin glass or antiferromagnetic state. The depth of the minimum is much greater than the elastic constant depression observed in transition metal alloy spin glasses (TMASG). This may be due to electrons (or holes) in large orbits around shallow-level impurities affecting the Mn magnetic moments.

Ultrasonic velocity measurements have proved useful for investigating magnetic phase transitions including those to the antiferromagnetic state in various insulating compounds<sup>1</sup> and to the spin glass state in transition metal alloys.<sup>2</sup>

In this paper we present the first ultrasonic velocity measurements on  $\text{Cd}_{1-x}\text{Mn}_x\text{Te}$ , a so-called semimagnetic-semiconductor which is paramagnetic at all temperatures for  $x < 0.17$ , becomes a spin glass below  $T_{\text{sg}}$  when  $0.17 < x < 0.62$  and is antiferromagnetic at low temperatures when  $0.62 < x < 0.71$ .<sup>3</sup> Our results should contribute to understanding phase transitions in spin-glass insulators which are due presumably to the frustration of antiferromagnetic alignment of ionic spins.<sup>3-5</sup>

We have measured the transit times of 30 MHz longitudinal and shear ultrasonic waves propagating normal to the (110) cleavage plane in  $\text{Cd}_{1-x}\text{Mn}_x\text{Te}$  samples with  $x = 0.05, 0.20, 0.35, 0.55, 0.57$ , and  $0.65$ . Laue x-ray photographs, and visual microscopic examination after etching at room temperature, reveal many small twins with (111) bounding planes in samples with  $x = 0.20$  and  $0.35$  and many small trills or hexagonalings with cubic (111) bounding planes (or hexagonal (0001) bounding planes because we have seen an apparent hexagonal structure with  $c/a$  ratio of  $\sqrt{5}$ ) in samples with  $x = 0.55$  and  $0.65$ . However, we believe that these structural imperfections are not the cause of the elastic moduli anomalies reported herein since elastic anomalies were also found in the  $x = 0.05$  and  $0.57$  single crystal samples and in the  $x = 0.20$  sample whose faster shear wave modulus has a value very close to those of the fast shear wave modulus in the single crystal samples.

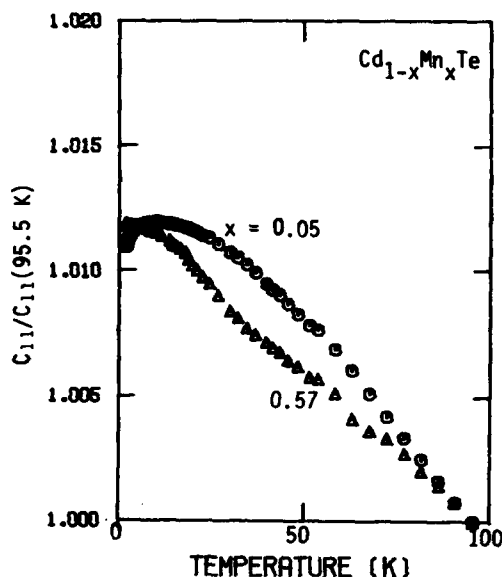


Fig. 1.  $C_{11}/C_{11}(95.5 \text{ K})$  vs  $T$  for single crystal samples. Values for  $C_{11}(95.5 \text{ K})$  are 5.56, and  $5.15 \times 10^{11} \text{ dyn/cm}^2$  for  $x = 0.05$  and 0.57, respectively.

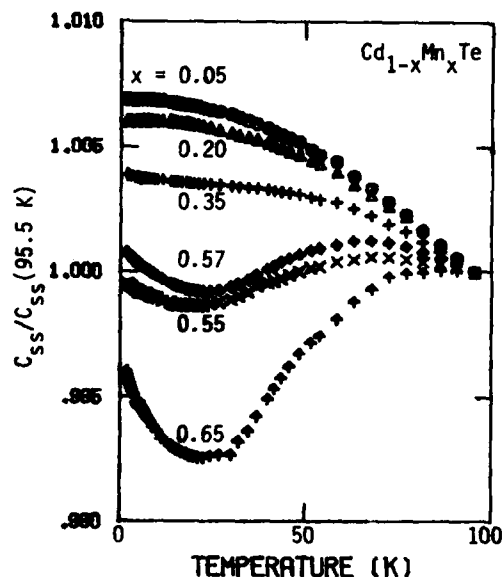


Fig. 2.  $C_{ss}/C_{ss}(95.5 \text{ K})$  vs  $T$  for the slower shear waves. Values for  $C_{ss}(95.5 \text{ K})$  are 9.03, 8.29, 9.40, 11.03, 7.94, and  $10.71 \times 10^{10} \text{ dyn/cm}^2$  for  $x = 0.05, 0.20, 0.35, 0.55, 0.57,$  and 0.65, respectively.

The elastic stiffness moduli of longitudinal and two shear waves were deduced from transit time data using the thermal expansivity of CdTe to correct for sample density and length changes. For single crystals,  $C_{\text{long}} = (C_{11} + C_{12} + 2C_{44})/2$ ,  $C_{fs} = C_{44}$  and  $C_{ss} = (C_{11} - C_{12})/2$ , where fs means fast shear and ss slow shear.

From Fig. 1 it can be seen that the normalized  $C_{11}$  longitudinal wave modulus obtained for single crystal samples has a depression at lowest temperatures for  $x = 0.05$  and between 20 K and 50 K for  $x = 0.57$ , indicating the presence of some volumetric magneto-elastic coupling.

The stiffness moduli of both the slower and faster traveling shear waves,  $C_{ss}$  and  $C_{fs}$ , respectively, have generally similar temperature dependences so we show only  $C_{ss}$  data in Fig. 2. The shear moduli exhibit anomalies which include flattening of the temperature dependence for  $x = 0.20$  and 0.35 and a wide minimum centered around about 22 K for  $x \geq 0.55$ . Each minimum includes the region where the magnetic susceptibility<sup>3,6</sup> indicates a magnetic transition. Our minima are much deeper than the elastic constant depression observed in transition metal alloy spin glasses (TMASG). This may be due to electrons (or holes) localized in large orbits around shallow-level impurities affecting the alignment of Mn spins<sup>7</sup> combined in the  $x = 0.55$  and 0.57 samples with frustration of the antiferromagnetic interaction by the lattice in semiconducting  $\text{Cd}_{1-x}\text{Mn}_x\text{Te}$ , whereas a free electron RKKY interaction occurs in TMASG.

For the  $x = 0.55$  sample we also measured the shear wave moduli  $C_{fs}$  and  $C_{ss}$  as a function of temperature in the presence of 780 G. A minimum was observed similar to that which occurred in zero applied field. This implies that it is not related to the "zero" field-cooled ac susceptibility,<sup>3</sup>  $\chi_{ac}$ , but rather to the  $\chi^{-1}$  anomaly observed at 8.5 kG.<sup>6</sup>

The gradual change in elastic anomalies with increasing Mn concentration seems to indicate that the transition from spin glass to antiferromagnetic phase is a smooth function of  $x$ . On the other hand, since we find no indication of a sharp, inverted  $\lambda$ -type elastic anomaly even in our  $x = 0.65$  sample, which presumably has an antiferromagnetic transition, the broad minimum we observe may indicate that our samples contain both spin-glass and antiferromagnetic regions instead of consisting of a single homogeneous phase.

Acknowledgment.— Support for this work was provided by the National Science Foundation via Grant No. DMR79-08538A1. Thanks are due to Professors J. K. Furdyna and W. M. Becker for making available the samples used in this investigation.

#### References

1. B. Lüthi, T. J. Moran, and R. J. Pollina, J. Phys. Chem. Solids, **31**, 1741 (1970).
2. See for example, G. F. Hawkins, R. L. Thomas, and A. M. de Graaf, J. Appl. Phys. **50**(3), 1709 (1979), and references cited therein.
3. R. R. Galazka, S. Nagata, and P. H. Keesom, Phys. Rev. **22**, 3344 (1980).
4. L. de Seze, J. Phys. C: Solid State Phys. **10**, L353 (1977).
5. G. S. Grest and E. G. Gahl, Phys. Rev. Lett. **43**, 1182 (1979).
6. S. B. Oseroff, R. Calvo, W. Giriat, and Z. Fisk, Solid State Commun. **35**, 539 (1980).
7. A. Gołnik, J. A. Gaj, M. Nawrocki, R. Planel, and C. Benoit à la Guillaume, Proc. 15th Int. Conf. Physics of Semiconductors, Kyoto, 1980, J. Phys. Soc. Japan **49**, Suppl. A, 819 (1980).

## AB INITIO FORCE CONSTANTS OF GERMANIUM

K. Kunc and R.M. Martin

CNRS and Université P. et M. Curie, Tour 13-22, 4 pl. Jussieu, 75230 Paris  
cedex 05, FranceXerox Research Center, 3333 Coyote Hill Road, Palo Alto, California 94304,  
U.S.A.

**Abstract.** - Using the local density-functional formalism, phonon frequencies can be predicted *ab initio* by comparing the energy of the equilibrium configuration with the one having the atoms displaced in a pattern corresponding to a "frozen" phonon. Here we show that by using less symmetric displacement patterns and by applying the Hellman-Feynman theorem to the self-consistent electronic charge densities, one can obtain *all force constants* determining the entire branches of phonon spectra corresponding to a selected direction of propagation. Our method is illustrated on the example of  $\Gamma$ -X branches of phonon spectra in Ge.

The local density-functional formalism [1] which was recently applied to *ab initio* evaluation of phonon frequencies in Si [2] and GaAs [3] showed an astounding accuracy in predicting total energies of semiconductors: Not only the phonon energies (given in the "frozen phonon" approach as a difference between the energies of two configurations of atoms) but also Gruneisen parameters were accurately determined. The (unknown) eigenvectors of the TO(X) and TA(X) modes in GaAs were established and their comparison with (extremely varied) predictions of different phenomenological models made it possible to judge the physical realism of the latter. The method also proved to be useful for determination of effective charges [3], for studying anharmonicity, and for predicting [3] a phase transition of GaAs to orthorhombic structure, not yet known experimentally. In this paper we show that it is possible to go still further by applying the Hellman-Feynman theorem to the same functional of the electronic density; by proceeding in terms of forces on all the ions we can obtain much more complete picture of interactions in solid than from the energies alone - providing that we study *less symmetric* displacement patterns than those of isolated phonon eigenmodes.

Let us consider phonon propagating in Ge along the [100] direction; then at any  $\mathbf{k} = (k, 0, 0)$  the (100) atomic planes vibrate as rigid units with respect to each other and oscillations of the set of (100) planes can be assimilated to vibrations of linear chain. The interplanar force constants needed for writing down the dynamical matrix of such a chain can be obtained in geometry shown in Fig. 1: The elementary unit cell of Ge was quadrupled along the [100] direction and one of the atoms was displaced from the equilibrium position by  $u = -0.01 a$  in the direction [011]. With this periodic supercell and using the Berkeley ionic pseudopotential [4] the self-consistent charge densities were evaluated in very much the same way as e.g. in Ref. 5.

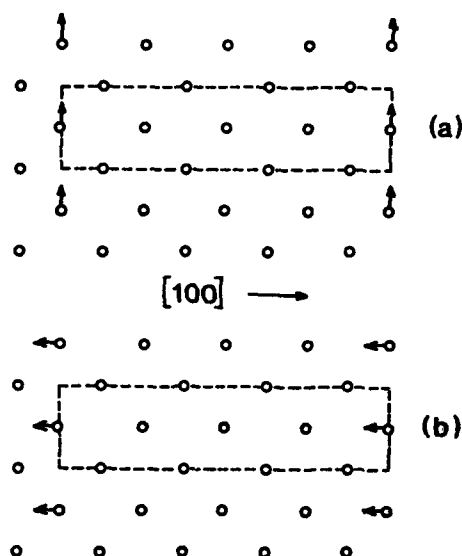


Fig. 1: Description of all phonons propagating in the [100] direction requires self-consistent charge densities determined on periodic supercells which can be constructed by repeating the elementary unit cell along the [100] direction. Present calculations were performed on this quadrupled cell containing 8 atoms of basis.

(a) Displacement pattern allowing to establish the forces determining the transverse vibrations.

(b) Pattern leading to longitudinal force constants.

Applying the Hellman-Feynman theorem we obtained the forces acting on all the neighboring planes extending up to the fourth neighbors. The  $2 \times 2$  dynamical matrix of the "linear chain" is easily constructed and by diagonalizing it for different wavevectors  $k$  we obtain the transverse acoustic and optical branches given in Fig. 2 (solid lines). Starting from the longitudinal configuration of Fig. 1b one obtains a different set of force parameters - which determine the longitudinal branches given in Fig. 2, as well.

Internal consistency of our calculations can be judged from the fact that the two sets of force parameters, which were provided by two independent and completely different calculations, give the LO and TO branches converging to the same LTO( $\Gamma$ ) frequency - degenerate to within 1.1 %. The energy of this mode agrees with our prediction using the "frozen phonon" approach (i.e. proceeding via the total energies) to within 0.2 % - which illustrates the consistency of both methods.

The main reason for an imperfect agreement between the experiment and theory is in the pseudopotential of Ge which was shown in [5] to predict the equilibrium lattice constant of Ge by 8 % too short; this gives a spurious contribution to all forces. Correcting for this term we obtain a second set of dispersion curves plotted in Fig. 2 (broken lines). The agreement with experiment is still imperfect - for which four mechanisms can be suspected to be responsible: (1, merely computational problems: sampling (8 special points were used in the transverse and 4 in the longitudinal case), plane wave expansions ( $\approx 580$  waves), self-consistency (to within less than  $2 \times 10^{-5}$  Ry in the components of potential with small G-vectors and less than 0.1 % in the other ones); (2) anharmonicity; (3) method of correcting the inadequacy of pseudopotential and (4) limited range of force constants considered.



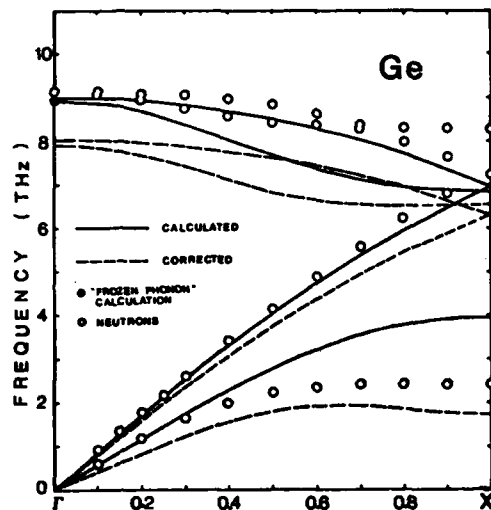


Fig. 2: Phonon dispersion along [100] predicted from forces acting on 8 atoms of the periodic supercell in the displacement patterns of Fig. 1a,b (solid line). The LO and TO branches - although provided by two different and completely independent calculations converge to the same frequency at  $\Gamma$  to within 1.1 %. This limit is consistent with the energy of the degenerate LTO( $\Gamma$ ) mode determined by the alternative "frozen phonon" approach, in the framework of the same local charge-density functional and using the same pseudopotential. The ionic potential used for determination of electronic charge-densities predicts the bonds by 8 % too short, therefore we have added approximate corrections for the contribution caused by the inadequacy of the potential (broken lines). Experimental points taken from Ref. 7 correspond to 80 K.

Presently we can eliminate the anharmonicity because, after repeating the transverse calculations with displacement  $u = -0.005 a$ , we obtained the same force constants to within less than 1 %. We believe (3) and (4) to be the principal causes of the remaining discrepancies: Our method of correcting assigned the spurious contribution to only the first neighbor interactions - which is likely to be a simplification of reality, and which is merely the least artificial among all possible assumptions. On the other hand, by performing calculations on quadrupled unit cell (rather than sextupled or octupled) we have limited the range of interactions to 4th neighbors while Herman [6], on the basis of the neutron data, has shown that inclusion of the 5th neighbors is essential for the lattice dynamics of Ge. Calculations on larger cells to determine longer range force constants are in progress.

#### References

- [1] P. Hohenberg and W. Kohn, Phys. Rev. 136, B864 (1964); W. Kohn and L. J. Sham, *ibid.* 140, A1133 (1965).
- [2] H. Wendel and R. M. Martin, Phys. Rev. B 19, 5251 (1979); M. T. Yin and M. L. Cohen, Phys. Rev. Lett. 45, 1004 (1980); B. N. Harmon, W. Weber, D. R. Hamann, to be published.
- [3] K. Kunc and R. M. Martin, Phys. Rev. B (to be published, August 15th, 1981).
- [4] W. E. Pickett, S. G. Louie and M. L. Cohen, Phys. Rev. B 17, 815 (1978).
- [5] K. Kunc and R. M. Martin, Phys. Rev. B (to be published, Sept 15th, 1981).
- [6] F. Herman, J. Phys. Chem. Solids 8, 405 (1959).
- [7] G. Nilsson and G. Nelin, Phys. Rev. B 3, 364 (1971).

## VOLUME AND TEMPERATURE DEPENDENCE OF THE TRANSVERSE CHARGE AND THE IONICITY OF TETRAHEDRAL SEMICONDUCTORS

D. Olego, M. Cardona and P. Vogl\*

*Max-Planck-Institut für Festkörperforschung, Stuttgart, F.R.G.**\*University of Graz, Austria*

**Abstract.**—The transverse charge  $e_T^*$  and thus the ionicity of most tetrahedral semiconductors (e.g. GaAs) decreases with decreasing volume. We have measured the volume dependence of  $e_T^*$  in 3C-SiC and found  $d \ln e_T^* / d \ln V = -0.67$ , with a sign opposite to the usual one. These results have been interpreted with pseudopotential calculations of  $e_T^*$  vs. volume. Semiempirical bond orbital models, (e.g. Harrison), are not able to explain this anomalous behavior of  $e_T^*$ . We also report the temperature dependence of  $e_T^*$  and interpret it with pseudopotential theory ( $de_T^*/dT = -9.0(5) \times 10^{-6} \text{ K}^{-1}$ ).

**1. Introduction.** — The LO-TO splitting of the Raman phonons can be used to obtain the corresponding Born transverse effective charges  $e_T^*$ . Measurements in a diamond anvil cell yield the dependence of  $e_T^*$  on volume. They have been performed for several III-V and II-VI compounds (1,2) and lead, in all cases, to a decrease in  $e_T^*$  with pressure which corresponds to a decrease in ionicity. These results have been interpreted with semiempirical bond models (3) as well as with "microscopic" pseudopotential calculations (4). Here we extend this work to 3C-SiC (zincblende). We found that, contrary to the other materials mentioned,  $e_T^*$  in 3C-SiC increases with increasing pressure. This anomaly can also be accounted for with pseudopotential theory. We also report the temperature dependence of  $e_T^*$ . It can be explained with pseudopotential theory by multiplying the form factors by Debye-Waller terms.

**2. Results.** — Figure 1 displays typical spectra of the TO and LO phonons of 3C-SiC in a way which reveals the increase of the LO-TO splitting with pressure ( $p$ ). The variation of the frequency of these phonons with  $p$  is shown in Fig. 2. The corresponding variation of lattice constant  $a$ , calculated with Murnaghan's equation (1) using  $B_0 = 322 \text{ GPa}$  and  $B'_0 = 3.43$  (average values of Si and diamond), is also given as an abscissa. We find from Fig. 2 the Grüneisen parameters  $\gamma_{TO} = 1.56(1)$ ,  $\gamma_{LO} = 1.55(1)$ . The increase in the LO-TO splitting can also be seen in Fig. 2. The " $\gamma$ " corresponding to LO-TO is  $\gamma_{LO-TO} = 1.52(5)$ . The charge  $e_T^*$  is given by:

$$e_T^* = \left[ \frac{\epsilon_\infty a^3 M_{\text{red}}}{16} (\omega_{LO}^2 - \omega_{TO}^2) \right]^{1/2} \quad (1)$$

where  $M_{\text{red}}$  is the reduced mass of the unit cell. From the variation of  $\omega_{\text{LO}} - \omega_{\text{TO}}$  with volume we evaluate with Eq. 1 the dependence of  $e_T^*$  on volume using the volume coefficient of the ir dielectric constant  $\text{dln } \epsilon_\infty / \text{dln } a = 1.8$  (the average of Si and diamond). The results are displayed in Fig. 3. A linear fit yields:

$$e_T^* = 2.697(4) - 5.45(10) \frac{\Delta a}{a_0} . \quad (2)$$

From Eq. (2) we calculate  $\gamma_{e_T^*} = -\text{dln } e_T^* / \text{dln } V = 0.67(2)$ .

The charge  $e_T^*$  can be related to the pseudopotential form factors  $v(G)$  of Si and C with the approximate expression (4):

$$e_T^* = -4 \frac{v_{\text{Si}}^2(3) - v_{\text{C}}^2(3)}{v_{\text{Si}}^2(3) + v_{\text{C}}^2(3)} \quad (3)$$

We use form factors similar to those of (5) and interpolate them smoothly, so as to obtain the derivatives of  $v(G)$  with respect to  $G$ . By differentiating Eq. (3) with respect to  $a$  we obtain the dashed line of Fig. 3 which represents reasonably well the experiment. The squares in this figure give the results of a full numerical pseudopotential calculation (1,4). The circles represent bond orbitals model calculations (3): They strongly deviate from the experiment.

The reason for the difference in the volume dependence of  $e_T^*$  between 3C-SiC and the other zincblende-semiconductors is to be sought in the different origin of their ionicity. In SiC the ionicity is related to the large difference in the radii of Si and C. Consequently part of the electronic charge of Si lies in the Wigner-Seitz sphere of C. A decrease in the lattice constant pushes more of this charge into the WS sphere of C and thus increases the ionicity and  $e_T^*$ .

For completeness we show in Fig. 4 the experimental points obtained for  $e_T^*$  at several temperatures together with a least squares fit:  $(\text{d}e_T^* / \text{d}T)_p = -9.0(5) \times 10^{-6} \text{K}^{-1}$ . This coefficient is very small due to a compensation between the thermal expansion and the explicit temperature effects. The latter can be calculated with pseudopotential theory using Debye-Waller factors (6). We find:

$$\left( \frac{\partial e_T^*}{\partial T} \right)_V = \begin{array}{ll} 1.28(50) \times 10^{-5} \text{K}^{-1} & \text{(experiment)} \\ 2.3 \times 10^{-5} \text{K}^{-1} & \text{(theory).} \end{array}$$

We thank W.J. Choyke for supplying us the samples of 3C-SiC.

#### References

1. R. Trommer, H. Müller, M. Cardona, and P. Vogl, Phys. Rev. **B21**, 4869 (1980)
2. B.A. Weinstein, Solid State Comm. **24**, 595 (1977)
3. W. Harrison, Electronic Structure and Properties of Solids, (Freeman, San Francisco, 1980)

4. P. Vogl, J. Phys. C **11**, 251 (1978)
5. H.G. Junginger and W. van Haeringer, Phys. Stat. Sol. **37**, 709 (1970)
6. D. Olego and M. Cardona, to be published

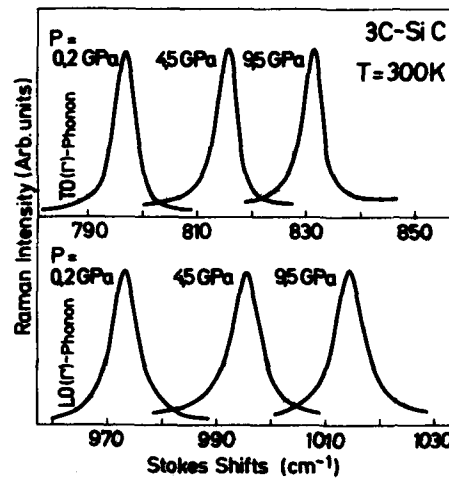


Fig. 1 LO and TO Raman lines of 3C-SiC at several pressures.

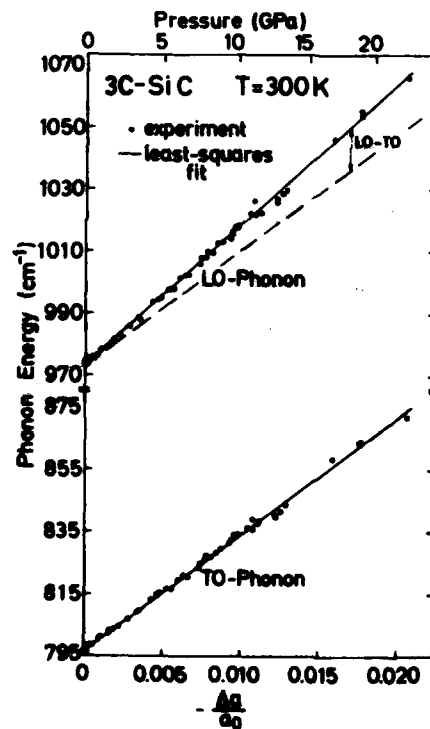


Fig. 2 Dependence of the LO and TO frequencies on pressure and lattice constant for 3C-SiC

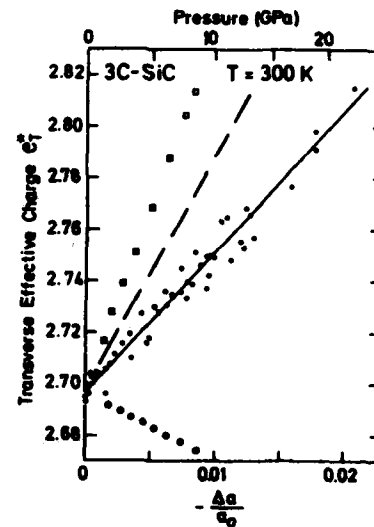


Fig. 3 Dependence of  $e_t^*$  on pressure and lattice constant measured for 3C-SiC (points). Dashed line: calculation with Eq. 3. Circles: bond orbital model. Squares: Full pseudopotential calculation.

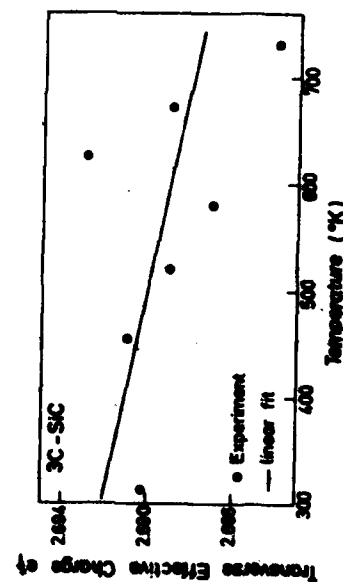


Fig. 4 Measured temperature dependence of  $e_t^*$  for 3C-SiC (points). Line: least squares fit.

## EFFECT OF THE PROPAGATION OF ULTRASOUNDS ON MAGNETOACOUSTIC PHENOMENA IN DEGENERATE SEMICONDUCTORS\*

Chhi-Chong Wu

Department of Applied Mathematics, National Chiao Tung University, Hsinchu, Taiwan, 300, China

**Abstract.**— The effect of ultrasounds propagating at an angle  $\theta$  relative to the direction of a dc magnetic field  $\vec{B}$  in degenerate semiconductors such as n-type InSb has been studied by using a quantum treatment which is valid at high frequencies and in strong magnetic fields. The interaction of conduction electrons with ultrasounds is via deformation-potential and piezoelectric couplings. Results show that the absorption coefficient and change in sound velocity oscillate with the dc magnetic field. However, when the direction of the propagation of ultrasounds is not the same as that of the field, both absorption coefficient and change in sound velocity will diminish and become insignificant in the intermediate-magnetic-field region. These results are quite different from those of nondegenerate semiconductors.

Several experiments in n-type InSb on the absorption coefficient and change in sound velocity for ultrasounds propagating parallel to or perpendicular to a dc magnetic field have revealed a magnetic-field dependence over a wide range of field strengths.<sup>1-3</sup> In an earlier paper,<sup>4</sup> it has been shown that the absorption coefficient and change in sound velocity depend on the direction of the propagation of ultrasounds relative to the dc magnetic field in nondegenerate semiconductors. When the ultrasonic wave vector  $\vec{q}$  approaches ninety degrees to the direction of the field, the absorption coefficient becomes small. In our present study, we investigate the effect of the propagation of ultrasounds on magnetoacoustic phenomena in degenerate semiconductors using a quantum treatment which is valid at high frequencies and in strong magnetic fields. The interaction between ultrasounds and conduction electrons is assumed via the piezoelectric and deformation-potential coupling mechanisms. For degenerate semiconductors, the distribution function of electrons is represented by the Fermi-Dirac statistics. The interesting temperature is very near absolute zero. Since we are interested in the high-frequency region such that  $|\vec{q}|\ell \gg 1$ , where  $\ell$  is the electron mean free path, the effect of collisions is neglected in our present case.

The eigenfunctions and eigenvalues for the nonparabolic band structure can be expressed as<sup>4</sup>

$$\psi_{\vec{k}\vec{n}} = \exp(ik_y y + ik_z z) \phi_n [x - (Hc/eB)k_y], \quad (1)$$

$$E_{\vec{k}\vec{n}} = -\frac{1}{2}E_g \{1 - [1 + (4/E_g) \{ (n + \frac{1}{2})H\omega_c + H^2 k_z^2 / 2m^* \}]^{-1/2}\}, \quad (2)$$

where  $m^*$  is the effective mass of electrons at the minimum of the conduction band,

$E_g$  is the energy gap between the conduction and valence bands, and  $\omega_c$  is the cyclotron frequency of electrons. Following the same method of quantum treatment as in our previous paper,<sup>4</sup> the linear longitudinal conductivity can be obtained as

$$\sigma_{zz}(\vec{q}, \omega) = \frac{\omega_p^2}{4\pi i \omega n_0} \left[ \sum_{\vec{k}, n} f_{\vec{k}, n} \theta_{\vec{k}, n} - \frac{n^2}{4m^*} \sum_{\vec{k}, n, n'} \frac{(f_{\vec{k}, n} - f_{\vec{k}+\vec{q}, n'}) \theta_{\vec{k}, n} \theta_{\vec{k}+\vec{q}, n'}}{E_{\vec{k}+\vec{q}, n'} - E_{\vec{k}, n} - \hbar\omega} (2k_z + q \cos \theta)^2 M_{n', n} \right] \quad (3)$$

where  $n_0$  is the electron density,  $\omega_p^*$  is the plasma frequency of the electron,  $\omega$  is the frequency of ultrasounds,  $f_{\vec{k}, n}$  is the distribution function of electrons,  $\theta$  is the angle between the ultrasonic wave vector  $\vec{q}$  and the magnetic field  $\vec{B}$ , and  $\theta_{\vec{k}, n}$  is given by  $\theta_{\vec{k}, n} = (1 + 2E_{\vec{k}, n}/E_g)^{-1}$ . (4)

The factor  $M_{n', n}$  is defined by

$$M_{n', n} = (n!/n'!) (L^2 q^2 \sin^2 \theta)^{n'-n} \exp(-L^2 q^2 \sin^2 \theta) [L_n^{n'-n} (L^2 q^2 \sin^2 \theta)]^2 \text{ for } n' \geq n, \quad (5a)$$

$$M_{n', n} = (n'/n!) (L^2 q^2 \sin^2 \theta)^{n-n'} \exp(-L^2 q^2 \sin^2 \theta) [L_{n'}^{n-n} (L^2 q^2 \sin^2 \theta)]^2 \text{ for } n' < n, \quad (5b)$$

where  $L = (m/m^* \omega_c)^{1/2}$  is the classical radius of the lowest Landau level and  $L_n^m(x)$  is the associated Laguerre polynomial.

The relation between the absorption coefficient  $\alpha_n$  and the linear longitudinal conductivity  $\sigma_{zz}$  is given by<sup>5</sup>

$$\alpha_n = -(4\pi q / \rho v_s^2) [\beta^2 + (C\omega\epsilon / 4\pi v_s)^2] \text{Im} [1 - (4\pi\sigma_{zz} / i\omega\epsilon)]^{-1}, \quad (6)$$

where  $\rho$  is the density of the material,  $\epsilon$  is the static dielectric constant,  $v_s$  is the sound velocity,  $C$  is the deformation potential, and  $\beta$  is an appropriate piezoelectric constant. The change in sound velocity is also related to the linear longitudinal conductivity  $\sigma_{zz}$  as<sup>5</sup>

$$\Delta v_s / v_s = (2\pi / \rho v_s^2) [\beta^2 + (C\omega\epsilon / 4\pi v_s)^2] \text{Re} [1 - (4\pi\sigma_{zz} / i\omega\epsilon)]^{-1}. \quad (7)$$

The relevant values of physical parameters for n-type InSb are  $n_0 = 10^{19} \text{ cm}^{-3}$ ,  $m^* = 0.039m_0$  ( $m_0$  is the free electron mass),  $E_g = 0.5 \text{ eV}$ ,  $E_F = 0.434 \text{ eV}$ ,  $\epsilon = 18$ ,  $\beta = 2.078 \times 10^4 \text{ esu/cm}^2$  for  $\vec{q} // [111]$ ,  $\rho = 5.8 \text{ gm/cm}^3$ ,  $v_s = 4 \times 10^5 \text{ cm/sec}$ , and  $C = 4.5 \text{ eV}$ . In Fig. 1 the absorption coefficient is plotted as a function of the dc magnetic field  $B$ . It can be seen that the absorption coefficient oscillates with the magnetic field. However, when the angle  $\theta$  is different from zero, the absorption coefficient diminishes to very small values in the intermediate magnetic fields. Hence the absorption coefficient can be observed only in stronger magnetic fields when the angle  $\theta$  increases. In Fig. 2, it shows that the change in sound velocity oscillates with the magnetic field. When the angle  $\theta$  increases, the change in sound velocity diminishes to very small values in the intermediate magnetic fields. Consequently, if the direction of propagation of ultrasounds is not the same as that of the dc magnetic field, the magnetoacoustic effect becomes insignificant in the intermediate-magnetic-field region.

\* Partially supported by National Science Council of China in Taiwan.

## References

1. K. W. Nill and A. L. McWhorter, J. Phys. Soc. Japan Suppl. 21, 755 (1966); K. W. Nill, Phys. Rev. Lett. 21, 82 (1968).
2. J. Gorelik, H. Zinman, B. Fisher, and A. Many, J. Appl. Phys. 41, 445 (1970).
3. H. G. Hafele, R. Grisar, C. Irslinger, H. Wachring, S. D. Smith, R. B. Dennis, and B. S. Wherrett, J. Phys. C: Solid St. Phys. 4, 2637 (1971).
4. C. C. Wu and J. Tsai, J. Appl. Phys. 51, 3751 (1980).
5. Y. Abe and N. Mikoshiba, J. Appl. Phys. 42, 190 (1971).

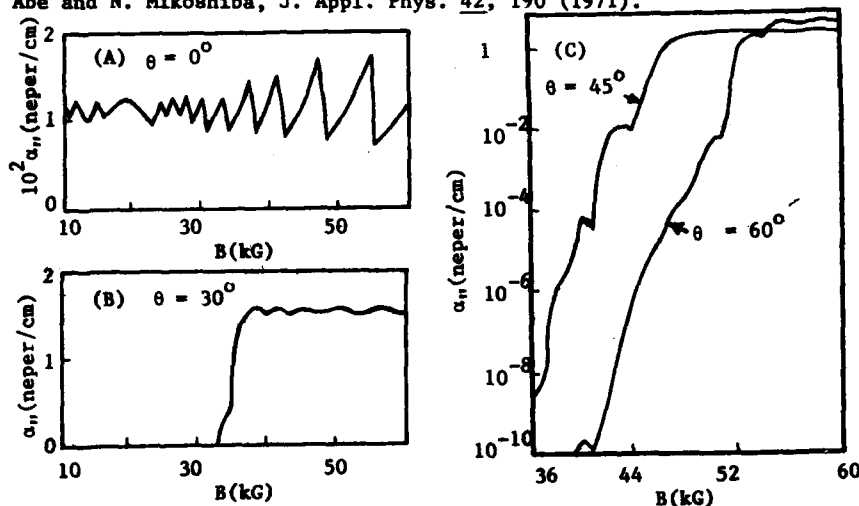


Fig. 1. Absorption coefficient as a function of dc magnetic field  $B$  in degenerate n-type InSb with  $q \parallel [111]$  at  $\omega = 2 \times 10^{12}$  rad/sec.

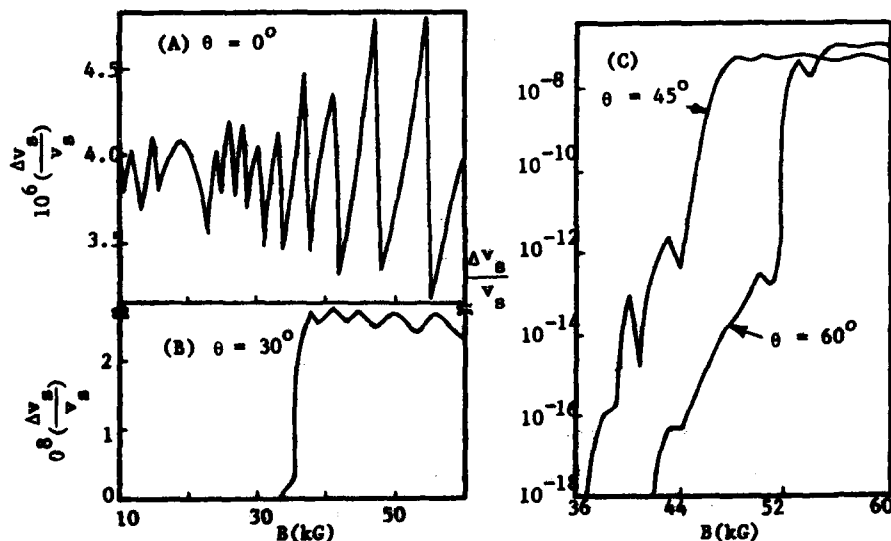


Fig. 2. Change in sound velocity as a function of dc magnetic field  $B$  in degenerate n-type InSb with  $q \parallel [111]$  at  $\omega = 2 \times 10^{12}$  rad/sec.

EFFECT OF MAGNETIC FIELD ON BALLISTIC HEAT-PULSE SCATTERING IN  
n-TYPE GERMANIUM

T. Miyasato\*, M. Tokumura and F. Akao

*The Institute of Scientific and Industrial Research, Osaka University, Suita  
565 Osaka, Japan*

**Abstract.**— The scattering of ballistic heat-pulse propagating along the (100) axis of lightly Sb or As doped Ge has been studied as a function of (100) magnetic field and the heater temperatures ranging from 4.6 to 8.6 K for Sb doped Ge (6.6 to 9.3 K for As doped Ge). It is shown that the transmitted ballistic heat-pulse intensity detected by CdS thin film bolometer increases with increasing magnetic field up to 60 kG with sample temperatures ranging from 1.8 to 4.2 K, and the behavior depends on the concentration of donor atom even at such a low concentration region. The behavior of the detected ballistic heat-pulse amplitude is compared with a calculation based on the Suzuki-Mikoshiba theory, taking into the shrinkage effect of the donor wave function and the resulting change of the value of the valley-orbit splitting.

**1. Introduction.**— The donor atoms of V-group in Ge have shallow donor levels, and the ground state of which splits into the lowest singlet ( $A_1$ ) and the higher lying triplet ( $T_2$ ). This is called the valley-orbit splitting, and the separation of which is denoted by  $4\delta$ , with the values of 0.32 meV for Sb doped Ge and 4.23 meV for As doped Ge. The donor electrons in the ground state of many-valley semiconductor such as Ge or Si are coupled with the acoustic phonons through a deformation potential coupling. When the magnetic field is applied, the energy level of the ground state undergoes the Zeeman splitting, and the shrinkage effect of the donor wave function should be considered simultaneously. Consequently, the value of  $4\delta$  and the cut-off function are changed by the magnetic field.

**2. Experimental Technique and Procedure.**— CdS thin film bolometer(1) was used for the detection of ballistic heat-pulse. The Au-thin film was evaporated onto one surface of the sample as a heater. The phonon flux emitted from the Au-heater travels ballistically in the sample and arrives at the CdS film. The release of the electrons in the trapping centers of CdS by this heat-pulse phonons gives rise to the variation of the electric resistance. The observed pulse amplitude, that is measured as a peak resistance change in CdS bolometer, represents the transmitted phonon power. The experimental results of the pure Ge showed the change of the signal height of 2-3 %, which means that the magnetic field effect on the generating and detecting systems can be neglected in the present experiments.

\*Present address : Department of Physics, University of Lancaster, Lancaster LA1 4YB, England



**3. Experimental Results.**— The experimental results for Sb doped Ge is shown in Fig.1, and those for As doped Ge are shown in Fig.2 and 3, and summarized as follows: (i) In Sb doped Ge, the signal echo height increases with the magnetic field for all heater temperature  $T_h$ 's, and the ratio of the change in the signal echo height increases with increasing  $T_h$ . (ii) In As doped Ge, the signal echo height decreases at 5 kG and then increases in  $1.5 \times 10^{14} \text{As/cm}^3$  doped sample, but monotonically increases in  $0.9 \times 10^{15} \text{As/cm}^3$  doped sample. Namely, there is a concentration dependence in such a low concentration region.

**4. Discussion and Conclusions.**— (a) Energy of ground state: When the magnetic field is applied along the (100) axis of n-type Ge, the equivalence of the four conduction band minima is kept and the degeneracy of the triplet state is not removed except for the spin splitting. In this configuration,  $4\Delta$  is changed through the shrinkage of the donor wave function by the magnetic field, and the magnetic field dependence of  $4\Delta$  for this configuration was given by Lee et al(2). The cut-off function in the donor electron-phonon interaction is also changed through this shrinkage. Therefore, the phonon scattering by donor electrons through process unaccompanied with donor spin reversal is strongly affected due to the shrinkage effect. (b) Scattering of heat-pulse in n-type Ge under magnetic field: The phonon relaxation rate in the ballistic heat-pulse propagation along the (100) axis under (100) magnetic field is calculated on the basis of ref.(3) and shown in ref.(4). The calculated curves are shown in Fig.3 for As doped Ge, and in Fig.4 for Sb doped Ge, and summarized as follows. For Sb doped Ge, the calculated results by this theory (denoted by B) show opposite sense to the experimental results, and for As doped Ge, the calculated curve shows smaller change compared with

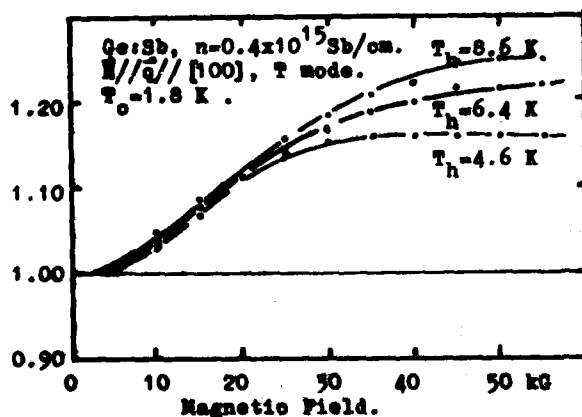


Fig. 1 : Magnetic field dependence of transmitted heat-pulse (T mode) amplitude in Sb( $n=0.4 \times 10^{15} \text{cm}^{-3}$ ) doped Ge. Sample temperature  $T_0=1.8 \text{ K}$ , heater temperature  $T_h$ 's are 4.6, 6.4 and 6.8 K.

the experimental results.

(c) Scattering by the homopolar-pair: The phonon scattering by homopolar pair(5,6,7) was calculated using appropriate parameters for Sb doped Ge, and shown in Fig.4 by A. As seen from these curves, it is necessary to take into consideration the scattering of phonons by homopolar-pair even in such a very low concentration region in addition to the scattering by the neutral shallow donors. Acknowledgements: We would like to express our deep thanks to Dr. Katsuo Suzuki for his helpful

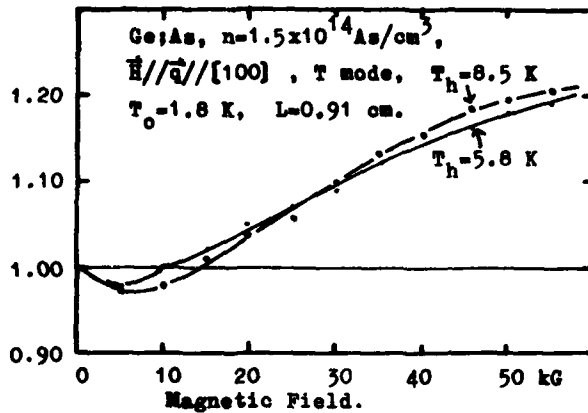


Fig. 2 : Magnetic field dependence of transmitted heat-pulse (T mode) amplitude in As ( $n=1.5 \times 10^{14}/\text{cm}^3$ ) doped Ge.

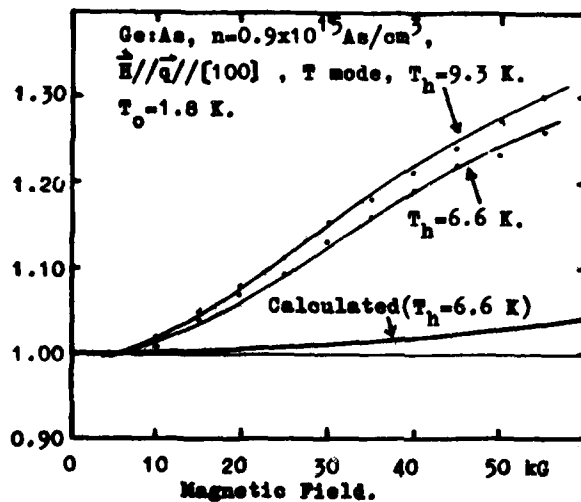


Fig. 3 : Magnetic field dependence of transmitted heat-pulse (T mode) amplitude in Sb ( $n=0.9 \times 10^{15}/\text{cm}^3$ ) doped Ge. Sample temperature is 1.8 K, and heater temperatures are 6.6 and 9.3 K. Theoretical curve was calculated based on Suzuki-Mikoshiba theory using appropriate parameters for  $T_h=6.6$  K.

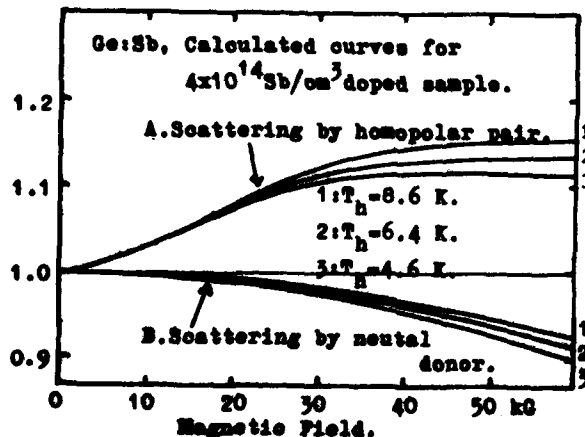


Fig. 4 : Theoretically calculated curves for Sb ( $n=0.4 \times 10^{15}/\text{cm}^3$ ) doped Ge. Upper curves show the magnetic field dependence of scattering of phonons by homopolar pair, and lower curves show that of scattering by neutral shallow donor electron (Suzuki-Mikoshiba theory). To explain the experimental results fully, it will be necessary to consider both scatterings.

discussions and encouragements.

References.- (1) T. Ishiguro & S. Morita: Appl. Phys. Lett. **25** (1974) 533. (2) N. Lee, D. M. Larsen & B. Lax: J. Phys. Chem. Solids **34** (1973) 1817. (3) K. Suzuki & N. Mikoshiba: J. Phys. Soc. Jpn. **28** (1970) 1248. (4) T. Miyasato, M. Tokumura, M. Toguchi & F. Akao: J. Phys. Soc. **50** (1981) 1986. (5) Z. W. Gortel: J. Phys. C **2** (1976) 707. (6) A. Kobayashi & K. Suzuki: Phys. Rev. **B20** (1979) 3278. (7) K. Suzuki: private communication.

## LOCAL-FIELD EFFECTS AND ZONE-CENTER PHONONS IN POLAR AND COVALENT CUBIC SEMICONDUCTORS

R. Resta and A. Baldereschi

*Institut de Physique Appliquée, EPFL, 1015 Lausanne, Switzerland*

**Abstract.**— Microscopic lattice-dynamics calculations based on first-principle dielectric matrices are presented for Si, Ge, GaAs, and ZnSe. Phonon frequencies are calculated in the limit of long wavelength and compare well with experimental data. Local-field effects are essential to explain the trends with increasing ionicity in the Ge isoelectronic series. The electronic polarization density associated to zone-center phonons is analyzed in real space.

**1. Introduction.**— Recent first-principle investigations of the lattice dynamics of solids are based either on the self-consistent scheme<sup>1</sup> or on the linear-response approach<sup>2</sup>. Advantages and shortcomings of both techniques are presently being studied.

The microscopic linear-response scheme is based on the inverse dielectric matrix (IDM) of a solid and amounts to evaluate the electronic response to the lattice distortion of a frozen-in phonon. The few first-principle calculations available to date<sup>3</sup> refer to Si only and give conflicting results on the accuracy attainable.

Here we present a first-principle linear-response study of zone-center phonons in both covalent (Si and Ge) and polar (GaAs and ZnSe) cubic semiconductors. Besides phonon frequencies, we also compute in  $r$  space the electronic polarization associated to phonon modes. This quantity, up to now available for Si only<sup>4</sup>, is essential for a better understanding of the electronic contribution to interatomic force constants and for developing more realistic models in lattice dynamics.

**2. Phonon frequencies at Brillouin-zone center.**— We have calculated phonon frequencies at  $q = 0$  using the linear-response scheme<sup>2</sup> based on the Appelbaum-Hamann ionic pseudopotentials<sup>5</sup> and recently calculated IDM's of order 113<sup>6</sup>. The latter have been extended by adding the Lindhart free-electron contribution of 116 additional reciprocal lattice vectors. The resulting phonon frequencies are reported in Table I together with experimental data. The overall relative error is about 10 % (20 % in ZnSe).

The TA frequency is vanishing and only the TO one is of interest. We analyze  $\omega_{TO}^2$  in Table II and find that (i) local fields (i.e. off-diagonal IDM elements) are more important in more ionic materials, indeed they are responsible for the lowering of  $\omega_{TO}$  with ionicity in the Ge isoelectronic series, and (ii) local-field effects are more relevant in Ge than in Si.

Opposite to the transverse case, the dynamical matrix for longitudinal phonons at  $q = 0$  depends also on the nonanalytic part of the IDM through the Born effective charges<sup>2</sup>  $Z_A^*$  and  $Z_C^*$  (the A,C labels indicate anion or cation) which should satisfy the relationship  $Z_A^* + Z_C^* = 0$  as required by the acoustic sum rule (ASR). In our first-principle calculation without adjustable parameters the ASR is not exactly fulfilled (cf. the calculated values of  $Z^*$  given in the lower portion of Table I) and this is why we obtain  $\omega_{LA} \neq 0$ . The largest ASR violation is 16 % in ZnSe; similar deviations were previously obtained for Si<sup>3,7</sup>. For the LO frequency we obtain  $\omega_{LO} = \omega_{TO}$  in covalent crystals (a result of symmetry alone) and we predict reasonably well the LO - TO splitting in polar materials. Due to the ASR violation, the calculated longitudinal eigenvectors are not exactly the acoustic and optic modes. The mixing however is small.

Tab. 1 : Calculated (upper) and expt. (lower) phonon frequency at the Brillouin zone center, in THz. The calculated Born effective charges are also shown.

	Si	Ge	GaAs	ZnSe
$\omega_{TA}$	0 0	0 0	0 0	0 0
$\omega_A$	1.32 0	0.82 0	0.74 0	1.19 0
$\omega_{TO}$	17.23 15.53	8.09 9.11	7.47 8.06	4.81 6.09
$\omega_{LO}$	17.23 15.53	8.09 9.11	8.00 8.75	6.51 7.55
$Z_A^*$	0.49	0.60	-1.24	-0.96
$Z_C^*$	0.49	0.60	2.19	2.21

Tab. 2 : Partial contributions (THz<sup>2</sup>) to  $\omega_{TO}^2$ : a) bare ions; b) and c) diagonal and off-diagonal up to 113  $\vec{G}$  vectors; d) diagonal free-electron from 116 additional  $\vec{G}$  vectors.

	Si	Ge	GaAs	ZnSe
a)	415.9	142.1	135.3	108.7
b)	-137.4	-69.2	-59.5	-33.2
c)	-14.4	-19.0	-31.5	-64.0
d)	32.9	11.5	11.4	11.6

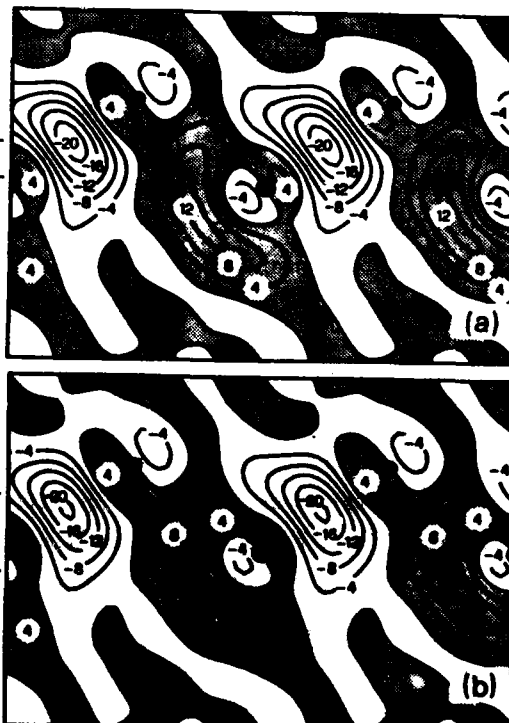


Fig. 1 : Polarization electron density (0.01 electrons/cell) induced in ZnSe in the (1,1,0) plane by optical phonons at the zone center. Larger dots indicate anion sites. (a) TO mode; (b) LO mode.

AD-A126 574

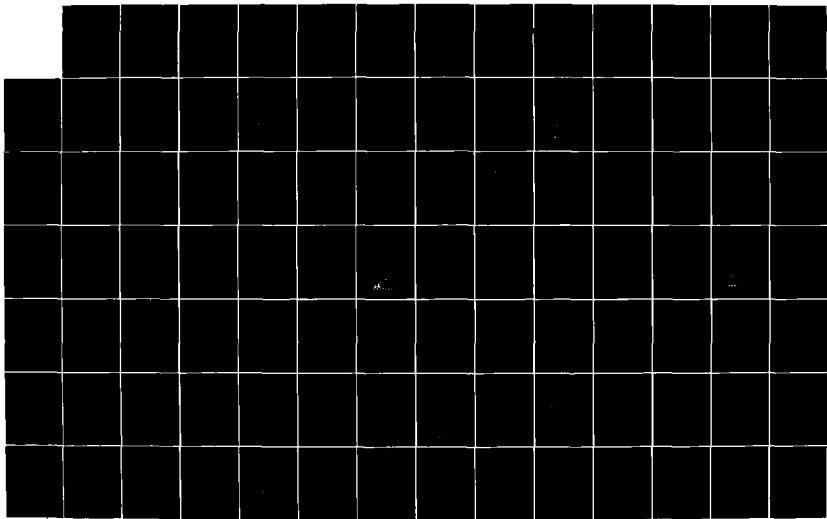
INTERNATIONAL CONFERENCE ON PHONON PHYSICS 31 AUGUST-3  
SEPTEMBER 1981 BLOOMINGTON INDIANA(U) INDIANA UNIV AT  
BLOOMINGTON W E BROW DEC 81 ARO-17340.1-PH  
MIPR-ARO-43-80

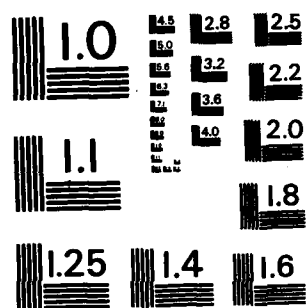
8/10

UNCLASSIFIED

F/G 20/2

NL





MICROCOPY RESOLUTION TEST CHART  
NATIONAL BUREAU OF STANDARDS-1963-A

3. Electronic polarization associated to zone-center phonons. - We do not consider here  $q = 0$  acoustic phonons since they correspond to rigid translations of the lattice and induce therefore the same rigid translation of the electron density. The  $q = 0$  LO and TO modes differ on a macroscopic scale but their ionic displacements in the unit cell are the same for  $q \rightarrow 0$  and are given by  $\vec{u}_A = -\beta^{-1}\vec{u}$  and  $\vec{u}_C = \beta\vec{u}$  where  $\beta^2 = M_A/M_C$  is the nuclear mass ratio, and  $\vec{u}$  is an effective amplitude of the frozen-in phonon which in the computations has been chosen as  $\vec{u} = 0.005 (1,1,1)$  in a.u.. Electronic polarization densities induced by these displacements have been calculated by inserting the linear-response electronic screening potential into Poisson equation.

In covalent materials the polarization densities associated to LO and TO modes are the same for  $q \rightarrow 0$  and they are similar to the result already known for Si<sup>4</sup>. Electronic screening mostly corresponds to a transfer from stretched to compressed bonds.

In polar materials the LO and TO modes for  $q \rightarrow 0$  induce the same macroscopic polarization but a different microscopic response (Fig. 1), the difference being the same electronic polarization density as the one induced by an effective external uniform field  $\vec{U} = -4\pi (Z_A^* \vec{u}_A + Z_C^* \vec{u}_C) / \Omega$  where  $\Omega$  is the unit cell volume. The electronic response is stronger for the TO than for the LO mode in agreement with energy considerations. Electronic response in ZnSe is mostly given by dipoles at the atomic sites as one expects in an ionic material and contains a very large local-field contribution. The results for GaAs are intermediate between those of Ge and ZnSe.

4. Acknowledgement. - Work supported in part by the Swiss National Foundation, and the GNSM - CNR, Pisa, Italy.

#### References

1. H. Wendel and R. M. Martin, *Festkörperprobleme* **19**, 21 (1979); M.T. Yin and M.L. Cohen, *Phys. Rev. Lett.* **45**, 1004 (1980).
2. R.M. Pick, M.H. Cohen and R.M. Martin, *Phys. Rev. B* **1**, 910 (1970).
3. S.G. Louie and M.L. Cohen, *Phys. Rev. B* **17**, 3174 (1978); P.E. Van Camp, V.E. Van Doren and J.T. Devreese, *Phys. Rev. Lett.* **42**, 1224 (1979).
4. A. Baldereschi and K. Maschke, *Proc. Int. Conf. Lattice Dynamics* (Flammarion, Paris, 1978) p. 36.
5. J.A. Appelbaum and D.R. Hamann, *Phys. Rev. B* **8**, 1777 (1973) and private communication.
6. A. Baldereschi and E. Tosatti, *Phys. Rev. B* **17**, 4710 (1978); R. Resta and A. Baldereschi, *Phys. Rev. B* **23**, 6615 (1981).
7. K. Shindo and H. Nara, *J. Phys. Soc. Jpn.* **43**, 899 (1978).

PHONON SPECTROSCOPY OF CHROMIUM-DOPED GALLIUM ARSENIDE USING  
SUPERCONDUCTING TUNNEL JUNCTIONS

M. Hamdache, P.J. King, D.T. Murphy and V.W. Rampton

*Department of Physics, University of Nottingham, University Park, Nottingham,  
NG7 2RD, England*

**Abstract:** Phonon spectroscopy measurements have been made on a variety of chromium-doped gallium arsenide samples over the range  $3\text{ cm}^{-1}$  (90 GHz) to  $24\text{ cm}^{-1}$  (720 GHz) at 1 K. In semi-insulating samples and in weakly p-type samples a cluster of three partially resolved resonant absorptions at  $4.2\text{ cm}^{-1}$ ,  $4.9\text{ cm}^{-1}$  and  $5.6\text{ cm}^{-1}$  are found, together with a weaker but broader absorption at  $10\text{ cm}^{-1}$ . These absorptions are not affected by sub-band gap illumination. In n-type samples these features are not found under dark conditions, but may be induced by illumination.

Chromium has often been introduced into gallium arsenide to compensate shallow donors in the production of semi-insulating (SI) device substrates. The numerous charge states of chromium have been studied by a wide range of techniques which have included electron spin resonance (epr), optical absorption, photoluminescence and far infra-red spectroscopy. Techniques which involve the coupling of chromium ions to 'phonons' have included acoustic relaxation, acoustic paramagnetic resonance (apr), thermal conduction and heat pulse techniques.

Many experimental results have been explained on a model where chromium substitutes (s) for gallium in the GaAs lattice.  $\text{Cr}_s^{2+}$  has been used to explain epr, far infra-red spectroscopy, the 0.82 eV optical absorption line, and an acoustic relaxation peak.  $\text{Cr}_s^{3+}$  and  $\text{Cr}_s^{4+}$  have been reported to give distinctive epr lines while  $\text{Cr}_s^{1+}$  has been observed only under large hydrostatic pressure. The dominant state is found to depend on the nature of the material,  $\text{Cr}_s^{2+}$  dominating in n-type material,  $\text{Cr}_s^{4+}$  dominating in strongly p-type material, while SI material contains a mixture of  $\text{Cr}_s^{2+}$  and  $\text{Cr}_s^{3+}$ . Valence changes can be induced by suitable illumination (see 1, 2, 3, 5 and 6 and references therein).

Dynamic Jahn-Teller models, which have replaced the original static Jahn-Teller models of  $\text{Cr}_s^{2+}$  and  $\text{Cr}_s^{3+}$ , are now well developed<sup>2</sup>.

Some phonon results have, however, not received a satisfactory explanation, these including apr<sup>1</sup> and for example the frequency crossing results of Challis and Ramdani<sup>3</sup>.

One technique which has not been widely applied to this system is phonon spectroscopy using tunnel junctions, although Narayanaswurti has described a measurement made on semi-insulating (SI) material<sup>4</sup>.



We have made measurements on n-type, SI and lightly p-type material using aluminium detectors and lead bismuth alloy generators both in the dark and in sub-band gap illumination. The results reported here were obtained using low frequency sine wave modulation of the generator junction, and detection of that frequency using phase sensitive detection techniques, although pulse measurements have also been made (see for example Eisenmenger<sup>5</sup>).

The samples used originated either from Czechoslovakia or from the Plessey Company in England<sup>1,3,6</sup>. The results here were made on CS-B, an SI Czechoslovakian sample, GA781, a lightly p-type sample containing zinc which is semi-insulating at helium temperatures, GA735-1, an SI sample and GA735-1, an n-type sample which remains n-type down to 1 K.

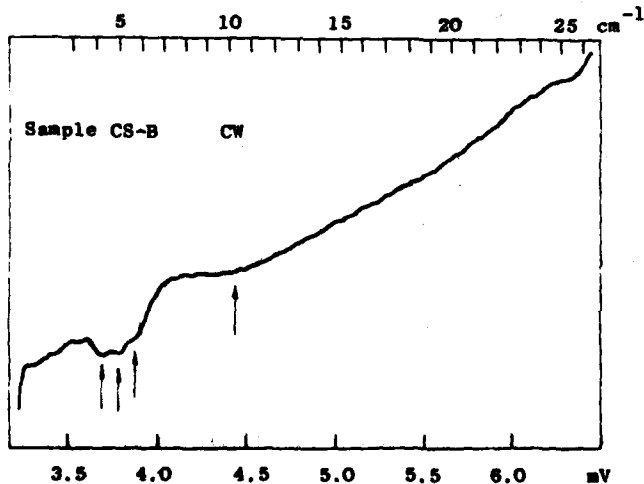


Figure 1:  
Detected signal as a  
function of generator bias.  
The sample was cut for  
<100> propagation.

The results on the p-type and semi-insulating samples were essentially similar and a spectrum obtained on CS-B is shown in Figure 1. The onset of detector sensitivity at  $\sim 3 \text{ cm}^{-1}$  is masked by a group of three strong and partially resolved resonant absorptions, indicated by arrows. A higher energy absorption in the region of  $10 \text{ cm}^{-1}$  is also indicated. In SI samples these lines are little affected by sub-band gap illumination provided by an optic light guide from a quartz iodine lamp through a silicon filter, this arrangement providing a band pass of 0.8 eV to 1.1 eV.

In n-type material none of the resonances described above are found if the sample is cooled to 1 K in total darkness. If, however, the sample is then illuminated with sub-band gap light all of the arrowed features in Figure 1 appear in a time dependent on the light intensity. On removal of the light the features decay, the time taken to reach half height being of order three hours. It is possible to digitally subtract the spectra at different times after illumination and such subtractions are shown in Figure 2. I is the result

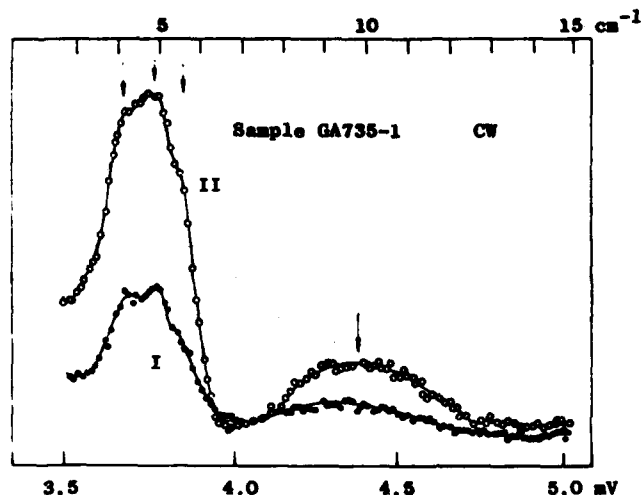


Figure 2:  
Subtracted spectra as a  
function of generator bias.  
The sample was cut for  
<100> propagation.

of light - 1½ hours dark and II is the result of light - 3 hours dark. The three features at 4.2, 4.9 and 5.6  $\text{cm}^{-1}$  are clearly visible and the broad band at 10  $\text{cm}^{-1}$  is reproduced. A lower shoulder on the three line band is also in evidence. All lines appear to be created and decay in proportion. The light dependence of these results resembles that of the apr on the same samples in that in SI material resonances are seen which can be light induced in n-type samples. Challis and Ramdane have reported a phonon absorption at 5  $\text{cm}^{-1}$  although they were unable to resolve any structure<sup>6</sup>. Our lower shoulder may be the upper wing of their line at 2.7  $\text{cm}^{-1}$ . They attribute these two lines and one at 13.3  $\text{cm}^{-1}$  to  $\text{Cr}^{3+}$ , although it seems improbable that this Kramers ion is also responsible for the apr.

#### References

1. Bury, P., Challis, L. J., King, P. J., Monk, D. J., Ramdane, A. Rampton, V. W. and Wiscombe, P., "Semi-Insulating III-V Materials", Shiva Press, 1980, p. 213.
2. Abkhani, A. S., Austen, S. P., Bates, C. A., Parker, L. W. and Pooler, D. R., "The Dynamic Jahn-Teller Theory for Substitutional  $\text{Cr}^{3+}$  in GaAs", submitted for publication to J. Phys. C: Solid State Phys., 1981.
3. Challis, L. J. and Ramdane A., "Phonon Scattering in Condensed Matter", ed. H. J. Maris, Plenum Press, 1980, p. 121.
4. Narayanaswurti, V., "Phonon Scattering in Condensed Matter", ed. H. J. Maris, Plenum Press, 1980, p. 385.
5. Eismenger, W., "Physical Acoustics", 12, Academic Press, 1976, p. 79.
6. Challis, L. J., Locatelli, M., Ramdane, A. and Salce, B., "Phonon Scattering by Cr ions in GaAs", submitted for publication to J. Phys. C: Solid State Phys., 1981.

# ULTRASONIC PHONONS IN $\text{Hg}_{0.8}\text{Mn}_{0.2}\text{Te}$ : DEPENDENCES OF ELASTIC MODULI ON PRESSURE AND TEMPERATURE

M.H. Chao and R.J. Sladek

*Department of Physics, Purdue University, West Lafayette, Indiana 47907, U.S.A.*

**Abstract.** - Ultrasonic transit times have been measured for  $\text{Hg}_{0.8}\text{Mn}_{0.2}\text{Te}$ , a semimagnetic semiconductor, as a function of pressure up to 4 kbar at 296 K and of temperature from 1.5 to 296 K. They are used to deduce the second order elastic stiffness constants SOEC and also force constants and third order elastic constants at 296 K. The shear modulus  $C_s = (C_{11} - C_{12})/2$  is decreased by pressure implying a structural transformation at 10 kbar. No elastic effects attributable to the magnetic moments of the Mn ions are observed even at low temperatures.

$\text{Hg}_{1-x}\text{Mn}_x\text{Te}$  crystals with  $x \leq 0.35$  have the cubic zinc-blende structure. The magnetic susceptibility,  $\chi$ , and heat capacity of  $\text{Hg}_{1-x}\text{Mn}_x\text{Te}$  exhibit effects at low temperatures<sup>1</sup> which depend on the magnetic moments of the Mn ions. Since the elastic properties of  $\text{Hg}_{1-x}\text{Mn}_x\text{Te}$  are unknown for  $x > 0$ , we have begun studying them in crystals with different concentrations of Mn and report herein the elastic behavior of semiconducting  $\text{Hg}_{0.8}\text{Mn}_{0.2}\text{Te}$ .

The transit times of 30 MHz longitudinal and transverse ultrasonic waves propagating along the [110] direction were measured as a function of hydrostatic pressure up to 4 kbar at 296 K and of temperature from 1.5 to 296 K at 1 bar.

We obtain values of  $C_{11}$ ,  $C_{12}$ ,  $C_{44}$  and  $C_s = (C_{11} - C_{12})/2$  for  $\text{Hg}_{0.8}\text{Mn}_{0.2}\text{Te}$  within 8% of those for HgTe.<sup>2</sup> All elastic stiffness moduli of  $\text{Hg}_{0.8}\text{Mn}_{0.2}\text{Te}$  have linear dependences on pressure. As can be seen from Table I, the shear moduli  $C_s$  and  $C_{44}$  decrease, while  $C_{11}$  and  $C_{12}$  increase with increasing pressure. For  $\text{Hg}_{0.8}\text{Mn}_{0.2}\text{Te}$  the pressure derivatives of  $C_{11}$ ,  $C_{12}$ , and  $C_s$  are within 9% of those for HgTe.<sup>3</sup> However,  $dC_{44}/dp$  is much smaller in  $\text{Hg}_{0.8}\text{Mn}_{0.2}\text{Te}$  than in HgTe in which it equals -0.12. Our results, along with the fact that HgTe transforms to the cinnabar structure at 14 kbar,<sup>4</sup> implies that  $\text{Hg}_{0.8}\text{Mn}_{0.2}\text{Te}$  will have a similar transformation at somewhat lower pressure which we estimate to be 10 kbar by assuming it occurs<sup>5</sup> when  $C_s/B$  reaches 0.17 as in HgTe. ( $B$  is the bulk modulus  $(C_{11} + 2C_{12})/3$ .) Elastic gammas calculated from our data using the relation  $\Gamma_{ij} = \frac{1}{2} B \partial \ln C_{ij} / \partial P - 1/6$  are listed in Table I also. The negative shear mode gammas imply that the thermal expansion coefficient of  $\text{Hg}_{0.8}\text{Mn}_{0.2}\text{Te}$  will be negative at low temperatures as is the case for HgTe.<sup>6</sup>

Using equations from the literature,<sup>7</sup> which we corrected for some errors, and our data we deduced the force constants and third order elastic stiffness constants

Table I. Values and pressure derivatives of elastic stiffness moduli and the anharmonicity parameters (elastic gammas) of  $\text{Hg}_{0.8}\text{Mn}_{0.2}\text{Te}$  at 296 K.

	$C_{ij} (10^{11} \text{ dyn/cm}^2)$	$ \partial C_{ij} / \partial P _{P=1 \text{ bar}}$	$\Gamma_{ij}$
$C_{11}$	5.15	3.51	1.23
$C_{12}$	3.55	4.25	2.28
$C_{44}$	1.96	-0.29	-0.47
$(C_{11} - C_{12})/2$	0.80	-0.37	-1.12

(TOEC) for our  $\text{Hg}_{0.8}\text{Mn}_{0.2}\text{Te}$  sample as shown in Table II --  $\alpha$  and  $\gamma$  are bond-stretching while  $\beta$  and  $\delta$  are bond-bending constants, whereas  $\epsilon$  is a mixed bond stretching-bending constant.

Table II. Harmonic force constants  $\alpha$  and  $\beta$  (in  $10^4 \text{ dyn/cm}$ ), anharmonic force constants  $\gamma$ ,  $\delta$ , and  $\epsilon$ , and third order elastic stiffness constants  $C_{ijk}$  (in  $10^{12} \text{ dyn/cm}^2$ ) of  $\text{Hg}_{0.8}\text{Mn}_{0.2}\text{Te}$  at 296 K.

$\alpha$	$\beta$	$\gamma$	$\delta$	$\epsilon$	$C_{111}$	$C_{112}$	$C_{123}$	$C_{144}$	$C_{166}$	$C_{456}$
2.687	0.247	-1.609	-0.205	-0.221	-3.32	-1.62	-1.46	-1.06	-0.106	-0.004

Our value of  $\beta/\alpha$  for  $\text{Hg}_{0.8}\text{Mn}_{0.2}\text{Te}$  is equal to that found for  $\text{HgTe}^3$  implying that both materials have the same Phillips ionicity (0.65) in view of Ref. 8. Our values of  $\delta/\gamma$  and  $\epsilon/\gamma$  for  $\text{Hg}_{0.8}\text{Mn}_{0.2}\text{Te}$  are consistent with how these ratios depend on  $f_1$  for various III-V and II-VI compounds.<sup>7</sup> The SOEC, the force constants, and three of the TOEC are smaller in  $\text{Hg}_{0.8}\text{Mn}_{0.2}\text{Te}$  than in  $\text{HgTe}$ . This seems consistent with the lower transition pressure we have deduced for  $\text{Hg}_{0.8}\text{Mn}_{0.2}\text{Te}$  compared to  $\text{HgTe}$ .

The SOEC of  $\text{Hg}_{0.8}\text{Mn}_{0.2}\text{Te}$  increase smoothly in the usual manner as temperature is decreased from 296 K to 1.5 K. The overall temperature dependences of the SOEC are somewhat smaller than in  $\text{HgTe}$ . This may be due to the  $\Gamma_{ij}$  and TOEC<sup>9</sup> having different values in the two materials. To look more closely for possible effects associated with the increase of magnetic susceptibility<sup>1</sup> at low temperatures we show in Fig. 1 data only for 100 K and below. From Fig. 1 there seems to be no evidence for effects which might be associated with the magnetic moments of the Mn ions. The absence of anomalies in the SOEC is consistent with there being no cusp in  $\chi$  and no spin glass transition for  $x = 0.20$  at low temperatures.<sup>1</sup>

In summary, from our ultrasonic measurements on  $\text{Hg}_{0.8}\text{Mn}_{0.2}\text{Te}$  we conclude that its bonding is weaker and transition pressure smaller than in  $\text{HgTe}$  and that the SOEC are not affected appreciably by the magnetic moments of the Mn ions.

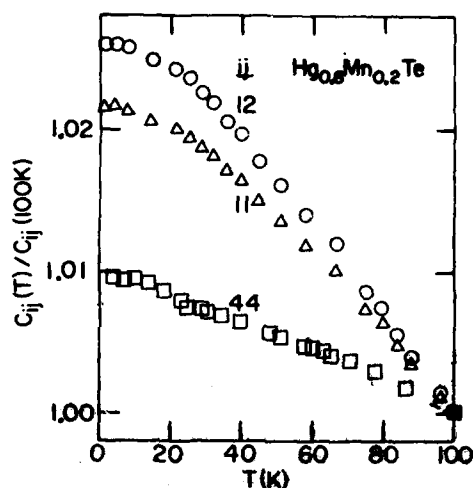


Fig. 1. Temperature dependences of normalized second order elastic constants. At 100 K,  $C_{11} = 5.503$ ,  $C_{12} = 3.845$ , and  $C_{44} = 2.027$ , all in units of  $10^{11}$  dyn/cm<sup>2</sup>.

**Acknowledgments.**— This work was supported by the National Science Foundation Materials Research Laboratory Program Grant No. DMR77-23798 and DMR80-20249. Thanks are due to Professor J. K. Furdyna for the samples and for a number of discussions.

#### References

1. S. Nagata, R. R. Galazka, D. P. Mullin, H. Akbarzadeh, G. D. Khattak, J. K. Furdyna, and P. H. Keesom, *Phys. Rev.* **B22**, 3331 (1980).
2. R. I. Cottam, and G. A. Saunders, *J. Phys. Chem. Solids* **36**, 187 (1975).
3. A. J. Miller, G. A. Saunders, Y. K. Yöğurtcu, and A. E. Abey, *Phil. Mag.* **A43**, 1447 (1981).
4. A. Jayaraman, W. Klement, Jr., and G. G. Kennedy, *Phys. Rev.* **130**, 2277 (1963).
5. Using a criterion of H. H. Demarest, R. Ota, and O. L. Anderson, in *High Pressure Research Applications in Geophysics*, edited by M. H. Manghant (Academic Press, N.Y. 1977), p. 281.
6. J. G. Collins, G. K. White, J. A. Birch, and T. F. Smith, *J. Phys. C: Solid State Phys.* **13**, 1649 (1980).
7. D. Gerlich, in *Proceedings of 6th Symposium of Thermophysical Properties*, Atlanta, GA, U.S.A., 1973, edited by P. E. Liley, p. 305.
8. R. M. Martin, *Phys. Rev.* **B1**, 4805 (1970).
9. See for example, J. A. Gerber and A. V. Granato, *Phys. Rev.* **B11**, 3990 (1975).

## PHONON ASSISTED TRANSITIONS IN THE FREE CARRIER ABSORPTION OF SEMICONDUCTORS IN QUANTIZING MAGNETIC FIELDS

H.N. Spector<sup>\*</sup> and T.M. Rynee<sup>\*</sup>

I.I.T.

<sup>\*</sup>TRWAbstract.-

We have investigated the effect of the scattering of free carriers in semiconductors by both acoustic and optical phonons on the free carrier absorption in quantizing magnetic fields. We find that for electromagnetic radiation polarized either parallel or perpendicular to the magnetic field, the free carrier absorption is an oscillatory function of the magnetic field. The origin of this oscillatory magneto-absorption is due to phonon assisted transitions between the various Landau levels of the free carriers in quantizing magnetic fields. From the periods of the oscillations in the free carrier absorption, the frequencies of those phonons which interact most strongly with the free carriers can be found.

The absorption of electromagnetic radiation by free carriers in intraband transitions in semiconductors can only take place with the simultaneous scattering of the carriers by imperfections in the crystal<sup>1,2</sup>. Therefore, the dependence of the free carrier absorption coefficient on temperature and wavelength of the radiation field will depend critically on the scattering mechanisms which are dominant in a particular semiconductor<sup>3</sup>. In strong magnetic fields, the energy levels of the free carriers, which form a continuum in a particular band in the absence of the field, are quantized into Landau subbands. Because of this quantization, the absorption coefficient will become a function of magnetic field as well as photon frequency and temperature. Intraband transitions can occur not only to states in the same Landau subband but also to states in other Landau subbands if the energy of the photon being absorbed,  $\hbar\Omega$ , is greater than the energy separation between subbands, which is  $\hbar\omega_c$ , where  $\omega_c$  is the cyclotron frequency of the carriers, for parabolic energy bands. An oscillatory dependence of the free carrier absorption with magnetic field is predicted<sup>4</sup> where the absorption has peaks when  $\Omega = n\omega_c$ . This oscillatory dependence arises from oscillations in the free carriers density of states whenever transitions can take place to a new Landau subband.

In most semiconductors, there is a range of temperatures and doping levels for which either acoustic phonons or optical phonons will dominate the scattering of the free carriers. Intraband transitions can occur with either the absorption or

<sup>\*</sup> This research was supported in part by a grant from the NSF Materials Research Laboratory Program, Grant No. DMR 76-24466.

emission of a phonon. When this occurs, the peaks in the free carrier absorption coefficient occur when  $\Omega\omega_0 = n\omega_c^5$ , where  $\omega_0$  is the frequency of the phonon being absorbed (plus sign) or emitted (minus sign). Therefore, from the periods of the oscillation of the free carrier absorption in quantizing magnetic fields, the frequencies of those phonons, whether acoustic and optical, which dominate the scattering of the free carriers can be determined.

The free carrier absorption coefficient is given by

$$K = \frac{e^2}{nc} \sum_i (W_i^a - W_i^e) \quad (1)$$

where  $W_i^{a,e}$  is the transition probability given by second order perturbation theory for absorption or emission of a photon,

$$W_i^{a,e} = \frac{2\pi}{\hbar} \int_f \left[ | \langle f | M_+ | i \rangle |^2 \delta(E_f - E_i + \hbar\Omega - \hbar\omega_0) + | \langle f | M_- | i \rangle |^2 \delta(E_f - E_i + \hbar\Omega + \hbar\omega_0) \right] \quad (2)$$

$f_i$  is the free carrier distribution function,  $\epsilon$  is the dielectric constant,  $n$  the number of photons in the radiation field and  $\langle f | M_{\pm} | i \rangle$  is the transition matrix element for the electron-photon interaction with the simultaneous absorption or emission of a phonon. Because the form of the interaction Hamiltonian between the radiation field and the carriers depends upon the polarization of the radiation, we find that the free carrier absorption depends not only on the magnitude of the magnetic field but the orientation of the field relative to the direction of polarization of the radiation. For the radiation polarized along the direction of the magnetic field and for either acoustic or optical phonon scattering via deformation potential scattering, the free carrier absorption coefficient is

$$K(B) = \frac{8\pi e^2 E_d^2 \omega_0^2 n}{\rho u^2 c \Omega^3 \hbar^3} \left( \frac{n}{2\pi k_B T} \right)^{1/2} \sinh \left( \frac{\hbar\omega_c}{2k_B T} \right) \sum_{n_1=0}^{\infty} \exp \left[ - \left( n_1 + \frac{1}{2} \right) \frac{\hbar\omega_c}{k_B T} \right] \exp \left[ \frac{n}{2k_B T} (\Omega + \omega_0) \right] \left\{ \sum_{n_f=0}^{n_1} \left( \frac{\hbar\omega_c}{2k_B T} \left[ \frac{\Omega + \omega_0}{\omega_c} - (n_f - n_1) \right] \right) \exp \left[ - (n_f - n_1) \frac{\hbar\omega_c}{2k_B T} \right] K_1 \left( \frac{\hbar\omega_c}{2k_B T} \left[ \frac{\Omega + \omega_0}{\omega_c} - (n_f - n_1) \right] \right) + \sum_{n_f=0}^{n_1} \left( \frac{\hbar\omega_c}{2k_B T} \left[ \frac{\Omega - \omega_0}{\omega_c} - (n_f - n_1) \right] \right) \exp \left[ - (n_f - n_1) \frac{\hbar\omega_c}{2k_B T} \right] K_1 \left( \frac{\hbar\omega_c}{2k_B T} \left[ \frac{\Omega - \omega_0}{\omega_c} - (n_f - n_1) \right] \right) \right\} \quad (3)$$

for lightly doped semiconductors when the carriers are nondegenerate and

$$K(B) = \frac{e^2 n^2 \epsilon_d^2 E_d^2 \omega_0^2}{2\pi^2 \hbar^3 \rho u^2 c \Omega^3} \sum_{n=0}^{n_1} \left[ E_f - \left( n + \frac{1}{2} \right) \hbar\omega_c \right]^{1/2}$$

$$\left\{ \sum_{n=0}^{n_2^+} [E_f + \hbar\Omega + \hbar\omega_0 - (n + \frac{1}{2})\hbar\omega_c]^{\frac{1}{2}} n_0 + \sum_{n=0}^{n_2^-} [E_f + \hbar\Omega - \hbar\omega_0 - (n + \frac{1}{2})\hbar\omega_c]^{\frac{1}{2}} (n_0 + 1) \right\} \quad (4)$$

for heavily doped semiconductors where the carriers are degenerate. Here,  $n_1$ ,  $n_2$  and  $n_2^{\pm}$  are the largest integers satisfying the conditions

$$n_1 = n_1 + \frac{\Omega \pm \omega_0}{\omega_c}, \quad n_1 = \frac{E_f}{\hbar\omega_c} - \frac{1}{2} \text{ and } n_2 = \frac{E_f}{\hbar\omega_c} + \frac{\Omega \pm \omega_0}{\omega_c} - \frac{1}{2} \text{ and the rest of the symbols}$$

are as defined in previous work<sup>4,5</sup>. The frequency  $\omega_0$  is the optical phonon frequency when optical phonon scattering or intravalley scattering is important and is the frequency of the acoustic phonon which interacts most strongly with the free carriers when acoustic phonon scattering is dominant. In very strong fields, these are phonons whose wave vector  $q \sim (\frac{m_0 c}{\hbar})^{\frac{1}{2}}$ . For both degenerate and nondegenerate semiconductors, the absorption coefficient is an oscillatory function of magnetic field with the period of oscillation depending upon the frequency of the phonons which interact most strongly with the free carriers. However, the detailed dependence of the absorption on field and the amplitude and periodicity of the oscillations differs between degenerate and nondegenerate materials.

#### References

1. H. Meyer, Phys. Rev. **112**, 298 (1958).
2. R. Rosenberg and M. Lox, Phys. Rev. **112**, 843 (1958).
3. H.Y. Fan, in "Semiconductors and Semimetals", edited by A. Beer and R. Willardson (Academic Press, NY, 1967) Vol.3, p.402.
4. E.R. Generazio and H.N. Spector, Phys. Rev. B **20**, 5162 (1979).
5. T.M. Rynne and H.N. Spector, J. Phys. Chem. Solids **42**, 121 (1981).



## VIBRATIONS OF SUBSTITUTIONAL IMPURITIES IN SEMICONDUCTORS

O.H. Nielsen

*Institute of Physics, University of Aarhus, DK-8000 Aarhus C, Denmark*

**Abstract** - The Green's function technique has been studied in detail, permitting numerical calculations of mean-square amplitudes in perfect and impure lattices. The  $^{119}\text{Sn}$  substitutional atom is distinguished by being an isoval impurity in Si, Ge and  $\alpha\text{-Sn}$ , and by being an amphoteric dopant in the III-V semiconductors. Several impurity models are employed for quantitative interpretation of Mössbauer Debye-Waller factors from a systematic study by Weyer al.

1. Green's functions. - The well known Green's function technique<sup>1</sup> for vibrations correlation functions (mean-square amplitudes) can be amended with a few expressions facilitating actual calculations.<sup>2</sup> The Green's function eqs. (2.4.44), (8.5.5) of Ref. 1 can be written for real  $\omega$  as

$$G_{\alpha\beta}(\mathbf{l}\kappa, \mathbf{l}'\kappa'; \omega \pm i0) = \frac{1}{\sqrt{M_{\mathbf{l}\kappa} M_{\mathbf{l}'\kappa'}}} \left[ \text{P} \int_0^\infty \frac{g_{\alpha\beta}(\mathbf{l}\kappa, \mathbf{l}'\kappa'; \omega')}{\omega^2 - \omega'^2} d\omega' + \frac{i\pi}{2\omega} g_{\alpha\beta}(\mathbf{l}\kappa, \mathbf{l}'\kappa'; \omega) \right] \quad (1)$$

$g_{\alpha\beta}(\mathbf{l}\kappa, \mathbf{l}'\kappa'; \omega)$  is a generalized density of states (DOS) function which for the perfect lattice is calculated as a Brillouin-zone sum.<sup>2</sup>  $\text{P} \int$  denotes a principal value integral which may be evaluated numerically as in Ref. 2. The impurity Green's function  $\bar{U}$  is found by solving eq. (8.5.2) of Ref. 1

$$\left[ \bar{I} - \bar{G} \cdot (\bar{\Delta}\bar{\Phi} + \bar{\Delta}\bar{M} \cdot \omega^2) \right] \bar{U} = \bar{G} \quad (2)$$

which for practical purposes may be separated into two coupled equations for the real and imaginary parts using eq. (1), see eq. (9) of Ref. 2. Correlation functions are easy to obtain when the DOS functions have been calculated, since the fluctuation-dissipation theorem yields with eq. (1)

$$\langle u_\alpha(\mathbf{l}\kappa) u_\beta(\mathbf{l}'\kappa') \rangle = \frac{1}{2\sqrt{M_{\mathbf{l}\kappa} M_{\mathbf{l}'\kappa'}}} \int_0^\infty \frac{1}{\omega} g_{\alpha\beta}(\mathbf{l}\kappa, \mathbf{l}'\kappa'; \omega) \cdot \coth(\frac{1}{2}\hbar\omega/k_B T) d\omega \quad (3)$$

In particular, the mean-square vibrational amplitude of a lattice atom or an impurity is given by eq. (3) using the  $g_{\alpha\alpha}(\mathbf{l}\kappa, \mathbf{l}\kappa; \omega)$  matrix element of the DOS function. For comparison with experimental data it is often convenient to expand the coth-factor to obtain an expression for  $\langle u_\alpha(\mathbf{l}\kappa)^2 \rangle$  at high temperatures ( $k_B T > \hbar\omega_{\text{max}}/2\pi$ ) in terms of weighted moments of the DOS.<sup>3</sup> The moments can be recast in terms of Debye temperatures rigorously defined by<sup>2-4</sup>

$$\theta_D(N) = \frac{N}{k_B} \cdot \left[ \frac{N+3}{3} \int_0^\infty \omega^N g_{\alpha\alpha}(\mathbf{l}\kappa, \mathbf{l}\kappa; \omega) d\omega \right]^{1/N} ; N \geq -3. \quad (4)$$

The indices ( $\alpha\mathbf{k}$ ) are understood for  $\theta_D(N)$  (which can vary significantly with  $N$ ).

The expansion of eq. (3) becomes

$$\langle u_{\alpha}(\mathbf{k})^2 \rangle = \frac{3k_B T}{M_{\mathbf{k}\mathbf{k}}} \cdot \left[ \frac{M}{k_B \theta_D(-2)} \right]^2 \cdot \left[ 1 + \left( \frac{\theta_D(-2)}{6T} \right)^2 - \left( \frac{\theta_D(-2)\theta_D(2)}{60T^2} \right)^2 + \dots \right] \quad (5)$$

The terms indicated usually give accurate values when  $T \gg \frac{1}{2}\theta_D(-2)$ . Fitting high-temperature  $\langle u_{\alpha}(\mathbf{k})^2 \rangle$  data will thus determine a  $\theta_D(-2)$  value. An interesting observation is that by eq. (1) the  $N = -2$  moment of the DOS is simply given by  $-M_{\mathbf{k}\mathbf{k}} G_{\alpha\alpha}(\mathbf{k}, \mathbf{k}; \omega = 0)$ . Applying this to a substitutional impurity yields by eq. (2) the relation<sup>2</sup>

$$\theta_D'(-2) = \theta_D(-2) \cdot \sqrt{\frac{M_{\mathbf{k}\mathbf{k}}}{M_{\mathbf{k}\mathbf{k}}'}} \cdot F(\bar{G}; \bar{\Delta\phi}) \quad , \quad (6)$$

where a prime refers to the impurity. The function  $F$  is found by solving eq. (2) at  $\omega = 0$ . A mass defect with  $\bar{\Delta\phi} = 0$  has  $F = 1$ . A model for impurity mean-square amplitudes at high temperatures would aim at calculating  $F$  for various  $\bar{\Delta\phi}$ .

**2. Interpretation of Mössbauer data.**— The  $^{119}\text{Sn}$  substitutional impurity in both group IV<sup>5</sup> and group III-V<sup>6</sup> semiconductors has been investigated by Mössbauer spectroscopy, determining the temperature variation of the Debye-Waller factor. For Si, Ge and  $\alpha$ -Sn, Weber's adiabatic bond-charge model<sup>7</sup> was applied for the perfect lattice phonons to yield the  $\theta_D(N)$ .<sup>2,5</sup> A hierarchy of impurity vibration models have been considered: (1) The mass defect model (see above) proved insufficient for Si, Ge, but of course good in  $\alpha$ -Sn. (2) The simple and analytical Mannheim model<sup>3,5</sup> quantified the  $\theta_D'(-2)$  in terms of force constant weakenings. However, this model assumes n.n. central forces making the diamond structure unstable. Furthermore, the force constant changes, necessary within this model, were rather large, and better models seem warranted for the semiconductors. (3) A model using the bond charge model concepts was constructed,<sup>2</sup> neglecting any changes in the long-range Coulomb forces. Changing simultaneously all impurity potentials to fit  $\theta_D'(-2)$ , resulted in force constant changes of -26% (Si) and -27% (Ge). For GaP, GaAs, GaSb, InP, InAs, and InSb a number of phonon models were compared with neutron diffraction determinations of  $\langle u_{\alpha}(\mathbf{k})^2 \rangle$ , rendering the rigid ion and deformation dipole models insufficient.<sup>6</sup> Some of the shell models gave reasonable results. Site-selective implantation of  $^{119}\text{Sn}$  yielded a complete set of  $\theta_D'(-2)$  values which were analyzed using eq. (6) to determine the values of  $F$ . The III- and V-impurity sites were clearly distinguishable in terms of  $F$ , and showed an unexpected qualitative difference between  $^{119}\text{Sn}$  being in a Ga- or an In-compound.

#### References.

1. A.A. Maradudin, E.W. Montroll, G.H. Weiss, and I.P. Ipatova, Solid State Physics, Suppl. 3, 2nd ed. (1971).
2. O.H. Nielsen, Phys.Rev. B (in print).
3. J.M. Grow, D.G. Howard, R.H. Nussbaum, and M. Takeo, Phys.Rev. B **17** (1978) 15.
4. T.H.K. Barron, W.T. Berg, and J.A. Morrison, Proc.Roy.Soc (London) **A242** (1957) 478.

5. J.W. Petersen, O.H. Nielsen, G. Meyer, E. Antoncik, and S. Damgaard, Phys.Rev. B 21 (1980) 4292; *ibid.* 22 (1980) 3135E.
6. O.H. Nielsen, F.K. Larsen, S. Damgaard, J.W. Petersen, and G. Meyer, to be published in Phys.Rev. B.
7. W. Weber, Phys.Rev. B 15 (1977) 4789.

## PARAMETRIC AMPLIFICATION OF MICROWAVE PHONONS IN SEMICONDUCTORS

H.N. Spector\*

*Illinois Institute of Technology, Chicago, IL, U.S.A.*Abstract.-

Two different nonlinear processes involving the interactions of phonons with electrons in a semiconductor in the presence of a d.c. electric field have been theoretically investigated. The first process involves the mixing of ultrasonic waves to generate new ultrasonic waves at the sum or difference frequencies of the original waves. The mechanisms which couples the waves together involves the interaction of the carriers bunched by one of the waves with the fields induced by the other wave. The second process involves the interaction between a forward traveling ultrasonic wave and a microwave radiation field to generate a backward traveling ultrasonic wave (phonon echo) and an amplification of the forward traveling wave. In piezoelectric semiconductors in the presence of a d.c. electric field, the need for a threshold microwave field for the generation of the echo wave and the amplification of the forward traveling wave can be eliminated under certain circumstances.

Nonlinear processes involving the interaction of phonons with each other or with photons provide a mechanism for generating high frequency phonons in the microwave frequency range. These nonlinear processes can be drastically effected by the presence of drifting carriers in a semiconductor. The nonlinearities which give rise to the parametric amplification of microwave phonons in semiconductors originate either from the nonlinear properties of the media (such as the existence of third order elastic coefficients, electro-optical coefficients, photoelastic coefficients, etc.) or from the nonlinear currents generated when charge carriers bunched by one wave interact with the fields induced by the other wave.

The basic equations which govern the behavior of the system of phonons interacting with each other, as well as with electrons and photons, are the equation of motion of the lattice in the elastic continuum approximation

$$\rho \frac{\partial^2 u_1}{\partial t^2} = \frac{\partial T_{1j}}{\partial x_j} \quad (1)$$

where  $u_1$  is the amplitude of the ultrasonic wave and  $T_{1j}$  is the stress tensor, Maxwell's equations for the electric and magnetic fields, and the constitutive relations between the stress tensor, polarization  $\vec{P}$ , magnetization  $\vec{M}$  and current density  $\vec{J}$  and the strain tensor  $S_{1j}$ , electric field  $\vec{E}$  and magnetic field  $\vec{H}$ . In a

\* Supported by a grant from the NSF Material Research Laboratory Program, Grant No. 76-24466.

nonferroelectric material, the free energy  $F$  can be expanded in powers of the strain and the electric field <sup>1</sup> while in a ferroelectric material, it can be expanded in powers of the strain and the polarization <sup>2</sup>. The stress tensor can be obtained from the free energy using the relation <sup>1</sup>

$$T_{ij} = \frac{\partial F}{\partial S_{ij}} \quad (2)$$

while the electric displacement vector <sup>1</sup> and electric field vector <sup>2</sup> can be obtained from the free energy using the relations

$$D_i = 4\pi \frac{\partial F}{\partial E_i} \quad (3)$$

and

$$E_i = \frac{\partial F}{\partial P_i} \quad (4)$$

The current density induced at a frequency  $\omega_3$  can also be expanded in powers of the electric field

$$J_i(\omega_3) = \sigma_{ij}(\omega_3)E_j + \Lambda_{ijk}(\omega_1, \omega_2)E_j(\omega_1)E_k(\omega_2) \quad (5)$$

where  $\omega_1 + \omega_2 = \omega_3$ . The nonlinear term in the current density arises from the mixing of waves of different frequencies to generate waves at the sum or different frequency. By expanding the free energy up to terms of third order in the product of the strain and electric or polarization fields, we can obtain the terms in the interaction which couple the phonons, photons and electrons together in the lowest order to give rise to parametric amplification of phonons in semiconductors.

We now consider two different processes in which waves can be coupled together by the nonlinear terms to generate new waves at the sum and difference frequencies of the original waves. In the first process, two ultrasonic waves are coupled together to generate either harmonics or subharmonics of the original waves <sup>3</sup>. The electric fields which appear in the second term of the current density, Eq.(5), are then the piezoelectric fields induced by each of the ultrasonic waves. In the second process, there is an interaction between an ultrasonic wave and a microwave electromagnetic wave to generate an echo ultrasonic wave <sup>1,2</sup> or between two oppositely directed ultrasonic waves to generate a microwave radiation field <sup>4</sup>. The electric fields in the second term of the current density are the radiation field and the piezoelectric field accompanying the ultrasonic waves. If the nonlinear coupling terms are small, we can write the displacement due to the ultrasonic wave and the electric fields due to the electromagnetic wave as plane waves modulated by a slowly varying amplitude  $A$ ,

$$E(z,t), u(z,t) = A(z)\exp(iqz - \omega t) \quad (6)$$

where  $q$  and  $\omega$  are the wave vector and frequency of the particular wave. The slowly varying amplitudes of the waves obey a differential equation of this form

$$\frac{dA_i}{dz} = -\alpha_i A_i + \eta_{ijk} A_j A_k \quad (7)$$

Here  $A_i$ ,  $A_j$  and  $A_k$  are the slowly varying amplitudes of the waves which are coupled together,  $\alpha_i$  is the linear loss coefficient for the  $i$ th wave and  $\eta_{ijk}$  is the nonlinear coupling coefficient which couples the three waves together. These coupled equations have been solved to obtain the generation of ultrasonic waves for the different processes mentioned above<sup>1-4</sup>. The results obtained depend upon the magnitude, frequency and electric field dependence of the nonlinear coupling coefficient  $\eta_{ijk}$ .

For the first process, which involves the mixing of ultrasonic waves to generate ultrasonic waves at the sum or difference frequency, the nonlinear coupling coefficient gives rise to a nonlinear gain which depends on the strain field accompanying the initial wave

$$\alpha_{NL} = -\alpha + \frac{|\eta|}{2q} |S(o)| \quad (8)$$

The nonlinear coupling is enhanced in paraelectric and ferroelectric materials because of the larger nonlinear material parameters in these substances. Eq.(8) gives the nonlinear for the case of subharmonic generation. For harmonic generation, the intensity of the generated wave is directly proportional to  $\eta$ .

For the second process, which involves the mixing of ultrasonic waves with a microwave radiation field to generate an echo wave and amplify the original ultrasonic wave, we have found that for piezoelectric semiconductors in the presence of an applied d.c. field the need for a threshold microwave field for generation of the echo and amplification of the initial wave can be eliminated under certain circumstances<sup>1</sup>. The condition for the amplification of the initial wave and the generation of the echo is

$$\text{Re}N > \alpha_i + \alpha_e \quad (9)$$

where

$$N = [(\alpha_i - \alpha_e)^2 + 4\eta_i \eta_e |E_M|^2]^{-1/2} \quad (10)$$

and  $E_M$  is the amplitude of the microwave field. In the presence of drifting carriers,  $\alpha_i > \alpha_e$ , where the subscripts  $i$  and  $e$  denote quantities associated with the initial and echo waves, and the condition given in Eq.(9) can be satisfied with negligibly small threshold microwave electric fields.

#### References

1. J.E. Economou and H.N. Spector, Phys. Rev. B 18, 5578 (1978).
2. J.E. Economou and H.N. Spector, Phys. Rev. B 20, 2061 (1979).
3. G. Johri and H.N. Spector, Phys. Rev. B 15, 4955 (1977).
4. J.E. Economou and H.N. Spector, Wave Electron, 4, 31 (1979).
5. J.E. Economou and H.N. Spector, J. Appl. Phys. 50, 6969 (1979).

## THE LOCALIZED MODES DUE TO PHOSPHEROUS DEFECTS IN CADMIUM TELLURIDE

K. Ramachandran and T.M. Haridasan

*School of Physics, Madurai Kamaraj University, Madurai 625021, India*

**Abstract.**— Dutt and Spitzer have experimentally observed the localized vibrational modes related to the phosphorous defect in CdTe and reported that this defect may go either to substitutional or interstitial site. In this paper we study theoretically this phosphorous defect behaviour for these two possible sites by Green's function technique and we believe that phosphorous goes interstitially rather than substitutionally. The localized modes paired with Ga, In and Al are also investigated and discussed in the light of the experimental results.

**1. Introduction.**— Dutt and Spitzer<sup>1</sup> measured the infrared active localized vibration modes (LVM) in CdTe when defects of phosphorous paired with In, Ga or Al are introduced. Their studies on LVM could not rule out the possibilities of the P defect going to interstitial or substitutional sites. It may further go to Te or Cd sites. For interstitial configuration it may be surrounded by 4 Cd neighbours or alternatively by 4 Te neighbours. The site symmetry in all these cases is  $T_d$  and the LVM falls under the  $F_2$  representation. To throw more light on the defect configuration in the light of the experimental results, we have made some theoretical investigations on these LVMs using lattice Green's functions and the results are presented here.

**2.a) Isolated substitutional P centre.**— Using the theory of Maradudin et al<sup>2</sup> the LVM frequencies can be obtained from the solution of the determinantal equation  $|I - g(\omega) \tilde{L}(\omega)| = 0$  where  $g$  refers to the Green's function of the host lattice entering the defect space (constituted by the defect and its 4 neighbours) and  $\tilde{L}$  the corresponding matrix for the force constant changes in the same defect space. Using the symmetry coordinates these matrices can be blockdiagonalized and the blocks of interest correspond to a  $3 \times 3$  matrix corresponding to  $F_2$  representations. The relevant Green's functions are computed using the phonons and eigenvectors of the modified rigid ion model of Plumble et al<sup>3</sup>. Assuming no relaxation the force constant changes can be expressed with one parameter  $\Delta A$ . If we fit the experimental LVM to this configuration we noticed an unusual increase of the force constant. When one

normally expects a force constant weakening for a lighter impurity such a large increase in the present case ( About 74% ) prompted us to examine the interstitial situation using lattice Green's functions.

b) Interstitial case.- Here also the nearest neighbour approximation with  $T_d$  symmetry gives the LVM under  $F_2$  representation. Using the theory of Brice<sup>4</sup> adapted for this case gave a force constant between interstitial and the host atom first neighbour around  $3.8468 \times 10^4$  dynes/cm as against  $6.0 \times 10^4$  dynes/cm between Cd and Te. The inclusion of the second neighbours did not alter the situation very much. This reveals that the LVM mode can be accounted in an interstitial configuration with a weaker force constant between the defect and the first neighbour. This is what one expects for a lighter impurity. In order to throw more light we have also computed the LVM modes due to the additive impurities of Ga, In and Al in both these configurations.

c) Substituted P defect paired with Ga, In and Al.- We assume P to Te site with Ga, In or Al going in any one of the 4 neighbouring Cd sites. We have now 2 LVMS associated with P centre due to the reduction of the point symmetry. Using the fitted force constants from isolated substitutional cases the LVMS are calculated for this configuration. However in these cases also one noticed Al-Te Ga-Te interactions to be larger than Cd-Te interaction.

d) Interstitial P defect paired with substitutional Ga, In and Al.- The interstitial P atom is assumed to be surrounded by 4 Cd atoms one of which is now replaced by Ga, In or Al. Now as in (c) knowing P-Cd interaction from isolated interstitial case and interaction of the type Ga-Te from isolated substitutional case and Ga-P interaction from crystal data of GaP, the modified LVM frequencies are calculated.

3. Results and conclusions.- The results are summarised in Table 1. A perusal of the results indicate that for the paired case the LVMS are satisfactorily accounted for by both the configurations.

But we should bear in mind that for the substitutional cases, one encountered unusually large force constants for Cd-P, Ga-Te and Al-Te. Eventhough for these lighter impurities, due to the fact that Group III or V elements enter in CdTe, one expects some long range coulomb contributions, still such extreme force constant changes of 74% are unexpected. Taken from this angle if one looks at the interstitial results,



Table 1.

System	Calculated LVM frequencies ( in $\text{cm}^{-1}$ )		Expt
	Substitutional	(Interstitial)	
P-Ga <sub>Cd</sub>	318.97	318.92	301.5
	349.21	345.97	352.5
P-In <sub>Cd</sub>	308.99	322.4	357.5
	345.97	352.7	305
P-Al <sub>Cd</sub>	399.98	352.72	331.5
	430.36	420.23	-

the pair modes are fairly well explained with a weaker P-Cd interaction. Thus we feel that P may go to the interstitial site rather than to a substitutional site. A recent calculation by Vandevyer and Talwar for substitutional configuration also gave a negative result. But they had not considered the case of the interstitial configuration. More data from experimental studies such as from Raman scattering would be highly desirable to throw more light on the P defect configuration in CdTe.

#### References.-

1. Dutt, B.V. and Spitzer, W.G., J. Appl. Phys 48, 954 (1977)
2. Maradudin, A.A., Montroll, E.W., Weiss, G.H. and Ipatova, I.P., Theory of lattice dynamics in the harmonic approximations, 2nd Edn, Academy Press, New York (1971)
3. Plumble, P. and Vandevyer, M., Phys. Stat. Solidi B73, 271 (1976)
4. Brice, D.K., Phys. Rev 140A, 1211 (1965)
5. Vandevyer, M. and Talwar, D.N., Phys. Rev B21, 3405 (1980)

RESONANT RAMAN SCATTERING IN  $\text{TiO}_2$ 

J. Camassel, B. Gil, P. Merle, H. Mathieu and J. Pascual\*

*Université des Sciences et Techniques du Languedoc, C.E.E.S., U.S.T.L., 34060 Montpellier-Cedex, France**\*Universitat Autònoma de Barcelona, Bellaterra, Barcelona, Spain*

**Abstract.** - One investigates the resonant behavior of Raman active phonons in  $\text{TiO}_2$  for incident laser energies ranging between 2.0 and 2.75 eV. One finds the enhancement to be dominated by the quadrupolar interaction.

$\text{TiO}_2$  (rutile) is a wide band gap semiconductor which belongs to the  $D_{4h}^{14}$  symmetry group. The fundamental absorption edge has been well characterized from experiments performed at liquid helium temperature<sup>(1)</sup>. The result of both experiments and theoretical calculations<sup>(2)</sup> concerning the ordering of electronic energy levels at the center of the Brillouin zone is schematically drawn in Fig.1. The lowest absorption edge is associated with a first-order forbidden quadrupolar interaction. Dipole-allowed transitions correspond to perturbations with  $\Gamma'_2$  ( $E//\bar{c}$ ) and  $\Gamma'_5$  ( $E \perp \bar{c}$ ) symmetry, respectively. If one refers to the crystallographic directions, the polarizability tensor of the first-order non-resonant Raman process corresponds to<sup>(3)</sup>:

$$\alpha_{yy}^{xx} (\Gamma^x_{5'} \quad x \quad \Gamma^x_{5'}) \longrightarrow \Gamma_1 (A_{1g}) + \Gamma_3 (B_{1g})$$

$$\alpha^{xy} (\Gamma^x_{5'} \quad x \quad \Gamma^y_{5'}) \longrightarrow \Gamma_4 (B_{2g})$$

$$\alpha^{zz} (\Gamma_{2'} \quad x \quad \Gamma_{2'}) \longrightarrow \Gamma_1 (A_{1g})$$

$$\alpha_{(yz)}^{xz} (\Gamma^x_{5'} \quad x \quad \Gamma_{2'}) \longrightarrow \Gamma_5 (E_g)$$

We have studied the resonant scattering tuning the incident phonon energy  $\hbar\omega_i$  close to the exciton energy of the fundamental gap. In this case, of the six terms contributing to the scattering probability per unit time<sup>(4)</sup> one becomes the strongest compared to all other terms which can be approximated by a constant C. Thus, in resonant Raman scattering (RRS) the scattering probability is written as:

$$P(\omega_i, \omega_s) \sim \left[ \sum_{j,k} \frac{\langle \Gamma_1 | H_3 | k \rangle \langle k | H_2 | j \rangle \langle j | H_1 | \Gamma_1 \rangle}{(\omega_k - \omega_s)(\omega_j - \omega_i)} \right]^2 \delta(\omega_i - \omega_s - \Omega)$$

where  $|\Gamma_1\rangle$  corresponds to the unperturbed ground state of the crystal;  $H_{1(3)}$  and  $H_2$  are the exciton-radiation and exciton-phonon interactions, respectively;  $|j\rangle$  and  $|k\rangle$

denote intermediate states in which excitations are created in the solid ;  $\omega_1(\omega_s)$  is the energy of the incident (scattered) light,  $\Omega$  the energy of the phonon and  $\omega_j(\omega_k)$  the energy of the intermediate state.

All experiments have been performed using previously described techniques<sup>(3)</sup>. The incident propagation was along the c axis, the collected one along a. All incident frequencies were provided by i) an argon-ion laser, ii) a C.W. dye laser using R6G in the range 5700-6000 Å, iii) a pulsed dye laser pumped by 1 MWatt nitrogen laser.

$$\Gamma_4(A_{1g}) : 76 \text{ meV}/612 \text{ cm}^{-1} \text{ Raman-line}$$

The most resonant electronic process first includes the creation of a direct exciton in an excited state of symmetry  $|j = \Gamma_3\rangle$  by means of a quadrupolar interaction  $H_1(\Gamma_3)$ . The exciton is next scattered to the exciton ground state  $|k = \Gamma_1\rangle$  by the  $\Gamma_1$  phonon. Finally the exciton annihilates by quadrupolar interaction  $H_3(\Gamma_3)$ . Other processes involving two dipolar interactions from the ground state to higher excited states with symmetry  $\Gamma_5$ , are far from resonance. The scattering probability is then given by :

$$P(A_{1g}) \sim \left[ \frac{\langle \Gamma_1 | H_3(\Gamma_3) | \Gamma_3 \rangle \langle \Gamma_3 | H_2(\Gamma_1) | \Gamma_3 \rangle \langle \Gamma_3 | H_1(\Gamma_3) | \Gamma_1 \rangle}{(3.05 + 0.076 - \hbar\omega_1)(3.05 - \hbar\omega_1)} \right. \\ \left. + \frac{\langle \Gamma_1 | H_3(\Gamma_5) | \Gamma_5 \rangle \langle \Gamma_5 | H_2(\Gamma_1) | \Gamma_5 \rangle \langle \Gamma_5 | H_1(\Gamma_5) | \Gamma_1 \rangle}{(5 + 0.076 + \hbar\omega_1)(5 - \hbar\omega_1)} + C \right]^2$$

Near resonance :

$$P(A_{1g}) \sim \frac{A^2}{(3.05 + 0.076 - \hbar\omega_1)^2 (3.05 - \hbar\omega_1)^2}$$

The solid line in Fig.2 has been calculated using  $A^2 = 0.16$  and accounts satisfactorily for the dispersion of experimental cross section.

$$\Gamma_5(E_g) : 56 \text{ meV}/449 \text{ cm}^{-1} \text{ Raman-line}$$

The different excitation processes involve different immediate states. Two of them are summarized in the expression of the scattering probability :

$$P(E_g) \sim \left[ \frac{\langle \Gamma_1 | H_3(\Gamma_5) | \Gamma_5 \rangle \langle \Gamma_5 | H_2(\Gamma_5) | \Gamma_3 \rangle \langle \Gamma_3 | H_1(\Gamma_3) | \Gamma_1 \rangle}{(5 + 0.056 - \hbar\omega_1)(3.05 - \hbar\omega_1)} \right. \\ \left. + \frac{\langle \Gamma_1 | H_3(\Gamma_2) | \Gamma_2 \rangle \langle \Gamma_2 | H_2(\Gamma_5) | \Gamma_5 \rangle \langle \Gamma_5 | H_1(\Gamma_5) | \Gamma_1 \rangle}{(5 + 0.056 - \hbar\omega_1)(5 - \hbar\omega_1)} + C \right]^2$$

The first contribution is semiresonant (only one energy denominator cancels) and the second is not. Then the scattering probability can be written :

$$P(E_g) \sim \frac{B^2}{(5 - \hbar\omega_1)^2 (3.05 - \hbar\omega_1)^2}$$

The solid curve in Fig. 3 has been calculated using  $B^2 = 1.75$  and, again, compares satisfactorily with the experimental results.

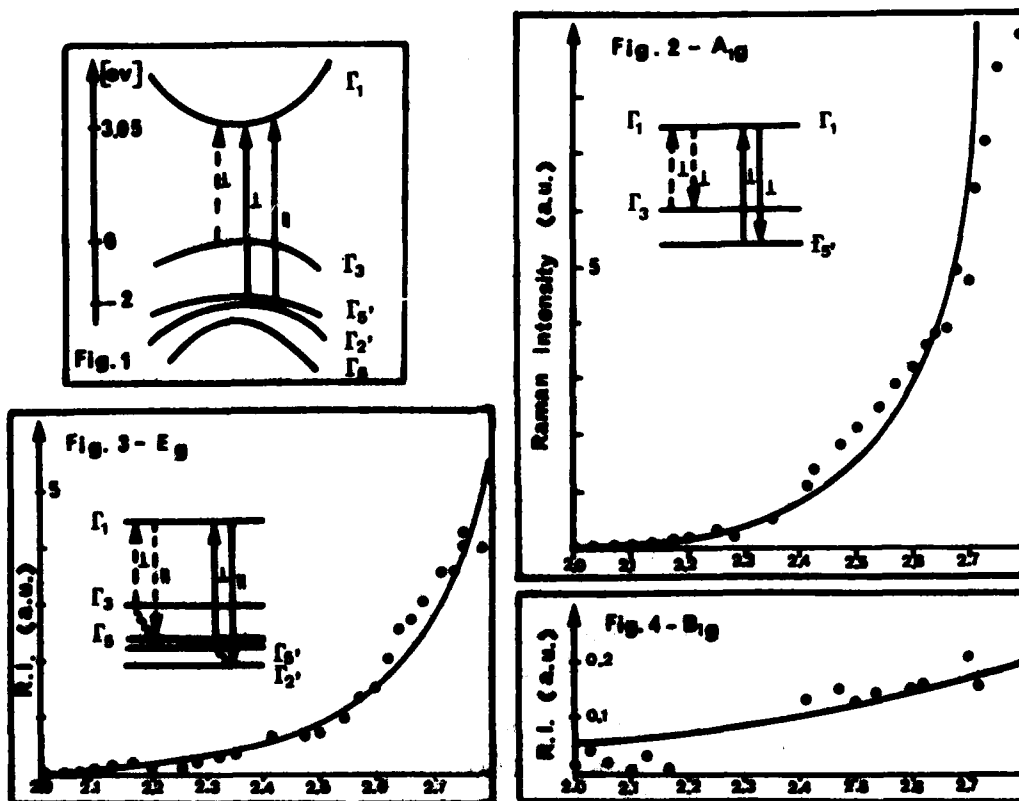
$$\Gamma_3(B_{1g}) : 18 \text{ meV}/143 \text{ cm}^{-1} \text{ Raman-line}$$

We did not find a process which permits the enhancement of phonons with symmetry  $\Gamma_3$  with quadrupolar-allowed transitions. The allowed process with lowest exciting energy includes two dipolar interactions with excited states of symmetry  $\Gamma_{5'}$  :

$$P(\Gamma_3) \sim \left[ \frac{\langle \Gamma_1 | H_3(\Gamma_{5'_L}) | \Gamma_{5'} \rangle \langle \Gamma_{5'} | H_2(\Gamma_3) | \Gamma_{5'} \rangle \langle \Gamma_{5'} | H_1(\Gamma_{5'_L}) | \Gamma_1 \rangle}{(5 - \hbar \omega_1)(5 - \hbar \omega_1)} + C \right]^2$$

In agreement with experimental data, the solid line in Fig. 4 displays a negligible dispersion in our range of investigation

- References : 1) J. Pascual, J. Camassel and H. Mathieu, Phys. Rev. Let. **39**, 1490, 1977.  
 2) N. Daudé, C. Gout and C. Jouanin, Phys. Rev. **B15**, 3229, (1977).  
 3) P. Merle, J. Pascual, J. Camassel and H. Mathieu, Phys. Rev. **B.21**, 1617, 1980.  
 4) P.Y. Yu, "Excitons", K.Cho ed. Springer Verlag, Berlin, p. 214, 1979.



## THE LOW FREQUENCY ABSORPTION OF GALLIUM PHOSPHIDE INDUCED BY IMPURITIES AND RADIATION DAMAGE

G.A. Gledhill\*, S.S. Kudhail\*, R.C. Newman\*\*, J. Woodhead\*\* and G.Z. Zhang\* \*

\* *Westfield College, University of London, Kidderpore Avenue, London NW3 7ST, England.*\*\* *J.J. Thomson Physical Laboratory, University of Reading, Reading RG6 2AF, England*

**Abstract.**— Irradiation of GaP by fast neutrons or 2MeV electrons induces infrared absorption corresponding to acoustic modes in the density of vibrational states. The dependence on radiation dose of other absorption lines induced just above and just below the Reststrahlen band is examined. Observations of previously unreported lines in the gap mode region are presented; lines at  $253\text{cm}^{-1}$  and  $304\text{cm}^{-1}$  being assigned to Si impurity on Ga sites and a B impurity complex respectively.

Absorption on the high frequency side of the Reststrahlen band in GaP induced by impurities and radiation damage has been investigated in some detail; however, relatively little work has been done at lower frequencies. In the spectral region just below  $300\text{cm}^{-1}$  gap modes, attributed to B and As impurities and to radiation damage defects, have been observed (1,2) and in the region of low density of states just above the TA phonon cut-off an absorption band due to a B resonance has been reported at  $158\text{cm}^{-1}$  (3). (These features are present in spectrum (b), Fig.1.).

In this paper we report the results of infrared absorption measurements at 80K in the spectral range  $30\text{--}700\text{cm}^{-1}$  on 20 bulk GaP samples prepared and examined by interferometric techniques described in (3). The samples contained various combinations of impurities including B, Si, C, Al and As and all but one had been irradiated by either 2MeV electrons or fast neutrons. The interpretation of the spectra was difficult for the following reasons: a very limited range of samples was available; all the samples contained at least two impurities and had been irradiated with a dose sufficient to render them transparent making it difficult to determine which features arose from damage and which arose from the various impurities; the samples were too thick to measure the strengths of strong lines accurately but not thick enough to measure the weakest lines; many of the lines overlapped, weaker ones fell on or near strong lines, with the result that some of the line strengths were estimated from unresolved features. The best measurements of line strengths had an error estimated at 10% but for the reasons just stated some had an error of 50%

In addition to the lines due to As ( $273\text{cm}^{-1}$ ) and B ( $284\text{cm}^{-1}$ ), features were observed at 234, 253, 264, 279, 283, 294, 299, 304, 316 and  $323\text{cm}^{-1}$ . The lines at 279, 316, and  $323\text{cm}^{-1}$  were present in all samples and are attributed to two-phonon lattice bands.

\* On leave from Dept. of Physics, Zhongshan University, Guangzhou, China

The line at  $253\text{cm}^{-1}$  (Fig.1 spectrum (c)) was observed only in samples containing Si impurity. Its strength was correlated with that of the line at  $465\text{cm}^{-1}$  and was not correlated with any lines arising from other defects, leading us to conclude that the feature at  $253\text{cm}^{-1}$  is a gap mode arising from the impurity centre  $^{28}\text{Si}_{\text{Ga}}$ . The strength-ratio of the local mode to gap mode is 3:1 for  $^{28}\text{Si}_{\text{Ga}}$  compared with 2:1 for  $^{10+11}\text{B}_{\text{Ga}}$ . If we assume that any gap mode associated with the impurity centre  $^{27}\text{Al}_{\text{Ga}}$  has approximately the same strength-ratio with respect to the Al local mode ( $444\text{cm}^{-1}$ ), then the failure to observe any feature in the gap which can be correlated with Al leads us to speculate that for this impurity centre no mode rises from the acoustic branch. In fact the asymmetric shape of the Si gap mode, consistent with its proximity to the LA cut-off, suggests that the Si mode is scarcely able to rise from the continuum. The comparison is not unreasonable since the  $^{28}\text{Si}_{\text{Ga}}$  local mode has a higher frequency than the  $^{27}\text{Al}_{\text{Ga}}$  local mode even though Si has the greater mass.

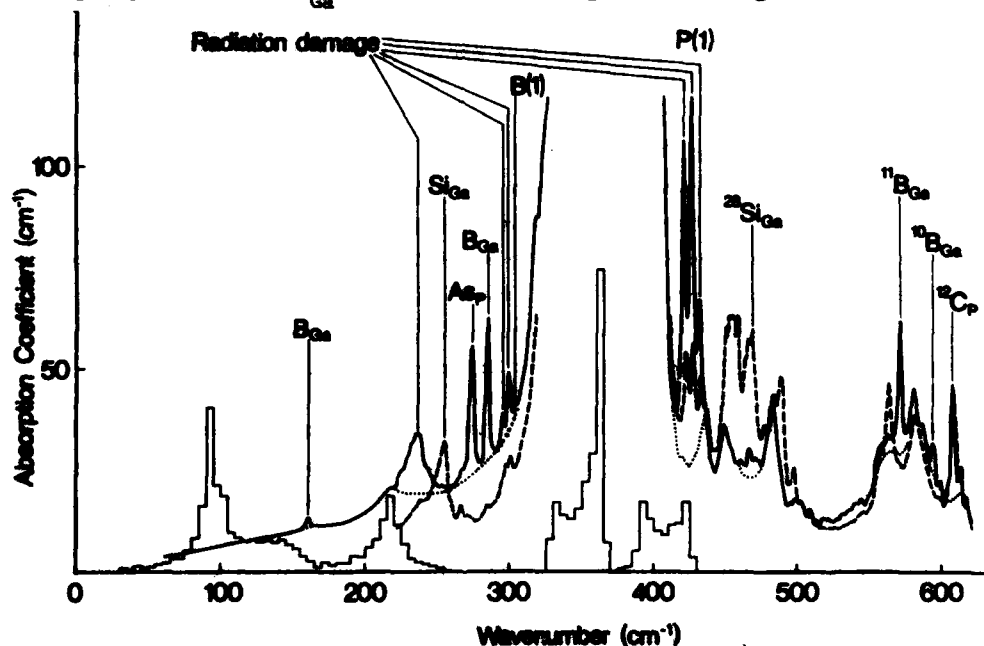


Fig.1. The one-phonon density of states in GaP at 300K calculated by Kunc et al.(4) (Histogram), Infrared absorption spectra measured at  $1\text{cm}^{-1}$  resolution at 80K of (a) pure, unirradiated GaP(.....), deduced from measurements on numerous samples, (b) a GaP crystal containing B,As,C and Si impurities and irradiated with a dose of  $10^{19}$  electrons (—) and (c) polycrystalline GaP sample containing Si and C and irradiated with  $4 \times 10^{18}$  electrons (- - -).

Radiation damage causes lattice deformation which lowers the crystal symmetry enabling previously forbidden absorption processes to occur. In particular one-phonon absorption is no longer restricted to the optic mode region as in the undamaged crystal so it is expected that radiation damage will induce absorption similar in structure to the one-phonon density of states in the acoustic mode region as reported by us previously for GaAs (5). This indeed occurs, as shown in Fig.1 spectrum (b), where

the band at  $234\text{cm}^{-1}$ , present in all samples subjected to either electron or neutron irradiation, is attributed to one-phonon absorption corresponding to the LA branch of the density of states.

Radiation damage is known to induce other features in GaP including the three lines at  $419.5$ ,  $429.0$  and  $430.5\text{cm}^{-1}$  (designated P(1) lines) on the high frequency side of the Reststrahlen band (6) and the lines at  $294$  and  $299\text{cm}^{-1}$  on the low frequency side. We find, for a range of samples, that all these features increase linearly in strength with radiation dose up to the limit imposed by our measuring techniques. Furthermore, the P(1) lines increase linearly in strength with radiation dose for a given sample. We conclude that the P(1) lines and the lines at  $294$  and  $299\text{cm}^{-1}$  involve intrinsic radiation damage defects only but the nature of the defects is not yet determined.

The line at  $304\text{cm}^{-1}$  was present only in samples which both contained B and had been exposed to a substantial dose of radiation. It increased in strength with radiation dose but its strength showed no correlation with the strength of the lines arising from B impurity on Ga sites, suggesting that it originated from a B impurity complex. Due to the presence of the adjacent line at  $299\text{cm}^{-1}$  induced by radiation damage, it was difficult to measure the strength of the  $304\text{cm}^{-1}$  line accurately. However, within experimental error, the strength of the line at  $304\text{cm}^{-1}$  increased linearly with the strength of the local mode line at  $850\text{cm}^{-1}$  which arises from the B impurity complex designated B(1)(7), suggesting that the  $304\text{cm}^{-1}$  line also originates from B(1). The other lines observed in this region ( $264$  and  $283\text{cm}^{-1}$ ) were found to be sample dependent; however, due to the weakness of these lines and the limited availability of samples it was not possible to make assignments.

Observations such as these of different modes of vibration of impurity or damage centres can be of considerable value in the correct formulation of theoretical models as opposed to the conventional attempts to adjust model parameters to fit local mode measurements.

We wish to thank Dr. D.R.Wight of RSRE(Malvern) and Mr. B.H.L.Wilson of Plessey Research(Caswell) for supplying GaP samples, Mr. A.Holman for help with electron irradiations and the Science Research Council for financial assistance.

#### References

1. Hayes W., Macdonald H.F. and Sennett C.T., J.Phys.C:Solid St.Phys.2, 2402 (1969).
2. Thompson F. and Newman R.C., J.Phys.C:Solid St.Phys.4, 3249 (1971).
3. Gledhill G.A., Kudhail S.S., Newman R.C. and Zhang G.Z., Int.J.of Infrared and Millimeter Waves. (In press) (July 1981).
4. Kunc K., Balkanski M. and Nusimovici M.A., Phys.Stat.Sol.(b)72, 229 (1975).
5. Gledhill G.A., Angress J.F., Brozel M. and Newman R.C., Proc.Int.Conf.on Lattice Dynamics, Paris, Flammarion. (1977).
6. Newman R.C. and Totterdell D.H.J., J.Phys.C:Solid St.Phys.8, 3944 (1975).
7. Woodhead J. and Newman R.C., J.Phys.C:Solid St.Phys.14, L345 (1981).

## RESONANT ENHANCEMENT OF THE RAMAN LINEWIDTH OF PHONON MODES INDUCED BY HYDROSTATIC PRESSURE

D. Petritis, C. Deville Cavellin and G. Martinez

*Laboratoire de Physique des Solides, associé au C.N.R.S., Université Pierre et Marie Curie, 4, place Jussieu, Paris VI, 75230 Paris Cedex 05, France*

**Abstract.**— It is shown that, under special circumstances, the pressure can induce in the RAMAN spectrum of a compound, a resonant variation of the linewidth of modes.

This effect can be interpreted by a model which then provides the value of some third order deformation potentials of the crystals.

The effect of the hydrostatic pressure on the phonon modes linewidth of semiconductors is studied. Under special circumstances this linewidth exhibits a resonant behaviour as a function of the pressure. Two experimental evidences of this effect are shown in the  $\text{Cu}_3\text{VS}_4$  and  $\text{ZrS}_3$  compounds. This effect is explained by the evidence, induced by pressure of a single phonon mode and a double phonon structure. The quasi harmonic approximation introduces a complex self energy,  $\Delta + i\Gamma$ .  $\Delta$ , a small shift of the harmonic frequency and  $\Gamma$  the linewidth characterize the anharmonicity. Two different kind of processes involving either virtual or real transitions contribute<sup>(1)</sup> to this self energy. Among them, only those which deal with real transitions give a contribution to  $\Gamma$ . The simplest diagram of this kind represents the decay of a single phonon  $\omega_0$  in two. The pressure cannot induced by itself any transitions between the different states of the system. Then it is expected that pressure acts directly on  $\Delta$  but not on  $\Gamma$ . This is confirmed by the majority of experimental results. However the inspection of the formalism which gives  $\Gamma$  for the process described above, shows that the expression can become resonant when  $\omega$  is closed to  $\omega_1 + \omega_2$ . Two examples of such a resonance have been studied in our laboratory, by performing Raman scattering experiments in diamond anvil cells.

The first one is that of the  $A_1$  mode of the  $\text{Cu}_3\text{VS}_4$ <sup>(2)</sup>. (Figure 1). Around 20 kbars the energy on the  $A$  mode equals the sum of the energies of the two lower  $F_2$  modes and the linewidth  $\Gamma$  exhibit a resonant enhancement. The figure 2 shows the example of the highest frequency  $A_g$  mode of  $\text{ZrS}_3$  which coincide with 2  $B_g$  modes. Notice the concomitant variation of the frequency in both cases.



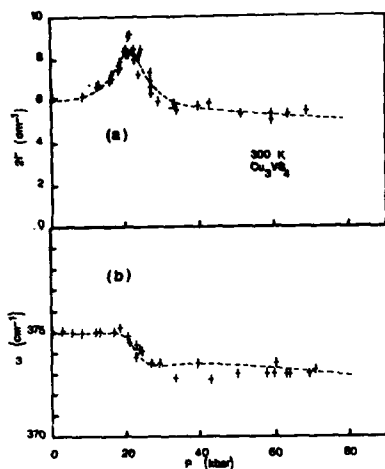


Figure 1. Variation of the linewidth (a) and the frequency (b) of the A mode of  $\text{Cu}_3\text{VS}_4$  as a function of the pressure.

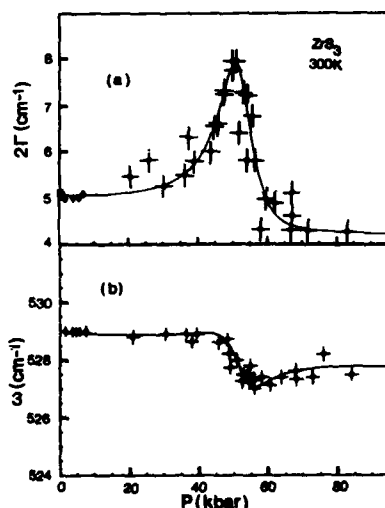


Figure 2. Variation of the linewidth (a) and the frequency (b) of an Ag mode of  $\text{ZrS}_3$  as a function of the pressure.

The theory of the coupled Raman scattering can be performed exactly and shows that if  $V_1$  represents the strength of the first order Raman effect,  $V_2$  that of the second order Raman effect and  $W$  the coupling between them, there are two different regimes: when  $\frac{V_1}{V_2} \ll \frac{\omega_0 - \omega}{2}$  the enhancement of the line-

width occurs without any noticeable asymmetry in the observed peak. This is the case for the two examples we are dealing with. If  $\frac{V_1}{V_2} \gg \frac{\omega_0 - \omega}{2}$  the asymmetry is effective and explains probably the line shape of the TO mode of GaP. In the absence of such an asymmetry the experimental results on  $\Gamma$  can be easily interpreted and fitted by the expression :

$$\Gamma(\omega_0(P)) = \frac{\phi}{\omega_1 \omega_2} (n_1 + n_2 + 1) \times$$

$$\frac{\gamma + b (\omega - \omega_1 - \omega_2)}{(\omega - \omega_1 \omega_2)^2 + \gamma^2}$$

$\phi$  characterizes the strength of the anharmonic potential for this process,  $\gamma$  the width of the double phonon structure and  $b$  the asymmetric parameter for the density of states of the double phonon structure.  $\phi$ ,  $\gamma$  and  $b$  are fitted to reproduce the experimental variation of  $\Gamma$  (fig. 1a and 2a). When the fit is correct, the Kramers Kronig transformation of this analytical expression should also fit the variation of the frequency (fig. 1b and 2b). It is also checked that by symmetry the single phonon  $\omega_0$  can decay into the two phonons  $\omega_1 + \omega_2$  and eventually that this double structure is experimentally seen independently which is the case for  $\text{Cu}_3\text{VS}_4$  with infrared and for  $\text{ZrS}_3$  with Raman scattering experiments<sup>(3)</sup>.

We obtained for  $\text{Cu}_3\text{VS}_4$   $\phi = 1.2 \cdot 10^5 \text{ cm}^{-4}$   $b = 0$  and for  $\text{ZrS}_3$   $\phi = 4 \cdot 10^4 \text{ cm}^{-4}$   $b = 0,45$   $\gamma$  being in both cases of the order of the sum of the individual linewidth of each phonon. The important result is that  $\phi$  is found practically pressure independent. We think that the surprising large variation of  $\phi$  with pressure found for  $\text{GaP}^{(4)}$  where the same model was tentatively applied to reproduce the experiments is just due to the fact that this model should not reproduce the situation for  $\text{GaP}$  where the asymmetry of the lines is very well defined.

#### References

1. WALLIS R.F., IPATOVA, I.P., MARADUDIN, A.A., Sov. Phys. Solid. State 8, 850 (1966).
2. PETRITIS D., MARTINEZ G., LEVY-CLEMENT C., GOROCHOV, O., Sol. St. Commun. 35, 273 (1980).
3. ZWICK A., RENUCCI M.A., CARLES R., SAINT CRICQ N., RENUCCI J.B., Proceedings of the Conference on Physics and Chemistry of layered materials, Sendai (1980).
4. WEINSTEIN B.A., Sol. Stat. Commun., 20, 999 (1976).

THE ROLE OF PHONONS IN PHASE TRANSITIONS

## THE ROLE OF PHONONS IN INCOMMENSURATE PHASE TRANSITIONS

R. Currat

*Institut Laue-Langevin, 156X, 38042 Grenoble Cedex, France*

**Abstract.**— The various classes of incommensurably-modulated solids are reviewed with particular emphasis given to the case of insulators. We discuss examples of incommensurate ordering transitions of the displacive and order-disorder types. Below the ordering temperature, the concepts of amplitude and phase susceptibilities are recalled. Neutron evidence for propagating phase modes in biphenyl and  $\text{ThBr}_4$  are presented.

1. **Introduction.**— Over the last few years, there has been a growth of interest in incommensurably modulated structures and much effort has been devoted to the characterization of their static and dynamical properties. Typically, incommensurate structures are stable over a temperature interval bounded by an upper ordering temperature  $T_i$  and a lower "lock-in" temperature  $T_c$ . Below  $T_c$  the wavelength of the modulation locks onto some rational fraction of the underlying lattice periodicity. Deviations from the above prototypical behaviour are numerous : some systems remain in the incommensurate state down to OK (e.g.  $\text{BaMnF}_4$ ), others undergo a succession of lock-in and unlocking transitions (e.g. thiourea).

The two transitions, at  $T_i$  and  $T_c$ , are markedly different in nature : while the transition at  $T_i$  has a well defined order parameter and a corresponding divergent susceptibility, the lock-in transition is either strongly discontinuous (no order parameter) or may correspond to the disappearance of phase defects, depending upon the symmetry of the soft-mode dispersion around the commensurate wavevector<sup>(1,2)</sup>. In what follows we shall be concerned with the dynamical behaviour of systems near their ordering temperature; this is where one expects to observe soft-modes and consequently, this is the regime which experimentally has been most extensively investigated.

From a microscopic standpoint it is important to distinguish between the two different types of ordering mechanisms which occur in low-dimensional metals and in insulators. In the former case, the incommensurability of the charge density wave (and of the associated lattice distortion), reflects the incommensurability of the Fermi wavevector, arising from non-stoichiometry (as in KCP), charge-transfer (as in TTF-TCNQ) or just energy band structure (as in the transition metal dichalcogenides).

In spite of their electronic origin, Peierls instabilities do give rise to lattice dynamical precursor effects, usually observed as a local softening of the longitudinal acoustic branch, in the vicinity of the ordering wavevector  $2\vec{k}_F$ .

In the case of insulators, a case which shall be emphasized below, the incommensurate ordering must be viewed as originating either from an intrinsic lattice dynamical instability (displacive limit) or from some collective ordering mode (order-disorder limit), both of general wavevector.

2. Soft-mode behaviour above  $T_i$ .— The 129°K transition in  $K_2SeO_4$  is one of the best documented<sup>(3)</sup> incommensurate transition of the displacive-type. Above  $T_i$ , the soft branch, shown in Fig. 1, displays a broad temperature-dependent minimum in the vicinity of  $\frac{1}{3} a^*$ . In the incommensurate state the modulation wavevector, equal to  $0.31a^*$  at  $T_i$ , increases steadily upon cooling and eventually locks onto the commensurate value  $\frac{a^*}{3}$  at  $T_c = 93$  K.

Within this soft-mode picture the incommensurate ordering transition appears simply as a natural extension of the conventional ferro- and antiferrodistortive transitions. In fact it is well-known that in the presence of competing interactions of different characteristic ranges, phonon dispersion curves may develop local minima around arbitrary wavevectors. Furthermore the exact position of such minima does not in general provide any direct insight into the nature of the competing forces.

As an alternative approach one may inquire whether there exists particular symmetry criteria associated with the occurrence of modulated phases. For instance, many modulated phases originate from non-symmorphic space groups where most of the special zone-boundary wavevectors are ruled out as possible candidates for a lattice instability on the grounds that they do not fulfill Lifshitz's criterion. In phonon language, this criterion reflects the fact that modes propagating in high-symmetry directions experience a pseudo-periodicity which is shorter than the lattice periodicity. This leads to the absence of gaps at the corresponding zone-boundaries, i.e., in a reduced zone scheme, to pairwise degeneracies of the zone boundary modes. Since the merging phonon branches are no longer constrained to have a zero slope, any zone-boundary phonon softening leads first to the appearance of a modulated structure, with a wavevector close to the high-symmetry zone-boundary point. This type of mechanism is illustrated by systems such as  $(NH_4)_2BeF_4$ <sup>(4)</sup> and biphenyl<sup>(5)</sup>. On the other hand it fails to account for the occurrence of modulated phases with wavevectors

close to  $\vec{q} = 0$ , as in  $NaNO_2$ <sup>(6)</sup> or Thiourea<sup>(7)</sup>, and alternative mechanisms have been proposed<sup>(8,9)</sup>, based on two-mode interactions.

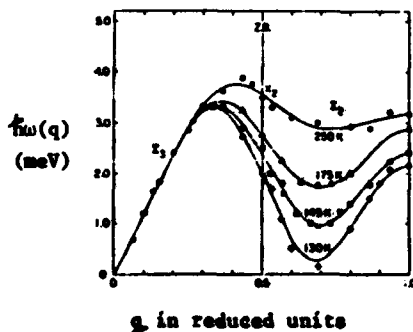


Fig. 1 : Dispersion of  $\sum_2, \sum_3$  soft mode branches in  $K_2SeO_4$  in an extended zone scheme (after ref. 3).

In the specific context of ionic crystals, it is customary to distinguish between long-range Coulomb interactions and short-range overlap forces. Thus the requirement of competing interactions of different ranges would seem to be systematically fulfilled in the case of ionic crystals, with some potential insight to be gained by means of conventional lattice dynamical modeling. Following this approach, Haque and Hardy <sup>(10)</sup> have investigated the microscopic origin of the  $K_2SeO_4$  soft-mode. To this end they have constructed a rigid-ion model of  $K_2SeO_4$  where the (numerous) short-range force-constants were determined using static equilibrium conditions as well as some observed Raman frequencies. On the basis of their model they were able to reproduce the soft  $\Gamma_2$ -branch in the  $[1,0,0]$  direction. The soft branch frequencies, however, were obtained as differences between two very large terms (with almost identical  $q$ -dependences), representing the Coulomb and short-range contributions to the dynamical matrix, respectively (see fig. 8 in ref. 10). Because of this large cancellation effect the soft mode minimum around  $\frac{a^*}{3}$  appears as accidental and no simple physical picture can be drawn from the model. Obviously, what is needed is a simpler model system.

Before closing this section, one should mention the existence of systems undergoing incommensurate order-disorder transitions as illustrated by  $NaNO_2$  <sup>(6)</sup>. Above  $164^\circ C$ , the structure of  $NaNO_2$  is disordered with respect to the orientation of the  $NO_2^-$  groups (parallel or antiparallel to  $b$ ). Between  $T_i = 164 K$  and  $T_c = 162.5^\circ C$  a modulated structure appears, characterized by the onset of an orientational probability wave. The wave appears to be essentially sinusoidal, with a wavevector varying smoothly <sup>(11)</sup> between  $\sim \frac{a^*}{8}$  and  $\frac{a^*}{10}$ . Yamada and Yamada <sup>(12)</sup> have shown that dipolar interactions between  $NO_2^-$  groups would, by themselves, favor a polarization wave of wavevector  $\sim \frac{a^*}{5}$ . This value represents a compromise between ferroelectric and antiferroelectric interactions between neighbouring dipoles. The observed value of the wavevector results from an additional compromise between dipolar forces on one hand and short range overlap forces on the other. Yamada's model is however not unique and a rather different picture, based on 2 coupled order parameters (polarization and shear waves) has also been proposed <sup>(13)</sup>.

The ordering transition at  $T_i$  is characterized by a critical slowing-down of the polarization fluctuation and no soft-phonon is observed as is typical for order-disorder transitions.

Finally one should emphasize that just above the ordering temperature, the dynamical behaviour of displacive systems is known to deviate from the simple soft-mode model. Due to coupling with defects the quasi-harmonic soft-mode frequency is expected to level off while a narrow quasielastic ("central") component develops. Halperin and Varma <sup>(13)</sup> have investigated the consequences of this coupling in cases where the defects are slowly relaxing as well as for frozen defects. In addition, Imry and Ma <sup>(14)</sup> have pointed out that in systems where the order-parameter has continuous symmetry (e.g. the Heisenberg ferromagnet) the presence of frozen

impurities is such as to destroy long range order at any temperature. This remark is of particular relevance here, since the incommensurate order parameter has continuous phase symmetry and since local defects, whether relaxing or frozen in the Halperin and Varma sense, will to some extent behave as frozen defects. Indeed any defect whose energy depends upon the local amplitude of the distortion will either diffuse towards a region where this amplitude is optimized, or alternatively distort the phase of the wave. As a result the modulation may lose its long-range phase coherence, a situation which may seriously affect the propagation of long-wavelength phase modes below  $T_i$ . Analogous arguments<sup>(15)</sup> have been developed in the context of charged impurities interacting with a CDW.

3. Excitations below  $T_i$ .— Despite the loss of translational invariance at  $T_i$ , there is experimental evidence for the existence of sharp excitations in the incommensurate state. At the moment there is no general theoretical framework within which these excitations may be discussed. Most of the current work is aimed at clarifying the way in which the soft branch renormalizes below  $T_i$ . Using the simplest kind of quasi-harmonic approximation, one may readily show<sup>(16)</sup> that the condensation of the soft mode coordinates  $Q(q_i)$  and  $Q(-q_i)$  induces a bilinear coupling between the neighbouring coordinates  $Q(q_i+q)$  and  $Q(-q_i+q)$ . The near-degeneracy between the latter coordinates is lifted by the interaction term and in the limit of small  $q$ , two new normal modes emerge :

$$A_q = \frac{1}{\sqrt{2}} (Q(q_i+q) + Q(-q_i+q))$$

$$\phi_q = \frac{1}{\sqrt{2}} (Q(q_i+q) - Q(-q_i+q))$$

Expanding the soft-mode dispersion ( $T > T_i$ ) in powers of  $q$  :

$$\omega^2(\pm q_i+q) = a(T-T_i) + q \bar{\Lambda} q + O(|q|^3) \quad (1a)$$

the dispersion laws for the new normal modes are obtained, to leading order in  $q$ , as :

$$\omega_A^2(q) = 2a(T_i-T) + q \bar{\Lambda} q \quad (1b)$$

$$\omega_\phi^2(q) = q \bar{\Lambda} q \quad (1c)$$

Bruce and Cowley<sup>(16)</sup> have discussed the limits of validity of the above picture and the extent to which the two new normal modes can be identified with fluctuations in the amplitude and phase of the frozen wave, respectively.

On the experimental side many attempts have been made at testing those simple predictions. In principle both  $q = 0$  modes may be observed by means of light scattering. While this would seem fairly obvious in the case of the (totally symmetric) amplitude mode, a rather more careful analysis is required in so far as the Brillouin

activity of the phase mode is concerned<sup>(17)</sup>. In practice attempts to observe the amplitude mode by Raman scattering have been generally successful, whereas Brillouin measurements of the phase mode in systems such as  $K_2SeO_4$  and  $BaMnF_4$  have yielded negative or controversial results<sup>(18,19)</sup>. Fortunately there are at least two systems in which a propagative phase mode could be observed by means of inelastic neutron scattering.

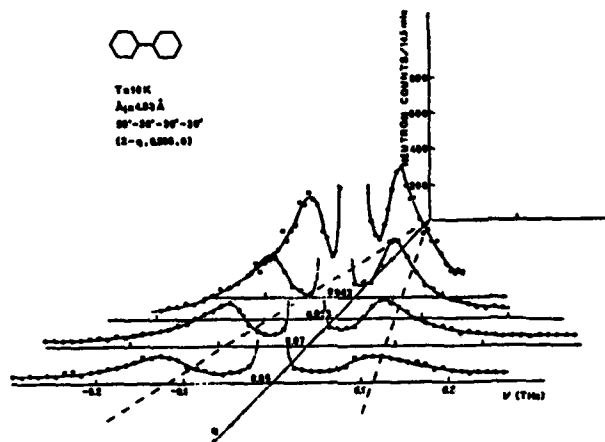


Fig. 2 : Energy scans for different reduced wavevectors along  $a^*$  in phase III of biphenyl (after ref. 20).

Fig. 2 shows some of the observed spectra as a function of wavevector in the  $a^*$  direction. The observed excitation is unambiguously identified as a phason since :

- i) its intensity is too large for it to be an acoustic branch originating from the  $(2, 0.536, 0)$  satellite reflection.
- ii) its slope is lower by a factor  $\sim 2$  compared to the slope of the lowest energy acoustic mode propagating in the  $a^*$ -direction, and agrees well with the corresponding soft mode dispersion above  $T_I$  (cf. eq. 1a and 1c).

The other system is  $ThBr_4$  which has a tetragonal ( $D_{4h}^{19}$ ) space group in the high-temperature phase (cf. Fig. 3) and becomes incommensurate<sup>(21)</sup> below  $T_I = 95$  K, with the modulation wavevector along the 4-fold screw-axis :

$$q_I = 0.31 c^*$$

$q_I$  is found to be independent of temperature and no lock-in transition was detected at least down to 10K. Above  $T_I$ , one observes temperature-dependent softening of a low lying optic branch (see Fig. 4).

The analysis of the room temperature infra-red and Raman spectra<sup>(22)</sup> together with the satellite reflection extinction rules, allows the symmetry assignment at the soft optic branch ( $\tau^4$  in Kovalev's notation) to be made. The soft-mode eigenvector consists of a simple linear combination of  $B_{1u}$ -type and  $B_{2g}$ -type bromine motions,

The first such system is deuterated biphenyl, a molecular crystal which undergoes a displacive transition at  $T_I = 38$  K into a modulated structure, followed by a partial lock-in transition at  $T_{II} = 2$  K. The best inelastic results<sup>(20)</sup> have been obtained in phase III (below  $T_{II}$ ), where the wavevector of the modulation is equal to  $\frac{1}{2} (1 - \delta_b) b^*$  with  $\delta_b = 0.07$ .



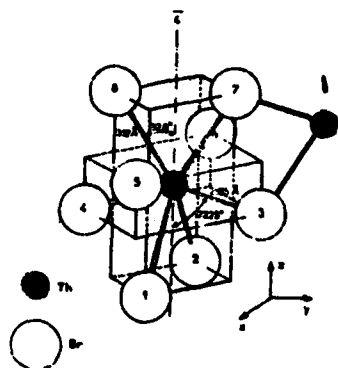


Fig. 3 : Structure of  $\text{ThBr}_4$  at room temperature.

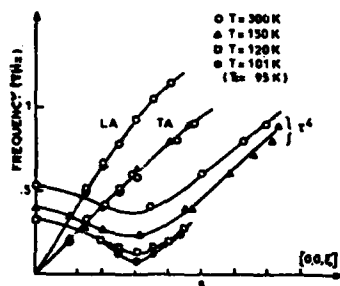


Fig. 4 : Soft mode dispersion in  $\text{ThBr}_4$

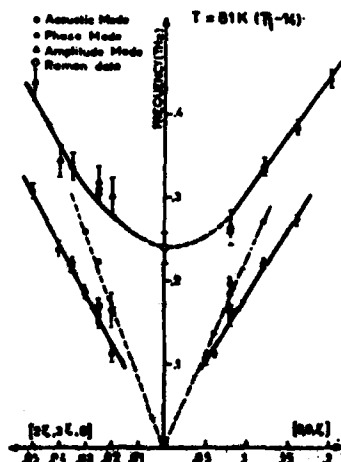


Fig. 5 : Constant Q-scans for wavevectors along  $c^*$  ( $\text{ThBr}_4$ ; 81 K)

Fig. 6 : Phase and amplitude mode dispersions in  $\text{ThBr}_4$ . Acoustic modes measured near (2,3,1) are shown for comparison.

the Thorium ions remaining at rest. Thus, while the high-temperature structure can be characterized in terms of only 3 parameters ( $c/a$  ratio,  $x$  and  $z$  coordinates of one Bromine ion), the description of the ionic displacements below  $T_i$ , in the single plane-wave approximation, requires only 3 additional parameters (wavevector, amplitude and  $B_{1u}/B_{2g}$  ratio).

Fig. 5 shows inelastic spectra obtained at 81 K near the  $(2,3,1-q_i)$  satellite reflection. The lower branch is too intense by 2 orders of magnitude to be of acoustic origin. Fig. 6 shows the experimental dispersion curves, which summarize the 81 K data. In both propagation directions, i.e.  $[0,0,\xi]$  and  $[2\xi, 3\xi, 0]$ , the observed slopes are in excellent agreement with the soft mode dispersion above  $T_i$ .

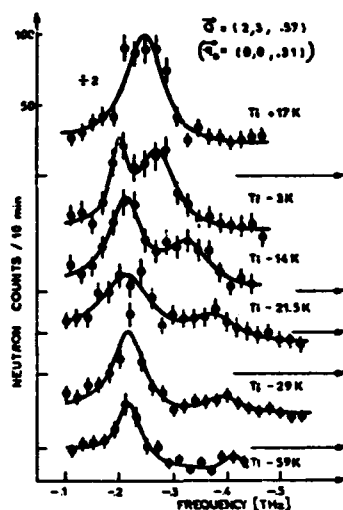


Fig. 7 : Inelastic spectrum at  $(2,3,0.57)$  as a function of temperature.

Fig. 7 shows the evolution of the spectrum at  $(2,3,1-q_1-\xi)$ , with  $\xi = 0.12$ , as a function of temperature : whereas the upper mode frequency hardens upon cooling, as expected for an amplitude mode, the lower mode remains essentially unchanged both in frequency and strength.

**4. Conclusion.**— While the dynamics of incommensurate phase transitions is rather well understood above  $T_i$ , many questions remain open regarding the nature and observability of the soft excitations below  $T_i$ . One of the important unsolved questions concerns the role of defects and the way in which they affect the phase coherence of the incommensurate wave. By analogy with the Heisenberg ferromagnet<sup>(23)</sup>, where long-wavelength magnons are found to be most affected by the lack of long range order above the Curie point, we expect long-wavelength phasons to be the most sensitive to the lack of long-range phase coherence

#### References

1. W.L. McMillan, Phys. Rev. B **14**, 1496 (1976); P. Bak and V.J. Emery, Phys. Rev. Lett. **36**, 978 (1976).
2. A.D. Bruce, R.A. Cowley and A.F. Murray, J. Phys. C. **11**, 3591 (1978).
3. M. Iizumi, J.D. Axe, G. Shirane and K. Shimaoka, Phys. Rev. B **15**, 4392 (1977).
4. M. Iizumi and K. Gesi, Solid State Comm. **22**, 37 (1977).
5. H. Cailleau, F. Moussa and J. Mons, Solid State Comm. **31**, 521 (1979).
6. Y. Yamada, I. Shibuya and S. Hoshino, J. Phys. Soc. Japan, **18**, 1594 (1963).
7. M.M. Elcombe and J.C. Taylor, Acta Cryst. A **24**, 410 (1968); F. Denoyer, A.H. Moudden, R. Currat, C. Vettier, A. Bellamy and M. Lambert, to be published in Phys. Rev.
8. A.P. Levanyuk and D.G. Sannikov, Fiz. Tverd. Tela **18**, 1927 (1976).
9. V. Heine and J.D.C. McConnell, Phys. Rev. Lett. **46**, 1092 (1981).
10. M.S. Haque and J.R. Hardy, Phys. Rev. B **21**, 245 (1980).
11. D. Durand, F. Denoyer, M. Lambert, L. Bernard and R. Currat, to be published.
12. Y. Yamada and T. Yamada, J. Phys. Soc. Japan, **21**, 2167 (1966).
13. B.I. Halperin and C.M. Varma, Phys. Rev. B **14**, 4030 (1976).
14. Y. Imry and S. Ma, Phys. Rev. Lett. **35**, 1399 (1975).
15. P.A. Lee, T.M. Rice and P.W. Anderson, Solid State Comm. **14**, 703 (1974).

16. A.D. Bruce and R.A. Cowley, J. Phys. C. 11, 3609 (1978).
17. H. Poulet and R.M. Pick, J. Phys. C. 14, 2675 (1981).
18. K.B. Lyons, T.J. Negran and H.J. Guggenheim, J. Phys. C. 13, L415 (1980).
19. D. J. Lockwood, A.F. Murray and N.L. Rowell, J. Phys. C. 14, 753 (1981).
20. H. Cailleau, F. Moussa, C.M.E. Zeyen and J. Bouillot, Solid State Comm. 33, 407 (1980); and this conference.
21. L. Bernard, R. Currat, P. Delamoye, C.M.E. Zeyen, S. Hubert and R. de Kouchkovsky, to be published.
22. S. Hubert, P. Delamoye, S. Lefrant, M. Lepostollec and M. Hussonnois, J. of Solid State Chem. 36, 2150 (1981).
23. J.W. Lynn, Phys. Rev. B 11, 2624 (1975).

## ARE PHASONS IN BIPHENYL DETECTABLE BY LIGHT SCATTERING ?

H. Poulet and R.M. Pick

Département de Recherches Physiques, Laboratoire associé au C.N.R.S. n°71,  
Université P. et M. Curie, 75000 Paris, France

**Abstract.**— Phenomenological Raman tensors for phasons and amplitons in the incommensurate phases of biphenyl are derived. The former are shown to be negligibly small when compared to the normal ampliton.

1. Introduction.— Biphenyl crystallizes in the  $P2_1/a$  space group. At  $T_i = 38$  K, a displacive second order phase transition leads to an incommensurate structure (Phase II), characterized by a distortion with wave vectors  $\pm \underline{q}_1 = \pm \frac{1}{2} [ \underline{b}^* (1 - \delta^b) + \underline{a}^* \delta^a ]$  and/or  $\pm \underline{q}_2 = \pm \underline{q}_1 \mp \underline{a}^* \delta^a$ . The distortion along  $\underline{a}^*$  locks in (Phase III) at 21 K, but that along  $\underline{b}^*$  never does. An acoustic-like phason has been detected in phases II and III by neutron scattering<sup>1</sup> but only the corresponding ampliton(s) have been seen by light scattering, even far below  $T_i$ . We shall show that this negative result for the phason<sup>2</sup> is predictable from intensity considerations.

2. Light scattering in displacive incommensurate phases (summary). — The theory of light scattering by amplitons and phasons has been recently developed<sup>3</sup> for the case when the star of  $\underline{q}_0$ , the static modulation wave vector, contains only  $\pm \underline{q}_0$ . The basic idea is that 1<sup>st</sup> order Raman scattering in the incommensurate phase can be viewed as the continuation of a high temperature 2<sup>nd</sup> order process involving the two soft phonons at  $\underline{q}_0$  and  $-\underline{q}_0$ , one of them becoming, below  $T_i$ , the static distortion (with amplitude  $\eta$ ). The starting point is thus the corresponding Raman tensor  $R_{jj}^{\alpha\beta}(\underline{k})$  where  $j$  labels the soft phonon, with normal coordinate  $Q_k^j$ , in the vicinity of  $\pm \underline{q}_0$ . Taking into account the symmetry properties of the ampliton and phason eigenvectors, as well as the temperature variation of the frequency of those excitations, the light scattering intensities turn out to be proportional to  $|R_{jj}^{\alpha\beta}(\underline{q}_0)|^2$  for the ampliton, and  $\left[ \eta \left| \frac{\partial R_{jj}^{\alpha\beta}(\underline{q})}{\partial q^\gamma} \right|_{\underline{q}_0} q^\gamma \right]^2$

for a phason propagating along  $\hat{q}$ ; the symmetry of the preceding tensors are those of second and third rank tensors in the group of  $\underline{q}_0$ .

3. Application to biphenyl. - The preceding theory directly applies to phase III. One must extend it, in phase II, because the star of  $\underline{q}_0$  contains four vectors. One starts from

$$F = \omega_0^2 (|Q_{\underline{q}_1}^j|^2 + |Q_{\underline{q}_2}^j|^2) + \frac{\beta}{4} (|Q_{\underline{q}_1}^j|^4 + |Q_{\underline{q}_2}^j|^4) + \gamma |Q_{\underline{q}_1}^j|^2 |Q_{\underline{q}_2}^j|^2$$

with  $\omega_0^2 = \bar{\omega}^2(T - T_i)$ . For  $T < T_i$ , two different phases are possible (cf. Table). Extending  $F$  in the vicinity of  $\pm \underline{q}_1$  and  $\pm \underline{q}_2$ , one obtains the dynamics of the four lowest frequency excitations:

- if  $4\gamma^2 > \beta^2$ , the distortion involves only  $\underline{q}_1$  (or  $\underline{q}_2$ ); one phason and one ampliton are 1<sup>st</sup> order Raman active, while two degenerate modes, localized around  $\underline{q}_2$  (or  $\underline{q}_1$ ) are only 2<sup>nd</sup> order Raman active.

- if  $4\gamma^2 < \beta^2$ , the distortion involves  $\underline{q}_1$  and  $\underline{q}_2$ ; it exists two uncoupled phasons and two coupled amplitons (cf. Table). The uncoupled phason and ampliton Raman tensors are the same as above, but they involve now  $\underline{q}_1$  and  $\underline{q}_2$ , and, when  $4\gamma^2 < \beta^2$ , the coupling between the amplitons must be dealt with. As  $\underline{q}_1$  and  $\underline{q}_2$  are in the vicinity of  $\underline{b}^*/2$ , one may expand these tensors in series of  $\underline{\delta}$  and take into account the  $C_{2h}$  symmetry of  $\underline{b}^*/2$ .

The final results appear in the table.<sup>4</sup> For both phases, the phason tensors are proportional to some cartesian coordinate of  $\underline{\delta}$  (expressed in reduced units) as well as to  $\eta$ : this leads to integrated intensities typically smaller by a  $\delta^2$  factor than that of the normal ampliton, while  $\delta^\alpha < 0.08$ . This factor becomes  $\delta^4$  when comparing, for  $4\gamma^2 < \beta^2$ , the two amplitons.


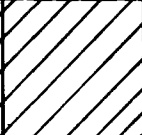
	$\underline{q}_1$	$\underline{q}_2$	Eigenvectors and Raman tensors			
$\gamma^2 > \frac{\beta^2}{4}$	$\eta$	0	$A_{\underline{q}_1}$ $R_{jj}^{\alpha\beta}$	$\varphi_{\underline{q}_1}$ $\eta B^{\alpha\beta\gamma\epsilon} \hat{q}^\gamma \delta^\epsilon$	$Q_{\underline{q}_2}^j$ $\blacktriangle$	$Q_{-\underline{q}_2}^j$ $\blacktriangle$
$\gamma^2 < \frac{\beta^2}{4}$	$\eta$	$\eta$	$\frac{1}{\sqrt{2}}[A_{\underline{q}_1} + A_{\underline{q}_2}]$ $R_{jj}^{\alpha\beta}$	$\frac{1}{\sqrt{2}}[A_{\underline{q}_1} - A_{\underline{q}_2}]$ $B^{\alpha\beta ab} \delta^a \delta^b$	$\varphi_{\underline{q}_1}$ $\eta B^{\alpha\beta\gamma\epsilon}$	$\varphi_{\underline{q}_2}$ $\hat{q}^\gamma \delta^\epsilon$
			$A_{\underline{q}_0}$ $R_{jj}^{\alpha\beta}$	$\varphi_{\underline{q}_0}$ $\eta B^{\alpha\beta\gamma\epsilon} \hat{q}^\gamma \delta^\epsilon$		

Table. - Phases II and III low frequency excitations. First two columns: static distortion amplitudes in phase II for  $q_1$  and  $q_2$ . Last four columns: eigenvector for each excitation (above) and corresponding Raman tensor (below). The same results for the phase III excitations appear in the lower part of the table.

$$\text{Here } \left\{ \begin{matrix} A_{q_i} \\ \varphi_{q_i} \end{matrix} \right\} \equiv \frac{1}{\sqrt{2}} [Q_{q_i}^j + Q_{-q_i}^j] ; B^{\alpha\beta\gamma\epsilon} \equiv \left| \frac{\partial R_{jj}^{\alpha\beta}}{\partial q^\gamma \partial q^\epsilon} \right|_{q_0} ;$$

$\Delta$  indicates no 1st order Raman scattering. Each tensor belongs to the unity representation of the  $C_{2h}$  point group.

#### References.

1. Cailleau H. *et al.*, Sol. State Commun. **33** (1980) 407.
2. Ecolivet Cl. Thesis (Rennes 1981) *unpublished*.
3. Poulet H. and Pick R.M., J. Phys. C: Solid State Phys. **14** (1981) 2675.
4. For simplicity, the tensors are not all written in the same units. This is taken into account when comparing the various intensities.

## DYNAMICS OF INCOMMENSURATE PHASES IN BIPHENYL

H. Cailleau, F. Moussa\*, C.M.E. Zeyen\*\* and J. Bouillot\*\*

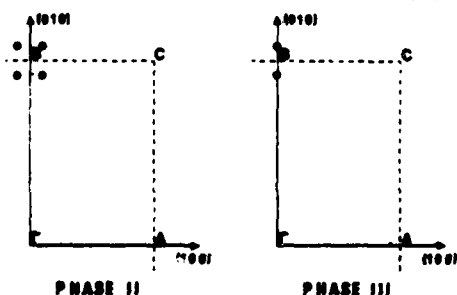
*Groupe de Physique Cristalline, E.R.A. au C.N.R.S. n°070015, Université de Rennes, Campus de Beaulieu, 35042 Rennes Cedex, France**\*Laboratoire Léon Brillouin, C.E.N. Saclay, 91191 Gif sur Yvette Cedex, France**\*\*Institut Max Von Laue-Paul Langevin, B.P. 156 X, 38042 Grenoble Cedex, France*

**Abstract** An excitati presenting the characteristics of a phason has been observed in the incommensurate phases of biphenyl using a cold source triple-axis neutron spectrometer.

Dynamics of incommensurate phases are expected to display a number of novel features. As a consequence of the continuous broken phase symmetry new hydrodynamic-like excitations appear, the phase modes or phasons, with a vanishing frequency in the long-wavelength limit. In this paper we report upon the observation by inelastic neutron scattering of excitations in the incommensurate phases of biphenyl which exhibit all the characteristics of a phason.

Biphenyl undergoes a displacive structural phase transition due to a molecular conformation instability with respect to a torsional angle between the planes of the phenyl rings <sup>[1,2]</sup>. In the high temperature phase, the soft mode is located around the B (0,1/2,0) zone boundary point. The space group  $P2_1/a$  is non-symmorphic and at the B point the Lifshitz condition is not satisfied : two torsional modes which are degenerate at the zone boundary come in with opposite but finite slopes <sup>[1,3]</sup>. On the lower soft phonon branch the minimum is away from the B point. In fact, two low temperature incommensurate phases are observed in biphenyl <sup>[4]</sup>. In phase II, which exists between  $T_{II} = 21$  K and  $T_I = 38$  K (deuterated sample), the wave vectors characterizing the incommensurate modulation are  $\vec{q}_s = \pm \delta_a \vec{a}^* \pm 1/2(1-\delta_b) \vec{b}^*$  (fig.1) ; no higher-order satellites could be observed in this phase. At  $T_{II}$ , a partial lock-in phase transition in the  $\vec{a}^*$  direction takes place and below  $T_{II}$  the satellite location becomes  $\vec{q}_s = \pm 1/2(1-\delta_b) \vec{b}^*$  (fig.1) ; in this phase III, we have been able to measure higher-order satellites up to third-order <sup>[2]</sup>. The variations of  $\delta_a$  and  $\delta_b$  with temperature

are small ;  $\delta_a$  lies between 0.04 and 0.05 (phase II) and is zero below  $T_{II}$ , while  $\delta_b$  falls in the range 0.07-0.085 (phases II and III). Unlike many other insulating materials, the biphenyl incommensurate modulation subsists at least down to 1.6 K. This

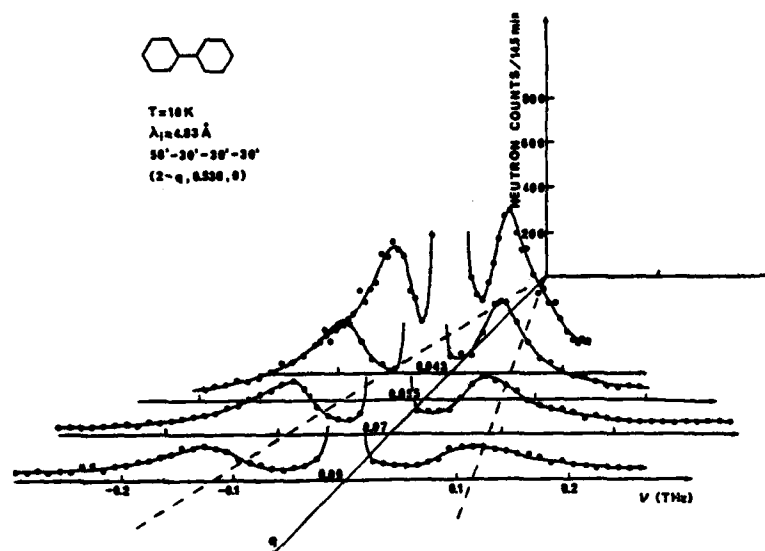


**Fig. 1** Location of satellite reflections in the incommensurate phases of biphenyl.

static behaviour is in agreement with the anisotropic shape of the soft mode dispersion surface : the minimum is well pronounced in the  $\vec{b}^*$  direction while in the  $\vec{a}^*$  direction the dispersion curve is flat <sup>[1,2]</sup>. It is also interesting to notice that the soft mode becomes overdamped only close to the transition temperature.

The study of the dynamics of the incommensurate phases was performed on the triple-axis spectrometer IN 12 installed at the cold source of the ILL.

We have observed low-energy excitations in phases II and III <sup>[5]</sup>. Figure 2 shows energy-scans for different reduced wave vectors  $\vec{q}$  along the  $\vec{a}^*$  direction, near a satellite reflection at 10 K. The inelastic peaks are well measured both for neutron





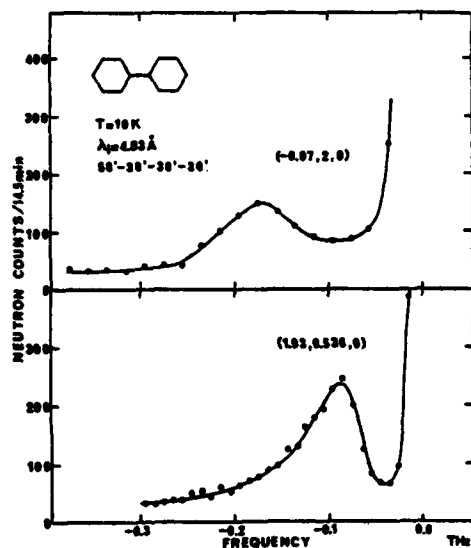


Fig. 3 Inelastic peaks near a satellite reflection (below) and a main Bragg reflection (above).

The experimental energy range limited by the use of cold neutrons did not allow us to observe the amplitude mode which frequency should be higher according to the Raman scattering results [7].

One reason explaining our observation of a phason in biphenyl might be the fact that material remains incommensurate even down to 1.6 K. Thus the experiment could be performed at very low temperature where the damping is small. Moreover the system must stay far away from a complete "devil's staircase" regime which can appear on approaching a commensurate lock-in transformation with no phasons at zero frequency [8].

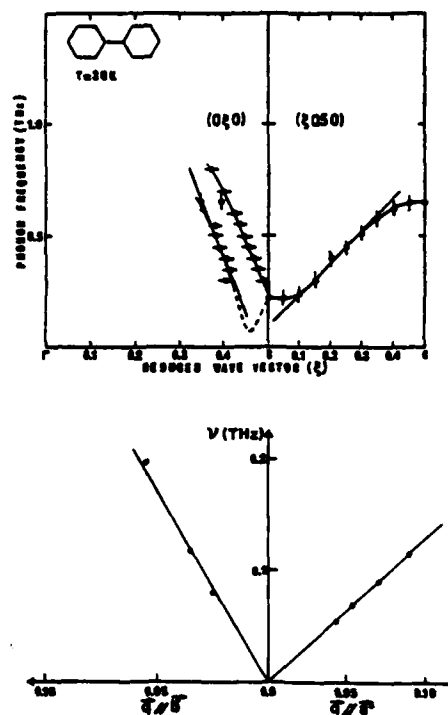


Fig. 4 Dispersion laws for the soft mode at 38 K (above) and the phason at 10 K (below). Both scales are homothetic

1. H. CAILLEAU, J.L. BAUDOUR, J. MEINDEL, A. DWORKIN, F. MOUSSA and C.M.E. ZEYEN, *Far. Disc.* 69, 7 (1980).
2. H. CAILLEAU, Thesis, Univ. Rennes (1981).
3. I. NATKANIEC, A.V. BIELUSHKIN and T. WASIUTYNSKI, *Phys. Stat. Sol.* 105, 413 (1981).
4. H. CAILLEAU, F. MOUSSA and J. MONE, *Solid State Comm.* 31, 521 (1979).
5. H. CAILLEAU, F. MOUSSA, C.M.E. ZEYEN and J. BOUILLLOT, *Solid State Comm.* 33, 407 (1980).
6. C. ECOLIVET, Thesis, Univ. Rennes (1981).
7. M. WADA, A. SANADA and Y. ISHIBASHI, *J. Phys. Soc. Jpn* 50, 3 (1981).
8. S. AUBRY, in "Seminar on the Riemann Problem, Spectral Theory and Complete Integrability", G.D. Chadnovsky ed., Lecture notes in mathematics, Springer-Verlag (1980).

## ON THE MODE SOFTENING IN SnTe AND PbTe

D. Strauch and U. Schröder

*Institut für Theoretische Physik, Universität Regensburg, D-8400 Regensburg, F.R.G.*

**Abstract.**— The softening of the  $T_0(\Gamma)$  mode in SnTe and PbTe with decreasing temperature is analyzed in terms of a shell model with a non-linear polarizability of the Te ion. The simultaneous stiffening of the elastic constants drastically influences the results.

1. **Introduction.**— We have investigated the temperature dependence of the  $T_0(\Gamma)$  mode frequency in the narrow-gap materials SnTe and PbTe. These modes become nearly soft at low temperature.<sup>1,2</sup> This is opposed by the overall stiffening of the elastic constants<sup>3,4</sup> with decreasing temperature. Tracing this different behaviour back to the different quantities involved in the elastic and optical properties one is primarily led to the different kinds of deformations of the electronic distribution.

For example, the phonon dispersion curves in SnTe<sup>5</sup> and PbTe<sup>6</sup> have been analyzed in terms of a shell model. This model involves the dipolar deformability of the ions which (at  $\vec{q} = 0$ ) influences only the optical frequencies but not the elastic constants. To account for a temperature-dependent polarizability in perovskite crystals a non-linear intra-ionic force constant was introduced by Migoni et al.<sup>7</sup> A simplified model has been discussed in Refs. 8 and 9.

Another indication towards a temperature-dependent polarizability stems from the shell-model expressions for the  $L_0$  and  $T_0$  mode frequencies at  $\vec{q} = 0$ ,

$$\mu\omega^2 = [R'_0 - \lambda \frac{4\pi}{3} Z'^2 / (1 - \lambda \frac{4\pi}{3v} \alpha)] e^2 / v, \quad (1)$$

with the reduced mass  $\mu$ , effective force constant  $R'_0$ , effective charge  $Z'$ , electronic polarizability  $\alpha$ , unit-cell volume  $v = 2r_0^3$ , and  $\lambda = 1$  or  $-2$  for the  $T_0$  and  $L_0$  frequency, respectively. With numbers for PbTe taken from Ref. 6 one finds  $R'_0 = 16.9$ ,  $Z' = 0.59$ ,  $(4\pi/3v)\alpha = 0.91$ , and thus

$$\mu\omega_{L_0}^2 = 16.9 + 1.0 = 17.9, \quad \mu\omega_{T_0}^2 = 16.9 - 15.8 = 1.1 \text{ (in units of } e^2/v \text{)}.$$

Thus PbTe (and similarly SnTe) seems to be close to the (electronic) polarization catastrophe, the connection of which to soft modes was first pointed out by Cochran.<sup>10</sup> The fact that a small variation in  $\alpha$  has a much larger effect on  $\omega_{T_0}$  than on  $\omega_{L_0}$  is in accordance with a relatively weak change of  $\omega_{L_0}$  with temperature in PbTe.<sup>2</sup>

2. **Theory.**— In the present case the contribution from the intra-ionic potential of the Te ion is of the form ( $\alpha = x, y, z$ )

$$V = \frac{1}{2} \sum_{\alpha} k_2 u_{\alpha}^2 + \frac{1}{4!} \sum_{\alpha} k_4 u_{\alpha}^4 + \frac{1}{8} \sum_{\alpha\beta} h_4 u_{\alpha}^2 u_{\beta}^2 \quad (2)$$

where  $\vec{u}$  is the relative shell-core displacement.

To first order in the anharmonicity, one obtains the renormalized force constant

$$k = k_2 + \frac{1}{2} (k_4 + 2h_4) \langle u_{\alpha}^2 \rangle \quad (3)$$

replacing  $k_2$  in the shell-model equations, in particular in  $R_0'$ ,  $Z'$ , and  $\alpha$  in eq. (1). The brackets  $\langle \dots \rangle$  denote the thermal average.

3. Results.— The equations of the shell model and eq. (3) have to be solved self-consistently. From the observed<sup>1,2</sup> values of  $\omega_{T0}$  we have determined  $k$  and  $\langle u_{\alpha}^2 \rangle$  as a function of temperature and have taken their expected linear relationship, eq. (3), as a test of the model. Indeed, most of the data fall on a straight line, see Fig. 1 (curves  $c_{ij} = \text{const}$ ), given by

$$k = 109.4 \left( 1 + \frac{1}{2} (270 \pm 120) \langle u_{\alpha}^2 \rangle / r_0^2 \right) e^2 / v \text{ for SnTe } (T \leq 100 \text{ K}), \quad (4)$$

$$k = 37.9 \left( 1 + \frac{1}{2} (100 \pm 30) \langle u_{\alpha}^2 \rangle / r_0^2 \right) e^2 / v \text{ for PbTe.}$$

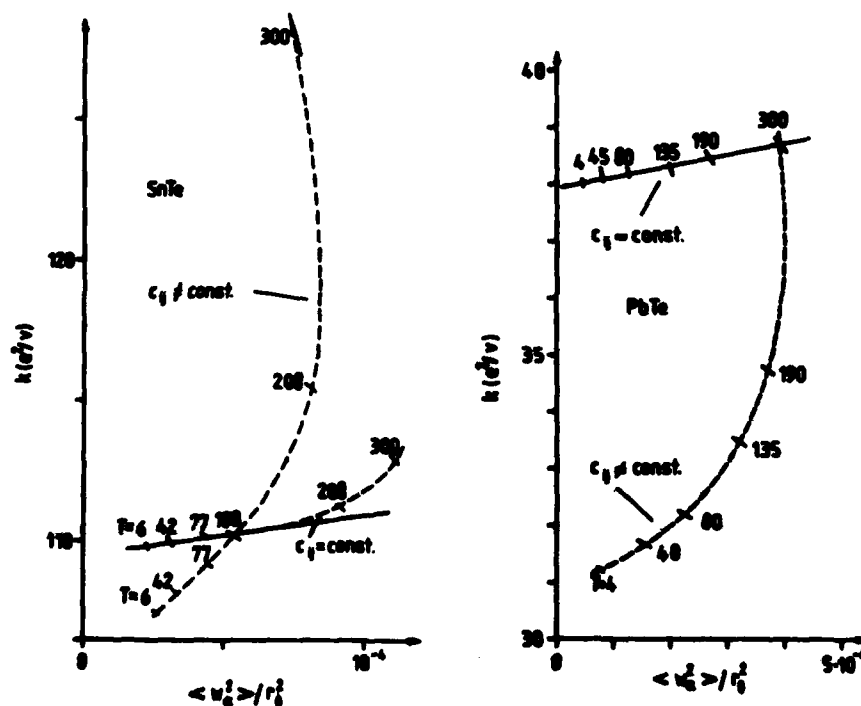


Fig. 1: Test of eq. (3) for SnTe and PbTe with and without taking account of the temperature dependence of the elastic constants  $c_{ij}$ . Straight lines show the fit of the calculated data appearing in eq. (3) by eqs. (4). Dashed lines are guides to the eye. Error bars result from those of  $\omega_{T0}$  as given in Refs. 1 and 2. Temperatures  $T$  are in K.

Since the variation of the intra-ionic force constant  $k$  turns out to be very small it seems necessary to investigate the change of the inter-ionic force constants as obtained from the elastic constants.<sup>3,4</sup> The simple procedure of accordingly changing, for example,  $A(12)$ ,  $B(12)$ , and  $A(11) + A(22)$  (in the notation of Refs. 5 and 6) does not seem to be a step in the right direction: The linear relationship between  $k$  and  $\langle \omega_{\alpha}^2 \rangle$  is largely lost, see Fig. 1 (curves  $c_{ij} \neq \text{const}$ ), and the temperature variation<sup>2</sup> of  $\omega_{T0}$  for  $\vec{q} = 0.1(1,1,1)\pi/a$  has the wrong sign. Changing another reasonable set of parameters leads to similar conclusions.

4. Discussion.— It seems that a very small non-linearity in the Te polarizability is able to describe the TO mode softening in SnTe and PbTe but that there is at present no model to consistently account for the temperature dependence of the optical and acoustical modes. Right now we can only speculate about ways out of the dilemma:

(a) The approximation given by eq. (3) may be insufficient. In the next order decay processes are added which render the self-energy depending on temperature and frequency; they complicate matters in that they lead to a non-local  $k$ . Possibly the potential (2) has to be augmented by higher-order terms. (b) The elastic constants and their temperature dependence may be at least partially due to deformabilities not contained in the shell model used.<sup>5,6</sup> (c) A microscopic treatment, when interpreted in shell-model terms, may lead to temperature-dependent charges.

Acknowledgements.— We are grateful to W.Kress for supplying us with the shell-model program.

#### References

- 1 G.S.Pawley, W.Cochran, R.A.Cowley, and G.Dolling, Phys.Rev.Letters **17**, 753 (1966).
- 2 H.A.Alperin, S.J.Pickart, J.J.Rhyne, and V.J.Minkiewicz, Phys.Letters **40A**, 295 (1972).
- 3 A.G.Beattie, J.Appl.Phys. **40**, 4818 (1969).
- 4 B.Houston, R.E.Strakna, and H.S.Belson, J.Appl.Phys. **39**, 3913 (1968).
- 5 E.R.Cowley, J.K.Darby, and G.S.Pawley, J.Phys.C (Solid State Phys.) **2**, 1916 (1969).
- 6 W.Cochran, R.A.Cowley, G.Dolling, and R.M.Elcombe, Proc.Roy.Soc. **A293**, 433 (1966).
- 7 R.Migoni, H.Bilz, and D.Bäuerle, Phys.Rev.Letters **37**, 1155 (1976); in: Lattice Dynamics, M.Balkanski, ed., Flammarion, Paris, 1978, p. 650.
- 8 H.Bilz, A.Bussmann, G.Benedek, H.Böttner, and D.Strauch, Ferroelectrics **25**, 339 (1980).
- 9 A.Bussmann-Holder, H.Bilz, and W.Kress, J.Phys.Soc.Japan **49** Suppl.A, 737 (1980).
- 10 W.Cochran, Phys.Rev.Letters **3**, 412 (1959); Adv.Phys. **9**, 387 (1960).

PRESSURE DEPENDENCE OF THE COUPLED OPTIC AND ACOUSTIC MODES NEAR THE FERROELASTIC TRANSITIONS OF  $\text{LaP}_5\text{O}_{14}$ 

G. Errandonea

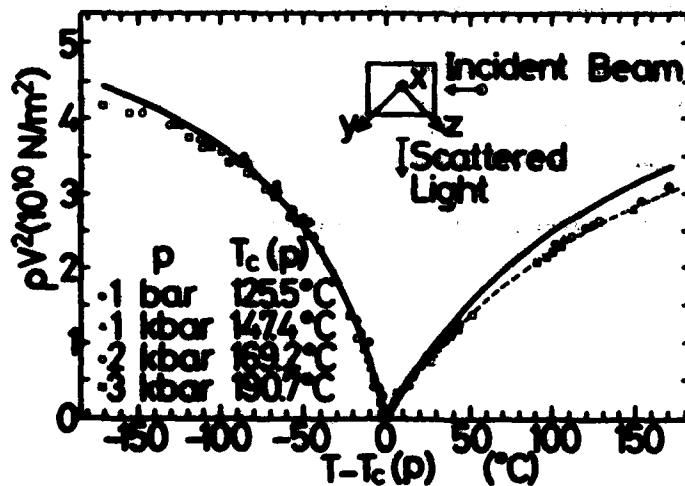
C.N.E.T., 196 rue de Paris, 92220 Bagneux, France

**Abstract.**— We report a thorough Raman and Brillouin scattering study, under high hydrostatic pressure, of the coupled soft-optic-acoustic modes of ferroelastic  $\text{LaP}_5\text{O}_{14}$  in order to clarify the unusual positive pressure dependence of the transition temperature :  $dT_c/dp = + 21.75 \pm 0.25^\circ\text{C/kbar}$ .

Lanthanum pentaphosphate undergoes a second order ferroelastic transition ( $\text{mmm} \rightarrow 2/m$ ), at  $T_c = 125^\circ\text{C}$  at atmospheric pressure, with no change of the translation symmetry. This "proper" transition is driven by a soft zone center optic mode which is linearly and strongly coupled to a soft acoustic mode <sup>1,2,3</sup>. The influence of a hydrostatic pressure on this coupled modes system has been investigated using Raman (0-2 kbar, 20-200°C) and Brillouin (0-3 kbar, 20-300°C) scattering experiments. More detailed informations are given in references 4 and 5.

The temperature and pressure dependences of the squared velocity  $v$  and frequency  $\omega$  of the respective soft acoustic and optic modes are plotted on figures 1 and 2.

The main effect of the pressure is to shift upward the transition temperature  $T_c$  which can be determined with an accuracy of  $\pm 0.5$  K or  $\pm 0.4$  K from respective Raman and Brillouin measurements. On fig.3, we



**Fig.1 :** Temperature and pressure dependences of  $pv^2$  of the soft acoustic mode. Dashed line : fit of the formula (1) with  $A = 3.62 \cdot 10^8 \text{ Nm}^{-2} \text{ K}^{-1}$  and  $g = 0.0062 \text{ K}^{-1}$ . Continuous line : fit of the phenomenological model of reference 3.

TABLE I. : Values<sup>9</sup> of the coefficients of formulas (1) and (2) used to fit Raman and Brillouin measurements.

(kbar)	Raman data			Brillouin data			$\frac{a-g\omega_0^2}{(\text{cm}^{-2}\text{K}^{-1})}$
	(°C)	( $\text{cm}^{-1}$ )	( $\text{cm}^{-2}\text{K}^{-1}$ )	(°C)	( $10^8 \text{Nm}^{-2}\text{K}^{-1}$ )	( $10^8 \text{K}^{-1}$ )	
0	125.6±.5	19.7 ±.2	2.41±.12	125.5±.4	3.69±.15	63±8	2.38±.30
1	147.8±.5	19.75±.2	2.36±.16	147.4±.4	3.67±.13	62±8	2.43±.35
2	169.2±.5	19.8 ±.2	2.39±.22	169.2±.4	3.57±.08	58±6	2.26±.29
3	—	—	—	190.7±.4	3.55±.10	60±6	2.38±.30

can see that  $T_c$  linearly increases with the pressure with a slope :

$$dT_c/dp = 21.75 \pm 0.25 \text{ K/kbar}.$$

This value is significantly smaller than the one obtained by Asaumi<sup>6</sup> on  $\text{NdP}_5\text{O}_{14}$  ( $dT_c/dp \sim 38 \text{ K/kbar}$ ) with a less accurate high pressure technique but it is close to the partial Raman measurements performed by Peercy<sup>7</sup> on  $\text{La}_{0.5}\text{Nd}_{0.5}\text{P}_5\text{O}_{14}$  ( $dT_c/dp \sim 18 \text{ K/kbar}$ ). It also agrees with the thermodynamic Ehrenfest formula which leads to  $dT_c/dp = 18.9 \text{ K/kbar}$  using the Landau free energy of the transition whose coefficients are numerically known<sup>3</sup>.

This phenomenological model<sup>3</sup> provides also an interpretation of our experimental data. In particular  $v$  and  $\omega$ , in the prototype phase, are given by :

$$\rho v^2 = C_{55} = A(T - T_c(p)) / [1 + g(T - T_c(p))] \quad (1)$$

$$\text{and} \quad \omega^2 = \omega_0^2 + a(T - T_c(p)) \quad (2) \quad \text{with } g = a/\omega_0^2 \quad (3)$$

Our measurements have been fitted to these formulas with the coefficients given in table I. They appear to be pressure independent or very slightly so.

As noticed by Samara<sup>8</sup>, the positive sign of  $dT_c/dp$  is exceptional for a transition driven by a soft zone center optic mode.

A decomposition<sup>8</sup> of  $\omega^2$  between a temperature independent harmonic

FIG.2 : Temperature and pressure dependences of the soft optic mode squared frequency

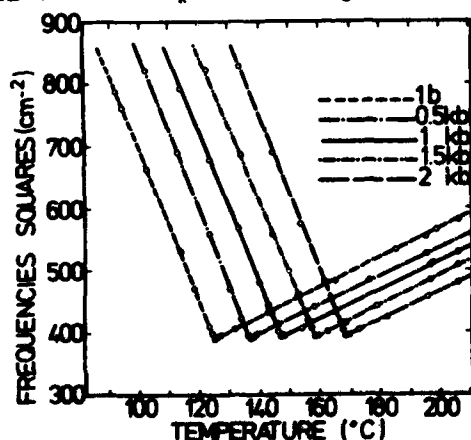
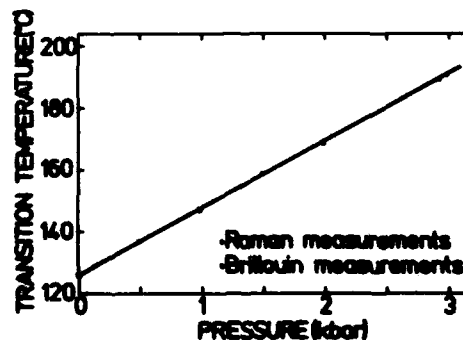


FIG.3 : Pressure dependence of the transition temperature leading to  $dT_c/dp = +21.75 \pm 0.25 \text{ K/kbar}$



contribution and an anharmonic one shows <sup>4</sup> that the transition temperature is given by :  $T_c = (\omega_o^2 - \omega_h^2)/a$  (4)

The negligible pressure dependence of  $\omega_o$  rules out the role of the strong coupling between the soft optic mode and the ferroelastic shear as a possible cause of this unusual behaviour.

Writing  $\omega_h^2$  as the difference between positive short range interactions and negative long range ones <sup>8</sup>, leads <sup>4</sup> in the most favourable case to  $dT_c/dp \sim +1$  K/kbar, an order of magnitude smaller than the experimental value.

By contrast, a decrease of only 4.5 %/kbar of the a coefficient in formula (2) is needed to induce the required shift. Though our experimental data did not detect any change of a, such a decrease could be consistent with our experimental uncertainties. Accurate measurements performed at higher pressures are needed to confirm this possibility.

#### REFERENCES

1. J.F. Scott, Ferroelectrics, **20**, 69 (1978)
2. G. Errandonea, J. Sapriel, Solid State Comm. **29**, 601 (1979)
3. G. Errandonea, Phys. Rev. **B21**, 5221 (1980)
4. G. Errandonea, H. Savary, Phys. Rev. **B24**, (1er Août 1981)
5. G. Errandonea, H. Savary, Proceedings of IMP5, (State College 1981) to be published in Ferroelectrics.
6. K. Asaumi, S. Kojima, T. Nakamura, J. Phys. Soc. Jpn. **48**, 1298 (1980)
7. P.S. Peercy, Proceedings of the High Pressure and Low Temperature Physics Conference (Plenum, New York, 1978) p. 279
8. G.A. Samara, Comments Solid State Phys. **8**, 13 (1977)
9. The uncertainties correspond to a significant departure of the fit to the experimental data.

## LATTICE INSTABILITIES AND PHASE TRANSITIONS IN FLUORIDE PEROVSKITES

R. Geick, H. Rauh, N. Lehner\*, J. Bouillot\*, W.G. Stirling\* and G. Heger\*\*

*Physik. Institut Universität Würzburg, Roentgenring 8, D-8700 Würzburg, F.R.G.*

\*ILL, F-38042 Grenoble, France

\*\*IAKI, Kernforschungszentrum, D-7500 Karlsruhe, F.R.G.

Abstract

One of the main differences in the physical behavior between  $\text{KMnF}_3$  and  $\text{KZnF}_3$  is that the former shows structural phase transitions while the latter does not. We have measured the phonon dispersion of both materials by means of inelastic neutron scattering at room temperature. In addition, we have found an anomalous temperature dependence of the  $R_{15}$  and  $M_2$  modes in  $\text{KZnF}_3$ , which are the modes softening in the phase transition of  $\text{KMnF}_3$ . This result indicates that there is a tendency towards a phase transition in all fluoride perovskites and favours the model of the displacive character of this phase transition.

We have measured the phonon dispersion of the fluoride perovskites  $\text{KMnF}_3$  and  $\text{KZnF}_3$  by means of inelastic neutron scattering at ILL, Grenoble, France and at Kernforschungszentrum Karlsruhe, FRG, at room temperature. Our results are shown in Fig. 1.

The experimental data are analyzed and completed by lattice dynamical shell model calculations. Our model was originally developed by Cowley /1/ and Stirling /2/. The number of adjustable parameters could be reduced to 6 by

1. keeping the ionic charges fixed to  $\pm e$ ,  $+2e$ , respectively;
2. making use of the electronic polarizabilities given by Tessmann et al. /3/;
3. calculating the force constants of the short range interaction between  $\text{K}^+ - \text{F}^-$  and  $\text{F}^- - \text{F}^-$  by means of interionic potentials /4,5,6/.

We would like to point out that a good fit could be obtained with physically reasonable values for all fitting parameters:

	short range force constant (N/m)						shell charge (e)			shell-core force constant (N/m)		
	K-F		Me-F		F-F		K	Me	F	K	Me	F
	$A_1$	$B_1$	$A_2$	$B_2$	$A_3$	$B_3$						
$\text{KMnF}_3$	12.15	-1.12	163.3	-22.3	0.12	0.23	-4.88	-4.62	-2.38	4520	33500	1640
$\text{KZnF}_3$	17.09	-1.64	181.1	-23.8	2.41	0.20	-4.89	-2.51	-2.43	4540	10690	1670

Measuring the phonon dispersion of  $\text{KMnF}_3$  and  $\text{KZnF}_3$ , we have provided an experimental basis for further theoretical considerations concerning anharmonic effects. In this context, theoretical work on phase transitions is of special interest, for example the contribution of hard and soft phonon modes to the Raman cross section of Raman active hard modes which have been used to study precursor order in  $\text{KMnF}_3$  /11/.



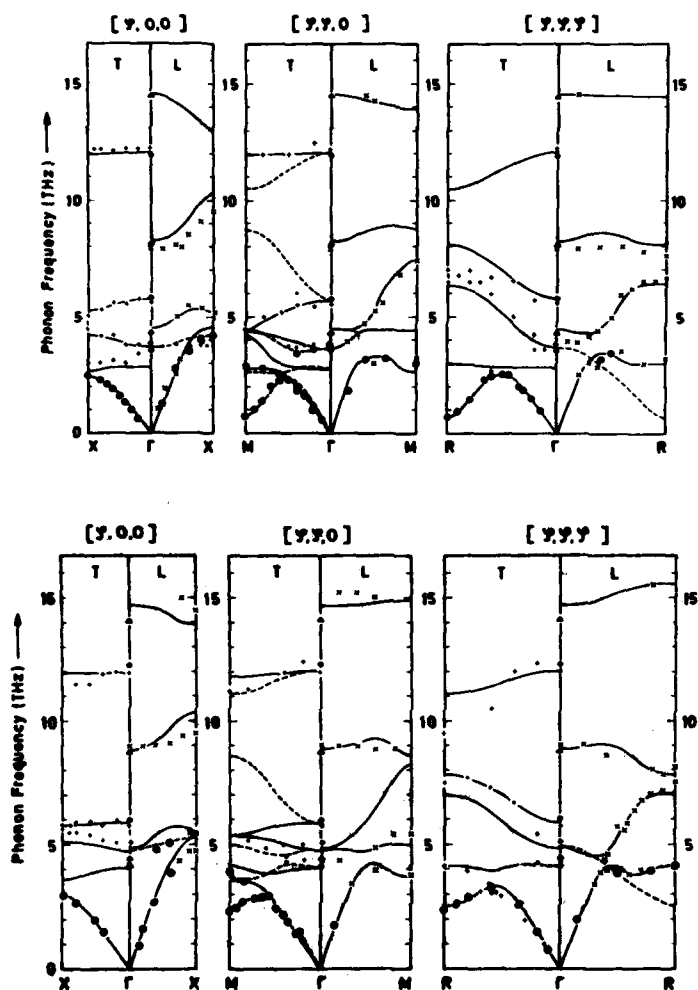


Fig. 1: Phonon dispersion of  $\text{KMnF}_3$  (upper part) and  $\text{KZnF}_3$  (lower part) for the main symmetry directions  $[0,0,0]$ ,  $[0,0,1]$  and  $[0,1,1]$ . The symbols +, x represent experimental data gained by inelastic neutron scattering. For the sake of completeness we have also drawn the low energy phonons measured by other groups [7,8], and, at  $\Gamma$ , the phonon frequencies obtained by FIR spectroscopy (L:  $\Delta$ , T:  $\diamond$ ) [9,10]. The solid and broken lines distinguish between phonon dispersion curves of different symmetry, as calculated with our shell model.

As it is well known, the  $R_{25}$  and  $M_2$  modes are the ones which show an anomalous temperature dependence and become soft at the phase transition temperature in  $\text{KMnF}_3$ . Studying the same modes in  $\text{KZnF}_3$ , where no structural phase transition is observed, we have found a similar anomalous temperature dependence (cf. Fig. 2) like in  $\text{KMnF}_3$ . The essential difference between  $\text{KMnF}_3$  and  $\text{KZnF}_3$  is not qualitative, but quantitative, namely the anomalous temperature dependence in  $\text{KMnF}_3$  is so strong that the frequency

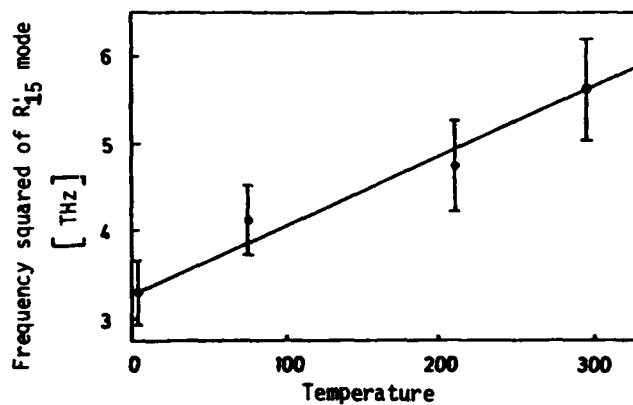


Fig. 2: Temperature dependence of the squared frequency of the  $R'_{15}$  mode in  $KZnF_3$ .

of the  $R'_{15}$  mode approaches zero at the phase transition temperature, while it would approach zero for  $T < 0$  in  $KZnF_3$ . This shows that there seems to be a tendency towards an instability against octahedra rotations in all fluoride perovskites regardless whether they undergo a phase transition or not. This result confirms the displacive character of the phase transition.

#### References

- /1/ R.A. Cowley, Phys.Rev. 134, A 981 (1964)
- /2/ W.G. Stirling, J.Phys.C 5, 2711 (1972)
- /3/ J.R. Tessmann, A.H. Kahn, and W. Shockley, Phys.Rev. 92, 890 (1953)
- /4/ M.J.L. Sangster and R.M. Atwood, J.Phys. C 11, 1541 (1978)
- /5/ C.R.A. Catlow, K.M. Diller, and M.J. Norgett, J.Phys. C 10, 1395 (1977)
- /6/ C.R.A. Catlow, M.J. Norgett, and I.A. Ross, J. Phys. C 10, 1627 (1977)
- /7/ K. Gesi, J.D. Axe, G. Shirane, and A. Linz, Phys.Rev. 85, 1933 (1972)
- /8/ M. Rousseau, J.Y. Gesland, B. Hennion, G. Heger, and B. Renker, Sol. State Comm.: to appear (1981)
- /9/ C.H. Perry and E.F. Young, J.Appl.Phys. 38, 4616 (1967)
- /10/ J.D. Axe and G.D. Petit, Phys.Rev. 157, 453 (1967)
- /11/ A.D. Bruce, W. Taylor, and A.F. Murray, J.Phys.C 13, 483 (1980)

LOCK-IN TYPE PHASE TRANSITION IN  $\text{KFeF}_4$ 

A. Maciel and J.F. Ryan

*Clarendon Laboratory, University of Oxford, Oxford, U.K.*

**Abstract.** - The Raman spectrum of  $\text{KFeF}_4$  reveals a low frequency phonon which softens as the temperature is raised towards a phase transition near 390K. Whereas the softening is incomplete the intensity decreases continuously but rapidly near  $T_c$  and the mode is not observed at higher temperatures. A symmetry analysis shows that it may be a lock-in type transition.

$\text{KFeF}_4$  has a layer structure composed of sheets of corner-sharing  $\text{FeF}_6^-$  octahedra separated by  $\text{K}^+$ . The structure is related to the tetragonal  $\text{TlAlF}_4$  structure but differs from it in that the stacking order along  $c$  shows alternate layers displaced relatively by  $b/2$ . These structures are of great interest from a dynamics point of view because of their intrinsic instability against librational modes of the  $\text{FeF}_6^-$  octahedra. For example,  $\text{CsFeF}_4$  shows a series of cell-doubling phase transitions involving staggered rotations of the  $\text{FeF}_6^-$  groups<sup>(1)</sup>. Heger et al<sup>(2)</sup> have found that at ambient temperatures the octahedra in  $\text{KFeF}_4$  are not fully aligned but are tilted about  $b$  to give the orthorhombic  $D_{2h}^{17}$  (Amma) structure shown in Figure 1. Recently, Hidaka et al<sup>(3)</sup> found an additional superlattice caused by rotations of the octahedra about  $a$  and staggered along  $b$ ; this structure is no longer centred and the space group  $D_{2h}^{13}$  (Pmmn) was proposed. A second-order transition between these two phases was reported to occur at  $T_c = 368\text{K}$ <sup>(3)</sup>. In this paper we present Raman scattering evidence for this transition and discuss a classical Landau model which shows that the transition is an example of a lock-in type between phases which would otherwise be separated by an incommensurate phase.

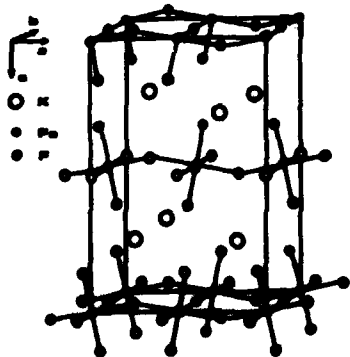


Fig. 1: High-temperature structure of  $\text{KFeF}_4$ .

Raman spectra were obtained from small flux-grown samples over a range of temperatures up to 500K, above which surface degradation occurred. At room temperature the spectrum is found to be considerably more complex than that expected from the  $D_{2h}^{17}$  structure, but the data are insufficient to test the  $D_{2h}^{13}$  proposal. Very intense features at  $210\text{cm}^{-1}$  and  $220\text{cm}^{-1}$  can be assigned to uniform librational modes of the  $\text{FeF}_6^-$  groups about the  $b$  and  $a$  axes respectively. At lower energies we observe the spectrum shown in Figure 2. The

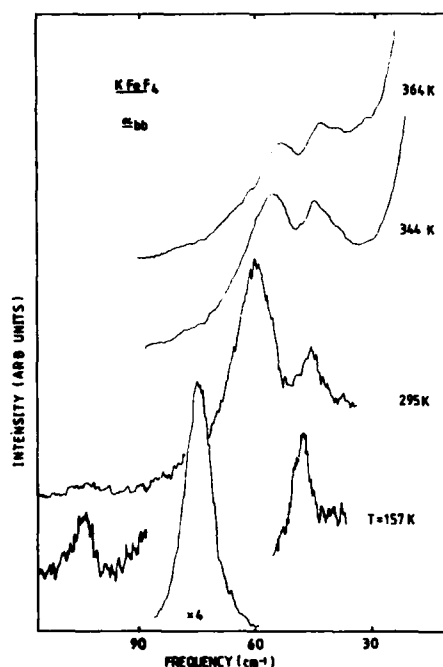


Fig. 2: Temperature dependence of the  $\alpha_{bb}$  spectrum of  $\text{KFeF}_4$ .

transition where we are unable to resolve the modes clearly.

The change of symmetry which occurs at  $T_c$  is consistent with a phonon instability at the critical wavevector  $\underline{k}_c = (\frac{1}{2}, \frac{1}{2}, 0)$ . The star of this vector has two components,  $\pm \underline{k}_c$ , and the order parameter has two components:  $Q_1 = Q_2^* = (A/\sqrt{2})\exp i\phi$  where  $A$  represents the amplitude and  $\phi$  the phase of the structural modulation. The thermodynamic free energy for this system can be expressed in terms of  $A$  and  $\phi$  as:

$$G = G_0 + \frac{1}{2}a(T-T_c)A^2 + uA^4 + vA^4(\cos 4\phi) \quad (1)$$

where we have included only terms up to fourth order in  $A$ . Applying the usual stability criteria leads to the following set of structures for  $T < T_c$ :

$$\begin{array}{lll} v < 0 & \phi_0 = n\pi/2 & (n = 0, 1, 2, 3) \\ v > 0 & \phi_0 = (2n+1)\pi/4 & (n = 0, 1, 2, 3) \end{array}$$

There are two distinguishably different structures; the solution  $v < 0$ ,  $\phi_0 = 0$  corresponds to the proposed  $D_{2h}^{13}$  structure<sup>(3)</sup>.

The frequency of the doubly-degenerate soft-mode obtained from (1) is:

$$\omega_0^2 = \chi^{-1} = a(T-T_c), \quad T > T_c \quad (2)$$

In the ordered phase the frequencies are:-

$$\omega_0^2 = \chi_0^{-1} = 2a(T_c-T), \quad T < T_c \quad (3a)$$

$105 \text{ cm}^{-1}$  line, which appears strongly in  $\alpha_{aa}$  and  $\alpha_{cc}$  spectra, is not very temperature dependent; it is observed quite clearly above the transition and is apparently not involved in the transition mechanism. The lowest energy line, which is also strong in  $\alpha_{aa}$  and  $\alpha_{cc}$  spectra, is not very temperature dependent, except that near 390K its intensity decreases rapidly and it is not observed at higher temperatures. The third mode which appears in  $\alpha_{bb}$ , is highly temperature dependent as shown in Figure 3; near  $T \sim (T_c - 20K)$  it merges with the lowest line, and as  $T_c$  is approached both lines disappear rapidly but apparently continuously. An interaction between the two modes is expected on symmetry grounds, but we observe neither a clear transfer of intensity between modes nor a strong level repulsion. These effects may however occur very close to the

$$\omega_1^2 = \chi_1^{-1} = -4va(T_c - T)/(u+v), \quad T < T_c \quad (3b)$$

$\omega_1$  appears in the  $A_g$  spectrum;  $\omega_1$  transforms as  $B_{2u}$  and is not Raman active.

Since the critical wavevector does not lie at the zone centre or the zone boundary there is no symmetry condition requiring the soft mode dispersion branch to have a minimum at  $k = k_c$ . For a second-order phase transition this minimum will in general be close to  $k_c$  so that an incommensurate phase occurs; at a lower temperature locking-in of the critical wavevector to  $k_c$  may occur. In  $KFeF_4$  there is no evidence for an intermediate incommensurate phase (al-

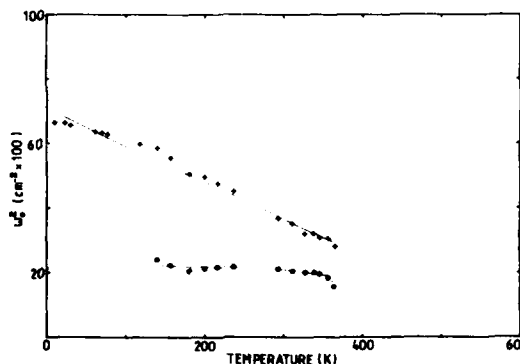


Fig. 3: Temperature dependence of the low frequency phonons in  $KFeF_4$ .

though there is a difference between the values of  $T_c$  obtained here and in (3)). In this sense the transition in  $KFeF_4$  can be regarded as a direct locking-in to the commensurate phase. This requires the fourth order Umklapp term,  $v$ , in (1) to dominate i.e.  $|v| > u$ , which causes the transition to be first order. The data presented here suggest that the transition is sharp although possibly continuous.

#### References

1. M. Hidaka, I. Wood, B.M. Wanklyn and B.J. Garrard. J. Phys. C: Solid State Physics 12, 1799 (1979)
2. G. Heger, R. Geller and D. Babel. Solid State Commun. 9, 335 (1971)
3. M. Hidaka, B.J. Garrard and B.M. Wanklyn. J. Phys. C. Solid State Physics 12, 2737 (1979)

# GRUNEISEN PARAMETER AND DEFORMATION POTENTIALS OF RAMAN ACTIVE MODES IN RUTILE STRUCTURE COMPOUNDS

J. Pascual, J. Camassel\*, P. Merle\* and H. Mathieu\*

Universitat autònoma de Barcelona, Bellaterra, Barcelona, Spain

\*Université des Sciences et Techniques du Languedoc, C.E.E.S., U.S.T.L., 34060 Montpellier-Cedex, France

**Abstract.** - We report a systematic calculation of the shear deformation potentials and mode Gruneisen parameters associated with the first order Raman active modes of  $\text{XO}_2$  and  $\text{YF}_2$  rutile compounds.

Many  $\text{XO}_2$  dioxides where X stands for Pb, Ge, Sn or Ti and  $\text{YF}_2$  difluorides with Y = Mg, Mn, Zn, Fe, Ni or Co crystallise in the rutile structure. Usual selection rules show that  $\Gamma_1$  ( $A_{1g}$ ),  $\Gamma_3$  ( $B_{1g}$ ),  $\Gamma_4$  ( $B_{2g}$ ) and  $\Gamma_5$  ( $E_g$ ) lattice modes are first-order Raman-active. Their energy is given by the dynamical equation :

$$\frac{vm}{2} \omega_i^2 = R_i + Q_i \quad (1)$$

$R_i$  corresponds to the short range interaction and includes bond stretching and bond bending effects (1), while  $Q_i$  summarizes all Coulomb contributions. Various experiments associate to  $\Gamma_3$  ( $B_{1g}$ ) a soft-mode behavior. In an attempt to understand this softening we undertaken on  $\text{TiO}_2$  a series of experimental studies under uniaxial stress (1). We completed this by theoretically computing all deformation potentials associated with the symmetrized components of the deformation tensor (2) :

$$\begin{aligned} \Delta\omega_i &= \left( \frac{e^2}{vm} \right) \frac{1}{2\omega_i} \left[ \Delta R_i + \Delta Q_i \right] - \frac{1}{2\omega_i} (e_{xx} + e_{zz}) \\ &= a_i e_{xx} + b_i e_{zz} + c_i (e_{xx} - e_{yy}) + d_i e_{xy} \end{aligned} \quad (2)$$

The results showed that the softening of the  $\Gamma_3$  ( $B_{1g}$ ) Raman-modes comes directly from the angular displacement associated with this pure rotation mode. Using a simple rigid ion model (RIM) and neglecting the stress induced change in the long range Coulomb interaction, one computed for  $\text{TiO}_2$  deformation potentials in qualitative agreement with the experimental data (2).

In this work we extend the experiments to  $\text{MgF}_2$  and report new calculations performed for  $\text{MgF}_2$ ,  $\text{MnF}_2$ ,  $\text{ZnF}_2$ ,  $\text{CoF}_2$ ,  $\text{TiO}_2$ ,  $\text{SnO}_2$  and  $\text{GeO}_2$ . All results are summarized in table 1. In order to render the comparison meaningful, we systematically use the force constants between first-nearest neighbors listed by Striefler and Barsch for difluorides (3) and dioxides (4) and assume a Born potential  $\phi_{S.R.} \sim r^{-5}$  for both series of compounds. We lastly include the change in long-range interaction.

Experimental results permit to collect 8 deformation potentials for  $\text{MgF}_2$  and  $\text{TiO}_2$ . In both cases,  $\Gamma_1$  and  $\Gamma_5$  which stiffen versus pressure exhibit negative deformation potentials while  $\Gamma_3$  which softens, has positive ones. The calculation satisfactorily reflects these results. Moreover it indicates that, within a family, all experimental values should be roughly independent of the cation. For instance we compute deformation potentials  $a_i \sim 1000 \text{ cm}^{-1}$  for the difluorides and  $\sim 1450 \text{ cm}^{-1}$  for the dioxides. All series of parameters reflect qualitatively similar trends. Concerning  $\Gamma_3$ , the calculation shows that the softening comes from the lack of restoring forces between the two anions associated with the bond 3-4. This is the only one to experience a stretching effect during a rotation of anions around the C axis.

To some extends,  $\Gamma_5$  can also be viewed as a rotational mode about the  $a'$  (110) axis. However, in this case, both anion-anion 3-4 and anion-cation 2-3 bonds give stretching contributions : the one associated with the last bond is strong enough to preclude a softening of the mode.

For the shake of completeness, we list in table II the Gruneisen parameter obtained from this calculation and compare with experimental data when they are available. Theoretical values obtained from refs. 3 and 4 are also given for comparison purpose.

#### References :

1. P. Merle, J. Pascual, J. Camassel and H. Mathieu, Phys. Rev. B21, 1617, (1980).
2. J. Pascual, J. Camassel, P. Merle and H. Mathieu, Phys. Rev. B21, 2439, (1980).
3. M.E. Striefler and G.R. Barsch, Physica Status Solidi, B59, 209, (1973).
4. M.E. Striefler and G.R. Barsch, Physica Status Solidi, B67, 143, (1975).

Raman mode Deformation potentials (cm <sup>-1</sup> )	$\Gamma_1 (A_{1g})$		$\Gamma_3 (B_{1g})$		$\Gamma_4 (B_{2g})$		$\Gamma_5 (E_g)$			
	$a_1$	$b_1$	$a_3$	$b_3$	$a_4$	$b_4$	$a_5$	$b_5$	$c_5$	$d_5$
<u>MgF<sub>2</sub></u> Ex(a)	-1100 ± 60	-470 ± 70	480 ± 60	365 ± 70	-	-	-450 ± 60	-775 ± 70	155 ± 10	-500 ± 75
Th(a)	-1065	-700	638	276	-998	-802	-530	-757	71	-397
Th(b)	-1029	-787	553	502	-	-	-537	-760	146	-556
<u>ZnF<sub>2</sub></u> Th(a)	-1011	-632	621	305	-820	-666	-527	-867	15	-446
<u>MnF<sub>2</sub></u> Th(a)	-983	-623	664	353	-812	-650	-471	-791	22	-440
<u>CoF<sub>2</sub></u> Th(a)	-1015	-688	607	321	-883	-727	-555	-876	15	-592
<u>TiO<sub>2</sub></u> Ex(c)	-610 ± 240	-820 ± 310	620 ± 120	330 ± 150	-	-	-1170 ± 370	-1840 ± 430	35 ± 35	-230 ± 300
Th(a)	-1545	-1290	966	407	-1464	-1399	-1007	-1451	126	-953
Th(d)	-1112	-736	383	1839	-	-	-780	-642	95	-1350
<u>SnO<sub>2</sub></u> Th(a)	-1398	-1112	891	451	-820	-787	-863	-1329	111	-677
<u>GeO<sub>2</sub></u> Th(a)	-1402	-1445	1020	718	-1421	-1570	-949	-1334	80	-899

Table I : Deformation potentials of Raman active modes of Rutile compounds.

a) This work ; b) J. Pascual et al, Phys. Rev. B15, in press, using force-constants extracted from a shell model ; c) ref. 1 ; d) ref. 2, neglecting the Coulomb contribution and assuming  $\phi_{S.R.} \sim r^{-4}$ .

	$\text{MgF}_2$		$\text{ZnF}_2$		$\text{MnF}_2$		$\text{CoF}_2$		$\text{TiO}_2$		$\text{SnO}_2$		$\text{GeO}_2$	
	Exp	Th.	Th.	Th.	Exp	Th.	Th.	Th.	Exp	Th.	Exp	Th.	Th.	Th.
	a	a b c	a c	a c	c a c	a c	d e a f g	h a g	a g					
$\gamma_1$	2.3 $\pm 0.2$	2.4 2.4 1.24	2.7 1.6	2.9 2.7 1.17	2.6 1.87	1 1.6 2.4 1.7 0.52	3.64 2.1 1.3	2.0 1.51						
$\gamma_3$	-4.9 $\pm 0.7$	-5.8 -4.9 -5.22	-8.1 -5.6	-12.2 -9.9 -7.0	-8.1 -6.66	-4 -5.03 -6.0 -4.6 -1.44	-10.4 -6.7 -7.5	-5.7 -3.0						
$\gamma_4$	-	1.8 - 1.05	1.5 1.43 2.3	1.6 1.09	1.7 1.61	-	- 1.6 - 1.24	2.58 1.0 1.15	1.7 1.41					
$\gamma_5$	1.8 $\pm 0.2$	2.0 2.0 1.61	2.4 2.35 3.1	2.1 1.68	2.5 2.63	2.9 2.43 2.2 1.7 0.33	3.20 2.0 1.42	1.5 0.64						

Table II: Gruneisen-mode parameters for Raman-active modes of rutile compounds.

a) this work ; b) J. Pascual et al, Phys. Rev. B15, in press, using force constants extracted from a shell model ;  
c) M.E. Striefeler and G.R. Barsch, Phys. Stat. Sol. B67, 417, 1975 and ref. therein ; d) ref. 1 ; e) G.A. Samara and  
P.S. Peercy Phys. Rev. B7, 1131, 1973 ; f) ref. 2, neglecting the Coulomb contribution and assuming  $\phi_{S.R.} \sim r^{-3}$  ;  
g) ref. 4 ; h) P.S. Peercy and B. Morosin, Phys. Rev. B7, 2779, 1973.



PIEZOSPECTROSCOPIC STUDY OF THE RAMAN SPECTRUM OF  $\text{LiIO}_3$ 

F. Cerdeira\*, F.E.A. Melo\*\* and R.S. Katiyar

*Instituto de Física, UNICAMP, 13.100, Campinas, SP, Brazil*

**Abstract.** - We studied the effect of stress on the Raman Spectrum of  $\alpha\text{-LiIO}_3$ , with the external force directed both parallel and perpendicular to the crystallographic c-axis. The low frequency part of the spectrum ( $\omega < 200\text{cm}^{-1}$ ), consisting of translational modes, exhibits the largest frequency changes and is selected for detailed discussion. These changes are well described by a linear deformation potential theory which allows calculation of Grüneisen parameters and other anharmonic coefficients. The former are in good agreement with those obtained independently using hydrostatic pressure. No significant difference in the value of these parameters was found when comparing results from data taken at two different temperatures (77K and 300K).

The  $\alpha$ -phase of  $\text{LiIO}_3$  belongs to the  $C_6^6$  space group with two formula units per unit cell.<sup>1</sup> The Raman-active phonons are distributed among the irreducible representations of the factor group,  $C_6$ , as:  $4A + 4E_1 + 5E_2$ . The first two types are simultaneously Raman and infrared active (hence split into TO-LO doublets) while  $E_2$  modes are Raman-active only. All modes have been previously identified by Raman and infrared spectroscopy<sup>2,3</sup>. We selected for detailed discussion a mode from each symmetry type among the lowest lying translational vibrations. These modes are referred to by the symbol of its irreducible representation followed by its room temperature frequency value (in parenthesis) rounded off to the nearest integer. Experiments were performed with  $\vec{E} \parallel \vec{z}$  (c-axis) at 77K, with the sample immersed in liquid nitrogen and at 300K. Experiments at 77K were also performed with the external force perpendicular to the hexagonal axis ( $\vec{E} \parallel \vec{x}$ ). The experimental arrangement is described elsewhere.<sup>4</sup>

The changes in the Raman spectrum produced by stress are well described in first order perturbation theory using an effective stress Hamiltonian dependent upon a number of constant parameters

\*CNPq Research Fellow

\*\*On leave from the Physics Department, Universidade Federal do Ceará

called deformation potentials.<sup>5</sup> For the  $C_6$  factor group of  $\alpha$ -LiIO<sub>3</sub> this yields<sup>4</sup>:

$$\Delta\omega_A = a'(\sigma_{xx} + \sigma_{yy}) + b'\sigma_{zz} \quad , \quad (1)$$

for A modes and:

$$\Delta\omega_E = a'(\sigma_{xx} + \sigma_{yy}) + b'\sigma_{zz} + c'[(\sigma_{xx} - \sigma_{yy})^2 + 4\sigma_{xy}^2]^{1/2} \quad , \quad (2)$$

for both types of E modes. Here  $\sigma_{ij}$  are the components of the stress tensor and  $a'$ ,  $b'$  and  $c'$  are deformation potentials to be determined from the experimental data. Mode Grüneisen parameters are obtained from these deformation potentials as

$$\gamma_j = -\frac{d \ln \omega_j}{d \ln V} = \frac{B}{\omega_{oj}} (2a' + b') \quad , \quad (3)$$

where  $B$  is the bulk modulus

In Fig. 1 we show Raman spectra for the frequency region under study taken at 77K for the unstrained crystal and for the maximum value of stress attained in both cases:  $\bar{F} \parallel \hat{z}$  and  $\bar{F} \parallel \hat{x}$ . Frequency vs. stress for the different modes are shown in Fig. 2, also at 77K. All frequencies are seen to change linearly with stress, within the limits of experimental accuracy. In these figures dots represent experimental data while straight lines are linear least-squares fits using eqs. (1) and (2). These fits yield values for the deformation potentials  $a'$ ,  $b'$  and  $c'$ , listed in Table I. Also listed in Table I are Grüneisen parameters calculated with eq. (3) and elastic constants of ref. 6. They are in excellent agreement with those of Lemos et al.<sup>7</sup> obtained from room temperature hydrostatic pressure measurements (Table I).

In conclusion we studied the effect of uniaxial stress on representative phonons of each symmetry type in  $\alpha$ -LiIO<sub>3</sub>. Our measurements render numerical values for the deformation potentials. These constants are anharmonic parameters of great importance in the lattice dynamical description of the material, owing to its well-documented history of nonlinear optical properties and to the possible existence of a high temperature superionic phase.<sup>3</sup> This led us to measure one of the deformation potentials at two different temperatures: 300K and 77K. No significant variation in the numerical value of the parameter was observed. Attempts to obtain

stress data at temperatures of 470K or more failed because the sample deformed plastically at low stresses when heated.

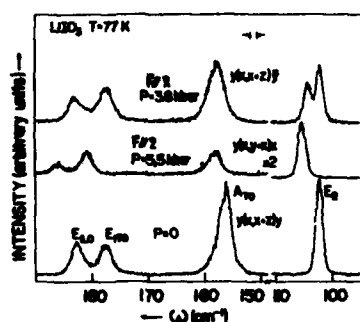


Fig. 1 - Raman spectrum of  $\text{LiIO}_3$  with and without pressure

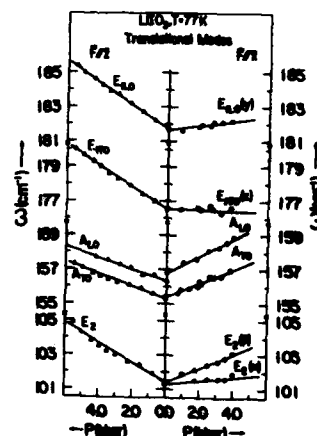


Fig. 2 - Pressure dependence of phonon frequencies

Table I. - Deformation potentials, in  $\text{cm}^{-1} \text{kbar}^{-1}$ , and Gruneisen parameters for translational modes in  $\text{LiIO}_3$

Mode	b'		a'	c'	γ	
	300K	77K			Uniaxial	hydrostatic
$E_2$ (94)	0.58	0.58	0.34	0.60	4.0	4.0
$A_{TO}$ (145)	0.40	0.35	0.40	---	2.4	3.0
$A_{LO}$ (146)	----	0.33	0.50	---	2.7	
$E_{ITO}$ (170)	0.69	0.63	0.04	0.17	1.3	1.3
$E_{ILO}$ (176)	0.61	0.66				

#### References

1. S. Matsumura, Mat. Res. Bull 6, 469 (1971) and references therein.
2. W. Otaguro, E. Wiener - Avnear, C.A. Arguello and S.P.S. Porto. Phys. Rev. B12, 4542 (1971).
3. J.P. Misset and M. Rembissenet, Solid State Commun. 20, 443 (1976).
4. F.A.E. Melo and F. Cardeira, to be Published.
5. von S. Haussuhl, Acustica 23, 165 (1970).
6. V. Lemos, F.A.E. Melo and F. Cardeira, to be Published.

OBSERVATION OF COUPLED AMPLITUDE MODES IN THE RAMAN SPECTRUM OF INCOMMENSURATE  $\gamma$ - $\text{Na}_2\text{CO}_3$ 

A. Maciel and J.F. Ryan

*Clarendon Laboratory, University of Oxford, Oxford, U.K.*

**Abstract.** - The Raman spectrum of incommensurate  $\gamma$ - $\text{Na}_2\text{CO}_3$  reveals an additional number of modes which are activated by the distortion. A complex coupled mode spectrum observed at low frequencies is interpreted as arising from an interaction of acoustic and librational dispersion branches at the incommensurate wavevector. The high-frequency internal mode  $\nu_1$  of the  $\text{CO}_3^{2-}$  ions is observed as a doublet whose splitting varies with temperature as  $(T_1 - T)^{2\beta}$  with  $\beta = 0.35$ .

The disordered  $\beta$  structure of sodium carbonate, which forms the basic structure for the incommensurate phase, is derived from the hexagonal  $\alpha$  form by a monoclinic distortion consisting mainly of rotations of the  $\text{CO}_3^{2-}$  groups about the  $(100)_{\text{hex}}$  axis<sup>(1)</sup>. The incommensurate distortion which sets in at  $T_1 = 633$  K is known to consist of rotations of the carbonate ions about axes normal to this direction and displacements of both the sodium and carbonate ions along this direction<sup>(2)</sup>. The critical wavevector varies continuously with temperature: for example, at room-temperature it has the value  $q^* = (0.182a^* + 0.318c^*)$ , while below  $\sim 130$  K it attains the approximately constant value  $(\frac{1}{6}a^* + \frac{1}{3}c^*)$  without there being a sharp lock-in<sup>(3)</sup>. At the onset of such an incommensurate structural modulation an additional number of vibrational modes with non-zero wavevector are expected to become Raman active. To date experimental studies have concentrated mainly on the behaviour of amplitude and phase modes which are primarily responsible for the distortion. In principle, however, modes originating from wavevectors  $nq^*$  ( $n = 1, 2, \dots$ )

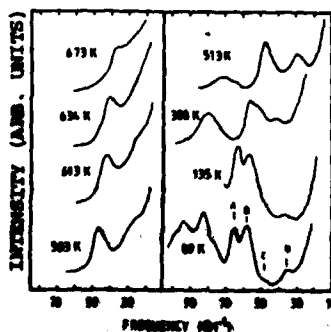


Fig. 1: Unpolarised Raman spectra of  $\text{Na}_2\text{CO}_3$  at various temperatures (K).

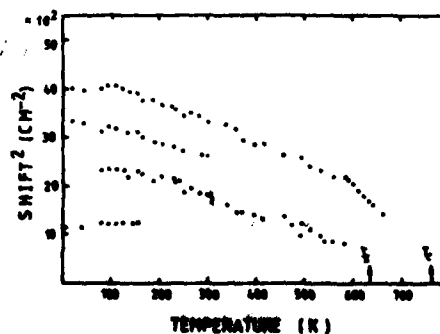


Fig. 2: Temperature dependence of the low-energy modes in  $\text{Na}_2\text{CO}_3$ .

on dispersion branches with appropriate symmetry may become active and can provide information about the distortion. In this paper we report Raman data for  $\gamma\text{-Na}_2\text{CO}_3$  which show evidence of these modes both in the low frequency spectrum and in the high-frequency internal mode spectrum of the  $\text{CO}_3^{2-}$  ions.

The spectrum of  $\gamma\text{-Na}_2\text{CO}_3$  (Fig. 1) shows two quite heavily damped modes below  $50\text{ cm}^{-1}$  which soften with increasing temperature. The plot of their energies versus temperature given in Fig. 2 suggests that they are soft modes for the  $\alpha$ - $\beta$  transition at  $T_c = 763\text{ K}$ . At low temperatures extra lines appear in the spectrum which are associated with the incommensurate phase. The energy of line D in Fig. 1 is relatively temperature independent (Fig. 2) up to about 160 K at which point it is obscured by the wings of the much more intense higher frequency modes. Line C is also very weak at low temperature but its strength increases with temperature as that of B decreases; the latter is not resolved clearly above room temperature. The spectra presented in Fig. 1 are unpolarised and it is not possible to determine the symmetry of the lines. However, an interpretation of the  $\beta$ -phase data can be suggested since on symmetry grounds two Raman-active soft modes ( $\text{Ag}+\text{Bg}$ ) are predicted<sup>(4)</sup> corresponding to rotations of the  $\text{CO}_3^{2-}$  ions about  $(100)_{\text{hex}}$  and  $(120)_{\text{hex}}$  respectively. Because of the complexity of the mode interactions and the lack of polarization data the spectra of the incommensurate phase are more difficult to interpret; however, the temperature dependence of the extra modes is consistent with the model in which a coupling of acoustic and librational dispersion branches at  $q^*$  gives rise to two coupled amplitude modes in the incommensurate phase. This librational branch is expected to be low lying in  $\text{Na}_2\text{CO}_3$  just as in  $\text{K}_2\text{CO}_3$  where an antiferrodistortive transition occurs<sup>(5)</sup> due to a softening of this branch at the Brillouin zone boundary.

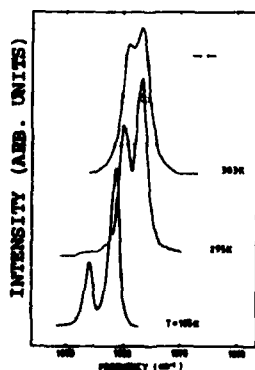


Fig. 3: Raman spectrum of the totally symmetric  $\nu_1$  mode of the  $\text{CO}_3^{2-}$  ion in  $\text{Na}_2\text{CO}_3$ . The data are unpolarized. Spectrometer bandpass is  $1\text{ cm}^{-1}$ .

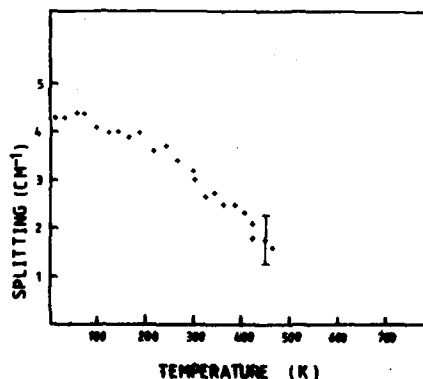


Fig. 4: Temperature dependence of  $\Delta\nu$ , the splitting of the  $\nu_1$  mode in the incommensurate phase.

Additional lines are also observed in the spectrum of the incommensurate phase in the neighbourhood of the  $\text{CO}_3^{2-}$  internal modes. The most obvious of these is the apparent splitting of the nondegenerate symmetric breathing mode  $\nu_1$  (Fig. 3). The temperature dependence of the splitting shown in Fig. 4 shows that it tends to zero near  $T_I$  although we are in fact unable to resolve the components above  $\sim 500$  K. In the  $\beta$  phase we observe only a single line, albeit quite broad. A log-log plot of  $\Delta\nu$  versus  $(T - T_I)$  yields a slope  $0.70 - 0.76$  depending on the choice of  $T_I$  as  $619$  K<sup>(3)</sup> or  $633$  K<sup>(2)</sup> respectively. Assuming a relationship  $\Delta\nu \propto (T_I - T)^{2\beta}$  yields a critical exponent  $\beta = 0.35 - 0.38$ . Similar values of  $\beta$  have been obtained for other incommensurate systems.

#### References

1. C.J. de Pater, *Physica* **96B**, 89 (1979)
2. W. van Aalst, J. den Hollander, W.J.A.M. Peterse and P.M. de Wolff  
*Acta. Cryst.* **32B** 47 (1976)
3. C.J. Pater and R.B. Helmholtz *Phys. Rev. B* **19** 5735 (1979)
4. Angela Maciel and J.F. Ryan. *J. Phys. C.* **14** L 509 (1981)
5. Angela Maciel and J.F. Ryan. *J. Phys. C.* **14**, 1611 (1981)

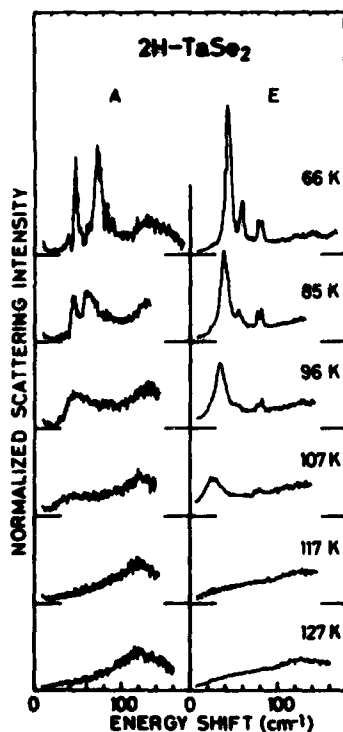
# INVESTIGATION OF THE CHARGE DENSITY WAVES IN $2H-TaSe_2$ BY ONE AND TWO PHONON RAMAN SCATTERING

S. Sugai<sup>\*\*</sup>, K. Murase<sup>\*</sup>, S. Uchida<sup>\*\*</sup> and S. Tanaka<sup>\*\*</sup>

<sup>\*</sup>Department of Physics, Osaka University, Toyonaka, 560 Japan

<sup>\*\*</sup>Department of Applied Physics, University of Tokyo, Tokyo, 113 Japan

**Abstract.** - One and two phonon Raman scattering was investigated in  $2H-TaSe_2$  at the normal and the charge density wave (CDW) phases. The temperature dependence of the generalized susceptibility was obtained from the integrated scattering intensity of the two phonon peaks relating to the Kohn anomaly mode. The temperature dependence of the phonon energies calculated from this susceptibility shows excellent agreement with the experimental data obtained from one phonon Raman scattering in the soft  $A_{1g}$  and  $E_{2g}$  - modes in the CDW phase and the Kohn anomaly mode in the normal phase.



**Fig.1** : Lower energy part of Raman spectra in the normal (127 K), ICDW (117 K), SCCDW (107, 96 K) and TCCDW (85, 66 K) phases. The dotted curves are duplications of the 127 K spectra.

Transition metal dichalcogenide  $2H-TaSe_2$  is a typical layered compound with a CDW phase transition. The crystal structure changes from the original hexagonal phase  $D_{6h}^4$  to the incommensurate charge density wave (CDW) phase at 122 K, followed by the triply commensurate CDW (TCCDW) phase of  $3a_0 \times 3a_0 \times c_0$  at 90 K.<sup>(1)</sup> On warming only the stripe domain structure (SCCDW), in which one CDW is commensurate and the other two are incommensurate, was observed by x-ray diffraction between 90 K to 112 K.<sup>(2)</sup>

The experiment was made in the back scattering configuration on the layer plane with 5145 Å Ar-ion laser and micro-computer associated system. Using this experimental configuration, one  $A_{1g}$  and two  $E_{2g}$  modes are observed in the normal phase. In the TCCDW phase six points on the E-lines and the two K-points in the original phase are folded into the  $\Gamma$ -point.

<sup>\*</sup> Present address: Div. Engineering, Brown University, Providence, RI 02912

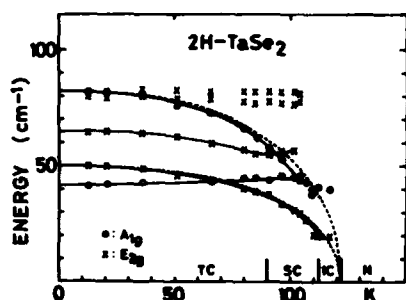


Fig. 2 : Temperature dependence of the phonon energies in the CDW phase. The dotted curves are calculated from the obtained susceptibility.

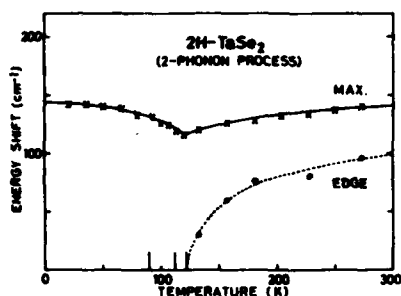


Fig. 3 : Temperature dependence of the energy shift of the maximum position and the edge of the lower energy foot of the two phonon Raman peak. The dotted curve is calculated using the susceptibility.

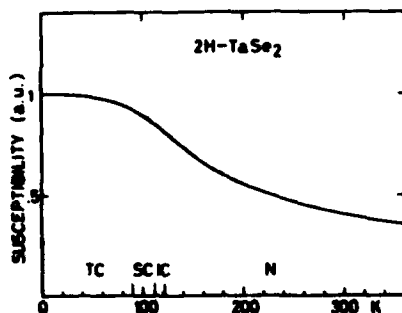


Fig. 4 : Temperature dependence of the generalized susceptibility obtained from the integrated scattering intensity of the two phonon Raman peak.

Figure 1 shows the Raman spectra below  $100 \text{ cm}^{-1}$ . The  $A_{1g}$ -spectra were obtained by subtracting the perpendicularly polarized spectra  $Z(XY)\bar{Z}$  from the parallel polarized spectra  $Z(XX)\bar{Z}$ . The normalized intensity was obtained by dividing the experimentally obtained intensity by  $n + 1$ , where  $n$  is the Bose-Einstein factor. The small peak at  $24 \text{ cm}^{-1}$  in the  $E_{2g}$ -spectra is due to the natively active rigid layer mode. The broad peak at  $110 \text{ cm}^{-1}$  is due to the two phonon process. On decreasing the temperature, two  $A_{1g}$ -modes and four  $E_{2g}$ -modes become strong. Figure 2 shows the temperature dependent phonon energies of these modes. The  $A_{1g}$ -mode at  $82 \text{ cm}^{-1}$  and the  $E_{2g}$ -mode at  $50 \text{ cm}^{-1}$ , at low temperatures, show softening toward the CDW to the normal phase transition temperature at 122 K. The  $50 \text{ cm}^{-1}$  mode is overdamped above 110 K. The  $82 \text{ cm}^{-1}$   $A_{1g}$ -mode approaches the  $42 \text{ cm}^{-1}$   $A_{1g}$ -mode and merges at 100 K.

The strong two phonon scattering intensity relating to the Kohn anomaly is the distinctive feature of 2H-compounds with CDW phase transitions. The maximum position and the edge of the foot of the two phonon scattering peaks are shown in Fig. 3. The energy of the edge shows strong temperature dependence. The half of this energy corresponds to the energy of the Kohn anomaly  $\Sigma_1\text{LA}$ -mode. The integrated scattering intensity increases with decreasing temperature, if the intensity is normalized by the statistical factor of the two phonon emitting process. The two phonon scattering intensity is related to the generalized electronic susceptibility  $\chi_{q\lambda}^{(4)}$  by

$$I \propto \chi_{q\lambda}^2 (n + 1)^2.$$



Figure 4 shows the obtained susceptibility. Phonon energies renormalized by the electron - phonon interaction are expressed<sup>(5)</sup> by

$$\tilde{\omega}_q^2 = \omega_{q\lambda}^2 - \alpha_{q\lambda} \chi_{q\lambda},$$

where  $\tilde{\omega}_q^2$  and  $\omega_{q\lambda}$  are the renormalized and bare phonon frequency, respectively. The calculated phonon energies are shown in Fig. 2 and Fig. 3 by dotted curves. The agreement with the experimental results is excellent.

Our results are summarized in the following.

1. The generalized electronic susceptibility was obtained from the second order Raman scattering intensity. The energy of the Kohn anomaly mode was calculated above and below the CDW phase transition temperature using the susceptibility. The agreement with the experimental data was excellent.
2. In the CDW phase, the  $A_{1g}$ -mode at  $82 \text{ cm}^{-1}$  at 12 K and the  $E_{2g}$ -mode at  $50 \text{ cm}^{-1}$  shows strong softening and their intensity curves have shoulders at about 90 K. They might be assigned to the amplitude modes. The  $42 \text{ cm}^{-1}$   $A_{1g}$ -mode and the  $64 \text{ cm}^{-1}$   $E_{2g}$ -mode might be assigned to the phase modes.
3. No hysteresis was observed in the phonon energy, scattering intensity and line width in the temperature range of the SCCDW phase. This suggests the existence of the domain structure in which the CDW is almost commensurate.
4. The Kohn anomaly phonon energy above the CDW transition temperature was obtained from the lower energy foot of the second order Raman peak.

#### References

1. D. E. Moncton, J. D. Axe and F. J. DiSalvo, Phys. Rev. B16 (1977) 801.
2. R. M. Fleming, D. E. Moncton, D. B. McWhan and F. J. DiSalvo, Phys. Rev. Letters 45 (1980) 576.
3. J. A. Holy, M. V. Klein, W. L. McMillan and S. F. Meyer, Phys. Rev. Letters 17 (1976) 1145.
4. P. F. Maldague and J. C. Tsang, Proc. Int. Conf. on Lattice Dynamics, edited by M. Balkanski, Flammarion Science (1978), p. 602.
5. S. K. Chan and V. Heine, J. Phys. F: Metal Phys., 3 (1973) 795.

# BRILLOUIN SCATTERING STUDY OF THE INCOMMENSURATE (ANTIFERROELECTRIC) PHASE TRANSITION IN SODIUM NITRITE

T. Yagi, Y. Hidaka\* and K. Miura\*\*

Kyushu University, Hakozaki, Fukuoka, Japan 812

**Abstract.**— The Brillouin scattering spectra of  $\text{NaNO}_2$  have been observed as a function of temperature near the two phase transition points; normal (paraelectric)-incommensurate (antiferroelectric) and incommensurate-commensurate (ferroelectric) phase transition points. A simple temperature dependence of the Brillouin frequency shifts has been found in the incommensurate phase indicating existence of a dispersion of the sound velocity in hypersonic frequency.

**1. Introduction.**— The phase transition in ferroelectric sodium nitrite ( $\text{NaNO}_2$ ) crystal has been regarded as a typical example of the order-disorder type transition. The flip-flop motion of electric dipoles = each of which is composed of a  $\text{NO}_2^-$  ion and the nearest neighbouring  $\text{Na}^+$  ion - is capable of being treated theoretically as a motion of the Ising spins. On the other hand the phase transition of  $\text{NaNO}_2$  is not so simple as expected from the simple mechanism mentioned above. With lowering temperature, the crystal symmetry changes from the disordered paraelectric (normal)  $D_{2h}^{25}-I_{mmm}$  to the sinusoidal-antiferroelectric (incommensurate) phase at  $T_N$  (437.7 K) and then undergoes a 1st order transition to the ordered-ferroelectric (commensurate)  $C_{2v}^{20}-I_{m2m}$  at  $T_C$  (436.3 K). In the incommensurate phase, the electric polarization has an incommensurate wavenumber  $k = a^*/8$ , where  $a^*$  is the magnitude of the reciprocal lattice vector parallel to the orthorhombic  $a$ -axis.

The observation of sound wave propagation is a powerful method for investigating the dynamic property of the incommensurate phase, because elastic waves are always coupled with the order parameter. Several studies on the sound wave propagation in  $\text{NaNO}_2$  have been reported.<sup>1-6)</sup> The purpose of the present paper is to observe the sound wave propagation in a gigahertz region by the Brillouin scattering in order to extend the frequency region covered by the recent ultrasonic studies in the incommensurate phase.<sup>3,4)</sup>

**2. Experiment.**— The sample crystals of  $\text{NaNO}_2$  were grown by the Bridgman method. During the course of the crystal growth, the temperature of the electric furnace was controlled to keep the cooling speed slow.

\*Present address : Ibaraki Electrical Communication Lab., NTT, Japan 319-11

\*\*Present address : Atsugi Plant, Sony Corp., Atsugi, Japan 243

After being cut to a cubic shape with a wet-thread saw, the surfaces of the sample crystal were finely polished in order to reduce the light scattered there. The sample crystal mounted in a light scattering cell was illuminated by a beam of the longitudinal single-mode  $\text{Ar}^+$  ion laser operated at an average output power of about 100 mW. A 5145 Å line, polarized vertically, was mainly used as the incident beam. The scattered light was analyzed an ordinary  $90^\circ$  Brillouin spectroscopic system which is essentially the same as the one described elsewhere.<sup>6,7)</sup> Figure 1 shows a typical example of the spectrum of  $\text{NaNO}_2$  observed at room temperature.

3. Results and Discussion. - The Brillouin frequency shift ( $\Delta\nu$ ) of the longitudinal modes was observed as a function of temperature for each of the three directions [100], [010] and [001] in a temperature range from 360 to 480 K. The temperature dependence of  $\Delta\nu$  in the [010] direction shows a qualitative agreement with the previous result except for the results very near the transition points  $T_C$  and  $T_N$ .<sup>5)</sup> The results near the transition points  $T_C$  and  $T_N$  are shown in Fig.2. In the incommensurate phase, a gradual decrease of  $\Delta\nu$  along with increasing temperature is seen in each of the three directions. Taking account of the temperature dependence of the refractive indices, we can see a rather smooth change of the sound velocity along with temperature in

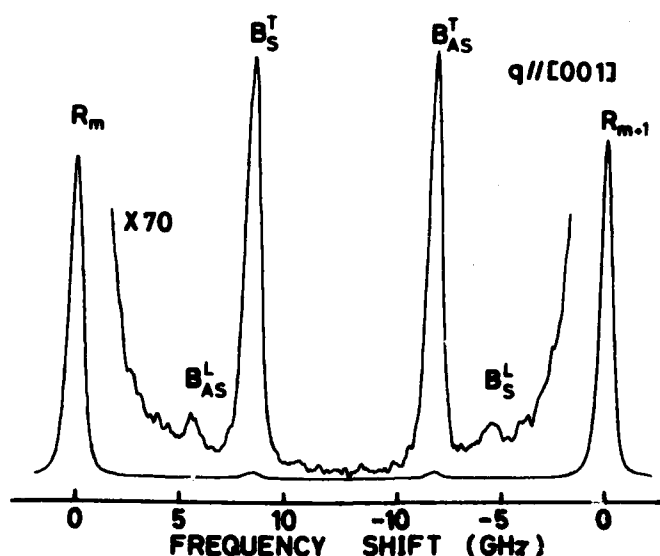
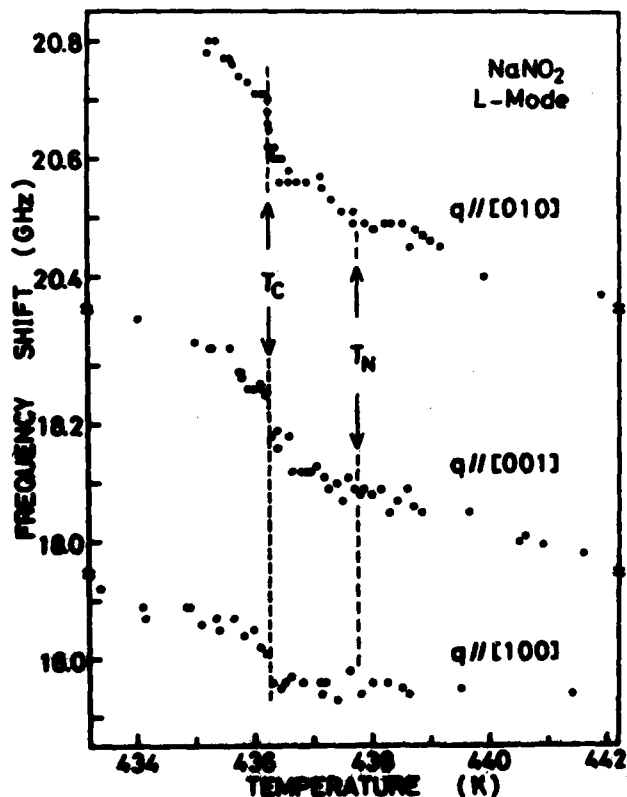


Fig. 1 : Brillouin spectrum of  $\text{NaNO}_2$  at room temperature. The phonon vector  $q$  is parallel to the [001] direction. The capital letters R and B denote Rayleigh and Brillouin lines. The superior and inferior letters m, T, L, S and AS mean the order of interference, transverse, and longitudinal modes, Stokes and anti-Stokes lines, respectively.

the incommensurate phase, because  $\Delta v$  is proportional to the hypersonic velocity. On the other hand, the distinct anomalies near  $T_C$  and  $T_N$  were reported in the recent ultrasonic study of the longitudinal wave propagating along the [010] direction.<sup>3,4)</sup> The relative change of the sound velocity at  $T_C$  in the ultrasonic data is estimated to be 3 ~ 4 %. On the other hand, the relative change in the present hypersonic data is about 0.5 % at  $T_C$ . At the normal-incommensurate phase transition point  $T_N$ , a continuous minimum in the velocity of the longitudinal sound wave in the [010] direction was reported.<sup>3,4)</sup> However no minimum was observed in the present data as shown in Fig.2.

The difference between the ultrasonic and the present hypersonic result indicates clearly the frequency dependence of the sound velocity in the incommensurate phase. Thus it is concluded that the dispersion frequency of the sound wave exists below a hypersonic region. Therefore, the amplitude mode which is expected to couples to the

sound wave in the incommensurate phase becomes sufficiently over damped in the frequency region considered here.



#### References.

1. I.Hatta, T.Ishiguro and N.Mikoshiba, Phys.Lett., **A29**, 421 (1969).
2. K.Ota, Y.Ishibashi and Y.Takagi, J.Phys.Soc.Jpn., **29**, 1545 (1970).
3. I.Hatta, Y.Shimizu and K.Hamano, J.Phys.Soc.Jpn., **44**, 1887 (1978).
4. I.Hatta, M.Hanami and K.Hamano, J.Phys.Soc.Jpn., **48**, 160 (1980).
5. H.Shimizu, M.Tsukamoto, Y.Ishibashi and M.Umeno, J.Phys.Soc.Jpn., **36**, 498 (1974).
6. T.Yagi, Y.Hidaka and K.Miura, J.Phys.Soc.Jpn., **48**, 2165 (1980).
7. M.Cho and T.Yagi, J.Phys. Soc.Jpn., **50**, 543 (1981).

Fig. 2 : Temperature dependence of the Brillouin frequency shift of the three longitudinal acoustic modes in the incommensurate (antiferroelectric) phase of  $\text{NaNO}_2$ . The phase lies in the temperature region between  $T_N$  and  $T_C$ .

## SOFT PHONON VALLEY NEAR THE TRANSITION TO AN INCOMMENSURATE PHASE IN BARIUM SODIUM NIOBATE

J. Schneck, J.C. Toledano, J. Aubree, B. Joukoff and C. Joffrin\*

C.N.E.T., 196 rue de Paris, 92220 Bagneux, France

\*I.L.L., Grenoble, France

**Abstract :** The dynamic characteristics of the tetragonal to incommensurate transition in Barium Sodium Niobate has been investigated. The precursor effects consist, in the tetragonal phase, of a soft phonon and a central peak.

Barium Sodium Niobate was known to undergo in the vicinity of 300°C a ferroelastic transition with the symmetry change  $4mm \rightarrow mm2$  <sup>(1)</sup>.

However it has been recently shown that there were actually two transitions in the 300°C range <sup>(2)</sup>. The upper one nearby 300°C which is continuous corresponds to the onset of an incommensurate phase with the modulation vector  $\vec{k} = (a^* + b^*)(1+\delta)/4 + c^*/2$  (referred to the tetragonal lattice).

The stability range of this phase is  $\sim 30^\circ\text{C}$ , where  $\delta$  varies on heating from 8 % to 12.5 %. The orthorhombic symmetry previously observed is only that of the "average" crystalline structure. The lower transition which is discontinuous leads to another incommensurate phase with identical point-symmetry and the same direction of modulation but with a different periodicity very close to a commensurate one ( $\delta \sim 1$  %).

By means of inelastic neutron scattering the dynamics of the upper transition has been studied in the high temperature tetragonal phase up to 660°C. In the investigated sample this transition occurs at  $T_I \sim 288^\circ\text{C}$ , the lower one being at  $T_{II} \sim 250^\circ\text{C}$ . Above  $T_I$ , energy scans has been performed near the vector  $(4 - (1+\delta)/4, 4 - (1+\delta)/4, 1/2)$  which corresponds to one of the strongest satellites observed, below  $T_I$ , in the  $[1\bar{1}0]$  scattering plane.

The critical wavevector has been found at  $\vec{k}_c = (3.72, 3.72, 0.5)$  and is temperature independent. For  $T < T_I$ ,  $\vec{k}_c$  corresponds to the temperature dependent position of the satellite reflection.

For  $T > T_I$ , inelastic scans reveal the presence of a damped soft phonon mode as well as that of a central component with a critical behavior. The soft phonon becomes overdamped below 400°C. The central component exhibits a steep increase of intensity on approaching  $T_I$  whereas its width is determined by the instrumental resolution ( $\sim 0.15$  THz).

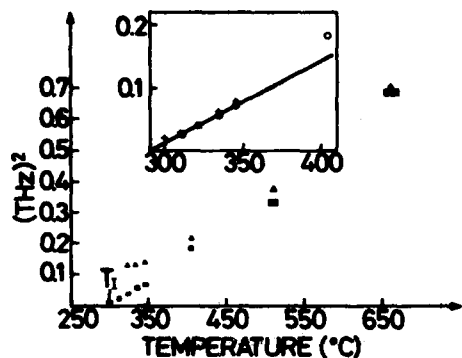


Fig.1 : Variations of the squared frequencies of the undamped renormalized soft mode,  $\omega_{\infty}^2$  (filled triangles), and  $\omega_0^2$  (squares). The insert shows  $\omega_0^2$  in a range of 60°C above  $T_I$ .

The contribution of the two former features have been separated through a fit of the energy scans<sup>(3)</sup>. The plot of the fitted squared frequency of the soft phonon  $\omega_{\infty}^2$  is shown on fig.1.  $\omega_{\infty}^2$  decreases markedly from 660°C to 350°C. Below 350°C,  $\omega_{\infty}^2$  remains nearly constant because below this temperature the phonon contribution seems to remain constant. This saturation of  $\omega_{\infty}^2$  is probably due to the interaction of the soft-phonon with a relaxing degree of freedom giving rise to a central peak.

The inverse of the static susceptibility  $\chi \sim 1/\omega_0^2$ <sup>(3)</sup> has been obtained through the measurements of the total intensity  $I$  scattered in both the central peak and the soft mode peak. We have  $\omega_0^2 \sim T/I$ <sup>(4)</sup>. As it is shown on fig.1 the temperature variations of  $\omega_0^2$  are in good agreement with a linear law below 350°C.

The set of fitted  $\omega_{\mathbf{k}}$  frequencies obtained for various  $\mathbf{k}$  vectors along the  $[110]$  direction gives the dispersion curve represented on fig.2.

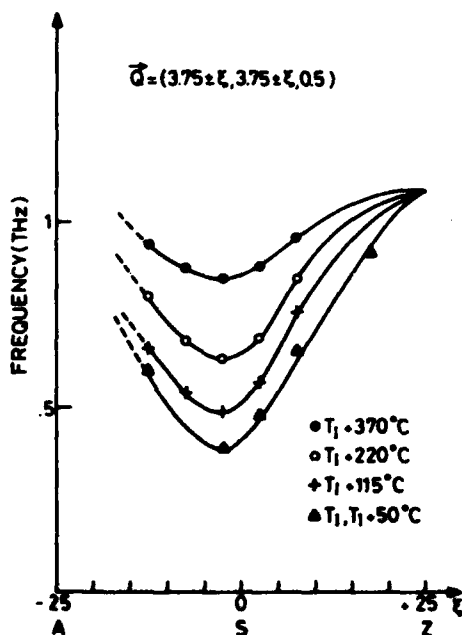


Fig.2 : Dispersion curve of the soft-phonon branch along the  $[110]$  direction.

Previous X-ray experiments <sup>(2)</sup> have shown in the high temperature phase precursor effects of the transition at  $T_I$  as strong rods of diffused scattering approximately along  $[1\bar{1}0]$ . In these rods a strong temperature dependence of the soft mode is observed showing that the dispersion curve along the direction is very flat.

On the basis of the preceding results, the nature of the diffused scattering observed in the X-ray experiment is clarified. Close to the critical wavevector  $\vec{k}_C$  and near  $T_I$  it is essentially due to the central peak distinct from the overdamped phonon contribution. On going away from  $\vec{k}_C$  in the  $[1\bar{1}0]$  direction the contribution of the soft phonon increases and makes an important fraction of the scattering. Over  $100^\circ\text{C}$  above  $T_I$  the diffused rods essentially reflect the valley shaped dispersion surface of the soft phonon branch.

These diffused rods reveal the occurrence of strong correlations in the (ac) orthorhombic plane. A possible structural basis for a correlation along the c direction could be in the fact that at microscopic level the soft mode has been assigned to a collective shearing of the oxygen octahedra in the structure <sup>(5)</sup>. This feature could establish strong correlations in the chains of oxygen octahedra parallel to c, through the corner sharing of the consecutive octahedra.

By contrast no obvious mechanism accounts for the correlation along the  $[110]$  direction.

#### REFERENCES

1. J.C. Tolédano, Phys. Rev. B, 12, 943 (1975) and references therein.
2. J. Schneck and F. Denoyer, Phys. Rev. B23, 383 (1981)
3. A.D. Bruce and P.A. Cowley, Adv. in Physics, 29, 219 (1980)
4. B. Dorner, J.D. Axe, G. Shirane, Phys. Rev. B6, 1950 (1972)
5. J. Schneck, J.C. Tolédano, C. Joffrin, J. Aubrée, B. Joukoff and A. Gabelotaud (to be published).

## VIBRATION SPECTRA OF CRYSTALS IN AN INCOMMENSURATE PHASE

T. Janssen and C. de Lange

*Institute for Theoretical Physics, University of Nijmegen, Toernooiveld, 6525 ED Nijmegen, The Netherlands*

**Abstract.**— The solutions of the equations of motion and the structure of the spectra of incommensurate crystal phases is exemplified on a model in one dimension. Use is made of the superspace symmetry of the problem.

**1. Equations of motion.** An incommensurate crystal phase is characterized by the simultaneous occurrence of 2 or more, mutually incommensurate, periodicities. As a consequence the translation symmetry is lost. Nevertheless, the symmetry is a space group, but in 4 (or more) dimensions<sup>1,2</sup>. If the modulation is displacive and one-dimensional, the position of the  $j$ th atom in the unit cell  $\vec{n}$  is  $\vec{n} + \vec{r}_j + \vec{f}_j(\vec{q} \cdot \vec{n})$ , where  $\vec{f}_j$  is a periodic function with period  $2\pi$ , and  $\vec{q}$  is the modulation wave vector which is incommensurate with the basic lattice. As additional dimension we take the phase  $\tau$  of  $\vec{f}_j$ . Then the positions can be seen as the intersection of 3-dimensional space with lines given by  $(\vec{n} + \vec{r}_j + \vec{f}_j(\vec{q} \cdot \vec{n} + \tau), \tau)$ . This 4-dimensional structure has again translation symmetry with basis vectors  $(\vec{a}_j, -\Delta\vec{a}_j), (0, 2\pi), (\vec{a}_j$  are the 3 basis vectors of the basic structure), where  $\Delta\vec{a}_j = \vec{q} \cdot \vec{a}_j$ .

This 4-dimensional translation symmetry can be exploited to study the vibrations of the incommensurate phase. We do this in the harmonic approximation. This approximation cannot throw light on the origin of the modulation, but can be used once the modulated configuration is established. We denote the displacement from the equilibrium position of atom  $\vec{n}, j$  for a phase  $\tau$  by  $\vec{u}(\vec{n}, j, \tau)$ . Then

$$m\omega^2 \vec{u}(\vec{n}, j, \tau) = \sum_{\vec{n}', j'} \Phi(\vec{n}, j, \vec{n}', j', \tau) \vec{u}(\vec{n}', j', \tau) \quad (1)$$

is the equation of motion with dynamic tensor  $\Phi$ . This equation and the properties of  $\Phi$  have been discussed in ref.3. Here we want to apply this equation to investigate the spectra. Because of the translation symmetry we can use a Bloch Ansatz for  $\vec{u}(\vec{n}, j, \tau)$ . As has been shown in ref.3,  $\vec{u}$  has the form

$$\vec{u}^{\vec{k}\lambda}(\vec{n}, j, \tau) = \exp(i\vec{k} \cdot \vec{n}) \vec{U}_j^{\vec{k}\lambda}(\tau + \vec{q} \cdot \vec{n}), \quad (2)$$

where  $\vec{k}$  is a vector in the Brillouin zone of the basic structure and  $\lambda$  an integer labelling the solutions. The function  $\vec{U}$  has lattice periodicity. In particular, it has periodicity in  $\tau$ :  $\vec{U}_j^{\vec{k}\lambda}(\tau) = \vec{U}_j^{\vec{k}\lambda}(\tau + 2\pi)$ . This implies that

$$\vec{U}_j^{\vec{k}\lambda}(\tau) = \sum_m \vec{K}_m^{\vec{k}\lambda} \exp(im\tau). \quad (3)$$



Substituting eqs.(2) and (3) into eq.(1) we get equations for  $\vec{U}$  and  $\vec{A}$ , which form for incommensurate  $q$  an infinite set of coupled difference equations. For commensurate  $q$ , this set is finite, because  $U(\tau)$  is coupled only to the finite set  $U(\tau+\vec{q}, \vec{n})$ . The number of equations then is exactly equal to the number of degrees of freedom in the supercell. Nevertheless it makes sense to use the description in the 4-dimensional superspace.

**2. Modulated spring model.**— As an example we consider a linear chain of identical particles with potential energy  $V = \sum \alpha_n(\tau) |u_n(\tau) - u_{n-1}(\tau)|^2 / 2$ , where the spring constants vary as a consequence of the modulation. Notice that we do not discuss the equilibrium positions themselves, but only the displacements. To make the model as simple as possible we assume a sinusoidal variation of the spring constants:

$$\alpha_n(\tau) = \alpha(1 + \epsilon \cos(qn + \tau)) \quad (4)$$

Eq.(2) gives  $u_n^{k\lambda}(\tau) = \exp(ikn) U^{k\lambda}(\tau + qn)$ . For the unmodulated crystal ( $\epsilon=0$ ) we get, of course, the usual solutions in the form of harmonic waves. These do not depend on  $\tau$ :  $u_n^k = u_0^k \exp(ikn)$ , which implies  $U^k(\tau) = u_0^k$ . For  $\epsilon \neq 0$  these waves are coupled to each other. Now it is important to notice that the description in eq.(2) is not unique. If one replaces  $k$  by  $k + \pi q$  and  $U^k(\tau)$  by  $U^k(\tau) \exp(-i\pi\tau)$ , the displacements for  $\tau=0$  are the same. This implies that for incommensurate  $q$ ,  $k$  can be taken to be zero. For commensurate  $q=s/N$ , one can take  $0 \leq k < 2\pi/N$ .

For  $\epsilon=0$  the solutions are  $U^{k\lambda}(\tau) = u_0^k \exp(-i\lambda\tau)$ . For  $\epsilon \neq 0$ , the solutions are no longer simply sinusoidal. An example is given in Fig.1 for the case  $q=0.3\pi$ ,  $\epsilon=0.316$  and  $\lambda=1$ . The label  $\lambda$  corresponds to that of the solution to which this solution tends for  $\epsilon \rightarrow 0$ . It is only ambiguous because of the degeneracy of modes with  $\lambda, -\lambda$ .

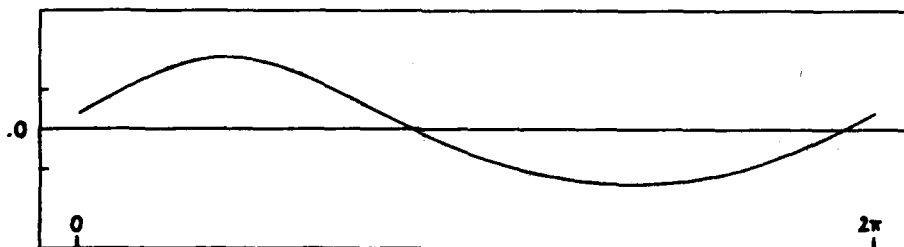


Fig.1 : The function  $U(\tau)$  for the  $k=0, \lambda=1$  mode of the modulated spring model with  $q=0.3\pi$ ,  $\epsilon=0.316$ ,  $u_0^k=0.7934$  (cf. Table 1).

The characterization of the modes is more transparent for the Fourier components  $A_n$ . For  $\epsilon=0$  there is only one component (or two if one combines the degenerate modes with  $\lambda$  and  $-\lambda$ ). For  $\epsilon \neq 0$  the number of components increases (Table 1). However, for  $\epsilon \ll 1$  a mode is well characterized by its biggest component. For  $\epsilon=1$ , this is no longer the case (see  $\lambda=2$  in Table 1 for  $\epsilon=1$ ).

$\lambda$	0	1			2			10		
$\epsilon$	0.0-1.0	0.0	0.316	1.0	0.0	0.316	1.0	0.0	0.316	1.0
$\mu_1$	0.000	0.824	0.793	0.383	2.618	2.445	1.968	4.000	4.494	6.239
$\mu_0$	0.224									
$\mu_1$		0.158, -.009	.146, .057	.094, .048		.020, .004	.022, -.044			.006, .001
$\mu_2$			-.014, -.016	-.037, .051	.158, .003	.111, .090	.062, -.046			.033, .025
$\mu_3$			.001, .003	.006, .040		-.024, -.053	-.054, .009			.040, .083
$\mu_4$			.000, -.001	.007, -.020		-.001, .022	-.009, -.003			-.002, .079
$\mu_5$				.004, -.004		-.011, .018	.062, .062			-.012, .022
$\mu_6$				-.080, .026		-.001, .001	.008, .023			-.002, .001
$\mu_7$				.024, .004			-.001, .004			0.0, 0.0
$\mu_8$				-.006, -.004			-.032, .044	.005, -.007		.007, -.010
$\mu_9$				.001, .002			-.027, .014	.074, -.038		.052, -.027
$\mu_{10}$							.052, .000	.224, .000	.190, 0.	.093, .000

Table 1. Real and imaginary parts of  $A_{\mathbf{m}}^{k\lambda}$  for  $k=0$ . Notice that  $A_{-\mathbf{m}}^{k\lambda} = A_{\mathbf{m}}^{k\lambda*}$ .

3. **Spectra.**— To study the spectra we have used the same modulated spring model. An extensive discussion has been given in ref.4. Here we present some results for a simple case. One way of doing is to use perturbations methods for small  $\epsilon$  but arbitrary  $q$ , another way is to approximate an irrational  $q$  by a rational one and to study the successive approximations. In Table 2 are given the  $^2$ -spectra for a superstructure

with  $q=0.3\pi$ . For  $\epsilon=0$  there are no gaps. For  $\epsilon \neq 0$ , there are in principle 19 gaps, but for  $\epsilon \neq 1$  only 5 gaps show up. If  $\epsilon$  increases the number of gaps increases, but the number of substantial gaps remains the same: the levels cluster. In the extreme limit  $\epsilon=1$  this can be seen clearly. It is remarkable that the clustering is governed by the continued fraction expansion of  $q$ . Since here  $q/2\pi = 1/(6+2/3)$  the cluster pattern in first approximation is 3-2-3-3-3-3-3. In a second approximation the 3-clusters split up in a 2-cluster and a single level.

To see the influence of the commensurate approximation, in Table 2 the spectra for  $q=0.3\pi$  are compared with those for  $2\pi/7$  and  $2\pi/6$ . It is clear that the gap structures are very similar.

The spectra for this simple model have also the main characteristics as for another model with nonlinear forces.<sup>5</sup>

$q/2\pi$	0.15	0.15	1/7	1/6	0.15	1/7
$\epsilon$	0.000	0.316	0.316	0.316	1.000	1.000
$^2$	4.000	4.494	4.525	4.427	6.238702	6.3163
		4.481	4.515	4.400	6.238686	
		3.370	3.439	3.288	3.65959	
					3.65953	3.8118
		3.325	3.319	3.037	3.65926	
		2.749	2.805	2.614	1.9710	
					1.9686	2.1292
		2.232	2.360	1.930	1.9680	
		2.128	2.236	1.863	0.9469	
					0.9435	1.0734
		1.326	1.489	0.963	0.9301	
		1.317	1.478	0.960	0.4150	
					0.3833	0.4554
			0.725		0.3727	
			0.725		0.1956	0.2139
		0.246	0.223	0.302	0.1878	
		0.177	0.161	0.218	0.0180	
					0.0052	
	0.000	0.000	0.000	0.000	0.0000	0.0000

Table 2. Spectra for the modulated spring model. A line between numbers indicates a continuous band.

#### References.

1. P.H.de Wolff, *Acta Cryst.*, A30,777(1974), A33,493(1977)
2. A.Janner and T.Janssen, *Phys.Rev.*, B15,643(1977), *Physica*, A99,47(1979)
3. T.Janssen, *J.Phys.C*, 12,5381(1979)
4. C.de Lange and T.Janssen, *J.Phys.C*, (to appear)
5. T.Janssen and J.A.Tjon, *Phys.Rev.*, B24, (to appear)

# INVESTIGATION OF THE CHARGE DENSITY WAVES IN $1T-VSe_2$ BY RAMAN SCATTERING

S. Sugai<sup>\*\*</sup>, K. Murase<sup>\*</sup>, S. Uchida<sup>\*\*</sup> and S. Tanaka<sup>\*\*</sup>

<sup>\*</sup>Department of physics, Osaka University, Toyonaka, 560 Japan

<sup>\*\*</sup>Department of Applied Physics, University of Tokyo, Tokyo, 113 Japan

**Abstract.**— The lattice dynamics in  $1T-VSe_2$  was investigated by Raman scattering in the normal phase ( $> 112$  K), the incommensurate charge density wave (ICDW) phase (80 - 112 K) and the commensurate charge density wave (CCDW) phase of  $4a_0 \times 4a_0$  ( $< 80$  K). Recently the stacking of the layers was observed to be incommensurate even in the lowest temperature phase. In the normal phase two modes were observed. In the CDW phase new peaks appear in the  $A_{1g}$  - symmetry at 50, 62 and  $174\text{ cm}^{-1}$  due to the formation of the superlattice. The  $50\text{ cm}^{-1}$  mode showed softening toward the CDW to normal phase transition temperature. The observed CDW peaks are broad reflecting the incommensurability along the direction perpendicular to the layer. A central peak was observed in the CDW phase.

The two dimensional transition metal diselenide  $1T-VSe_2$  is known to show the charge density wave (CDW) phase transition. On cooling, the ICDW is formed at 112 K and successively the CCDW of  $4a_0 \times 4a_0$  is constructed in a layer, but the stacking of layers along the C - axis is still incommensurate.<sup>(1)</sup> The calculation of the band structure shows a pancake-like Fermi surface near the  $\Gamma$ -point<sup>(2)</sup> as in the case of  $1T-TaSe_2$ . This might be the origin of the incommensurate stacking. The electronic resistivity is metallic even at low temperature, and the temperature dependence resembles  $2H-TaSe_2$ .

The experiment was made in the back scattering configuration on a cleaved layer surface, using a 5145 Å Ar - ion laser of 100 mW and a microcomputer associated Raman spectroscopy system. The scattering intensity from  $1T-VSe_2$  was weak by about one-tenth of that of  $2H-TaSe_2$ .

The crystal structure in the normal phase is trigonal  $D_{3d}^3$  and the unit cell contains one formula unit. One  $A_{1g}$  and one  $E_g$  - mode are Raman active. The  $A_{1g}$  - mode is observed in the parallel polarization configuration of the incident and the scattered lights. The  $E_g$  - mode is active both in the parallel and perpendicular polarization configurations. The  $A_{1g}$  - symmetry spectra were obtained by subtracting the perpendicular polarization spectra from the parallel polarization spectra after correcting for the apparatus efficiency about the polarization direction for each wavelength point.

<sup>\*</sup>Present address: Div. Engineering, Brown University, Providence, RI 02912

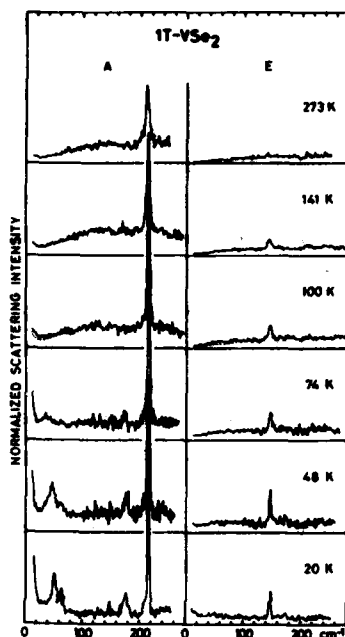


Fig. 1 : The  $A_{1g}$  and  $E_g$  symmetry spectra of  $1T-VSe_2$  in the normal ( $> 112$  K) incommensurate (80 K - 112 K) and commensurate-in-a-layer ( $< 80$  K) phases.

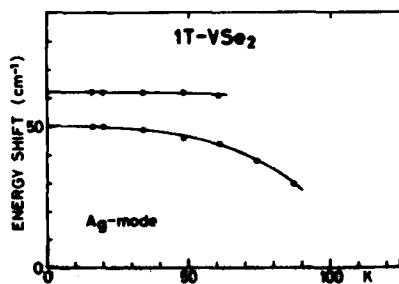


Fig. 2 : Temperature dependence of the energies of the  $A_{1g}$  - modes which appear in the CDW phase.

Figure 1 shows the  $A_{1g}$  and  $E_g$  - symmetry spectra in  $1T-VSe_2$ . The scattering intensity was corrected for the phonon distribution function  $n$ , as

$$I(\omega) = I_0(\omega) / (n(\omega, T) + 1),$$

where  $I_0(\omega)$  is the observed scattering intensity. At room temperature the  $A_{1g}$  - mode is observed at  $211 \text{ cm}^{-1}$  and the  $E_g$  - mode at  $143 \text{ cm}^{-1}$ . The peak of the  $E_g$  - mode is small and broad at room temperature, but becomes strong with cooling the crystal. The broad peak near  $130 \text{ cm}^{-1}$  is assigned to the second order Raman peak relating to the Kohn anomaly. Below the CDW phase transition temperature new peaks appear because of the increase of the unit cell. The new peaks were observed only in the  $A_{1g}$  - symmetry with the energy of  $50 \text{ cm}^{-1}$ ,  $62 \text{ cm}^{-1}$  and  $174 \text{ cm}^{-1}$  at 20 K. These peaks are broad even at 20 K, reflecting the incommensurability along the C- axis. The  $50 \text{ cm}^{-1}$  mode at low-temperatures shows strong softening toward the ICDW to the normal phase transition temperature of 112 K as shown in Fig. 2.

Figure 3 shows the normalized integrated scattering intensity and the full line width at half maximum. Figure 3(a) is concerned with the CDW state activated modes and Fig. 3(b) the native modes. At low temperatures the CDW state activated modes of  $50 \text{ cm}^{-1}$  and  $62 \text{ cm}^{-1}$  decrease their scattering intensity and increase their line width with temperature. The intensity of the modes active even in the original phase decreases with temperature. The point of inflection is about 130 K. The  $147 \text{ cm}^{-1}$   $E_g$  - mode almost merges into the background at room temperature. This temperature behavior is similar to the native mode of  $240 \text{ cm}^{-1}$   $A_{1g}$  - mode in

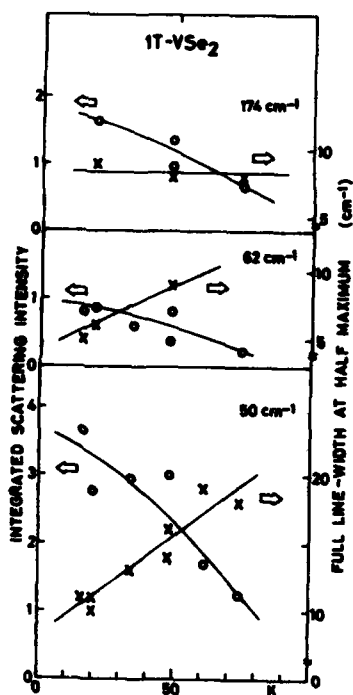


Fig. 3(a)

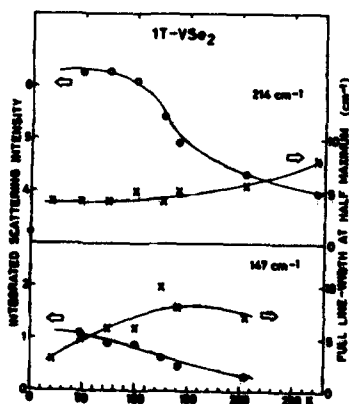


Fig. 3(b)

Fig. 3 : Temperature dependence of the integrated scattering intensity and the full line width at half maximum of the CDW - activated modes (a) and the originally active modes (b).

2H-TaSe<sub>2</sub>.

Below the CDW phase transition temperature a central peak appears below 10 cm<sup>-1</sup>, and its intensity increases with decreasing temperature. The central peaks accompanying the CDW phase transition was observed by Sooryakumer, Bruns and Klein in the ICDW phase of 2H-TaSe<sub>2</sub>.<sup>(3)</sup> In the naive theory of the one dimensional CDW, the phase mode has vanishing energy at zero wave vector. In two dimensional materials, the energy of the phase mode are not well known due to the interaction of the triple CDW's. The observed central peak might be related to the phonon or to some defects in the crystal.

The authors thank A. Toriumi for the preparation of good crystals.

#### References

- (1) K. Tsutsumi, T. Sambongi, A. Toriumi and S. Tanaka, *Physica*, **105B** (1981) 419
- (2) A. M. Wolley and G. Wexler, *J. Phys.C: Solid State Physics* **10** (1977) 2601.
- (3) R. Sooryakumer, D. G. Burns and M. V. Klein, *Proceedings of the Second Joint USA - USSR Symposium*, edited by J.L. Birman, H. A. Cummins and K. K. Rebane, Plenum Press 1979, p.347.

PRESSURE DEPENDENCE OF IMPURITY INDUCED RAMAN SCATTERING SPECTRA IN  
ZnS CRYSTALS

M. Zigone, M. Vandevyver\* and D.N. Talwar\*

*Laboratoire de Physique des Solides, associé au C.N.R.S., Université Pierre  
et Marie Curie, 4, Place Jussieu, 75230 Paris Cedex 05, France**\*C.E.A., C.E.N.S., Boite Postale n° 2, 91190 Gif-sur-Yvette, France*

**Abstract.** - Raman scattering from zinc sulphide crystals containing a transition metal substitutional impurity (Mn and Co) is reported at different pressures up to 40 kbar. Numerical calculations of these impurity induced Raman intensities are also made on the basis of Green's function theory. It is shown that the features observed in the Raman spectra of the above crystals may be interpreted as a series of resonant modes due to the weakening of the impurity-sulfur bonds by about 20 %.

1. **Introduction.** - When impurity atoms are introduced into a crystal, new phonons are induced which were either inactive or inexistent in the perfect crystal. There may arise two possibilities that a) all the modified modes lie within the band mode region, or b) some new modes occur at frequencies in between or greater than the bands of the allowed frequencies of the host system.

In the recent years, these impurity induced modes have intensively been investigated in numerous crystals using both infrared (i.r.) absorption and Raman scattering methods<sup>1</sup>. Most of the works have concerned isolated or complex defects in crystals at atmospheric pressure. Rather sparse are the studies of the influence of a reversible perturbation as hydrostatic pressure on the defect modes.

The present communication is devoted to the effect of hydrostatic pressure up to  $\approx 40$  kbar on the Raman spectra of ZnS containing transition-metal atomic-substitutions (Mn and Co). It is shown that the pressure dependence of the vibrational modes is a useful tool in the assignment of the impurity-induced modes.

A calculation of the impurity induced first-order Raman scattering (IFOR) is also performed here for the above crystals, at 40 kbar pressure. As a result, our calculation reproduces very well the experimental results by assuming a weakening of  $\approx 20$  % of the impurity-host bonding.

2. **Experimental.** - The Raman spectra were measured using a "Spectra Physics" Ar<sup>+</sup> laser and a "Coderg" double monochromator. The experimental resolution was usually of  $\approx 1$  cm<sup>-1</sup>. The high pressure cell was a gasketed diamond-anvil cell. The pressure determination is accurate to  $\pm 1$  kbar at 40 kbar.

The effect of hydrostatic pressure on the impurity induced Raman spectra has been studied for ZnS:Mn and ZnS:Co systems. The results are shown in figs. 1 and 2 for ZnS:Mn only. The measurements have been performed up to  $\approx 40$  kbar, at room tempera-

ture. The important result concerns the defect phonons, all of them exhibit the same blue shift under pressure application without any other modifications. Moreover, the blue shift is very similar to that of the  $LO(\Gamma)$  phonon.

The frequencies of peaks found in the defect spectra (see Table 1) fall into the range where the one-phonon density of states is high or rapidly varying<sup>2, 4</sup>.

Then, we might conclude that we do see the IFOR scattering which is due to the relaxation of the wave-vector conservation rule in the presence of the defect ("defect activated phonon density"). Nevertheless, the alternative hypothesis of "true defect modes" cannot be excluded. First, the phonon density shows a narrow gap in the optical region which suggests the possibility of gap modes<sup>2</sup>.

Secondly, resonant modes characterized by a

strong enhancement of amplitude of vibration in the vicinity of the defect, could also be responsible for the observed defect spectra. We expect that, upon pressure application, the Raman spectrum of the "defect activated phonon density" should reflect the variations with pressure of the dispersion curves at zone edges, and thus present a modification of its structure because each of the high symmetry points of the Brillouin zone has a different pressure dependence coefficient<sup>4</sup>. We have seen that, in fact, it is not what we have observed in the experiments under

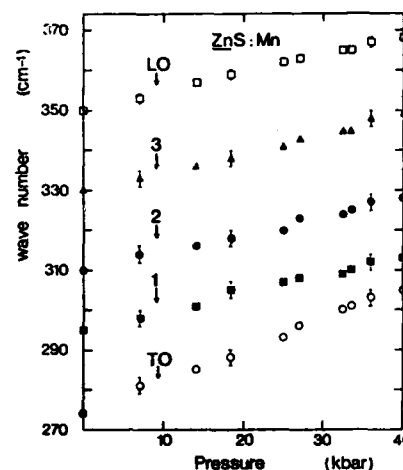


Fig. 1. Pressure dependence of phonon frequencies in ZnS:Mn (3 %). The notation 1, 2, 3 correspond to the defect phonon peaks that are listed in Table 1.

TABLE I

Comparison of the experimental perfect crystal and impurity frequencies with those of the modes predicted by calculation at two values of the pressure: 1 bar and 40 kbar. The measured and calculated frequency shifts  $\Delta\omega$  between 1 bar and 40 kbar are also indicated. All the frequencies are given in  $\text{cm}^{-1}$ . A numerical agreement of frequencies at 40 kbar is achieved for the same value of the defect parameter  $t(P) = (\Delta\omega - \Delta\omega(P))/\Delta\omega(P)$  that has been found at atmospheric pressure. The calculation reproduces also very well the measured frequency shifts  $\Delta\omega$ .

features (see figs. 4 and 5)	ZnS:Mn						ZnS:Co					
	1 bar		40 kbar		$\Delta\omega = \omega_{40} - \omega_1$		1 bar		40 kbar		$\Delta\omega = \omega_{40} - \omega_1$	
	exp.	calc. for $t=0.20$	exp.	calc. for $t=0.20$	exp.	calc.	exp.	calc. for $t=0.10$	exp.	calc. for $t=0.10$	exp.	calc.
TO( $\Gamma$ ) +	274	274	305	305	+ 31	+ 31	274	274	305	305	+ 31	+ 31
1 +	299	296	313	315	+ 18	+ 19	303	304	321	323	+ 18	+ 19
		300		319		+ 19		308		327		+ 19
2 +	310	311	328	330	+ 18	+ 19	315	314	333	333	+ 18	+ 19
3 +	330	331	349	350	+ 19	+ 19	335	334	352	353	+ 17	+ 19
		339		350		+ 19		344		363		+ 19
LO( $\Gamma$ ) +	350	350	368	369	+ 18	+ 19	350	350	368	369	+ 18	+ 19

compression (c.f. Figs. 1 and 2).

This behaviour under pressure is an argument in favor of our second hypothesis of "true defect modes".

3. Calculation. - In this section we attempt to calculate the IFOR spectra due to the above impurities on the basis of the Green's function technique, by using a rigid ion model of 11 parameters (RIM 11) for description of the perfect crystals<sup>2</sup>. Among the possible one-parameter defect models, we consider the one proposed by Grimm et al.<sup>5</sup>. In this model, the defect can be described by a single dimensionless parameter  $t$  as :  $t = -\Delta f/f$ . Details on numerical computations of the impurity induced Raman intensity are given in ref.

3. In an earlier paper<sup>4</sup> we have reported a lattice dynamical study of zinc-chalcogenides under compression. Therefore, a set of model parameters is available at any pressure, and this allow us to calculate the IFOR scattering at high pressure.

The calculation of the IFOR spectra of the above crystals at atmospheric pressure has already been

given in a previous work<sup>3</sup>. We have shown that the calculated results provide an excellent agreement with the experimental structure for the value  $t \approx 0.2$  of the defect parameter, i.e. a weakening of the impurity-host bonding by a factor 0.8. This calculation predicts also no gap modes for the selected value of  $t$  and in the frequency range under study. Therefore, the only "true defect modes" which could be responsible for the observed structure are the resonant modes.

In order to clarify this question furthermore, we have calculated the IFOR spectra from Mn and Co impurities at 40 kbar ; the shift of defect modes with pressure is in a very good agreement with the one observed experimentally (cf. fig. 2 and Table 1) for the value of  $t$  determined in the calculation at 1 atm. pressure<sup>3</sup> :  $t \approx 0.2$ .

This constitutes a supplementary test for the chosen models of the perfect lattice and of the defect.

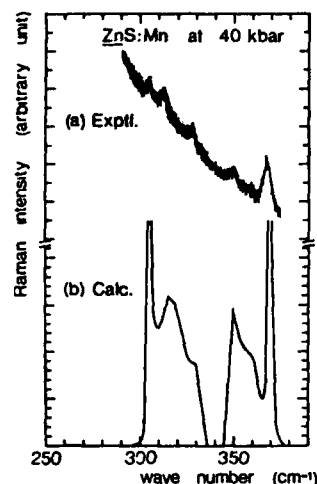


Fig. 2. Comparison between the measured and calculated Raman intensities of ZnS:Mn (3 %) at 40 kbar pressure. (a) represents the experimental spectrum obtained at 40 kbar ; whereas in b) the calculated sum  $A_1 + E + F_2^{bb}$  is plotted.

#### References

1. For review see e.g. A.S. Barker Jr. and A.J. Sievers, Rev. Mod. Phys. **47**, suppl. n° 2 (1975).
2. K. Kunc, Ann. Phys. (Paris) **8**, 319 (1973).
3. D.N. Talwar, M. Vandevyver and M. Zigone, J. Phys. C **13**, 3775 (1980) ; Phys. Rev. B **23**, 1743 (1981) ; M. Zigone, M. Vandevyver and D.N. Talwar, to appear in Phys. Rev. B.
4. D.N. Talwar, M. Vandevyver, K. Kunc and M. Zigone, to appear in Phys. Rev. B, (July issue).
5. A. Grimm, A.A. Maradudin, I.P. Ipatova, and A.V. Subashiev, J. Phys. Chem. Solids **33**, 775 (1972).



## SIMULTANEOUS CONDENSATION OF SEVERAL MODES AT STRUCTURAL PHASE TRANSITIONS

P. Toledano, G. Pascoli and M. Coiret

*Groupe de Physique Théorique, Faculté des Sciences, 80000 Amiens, France*Abstract.-

The structural transitions in a number of materials has been explained by the simultaneous condensation of several modes at the transition temperature. The various types of couplings between the order-parameters corresponding to this mechanism are discussed.

Most of the observed structural phase transitions have been related to the condensation of a single normal mode of the crystal. This confirms the basic assertion of the Landau theory<sup>1</sup> which states that when the space-groups of two phases are group-subgroup related, the transition from one to another phase can be described by a single order-parameter(OP). In other words, the number of phenomenological variables that have to be introduced in the description of the transition is minimal and cannot be reduced. However, a small fraction of the materials undergoing structural transitions does not comply with the preceding scheme. This is, for example, the case of families of compounds such as the Boracites<sup>2</sup>, the Langbeinites<sup>3</sup> and part of the Perovskites<sup>4</sup>; of isolated compounds such as Benzil<sup>5</sup> or Bismuth titanate<sup>6</sup>; and also of incommensurate systems, such as Sodium nitrite and Thiourea<sup>8</sup>.

In these materials, the structural changes cannot be interpreted with a single OP and several modes related to distinct OP seem to be simultaneously involved. As each OP expresses a set of atomic displacements (a degree of freedom) associated to a certain normal mode of the system, the fact that several OP are involved signifies that the displacements related to one OP brings about an instability in parameters inducing other displacements. Due to the non-linear interaction between the various parameters, the modifications accompanying the transition (symmetry change, dielectric or elastic anomalies...) will require for their description an increasing number of thermodynamic variables. Thus, it can be asked to what extent a Landau-type theory involving several OP may still have a predictive value. In this paper we briefly discuss the case of transitions induced by two OP whose characteristics have been precised by a number of recent studies<sup>7-13</sup>.

As we have in mind a qualitative description, we can restrict to consider only single component OP's, namely  $p$  and  $q$ . The free-energy(FE) of the transition will contain, in addition to invariants of each OP, mixed invariants expressing the coupling between  $p$  and  $q$ . As it is the lowest degree coupling term which determines the essential features of the transition, we can therefore distinguish two main cases:

1) The FE is of the type:

$$F = A_1 p^2 + A_2 p^4 + A_3 p^6 + B_1 q^2 + B_2 q^4 + B_3 q^6 + C p^2 q^2 \quad (1)$$

Such a case is encountered when lower couplings of the type  $pq, pq^2$  or  $p^2 q$  are forbidden by symmetry. It is realized, for instance, for two non-unit one dimensional real irreducible representations (IR) of the space-group  $G_0$  describing the more symmetric (high temperature) phase.

When  $A_3 = B_3 = 0$ , (1) is related to an experimentally unrealistic set of two successive second order transitions. When only one of the sixth-degree coefficients (let say  $B_3$ ) is non-zero, we obtain an asymmetric FE which has been used by Holakovskiy<sup>9</sup> to describe the simultaneous onset of spontaneous values for  $p$  and  $q$  at a first order transition. More precisely, when one assumes a single temperature-dependent coefficient ( $A_1$ ), the softening of this coefficient triggers two phase transitions either at different or at the same temperature. In this latter case, which is realized for sufficient large values of the coupling coefficient  $C$ , the spontaneous values of  $p$  change the coefficient at  $q^2$  inducing a transition in  $q$ . The soft vibrational mode of the high symmetry phase remains related to the "primary" OP, but the space group of the low symmetry phase is the intersection of the symmetries determined separately by  $p$  and  $q$ . In addition to this remarkable property, other features allow the identification of "triggered" phase transitions, namely a complex domain structure depending on the possible orientation of two OP having different symmetry properties; or the mixed behaviour of the dielectric constant (proper below the Curie point, improper above). Bismuth titanate<sup>6</sup> has been proposed as an illustrative example of the preceding model though the available data are still incomplete for this material.

The phase diagram of (1) when  $A_3 \neq B_3 \neq 0$  has been discussed by Gufan and Larin<sup>10</sup>. It displays various sets of successive (and possibly simultaneous) transitions with intersecting lines of second and first order transitions.

2) The FE is of the type:

$$F = A_1 p^2 + A_2 p^4 + A_3 p^6 + B_1 q^2 + B_2 q^4 + B_3 q^6 + C p q^2 \quad (2)$$

with a linear-quadratic coupling term which can be formed if at least one of the two OP is spanned by a multidimensional IR. On the theoretical ground this FE has been shown to be connected to the simultaneous condensation of two modes<sup>11,13</sup>. Besides, it has been used to describe accurately the experimental data of particular systems. In Boracites<sup>2</sup> the low temperature phases and the dielectric anomaly have been explained by a mechanism in which the components of the polarisation play the role of the primary OP triggering a six components OP associated to an IR of the cubic space group  $T_d^5$  at the Brillouin zone boundary. In Bismut<sup>5</sup> for which a detailed numerical model has been proposed, the primary and triggered OP possess respectively two and three components. In this material, the coupling to macroscopic quantities which are not symmetry breaking parameters has been considered. It has been shown that such a coupling does not affect the dynamical properties of the

crystal while the coupling between the OP  $p$  and  $q$  is likely to be active both in its static and dynamic behaviours. On the other hand quantitative values show<sup>5</sup> that in Bensil, the triggering though essential to explain the symmetry characteristics of the transition influences only weakly the other physical properties.

The two FE considered in 1) and 2) summarize the qualitative situations which may be encountered for structural transitions induced by two OP. Numerical models should also take into account the actual symmetry of the OP and higher degree couplings. Besides when dealing with transitions towards incommensurate phases other type of coupling, involving the space derivatives of the OP, must be considered. This brings us to a third case.

3) The onset of intermediate incommensurate phases, such as in Sodium nitrite or Thiourea<sup>8</sup>, has been attributed to the coupling of two distinct OP whose transformation properties allow an antisymmetric invariant of the type:

$$\frac{pdq}{dx} - \frac{qdp}{dx} \quad (3)$$

If we consider  $p$  and  $q$  as the amplitudes of two different normal modes of the crystal, (3) expresses the existence of a relative maximum in the lowest mode due to their interaction. This situation can be recognised when a commensurate phase, generally stable at lower temperature, is related to an IR of the high temperature commensurate phase which does not transform like (3). In Sodium nitrite and Thiourea the low temperature commensurate phase is connected to a one dimensional IR of the orthorhombic Brillouin zone center so that the construction of an invariant of type (3) needs to recourse to two distinct IR at that point. The preceding model is however far from being experimentally confirmed as it does not explain the complex set of phases which is for instance observed in Thiourea.

#### REFERENCES

1. L.D. Landau and E.M. Lifshitz, Statistical Physics (Pergamon Press, Oxford, 1958).
2. A.P. Levanyuk and D.G. Sannikov, Sov. Phys. Solid State, 17, 327 (1975).
3. Yu.M. Gufan, V.P. Dmitriev, and V.I. Torgashev, Sov. Phys. Crystallogr. 24, 342 (1979).
4. W. Cochran and A. Zia, Phys. Stat. Sol. 25, 273 (1968).
5. J.C. Toledano, Phys. Rev. B20, 1147 (1979).
6. J. Holakovsky, Phys. Stat. Sol. (b) 69, 575 (1975).
7. G. Pascoli, These de troisieme cycle (University of LILLE I, 1981), unpublished.
8. A.P. Levanyuk and D.G. Sannikov, Sov. Phys. Solid State, 18 1122 (1976).
9. J. Holakovsky, Phys. Stat. Sol. (b) 56, 615 (1973).
10. Yu.M. Gufan and E.S. Larin, Sov. Phys. Solid State, 22, 290 (1980).
11. Yu.M. Gufan and V.I. Torgashev, Sov. Phys. Solid State, 22, 951 (1980).
12. P. Toledano and G. Pascoli, in: N. Boccara, Symmetries and Broken Symmetries in Condensed Matter Physics (IDST, Paris, 1981).
13. D.G. Sannikov, Pis'ma Zh. Eksp. Teor. Fiz. 31, 342 (1980).

LATTICE DYNAMICS OF THE CUBIC-TETRAGONAL PHASE TRANSITION IN  $\text{KNbO}_3$ 

M.D. Fontana, G.E. Kugel and C. Carabatos

University of Metz, Ile du Saulcy, 57045 Metz, France

**Abstract.** - The dynamical properties in the cubic and the tetragonal phases of  $\text{KNbO}_3$  are described on the basis of the same shell model. Calculations clearly show the strong influence of the intraionic oxygen polarizability on the ferroelectric mode behaviour in both phases.

**1. Introduction.** -  $\text{KNbO}_3$  continues to be of a particular interest among ferroelectric (FE) materials because it undergoes three successive phase transitions, whose mechanism is the object of many controversies. Inelastic neutron scattering measurements<sup>1</sup> performed in the tetragonal phase ( $T = 245^\circ\text{C}$ ) reveal the presence of a low-frequency E(TO) zone center mode together with an high anisotropy in the lowest phonon branches which can be related to the existence of strong correlations along the  $\langle 100 \rangle$  axes between the large motions associated to the soft modes. Recent infrared reflectivity measurements<sup>2</sup> clearly show the softening of the lowest-frequency  $F_{1u}$  phonon with decreasing temperature in the entire range of the cubic phase ( $425^\circ\text{C} < T < 910^\circ\text{C}$ ).

Lattice-dynamical calculations are carried out for the cubic ( $O_h^1$  space group) and the tetragonal ( $C_{4v}^1$  space group) phases in order to explain the main experimental features. The aim of this paper is to show, for the first time, that the dispersion curves for both phases can be described satisfactorily by the same harmonic model.

**2. Description of the model.** - In this work for the cubic phase we use the model developed by Cowley<sup>3</sup> for  $\text{SrTiO}_3$  with axially symmetric short-range force constants A and B between nearest neighbours (K-O, Nb-O, O-O). In addition we allow an anisotropy in the oxygen core-shell coupling constant  $k(O)$  as previously suggested by Migoni et al.<sup>4</sup> for both  $\text{SrTiO}_3$  and  $\text{KTaO}_3$ . Therefore the components of the tensor  $k(O)$  in the directions of neighbouring K and Nb ions are denoted  $k(O-K)$  and  $k(O-Nb)$  respectively. This leads to a 15 parameters model for the cubic phase (Table 1).

Since the symmetry is lower in the tetragonal phase (Figure 1), the number of parameters is, in principle, larger than in the cubic phase. Using simple geometry arguments we are able to derive the parameters of the tetragonal phase from those of the cubic structure. Consequently, the short-range constants of the tetragonal phase are expressed as functions of the lattice parameters  $c$  and  $a$ , of the

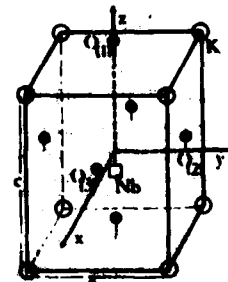


Fig. 1 : Tetragonal unit cell

spontaneous ionic displacements  $\delta$ , measured by Hewat<sup>5</sup>, and of the set of parameters A and B, already defined in the cubic phase. Furthermore, in the tetragonal phase, we distinguish two kinds of oxygen ions,  $O_{(1)}$  (located on the polar axis passing through the Nb ion) and  $O_{(2)}$  or  $O_{(3)}$  (in the plane perpendicular). Consequently we allow the parameter  $k(O_{(1)}-Nb)$  to be different from the parameters  $k(O_{(2)}-Nb)$  and  $k(O_{(3)}-Nb)$ .

3. Results and discussion. - For the tetragonal phase, the dispersion curves are calculated with parameters adjusted to the results of inelastic neutron<sup>1</sup> and Raman<sup>6</sup> scattering measurements. The experimental data are quite satisfactorily reproduced by the model calculations (Fig.2) except for the  $\Delta_2$  (TO) branch near the zone boundary. This failure may be due to the large anharmonic coupling between acoustic and soft optic phonons in this direction. The strong anisotropy in the lowest dispersion branches is interesting to notice together with an anticrossing and eigenvector exchange between optic and acoustic  $\Delta_2$  branches, which take place approximately at 1/3 of the Brillouin zone edge. The soft  $E(TO)$  phonon at  $q=0$  is essentially characterized by a large vibrationnal amplitude of the niobium ion relative to the oxygen ion located along the mode polarization direction. Moreover the Einstein oscillator response of this mode in the whole Brillouin zone confirms the presence of dynamical correlation chains Nb-O-Nb directed along the  $[100]$  and  $[010]$  axes<sup>1</sup>. This shows the validity of the linear chain model for describing the soft mode behaviour in perovskites, as emphasized by Bilz et al.<sup>7</sup> for  $KTaO_3$ .

For the cubic phase, the phonon branches are obtained with the parameter values previously used in the tetragonal phase, except for the coupling  $k(O-Nb)$  (Table 1). In figure 2 the calculations are compared with the experimental data of Nunes et al.<sup>8</sup> In addition to the large anisotropy in the phonon dispersion surface, we can also note the softening of the lowest  $F_{1u}$  phonon with a relatively slight

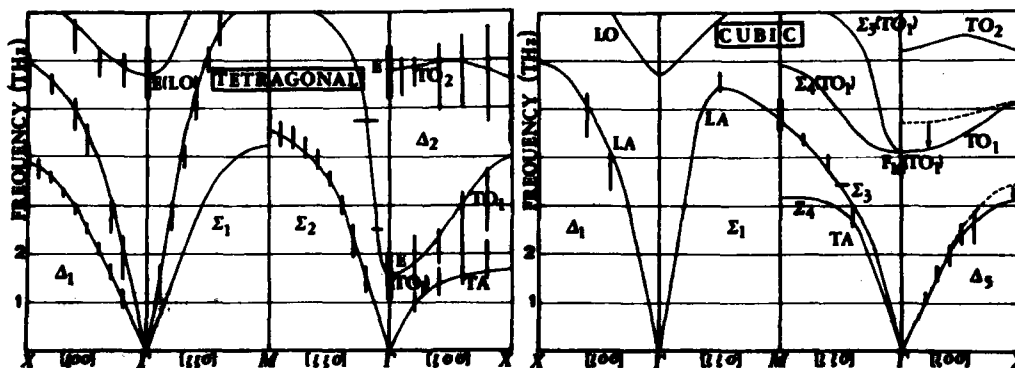


Figure 2 : Calculated dispersion curves of  $KNbO_3$  in the tetragonal and cubic phases compared with experimental data of Refs 1,6 and Ref. 8 respectively. The dotted curves correspond to  $k(O-Nb) = 131$

$e^2/2v$						$e$						$e^2/v$			
$A_{K-O}$	$B_{K-O}$	$A_{Nb-O}$	$B_{Nb-O}$	$A_{O-O}$	$B_{O-O}$	$Z_K$	$Z_{Nb}$	$Y_K$	$Y_{Nb}$	$Y_O$	$k_K$	$k_{Nb}$	$k_{O-K}$	$k_{O_1-Nb}$	$k_{O_2-Nb}$
26	-2.9	385	-80	2.2	0.7	1	4.1	2.2	-1.5	-2.7	65	1466	560	155	128.8
														(129)	(129)

Table 1 : Shell model parameters. The values into brackets correspond to the cubic phase.

change in the value of  $k(\text{O-Nb})$ . The other zone-centre modes are nearly insensitive to this variation.

At the cubic-tetragonal phase transition, therefore, the splitting and the frequency shift<sup>6</sup> of these phonons depend only on the geometrical effect in the force constants. On the contrary, the large separation of the FE soft  $F_{1u}$  phonon into a soft E component (1.55 THz) and a hardened  $A_1$  (8.35 THz) essentially originates from a  $k(\text{O}_{(1)}-\text{Nb})$  value larger than  $k(\text{O}_{(2)}-\text{Nb})$  (Table 1).

All these results emphasize the role of the intraionic oxygen polarizability in the phase transition mechanism of  $\text{KNbO}_3$ . This polarizability is dynamically enhanced by the hybridization of oxygen 2p states with niobium 4d states<sup>9</sup> in the direction of the chain like coupling Nb-O-Nb. This leads to a softening of the lowest cubic  $F_{1u}(\text{TO})$  and tetragonal  $E(\text{TO})$  modes. At the phase transition, the disappearance of the  $[001]$  correlation due to the asymmetry of the Nb-O-Nb bond is related to the abrupt change in the value of  $k(\text{O-Nb})$  along the polar direction, and therefore to the stabilization of the ferroelectric  $A_1(\text{TO})$  component.

In order to specify the behaviour of the oxygen polarizability, calculations with a model including the temperature dependence of the soft mode are actually in progress.

#### Acknowledgments

The authors are grateful to Prof. M. Bilz and Drs W. Kress and R. Migoni for many fruitful discussions, and also to Dr G. M  trat for providing the excellent samples used in the experiments.

#### References :

1. M.D. Fontana, G Dolling, G.E. Kugel and C. Carabatos, Phys. Rev. **B20**, 3850 (1979)
2. M.D. Fontana, G. M  trat, J.L. Servoin and F. Gervais, Fifth International Meeting on Ferroelectricity, submitted to Ferroelectrics (1981)
3. R.A. Cowley, Phys. Rev. **134A**, 981 (1964)
4. R. Migoni, H. Bilz and D. B  uerle, Phys. Rev. Lett. **37**, 1155 (1976)
5. A.W. Hewat, J. Phys. C **6**, 2559 (1973)
6. M.D. Fontana, G.E. Kugel, G. M  trat and C. Carabatos, Phys. Stat. Sol. (b) **103**, 211 (1981)
7. H. Bilz, A. Bussmann, G. Benedek, H. B  ttner and D. Strauch, Ferroelectrics **25**, 339 (1980)
8. A.C. Nunes, J.D. Axe and G. Shirane, Ferroelectrics, **2**, 231 (1971)
9. A. Bussmann, H. Bilz, R. Roenspiess and K. Schwarz, Ferroelectrics, **25**, 343 (1980)

ON THE Si-O-Si BOND ANGLE IN  $\alpha$ - AND  $\beta$ -QUARTZ

B. Dorner, H. Boysen\*, F. Frey\* and H. Grimm\*\*

ILL Grenoble, France

\*Inst. f. Kristallographie, Univ. München, F.R.G.

\*\*IFF-KFA Jülich, F.R.G.

**Abstract.**— The structural change from  $\alpha$  to  $\beta$ -quartz is accompanied by an enlargement of the Si-O-Si bond angle with increasing temperature. At the same time the  $\text{SiO}_4$  tetrahedra shrink. The speculative explanation is that with increasing temperature the electron density on the Si atom adopts some d-type components. The soft mode at  $\Gamma$  and another strongly temperature dependent mode at M reflect the structural changes.

Quartz undergoes a structural phase transition of first order at  $573^\circ\text{C}$  from a trigonal  $\alpha$ -phase to the hexagonal  $\beta$ -phase. The  $\Gamma$ -point soft mode in  $\alpha$ -quartz and its temperature dependence was observed by Raman scattering /1,2/. An eigenvector determination /3/ confirmed that the mode at 6.25 THz at room temperature has the displacements as expected from the structural change /4/ for the soft mode.

Grimm and Dorner /5/ conceived a model of regular rigid  $\text{SiO}_4$  tetrahedra assuming that the tetrahedra stay undeformed at all temperatures. The  $\alpha$ -phase is produced out of the  $\beta$ -phase by rotations of the tetrahedra around two-fold axes which are parallel to the hexagonal plane. The tilt angle  $\delta$  can be interpreted as the order parameter. The order parameter connected to a first order phase transformation

$$\delta^2 = \frac{2}{3} \delta_0^2 \left[ 1 + \sqrt{1 - \frac{3}{4} \frac{T - T_0}{T_c - T_0}} \right]$$

was fitted to the structural data /4/. Here  $T_0$  is the temperature at which the phase transformation occurs. At  $T = T_c$  the coefficient of the quadratic term in a Landau expansion of the free energy goes to zero.

$\delta_0$  is the step in the order parameter which appears at  $T_0$ . There are two parameters to be fitted:  $\delta_0 = 7.3^\circ$  and  $T_0 - T_c = 10^\circ\text{C}$ . This model is very successful as it describes the structural parameters, one for Si and three for O, versus temperature very well. The components of the eigenvector of the soft mode at room temperature as determined experimentally /3/, could be calculated in perfect agreement including the coupling of the secondary order parameter. But the temperature dependence of the lattice constants  $a$  and  $c$  /6/ differs strongly from the predictions of the model, see Fig. 1.

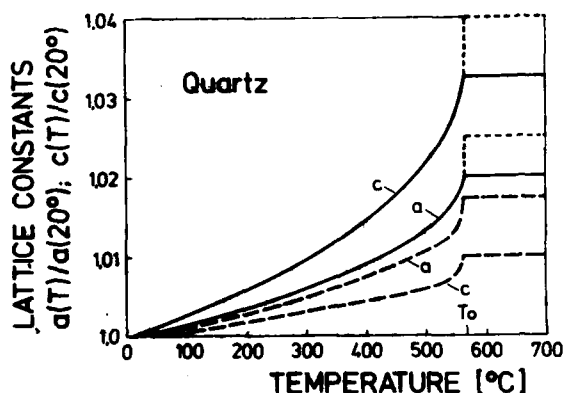


Fig. 1: Lattice expansion.  
 — model /5/ of rigid  $\text{SiO}_4$  tetrahedra, in  $\beta$ -quartz for the disordered structure, --- for the ideal  $\beta$ -phase, — ex-perimental data /6/.

Apparently the lattice expands less than predicted from the model. Note that the usual thermal expansion by anharmonicity is not considered by the model. As the structure is built up by corner connected tetrahedra, the only possible conclusion is that the tetrahedra shrink with increasing temperature. Obviously the deformation of the tetrahedra is anisotropic and much stronger for components contributing to  $c$ .

Another important feature is the bond angle (BA) Si-O-Si being  $143.6^\circ$  at room temperature and having a maximum possible within the quartz structure, with  $153.1^\circ$  in the ideal  $\beta$ -structure. The soft mode in the  $\beta$ -phase, overdamped at all accessible temperatures /3/, has an eigenvector which leaves the tetrahedra rigid and does not vary the BA. This means that adjacent tetrahedra move only perpendicular to the Si-O-Si plane with a small restoring force.

Recently we discovered another strongly temperature dependent mode at the M points /7/. It softens from 3.61 THz at room temperature to 0.82 THz in the  $\beta$ -phase. An eigenvector determination revealed that this mode in  $\beta$ -quartz leaves the  $\text{SiO}_4$  tetrahedra rigid and does not bend the BA just like the real soft mode.

Model calculations /8/ included this bond angle force (essentially a three body force) by a central force between Si-Si atoms. A calculation of the temperature dependence for the soft mode and for the mode at the M-point /8/ was performed by using the force constants as fitted at room temperature /9/ and inserting atomic positions corresponding to the structure at each temperature. The calculated modes soften with increasing temperature. An inspection of the calculated eigenvectors showed that the Si-Si displacement got smaller with increasing temperature, this means that the BA has smaller amplitudes at higher temperature. Only in the  $\beta$ -phase the two modes do not bend the BA in the Si-O-Si plane.

Very probably the Si-O-Si bonds play a dominant role in the struc-



tural changes of quartz. It has been suggested /10/ that the electron density on the Si atom may change with temperature such that from the basic  $sp^3$  hybridisation some density becomes d-type. The d-type components would build  $\pi$ -bonds to the oxygen p-electrons leading to a  $180^\circ$  BA while the  $sp^3$  hybridisation would produce  $\sigma$ -bonds leading to a BA near  $90^\circ$  if the structure would allow. This speculation explains why the BA increases to a maximum with temperature. The maximum (extremum) of the BA is connected to a higher symmetric phase. Thus there has to appear a phase transformation and as it is a displacive one, we expect a soft mode. The driving mechanism is the electron density on the Si-atom. The speculation does not explain why the  $\beta$ -phase has a slightly disordered structure /11/ with a BA =  $150.1^\circ$  rather than  $153.1^\circ$ . On the other hand this increasing contribution of  $\pi$ -bond character explains the fact that the tetrahedra shrink with increasing temperature because the  $\pi$ -bond tightens the Si-O bond.

- /1/ S.M. Shapiro, D.C. O'Shea and H.Z. Cummins; Phys. Rev. Lett. 19, 361 (1967)
- /2/ J.F. Scott; Phys. Rev. Lett. 21, 907 (1968)
- /3/ J.D. Axe and G. Shirane; Phys. Rev. B1, 342 (1970)
- /4/ R.A. Young; Air Force Office of Scientific Res. Rep. 2569 (1962)
- /5/ H. Grimm and B. Dorner; J. Phys. Chem. Solids 36, 407 (1975)
- /6/ C.A. Sorrell, H.U. Anderson and R.J. Ackermann; J. Appl. Cryst. 7, 468 (1974)
- /7/ H. Boysen, B. Dorner, F. Frey and H. Grimm; J. Phys. C 13, 6127 (1980)
- /8/ T.H.K. Barron, C.C. Huang, and A. Pasternak; J. Phys. C 9, 3925 (1976)
- /9/ B. Dorner, H. Grimm and H. Rzany; J. Phys. C, 13, 6607 (1980)
- /10/ D.W.J. Cruickshank; J. Chem. Soc. 1077, 5486 (1961)
- /11/ A.F. Wright and M. Lehmann; J. Solid St. Chem.

## DYNAMICS IN DISPLACIVE PHASE TRANSITIONS

R. Englman

Israel Atomic Energy Commission, Soreq  
Nuclear Research Center, Yavne, Israel

**Abstract.**— First passage rates of an interacting, anharmonic system of phonons (some of which are unstable, soft) are calculated as function of temperature. The classical equations of motion are amended by a non-local term representing tunnelling.

1. Introduction.— Studies<sup>(1,2)</sup> of the approach of large systems to a new configuration present pictures of a limited number of degrees of freedom (soft modes) that have several points of stability and are in interaction with other (hard) degrees of freedom or with a random force-field. The theoretical methods utilize Fokker-Planck or master-equations. Experimentally soft mode dynamics have been investigated, e.g. by Raman scattering.<sup>(3)</sup> Times of passage to the new equilibrium point<sup>(4)</sup> vary widely, between  $10^0$ - $10^8$  times inverse lattice frequencies,<sup>(5)</sup> and the factors that influence this variation are of interest.

For phonon-physics and in studies of displacive first order transitions (as in Cu or Fe-doped spinels) theories of fluctuation-induced phase-transitions are insufficiently productive since (a) they treat mainly the vicinity of the bifurcation point, whereas most of the passage time is taken up far from this point and (b) quantum mechanical tunnelling is not included in the classical studies.

2. Description.— Our treatment (which follows on a previous work<sup>(6)</sup>) is for a monatomic, anharmonic lattice which is unstable in some low-frequency modes. The modes are admixed by qxqxq-type anharmonic terms whose strengths are about .1 in units of zero point motion, the mode mixing operating among adjacent, as well as within, wave-number shells and are critical for the transition. In our computation the Brillouin zone is divided into cells, numbering up to  $10^3$ . The soft modes possess cubic terms (of strengths .02-.06) whose physical effect on the passage resembles that of a second minimum (see Fig. 1). In the equations of motion of the soft modes we add to the kinematic velocity a tunnelling term

$$v_t = (\hbar\omega/M)^{1/2} \exp[-(V_{\max}-V)/\hbar\omega] \quad (1)$$

where  $\omega$  is the (harmonic) soft mode frequency,  $M$  the atomic mass,  $V$  the local potential and  $V_{\max}$  the height of the maximum in the potential being a function of the remaining coordinates. The exponential form is exact in the WKB-approximation for a parabolic barrier.<sup>(7)</sup> Initial conditions for the modes at their minima assume a thermal distribution in the velocities squared.

3. Results.— First passage rates have been calculated for a monatomic, Debye-type lattice having dynamic properties and mean mass equal to those of MgO. As is well known,<sup>(2)</sup> the rates depend heavily on the initial conditions and emphasis is placed on fast passage conditions (leftward initial velocities). Rates shown in Fig. 2 as function of temperature  $T$  are those for soft modes occupying about 1.5% of the Brillouin zone. To test the effect of the tunnelling, Eq. (1), calculations were also made for a lattice whose mean mass is reduced by 20, i.e. for a proton lattice with the bonding properties of MgO. Down to 1.2°K ( $\sim .8 \text{ cm}^{-1}$ ) the effect of tunnelling on the transition is small but is still distinguishable below 20°K.

#### 4. References

- (1) H. Haken, Synergetics (Springer, Berlin, 1978)
- (2) R. Kubo et al. (Ed.), Nonlinear Nonequilibrium Statistical Mechanics, Kyoto Seminar in Prog. Theor. Phys. Suppl. 64 (1978)
- (3) K. Hisano and K. Toda, Solid State Commun. 27, 915 (1978)
- (4) M.I. Dykman and M.A. Krivoglas, Physica A 104A, 480 (1980)
- (5) A.D. Bruce, K.A. Müller and W. Berlinger, Phys. Rev. Letters 42, 185 (1979)
- (6) R. Englman, Chem. Phys. 58, 227 (1981)
- (7) R. Englman, D. Magnai and A. Ranfagni, (to be published).

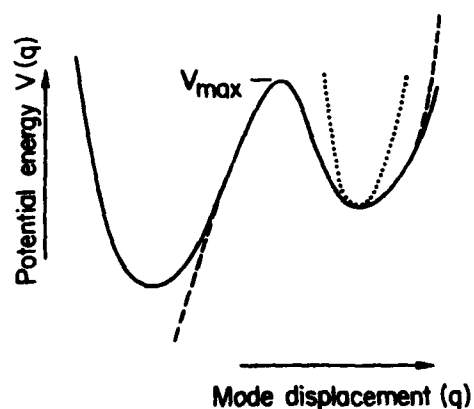


Fig. 1.- Forms of potentials used for soft modes (full curve) and hard modes (dotted curve). The broken curve is a cubic approximation to the soft-mode potential.

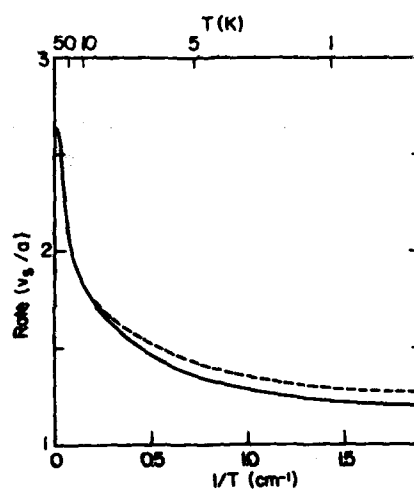


Fig. 2.- Phase transition rates (in units of sound-velocity over lattice spacing) for an unstable (mass averaged)  $\text{MgO}$ -type lattice (full line) and for the same lattice with proton-masses (drawn by broken line) in which tunnelling is perceptible.

# PHONON INDUCED ANOMALOUS RESISTIVITY IN STRUCTURAL PHASE TRANSITION OF PbSnTe

T. Suski and S. Katayama\*

*High Pressure Research Center, Polish Academy of Sciences, Warsaw, Sokołowska 29, Poland*

*\*Department of Physics, Osaka University, 1-1 Machikaneyama, Toyonaka, 560 Japan*

**Abstract.**— We report an anomalous electrical resistivity increment  $\Delta\rho$  on PbSnTe near the vicinity of the structural phase transition temperature  $T_C$ . Applying hydrostatic pressure lowers  $T_C$  and leads to a decrease of  $\Delta\rho$ . It is reasonably interpreted that  $\Delta\rho$  is due to the free carrier scattering from the soft TO phonon. The observed initial slope of  $T_C$  with increasing pressure is also discussed by using the Littlewood formula.

1. **Introduction.**— The IV-VI compound semiconductors such as (Pb,Ge,Sn)-Te alloys exhibit a structural phase transition from rocksalt structure to rhombohedrally distorted structure.<sup>1</sup> The softening of the transverse optical (TO) phonon at  $q=0$  indicates the structural instability in the small gap materials. A sequence of recent experiments have elucidated the nature of instability associated with the inter-band electron-phonon coupling.<sup>2</sup> In particular PbSnTe has attracted our attention on the "zero" gap nature as well as on the phase transition. The purpose of present paper is to report the electrical transport measurements on  $\text{Pb}_{1-x}\text{Sn}_x\text{Te}$  ( $x=0.44, 0.54, 0.80$  and  $0.86$ ) from 4.2 to 150 K by applying hydrostatic pressure. From the anomalous portion of resistivity near  $T_C$  under pressure, we explore the pressure dependence of  $T_C$  as well as the free carrier scattering mechanism giving rise to  $\Delta\rho$ .

2. **Experiments.**— Measurements of Hall coefficient  $R_H$  and resistivity  $\rho$  were made for solution grown single crystal by using the technique of helium gas compression to produce the hydrostatic pressures. Details of crystal characterization were given elsewhere.<sup>3,4</sup>

3. **Results and Analysis.**— Since Kobayashi et al.<sup>5</sup> found a resistivity anomaly near 100 K in SnTe, many authors have investigated the anomalous increase in  $\rho(T)$  on PbSnTe<sup>3,6</sup> and PbGeTe<sup>6</sup> near  $T_C$ . Suski et al.<sup>7</sup> have observed  $\Delta\rho$  in PbSnTe by applying pressure. In Fig.1, as a typical example, we show  $\rho(T)$  vs. temperature ( $T$ ) in  $\text{Pb}_{0.56}\text{Sn}_{0.44}\text{Te}$  with carrier concentration  $p=2.3 \times 10^{19} \text{ cm}^{-3}$  at four different pressures.

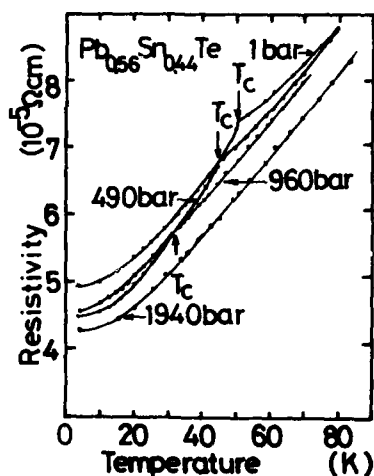


Fig. 1 :  $\rho$  vs.  $T$  at four pressures.

There appears a prominent cusp-like anomaly  $\Delta\rho$  for each pressure. The lowering peak shift with increasing pressure corresponds to decrease of  $T_c$ . According to earlier theoretical analysis on  $\text{SnTe}$ <sup>8</sup>,  $\Delta\rho$  in  $\text{PbSnTe}$  may also be due to the carrier scattering from the soft TO mode. Explicit form of resistivity by the TO phonon scattering  $\rho_{\text{TO}}$  is given by<sup>8</sup>

$$\rho_{\text{TO}} = \frac{2\hbar^3 k_F^2 \pi^2}{15 p^2 e^2 k_B T} N(E_F)^2 \langle (m_{\text{TO}})^2 \rangle \int_0^2 d\eta n^3(\omega_{\text{TO}}(k_F \eta)) [1 + n(\omega_{\text{TO}}(k_F \eta))], \quad (1)$$

where  $\omega_{\text{TO}}(q)$  is the TO phonon frequency as  $\omega_{\text{TO}}^2(q) = \omega_{\text{TO}}^2(T) + Aq^2$ ,  $k_F$ ,  $N(E_F)$  and  $m_{\text{TO}}$ , respectively, are the Fermi wave number, the density of state at the Fermi level  $E_F$  and the matrix element involving the inter-band electron-phonon deformation potential  $\tilde{\epsilon}_{\text{cv}}$ . If we used a high temperature expression for the Planck distribution function as  $n(\omega) = k_B T / \hbar \omega$

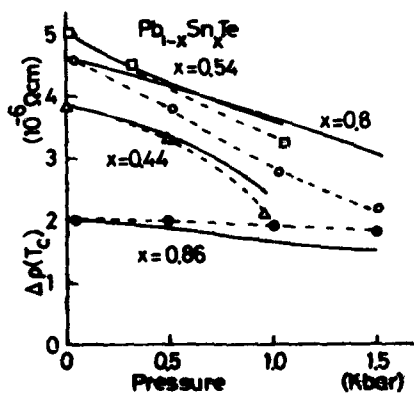


Fig. 3 :  $\Delta\rho(T_c)$  vs. pressure.

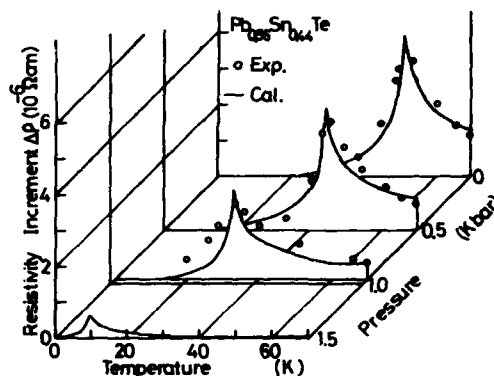


Fig. 2 : Temperature dependence of  $\Delta\rho$  at four pressures. Solid lines and  $\circ$  denote calculations and experiments which are obtained by subtracting the smooth background from  $\rho$  in Fig. 1.

in Eq.(1),  $\rho_{\text{TO}}$  is proportional to  $T$ .

Figure 2 shows the calculated  $\rho_{\text{TO}}$  by Eq. (1) and the experimental points from Fig.1 as a function of  $T$  at four pressures on  $\text{Pb}_{0.56}\text{Sn}_{0.44}\text{Te}$ . The value of  $|\tilde{\epsilon}_{\text{cv}}|/\sqrt{A}$  is estimated to be  $2.44 \times 10^{-6} \text{ eV cm}^{-1} \text{ sec}$  which is obtained by fitting  $\rho_{\text{TO}}$  with  $\Delta\rho$  at 1 bar. The overall feature in  $\Delta\rho$  is well reproduced by  $\rho_{\text{TO}}$  so that  $\Delta\rho$  mainly comes from the soft mode scattering. Note that the cusp-like anomaly around  $T_c$  in  $\rho_{\text{TO}}$  is produced by the mean field behavior of  $\omega_{\text{TO}}$  as

AD-A126 574

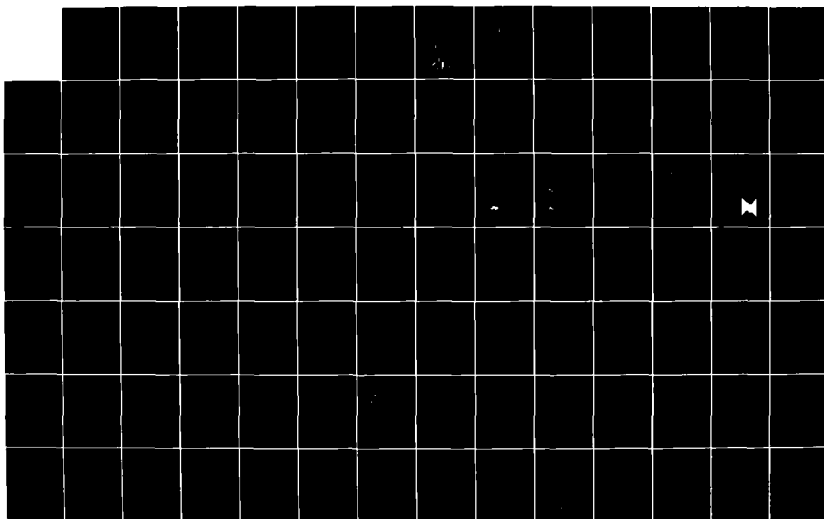
INTERNATIONAL CONFERENCE ON PHONON PHYSICS 31 AUGUST-3  
SEPTEMBER 1981 BLOOMINGTON INDIANA(U) INDIANA UNIV AT  
BLOOMINGTON W E BROW DEC 81 ARO-17340.1-PH  
MIPR-ARO-43-80

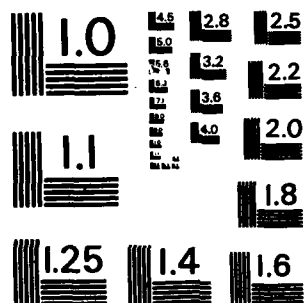
9/10

UNCLASSIFIED

F/O 20/2

NL





MICROCOPY RESOLUTION TEST CHART  
NATIONAL BUREAU OF STANDARDS-1963-A



$\omega_{TO}^2 = \alpha(T - T_C)$  for  $T > T_C$  and  $\omega_{TO}^2 = 2\alpha(T_C - T)$  for  $T < T_C$ . In Fig.3, we plotted  $\Delta\rho$  at  $T_C$ ;  $\Delta\rho(T_C)$  vs. pressure for all samples. The solid curves denote the calculations by using  $\rho_{TO}(T_C) = gT_C$  with the observed values of  $T_C$ .  $g$  is adjusted for each curve to agree with  $\Delta\rho$  at 1 bar. We ignored the pressure dependence of the energy gap  $E_g$ , effective mass  $m^*$  and  $A$  which give  $g$  in some combination. This approximation may be permitted as long

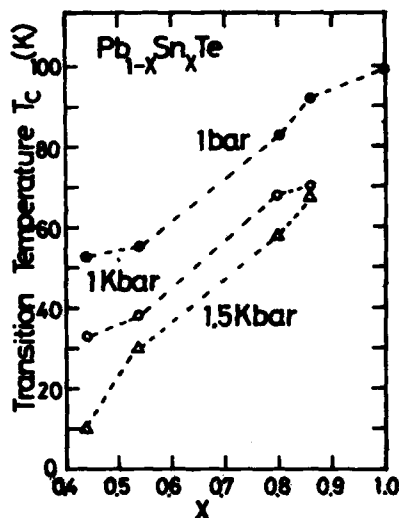


Fig.4:  $T_C$  vs.  $x$  under pressure.

as we are concerned with the carrier concentrations higher than  $10^{19} \text{ cm}^{-3}$  as well as low pressure less than 1 Kbar. We can see a good correlation between data and calculations. There appears a small discrepancy above 0.5 Kbar which may be attributed to our ignoring of the pressure dependence of  $E_g$ ,  $m^*$  and  $A$ .

In Fig.4, we summarized  $T_C$  vs. tin compositions  $x$  at 0.001, 1 and 1.5 Kbar in the four compositions with adding  $T_C = 98.5 \text{ K}$  in SnTe at 1 bar.<sup>5</sup> When we do not have data just at 1 and 1.5 Kbar, the values estimated by inter- and extrapolation are plotted. The observed initial slope of  $T_C$  with increasing pressure are

estimated to be -14.5, -15.1, -13.4 and -15.0 K/Kbar for  $x=0.44$ , 0.54, 0.80 and 0.86, respectively. According to the Littlewood formula<sup>9</sup>,  $dT_C/dp$  for  $x=0.44$ , 0.54, 0.80 and 0.86, respectively, are -12.5, -11.6, -11.8 and -11.9 K/Kbar. The trend and order of magnitude agree well with experiments.

In conclusion we reemphasize that the observed behavior of  $\Delta\rho$  under pressure in PbSnTe near  $T_C$  is well understood by assuming the soft TO phonon scattering with  $\omega_{TO}$  described by the mean field scheme.

The important contribution of Dr.M.Baj is gratefully acknowledged. One of us (S.K.) thanks Prof.K.Murase for his fruitful discussions. We are also indebted to Drs. K.L.I.Kobayashi and K.F.Komatsubara for supplying specimens.

#### References

1. See the recent article by K.Murase, J.Phys.Soc.Jpn., **49** Suppl.A (1980) 725, and the references contained therein.
2. H.Kawamura, Proc.Int.Summer School on Narrow Gap Semiconductors, Nimes 1979 (Berlin, Springer Verlag, 1980).
3. K.L.I.Kobayashi, Y.Kato and K.F.Komatsubara, Prog.Crystal Growth Charact. **1** (1978) 117.
4. T.Suzuki, L.Dmowski and M.Baj, Solid State Commun., **38** (1980) 59.
5. K.L.I.Kobayashi, Y.Kato, Y.Katayama and K.F.Komatsubara, Solid State Commun., **17** (1975) 875.
6. S.Takaoka and K.Murase, Phys. Rev., **B20** (1979) 2823.
7. T.Suzuki, M.Baj, W.Zuczkowski, K.L.I.Kobayashi and K.F.Komatsubara, Solid State Commun., **30** (1979) 77.
8. S.Katayama and D.L.Mills, Phys. Rev., **B22** (1980) 336.
9. P.B.Littlewood, J. Phys. C, Solid St. Phys., **13** (1980) 4875.

# A RAMAN STUDY OF THE STRUCTURAL PHASE TRANSITION IN DISORDERED $\text{KMn}_{0.85}\text{Ni}_{0.15}\text{F}_3$

D.J. Lockwood and G.J. Coombs\*

*Physics Division, National Research Council, Ottawa, Canada K1A 0R6*

*\*Physics Department, University of New South Wales, Kensington, Australia*

**Abstract.**—  $\text{KMn}_{1-x}\text{Ni}_x\text{F}_3$  has been studied to investigate the effect of disorder on the structural phase transition at 186 K in  $\text{KMnF}_3$ . This transition was found at ~130 K in  $\text{KMn}_{0.85}\text{Ni}_{0.15}\text{F}_3$  but was not observed in other crystals having  $x > 0.5$ . Disorder mainly affects  $T_c$  and not the phonon behaviour. Present results are consistent with a linear extrapolation of  $T_c$  to 0 K at  $x = 0.5$ .

1. **Introduction.**— The presence of defects can substantially alter structural phase transition temperatures. Although the origins of this change are poorly understood it is now believed that defects influence phase transitions in different ways depending on the sign of the specific heat exponent.<sup>1</sup> We have investigated the disordered system  $\text{KMn}_{1-x}\text{Ni}_x\text{F}_3$  where the critical properties should be the same as those of pure  $\text{KMnF}_3$ , which possesses two structural phase transitions.<sup>2</sup>

2. **Experiment and Results.**— Raman measurements were performed on several alloys following the procedure given in Ref. 3. The incident and scattered beams were directed along the cubic principal axes (X and Y, say).

A structural phase transition was observed in only one ( $x = 0.15$ ) of the mixed crystals studied at temperatures  $> 5$  K. Low temperature spectra for this crystal are shown in figure 1. Spectra in off-diagonal polarisations were essentially identical because of domain induced mixing. The broad peaks near 330 and 145  $\text{cm}^{-1}$  arise from two-magnon excitations<sup>3</sup> while those to lower frequency (near 25 and 70  $\text{cm}^{-1}$ ) are probably two-phonon bands. The narrow lines are assigned to first-order phonon scattering (see table 1). The 127 and 238  $\text{cm}^{-1}$  lines in off-diagonal polarisation are too strong to be attributable to depolarisation of lines at similar frequencies in the (ZZ) spectrum. All of these lines diminish in intensity and eventually vanish with increasing temperature as is shown, for example, in figure 2. These results indicate  $T_c = 130 \pm 5$  K. The peak frequency of the soft mode at 17.4  $\text{cm}^{-1}$  renormalises relatively slowly at first with increasing temperature but is overdamped by 60 K (see figure 5(a) of Ref. 3). This, together with the low frequency, made it difficult to extract a detailed temperature dependence. The remaining modes shift little in frequency with increasing temperature.

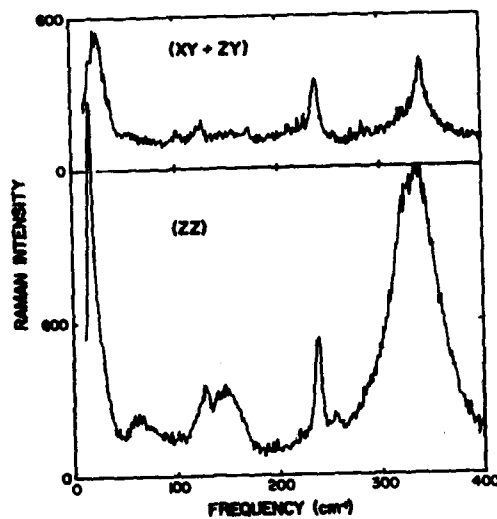


Fig. 1: Raman spectrum of  $\text{KMn}_{0.85}\text{Ni}_{0.15}\text{F}_3$  recorded at 6 K with a resolution of  $2.8 \text{ cm}^{-1}$ .

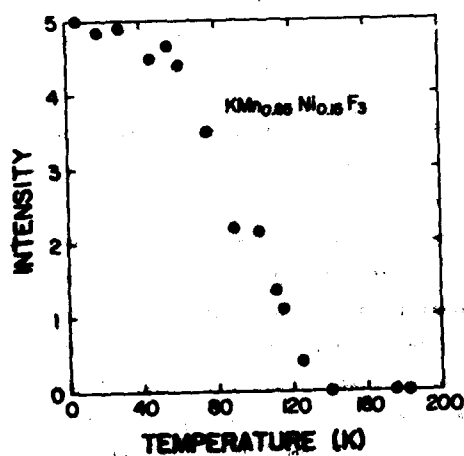


Fig. 2: Temperature dependence of the  $230 \text{ cm}^{-1}$  (ZZ) mode intensity.

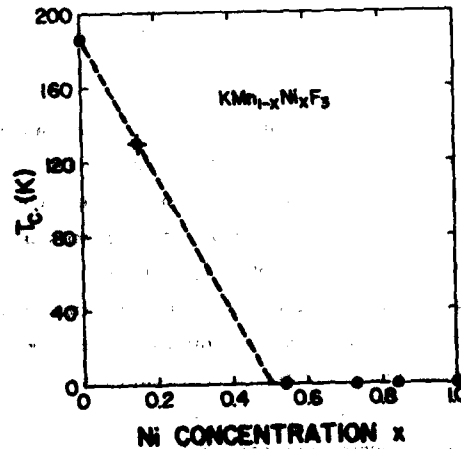


Fig. 3: Concentration dependence of  $T_c$ .

Table 1. Assignments and peak frequencies ( $\text{cm}^{-1}$ ) of Raman active modes in tetragonal  $\text{KMn}_{1-x}\text{Ni}_x\text{F}_3$ .

Assignment	$x = 0^3$ (100 K)	$x = 0.15$ (6 K)
$E_g$	20.5 (ZX)	-
$A_{1g}$	62 (ZZ)	17.4 (ZZ)
$E_g$	116 (ZX)	127 (XY+ZY)
$B_{2g}$	124 (YY)	127.9 (ZZ)
$E_g$	227.5 (ZX)	238 (XY+ZY)
$B_{2g}$	231 (YY)	238.2 (ZZ)
$B_{1g}$	327.5 (YX)	340.5 (XY+ZY)

3. Discussion.— Comparison with results obtained from pure  $\text{KMnF}_3$  (see table 1) indicates that the 130 K phase transition in  $\text{KMn}_{0.85}\text{Ni}_{0.15}\text{F}_3$  derives from the same cubic-tetragonal phase change associated with condensation of the cubic-phase  $E_{15}$  modes.<sup>3</sup> The intensity of the hard mode at  $238 \text{ cm}^{-1}$  has a similar reduced temperature dependence to that found for the analogous line in  $\text{KMnF}_3$ <sup>3</sup> and provides a measure of the order parameter. The  $A_{1g}$  soft modes in  $\text{KMnF}_3$  and  $\text{KMn}_{0.85}\text{Ni}_{0.15}\text{F}_3$  also have a similar temperature dependence. Furthermore, the hard and soft mode damping for  $x = 0.15$  is comparable with that found for  $x = 0$ . Thus the critical properties of the mixed crystal are the same as those of pure  $\text{KMnF}_3$ , as predicted by theory. The main effect of disorder appears as a lowering of the phase transition temperature and a smaller anisotropy in  $B_{2g}$  -  $E_g$  mode frequencies, implying an increased resistance against  $E_{15}$  mode softening. Present results are consistent with a linear extrapolation of  $T_c$  from 186 K at  $x = 0$  to 0 K at  $x = 0.5$ , as is shown in figure 3.

Acknowledgment.— The experimental work was performed at the Edinburgh University Physics Department with support from the SRC and the US Army Office of Scientific Research.

#### References

1. A.B. Harris, J. Phys. C **7**, 1671 (1974).
2. D.J. Lockwood and B.H. Torrie, J. Phys. C **7**, 2729 (1974).
3. D.J. Lockwood, G.J. Coombs and R.A. Cowley, J. Phys. C **12**, 4611 (1979).

# "NON-CENTRAL" PEAKS IN LIGHT SCATTERING SPECTRA OF LITHIUM TANTALATE AND QUARTZ AT PHASE TRANSITION

V.S. Gorelik, B.S. Umarov\* and M. Umarov\*

P. Lebedev Physical Institute, Moscow, U.S.S.R.

\*S. Umarov Physicotechnical Institute, Dushanbe, U.S.S.R.

In a number of works /1-3/ anomalous increasing of the central peak intensity was found. One of the reasons of this anomaly may be a dynamical effect /4,5/, caused by the softening of one of the vibrations of crystal lattice, responsible for the structural phase transition in the crystal.

To separate these effects the study of the temperature dependence of noncentral peak ( $\omega' = \omega_0 - \Omega$ , where  $\omega_0$  is exciting light frequency,  $\Omega$  is frequency shift) intensity has been carried out in the present work. The value of the frequency shift  $\Omega$  remained unchanged during scattered light registration by the Raman spectrometer /6/. So the gratings of the spectrometer are in a fixed position when the temperature is changed. We call spectra obtained by this method isofrequency spectra.

Analysis of the RS isofrequency dependence may be carried out using the general theory of light scattering near the second order phase transition point /4,5/. In one soft mode approximation in this theory the following expression for the RS spectral intensity was obtained:

$$J(\Omega, T) = I(T) \frac{\Gamma \Omega_0^2}{\Gamma^2 (\Omega_0^2 - \Omega^2)^2 + \Gamma^2 \Omega^2} \quad (1)$$

where  $J(\Omega, T)$  is the observed spectral intensity,  $I(T)$  is the integral scattering intensity,  $\Omega_0$  and  $\Gamma$  are corresponding soft mode parameters,  $T$  is the crystal temperature. Below the transition point expression (1) may be written as follows:

$$i(\Omega, X) = \frac{2A_0 |X| \Gamma}{[2A_0 |X| - \Omega^2]^2 + \Gamma^2 \Omega^2} \quad (2)$$

Here,  $A_0$  is the corresponding coefficient in the thermodynamical potential decomposition according to the order parameter,  $X = \Theta - T$ ,  $\Theta$  is phase transition temperature; besides, in (2) instead of the

observed spectral intensity  $I(\Omega, X)$  reduced spectral intensity is used:

$$i(\Omega, X) = K \frac{I(\Omega, T)}{T} \quad (3)$$

where  $K$  is some coefficient independent of the temperature.

Fig. 1 shows the calculated results of the RS isofrequency dependence according to (2), obtained for the frequency values  $\Omega = 1, 3, 5$  and  $10 \text{ cm}^{-1}$  for certain values of the parameters  $A_0$  and  $\Gamma$ . This choice of the parameters corresponds to the strongly overdamped soft vibration for  $X \leq \frac{\Gamma^2}{A_0} = 20\text{K}$ . As one can see from Fig. 1 dependencies under discussion have a well-expressed maximum,  $X_0$  co-ordinate of which tends to zero when  $\Omega$  decreases. At the same time intensity of the maximum  $i(X_0)$  increases and the width of the corresponding contours decreases (see Fig. 1). Experimental results of the isofrequency

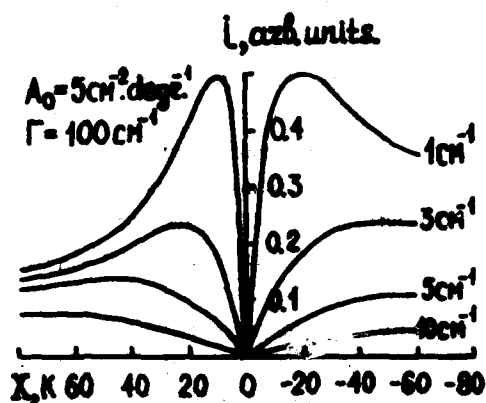


Fig. 1. Isofrequency dependencies, calculated according to (2) for frequency values  $\Omega = 1, 3, 5$  and  $10 \text{ cm}^{-1}$  when  $A_0 = 5 \text{ cm}^{-2} \text{ degree}^{-1}$  and  $\Gamma = 100 \text{ cm}^{-1}$ , where  $X = \Theta - T$ ,  $\Theta$  is transition temperature.

cy temperature dependence  $I(\Omega, T)$  in the lithium tantalate and quartz crystals are shown in Fig. 2 and Fig. 3. In both cases the increase of

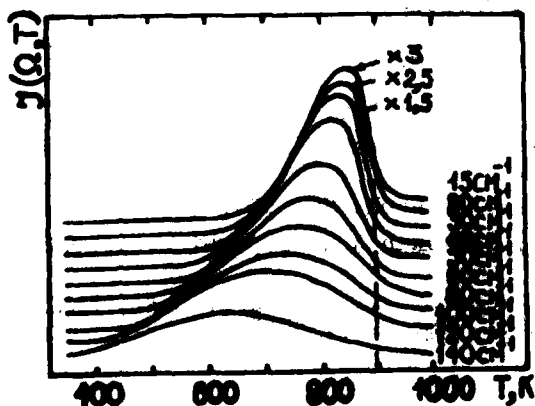


Fig. 2. Observed isofrequency dependencies of RS intensity  $I(\Omega, T)$  in lithium tantalate crystals;  $\Theta = 898\text{K}$ .

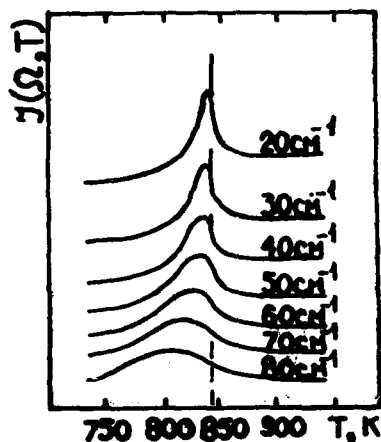


Fig. 3. Observed isofrequency dependencies of RS intensity  $J(\Omega, T)$  in quartz crystals;  $\Theta = 846\text{K}$ .

the scattering intensity is observed when the crystal temperature approaches the phase transition point. Maximum of the intensity is observed at  $T \neq \Theta$ ; the less is  $\Omega$  the nearer to the transition point is the position of maximum (in Fig. 2, 3 shown on the right). Beside this, at the phase transition point in quartz additional sharp maximum is observed for small values  $\Omega$ . This maximum appears to be of static origin. On the whole, the dependencies observed are in agreement with theoretical values (Fig. 1) for certain values of  $\Lambda_0$  and  $\Gamma$  parameters.

Thus, the study of the isofrequency Raman scattering spectra allows to reveal dynamical effects, responsible for the scattered light intensity increasing and to obtain quantitative information on soft mode parameters in the direct proximity to the phase transition point in the crystal.

#### REFERENCES

1. Yakovlev I.A., Mikheeva L.M., Velichkina T.S. Doklady AN SSSR, **107**, 675, 1956.
2. Shapiro S.M., Cummins H.Z. - Phys. Rev. Lett., 1968, v. 21, p. 1578.
3. Lyons K.B., Fleury P.A. In light Scattering in Solids. Plenum Press, New York, 1979, p. 357.
4. Ginsburg V.L. Uspekhi Fizicheskikh nauk, **77**, 621, 1962.
5. Ginsburg V.L., Levanyuk A.P., Solovyan A.A. Uspekhi Fizicheskikh nauk, **130**, 614, 1980.
6. Gorelik V.S., Ivanova S.V., Kuchezuk I.P., Strukov B.A., Khalesov A.A. - Sol. St. Phys. (Soviet), **15**, 2297, 1976.

# RAMAN SCATTERING STUDY OF LOW FREQUENCY PHONON POLARITONS IN SEVERAL CRYSTALS

S. Kojima and T. Nakamura\*

*Institute of Applied Physics, University of Tsukuba, Sakura, Ibaraki 305, Japan*

*\*The Institute for Solid State Physics, The University of Tokyo, Roppongi, Minato-ku, Tokyo 106, Japan*

**Abstract.**- Dispersion relations of low-frequency phonon polaritons have been investigated by the near-forward Raman scattering technique. The results of measurements are given for the crystals  $\text{Sr}_2\text{Nb}_2\text{O}_7$ ,  $\text{LiTaO}_3$  and  $\text{Gd}_2(\text{MoO}_4)_3$ .

**1. Introduction.**- Dispersion relations of low-frequency phonon polaritons in the crystals, which undergo structural phase transitions, give important information about the mechanism of the transitions. However, in fact, measurements of low-frequency polaritons require observations of near-forward Raman scattering at very small angles. So polariton peaks are obscured by the wing of the Rayleigh line. For such a problem, the iodine filter technique has been used to reject the Rayleigh component. In that case complicated compensations are required. On the other hand, the recent development of concave holographic gratings enables a double monochromator to improve the stray light rejection up to  $10^{-14}$  (usually  $10^{-10} \sim 10^{-12}$ ). In this work, low-frequency polaritons have been measured by the combination of the double monochromator and the optical system designed for this purpose.

**2. Experimentals.**- The samples were excited by an incident beam at 5145Å from Ar ion laser. The scattered light from the samples was selected by a stopper with two cocentric arc-shaped symmetric holes and was collected onto the entrance slit of a double monochromator (Jobin Yvon Ramanor Hg.2S). The detector used was cooled photomultiplier (HTV-R649S) and the output current was analysed with the usual photon counting technique.

## 3. Results.

### 3-1. $\text{Sr}_2\text{Nb}_2\text{O}_7$

Strontium Niobate  $\text{Sr}_2\text{Nb}_2\text{O}_7$  is one of the  $\text{A}_2\text{B}_2\text{O}_7$  type oxide compounds with a perovskite slab structure. It undergoes a ferroelectric phase transition at about 1342°C with a point group change from mm to



mm<sup>2</sup> and has a spontaneous polarization along the c-axis.<sup>1</sup> At about 215°C, another transition occurs and transforms into an incommensurate phase modulated with the wave vector  $\vec{k} = \pm(1-\delta)\frac{1}{2}\vec{a}^*$  (where  $\vec{a}^*$  is a reciprocal lattice vector).<sup>2</sup>

As to the lattice instability, Kojima et al. has found an amplitude mode responsible for the normal-incommensurate phase transition at 215°C by the backward Raman scattering technique.<sup>3</sup> Namely, a mode located at 44cm<sup>-1</sup> in b(cc) $\bar{b}$  scattering spectra shows softening at first with increasing temperature from room temperature. Next, level repulsion and intensity transfer take place between the soft mode and another mode located at 28cm<sup>-1</sup>. With further increasing temperature, the lower mode begins to soften toward 215°C.

In the present work, near-forward Raman scattering measurements have been made for studying  $A_1(z)$  polaritons. In the low frequency region, the polariton effect has been observed for the amplitude mode located at 44cm<sup>-1</sup> and the mode located 54cm<sup>-1</sup> at b(cc)b+ $\Delta$ a scattering geometry. As the peak at 54cm<sup>-1</sup> approaches to the peak at 44cm<sup>-1</sup> in the spectra, an intensity transfer between the two modes occurs. Then the peak at 44cm<sup>-1</sup> tends to zero in decreasing q. No anomaly of polariton line shapes induced by a coupling to another lower mode at 28cm<sup>-1</sup> has been detected, although, in the case of temperature dependence, anti-crossing between the mode 44cm<sup>-1</sup> and the mode at 28cm<sup>-1</sup> occurs. The absence of anti-crossing in polariton dispersion curves suggests that the mode at 28cm<sup>-1</sup> of which oscillator strength is extremely weak does not interact with photon.

The high-temperature behavior of the low frequency parts in b(cc) $\bar{b}$  scattering spectra has also been investigated. The remarkable softening and the line-broadening of the mode at 54cm<sup>-1</sup> have been clearly observed in approaching the transition point 1342°C.

### 3-2. LiTaO<sub>3</sub>

Litium Tantalate LiTaO<sub>3</sub> is one crystal of technological importance. It undergoes a ferroelectric phase transition at about 620°C. Recently, Penna et al. reported the anomalous leveling in the low wave number region of the  $A_1(z)$  polaritons, which was attributed to finite propagation lengths of polaritons.<sup>4</sup> The propagation length of polaritons was introduced by Penna et al. and is determined by the destruction of polaritons due to domain wall distributions.

The lowest branch of the  $A_1(z)$  polaritons has been accurately measured. Polariton peaks were clearly observed in the region  $\omega_p > 14\text{cm}^{-1}$ . The obtained relation  $\omega_p$  vs. q is nearly straight in the

region  $q > 100\text{cm}^{-1}$  and such an effect reported by Penna et al. has not been observed.

### 3-3. $\text{Gd}_2(\text{MoO}_4)_3$

Gadolinium Molybdate  $\text{Gd}_2(\text{MoO}_4)_3$  undergoes a ferroelectric phase transition at about  $160^\circ\text{C}$ .<sup>5</sup> Neutron scattering studies have shown that above  $T_c$  there is a doubly degenerate soft phonon at Brillouin zone-boundary (M point) associated with the transition. Fleury reported a soft mode with  $A_1(z)$  symmetry at about  $46\text{cm}^{-1}$  at room temperature.<sup>6</sup> He found by the single damped oscillator fitting that the temperature dependence of the mode frequency is not remarkable, however, the line-width of the mode increases rapidly toward  $T_c$  with increasing temperature.

In the present study, the polariton effect for the soft mode has been investigated at room temperature. Near-forward Raman scattering measurements have been made at  $a(cc)a+\Delta b$  geometry. With decreasing the polariton vector  $q$ , the anomalous line-broadening of the polaritons at about  $46\text{cm}^{-1}$  has been observed. The result suggests the strong frequency dependence of the damping factor of the soft mode.

The detailed experimental procedure and analysis will be published elsewhere.

### REFERENCES

1. S.Nanamatsu, M.Kimura and T.Kawamura, J. Phys. Soc. Jpn. **38** (1975) 817
2. N.Yamamoto, K.Yagi, G.Honjo and M.Kimura, J. Phys. Soc. Jpn. **48** (1980) 185
3. S.Kojima, K.Ohi, M.Takashige, T.Nakamura and H.Kakinuma, Solid State Commun. **31** (1979) 755
4. A.F.Penna, S.P.S.Porto and E.Wiener - Avnear, Solid State Commun. **23** (1977) 377
5. H.J.Brochrdt and P.E.Bierstedt, Appl. Phys. Lett. **9** (1966) 50
6. P.A.Fleury, Solid State Commun. **8** (1970) 601

SOFT PHONONS AND MAGNETIC ORDERING IN THE  $\gamma$ -PHASE TRANSITION METAL ALLOYS  $\text{Fe}_{1-x}\text{Pd}_x$ M. Sato<sup>\*\*</sup>, B.H. Grier<sup>\*</sup>, S.M. Shapiro<sup>\*</sup> and H. Miyajima<sup>\*\*</sup><sup>\*</sup>Brookhaven National Laboratory, Upton, New York 11973, U.S.A.<sup>\*\*</sup>The Institute for Solid State Physics, the University of Tokyo, Roppongi, 7-22-1, Minato-ku, Tokyo 106, Japan

**Abstract.** - Neutron inelastic scattering measurements have been performed on two single crystals of the thermally quenched  $\gamma$ -phase (fcc) alloy,  $\text{Fe}_{1-x}\text{Pd}_x$  with  $x = 0.28$  and  $x = 0.37$ . The  $x = 0.28$  sample which orders ferromagnetically at  $T_C = 575$  K exhibits a smeared structural transition into an fct phase near  $T_M = 265$  K. An anomalous dispersion of the  $[\bar{1}10]\text{TA}_1$  branch due to the decrease of the phonon energy around the  $\Gamma$  point develops below  $T_C$ . As the temperature decreases, the branch decreases in energy. The anomalous part of the elastic constant,  $\Delta(C_{11}-C_{12})/2$ , follows the same temperature dependence as the square of the magnetization. On the  $x = 0.37$  sample which has no structural transition, the phonon anomaly is much weaker. For both crystals the other branches exhibit normal behavior.

The iron-based Invar alloys,  $\text{Fe}_{1-x}\text{Ni}_x$ ,  $\text{Fe}_{1-x}\text{Pt}_x$ , and  $\text{Fe}_{1-x}\text{Pd}_x$  undergo a martensitic fcc to bcc first-order phase transformation at temperature  $T_M$  well below the magnetic ordering temperature  $T_C$ . The lattice dynamics of  $\text{Fe}_{1-x}\text{Ni}_x$  and  $\text{Fe}_{1-x}\text{Pt}_x$  alloys have been extensively studied by ultrasonic<sup>1,2</sup> and inelastic neutron scattering techniques<sup>3,4</sup> with the goal of understanding the relationship between the Invar properties, the magnetization  $M$  and the martensitic transition. In Haensch's ultrasonic study of  $\text{Fe}_{1-x}\text{Ni}_x$  and  $\text{Fe}_3\text{Pt}$ <sup>2</sup> he observed an anomalous decrease of the elastic constants  $C_{44}$  and  $\frac{1}{2}(C_{11}-C_{12})$ , which has the same temperature dependence as  $M^2$ . This was explained as due to a strain dependent exchange coupling in the Heisenberg spin system. Endoh et al.<sup>4</sup> also observed an anomalous behavior of  $\frac{1}{2}(C_{11}-C_{12})$  in  $\text{Fe}_{1-x}\text{Ni}_x$  by neutron scattering measurements, but emphasized that the anomalous part of  $\frac{1}{2}(C_{11}-C_{12})$  varies linearly in  $M$ . Their explanation was based more on the dynamical response of the conduction electrons to the strain.

Recent measurements<sup>5,6</sup> on  $\text{Fe}_{1-x}\text{Pd}_x$  alloys have shown that another phase, a face-centered tetragonal (fct) phase, exists between the fcc and bcc phases. In this paper, we report on the lattice dynamics of  $\text{Fe}_{1-x}\text{Pd}_x$  studied by inelastic neutron scattering and show that the anomalous part of  $\frac{1}{2}(C_{11}-C_{12})$  follows the temperature dependence of  $M^2$ .

The measurements were performed on two single crystals of  $\text{Fe}_{1-x}\text{Pd}_x$  with  $x = 0.37 \pm 0.01$  (crystal 1) and  $x = 0.28 \pm 0.01$  (crystal 2). The concentration of crystal 1 is such that it does not exhibit any structural phase transformation below the Curie point. Crystal 2 exhibits an fcc to fct transition near  $T_M = 265$  K but because of concentration gradients the transition is smeared out over 35 K. In addition, a

<sup>\*</sup>On leave from the Institute for Solid State Physics, The University of Tokyo, 7-22-1, Roppongi, Minato-ku, Tokyo 106, Japan

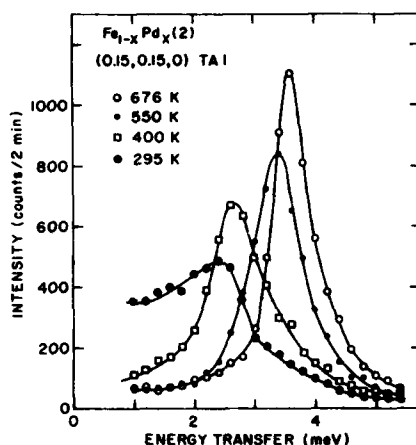


Fig. 1. Examples of the observed profiles of the  $[\zeta\zeta 0]$ TAI soft phonon branch.

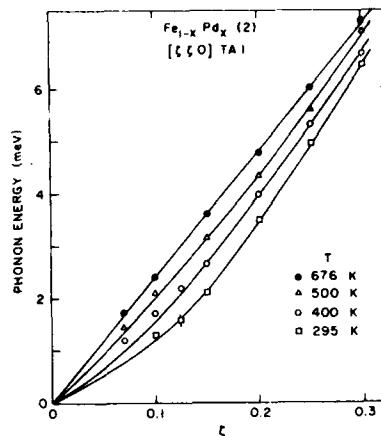


Fig. 2. Dispersion of the  $[\zeta\zeta 0]$ TAI phonon branch at various temperatures.

bcc phase also appears at lower temperatures. Because of this, it was not possible to study any of the details of the critical dynamics associated with the martensitic transition near  $T_M$ .

Fig. 1 shows the observed spectra of the  $[\zeta\zeta 0]$ TAI phonons for  $\zeta = 0.15$  measured at several temperatures. This branch corresponds to the elastic constant  $\frac{1}{2}(C_{11}-C_{12})$ . At  $T = 676$  K, which is greater than  $T_c = 575$  K, the spectrum is symmetric and relatively narrow. As  $T$  is lowered, the frequency decreases and the linewidth increases. This is opposite to that expected from normal anharmonic processes. The small  $q$  portion of the dispersion curve for this branch is shown in Fig. 2. Above  $T_c$ , the dispersion curve is linear. As  $T$  decreases, an anomalous upward curvature develops.

We can compare the anomalies in  $\frac{1}{2}(C_{11}-C_{12})$  to the magnetization by defining the quantity  $\delta_\zeta^2 = \frac{\omega^2(T > T_c) - \omega^2(T)}{\omega^2(T > T_c)}$  where  $\omega(T)$  is the  $[\zeta\zeta 0]$ TAI phonon energy. The extrapolation of  $\delta_\zeta^2$  to  $\zeta=0$ ,  $\delta^2$ , is the amount that the elastic constant changes below  $T_c$ . Fig. 3 shows the behavior of  $\delta^2$  as a function of temperature. This is compared with  $M(T)$  and  $M^2(T)$  and it can be seen that the anomalous contribution to  $\frac{1}{2}(C_{11}-C_{12})$  has the same temperature dependence as  $M^2(T)$ . This agrees with the results of Hausch for  $Fe_{1-x}Ni_x$  and  $Fe_3Pt$ , but differs from those of Endoh et al. on  $Fe_{0.65}Ni_{0.35}$  where  $\delta^2 \sim M(T)$ .

When the quantity  $\delta^2$  approaches 1, the elastic constant  $\frac{1}{2}(C_{11}-C_{12})$  goes to 0. In Fig. 3, the extrapolation of  $\delta^2$  to unity occurs at a temperature very near the martensitic transition temperature. This implies that the coupling to the magnetization which is responsible for the phonon softening is intimately related to the driving mechanism of the fcc-fct transition. Evidence to support this comes from the fact that in crystal 1,  $x = 0.37$ , no martensitic (fcc-fct) transition occurs and the anomalous phonon behavior is much weaker.

No significant phonon anomaly has been observed in the other branches for either crystal. In both crystals, we observed a large increase of the linewidth of

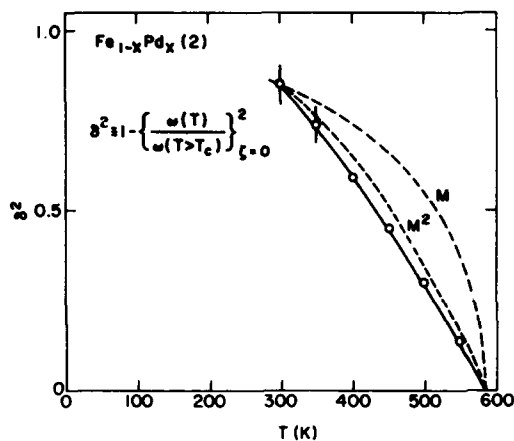


Fig. 3. The amount of the softening of the elastic constant  $1/2(C_{11}-C_{12})$  normalized by the values above  $T_c$  is shown. This is determined by the extrapolation of  $\delta^{-2} = [1 - \omega^2(T)/\omega^2(T_c)]^{-1}$  to  $\zeta=0$ . The temperature dependence of  $M$  and  $M^2$  is shown by the broken lines.

the  $[\zeta\zeta 0]$  TA1 phonons as  $T$  decreases below  $T_c$ . This cannot be explained by a macroscopic inhomogeneity of  $x$ . However a coupling of the phonons to some other fluctuations, such as spin fluctuations or charge density waves, can explain the  $T$  and  $q$  dependences of the linewidth.<sup>7</sup>

The detailed study of the linewidth remains a future problem.

**Acknowledgments** - The authors are indebted to M. Matsui for providing them with useful information. They are grateful to G. Shirane for his support and to S. K. Sinha for useful discussions. Work at Brookhaven was supported by the Division of Basic Energy Sciences, U. S. Department of Energy, under Contract no. DE-AC02-76CH00016.

#### References-

1. G. Hausch, *phys. stat. sol. (a)* **15**, 501 (1973).
2. G. Hausch, *J. Phys. Soc. Jpn* **37**, 819 (1974).
3. K. Tajima, Y. Endoh, Y. Ishikawa, and W. G. Stirling, *Phys. Rev. Lett.* **37**, 519 (1976).
4. Y. Endoh and Y. Noda, *J. Phys. Soc. Jpn* **46**, 806 (1979).
5. M. Matsui, T. Shimizu, H. Yamada, and K. Adachi, *J. Magn. Mag. Mat.* **15-18**, 1201 (1980).
6. M. Matsui, H. Yamada, and K. Adachi, *J. Phys. Soc. Jpn* **48**, 2161 (1980).
7. S. K. Sinha, *Dynamical Properties in Solids*, ed. G. K. Horton and A. A. Maradudin, Chap. 1 (North-Holland, 1980).

## ROLE OF PHONONS IN STRUCTURAL PHASE TRANSITIONS OF TRANSITION METAL DICHALCOGENIDES

K. Motizuki, Y. Yoshida and Y. Takaoka

*Department of Material Physics, Faculty of Engineering Science, Osaka University, Toyonaka 560, Japan*

**Abstract.**— To study the lattice instability of 1T-TiSe<sub>2</sub>, phonon dispersion curves are calculated as functions of temperature by taking into account the effective ion-ion interactions caused by electron-lattice interaction. From the standpoint of the softening of phonon frequency we conclude that one of the transverse modes at the L point freezes as the distortion at the phase transition.

### 1. Introduction.

Semimetallic 1T-TiSe<sub>2</sub> transforms at about 200 K into a 2a×2a×2c superlattice structure<sup>1</sup> that is described as the condensed state of one of the transverse phonons at the L point in the Brillouin zone ( $L_1^-(1)$  mode). For the formation of the superlattice we have presented a theory<sup>2,3</sup> which is based on the band-type Jahn-Teller mechanism, and we have emphasized the role of the electron-lattice interaction. For several lattice distortions described by wave vectors at the symmetry points in the Brillouin zone we have calculated the generalized electronic susceptibility  $\chi$ , in which the wave number and mode dependences of the electron-lattice interaction are included. We used the electronic band obtained by the tight-binding fit to the Zunger and Freeman's band.<sup>4</sup> We found that the decrease of the electronic energy due to lattice distortion is the largest for the  $L_1^-(1)$  mode with an amplitude ratio of 3:1 for the Ti and Se displacements. This result is consistent with the observation by neutron diffraction.<sup>1</sup> However, since the phase transition would occur when the decrease of the electronic energy due to the distortion exceeds the increase of the lattice energy, the study of the lattice dynamics is necessary to discuss the phase transition in more detail. In this paper we study the lattice dynamics of 1T-TiSe<sub>2</sub> by taking account of the effective ion-ion interactions caused by the electron-lattice interaction. We calculate the phonon dispersion curves as functions of temperature and discuss the results in connection with the structural phase transition.

### 2. Effective ion-ion interaction caused by electron-lattice interaction.

By using the adiabatic approximation and by calculating the second order perturbation with respect to the electron-lattice interaction, the effective ion-ion interaction is obtained as

$$V_{\text{eff}} = \frac{1}{2} \sum_q \sum_{\mu, \nu} \sum_{\alpha, \beta} \chi^{\alpha\beta}(\mu\nu, q) u_{\mu}^{\alpha}(q) u_{\nu}^{\beta}(-q), \quad (1)$$

where  $\alpha$  and  $\beta$  are Cartesian coordinates and  $u_{\mu}^{\alpha}(q)$  denote the Fourier amplitude of the  $\alpha$ -component of the displacement  $u_{\ell\mu} (= \sqrt{m_{\ell}} \delta R_{\ell\mu})$  of the  $\mu$ th atom in the  $\ell$ th unit cell.  $\chi^{\alpha\beta}(\mu\nu, q)$  in eq. (1) is as follows:

$$\chi^{\alpha\beta}(\mu\nu, q) = \sum_{n,k} \sum_{n'} \left\{ \frac{1}{E_{nk}^0 - E_{n'k-q}^0} g^{\mu\alpha}(nk, n'k-q, E_{nk}^0) [g^{\nu\beta}(nk, n'k-q, E_{nk}^0)]^* \right. \\ \left. + \frac{1}{E_{nk}^0 - E_{n'k+q}^0} g^{\nu\beta}(nk, n'k+q, E_{nk}^0) [g^{\mu\alpha}(nk, n'k+q, E_{nk}^0)]^* f(E_{nk}^0) \right\}, \quad (2)$$

where  $E_{nk}^0$  etc. are the band energies of the undistorted lattice,  $n$  and  $n'$  specify the bands,  $f(E_{nk}^0)$  is the Fermi distribution function and  $g$  is the coefficient of the electron-lattice interaction given by

$$g^{\mu\alpha}(nk, n'k-q, E_{nk}^0) = \xi^{\mu\alpha}(nk, n'k-q) - E_{nk}^0 \eta^{\mu\alpha}(nk, n'k-q). \quad (3)$$

$\xi^{\mu\alpha}$  and  $\eta^{\mu\alpha}$  are obtained in forms that include the derivatives of two-center transfer and overlap integrals with respect to  $u_{\ell\mu}^{\alpha}$ .

We have calculated  $\chi^{\alpha\beta}(\mu\nu, q)$  for  $T=0, 500$ , and  $1000$  K and for  $q=0$  ( $\Gamma$  point),  $\Gamma A$ ,  $\Gamma M$ ,  $\frac{1}{2}\Gamma M$ ,  $\Gamma L$ , and  $\frac{1}{2}AL$ .  $\mu$  (or  $\nu$ ) = 0, 1, and 2 denote the Ti, Se1, and Se2 ions in the unit cell. We take the  $x$ -axis along the  $\Gamma M$  line, the  $y$ -axis perpendicular to the  $\Gamma M$  line in the  $c$ -plane, and the  $z$ -axis perpendicular to the  $c$ -plane. As for the derivatives of the overlap integrals (denoted as  $(pd\pi)'$ , etc.) and those of the transfer integrals ( $t'(pd\pi)$ , etc.), only  $pd\pi$ ,  $pp\sigma$ ,  $pp\pi$  are taken into consideration, because only these mainly contribute to  $\chi$ . For  $(pd\pi)'$  etc. we use the values of  $1/\sqrt{2}$  times those evaluated by using the Slater functions.  $t'(pd\pi)$  etc. are now parameters and we take  $t'(pd\pi) = 2$  eV/A,  $t'(pp\sigma) = -2t'(pp\pi) = -3.5$  eV/A. We show in Fig. 1 the calculated temperature dependence of the  $yy$ -component of  $\chi$  for  $q=\Gamma L$  and  $\Gamma M$ .  $\chi^{yy}(01, \Gamma L)$  and  $\chi^{yy}(00, \Gamma L)$  are most sensitive to temperature and play an important role in the softening of the  $L_1^{-}(1)$  mode.

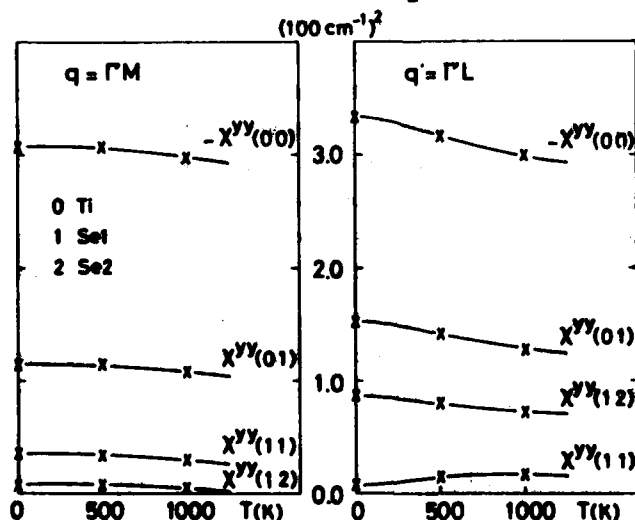


Fig.1  
Temperature variation of  
 $\chi^{yy}(\mu\nu, q)$  for  $q=\Gamma M, \Gamma L$ .

### 3. Phonon dispersion curves.

The dynamical matrix is assumed to be the sum of the matrix  $\chi^{\alpha\beta}(\mu\nu, q)$  obtained above and the matrix  $R^{\alpha\beta}(\mu\nu, q)$  for short-range forces between ion-cores. In the calculation of the phonon dispersion curves, we do not use  $\chi$  of the whole  $q$  values but introduce instead long-range forces between ions which reproduce the calculated  $\chi$  at the symmetry points of  $q=0, \Gamma, A$ , etc. cited above. These forces are found non-central and temperature-dependent. As for the matrix  $R$  we take five short-range potentials  $\phi_{01}, \phi_{12}, \phi_{12}', \phi_{00}$ , and  $\phi_{11}$ <sup>5</sup> and we specify these potentials by several parameters. We determined these parameters so as to get a good fit to the observed transverse phonon frequencies<sup>6</sup> at the  $\Gamma, A, M, L$  points. The phonon dispersion curves calculated at 500 K are shown by solid curves in Fig. 2. The agreement with the observation is reasonably good. The dotted curves in Fig. 2 show the results for 0 K. As seen from the figure, all frequencies except those of the lowest dispersion curve along the  $\Gamma L$  line are insensitive to temperature. The  $L_1^-(1)$  mode frequency becomes imaginary at 0 K. Thus, we conclude that the  $L_1^-(1)$  mode freezes as lattice distortion at a certain temperature which is found to be 220 K.

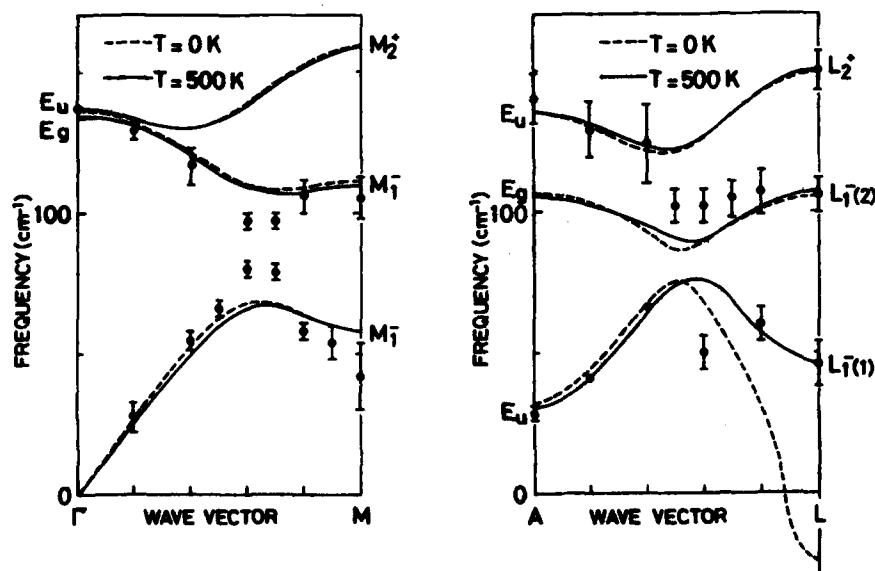


Fig.2 The transverse phonon dispersion curves.  
Dots denote experimental data obtained by  
Wakabayashi et al.<sup>6</sup>

#### References

1. DiSalvo F.J., Moncton D.E. and Waszczak J.V., Phys. Rev. B14, 4321 (1976).
2. Yoshida Y. and Motizuki K., J. Phys. Soc. Japan 49, 898 (1980).
3. Motizuki K., Yoshida Y. and Takaoka Y., to be published in Physica (1981).
4. Zunger A. and Freeman A.J., Phys. Rev. B17, 1839 (1978).
5. Takaoka Y. and Motizuki K., J. Phys. Soc. Japan 49, 1838 (1980).
6. Wakabayashi N., Smith H.G., Woo K.C. and Brown F.C., Solid State Commun. 28, 923 (1978).



OBSERVATION OF PRETRANSITIONAL EFFECTS ON THE SHAPE OF THE  $E_2$  ( $17 \text{ cm}^{-1}$ ) OPTICAL MODE IN  $\beta$ -AgI BY RAMAN SPECTROSCOPY

E. Cazzanelli, A. Fontana, G. Mariotto, F. Rocca\* and M.P. Fontana\*\*

Dipartimento di Fisica e Unità G.N.S.M. - C.N.R., Trento, Italy

\*Istituto per la Ricerca Scientifica e Tecnologica, Trento, Italy

\*\*Istituto di Fisica e Unità G.N.S.M. - C.N.R., Parma, Italy

**Abstract.**— Resonance interference between the  $E_2(17 \text{ cm}^{-1})$  optical mode and the continuum of one-phonon density of state has been observed in  $\beta$ -AgI. From a fitting of the  $E_2$  optical mode shape with a "Fano" formula we have obtained the temperature behaviour of the coupling parameter  $q$  and the true half-width which show substantial change near the  $\beta$ - $\alpha$  transition temperature.

The lattice dynamics of AgI has been extensively studied in recent years<sup>(1)</sup>. On particular interest is to understand the vibrational dynamics near the superionic transition. Since the ionic conductivity jump at  $T_0 \approx 147^\circ\text{C}$  is coupled with a change in the crystal structure<sup>(1)</sup> it is reasonable to assume that phonons play an important role in driving the transition. However no detectable pre-transitional effects have been observed in Raman spectra upon approaching  $T_0$ .

The nature of the Raman spectra in AgI and its change with temperature is clearly anomalous and has been the subject of some controversy. Recently we have shown that the anomalous features in the Raman spectra and their temperature dependence were connected with a first order phonon partial density of states, activated in the  $\beta$ -phase by a local low temperature disordering of the  $\text{Ag}^+$  ions<sup>(2-3)</sup>. In Fig. 1 we show the temperature dependence of Raman spectra in  $\beta$ -AgI. It is clear from the figure that the perfectly normal spectrum due to zone center optical modes changes continuously into a continuum of vibrational states, as temperature is increased, with the sole exception of the  $E_2(17 \text{ cm}^{-1})$  optical mode. Thus such optical mode is barely affected by the local disordering of  $\text{Ag}^+$  ions: this is probably due to the extreme flatness of dispersion curve<sup>(4)</sup>. Bührer and Bruesch<sup>(4)</sup> argue that the sharp  $E_2$  optical mode induce the phase transition by favouring of Frankel pairs in the Ag sublattice. In fact the  $E_2$  mode has the appropriate eigenmode structure and disappears discontinuously at  $147^\circ\text{C}$ . However the "coupling" of such mode to jumping cations does not appear to produce important effects on the mode dynamic structure factor as the phase transition is approached. One reason for apparent insensitivity of  $E_2$  mode may be that overall vibrational response of AgI is similar in two  $\beta$  and  $\alpha$ -phase<sup>(3,5)</sup>. However, a finer experimental analysis of

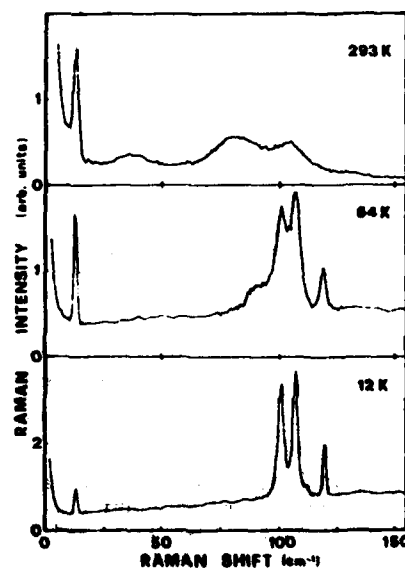


Fig. 1: Experimental Raman spectra at various Temperature from 5 to 150  $\text{cm}^{-1}$ .

$E_2$  mode spectral region does show some pretransitional effects as  $T_0$  is approached (fig. 2). From these experimental data we see that:

- 1 - the  $E_2$  mode damping increases considerably;
- 2 - the shape of  $E_2$  line is visibly asymmetric;
- 3 - there is a slight shift towards low frequencies;
- 4 - the total Raman Intensity divided by the Bose-Einstein factor remains constant.

In order to interpret these data we hypothesize a Fano interference<sup>(6)</sup> between the  $17\text{ cm}^{-1}$  peak and the underlying continuum of vibrational states. From inelastic neutron scattering we can assume that such continuum is due to the phonon density of states associated with an acoustical branch: such branch has, at zone edge, the same symmetry and nearly the same energy as the almost flat branch of the  $E_2$  optical mode. For a given temperature the Fano spectral shape can be written as<sup>(7)</sup>

$$1) \sigma(\epsilon) = \frac{(q + \epsilon)^2}{1 + \epsilon^2} + \sigma'$$

where  $\sigma'$  is the cross section for the underlying continuum which does not interact with the discrete state, and

$$q = \frac{\langle 1|\alpha_1|0\rangle}{\pi \langle 1|w|2\rangle \langle 2|\alpha_2|0\rangle}$$

2)

$$\epsilon = \frac{E - E_1}{\pi \langle 2|\alpha_2|0\rangle |Z|}, \quad E_1 = E_q + F$$

where  $E_q$  is the eigenvalue of the uncoupled one-phon state (i.e. the energy of the  $E_2$  mode) and  $F$  is the slight shift from  $E_q$  due to admixture of states. A simple scheme of Fano interference is to view the like shape of a discrete mode interacting with a continuum as due to interference between two coherent scattering channels into the same heavily damped final state: the first is a direct channel  $\langle 2|\alpha_2|0\rangle$  coupling the ground state  $|0\rangle$  to the continuum  $|2\rangle$ ; the second is an indirect one, coupling states  $|0\rangle$  and  $|2\rangle$  via the discrete state  $|1\rangle$  and is given by

a second order matrix element  $\langle 2|w|1\rangle \langle 1|\alpha_1|0\rangle$  where  $\langle 2|w|1\rangle$  describes a non radiative transition from the discrete level into the continuum degenerate with it. Such non radiative transition is connected with the true width of the line

$$\Gamma = 2\pi |\langle 2|w|1\rangle|^2$$

In the figure 3 we show a typical fit of the spectra for  $T = 403^\circ\text{K}$  together with the calculated true experimental band shape.

If the reasonable assumption that  $\langle 1|\alpha_1|0\rangle$  and  $\langle 2|\alpha_2|0\rangle$  are independent or weakly dependent on temperature is also made, then we have that 3)  $q \sim \Gamma^{-1}$  and thus the main contribution to the temperature dependence in the Fano fitting of the  $E_2$  mode lineshape will be connected with the behaviour of the true linewidth. We have verified the assumptions leading to (3) by fitting the  $E_2$  lineshape using (1) with both

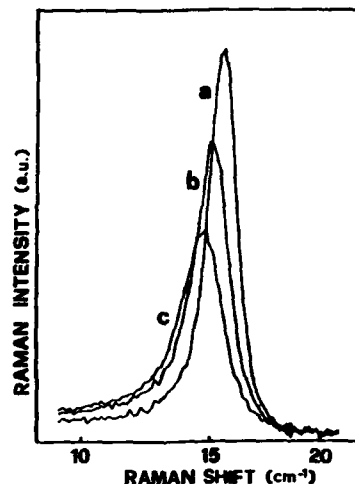


Fig. 2: Experimental  $E_2$  optical mode at various temperature near transition. a =  $303^\circ\text{K}$ ; b =  $380^\circ\text{K}$ ; c =  $417^\circ\text{K}$ .

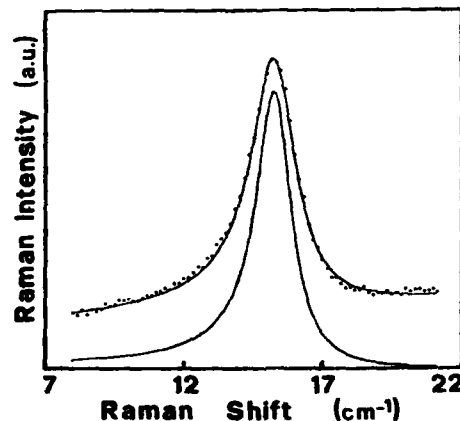


Fig. 3: The  $E_2$  mode line shape at  $403^\circ\text{K}$ . Dots: experimental data; solid line: fit using eq. (1). Lower solid line: true line shape.

$q$  and  $\Gamma$  as free parameters. We have found that the product  $q \Gamma^{-1}$  was independent temperature within our 10% estimated error.

In fig. 4 we show separately the behaviour of the coupling parameter  $q$  and the halfwidth  $\Gamma$  vs temperature.

From inelastic neutron scattering data <sup>(4)</sup> we found that the  $E_2$  optical mode and the density of states associated with the acoustical branch change little with temperature. Thus the change in the  $\langle 1|w|2 \rangle$  matrix elements as  $T_0$  is approached cannot be due to changes in the vibrational dynamics. Rather the increase in the coupling must be connected with a "static" property of the system, such as an order parameter.

In the framework of our interpretation of the anomalous features in the Raman spectrum of  $\beta$  and  $\alpha$ -AgI, we are led to associate the behaviour of  $q$  (or  $\Gamma$ ) to the jump motion of the  $\text{Ag}^+$  ions and to the associated degree of disorder. Thus the appropriate order parameter could be the concentration of Frenkel pairs, itself connected with macroscopic ionic conductivity.

Work supported in part by CNR contract N. 80.00816.11.

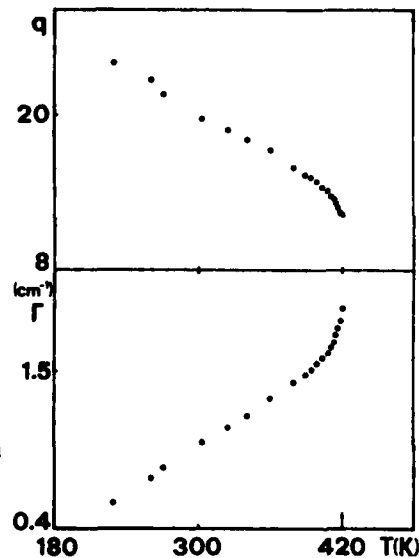


Fig. 4: Behaviour of the  $q$  and  $\Gamma$  parameters versus temperature.

#### References

- 1) G.D. Mahan, W.L. Roth, Editors, "Superionic Conductors", Plenum Press, N.Y. (1976)  
P. Vashista, J.N. Mundy, Editors, "Fast ion transport in solids", North Holland, Amsterdam (1979)
- 2) A. Fontana, G. Mariotto, M. Montagna, V. Capozzi, E. Cazzanelli, M.P. Fontana  
Solid State Commun. **28**, 35 (1978)
- 3) G. Mariotto, A. Fontana, E. Cazzanelli, M.P. Fontana, Phys. Stat. Sol. (b) **101**,  
341 (1980)
- 4) W. Bührer, R.M. Nicklow, P. Brüesch, Phys. Rev. **B17**, 3362 (1978)
- 5) A. Fontana, G. Mariotto, M.P. Fontana, Phys. Rev. **B21**, 1102 (1980)
- 6) U. Fano, Phys. Rev. **124**, 1866 (1961)  
U. Fano, J.W. Cooper, Phys. Rev. **137**, 1364 (1965)
- 7) J.F. Scott, Rev. Modern Phys. **46**, 86 (1974)  
P.L. Rousseau, S.P.S. Porto, Phys. Rev. Lett. **20**, 1354 (1968)

## BRILLOUIN SCATTERING STUDY OF PHASE TRANSITIONS IN p-POLYPHENYLS

C. Ecolivet, B. Toudic and M. Sanquer

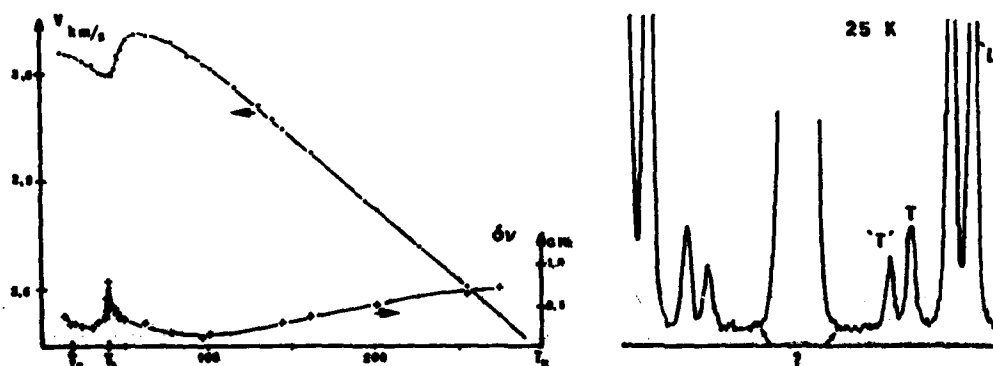
*Groupe de Physique cristalline, E.R.A. au C.N.R.S. n°070015, Université de Rennes, Campus de Beaulieu, 35042 Rennes Cedex, France*

**Abstract** A Brillouin scattering study of the various phase transitions in p-polyphenyls reveals different kinds of elastic anomalies depending on the nature of these transitions.

**INTRODUCTION** The first elements of the p-polyphenyls series undergo phase transitions through a change of their molecular conformation. This change happens by an antiferrodistorsive rotation of aromatic rings about the molecular long axis, which effect is the stabilization at low temperatures of a non-planar molecular conformation. Despite their isomorphism, p-polyphenyls present different kinds of transitions and critical behaviours. We report here some results of a Brillouin scattering investigation of these transitions and their effect on the elastic properties of these crystals.

**INCOMMENSURABLE PHASES OF BIPHENYL** Biphenyl undergoes a first incommensurate phase transition at  $T_1 = 42$  K with modulation vectors along  $\vec{a}$  and  $\vec{b}$  (4 satellites). This displacive transition is related to a soft mode which happens at the satellites near the Z point (0, 1/2, 0) of the first Brillouin zone. A partial lock-in transition happens at  $T_2 = 17$  K where the incommensurability along  $\vec{a}$  disappears (<sup>1</sup>).

The major sound velocity anomaly occurs for the quasi longitudinal mode propagating along  $\vec{a}$  (figure 1). This kind of elastic anomaly has been observed in many other materials presenting such phases like  $K_2S_8O_4$ ,  $Rb_2ZnCl_4$ .



**Fig. 1** (left) - Biphenyl quasi-longitudinal sound velocity (upper) and its Brillouin total linewidth ( $\Delta\nu$ ) versus temperature.

**Fig. 2** (right) - Spectrum of biphenyl at 25 K by phonons propagating along  $\vec{a}$ . The ar-

rows at the foot of the Rayleigh indicate the expected location of the phason line, whereas "L", "T" and T designates the quasi-longitudinal, quasi-transverse and transverse modes.

As a phason was previously observed by neutron scattering (<sup>1</sup>), we have tried to see it by light scattering. Our experiment failed to find this component and what we can say, if the phason has really a propagation velocity of 1000 m/s, is that it scatters less than 1/10 of the light scattered by the weakest transverse mode.

**IMPROPER FERROELASTIC TRANSITION OF p-TERPHENYL** p-terphenyl undergoes at 193 K an improper ferroelastic transition labelled  $2/m \bar{1}' F \bar{1}'$  according to Aizu. This transition is characterized by a superstructure which appears at the C point  $(1/2, 1/2, 0)$  of the first Brillouin zone leading to the existence of two crystallographically different kinds of domains (Fig.3) depending on the orientation of the molecule central ring (<sup>2</sup>).

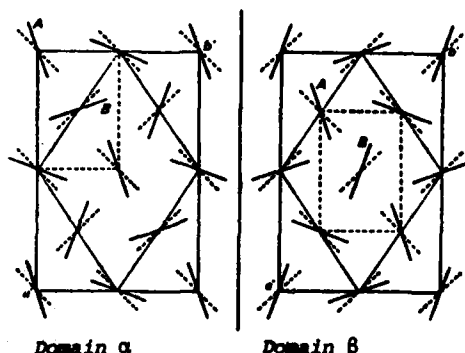


Fig. 3 - Projection on the (001) plane of the central ring orientations in both phases ; dashed lines for the high temperature phase and full lines for the low temperature phase.

One of the elastic anomalies created by this order-disorder transition is related to the differentiation of the  $|110|$  and  $|1\bar{1}0|$  directions as it can be seen on the figure above. For one of these directions depending on the domain, central rings are perpendicular to their neighbours whereas along the other direction the angle between central rings is much less. This difference and the presence of several domains in the scattering volume are at the origin of the presence of two distinct and simultaneous longitudinal Brillouin lines in the spectrum (Fig. 4).

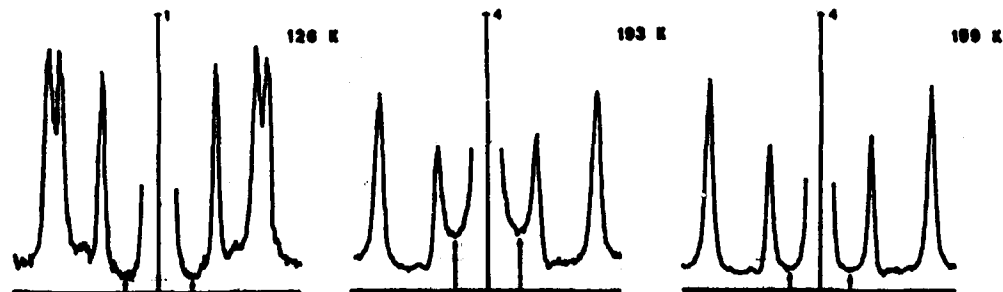


Fig.4 - Right angle Brillouin scattering spectrum in the  $a(c,c)b$  geometry at 3 different temperatures showing the "longitudinal" Brillouin lines (from the next order) and the "transverse" Brillouin lines near the Rayleigh line ; notice also a quasi elastic component which goes through a maximum at  $T_C = 193$  K. The frequency interval shown is 35.5 GHz.

A fit performed on these spectra between 90 K and 193 K shows a  $(T_C - T)^{0.29}$  variation of this splitting ; it corresponds to the numerical value of 0.30 obtained for the superstructure intensity recorded by neutron scattering <sup>(1)</sup>. This value reflects a slight discontinuity of the transition.

**THE p-QUATERPHENYL TRANSITION** p-quaterphenyl undergoes a transition similar to the p-terphenyl in the sense it is also an order-disorder transition between the  $P 2_1/a$  high temperature phase and probably a  $P \bar{1}$  low temperature phase with also coexistence of domains <sup>(3)</sup>. But here two central rings are moving in opposite directions inside each molecule and the difference between the  $|110|$  and the  $|\bar{1}\bar{1}0|$  is not as obvious as for p-terphenyl and two different longitudinal Brillouin lines are not observed. Generally the elastic anomalies are also weaker. The figure 5 shows an anomaly of the "longitudinal" sound velocity recorded along  $\vec{a}$  which shows a small change of slope at  $T_C = 240$  K ; there is no complete explanation for this kind of behaviour, but it is could be due to some relaxation mechanism.

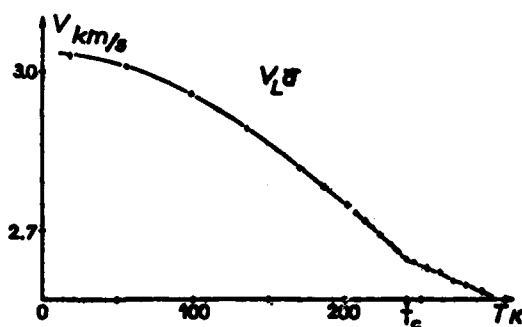


Fig. 5 - Sound velocity of the quasi longitudinal mode propagating along  $\vec{a}$ .

#### References

1. H. CAILLEAU, Thesis Rennes 1981.
2. J.L. BAUDOUR, Y. DELUGEARD, H. CAILLEAU, Acta Cryst. (1976), B32, 150.
3. J.L. BAUDOUR, Y. DELUGEARD, P. RIVET, Acta Cryst. (1978), B34, 625.

PHONON DISPERSION AND TRANSVERSE MODE SOFTENING IN  $\text{RbFeCl}_3$ 

D. Petitgrand, B. Hennion, C. Escribe-Filippini\* and S. Legrand\*\*

*Laboratoire Léon Brillouin, CEN-Saclay, 91191 Gif-sur-Yvette, France**\*Institut Laue-Langevin, 156X, Centre de Tri, 38042 Grenoble Cedex, France**\*\*DPHG/PSRM, CEN-Saclay, 91191 Gif-sur-Yvette, France*

**Abstract.**— Phonon dispersion curves of  $\text{RbFeCl}_3$  have been measured by neutron scattering. For wave vectors in the hexagonal plane the transverse phonons polarized along  $z$  are found to have very low energies. Furthermore the shape of this branch changes drastically as the temperature is lowered from room temperature to 20K, the zone boundary energy at the K point being decreased by a factor of two. However no Bragg reflection indicative of a phase transition has been detected at this point. These features are interpreted as showing evidence that  $\text{RbFeCl}_3$  is at the border of a phase transition for which a microscopic mechanism will be discussed.

1. **Introduction.**— Phonon softening has been extensively studied in  $\text{AMX}_3$  compounds of cubic perovskite structure<sup>(1)-(3)</sup> in connection with structural phase transitions. More recently it has been reported that some  $\text{AMX}_3$  crystals with hexagonal structures also undergo structural phase transitions<sup>(4)</sup>. In this paper we give the first experimental report of the observation of a phonon softening in the hexagonal  $\text{RbFeCl}_3$  compound.

2. **Experiments and Results.**— The  $\text{RbFeCl}_3$  single crystals used in these experiments are the same as those grown for the spin wave investigation<sup>(5)</sup>. The inelastic neutron scattering experiments have been carried out on the triple-axis spectrometer IN 3 at the Institut Laue-Langevin. The experiments were performed with incident neutron wave-vectors of  $2.3$  or  $2.66 \text{ \AA}^{-1}$  and collimations of  $30'/20'/20'/20'$ . The sample was mounted in a pumped  $^4\text{He}$  cryostat with the  $c$ -axis horizontal so that the  $[h0l]$  plane was in the scattering plane.

The dispersion curves of acoustic phonon measured at room temperature are shown in Fig.1.

Since our measurements in the  $c$  direction do not extend to very small  $q$ , the sound velocity of the TA (001) branch (broken line in Fig.1) was set equal to that of the TA (110) branch as required by elastic theory. Obviously this sound velocity is smaller than the phase velocity derived from our lowest experimental point, which means that this transverse mode must have an upward curvature. This peculiarity, unexpected from classical elastic theory, is similar to that first observed in Graphite<sup>(6)</sup> and more recently in  $\text{CaNiF}_3$ <sup>(7)</sup>. This is a consequence of the inhomogeneous structure which can be regarded as made up of strongly coupled  $\text{FeCl}_6$  octahedra making infinite fibres along the  $c$ -axis. These fibres are much more loosely coupled to the neighbouring ones via Rb ions. The bending of a fibre requires an elastic

energy  $EI \frac{\partial^4 u}{\partial z^4}$  ( $E$  being the Young modulus and  $I$  the momentum of inertia of the fibre) in addition to the shear energy  $C_{44} \frac{\partial^2 u}{\partial z^2}$  of the  $\text{FeCl}_6\text{-Rb-FeCl}_6$  bonds. Thus the transverse phonons dispersion takes the form  $\omega_c^2 = \rho^{-1}(C_{44}k_z^2 + EI k_z^4)$ , which explains the positive curvature at low  $q$ .

For phonons propagating in the hexagonal plane, the most striking feature is the very low value of the transverse mode ( $e//Z$ ) energies compared with those of the longitudinal mode. From the slope at small  $q$  we deduce  $C_{11}/C_{44} = 17$ , a value much larger than typical values ( $4 < C_{11}/C_{44} < 6$ ) for ionic crystals. We have carried out a systematic investigation of this transverse phonon between 1.5 and 300 K the results of which are illustrated in Fig.2. The whole branch gradually flattens as the temperature is lowered from 300 K to 20 K and then becomes almost temperature independent at lower temperatures. Furthermore, the decrease in energy appears to be stronger at the K point with the consequence that this point becomes a minimum for  $T \leq 150$  K, instead of a maximum at room temperature. Down to 50 K, the lowering of the phonon energies is strongly reminiscent of the behaviours observed in cubic crystals  $\text{SrTiO}_3$ <sup>(1)</sup>,  $\text{KMnF}_3$ <sup>(2)</sup>,  $\text{RbCaF}_3$ <sup>(3)</sup> ... for which the lowering is achieved by a complete softening of the mode giving rise to a structural phase transition. Thus we have carefully checked the elastic scattering, but we found no evidence of Bragg scattering at the K point.

3.- Discussion. - In the above mentioned cases of cubic  $\text{AMX}_3$  compounds, the soft mode has been identified as a coherent rotation of the  $\text{MX}_6$  octahedral. But in the hexagonal  $\text{AMX}_3$  structure two neighbouring octahedra share a triangular face and a coherent rotation of the octahedra thus involves a strong coupling with internal modes of  $\text{MX}_6$  giving rise to a high frequency mode. In fact the only possibility which let the internal modes frozen and is compatible with our observations is a mode involving translations of the whole fibre along  $c$ . For the special case of  $q = (\frac{1}{3} \frac{1}{3} 0)$ , which is the sensitive point, the motions of the 3 fibres situated on the vertex of a triangle are out of phase by  $120^\circ$ . The fact that this mode is of low energy can be explained by repulsive interactions between chains in their vertical motion. Indeed we anticipate that such a repulsion arises from the mismatch of the ionic radii of  $\text{Rb}^+$  and  $\text{Cl}^-$ . This interpretation is strongly supported by the fact that below 120K  $\text{RbFeBr}_3$  undergoes a structural phase transition which just has the point K as a superlattice reflection. Thus one must conclude that  $\text{RbFeCl}_3$  would be slightly below and  $\text{RbFeBr}_3$  beyond the stability threshold.

One of the remaining problems is the description of the anharmonic behaviour of such a system. We plan to do accurate measurements of the temperature dependence of the energies and widths of these unusual phonons in order to investigate this point.

- (1) G. SHIRANE and Y. YAMADA, Phys. Rev. 117 (1969) 858.
- (2) G. SHIRANE, V. J. MINKIEWICZ and A. LINEZ, Solid State Comm. 8 (1970) 1941.
- (3) M. ROUSSEAU, J. NOUET, R. ALMAIRAC and B. HENNION, J. de Phys. Lett. 37 (1976) L-33;  
M. ROUSSEAU, J. NOUET and R. ALMAIRAC, J. de Phys. 38 (1977) 1423.
- (4) J. M. PEREZ-MATO, J. L. NAVES, M. J. TELLO and F. J. ZUNIGA, J. of Phys. C, Solid State Phys. 14 (1981) 1121 and references included.
- (5) D. PETITGRAND, B. HENNION, P. RADHAKRISHNA, C. ESCRIVE and S. LEGRAND, Recent developments in Condensed matter Physics (Plenum Publ. Corp., New-York) 5 (1981) 205.
- (6) R. WICKLOW, N. WAKAMATSU and E. C. SMITH, Phys. Rev. B5 (1972) 4951.



- (7) B.DORNER and M.STEINER, J.of Phys.C,Solid State Phys. 9 (1976) 15.  
 (8) M.EIBSCHUTZ, G.R.DAVIDSON and D.E.COX, AIP Conf.Proceedings 18 (1973) 386.

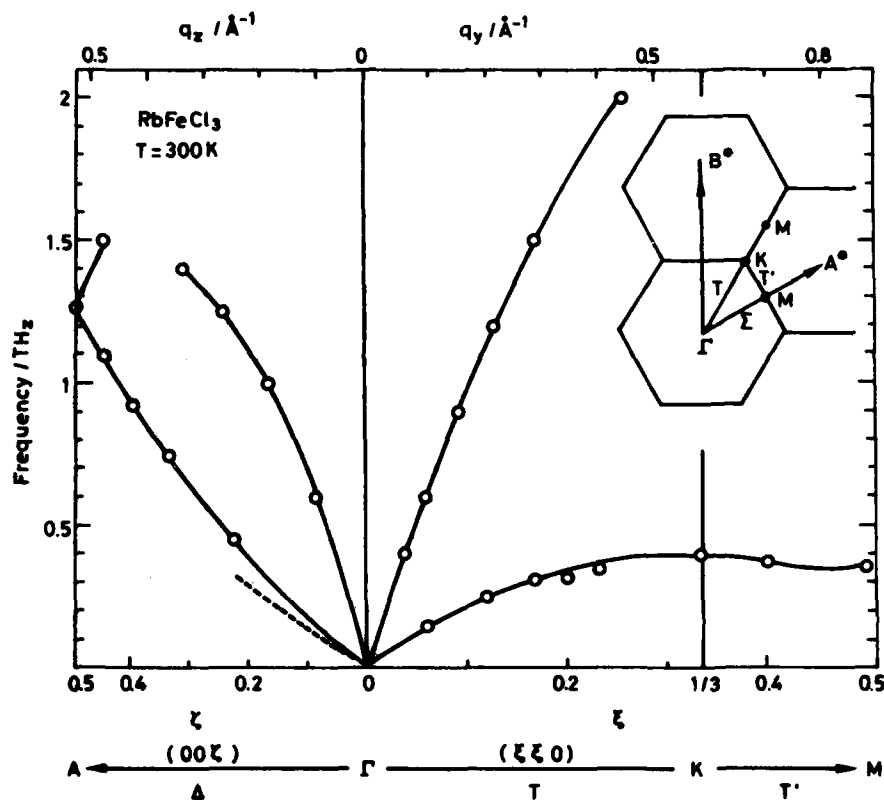


Fig.1 - Dispersion of acoustic phonons polarized in the [h0l] plane at 300 K.

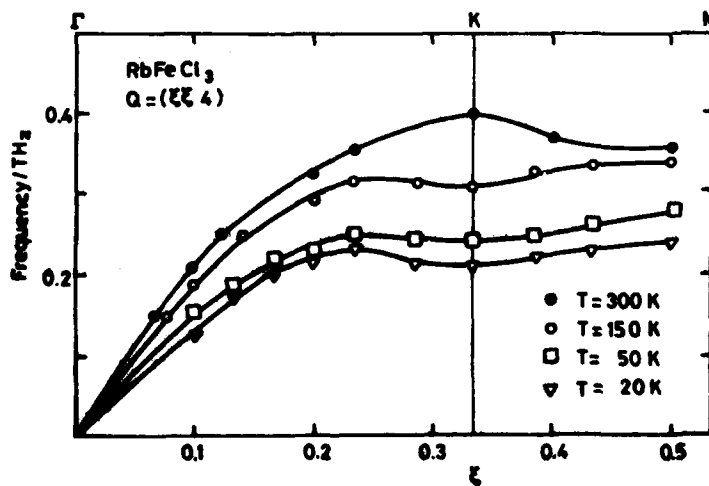


Fig.2 - Temperature dependence of the  $q = (\xi\xi 0)$ ,  $e = (001)$  transverse phonon.

# A RAMAN SCATTERING STUDY OF THE SOLID TO SOLID PHASE TRANSITION IN BENZIL

D.R. Moore, V.J. Tekippe\*, A.K. Ramdas\*\* and J.C. Toledano\*\*\*

University of Illinois at Chicago Circle, U.S.A.

\*Gould Laboratories

\*\*Purdue University

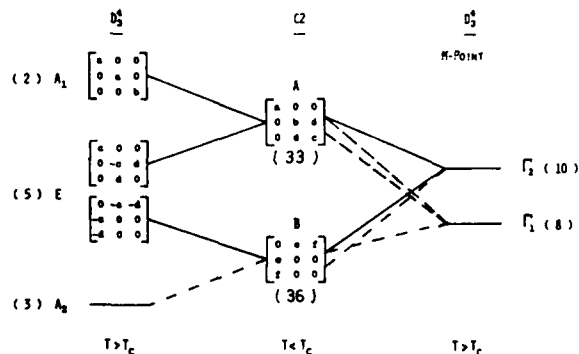
\*\*\*C.N.E.T., France

**Abstract.**--At 84°K, benzil undergoes a first order phase transition from  $D_3$  space group symmetry in the upper phase to C2 symmetry in the lower temperature phase with a simultaneous four-fold expansion of the primitive unit cell. In addition to the effects of the phase transition on the zone center optical modes which are Raman active above  $T_c$ , our polarized Raman studies do indeed show the emergence of new modes, including a second soft mode, which are related to the enlargement of the unit cell.

## I. Introductory Remarks

Room temperature benzil ( $C_6H_5COCOC_6H_5$ ) has a trigonal structure belonging to the space group  $D_3$ . At  $T_c=84$  K, benzil undergoes a solid to solid phase transition in which the trigonal phase converts to a monoclinic one of space group symmetry C2. A previous Raman scattering study<sup>1</sup> of this phase transition revealed a pronounced, nonlinear softening of the lowest frequency optic mode on both sides of  $T_c$ . This soft mode is associated with the center of the Brillouin zone and typically induces a phase transition that preserves the number of atoms per unit cell. However, x-ray diffraction studies show that the phase transition is accompanied by a four-fold expansion of the primitive unit cell<sup>2</sup>. This point was recently addressed by Toledano<sup>3</sup> in a phenomenological model of the phase transition in benzil. In this dual order parameter model, the primary order parameter is associated with the observed zone center soft mode and determines the trigonal to monoclinic symmetry change. The secondary order parameter corresponds to the star of  $\vec{k}$  vectors ( $\vec{k}_M^*$ ) at the M point of the Brillouin zone and is related to the observed four-fold expansion of the unit cell. The model allows a nonlinear coupling between the two order parameters and the mechanism of the phase transition is assumed to proceed through a "triggering" of the M point instability by the one at the  $\Gamma$  point. Although the phonon modes associated with  $\vec{k}_M^*$  are Raman inactive above  $T_c$ , they are expected to become Raman active below  $T_c$ . In addition, the model predicts that the soft optic mode at  $|\vec{k}|=0$  will trigger a second soft mode related to  $\vec{k}_M^*$ . Since neither this second soft mode

Fig. 1: Group theoretical analysis of the phase transition in benzil. The lines indicate the correlation of the modes in the trigonal phase above  $T_C$  with those in the monoclinic phase below  $T_C$ . The solid lines indicate those modes which are expected to show strong Raman activity.



nor the additional modes associated with the unit cell expansion had been observed in previous studies, a more comprehensive study of the phase transition by Raman scattering techniques was clearly indicated.

## II. Experimental Results & Discussion

The decomposition of the lattice modes at the  $\Gamma$  and M points of the hexagonal Brillouin zone of the trigonal phase into the A and B irreducible representations at the  $\Gamma$  point of the monoclinic phase is summarized in Figure 1. The numbers in parentheses indicate the number of modes of each symmetry type. At the transition temperature the decomposition proceeds as follows:  $A_1 \rightarrow A$ ,  $A_2 \rightarrow B$ ,  $E \rightarrow A+B$ ,  $\Gamma_1 \rightarrow 2A+B$  and  $\Gamma_2 \rightarrow A+2B$ .

The temperature dependence of the polarized Raman spectra recorded in the  $Y(XY+XZ)X$  scattering geometry is shown in Figure 2a. As the temperature is lowered to  $T_C$  (dashed line) the intensity of the lowest E mode (1e) increases dramatically while its frequency decreases sharply. This anomalous behavior is characteristic of a soft optic mode inducing a phase transition and is similar to the results observed by Sapriel et al.<sup>1</sup> The emergence of an additional mode (2b) positioned on the shoulder of the B component of the soft E mode (1b) is also observed at  $T_C$ . This new mode is interpreted as the stronger B component of the soft  $\Gamma_2$  mode predicted by Toledano<sup>3</sup>. The two soft mode components are clearly distinguishable since they exhibit a temperature dependence different from that of the other modes. As the temperature decreases, both modes become less intense and move towards higher frequency. This opposes the general increase in intensity exhibited by all of the other external modes. Since a maximum of eight B modes can be associated with the zone center modes of the trigonal phase, at least eleven of the modes observed in the spectrum at  $T=16^\circ K$  correspond to  $\bar{K}_M^*$  and, hence, to the enlargement of the unit cell. Similar results were obtained for the modes of  $A_1$  symmetry above  $T_C$  and A symmetry below  $T_C$ . The corresponding spectra were

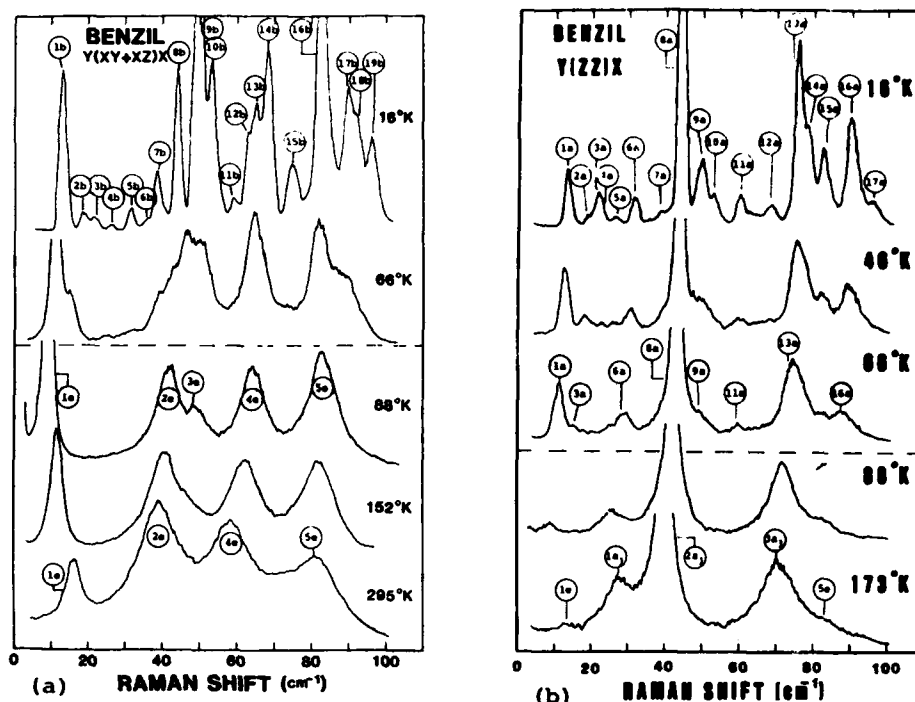


Fig. 2: The polarized Raman spectra exhibited by benzil at selected temperatures above and below  $T_C$ . The spectra were excited with 5145 Å radiation and recorded in a  $90^\circ$  scattering geometry. The scattering geometries used allow a) E modes above  $T_C$  and B modes below  $T_C$  and b)  $A_1$  modes above  $T_C$  and A modes below  $T_C$ .

recorded in a Y(ZZ)X scattering geometry and are shown in Figure 2b. The A components of the two soft modes are denoted as 1a and 3a. Additional theoretical considerations predict that of the sixty-nine Raman active modes expected for  $T < T_C$ , seventeen A modes and eighteen B modes will be intense enough to observe<sup>4</sup>. This is in excellent agreement with the seventeen A modes and nineteen B modes observed in the present study.

In conclusion, our Raman scattering study of the phase transition in benzil has revealed effects due to both the symmetry change and the expansion of the unit cell, in excellent agreement with the predictions of a dual order parameter model.

#### References:

1. J. Sapriel, A. Boudou and A. Perigaud, Phys. Rev. B19, 1484 (1979).
2. G. Odou, M. More and V. Warin, Acta. Cryst. A34, 459 (1978).
3. J. C. Toledano, Phys. Rev. B20, 1147 (1979).
4. D. R. Moore, Ph.D. Thesis (University of Illinois at Chicago Circle, 1981) unpublished.

## SPECTROSCOPIC IONICITY AND LATTICE INSTABILITY IN III-VI LAYER COMPOUNDS

N. Kuroda, S. Hashimoto and Y. Nishina

*The Research Institute for Iron, Steel and Other Metals, Tohoku University, Sendai 980, Japan*

**Abstract.** - III-VI compounds with the sandwich-type layer structure should have Phillips' electronegativity difference in the range from 0.55 to 0.95. In a certain range of ionicity of valence bonds, however, shear mode phonons are bound to be unstable by the long range Coulomb force, so that InS crystallizes in a nonlayer structure. Three other examples of such nonlayer compounds have been found from experimental phase analysis of  $(\text{GaSe})_x(\text{InSe})_{1-x}$ .

1. Nature of Chemical Bonds. - Group III-VI excess valence compounds, GaS, GaSe and InSe, crystallize in a sandwich-type layer structure. Despite of its strong anisotropy, the electronic coordination with respect to both anion and cation can be regarded as tetrahedral since nonbonding orbitals are formed at anion sites by the excess electrons. Figure 1 shows the dependence of force constants on the bond length  $\ell$ . The  $\ell^{-8/3}$  rule<sup>1)</sup> holds well in III-VI layer compounds as well as in group III-V and II-VI compounds. Besides, the force constants indicate that the strength of bonding is comparable to the proper tetrahedral bonding. The similarity of bonding is evidently shown by the ratio of bending to stretching force constants: Experimental values in the layer compounds agree well with those in such tetrahedral compounds if scaled by the spectroscopic ionicity  $f_i$ ,<sup>2)</sup> as shown in figure 2.

If we pay attention to the heteropolar energy gap,<sup>2)</sup>  $C$ , we find that all three layer compounds have  $C = 4.7$  eV. This value agrees well with  $C$  in tetrahedral compounds with the same value of Phillips' electronegativity difference  $\Delta$  as shown in figure 3. The heteropolar energy gap in GaTe is of particular interest because GaTe crystallizes at ambient conditions in a monoclinic layer structure modified strongly from the sandwich-type one. Its dielectric constant  $\epsilon_\infty$  of 9.0<sup>3)</sup> gives  $C = 4.0$ , being close to 4.7 eV despite that  $\Delta = 0.34$  in GaTe is smaller by a factor of about two than  $\Delta = 0.80$  in InSe. This fact suggests that the sandwich-type layer structure requires  $C$  of the anion-cation bond to be rather constant in order to maintain the

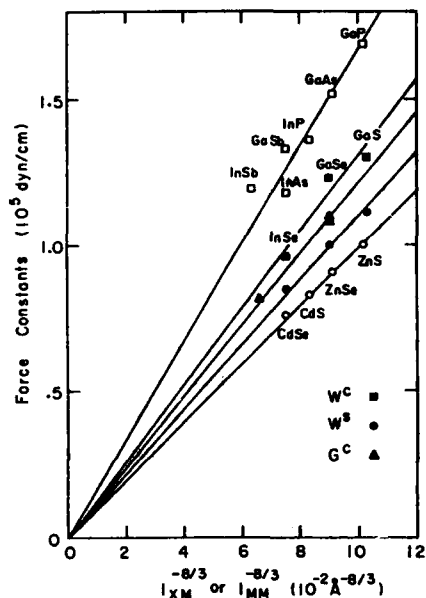


Fig. 1: Force constants vs  $l^{-8/3}$ . The force constants in III-V and II-VI compounds are represented by  $\mu\omega^2$ , where the frequencies,  $\omega$ , of TO phonons are referred to literatures. W and G are force constants associated with anion-cation and cation-cation bonds, respectively, in III-VI compounds. Suffices c and s denote the compressional and shear components with respect to the basal plane, respectively.

balancing of charge distribution against the van der Waals bond and the cation-cation homopolar bond; the sandwich-type layer structure is stable only if  $\Delta = 0.55$  to  $0.95$ . InTe is known to crystallize in a nonlayer structure. The instability of the layer structure may be attributed in part to the fact that  $\Delta = 0.48$  in InTe. In InS, on the

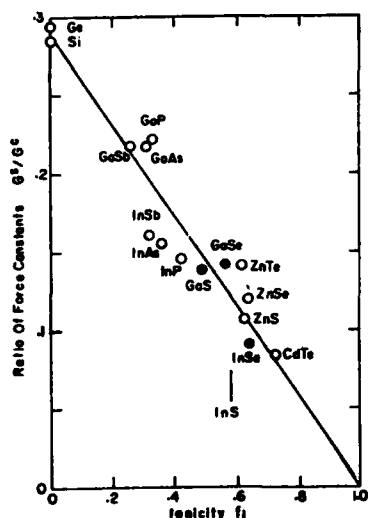


Fig. 2: The ratio of bending to stretching force constants vs ionicity.

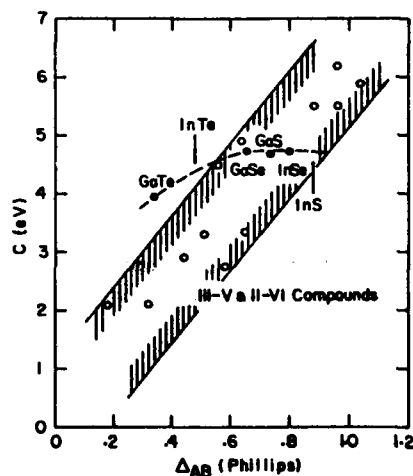


Fig. 3: Heteropolar energy gap vs Phillips' electronegativity difference.

other hand, we have  $\Delta = 0.88$  which lies in the stable region for the layer structure. Furthermore we find  $f_i = 0.58$  in InS provided that it crystallizes in the layer structure with  $C = 4.7$  eV. The value of  $f_i$  is even smaller than that in InSe, so that the Coulomb repulsion between cations would not be strong enough to break up the layer structure. Nevertheless InS crystallizes in a three dimensional structure at ambient conditions. Thus the lattice instability of group III-VI compounds can not be explained in terms of the nature of chemical bond alone.

2. Phase Diagram of  $(\text{GaSe})_x(\text{InSe})_{1-x}$ . - Present authors (Y.N. and N.K.)<sup>4)</sup> have predicted that the sandwich-type layer structure is unstable in the pseudobinary system  $(\text{GaSe})_x(\text{InSe})_{1-x}$  for a wide range of  $x$  due to the instability of shear mode phonons induced by the long range Coulomb interaction. If it is the case, the layer structure should be unstable also in InS because InS corresponds in its electronic polarizability to the pseudobinary compound with  $x \approx 0.6$ . In order to examine the validity of this prediction, we have determined the phase diagram of  $(\text{GaSe})_x(\text{InSe})_{1-x}$  by means of DTA. According to the phase diagram thus obtained (figure 4), GaSe and InSe are miscible only for  $0 \leq x \leq 0.13$  and  $0.9 \leq x \leq 1.0$ . In the immiscible region there appear three new phases  $\text{GaIn}_3\text{Se}_4$ ,  $\text{Ga}_2\text{InSe}_3$  and  $\text{Ga}_3\text{InSe}_4$ , which probably have nonlayer structures. In addition, they exhibit phase transitions at 738, 592 and 543 °C as seen in figure 4. All these observations are consistent with our theoretical prediction. The present results strongly suggest that the three dimensional structure of InS is caused by the instability of shear mode phonons.

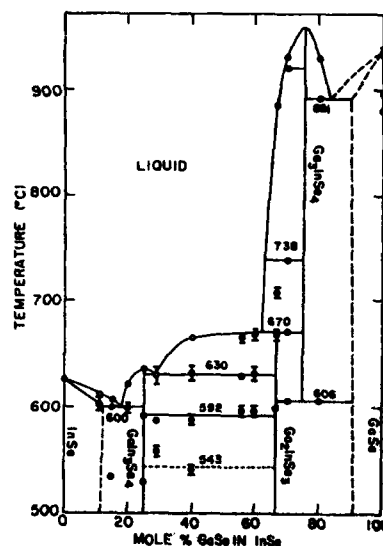


Fig. 4: Phase diagram of  $(\text{GaSe})_x(\text{InSe})_{1-x}$ .

#### References

- 1) K.M. Guggenheimer, Proc. Phys. Soc. (London) **58**, 456 (1946).
- 2) J.C. Phillips, Bonds and Bands in Semiconductors (Academic Press, New York, 1973).
- 3) C. Tatsuyama, Y. Watanabe, C. Hamaguchi and J. Nakai, J. Phys. Soc. Japan **29**, 150 (1970).
- 4) Y. Nishina and N. Kuroda, Physica B **99**, 291 (1980).

PHONONS AT SURFACES AND INTERFACES



## THE SPECTROSCOPY OF SURFACE PHONONS BY INELASTIC ATOM SCATTERING

G. Benedek, G. Brusdeylins\*, R.B. Doak\* and J.P. Toennies\*

*Gruppo Nazionale di Struttura della Materia del Consiglio Nazionale delle Ricerche, Istituto di Fisica dell'Università, I-20133 Milano, Italy**\*Max-Planck-Institut für Strömungsforschung, Böttinger Str. 4-8, D-3400 Göttingen, F.R.G.*

**Abstract.**— The recent great advance in the production of highly monochromatic atomic beams is opening new perspectives in surface physics, having made way to a full determination of the surface vibrational structure. After a short review of the earlier attempts to detect surface phonons from the angular distributions of scattered atoms, we report on the direct measurement of surface phonon dispersion curves, first achieved by Brusdeylins, Doak and Toennies in alkali halides, from time-of-flight (TOF) spectra of scattered He atoms. A comparison is made with the existing theories of surface phonons in ionic crystals. The state of the art in the theory of inelastic scattering processes is briefly illustrated in order to discuss the theoretical interpretation of TOF spectra. The one-phonon energy-loss spectra of He scattered from LiF(001) calculated for a hard corrugated surface model are found to be in good agreement with TOF spectra at all the incidence angles. Evidence is given that, in addition to Rayleigh waves, important contributions to the inelastic scattering come from the surface-projected density of bulk phonons. The possible observation of optical surface modes in KCl(001) is finally discussed.

**1. Introduction.**— Although surface phonons have since long attracted much attention due to their role in several surface and interface phenomena and in various technological applications,<sup>1</sup> their spectroscopy in the dispersive region has been considered till now much more difficult than that of bulk phonons. Indeed the conventional probes of bulk phonons, such as neutrons<sup>2</sup> and light, are only weakly sensitive to the surface owing to their large penetration into the solid. In the plasma spectral region photons become surface sensitive but couple only to very long-wave surface excitations.<sup>3,4</sup> Also electron energy loss spectroscopy, which has given us the first evidence of surface electromagnetic modes in monocrystals,<sup>5</sup> and inelastic electron tunneling spectroscopy<sup>6</sup> are actually restricted to long waves by unfavorable kinematical conditions.

The great potentialities of atom scattering in surface phonon spectroscopy have been apparent since the theoretical work of Cabrera, Celii and Manson,<sup>7</sup> but only the recent great advance in the production and detection of highly monochromatic atomic beams, triggered off by the studies in rarified gas dynamics,<sup>8</sup> has made way for a full determination of the surface vibrational structure. Today atoms can do for surface phonons the same job that slow neutrons do for bulk phonons.

Alongside, various theoretical problems had to be considered, since the assessment of such a powerful technique in surface phonon analysis required an accurate comparison with the predicted energy-loss profiles and related surface phonon densities. This in order to answer

two urgent questions: 1) Whether and when are single-phonon processes predominant; 11) in how distorted a way do energy-loss spectra reflect the surface projected phonon density.

2. Inelastic processes in angular distributions.— The early experiments carried out by Subbarao and Miller<sup>9</sup> with cold He beams on Ag(111) provided a first clear separation between elastic and inelastic scattering, the latter displaying a clear multiphonon nature.

On the contrary, the data obtained by Williams and Mason for He scattering from LiF(001)<sup>10</sup> and NaF(001)<sup>11</sup> were indicative of one-phonon processes. The phonon frequencies, derived from a sophisticated analysis of the out-of-plane angular distributions (AD) around the diffraction peaks, are in fair agreement with the calculated Rayleigh wave (RW) dispersion curves.

In fig. 1a the data for NaF are compared to the theoretical curve obtained by the Green's function method<sup>12</sup>, using the breathing shell model (BSM) and room temperature data. Shell model slab calculations<sup>13</sup> give almost identical results.

The results of Williams and Mason are quite remarkable when considered in light of the recent data obtained by Doak *et al*<sup>14</sup> by the time-of-flight (TOF) technique and a much better resolution (fig. 1b).

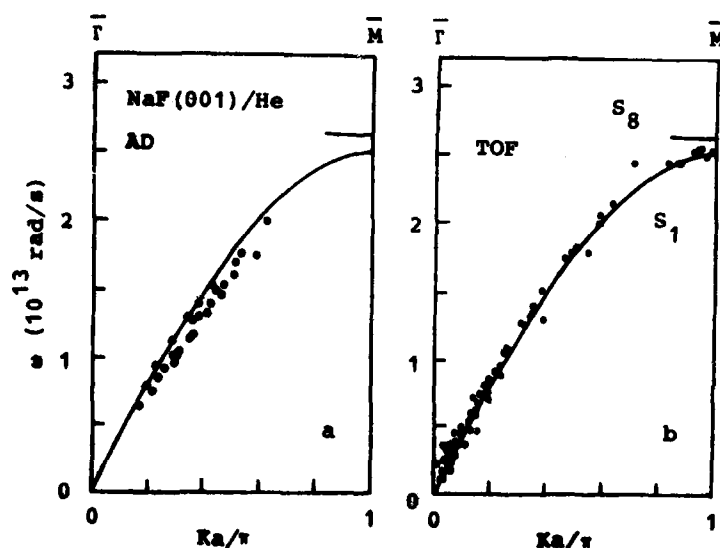


Fig. 1 : Calculated Rayleigh wave dispersion curves in NaF(001) compared to He<sup>4</sup> scattering data obtained from angular distributions (a: ref. 11) and time-of-flight spectra (b: ref. 14).

According to Avila and Lagos<sup>15</sup>, the systematic deviation in fig. 1a from the theoretical curve is removed when the data are analyzed in terms of kinematical focussing.

The kinematical focussing (KF) occurs with any particular scattering geometry for which the paraboloid representing the energy-loss versus momentum transfer relation

$$\omega/\omega_1 = 1 - \left[ (1 - K_p/K_1)^2 + K_{np}^2/K_1^2 \right] (\sin\theta_1/\sin\theta_f)^2 \quad (1)$$

is tangent to a surface-phonon dispersion surface  $\omega = \omega(\vec{K})$ .<sup>16</sup> Here  $\omega_1$  and  $K_1$  are energy and parallel momentum of the incident atom ( $\hbar = 1$ ),  $\theta_1$  and  $\theta_f$  the incidence and outgoing angles, respectively.  $K_p$  and  $K_{np}$  are the components of the transferred parallel momentum  $\vec{K} = (K_p, K_{np})$ , respectively parallel and normal to the incidence plane.

KF yields singularities in the angular distribution due to the vanishing of the Jacobian transforming momentum-space coordinates into angular coordinates.

For planar scattering ( $K_{np} = 0$ ), KF may occur only along symmetry directions. For relatively heavy probes, like Ne, and large  $\theta_f$  and  $\theta_1$ , KF occurs at small phonon group velocities, i.e. for phonons close to the critical points, where the phonon density is large.<sup>16</sup> Avila and Lagos have discussed another important enhancement mechanism for non-planar KF which explains Williams and Mason's data.<sup>15</sup>

Boato and Cantini<sup>17</sup> performed a careful investigation of the angular distributions of Ne planar scattering from LiF(001), finding a rich fine structure in addition to the elastic diffraction pattern. Although interpreting such inelastic features as due to KF yielded frequencies of surface modes in reasonable agreement with the theoretical prediction for Rayleigh and Lucas modes at  $\bar{M}$  and  $\bar{\Gamma}$  critical points<sup>18</sup>, Cantini, Felcher and Tatarek found a more convincing explanation of the fine structure in terms of inelastic resonances with surface bound states<sup>19</sup>. In addition, their kinematical analysis led to a rough determination of KW dispersion. Cantini and Tatarek have made a similar analysis for the inelastic resonances of He scattered from graphite (0001).<sup>20</sup>

The high-resolution angular distributions recently obtained by Brusdeylins *et al* for He scattering from LiF(001) and NaF(001)<sup>21</sup> give only a faint evidence of KF effect, its features being hardly distinguishable from the complicated pattern of inelastic resonances.

Thus KF could be visible only where the channels to bound states are extremely weak, as in metals, but we do not know of any example, apart from some poorly understood data on He-Au (111).<sup>22</sup>

However, in view of the recent advance in the theory and design<sup>8</sup> of highly monochromatic nozzle beam sources, the KF way to surface phonons has been abandoned in favour of TOF spectroscopy.

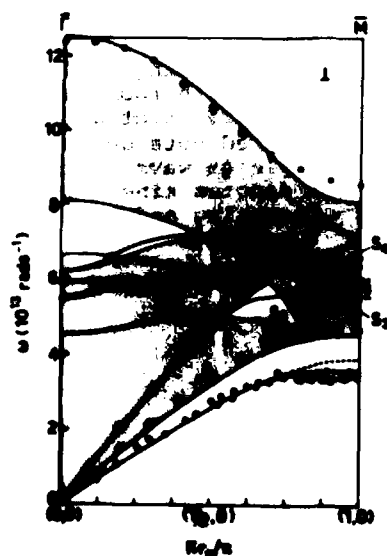


Fig. 2 : Surface phonon dispersion curves in LiF(001) along (100) for sagittal polarisation. Comparison is made with He<sup>4</sup> scattering data (o) and neutron data (e).

3. The analysis of time-of-flight spectra.— In the late seventies TOF measurements provided a *direct* evidence of Rayleigh waves in the THz range<sup>23,24</sup>. The high-resolution spectra measured by Toennies group in Göttingen led for the first time to the full determination of the RW dispersion as well as of the energy loss profiles in LiF<sup>25</sup>, NaF (fig. 1b) and KCl.<sup>14</sup>

These experiments have stimulated a new effort in the theory of inelastic processes<sup>26-30</sup>. Most of the features found in TOF spectra—dominance of RWs and cut-off of optical frequencies—were predicted already in the framework of the distorted wave Born approximation (DWBA)<sup>31</sup>.

The validity of this theory for ionic crystals, where the surface is quite corrugated, is in question, however, since the non-specular part of the potential works as a perturbation. Physically it would mean that unklapp processes involving surface-reciprocal lattice vectors  $G \neq 0$  have to be less probable, which is clearly in contrast with the observation of strong quantum rainbow effects.<sup>17</sup>

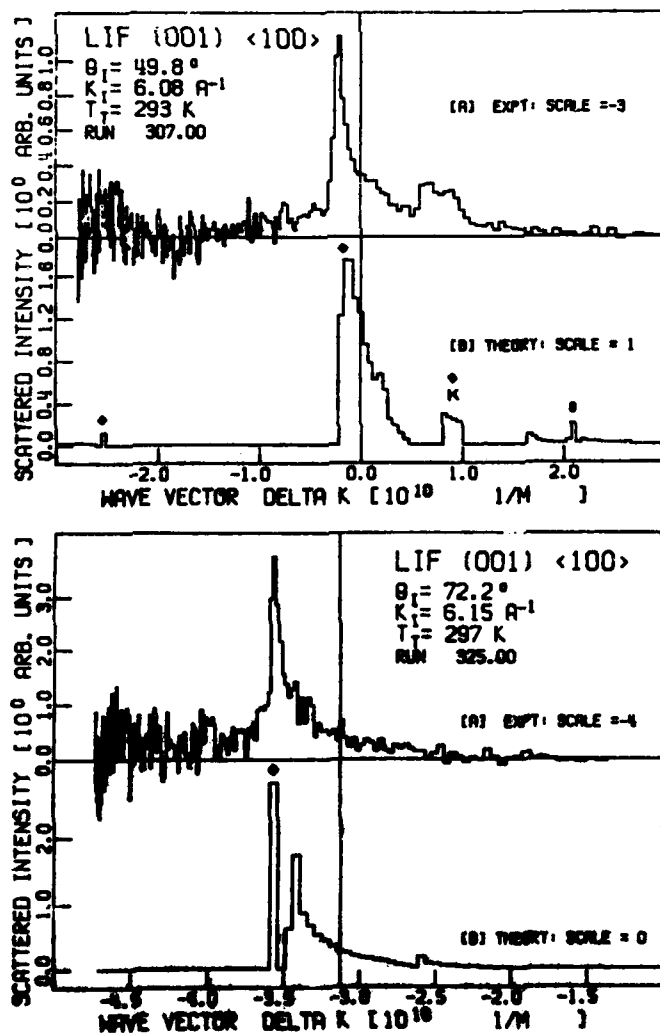


Fig. 3 : Time-of-flight spectra of He scattered from LiF (001) surface along (100) for incidence angle  $\theta_i = 49.8^\circ$  and  $72.2^\circ$  (from ref. 14) and calculated one-phonon reflection coefficient for a hard corrugated surface model. The calculation of the phonon densities is based on the Green's function method and the breathing shell model with room temperature input data. Squared dots denote Rayleigh wave peaks, K denotes kinematical focussing and 0 labels Lucas mode.

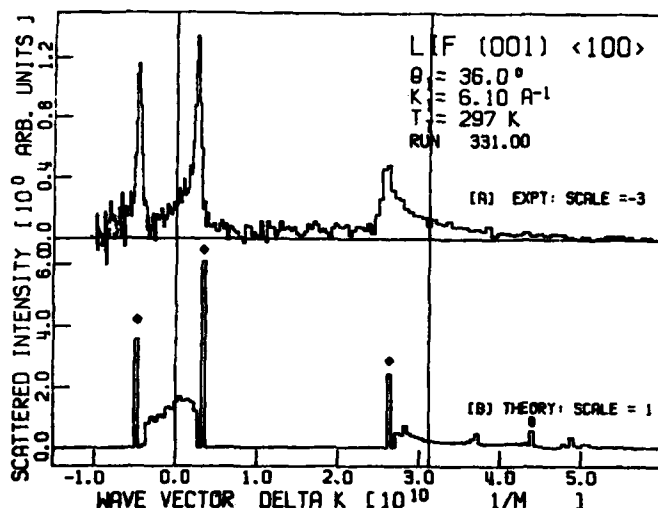


Fig. 4 : Same as fig. 3 for incidence angle  $\theta_i = 36.0^\circ$ .

Thus in the theoretical interpretation of TOF data our main concern is the non-perturbative treatment of the static corrugated potential. We work in a DWBA where only the phonon-induced corrugation acts as a perturbation. The one-phonon reflection coefficient for a process casting an incident atom of momentum  $\vec{k}_i$  into a final state  $\vec{k}_f$  oriented within a solid angle  $d\Omega$ , is expressed by<sup>28</sup>

$$\frac{d^2R(1)}{d\omega d\Omega} = \frac{k_z^2}{8\pi^3} \left| \frac{k_f}{k_{iz}} \right| \left| 1 + \coth \frac{\omega}{2k_B T} \right| \sum_{\kappa\kappa',\alpha\beta} g_{\kappa\alpha}(\vec{k}) g_{\kappa'\beta}^*(\vec{k}) \rho_{\kappa\alpha,\kappa'\beta}(\vec{k},\omega), \quad (2)$$

where  $T$  is the surface temperature, and  $\rho_{\kappa\alpha,\kappa'\beta}(\vec{k},\omega)$  are the elements of surface-projected phonon density matrix.

If  $z = D_0(\vec{R})$  represents the static surface profile,  $D_0(\vec{R})$  being a periodic function of the position vector  $\vec{R} = (x,y)$ , the coupling coefficients are given by

$$g_{\kappa\alpha}(\vec{k}) = \int d\vec{R} \exp(-W(\vec{R}) - i\vec{k} \cdot \vec{R} + ik_z D_0(\vec{R})) g_0(\vec{R}) \partial D_0(\vec{R}) / \partial u_{\kappa\alpha}, \quad (3)$$

where  $\partial D_0(\vec{R}) / \partial u_{\kappa\alpha}$  is the distortion of the surface profile due to a unit displacement  $\vec{u}_{\kappa\alpha}$  of the  $\kappa$ -th ion, and  $W(\vec{R})$  is the Debye-Waller factor. The scattering amplitude  $g_0(\vec{R})$  is obtained by solving numerically the Lippmann-Schwinger equation in the direct space for the static corrugated surface, using a method developed by Garcia and Cabrera.<sup>32</sup>

The surface-projected phonon densities are calculated by the Green's function method,<sup>12</sup> for 33 values of  $\vec{k}$  in the irreducible segment  $\Gamma\bar{M}$  lying in the scattering plane, and for 100 equally-spaced values of  $\omega$  between 0 and the maximum crystal frequency. This calculation is equivalent to a slab calculation with 192 layers.

Fig. 2 shows the dispersion curves along (100) of LiF(001) surface modes with sagittal polarization - the one involved in planar scattering. Heavy lines are surface modes. Thin lines are band edges of bulk modes having non-vanishing sagittal component. When a dispersion curve enters a band, the surface-localized mode transforms into a reso-

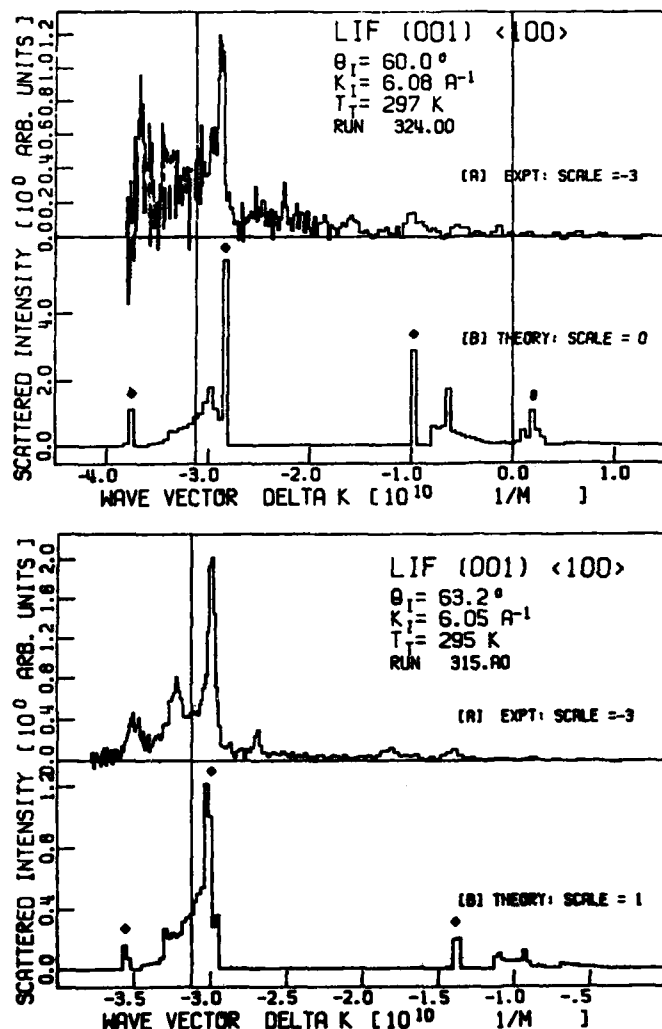


Fig. 5 : Same as fig.3  
for incidence angles  
 $\theta_i = 60.0^\circ$  and  $63.2^\circ$ .

nance. The RW dispersion curve is compared to the atom scattering data (open circles)<sup>25</sup>. The broken line shows the shell model slab calculation by Chen *et al.*<sup>13</sup>. The quality of bulk dynamics can be judged by comparing to neutron data (black points) the band edges which correspond to bulk dispersion curves along symmetry directions.

In this calculation, based on BSM and room temperature data, bulk ( $\alpha_{\pm}^B$ ) and surface ( $\alpha_{\pm}^S$ ) ion polarizabilities are equal ( $\alpha_{\pm}^B = \alpha_{\pm}^S$ ) and taken from the classical compilation of Tessmann, Kahn and Shockley<sup>33</sup> (TKS).

If  $\alpha_{\pm}^S$  is allowed to be larger than  $\alpha_{\pm}^B$  and both are adjustable, the residual discrepancies at the  $\bar{M}$  point can be removed in both bulk and RW dispersion curves.<sup>29</sup> Despite the general argument that surface polarizabilities should be larger than bulk polarizabilities owing to the smaller coordination, we did not use this fitting procedure here, since TKS values yield an excellent fit in NaF and KCl and a reasonable compromise in LiF.

In evaluating  $d^2R^{(1)}/d\omega d\theta$ , we use the static surface profile  $D_0(\vec{R})$

which gives the best fit to diffraction amplitudes according to Garcia<sup>32</sup>. The kinematical parameters ( $k_1 = 6.1 \text{ \AA}^{-1}$ ;  $\theta_1 = 90^\circ - \theta_f = 49.8^\circ, 72.2^\circ, 36.0^\circ, 60.0^\circ$  and  $63.2^\circ$ ) correspond to a selected set of TOF spectra measured by Brusdeylins, Doak and Toennies with the apparatus of ref. 25. Experimental and theoretical spectra are shown together in figs 3-5 as functions of  $K$ . The phonon energy is readily obtained from eq. 1 with  $K_p = K$  and  $K_{np} = 0$ . The vertical lines correspond to  $K = G = \text{integer} \times 2\pi/a$  where  $a$  is the interionic distance.

The theoretical RW peaks are represented by isolated rectangular peaks (marked by  $\diamond$ ). At low energy ( $K$  close to  $G$ ) the RW peak is not resolved from the continuous bulk density. Close to KF condition the RW peak may extend over several bins. This is seen in fig. 3 ( $\theta_1 = 49.8^\circ$ ), where the KF induced broadening of the RW peak  $K$  reflects fairly well the experimental structure. Here the RW peak at  $K \sim -0.2$  is not resolved, but the spectra appear to be in reasonably good agreement.

At  $\theta_1 = 72.2^\circ$ , the single RW peak is well resolved letting one appreciate how important is the bulk phonon contribution forming the long tail above  $K = -3.4$ .

A richer structure is found for  $\theta_1 = 36.0^\circ$  (fig. 4). Here the intensities of the three distinct RW peaks are in very good agreement with the predicted intensities. Again the experimental tails aside the RW peaks are seen to correspond to bulk phonon structures. While the band around  $K = 0$  contains acoustic phonons, the long tail above  $K = 2.8$  comes essentially from optical phonons. The small theoretical peak 0 is a Lucas optical surface mode ( $S_4$  in fig. 2); this is also predicted for  $\theta_1 = 49.8^\circ$  and  $60.0^\circ$  (fig. 5) but no evidence is found in TOF spectra.

A similar overall agreement is found also in fig. 5 ( $\theta_1 = 60.0^\circ, 63.2^\circ$ ). However, once we fit the maximum intensities around  $K = -3$ , we note that the RW intensity at larger (smaller) absolute momentum transfer is weaker (stronger) than the observed one.

The general good agreement between theory and experiment means, for the experimentalist, that *one-phonon processes are dominant* and, for the theoretician, that the Green's function method for surface dynamics and the HCS model employed in scattering theory work quite well. However, the future interest is on the discrepancies.

Why does theory predict too large (small) intensities at small (large) momentum transfers? Why are the predicted Lucas mode peaks not (yet) seen in the experiments?



Fig. 6 : Surface phonon dispersion curves of KCl(001) along the symmetry directions for sagittal (I) and parallel (II) polarization.

An answer to these questions will probably come from a better description of the surface-atom potential, including the attractive part and the effects of bound-state resonances. For example, the weakness of Lucas modes in scattering could mean that  $\text{Li}^+ - \text{He}$  interaction is even weaker than that schematically described by the chosen surface profile. Actually, the difficulty existing in LiF for the observation of optical modes is that the radius and the polarizability of Li ion (the ion which moves in optical modes) are too small and consequently so are both repulsive and attractive interactions with He atoms.

A better situation occurs in crystals like KCl, where the ions have approximately the same mass and are both polarizable. Moreover in KCl optical frequencies are smaller than  $k_B T$  (room temperature) and  $\omega_1$ , and can therefore be observed in both energy loss and gain processes. Indeed in KCl(001), besides sharp RW peaks, additional structures corresponding to the strong resonance  $S_8$  are observed in TOF spectra:<sup>14</sup> such experimental points are compared to the calculated dispersion curves in fig. 6. Further weak and barely resolved features can be related to optical modes of higher frequency ( $S_2$ ,  $S_6$  and  $S_4$ ), but such interpretation is still *sub judice*. We hope that future measurements will confirm this stimulating observation.

#### References

1. G. Benedek, Proc. Int. School of Physics "E. Fermi", Course LVIII, ed. F.O. Goodman (Compositori, Bologna 1974), p. 605.
2. K.H. Rieder, Surface Sci. 26, 637 (1971).
3. J. Sandercock, Solid State Comm. 26, 547 (1978).
4. A. Otto, Z. Physik 216, 398 (1968).
5. H. Ibach, Phys. Rev. Letters 24, 1416 (1970).
6. T. Wolfram, Inelastic Electron Tunnel Spectroscopy (Springer V.1978)
7. N. Cabrera, V. Celli and R. Manson, Phys. Rev. Letters 22, 346 (1969).
8. J.P. Toennies and K. Winckelmann, J. Chem. Phys. 66, 3965 (1977).
9. R.B. Subbarao and D.R. Miller, J. Chem. Phys. 51, 4679 (1969).
10. B.R. Williams, J. Chem. Phys. 55, 1315 and 3220 (1971).
11. B.F. Mason and B.R. Williams, J. Chem. Phys. 61, 1435 (1974).
12. G. Benedek, Surface Sci. 61, 603 (1976).
13. T.S. Chen, F.W. de Wette and G.P. Alldredge, Phys. Rev. B15, 1167 (1977)
14. R.B. Doak, Thesis (M.I.T. 1981, unpublished) and private comm.
15. R. Avila and M. Lagos, Surface Sci. 103, L104 (1981).
16. G. Benedek, Phys. Rev. Letters, 35, 234 (1975).
17. G. Boato and P. Cantini, Proc. Int. School of Physics "E. Fermi", Course LVIII, ed. F.O. Goodman (Compositori, Bologna 1974), p. 707.
18. Ref. 13, footnotes 41 and 42.
19. P. Cantini, G.P. Felcher and R. Tatarek, Phys. Rev. Letters 37, 606 (1979)
20. P. Cantini and R. Tatarek, Phys. Rev. B 23, 3030 (1981).
21. G. Brusdeylins, R.B. Doak and J.P. Toennies, J. Chem. Phys. 75 (A), 1781 (1981).
22. D.R. Miller and J.M. Horne, Proc. 7th Intern. Vac. Congr. and 3rd Int. Conf. Solid Surfaces (Vienna 1977) p. 1385.
23. J.M. Horne and D.R. Miller, Phys. Rev. Letters 41, 511 (1978).
24. B. Feuerbacher, M.A. Adriaens and H. Thuis, Surf. Sci. 94, L171 (1980).
25. G. Brusdeylins, R.B. Doak and J.P. Toennies, Phys. Rev. Letters 44, 1417 (1980) and 46, 437 (1981).
26. G. Armand and J.R. Manson, Surface Sci. 80, 532 (1979).
27. M. Lagos and L. Birstein, Surface Sci. 51, 469 (1975).
28. A.C. Levi, Nuovo Cim. B 54, 357 (1979).
29. G. Benedek and N. Garcia, Surf. Sci. 80, 543 (1979); 103, L143 (1981).
30. H.D. Meyer, Surface Sci. 104, 117 (1981).
31. G. Benedek and G. Seriani, Jpn. J. Appl. Phys. Suppl. 2, pt. 2, 545 (1974)
32. N. Garcia and N. Cabrera, Phys. Rev. B18, 576 (1978).
33. J.R. Tessman, A.H. Kahn and W. Shockley, Phys. Rev. 92, 890 (1953).



## GRAPHITE SURFACE PHONONS STUDIED THROUGH He ATOMS RESONANT SCATTERING

P. Cantini, G. Boato and R. Tatarek

*Istituto di Scienze Fisiche dell'Università di Genova, Viale Benedetto XV,  
5 - 16132 Genova, Italy*

Abstract.— He atom scattering has been used to study phonon-assisted bound state resonances and the Debye-Waller factor for the basal plane of graphite. A dispersion relation is reported for the surface phonons involved in the resonances. The attenuation of the specular peak in the temperature range from 20 to 315 K is used to derive the mean-square displacement  $\langle u_{\perp}^2 \rangle$  of surface atoms, perpendicular to the (0001) plane. The anomalous thermal behaviour of  $\langle u_{\perp}^2 \rangle$  is explained by considering the layered structure of the crystal.

Light atom scattering is in principle a powerful technique to study surface lattice dynamics. Detailed information on the dispersion relation of surface phonons can be obtained in special cases with the only study of angular distribution of the scattered particles, without any energy analysis. This is just what happens with the study of phonon assisted resonances, a process that was extensively studied recently for the He/graphite system [1].

We recall that the kinematic conditions for a scattering process involving the exchange of a single phonon are:

$$k^2 = k_0^2 \pm 2M\omega_q/\hbar, \quad \vec{k}_G = \vec{k}_0 + \vec{G} \pm \vec{Q} \quad (1a-b)$$

where  $\vec{k}=(\vec{k}, k_z)$  is the wave vector of the gas atom of mass  $M$ , while  $\hbar\omega_q$  and  $\vec{Q}$  are the energy and parallel wave vector of the exchanged phonon;  $\vec{G}$  is a surface reciprocal lattice vector. For in-plane scattering, a resonant structure in the angular distribution of the scattered atom, located at the polar angle  $\vartheta_f^*$  and observed at incident angle  $\vartheta_0$  must permit to obtain  $\hbar\omega_q^*$  and  $\vec{Q}^*$  for the involved phonon through the solution of the two equations

$$k_0^2 \pm 2M\omega_q^*/\hbar - (\vec{k}_0 + \vec{N} \pm \vec{Q}^*)^2 - 2M\varepsilon_j/\hbar^2 = 0 \quad (2)$$

$$k_0^2 + 2M\omega_q^*/\hbar - (\vec{k}_0 + \vec{F} \pm \vec{Q}^*)^2 / \sin^2 \vartheta_f^* = 0 \quad (3)$$

where Eq.2 represents the condition for an atom to enter a bound state  $(\epsilon_j, \vec{N})$  while Eq.3 is the condition for the atom to be scattered at a given final angle  $\vartheta_f$  through the final  $\vec{F}$  diffraction channel. The resonant state labeled  $(\epsilon_j, \vec{N})$  is an intermediate state in which the atom is diffracted in a closed channel  $\vec{N}$ , with its perpendicular energy negative and equal to an energy level  $\epsilon_j$  of the atom-surface potential  $\hbar^2 k_{Nz}^2 / 2M = \epsilon_j < 0$ .

For He/graphite system we selected and analysed about 120 angular distributions, where about 180 resonance structures were identified. Details of the experiment are reported elsewhere [1,2]. The angular positions of the resonant structures  $(\vartheta_o, \vartheta_f^*)$  gave, through Eqs.2 and 3 the  $\hbar\omega_q^*$  and  $\vec{Q}^*$  of the phonon involved in the resonance. All the observed points belong to a limited region of the surface projected phonon dispersion relation  $\omega(\vec{Q})$ . The best fit region of the experimental points is reported in Fig.1 as a dashed area, and compared with the dispersion relations  $\omega(\vec{Q})$  for bulk phonons travelling along the  $\Gamma M$  direction, as obtained by neutron scattering [3]. The experimental region contains the transverse acoustic mode  $TA_1$  for bulk phonons; this seem to indicate a strong contribution of Rayleigh phonons to surface scattering.

In order to study the thermal vibration at the surface, the specularly reflected intensity was also measured at several incident angles, for surface temperatures  $20 \text{ K} < T_s < 315 \text{ K}$ . The thermal attenuation of the specular beam was represented by the conventional Debye-Waller formula  $P_{\text{exp}} = P_{\text{el}} \exp(-2W)$ , where the D-W coefficient for atom scattered by surfaces is  $2W = q_z^2 \langle u_1^2 \rangle$ ,  $q_z$  being the momentum transfer perpendicular to the surface. The elastic probability  $P_{\text{el}}$  was calculated in the eikonal approximation and the  $\langle u_1^2 \rangle$  values were obtained from  $P_{\text{exp}}$ . The average values obtained at different surface temperatures are reported in Fig.2 with their statistical error. The  $\langle u_1^2 \rangle$  value at room temperature is in agreement with the bulk value obtained by Chen and Trucano [4], who evaluated a Debye temperature of about 530 K. However the temperature dependence does not follow the Debye curve, reported in Fig.2 (curve (a)). We tried to explain the appreciable

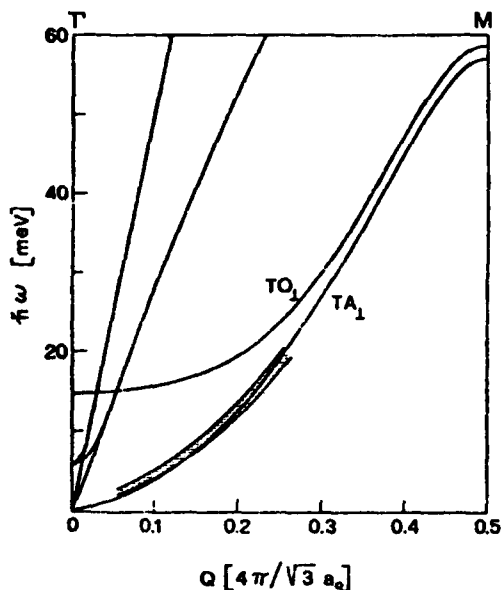


Fig. 1 : Most probable experimental dispersion relation of surface phonon (dashed region) compared with the bulk phonon spectrum in the  $\Gamma M$  direction (Ref.3).

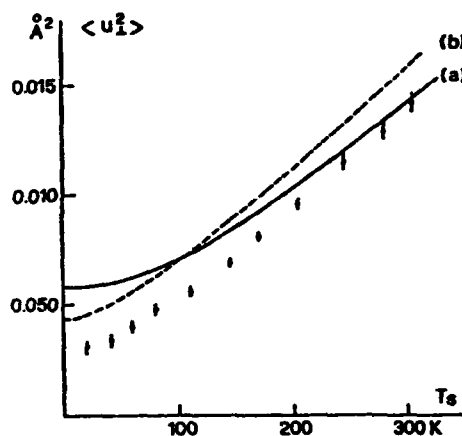


Fig. 2 : Mean-square displacement of surface atoms  $\langle u_1^2 \rangle$  vs surface temperature, compared with the Debye curve (a) and the curve calculated in the text (b).

decrease of  $\langle u_1^2 \rangle$  at low temperature taking into account of the anisotropy and the layered structure of graphite crystal. We assumed a quadratic dispersion relation at low  $Q$ , as obtained by neutron data [3] and by atom scattering. Details of this calculation are reported elsewhere [2]. The  $\langle u_1^2 \rangle$  so calculated is reported in Fig.2 (curve (b)). It appears that the temperature dependence of the experimental points is now well reproduced. The remaining shift of curve (b) can be attributed to both some uncertainty in the absolute experimental intensities and to the simplified assumed phonon spectrum.

#### References

- 1 P. Cantini and R. Tatarek, Phys.Rev. B 23 (1981) 3030.
- 2 G. Boato, P. Cantini, C. Salvo, R. Tatarek and S. Terreni, to be published.
- 3 R. Nicklow, N. Wakabayashi and H.G. Smith, Phys.Rev.B 5 (1972) 4951.
- 4 R. Chen and P. Trucano, Acta Crystallografica A 34 (1978) 979.

## THEORY OF ACOUSTIC PHONONS AT INTERFACES AND BRILLOUIN SCATTERING

V. Bortolani, F. Nizzoli, G. Santoro and A. Marvin\*

*Istituto di Fisica and G.N.S.M.-C.N.R., Università di Modena, 41100 Modena, Italy**\*Istituto di Fisica Teorica, Università di Trieste, 34014 Miramare-Grignano, Trieste, Italy*

**Abstract.**- We present calculations of the Brillouin cross section for a metallic thin film (Al and Au) on a Si substrate. The results for the Al coating are explained in terms of scattering from the surface corrugation due to the thermally excited acoustic phonons. In the case of Au we find an appreciable contribution from the elasto-optic coupling in the film.

1. Introduction.- For clean surfaces, it has been found that the light is inelastically scattered both from the dynamical corrugation of the surface due to the phonon field (ripple effect)<sup>(1)</sup> and from the dielectric inhomogeneity of the medium (elasto-optic effect)<sup>(2)</sup>. In both cases the spectral function shows structures related to the surface modes (Rayleigh waves-RW) and to combinations of bulk modes with modes localized near the surface (the so called mixed modes)<sup>(3,4)</sup>. In this paper we consider the case of coated surfaces and we show that the interface existing between the coverage and the substrate causes new modes to appear in the Brillouin spectra<sup>(5,6)</sup>. The calculations will refer to a (001) Si substrate and to backscattering geometry, that is the scattered light is assumed to be collected in a certain solid angle around the incidence direction, making an angle  $\theta$  to the surface normal. Under these conditions the experiment probes the Fourier components of the phonon field with a fixed parallel wavevector  $\vec{Q}_{\parallel}$ , equal to minus twice the parallel component of the wavevector of the incident light<sup>(7)</sup>. Conversely, due to the lack of translational invariance along the surface normal, all the complex normal wavevectors  $q_{\perp}$  of the phonon field are mixed in the experiment and contribute to the spectra. We consider here a parallel wavevector  $\vec{Q}_{\parallel}$  directed along [100] and TM light of wavelength 5145 Å. The angle  $\theta$  is equal to 70°.

2. Calculation of the cross section.- The computed cross section for a coated surface is found to be the square modulus of the sum of four contributions<sup>(8)</sup>, due to: a) scattering from the surface ripples (proportional to  $|v_z|^2$  computed at the film surface), b) scattering from the interface ripples (proportional to  $|v_z|^2$  at the interface), c) and d) elasto-optic coupling in the film and substrate respectively. The latter two terms are complicated combinations of the normal modes of the two media. Let us first show a comparison between experiment and theory in the case of an Al coating. A tandem multipass interferometer (5 pass plus 2 pass) has been used<sup>(7)</sup>. The fig.1 refers to film thickness of 2000 Å. The experimental points are compared with the cross sec-

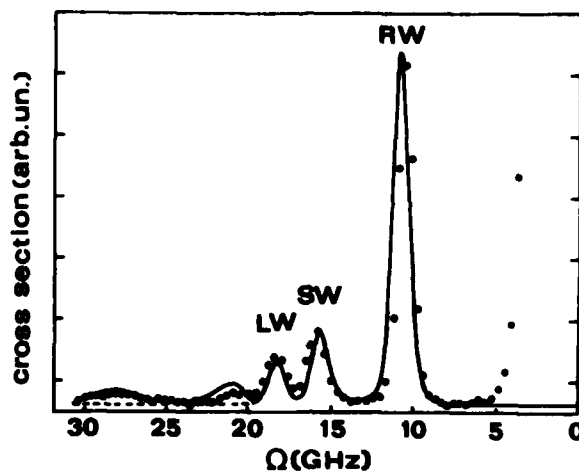


Fig. 1 : Experimental (dots) and computed (full line) Brillouin cross section for a 2000 Å film of Al deposited on Si (Stokes spectrum). The broken line shows the spectrum without the contribution of the continuum of phonon mixed modes.

tion computed by including the contribution a) only. This is in fact very reasonable for the Al surface, due to the high value of its dielectric constant<sup>(1,3,4)</sup>. Also in our case of a supported film, an explicit calculation with the elasto-optic coefficients of Al and Si confirmed that the only important term is a). Although this term depends on the displacement field at the film surface, it shows important features due to the presence of the interface. In Fig.1 the frequency of the RW, nearly 11.3 GHz, is strongly different from that of Al, that is 10.4 GHz. Indeed the most dramatic effect due to the interface is the appearance of a Sezawa wave (SW1)<sup>(9)</sup> at about 16 GHz and of a Lamb wave (LW1) at 18 GHz. They are followed at higher frequencies by a continuum of phonons, extending from 21 to 30 GHz. These modes eventually give rise to new thin-film modes, on further increasing the thickness.

We pass now to a gold thin-film. The dielectric constant of gold at 5145 Å is very small ( $\epsilon = -3.19 + i2.47$ ) and we expect an appreciable contribution from the term c). This is clearly shown in Fig.2 for 1000 Å of gold deposited over Silicon. The position of the RW, of the Sezawa and Lamb waves and of the resonance in the continuous spectrum (nearly 21 GHz) are well accounted for, but the relative amplitudes of various peaks is not reproduced. This is a clear indication of the importance of the elasto-optic coupling in the film. Unfortunately the elasto-optic coefficients of Au are not known and this prevents a quantitative comparison between the full theory and the measured spectrum. However, calculations of the Brillouin cross section with the elasto-optic coefficients of gold in the realistic range 1-10 gave strong modifications in the relative amplitudes of the peaks. In particular, the waves having a strong longitudinal character (SW, LW1, LW2 and LW3) can be affected by the introduction of the elasto-optic contribution. Instead RW and LW4, mostly transverse, do

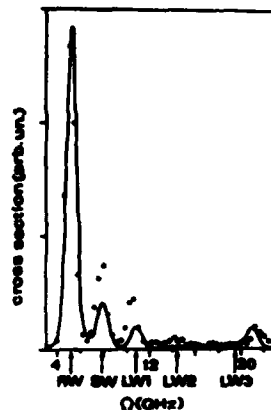


Fig. 2 : As in Fig.1. Gold film thickness 1000 Å (anti-Stokes spectrum).

not depend on the latter coupling.

In conclusion, we have shown that the Brillouin spectra from thermally excited acoustic phonons in coated surfaces differ considerably from those obtained in clean surfaces. In particular, we have found important structures whose number increases as the film becomes thicker. These structures have been explained in terms of thin-film waves polarized in the sagittal plane (Sezawa and Lamb modes).

#### References

1. R Loudon, Phys. Rev. Lett. **40**, 581 (1978)
2. V Bortolani, F Nizzoli and G Santoro, Phys. Rev. Lett. **41**, 39 (1978)
3. A Marvin, V Bortolani and F Nizzoli, J. Phys. C **13**, 299 (1980) and references therein
4. A Marvin, V Bortolani, F Nizzoli and G Santoro, J. Phys. C **13**, 1607 (1980)
5. V Bortolani, F Nizzoli, G Santoro, A Marvin and J R Sandercock, Phys. Rev. Lett. **43**, 224 (1979)
6. N L Rowell and G I Stegeman, Phys. Rev. Lett. **41**, 970 (1978)
7. J R Sandercock, Solid St. Commun. **26**, 547 (1978)
8. V Bortolani, F Nizzoli, G Santoro, J R Sandercock and A Marvin, to be published
9. G W Farnell and E L Adler, Physical Acoustic, vol. IX, pp. 33-127, Academic Press, New York (1972)

# HOW MUCH INFORMATION CAN LOW ENERGY ION SCATTERING GIVE ABOUT SURFACE PHONONS ?

D.J. Martin and R.P. Walker\*

*Department of Pure and Applied Physics, University of Salford, Salford, Lancashire M5 4WT, U.K.*

*\*Daresbury Laboratory, SERC, Warrington WA4 4AD, U.K.*

**Abstract** - Using correlation coefficients calculated in the Born von-Kármán model, the temperature variation of low energy ion scattering spectra is shown to be capable of giving information on surface Debye temperatures but not on detailed aspects of surface phonons.

1. Introduction. - Low energy ion scattering [1] can be exploited to give information on surface phonons [2]. We have shown, [3] using the Debye model, that correlations between atomic vibrations have a significant influence on these results and now extend these studies by using the Born von-Kármán model for the phonons. The results for the ion scattering using this model, differ from the Debye case and it should be possible to obtain information on the correlations. However, the technique cannot readily give information on details such as the force constant ratios.

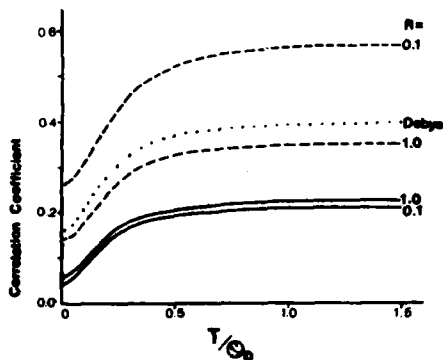
2. Mean square atomic displacements and correlations. - On the basis of an earlier study [4] we have developed a Born von-Kármán calculation for  $\langle u^2(T) \rangle$  and the correlation coefficients  $\rho(u_\alpha, u_\beta)$  in a simple model of bulk monatomic FCC and BCC crystals. Only the next-nearest neighbour and nearest neighbour force constants, of ratio  $R$ , are used. This model is crude for surface phonons but it allows us to examine the influence of the two major parameters  $T/\theta_D$  ( $\theta_D$  set to agree with the Debye result for  $\langle u^2(T \rightarrow \infty) \rangle$ ) and  $R$ .

The results for  $\langle u^2(T/\theta_D) \rangle$  are insensitive to  $R$ ; they deviate only a few percent from the Debye result. In general the correlations are, as expected, much more sensitive to  $R$  and differ markedly from the Debye result, as shown in figure (1). However, the particular correlation coefficient which is important for ion scattering is that for displacements perpendicular to the atomic row and, as shown in

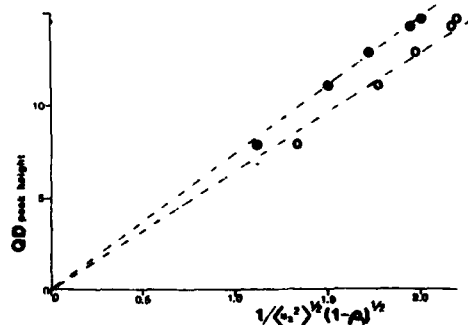
figure (1), this is particularly insensitive to change in  $R$ . Studies in other directions and also in FCC crystals reveal a similar pattern: for orthogonal displacements  $\rho$  is  $\sim 60\%$  of the Debye value and changing  $R$  from 0.1 to 1.0 changes  $\rho$  by only  $\sim 20\%$ .

3. Quasi-double and quasi-triple ion scattering. - It is possible to characterize peaks in the intensity against energy measurements of ion scattering spectra as quasi-double (QD) and quasi-triple (QT) [1]. On the basis of a simple two-atom model [3] the QD peak height is found to vary as  $A / \langle u_z^2 \rangle^{1/2} (1 - \rho_1)^{1/2}$  where  $A$  is an (inaccurately known) constant, related to the neutralization probability and scattering cross-section,  $\langle u_z^2 \rangle$  refers to displacements perpendicular to the chain and  $\rho_1$  is the correlation coefficient for nearest neighbour displacements perpendicular to the chain. Provided the measurements are extended to  $T < \theta_D$  it should be possible to measure surface Debye temperatures. Figure 2 shows a plot of the QD peak height for  $Kr^+$  scattering from Cu  $\langle 100 \rangle$  row, as obtained from "chain" simulation [3], against  $1 / \langle u_z^2 \rangle^{1/2} (1 - \rho_1)^{1/2}$ . The solid circles are the results for the correct  $\theta_D$ ; the open circles are the results if  $\theta_D$  is 20% too high. In practice  $\theta_D$  would be adjusted to give the best straight line through the origin. Unfortunately, it is difficult to extract separate information on  $\theta_D$  and  $\rho$  from QD results and lack of knowledge on  $\rho$  leads to errors in  $\theta_D$ .

A simple three atom model [3] gives for the QT peak height:



**Fig.1:** The correlation coefficients as a function of  $T/\theta_D$  for atoms of separation  $\langle 111 \rangle$  in a BCC monatomic crystals with  $R=0.1$  and  $1.0$ . The dotted curve is the Debye result. The broken curves are for displacements in the  $\langle 111 \rangle$  direction. The solid curves are for  $\langle 1\bar{1}0 \rangle$  displacements.



**Fig.2:** QD peak height from a computer simulation for 10keV  $Kr^+$  scattered for a  $\langle 100 \rangle$  row of Cu atoms for a scattering angle  $\theta = 30^\circ$ , plotted against  $1 / \langle u_z^2 \rangle^{1/2} (1 - \rho_1)^{1/2}$  for the correct value of  $\theta_D = 300K$  (solid circles) and for  $\theta_D = 360K$  (open circles).



$$\frac{D\theta_D}{\langle v_z^2 \rangle (3-4\rho_1-2\rho_2+4\rho_1\rho_2-\rho_2^2)} \exp \left\{ \frac{-\alpha\theta_D}{\langle v_z^2 \rangle (3-4\rho_1+\rho_2)} \right\} \quad (1)$$

where  $\langle v_z^2 \rangle = \langle u_z^2 \rangle mk \theta_D / \hbar^2$  and  $\alpha = \delta^2 mk / \hbar^2$

$D$  is a constant related to the scattering cross section and neutralization probability,  $\rho_2$  the correlation coefficient for displacements of second nearest neighbours in the row and  $\delta$  the depth of the "thermal pit" giving QT scattering. For  $T \gg \theta_D$  a plot of  $\ln(\text{QT peak height}) + \ln(T)$  against  $1/T$  will have slope  $\delta^2 mk \theta_D^2 / 3 \hbar^2 (3-4\rho_1+\rho_2)$ . Again separate information on  $\theta_D$  and  $\rho$  cannot be obtained. However, by choosing the scattering conditions to give QT scattering for  $T \ll \theta_D$  it is in principle possible to see evidence of the correlations and to measure them as shown in figure (3) where the predictions of equation (1) are compared with simulation results. Unfortunately, because the relevant correlation coefficients are insensitive to  $R$ , this information is of limited value.

If these results are true in general it follows that low energy ion scattering is only intrinsically capable of giving information on surface Debye temperatures and that QD peak measurements, extended to  $T \ll \theta_D$ , may be superior to QT measurements.

We are grateful to Drs G J Keeler, D G Armour, S A Cruz and E V Alonso for discussions and the SERC for grant support.

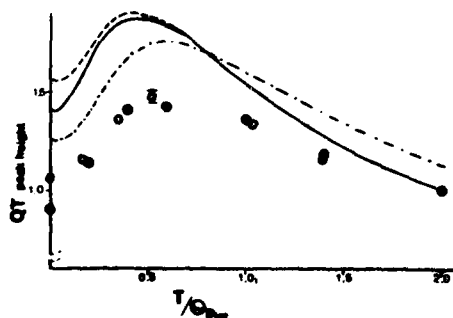


Fig.3. QT peak height for 4KeV  $\text{Ar}^+$  scattered from a  $\langle 111 \rangle$  row of Na atoms for  $\theta = 39.7^\circ$  and  $E_f = 2.93$  to 3.01keV. The curves show the predictions of equation (1), the points are simulation results. Solid curve and solid circles: uncorrelated Debye model  $\theta_D = 51\text{K}$ . Chain curve: correlated Born von-Karman model, same  $\theta_D$ . Broken curve and open circles: correlated Born von-Karman model  $\theta_D = 44.4\text{K}$ . N.B. simulations diverge for  $T \rightarrow 0$  due to change of  $\rho$  with  $T$

#### References

1. Boers, A.L., Surface Sci. **63** (1977) 475.
2. Poelsema, B., Verheij, L.K. and Boers, A.L., Nuclear Instr. Methods, **132**, (1976) 623.
3. Martin, D.J., Surface Sci. **97** (1980) 586 and Walker, R.P., and Martin, D.J. paper submitted to Surface Sci.
4. Keeler, G.J., in Physics Programs, ed. Boardman, A.D., (John Wiley, 1980).

## RESONANT BRILLOUIN SCATTERING IN OPAQUE REGION OF CdS

Y. Itoh, C. Hamaguchi and Y. Inuishi

*Faculty of Engineering, Osaka University, Suita City, Osaka 565, Japan*

**Abstract.** - Resonant Brillouin scattering has been investigated in CdS above and below the fundamental absorption edge at room temperature using acousto-electrically amplified phonon domains. Experimentally observed resonant behaviour has been analyzed on the basis of light-scattering theory and piezobirefringence theory. A good agreement is found when we take into account both the real and imaginary parts of the Brillouin tensor and piezobirefringence coefficients, especially near the absorption edges.

**1. Experiment.** - Resonant Brillouin scattering studies making use of the acousto-electrically amplified phonon domains have been reported by many workers.<sup>1-5)</sup> In these experiments, the incident photon energies were restricted to the region in which the samples were transparent because of the experimental conditions that the transmitted light signals were measured. Therefore, it is difficult to obtain the dispersion of the Brillouin scattering cross section in the opaque region due to the strong absorption. To overcome this restriction, Chang et al. proposed to utilize the scattering of reflected light and a high intensity Ar ion laser line between 457.9 nm and 514.5 nm.<sup>6)</sup> In the present work we adopted similar method except Fabry-Perot interferometer. The samples used in the present work are single crystals with  $\sim 20$  ohm-cm resistivity and with the scattering surface of optical flat mechanically polished and etched. The T2-mode phonons amplified through acoustoelectric effect propagate in the direction perpendicular to the c-axis with shear polarization parallel to the c-axis. The laser light beam is incident on a polished surface parallel to the c-axis and the scattering plane was perpendicular to the c-axis. Here, the Brillouin scattering process produces a scattered light out of the propagation direction of the reflected light beam. The light scattered by the ripple mechanism shows no rotation of the polarization, but the scattering by the elasto-optic mechanism is rotated by 90°. <sup>6)</sup> Our main interest in the present work is the latter mechanism in the opaque region. Therefore, we choose the polarization direction of the scattered light perpendicular to the incident light. The interaction length between phonon and photon is comparable to the penetrating depth ( $\alpha^{-1}$ ) and restricted to the surface region. Thus the scattering is induced by the surface acoustic waves. The identification of the surface acoustic waves was made by the sound velocity  $v(T2) = \sqrt{C_{44}/\rho} = (1.80 \pm 0.05) \times 10^5$  cm/sec and selection rules of the light polarization. Experiments in the transparent region were made by

using the method reported elsewhere.<sup>1-5)</sup>

**2. Discussions.** - Figure 1 shows wavelength dependence of the Brillouin scattering cross section  $\sigma_B$  (in arbitrary units) for 0.5 GHz T2-mode phonons at room temperature, where the open circles with error bars are obtained by the reflected light scattering geometry and the solid circles are the experimental data obtained by the transmission light scattering geometry. These two independent data were plotted by comparing with the theoretical curves. According to the theory for surface elasto-optic scattering in isotropic opaque materials, the cross section varies with absorption coefficient  $\alpha$ , as  $[1 + (\alpha\lambda/2\pi n)^2]^{-1}$ .<sup>6)</sup> For CdS at room temperature, the refractive index  $n=2.8$  and  $\alpha$  is nearly constant  $\sim 10^5 \text{ cm}^{-1}$ , for  $450 \text{ nm} < \lambda < 500 \text{ nm}$ . In the region, the measured Brillouin scattering cross section is reduced by less than  $\approx 5\%$ .<sup>6)</sup> Therefore, absorption correction can be neglected. In the wavelength region below the fundamental absorption edge, the Brillouin scattering cross section has a deep minimum (resonant cancellation) at around  $560 \text{ nm}$ .<sup>2)</sup> At shorter wavelengths, a resonant enhancement is observed in the neighbourhood of the absorption singularities. We find in Fig. 1 a clear resonant enhancement in the opaque region, where the three absorption edges  $506 \text{ nm}$ ,  $503 \text{ nm}$ , and  $491 \text{ nm}$  exist. Similar enhancement in this region is observed in CdS by Chang et al.<sup>6)</sup> The resonant features (resonant cancellation and resonant enhancement) in the transparent region have been well explained by the following light scattering theory. It is interesting to check whether the resonant enhancement in opaque region is explained by the same theory

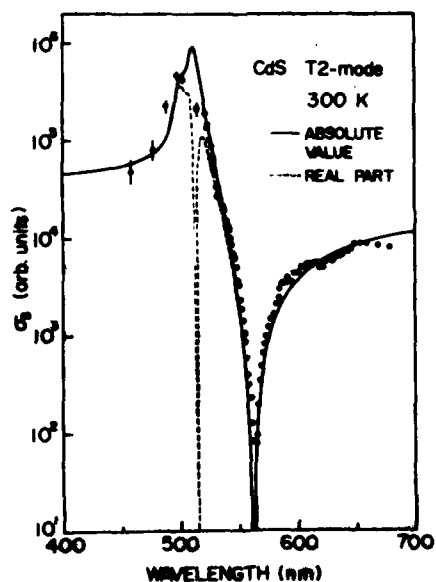


Fig. 1.-Dispersion curves of Brillouin scattering cross section for 0.5 GHz acoustic phonons. The present data in the opaque region is shown by open circles, while the data in the transparent region is shown by closed circles.

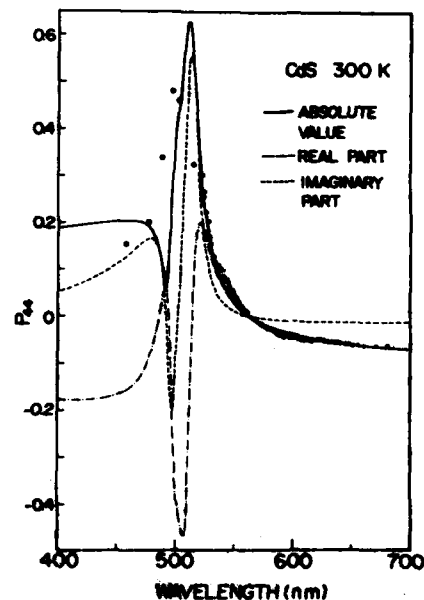


Fig. 2.-Dispersion curves of photoelastic constant  $P_{44}$  obtained from the data shown in Fig. 1. The present data in the opaque region is shown by open circles, while the data in the transparent region is shown by closed circles.

with the same parameters. In order to clarify this problem, we extend the existing theory in the opaque region. The scattering cross section  $\sigma_B$ , derived by Loudon has the form:<sup>1-5,7)</sup>

$$\sigma_B \propto |R_{is} + R_o|^2, \quad R_{is} = \frac{1}{V} \sum_{\alpha, \beta} \frac{P_{o\beta} \Xi_{\beta\alpha} P_{\alpha o}}{[\omega_\beta - (\omega_s + i\Gamma)][\omega_\alpha - (\omega_i + i\Gamma)]} \quad (1)$$

where  $R_{is}$  is the frequency dependent Brillouin tensor,  $\hbar\omega_i$  and  $\hbar\omega_s$  are the energy of the incident and scattered photons,  $\hbar\omega_q$  is the phonon energy,  $\Xi_{\beta\alpha}$  is the matrix element of the deformation potential scattering,  $P_{o\beta}$  and  $P_{\alpha o}$  are the appropriate momentum matrix elements, and  $R_o$  is the non-resonant term arising from far off critical points. Equation (1) indicates that the scattering cross section increases as the incident photon energy  $\hbar\omega_i$  approaches the electron-hole pair energy  $\hbar\omega_\alpha$  or  $\hbar\omega_\beta$ . The resonant cancellation ( $\sigma_B = 0$ ) occurs when  $R_{is} + R_o = 0$ .  $\Gamma$  is a phenomenological damping factor which is important in the resonant regions. A solid curve in Fig. 1 is calculated by eq. (1) including both the real and imaginary parts of  $R_{is}$ , where the exciton effect is taken into account in the manner derived by Zeyher et al.<sup>4,8)</sup> On the other hand, a dashed curve is calculated by taking into account the real part of eq. (1) only. The experimental data show a good agreement with the former results but a poor agreement with the latter calculation. From these results, we conclude that the imaginary part of  $R_{is}$  plays an important role, in particular, in the region of the absorption edges.

It has been shown that the Brillouin scattering cross section is analyzed from phenomenological aspect by incorporating the piezobirefringence theory.<sup>3-5)</sup> In Fig. 2 we show the dispersion curves of the photoelastic constant  $P_{44}$  determined by the relation  $\sigma_B(T2) \propto |P_{44}^r + iP_{44}^i|^2$ , where the superscript r and i indicate the real and imaginary part of  $P_{44}$ , respectively. Since the present method does not give signs and absolute values of the photoelastic constant but relative values, they are adjusted to the values of Yu and Cardona,  $P_{44}^r = -0.054$  at 630 nm.<sup>9)</sup> The theoretical curve of the absolute value of  $P_{44}$  ( $|P_{44}^r + iP_{44}^i|$ ) obtained from piezobirefringence analysis shows a good agreement with the experimental data in the region investigated. This indicates again that the imaginary part of the photoelastic constant plays an important role to determine the dispersion and thus the dispersion of the Brillouin scattering cross section in the resonant enhancement region.

#### References.

- 1) D.K.Garrod and R.Bray, Phys. Rev. B6 (1972) 1314.
- 2) K.Ando and C.Hamaguchi, Phys. Rev. B11 (1975) 938.
- 3) S.Adachi and C.Hamaguchi, Phys. Rev. B19 (1979) 938.
- 4) Y.Itoh, M.Fujii, C. Hamaguchi, and Y.Inuishi, J. Phys. Soc. Jpn. 48 (1980) 1972.
- 5) R.Berkowicz and T.Skattrup, Phys. Rev. B11 (1975) 2316.
- 6) W.C.Chang, S.Mishra and R.Bray, Proc. 15th Int. Conf. Physics of Semiconductors, Kyoto, J. Phys. Soc. Jpn. 59 (1980) Suppl. A, p711.
- 7) R.Loudon, Proc. Roy. Soc. A275 (1963) 218; J. Phys. 26 (1973) 29.
- 8) R.Zeyer, C.Ting and J.L.Birman, Phys. Rev. B10 (1974) 1725.
- 9) P.Y.Yu and M.Cardona, J.Phys. Chem. Solids 34 (1973) 29.

## THERMALIZATION OF HIGH-FREQUENCY PHONONS IN SILICON SINGLE CRYSTALS

R.E. Horstman and J. Wolter

*Philips Research Laboratories, Eindhoven, The Netherlands*

**Abstract.**— Heat pulses generated by means of small constantan heaters were transmitted through long silicon single crystals. Despite isotope scattering we find the transmitted energy to depend linearly on the applied heater power for heater temperatures between 5 K and 30 K. We obtain evidence that rapid thermalization of the phonon pulse takes place in the vicinity of the heater.

We report on experiments performed to study the influence of isotope scattering on the transmission of high-frequency phonons through long silicon crystals. The observed pulse shapes cannot be described with simple models for ballistic or diffusive phonon propagation. The experiments indicate that frequency down-conversion of high-frequency phonons takes place within several microseconds in the neighbourhood of the phonon generator.

The experiments were carried out on two dislocation-free silicon single crystals with cylindrical shape (5 cm diameter). One crystal (10 cm long) was grown along the [111] direction, the other (6 cm long) along the [100] direction. Constantan heaters (impedance 50 ohms) and aluminium bolometers ( $0.5 \times 0.2 \text{ mm}^2$ ) were evaporated onto opposite crystal ends. The crystals were immersed in liquid helium. Only the heater and the bolometer were mounted in vacuum cans.

Voltage pulses (50 ns duration) were applied to the heater. The detected signals were recorded by means of a Biomation 8100 transient recorder and stored in the memory of a Nicolet 1170 digital signal averager connected to a computer system for further data handling.

Typical signals for several heater temperatures are displayed in Fig.1 for the [111] crystal. The amplitudes of the pulses have been scaled to the same height to allow a better comparison of the pulse shapes. The arrows indicate the expected arrival times for ballistic phonon propagation of the transverse phonon modes [1]. These times are in good agreement with the observed onsets of the heat pulses. However, the observed signals are substantially broader than the duration (50 ns) of the original pulse applied to the heater. A negligible part of this broadening is due to the time constant of the bolometer (100 ns) and the finite dimensions of the heater and the bolometer. From the data [2] for the isotope scattering time we calculate the arrival times for the maximum amplitude in the phonon flux at the dominant phonon frequency in the Planck spectrum for different heater temperatures

(Table I). These times are much longer than the times observed for the arrival of the maximum phonon flux. Thus simple diffusive phonon propagation caused by isotope scattering does not explain the observed pulse shapes.

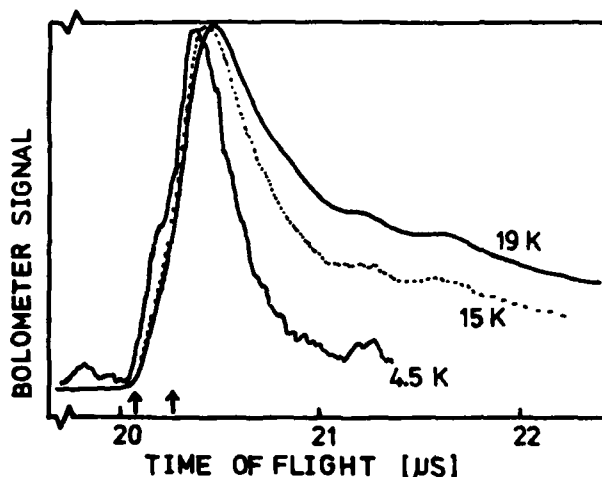


Figure 1: Bolometer signal for transverse phonons as a function of time for different heater temperatures.

$T_H/K$	$f_d/THz$	$\lambda/mm$	$t_a/\mu s$
3.8	0.2	100	20
6.7	0.4	10	100
12.0	0.7	1	1000
21.0	1.3	0.1	10000

Table I: Calculated mean free path  $\lambda$  and expected arrival time  $t_a$  of the maximum phonon flux for the dominant phonon frequency  $f_d$  in the Planck spectrum of a heater with temperature  $T_H$ .

We also determined the total energy arriving at the detector by integrating the phonon signal for different heater temperatures. For the L and T phonons in the [111] crystal Fig.2 shows the energy in the phonon signal as a function of the energy applied to the heater. The absolute energy scale was obtained from absolute measurements in the manner described in ref.3. We find that, independent of heater area and crystallographic direction, the detected energy is directly proportional to the applied heater energy. From the strong frequency dependence of the isotope scattering, however, we expect that, with increasing heater temperature, a decreasing fraction of the phonons propagates ballistically from the heater to the bolometer (dashed line in Fig.2).

The existence of isotope scattering in silicon was clearly observed in heat pulse reflection experiments [4,5]. The fact that it does not show up in our experiments suggests that the propagating phonons have much lower frequencies than the phonons generated in the heater. From experiments with an Al-Pb tunneljunction with tunable detection threshold [6] we obtained evidence that thermalization of the heat pulse takes place: for all bias voltages the detector signal depends linearly on the applied heater power indicating that the tunneljunction is simply warmed up.

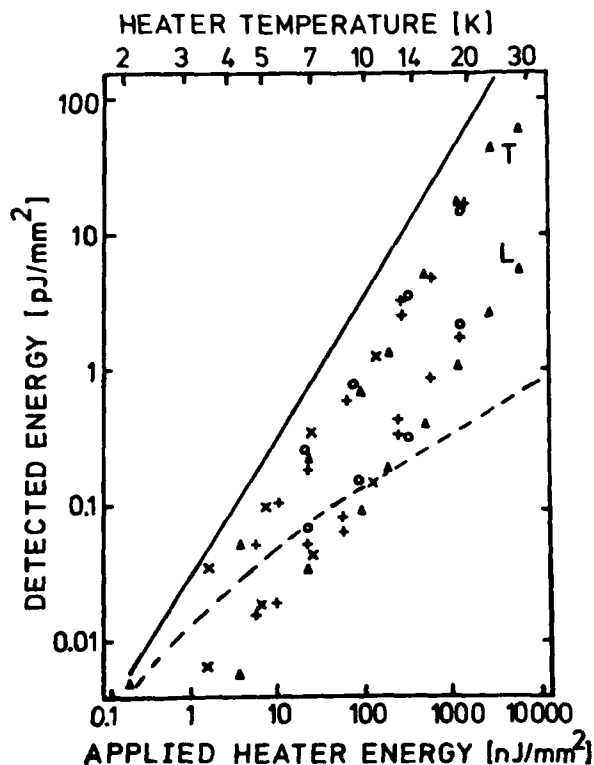


Figure 2: Transmitted energy for longitudinal and transverse phonons as a function of applied heater energy. Pulse length 50 ns. Upper axis shows calculated heater temperatures. (0) Absolute measurements for  $1 \times 1 \text{ mm}^2$  used for calibration. Relative measurements with heaters of dimensions  $2 \times 2 \text{ mm}^2$  (x);  $1 \times 1 \text{ mm}^2$  ( $\Delta$ );  $0.5 \times 0.5 \text{ mm}^2$  (+). Calculated transmitted energy: (fully drawn line) all transverse phonons propagate ballistically; (dashed line) taking into account isotope scattering

To explain our results we suggest the following model. Due to isotope scattering a hot phonon cloud [7,8] is formed in front of the heater. Inside the cloud strong phonon scattering with efficient frequency conversion takes place. This is likely, because in many crystals anharmonic decay of L phonons at 1 THz takes place within one microsecond [9]. Direct decay of T phonons is much less likely, but due to isotope scattering T phonons can be rapidly converted into L phonons, which subsequently decay. The dimensions of the cloud are defined by the isotope scattering. From this cloud low-frequency phonons escape and propagate ballistically through the crystal. The observed broadening of the phonon signal at the opposite crystal surface is determined by the lifetime of the high-frequency phonons inside the cloud.

#### References:

- [1] R.E.Horstman, Phys.Lett.79A (1980) 229
- [2] M.G.Holland, Phys.Rev.132 (1963) 2461
- [3] J.Wolter and R.E.Horstman, Phys.Lett.61A (1977) 238
- [4] R.E.Horstman and J.Wolter, Phys.Lett.62A (1977) 279
- [5] C.J.Guo and E.J.Maris, Phys.Rev.A10 (1974) 960
- [6] W.Dietsche, Phys.Rev.Lett.40 (1978) 786
- [7] W.E.Bron, J.A.Patel and W.L.Schaich, Phys.Rev.B20 (1979) 5394
- [8] W.L.Schaich, J.Phys.C: Solid State Phys.11 (1978) 4341
- [9] W.E.Bron, Phys.Rev.B21 (1980) 2627

## SURFACE ROUGHNESS KAPITZA CONDUCTANCE : DEPENDENCE ON MATERIAL PROPERTIES AND PHONON FREQUENCY

N.S. Shiren

IBM Thomas J. Watson Research Center, Yorktown Heights, NY 10598, U.S.A.

**Abstract.** - A recent calculation of the surface roughness contribution to Kapitza conductance is compared with measurements on several different solid materials in contact with He II.

In a recent publication<sup>1</sup> I have presented some results of a first order perturbation calculation of the effect of a statistically rough surface on Kapitza resistance. These results were compared with previously published data on Cu - He<sup>3</sup>, Cu - He II, and NaF-He II interfaces. Excellent agreement in magnitude, temperature dependence, and pressure dependence, was found at temperatures above 0.2 K for reasonably realistic values of the parameters (r.m.s. amplitude and correlation length) characterizing the roughness.

In this paper I compare the calculated Kapitza conductances for several materials with measured values compiled by Snyder,<sup>2</sup> and also discuss the frequency dependence of the scattered phonons.

Let  $M$  indicate the wave polarization in the solid;  $M = l$  for longitudinal waves;  $M = \sigma, \pi$  for waves polarized perpendicular or parallel to the plane of scattering, respectively. Then, from reference 1, for an incident power per unit surface area per unit solid angle per unit frequency,  $\partial \mathcal{P}_i / \partial \Omega_i$ , at frequency  $\omega$  in the liquid, the fractional differential scattered flux into mode  $M$  in the solid is,

$$D_M = \frac{\partial \mathcal{P}_M / \partial \Omega_M}{\partial \mathcal{P}_i / \partial \Omega_i} = k_M^4 F_M G(|\vec{k}_M^l - \vec{k}^l|). \quad (1)$$

$\vec{k}^l$  and  $\vec{k}_M^l$  are the components of the wave vectors in the liquid and solid, respectively, parallel to the interface. The  $F_M$  are dimensionless expressions which are functions of all the various scattering and input angles as well as the velocities and densities.  $\partial \mathcal{P}_M / \partial \Omega_M$  is the scattered power per unit surface area per unit solid angle per unit frequency.



$G(K)$  is the spectral density of the roughness modes with wave vector  $K$  and amplitude  $\zeta_K$ . For a simple exponential surface correlation function with correlation length  $l$  and mean square amplitude  $\langle \zeta^2 \rangle$  ( $\langle \rangle$  indicates an average over an ensemble of representations of the surface),  $G(K)$  is given by

$$G(K) = \partial \langle \zeta_K^2 \rangle / \partial K^2 = 2\pi \frac{\langle \zeta^2 \rangle l^2}{(1 + K^2 l^2)^{3/2}} \quad (2)$$

The frequency dependence of  $D_M$  is completely determined by the factor  $k_M^4 G$ . Let  $H = (|k_M^{\parallel} - k^{\parallel}|) / k_M$ , then  $H$  is independent of frequency, and

$$k_M^4 G(k_M H) = 2\pi \frac{\langle \zeta^2 \rangle}{l^2} \frac{(k_M l)^4}{[1 + H^2 (k_M l)^2]^{3/2}} \quad (3)$$

Thus  $D_M$  is directly proportional to the mean square of the perturbation parameter  $k_M l$ , and  $l$  appears as a scale factor on the frequency.

The total power per unit surface area scattered into the solid is

$$Q_s = \sum_{M=\sigma, \pi, l} \int d\Omega_i \int d\Omega_M \int d\omega D_M (\partial \mathcal{P}_i / \partial \Omega_i) \quad (4)$$

Its contribution to the Kapitza conductance is

$$h_K^s = \partial Q_s / \partial T \quad (5)$$

and the total thermal resistance of the interface is

$$R = h_K^{-1} = (h_K^{AM} + h_K^s)^{-1} \quad (6)$$

Fig. 1 shows the frequency dependence of  $Q_s$  for single frequency inputs. At the low frequency end  $Q_s \propto (k l)^4 (\langle \zeta^2 \rangle / l^2)$  as expected from Eq. (2). However, for large  $(k l)$  small values of  $H$  are emphasized and  $Q_s$  tends to vary as the integral of Eq. (2) (over  $H dH$ ), i.e.  $Q_s \propto (k l)^2 (\langle \zeta^2 \rangle / l^2)$ . Since, as shown by Fig. 1, the scattering probability increases monotonically with frequency, for thermal inputs the scattered frequency distribution is shifted towards higher frequencies. However, thru  $H$  the amount of the shift is angle dependent; large angle inputs (from the helium) are shifted less than small angle inputs. These results are not dependent on the specific form of  $G(K)$  used here. They hold for any normalized  $G(K)$  which decreases monotonically with increasing  $K$ .

Snyder<sup>2</sup> has tabulated the largest reported values of  $h_K$  for several materials. I have chosen to compare the theory with these data (rather than, e.g. the smallest reported

values) because it is more likely that  $h_K^s \gg h_K^{AM}$ . The integrations required for evaluation of Eq. (5) were all computed numerically assuming  $\mathcal{P}_i$  proportional to a Debye density of states and equilibrium phonon populations. Of course, actual values of  $\langle \xi^2 \rangle$  and  $l$  are not known so some choice has to be made. I have used the same values of  $\langle \xi^2 \rangle / l^2$  and  $l/v_t$  ( $v_t$  is the shear wave velocity) for all the materials.

Fig. 2 shows the relative values of  $h_K^s$  plotted against relative  $h_K^{max}$  (from Snyder<sup>2</sup>). Obviously, we cannot expect exact agreement because of the unknown quantities  $\langle \xi^2 \rangle$  and  $l$ , however the general trend is correct.

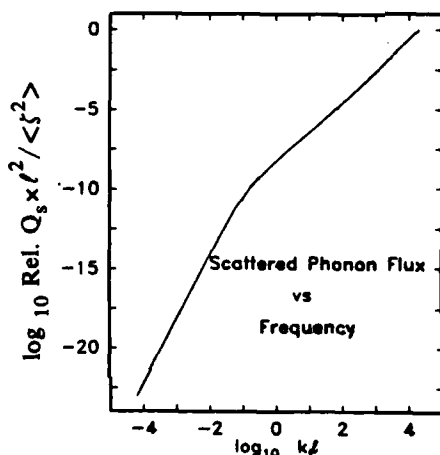
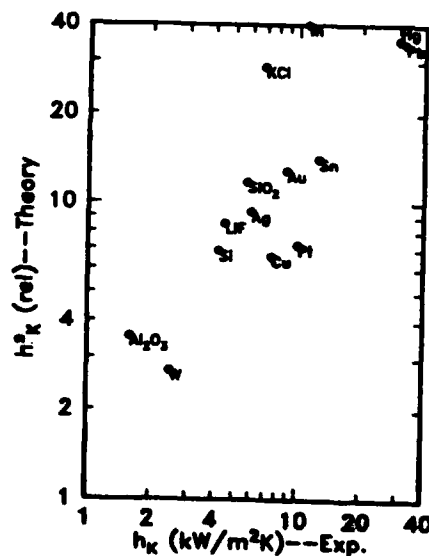


Fig. 1 : Relative values of total transmitted intensity ( $Q_s \times l^2 / \langle \xi^2 \rangle$ ) for He II to NaF, versus  $k_t l$ .  $k_t$  is the shear wave vector in the solid.

Fig. 2 : Relative values of scattering contribution to Kapitza conductance,  $h_K^s$ , versus largest measured values<sup>2</sup> of  $h_K$  for the indicated materials in contact with He II.



#### References

1. N. S. Shiren, Phys. Rev. Letters, submitted.
2. N. S. Snyder, NBS Technical Note 385 (U. S. Govt. Printing Office, Washington, 1969).
3. I. M. Khalatnikov, Introduction to the Theory of Superfluidity (W. A. Benjamin, Inc., New York 1965), Chap. 23.

## EFFECT OF SURFACE ROUGHNESS ON THE KAPITZA RESISTANCE

T.J. Shen, D. Castiel and A.A. Maradudin

*Department of Physics, University of California, Irvine, California 92717, U.S.A.*

**Abstract.**— The Kapitza resistance due to acoustic phonons crossing a rough planar interface from liquid He into an isotropic solid is investigated, and its characteristic function, viz. the penetration coefficient is calculated as a function of the frequency of the incident phonons and their angle of incidence.

The propagation of acoustic phonons across the interface between liquid HeII and a solid has been proposed as the mechanism giving rise to the thermal boundary (Kapitza) resistance at this interface<sup>1</sup>. However, this process predicts a Kapitza resistance 10-100 times higher than the experimental results. This indicates the existence of additional heat conduction mechanisms. Among the possible candidates are the diffusely scattered phonons, which are observed in phonon reflection<sup>3</sup> and transmission<sup>4</sup> experiments. To account for the diffuse phonons, the theory of a rough interface has been introduced in some simplified versions.<sup>5,6</sup> Here we re-examine the effects of roughness. We consider a system in which the region  $x_3 > \zeta(\vec{x}_\parallel)$  is filled with liquid HeII, while the region  $x_3 < \zeta(\vec{x}_\parallel)$  is filled by an isotropic elastic medium. We treat both media as non-dissipative.

The surface profile function  $\zeta(\vec{x}_\parallel)$  is taken to be a stationary stochastic process with the following statistical properties. (1)  $\langle \zeta(\vec{x}_\parallel) \rangle = 0$ ; (2)  $\langle \zeta(\vec{x}_\parallel) \zeta(\vec{x}'_\parallel) \rangle = \delta^2 \exp(-|\vec{x}_\parallel - \vec{x}'_\parallel|^2/a^2)$ , where  $\delta$  and  $a$  are the root mean square departure of the surface from flatness and the transverse correlation length, respectively.

The heat flux  $Q$  across the interface is given by<sup>2</sup>

$$Q = \frac{\kappa c_o^2}{(2\pi)^2} \int_0^\infty dk k^3 n\left(\frac{\kappa c_o k}{k_B T}\right) \int_0^\pi d\cos\theta \cos\theta P(k, \theta), \quad (1)$$

where  $n$  is Planck's function,  $c_o$  is the sound velocity in liquid He,  $P(k, \theta)$  is the penetration coefficient of a phonon with momentum  $\hbar \vec{k}(k = |\vec{k}|)$  incident from the liquid side at an angle  $\theta$  into the solid and is given by

$$P(k, \theta) = \frac{\langle s_3^{\text{trans}} \rangle}{s_3^{\text{inc}}} \quad (2)$$

where  $S_3^{\text{inc}}$  and  $\langle S_3^{\text{trans}} \rangle$  are the normal components of the incident and the statistically averaged transmitted energy fluxes. These energy fluxes depend on the velocity potential  $\phi(\vec{x}, t)$  in the liquid and the displacement field  $\vec{u}(\vec{x}, t)$  in the solid which are, for  $x_3 > \zeta_{\text{max}}$ ,

$$\phi(\vec{x}, t) = e^{-i\omega t} \left\{ e^{i\vec{k}_1 \cdot \vec{x}_1 - i\alpha_0(k_1)x_3} + \int \frac{d^2 q_1}{(2\pi)^2} A_1 e^{i\vec{q}_1 \cdot \vec{x}_1 + i\alpha_0(q_1)x_3} \right\}, \quad (3a)$$

and for  $x_3 < \zeta_{\text{min}}$ ,

$$(u_1(\vec{x}, t), u_2(\vec{x}, t), u_3(\vec{x}, t)) = e^{-i\omega t} \int \frac{d^2 q_1}{(2\pi)^2} e^{i\vec{q}_1 \cdot \vec{x}_1} \left\{ e^{-i\alpha_l(q_1)x_3} \times \right. \\ \left. \times \left( \hat{q}_1, \hat{q}_2, -\frac{\alpha_l(q_1)}{q_1} \right) A_2 + e^{-i\alpha_t(q_1)x_3} \left( \hat{q}_1 A_3 - \hat{q}_2 A_4, \hat{q}_2 A_3 + \hat{q}_1 A_4, \frac{q_1}{\alpha_t(q_1)} A_3 \right) \right\}, \quad (3b)$$

where we have denoted  $A_j(\vec{q}_1 | \vec{k}_1)$  ( $j = 1, 2, 3, 4$ ) by  $A_j$  for simplicity. In these expressions  $\hat{q}_\alpha = q_\alpha / q_1$ ,  $\alpha = 1, 2$ , and  $\alpha_p(q_1) = [\omega^2 / c_p^2 - q_1^2]^{1/2}$  for  $q_1 < \omega / c_p$  and

$i[q_1^2 - \omega^2 / c_p^2]^{1/2}$  for  $q_1 > \omega / c_p$ , with  $p = o, l, t$ , and  $c_l$ ,  $c_t$  and  $c_o$  are the longitudinal, transverse sound velocities in the solid and the sound velocity in liquid He. These coefficients are determined by the boundary conditions, viz. the continuity of the normal components of the velocity and the stresses acting on the surface  $x_3 = \zeta(\vec{x}_1)$ , and the perturbative solutions for them can be written in the following forms

$$A_j(\vec{q}_1 | \vec{k}_1) = a_j^{(0)} \left\{ (2\pi)^2 \delta(\vec{q}_1 - \vec{k}_1) + \zeta(\vec{q}_1 - \vec{k}_1) a_j^{(1)}(\vec{q}_1 | \vec{k}_1) + \right. \\ \left. + \int \frac{d^2 \gamma_1}{(2\pi)^2} \zeta(\vec{q}_1 - \vec{\gamma}_1) \zeta(\vec{\gamma}_1 - \vec{k}_1) a_j^{(2)}(\vec{q}_1, \vec{\gamma}_1 | \vec{k}_1) + \dots \right\}, \quad j = 1, 2, 3 \quad (4a)$$

$$A_4(\vec{q}_1 | \vec{k}_1) = \zeta(\vec{q}_1 - \vec{k}_1) a_4^{(1)}(\vec{q}_1 | \vec{k}_1) + \int \frac{d^2 \gamma_1}{(2\pi)^2} \zeta(\vec{q}_1 - \vec{\gamma}_1) \zeta(\vec{\gamma}_1 - \vec{k}_1) a_4^{(2)}(\vec{q}_1, \vec{\gamma}_1 | \vec{k}_1) + \dots, \quad (4b)$$

where the superscripts denote the order of the corresponding term in  $\zeta(\vec{x}_1)$ , and  $\zeta(\vec{k}_1)$  is the Fourier transform of  $\zeta(\vec{x}_1)$ . In terms of these coefficients,  $P(k, \theta)$  can be separated into a specular part and a diffuse part

$$P(k, \theta) = P_s(k, \theta) + P_d(k, \theta), \quad (8)$$

where

$$P_s(k, \theta) = \frac{\rho}{\rho_o k \cos \theta} |a_2^{(0)}(k_1)|^2 \operatorname{Re} \left\{ [2\alpha_l(k_1) - \frac{k_1^2 - \alpha_l^2(k_1)}{k_1^2} \alpha_s(k_1)] \right\}$$

$$\begin{aligned}
& \times \left[ 1 + 2\delta^2 \operatorname{Re} \int \frac{d^2 q_1}{(2\pi)^2} g(|\vec{k}_1 - \vec{q}_1|) a_2^{(2)}(\vec{k}_1, \vec{q}_1 | \vec{k}_1) + \dots \right] \\
& + |a_3^{(0)}(k_1)|^2 \operatorname{Re} \left\{ \left[ \frac{2k_1^2}{\alpha_t(k_1)} - \frac{k_1^2 - \alpha_t^2(k_1)}{\alpha_t(k_1)} \right] \right. \\
& \times \left. \left[ 1 + 2\delta^2 \operatorname{Re} \int \frac{d^2 q_1}{(2\pi)^2} g(|\vec{k}_1 - \vec{q}_1|) a_3^{(2)}(\vec{k}_1, \vec{q}_1 | \vec{k}_1) + \dots \right] \right\}, \quad (6a) \\
P_d(k, \theta) &= \frac{\rho_s^2}{\rho_0 k \cos \theta} \operatorname{Re} \int \frac{d^2 q_1}{(2\pi)^2} g(|\vec{k}_1 - \vec{q}_1|) \left\{ [2\alpha_t(q_1) - \frac{q_1^2 - \alpha_t^2(q_1)}{q_1} \alpha_t(q_1)^*] \right. \\
& \times |a_2^{(0)}(k_1) a_2^{(1)}(\vec{q}_1 | \vec{k}_1)|^2 + \left[ \frac{2q_1^2}{\alpha_t(q_1)} - \frac{q_1^2 - \alpha_t^2(q_1)}{\alpha_t(q_1)} \right] |a_3^{(0)}(k_1) a_3^{(1)}(\vec{q}_1 | \vec{k}_1)|^2 \\
& \left. + \alpha_t(q_1) |a_4^{(1)}(\vec{q}_1 | \vec{k}_1)|^2 + \dots \right\}, \quad (6b)
\end{aligned}$$

where  $\rho$  and  $\rho_0$  are the mass densities of the solid and liquid He, and the result that  $\langle \zeta(\vec{k}_1) \zeta(\vec{k}_1') \rangle = \delta^2 (2\pi)^2 \delta(\vec{k}_1 + \vec{k}_1') g(k_1)$  has been used. We use an adaptive numerical integration scheme to evaluate the diffuse part of the penetration coefficient, which is shown in Fig. 1 for  $\delta = a$ , and will present the results for the Kapitza resistance elsewhere. In Fig. 1, the two peaks at the angles of  $6.4^\circ$  and nearly  $90^\circ$  come from the excitation of generalized Rayleigh waves and stoneley waves, respectively.

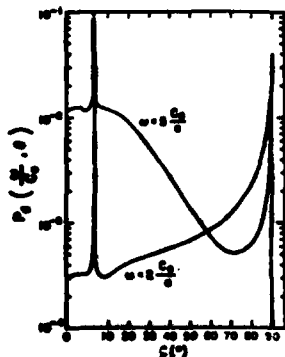


Fig. 1. The diffuse part of the penetration coefficient versus the angle of incidence for two different frequencies  $\omega (=c_0 k)$ .

#### References

1. Kapitza, P. L., *zh. Eksp. Teor. Fiz.* **11**, 1 (1941)
2. Khalatnikov, I. M., *Theory of Superfluidity*.
3. Weber, J., Sandmann, W., Dietsche, W. and Kinder H., *J. Phys. Coll.* **39**, C-6, 242 (1978).
4. Taborak, P. and Goodstein, D. L., *Phys. Rev.* **B22**, 1550 (1980).
5. Little, W. A., *Phys. Rev.* **123**, 1909 (1961).
6. Adamenko, I. N. and Faks, I. M., *zh. Eksp. Teor. Fiz.* **59**, 2071 (1970).
7. Rayleigh, L., *Proc. Roy Soc.* **A79**, 399 (1907).

PHONONS OF THE METAL/AMORPHOUS SILICON INTERFACE STUDIED BY  
INTERFERENCE ENHANCED RAMAN SCATTERING

R.J. Nemanich and C.C. Tsai

*Xerox Palo Alto Research Center, 3333 Coyote Hill Road, Palo Alto, California  
94304, U.S.A.*

**Abstract.** - The interference enhanced Raman scattering (IERS) configuration is used to study the initial interfacial interactions of thin films of Pd or Pt on hydrogenated amorphous silicon (a-Si:H). Sharp spectral features are observed in the Raman spectrum of as-deposited Pd on a-Si:H which are attributed to crystalline Pd<sub>2</sub>Si. In contrast, for as-deposited Pt on a-Si:H, broad spectral features are observed which are attributed to an intermixed Pt-Si phase.

Silicide formation at metal-semiconductor interfaces is an important aspect of future technologies and relates to the nature of Schottky barrier formation. Most work has been concerned with interactions at metal-crystalline silicon interfaces.<sup>1,2</sup> However, since hydrogenated amorphous silicon (a-Si:H) has exhibited true semiconductor properties, interactions at the metal/a-Si:H interface will also be important and could be quite different from interactions on crystalline Si. In this study Raman scattering is used to probe the initial interactions at the interface of Pd and Pt on a-Si:H.

Although light scattering has proved a very useful probe of lattice vibrations of insulators, semiconductors and even some metals, this probe has only recently achieved any success in studying the physical interactions at interfaces and surfaces. In particular, the metal-semiconductor interface has proven to be a particularly difficult configuration, but the interactions at a metal-semiconductor interface are both physically varied and technologically important. There are several major experimental problems with light scattering in a standard backscattering configuration. Firstly, the interface region is a small portion of the sample, and excitations of the region are often "masked" by those of the semiconductor. In addition, because of the high reflectivity and absorption of visible light from metals (or semiconductors), it is difficult to illuminate the "buried" interface. Furthermore, the scattering that does occur is strongly absorbed. While there has been recent success using standard Raman backscattering techniques to explore the metal-semiconductor interface, a new technique called interference enhanced Raman scattering (IERS)<sup>3</sup> holds the possibility of routine application to many problems in this area.

The IERS configuration utilizes a multilayer sample configuration which enhances the signal by optical interference properties. For scattering from a metal/a-Si:H interface, a four-layer structure is used and a schematic of this structure is shown in Fig. 1a. This

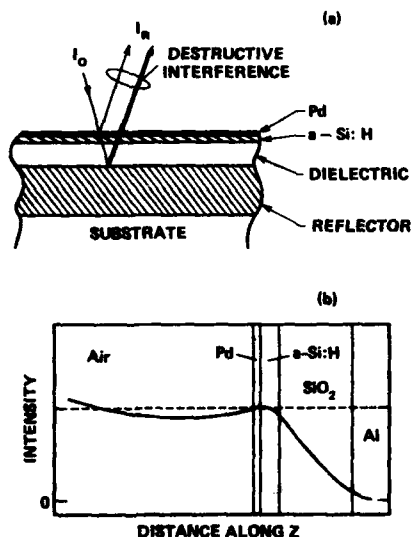


Fig. 1 : (a) A schematic of the four-layer sample configuration used to obtain interference enhanced Raman scattering (IERS); (b) the electric field intensity due to 514.5 nm light impinging on the multilayer sample shown in (a) at normal incidence. The dashed lined represents the light intensity if no sample were present.

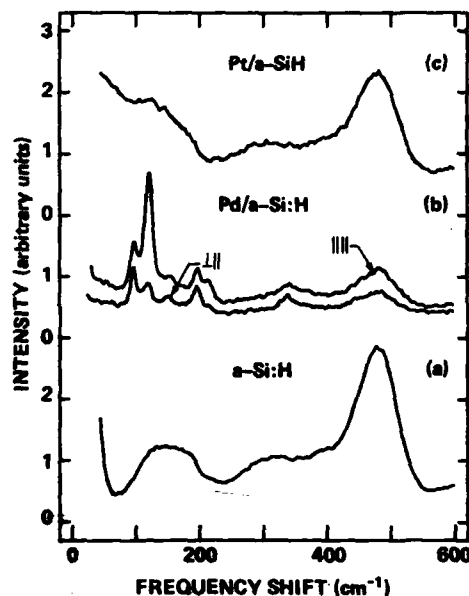


Fig. 2: The Raman spectra of (a) a-Si:H, (b) 2 nm Pd on a-Si:H and (c) 5nm Pt on a-Si:H. Polarized spectra are shown in (b) and the symbols refer to the polarization of the incident and scattered light with respect to the scattering plane.

configuration consists of an optically thick aluminum layer, a 40 nm  $\text{SiO}_2$  layer, a 10 nm a-Si:H layer and a Pd or Pt layer of 2 to 6 nm. Using the bulk optical properties of these films, we can calculate the light intensity inside the sample due to the incident 514.5 nm radiation. The results of this calculation indicated in Fig. 1b show that the light intensity is a maximum at the interface and is actually equal to the incident light intensity. This intensity could be 5 to 50 times stronger than that at a similar metal interface on a thick semiconductor. In addition, the same interference conditions that cause the optimization of the incident light also causes enhanced normal emission of the Raman scattered light which originates at the interface. This can cause an additional enhancement of up to a factor of 4. Thus, the Raman scattering signal from the interface using IERS may be 200 times stronger than from normal backscatter configurations.<sup>3</sup> The IERS configuration holds the additional benefit of reducing the substrate excitations on two grounds: the semiconductor is very thin and the optical interference is destructive for excitations deeper in the sample.

The a-Si:H used in this study was deposited by plasma decomposition of pure silane where 1 to 2W of rf power sustained the plasma, and the substrates were held at the anode at a temperature of 230°C. The resultant material is known to have low defect densities and contain ~8 at. % H.<sup>4</sup> The Pd was thermally evaporated after the a-Si:H

deposition, and the a-Si:H film suffered an exposure to air for less than 15 min.

The Raman spectrum of a-Si:H in the IERS configuration is shown in Fig. 2a. The broad continuous spectrum obtained from the a-Si:H is essentially identical to that obtained from thick a-Si:H films. And while not shown here, the second order Si network vibrations and Si-H vibrations are also identical to corresponding features from similarly prepared thick a-Si:H films.<sup>5</sup> Thus, the 10 nm a-Si:H film is essentially "bulk-like" in its vibrational excitations.

The deposition of 2 nm of Pd on this film causes dramatic changes in the Raman spectra. Polarized Raman spectra shown in Fig. 2 b display several sharp features. Since Pd has no first order Raman spectrum, these features are attributed to a crystalline Pd-silicide compound which forms at the interface of the Pd and a-Si:H film. By comparison with thick silicide films formed on crystalline Si, these features can be attributed to a form of  $\text{Pd}_2\text{Si}$ .<sup>6</sup> It should be emphasized that the sharp lines indicate the presence of a crystalline compound. To determine the extent of the initial silicide formation, 3 nm and 6 nm Pd films on a-Si:H were also examined, and it was found that ~2 nm of the Pd was initially consumed to form a silicide.<sup>6</sup>

The chemical similarity of Pd and Pt would suggest that a corresponding result might be obtained. As is shown in Fig. 2c, there are no additional sharp spectral features after Pt deposition on a-Si:H. There is, however, a significant broad, low frequency contribution not evident in any of the other spectra. This feature is attributed to an intermixed Pt-silicon phase which lacks long-range order. Annealing of this sample to 200°C causes the appearance of sharp spectral features which are attributed to crystalline compounds  $\text{Pt}_2\text{Si}$  and PtSi. It should be noted that annealing both the Pt or Pd/a-Si:H structure leads to improved Schottky barrier properties.<sup>7</sup>

We are certainly encouraged by the success of the IERS technique. Its major limitation is that thin film structures are required. Thus, it is easier to work with amorphous semiconductors, but with the use of molecular beam epitaxy the scope of the IERS technique may be broadened to examine crystalline interfaces.

#### References

1. Tu, K. N. and Mayer, J. W., in Thin Films Interdiffusion and Reactions, edited by Poate, J. M., Tu, K. N., and Mayer, J. W. (Wiley, New York, 1978), p. 359.
2. Ottaviani, G., J. Vac. Sci. Technol. **16**, 1112(1979).
3. Connell, G. A. N., Nemanich, R. J., and Tsai, C. C., Appl. Phys. Lett. **38**, 31(1980).
4. Knights, J. C., and Lucovsky, G., CRC Crit. Rev. Solid State Mat. Sci. **9**, 211(1980).
5. Tsai, C. C., and Nemanich, R. J., J. Non-Cryst. Solids, **35 & 36**, 1203(1980).
6. Nemanich, R. J., Tsai, C. C., and Sigmon, T. W., Phys. Rev. B, **23**, 6828(1981).
7. Tsai, C. C., Thompson, M. J., and Nemanich, R. J., Proc. Ninth International Conference on Amorphous and Liquid Semiconductors, (1981) (in press).



## FILM THICKNESS DEPENDENCE OF HEAT TRANSMISSION INTO HELIUM\*

P. Taborék, M. Sinvani, M. Weimer and D. Goodstein

*California Institute of Technology, Pasadena, CA 91125, U.S.A.*

**Abstract.**— A heater is pulsed at the interface between a sapphire crystal and an adsorbed  $^4\text{He}$  film. For short pulses, the amount of heat absorbed by the film saturates when the film thickness reaches a few layers, just as observed in phonon reflection experiments. For longer pulses, however, there is little difference between thin film and vacuum results, while substantial heat is transferred to the bulk liquid.

After a decade of fast heat pulse phonon reflection experiments in many laboratories, one of the most striking and persistent results is what might be called the three layer effect. Narrow heat pulses (50 - 100 nsec) traverse a crystal ballistically, are reflected from a surface, and return to be detected by a bolometer. The maximum bolometer signal is seen when the surface is in vacuum. If the surface is coated with a thin film of helium, the signal diminishes, indicating that some of the heat incident upon the surface has been transmitted into the helium. This change in the signal saturates at about three atomic layers of adsorbed helium. No further change is seen as the film thickness increases to infinity (bulk liquid).

We have performed a series of experiments which throw new light on this three layer effect. In these experiments, an ohmic heater is evaporated directly onto a crystal surface upon which the He film thickness may be manipulated. On the far surface of the crystal, a superconducting transition bolometer in a constant temperature superfluid bath detects that portion of the heat which enters the crystal rather than being carried away by the helium. The crystal is a sapphire cylinder, 57 mm in diameter and 9.5 mm thick, oriented with the heater and bolometer along the crystallographic y-axis. Since the power dissipated in the heater is shared between the crystal and the helium, we call this the "power sharing" geometry.<sup>(1)</sup> (See Fig. 1 inset).

The results of these experiments may be summarized briefly as follows: when narrow heat pulses (150 nsec) are used, the bolometer signal is much like that in reflection experiments, most of the change being due to the first three layers (see Fig. 1). On the other hand, when wide heat pulses ( $\sim 10$   $\mu\text{sec}$ ) at the same power density are used, the bolometer signal for a three layer film barely differs from the vacuum result, while substantial transmission is observed into bulk

\*Supported in part by ONR Contract # N00014-80-C-0447.

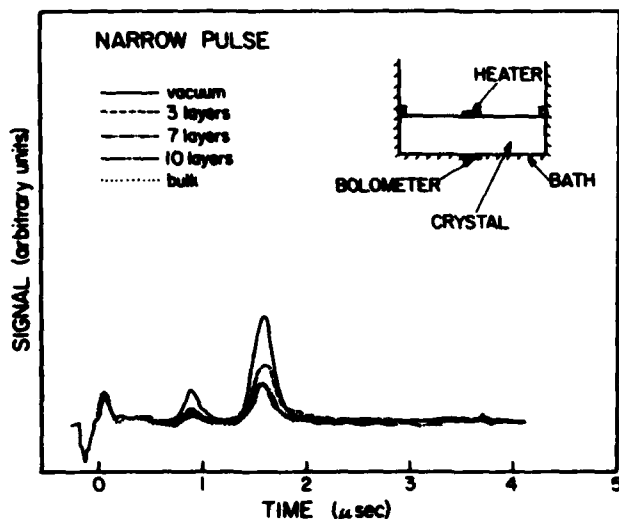


Fig. 1 : Phonon signal in power sharing geometry for various He film thicknesses on heater. Heater pulse width 150 nsec, heater power density 0.2 watts/mm (typical power density in reflection experiments: .02 W/mm<sup>2</sup>).

liquid (see Fig. 2).

These observations imply that the three layer effect is a consequence of the kinetics of film desorption. A detailed calculation indicating that this is indeed the case will be discussed briefly below, and presented in full in a subsequent publication.

Previous investigators have attributed the three layer effect to other causes. Guo and Maris<sup>(2)</sup> reported a correlation between heat transmission and film thickness. That observation implies that the coupling of heat across the crystal-helium interface (i.e., the anomalous Kapitza effect) comes into play in the first three layers or 10 Å of film. Dietsche and Kinder<sup>(3)</sup> argue instead that the transmission of heat is determined by the pressure in the helium gas, which governs the effective interfacial resistance between the helium film and the gas. The latter hypothesis alone does not explain our long heat pulse power sharing results, since the pressure in the gas is not affected by our heat pulses.

To account for these and other experiments, we have formulated a model of the kinetics of thermal behavior in the film-gas system, when heat is injected into the film. Equations are written for the conservation of energy and mass in the film, the dynamical variables being the film thickness and temperature. Energy flows across the film-solid interface mediated by the Kapitza resistance, which is assumed to be independent of the film thickness. The equations can be linearized and solved analytically for reflection experiments. In the power sharing experiments, where the power densities may be much higher, they are solved numerically.

The central result of the calculation is that when heat is injected into the film, it evolves toward steady state behavior with a characteristic time,  $\tau_0$ , which is typically of order 1 μsec. At times short compared to  $\tau_0$ , energy is consumed by

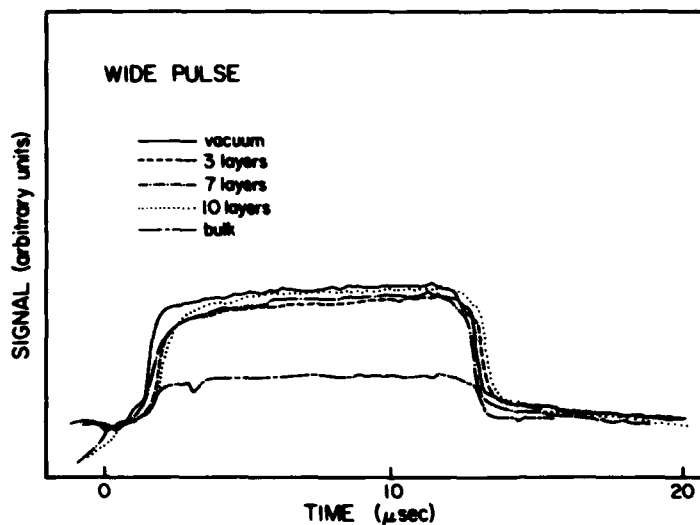


Fig. 2 : Phonon signal in power sharing geometry. Conditions identical to those in Fig. 1 except heater pulse 12  $\mu$ sec.

the latent heat and heat capacity of the film. At longer times, much less energy is transmitted out of the solid since the only remaining mechanism to carry it away is the excess kinetic energy of desorbed atoms over adsorbed atoms in the steady state. In this way, the model accounts for the results in Figs. 1 and 2 of this paper. It also predicts the three layer effect in narrow heat pulse reflection experiments. In particular, it is in quantitative agreement both with the results of Guo and Maris<sup>(2)</sup>, and with those of Dietsche and Kinder.<sup>(3)</sup>

In conclusion, then, we believe the three layer effect is not a consequence of the evolution of the Kapitza effect. It is due instead to the kinetics of the desorption process. No new information is revealed about the mysterious Kapitza resistance, but we see that heat pulse techniques using fast heaters and bolometers constitute an excellent way of studying the important problem of desorption kinetics.

- References:**
1. T. Ishiguro and T. A. Fjeldly, Physics Letters **45A**, 127 (1973).
  2. C. J. Guo and H. J. Maris, Phys. Rev. **A10**, 960 (1974).
  3. W. Dietsche and H. Kinder, J. Low Temp. Phys. **23**, 27 (1976).

## PHONONS AT METAL SURFACES

C. Schwartz and W.L. Schaich

Physics Department, Indiana University, Bloomington, IN 47405, U.S.A.

**Abstract.** - We examine phonons at metal surfaces using hydrodynamic equations. The principle focus is on the strength of the electric field produced outside the metal by such oscillations. We find that the magnitudes of these coupling strengths for both surface and bulk modes depend crucially on the boundary conditions imposed at the surface.

1. Hydrodynamic model. - Our linearized continuum model of the coupled motion of electrons and ions is defined by the equations:

$$\frac{\partial \vec{J}_1}{\partial t} = \frac{\Omega^2}{4\pi} \vec{E} + \rho_0 [c_L^2 \vec{\nabla} (\vec{\nabla} \cdot \vec{\xi}_1) - c_T^2 \vec{\nabla} \times (\vec{\nabla} \times \vec{\xi}_1)] \quad (1a)$$

$$\frac{\partial \vec{J}_e}{\partial t} = \frac{\omega_p^2}{4\pi} \vec{E} - \rho_0 [\beta_e^2 \vec{\nabla} (\vec{\nabla} \cdot \vec{\xi}_e)] \quad (1b)$$

$$\vec{\nabla} \cdot \vec{E} = 4\pi\rho_0 (\vec{\nabla} \cdot \vec{\xi}_e - \vec{\nabla} \cdot \vec{\xi}_1) \quad (1c)$$

where e and i subscripts refer, respectively, to electrons and ions;  $\vec{E}$  is the (longitudinal) electric field;  $\rho_0$  the (constant) equilibrium ion charge density,  $\Omega_p$  and  $\omega_p$  are the ion and electron plasma frequencies; the c's and  $\beta_e$  parametrize short range restoring forces; and the  $\xi$ 's are displacement fields related by a time derivative to the current densities  $\vec{J}$ :  $\vec{J}_1 = \rho_0 \frac{\partial \vec{\xi}_1}{\partial t}$  and  $\vec{J}_e = -\rho_0 \frac{\partial \vec{\xi}_e}{\partial t}$ . Note that we have neglected retardation and discrete lattice effects and that only the ions sense transverse forces, via  $c_T$ . In bulk material at a general frequency  $\omega$ , one has electronic longitudinal waves and ionic longitudinal and transverse waves. When one considers excitations near a surface, where  $\rho_0$  drops discontinuously to zero, linear combinations of these bulk modes plus excitations varying as  $e^{iQ \cdot \vec{x}_e - Q|x|}$  must be used. Here  $\vec{x}$  (and the wavevector  $Q$ ) lies in the surface plane while  $x$  is normal to it. The coupled modes are labeled by  $\omega$ ,  $Q$ , and polarization indices. To determine the eigenmodes of (1) requires in general the imposition of five independent surface boundary conditions. For the first two, we use continuity of the potential  $\phi$  ( $\vec{E} = -\vec{\nabla}\phi$ ) and continuity of the normal component of the displacement field. This last is equivalent to  $\Delta(\vec{E} \cdot \hat{x}) = 4\pi\sigma_s$ , where  $\sigma_s$  is the induced surface charge density and  $\Delta(\dots)$  means the discontinuity in  $(\dots)$ . For the other boundary conditions we have examined several possibilities. Consideration of metal or plasma physics suggests we set  $c_T = 0$ , which eliminates the transverse modes and

one boundary condition, and for the remaining two conditions require at the surface,

$$\vec{f}_i \cdot \hat{x} = 0 = \vec{f}_e \cdot \hat{x}, \quad (2)$$

which we call case C. Note that (2) implies  $\sigma_s = 0$ . On the other hand, elasticity theory suggests we keep  $c_T \neq 0$  and instead require (case S)

$$\vec{\sigma}_i \cdot \hat{x} = 0 = \vec{\sigma}_e \cdot \hat{x} \quad (3)$$

where  $\vec{\sigma}$  is the stress tensor that leads to (1).

2. **Results.** - The different boundary conditions (2) and (3) lead to dramatically different predictions. Consider first possible surface modes. With (2) there is a surface mode just below (at each  $Q$ ) the bulk longitudinal modes. This mode has been found also in less general ( $c_L = 0$ ) models.<sup>1,2</sup> With (3) a surface mode only appears below the bulk transverse modes. This surface mode is in essence a (stiffened) Rayleigh wave. It requires a finite  $c_T$  and the effective longitudinal sound speed is  $v_L^2 = c_L^2 + c_S^2$  where  $\Omega_p = c_S k_S$  with  $k_S = \omega / \beta_e$ . To discuss the possible external coupling to these modes we have quantized them and write the external potential as  $\phi(\vec{x}) = \sum_Q \Lambda_Q e^{iQ \cdot \vec{x}} e^{-Qx} (a_Q + a_Q^\dagger)$  where  $a^\dagger$  ( $a$ ) is a creation (annihilation) operator for the surface mode  $Q$ . A similar expression holds for the coupling to bulk modes. In figure 1 we plot  $\Lambda_Q$  vs.  $Q$  for the cases C and S and also an analogous quantity from the theory of Rahman and Mills<sup>3</sup>, case R.

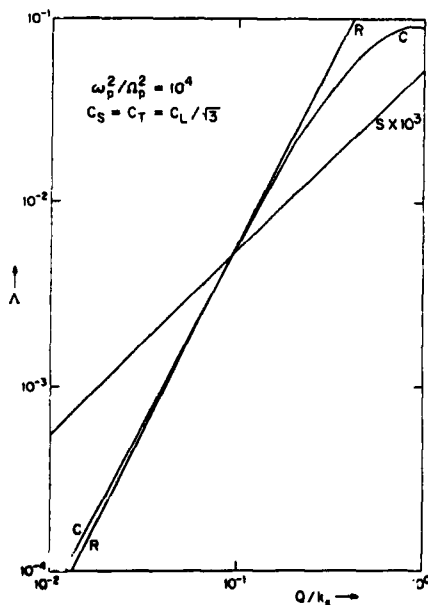
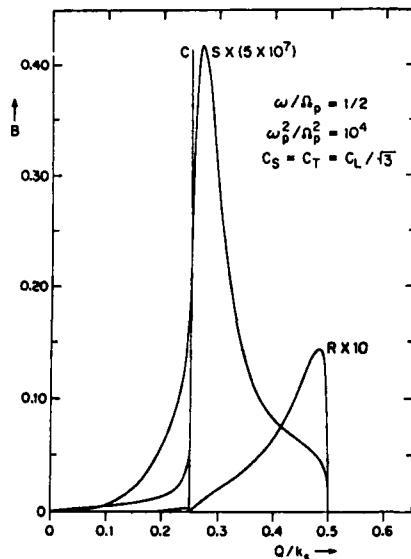


Fig. 1: External coupling strength parameter  $\Lambda$  for surface modes resulting from different boundary conditions versus surface wavevector  $Q$ . All  $\Lambda$ 's are in the same arbitrary units. Other symbols are defined in the text.

In figure 2 we plot a quantity  $B$ , proportional to the sum of the squares of all the finite  $\Lambda$ 's for the bulk modes at each  $\omega$  and  $Q$ . Simple integrals of  $B$  determine experimental quantities such as image potentials, electron loss spectra, or thermal diffuse scattering.



**Fig. 2:** External coupling strength parameter  $B$  (dimensionless) for bulk modes subject to different boundary conditions versus surface wavevector  $Q$  at fixed frequency  $\omega$ . See text for definition of the other symbols.

The most striking feature of both figures (1) and (2) is the small relative size of the  $\Lambda$ 's for case S. They are reduced by roughly  $\Omega_p^2/\omega^2$  compared to those for cases C or R. Closer study shows that the condition  $\hat{\sigma}_e \cdot \hat{x} = 0$  is the cause of this reduction. Requiring the electrons to sense zero stress at the surface essentially suppresses any external fields at frequencies comparable to  $\Omega_p \ll \omega_p$ .

This work was supported in part by the NSF through grant DMR 78-10235.

#### References

1. W.L. Schaich, Phys. Rev. **B24**, 686 (1981).
2. J.B. McBride and P.K. Kaw, Phys. Letts. **33a**, 72 (1970).
3. T.S. Rahman and D.L. Mills, Phys. Rev. **B21**, 1432 (1980).

## SURFACE LATTICE DYNAMICS OF NICKEL

V. Bortolani, A. Franchini, F. Nizzoli and G. Santoro

*Istituto di Fisica and G.N.S.M.-C.N.R., Università di Modena, 41100 Modena, Italy*

**Abstract.**- In the framework of a central and angular force constants model, we have evaluated the phonon spectrum and the loss function of the Ni(111) surface covered with Oxygen. We explain quantitatively the main features of the observed electron energy loss spectra.

**1. Introduction.**- In this work we are interested in the surface optical phonons of the Ni(111) surface for which very accurate high resolution electron energy loss (EELS) experiments are available<sup>(1)</sup>. The detection of these surface vibrations with EELS occurs through the dipole coupling. The dipole is provided by fraction of monolayers of Oxygen adsorbed on the metallic surface. As a consequence there are problems of interpretation of the experimental spectra because one has to discriminate between the modes of the substrate and the modes induced by the adsorbate. In order to solve this problem we show here that a realistic surface phonon calculation is needed. Our results indicate that the observed peaks relate to the phonons of the substrate for the Rayleigh wave, but otherwise are due to the adsorbed layer.

**2. Calculation of the EELS spectrum.**- In the dipole coupling approximation, the EELS scattering cross section has the form:

$$\frac{d\sigma}{d\Omega} \propto \frac{k_B T}{\omega^2} \left| \frac{w_z(\vec{Q}_{\parallel}, l_z=0, \omega)}{\sqrt{m_{l_z=0}}} - \frac{w_z(\vec{Q}_{\parallel}, l_z=1, \omega)}{\sqrt{m_{l_z=1}}} \right|^2$$

Here  $w_z$  is the normal component of the polarization vector of the excited phonon with parallel momentum  $\vec{Q}_{\parallel}$  and frequency  $\omega$ .  $l_z$  labels the atomic planes and  $m_{l_z}$  is the mass of the atoms in the  $l_z$  plane. It is clear from this equation that the modes which are detectable are those having a non zero normal component of the sum of the polarization vectors in the surface unit cell. In order to evaluate the surface phonon field of Ni we use the slab method, in the framework of a central and angular force constants parametrization<sup>(2)</sup>. We present here the calculations for the measured EELS spectra relative to the Ni(111):O p(2x2) and to the Ni(111):O ( $\sqrt{3} \times \sqrt{3}$ )R30° geometries, depicted in Fig.1. In both configurations the Oxygen is bound to three Ni in a  $C_{3v}$  position.

We firstly consider the p(2x2) geometry. In this case the M point of the 2-dimensional Brillouin zone of the ideal (111) surface is folded in  $\Gamma$ , so that EELS detects the M phonons. The experimental results<sup>(1)</sup> are reported in Fig.2a. Three peaks are

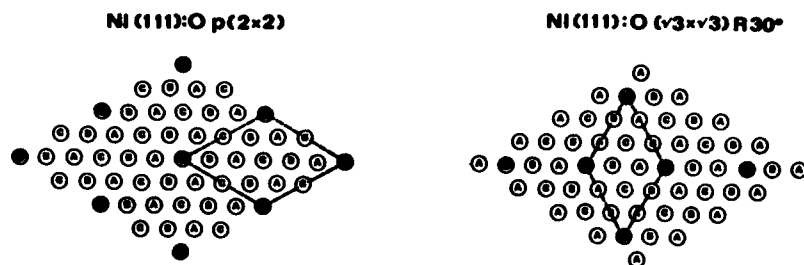


Fig. 1 : a) Ni(111):O p(2x2) geometry. ● Oxygen atoms, (A), (B), (C) Ni atoms in the first three layers. b) the same for the  $(\sqrt{3}\times\sqrt{3})R30^\circ$  geometry.

present. The one at 72 meV, which is far outside the phonon spectrum of Ni, is clearly due to the motion of the Oxygen relative to the three coordinate Ni atoms. It corresponds to the  $A_1$  normal mode of a pyramidal  $x_3y$  molecule<sup>(3)</sup>. As it can be seen from Fig.3, this mode gives a dipole moment along the  $C_{3v}$  axis, i.e. the surface normal. The lowest peak can be interpreted in terms of the surface phonons of the clean Ni(111) surface<sup>(2)</sup>. In fact, near this frequency there is the Rayleigh wave of the M point which is mainly polarized normal to the surface. The other peak at 32.8 meV, inside the phonon spectrum of Ni, cannot be explained in terms of the phonons of the clean surface. The modes of the M point around this frequency are longitudinal and do not couple with the impinging electrons. To clarify the nature of this peak we have performed a full calculation of the phonons of the covered surface. We have considered the interaction of Oxygen with the three nearest neighbouring Ni atoms by introducing one central and one angular force constant. By any arbitrary choice of these force constants the calculated EELS cross section shows three structures. The one at lowest frequency remains related to the Rayleigh mode of the substrate. The other two peaks are connected with the  $A_1$  (higher frequency peak) and  $A_2$  (central peak) modes of the  $x_3y$  molecule. For this molecule, the frequency of the  $A_1$  mode is mainly due to the value of the Ni-O central force constant, while the frequency of  $A_2$  depends on the Ni-O-Ni angular force constant. To determine the force constants of the  $x_3y$  molecule we note that, even if the free  $Ni_3O$  molecule does not exist, the surface potential is able to stabilize such a molecule. By using the EELS data relative to a very low disordered coverage of Oxygen we fit the peak at 72 meV with the central force constant and the peak at 30 meV with the angular force constant. The results obtained with these parameters are reported in Fig.2b. The lowest peak is still related to the Rayleigh wave of the clean surface. The presence of the Oxygen atom does not modify the frequency and polarization of this mode. The highest peak remains at the energy position of the  $A_1$  mode of the molecule. The other peak at 32.8 meV, in perfect agreement with the experiment, results slightly shifted with respect to the energy of the  $A_2$  mode of the free molecule, while the polarization remains the same. The frequency shift can be understood in terms of the indirect O-O interaction caused by the sub-



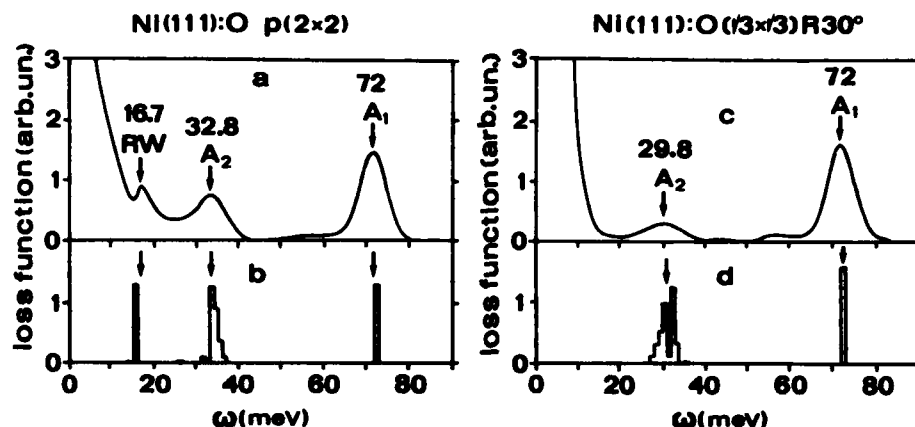


Fig. 2 : a) and b) experimental and calculated EELS intensities for the p(2x2) geometry. c) and d) the same for the  $(\sqrt{3}\times\sqrt{3})R30^\circ$  geometry.

strate.

The same analysis has been carried out for the  $(\sqrt{3}\times\sqrt{3})R30^\circ$  geometry. The experimental and calculated intensities are compared in Fig.2c and Fig.2d respectively. The two observed modes are related to the  $A_1$  and  $A_2$  modes of the molecule. The 29.8 meV peak is slightly shifted with respect to the corresponding mode of the p(2x2) geometry because of the different O-O interaction.

In conclusion, we have shown that a detailed calculation allows to explain the loss spectra of coated systems and to identify the origin of the experimental structures in terms of the modes of the substrate and those of the adsorbate species.

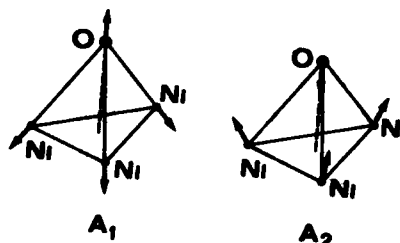


Fig. 3 : Normal modes of the  $x_3y$  pyramidal molecule that contribute to the EELS cross section.

#### References

- 1) H Ibach and D Bruchmann, Phys.Rev.Lett. **44**, 36 (1980)
- 2) V Bortolani, A Franchini, F Nizzoli and G Santoro, Proceedings of the Summer School on the Dynamics of Gas-Surface Interaction, Erice (1981), to be published
- 3) G Herzberg, "Molecular spectra and molecular structure" vol.2, p.155, Van Nostrand Inc., New York (1945)

## MICROSCOPIC THEORY OF LATTICE DYNAMICS AND RECONSTRUCTION OF SEMICONDUCTOR SURFACES

A. Muramatsu and W. Hanke

*Max-Planck-Institut für Festkörperforschung, 7000-Stuttgart-80, F.R.G.*

**Abstract.**— On the basis of a microscopic theory of surface density response including local-field and excitonic effects we calculate the phonon spectrum of an ideal Si(111) slab. A drastic enhancement of the non-local response is obtained for wavevectors corresponding to 2x1 and 7x7 superstructures, signalling an excitonic insulator instability of the metallic dangling bond surface state. The coupling of the resulting charge-density wave to the lattice produces a soft surface mode with atomic displacements supporting the ionic buckling model.

In this contribution we present a) a calculation of the phonon spectrum for an 8-layer ideal Si(111) slab starting from an accurate description of the surface electronic states and b) a detailed study of the implications for a microscopic understanding of the surface 2x1 and 7x7 reconstructions.

It has already been established that in a Wannier or LCAO basis for the wave functions, the non-interacting surface polarizability is of the separable form  $\tilde{\chi} = A N A^{\dagger}$ . The separability enables one to solve the integral equation for the density response  $\chi = \tilde{\chi} + \tilde{\chi} v \chi$ , which determines the electronic contribution to the dynamical matrix given by<sup>2</sup>

$$D_{\alpha\beta}^E(\kappa\kappa', \vec{q}) = -\frac{1}{M} \sum_{ss'} F_{\alpha}^s(\kappa, \vec{q}) \{N^{-1}(\vec{q}) + v^{xc}(\vec{q})\}_{ss'}^{-1} F_{\beta}^{s'\dagger}(\kappa', \vec{q}) \quad (1)$$

Here  $\alpha$  and  $\beta$  denote Cartesian coordinates and  $\kappa$  an ion in the 3-D basis of the slab.  $F_{\alpha}^s(\kappa, \vec{q})$  corresponds to the force experienced by the ion  $\kappa$  due to interaction through the ionic potential with the density wave  $A$  in direction  $\alpha$ .  $N^{-1}$  is the inverse non interacting polarizability and  $v^{xc}$  is the Coulomb interaction matrix which includes both RPA local-field effects as well as electron-hole interaction<sup>3</sup>. In Fig. 1 we present the phonon spectrum in the (0,1) direction obtained for an ideal 8-layer slab of Si(111). In the region where  $q \lesssim 1/l$ , being  $l$  the thickness, we obtain phonon instabilities related to violation of infinitesimal rotational (unrelaxed surface)<sup>4</sup> and translational (a surface<sup>5</sup> acoustic sum rule<sup>6</sup> was not implemented) invariance. On the other hand, the interplay between local-field and excitonic effects

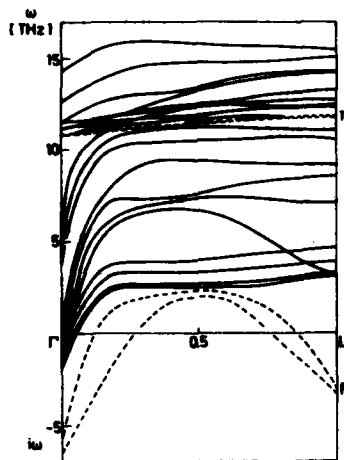


Fig. 1 Phonon spectrum for  $q=(0,1)$  for an ideal 8-layer slab of Si (111). Dashed lines: surface modes.

face.<sup>8</sup> But no structure corresponding to the  $2 \times 1$  superstructure is observable. The RPA local-field effects give a large correction (Fig. 2(b)) due to the extremely localized nature of the DB-orbitals. The features present before disappear and no electronic instability is observable. Beyond RPA, the system shows a strong tendency to an excitonic insulator instability when electron-hole attraction is considered. In this approximation the excitation energy of the system is lowered giving an enhancement of density response (Fig. 2(c)) and a tendency of the DB's to form a CDW. We can distinguish two features connected with commonly observed superstructures. First, we obtain a saddle-point at L. This enhancement of the susceptibility is responsible for the surface phonon instabilities at the L point (Fig. 1). But being a saddle-point, the

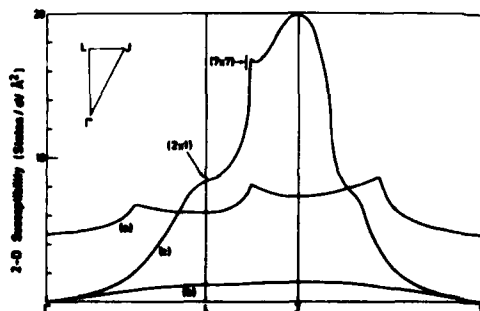


Fig. 2. 2-D susceptibility for a) non-interacting el-hole system; b) plus local field effects and c) plus el.-hole attraction. The inset shows the irreducible part of the Brillouin zone.

produces an instability of surface modes at the zone boundary. An analysis of the eigenvectors of these modes, which are elliptically polarized in the sagittal plane and strongly localized in the outmost layer, shows that the displacements of the surface atoms give rise to a "buckled" surface, supporting thus Haneman's<sup>7</sup> model for the  $2 \times 1$  surface reconstruction.

In order to obtain a better understanding of the mechanism which produces a softening of the surface modes at  $q_{BZ}$ , we concentrate on the top layer of the slab and take into account only the dangling-bond (DB) orbitals. In Fig. 2 (a) we show the contribution to the susceptibility from the non-interacting electron-hole system. The band structure gives rise to maxima near to wavevectors that correspond to the  $7 \times 7$  reconstruction due to "nesting" of the Fermi surface.<sup>8</sup>

But no structure corresponding to the  $2 \times 1$  superstructure is observable. The RPA local-field effects give a large correction (Fig. 2(b)) due to the extremely localized nature of the DB-orbitals. The features present before disappear and no electronic instability is observable. Beyond RPA, the system shows a strong tendency to an excitonic insulator instability when electron-hole attraction is considered. In this approximation the excitation energy of the system is lowered giving an enhancement of density response (Fig. 2(c)) and a tendency of the DB's to form a CDW. We can distinguish two features connected with commonly observed superstructures. First, we obtain a saddle-point at L. This enhancement of the susceptibility is responsible for the surface phonon instabilities at the L point (Fig. 1). But being a saddle-point, the

corresponding  $2 \times 1$  superstructure should be still unstable against other configurations. In fact we observe that the next local maximum appears for a wavevector nearly corresponding to the  $7 \times 7$  reconstruction. An other maximum appears at J, corresponding to a  $(\sqrt{3} \times \sqrt{3}) 30^\circ$  superstructure, which is occasionally observed<sup>9</sup>.

The coupling of the CDW with the lattice, given by the form factor  $F_\alpha^S(\kappa, \vec{q})$  determines the type of reconstruction. We observed that the coupling factor of the DB-CDW to displacements parallel to the surface is zero at the zone boundary. The only contribution for displacements parallel to the surface comes from interactions of the DB's with the "back bonds" which are much smaller than the first ones. This fact indicates that the CDW can almost only couple with displacements perpendicular to the surface as corroborated in the full calculation, discarding thus the "covalent bonding" model.

#### References

1. Wu, C.H. and Hanke, W., Sol. St. Comm. 23, 829 (1977)
2. Hanke, W. and Wu, C.H., Proc. Int. Conf. Latt. Dynamics (Flammarion, Paris), 292 (1977)
3. Hanke, W. and Sham, L.J., Phys. Rev. B 21, 4656 (1980)
4. Ludwig, W. and Langeler, B., Sol. St. Comm. 2, 83 (1964)
5. Muramatsu, A., to be published in Phys. Rev. B
6. Sham, L.J., Phys. Rev. 188, 1431 (1969); Pick, R., Cohen, M.H. and Martin, R.M., Phys. Rev. B 1, 910 (1970)
7. Haneman, D., Phys. Rev. 170, 705 (1968)
8. Tosatti, E. and Anderson P.W., Sol. St. Comm. 14, 713 (1974)
9. For a recent review: Chadi, D.J., Surf. Sci. 99, 1 (1980)

## ATOMIC VIBRATIONS AT (100) SURFACES OF FCC AND BCC METALS

J.E. Black\*, D.A. Campbell and R.F. Wallis

University of California, Irvine, California 92717, U.S.A.

**Abstract.** - We have studied the dynamics of atom motion at metal (100) surfaces. The interactions between atoms are modelled with central forces and angle bending forces. Results for frequencies and polarizations of surface modes have been obtained for the following metals: body centered Cr, Fe, K, Mo, Na, V, W; face centered Ag, Al, Au, Cu, Ir, Ni, Pd, Pt, Rh. Specific results are presented for Cr and Ni.

1. Introduction. - In the last few years we have seen the development of experimental techniques which are sensitive to surface phonons. The electron energy loss spectroscopy experiments of Ibach and Bruchmann [1] and of Andersson [2] have revealed surface phonons on nickel. Helium scattering experiments by Brusdeylins, Doak, and Toennies [3] have yielded data on surface vibrations on LiF. This latter technique may soon be applied to a study of metal surfaces [4]. It is clear that there will be a need for a tabulation of important surface phonon frequencies for a variety of metals. Such a tabulation can serve as a guide to the interpretation of spectral features. In addition, it may serve as a starting point from which to recognize that surface relaxation or reconstruction has occurred. It is the tabulation of important surface phonon frequencies which is the objective of this work.

2. Lattice Dynamical Models. - We have used several models in calculating the atomic force constants. In the present paper, we present results for only a single model consisting of first and second neighbor central interactions together with angle bending interactions. The five force constants  $\alpha_1$ ,  $\alpha_2$ ,  $\beta_1$ ,  $\beta_2$ , and  $\gamma$  were determined by first calculating  $\gamma$  from the elastic constants, and then using the equilibrium condition, along with experimentally determined frequencies at high symmetry points in the bulk dispersion curves. The frequencies that gave the best overall fit are  $v_T(\frac{\pi}{2}, \frac{\pi}{2}, 0)$ ,  $v(s, 0, 0)$  and  $v(\frac{\pi}{2}, \frac{\pi}{2}, \frac{\pi}{2})$ . We measured the goodness of fit by comparing

\*Present address : Physics Department, Brock University, St. Catharines, Ontario L2S 3A1, Canada

the experimental bulk dispersion curves with our theoretically generated dispersion curves. For the case of FCC metals, we also used a two neighbor model with angle bending. The development is analogous to that for the BCC metals.

With the models in hand, the surface phonon frequencies can now be calculated. We employ the slab method in which the crystal consists of 20 atomic layers parallel to the (001) surface [5]. Each atomic layer is assumed to be infinite in extent.

3. Results for BCC Metals. - The dispersion curves of Fig. 1 are

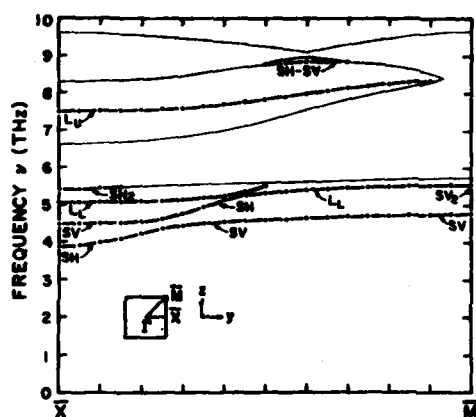


Fig. 1. Dispersion data along the  $\bar{M}\bar{K}$  direction in the surface Brillouin zone of Cr. Dashed lines indicate surface modes, and the cross-hatched areas are those in which bulk phonons are found.

qualitatively fairly typical. They are for Cr in the region between  $\bar{X}$  and  $\bar{M}$  on the zone boundary. The modes have been named according to their shear or longitudinal character at  $\bar{X}$ . The modes that begin as shear horizontal (SH) and shear vertical (SV) at  $\bar{X}$  approach one another as we move to the right of  $\bar{X}$ . At their point of closest approach each mode has both vertical and horizontal shear. Thereafter the mode which is lower in frequency becomes completely SV while the mode which began as SV becomes SH. It is as if the two modes had "crossed" one another. It seems useful in the remainder of this discussion to speak of such encounters as mode "crossings" even though there is no actual intersection of the modes. "Crossing" will mean that the modes have altered their polarization when they encounter one another in the dispersion plots. In this language we see the mode which begins as  $L_1$  at  $\bar{X}$  (a lower longitudinal vibration) crosses SH. The  $L_1$  mode gradually loses its amplitude in the surface layer, until at  $\bar{M}$  it is vibrating entirely parallel to the surface in the second layer--denoted as  $SH_2$ . The mode  $L_2$  (upper longitudinal) exists over much of the zone boundary, but loses its surface character before reaching  $\bar{M}$ . The mode  $SH_2$  at  $\bar{X}$  loses its surface character at

$\phi_3 = 0.24$  radians. As we move toward  $\bar{M}$ , the SH mode vibrates perpendicular to the  $\bar{\Gamma}\bar{X}$  direction, not perpendicular to the wave vector. Similarly, modes labelled longitudinal vibrate along the  $\bar{\Gamma}\bar{X}$  direction, not parallel to the wave vector, at points away from  $\bar{X}$ . Thus the mode marked SV-SH at high frequencies in the center of the zone edge has components parallel and perpendicular to  $\bar{\Gamma}\bar{X}$  in the plane of the surface. All BCC metal results are qualitatively similar to those for Cr.

4. Results for FCC Metals. - The results are qualitatively very similar to those obtained for the BCC metals. The most striking difference between FCC and BCC metals is the absence of the mode  $L_L$  at  $\bar{X}$ .

A typical set of dispersion curves is shown in Fig. 2 for Ni.

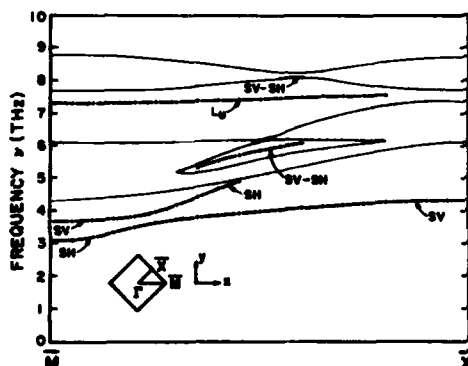


Fig. 2. Dispersion data along the  $\bar{M}\bar{X}$  direction in the surface Brillouin zone of Ni. Dashed lines indicate surface modes, and the cross-hatched areas are those in which the bulk phonons are found.

Note that the mode  $SV_2$  at  $\bar{M}$  now exists only at  $\bar{M}$  and is no longer a continuation of  $L_L$  as it was in the body centered case. Also the mode of SV-SH character is found near the zone edge center in all cases.

Acknowledgements - This research was supported by grants from the Department of Energy, through Contract No. DE-AT0379-ER1032, from the National Science and Engineering Research Council of Canada, and from the National Science Foundation under Grant No. DMR-7809430.

#### References

1. H. Ibach and D. Bruchmann, Phys. Rev. Letters 44 (1980) 36.
2. S. Andersson, Surface Sci. 79 (1979) 385.
3. G. Brusdeylins, R. B. Doak and J. P. Toennies, Proceedings of the Fourth Interaction Conference on Solid Surfaces, eds. D. A. Degral and M. Costa, Cannes, 1980, p. 842.
4. J. P. Toennies, private communication.
5. J. E. Black, D. A. Campbell and R. F. Wallis, Surface Sci. 105 (1981) 629.

## EFFECTIVE MASS APPROXIMATION FOR SURFACE PHONON STATES

A. Fasolino\*, G. Santoro\*\* and E. Tosatti\*\*

\*GNSM-CNR and SISSA, Istituto di Fisica Teorica, Università di Trieste, 34014 Miramare-Grignano, Trieste, Italy

\*\*Istituto di Fisica and GNSM-CNR, Università di Modena, 41100 Modena, Italy

+International Centre for Theoretical Physics, 34014 Miramare-Grignano, Trieste, Italy

**Abstract.**— We show how effective mass concepts borrowed from the theory of impurity states in semiconductors can usefully be applied to the calculation of surface phonon states.

1. **Introduction.**— Given an infinite crystalline solid, two independent surfaces can be created by adding a localized perturbation  $V$ , which consists of cutting all bonds that cross a plane. Historically the effect of localized perturbations on an infinite Bloch problem have been dealt with first in connection with impurity states in semiconductors<sup>(1,2)</sup>. When dealing in particular with the bound states that the impurity potential is able to split from the Bloch bands, the popular effective mass approximation has been most useful in providing a qualitative understanding of the problem<sup>(1,2)</sup>. A surface state — electronic, vibrational, whatever its microscopic nature — is, in principle, a bound state of the same kind; only the perturbation has infinite extension along  $(x,y)$  and is localized just along  $z$ .

This work represents an attempt to apply the concepts typical of the effective mass formulation to the study of a surface state problem. In order to make our study more definite and provide ourselves with accurate numerical reference calculations to use as a check, we shall concentrate in the following on a surface phonon problem, in particular the phonons of a bcc (100) surface.

2. **Method.**— We start by formally writing the surface phonon eigenvector as a linear combination of bulk phonon states  $\vec{u}$  with the same in-plane momentum  $\vec{q}$  and variable normal component  $k$ :

$$\vec{v}_{\vec{q}}(\vec{R}) = \sum_{k,\lambda} \phi_k^{\lambda} \vec{u}_{\vec{q}k\lambda}(\vec{R}) \quad (1)$$

Here  $\vec{R}$  is an atomic site and  $\lambda$  denotes the branch. The "envelope" function  $\phi$  then satisfies:

$$\sum_{k',\lambda'} [(\omega^2 - \omega_{\vec{q}k\lambda}^2) \delta_{kk'} \delta_{\lambda\lambda'} + v_{kk'}^{\lambda\lambda'}] \phi_{k'}^{\lambda'} = 0 \quad (2)$$

where  $v_{kk'}^{\lambda\lambda'} = \langle \vec{u}_{\vec{q}k\lambda} | V | \vec{u}_{\vec{q}k'\lambda'} \rangle$  is taken between bulk states. For a general  $\vec{q}$ -direction and for a Bravais lattice, Eq.(2) constitutes a set of three coupled equations. For particular  $\vec{q}$  values, however, symmetry may allow a decoupling. Such is the case for



example of  $\vec{q} = (\frac{1}{2}, \frac{1}{2}) 2\pi/a \equiv M$  on the bcc (100) surface, that is our test case. At that point we have a non-degenerate  $\vec{v} \parallel \hat{z}$  mode ( $M_1$ ) and a twofold degenerate  $\vec{v} \perp \hat{z}$  mode ( $M_5$ ). The symmetry labels are those of  $C_{4v}$ , that is the two-dimensional part of the crystal symmetry group as reduced by the surface perturbation  $V$ . We now develop this particu-

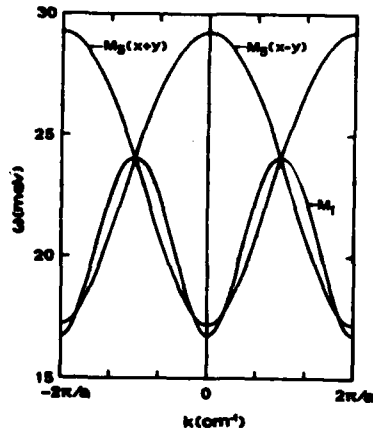


Fig. 1 : Bulk phonon branches of  $W$  for  $\vec{q} \equiv M$

lar case as an instructive exemplification. For comparison, we also perform accurate numerical surface state calculations with the usual slab technique using the parameters of  $W(100)$ <sup>(3)</sup>. We use variable intra-surface force constants  $\alpha_s$  and  $\beta_s$ <sup>(4)</sup> to control the actual surface state energy and eigenvector.

The bulk bands  $\omega_{\vec{q}k\lambda}$  for  $\vec{q} \equiv M$  are shown in Fig.1. Here  $k$  spans twice the Brillouin zone (from  $-2\pi/a$  to  $2\pi/a$ ) as required by having two alternating types of layers in the problem. We note that this give rise to two equiva-

lent minima at  $k_0=0$  and  $k_0=2\pi/a$  for both the  $M_1$  symmetry and the  $M_5$  symmetry and in fact for all other zone-border  $\vec{q}$ -points as well. However, the two minima are orthogonal by symmetry (belonging to the two different rows  $(x-y)$  and  $(x+y)$  of the twofold degenerate irreducible representation  $M_5$ ) and do not mix in the  $M_5$  case, while they are mixed by  $V$  in the  $M_1$  case. The  $V$ -matrix is given by all those slab matrix elements that are removed by creating the surface, taken with negative sign. We obtain analytical expressions for  $V_{kk'}$  at the  $M$  point as a function of  $\alpha_s$  and  $\beta_s$ . However they are too long to be reported here<sup>(5)</sup>; we shall just proceed to discuss the results.

3. Bound state problem: solutions.- a) variational : we try exponentially decaying solutions:

$$\phi_{M_5}^{\pm}(z) = \exp(-|z|[\lambda^{-1} + i(\pi/a)(1 \pm 1)]) \quad (3)$$

and:

$$\phi_{M_1}^{\pm}(z) = \exp(-|z|\lambda^{-1}) \{1 \pm \exp[2i\pi|z|/a]\} \quad (4)$$

where the "+" and "-" signs in Eq.(3) correspond to  $x+y$  and  $x-y$  respectively, the two terms in the  $M_1$  case are necessary in order to include intervalley mixing (that removes the degeneracy between the "+" and "-" case) and the variational parameter is the penetration depth  $\lambda$ .

b) Effective mass approximation : For shallow bound states, one may approximate

$\omega_{\vec{q}k\lambda}^2 \approx \omega_{\vec{q}k_0\lambda}^2 + \hbar^2(k-k_0)^2 \omega_{\vec{q}k_0\lambda}^2 / m^*$ . The Schrodinger-like problem (2) can be solved variationally, with trial functions such as (3) and (4).

c) Koster-Slater approximation : If we further replace  $V_{kk'}$  with  $V_{k_0 k_0}$ , where  $k_0$  is the relevant extremum, the solution becomes similar to the well known Koster-Slater problem (except for a cutoff at  $\pm 2\pi/a$ ), that is straightforward to evaluate analytically.

Fig.2 presents a comparison of the approximate solutions a), b) and c) with the exact numerical slab surface phonon "binding energy". This quantity, introduced in

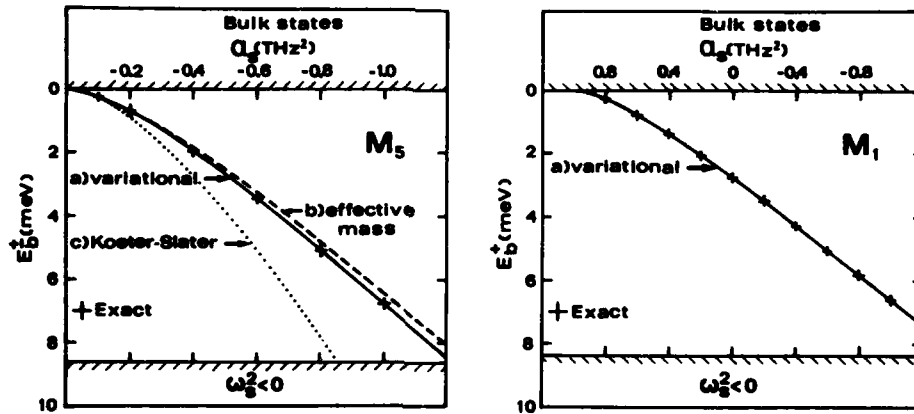


Fig. 2 : Surface phonon "binding energies" calculated at the Mpoint of W(100) for  $\beta_s = 3.7$  and  $\alpha_s = 4.222$

analogous to the impurity binding energy in the usual effective mass theory<sup>(1,2)</sup>, is defined as  $E_B = (\omega_s^2 - \omega_{qk_0}^2) / 2\omega_{qk_0}^2$ . The variational result is in perfect agreement with the exact calculation over the whole range of parameters that have been tested. This means that the straight exponentials (3) and (4) in fact represent extremely well the behaviour of the surface phonon. We have checked that this is indeed the case.

The approximations b) and c) are clearly acceptable only for shallow surface states. However, the effective mass approximation b) remains fairly accurate in the whole range, while the Koster-Slater result c) fails appreciably already for  $E_B/\text{band width} \approx 0.1$ . We note that while for  $M_5$  the two states  $\phi_{M_5}^{\pm}$  are degenerate, only  $\phi_{M_1}^+$  leads to a bound state in the  $M_1$  case, where  $\phi_{M_1}^-$  yields  $E_B = 0$ .

#### References

1. F Bassani, B Preziosi and G Iadonisi, Repts. Prog. Phys. **37**, 1099 (1974)
2. M Altarelli, A Baldereschi and N O Lipari, Solid State Phys., to appear
3. D Castiel, L Dobrzynski and D Spanjard, Surf. Sci. **59**, 252 (1976)
4. This parametrization has been explained and used earlier for a study of the W(100) surface reconstruction. See A Fasolino, G Santoro and E Tosatti, Phys. Rev. Lett. **44**, 1684 (1980)
5. These and other details will be reported extensively elsewhere.

# ADSORBATE INDUCED VIBRATIONS MEASURED BY EELS ON A CuZn $\alpha$ 75/25 (110) SURFACE DURING ITS EARLY STAGE OF OXIDATION

P.A. Thiry, S. Maroie\*, J.J. Pireaux\*, R. Caudano and A. Adnot\*\*

*Institute for Research in Interface Sciences, Facultés Universitaires Notre-Dame de la Paix, B-5000 Namur, Belgium.*

*\*\*I.S.A. Riber, B.P. 231, F-92505 Rueil, France.*

**Abstract.** - Using high resolution electron energy loss spectroscopy (EELS), we have measured three vibrational bands on a clean  $\alpha$ -CuZn 75/25 (110) surface after O<sub>2</sub> exposure. The band at 420 cm<sup>-1</sup> is related to the metal-O stretching vibration. The band around 3630 cm<sup>-1</sup> is interpreted as the O-H stretching vibration arising from water contamination. At higher coverages, a third band emerges (550 cm<sup>-1</sup>). It is attributed to an optical surface phonon and associated with a preliminary stage of bulk oxide formation.

1. **Introduction.** - Brass alloys of Cu/Zn are largely used for industrial applications. There is great interest in understanding the reaction of such materials with oxygen. In order to start from a fundamental point of view, the experiments reported here were performed on a single crystal of CuZn  $\alpha$  brass 75/25. Although it crystallizes in the f.c.c. lattice, it is a solid substitutional solution of Zn in Cu.

2. **Experimental.** - EELS experiments were carried out with an hemispherical RIBER-SEDRA spectrometer, capable of an energy resolution of 35 cm<sup>-1</sup> (4 meV) /5/. The analyzer is rotatable in the plane of incidence. All spectra were taken with 4 eV impact energy, a monochromator current of  $3 \times 10^{-10}$  A, and an energy resolution of 60 cm<sup>-1</sup>. The spectrometer is mounted in an UHV chamber (10<sup>-11</sup> Torr range), where other techniques are available, such as LEED, AES using retarding field analyzer, Kelvin probe for work function measurements and quadrupole mass analyzer. Water contamination in oxygen (nominal purity : 99,998 %) was measured to be lower than 0.5 %. Pressure indications are uncorrected gauge readings. The polished crystal was cleaned by cycles of Ar<sup>+</sup> bombardment and annealing up to 430 K. The consecutive Auger spectra showed no observable contamination. Sharp LEED patterns were observed in agreement with the (110) face. During O<sub>2</sub> admission, LEED did not reveal any superstructure. A maximum of the work function was found at 20 L (1 Langmuir = 10<sup>-6</sup> Torr.s).

3. **EELS results and interpretation.** - EELS results are summarized on fig. 1. One peak (420 cm<sup>-1</sup>) was observed to grow regularly without

\* Resp. Research Assistant & Research Associate of the Belgian NFSR.

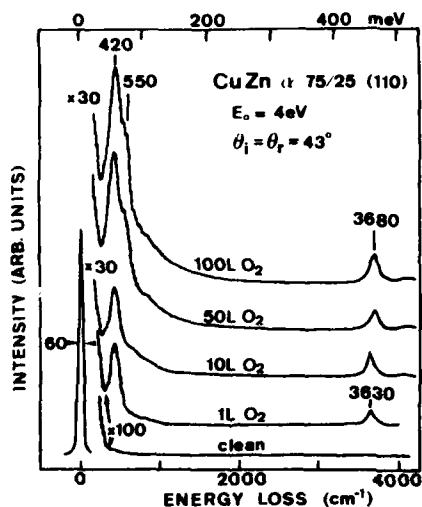


Fig. 1 : Energy loss spectra of the clean surface, and after exposure to  $O_2$  at room temperature.

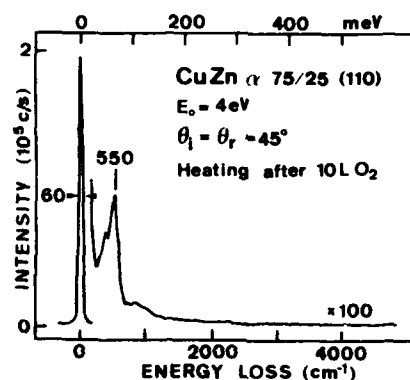


Fig. 2 : Energy loss spectrum of the surface exposed to 10 L  $O_2$  and annealed to 430 K.

any frequency shift. It is attributed to the stretching vibration of atomic oxygen adsorbed on the surface. Dissociative adsorption is inferred from the absence of molecular  $O_2$  vibration. This frequency ( $420\text{ cm}^{-1}$ ) lies in the range of atomic oxygen vibrations measured on other metallic substrates /1,2/. Off specular experiments ( $10^\circ$ ,  $20^\circ$  and  $30^\circ$ ) indicate clearly that it is excited by dipole scattering, because its intensity peaks strongly in the specular direction. The observation of only one vibration imposes that only one site is activated. Four sites are available : on-top, short bridge, long bridge and the deep center site where the oxygen may have 5 nearest neighbours. Following a general rule, the atom is most likely to choose the site offering the highest coordination. This would favour the center site, although for  $O\text{-Cu}(110)$  a long bridge site /1/ and for  $O\text{-Ni}(110)$  a short bridge one have been reported.

From the very beginning of  $O_2$  exposure, a peak at  $3630\text{ cm}^{-1}$  was observed. It is assigned to the stretching vibration of OH species adsorbed on the surface. Separate measurements were made with exposure to  $H_2O$  : on the clean surface, they did not reveal any loss feature; if the surface was previously dosed with  $O_2$ , a small increase was observed for the OH peak. It is believed that some amount of  $H_2O$  contaminant in the admitted gas can interact with the surface only during the adsorption of  $O_2$  itself. A similar mechanism of assisted selective adsorption has been reported for stainless steel /3/. The OH is adsorbed on the same

site as the atomic oxygen, since only one adsorbate-metal vibration is observed at low exposure. The relatively low frequency with respect to the free OH is an indication of the existence of H-bonding with oxygen adsorbed on adjacent sites.

When the O<sub>2</sub> exposure varied from 10 L to 100 L, the EELS spectra changed substantially. The relative intensity of the OH vibration saturated and its frequency shifted from 3630 cm<sup>-1</sup> to 3680 cm<sup>-1</sup>. A third peak emerged at 550 cm<sup>-1</sup>, very close to the frequency of the surface optical phonon of ZnO /4/. It is interpreted as the vibration of oxygen incorporated in the surface during a preliminary stage of oxide formation. The decrease of the 3630 cm<sup>-1</sup> peak intensity indicates that the mechanism of H<sub>2</sub>O assisted selective adsorption must then be inhibited : this is explained as an incorporation of the oxygen atoms ( $\Delta\phi$  decrease), relaxing the H-bonding, as the OH frequency shifts by 50 cm<sup>-1</sup>.

Annealing of the sample after O<sub>2</sub> adsorption lead to the following observations (Fig. 2) : the oxide-like peak at 550 cm<sup>-1</sup> was enhanced and its intensity became higher than the 420 cm<sup>-1</sup> one, that shifted to low energy; the OH vibration vanished. This is consistent with our interpretation : the occupation of the 550 cm<sup>-1</sup> site inhibits the OH- and the 420 cm<sup>-1</sup> vibrations at the same time.

**Acknowledgements.** - The authors are indebted to F. Eckstein (Max Planck Institute, Stuttgart FRG) for providing the crystal. This work is supported by the Belgian Fund for Joint Basic Research (FRFC).

#### References

- /1/ Wendelken, J.F., Surface Sci. 108 (1981) 605.
- /2/ Sexton, B.A., Surface Sci. 88 (1979) 299.  
Erley, W. and Ibach, H., Solid State Commun. 37 (1981) 937.  
Andersson, S., Solid State Commun. 20 (1976) 229.
- /3/ Adnot, A., Ph.D. Thesis, Université Laval, Québec (1977).
- /4/ Ibach, H., Phys. Rev. Lett. 24 (1970) 1416.
- /5/ Thiry, P.A., Pireaux, J.J. and Caudano, R., Physica Mag. 4, 1 (1981) in press.

## SURFACE PHONONS AND THE INCOMMENSURATE RECONSTRUCTION OF CLEAN Mo (100)

A. Fasolino\*, G. Santoro\*\* and E. Tosatti\*\*

\*GNSM-CNR and SISSA, Istituto di Fisica Teorica, Università di Trieste, 34014 Miramare-Grignano, Trieste, Italy

\*\*Istituto di Fisica and GNSM-CNR, Università di Modena, 41100 Modena, Italy

+International Centre for Theoretical Physics, 34014 Miramare-Grignano, Trieste, Italy

**Abstract.**— We present a model lattice dynamical study of the Mo(100) incommensurate reconstruction. We find that both the predicted periodicity and polarization of the incommensurate distortion agree with experiment. Interesting changes of the periodicity are predicted in presence of an electric field of magnitudes such as those used in Field-Ion-Microscopy.

1. **Introduction.**— The Mo(100) displacive reconstruction is peculiar, because it is incommensurate, with a temperature independent periodicity, roughly given by  $k=(0.44, 0.44)2\pi/a$ <sup>(1)</sup>. It was earlier supposed that the incommensurability could be due to intra-surface long-range forces, connected with a partly filled surface state band and related 2-dimensional Fermi surface<sup>(2)</sup>. In a subsequent model study of the lattice-dynamical aspects of the commensurate  $(\sqrt{2}\times\sqrt{2})R45^\circ$  reconstruction of W(100), it was found, however, that incommensurate surface phonon instabilities may also occur with strictly short-range surface forces. In this work we pursue the idea that incommensurability of Mo(100) could be due to this latter elastic reason. We still envisage the chemically unbounded surface electrons and 2-dimensional Fermi surface, to be the driving force of this phenomenon<sup>(3)</sup>. However, the actual surface distortion and its periodicity will be finally determined by a compromise between the driving force and the deformation energies involved. In the present approach one assumes a simple model for the driving forces (simulated by a first neighbor intra-surface repulsion) and one determines the distorted state by a careful study of the lattice energies, via a surface phonon calculation. We follow here the conventional soft-mode approach to structural phase transitions, whose basic ingredients are: a) the harmonic vibration spectrum of the ideal surface and its instabilities, b) the anharmonic forces that intervene to stabilize the surface once the distortion is introduced by freezing-in the soft mode.

2. **Mo(100) surface instabilities.**— Our model is the same introduced earlier for the W(100) surface<sup>(4)</sup>. We have an n-layer slab ( $n>15$ ) with bulk-like intratomic forces, except for the outer surface layer. The force constants  $\alpha_s = \frac{1}{R} \left( \frac{\partial U}{\partial R} \right)_{R=a}$  and  $\beta_s = \left( \frac{\partial^2 U}{\partial R^2} \right)_{R=a}$  between two surface first neighbors (distance  $a$ ) are adjustable to represent the extra surface forces. By looking for imaginary surface phonon modes we can construct a "phase diagram" as a function of  $\alpha_s$  and  $\beta_s$ . The result is shown in Fig.1. Beside the stable region and the regions  $M_1$ ,  $M_5$  and  $L_2$  where the corresponding zone-border modes are unstable, we find two regions  $I_1$  and  $I_2$  where the instability occurs first

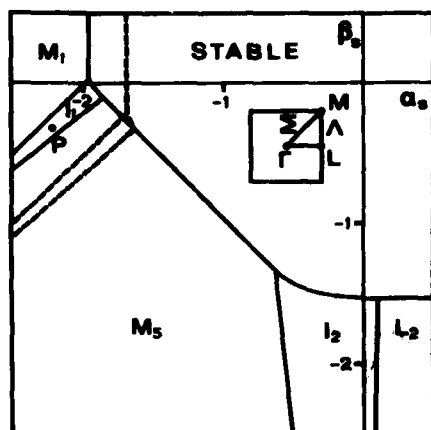


Fig. 1 : T=0 phase diagram as a function of the surface force constants of Mo(100).

at an incommensurate wavevector.

However in the  $I_2$  region, the instability occurs along the  $\Lambda$ -line ( $q_\Lambda = (\frac{1}{2}, \frac{1}{2} - \delta)2\pi/a$ ). This disagrees with experiment, that shows a  $\Sigma$ -type distortion ( $q_\Sigma = (\frac{1}{2} - \delta, \frac{1}{2} - \delta)2\pi/a$ ) with  $\delta = 0.06$ . In the region  $I_1$ , on the other hand, two instabilities occur almost simultaneously along the  $\Lambda$ -line and along the  $\Sigma$ -line. We have previously argued<sup>(5)</sup>, however, that in this circumstance one should expect a  $\Sigma$ -distortion, because the anharmonic restoring forces are weaker for  $\Sigma$  than for  $\Lambda$ . We are thus led to assume that the Mo(100) incommensurate distortion corresponds to the  $I_1$  phase. We now consider some of the consequences

of this model.

**3. Surface lattice distortion.**— The nature of the expected surface lattice distortion is best understood by considering in detail the mechanisms through which the incommensurability occurs. Fig.2 shows how an absolute minimum in  $\omega$  can occur slightly off the  $M$  point, whenever an  $M_5$  (in-plane) and an  $M_1$  (vertical) soft modes happens to come sufficiently close in energy. At the  $M$  point itself,  $M_1$  and  $M_5$  are orthogonal by symmetry. Away from  $M$ , however, they interact producing a minimum in the lowest  $\Sigma_1$  or  $\Lambda_1$  branch, while the  $\Sigma_2$  and  $\Lambda_2$  branches remains higher. Therefore the incommensurate distortion is predicted to have  $\Sigma_1$  symmetry. This mode consists of an admixture of in-plane longitudinal (110) motion and of vertical (001) motion. This is precisely the symmetry found by careful analysis of LEED data by Barker and Estrup<sup>(6)</sup>. The present mechanism bears several analogies with that invoked in incommensurate ferroelectrics<sup>(7)</sup>, with a noticeable difference: the twofold degeneracy is here broken quadratically rather than linearly, by moving away from the high symmetry point. The implications of this fact on the presence of discommensurations as well as on the behaviour of the distortion periodicity with temperature are presently under investigation and will be reported elsewhere<sup>(8)</sup>.

**4. Effects of electric fields.**— A possible test of the present model could consist in trying to change artificially the periodicity of the surface distortion. This could be done, for example, by applying a very strong surface electric field such as one finds in FIM experiments. We have evaluated how the surface phonon modes are altered by the field by supposing the first layer atom to acquire a charge  $\rho = -e$  ( $\vec{u} - \vec{u}_{21}$ )  $\cdot \vec{z}$  where  $\vec{u}$  is its displacement and  $\vec{u}_{21}$  are the displacements of its four first neighbors

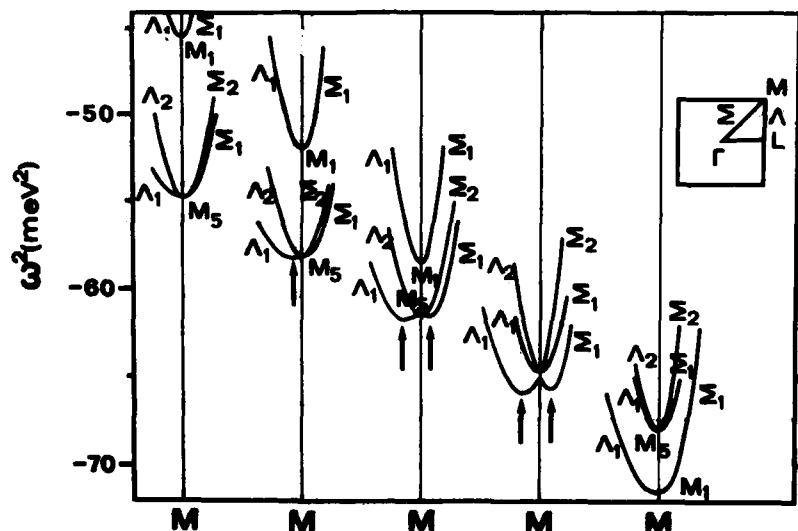


Fig. 2 : Surface phonon branches of Mo(100) along the  $\Sigma$  and  $\Lambda$  directions

in the second layer. We believe that  $\alpha$  is positive, so that a raised atom becomes positively charged, but the same reasoning would apply for  $\alpha < 0$  with a reversed electric field. In the new phonon spectrum all modes involving a vertical displacement are softened by the field. The new phase diagram is drawn (dashed line) in Fig.1 for a sufficiently strong field whose absolute magnitude is  $E = 3 \times 10^7$  V/cm if we take  $\alpha = 1$  e/Å. For increasing field we expect the reconstruction  $\vec{q}$ -vector to shift, the distortion acquiring more and more  $z$  component, until at some critical field  $E_c$  the distortion should become  $M_1$ -like (commensurate  $c(2 \times 2)$ ), with strictly vertical displacements. This is made clear in Fig.1 if one supposes the point P to represent the actual Mo(100) surface. Once the field is applied P falls inside the  $M_1$  region. The new commensurate field-induced phase should become particularly evident e.g. by field etching. An observation in this direction has actually been reported<sup>(9)</sup> for W(100) where, however the reconstruction is commensurate even at zero field.

#### References

1. T E Felter, R A Barker and P J Estrup, Phys.Rev.Lett. **38**, 1138 (1977)
2. E Tosatti, Solid.St.Comm. **25**, 881 (1978)
3. An alternative explanation is given in: J E Inglesfield, J.Phys. C **12**, 149 (1979)
4. A Fasolino, G Santoro and E Tosatti, Phys.Rev.Lett. **44**, 1684 (1980)
5. A Fasolino, G Santoro and E Tosatti, La vide, Le couches minces (suppl.) **201**, 679 (1980)
6. R A Barker, S Semencik and P J Estrup, Surf. Sci. **94**, L162 (1980)
7. V Dvorák, in "Modern trends in the theory of condensed matter", ed.by A Pekalski and J Przystawa, Springer (Berlin), p.447 (1980)
8. A Fasolino and E Tosatti, to be published
9. A J Melmed, R J Tung, W R Graham and G D W Smith, Phys.Rev.Lett. **43**, 1521 (1979)



## MODE CONVERSION COEFFICIENTS OF ACOUSTIC WAVES AT A CRYSTAL-VACUUM INTERFACE

J. Throwe and W.E. Bron

Indiana University, Bloomington, IN 47405, U.S.A.

**Abstract.**—Recent work by Taborek<sup>1</sup> et al has shown that the reflection of acoustic phonons from a sapphire-vacuum interface is divided between a specular component which is predicted by elastic theory and a diffuse component. Knowledge of the magnitude and direction of the specular component is useful in the design of experiments to study the frequency dependence of the reflection process. We have generated mode conversion coefficients for infinite plane waves traveling initially in the x direction and incident at various angles on perfect surfaces in quartz, sapphire, and ZnO. For waves propagating in the xy-plane, ZnO behaves as an isotropic solid whereas quartz, because of its anisotropy, exhibits new transverse reflections beyond the critical angle.

Coherent collimated phonons pulses can be generated via the piezoelectric interaction of an FIR laser beam with a crystal surface. As a first approximation the reflection of such a pulse from the opposite surface after traversing the crystal can be treated as the reflection of an infinite plane elastic wave from a perfectly flat crystal-vacuum interface. The conditions governing such a reflection have been treated extensively in the literature<sup>2,3,4</sup> and can be summarized as follows:

1. The component of the incident wave vector parallel to the surface is conserved.
2. The group velocities of the reflected waves must point into the crystal, although their wave vectors need not do so.
3. The vacuum exerts no stresses on the crystal.

In general, the energy of the incident wave is divided among reflections from each of the three acoustic branches. Beyond certain critical angles of incidence, however, it is no longer possible to satisfy the first two conditions for all three branches. It is then necessary to introduce evanescent modes in order to maintain the stress free boundary condition. These modes carry no energy away from the surface, leaving the incident energy to be divided between the remaining bulk wave reflections.

Figures 1a, 2a and 3a show the energy reflection coefficients in ZnO, sapphire and quartz for T2 waves traveling in the x direction incident on planes containing the z-axis. Because it has hexagonal symmetry ZnO is elastically isotropic with respect to rotation about the z-axis<sup>4</sup> (Figure 1b). In the xy-plane

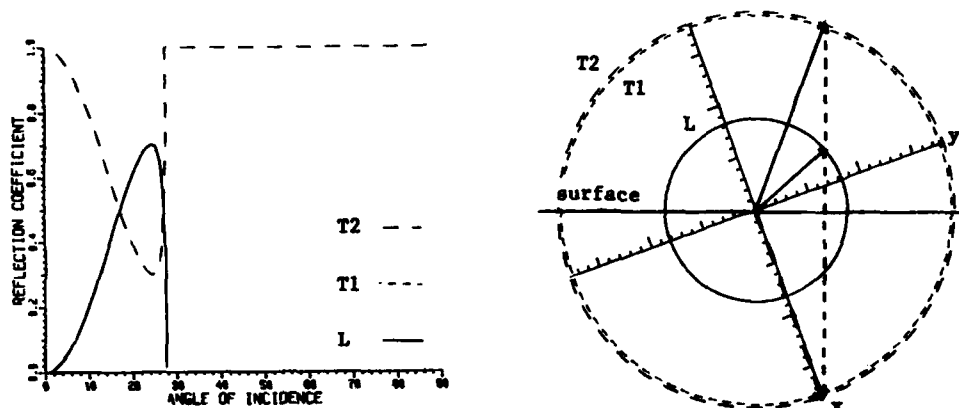


Figure 1. a) Energy reflection coefficients for T2 phonons traveling in the x direction in ZnO. b) Slowness surface for ZnO in the xy-plane showing possible reflected wave vectors (solid arrows) for a T2 wave (dashed arrow) incident at  $20^\circ$  to the surface normal. The T1 reflection has been omitted.

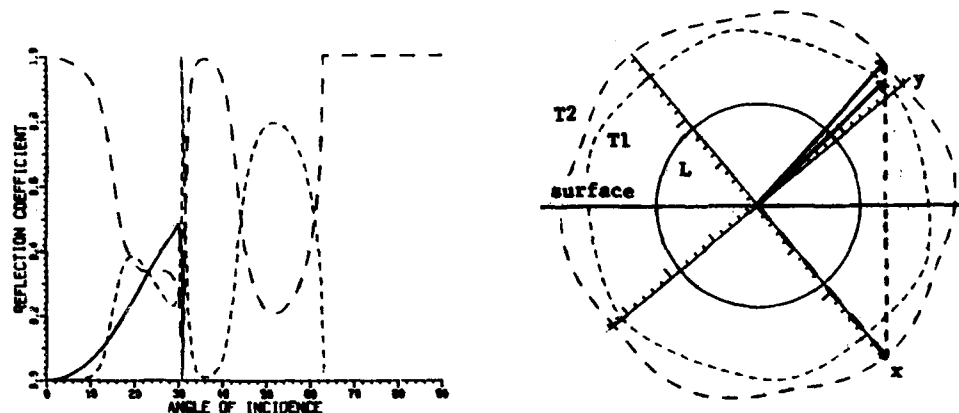


Figure 2. a) Energy reflection coefficients for T2 phonons traveling in the x direction in sapphire. b) Slowness surface for sapphire in the xy-plane showing possible reflected wave vectors (solid arrows) for a T2 wave (dashed arrow) incident at  $40^\circ$  to the surface normal. There is no possible L reflection.

the T1 mode is polarized perpendicular to the plane of incidence and thus is not coupled to the other modes by reflection. Accordingly, the energy of the incident T2 wave is therefore divided between T2 and L reflections. Beyond the T2-L critical angle of  $26^\circ$  the only bulk wave available for reflection is the T2 mode, i.e., with an energy reflection coefficient of 1.

In sapphire the transverse modes are polarized at oblique angles to the plane of incidence. The incident energy is therefore shared by all three reflected modes up to the T2-L and T2-T1 critical angles of  $31^\circ$  and  $63^\circ$  respectively.

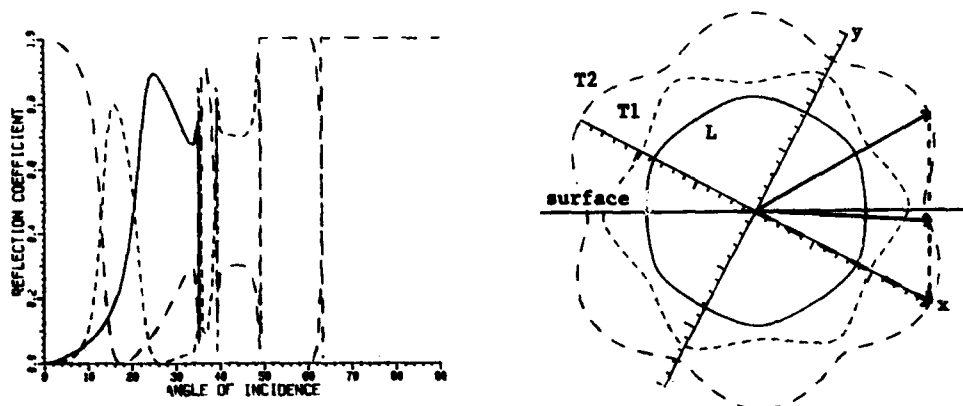


Figure 3. a) Energy reflection coefficients for T2 phonons traveling in the x direction in quartz. b) Slowness surface of quartz showing possible reflected wave vectors (solid arrows) for a T2 wave (dashed arrow) incident at  $62^\circ$  to the surface normal. One reflected mode has a wave vector pointing out of the crystal.

The situation in quartz is more complex due to the high curvature of the slowness surface (Figure 3b). As noted by Jones and Henneke<sup>5</sup>, it is possible for a single branch to contribute more than one reflected wave for a given angle of incidence. The most clearcut case occurs in the T2 branch between  $60^\circ$  and  $63^\circ$ . At  $60^\circ$  a new reflection appears with wave vector pointing out of the crystal but with its group velocity directed inward. This shares the energy with the original T2 reflection until  $63^\circ$ , where the original reaches its critical angle. At  $39.4^\circ$  a slightly different situation creates two T1 modes with wave vectors pointing into the crystal which coexist over a range of less than  $.01^\circ$ . The T2-L and T2-T1 critical angles are  $35^\circ$  and  $49^\circ$ .

Reflection coefficients for incident T1 and L waves show, as expected, fewer critical angle features. Coefficients for GaAs are also available.

Funded by ONR Contract N14-78-0249.

#### References

1. Zaborak, P. and Goodstein, D., J. Phys. C **12**, 4737(1979).
2. Weis, O., Z. Physik B **34**, 55(1979).
3. Henneke II, E.G., J. Acoust. Soc. Amer. **51**, 210(1972).
4. Masgrave, M.J.P., Crystal Acoustics, Holden-Day(1970).
5. Jones, C.L. and Henneke II, E.G., IEEE Trans. on Sonics and Ultrasonics, **SU-20**, 267(1973).

## TIME CONSTANT FOR PHONON INDUCED DESORPTION OF HELIUM\*

P. Taborek, M. Sinvani, M. Weimer and D. Goodstein

*California Institute of Technology, Pasadena, CA 91125, U.S.A.*

**Abstract.**— We have made direct measurements of the time constant for thermal desorption of thin helium films as a function of substrate temperature and film binding energy. We find that the attempt frequency for desorption  $\tau_0^{-1}$  is several orders of magnitude larger than previously reported values.

Phonons impinging on a solid surface which is covered with a helium film can cause some of the atoms to be ejected. The physics of this process is important for an understanding of the dynamics of desorption and energy transport at solid/helium interfaces. We have used pulsed phonon techniques to study the rate of desorption from a nichrome surface. The experimental apparatus consists of a rectangular thin film nichrome heater deposited on a sapphire crystal which forms the bottom of a vacuum can (see Fig. 1, inset). A superconducting transition bolometer with a thermal response time of  $\sim 10$  nsec is mounted  $\sim 1$  mm above the heater. By admitting known quantities of helium gas, the thickness of the film which covers all the surfaces in the cell can be controlled in the range 1-3 layers. The ambient temperature is 3.5 K and the pressure is always sufficiently low that the atoms travel ballistically to the detector. A current pulse with a

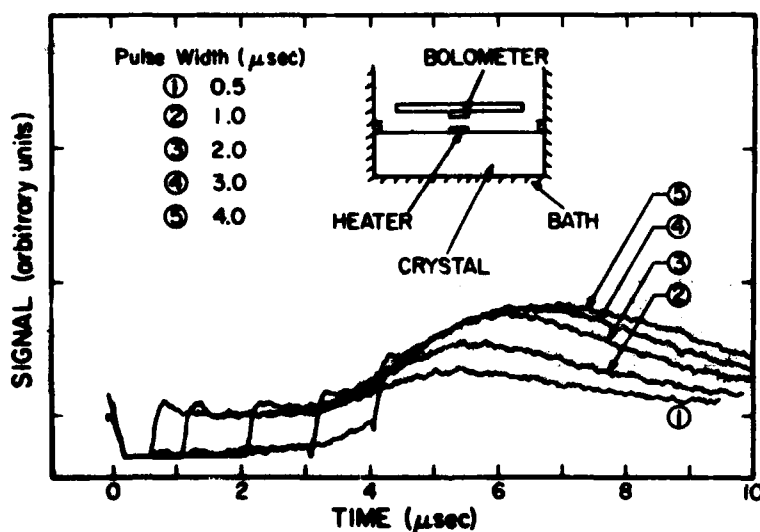


Fig. 1 : Bolometer signal as a function of time for various heater pulse widths. Heater temperature = 6.2 K. The inset shows the experimental geometry.

\*Supported in part by ONR Contract # N00014-80-C-0447

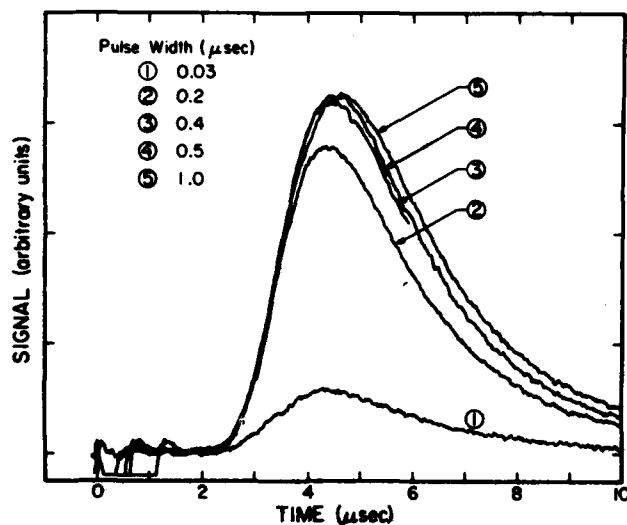


Fig. 2 : Bolometer signal as a function of time for various heater pulse widths. Heater temperature = 8.1 K. The pulse shape is described by Eq. 1. No further change in the signal is observed for pulses longer than 1 μsec.

known power and duration is applied to the heater, which raises the heater temperature and causes desorption of the film; typical bolometer signals are shown in Figs. 1 and 2. The temperature of the heater film is a function of the power and can be calculated from acoustic mismatch theory<sup>(1)</sup> and can also be deduced independently from the time of flight of the desorbed atoms. The calculated temperature of the nichrome film and the measured temperature of the desorbed atoms are in good agreement. Because the heater film is in contact with a single crystal substrate, the heater temperature can be raised and lowered with a time constant of  $\sim 10$  nsec. When the heater temperature is higher than the ambient, the number of atoms/cm<sup>2</sup> in the helium film  $n(t)$  relaxes to a new steady state value  $n_{ss}$  in a characteristic time  $\tau$ .

For heater pulse widths  $\leq \tau$ , the desorption signal is a sensitive function of the pulse width, but for long pulses, the signal saturates. By slowly increasing the pulse width from a minimum of 30 nsec, the pulse width which causes saturation is easily observed. We have used this technique to measure  $\tau$  as a function of film thickness and heater temperature. Typical data shown in Figs. 1 and 2 give  $\tau \sim 1$  μsec for  $T_{\text{heater}} = 6.2$  K and  $\tau \sim .2$  μsec for  $T_{\text{heater}} = 8.1$  K.

Theories for the desorption time  $\tau$  can be quite complicated,<sup>(2)</sup> but the results can be described using a simple thermal activation model<sup>(3)</sup>  $\tau = \tau_0 e^{E_b/T}$  where  $\tau_0$  is a characteristic attempt frequency and  $E_b$  is the binding energy of the atom to the substrate. In order to compare our results with previous indirect experimental measurements<sup>(4)</sup> and theoretical calculations<sup>(2)</sup> it is necessary to measure an average  $E_b$  for the desorbed films. We have estimated  $E_b$  in two independent ways. First,  $E_b$  can be extracted by fitting the time of flight distribution to a theoretical model which assumes that the helium film is heated to the

temperature of the substrate and the atoms desorb with a Maxwellian distribution. The expected bolometer signal has the form

$$S(t) \propto T^{-3/2} e^{-(\frac{mv^2}{2} + E_b)/kT} v^4 (\frac{1}{2} mv^2 + E_b) \quad (1)$$

with  $v = \ell/t$  where  $\ell$  is the distance to the detector.  $E_b$  may also be deduced from the chemical potential of the gas, which can be determined by measuring  $P$  and  $T$ . Using these methods we find that  $E_b \geq 35$  K for the data shown in Figs. 1 and 2. From  $\tau = \tau_0 e^{E_b/T}$ , we find  $\tau_0 < 5 \times 10^{-9}$  sec, at least two orders of magnitude smaller than the value deduced in reference (4) and explained in reference (2). The technique used in that experiment is very insensitive to the small time constants which are observed for heater temperatures above 6 K. Our measurements are consistent with their data, but yield much more precise values of  $\tau$  in this regime.

- References:
1. O. Weis, Z. Ang. Phy. 26, 325, 1969.
  2. Z. W. Gortel, H. J. Kreuzer, and D. Spaner, J. Chem. Phys. 72, 234, 1980.
  3. J. Frenkel, Kinetic Theory of Liquids, Dover, New York, 1946.
  4. S. A. Cohen and J. G. King, Phys. Rev. Lett. 31, 703, 1973.

## POLARIZATION DEPENDENCE OF PHONON INDUCED DESORPTION OF He ATOMS AT LOW TEMPERATURES\*

P. Taborek, M. Sinvani, M. Weimer and D. Goodstein

*California Institute of Technology, Pasadena, CA 91125, U.S.A.*

**Abstract.**— We directly observe the desorption of He atoms from a thin film on the surface of a solid by both longitudinal and transverse ballistic phonons. Ballistic propagation of the He atoms, sound in the vapor and second sound in the bulk liquid are all separately observed. Comparison of the data reveals that the efficiency of conversion of L and T phonons is the same for these three different modes of coupling.

The heat pulse technique has previously been used by several authors to study the transmission of thermal energy, via longitudinal (L) and transverse (T) ballistic phonons generated in a solid, across an interface with bulk superfluid helium. Schwanenburg and Wolter<sup>(1)</sup> first made a direct measurement of the relative L/T phonon transmission coefficient into He II by observing two peaks in the collective second sound signal corresponding to the two incident phonon polarizations. In a later experiment Salemink, van Kempen and Wyder<sup>(2)</sup> studied the conversion of both L and T ballistic phonons incident from the solid to first sound (ballistic phonon propagation) in He II.

Using essentially similar techniques we have studied the desorption of thin films (1-3 layers) of He adsorbed on the surface of sapphire. The experimental arrangement consists of a resistive thin film Nichrome ( $\sim .1 \text{ mm}^2$ ) heater evaporated onto a single crystal sapphire cylinder 57 mm in diameter and 9.5 mm thick whose crystallographic y-axis coincides with the direction of phonon propagation. The far side of the crystal is in a vacuum can where He gas may be admitted. The adsorbed film thickness is controlled via the He gas pressure. The entire cell is immersed in a helium bath at about 2 K. Pulsing the heater, ballistic longitudinal and transverse phonons propagate through the crystal arriving at the far surface at different times (see inset Fig. 1). He atoms are desorbed, and their arrival time spectrum detected by a superconducting bolometer above the crystal surface in the gas. When the mean free path in the gas is long compared to the distance to the bolometer the desorbed atoms travel ballistically to the detector. In this low pressure regime we observed two peaks in the desorption signal (Fig. 1). The difference in arrival time for these two peaks is precisely the same as the difference in times of flight across the sapphire of the two phonon polarizations, as measured by a bolometer evaporated directly on the surface of the crystal. The

\*Supported in part by ONR Contract #N00014-80-C-0447

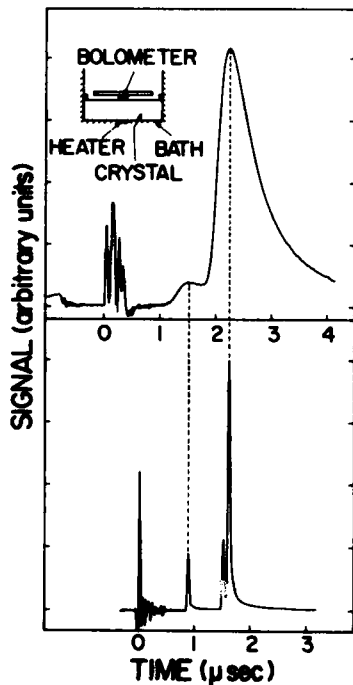


Fig. 1 : Bolometer signal vs. time.  
Top: Desorbed atoms travel ballistically to bolometer in gas.  $T = 2$  K, pulse 200 nsec, heater power 2 watts, distance to bolometer  $5.8 \times 10^{-3}$  cm. Arrival time of peaks corresponds to two phonon polarizations shifted by TOF through crystal.  
Bottom: Phonons propagating through crystal: bolometer on opposite face.  $T = 2$  K, pulse 30 nsec.

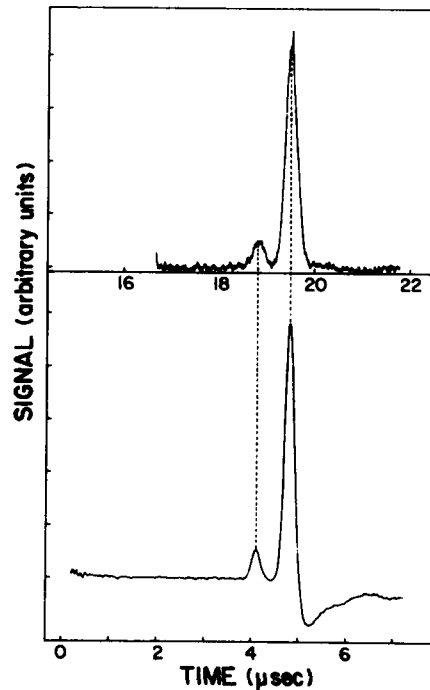


Fig. 2 : Bolometer signal vs. time.  
Top: Second sound  $T = 2$  K, pulse 250 nsec, heater power 2 watts, distance to bolometer  $2.8 \times 10^{-2}$  cm.  
Bottom: Sound in gas,  $T = 2.86$  K, pulse 100 nsec, heater power 2 watts, gas pressure 5 torr. Arrival time of peaks for sound and second sound separated by TOF difference of two phonon polarizations through crystal. Absolute times coincide with TOF through crystal and speeds of sound and second sound at temperatures indicated.

detector must be sufficiently close to the crystal to resolve the signal due to L and T phonons in spite of pulse broadening effects.

As the gas pressure in the cell is increased the desorption signal undergoes a transition to collective motion in the gas, that is, sound. Two sound peaks, generated by the L and T phonons are likewise observed (Fig. 2). Finally, when the cell is filled with bulk liquid He II two second sound pulses are observed.<sup>(1)</sup> The most striking feature of these observations is that the relative transmission coefficient of L and T phonons, as deduced from the amplitude of the two peaks, is very nearly the same for three very different modes of heat transport -- ballistic propagation in the gas, collective propagation in the gas, and collective propa-



AD-A126 574

INTERNATIONAL CONFERENCE ON PHONON PHYSICS 31 AUGUST-3  
SEPTEMBER 1981 BLOOMINGTON INDIANA(U) INDIANA UNIV AT  
BLOOMINGTON W E BRON DEC 81 ARO-17340.1-PH  
MIPR-ARO-43-80

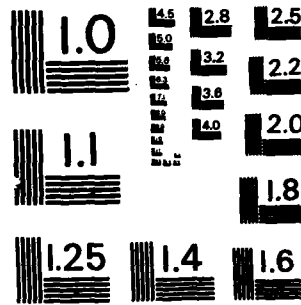
10/10

(UNCLASSIFIED)

F/G 20/2

NL

END  
DATE  
FILMED  
C 83  
DT 6



MICROCOPY RESOLUTION TEST CHART  
NATIONAL BUREAU OF STANDARDS-1963-A

gation in the liquid. Further, this ratio is roughly equal to the relative amplitude of L and T phonon pulses in the crystal. Thus the coupling of these two polarizations across the interface is approximately equal. The similarity of the L/T ratio for desorption, sound, and second sound generation suggests that the same mechanism of coupling across the interface operates in all three cases.

- References:**
1. T. J. B. Schwanenburg and J. Wolter, Phys. Rev. Lett. 31, 693 (1973).
  2. H. W. M. Salemink, H. van Kempen, and P. Wyder, Phys. Rev. Lett. 41, 1733 (1978).

## LOW FREQUENCY PHONONS IN SINTERED COPPER

B. Frisken, F. Guillon, J.P. Harrison and J.H. Page

*Physics Department, Queen's University, Kingston, Ontario, Canada, K7L 3N6*

**Abstract.** - Measurements of Young's Modulus and sound velocity of a range of sintered copper powder samples have demonstrated the existence of low frequency soft phonon modes that could explain the low temperature anomaly in the Kapitza resistance between liquid  $^3\text{He}$  and sintered metal heat exchangers below 10 mK.

**Introduction.** All measurements of the Kapitza resistance, or thermal boundary resistance, between liquid  $^3\text{He}$  and solids in the region of 1 mK have been anomalously small when compared with the predictions of acoustic theory. In addition, the measured resistances have generally been proportional to  $T^{-1}$  rather than  $T^{-3}$  as given by acoustic theory<sup>(1)</sup>. This is a low temperature effect since the acoustic theory seems to describe experimental results quite well in the 30-100 mK temperature range. Either there is an extra channel for heat flow across the boundary or there is a problem with the acoustic theory when  $T \lesssim 10$  mK. It has been argued by others that magnetic coupling is the extra channel. However, this is unlikely since the anomalous resistance is independent of magnetic field,  $^3\text{He}$  pressure, phase of the  $^3\text{He}$  (A, B or normal) or magnetic impurity content of the solid. We are instead pursuing the possibility that the usual acoustic mismatch theory is inappropriate at the lowest temperatures for the solids that have been investigated; all experiments have been made with solids that were either sintered metal powders or powdered cerium magnesium nitrate. In all cases the powder diameter ( $d$ ) was smaller than or comparable with the dominant phonon wavelength at 1 mK ( $\sim 30 \mu\text{m}$  in bulk solids). Therefore the usual Debye spectrum has a long wavelength cut-off at  $\lambda_{\text{ph}} \sim d$ , with a consequent low energy cut-off at  $E/k_B \sim \hbar v_D/k_B d$  ( $\sim 100$  mK when  $d = 1 \mu\text{m}$ ) where  $k_B$  is Boltzmann's constant and  $v_D$  is the Debye sound velocity. A consequence is that essentially no bulk phonons are excited at 1 mK. Instead there should be new normal modes associated with the powder particles as lumped masses and the necks between particles as weak springs. We present here the results of an investigation of these new modes.

**Sample Preparation.** A variety of copper and silver powder diameters, packing factors and sintering processes have been used by various groups in the past<sup>(1)</sup>. This work was done with 700 Å copper powder<sup>(2)</sup> and with a range of packing factors and sintering temperatures. The powder was first cleaned in trichloroethylene and then in

acetone (10 minutes in an ultrasonic bath). The powder was dried, placed loosely in aluminum foil boats in a furnace tube and the tube evacuated. When the pressure had dropped to  $10^{-4}$  torr the furnace was switched on and brought up to its working temperature (usually  $200^{\circ}\text{C}$ ). Then hydrogen was allowed to stream through the tube for 15 minutes at which time the furnace tube was quickly cooled. As soon as possible the pre-sintered powder was packed into a clean mold. Apart from varying the sinter temperature the sinter process was the same as the pre-sinter process described above. The final samples were in the form of 2 mm thick discs or beams 70 mm x 5 mm x 2 mm.

Method and Results. In order to investigate the low frequency modes, measurements were made of the Young's modulus (zero frequency) and the velocity of longitudinal sound (15 MHz).

(1) Young's Modulus. The sinters are quite stiff and to obtain a measurable distortion with reasonable loads the sinter was formed into long thin beams that were supported at the ends and loaded in the centre. The beams were loaded in 2 gm increments to about 40 gm and then unloaded in increments while the deformations were measured with a travelling microscope. Young's Modulus (Y) was determined from a deformation versus load plot. The results are shown in figure 1, plotted as  $Y/Y_{\text{Cu}}$  where  $Y_{\text{Cu}}$  is the Young's modulus of copper ( $12.5 \times 10^{10} \text{ Nm}^{-2}$ ).

(ii) Sound Velocity. The ultrasonic velocity was measured in the frequency range 12-20 MHz on thin disc-shaped samples. The sinters were dry polished flat and parallel using fine silicon carbide paper. The samples were then placed between two quartz delay rods and the velocity was measured from the time delay between a reflected pulse, which has travelled up and down the quartz rod only, and a transmitted pulse, which has passed through the specimen and each quartz rod. The transmitted signals were generally weak and often broad, in part due to interference effects caused by inhomogeneities in the sinters, and consequently the leading edge of the pulses was used in all measurements. To prevent bonding fluid from penetrating the pores of the sinter thin latex membranes were inserted between the sinter and the quartz rod, with a layer of Nonaq stopcock grease or glycerol between the quartz and the membrane but not between the membrane and the sinter. A measured correction of  $0.07 \mu\text{s}$  was applied for the delay in the membranes. The technique worked well for both Ag and Cu sinters over a range of packing factors  $f$ ; for a Ag sinter with  $f = 55\%$ , we obtain the velocity  $v_s = (1.73 \pm .05) \times 10^3 \text{ ms}^{-1}$  and for Cu sinters with  $f = 48\%$  and  $42\%$  we measure  $v_s = (1.6 \pm .1)$  and  $(1.2 \pm .2) \times 10^3 \text{ ms}^{-1}$  respectively. Measurements were also made on a Cu sinter of 33% filling factor, but even with the sample thickness reduced to 0.53 mm, the ultrasonic attenuation was so great that the membranes had to be removed for a transmitted signal to be observed; in this case, the bond was made with Nonaq which is sufficiently viscous to cause minimal contamination in the sinter. For this sample  $v_s = 0.75 (\pm .2) \times 10^3 \text{ ms}^{-1}$ . The results for these samples have been converted to a reduced elastic modulus  $\rho v_s^2 / (\rho v_s^2)_{\text{bulk}}$  where bulk refers to bulk copper or silver.

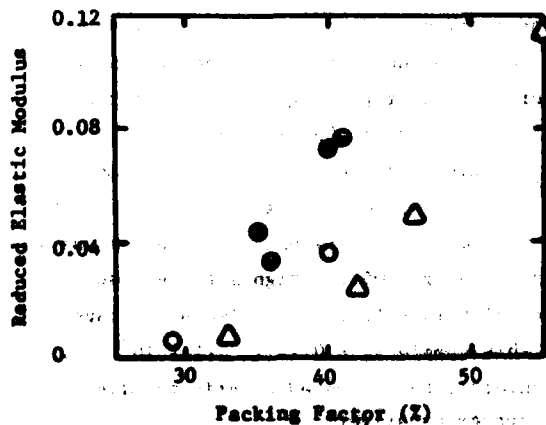
**Discussion of Results.** First of all the sinters are elastic and considerably softer than bulk copper. There is a marked, but not unexpected<sup>(3)</sup>, dependence upon packing factor. This has been confirmed in more recent work on both copper and silver<sup>(4)</sup>. The sound velocity and elastic modulus measurements are in satisfactory agreement; the agreement is better in the more recent work in which sample preparation was more consistent.

For these soft modes to be significant in heat transfer at  $\approx 10$  mK they would have to exist to  $v > 10^{-2}(k_B/h)$  or 200 MHz. Their upper limit can in fact be estimated by applying Debye theory. With  $N/V \sim 10^{18} \text{m}^{-3}$ <sup>(4)</sup> we find  $v_D \sim 500$  MHz. Therefore these modes should completely dominate the phonon spectrum below 10 mK. They are softer modes and have a density of states up by  $\sim 50$  when compared to bulk copper and it is not surprising therefore that acoustic mismatch theory with bulk copper parameters fails to agree with experimental results.

In conclusion it is emphasised that these are continuum modes of the sinter plus whatever occupies the pores (usually liquid helium). For a full understanding of heat transfer below 10 mK a study is now required of the coupling of these modes to the electron gas in the metal and to the quasiparticle excitations in the liquid  $^3\text{He}$  or  $^3\text{He}/^4\text{He}$  mixtures.

**Acknowledgements.** This work has been supported by N.S.E.R.C. and by C.R.A.D. of the D.N.D. We would like to thank John Robertson for preparing the samples used for the sound velocity measurements and Christian Frénois for assistance with some of the velocity measurements.

1. Detailed references are given in the review article: J.P. Harrison, J. Low Temp. Phys. **37**, 467 (1979).
2. Ul-Vac Vacuum Metallurgical Co. Ltd., Tokyo, Japan.
3. David Wood (private communication), E. Domany, J.A. Gubernatis and J.A. Krumhansl, Journal of Geophysical Research **80**, 485 (1975).
4. J. Robertson, F. Guillon and J.P. Harrison (to be published).



**Figure 1.** Circles are the beam bending results with sintering temperatures as follows:

Open circles, 175°C  
Half-open circles, 200°C  
Closed circles, 225°C.

Triangles are the sound velocity results with a sintering temperature of 200°C. The 55% result is for silver.

**PHONON ECHOES**

## PHONON ECHOES IN BULK AND POWDERED MATERIALS

K. Kajimura

*Electrotechnical Laboratory, Sakura-mura, Ibaraki 305, Japan*

**Abstract.**— Experimental and theoretical studies of phonon echoes in bulk and powdered materials are reviewed. Phonon echoes have been observed in many materials such as bulk piezoelectric crystals, paramagnets, glasses, doped semiconductors, and piezoelectric, magnetic, and metallic powders, etc. The echoes arise from a time reversal of the phase, like spin echoes, of a primary pulsed acoustic excitation due to a second acoustic or rf pulse. The phase reversal occurs through the nonlinear interactions of acoustic oscillations with either themselves or electromagnetic fields. The diversing phonon echo phenomena can be classified into two general classes depending on the type of nonlinear mechanism responsible for echo formation: In parametric "field-mode" interaction systems the applied rf field of the second pulse interacts with the modes excited by the primary pulse to cause phase reversal. The echo amplitude of this class decreases monotonously with the time separation of applied two pulses,  $\tau$ . Backward and forward propagating wave echoes in bulk materials belong to this class. In "anharmonic oscillator" systems different oscillation modes nonlinearly couple to one another to cause subsequent echo formation. The echo amplitude initially increases with  $\tau$  and takes a maximum before decreasing exponentially for large  $\tau$ . Only the powder echoes are in this class. In addition to these dynamic echo phenomena there are quasistatic three-pulse echoes in which phases are stored for days and years, phenomena being applicable to mass storage devices. The essential physics of phonon echo phenomena seems to be well understood although precise quantitative descriptions of each phenomenon are still required. The phonon echo studies are now being applied to a tool for physics and to technology.



## STATIC POLARIZATION ECHOES IN METAL POWDERS

F. Tsuruoka\* and K. Kajimura

*Electrotechnical Laboratory, Sakura-mura, Ibaraki 305, Japan*

**Abstract.**— Static polarization echoes with long time storage in metal powders placed in steady magnetic field have been studied. The echo amplitudes were found to be unstable when the surrounding He gas pressures were less than 10 Pa, whereas they were stabilized by introducing a small amount of He gas of  $\geq 100$  Pa at 4.2 K. The phenomenon can be understood if the process involves the macroscopic reorientation of individual particles and if the mechanical rotation of the individual particles is stabilized by the increase in inter-particle friction due to the presence of He gas molecules on the particles. A particular base axis of the rotation is proposed to be specified by an anisotropic magnetic dipole caused by electric currents associated with the mechanical oscillation of particles.

1. **Introduction.**— In powder samples consisting of a large number of particles ( $>10^5$ ) of piezoelectric, magnetoelastic, normal metallic, and superconducting materials, two-pulse polarization echoes occur at  $t = \tau$  ( $m=2,3,4,\dots$ ) and stimulated three-pulse echoes at  $t = p\tau + r\tau$  ( $p,r=1,2,3,\dots$ ) following applied rf pulses at times  $t=0$ ,  $\tau$ , and  $T > \tau$ . The primary pulse at  $t=0$  excites resonant acoustic oscillations in the particles. Only the powder particles having sizes of an order of the acoustic wavelength excited in the particles are responsible for the echo formation. Powder echoes are separated into two general types. Dynamic echoes<sup>1</sup> have relaxation times  $T_2$  associated with acoustic oscillations of the particles. The relaxation time  $T_2$  coincides with the decay time of free oscillation of the constituting particles. Static or memory echoes<sup>2</sup> are those for which the relaxation time  $T_1$  of the stimulated three-pulse echo at  $t=T+\tau$  exceeds the lifetime of any dynamic process. The static polarization echoes were observed in powders of piezoelectric,<sup>2</sup> ferromagnetic,<sup>3</sup> and normal metallic materials.<sup>4</sup> The echo formation mechanism and long time storage proposed by Melcher and Shiren<sup>2</sup> for piezoelectric powders assume mechanical reorientation of particles caused by the torque exerted on an oscillating dipole by an external rf pulse. This model, referred to as the torque-rotation model, has been successful in explaining the properties of the static echoes in piezoelectric powders.<sup>5</sup> The model is readily applicable to the static echoes of magnetoelastic powders in which the magnetostrictive axis behaves as a base axis for an oscillating dipole. In metal powders, however, it has not been clear so far that what types of information are stored in the individual particles. In this paper we report experimental results on the static polarization echoes of metal powders of Al, Sn, and Nb and of type II

\*Permanent address : Faculty of Science, Tokyo Institute of Technology, Oh-okayama, Meguro-ku, Tokyo 152, Japan

superconducting powder of  $V_3Si$  which suggest mechanical reorientation of individual particles. We also propose that a particular base axis for the torque rotation can be specified by the anisotropic magnetic dipole caused by the electric current associated with the acoustic oscillations of the particles.

2. Experimental results.— A detailed description of experimental procedure and results were published in Refs. 6 and 7. We summarize only the essential experimental result indicating the macroscopic reorientation of metal particles in the following: (i) The echo amplitude took a maximum when the resonance condition was met for the acoustic vibration of individual particles. (ii) Integration of the static echo amplitude,  $e_3$ , to its maximum value by repetitive application of a two-pulse sequence with the relative phase strictly fixed was required to observe  $e_3$  with reasonable signal to noise ratio under He-gas pressures  $> 100$  Pa. (iii) In a vacuum of  $10^{-4}$  Pa  $e_3$  was not detected even for repetitive application of a two-pulse sequence. Under He gas pressures less than 10 Pa  $e_3$  was unstable in a sense that the integration by the two-pulse sequence and the destruction by the third-pulse sequence occurred irregularly in time. Actually, when a third probing pulse was applied after turning off the repetitive two-pulse sequence,  $e_3$  died out immediately. Above 100 Pa integration of  $e_3$  to its saturation was observed although the integration rate was very low. The storage was able to be read out nondestructively by the third-pulse sequence after turning off the two-pulse sequence and erased only when the surrounding gas pressure was reduced and an rf pulse was applied.

3. Discussion.— In the presence of surrounding gases the oscillation energy is transferred from a particle to them through its surface and consequently the oscillation amplitude is damped as has been investigated in the study of dynamic echoes.<sup>1,6</sup> When the surrounding gas is pumped out to a vacuum, the oscillation amplitude becomes large enough for particles jumping around their unstable sitting positions, resulting in irreversible disturbance of the stored pattern. When He gas is introduced, both the damping of oscillation,  $\Gamma$ , and the interparticle friction against the mechanical rotation,  $\Gamma_a$ , in the torque-rotation model increase. The measured increase in  $\Gamma$  was at most 50 % when the He pressure was increased from  $10^{-4}$  to  $10^5$  Pa.<sup>6</sup> The striking effect of the presence of surrounding gases on the static echoes comes from the sudden increase in  $\Gamma_a$ , which prevents the irreversible disturbances of the stored pattern. In fact the integration rate became much lower than that expected from only the increase in  $\Gamma$ . It is noted that the effect of surrounding gases takes place outside the metal powders but not inside the particles similar in nature to holographic processes<sup>8</sup> or dislocation motions.<sup>9</sup>

We propose that the anisotropic dipole moment is caused by the electric current flowing around the metal surface associated with mechanical oscillation of individual particles along the direction to which the resonance condition is met. The base axis of the magnetic dipole for the mechanical rotation, therefore, originates from the geometric and elastic anisotropy of irregularly shaped powder particles. The

mechanical oscillation is excited by Lorentz force acting on conduction electrons and positive ions due to the rf and steady magnetic field as was investigated earlier by Meredith et al.<sup>10</sup> This mechanism was applied to powders by the present authors.<sup>6</sup> An electric current is induced at the surface of an oscillating particle placed in the steady magnetic field due to the acoustoelectromagnetic response of electrons and ions in the direction normal to both the surface and the direction of projection of the rf magnetic field on the metal surface. The induced current then causes a magnetic dipole moment along the latter direction. The theoretical calculation based on the torque-rotation model<sup>1</sup> with the above mentioned dipole moment gives a result in satisfactory agreement with the experimental results on the dependences of the static echo amplitude,  $e_3$ , on the rf pulse amplitudes and the strength of the steady magnetic field.<sup>7</sup>

In conclusion we found that surrounding He gas strongly affected the stability of the static echoes at 4.2 K. Based on this experiment we conclude that the static echoes in metal powders are understood by the torque-rotation model in which the base axis for rotation is specified to be along the anisotropic dipole moment caused by the electric current associated with the mechanical vibration of individual particles.

The authors would like to acknowledge Professor T. Fukase for his supply with  $V_3Si$  samples. One of the authors (FT) is gratefully indebted to Dr. T. Ishiguro and Professor Y. Hiki for their giving him an opportunity to stay at Electrotechnical Laboratory.

#### References.-

1. K. Fossheim, K. Kajimura, T.G. Kazyaka, R.L. Melcher, and N.S. Shiren, Phys. Rev. B **17** 964 (1978) and references quoted therein.
2. R.L. Melcher and N.S. Shiren, Phys. Rev. Lett. **36**, 888 (1976) and references therein.
3. R.L. Melcher and N.S. Shiren, Phys. Lett. **57A**, 377 (1976) and references therein.
4. S. Kupca, I. Maertense, H.P. Kunkel, and C.W. Searle, Appl. Phys. Lett. **29**, 224 (1976).
5. K. Fossheim, K. Kajimura, and R.L. Melcher, Solid State Commun. **27**, 753 (1978).
6. F. Tsuruoka and K. Kajimura, Phys. Rev. B **22**, 5092 (1980).
7. F. Tsuruoka and K. Kajimura, Appl. Phys. Lett. **38**, 1025 (1981).
8. N.S. Shiren and R.L. Melcher, 1974 Ultrasonics Symposium Proceedings, IEEE Catalogue No. 74 CHO 896-1au (IEEE, New York, 1974), p.556.
9. Ya.Ya. Asadullin, Phys. Lett. **79A** 115 (1980).
10. D.J. Meredith, R.J. Watts-Tobin, and E.R. Dobbs, J. Acoust. Soc. Am. **45**, 1393 (1969).

## ECHO PROPERTIES OF BGO AND CdS

J.O. Fossum, H.J. Aune, K. Fosheim and R.M. Holt

*The Norwegian Institute of Technology, 7034 Trondheim-NTH, Norway*

**Abstract.**— A brief discussion is given of the theory of echo generation in insulators and semiconductors. For semiconductors it is shown that  $\omega, 2\omega$  echo generation may occur without dc-field present. In this case the echo amplitude is directly proportional to the electronic conductivity and the applied fields. Experiments in CdS support the predictions. From measurements on BGO it is concluded that interactions with vacancies which is responsible for strong acoustic attenuation at low temperatures, does not contribute in the echo generation.

1. **Introduction.**— Wavevector reversed phonon echoes have recently been used as a powerful tool in studying phase transitions<sup>1,2</sup>. The present work is aimed at a further mapping of echo properties of single crystals in order to find proper materials for such use. In addition it is of great interest to attain an improved understanding of the origin of the echo mechanism itself. For a more general discussion of phonon echoes we refer to a forthcoming review<sup>3</sup>.

2. **Theory.**— Starting from a free energy expansion in strain  $S$  and electric field  $E$ , and applying Poisson's equation, Newton's 2nd law (in one dimension) can be written:

$$\rho \frac{\partial^2 u}{\partial t^2} - c_0 \frac{\partial^2 u}{\partial z^2} = c_1 E S + c_2 E^2 S + \frac{eQ}{\epsilon} n_s (1 + \kappa E + \dots) + \dots \quad (1)$$

where  $u$  is the mechanical displacement,  $\rho$  is the mass density,  $c_0$  is the piezoelectrically stiffened elastical constant,  $c_1$ ,  $c_2$  and  $\kappa$  are functions of various electroacoustic coupling constants,  $e$  is the piezoelectric constant,  $Q$  is the elementary charge,  $\epsilon$  the dielectric constant and  $n_s$  denotes the space charge density.

In insulating dielectrics  $n_s = 0$ . A term associated with an electroacoustic nonlinearity  $c_n$  in this case gives rise to an  $\omega, 2\omega/n$  echo ( $n$  is an integer). This means that a forward propagating strain wave of frequency  $\omega$ ,  $S_f \sim S_0 \cos(\omega t - kz)$  is mixed with an electric field of frequency  $2\omega/n$  i.e.  $E^n \sim E_0^n \cos^n \frac{2\omega}{n} t$ , to produce a backward wave echo

$$S_b \sim S_0 E_0^n \sin(\omega t + kz) \quad (2)$$

In centrosymmetric crystals all odd numbered constants  $c_{2n+1}$  vanish, so the lowest order echo will be an  $\omega, \omega$  echo. Otherwise,  $\omega, 2\omega$  echoes are of lowest order.

In semiconductors  $n_s \neq 0$ . In addition to the mechanism discussed above, the last terms in (1) now provide sources for echo generation. As explained by Melcher and Shiren<sup>4</sup>,  $n_s$  will contain a backward wave component if the applied strain and field have the same frequency  $(\omega, \omega)$ . They found that  $\omega, \omega$  echoes as well as  $\omega, \omega/n$  echoes may originate from the term  $\frac{eQ}{\epsilon} n_s$  in (1). This term can not give rise to for instance  $\omega, 2\omega$  echoes except with application of a dc-field. We find, however, that unbiased  $\omega, 2\omega$  echo generation may occur from the term  $\frac{eQ}{\epsilon} n_s \kappa E$ . From the equation of charge continuity and the expression for the current density,  $n_s$  is found to contain a term proportional to  $\sigma_0 S_0 \cos(\omega t - kz)$ .  $\sigma_0$  is the static electronic conductivity. Making  $n_s$  with  $E$ , a backward echo is formed:

$$S_b = \sigma_0 S_0 E_0 \sin(\omega t + kz).$$

$\sigma_0$  generally depends on illumination, temperature and possibly on field amplitudes  $S_0$  and  $E_0$ , as well as pulse widths and repetition rate.

When  $n_s = 0$ , storage echo phenomena may also occur<sup>5</sup>.

3. Echoes in BGO ( $\text{Bi}_{12}\text{GeO}_{20}$ ). In the present work,  $\omega, 2\omega$  echoes have been observed in BGO with several modes of sound propagation in broad ranges of frequency and temperature.

The echo amplitude dependence on strain and electric field has proved to be bilinear, as expected from Eq. (2). No saturation effects are seen.

With pulsed fields the resulting echo is shown experimentally to be the convolved product of the input pulses, with the time scaled by a factor two for the second (E) pulse.

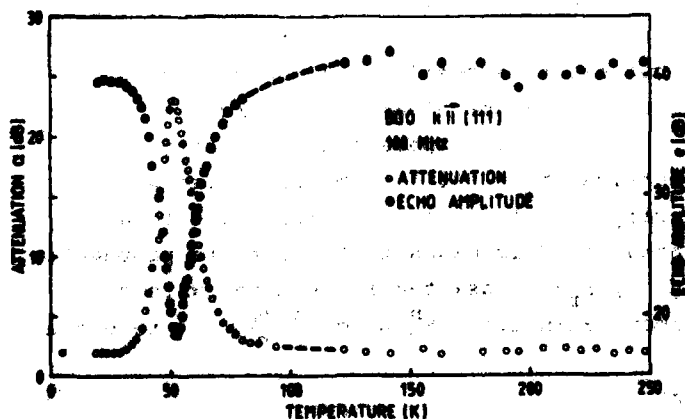


Fig. 1 : Echo and attenuation vs. temperature in BGO. From Ref. 3.

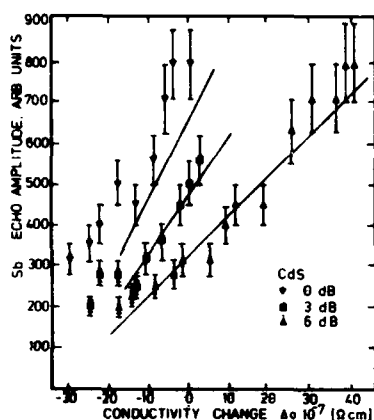


Fig.2 :  $\omega, 2\omega$  echo amplitude in CdS at room temperature versus electronic conductivity for various  $2\omega$  fields. The fully drawn lines are predicted from Eq.(3).

The temperature dependence of the echo at 100 MHz is given in Fig.1. The reduction in measured echo amplitude near 55 K is completely attributed to the increased absorption in this temperature region<sup>6</sup>. Hence vacancy diffusion in the Ge sublattice, which is responsible for

the attenuation peak, does not have any influence on the formation of phonon echoes.

**4. Echoes in CdS.**— Measurements are performed with 4 different CdS-crystals of high dark resistivity ( $10^8$ – $10^{10} \Omega \text{ cm}$ ), supplied from 3 different sources. All these crystals show strong unbiased  $\omega, 2\omega$  echoes, and also  $\omega, \omega$  echoes at room temperature.

The  $\omega, 2\omega$  echo amplitude is found to be proportional to the electronic conductivity, in agreement with the prediction in Eq.(3). This is illustrated in Fig.2, where the conductivity is changed by continuously varying the voltage of a white light lamp. The relative change in conductivity,  $\Delta\sigma$ , is measured by detecting the change in ultrasonic attenuation,  $\Delta\alpha$ . In all our CdS-crystals, the attenuation increases with increasing conductivity. Theory<sup>7</sup> predicts:

$$\Delta\alpha = \frac{K^2}{2\varepsilon v_s} \Delta\sigma \quad (4)$$

where  $K^2$  is the electromechanical coupling constant and  $v_s$  is the sound velocity. The deviation from the predicted line for maximum field (0dB) is due to field-dependent photoconductivity for this crystal.

For two of the crystals the photoconductivity and accordingly the echo amplitude is seen to depend nonlinearly on excitation field amplitudes and pulse widths as well as the rf-repetition rate.

#### References.

1. K. Fossheim and R.M. Holt, Phys.Rev.Letters **45**, 730 (1980).
2. R.M. Holt and K. Fossheim, Ferroelectrics **25**, 515 (1980).
3. K. Fossheim and R.M. Holt, Physical Acoustics Vol. XVI (in press).
4. R.L. Melcher and N.S. Shiren, Phys.Rev.Letters **34**, 731 (1975).
5. R.L. Melcher and N.S. Shiren, Ultrasonic Symposium Proceedings, IEEE 74CHO, 896 - 15V, 557 and 572 (1974).
6. W. Rehwald, J.Appl.Phys. **44**, 3017 (1973).
7. A.R. Hutson and D.L. White, J.Appl.Phys. **33**, 40 (1962).

BACKWARD WAVE PHONON ECHOES AT 17 GHz IN SINGLE CRYSTALS OF  $\text{LiTaO}_3$ ,  $\text{LiNbO}_3$  AND  $\text{Bi}_{12}\text{SiO}_{20}$ 

D.J. Meredith, J.A. Pritchard and J.K. Wigmore

University of Lancaster, U.K.

**Abstract.**— From measurements of the power and time dependence of  $\omega$ - $\omega$  2 pulse echoes at 17 GHz, we inferred that, at low powers, an intrinsic non-linearity  $\gamma s^2 E^2$  was responsible for their generation in  $\text{LiTaO}_3$  and  $\text{LiNbO}_3$ . However, this model could not explain either the high power data in these materials, or any of the results in  $\text{Bi}_{12}\text{SiO}_{20}$ .

It is now well established that there are several different microscopic mechanisms which are all capable of producing phonon echoes, depending on the nature of the material and the form of the specimen. Thus, it has been suggested that, in macroscopic single crystals of non-centrosymmetric materials, the non-linearity responsible for backward wave phonon echoes could be an intrinsic feature of the crystal lattice potential<sup>1</sup>, or it could be due to defect centres that are strongly coupled to the phonons<sup>2</sup>. In an attempt to understand both the details of these mechanisms and the conditions under which they might be important, we have been studying  $\omega$ - $\omega$  backward wave echoes in lithium tantalate ( $\text{LiTaO}_3$ ), lithium niobate ( $\text{LiNbO}_3$ ) and bismuth silicon oxide ( $\text{Bi}_{12}\text{SiO}_{20}$ ).

In the intrinsic theory of the origin of such echoes<sup>1</sup>, phonons and photons, both at the same angular frequency,  $\omega$ , are coupled through the term  $\gamma s^2 E^2$  in the expansion of the crystal free energy as powers of strain,  $s$ , and electric field,  $E$ . The intensity,  $I_e$ , of the echo is found to be proportional to  $\gamma^2 \omega^2 I_u I_m^2$ , where  $\gamma$  is the coupling parameter,  $I_u$  the intensity of the forward travelling ultrasonic wave, and  $I_m$  the intensity of the (microwave) photon pulse. Bajak<sup>3</sup> later showed that this type of  $\omega$ - $\omega$  phonon echo is a special case of the more general interaction involving 2 phonons and  $N$  photons, coupled weakly through a non-linearity of the pure crystal lattice.

By contrast, Shiren et al<sup>2</sup> suggested that the presence in the crystal of strongly coupled impurities might give rise to non-linear dispersion and absorption which could be equally effective in coupling phonons and photons. The dependence of the echo intensity on  $I_u$  and  $I_m$  would not be the simple form predicted by Fedders and Lu, but would be a complicated expression depending on the precise characteristics of the defect. In addition, a three-pulse, or "storage" echo, might be observed.

In our experiments the specimen was contained wholly within the microwave cavity, which was immersed directly in liquid helium at 1.25 K to minimise acoustic attenuation in the sample. The two exciting pulses had lengths typically of 200 nsec and a separation of 1-10  $\mu\text{sec}$ . Microwave powers up to 1 kW could be obtained from a

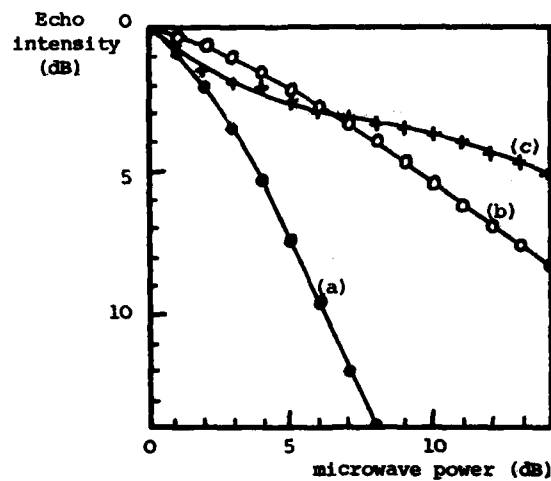


Figure 1. Dependence of the echo intensity on the power of the exciting pulses, (a) LiTaO<sub>3</sub> (P<sub>2</sub>), (b) LiNbO<sub>3</sub> (P<sub>1</sub>), (c) Bi<sub>12</sub>SiO<sub>20</sub> (P<sub>2</sub>).

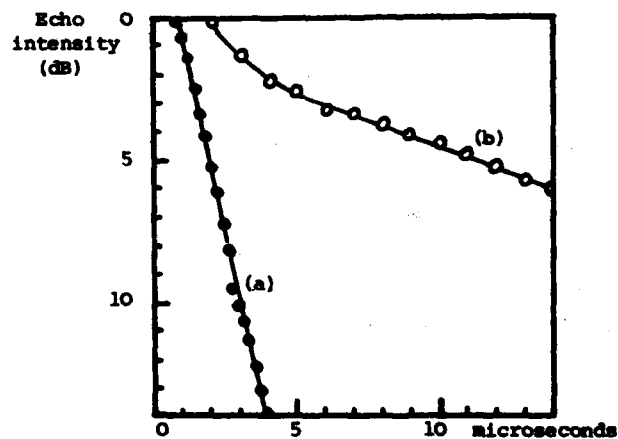


Figure 2. Dependence of the echo intensity on the time separation of the two exciting pulses, (a) LiTaO<sub>3</sub>, (b) Bi<sub>12</sub>SiO<sub>20</sub>.



Litton 624 travelling wave tube amplifier, and a second, low noise TWTA (MO valve TWJ30) preamplified the echo before its detection with a self oscillating Gunn diode mixer.

The intensity of the echo was measured as a function of the power levels of the two exciting pulses, which determined  $I_u$  and  $I_m$ . Typical results are shown in figure 1. At low powers and with exciting pulses no longer than about 200 nsec,  $\text{LiTaO}_3$  fitted the intrinsic model very well. Below a slight flattening at high powers, the dependence on  $I_m$  was closely quadratic, and that on  $I_u$  (not shown) linear. In addition, the pulse shape of the echo was the predicted trapezoid. We estimated the coupling constant  $\gamma$  to be about  $10^{-8} \text{ F m}^{-1}$ ; more details are published elsewhere.<sup>4</sup>

$\text{LiNbO}_3$  behaved similarly, but with a considerably broader region of curvature. Indeed, the dependence of  $I_e$  on  $I_u$  hardly reached the linear regime in the range of powers that were accessible (figure 1). The origin of the curvature is not understood since such power levels should still be in the small signal limit considered by Fedders and Lu. It is possible that some additional channel which couples  $\omega$  photons and  $\omega$  phonons and removes energy from the  $\omega$  echo, could exist within Bajak's model.

The echo obtained in  $\text{Bi}_{12}\text{SiO}_{20}$  had a totally different power dependence (figure 1) which could not be fitted to any simple functional form. The dependence of the echo on the pulse separation also showed anomalous behaviour (figure 2). Unlike those for  $\text{LiTaO}_3$  and  $\text{LiNbO}_3$ , the curve did not fit a single exponential but appeared to consist of a rapid decay superimposed on a much more gradual slope. Since, even qualitatively,  $\text{Bi}_{12}\text{SiO}_{20}$  behaves in so different a manner to  $\text{LiTaO}_3$  and  $\text{LiNbO}_3$ , it is tempting to suggest that our sample is behaving extrinsically. However, no 3 pulse echo has yet been observed.

We are grateful to the Science Research Council (London) for support.

1. P.A.Fedders and E.Y.C.Lu, App.Phys.Letters 23 502 (1973)
2. N.S.Shiren, W.Arnold, and T.G.Kazyaka, Phys.Rev.Letters 39 239 (1977)
3. I.L.Bajak, Phys.Rev.B18 2405 (1978)
4. D.J.Meredith, J.A.Pritchard and J.K.Wigmore (to be published)

## DIPOLAR FIELD FLUCTUATION EFFECTS ON PHONON ECHOES IN PIEZOELECTRIC POWDER

S. Yoshikawa and T. Kimura\*

*Technological Univ. of Nagaoka, Nagaoka, Niigata, Japan**\*Musashino Electrical Comm. Lab., N.T.T., Musashino, Tokyo, Japan*

**ABSTRACT:** One-shot phonon echo in piezoelectric powder was studied in order to simplify the experimental condition and clarify the basic mechanism on this phenomenon. One-shot phonon echo is observed by the application of the single sequence of the incident electric pulses. The one-shot two-pulse echo was observed to have relaxation characteristics with the function of  $\exp(-\alpha\tau^2)$ . The dynamic relaxation is clarified to originate in the effect of the local field fluctuation in a large number of the oscillating piezoelectric particles.

1. **EXPERIMENTS.** -  $\text{LiNbO}_3$  and  $\text{LiTaO}_3$  powder with 74-88  $\mu\text{m}$  center grain size was dehumidified at 250°C, enclosed into 0.1 Pa ( $10^{-5}$  Torr) glass tubes with a diameter 15 mm. The number of particles were about  $10^7$ . The echo signal measurements were made by using a transient recorder, which can sample a real time signal at a rate of 8 bits/0.2  $\mu\text{s}$ , and carries out the one-shot echo observation. The relation between the incident two-pulse separation and the observed two-pulse echo height  $e_2$  was studied. Furthermore, the relation was measured as a function of the driving frequency. The three-pulse echo characteristics were also measured in the one-shot experiment.

2. **RESULTS.** - The measured relation between  $\tau$  and  $e_2$  is shown in Fig.1. This result indicates that the observed relation is expressed as  $e_2 \propto \exp(-\alpha\tau^2)$ . Coefficient  $\alpha$  changes as the driving frequency  $f$  changes. The relation between  $\alpha$  and  $f$  is shown in Fig.2. Figure 2 indicates that  $\alpha \propto f^2$ . On the contrary, three-pulse echo  $e_3$  characteristics are quite different from those for  $e_2$ . The one-shot experimental results are shown in Fig.3. Figure 3 indicates that the decay of  $e_3$  does not depend on the driving frequency. It also suggests that the one-shot phonon echo has long life time, as has been observed in the ordinary experiment. Further, the mechanism for the decay behavior in the one-shot two-pulse echoes originates in the quite different mechanism from that for  $e_3$ .

3. **DIPOLAR FIELD FLUCTUATION MECHANISM.** - The two-pulse echo decay with the function of  $\exp(-\alpha\tau^2)$ , where  $\alpha \propto f^2$ , suggests that the phonon echo in piezoelectric powder possibly has a similar mechanism to that of spin echo<sup>1</sup>.

In the present study, a dipolar field fluctuation mechanism is assumed and developed on the basis of the torque rotation<sup>2</sup> and the dipolar field<sup>3</sup> models.

For the particle with resonant frequency  $\Omega$ , the angle  $\theta$  between the incident pulse field and the induced dipolar orientation is given by the following dynamic equation<sup>3</sup>.

$$\ddot{\theta} + \Gamma \dot{\theta} = \frac{1}{I} F(t, \Omega) \sin \theta \cos \theta \\ = \frac{1}{I} F(t, \Omega) (\sin \theta_0 \cos \theta_0 + \theta \cos 2\theta_0) \quad (1)$$

where  $F(t, \Omega)$  is the force associated with the induced dipole oscillation, and  $\theta_0$  is the initial orientation. It is considered that the second force is small because, through the one-shot experiment within the interval in the order of  $\tau$ , displacement  $\theta$  is not expected to reach a value which definitely changes the orientation of the induced dipolar field. Furthermore, the force is not always known to excite the particle positively, together with the local dipolar field, because any values of the initial orientation  $\theta_0$  may be possible in powder system. Therefore, the second excitation is assumed to be stationary Gaussian or a kind of noise. According to this assumption, the displacement  $\theta$  is divided into two components,  $\theta_f$  and  $\delta\theta$ . They are derived from the first and the second forces given in Eq.1. Component  $\delta\theta$  is defined to be the fluctuated angle caused by the noise. Fluctuated angle  $\delta\theta$  is assumed to be independent on  $\theta_f$  and a random variable. These two variables,  $\delta\theta$  and  $\dot{\delta\theta}$ , are assumed to be independent from time. The fluctuating effect also induces the fluctuation  $\dot{\delta\theta}$  on the angular momentum. This process is a Markoff process. The conditional probability density is given by<sup>4</sup>:

$$P(\delta\theta, \dot{\delta\theta}) = C \exp \left\{ -\frac{2}{I^2 W} (\dot{\delta\theta}^2 + \frac{\delta\theta^2}{I} F(t, \Omega) \cos 2\theta_0) \right\} \quad (2)$$

where  $C$  is the coefficient, and  $W$  is the noise power. From fluctuation for the angular momentum, the expected dipolar field strength is derived as follows.

$$\langle P_z(\Omega, \theta, t) \rangle_{\delta\theta, \dot{\delta\theta}} \sim C \sqrt{\frac{1}{I^2 W}} \exp \left( -\frac{1}{I^2 W} t^2 - \frac{t}{T_2} \right) \sin 2\Omega t \\ \times \text{other term dependent on } \Omega \text{ and } \theta_0. \quad (3)$$

If  $1/I^2 W \gg 1/T_2$ , where  $T_2$  is the intrinsic relaxation constant, is satisfied in  $\text{LiNbO}_3$  and  $\text{LiTaO}_3$  powder, decay with function  $\exp(-t^2/I^2 W)$  is realized. Therefore, coefficient  $\alpha$ , observed in the present experiment, can be defined to be  $\alpha = 1/I^2 W$ . This theoretical result further explains the dependence of  $\alpha$  on driving frequency  $f$ . The relevant moment of inertia  $I$  is given by  $I \sim \rho d^2$ , where  $\rho$  is the averaged grain density and  $d$  is the diameter. The piezoelectric resonant condition has been observed to be  $f \sim 1/d$ , as reported in Ref.5. The observed relation of  $\alpha \sim f^2$  is explicitly explained by these physical relations.

In summary, it is concluded that a large number of dipoles, which are caused by induced piezoelectric oscillation, should be considered in the light of dipolar field fluctuation. The effect like this short time fluctuation mechanism is further expected to explain the real complicated phenomena on phonon echoes in piezoelectric powder.

1. P.Hu and S.R.Hartmann, Phys. Rev. **B9**, 1 (1974)
2. R.L.Melcher and N.S.Shiren, Phys. Rev. Lett., **36**, 888 (1976)
3. T.Kimura and S.Yoshikawa, J. Appl. Phys., **51**, 2817 (1980)
4. T.K.Caughey, J. of Acoust. Soc. of Amer., **35**, 1683 (1963)
5. N.S.Shiren and R.L.Melcher, 1975 IEEE Proc.SU Symp., 572 (1975)

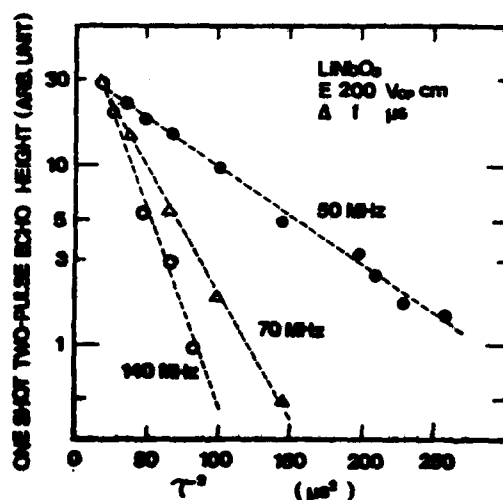


Fig. 1 Relation between one-shot two-pulse echo  $e_2$  and pulse separation  $\tau$ .

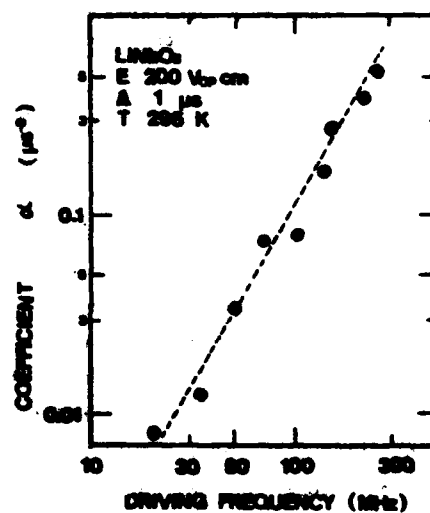


Fig. 2 Relaxation coefficient dependence on driving frequency.

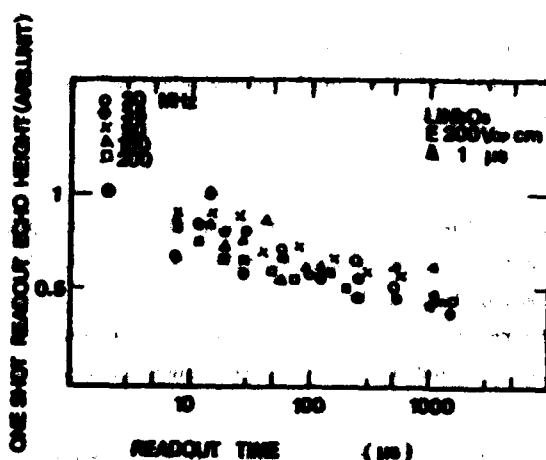


Fig. 3. One-shot three-pulse echo relaxation

ATTENUATION OF A STATIC POLARIZATION ECHO BY  $^4\text{He}$  FILMM. Poirier<sup>++</sup>, J.D.N. Cheeke<sup>\*</sup>, P. Morisseau<sup>\*</sup> and A. Hikata<sup>\*\*</sup><sup>\*</sup>Département de Physique, Université de Sherbrooke, Sherbrooke, Prov. Québec, Canada, J1K 2R1<sup>\*\*</sup>Brown's University, Providence, R.I., U.S.A.

**Abstract.** - We have measured by the phonon echo technique the attenuation of an adsorbed  $^4\text{He}$  film on silica powder against pressure at 35 MHz and low temperatures. The attenuation curves present the typical shape of a multilayer adsorption isotherm of type II according to the BET classification. Because of relatively high RF power no onset of superfluidity has been observed in these films. The attenuation decreases with temperature following the normal viscosity and thermal conductivity contributions to the ultrasonic absorption by  $^4\text{He}$ .

1. **Experiment.** -  $\text{SiO}_2$  powder ( $\phi \sim 70 \mu\text{m}$ ) is introduced in a copper capacitive cell to which we apply a sequence of three RF pulses ( $f \sim 35 \text{ MHz}$ ) supplied by a Matec 6600 pulse modulator and receiver. The first two pulses (15  $\mu\text{sec}$  separation time and 2  $\mu\text{sec}$  width) produce the dynamic polarization echo  $e_2$  and the third pulse, the static polarization (or memory) echo  $e_3$  when it is applied a long time after the first two<sup>1</sup>. Because of stability the memory echo has been chosen for monitoring the attenuation produced by an adsorbed  $^4\text{He}$  film on the individual particles. The film is built up when  $^4\text{He}$  gas is admitted in the capacitive cell. The attenuation is measured by a Matec attenuation recorder as a function of the cell gas pressure for different temperatures.

The adsorption isotherm measurement is done with 13 g of  $\text{SiO}_2$  powder in a Copper cell of 11  $\text{cm}^3$  volume. By admitting precise amounts of  $^4\text{He}$  gas, the volume adsorbed by the powder is obtained by measuring the pressure variation in the cell. The adsorption isotherm is obtained by plotting the total volume adsorbed as a function of the cell equilibrium pressure which takes a few minutes (3 - 5) to establish for both measurements.

2. **Results.** - The attenuation curves obtained for different temperatures are presented in Figure 1. They are the result of an adsorbed  $^4\text{He}$  film on the individual particles and not an effect of gas loading losses which would give a linear variation with pressure<sup>2</sup>. In Figure 1, there is first a rapid increase of attenuation for  $p/p_0 < 0.1$ , then a flattening up to 0.7 and a rapid increase when saturation pressure is approached.

An example of an adsorption isotherm of  $^4\text{He}$  on the same powder is shown in

<sup>+</sup> Permanent address : Conseil National de Recherche du Canada, IGM, 750 rue Bel-Air, Montreal, Prov. Québec, Canada, H4C 2K3

Figure 2. Because of small specific surface of adsorbant, residual gas effects contribute to the adsorbed volume especially at low pressures and high temperatures.

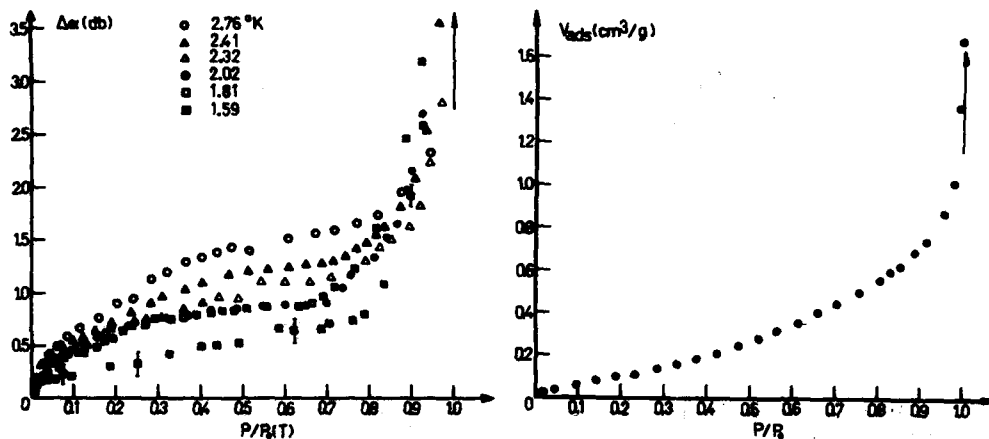


Fig. 1: Attenuation variation of memory echo versus relative cell pressure of  $^4\text{He}$ . Fig. 2: Adsorption isotherm of  $^4\text{He}$ : adsorbed volume at STP per g of adsorbent.

3. Discussion. - By comparing attenuation and adsorption isotherm results we conclude that we are really measuring the attenuation produced by the adsorbed  $^4\text{He}$  film on the individual particles. According to the classification of adsorption isotherms of BET<sup>3</sup> our results show evidence of multilayer adsorption. There is first at  $p/p_0 < 0.1$  completion of the first (or two) monolayer compressed in the van der Waals field of the substrate which gives a rapid increase of attenuation and also volume adsorbed. Up to  $p/p_0 \sim 0.7$  the completion of the first normal monolayer proceeds showing a flattening and for  $p/p_0 > 0.7$  multilayer formation is going on with a fast increase in attenuation and volume adsorbed. At saturation pressure, liquefaction occurs: attenuation is maximum and volume adsorbed goes to  $\infty$ . According to the slab theory of FHH<sup>4</sup> the volume adsorbed should be a linear function (slope - 1/3) of  $\ln(p_0/p)$  on a log-log scale when multilayer formation proceeds. One may verify that it is indeed the case by looking at Figures 3 and 4 where such plots have been done for both sets of results. The data align fairly well along the line - 1/3 with a slower approach for adsorbed volume because of gas effects at low pressures.

In Figure 1, the attenuation decreases with temperature which is the usual variation associated with the normal viscosity and thermal conductivity contributions to the ultrasonic absorption<sup>5</sup>. No onset of superfluidity is observed in these films because too much RF power is needed in phonon echo experiment. In figure 2 adsorbed volume is not only a film effect but there is a contribution from residual gas which will be discussed in a later paper.

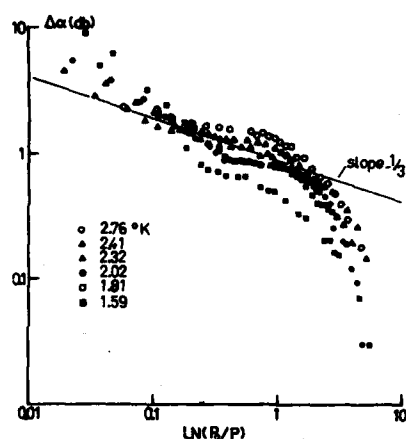


Fig. 3: Attenuation variation versus  $\ln (P_0/p)$  on a log-log scale.

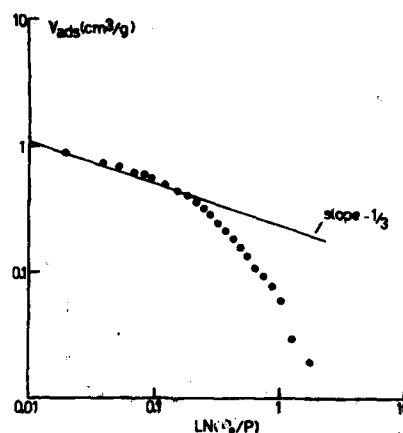


Fig. 4: Volume adsorbed per g at STP versus  $\ln (P_0/p)$  on a log-log scale.

In conclusion, we have shown that an adsorption isotherm model proceeding from a multilayer formation explains our phonon echo attenuation results. It shows that such a technique may be used to monitor the adsorption isotherm of  $^4\text{He}$  at low temperatures with an interesting sensitivity to detect monolayers.

This work was supported by the Natural Science and Engineering Research Council of Canada and the G.R.S.D. (Groupe de Recherches sur les semiconducteurs et les Diélectriques).

#### REFERENCES

- 1) See the article of Fosheim et al, Phys. Rev. B 17, 964 (1978).
- 2) Ch. Frénois, J. Joffrin and A. Levelut, Jour. de Physique Lett. 35, 221 (1974).
- 3) S. Brunauer, P.H. Emmett and E. Teller, J. Amer. Chem. Soc. 60, 309 (1938).
- 4) T.L. Hill, Advanc. Catalys. 4, 211 (1952).
- 5) S.G. Eckstein, Y. Eckstein, J.B. Ketterson in Phys. Acoustics, vol. 6, Mason (1970).

**PHONON IN INSULATORS**



## ON THE POSSIBLE USE OF OPTICAL ROTATION MEASUREMENTS FOR DETECTING WEAKLY IR ACTIVE MODES

V.C. Sahni

*Nuclear Physics Division, Bhabha Atomic Research Centre, Trombay, Bombay  
400 085, India*

**Abstract.**— IR activity of normal modes of a crystal is usually investigated through reflection or transmission measurements. We propose here another way which should be useful for studying modes of weak IR activity. The method involves measuring the rotation angle  $\theta$ , of the plane of polarization of a monochromatic beam of frequency  $\omega$ , as the beam traverses a crystal of thickness  $d$ . By studying  $\theta$  as a function of incident frequency  $\omega$  one would observe a 'resonance' close to each IR active frequency  $\omega_i$ . The method would be feasible if there is appreciable transmission of the beam that is the oscillator strength of the mode is small. We suggest a system, namely,  $\text{LiKSO}_4$ , where this idea could be applied. In particular we discuss how the symmetric stretching mode of  $\text{SO}_4$  which is IR inactive for a free ion but is weakly IR active in this crystal, could be investigated using different wavelengths of a  $\text{CO}_2$  laser. Potentiality of the proposed technique for investigating phase transitions, wherein certain Raman active modes acquire weak IR activity across the transition are mentioned.

1. **Introduction.**— The infra-red (IR) activity of long wavelength modes of a crystal is traditionally investigated via the first order process involving reflection or transmission measurements,<sup>1,2</sup> and a wealth of data has been accumulated in this way. Here we propose another way of detecting weakly IR active modes. The method involves monitoring the rotation  $\theta$  of the plane of polarization of a monochromatic beam of frequency  $\omega$  (as it passes through a crystal) as a function of  $\omega$ . From the resonances which will be exhibited by this function it should be possible to infer the IR dispersion frequencies. We will outline the physical basis of the method in section 2 and also point out the circumstances when the technique would be feasible. A possible test case, where the ideas suggested here could be applied, is discussed in section 3 and certain remarks are made regarding the utility of this technique in investigating certain phase transitions.

2. **Physical Basis of the Method.**— It is known that the phenomenon of optical rotation, viz. rotation of plane of

polarisation of a plane polarised beam in traversing a medium, can occur even for a medium whose real dielectric tensor is isotropic, purely on account of effects of spatial dispersion<sup>3</sup>. Born and Huang have shown that this effect can cause, in a crystal otherwise free from double refraction, the right and left circularly polarized beams to travel with differing phase velocities. Since a plane polarized beam can be expressed as a superposition of two such circularly polarized beams, the above difference in phase velocities results in a rotation of the plane of polarization as the beam traverses the medium. One can show<sup>3</sup> that even for uniaxial crystals when the beam propagates along the unique axis similar considerations hold, and further the rotation angle  $\theta$  is related to  $\vec{G}$  through

$$\theta \propto (\vec{G} \cdot \hat{k}) d \quad (1)$$

where  $\vec{G}$  is the gyration vector,  $\hat{k}$  a unit vector along the beam direction and  $d$  is the thickness of the crystal. The calculation of the gyration vector  $\vec{G}$  requires one to calculate the wave vector dependence of dielectric susceptibility  $\alpha_{\alpha\beta}(\vec{q}, \omega)$ ; that is effects of spatial dispersion have to be incorporated. Explicit calculations have been performed<sup>3</sup> (without including the damping effects) for the rigid ion model case. It emerges that the leading (linear)  $\vec{q}$  dependence originates from the imaginary part  $\alpha_{\alpha\beta}^I(\vec{q}, \omega)$  (of  $\alpha_{\alpha\beta}(\vec{q}, \omega)$ ), which is an antisymmetric tensor, and the components of gyration vector  $\vec{G}$  are defined through

$$G_{\alpha} = 4\pi \alpha_{\beta\gamma}^I(\vec{q}, \omega) = -4\pi \alpha_{\gamma\beta}^I(\vec{q}, \omega), \quad (2)$$

( $\alpha, \beta, \gamma$  are cyclic order of 1,2,3)

Within the limit of negligible damping, one can write a somewhat more general form (than for the rigid ion model) for the gyration vector  $\vec{G}$  and this turns out to be

$$\vec{G} = -\frac{1}{c} \sum_j \sum_{j'} \frac{f_j(j')}{\omega_j(j') - \omega^2} \cdot \vec{z}(j) \times \vec{z}(j') \quad (3)$$

(c/f Born and Huang's (44.69)) where  $\vec{z}(j)$  is the dipole moment of the  $j$ th mode and  $\omega(j)$  its dispersion frequency. (For an IR inactive mode  $\vec{z}(j) = 0$ , hence  $\vec{G}$  derives contribution only from IR active modes).  $f_j(j')$  involves the eigenvectors of the dispersion oscillators  $j$  and  $j'$  and the first derivatives of the dynamical matrix - excluding macroscopic field terms - w.r.t.  $q_j$  at  $q_j = 0$ .

Upon using equation (3) in equation (1) we find that if we study the  $\omega$  dependence of the rotation angle  $\theta$ , then it would show resonances close to each dispersion frequency. In this way, by experimentally measuring the rotation of plane of polarisation of a monochromatic beam of frequency  $\omega$  the dispersion frequencies of IR active modes can be located. Of course, it is obvious that for the method to be practical, the transmission of the beam should be appreciable. This means that the method would be feasible only for modes of rather weak IR activity. However, the important point to note is that resonant character of  $\theta$  as a function of  $\omega$  holds even for modes of weak activity, and hence the method could be useful in their study provided the attenuation coefficient is say  $\leq 50 \text{ cm}^{-1}$ .

3. Test Case and Utility.— A testing ground, where the technique suggested in this paper could be tried, is provided by the system  $\text{LiKSO}_4$ . This is a crystal belonging to the symmetry  $C_6$  at room temperature and there are two molecules per unit cell. In the free ion state we know that the symmetric stretching mode  $\nu_1$  is IR inactive. In  $\text{LiKSO}_4$ , however, because one of the oxygen atoms is inequivalent compared to other three, this mode too acquires IR activity. Of course, the IR activity is expected to be extremely weak and so the present method could be tried. From Raman measurements it is known that the frequency of this mode lies at  $1008 \text{ cm}^{-1}$ . A convenient source of monochromatic radiation would then be a  $\text{CO}_2$  laser which offers several wavelengths lying in the range  $960 \text{ cm}^{-1}$  to  $1060 \text{ cm}^{-1}$ . The beam could be made to pass along the unique axis of the crystal, whose faces are cut so as to be normal to the unique axis. By monitoring the rotation angle  $\theta$  as a function of  $\omega$  one can see whether IR activity of the mode can be established in this way.

If this technique proves feasible then one could employ it to study phase transitions wherein the inversion symmetry is lost/acquired across the transition point. Often in such cases certain Raman active modes lose/acquire IR activity but the effects are rather weak. In such situations, when the vibrational frequency is already known from Raman data, to establish whether the acquisition of IR activity by the mode has occurred or not could be ascertained by the proposed technique.

References:— 1. M. Born and K. Huang, Dynamical Theory of Crystal Lattices (Oxford Univ. Press) 1954.

2. G. Venkataraman, L.A. Feldkamp and V.C. Sahni, Dynamics of Perfect Crystals (MIT Press, Cambridge, Mass) 1975.

3. Ref. 1 Appendix IX and Chapter VII.

LATTICE DYNAMICS OF CUPRITE ( $\text{Cu}_2\text{O}$ )

G.E. Kugel, C. Carabatos and W. Kress\*

University of Metz, 57045 Metz, France

\*Max-Planck-Institut für Festkörperforschung, 7000 Stuttgart, F.R.G.

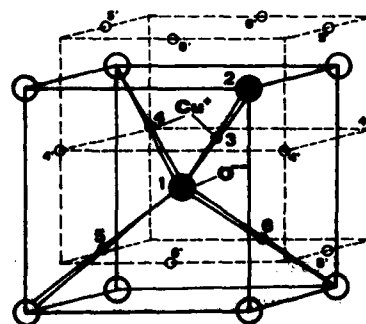
**Abstract.** - The phonon dispersion curves of  $\text{Cu}_2\text{O}$  have been calculated using a shell model which takes into account nearest neighbour O-Cu, Cu-Cu and O-O interactions, long range Coulomb interactions and the electronic polarizability of both the oxygen and the copper ions. The results are compared with the data obtained from ultrasound, infrared, Raman and inelastic neutron scattering measurements. The interrelations between fcc-Cu and  $\text{Cu}_2\text{O}$  are pointed out and the influence of deformations of the electronic charge density on the phonon dispersion curves is discussed.

**Introduction.** - For many years the extremely rich excitonic spectra of cuprous oxide have attracted considerable interest in the electronic properties of this compound<sup>1</sup>. Up to now only very few attempts<sup>2,3</sup> have been made to calculate the phonon dispersion curves and thus to give a unique interpretation of the different phonon frequencies deduced from recent ultrasound<sup>4</sup>, Raman scattering<sup>5,6</sup>, exciton luminescence<sup>7</sup> and inelastic neutron scattering<sup>8</sup> measurements. The calculation of Huang<sup>2</sup> is restricted to the  $\Gamma$ -point whereas the model of Carabatos<sup>3</sup> which gives a quite satisfactory description of the optical modes at the zone center does not reproduce the elastic and dielectric properties and shows serious disagreement with the neutron scattering data, in particular a softening of the acoustic branches at the R point. In this paper we show how the model has to be extended and modified in order to overcome the above mentioned deficiencies.

Cuprite crystallized in a simple but uncommon structure which belongs to the non symmorphic space group  $O_h^4$  and can be considered as being made out of two interpenetrating Bravais lattices: a fcc-Cu lattice and a bcc-O lattice (Fig. 1). Each oxygen is the center of a regular tetrahedron the corners of which are occupied by the four nearest neighbour Cu ions. The unit cell contains two formula units of  $\text{Cu}_2\text{O}$ .

At the center of the Brillouin zone the normal vibrations of  $\text{Cu}_2\text{O}$  decompose into

$$3\Gamma_{15}^{(3)} + \Gamma_{25}^{(3)} + \Gamma_{12}^{(2)} + \Gamma_2^{(1)} + \Gamma_{25}^{(3)}$$

Fig. 1. Crystalline structure of  $\text{Cu}_2\text{O}$ .

where the two optic  $\Gamma_{15}$  modes are infrared active and only the  $\Gamma'_{25}$  mode is Raman active. In contrast to the poor first order ordinary Raman spectrum which exhibits only one mode all odd-parity phonons can be observed in resonant Raman (RR) scattering on exciton lines. For a long time the interpretation of the RR spectra has been highly controversial. At present the different lines are well understood in terms of quadrupolar and dipolar transitions and specific polarization selection rules have been derived<sup>9</sup>.

**Lattice Dynamics.**— The phonon dispersion curves up to phonon energies of about 5 THz have been measured in the high symmetry directions  $\Delta$ ,  $\Sigma$  and  $\Lambda$  at room temperature by Beg and Shapiro<sup>8</sup>. Some complementary measurements in the intermediate energy region between 4 and 10 THz have been performed by ourselves in order to determine the branches connected to the  $\Gamma'_2$  mode. The results of the neutron scattering measurements are represented in Fig. 2 together with our model calculations.

In the following we will discuss the different parameters of the model. First of all we take into account the nearest neighbour O-Cu interactions. These interactions which have already been used in the rigid ion model of Carabatos and Prevot<sup>3</sup> are most important and have to be considered in any model for  $\text{Cu}_2\text{O}$ . This can be concluded from band structure calculations<sup>10</sup>

which reveal a strong hybridization of the Cu 3d orbitals with the O 2p states. This hybridization favours the cuprite structure and stabilizes the copper tetrahedra around the oxygen ions. The importance of the Cu-O interactions is also indicated by the high frequency (15.45 THz) of the Raman active  $\Gamma'_{25}$  mode in which the oxygen is displaced with respect to the rigid copper tetrahedron. In a rigid ion model this mode determines directly the force constant for the central O-Cu interaction. The second mode which is strongly dependent on the O-Cu force constants is the  $\Gamma'_2$  vibration which corresponds to an isotropic deformation of the copper tetrahedron. Naturally this mode is also influenced by the Cu-Cu interactions which we now discuss. It is interesting to note that the elastic constant  $c_{11}$ <sup>4</sup> scaled by the mass densities of Cu and  $\text{Cu}_2\text{O}$  is the same in both crystals whereas the shear constants  $\frac{1}{2}(c_{11}-c_{12})$  and  $c_{44}$  are considerably lowered in the oxide. This means that the LA and the lowest LO branch in the 100 direction are basically due to the same interactions as in metallic copper. It is

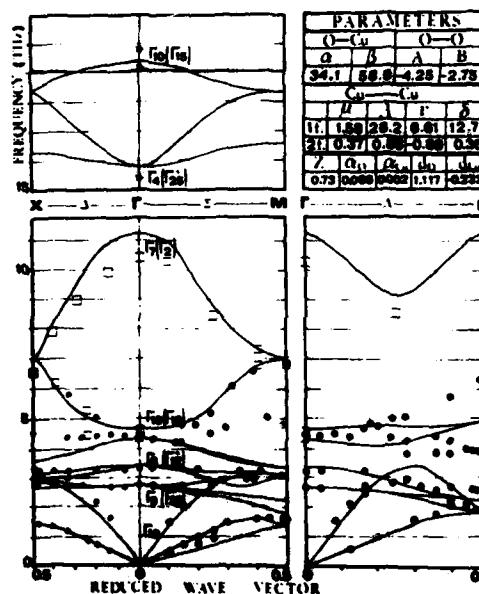


Fig. 2. Phonon dispersion curves in cuprite (○: ref. 8; □: our measurements; \* optical data). The full lines are the shell model calculations.

that the elastic constant  $c_{11}$ <sup>4</sup> scaled by the mass densities of Cu and  $\text{Cu}_2\text{O}$  is the same in both crystals whereas the shear constants  $\frac{1}{2}(c_{11}-c_{12})$  and  $c_{44}$  are considerably lowered in the oxide. This means that the LA and the lowest LO branch in the 100 direction are basically due to the same interactions as in metallic copper. It is

therefore essential to take into account the nearest neighbour Cu-Cu interactions and to take care of the fact that the Cu-Cu interactions in  $\text{Cu}_2\text{O}$  are split into two distinct families. In the first family the Cu-Cu forces act together with nearest neighbour Cu-O-Cu forces which are missing in the second family. It should be mentioned that it is not the Cu-Cu interaction itself which stabilizes the frequencies in the  $\Gamma$  and  $\Lambda$  directions and in particular at the R-point, but the fact that the force constants of the two families are different. Our calculations show that the considerable lowering of the shear elastic constants in  $\text{Cu}_2\text{O}$  as compared to fcc Cu is due to strong non central O-Cu interactions weak nearest neighbour O-O interactions and a strong enhancement of the interactions between those  $\text{Cu}^+$  ions, which are linked by Cu-O-Cu bindings. The large value of the dielectric constant  $\epsilon_\infty$  (6.46) arises from a substantial electronic polarizability which is essentially due to the oxygen ions. Minor contributions arise from the  $\text{Cu}^+$  ions. In our calculations it turns out that the shell change of the  $\text{Cu}^+$  ions is positive. This indicates a strong overlap of charge density near the  $\text{Cu}^+$  ion which is also indicated by the band structure calculations. The dipolar electronic polarizability acts mainly on the polar  $\Gamma_{15}^{(3)}$  modes. Band structure calculations and RR scattering experiments indicate that electronic deformations of other than dipolar symmetry, in particular the isotropic deformation of the charge density around the  $\text{O}^{--}$  ions, may become important. The effect of an isotropic  $\text{O}^{--}$  deformation is already included in our calculations since it corresponds essentially to a special combination of nearest neighbour force constants between those Cu-O-Cu bonds. The large values found for the Cu-Cu coupling constants  $\lambda$  and  $\delta$  for the first family support these ideas.

Conclusions. - With our model a realistic calculation of the phonon density of states and the specific heat will be possible. The inclusion of the scattering matrix elements will give the RR spectra. Investigations of the pressure dependence of the RR spectra are in progress and will yield the third order anharmonic contributions to the lattice potential.

#### References

1. V.T. Agekyan, Phys. Stat. Sol.(a) 43, 11 (1977). Earlier references are given here.
2. K. Huang, Z. Physik 171, 213 (1963)
3. C. Carabatos and B. Prevot, Phys. Stat. Sol.(b) 44, 701 (1971)
4. J. Hallberg and R.C. Ewanson, Phys. Stat. Sol. 42, 305 (1970)
5. A. Compaan and H.Z. Cummings, Phys. Rev. Lett. 31, 41 (1973)
6. M.A. Washington, A.Z. Genack, H.Z. Cummings, R.E. Bruce, A. Compaan, and R.A. Forman, Phys. Rev. B 15, 2145 (1977)
7. Y. Petroff, P.Y. Yu, and Y.R. Shen, Phys. Rev. Lett. 31, 41 (1973)
8. M.M. Beg and S.M. Shapiro, Phys. Rev. B 13, 1728 (1976)
9. J.L. Birman, Phys. Rev. B 9, 4518 (1974)
10. L. Kleinmann and K. Mednick, Phys. Rev. B 21, 1549 (1980)

## TIME REVERSAL SYMMETRY AND THE RAMAN SCATTERING BY CRYSTALS

A.K. Ramdas and S. Rodriguez

*Department of Physics, Purdue University, West Lafayette, Indiana 47907, U.S.A.*

**Abstract.**— A survey of the effect of time reversal symmetry on the phonon spectra of crystals is presented. The linear wave vector dependence of the dispersion curves of the zone center polar modes as well as splitting of shear acoustic modes are accessible to observation in the Raman and Brillouin spectra of selected lines in suitable crystals.

In perfect crystals, the symmetry of the lattice imposes restrictions on the nature of the normal modes of vibration. For example, phonons of infinite wave length can be either non-degenerate or at most doubly degenerate except for crystals belonging to one of the five cubic classes in which case, in addition to the above, there can exist triply degenerate phonons. These conclusions for these modes as well as their eigenvectors can be deduced from the knowledge of the symmetry of the crystal and the content of its primitive cell.

In addition to the geometrical symmetry operations of the group of the crystal under investigation, the equations of motion of the atoms (classical or quantal) are invariant under the operation of time reversal. This additional restriction has interesting consequences for the dispersion (dependence of the frequency of the phonons on their wave vectors  $\vec{q}$ ) of the normal modes.

Let each primitive cell of the crystal be denoted by a translation vector  $\vec{n}$  and let  $\alpha = 1, 2, \dots, 3f$  label the degrees of freedom of the  $f$  atoms in each cell. In the harmonic approximation, the equations of motion of the displacements  $u_{n\alpha}$  from the equilibrium configuration are

$$M_\alpha \ddot{u}_{n\alpha} = - \sum_{n', \alpha'} C_{\alpha\alpha'}(\vec{n} - \vec{n}') u_{n'\alpha'} \quad (1)$$

where  $C_{\alpha\alpha'}(\vec{n} - \vec{n}')$  are the force constants and  $M_\alpha$  the mass of the atom associated with the  $\alpha$  degree of freedom; translational symmetry requires that  $C_{\alpha\alpha'}(\vec{n} - \vec{n}')$  depend only on  $\vec{n} - \vec{n}'$ . Furthermore  $C_{\alpha\alpha'}(\vec{n} - \vec{n}')$  is symmetric in  $\alpha, \alpha'$  and  $\vec{n}, \vec{n}'$ . The propagating solutions of these equations with wave vector  $\vec{q}$  and angular frequency  $\omega(\vec{q})$  obey the eigenvalue equation

$$\sum_{\alpha'} [C_{\alpha\alpha'}(\vec{q}) - \omega^2(\vec{q}) \delta_{\alpha\alpha'}] u_{\alpha'} = 0 \quad (2)$$

where

$$\tilde{C}_{\alpha\alpha'}(\vec{q}) = \sum_{\vec{n}} (M_{\alpha} M_{\alpha'})^{-1/2} C_{\alpha\alpha'}(\vec{n} - \vec{n}') \exp[-i\vec{q} \cdot (\vec{n} - \vec{n}')] \quad (3)$$

$\tilde{C}(\vec{q})$ , the dynamical matrix, is Hermitian and positive definite. Time-reversal symmetry imposes, in addition,

$$\tilde{C}^*(-\vec{q}) = \tilde{C}(\vec{q}) \quad (4)$$

Pine and Dresselhaus<sup>1,2</sup> have shown that this requires the frequency of all optical phonons to vary quadratically with wave vector in the vicinity of  $\vec{q} = 0$  with the exception of the doubly degenerate polar phonons of crystal classes  $C_3, C_4, C_6, D_3, D_4$ , and  $D_6$  and the triply degenerate polar phonons of crystals with point group symmetries  $T$  and  $O$ . The frequencies of these phonons vary linearly with  $\vec{q}$  near  $\vec{q} = 0$ . The symmetry groups enumerated above possess only proper rotations. The presence of an improper operation is sufficient to invalidate the possibility of this behavior.

For acoustical phonons, since  $\omega(\vec{q})$  tends to zero as  $\vec{q} \rightarrow 0$  and the eigenvalue equation (2) gives  $\omega^2$ , solutions for all crystal classes are linear in wave vector near  $\vec{q} = 0$ . However, shear acoustic waves propagating along the optic axes of crystals of symmetry  $C_3, C_4, C_6, D_3, D_4$ , or  $D_6$  and along the  $\langle 100 \rangle$  or  $\langle 111 \rangle$  directions of crystals of classes  $T$  and  $O$ , corresponding to right- and left- circular polarizations have different phase velocities. This gives rise to the phenomenon of acoustical activity.<sup>3</sup>

Raman and Brillouin scattering are ideal techniques to investigate the behavior of phonons described above. The wave vector conservation rule establishes that the phonon involved in a given inelastic scattering has a wave vector equal to  $\sqrt{2} k_L$  for right-angle scattering and  $2 k_L$  for back-scattering where  $k_L$  is the wave vector of the incident radiation. The energy differences between the different phonon branches into which the zone center polar modes splits are small for  $0 < q < 2 k_L$ . This necessitates the study of appropriate narrow lines in the Raman spectra requiring temperatures in the liquid helium range and high resolution spectroscopy with a Fabry-Perot interferometer.

Studies on suitable Raman lines in  $\alpha$ -quartz<sup>1,3,4</sup> and  $\text{Bi}_{12}\text{GeO}_{20}$ ,<sup>5</sup> have clearly demonstrated the above phenomena. The latter material is cubic with point group symmetry  $T$ . The three-fold degenerate polar optical phonons at  $\vec{q} = 0$  are split isotropically according to an effective Hamiltonian interaction of the form

$$H' = A \vec{q} \cdot \vec{I} \quad (5)$$

where  $A$  is a phenomenological constant and  $\vec{I}$  the angular momentum matrix for unit spin. In addition one must take account of the splitting of such triply degenerate phonons, even for  $\vec{q} \rightarrow 0$ , into longitudinal and transverse optical branches. Further verification of the linear- $\vec{q}$  effects is provided by studies of the polarization features of the Raman spectra in the absence and presence of an applied uniaxial stress. Phenomenological constants describing the linear- $\vec{q}$  (e.g., the constant  $A$  in  $\text{Bi}_{12}\text{GeO}_{20}$ ) and the stress dependence have been obtained from such investigations.<sup>4,5</sup>



We note that in the presence of a magnetic field,  $\vec{B}$ , time reversal symmetry breaks down unless the time reversal operator is applied also to the sources of the magnetic field. Then, instead of Eq. (4) we have

$$\bar{C}^*(-\vec{q}, -\vec{B}) = \bar{C}(\vec{q}, \vec{B}) \quad (6)$$

A theoretical study of the effects of a magnetic field on the phonon modes of crystals at  $\vec{q} = 0$  has been carried out by Anastassakis *et al.*<sup>6</sup> The consequences regarding linear- $\vec{B}$  dependence of phonon frequencies are similar to those for the linear- $\vec{q}$  dependence discussed above, but occurs in a larger number of crystal classes. In general the changes in phonon energies due to the presence of a magnetic field are small. However, if an interaction of the resonant type occurs, i.e., if there are magnetic and phonon excitations of the crystal having approximately equal energies, the effects can be large. This is illustrated in the work of Schaack<sup>7</sup> on rare earth compounds.

Finally, an interesting case of linear- $\vec{q}$  dependence of phonon frequencies in helical chains has been investigated by Imaino.<sup>8</sup> In a model study he exhibited the linear dependence of doubly degenerate optical phonons in linear helical chains containing three atoms per turn with equal force constants between the first three nearest neighbors.

#### References

1. A. S. Pine and G. Dresselhaus, Phys. Rev. **188**, 1489 (1969).
2. A. S. Pine and G. Dresselhaus, Phys. Rev. **B4**, 356 (1971).
3. A. S. Pine and G. Dresselhaus, Proceedings of the International School of Physics "Enrico Fermi", Course 52, E. Burstein, ed., (Academic Press, New York, 1972), pp. 325-344.
4. M. H. Grimsditch, A. K. Ramdas, S. Rodriguez, and V. J. Tekippe, Phys. Rev. **B15**, 5869 (1977).
5. W. Imaino, A. K. Ramdas, and S. Rodriguez, Phys. Rev. **B22**, 5679 (1980).
6. E. Anastassakis, E. Burstein, A. A. Maradudin, and R. Minnick, J. Phys. Chem. Solids, **33**, 519, 1091 (1972).
7. G. Schaack, Proceedings, VIIth International Conference on Raman Spectroscopy, Ottawa, Canada (1980); W. F. Murphy, ed., (North Holland, Amsterdam, 1980), pp. 18-21.
8. W. I. Imaino, Ph.D. Thesis, Purdue University, 1980 (unpublished).

THE PHONON ANOMALY IN b.c.c.  $\text{He}^4$  : A PHONON SELF-TRAPPING ?

M. Héritier

*Laboratoire de Physique des Solides, Université de Paris-Sud, 91406 Orsay, France*

**Abstract.** - It is proposed that a longitudinal phonon in b.c.c.  $\text{He}^4$ , at wavevector  $|\vec{q}| = 2.3 \text{ \AA}^{-1}$  can be self-trapped in a liquid drop and form a roton-like excitation. This can account for anomalies observed in the phonon spectrum, in a sphere of momentum space.

The concept of self-trapping, well-known in the case of a single particle, can be extended to collective excitations (1): consider a system where one can define two phases which have almost equal thermodynamical potential,  $G_S$  in the stable phase and  $G_E$  in the excited one. Suppose than an elementary excitation as a lower energy  $\omega_E$  in the excited phase than in the stable phase  $\omega_S$ , so that  $\Delta\omega = \omega_S - \omega_E \gg \Delta G = G_E - G_S$ . The excitation energy lowering  $\Delta\omega$  tends to induce the formation of a volume of the excited phase, limited to a finite size by  $\Delta G$ . Taking into account the excitation localization energy  $E_{loc}$ , the excitation can be self-trapped if the thermodynamical potential balance is favourable.

We consider here longitudinal phonons in  $\text{He}^4$ , either in the b.c.c. solid or in the superfluid (the phonon-roton spectrum). This system seems a good candidate for collective excitation self-trapping: first, longitudinal phonons exist with a long lifetime in both phases (as "rotons" at large wavevectors in the superfluid). Secondly, in many respects, solid and liquid Helium behave very similar: Delrieu has noted striking analogies between the two phases (2) (orders of magnitude, types of interactions, types of defects). Castaing and Nozières have pointed out the "nearly solid" character of liquid  $\text{He}^3$  (3) (the same idea applies to liquid  $\text{He}^4$ ). A roton in superfluid  $\text{He}^4$  has been described as a longitudinal phonon self-trapped in a solid-like region of the liquid (4). Here, the stable phase is the b.c.c. solid at pressures only slightly higher than the melting pressure, so that the melting free enthalpy is much smaller than a typical atomic kinetic energy in the liquid  $E_{kin} = \hbar^2 k^2 / 2m$ , where  $m$  is the atomic mass and  $k \sim \pi/a$  ( $a$  is the interatomic spacing). The b.c.c. structure corresponds to the lowest solid-liquid surface tension.

The excitation spectrum of the liquid exhibits a minimum (the "roton minimum"), at a wavevector  $|\vec{q}| = q_0 = 2.1 \text{ \AA}^{-1}$ ,  $\omega = \omega_R = 7.3 \text{ K}$ . In the larger part of the momentum space, the phonon energies in the solid  $\omega_s(q)$  are much larger than  $\omega_R$  so that:

$$\Delta\omega(q) = \omega_s - \omega_R \gg \frac{\hbar^2 k^2}{2m} \gg \Delta G(p, T)$$

Therefore, conditions for self-trapping in a superfluid drop of radius  $R$  are favorable at wavevectors around the roton minimum. The free enthalpy balance condition can be written:

$$-\Delta\omega(q_0) + E_{\text{loc}}(R) + (4\pi/3)R^3\Delta G + 4\pi\sigma R^2 < 0$$

The second term is the energy necessary to localize the roton within the drop. The last term is the solid-liquid interface energy, which remains finite on the melting curve, and, therefore, predominates on the volume term. As estimated from ion mobility measurements (5),  $\sigma = 0.04$  erg/cm<sup>2</sup>. A roton can be pictured as a vortex ring of diameter  $2R_0$ , with a dipolar velocity field, except at small distances. In the Feynman model,  $2R_0 \sim a$ . However, in this work, it is more consistent to use the picture of a phonon self-trapped in a solid-like region of diameter  $2R_0$ . The estimate of  $R_0$  is about 4-5 interatomic distances on the melting curve. To localize the roton within the drop, it is necessary to perturb the dipolar backflow, which increases the fluid kinetic energy. Imposing that the velocity vanishes for  $r > R$ , and considering the fluid as continuous, perfect and incompressible, we obtain, as leading term:

$$E_{\text{loc}}(R) = (M^2 q_0^2 / 2m) / R^2 R$$

Minimization with respect to  $R$ , gives the free enthalpy of the self-trapped state:

$$G_{\text{ST}} = -\Delta\omega(q_0) + (3/2) (M^2 q_0^2 / 2m R^2)^{1/3} \times (8\pi\sigma)^{2/3}$$

the optimum drop radius is

$$R = a \left[ \frac{M^2 q_0^2}{2m} / 8\pi\sigma R^2 \right]^{1/3}$$

We expect about 120 atoms in the drop and a self-trapped phonon energy about 10K above the roton energy. Given the rough approximations involved these figures should be considered as orders of magnitude, rather than precise determinations.

Have these self-trapped phonons been observed experimentally? Indeed, anomalies have been seen in the phonon spectrum of b.c.c. He<sup>4</sup> in neutron scattering experiments (6): at equivalent points of the momentum space, non identical neutron profiles were observed. At  $|\vec{q}| \sim 2.3\text{\AA}^{-1}$ , on a sphere of the momentum space, the profiles were dissymmetric, with a higher intensity, and occurred at lower energy. While dissymmetries and changes in the peak intensities may be due to interference effect in the one-phonon scattering function (see Glyde (7)) the peak energy lowering cannot be interpreted so easily. The fact that the anomaly occurs at a constant value of the modulus of the wavevector, independently of its direction, agrees with our interpretation, since the roton spectrum of the liquid is isotropic. The value of the anomalous wavevector  $|\vec{q}| = 2.3\text{\AA}^{-1}$  is also in agreement with the roton wavevector, located at  $2.1\text{\AA}^{-1}$  on the melting curve and, therefore, at a higher value in the metastable liquid at pressures above the melting pressure. The value of the minimum energy,  $\epsilon = 15\text{K}$  is in remarkable agreement with our rough estimate, 10K above the roton energy, i.e. about 17K. Werthamer (8) has shown that the Debye-Waller factor in the solid closely resembles the structure of superfluid He<sup>4</sup>, exhibiting characteristic oscillations in the longitudinal modes (but much smaller ones in the transverse modes).

We propose that these effects are a manifestation of phonon self-trapping. It is obvious that our model is quite schematic and roughly approximate. What

we want to point out in this model are consequences of high non linearities. In this quantum crystal, the equations of motion should be non linear. Indeed, the physical condition  $\Delta\omega \gg \Delta G$  implies that the degrees of freedom involved in the excitation are strongly coupled to the order parameter of the phase transition (here the fourier components of the density at wavevectors belonging to the reciprocal lattice). The coupling is so large that a linearization is not possible. It is well known that, in such a case, a local solution is possible: the case of an electron in an ionic crystal embedded in a lattice polaron is a well known example. An electron in a magnetic insulator with a large s-d exchange, forming a magnetic polaron, is another one. In our case the collective excitation becomes local both in real space and in momentum space. In this local solution, the anharmonicity is so large that surprising similarities with the liquid phase are observed. This is what we want to modelize with our liquid drop picture.

#### REFERENCES

- 1) M. Héritier, P. Lederer and G. Montambaux, J. of Physics c, 13, L 703, (1980)
- 2) J.M. Delrieu, private communication
- 3) B. Castaing and P. Nozières, J. de Physique (Paris), 40, 257, (1979)
- 4) M. Héritier, G. Montambaux and P. Lederer J. de Physique (Paris) 40, L493, (1979)
- 5) R.M. Ostermeier and K.W. Schwartz, Phys. Rev. A5, 2510, (1972)
- 6) E.B. Osgood, V.J. Minkiewicz, T.A. Kitchens and G. Shirane, Phys. Rev. A5, 1537, (1972)  
V.J. Minkiewicz, T.A. Kitchens and E.B. Osgood, Phys. Rev. A8, 1513, (1973)
- 7) H.R. Glyde, Can. J. Phys, 49, 761, (1971)  
H. Börner, Phys. Rev. Letters, 29, 556, (1972)
- 8) N.R. Werthamer, Phys. Rev. Letters, 28, 1102 (1972)

## A STUDY OF THE Pb PRECIPITATION IN NaCl FROM THERMAL CONDUCTIVITY EXPERIMENTS

M. Locatelli, R. Suchail and E. Zecchi\*

*Service des Basses Températures, Laboratoire de Cryophysique, Centre d'Etudes Nucléaires de Grenoble, 85 X, 38041 Grenoble Cedex, France*

*\*Gruppo Nazionale di Struttura della Materia CNR, Istituto di Fisica dell'Università di Parma, Italy*

**Abstract.** - Phonon interactions are very useful in the study of large defects in dielectric crystals. We present here the study of the nucleation phenomenon of Pb in NaCl by means of thermal conductivity experiments between 50 mK and 50 K, and give some elements in favour of the hypothesis that the vacancy is the scattering center in the IV dipole ( $\text{Pb}^{2+}$  vacancy) phonon interactions.

**1. Introduction** - The interaction of phonons with large defects in dielectric crystals depends on the characteristics of the defect (dimensions, shape, density) and on the phonon frequency (1). Therefore thermal conductivity experiments can be very useful in the study of such defects. Since phonons interact with many different defects, it is necessary to know the different interaction processes available in the studied system, in order to analyse the results.

In previous work (2) on Pb nucleation in KCl we have deduced the presence of a cylindrical Suzuki like phase ( $\text{PbCl}_2$  superlattice), also we have observed phonon scattering by I.V. ( $\text{Pb}^{2+}$  vacancy) dipoles and formulated the hypothesis that the scattering center is the vacancy, as the resonance frequency does not depend on the cation (3).

It is interesting to confirm this hypothesis and in order to do this we have studied by the same technique the NaCl : Pb system, where the site of the vacancy is different from that in KCl : Pb (4).

**2. Experiments and Results** - All the samples were provided by Prof. R. CAPELLETTI from Parma University (Italy) and their characteristics are given in Table 1.

The thermal conductivity has been measured by the standard method in two thermal states for the doped crystals : as received and quenched. The thermal treatment at 500°C for two hours before quenching to LNT permits to dissolve some of the large defects.

I.V. dipole concentration in the different states and samples has been measured using Ionic Thermo Currents (ITC) technique by the Parma Group. A pure NaCl sample has been measured too as a reference.

The results are shown in Fig.1, and we can make the following remarks : 1) for the heavily doped sample it is impossible to dissolve all the lead by a quenching

this result is confirmed by ITC too, ii) for the sample with the lightest doping, the "dip" at high temperature, attributed to I.V. dipoles, is very small, while ITC experiments show the presence of I.V. dipoles.

3. Quantitative Analysis - We use the Debye model, as employed in (5), to analyse the results : in this model the different scattering processes are considered independent and the total inverse relaxation time is given by the relation :

$$\tau^{-1} = v/b + G\omega + A\omega^4 + \tau_{ph\ ph}^{-1} + \sum \tau_i^{-1}$$

$v/b$ ,  $G\omega$ ,  $A\omega^4$  and  $\tau_{ph\ ph}^{-1}$  correspond to the boundary, dislocation, point defect and phonon phonon scattering,  $v$  is the sound velocity,  $b$  the sample dimension ; only  $G$  and  $A$  can vary with the thermal state of the sample.

$\tau_{ph\ ph}^{-1}$  has been accurately determined using the results for the pure sample :

$$\tau_{ph\ ph}^{-1} = 84370 \omega^2 T \exp(-310/4.5 \times T)$$

$\tau_i^{-1}$  are related to the IV dipole and large defect scattering.

The following expressions have been used :

- IV dipole  $\tau_{IV}^{-1} = D\omega^4 / (\omega^2 - \omega_0^2)^2$  elastic scattering where  $D$  is proportional to the IV concentration and  $\omega_0$  is the resonance frequency,

- large defects : two types

. Spherical  $\tau_r^{-1} = N_r v^{-1} \sigma_r$  where  $N_r$  is the spherical defects concentration

$$\sigma_r = \pi r^2 \times \begin{cases} (1 + R \exp(-\frac{1}{3})) \times (r\omega/v)^4 & \text{for } \frac{2r\omega}{v} < 1.5 \\ (1 + R \exp(-\frac{r\omega}{3v})) & \text{for } \frac{2r\omega}{v} > 1.5 \end{cases}$$

where  $r$  is the radius of the defect and  $R$  a scattering efficiency coefficient.

. Cylindrical  $\tau_{ld}^{-1} = N_{ld} v^{-1} \sigma_{ld}$  where  $N_{ld}$  is the cylindrical defects concentration and  $\sigma_{ld} = \sigma_d + \sigma_e$

$$\text{with } \sigma_l = \begin{cases} gV^2 (\omega/v)^3 & \text{for } l\omega/v < 1.5 \\ gV^2 (\omega/v)^3 \exp(-c(\frac{\omega}{v} - \frac{1.5}{l})^2) & \text{for } \frac{l\omega}{v} > 1.5 \end{cases}$$

$$\sigma_d = \begin{cases} fd l (d\omega/1.5v)^4 & \text{for } d\omega/v < 1.5 \\ fdl & \text{for } d\omega/v > 1.5 \end{cases}$$

where  $l$  is the length,  $d$  the diameter and  $V$  the volume of the cylinder,  $v$  the sound velocity,  $g$ ,  $f$  are scattering efficiency coefficients,  $c$  an adjustable parameter.

The values of the main parameters corresponding to the curves in Fig.1 are given in the Table 1.

We note that the fits are good for the heavily doped sample, but not excellent for the two other samples. This can be attributed to the presence of impurity ions which modify the thermal conductivity mainly for the undoped or lightly doped sample. Nevertheless we can deduce the following results from the analysis 1) the lead nucleation gives rise to large defects with the dimension and shape depending on the Pb concentration : spherical at low concentration and cylindrical at high concentration.

ii) the IV dipole phonon scattering is weak and corresponds to a resonance temperature of 55 K.

This behaviour is different from the one observed in the KCl : Pb system where the scattering is stronger and at a resonance temperature of 29 K.

4. Conclusion - The scattering center in the IV dipole phonon interaction seems to be the vacancy, and a quantitative model will be developed in the future.

Moreover the Pb nucleation gives rise to large defects where the shape, spherical or cylindrical, seems to depend on the Pb concentration.

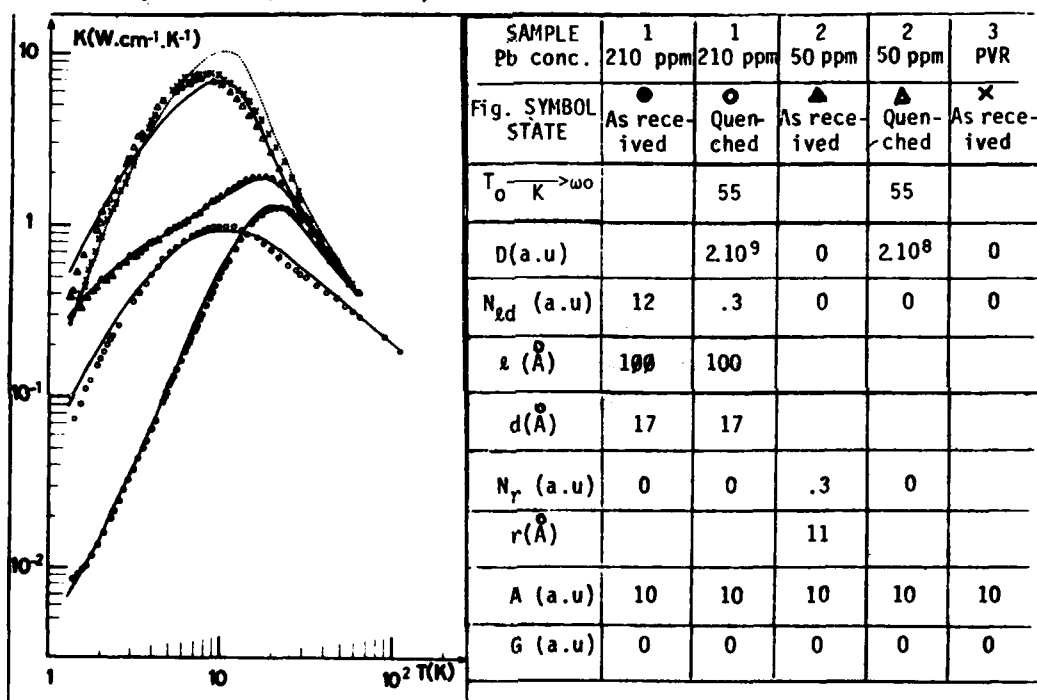


Fig.1 - Thermal conductivity versus the temperature for symbols see. Table 1

Table 1

#### References

- (1) ABOU GHANTOUS M., GUCKELBERGER K. and LOCATELLI M., J. Phys. Chem. Solids 41 (1980) 473
- (2) LOCATELLI M., ZECCHI E. and CAPELLETTI R., J. Phys. Colloq. 41 (1980) C6-371
- (3) WALKER C.T. and POHL R.O., Phys. Rev. 131 (1963) 1433
- (4) DRYDEN J.S. et al., J. Phys. C2 (1979) 603
- (5) LOCATELLI M., J. Physique Colloq. 37 (1976) C7-322

INTERACTION OF SOUND WITH VACANCIES IN bcc  $^3\text{He}$  CRYSTALS

I. Iwasa and H. Suzuki

*Department of Physics, University of Tokyo, Bunkyo-ku, Tokyo 113, Japan*

**Abstract.**— Longitudinal sound velocity was measured in bcc  $^3\text{He}$  crystals at frequencies of 10, 30 and 50 MHz as a function of temperature. Above 0.4 K, the velocity always decreased with increasing temperature and no systematic dependence on frequency was observed. The result was interpreted by taking into account the contribution of vacancies to the sound velocity.

We have measured the longitudinal sound velocities in bcc  $^3\text{He}$  crystals with a resolution of  $2 \cdot 10^{-5}$  at frequencies of 10, 30 and 50 MHz as a function of temperature. The relative change in the velocity  $\Delta v/v_0 = (v(T) - v_0)/v_0$  is plotted in Figs. 1 and 2. The data in Fig. 1 are taken for a crystal grown at 33 atm ( $24.4 \text{ cm}^3/\text{mole}$ ). The velocity change below 0.3 K is hysteretic and amplitude-dependent due to dislocations and is discussed elsewhere.<sup>1)</sup> Above 0.4 K the velocity decreases with temperature. The data in Fig. 2 taken for a crystal grown at 38 atm ( $23.8 \text{ cm}^3/\text{mole}$ ) show no systematic dependence on the frequency.

Our results are consistent with those of Wanner, Mueller and Fairbank.<sup>2)</sup> They analyzed the data by a 2-parameter equation

$$\rho[v^2(T) - v_0^2] = RT^4 + ST^6, \quad (1)$$

where  $\rho$  is the density and  $R$  and  $S$  are parameters. The equation was derived by using the Mie-Grüneisen equation of state for a solid together with the specific heat. The first term on the right-hand side was a direct consequence of the lattice specific heat and this  $T^4$ -dependence was observed in hcp  $^4\text{He}$  crystals.<sup>3)</sup> The second term was related to the excess specific heat (high-temperature anomaly) which was described by a  $T$ -dependent Debye temperature  $\theta(T) = \theta_0(1 - \alpha T^2)$ . Although eq.(1) was well fitted to their data, their derivation of the second term was unjustifiable because the term was comparable to or even greater than the first term.

The recent specific heat measurement of Greywall<sup>4)</sup> has shown that the high-temperature anomaly is primarily caused by vacancies. In the following we will show that the observed temperature dependence of the



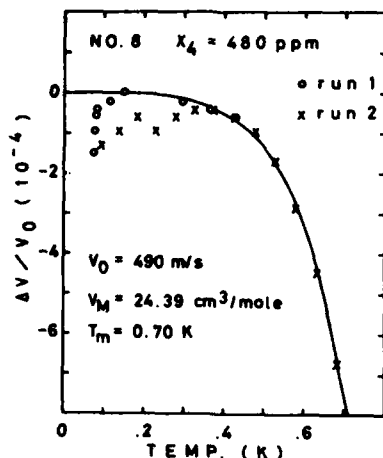


Fig. 1 : Temperature dependence of the velocity at 10 MHz on a cooling run (run 1) and a heating run (run 2). The drop in the velocity at 0.08 K and the hysteresis below 0.3 K are due to dislocations multiplied by phase separation. The curve is calculated from eq.(4) with  $k = -1.53$  and  $\ell = -0.51$ .

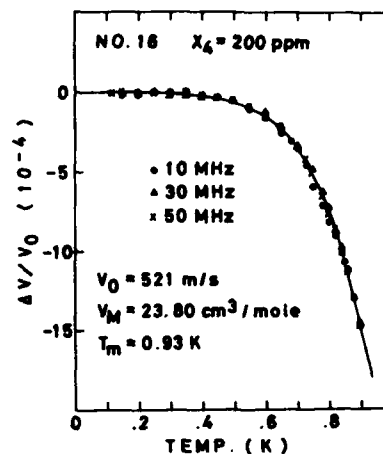


Fig. 2 : Temperature dependence of the velocity at 10, 30 and 50 MHz. Phase separation did not occur in this crystal. The curve is calculated from eq.(4) with  $k = -1.10$  and  $\ell = -0.55$ .

sound velocity is consistent with the specific heat which is composed of the lattice and vacancy terms.

According to Greywall the specific heat of a bcc  $^3\text{He}$  crystal is a sum of (1) the lattice term  $C_\theta$  with the Debye temperature  $\theta$ , (2) the vacancy term  $C_\phi$  with the vacancy formation energy  $\phi$ , (3) the exchange term  $C_J$  with the exchange energy  $J$ , and (4) the residual excess specific heat  $C_x$  whose origin is not given. Each of the first three major terms has a functional form  $f(\alpha/T)$  where  $\alpha = \theta, \phi$  or  $J$ . Then the generalized Mie-Grüneisen equation of state reads

$$\left(\frac{\partial P}{\partial T}\right)_V = \sum_{\alpha} \gamma_{\alpha} \frac{C_{\alpha}}{V}, \quad (2)$$

where  $V$  is the volume and  $\gamma_{\alpha} = -d \ln \alpha / d \ln V$ . For simplicity we neglect the exchange term which is appreciable only below 0.1 K. After several thermodynamical manipulations with an assumption that the number of vacancies does not change by the sound wave we obtain an expression for the adiabatic bulk modulus:

$$B_s(T) - B_0 = \frac{\gamma_{\theta}}{V} (\gamma_{\theta} - \gamma_{\theta}^0 + 1) \int C_{\theta} dT + \frac{\gamma_{\phi}}{V} (\gamma_{\phi} - \gamma_{\phi}^0 + 1) \int C_{\phi} dT \quad (3)$$

$$\equiv B_1 + B_2,$$

where  $\gamma'_\alpha = d \ln \gamma_\alpha / d \ln V$  and we set  $\gamma'_\alpha = 0$  for numerical estimations.

As the bulk modulus is a linear combination of the elastic constants which in turn are related to the sound velocity, the relative change in the velocity can be written as

$$\frac{\Delta v}{v_0} = k \frac{B_1}{B_0} + \ell \frac{B_2}{B_0}, \quad (4)$$

where  $k$  and  $\ell$  are adjustable parameters.  $B_0$ ,  $B_1$  and  $B_2$  are calculated from the data of the specific heat<sup>4)</sup> and the elastic constants.<sup>5)</sup> Equation (4) is then fitted to our velocity data. The curves in Figs. 1 and 2 are calculated for  $\ell = -0.51$  with  $k = 3\ell$  and  $\ell = -0.55$  with  $k = 2\ell$ , respectively.

Equation (4) is physically more reasonable than eq.(1): As the bulk modulus increases and the longitudinal sound velocity decreases with temperature, the shear modulus in the isotropic approximation should decrease. A simple interpretation of the second term in eq.(4) is then that the shear modulus is decreased by vacancies because there are no bondings at the vacant sites. As for the first term, the present values of  $k = -1.53$  and  $-1.10$  are comparable to those obtained for hcp  $^4\text{He}$  ( $-0.8 \sim -1.8$ ).

In conclusion, the contribution of vacancies to the velocity which was not considered by Wanner et al. should be taken into account. We thank R. Wanner for useful discussions.

#### References

- 1) I. Iwasa, N. Saito and H. Suzuki: to be published.
- 2) R. Wanner, K.H. Mueller, Jr. and H.A. Fairbank: J. Low Temp. Phys. 13, 153 (1973)
- 3) I. Iwasa and H. Suzuki: J. Phys. Soc. Jpn. 49, 1722 (1980).
- 4) D.S. Greywall: Phys. Rev. B15, 2604 (1977).
- 5) D.S. Greywall: Phys. Rev. B11, 1070 (1975).

## MEANS SQUARE DISPLACEMENTS OF A SUBSTITUTIONAL DEFECT AND ITS NEAREST NEIGHBOURS IN KI

S. Duraiswamy and T.M. Haridasan

*School of Physics, Madurai Kamaraj University, Madurai 625021, India*

**Abstract.**— The means square displacements of both the cation and anion substitutional defects and those of their nearest neighbours in KI are calculated in the frame work of a scattering matrix formalism. Our results show that the means square amplitudes of the defect atom, such as the  $\text{Rb}^+$  in KI is much larger than the value of  $\text{Rb}^+$  in RbI as also of  $\text{K}^+$  in KI. The means square displacements of the nearest neighbours in the defect environment are not that significantly altered from their values in the host crystal environment. The other salient features observed from our calculations are also discussed.

**1. Introduction.**— Even though many aspects associated with point defects in alkali halides are well investigated both theoretically and experimentally in the past, the means square displacements of point defects and their immediate neighbours are not explored that extensively so far. In this paper we report the results of our investigations on the means square displacements of  $\text{Na}^+$ ,  $\text{Rb}^+$ ,  $\text{Cl}^-$  and  $\text{Br}^-$  impurities and those of their nearest neighbours in KI using the lattice Green's functions in the scattering matrix formalism.

**2. Method of Calculation.**— It is well known that the impurity modes associated with a point defect in an alkali halide is given by the solutions of the determinantal equation  $|I - g(\omega) \delta l(\omega)| = 0$  for various  $\omega$  values. However following the same theory one can formulate a scattering matrix and show that the matrix associated with the scattered amplitude  $u_i$  of the defect and its neighbours can be written corresponding to the incident plane wave as<sup>1</sup>

$$u_i = [I + g \delta l (I - g \delta l)^{-1}] u_i^0 \quad (1)$$

Here  $g$  is the Green's function matrix of the host lattice in the defect space constituted by the impurity and its first six neighbours.  $\delta l$  is the matrix describing the perturbation in the same space due to the presence of the defect. So knowing  $\delta l$ ,  $g$  and the plane wave amplitude  $u_i^0(q, j)$  for the incident mode  $(q, j)$  one can compute  $u_i(K, \omega)$  and then obtain the means square amplitudes and the Debye Waller factors as

$$\langle u_i^2(K) \rangle = \frac{\hbar}{2} \int_0^\infty \frac{u_i^2(K, \omega)}{\omega} \coth\left(\frac{\hbar\omega}{2kT}\right) d\omega \quad (2)$$

$$B(K) = \frac{9\hbar^2}{2} \langle u_i^2(K) \rangle \quad (3)$$

The elements of  $g$  matrix in the (21x21) defect space are available from the early work on impurity modes<sup>2</sup>. The elements of  $\delta l$  matrix are also available likewise. The relevant elements of  $g$  matrix are evaluated using the phonon frequencies and eigenvectors from a shell model fitted to neutron scattering data<sup>3</sup>. The  $\delta l$  matrix involve only one unknown parameter  $\Delta A$ , the change of force constant between the defect and its first neighbour. These are fitted to the experimental gap modes<sup>4</sup>. The values of  $\Delta A$  obtained are given in Table 1. The  $u(q, j)$  are again fed from the shell model used in the estimation of  $g$ . Then using Eqs 2 and 3  $\langle u_i^2(K) \rangle$  and  $B(K)$  for the impurity ion and their first neighbours are computed.

**3. Results and discussion.**— The results of our calculations are given in Tables 2 and 3. The main conclusions are the following.

- a) The B factor for the impurity is in general larger than the corresponding B factor of the host atoms. For example B factor of Rb in KI is more than that of K in KI. Also it is larger than that of Rb in RbI.
- b) The B factor of  $Na^+$  in KI is greater than the B factor of  $Rb^+$  in KI whereas for the negative ion impurities the trend is reversed.
- c) The B factor of the first neighbour of the defect is different from the B factor of the same ion in the host crystal environment. However the difference in these two B factors is not that prominent.
- d) The occurrences of possible resonances in  $(I - g\delta l)^{-1}$  may be responsible for getting larger B factors for the defects.

In calculations such as diffusion where the jump frequency depends on the jumping atom (which is an impurity) and its neighbours one should employ these means square amplitudes. In the absence of experimental results we hope that these estimations would be of use to scattering experimentalists to see how the scattered intensities would be influenced by such defects.

Table 1. Change in force constant in KI

The defect	Change in $\Delta$ in units of $10^4$ dynes/cm
$Cl^-$	-0.111
$Br^-$	-0.595
$Na^+$	-1.000
$Rb^+$	0.435

Table 2. B factors of various defects and nearest neighbours  
in KI at 300 K in units of  $\text{\AA}^2$

Defect	B(Defect)	B(nearest neighbour)
Rb <sup>+</sup>	5.055	2.573
Na <sup>+</sup>	23.681	3.322
Cl <sup>-</sup>	2.979	6.427
Br <sup>-</sup>	3.355	3.843

Table 3. B factors in  $\text{\AA}^2$  for Rb<sup>+</sup> in KI at different temperatures.

Temperature	(B <sub>+</sub> ) <sub>Rb</sub> in RbI	(B <sub>+</sub> ) <sub>Rb</sub> in KI	(B <sub>-</sub> ) <sub>I</sub> in KI:Rb	(B <sub>-</sub> ) <sub>I</sub> in KI
50 K	0.684	1.396	0.487	0.541
100 K	1.265	2.076	0.885	1.014
150 K	1.867	2.891	1.302	1.501
200 K	2.475	3.747	1.724	1.992
250 K	3.085	4.622	2.148	2.484
300 K	3.697	5.055	2.573	2.977

#### References.-

1. Maradudin, A.A., Montroll, E.W., Weiss, G.H., and Ipatova, I.P.,  
Theory of lattice dynamics in the harmonic approximation, 2nd Ed,  
Academic Press, New York (1971)
2. Sebastian, R., Savariraj, G.A., and Haridasan, T.M., Phys. Stat. Solidi,  
91b, 371 (1979).
3. Dolling, G., Cowley, R.A., Schittenhelm, C. and Thorson, I.M., Phys.  
Rev 147, 577 (1966)
4. Kalyani, S. and Haridasan, T.M., J. Phys. Chem. Solids 28, 735 (1977).

ANOMALOUS TEMPERATURE DEPENDENCE OF A LO MODE IN  $\text{LiKSO}_4$ 

M.L. Bansal, S.K. Deb, A.P. Roy and V.C. Sahni

Nuclear Physics Division, Bhabha Atomic Research Centre, Trombay, Bombay 400 085, India

**Abstract.**— Raman scattering measurements for  $\text{LiKSO}_4$  over the temperature range 200 K to 725 K are reported. The results corroborate the occurrence of a phase transition at 700 K and also exhibit two unusual lattice dynamical features viz an inverted LO-TO splitting and an increase in the frequency of a normal mode with rise in temperature. A phenomenological explanation for these features is given.

1. **Introduction.**— We had recently<sup>1</sup> established a subtle first order low temperature phase transition in  $\text{LiKSO}_4$  ( $\sigma_6^6 \rightarrow \sigma_{3v}^4$ ) (at 201 K) using Raman scattering measurements and we have extended our measurements to high temperature region since additional phase transition ( $\sim 700\text{K}$ ) had been proposed for this crystal in the literature<sup>2</sup>.

In extending our measurements upto 725K while we have found evidence that a phase transition does occur around 700K, in addition, we have found two interesting features of vibrational modes in the temperature range between the transition points (crystal symmetry  $\sigma_6^6$ ). These features are: (i) the LO frequency of a  $\nu_2$  mode of  $\text{SO}_4$  appears below its TO counterpart and (ii) the frequency of this LO mode increases with the rise in temperature. Since these are somewhat unusual features we propose to discuss these in greater detail here and except for a brief mention, omit the discussion of the changes pertaining to high temperature phase transition.

In section 2 we describe experimental details and present the spectra. Discussion of the results and a possible explanation for the LO-TO frequency inversion and anomalous temperature dependence of the  $E_1(\text{LO})\nu_2$  mode are given in section 3.

2. **Experimental details.**— Polarized Raman Spectra were recorded using a home made 40 mW He-Cd laser and a grating double monochromator<sup>3</sup> with spectral bandpass of  $3.5\text{cm}^{-1}$ .

For high temperature studies, we used a cell, wherein the sample is mounted mechanically and its three faces are in contact with copper to ensure uniformity of temperature. The temperature was

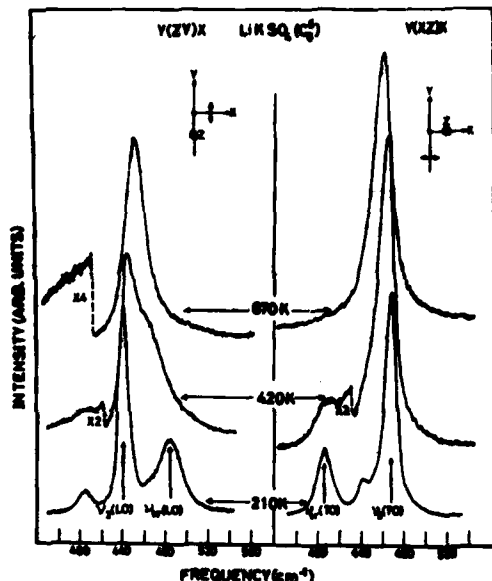


Fig. 1 Raman spectra at different temperatures for two orientations.

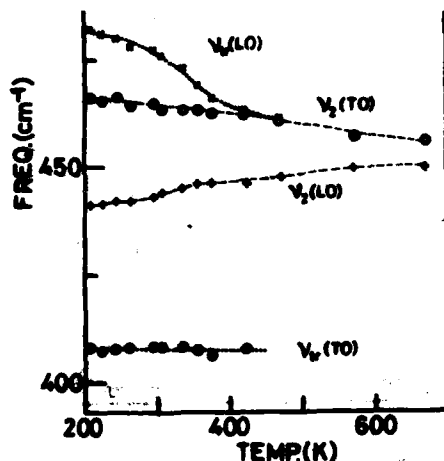


Fig. 2 Frequency variation of modes of Fig. 1 with temperature.

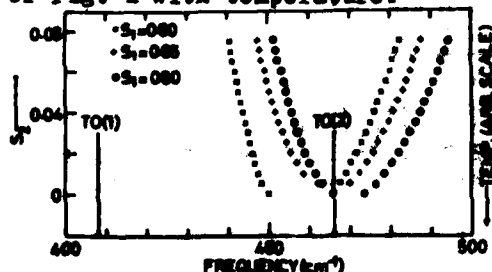


Fig. 3 Dependence of LO frequencies on  $S_1$  &  $S_2$ . Input TO frequencies are also shown.

monitored using a copper constant thermocouple and a proportional temperature controller was used to maintain it constant within  $\pm 0.5^\circ\text{C}$ . The reported temperature values refer to the temperature of the copper block; the sample temperature is somewhat lower (by  $\sim 10\text{K}$  at  $600\text{K}$ ).

**3. Results and Discussion.**— Fig. 1 shows the temperature dependence ( $210\text{K}$ – $675\text{K}$ ) of  $\text{Y}(\text{ZY})\text{X}$  and  $\text{Y}(\text{XZ})\text{X}$  spectra over the frequency range  $400\text{ cm}^{-1}$ – $520\text{ cm}^{-1}$ .  $\nu_{\text{tr}}$  and  $\nu_2$  label modes involving predominantly Li translation and  $\text{SO}_4$  internal vibration respectively. Further as is often the case with Li salts, the ionic conductivity increases considerably with the rise in temperature. So the former mode can be expected to broaden more rapidly with increasing temperature. The assignment of LO modes in Fig. 1 is based on this premise and is different from earlier assignments. Fig. 2 shows plot of frequencies versus temperature. Note that for the  $\nu_2$  mode LO–TO splitting is inverted. The behaviour can be understood using a picture of two nearby oscillators where one of them carries a much larger dipole moment. An approximate expression for the dielectric function, valid in this frequency range is

$$\epsilon(\nu) = \epsilon_{\infty} + \frac{S_1 \nu_{\text{tr}}^2(\nu_0)}{\nu_{\text{tr}}^2(\nu_0) - \nu^2} + \frac{S_2 \nu_2^2(\nu_0)}{\nu_2^2(\nu_0) - \nu^2} \quad (1)$$

The LO frequencies obtained from the series of eqn. (1) for a given set of TO frequencies and oscillator

strengths  $S_1$  and  $S_2$  are given in Table 1. Hiraishi et al<sup>4</sup> give values of  $S_1$  and  $S_2$  from an analysis of their room temperature IR reflection spectra. The values chosen by us at 210K are close to theirs.

The most notable feature about temperature variation of various modes (Figs. 1&2) is that both  $\nu_{tr}(LO)$  and  $\nu_2(LO)$  converge towards  $\nu_2(TO)$  as temperature is increased; the former decreases by  $17\text{cm}^{-1}$  whereas the latter increases by  $6\text{cm}^{-1}$  over the temperature interval 210K-420K. This behaviour can be quantitatively reproduced using eq.(1) assuming a decrease in the value of  $S_2$  from 0.065 to 0.015 (Table 1). In eqn(1), the damping has been neglected and to that extent choice of the initial values of  $S_1$  and  $S_2$  is somewhat uncertain. A glance at Fig.3 clearly shows that for predicting the observed relative shifts of  $\nu_2(LO)$  and  $\nu_{tr}(LO)$ ,  $S_2$  has to decrease with increasing temperature, irrespective of the uncertainty in the initial choice of  $S_1$  and  $S_2$ . Variation of  $S_1$  keeping  $S_2$  fixed leads to simultaneous increase or decrease of both  $\nu_2(LO)$  and  $\nu_{tr}(LO)$ , whereas experimentally  $\nu_2(LO)$  increases and  $\nu_{tr}(LO)$  decreases with increasing temperature. At still higher temperature ( $> 420\text{K}$ ) Li modes can not be traced experimentally but  $\nu_2(LO)$  moves progressively closer to  $\nu_2(TO)$ . Since the  $\nu_2$  mode is IR inactive in the free ion state, this continuous decrease in the oscillator strength implies that the  $\text{SO}_4$  distortion (from tetrahedral shape) diminishes with increasing temperature. Across 700K changes in the Raman spectra occur over the entire frequency range. Further, the widths of most of the modes change abruptly across the transition point. However, as the widths of the peaks are rather large (FWHM even as much as  $40\text{cm}^{-1}$ ) detailed examination of the transition by Raman scattering alone, seems unfeasible and other techniques may be necessary for elucidation of the transition.

Table 1: Observed and calculated LO frequencies (in  $\text{cm}^{-1}$ )

T(K)	obs(TO)	obs(LO)	cal(LO)	
210	408	440	441	$S_1 = 0.50$
	466	480	480	$S_2 = 0.065$
420	408	446	446	$S_1 = 0.50$
	462	463	466	$S_2 = 0.015$

- References.- 1. M.L. Bansal, S.K.Deb, A.P.Roy & V.C.Sahni, Sol. St. Comm., 36, 1047(1980).  
 2. D.P.Sharma, Pramana, 13, 223(1979), and references therein.  
 3. M.L.Bansal, T.R.Rao, V.C.Sahni & A.P.Roy, Ind.J.Phys. 50, 199(1976).  
 4. J.Hiraishi, N.Taniguchi and H. Takahashi, J. Chem. Phys. 65, 3821 (1976).



## A GREEN'S FUNCTION STUDY OF THE U CENTRE IN BaClF AND SrClF

K.R. Balasubramanian and T.M. Haridasan

*School of Physics, Madurai Kamaraj University, Madurai 625021, India*

**Abstract .-** A Green's function investigation of the localized and resonant modes due to U centres in the tetragonal BaClF and SrClF crystals is made for the first time. The lattice Green's functions are computed using the normal modes and eigenvectors obtained on a shell model which explained the long wavelength phonons satisfactorily. The U centre has  $D_{2d}$  point symmetry and the relevant matrices are blockdiagonalised group theoretically. The U centre modes come under E and  $B_2$  representations. The force constant weakening to fit the experimental E mode is 24% whereas for the  $B_2$  mode the weakening is only 12%. These are compared with earlier work on molecular model and on the U centres in fluorites. The possible phonon resonances are also examined and the possibility of their experimental detection is discussed.

**1. Introduction.-** Jumeau<sup>1</sup> observed experimentally the localized modes due to H<sup>-</sup> ion substitution in the tetragonal crystals of BaClF and SrClF. It was established that the H<sup>-</sup> ion enters the F<sup>-</sup> ion site. As it is customary to denote this point defect as U centre in alkali halides and fluorites we shall label this centre in these crystals also as U centre. Kalyani et al.<sup>2</sup> employed a molecular model to account for these modes. Since the lattice dynamics of these crystals has been discussed recently by the present authors<sup>3</sup> on the basis of a shell model, we thought it worthwhile to use a Green's function formalism to investigate these localized modes in BaClF and SrClF. We shall report the results of such an investigation in this paper.

**2. Theory.-** The localized modes due to point defect are obtainable from the solutions of the determinantal equation  $|I - g(\omega)\{f(\omega)\}| = 0$  by seeing to which value of  $\omega$  this condition is satisfied. Here  $g(\omega)$  is the lattice Green's function matrix of the host lattice in a partitioned space constituted by the U centre and its immediate neighbours with which it interacts directly.  $f(\omega)$  is the matrix denoting the force constant changes. So knowing  $g$  and  $f$  as functions of  $\omega$  we can use the above criterion to obtain the

defect modes. In the present case of BaClF and SrClF, they are tetragonal crystals with six atoms per unit cell. The dynamics of these crystals have been investigated by us on a shell model where the parameters were transferred suitably from corresponding parameters of  $\text{SrF}_2$  and  $\text{SrCl}_2$ . Such a model explained the long wavelength optic phonons fairly well. We have used this model to work out the phonons and their polarisation vectors at 1000 wavevector points in the Brillouin zone and these data are used in the computation of the relevant Green's functions.

If we look at the U centre it is surrounded by 4  $\text{Sr}^{++}$  ions as first neighbours, 4  $\text{F}^-$  ions as second neighbours and 4  $\text{Cl}^-$  ions as third neighbours. It is fairly realistic to assume that the change in force constants happens only between the U centre and the first neighbours. Thus  $g$  and  $\delta l$  would be of dimension (15x15). But since the U centre has the site symmetry of  $D_{2d}$  the following irreducible representations are possible.

$$\Gamma_{15} = 2A_1 + A_2 + B_1 + 3B_2 + 4E$$

The U centre modes come under the E and  $B_2$ .

Using group theory both the  $g$  and  $\delta l$  matrices are blockdiagonalized. The  $\delta l$  matrix involved only one unknown parameter  $\Delta A$ , which represents the force constant change between the U centre and its first neighbours.

**3. Calculations and results.**— The relevant determinants of the E and  $B_2$  blocks are calculated for various  $\omega$  values for a specific percent change of the force constant change ( $\Delta A/A$ ). The value of  $\omega$  for which the determinant vanishes is picked. This is repeated for different percentage of the force constant changes. A graph between the percentage of force constant change and the value  $\omega$  for vanishing determinant is drawn and from this the percent age change of force constant required to fit the experimental local mode frequency is obtained. The percentage force constant softening to fit the local mode under E representation came up to be 24% whereas the corresponding softening for the  $B_2$  mode was only 12%. We had extended the defect space to include the second and third neighbours in subsequent calculations. The trend of the results even with the extended space remains the same. The force constant weakening obtained in the present calculation is smaller than obtained by Kalyani et al in their molecular model calculations, but are of the same range as obtained by Hayes and Wirtshire<sup>4</sup> for the U centres in fluorites. Our also notices that the force constant softening obtained for the E mode does not

explain perfectly the  $B_2$  mode and vice-versa. It is felt that one should obtain the relaxations of the host atoms due to the U centre first and try to incorporate these relaxations in future calculations for obtaining force constant softening in order to explain the E and  $B_2$  mode simultaneously to the same degree of accuracy. However, such an investigation should await until more refined and realistic potential functions for the interatomic interaction in such crystals emerge. Nevertheless, with the present force constant weakening obtained from the localized mode studies the resonant modes under various irreducible representations are also computed. The condition of vanishing determinant followed by the estimation of the widths of such potential resonances gave us the following results. No resonances could be obtained for the  $A_1, A_2$  and  $B_1$  representations. A resonance at  $281 \text{ cm}^{-1}$  was obtained in SrClF for 24% force constant weakening under E representation. The corresponding resonance in BaClF was at  $257 \text{ cm}^{-1}$  for both 24% and 1% weakening. A low frequency resonance at  $25 \text{ cm}^{-1}$  was also obtained for SrClF alone with 24% softening under the  $B_2$  representation. At present there is no experimental data for comparison. However, the present estimation would give the region where one should look for such resonances either by optical spectroscopy or neutron spectroscopy.

#### References.

1. Jumeau, D., J. Phys. Chem. Solids **37**, 465 (1976)
2. Kalyani, S., Haridasan, T.M. and Krishnamurthy, N., Proc. Internat. conf on Lattice Dynamics (Flammarrion) p409 (1977)
3. Balasubramanian, K.R. and Haridasan, T.M. J. Phys. Chem. Solids In press (1981)
4. Hayes, W. and Wirtshire, M.C.K., J. Phys. C. (Solid state), **6**, 1149 (1973).

## PHONON DISPERSIONS IN CALCIUM TUNGSTATE

N. Krishnamurthy and K. Kesavasamy

*School of Physics, Madurai Kamaraj University, Madurai, India*

**Abstract:** External mode formalism is applied to study phonons in  $\text{CaWO}_4$ . The effective ionic charges of the Coulomb interactions and the effective ionic radii of Born-Mayer shortrange potential are determined so that the dynamical equilibrium conditions are satisfied and lattice energy is of right order in comparison with other complex ionic crystals. The calculated phonon dispersion relations along  $[001]$  and  $[110]$  directions are in reasonable agreement with the neutron data. The generalised LST relations computed with our model agree with the IR data. Zone centre phonons in few other scheelites are also investigated and compared with experimental data to study the influence of polarisability and a possible breakdown of external mode formalism.

1. Introduction:-  $\text{CaWO}_4$  belongs to  $(\text{C}_{6h}^2)$  with two formula groups in the primitive cell. The optical and neutron data are available<sup>1</sup>. Elastic properties have been studied experimentally and theoretically with Steinman et al's model parameters<sup>2</sup>. On the theoretical aspects of phonons, Kannamori et al. studied<sup>3</sup> the translational modes alone, ignoring the librations of tungstate ions and long range Coulomb inter-

Fig. 1. Phonon Dispersion along  $(00q)$   
 Theoretical —  $B_g$ ; ----  $A_g$ ; -.-.-  $E_g$   
 Experimental O  $B_g$ ; ●  $E_g$ ; +  $A_g$

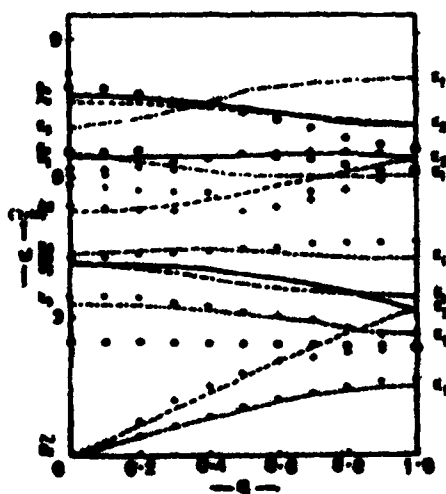


Fig. 2. Phonon Dispersions along  $(qq0)$   
 Theoretical -.-.-  $\Sigma_1$ ; ----  $\Sigma_2$   
 Experimental O acoustical; ● optical

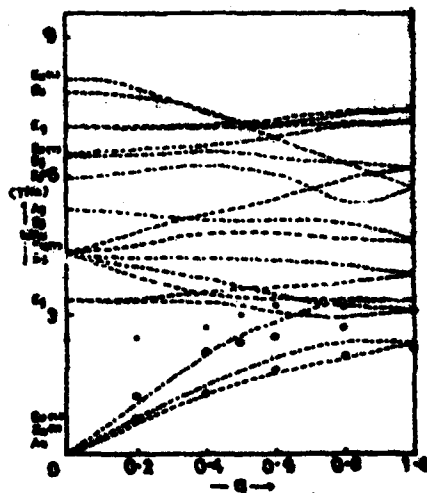


Table 1. Zone centre phonon frequencies in other scheelites (THz)

Effective radii (Å)  $R_{Ca}=1.50$ ;  $R_{Sr}=1.55$ ;  $R_{Pb}=1.60$ ;  $R_{Ba}=1.65$ ;  $R_{Mo}=0.80$ ;  $R_W=0.80$  and  $R_O=1.75$ Effective charges  $Z_{Ca}, Z_{Sr}, Z_{Pb}$  and  $Z_{Ba} = 1.55$ ;  $Z_{Mo}$  and  $Z_W = 0.33$ ;  $R_O = -0.47$ 

Mode	CaMoO <sub>4</sub>		SrMoO <sub>4</sub>		BaMoO <sub>4</sub>		BaMoO <sub>4</sub>		PbMoO <sub>4</sub>		PbMoO <sub>4</sub>			
	expt. [6]	cal.	expt. [6]	cal.	expt. [6]	cal.	expt. [6]	cal.	expt. [6]	cal.	expt. [6]	cal.		
A <sub>g</sub>	6.15	5.30	5.76	4.79	5.52	4.89	5.85	3.98	5.67	4.15	5.24	4.69	4.92	4.21
B <sub>u</sub>	---	7.81	---	7.05	---	7.20	---	6.05	---	6.32	---	6.97	---	7.71
B <sub>g</sub>	6.57	6.45	---	4.04	4.71	4.32	2.28	2.94	3.03	3.21	2.28	3.26	2.25	3.81
B <sub>g</sub>	3.30	5.13	2.28	3.39	2.94	3.99	2.01	2.47	2.07	2.92	1.56	2.66	1.92	2.65
A <sub>u</sub>	5.88	4.45	3.75	2.71	4.50	2.94	3.30	1.97	3.60	2.21	2.76	2.20	2.70	3.12
A <sub>u</sub> (L)	5.91	7.89	---	5.13	---	5.53	---	3.97	---	4.41	---	3.93	---	4.76
E <sub>g</sub>	7.89	7.13	4.05	5.61	4.23	5.77	4.65	4.07	4.80	4.29	5.61	5.27	5.70	5.40
E <sub>g</sub>	5.67	4.48	3.06	2.87	3.42	3.58	3.09	2.11	3.45	2.60	2.58	2.66	3.00	2.32
E <sub>g</sub>	4.35	3.92	2.28	2.56	2.94	2.60	2.28	1.42	3.03	1.52	1.83	1.63	1.83	1.22
E <sub>u</sub>	6.24	6.56	4.95	5.13	5.25	5.20	4.05	3.65	4.35	3.66	7.92	4.81	8.10	3.37
E <sub>u</sub>	4.50	4.27	3.54	2.67	3.84	2.89	2.94	1.48	3.24	1.76	3.60	1.97	3.24	1.51
E <sub>u</sub> (L)	4.68	5.78	---	4.75	---	4.82	---	3.58	---	3.62	---	3.76	---	3.18
E <sub>u</sub> (L)	7.83	8.38	---	5.47	---	5.83	---	3.82	---	4.23	---	4.84	---	4.05
q  c	2.84	3.14	---	3.58	---	3.54	---	4.06	---	3.98	---	3.19	---	2.33
q  b	2.43	2.99	---	3.60	---	3.50	---	6.41	---	5.65	---	3.69	---	6.41

actions. We take into account the inertia of ungstate ions, the long range Coulomb interactions in our computations based on the external mode formalism<sup>4</sup>.

2. Model and Results:- Following Rao et al.<sup>5</sup> we employ Born-Mayer shortrange potential, in addition to Coulomb potential.

$$V(r_{12}) = \frac{1}{4\pi\epsilon_0} \frac{Z_1 Z_2 e^2}{r_{12}} + a \exp \left[ \frac{-13.6}{1.1(R_1 + R_2)} r_{12} \right] \quad (1)$$

where  $a = 1822$  eV. The ionic charges and radii are the parameters of the model.

For  $Z_{Ca} = 1.55$ ,  $Z_W = 0.33$  and  $Z_O = -0.47$ ;  $R_{Ca} = 1.50$ ;  $R_W = 0.80$  and  $R_O = 1.75$ , it is found that there is a reasonable balance between long range and shortrange forces to satisfy dynamical equilibrium conditions and the cohesive energy is of the right order (-30.2 eV). With this set of parameters the dynamical matrix is solved, using group theoretical expressions,<sup>6</sup> for points along (00q) and (qq0) and plotted in Figs 1 & 2. In both directions all branches are explained satisfactorily, except the low  $B_g$  mode. This is understandable, as rigid ion model usually predicts a higher value for the frequency of longitudinal optical mode. The generalized LST relations<sup>6</sup> are also reasonably explained with the present model. The ratios of static dielectric constant to high frequency dielectric constant are 3.09(2.77) and 2.97(3.06) for q1c and q1b respectively where the experimental values are given in brackets.

In view of the reasonable success, the model is applied to study phonons in other scheelites and the results are compiled in Table 1. We find that the phonons in most of the scheelites can be explained satisfactorily excepting those in  $PbWO_4$  and  $PbMoO_4$  presumably due to ambiguities<sup>6</sup> in the optical data in these crystals. From the knowledge of polarisability of the ions<sup>6</sup> and external-internal modes separation we conclude that any further refinement may be possible only in  $SrWO_4$  and  $SrMoO_4$ , as both noninclusion of polarisability and decoupling of external-internal modes are not serious in these crystals. It is believed that this report will be, particularly, useful for the measurements of phonon spectra in (qq0) direction of  $CaWO_4$ . One of us (KK) thanks CSIR (India) for the award of a Senior Research Fellowship.

#### References:-

1. Steinman, D. K., King, J. S. and Smith, H. G. Intern. Conf. IAEA (SM/155/B-4), Grenoble, France, p.219 (1972).
2. Kesavasamy, K. and Krishnamurthy, N., Z. Phys. **B41**, 95 (1981).
3. Kanamori, H., Hayashi, S. and Ikeda, Y., J. Phys. Soc. (Japan) **36**, 511 (1974).
4. Venkatraman G. and Sahni, V. C., Rev. Mod. Phys. **42**, 409 (1970).
5. Rao, K. R., Chaplot, S. L., Iyengar, P. K., Venkatesh, A. H. and Vijayaraghavan, P. R., Pramana, **11**, 251 (1978).
6. Kesavasamy, K. and Krishnamurthy, N., Z. Physik B (Communicated).

## THE DIELECTRIC FUNCTION MATRIX AND THE LATTICE DYNAMICS OF KCl

M.A. Ball and W.N. Leung

D.A.M.T.P., University of Liverpool, Liverpool L69 3BX, U.K.

**Abstract.** - The RPA dielectric function matrix of KCl is calculated with a model in which the valence band consists of p-states on the Cl atoms and the conduction bands are either (i) a single OPW band or (ii) two OPW bands. Local field effects are approximately included. Results for the diagonal, some off-diagonal elements and the effective charges are presented. The long-range parts of the dynamical matrix are got from the calculations; the short-range parts are obtained by fitting to the transverse frequencies.

We report some model calculations of the dielectric function matrix  $\epsilon(\underline{q} + \underline{g}, \underline{q} + \underline{g}')$  of the ionic crystal KCl, including results for the diagonal and some off-diagonal elements. We also show how the dynamical matrix can be expressed in terms of these results.

The dielectric function  $\epsilon$  is given in the R.P.A. by

$$\epsilon(\underline{q} + \underline{g}, \underline{q} + \underline{g}') = \delta_{\underline{g}\underline{g}'} - \frac{4\pi e^2}{\tau|\underline{q} + \underline{g}|^2} \frac{2}{N} \sum_{\underline{k}, n_1, n_2} \frac{\langle \psi_{n_2 \underline{k}} | \exp[-i(\underline{q} + \underline{g}) \cdot \underline{r}] | \psi_{n_1 \underline{k} + \underline{q}} \rangle}{\langle \psi_{n_1 \underline{k} + \underline{q}} | \exp[i(\underline{q} + \underline{g}') \cdot \underline{r}] | \psi_{n_2 \underline{k}} \rangle} \frac{(f_{n_1 \underline{k} + \underline{q}} - f_{n_2 \underline{k}})}{E_{n_1 \underline{k} + \underline{q}} - E_{n_2 \underline{k}}} \quad (1)$$

where the sum is over the first Brillouin zone and the occupied and unoccupied bands  $n_2$  and  $n_1$  respectively. The most important of these bands are the uppermost valence (p-) band and the lowest conduction band. Fry /1/ and Lipari /2/ use for the valence band tight-binding wave-functions with p-like states centred on the Cl atoms.

$$\psi_{\underline{mk}}(\underline{r}) = \frac{1}{\sqrt{N}} \sum_{\underline{j}} \exp[i\underline{k} \cdot \underline{R}_{\underline{j}}] U_{\underline{pm}}(\underline{r} - \underline{R}_{\underline{j}}) \quad (2)$$

$$U_{\underline{po}}(\underline{r}) = ((2\delta)^5/24)^{1/2} \exp[-\delta r] \quad (3)$$

The exponent  $\delta$  in  $U_{\underline{po}}(\underline{r})$  is a parameter.

For the conduction band energies and wave-functions two separate models were used: -

(i) Only one band was considered, this being a parabolic (s-) band derived from a single orthogonalized plane wave (OPW)

$$E_c(\underline{k}) = E_c^0 + \alpha |\underline{k}|^2 \quad (4)$$

$$\psi_{c\underline{k}}(\underline{r}) = (a \frac{i\underline{k} \cdot \underline{r}}{(N\tau)^{1/2}} - \sum_{\underline{l}} \mu_{\underline{kl}} \psi_{\underline{lm}}(\underline{r}))/N(\underline{k}) \quad (5)$$

where  $N(k)$  is a normalization factor and  $\mu_{km}$  is the orthogonalization coefficient.

(ii) In this model two bands (s- and d-) were included; -

$$\psi_{sk} = \alpha_{k,g} \psi_{ck}(\underline{r}) + \beta_{k,g} \psi_{c(k+g)}(\underline{r}) \quad (6)$$

$$\psi_{dk} = \beta_{k,g} \psi_{ck}(\underline{r}) - \alpha_{k,g} \psi_{c(k+g)}(\underline{r}) \quad (7)$$

The reciprocal-lattice vector  $\underline{g}$  in (6) and (7) depends on  $\underline{k}$ .

Tight-binding expressions were used for the energies and the coefficients  $\alpha$  and  $\beta$  were determined by fitting to these energies. The advantage of this model over (i) is that it takes Brillouin Zone boundary effects into account.

The energy parameters in (i) and (ii) were determined by fitting to the energy-band calculations of Kunz /3/. The dielectric function  $\epsilon$  is then calculated by numerical integration over the first Brillouin Zone. This is more realistic than the procedures of Fry /1/ and Lipari /2/.

To invert the dielectric matrix, the following approximate formulae are used:-

$$1/\epsilon^{-1}(\underline{q}, \underline{q}) = \epsilon(\underline{q}, \underline{q}) - \sum_{\underline{g}} \epsilon(\underline{q}, \underline{q} + \underline{g}) \epsilon(\underline{q} + \underline{g}, \underline{q}) / \epsilon(\underline{q} + \underline{g}, \underline{q} + \underline{g}) \quad (7)$$

$$\epsilon^{-1}(\underline{q}, \underline{q} + \underline{g}) = -\epsilon^{-1}(\underline{q}, \underline{q}) \epsilon(\underline{q}, \underline{q} + \underline{g}) / \epsilon(\underline{q} + \underline{g}, \underline{q} + \underline{g}) \quad (8)$$

The parameter  $\delta$  in  $U_{po}(\underline{r})$  is determined by setting  $1/\epsilon^{-1}(0,0)$  equal to the experimental value. As the second term in (7) incorporates some of the local-field corrections, our calculation does include these approximately. Using 52 reciprocal lattice vectors, these corrections change the results by approximately 6% and 7% with models (i) and (ii) respectively. Some of our calculations are presented in Figs. 1 & 2. In these exchange and correlation have as yet been neglected.

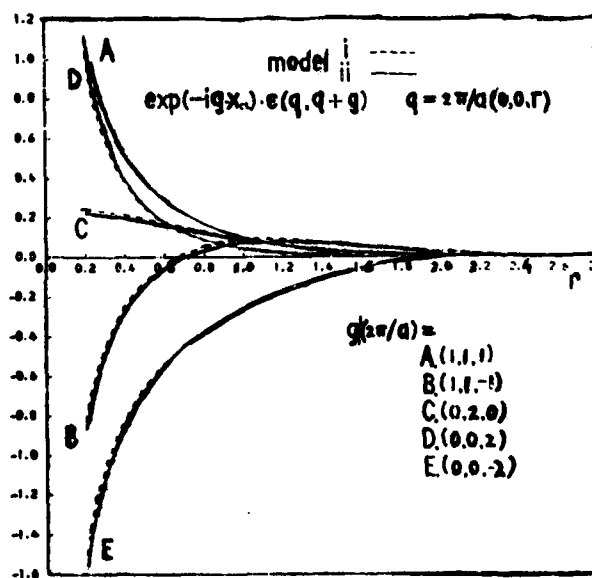


Fig. 1 Off-diagonal elements

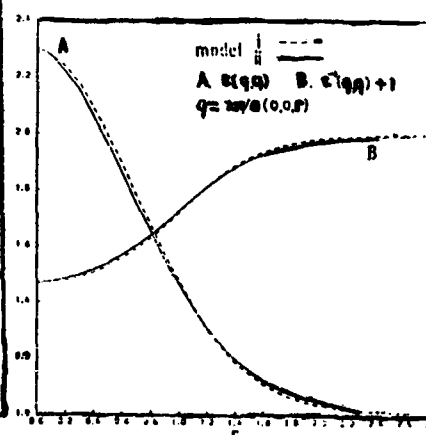


Fig. 2 (A)  $\epsilon(q, q)$ ; (B)  $\epsilon^{-1}(q, q) + 1$



A sensible test of our calculations of  $\epsilon$  is provided by the lattice dynamics. The effective charge tensor  $Z_{\alpha}^{\text{eff}}(\kappa)$  of an ion of type  $\kappa$  is got from the  $q \rightarrow 0$  limit of  $Z(q, \kappa)$ , the effective charge vector, where

$$Z_{\alpha}(q, \kappa) = \frac{-i}{v(q)} (q_{\alpha} W(q, \kappa) + \sum_{\underline{g}} \frac{\epsilon^{-1}(\underline{q}, \underline{q} + \underline{g})}{\epsilon^{-1}(\underline{q}, \underline{q})} W(\underline{q} + \underline{g}, \kappa) (q + \underline{g})_{\alpha} \exp[-i \underline{g} \cdot \underline{R}(\kappa)]) \quad (9)$$

and  $W(q, \kappa)$  is the unscreened pseudopotential. As a first approximation this has been taken as  $-Z(\kappa)v(q)$  with  $Z(\text{Cl}) = 5$  and  $Z(\text{K}) = 1$ . Our calculations give  $Z^{\text{eff}}(\text{Cl}) = -0.96(i), -1.24(ii)$  and  $Z^{\text{eff}}(\text{K}) = 1.21(i), 1.20(ii)$ . These results compare favourably, considering the approximations made, with the experimental values of  $\pm 1.123$ .

The dynamical matrix is

$$D_{\alpha\alpha'}(\underline{q}; \kappa, \kappa') = \frac{(M(\kappa)M(\kappa'))^{1/2}}{\tau} \{ \exp[i \underline{q} \cdot (\underline{R}(\kappa) - \underline{R}(\kappa'))] Z_{\alpha}^{*}(\underline{q}, \kappa') Z_{\alpha'}(\underline{q}, \kappa) v(q) \epsilon^{-1}(\underline{q}, \underline{q}) + (T_{\alpha\alpha'}(\underline{q}; \kappa, \kappa') - \delta_{\kappa\kappa'} \sum_{\kappa''} \tau_{\alpha\alpha''}(0; \kappa, \kappa'')) \} \quad (10)$$

in the notation of Sham /4/. In (10) the first and second terms represent the long- and short-range effects respectively. The latter can be described by the Lorentz field effect and some short-range force constants. These determine completely the transverse phonons, which can almost be fitted with two (the nearest-neighbour) parameters and can be fitted to within 5% by using 5 parameters.

At present we are trying to calculate the longitudinal frequencies using the above short-range forces and our calculated values of  $Z(q, \kappa)$  and  $\epsilon^{-1}(q, q)$ . We have added a small constant to  $Z(q, \text{Cl})$  to ensure that the acoustic sum rule is satisfied. At small  $q$  our results are reasonable but at larger values there is a large variation in  $Z(q, \text{Cl})$ , giving rise to imaginary frequencies. We are investigating the causes of this.

- /1/ Fry, J.L., Phys. Rev. 179 (1969) 892.
- /2/ Lipari, N.O., J. Chem. Phys. 53 (1970) 1040.
- /3/ Kunz, A.B., Phys. Rev. 175 (1968) 1147.
- /4/ Sham, L.J., Dynamical Properties of Solids I (1974) ed. by G.K. Horton and A.A. Maradudin (North-Holland, Amsterdam).

# CALCULATION OF DEFECT ENTROPIES IN IONIC CRYSTALS IN THE QUASIHARMONIC APPROXIMATION : APPLICATION TO FLUORITES

P.W.M. Jacobs, M.A.H. Nerenberg, J. Govindarajan and T.M. Haridasan

University of Western Ontario, London, Ontario, Canada N6A 5B7

**1. Outline of Theory** The dynamical matrix for a crystal containing an interstitial can be written in the form

$$\bar{L} = \begin{vmatrix} L & -\delta L & A \\ A^T & & \Lambda \end{vmatrix} \quad (1)$$

where  $L$  is the dynamical matrix of the perfect crystal,  $\Lambda$  is that part of  $L$  that refers exclusively to the interstitial and  $A$  is the matrix that connects the interstitial coordinates with those of the rest of the lattice.  $A^T$  is the transpose of  $A$ .  $\delta L$  is the matrix that describes the force constant changes which occur because of the relaxations of the lattice ions due to the presence of the interstitial. The Green matrix  $\bar{G} = \bar{L}^{-1}$  may also be written in partitioned form like that in (1), whence it may be shown that the determinant of  $\bar{G}$  is

$$|\bar{G}| = |I - G \delta L'| |G| |\Lambda|^{-1} \quad (2)$$

where  $\delta L' = \delta L + \Lambda \Lambda^{-1} A^T$  and  $I$  is the  $3N \times 3N$  unit matrix,  $N$  being the number of atoms in the crystal. Since static lattice calculations show that relaxations of the lattice ions are small except for the first and second neighbours, the non-zero elements of  $\delta L$  will be restricted to a small sub-space comprising these  $n$  ions that are perturbed appreciably by the interstitial. It then follows that

$$|I - G \delta L'| = |I - g \delta l'| \quad (3)$$

where  $I$  on the RS of (3) is now the  $3n \times 3n$  unit matrix.

$$\delta l' = \delta l + \Lambda^{-1} a^T \quad (4)$$

where

$$A = \begin{vmatrix} 0 \\ a \end{vmatrix} \quad (5)$$

and the dimensions of the matrix  $a$  are  $3n \times 3$ .

The entropy change associated with the introduction of an anion from  $\infty$  into an interstitial position in the high-temperature approximation may then be written in the form

$$s_1 = -\frac{1}{2} k \ln \lim_{\omega \rightarrow 0} |I - g \delta l'| + 3k \{1 - \ln (\hbar \omega_1 / kT)\} \quad (6)$$

where  $\omega_1$  is the hypothetical frequency of vibration of an interstitial in a lattice in which all the host-lattice ions are frozen at their (perfect lattice) equilibrium positions. In similar fashion the dynamical matrix of a crystal with a vacancy is

$$\bar{L}_v = L_c - \delta l \quad (7)$$

where  $L_c$  is the dynamical matrix  $L$  of the crystal without a vacancy, truncated by removing the three rows and columns belonging to the ion which is no longer present.  $\delta l$  is the matrix of force constant changed due to the relaxations of the ions caused by the vacancy. It includes as well the changes in the "self-terms" of the ions because of the removal from these sums the contributions due to the ion which has now been removed. By partitioning  $\bar{L}_v$ , and also the perfect crystal dynamical matrix  $L$ , into blocks such that one of the diagonal blocks of  $\bar{L}_v$  represents the 'defect space' (that is those ions that are perturbed by the presence of the vacancy - in practice this means its first and second neighbours) and the corresponding block of  $L$  represents the defect space-to-be (including the ion that will become a vacancy) it may be shown that the entropy change associated with the removal of a lattice anion to  $\infty$  is

$$s_v = -k \ln \lim_{\omega \rightarrow 0} \{ m^3 |g_v| | (g_v^{-1})_t - \delta l | (kT/h)^6 \} - 3k \quad (8)$$

The entropy of formation of a Frenkel defect is thus given by

$$s_F = s_i + s_v \\ = -k \ln \lim_{\omega \rightarrow 0} \{ |g_v| | (g_v^{-1})_t - \delta l | | I - g \delta l' | m^3 \omega_I^6 \} \quad (9)$$

In these expressions  $m$  is the mass of an anion,  $g_v$  is the perfect-lattice Green matrix for the defect space-to-be and  $(g_v^{-1})_t$  is the truncated version of the reciprocal of  $g_v$  (that is, with the 3 rows and columns deleted that correspond to the ion which is to be removed when the vacancy is found). We may not multiply out the first product of determinants in (9) since the operations of truncation and inversion do not, in general, commute.

**2. Calculation** The necessary Green functions were evaluated using shell model parameters fitted to the experimental phonon dispersion. These parameters were taken from the work of Elcombe and Pryor<sup>1</sup> and Elcombe<sup>2</sup>. For the calculation of  $\delta l$  we require the coordinates of the ions in the imperfect crystal which were obtained from the HADES program.<sup>3</sup> The changes in the short-range interaction were restricted to second neighbours, but in the calculation of the self-terms in the  $\delta l$  matrix, it was necessary to ensure that each ion had its full complement of first and second neighbours, even though these neighbours might lie outside the defect space. The short-range force constants were calculated using the two-body central potential of Catlow, Morgett and Ross<sup>4</sup>. The change in the coulomb interaction was calculated only between the ion at the origin (which later became the site of the vacancy) and its first and second neighbours (Benedek<sup>5</sup>). The defect space comprising the interstitial and its first and second neighbours consisted of 15 ions, but 95 ions had to be taken into account while calculating the diagonal terms of  $\delta l$ . The change in the coulomb force between the interstitial and only its first and second neighbours was included. Additionally, the presence of the interstitial is felt through the terms  $\Lambda^{-1} a^T$ , where  $\Lambda^{-1}$  was calculated from the self term of the interstitial.

The calculation is a quasiharmonic one in that the actual lattice parameter at each  $T$  was used in determining the relaxations of the ions. The Green matrix at each  $T$  was obtained by a scaling procedure<sup>6</sup>. This calculation yields an entropy of

Frenkel defect formation at constant volume,  $s^v$ . For comparison with experiment we need the corresponding entropy at constant pressure  $s^p$ . Since to first order in  $v^p$ , the volume change on forming a Frenkel defect at constant pressure, the Gibbs energy change  $g^p$  is equal to the Helmholtz energy change  $f^v$ ,  $s^p$  is related to by  $s^v$  by

$$s^p - s^v = - \left( \frac{\partial f^v}{\partial v} \right) \beta^p v \quad (10)$$

where  $v$  is the volume per molecule ( $=2r_0^3$ ,  $r_0$  being the  $F^- F^-$  nn distance) and  $\beta^p$  the expansivity. Since both the energy and entropy of defect formation at constant volume  $u^v$  and  $s^v$  are determined by our calculations,  $f^v$  and  $s^p$  may be found and compared with experimental values.

### 3. Results

CaF <sub>2</sub>	T/K	300	1000	1500	
	s <sup>v</sup> /k	0.73	2.88	5.30	
	s <sup>p</sup> /k	8.83	13.30	18.42	
SrF <sub>2</sub>	T/K	300	600	900	(1200) <sup>a</sup>
	s <sup>v</sup> /k	4.49	3.64	3.34	(2.97)
	s <sup>p</sup> /k	5.74	5.68	5.28	(4.15)

<sup>a</sup>Based on extrapolated values.

For CaF<sub>2</sub><sup>a</sup> the mean calculated value of  $s^p$  in the range 550 - 1000 K is ~0k, and the experimental value of  $s^p$  is about 5 k.<sup>a</sup> For SrF<sub>2</sub>  $s^p$  (expt) = 4.1 k in the range ~570 - 1100 K, and the calculated value of  $s^p$  is about 5 k. The quasiharmonic calculation depends critically on a knowledge of the temperature dependence of the lattice constant.

**Acknowledgement:** We acknowledge support of this research by the Natural Sciences and Engineering Research Council of Canada. T.M.H. is grateful to the Centre for Inter-disciplinary studies in Chemical Physics for the award of a Fellowship and for further financial support, and to Madurai Kamaraj University for leave of absence. We are most grateful to Dr. A.B. Lidiard and Dr. M. Hutchings for data on the lattice constant of CaF<sub>2</sub>.

### References

1. Elcombe M.M. and Pryor A.W., J.Phys. C (Solid State) **3**, 492 (1970).
2. Elcombe M.M., J.Phys. C (Solid State) **5**, 2702 (1972).
3. Norgett M.J., AERE Harwell Report R 7650 (1974).
4. Catlow C.R.A., Norgett M.J. and Ross T.A., J.Phys. C **10**, 1627 (1977).
5. Benedek G., Physics of Impurity Centres in Crystals (Tallinn), P.182 (1972).
6. Naridasan T.M., Govindarajan J., Harenberg M.A.H. and Jacobs P.W.M., J.Phys. C **12**, 5371 (1979).
7. Gillen M.J., Phil. Mag **43A**, 301 (1981).
8. Ong S.H. and Jacobs P.W.M., J.Phys. (Paris) **37**, C7-331 (1976).
9. Jacobs P.W.M. and Ong S.H., in course of publication.

## LIBRATIONAL MODES OF WATER IN CRYSTAL HYDRATES AND PHASE-TRANSITIONS

M.B. Patel and H.D. Bist

Department of Physics, Indian Institute of Technology, Kanpur-India

**Abstract:** Temperature dependence of infrared active librational modes of water in polycrystalline  $M(\text{ClO}_4)_2 \cdot 6\text{H}_2\text{O}$  ( $M=\text{Mg}$  and  $\text{Zn}$ , respectively) shows phase transitions at 225.5, 193 and 110 K in the former and at 284, 256.5 and 233K in the latter.

1. **Introduction.** In the isomorphous metal perchlorate hexahydrates<sup>1</sup> of general formula  $M(\text{ClO}_4)_2 \cdot 6\text{H}_2\text{O}$ , where  $M=\text{Mg}$ ,  $\text{Fe}$ ,  $\text{Co}$ ,  $\text{Ni}$  and  $\text{Zn}$ ; the Mössbauer<sup>2,3</sup>, magnetic susceptibility and anisotropy<sup>4</sup>, and EPR<sup>5,6</sup> studies have revealed that these systems undergo one (or more) phase transition(s) between 80-373K. There are two different views regarding the change in the perchlorate crystal structure at the phase transition (PT) below room temperature (RT). According to Mössbauer studies<sup>2,3</sup>, the water octahedron surrounding the metal ion in the crystal is trigonally stretched at higher temperature (HT) and it becomes trigonally compressed at lower temperatures (LT) after the PT. According to Choudhuri<sup>4</sup>, the water octahedron trigonally stretched at HT becomes tetragonally compressed after the PT, thus involving a structural change. However, EPR studies<sup>5</sup> show supporting evidence to one or another view point in the same series below and above RT<sup>6</sup>. Ross has reported the fundamental modes of  $\text{ClO}_4^-$  ion in various anhydrous and hydrated perchlorates.<sup>7</sup> No data are available for librational modes of water in hydrated perchlorates, except  $\text{LiClO}_4 \cdot 3\text{H}_2\text{O}$ <sup>8</sup> and  $\text{Zn}(\text{ClO}_4)_2 \cdot 6\text{H}_2\text{O}$ <sup>9</sup>. We have undertaken the study of water modes in perchlorates with a view to understand the dynamics of PT and the relative significance of polyatomic anions, water dipoles and cations for affecting the PT.

2. **Experimental.**  $\text{Mg}(\text{ClO}_4)_2 \cdot 6\text{H}_2\text{O}$  (MPHH) is prepared dissolving magnesium carbonate in dilute perchloric acid and purified by reported procedure<sup>9</sup>. Infrared spectra at RT and LT were taken by the KBr pellet technique using a Perkin Elmer 590 spectrophotometer and Specac variable temperature cell fitted with its automatic temperature control unit. The relevant bands are reported in Table 1.

3. **Results and Discussion.** The librational assignments are based on: (I) comparison of hydrated (RT & LT) spectra and anhydrous MPHH (Table 1A) showing that the bands at 602, 485, 423, 380 & 360  $\text{cm}^{-1}$  are the bands due to water molecules and at 640, 630 ( $\nu_4^p$ ) and 457  $\text{cm}^{-1}$  ( $\nu_2^p$ ) that of  $\text{ClO}_4^-$  ion; (II) the bands at 602, 485, 423 and 360  $\text{cm}^{-1}$  are assigned as rocking (R), wagging (W), twisting

TABLE 1. Observed bands in the IR spectrum of (A) hydrated and anhydrous and (B) partially deuterated magnesium perchlorate.

(A)						(B)						
Hydrated		Anhydrous		Assign- ment		Partially Deuterated					Assign- ment	
LT	RT	LT	RT			LT	RT		RT			
$\nu(\text{cm}^{-1})$	$\nu(\text{cm}^{-1})$	$\nu(\text{cm}^{-1})$	$\nu(\text{cm}^{-1})$			H <sub>2</sub> O	HOD	D <sub>2</sub> O	H <sub>2</sub> O	HOD	D <sub>2</sub> O	
360	40	356	23	--	M-O	360	351	345	355	--	--	M-O
380	21	--	--	--	M-O <sub>w</sub>	380	375	370	--	--	--	M-O <sub>w</sub>
423	31	--	--	--	T <sub>w</sub>	423	382	290	--	--	--	T <sub>w</sub>
457	13	--	--	461	v <sub>2</sub> <sup>p</sup>	485	450	335	470	445	330	W
485	100	470	100	--	W <sub>2</sub>	602	523	420	605	505	423	R <sub>w</sub>
602	85	605	73	--	R	1633	1441	1208	1634	1442	1209	v <sub>2</sub> <sup>w</sup>
630	26	630	18	630	v <sub>4</sub> <sup>p</sup>	2240	1945	--	2242	1950	--	v <sub>2</sub> +R
640	25	640	16	639								

(T) and M-O<sub>w</sub>, respectively, on the basis of intensity (I)<sup>8</sup>, sequence of frequency ( $\nu$ )<sup>8</sup>, frequency shift on partial deuteration<sup>8</sup> (Table 1B), expected M-O<sub>w</sub> vibration<sup>10</sup> of transition metal-aquo complexes, and (III) a new criterion using a combination band (of the bending & rocking modes of bound water) at 2235 cm<sup>-1</sup> corroborating that the 602 cm<sup>-1</sup> band is due to the R modes of water. Similar studies were made in ZPHN and have been discussed earlier<sup>9</sup>.

For structural studies of MPFH isotopic dilution technique<sup>11</sup> was used. Figure 1 shows the bands due to OD stretching fundamentals of isotopically dilute HDO in MPFH in the temperature range 303-100K. Between 303-100K the six water molecules are equivalent, confirmed by the single bending mode. The shoulder appearing at 225.5 ± 1.5K in the OD stretching modes that the water molecules are distorted due to non-equivalent hydrogen bonding,<sup>12</sup> as a result of which the space group of MPFH including hydrogen is no more C<sub>2v</sub><sup>7</sup> but one of the lower symmetry. At 193 ± 1K the water molecules are distorted further, due to the weakening of one hydrogen bond. The peak intensity enhancement at 110 ± 5K and width considerations suggest a positional ordering of hydrogen atoms in the system. The T mode shows similar behaviour as the OD stretch. The PT at 225.5K is being reported here for the first time.<sup>2,5</sup> Present study shows that all the PT are 2nd or higher order.

Figure 2 shows the bands in (A) stretching and (B) bending regions of water in ZPHN in the temperature range

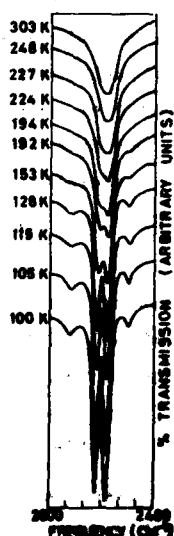


Fig. 1: Temperature dependence of OD stretch of HOD in partially deuterated  $\text{Mg}(\text{ClO}_4)_2 \cdot 6\text{H}_2\text{O}$  (H:D=95:5) pellet in NBr.

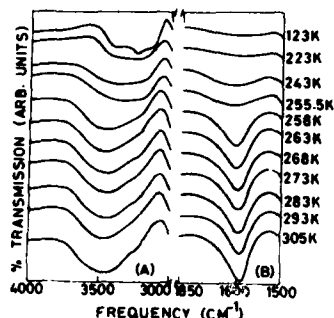


Fig. 2: Temperature dependence of the (A) stretching and (B) bending modes of water in  $\text{Zn}(\text{ClO}_4)_2 \cdot 6\text{H}_2\text{O}$ .

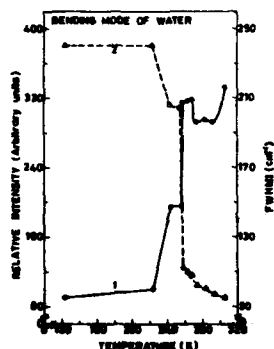


Fig. 3: A plot of (A) relative intensity vs. temperature (solid line) and (B) FWHM vs. temperature for bending mode of water in  $\text{Zn}(\text{ClO}_4)_2 \cdot 6\text{H}_2\text{O}$ .

305-123K. Detailed study of the variation of intensity, and full width at half maximum intensity (FWHMI) with temperature in the bending region (Fig. 3) broadly corroborates the discontinuous changes depicting the PT at 284, 256.5 and near 233K. Figures 2-3 show that (I) minor changes are taking place at 284K, which indicate that 2nd or higher order PT is taking place. This observation may be attributed to the axial compression of water molecules resulting due to distortion of  $\text{ClO}_4^-$  ion<sup>3</sup> in crystal hydrates, below 284K, without structural change,<sup>12</sup> (II) the sharp changes at 256.5K indicate that 1st order PT is taking place; changes in band shapes (Fig. 2) indicate that structural change<sup>12</sup> is taking place. Our observations support<sup>4</sup> that the space group  $C_{2v}^7$  of ZPHH at HT changes to space group  $C_{2h}^5$  below 256.5K, which is consistent with group theoretical calculations and experimental observations<sup>13</sup> in tutton salt having the same octahedral aquo-complex, (III) the discontinuity in between 243-223K shows that this PT is 2nd or higher order. The change in FWHMI in the stretching region indicates that the PT near 233K is order-disorder type.<sup>14</sup>

4. Acknowledgement. H. D. Bist expresses sincere thanks to Professor J. R. Durig for kind hospitality and facilities provided during finalization of the manuscript.

#### References

1. C. D. West: *Z. Kristallogr.*, 91A, 488 (1935).
2. I. Dezsi and L. Keszthelyi: *Solid State Commun.*, 4, 511 (1966).
3. W. M. Reiff, R. B. Frankel and C. R. Abeledo: *Chem. Phys. Lett.*, 22, 124 (1973).
4. B. K. Choudhuri: *Solid State Commun.*, 16, 767 (1975).
5. R. Dayal, D. R. Rao and P. Venkateswarlu: *J. Mag. Resonance*, 36, 99 (1979).
6. A. K. Jain and G. C. Upreti: *Phys. Stat. Sol.*, (a) 58, 155 (1980).
7. S. D. Ross: *Spectrochim. Acta* 22, 1949 (1966).
8. V. P. Tayal, B. K. Shrivastava, D. P. Khandelwal and H. D. Bist: *Applied Spectroscopy Review* (and the references therein), 16, 43 (1980).
9. H. B. Patel, V. M. Sarin and H. D. Bist: *Proceedings of VIIth International Conference on Raman Spectroscopy, Ottawa 1980*, p 126.
10. I. Nakagawa and T. Shimanouchi: *Spectrochim. Acta*, 20, 429 (1964).
11. H. Folk and T. A. Ford: *Can. J. Chem.*, 44, 1899 (1966).
12. J. Schiffer, Ph.D. Thesis, Princeton University, Princeton, New Jersey, 1963.
13. V. Ananthanarayanan: *Z. Phys.*, 163, 144 (1961).
14. D. F. Morning: *J. Chem. Phys.*, 17, 1346 (1949).

## BRILLOUIN SCATTERING IN SILVER HALIDES

T. Hattori, T. Imanishi, H. Kurokawa and A. Mitsuishi

*Department of Applied Physics, Osaka University, Suita, Osaka 565, Japan*

**Abstract.**— Polarized Brillouin scattering spectra in AgBr and AgCl crystals were measured in the temperature region from room temperature to liquid phase temperature above the melting point. The anomaly that the acoustic phonon frequency shows a marked decrease at high temperature cannot be interpreted by a quasi-harmonic approximation. The discussion is given on the relation between the anomalous features and the increasing Frenkel defects.

1. **Introduction.**— It is well known that silver halides show an anomaly in ionic conductivity[1], lattice constant[2], specific heat[3] and others at high temperature. The anomaly in the elastic constant  $C_{11}$  of AgBr was observed by using an ultrasonic pulse technique[4]. It is generally assumed that this anomaly is associated with Frenkel defect, but there seems to be no detailed discussion. In order to study the anomaly in the case of AgBr and AgCl, polarized Brillouin scattering spectra were measured in the temperature region from room temperature to liquid phase temperature above the melting point.

2. **Experiment.**— Spherical single crystals of AgBr and AgCl were grown by the Bridgman method. The orientation of crystal was determined by the observation of the etch pits and was checked by a Laue X-ray technique. The crystals were cut and polished so that the wavevector can be transferred along  $\langle 100 \rangle$  or  $\langle 110 \rangle$  directions. After polishing the crystals were annealed at about 350°C and then slowly cooled to room temperature. The crystal for the optical measurements was located in an electric furnace with fused quartz-windows. For the measurements at liquid phase temperature, the powder of AgBr or AgCl sealed in a small fused quartz-tube in high vacuum was melted in the furnace.

3. **Results.**— Three modes, which participate in the elastic constants  $C_{11}$ ,  $C_{44}$  and  $\frac{1}{2}(C_{11} + C_{12} + 2C_{44})$ , respectively, were observed in the polarized Brillouin scattering spectra, which were measured using a triple pass pressure scanning Fabry-Perot interferometer. The following three values for those three modes were obtained as a function on temperature: the value of the Brillouin shift, the half width of the



Brillouin band and the intensity ratio ( $I_L/I_T$ ) of the longitudinal acoustic (LA) phonon to the transverse acoustic (TA) phonon. Figure 1 shows the temperature dependence of the three values for both  $C_{11}$  and  $C_{44}$  modes of AgBr. Both values of the Brillouin shift for  $C_{11}$  and  $C_{44}$  modes decrease linearly with increasing temperature up to about 300°C and thereafter show a marked decrease to melting point. Together with the phenomena mentioned above, the value of  $I_L/I_T$  increases slightly with increasing temperature up to about 300°C and then increases rapidly as if it diverges at the melting point. On the other hand, the shape of each Brillouin band is a Lorentzian in whole temperature region measured including the liquid phase, and the half width of  $4 \times 10^{-2} \text{ cm}^{-1}$  hardly changes within experimental errors. In the case of AgCl, the same phenomena as AgBr was observed.

4. Discussion.— In general, the frequency of a phonon ( $\omega_j$ ) is a function of temperature (T) and volume (V). Therefore, its derivative  $d\omega_j$  is expressed as follows:

$$d\omega_j = \left(\frac{\partial \omega_j}{\partial V}\right)_T dV + \left(\frac{\partial \omega_j}{\partial T}\right)_V dT \quad \dots\dots(1)$$

Under the condition of the constant pressure, Eq(1) can be transferred to

$$\left(\frac{\partial \omega_j}{\partial T}\right)_P = -\alpha \gamma_j \omega_j + \left(\frac{\partial \omega_j}{\partial T}\right)_V \quad \dots\dots(2)$$

where,  $\alpha$  is the coefficient of volume thermal expansion and  $\gamma_j$  the mode-Grüneisen parameter, respectively. In silver halides, both physical constants of  $\alpha$  and  $\gamma_j$  were obtained by Lawson et al.[2] and by Loje et al.[5], respectively. Therefore, we can calculate the value of the first term of equation (2) as shown in figure 2 by the symbol  $\bullet$ . The second term of equation (2) shows the contribution of the anharmonicity. It is assumed that the calculated value of the second term is independent of temperature and is a constant, because

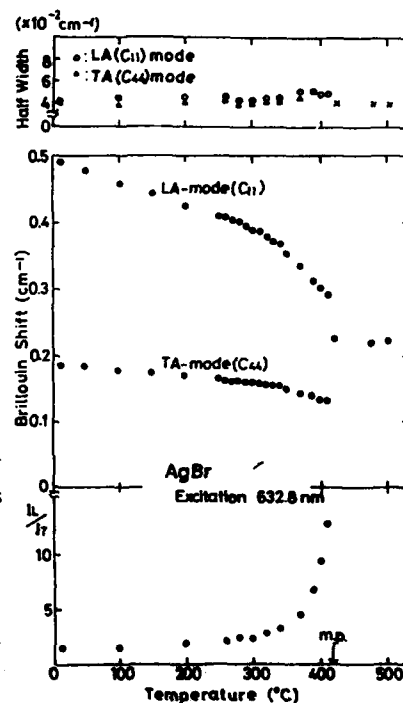


Fig.1 : Temperature dependence of LA and TA phonons propagating along the  $\langle 100 \rangle$  crystal axis of AgBr.

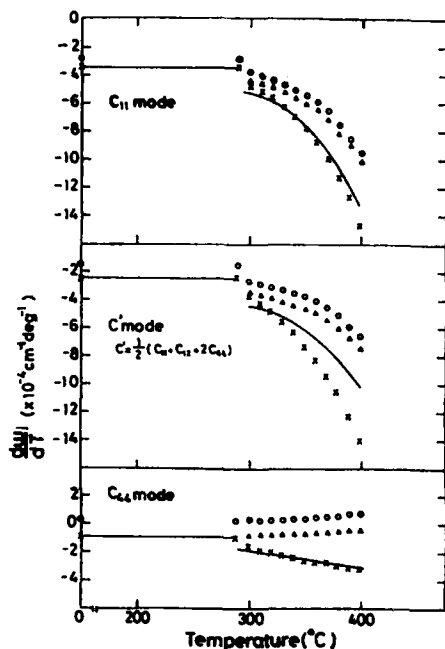


Fig.2 : The comparison between the experimental curve (solid line) and the calculated ones of the temperature derivative of the phonon frequency for each mode. The discontinuation of each curve at 290°C is not essential, because it is due to the fact that we put  $d\omega/dT$  to be constant at the temperature region under 290°C for convenience of the calculation. See the text concerning the calculated curves.

phonon of silver halides can be interpreted very well by the third term added newly in equation (2). The same analysis is made for the case of AgCl. To clarify the third term, further study is in progress.

\*Work supported in part by Grant-in-Aid for Scientific Research, the Ministry of Education, Japan.

#### References

- [1] J.K.Abeagy and R.J.Friauf, *Phys.Rev.*, **B11** (1975)1654.
- [2] A.W.Lawson, *Phys.Rev.*, **78** (1950)185.
- [3] h. Joet and P.Kubaschewski, *Z.Phys.Chem.Neue Folge* **60** (1968)69.
- [4] D.S.Tannhauser, L.J.Bruner and A.W.Lawson, *Phys.Rev.*, **102** (1956) 1274.
- [5] K.F.Loje and D.E.Schuele, *J.Phys.Chem.Solid*, **31** (1970)2051.
- [6] F.Seitz, *Phys.Rev.*, **56** (1939)1063.

the half width of each acoustic phonon band hardly changes as shown in figure 1. Therefore, the calculated curve of the equation (2) is as shown in figure 2 by using the symbol  $\Delta$ . This curve does not agree with the experimental curve at all. Namely, the anomaly that the acoustic phonons show a marked decrease at high temperature cannot be interpreted by a quasiharmonic approximation. And this anomaly was observed for all acoustic phonon modes. It is considered that the increasing Frenkel defect at high temperature plays a dominant role in this anomalous behavior. Therefore, the third term as  $(\partial\omega_j/\partial N)(dN/dT)$ , where  $N$  is the concentration of Frenkel defect, is added in equation (2) in order to interpret this anomaly. The values of  $(dN/dT)$  were already reported [6]. Because, the values of  $(\partial\omega_j/\partial N)$  cannot measure, it was taken as a fitting parameter. The best fit value is  $1.5\text{cm}^{-1}$ . And then, the calculated curve is obtained as shown in figure 2 by the symbol  $x$ . Therefore, it is considered that the anomalous features of the acoustic

## DETECTION OF IMPURITY TUNNELING IN SOLIDS VIA COHERENT PHONON COUPLING AND DIRECT NEUTRON SCATTERING

R.C. Casella

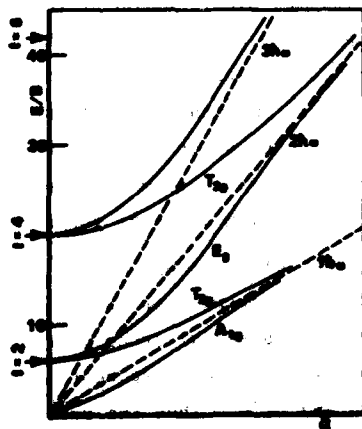
National Measurement Laboratory, National Bureau of Standards, Washington, D.C. 20234, U.S.A.

**Abstract.**— A theoretical treatment is given of the observation of molecular tunneling in solids by the coherent interaction of the tunnel-split excitations with acoustic phonons and by direct neutron inelastic scattering. Results are applied to the case of rotation tunneling of  $\text{CN}^-$  dumbbells in KBr and KCl, and to the motion of H atoms in two-well traps associated with oxygen impurities in niobium. Comparison is made with experiment.

Coherent forward resonant scattering of phonons from the tunnel-split ground and librionically excited configurations of impurity molecules in solids results in mixed modes, with non-zero component amplitudes for both the phonon and the coherently excited impurity complexes. When observed via inelastic neutron scattering, one sees a perturbed acoustic branch in the neighborhood of the wave vector  $\vec{k}$  at which the component modes are degenerate [1], [2]. The mixed mode  $|\Phi\rangle$  is given by relation (1), where  $|EX, \vec{k}\rangle$  represents the impurity excitation at site  $\vec{R}$ .

$$|\Phi\rangle = |\text{phonon}, \vec{k}\rangle + i \sum_{\vec{R}} |EX, \vec{k}\rangle \langle EX, \vec{R}|T|\text{phonon}, \vec{k}\rangle \quad (1)$$

where the sum on  $\vec{R}$  of the T-matrix elements extends only over lattice sites occupied by the dumbbell impurities. The mixed modes have been described in terms of vector cubic harmonics and analyzed group theoretically in terms of a model [2]



**Fig. 1.** Energy level schematic for the unperturbed impurity complex: the  $A_{1g}$  lowest level and the neutron-active low-lying  $E_g$  and  $T_{2g}$  states vs. the coupling strength  $g$  of the hindering potential for the model in which the impurity dumbbells are aligned along  $\langle 111 \rangle$  directions. The first excited librionic level is of type  $E_g$ . The tunnel split excitation within the librionic ground state is of type  $T_{2g}$ .  $B$  is the rotation constant;  $l$  is the angular-momentum quantum number when  $g = 0$ .

which accommodates the neutron scattering data [3], [4] as well as the infrared and Raman scattering data [5] for  $\text{KCl:CN}^-$  and  $\text{KBr:CN}^-$ . The more easily observed phonon admixture with the first vibronically excited tunnel state is determined to be of  $E_g$  character. (See Fig. 1.) If the tunnel-split second excited state ( $T_{2g}$  character) were to lie close to the  $E_g$  excitation in these systems it ought couple with equal strength [2]. The inability to observe the  $T_{2g}$  interaction via neutron scattering indicates that it lies above the potential barrier and is subject to lifetime broadening due to multi-phonon emission. This destroys the coherence required for its observation via the neutron probe. The observation of a broad  $T_{2g}$  state in the Raman spectra considerably above the  $E_g$  [5] is in accord with this picture. Moreover, the model leads to the conclusion that the tunnel-split ground state in these systems ought be observable by neutron scattering (via its coupling to the acoustic phonon) only in the  $T_{2g}$  configuration (Fig. 1). This prediction has been confirmed experimentally in  $\text{KBr:CN}^-$  [3].

At low temperatures, dilute ( $< 0.1\%$  concentration) hydrogen atoms in metals such as niobium and tantalum, also doped with  $0.1\%$  concentration oxygen atoms, become trapped at the latter sites in what are believed to be two-well centers. Tunneling of the hydrogen between the two potential minima near the oxygen provides another interesting system in which molecular (atomic) tunneling in solids can be studied under quite different conditions. Because of the very large low-energy  $n$  p scattering length it is possible to study the excitations directly via neutron scattering. This has been done both for transitions among the tunnel-split components of the vibronic ground state [6] and also for transitions from them to the first and second vibronically excited states [7]. Here the picture is complicated by local strains which can produce relative displacements in the energy of the component well minima. This greatly reduces the ratio of inelastic to elastic neutron scattering within the ground doublet according to a model developed in [6]. The reduction is by a factor  $\sin^2 2\theta$  where  $\theta$  is a mixing angle between the left and right single-well states, describing their admixture in tight-binding approximate tunneling eigenstates. (The average is over some assumed distribution of the strain induced relative displacements.) In principle, for zero strain (infinite dilution) the elastic and inelastic differential cross sections for scattering within the ground doublet ought to be comparable. It is important to understand theoretically the neutron induced transitions to the tunnel-split excited states in order to confirm the model directly. If separated considerably from the ground doublet, the excited doublet can be characterized by a mixing angle  $\phi$ , generally different from  $\theta$ . Matrix elements for transitions from either component of the ground doublet to either of the tunnel-split excitations depend upon both  $\theta$  and  $\phi$ . Under suitable experimental conditions, however, the differential cross section for excitations from both components of the ground doublet to either component of the excited doublet can be shown to be independent of  $\theta$  and of  $\phi$ . Thus the ratio  $\Lambda$  of inelastic cross sections,

$$\Lambda = \frac{d\sigma/d\Omega_{\text{excited}}}{d\sigma/d\Omega_{\text{inelastic}}} / \frac{d\sigma/d\Omega_{\text{ground}}}{d\sigma/d\Omega_{\text{inelastic}}} \quad (2)$$

is enhanced by a (concentration dependent) factor  $1/(\sin^2 2\theta)$ . The numerator in the expression for  $\Lambda$  is diminished by the transition form factor  $\tilde{F}(\vec{q}')$  where  $\vec{q}'$  is the momentum transfer in the higher energy inelastic neutron scattering experiment involving vibronic excitation. For small  $\vec{q}'$ ,  $\tilde{F}(\vec{q}') \sim (\vec{q}' \cdot \vec{D})^2$ , where  $\vec{D}$  is the dipole transition matrix element. For small momentum transfer  $\vec{q}$  in the lower energy experiment involving transitions within the ground doublet, the denominator  $\sim (\vec{q} \cdot \vec{F}/2)^2$  where  $\vec{F}$  denotes the spatial displacement of the well minima within each two-well complex. Thus, in the limit  $\vec{q}' \rightarrow 0$ ,  $\vec{q} \rightarrow 0$  such that ratio  $\rho$  of the larger to the smaller remains fixed,  $\Lambda$  remains finite. I find, in this limit,

$$\Lambda = (\rho^2/8) (k_F/k_I) (M\omega/V_0) / (\sin^2 2\theta). \quad (3)$$

Here,  $(k_F/k_I)$  is the ratio of the final to the initial momenta of the neutron in the higher energy experiment,  $M\omega$  is the vibronic excitation energy, and  $V_0$  is the barrier height between the potential minima. General expressions have also been derived for  $\Lambda$  and various other cross section ratios when the small  $\vec{q}$ ,  $\vec{q}'$  expansion is not justified [8]. Because of the disparate conditions under which the higher [0(100 meV)] and lower [0(0.2 meV)] energy neutron scattering experiments are run in Nb:0(1%) H, 0(1%) O, many difficult normalization problems have to be dealt with in order to determine  $\Lambda$  even semiquantitatively [7]. Nevertheless, it would appear worthwhile.

#### References

- [1] D. Walton, H. A. Mook, and R. M. Nicklow, Phys. Rev. Lett. **33**, 412 (1974).
- [2] R. C. Casella, Phys. Rev. B **20**, 5318 (1979).
- [3] J. M. Rowe, J. J. Rush, S. M. Shapiro, D. G. Hinks, and S. Sussman, Phys. Rev. B **21**, 4863 (1980).
- [4] R. M. Nicklow, W. P. Crummett, M. Mostoller, and R. F. Wood, Phys. Rev. B **22**, 3039 (1980).
- [5] D. Durand and F. Luty, Phys. Stat Solidi B **81**, 443 (1977).
- [6] H. Wipf, A. Magerl, S. M. Shapiro, S. K. Satija, and W. Tomlinson, Phys. Rev. Lett. **46**, 947 (1981).
- [7] A. Magerl, J. J. Rush, and J. M. Rowe, private communication (unpublished).
- [8] R. C. Casella, to be published.

# AUTHOR INDEX

- Abou-Ghantous (M.).- See Khoder (A.F.)..... C6-383
- Adnot (A.).- See Thiry (P.)..... C6-843
- Agrawal (B.K.).- Vibrational excitations in a-Si:F and a-Si:F:H alloys..... C6-93
- Aikawa (Y.).- See Nakamura (T.). C6-421
- Akao (F.).- See Miyasato (T.)... C6-658
- Alexandre (F.).- See Jusserand (B.)..... C6-43
- Alig (R.C.), Bloom (S.) and Inoue (M.).- Optical-mode deformation potential..... C6-484
- Aliotta (F.), Fontana (M.P.), Maisano (G.), Migliardo (P.), Vasi (C.) and Wanderlingh (F.).- Vibrational dynamics in ionic liquids..... C6-57
- Almond (D.P.) and West (A.R.).- A new interpretation of Ultrasonic Attenuation in Superionic Conductors  $\beta$  and  $\beta'$ -alumina.. C6-187
- Anastassakis (E.M.) and Cardona (M.).- Simulation of long-wavelength optical phonons by generalized internal strains. C6-537
- Anikiev (A.A.), Umarov (B.S.), Gorelik (V.S.) and Vetelino (J.F.).- Two-phonon bound states in ammonium chloride at finite temperatures..... C6-152
- Animalu (A.O.E.).- See Onwugba (B.N.)..... C6-401
- Appel (J.).- See Far (B.)..... C6-490
- Arnold (S.B.) and Manen (M.).- The local phonon density of states and its influence on superconducting properties.. C6-377
- Arnold (W.), Billmann (A.), Doussineau (P.), Frenois (C.) and Levelut (A.).- Ultrasonic absorption and dispersion in amorphous superconductors... C6-37
- Arnold (W.).- See v. Löhneysen (H.)..... C6-193
- Arora (A.K.).- See Sood (A.K.). C6-572
- Asai (N.).- See Inoue (K.)..... C6-430
- Ashkenazi (J.) and Dacorogna (M.).- Phonons in metals..... C6-355
- Aubree (J.).- See Schneck (J.).. C6-734
- Aune (H.J.).- See Fossum (J.O.). C6-867
- Ayache (C.) and Nuñez-Regueiro (M.).- Basal thermal conductivity of  $\text{TiSe}_2$ ..... C6-338
- Aydinli (A.).- See Compaan (A.). C6-453
- Balasubramanian (K.R.) and Haridasan (T.M.).- A green's function study of the U centre in  $\text{BaClF}$  and  $\text{SrClF}$ ..... C6-905
- Baldereschi (A.).- See Rosta (R.) C6-661
- Balkanski (M.).- See Brunel (L.C.)..... C6-412
- Balkanski (M.).- See Kanellis (G.)..... C6-341
- Ball (M.A.).- The generalized pseudomom formalism in lattice dynamics..... C6-519
- Ball (M.A.) and Leung (W.N.).- The dielectric function matrix and the lattice dynamics of  $\text{KCl}$ ..... C6-911

- Banerjee (P.K.), Bendow (B.), Drexhage (M.G.), Goltman (J.T.), Mitra (S.S.) and Moynihan (C.T.).- Polarized Raman scattering studies of fluoro-zirconate and fluorohafnate glasses..... C6-75
- Bansal (M.L.), Deb (S.K.), Roy (A.P.) and Sahni (V.C.).- Anomalous temperature dependence of a LO mode in  $\text{LiKSO}_4$ ..... C6-902
- Barchielli (A.) and Mulazzi (E.).- Homogeneous broadening of zero-phonon lines for a multilevel system in a crystal : the role of the electron-phonon interactions..... C6-475
- Basoon (S.A.).- See Kaplyanskii (A.A.)..... C6-439
- Basoon (S.A.).- See Kaplyanskii (A.A.)..... C6-462
- Batallan (F.), Rosenman (I.), Simon (C.), Furdin (G.) and Lauter (H.J.).- Phonons in graphite intercalated with bromine..... C6-344
- Bauernfeind (W.), Keller (J.) and Schröder (U.).- Theory of thermal conductivity in molecular crystals. Application to alkali cyanides..... C6-247
- Bauhofer (W.).- See Benedek (G.) C6-301
- Baumgartner (R.), Engelhardt (M.) and Renk (K.F.).- Observation of strongly frequency dependent lifetimes of acoustic phonons in  $\text{CaF}_2$ ..... C6-119
- Behera (S.N.).- Effect of non-magnetic impurities on the Raman scattering by superconducting gap excitations in layered compounds..... C6-292
- Behera (S.N.) and Khare (A.).- Dynamics and Thermodynamics of a one dimensional non-linear lattice in the continuum limit C6-314
- Behera (S.N.) and Samsur (Sk.).- Hybridization of the two-phonon bound state with the local mode in imperfect crystals..... C6-528
- Bellissent-Funel (M.C.).- See Maisano (G.)..... C6-51
- Belushkin (A.I.).- See Wasiutynski (T.)..... C6-599
- Bendow (B.), Lipson (H.G.), Brown (R.N.), Marshall (R.C.), Billard (D.) and Mitra (S.S.).- Temperature dependence of multi-phonon absorption in highly transparent cubic zirconia.. C6-140
- Bendow (B.).- See Banerjee (P.K.) C6-75
- Benedek (G.), Pollini (I.) and Bauhofer (W.).- Two-phonon progressions associated with vibronic excitons in layered 3d-metal compounds..... C6-301
- Benedek (G.).- See Bussmann-Holder (A.)..... C6-409
- Benedek (G.), Brusdeylins (G.), Doak (R.B.) and Toennies (J.P.).- The spectroscopy of surface phonons by inelastic atom scattering..... C6-793
- Berberich (F.) and Kinder (H.).- The phonon spectrum emitted by superconducting Sn tunnel junctions..... C6-374
- Beserman (R.).- See Schmeltzer (D.)..... C6-84
- Beserman (R.).- See Schmeltzer (D.)..... C6-158
- Beserman (R.).- See Teicher (M.) C6-46
- Bethoux (O.), Lasjaunias (J.C.) and Ravex (A.).- Effect of a thermal annealing on the lattice specific heat and thermal conductivity of superconducting amorphous  $\text{Zr}_{0.76}\text{Ni}_{0.24}$  alloys..... C6-60
- Beyeler (H.U.).- See v. Löhneysen (H.)..... C6-193
- Bielushkin (A.V.), Natkaniec (I.), Dolganov (V.K.) and Sheka (E.F.).- Vibrational density of states of amorphous and crystalline liquid crystal substances..... C6-34
- Biem (W.).- See Menn (K.)..... C6-87

- Billard (D.).- See Bendow (B.). C6-140
- Billmann (A.).- See Arnold (W.). C6-37
- Bilz (H.).- See Brunel (L.C.). C6-412
- Bilz (H.).- See Bussmann-Holder (A.). C6-409
- Bilz (H.).- See Büttner (H.). C6-111
- Bilz (H.).- See Kress (W.). C6-3
- Bilz (H.).- See Maradudin (A.A.). C6-137
- Bist (H.D.).- See Patel (M.B.). C6-917
- Black (J.E.), Campbell (D.A.) and Wallis (R.F.).- Atomic vibrations at (100) surfaces of FCC and BCC Metals. C6-837
- Blanchard (C.).- See Deville (A.). C6-465
- Bloom (S.).- See Alig (R.C.). C6-484
- Boatner (L.A.).- See Salce (B.). C6-424
- Boato (G.).- See Cantini (P.). C6-801
- Boissier (M.), Vacher (R.) and Perrin (B.).- Ultrasonic relaxation in  $\alpha$ -sulphur. C6-611
- Bokhenkov (E.L.), Kolesnikov (A.I.), Krivenko (T.A.), Sheka (E.F.) and Dementjev (V.A.).- Harmonic dynamics of anthracene and naphthalene crystals. C6-566
- Bokhenkov (E.L.), Kolesnikov (A.I.), Krivenko (T.A.), Sheka (E.F.), Dementjev (V.A.) and Natkaniec (I.).- Neutron spectroscopy of internal phonons of naphthalene and anthracene crystals. C6-605
- Bokhenkov (E.L.).- See Dorner (B.). C6-602
- Bömmel (H.E.).- See Strübel (B.). C6-404
- Bonjour (E.), Calemczuk (R.), Lagnier (R.) and Salce (B.).- Low temperature thermal properties of cyclohexanol : a glassy crystal system. C6-63
- Bortolani (V.), Franchini (A.), Nizzoli (F.) and Santoro (G.).- Surface lattice dynamics of nickel. C6-831
- Bortolani (V.), Nizzoli (F.), Santoro (G.) and Marvin (A.).- Theory of acoustic phonons at interfaces and Brillouin scattering. C6-804
- Bosio (L.).- See Copley (J.R.D.). C6-386
- Bouilliot (J.).- See Cailleau (H.). C6-704
- Bouilliot (J.).- See Geick (R.). C6-713
- Boysen (H.).- See Dorner (B.). C6-752
- Brafman (O.) and Livescu (G.).- A study of polaritons and phonon peculiarities in  $\text{CuCl}_{1-x}\text{Br}_x$ . C6-96
- Breazeale (M.A.) and Philip (J.).- Temperature dependence of phonon-phonon interaction in silicon. C6-134
- Brito-Orta (R.) and Klemens (P.G.).- Contribution of low-frequency longitudinal phonons to the lattice thermal conductivity of dielectric solids. C6-256
- Brito-Orta (R.) and Klemens (P.G.).- Contribution of low-frequency longitudinal phonons to the lattice thermal conductivity of dielectric solids. C6-256
- Bron (W.E.).- See Thrope (J.). C6-849
- Brown (R.A.).- The effect of dislocations on thermal conductivity. C6-271
- Brown (R.N.).- See Bendow (B.). C6-140
- Brüesch (P.), Hibma (T.) and Bühner (W.).- Phonons and ionic conductivity in the two-dimensional super-ionic conductor  $\text{AgCrS}_2$ . C6-178
- Brunel (L.C.), Landwehr (G.), Bussmann-Holder (A.), Bilz (H.), Balkanski (M.), Massot (M.) and Ziolkowicz (M.K.).- Influence of strong magnetic fields on ferroelectric phase transitions. C6-412
- Brusdeylins (G.).- See Benedek (G.). C6-793



- Buchenau (U.), Schober (H.R.) and Wagner (R.).- Coherent neutron scattering from polycrystals C6-395
- Bührer (W.).- See Brüesch (P.). C6-178
- Bussmann-Holder (A.), Benedek (G.), Bilz (H.) and Mokross (E.).- Microscopic polarizability model of ferroelectric soft modes..... C6-409
- Bussmann-Holder (A.).- See Brunel (L.C.)..... C6-412
- Büttner (H.) and Bilz (H.).- Some aspects of nonlinear lattice models..... C6-111
- Cailleau (H.), Moussa (F.), Zeyen (C.M.E.) and Bouillot (J.).- Dynamics of incommensurate phases in biphenyl..... C6-704
- Calemczuk (R.).- See Bonjour (E.)..... C6-63
- Calleja (J.M.), Vogt (H.) and Cardona (M.).- Absolute cross sections for one-phonon Raman scattering from several insulators and semiconductors... C6-487
- Camassel (J.), Gil (B.), Merle (P.), Mathieu (H.) and Pascual (J.).- Resonant Raman scattering in  $\text{TiO}_2$ ..... C6-682
- Camassel (J.).- See Pascual (J.) C6-719
- Campbell (D.A.).- See Black (J.E.)..... C6-837
- Cancela (L.S.G.), Ramos (J.G.) and Gualberto (G.M.).- Multi-phonon process in  $\text{NiSO}_4 \cdot 6\text{H}_2\text{O}$  C6-581
- Cantini (P.), Boato (G.) and Tatarak (R.).- Graphite surface phonons studied through He atoms resonant scattering... C6-801
- Carabatos (C.).- See Fontana (M.D.)..... C6-749
- Carabatos (C.).- See Kugel (G.E.)..... C6-884
- Cardona (M.).- See Anastassakis (E.M.)..... C6-537
- Cardona (M.).- See Calleja (J.M.) C6-487
- Cardona (M.).- See Olego (D.).. C6-652
- Cardona (M.).- See Pintschovius (L.)..... C6-634
- Cardona (M.).- See Oka (Y.).... C6-459
- Carles (R.), Saint-Cricq (N.), Zwick (A.), Renucci (M.A.) and Renucci (J.B.).- Low frequency Raman scattering in mixed  $\text{Ga}_{1-x}\text{Al}_x\text{As}$  and  $\text{Ga}_{1-x}\text{In}_x\text{As}$  alloys..... C6-105
- Carlone (C.), Hota (N.K.), Stolz (H.J.), Elbert (M.), Kuzmany (H.) and Hochheimer (H.D.).- Gas phase Raman spectrum of TCNQ and pressure dependence of the modes in crystals of TCNQ..... C6-323
- Carroll (P.J.) and Lamin (J.S.).- Second order Raman scattering in crystalline sulphur selenium and tellurium..... C6-643
- Casella (R.C.).- Detection of Impurity tunneling in solids via coherent phonon coupling and direct neutron scattering C6-923
- Castiel (D.).- See Shen (T.J.). C6-819
- Caudano (R.).- See Thiry (P.).. C6-843
- Cazzanelli (E.), Fontana (A.), Mariotto (G.) and Rocca (F.).- Vibrational dynamics of  $\text{RbAg}_4\text{I}_5$  by Raman spectroscopy..... C6-190
- Cazzanelli (E.), Fontana (A.), Mariotto (G.), Rocca (F.) and Fontana (M.P.).- Observation of pretransitional effects on the shape of the  $E_2(17 \text{ cm}^{-1})$  optical mode in  $\beta\text{-AgI}$  by Raman spectroscopy..... C6-776
- Cazzanelli (E.).- See Mazurati (V.)..... C6-196
- Celio (M.), Moanier (R.) and Wachter (P.).- Phonon and elastic anomalies in intermediate valent  $\text{Ta}_x\text{Se}$  and  $\text{TaSe}_{1-y}\text{Te}_y$ ..... C6-11

- Cerdeira (F.), Melo (F.E.A.) and Katiyar (R.S.).- Piezospectroscopic study of the Raman spectrum of  $\text{LiIO}_3$ ..... C6-722
- Challis (L.J.), Ghazi (A.A.) and Wybourne (M.N.).- Frequency crossing in bicrystals and inelastic scattering at surfaces..... C6-229
- Challis (L.J.).- See Ramdane (A.)..... C6-244
- Chao (M.H.) and Sladek (R.J.).- Ultrasonic phonons in  $\text{Hg}_{0.8}\text{Mn}_{0.2}\text{Te}$ ; dependences of elastic moduli on pressure and temperature..... C6-667
- Chaplot (S.L.), Mierzejewski (A.), Lefebvre (J.), Pawley (G.S.) and Luty (T.).- Internal and external phonons in monoclinic tetracyanoethylene..... C6-584
- Chaplot (S.L.).- See Dorner (B.) C6-602
- Chaplot (S.L.).- See Rao (K.R.) C6-637
- Cheeke (J.D.N.) and Madore (G.).- Acoustoelectric interaction in p-InSb at low temperature... C6-569
- Cheeke (J.D.N.).- See Poirier (M.)..... C6-876
- Chernyshov (A.A.).- See Dorner (B.)..... C6-365
- Chhi-Chong Wu.- Effect of the propagation of ultrasounds on magnetoacoustic phenomena in degenerate semiconductors... C6-655
- Chih-Yuan Lu.- Ground State energy of Frohlich electron-phonon system..... C6-481
- Chin (M.A.).- See Ulbrich (R.G.)..... C6-226
- Choi (B.K.).- See Kim (J.J.)... C6-427
- Ciplys (D.) and Prieur (J.Y.).- Ultrasonic properties of a superionic glass:  $\text{B}_2\text{O}_3$ ,  $0.5 \text{ Li}_2\text{O}$ ,  $0.7 \text{ LiCl}$ ..... C6-184
- Coiret (M.).- See Teledano (P.) C6-476
- Colvard (C.), Merlin (R.), Klein (M.V.) and Gossard (A.C.).- Light scattering from phonons in GaAs-AlAs superlattices..... C6-631
- Compaan (A.), Lo (H.W.), Lee (M.C.) and Aydinli (A.).- Pulsed Raman measurements of inhibited electron-phonon coupling at high plasma densities in silicon. C6-453
- Coombs (G.J.).- See Lockwood (D.J.)..... C6-761
- Copley (J.R.D.), Bosio (L.), Cortès (R.), Lefebvre (J.) and Teuchert (W.D.).- A neutron inelastic scattering study of phonons in metastable Beta-Galium..... C6-386
- Cortès (R.).- See Copley (J.R.D.)..... C6-386
- Couach (M.).- See Khoder (A.F.)..... C6-383
- Currat (R.).- The role of phonons in incommensurate phase transitions..... C6-693
- Czachor (A.).- Gaps in phonon dispersion curves for substitutional alloys..... C6-525
- Dacorogna (M.).- See Ashkenazi (J.)..... C6-355
- Dandolo (R.).- See Zeyer (R.) C6-40
- Dattagupta (S.).- See Sood (A.K.)..... C6-572
- Daudin (B.), Salce (B.) and Smith (S.H.).- Specific heat and thermal conductivity of  $\text{TmVO}_4$  and  $\text{DyVO}_4$  with an applied magnetic field..... C6-277
- Deb (S.K.).- See Bansal (M.L.) C6-902
- Dellepiane (G.).- See Mulazzi (E.)..... C6-493
- Delpech (P.).- See Jussierand (B.)..... C6-43
- Dementjev (V.A.).- See Bokhenkov (E.L.)..... C6-566
- Dementjev (V.A.).- See Bokhenkov (E.L.)..... C6-605

- Deville (A.), Gaillard (B.), Blanchard (C.) and Livaige (J.).- Comparison of electron spin-lattice relaxation in amorphous and crystalline materials..... C6-465
- Deville Cavellin (C.).- See Petritis (D.)..... C6-688
- Devreese (J.T.).- See Vanchamp (P.E.)..... C6-625
- Dierker (S.B.).- See Merlin (R.) C6-392
- Dietsche (W.), Kirch (S.J.) and Wolfe (J.P.).- Phonon spectroscopy of the electron-hole-liquid..... C6-447
- Dietsche (W.).- See Northrop (G.A.)..... C6-209
- Dietz (W.).- See Fritsch (G.).. C6-143
- Dixon (G.S.).- Two-Magnon-one-phonon scattering in the lattice thermal conductivity of magnetic insulators..... C6-262
- Dixon (M.).- See Elliott (R.J.) C6-175
- Doak (R.B.).- See Benedek (G.). C6-793
- Dolganov (V.K.).- See Rielushkin (A.V.)..... C6-34
- Dorner (B.), Bokhenkov (E.L.), Sheka (E.F.), Chaplot (S.L.), Pawley (G.S.), Kalus (J.), Schmelzer (U.) and Matkaniec (I.).- Phonon dispersion curves in the molecular crystals naphthalene and anthracene measured by inelastic neutron scattering..... C6-602
- Dorner (B.), Boysen (H.), Frey (F.) and Grimm (H.).- On the Si-O-Si bond angle in  $\alpha$ - and  $\beta$ -quartz..... C6-752
- Dorner (B.), Chernyshov (A.A.), Pushkarev (V.V.), Rmyantsev (A.Yu.) and Pynn (R.).- Electron-phonon coupling in the nontransition metal cadmium. C6-365
- Doussineau (P.).- Attenuation and velocity change of acoustic waves in the amorphous metal Pd Si Cu from 0.05 K to 90 K..... C6-72
- Doussineau (P.).- See Arnold (W.)..... C6-37
- Doussineau (P.).- See Prieur (J.-Y.)..... C6-33
- Drexhage (M.G.).- See Banerjee (P.K.)..... C6-75
- Duraiwamy (S.) and Haridasan (T.M.).- Means square displacements of a substitutional defect and its nearest neighbours in KI..... C6-899
- Dynes (R.C.).- See Hensel (J.C.) C6-212
- Dynes (R.C.).- See Hensel (J.C.) C6-308
- Ecolivet (C.).- Linear chain models and sound velocities in molecular organic crystals.. C6-578
- Ecolivet (C.), Toudic (B.) and Sanquer (M.).- Brillouin scattering study of phase transitions in p-polyphenyls C6-779
- Einsenmenger (W.).- Phonon imaging..... C6-201
- Elbert (M.).- See Carlone (C.) C6-323
- Elliott (R.J.) and Dixon (M.).- Vibrations and diffusion of atoms in superionic crystals and melts..... C6-175
- Engelhardt (M.).- See Baumgartner (R.)..... C6-119
- Englman (R.).- Dynamics in displacive phase transitions... C6-755
- Englman (R.).- Phonon pulses from a relaxing system..... C6-241
- Errandonea (G.).- Pressure dependence of the coupled optic acoustic modes near the ferroelastic transition of  $\text{LaF}_5\text{O}_{14}$ ..... C6-710
- Escribe-Filippini (C.).- See Petitgrand (D.)..... C6-782
- Etchepare (J.).- See Marian (M.) C6-608
- Every (A.G.).- Phonon focusing and the shape of the ray surface in cubic crystals..... C6-215

- Fain (B.).- Instabilities in thermal bath : Phonon enhancement and saturation in a three-level system..... C6-540
- Falter (C.), Ludwig (W.) and Selmke (M.).- Renormalized response theory with applications to phonon anomalies..... C6-516
- Fasolino (A.), Santoro (G.) and Tosatti (E.).- Effective mass approximation for surface phonon states..... C6-840
- Fasolino (A.), Santoro (G.) and Tosatti (E.).- Surface Phonons and the Incommensurate reconstruction of clean Mo(100)... C6-846
- Fay (D.) and Appel (J.).- Effect of phonons on the spin susceptibility..... C6-490
- Fishman (G.), Pinczuk (A.), Worlock (J.M.), Störmer (H.L.), Gossard (A.C.) and Wiegmann (W.).- Coupled electron-LO phonon excitation in a two dimensional electron system..... C6-305
- Fisk (Z.).- See Merlin (R.).... C6-392
- Fontana (A.).- See Cazzanelli (E.)..... C6-190
- Fontana (A.).- See Cazzanelli (E.)..... C6-776
- Fontana (A.).- See Mazzacurati (V.)..... C6-196
- Fontana (M.D.), Kugel (G.E.) and Carabatos (C.).- Lattice dynamics of the cubic-tetragonal phase transition in  $\text{KNbO}_3$ ..... C6-749
- Fontana (M.P.).- See Maisano (G.)..... C6-51
- Fontana (M.P.).- See Aliotta (F.)..... C6-57
- Fontana (M.P.).- See Cazzanelli (E.)..... C6-776
- Fosheim (K.).- See Fossum (J.O.) C6-867
- Fossum (J.O.), Anne (H.J.), Fosheim (K.) and Molt (R.M.).- Echo properties of  $\text{BiO}$  and  $\text{CdS}$ ..... C6-867
- Franchini (A.).- See Bortolani (V.)..... C6-831
- Freire (J.D.).- See Katiyar (R.S.)..... C6-433
- Frenois (C.).- See Arnold (W.). C6-37
- Frenois (C.).- See Prieur (J.-Y.) C6-33
- Frey (F.).- See Dorner (B.).... C6-752
- Friskén (B.), Guillon (F.), Harrison (J.P.) and Page (J.H.).- Low frequency phonons in sintered copper..... C6-858
- Fritsch (G.), Dietz (W.), Hering (R.) and Lüscher (E.).- Anharmonic contributions to the thermal diffuse X-Ray scattering intensity from single crystalline sodium..... C6-143
- Furdin (G.).- See Batallan (F.) C6-344
- Gaillard (B.).- See Deville (A.) C6-465
- Galeener (F.L.).- Vibrational selection rules in disordered solids : vitreous  $\text{GeO}_2$ ..... C6-24
- Geick (R.), Rauch (H.), Lehner (N.), Bouillot (J.), Stirling (W.G.), Heger (G.).- Lattice instabilities and phase transitions in fluoride perovskites C6-713
- Gerlinger (H.) and Schaack (G.).- Magnetic field dependent Raststrahlen spectra in paramagnetic  $\text{CeF}_3$ ..... C6-499
- Gervais (F.) and Servoin (J.L.).- Role of polar phonons in the chemical bond at structural phase transitions characterized by repetitive Fourier spectroscopy..... C6-415
- Ghazi (A.A.).- See Challis (L.J.) C6-229
- Gil (B.).- See Camassel (J.)... C6-682
- Gledhill (G.A.), Kudhail (S.S.), Newman (R.C.), Woodhead (J.) and Zhang (G.Z.).- The low frequency absorption of gallium phosphide induced by impurities and radiation damage..... C6-685

- De Goër (A.M.), Locatelli (M.) and Laermans (C.).- Thermal phonon transport study of the defects created in quartz single crystals by different irradiations ( $\gamma$  rays, electrons, neutrons)..... C6-78
- De Goër (A.M.), Locatelli (M.) and Lassmann (K.).- A Study of the ground state of acceptors in silicon from thermal transport experiments..... C6-235
- De Goër (A.M.), Locatelli (M.) and Nicolau (I.F.).- Low temperature thermal conductivity of Hg I<sub>2</sub> single crystals..... C6-265
- De Goër (A.M.).- See Salce (B.) C6-424
- Goltman (J.T.).- See Banerjee (P.K.)..... C6-75
- Gompf (F.) and Lannin (J.S.).- The vibrational spectra of crystalline and amorphous phosphorous..... C6-27
- Gompf (F.), Schmidt (H.J.) and Renker (B.).- Inelastic neutron scattering from amorphous Fe<sub>40</sub>Zr<sub>60</sub> doped with different concentrations of Krypton (0,1, 7 at %X)..... C6-49
- Goodstein (D.).- See Taborek (P.) C6-825
- Goodstein (D.).- See Taborek (P.) C6-855
- Goodstein (D.).- See Taborek (P.) C6-852
- Gorelik (V.S.), Umarov (B.S.) and Umarov (M.).- "Non-Central" peaks in light scattering spectra of lithium tantalate and quartz at phase transition.. C6-764
- Gorelik (V.S.).- See Anikiev (A.A.)..... C6-152
- Gossard (A.C.).- See Colvard (C.)..... C6-631
- Gossard (A.C.).- See Fishman (G.)..... C6-305
- Govindarajan (J.).- See Jacobs (P.W.M.)..... C6-914
- Granato (A.V.).- See Kneemel (G.A.)..... C6-250
- Greenstein (M.) and Wolfe (J.P.).- Modulation of ballistic phonon fluxes in Ge by a He Gas film at a solid/superfluid interface..... C6-274
- Greig (D.) and Hardy (N.D.).- The thermal conductivity of semicrystalline polymers at very low temperatures..... C6-69
- Grier (B.H.).- See Sato (M.)... C6-770
- Grimm (H.).- See Dorner (B.)... C6-752
- Gualberto (G.M.).- See Cancela (L.S.G.)..... C6-581
- Guillon (F.).- See Frisken (B.) C6-858
- Güntherodt (G.).- See Kress (W.) C6-3
- Gupta (O.P.).- Phonon dispersion and thermophysical properties of sodium..... C6-380
- Hamaguchi (C.).- See Itoh (Y.). C6-810
- Hamann (D.R.).- See Harmon (B.N.)..... C6-628
- Hamdache (M.), King (P.J.), Murphy (D.T.) and Rampton (V.W.).- Phonon spectroscopy of chromium-doped gallium arsenide using superconducting tunnel junctions..... C6-664
- Hanke (W.).- See Muramatsu (A.) C6-834
- Hardcastle (J.F.) and Zabel (H.).- Thermal expansion of Alkali-graphite intercalation compounds..... C6-326
- Hardy (N.D.).- See Greig (D.).. C6-69
- Haridasan (T.M.).- See Balasubramanian (K.R.)..... C6-905
- Haridasan (T.M.).- See Duraiswamy (S.)..... C6-899
- Haridasan (T.M.).- See Jacobs (P.W.M.)..... C6-914
- Haridasan (T.M.).- See Ramachandran (K.)..... C6-679
- Herring (R.).- See Fritsch (G.). C6-143

- Harmon (B.N.), Weber (W.) and Hamann (D.R.).- Vibrational frequencies via frozen phonons..... C6-628
- Harrison (J.P.).- See Friksen (B.)..... C6-858
- Hashimoto (S.).- See Kuroda (N.)..... C6-788
- Hatakeyama (S.).- See Horie (C.)..... C6-298
- Hattori (T.), Imanishi (T.), Kurokawa (H.) and Mitsuishi (A.).- Brillouin scattering in silver halides..... C6-920
- Hayes (W.).- Phonons in super-ionic conductors..... C6-167
- Heger (G.).- See Geick (R.).... C6-713
- Henkel (J.H.).- Lattice phonon lifetime calculation..... C6-146
- Hennion (B.).- See Petitgrand (D.)..... C6-782
- Hensel (J.C.), Dynes (R.C.) and Tsui (D.C.).- Absorption of ballistic phonons by the 2D electron gas in a Si mesfet. C6-308
- Hensel (J.C.), Dynes (R.C.), Unterwald (F.C.) and Simons (A.L.).- Singular effects in phonon focusing: formation of phonon focusing caustics.... C6-212
- Heritier (M.).- The phonon anomaly in b.c.c.  $\text{Ba}^2$ : a phonon self-trapping?..... C6-890
- Heritier (M.) and Montambaux (G.).- Interpretation of experiments in the solidon model for rotons..... C6-534
- Hibma (T.).- See Bräsech (P.).. C6-178
- Hidaka (Y.).- See Yagi (T.).... C6-731
- Hikata (A.).- See Peirier (M.). C6-676
- Hochheimer (H.B.).- See Carlone (C.)..... C6-323
- Holt (R.M.).- See Paoletti (J.O.) C6-867
- Horie (C.), Miyazaki (H.), Igarashi (S.) and Hatakeyama (S.).- Role of phonons in orientational intra-plane ordering in graphite intercalation compounds..... C6-298
- Horie (C.).- See Miyazaki (H.). C6-335
- Horstman (R.E.) and Wolter (J.).- Thermalization of high-frequency phonons in silicon single crystals..... C6-813
- Hota (N.K.).- See Carlone (C.). C6-323
- Hu (P.).- See Lax (M.)..... C6-161
- Hwang (D.M.) and Solin (S.A.).- Phonon Raman spectroscopy in graphite intercalation compounds..... C6-347
- Igarashi (S.).- See Horie (C.).. C6-298
- Imanishi (T.).- See Hattori (T.) C6-920
- Inoue (K.) and Asai (N.).- Hyper-Raman scattering study of ferroelectric phase transitions in  $\text{Sr Ti O}_3$  and  $\text{Ba Ti O}_3$ ..... C6-430
- Inoue (M.).- See Allig (R.C.)... C6-484
- Inuishi (Y.).- See Itoh (Y.)... C6-810
- Itoh (Y.), Hamaguchi (C.) and Inuishi (Y.).- Resonant Brillouin scattering in opaque region of  $\text{CdS}$ ..... C6-810
- Itoh (S.).- See Nakamura (T.).. C6-418
- Iwasa (J.) and Suzuki (H.).- Interaction of sound with vacancies in bcc  $\text{Fe}$  crystals C6-896
- Jacobs (P.W.W.), Norenberg (M.A.H.), Govindarajan (J.) and Narayanan (T.N.).- Calculation of defect entropies in ionic crystals in the quasiharmonic approximation: application to fluorites.... C6-914
- Jang (H.S.).- See Nakamura (T.) C6-418
- Janssen (T.) and de Lange (C.).- Vibration spectra of crystals in an incommensurate phase.. C6-737
- Jayaraman (A.).- See Kress (W.) C6-3

- Joffrin (C.).- See Schneck (J.) C6-734
- Johnstone (I.W.), Jones (G.D.) and Lockwood (D.J.).- Raman scattering from phonons in disordered  $\text{CaMg}_{1-x}\text{Co}_x\text{Cl}_3$ ..... C6-90
- Jones (G.D.).- See Johnstone (I.W.)..... C6-90
- Jørgensen (J.).- See Merlin (R.) C6-392
- Joakoff (B.).- See Schneck (J.). C6-734
- Jusserand (B.), Sapriel (J.), Alexandre (F.) and Dalpech (P.).- Raman study of the anharmonicity and disorder-induced effects in  $\text{Ga}_{1-x}\text{Al}_x\text{As}$ ..... C6-43
- Kajimura (K.).- Phonon echoes in bulk and powdered materials..... C6-863
- Kajimura (K.).- See Tsuruoka (F.)..... C6-864
- Kalus (J.).- See Dörner (B.)... C6-602
- Kamitakahara (W.A.), Wada (N.) and Solin (S.A.).- Neutron spectroscopy of phonons in  $\text{Rb C}_6$ .... C6-311
- Kanellis (G.), Morhange (J.F.) and Balkanski (M.).- Electrostatic energy and lattice vibration in thin ionic slabs..... C6-341
- Kaplyanskii (A.A.), Basoon (S.A.) and Shekhtman (V.L.).- Multiple resonant Raman spin-flip phonon scattering and  $29\text{ cm}^{-1}$  phonon transport in excited ruby in a magnetic field..... C6-462
- Kaplyanskii (A.A.), Basoon (S.A.) and Shekhtman (V.L.).- Phonons in excited ruby..... C6-439
- Katsuyama (S.).- See Sasaki (T.). C6-758
- Katiyar (R.S.) and Strada (J.D.).- Dynamical study of phonons in ferroelectric lead titanate..... C6-483
- Katiyar (R.S.).- See Cardona (P.)..... C6-722
- Keller (J.).- See Bavernfeind (W.)..... C6-247
- Kesavamoorthy (R.).- See Umadevi (V.)..... C6-81
- Kesavasamy (K.).- See Krishnamurthy (N.)..... C6-908
- Khare (A.).- See Behara (S.N.). C6-314
- Khoder (A.F.), Couach (M.), Locatelli (M.), Abou-Ghantous (M.) and Senateur (J.P.).- On the thermal and electrical conductivity of  $\text{V}_3\text{Si}$  and  $\text{V}_5\text{Si}_3$ ..... C6-383
- Kim (J.J.), Won (J.W.) and Choi (B.K.).- Soft-mode spectra and phase transition in KDP crystal with ADP impurities. C6-427
- Kimura (T.).- See Yoshikawa (S.)..... C6-873
- Kinder (H.).- See Berberich (F.) C6-374
- King (P.J.).- The effect of lattice strains on the acoustic relaxation losses in dielectric crystals due to magnetic ions..... C6-456
- King (P.J.).- See Hamdache (M.) C6-664
- Kirch (S.J.).- See Dietsche (W.) C6-447
- Klemens (P.G.).- Theory of the attenuation of elastic waves in inhomogeneous solids..... C6-102
- Klemens (P.G.).- See Erite-Orta (R.)..... C6-256
- Klein (M.V.).- Raman scattering from anomalous phonons in transition metals and compounds..... C6-368
- Klein (M.V.).- See Colvard (C.) C6-631
- Klein (M.V.).- See Merlin (R.). C6-392
- Klein (M.V.).- See Wada (N.)... C6-350
- Klein (P.B.).- See Stron (U.)... C6-36

- Klitsner (T.), Raychaudhuri (A.K.) and Pohl (R.O.).- Connection between the low temperature thermal properties of glasses and their glass transition temperature C6-66
- Kneezel (G.A.) and Granato (A.V.).- Phonon-Dislocation dipole interaction in Li F at low temperature..... C6-250
- Kohli (M.).- See Prohofsky (E.W.)..... C6-560
- Kojima (S.) and Nakamura (T.).- Raman scattering study of low frequency phonon polaritons in several crystals.... C6-767
- Kojima (S.).- See Nakamura (T.) C6-418
- Kolesnikov (A.I.).- See Bokhenkov (E.L.)..... C6-566
- Kolesnikov (A.I.).- See Bokhenkov (E.L.)..... C6-605
- Kress (W.), Bils (H.), Güntherodt (G.) and Jayaraman (A.).- Phonons in mixed valence compounds..... C6-3
- Kress (W.).- See Kugel (G.E.).. C6-884
- Krishnamurthy (N.) and Kasavamsy (K.).- Phonon dispersions in calcium tungstate..... C6-908
- Krivenko (T.A.).- See Bokhenkov (E.L.)..... C6-566
- Krivenko (T.A.).- See Bokhenkov (E.L.)..... C6-605
- Kshirsagar (S.T.) and Lannin (J.J.).- Raman scattering in anneal stable amorphous silicon..... C6-54
- Kuchte (B.) and Lotz (T.).- Harmonic and anharmonic representation of librational motions in molecular crystals..... C6-587
- Kudrall (S.S.).- See Gledhill (G.A.)..... C6-685
- Kugel (G.E.), Carabatos (C.) and Kress (W.).- Lattice dynamics of cuprite ( $\text{Cu}_2\text{O}$ )..... C6-884
- Kugel (G.E.).- See Fontana (M.D.) C6-749
- Kunc (K.) and Martin (R.M.).- Ab initio force constants of germanium..... C6-649
- Kunc (K.).- See Pollian (A.)... C6-295
- Kuroda (N.), Hashimoto (S.) and Mishina (Y.).- Spectroscopic ionicity and lattice instability in III-IV layer compounds..... C6-788
- Kuroda (N.) and Mishina (Y.).- Two-exciton process resonant Raman scattering in InSe.... C6-332
- Kurokawa (H.).- See Hattori (T.) C6-920
- Kuzmany (H.).- See Carlone (C.) C6-323
- Laermans (C.).- See De Goffr (A.M.)..... C6-78
- Lagnier (R.).- See Bonjour (E.)..... C6-63
- Landwehr (G.).- See Brunel (L.C.)..... C6-412
- de Lange (C.).- See Janssen (T.)..... C6-737
- Lannin (J.S.).- See Carroll (P.J.)..... C6-643
- Lannin (J.S.).- See Compf (F.). C6-27
- Lannin (J.S.).- See Kshirsagar (S.T.)..... C6-54
- Lasjaunias (J.C.).- See Bethoux (O.)..... C6-60
- Lassmann (K.).- See De Goffr (A.M.)..... C6-235
- Läuger (K.).- See Strübel (B.). C6-404
- Leuter (H.J.).- See Batallan (F.)..... C6-344
- Lax (M.), Narayanaswamy (V.), Hu (P.) and Weber (W.).- Lifetime of high frequency phonons..... C6-161
- Lee (H.C.).- See Compagn (A.)... C6-453
- Lefebvre (J.).- See Chaplot (D.L.)..... C6-584



- Lefebvre (J.).- See Copley  
(J.R.D.)..... C6-386
- Legrand (S.).- See Petitgrand  
(D.)..... C6-782
- Lehner (N.).- See Geick (R.)... C6-713
- Leisure (R.G.).- See Prieur  
(J.-Y.)..... C6-33
- Lengfellner (H.) and Renk  
(K.F.).- Detection of acoustic  
zone-boundary phonons by  
phonon difference absorption C6-259
- Leung (W.N.).- See Ball (M.A.). C6-911
- Levelut (A.).- See Arnold (W.). C6-37
- Levelut (A.).- See Prieur  
(J.-Y.)..... C6-33
- Lipson (H.G.).- See Bendow (R.) C6-140
- Livage (J.).- See Deville (A.). C6-465
- Livescu (G.).- See Braiman (O.) C6-96
- Lo (H.W.).- See Compaan (A.)... C6-453
- Locatelli (M.), Suchail (R.) and  
Zecchi (E.).- A study of the  
Pb precipitation in NaCl from  
thermal conductivity  
experiments..... C6-893
- Locatelli (M.).- See de Goeër  
(A.M.)..... C6-78
- Locatelli (M.).- See de Goeër  
(A.M.)..... C6-235
- Locatelli (M.).- See de Goeër  
(A.M.)..... C6-265
- Locatelli (M.).- See Khoder  
(A.F.)..... C6-383
- Locatelli (M.).- See Randane  
(A.)..... C6-244
- Lockwood (D.J.) and Coombs  
(G.J.).- A Raman study of the  
structural phase transition  
in disordered  $\text{KMnO}_3$ ,  $\text{MnO}_2$ ,  $\text{FeF}_2$  C6-761
- Lockwood (D.J.).- See Johnston  
(S.W.)..... C6-90
- Lorenz (H.).- See Sah  
(G.T.)..... C6-371
- v.Löhneysen (H.), Schink (H.J.),  
Arnold (W.), Bayeler (H.U.),  
Pietronero (L.), Strässler  
(S.).- Low-temperature spe-  
cific heat anomaly of the  
one-dimensional ionic con-  
ductor hollandite..... C6-193
- Lu (K.C.).- See Prohovsky  
(E.W.)..... C6-560
- Ludwig (W.).- See Falter (C.). C6-516
- Lüscher (E.).- See Fritsch (G.) C6-143
- Luty (T.).- Translational-  
rotational coupling in s-  
triazine crystal..... C6-590
- Luty (T.).- See Chaplot (S.L.) C6-584
- Luty (T.).- See Kuchta (B.)... C6-587
- Maciel (A.) and Ryan (J.F.).-  
Lock-in type phase transition  
in  $\text{KFeF}_4$ ..... C6-716
- Maciel (A.) and Ryan (J.F.).-  
Observation of coupled ampli-  
tude modes in the Raman spec-  
trum of incommensurate  
 $\gamma\text{-Na}_2\text{Co}_3$ ..... C6-725
- Madore (G.).- See Cheeks  
(J.D.N.)..... C6-569
- Magerl (A.) and Zabel (H.).-  
Lattice dynamics of graphite  
intercalation compound-mo-  
delled by the phonon dis-  
persion of linear chains... C6-329
- Magerl (A.).- See Zabel (H.)... C6-289
- Mahan (G.D.).- See Tam (P.F.). C6-122
- Maier (J.) and Sigwalt (R.).- The  
influence of the dynamical  
Jahn-Teller effect of  
acceptors onto the phonon-  
transport mechanism in  
cubic semiconductors..... C6-232
- Maisano (G.), Migliardo (P.)  
Wanderlingh (P.), Fontana  
(M.P.), Bellissent-Funel  
(M.-C.) and Roth (H.).-  
Local order and dynamics in  
liquid electrolytes : small  
angle neutron scattering... C6-51
- Maisano (G.).- See Aliotta  
(P.)..... C6-37

- Maradudin (A.A.), Martin (A.J.),  
Bils (H.) and Wallis (R.F.).-  
Non-linear dynamical  
excitation..... C6-137
- Maradudin (A.A.).- See Shen  
(T.J.)..... C6-819
- Maradudin (A.A.).- See Suzuki  
(Z.)..... C6-640
- Mariotto (G.).- See Caszanelli  
(E.)..... C6-776
- Mariotto (G.).- See Caszanelli  
(E.)..... C6-190
- Mariotto (G.).- See Mazzacurati  
(V.)..... C6-196
- Marole (S.).- See Thiry (P.)... C6-843
- Marshall (R.C.).- See Bandow  
(B.)..... C6-140
- Martin (A.J.).- See Maradudin  
(A.A.)..... C6-137
- Martin (D.J.) and Walker (R.P.).-  
How much information can low  
energy ion scattering give  
about surface phonons ?..... C6-807
- Martin (R.M.).- Recent advances  
in the theory of phonons in  
semiconductors..... C6-617
- Martin (R.M.).- See Kunc (K.).. C6-649
- Martinez (G.).- See Petritis  
(D.)..... C6-688
- Marvin (A.).- See Bortolani  
(V.)..... C6-804
- Massa (N.E.).- Raman scattering  
spectra of  $\text{Nb}_2\text{ZnCl}_4$  under  
uniaxial stress..... C6-593
- Massot (H.).- See Brunel  
(L.C.)..... C6-412
- Mathieu (H.).- See Camassel  
(J.)..... C6-682
- Mathieu (H.).- See Pascual  
(J.)..... C6-719
- Maurer (B.).- See Miller (V.).. C6-389
- Mazzacurati (V.), Ruocco (G.),  
Signorelli (G.), Caszanelli  
(E.), Fontana (A.) and  
Mariotto (G.).- A theoretical  
model for the continuous  
order-disorder transition at  
703 K in superionic  $\alpha\text{-AgI}$ ... C6-196
- Mei (M.N.).- See Prohovsky  
(E.W.)..... C6-560
- Melo (F.E.A.).- See Cerdeira  
(F.)..... C6-722
- Meltzer (R.S.).- See Sox  
(D.J.)..... C6-450
- Menn (K.) and Biem (W.).-  
Coherent potential approxi-  
mation and strongly anhar-  
monic systems : crystals of  
para-hydrogen and neon resp.  
hydrogen atoms..... C6-87
- Menon (M.).- See Arnold (G.B.). C6-377
- Meredith (D.J.), Pritchard  
(J.A.) and Wignore (J.K.).-  
Backward wave phonon echoes  
at 17 GHz in single crystals  
of  $\text{LiTaO}_3$ ,  $\text{LiNbO}_3$  and  
 $\text{Bi}_{12}\text{SiO}_{20}$ ..... C6-870
- Merian (M.) and Etchepare (J.).-  
A calculation of the phonon  
dispersion curves in trigonal  
and monoclinic selenium  
with the help of a single  
vibrational potential..... C6-608
- Merlin (R.).- See Colvard (C.). C6-631
- Merle (P.).- See Camassel (J.). C6-682
- Merle (P.).- See Pascual (J.).. C6-719
- Merlin (R.), Dierker (S.B.),  
Klein (M.V.), Jørgensen (J.),  
Mamussen (S.R.), Fisk (Z.)  
and Webb (G.W.).- Raman  
scattering in  $\text{V}_3\text{Si}$ ,  $\text{V}_3\text{Ge}$ ,  
 $\text{Nb}_3\text{Sb}$  and  $\text{Cr}_3\text{Si}$  : correlation  
of  $E_g$  optical phonon line-  
width with magnetic suscep-  
tibility..... C6-392
- Michard (F.).- See Durán (B.). C6-131
- Mietzajewski (A.).- See Chaplet  
(S.L.)..... C6-584
- Migliardo (P.).- See Abbotte  
(P.)..... C6-57

- |  |        |  |        |
|--|--------|--|--------|
| Migliardo (P.).- See Maisano (G.).....   | C6-51  | Moussa (F.).- See Cailleau (H.)  | C6-704 |
| Mitra (S.S.).- See Banerjee (P.K.).....  | C6-75  | Moynihan (C.T.).- See Banerjee (P.K.).....   | C6-75  |
| Mitra (S.S.).- See Bendow (B.).  | C6-140 | Mulazzi (E.), Tubino (R.) and Dellepiane (G.).- On the origin of the red shift of Raman excitation profile from the absorption spectrum  | C6-493 |
| Mitsubishi (A.).- See Hattori (T.).....  | C6-920 | Mulazzi (E.).- See Barchielli (A.).....  | C6-475 |
| Miura (K.).- See Yagi (T.).....  | C6-731 | Müller (V.), Schanz (G.), Unterhorst (E.J.) and Maurer (D.).- Nuclear acoustic resonance investigations of the longitudinal and transverse electron lattice interaction in transition metals and alloys..... | C6-389 |
| Miyajima (H.).- See Sato (M.)..  | C6-770 | Müller (V.).- See Strübel (B.).  | C6-404 |
| Miyasato (T.), Tokumura (M.) and Akao (F.).- Effect of magnetic field on ballistic heat-pulse scattering in n-type germanium.....                | C6-658 | Muramatsu (A.) and Hanke (W.).- Microscopic theory of lattice dynamics and reconstruction of semiconductor surfaces.....   | C6-834 |
| Miyazaki (H.) and Horie (C.).- Effect of electron-phonon interaction on Raman spectra of graphite intercalation compounds.....                   | C6-335 | Murase (K.).- See Sugai (S.)...  | C6-740 |
| Miyazaki (H.).- See Horie (C.).  | C6-298 | Murase (K.).- See Sugai (S.)...  | C6-320 |
| Mokross (B.).- See Bussmann-Holder (A.).....   | C6-409 | Murase (K.).- See Sugai (S.)...  | C6-728 |
| Monnier (R.).- See Celio (M.)..  | C6-11  | Murphy (D.T.).- See Hamdache (M.).....   | C6-664 |
| Montambaux (G.).- See Heritier (M.).....   | C6-534 | Mutsheller (W.).- See Wagner (M.).....   | C6-238 |
| Moore (D.R.), Tekippe (V.J.), Rendas (A.K.) and Toledano (J.C.).- A Raman scattering study of the solid to solid phase transition in benzil..... | C6-785 | Nakamura (T.), Kojima (S.), Jang (M.S.), Takashige (M.) and Itoh (S.).- $E(x)-A_1(z)$ oblique phonons in tetragonal $BaTiO_3$ .....  | C6-418 |
| Morhange (J.F.).- See Kanellis (G.).....   | C6-341 | Nakamura (T.), Takashige (M.) and Aikawa (Y.).- Raman scattering from amorphous state of ferroelectric $PbTiO_3$ and its change in the crystallization process.....  | C6-421 |
| Morissseau (P.).- See Poirier (M.).....  | C6-876 | Nakamura (T.).- See Kojima (S.)  | C6-767 |
| Mörke (I.) and Wichter (P.).- Phonon softening in intermediate valent $Su_2$ .....   | C6-14  | Narayanamurti (V.).- Transport of high energy phonons.....   | C6-221 |
| Motizuki (K.), Yoshida (Y.) and Takasaka (Y.).- Role of phonons in structural phase transitions of transition metal dichalcogenides.....         | C6-773 | Narayanamurti (V.).- See Lax (M.).....   | C6-161 |
| Mountfield (R.R.) and Rayne (J.A.).- Elastic moduli of linear antiferromagnet $CuNiCl_2$ .....   | C6-468 |  |        |

- Narayanamurti (V.).- See Ulbrich (R.G.)..... C6-226
- Natkaniec (I.).- See Bielushkin (A.V.)..... C6-34
- Natkaniec (I.).- See Bokhenkov (E.L.)..... C6-605
- Natkaniec (I.).- See Dorner (B.) C6-602
- Natkaniec (I.).- See Wasiutynski (T.)..... C6-599
- Nava (R.) and Rodriguez (M.).- Frequency dependence of acoustic saturation in smoky quartz.. C6-99
- Nemanich (R.J.) and Tsai (C.C.).- Phonons of the metal/amorphous silicon interface studied by interference enhanced Raman scattering..... C6-822
- Nerenberg (M.A.H.).- See Jacobs (P.W.M.)..... C6-914
- Newman (R.C.).- See Gladhill (G.A.)..... C6-685
- Nicolau (I.F.).- See de Goër (A.M.)..... C6-265
- Nielsen (O.H.).- Vibrations of substitutional impurities in semiconductors..... C6-673
- Nishina (Y.).- See Kuroda (N.) C6-332
- Nishina (Y.).- See Kuroda (N.) C6-788
- Nishina (Y.).- See Sasaki (Y.) C6-557
- Nizzoli (F.).- See Bortolani (V.)..... C6-804
- Nizzoli (F.).- See Bortolani (V.)..... C6-831
- Northrop (G.A.), Dietache (W.) Zdzis (A.D.) and Wolfe (J.P.).- Processing of dispersive phonons in Ge..... C6-209
- Nücker (N.).- See Yeh (C.T.).. C6-371
- Ruñez-Reguero (M.).- See Ayache (C.)..... C6-338
- Rasser (H.-K.).- See Wagner (M.) C6-238
- Oka (Y.) and Cardona (M.).- Raman scattering study of correlation between phonons and electron spins in CdS and ZnTe under resonance condition..... C6-459
- Olego (D.), Cardona (M.) and Vogl (P.).- Volume and temperature dependence of the transverse charge and the ionicity of tetrahedral semiconductors..... C6-652
- Onwuagba (B.N.) and Animalu (A.O.E.).- Screening of the short-range potential by the local field correction in the lattice dynamics of vanadium..... C6-401
- Padmanabhan (V.M.).- See Rao (K.R.)..... C6-637
- Page (J.H.).- See Frisken (B.) C6-858
- Page (J.B.).- See Schröder (U.)..... C6-496
- Parrinello (M.) and Rahman (A.).- Polymorphic transitions in alkali halides. A molecular dynamics study.. C6-511
- Pascoli (G.).- See Toledano (P.)..... C6-746
- Pascual (J.), Camassel (J.), Merle (P.) and Mathieu (H.).- Gruneisen parameter and deformation potentials of Raman active modes in rutile structure compounds..... C6-719
- Pascual (J.).- See Camassel (J.) C6-682
- Patel (M.B.) and Bist (H.D.).- Librational modes of water in crystal hydrates and phase-transitions..... C6-917
- Pawley (G.S.).- See Chaplot (S.L.)..... C6-584
- Pauley (G.S.).- See Dorner (B.) C6-602
- Pelous (J.).- See Vacher (R.).. C6-125
- Perrin (B.) and Michard (F.).- Phonon-phonon interactions in molecular crystals studied by ultrasonic methods..... C6-131

- Perrin (B.).- See Boissier (M.). C6-611
- Petitgrand (D.), Hennion (B.), Escribe-Filippini (C.) and Legrand (S.).- Phonon dispersion and transverse mode softening in  $\text{RbFeCl}_3$ ..... C6-782
- Petritis (D.), Deville Cavellin (C.) and Martinez (G.).- Resonant enhancement of the Raman linewidth of phonon modes induced by hydrostatic pressure..... C6-688
- Philip (J.).- See Breazeale (M.A.)..... C6-134
- Pick (R.M.).- See Poulet (H.).. C6-701
- Pietronero (L.).- See v.Lönnheysen (H.)..... C6-193
- Pinczuk (A.).- See Fishman (G.) C6-305
- Pintschovius (L.), Vergès (J.A.) and Cardona (M.).- Self-energy of phonons interacting with free carriers in silicon..... C6-634
- Pireaux (J.J.).- See Thiry (P.) C6-843
- Pohl (R.O.).- See Klitsner (T.) C6-66
- Poirier (M.), Cheeke (J.D.N.), Morisseau (P.) and Hikata (A.).- Attenuation of a static polarization echo by  $^4\text{He}$  film..... C6-876
- Pollian (A.), Kunc (K.) and Rossat-Mignod (J.).- Inelastic neutron scattering and lattice dynamics of the layer semiconductor  $\text{GaS}$ .... C6-295
- Pollini (I.).- See Benedek (G.) C6-301
- Poulet (H.) and Pick (R.M.).- Are phasons in biphenyl detectable by light scattering ?..... C6-701
- Prasad (P.N.).- Dynamics of phonon interactions inorganic solids..... C6-563
- Prieur (J.-Y.), Doussineau (P.), Frenois (C.), Levelut (A.) and Leisire (R.G.).- Low-temperature acoustical properties of  $\text{Mn}$  doped  $\beta\text{-Al}_2\text{O}_3$ ..... C6-33
- Prieur (J.-Y.).- See Ciplys (D.)..... C6-184
- Pritchard (J.A.).- See Meredith (D.J.)..... C6-870
- Prohofsky (E.W.), Van Zandt (L.L.), Kohli (M.), Lu (K.C.), Mei (M.N.) and Putman (B.).- Phonons in the DNA double helix..... C6-560
- Pushkarev (V.V.).- See Dorner (B.)..... C6-365
- Putman (B.).- See Prohofsky (E.W.)..... C6-560
- Pynn (R.).- See Dorner (B.).... C6-365
- Radhakrishnan (V.).- See Sharma (P.C.)..... C6-268
- Rahman (A.).- See Parrinello (M.)..... C6-511
- Ramachandran (K.) and Haridasan (T.M.).- The localized modes due to phosphorous defects in cadmium telluride..... C6-679
- Ramdane (A.), Salce (B.), Challis (L.J.) and Locatelli (M.).- Phonon scattering by Cr ions in  $\text{GaAs}$  and the effect of uniaxial stress.. C6-244
- Ramas (A.K.) and Rodriguez (S.).- Time reversal symmetry and the Raman scattering by crystals..... C6-887
- Ramas (A.K.).- See Moore (D.R.)..... C6-785
- Ramos (J.G.).- See Cancelli (L.S.G.)..... C6-581
- Rampton (V.W.).- See Handache (M.)..... C6-664
- Rao (K.R.), Padmanabhan (V.M.), Vijayaraghavan (P.R.) and Chaplot (S.L.).- Neutron, X-ray and lattice dynamical studies of  $\text{Sb}_2\text{S}_3$ ..... C6-637
- Rasmussen (S.R.).- See Marlin (R.)..... C6-392
- Rauh (H.).- See Geick (R.)..... C6-713
- Ravex (A.).- See Bethoux (O.)... C6-60

- Raychaudhuri (A.K.)-- See Klitsner (T.)..... C6-66
- Rayne (J.A.)-- See Mountfield (K.R.)..... C6-468
- Rebane (L.A.) and Rebane (K.K.)-- Phonons in resonant secondary emission of impurity molecules in crystals..... C6-505
- Rebane (K.K.)-- See Rebane (L.A.) C6-505
- Rebane (K.)-- See Saari (P.).... C6-502
- Reichardt (W.)-- See Yeh (C.T.) C6-371
- Reiger (R.)-- See Schröder (U.) C6-496
- Renk (K.F.)-- Voir Baumgartner (R.)..... C6-119
- Renk (K.F.)-- See Lengfellner (H.)..... C6-259
- Renker (B.)-- See Gompf (F.)... C6-49
- Renker (B.)-- See Yeh (C.T.)... C6-371
- Renucci (J.B.)-- See Carles (R.)..... C6-105
- Renucci (M.A.)-- See Carles (R.)..... C6-105
- Resta (R.) and Baldereschi (A.)-- Local-field effects and zone-center phonons in polar and covalent cubic semiconductors..... C6-661
- Rives (J.E.)-- See Sox (D.J.).. C6-450
- Rocca (F.)-- See Cassanelli (E.) C6-190
- Rocca (F.)-- See Cassanelli (E.) C6-776
- Rodriguez (H.)-- See Nava (R.).. C6-99
- Rodriguez (S.)-- See Ramdas (A.K.)..... C6-887
- Rogers (S.J.), Shaw (C.J.) and Wiederick (H.D.)-- Limitations on the usefulness of metallic thin film semiconductors for phonon detection..... C6-317
- Rosenman (I.)-- See Batallan (F.)..... C6-344
- Rossat-Mignod (J.)-- See Pollian (A.)..... C6-295
- Roth (M.)-- See Maisano (G.)... C6-51
- Roy (A.P.)-- See Bansal (M.L.).. C6-902
- Roy (K.P.)-- See Sharma (P.C.).. C6-268
- Rumyantsev (A.Yu.)-- See Dorner (B.)..... C6-365
- Ruocco (G.)-- See Mazzacurati (V.)..... C6-196
- Ryan (J.F.)-- See Maciel (A.).. C6-716
- Ryan (J.F.)-- See Maciel (A.).. C6-725
- Rynee (T.M.)-- See Spector (H.N.) C6-670
- Saari (P.) and Rebane (K.)-- Phonon relaxation in crystals studied by hot luminescence. C6-502
- Sahni (V.C.)-- On the possible use of optical rotation measurements for detecting weakly IR active modes..... C6-881
- Sahni (V.C.)-- See Bansal (M.L.) C6-902
- Saint-Cricq (N.)-- See Carles (R.)..... C6-105
- Salce (B.), De Goër (A.M.) and Boatner (L.A.)-- Study of "pure"  $\text{KTaO}_3$  and KTN single crystals by thermal conductivity measurement down to 50 mK..... C6-424
- Salce (B.)-- See Bonjour (E.).. C6-63
- Salce (B.)-- See Daudin (B.)... C6-277
- Salce (B.)-- See Randane (A.).. C6-244
- Samsur (Sk.)-- See Behera (S.N.)..... C6-528
- Sanquer (M.)-- See Ecolivet (C.) C6-779
- Santoro (G.)-- See Bortolani (V.)..... C6-804
- Santoro (G.)-- See Bortolani (V.)..... C6-831
- Santoro (G.)-- See Fasolino (A.) C6-840
- Santoro (G.)-- See Fasolino (A.) C6-846

- Sapriel (J.).- See Jusserand (B.)..... C6-43
- Sasaki (Y.) and Nishina (Y.).- Vibrational spectra of solid and liquid sulfur..... C6-557
- Sasaki (W.), Sasaki (Y.), Ushioda (S.) and Taylor (W.).- Low frequency light scattering spectra of AgI..... C6-181
- Sasaki (Y.).- See Sasaki (W.).. C6-181
- Sato (M.), Grier (B.H.), Shapiro (S.M.) and Miyajima (R.).- Soft phonons and magnetic ordering in the  $\gamma$ -phase transition metal alloys  $\text{Fe}_{1-x}\text{Pd}_x$ ..... C6-770
- Schaack (G.).- See Gerlinger (H.) C6-499
- Schaich (W.L.).- See Schwartz (C.)..... C6-828
- Schanz (G.).- See Müller (V.).. C6-389
- Schink (H.J.).- See v. Löhneysen (H.)..... C6-193
- Schmeltzer (D.) and Beserman (R.).- Anharmonic interaction in zinc selenide..... C6-158
- Schmeltzer (D.) and Beserman (R.).- Renormalization group method for vibrational behavior in mixed crystals..... C6-84
- Schmeltzer (D.).- See Suzuki (K.) C6-640
- Schmeltzer (D.).- See Teicher (M.)..... C6-46
- Schmelzer (U.).- See Dorner (B.)..... C6-602
- Schmidt (H.J.).- See Gompf (F.) C6-49
- Schneck (J.), Toledano (J.C.), Aubree (J.), Joukoff (B.) and Joffrin (C.).- Soft phonon valley near the transition to an incommensurate phase in barium sodium niobate.... C6-734
- Schober (H.R.).- See Buchenau (U.)..... C6-395
- Schröder (U.), Weiss (M.), Reiger (R.) and Page (J.B.).- Generalization of Fröhlich's operator for the electron-phonon coupling in polar crystals..... C6-496
- Schröder (U.).- See Bauernfeind (W.)..... C6-247
- Schröder (U.).- See Strauch (D.)..... C6-707
- Schwartz (C.) and Schaich (W.L.).- Phonons at metal surfaces..... C6-828
- Selmke (M.).- See Falter (C.).. C6-516
- Senateur (J.P.).- See Khoder (A.F.)..... C6-383
- Servoin (J.L.).- See Gervais (F.)..... C6-415
- Shapiro (S.M.).- See Sato (M.). C6-770
- Sharma (P.C.), Roy (K.P.) and Radhakrishnan (V.).- The effect of non-metal-metal transition due to doping on lattice thermal conductivity : applications to Ge-doped InSb..... C6-268
- Shaw (C.J.).- See Rogers (S.J.) C6-317
- Shaw (P.B.).- See Young (E.W.). C6-522
- Sheard (F.W.).- Spin-lattice interaction in cerium ethylsulphate..... C6-596
- Sheka (E.F.).- See Bielushkin (A.V.)..... C6-34
- Sheka (E.F.).- See Bokhenkov (E.L.)..... C6-566
- Sheka (E.F.).- See Bokhenkov (E.L.)..... C6-605
- Sheka (E.F.).- See Dorner (B.). C6-602
- Shekhtman (V.L.).- See Kaplyanskii (A.A.)..... C6-439
- Shekhtman (V.L.).- See Kaplyanskii (A.A.)..... C6-462

- Shen (T.J.), Castiel (D.) and Maradudin (A.A.).- Effect of surface roughness on the Kapitza resistance..... C6-819
- Shiren (N.S.).- Surface roughness Kapitza conductance : dependence on material properties and phonon frequency..... C6-816
- Sigmund (E.).- See Maier (J.).. C6-232
- Signorelli (G.).- See Mazzacurati (V.)..... C6-196
- Singh (T.J.) and Verma (G.S.).- Four-Phonon processes in solids..... C6-155
- Simon (C.).- See Batallan (F.). C6-344
- Simons (A.L.).- See Hensel (J.C.)..... C6-212
- Sinvani (M.).- See Taborek (P.) C6-852
- Sinvani (M.).- See Taborek (P.) C6-855
- Sinvani (M.).- See Taborek (P.) C6-825
- Sladek (R.J.).- See Chao (M.H.) C6-667
- Sladek (R.J.).- See Wu (A.Y.).. C6-646
- Smith (S.H.).- See Daudin (B.). C6-277
- Solin (S.A.).- Phonons in graphite intercalation compounds C6-283
- Solin (S.A.).- See Hwang (D.M.) C6-347
- Solin (S.A.).- See Kamitakahara (W.A.)..... C6-311
- Sood (A.K.), Arora (A.K.), Dattagupta (S.) and Venkataraman (G.).- Orientational dynamics of sulphate ions in potash alum..... C6-572
- Sood (A.K.).- See Umadevi (V.). C6-81
- Sox (D.J.), Rives (J.E.) and Maltzer (R.S.).- Stimulated emission of tunable high frequency phonons in  $\text{LaF}_3:\text{Er}^{3+}$ . C6-450
- Spector (H.N.).- Parametric amplification of microwave phonons in semiconductors... C6-676
- Spector (H.N.) and Rynee (T.M.).- Phonon assisted transitions in the free carrier absorption of semiconductors in quantizing magnetic fields..... C6-670
- Srivastava (G.P.).- Phonon conductivity due to non-diagonal energy-flux operator..... C6-253
- Srivastava (G.P.).- Role of thermal expansion in the phonon conductivity of solids..... C6-149
- Stirling (W.G.).- See Geick (R.)..... C6-713
- Stolz (H.J.).- See Carlone (C.). C6-323
- Stürmer (H.L.).- See Fishman (G.) C6-305
- Strässler (S.).- See v.Löhneysen (H.)..... C6-193
- Strauch (D.) and Schröder (U.).- On the mode softening in  $\text{SnTe}$  and  $\text{PbTe}$ ..... C6-707
- Strübel (B.), Lügner (K.), Bümmel (H.E.) and Müller (V.).- The ultrasound-induced electric field gradient (EFG) in metals..... C6-404
- Strom (U.), Klein (P.B.), Weiser (K.) and Wolf (S.A.).- Time-resolved phonon spectroscopy of amorphous  $\text{As}_2\text{S}_3$ ..... C6-30
- Suchail (R.).- See Locatelli (M.) C6-893
- Sugai (S.), Murase (K.), Uchida (S.) and Tanaka (S.).- Investigation of the charge density waves in  $\text{1T-VSe}_2$  by Raman scattering..... C6-740
- Sugai (S.), Murase (K.), Uchida (S.) and Tanaka (S.).- Investigation of the charge density waves in  $\text{2H-TaSe}_2$  by one and two phonons Raman scattering..... C6-728
- Sugai (S.), Ueda (T.) and Murase (K.).- Raman scattering in  $\text{MoS}_2$ ,  $\text{MoSe}_2$ , and  $\alpha\text{-MoTe}_2$  at high pressures..... C6-520



- Suski (T.) and Katayama (S.).- Phonon induced anomalous resistivity in structural phase transition of  $\text{PbSnTe}$ ... C6-758
- Suzuki (K.), Schmeltzer (D.) and Maradudin (A.A.).- Vibrational properties of vacancies in homopolar semiconductors..... C6-640
- Suzuki (H.).- See Iwasa (I.).. C6-896
- Taborek (P.), Sinvani (M.), Weimer (M.) and Goodstein (D.).- Film thickness dependence of heat transmission into helium..... C6-825
- Taborek (P.), Sinvani (M.), Weimer (M.) and Goodstein (D.).- Polarization dependence of phonon induced desorption of He atoms at low temperatures..... C6-855
- Taborek (P.), Sinvani (M.), Weimer (M.) and Goodstein (D.).- Time constant for phonon induced desorption of Helium..... C6-852
- Takaoka (Y.).- See Motizuki (K.)..... C6-773
- Takashige (M.).- See Nakamura (T.)..... C6-418
- Takashige (M.).- See Nakamura (T.)..... C6-421
- Talwar (D.N.).- See Zigone (M.)..... C6-743
- Tanaka (S.).- See Sugai (S.).. C6-728
- Tanaka (S.).- See Sugai (S.).. C6-740
- Tatarek (R.).- See Cantini (P.) C6-801
- Taylor (W.).- See Sasaki (W.). C6-181
- Teicher (M.), Schmeltzer (D.) and Beserman (R.).- Phonon-line-shape and disorder correlation in mixed  $\text{GaP}_{1-x}\text{As}_x$ ..... C6-46
- Tekippe (V.J.).- See Moore (D.R.)..... C6-785
- Teuchert (W.D.).- See Copley (J.R.D.)..... C6-386
- Thiry (P.), Maroie (S.), Pireaux (J.J.), Caudano (R.) and Adnot (A.).- Adsorbate induced vibrations measured by EELS on a  $\text{CuZn}$   $\alpha$  75/25 (110) surface during its early stage of oxidation C6-843
- Thorpe (M.F.).- Phonons in amorphous materials..... C6-19
- Throe (J.) and Bron (W.E.).- Mode conversion coefficients of acoustic waves at a crystal-vacuum interface.... C6-849
- Toennies (J.P.).- See Banadek (G.)..... C6-793
- Tokumura (M.).- See Miyasato (T.)..... C6-658
- Toledano (P.), Pascoli (G.) and Coiret (M.).- Simultaneous condensation of several modes at structural phase transitions..... C6-746
- Toledano (J.C.).- See Moore (D.R.)..... C6-785
- Toledano (J.C.).- See Schneck (J.)..... C6-734
- Tosatti (E.).- See Fasolino (A.)..... C6-840
- Tosatti (E.).- See Fasolino (A.)..... C6-846
- Toudic (B.).- See Ecolivet (C.) C6-779
- Tsai (C.C.).- See Nemanich (R.J.) C6-822
- Tsui (D.C.).- See Hensel (J.C.). C6-308
- Tsuruoka (F.) and Kajimura (K.).- Static polarization echoes in metal powders..... C6-864
- Tea (P.F.) and Mahan (G.D.).- Anharmonicity effects in  $\text{CaF}_2$  at low temperature..... C6-122
- Tubino (R.).- See Mulazzi (E.).. C6-493
- Tucker (J.W.).- Phonon scattering at frequencies near the exciton frequency of two-level defects C6-478
- Uchida (S.).- See Sugai (S.).... C6-740
- Uchida (S.).- See Sugai (S.).... C6-728

- Ueda (T.).- See Sugai (S.)..... C6-320
- Ulbrich (R.G.), Narayanamurti (V.) and Chin (M.A.).- Ballistic transport and decay of near zone-edge non-thermal phonons in semiconductors..... C6-226
- Umadevi (V.), Kesavameorthy (R.), Sood (A.K.) and Venkataraman (G.).- Surface polaritons in irradiated  $\alpha$ -quartz..... C6-81
- Umarov (B.S.).- See Anikiev (A.A.)..... C6-152
- Umarov (M.).- See Gorelik (V.S.) C6-764
- Umarov (B.S.).- See Gorelik (V.S.)..... C6-764
- Unterhorst (E.J.).- See Müller (V.)..... C6-389
- Unterwald (F.C.).- See Hensel (J.C.)..... C6-212
- Ushioda (S.).- See Sasaki (W.).. C6-181
- Vacher (R.) and Palous (J.).- Phonon damping in crystalline and amorphous solids at hypersonic frequencies..... C6-125
- Vacher (R.).- See Boissier (M.). C6-611
- Vallera (A.M.).- High temperature phonons in iron..... C6-398
- Van Camp (P.E.), Van Doren (V.E.) and Devraese (J.T.).- First principles calculation of the phonon spectra of solids..... C6-625
- Vandevyver (M.).- See Zigone (M.)..... C6-743
- Van Doren (V.E.).- See Van Camp (P.E.)..... C6-625
- Van Zandt (L.L.).- See Prohovsky (E.W.)..... C6-340
- Vasi (C.).- See Aliotta (F.).... C6-57
- Venkataraman (G.).- Phonons in molecular crystals..... C6-549
- Venkataraman (G.).- See Sood (A.K.)..... C6-572
- Venkataraman (G.).- See Umadevi (V.)..... C6-81
- Vergés (J.A.).- See Pintschovius (L.)..... C6-634
- Verma (G.S.).- See Singh (T.J.) C6-155
- Vetelino (J.F.).- See Anikiev (A.A.)..... C6-152
- Vijayaraghavan (P.R.).- See Rao (K.R.)..... C6-637
- Vogl (P.).- See Olego (D.)..... C6-652
- Vogt (H.).- See Calleja (J.M.).. C6-487
- Wachter (P.).- See Celio (M.)... C6-11
- Wachter (P.).- See Mürke (I.)... C6-14
- Wada (N.), Klein (M.V.) and Zabel (H.).- Raman scattering studies of folded shearing phonons in  $KC_{12}N$  ( $n = 2 \sim 6$ )..... C6-350
- Wada (N.).- See Kamitakahara (W.A.)..... C6-311
- Wagh (A.S.).- A Microscopic transport theory of electron-phonon systems..... C6-471
- Wagner (M.), Mutscheller (W.) and Nusser (H.-K.).- Phonon and pseudo-magnon transport in cooperative Jahn-Teller systems. C6-238
- Wagner (R.).- See Buchenau (U.). C6-395
- Walker (R.P.).- See Martin (D.J.) C6-807
- Wallis (R.F.).- See Black (J.E.). C6-837
- Wallis (R.F.).- See Maradudin (A.A.)..... C6-137
- Wallis (R.F.).- See Wanser (K.H.) C6-128
- Wanderlingh (F.).- See Aliotta (F.)..... C6-57
- Wanderlingh (F.).- See Maisano (G.)..... C6-51
- Wanser (K.H.) and Wallis (R.F.).- Harmonic and anharmonic properties of silicon..... C6-128

- Wasiutynski (T.).- Self-consistent phonon calculations in solid nitrogen..... C6-575
- Wasiutynski (T.), Natkaniec (I.) and Belushkin (A.I.).- Lattice dynamics calculations for solid biphenyl in the high temperature phase..... C6-599
- Webb (W.).- See Merlin (R.)... C6-392
- Weber (W.).- See Harmon (B.N.) C6-628
- Weber (W.).- See Lax (M.)..... C6-161
- Weimer (M.).- See Taborek (P.) C6-825
- Weimer (M.).- See Taborek (P.) C6-855
- Weimer (M.).- See Taborek (P.) C6-852
- Weiser (K.).- See Strom (U.).. C6-30
- Weiss (K.).- Attenuation of second sound in solids..... C6-531
- Weiss (M.).- See Schröder (U.) C6-496
- West (A.R.).- See Almond (D.P.) C6-187
- Wiederick (H.D.).- See Rogers (S.J.)..... C6-317
- Wiegmann (W.).- See Fishman (G.)..... C6-305
- Wignore (J.K.).- See Meredith (D.J.)..... C6-870
- Wolf (S.A.).- See Strom (V.).. C6-30
- Wolfe (J.P.).- See Dietzsch (W.) C6-447
- Wolfe (J.P.).- See Greenstein (M.)..... C6-274
- Wolfe (J.P.).- See Northrop (G.A.)..... C6-209
- Wolter (J.).- See Horstman (R.E.)..... C6-813
- Won (J.W.).- See Kim (J.J.)... C6-427
- Woodhead (J.).- See Gledhill (G.A.)..... C6-685
- Worlock (J.M.).- See Fishman (G.)..... C6-305
- Wu (A.Y.) and Sladek (R.J.).- Ultrasonic phonon velocities in  $\text{Cd}_{1-x}\text{Mn}_x\text{Te}$  between 1.5 and 96 K : anomalies near the magnetic transition..... C6-646
- Wybourne (M.N.).- See Challis (L.J.)..... C6-229
- Yagi (T.), Hidaka (Y.) and Miura (K.).- Brillouin scattering study of the incommensurate (Antiferroelectric). Phase transition in sodium nitrite C6-731
- Yeh (C.T.), Reichardt (W.), Renker (B.), Nicker (N.) and Loewenhaupt (M.).- Lattice dynamics of  $\text{YAl}_2$  and  $\text{LaAl}_2$  - a further contribution to the La-Y puzzle..... C6-371
- Yoshida (Y.).- See Motizuki (K.) C6-773
- Yoshikawa (S.) and Kimura (T.).- Dipolar field fluctuation effects on phonon echoes in piezoelectric powder..... C6-873
- Young (E.W.) and Shaw (P.B.).- A strong coupled acoustic deformation polaron in one dimension..... C6-522
- Zabel (H.) and Magerl (A.).- Phonons in alkali graphite intercalation compounds..... C6-289
- Zabel (H.).- See Hardcastle (S.E.)..... C6-326
- Zabel (H.).- See Magerl (A.)... C6-329
- Zabel (H.).- See Wada (N.)..... C6-350
- Zdetsis (A.D.).- See Northrop (G.A.)..... C6-209
- Zecchi (E.).- See Loratelli (M.)..... C6-893
- Zeyher (R.) and Dandolo (R.).- Entropy of disordered solids at low temperatures ..... C6-40
- Zeyen (C.M.E.).- Improved energy resolution with neutron spin echo triple-axis spectrometers C6-543
- Zeyen (C.M.E.).- See Cailliau (H.)..... C6-704

C6-949

Zhang (G.Z.)- See Gledhill  
(G.A.)..... C6-685

Zigone (M.), Vandevyver (M.)  
and Talvar (D.N.)- Pressure  
dependence of impurity induced

Raman scattering spectra in  
ZnS crystals..... C6-743

Ziolkiewicz (M.K.)- See Brunel  
(L.C.)..... C6-412

Zwick (A.)- See Carles (R.)... C6-105

SECURITY CLASSIFICATION OF THIS PAGE (When Data Entered)

REPORT DOCUMENTATION PAGE		READ INSTRUCTIONS BEFORE COMPLETING FORM
1. REPORT NUMBER 17340.1-PH	2. SOVT ACCESSION NO. N/A	3. RECIPIENT'S CATALOG NUMBER N/A
4. TITLE (and Subtitle)  International Conference on Phonon Physics		5. TYPE OF REPORT & PERIOD COVERED FR Proceedings
		6. PERFORMING ORG. REPORT NUMBER N/A
7. AUTHOR(s) Editor: W. E. Bron		8. CONTRACT OR GRANT NUMBER(s) ARO 43-80
9. PERFORMING ORGANIZATION NAME AND ADDRESS Indiana University Bloomington, IN		10. PROGRAM ELEMENT, PROJECT, TASK AREA & WORK UNIT NUMBERS  N/A
11. CONTROLLING OFFICE NAME AND ADDRESS U. S. Army Research Office P. O. Box 12211 Research Triangle Park, NC 27709		12. REPORT DATE Dec 81
		13. NUMBER OF PAGES 949
		14. MONITORING AGENCY NAME & ADDRESS (if different from Controlling Office)
		15. SECURITY CLASS. (of this report)  Unclassified
		15a. DECLASSIFICATION/DOWNGRADING SCHEDULE
16. DISTRIBUTION STATEMENT (of this Report)  Submitted for announcement only.		
17. DISTRIBUTION STATEMENT (of the abstract entered in Block 20, if different from Report)		
18. SUPPLEMENTARY NOTES		
19. KEY WORDS (Continue on reverse side if necessary and identify by block number)		
20. ABSTRACT (Continue on reverse side if necessary and identify by block number)		

END

DATE  
FILMED

583

DT